

Konferenzbeiträge / Atti / Proceedings

Building Simulation Applications BSA 2022

5th IBPSA-Italy Conference

Bozen-Bolzano, 29th June – 1st July 2022

Edited by

Giovanni Pernigotto, Francesco Patuzzi,

Alessandro Prada, Vincenzo Corrado, Andrea Gasparella

bu,press

bozen
bolzano
university
press



Konferenzbeiträge / Atti / Proceedings

Building Simulation Applications BSA 2022

5th IBPSA-Italy Conference

Bozen-Bolzano, 29th June – 1st July 2022

Edited by

Giovanni Pernigotto, Francesco Patuzzi,

Alessandro Prada, Vincenzo Corrado, Andrea Gasparella

bu,press

bozen
bolzano
university
press

Scientific Committee

Ian Beausoleil-Morrison, Carleton University, Canada
Jan L.M. Hensen, Technische Universiteit Eindhoven, The Netherlands
Gregor P. Henze, University of Colorado Boulder, USA
Ardeshir Mahdavi, Technische Universität Wien, Austria
Athanasios Tzempelikos, Purdue University, USA
Reinhard Radermacher, University of Maryland, USA
Francesco Asdrubali, Università degli Studi Roma Tre, Italy
Paolo Baggio, Università degli Studi di Trento, Italy
Francesca Cappelletti, Università IUAV di Venezia, Italy
Maurizio Cellura, Università degli Studi di Palermo, Italy
Cristina Cornaro, Università degli Studi di Tor Vergata, Italy
Vincenzo Corrado, Politecnico di Torino, Italy
Andrea Gasparella, Free University of Bozen-Bolzano, Italy
Livio Mazzarella, Politecnico di Milano, Italy
Adolfo Palombo, Università degli Studi di Napoli Federico II, Italy

Students Tutoring Scientific Committee

Matthias Schuss, Technische Universität Wien, Austria
Ulrich Pont, Technische Universität Wien, Austria
Alessia Arteconi, Università Politecnica delle Marche, Italy
Ilaria Ballarini, Politecnico di Torino, Italy
Annamaria Buonomano, Università degli Studi di Napoli Federico II, Italy
Marco Caniato, Free University of Bozen-Bolzano, Italy
Gianpiero Evola, Università degli Studi di Catania, Italy
Federica Morandi, Free University of Bozen-Bolzano, Italy
Francesco Patuzzi, Free University of Bozen-Bolzano, Italy
Giovanni Pernigotto, Free University of Bozen-Bolzano, Italy
Anna Laura Pisello, Università degli Studi di Perugia, Italy
Alessandro Prada, Università degli Studi di Trento, Italy

Organizing Committee

Paolo Baggio, Università degli Studi di Trento, Italy
Marco Baratieri, Free University of Bozen-Bolzano, Italy
Marco Caniato, Free University of Bozen-Bolzano, Italy
Francesca Cappelletti, Università IUAV di Venezia, Italy
Vincenzo Corrado, Politecnico di Torino, Italy
Andrea Gasparella, Free University of Bozen-Bolzano, Italy
Norbert Klamsteiner, Energytech G.m.b.H./S.r.l -Bozen, Italy
Federica Morandi, Free University of Bozen-Bolzano, Italy
Francesco Patuzzi, Free University of Bozen-Bolzano, Italy
Giovanni Pernigotto, Free University of Bozen-Bolzano, Italy
Alessandro Prada, Università degli Studi di Trento, Italy
Fabio Viero, Manens – Tifs, Italy

bu,press

Bozen-Bolzano University Press, 2022

Free University of Bozen-Bolzano

www.unibz.it/universitypress

Cover design: DOC.bz / bu,press

ISSN 2531-6702

ISBN 978-88-6046-191-9

DOI 10.13124/9788860461919



This work—excluding the cover and the quotations—is licensed under the Creative Commons Attribution-ShareAlike 4.0 International License.

Table of Contents

Preface	ix
Optimization of Daylighting and Energy Performance in Bangladesh Ready-Made Garment Factories: Use of Parametric Design, Simulation Modeling, and Genetic Algorithms <i>Md Ashikur Rahman Joarder, Md Monir Hossain, Aaron J.E. Bach, Jean P. Palutikof, Fahim Tonmoy</i>	1
Transient Three-Dimensional CFD Modelling of Ceiling Fans: A Comparison Between Detailed and Simplified Models <i>Francesco Babich, Akshit Gupta, Wilmer Pasut</i>	9
Intelligibility Prediction in Scholar Classrooms <i>Samantha Di Loreto, Fabio Serpilli, Valter Lori, Costanzo Di Perna</i>	17
Hybrid Heat Pump Systems: Is Predictive Control Worth Using? <i>Patricia Ercoli, Alice Mugnini, Fabio Polonara, Alessia Arteconi</i>	25
The Acoustic Adaptation of the Aula Magna at the University of Bologna: Auditorium and Conference Hall Scenarios Simulated in the Main Nave of Santa Lucia's Church <i>Antonella Bevilacqua, Ruoran Yan, Maria Cristina Tommasino</i>	33
Implementation and Calibration of a Model to Treat Naturally Ventilated Complex Fenestration Systems in TRNSYS <i>Ingrid Demanega, Giovanni Gennaro, Giuseppe De Michele, Francesco Isaia, Fabio Favoino, Stefano Avesani</i>	41
Heat and Mass Transfer Modelling for Moisture-Related Risks in Walls Retrofitted by Timber Materials <i>Gianpiero Evola, Alessandra Urso, Vincenzo Costanzo, Francesco Nocera, Luigi Marletta</i>	49
Multi-Objective Optimization Of Thermo-Acoustic Comfort Of School Buildings <i>Daniele Colarossi, Samantha Di Loreto, Eleonora Tagliolini, Paolo Principi, Fabio Serpilli</i>	67
A Review on the FIVA-Project: Simulation-Assisted Development of Highly-Insulating Vacuum Glass Windows <i>Ulrich Pont, Peter Schober, Magdalena Wölzl, Matthias Schuss, Jakob Haberl</i>	69
Influence of Sound-Absorbing Ceiling on the Reverberation Time. Comparison Between Software and Calculation Method EN 12354-6 <i>Nicola Granzotto, Paolo Ruggeri, Fabio Peron, Marco Caniato, Andrea Gasparella</i>	77
Simulation of Thermal and Acoustic Façade Insulation Starting From the Characteristics of the Individual Elements <i>Nicola Granzotto, Paolo Ruggeri, Fabio Peron, Marco Caniato, Andrea Gasparella</i>	85
Climate Change Impact on Historical Buildings: A Case Study Within the Interreg Ita-Slo Secap Project <i>Marco Manzan, Amedeo Pezzi</i>	95
Hourly Dynamic Calculation of the Primary Energy With Heat Pump Generation System (EN 15316-4-2): A Case Study in Italy <i>Giada Remia, Serena Summa, Luca Tarabelli, Costanzo Di Perna</i>	103
A Project Focused on Sound Diffusion: The Acoustics of the Auditorium Yves St Laurent of Marrakech in Combination With its Innovative Architectural Design <i>Lamberto Tronchin, Antonella Bevilacqua, Ruoran Yan</i>	111
On the Prints of Another Horseshoe-Shaped Historical Building: Acoustic Studies of the Bonci Theatre of Cesena <i>Antonella Bevilacqua, Ruoran Yan</i>	117
Acoustic Discoveries of Another Masterpiece by Antonio Galli Bibiena: The Communal Theatre of Bologna <i>Antonella Bevilacqua, Ruoran Yan</i>	123
In Situ Measurement of Wall Thermal Properties: Parametric Investigation of the Heat Flow Methods Through Virtual Experiments Data <i>Andrea Alongi, Luca Sala, Adriana Angelotti, Livio Mazzarella</i>	129

Investigating the Performance of Different Window Opening Styles for Single-Sided Wind-Driven Natural Ventilation Using CFD Simulations <i>Akshit Gupta, Annamaria Belleri, Francesco Babich</i>	137
The Management of the Energy Performance Simulation of a Complex Building Portfolio. The Case of the School Building Asset of an Italian Municipality <i>Claudia Bo, Enrico De Angelis, Andrea Augello</i>	145
Hourly-Simplified Calculation to Identify Cost-Optimal Energy Performance Requirements for the Italian Building Stock <i>Matteo Piro, Franz Bianco Mauthe Degerfeld, Giovanna De Luca, Ilaria Ballarini, Vincenzo Corrado</i>	153
A Novel Methodology for Risk Assessment of Airborne Transmission due to Covid-19 in University Classrooms <i>Giulia Lamberti, Roberto Rugani, Fabio Fantozzi</i>	161
Integrated Approach to Assess the Energy and Environmental Payback Time of Buildings Refurbishment: A Case Study <i>Marta Roncone, Francesco Asdrubali, Gianluca Grazieschi, Chiara Tonelli</i>	169
Comparison Between Measured and Calculated Values in Relation to Noise From Wind Turbines <i>Antonella Bevilacqua, Gino Iannace, Ilaria Lombardi, Amelia Trematerra</i>	177
Thermo-Hygrometric Comfort Analysis in a Real Public Conference Room to Support a Digital-Twin Targeted to Parametric Investigations <i>Roberto Bruno, Piero Bevilacqua, Daniela Cirone, Natale Arcuri</i>	185
Validation of Energy Simulations of a Sustainable Wooden House in a Mediterranean Climate <i>Piero Bevilacqua, Roberto Bruno, Daniela Cirone, Stefania Perrella, Natalia Shushunova, Natale Arcuri</i>	193
Thermal and Acoustic Simulation of a Technical Enclosure for High Voltage Control Equipment <i>Edoardo A. Piana, Somayan Basu, Francesco Palone, Simone Sacco, Roberto Spezie</i>	199
Investigating the Role of Humidity on Indoor Wellness in Vernacular and Conventional Building Typologies <i>Suchi Priyadarshani, Roshan R Rao, Monto Mani, Daniel Maskell</i>	207
An Investigation Into Thermal Performance of Buildings Built Using Upcycled End-Of-Life Photovoltaic Panels <i>Roshan R Rao, Suchi Priyadarshani, Monto Mani</i>	217
Determining the Energy Benefits from Passive Solar Design Integration through the Sensitivity Analysis of Different Case Studies <i>Giacomo Cillari, Alessandro Franco, Fabio Fantozzi</i>	225
A Novel Personal Comfort System: A Radiant Desk With a Loop Heat Pipe <i>Roberto Rugani, Marco Bernagozzi, Marco Picco, Giacomo Salvadori, Fabio Fantozzi</i>	233
Energy Signature Modeling Towards Digital Twins – Lessons Learned From a Case Study With TRV and GAHP Technologies <i>Massimiliano Manfren, Maria Cristina Tommasino, Lamberto Tronchin</i>	243
The Amintore Galli Theatre in Rimini: A Dataset of Building Simulation Tools for its Acoustic Design <i>Antonella Bevilacqua, Massimiliano Manfren, Maria Cristina Tommasino, Ruoran Yan, Lamberto Tronchin</i>	249
Data-Driven Building Energy Modelling – Generalisation Potential of Energy Signatures Through Interpretable Machine Learning <i>Massimiliano Manfren, Maria Cristina Tommasino, Lamberto Tronchin</i>	255
Estimated Versus Actual Heating Energy Use of Residential Buildings <i>Matthias Schuss, Martin Fleischhacker, Ardeshir Mahdavi</i>	265
Polyamide Waste Thermal and Acoustic Properties: Experimental and Numerical Investigation on Possible Reuse for Indoor Comfort Improvement <i>Manuela Neri, Eva Cuerva, Alfredo Zabaleta, Pablo Pujadas, Elisa Levi, Ondrej Sikula</i>	273
Assessment of Demand-Side Management on the Performance of a Single-Dwelling Mechanical Ventilation Plus Radiant Floor System <i>Paolo Bonato, Anton Soppelsa, Marta Avantaggiato, Roberto Fedrizzi</i>	281
Passive Design Strategies for the Improvement of Summer Indoor Comfort Conditions in Lightweight Steel-Framed Buildings <i>Nicola Callegaro, Max Wieser, Giovanni Manzini, Ivan Kharlamov, Rossano Albatici</i>	289
Energetic Optimisation of the Domestic Hot Water System in a Residential Building by Means of Dynamic Simulations <i>Paolo Valdiserri, Aminhossein Jahanbin, Giovanni Semprini</i>	299

Assessing the Climate Resilience of Passive Cooling Solutions for Italian Residential Buildings <i>Mamak P. Tootkaboni, Ilaria Ballarini, Vincenzo Corrado</i>	305
Ventilation of Residential Buildings in Alpine Region: A Comparison Between Natural, Mechanical, and Mixed-Mode Strategies <i>Francesca Avella, Paolo Bonato, Annamaria Belleri, Francesco Babich</i>	313
A Comparison Among Three Whole-Building Dynamic Simulation Software and their Applicability to the Indoor Climate Modelling of Historical Buildings <i>Francesca Frasca, Elena Verticchio, Michele Libralato, Paola D'Agaro, Giovanni Cortella, Anna Maria Siani, Cristina Cornaro</i>	321
QGIS-Based Tools to Evaluate Air Flow Rate by Natural Ventilation in Buildings at Urban Scale <i>Silvia Santantonio, Guglielmina Mutani</i>	331
Modeling Energy Consumption in a Single-Family House in South Tyrol: Comparison Between Hemp Concrete and Clay Bricks <i>Silvia Ricciuti, Irene Lara-Ibeas, Annamaria Belleri, Francesco Babich</i>	341
A Fully Automated and Scalable Approach for Indoor Temperature Forecasting in Buildings Using Artificial Neural Networks <i>Jakob Bjørnskov, Muhyiddine Jradi, Christian Veje</i>	349
Effects of Different Moisture Sorption Curves on Hygrothermal Simulations of Timber Buildings <i>Michele Libralato, Maja Danovska, Giovanni Pernigotto, Andrea Gasparella, Paolo Baggio, Paola D'Agaro, Giovanni Cortella</i>	357
Energy Performance Evaluation and Economical Analysis by Means of Simulation Activities for a Renovated Building Reaching Different Nzeb Definitions Targets <i>Riccardo Gazzin, Jennifer Adami, Mattia Dallapiccola, Davide Brandolini, Miren Juaristi Gutierrez, Diego Tamburrini, Paolo Bonato, Martino Gubert, Stefano Avesani</i>	367
Preliminary CFD Parametric Simulations of Low- and Medium-Density Urban Layouts <i>Ritesh Wankhade, Giovanni Pernigotto, Michele Larcher</i>	377
Smart Sensors and Auditory Sensitivity: Acoustic Optimization of Dedicated Spaces for Autistic Individuals <i>Federica Bettarello, Marco Caniato, Arianna Marzi, Giuseppina Scavuzzo, Andrea Gasparella</i>	387
Simulation Application for the Assessment of the Energy Performance of a Building Renovated Using I-BEST System (Innovative Building Envelope through Smart Technology) <i>Cristina Carpino, Mario Maiolo, Patrizia Piro, Roberto Bruno, Natale Arcuri</i>	395
Modeling Occupants' Behavior to Improve the Building Performance Simulation of Classrooms <i>Federica Morandi, Julian Donges, Ilaria Pittana, Alessandro Prada, Francesca Cappelletti, Andrea Gasparella</i>	403
Modeling and Measurements in Natural Ventilation of Massive Buildings: A Case Study <i>Francesco Asdrubali, Luca Evangelisti, Claudia Guattari, Marta Roncone, Lucia Fontana, Ginevra Salerno, Chiara Tonelli, Valeria Vitale</i>	411
Calibration of the Energy Simulation Model of a Library with a Meta-Model-Based Optimization Approach <i>Maja Danovska, Alessandro Prada, Paolo Baggio</i>	417
Development of a Detailed Model of Hybrid System Composed by Air-to-Water Heat Pump and Boiler <i>Erica Roccattello, Alessandro Prada, Marco Baratieri, Paolo Baggio</i>	427
The Role of Ventilation in Indoor Spaces During the Covid-19 Pandemic: Comprehensive Analysis of ASHRAE Standard 62.1 <i>Giovanni Francesco Giuzio, Giovanni Barone, Annamaria Buonomano, Gianluca Del Papa, Cesare Forzano, Adolfo Palombo, Giuseppe Russo</i>	437
Design of Energy-Neutral Smart Buildings: An Ontological Framework to Integrate LCA, BIM and PLM <i>Tarun Kumar, Monto Mani</i>	449
Assessing the Performance of a Simplification Algorithm for Urban Building Energy Modeling in Multi-Objective Optimization <i>Federico Battini, Giovanni Pernigotto, Andrea Gasparella</i>	457
Application of a Simplification Algorithm for Urban Building Energy Modeling to Complex-Shaped Educational Buildings <i>Matteo Merli, Federico Battini, Giovanni Pernigotto, Andrea Gasparella</i>	465
Numerical Investigation of Radiation Efficiency of a Cross-Laminated Timber Floor <i>Marco Caniato, Nicola Granzotto, Federica Bettarello, Arianna Marzi, Paolo Bonfiglio, Andrea Gasparella</i>	473

Assessment of Contagion Risk due to Covid-19 for a Multi-Zone Building Model of Offices <i>Riccardo Albertin, Alessandro Pernici, Giovanni Pernigotto, Andrea Gasparella</i>	479
Impact of Visual, Thermal, and Indoor Air Quality Conditions on Students' Wellbeing and Learning Performance in a Primary School of Bolzano, Italy <i>Giovanni Demozzi, Luca Zaniboni, Giovanni Pernigotto, Andrea Gasparella</i>	489
Performance Simulation of Desiccant Wheel under Dynamic Conditions: <i>Comparison between Detailed and Simplified Models</i> <i>Simone Dugaria, Andrea Gasparella</i>	499
BIM and Mixed Reality for Visualizing Building Energy Data <i>Dietmar Siegele, Paola Penna, Ilaria Di Blasio, Michael Riedl</i>	507
Impact of Solar Radiation Modelling on the Simulated Building Energy Performance in the Climate of Bolzano, Italy <i>Giovanni Pernigotto, Alessandro Prada, Aleksandr Gevorgian, Andrea Gasparella</i>	515
Effect of the Time Interval Base on the Calculation of the Renewable Quota of Building in an Alpine Context <i>Margherita Povolato, Alessandro Prada, Paolo Baggio</i>	525
Innovative Approaches for Teaching BPS: First Implementations of Business Game-Like Activities <i>Andrea Gasparella</i>	533

Preface

The participation of about 100 attendees at the fifth Building Simulation Applications BSA2022 Conference, one of the first IBPSA conferences held entirely in presence after the pandemic outbreak, can certainly be claimed as a step forward in the process of overcoming the constraints and limitations imposed by the years of the Covid-19 pandemic.

11 conference sessions in two parallel tracks, 66 presentations reporting the contributions by more than 180 authors are some of the most significant figures of this event. In addition, confirming an international profile and its inclusivity call, the Conference saw a small but significant presence of delegates from abroad, especially from Austria and India.

As the previous editions, BSA 2022 focused on providing an overview of the latest applications of building simulation in the following three main fields: the use of simulation for building physics applications, such as building envelope and HVAC system modelling and their design and operation optimization; global performance and multi-domain simulations; the development through simulation of new methodologies, regulations, as well as new calculation and simulation tools.

Nonetheless, the times urged to address indoor air quality, the main topic of this edition, emphasizing the role of simulation to assess strategies able to ensure healthy and safe indoor conditions for occupants.

The engaging opening speech about “The Role of IBPSA and Post-Covid Simulation” by Prof. Lori McElroy, President of IBPSA, was followed by two innovative and capturing keynotes, “Simulation and Optimization: Supporting Building Decarbonization” by Prof. Paolo Baggio, University of Trento, Italy, and “Going Digital – Infrastructure Modeling for Resilience and Decarbonization”, by Dr. Drury B. Crawley, vice-President of IBPSA.

The conference also devoted some time to the analysis and discussion of the use of building simulation among building professionals and specialists in terms of education: The “3rd Student School on Building Performance Simulation Applications” addressed the use of building performance simula-

tion in the context of building rating systems and in relation with BIM. We also had an interesting conversation with Lori McElroy on the topic of “Building Simulation in the Profession: Work in Progress”, discussing the current most critical aspects and challenges. Finally, after the conference closing ceremony on the third day, the “Round Table for Designers and Practitioners” featured four professional experiences about the use of building simulation, with a discussion about errors, challenges, and opportunities.

The fifth edition of the BSA conference represented an opportunity to restart and revitalize the process of reducing the gaps between academia and the professional world, of rethinking the role of building simulation in the design practice for future buildings, and of opening in the face of unprecedented challenges and opportunities of a new post-pandemic society.

Andrea Gasparella, Free University of Bozen-Bolzano

Optimization of Daylighting and Energy Performance in Bangladesh Ready-Made Garment Factories: Use of Parametric Design, Simulation Modeling, and Genetic Algorithms

Md Ashikur Rahman Joarder – Bangladesh University of Engineering and Technology, Bangladesh – ashikj2000@gmail.com; ashikjoarder@arch.buet.ac.bd

Md Monir Hossain – Bangladesh University of Engineering and Technology, Bangladesh – hossainmonir.2008@gmail.com

Aaron J.E. Bach – Griffith University, Australia – a.bach@griffith.edu.au

Jean P. Palutikof – Griffith University, Australia – j.palutikof@griffith.edu.au

Fahim Tonmoy – BMT Commercial pty, Brisbane, Australia – Fahim.Tonmoy@bmtglobal.com

Abstract

The ready-made garment (RMG) sector is an essential contributor to the economy of Bangladesh. Most RMG buildings in the country are often found to be inefficient in terms of natural light, energy consumption and the thermal comfort of the workers. Computational modeling, simulation and optimization analysis could be used during the building planning and design phases to effectively integrate these three issues and improve the working environment. This research first evaluates both daylighting and energy performance of a real-world existing air-conditioned RMG factory building in Dhaka. Next, an optimized design solution is proposed for the factory. Finally, we correlate the relationship between design variables and performance metrics. Nine independent variables (north, south, east and west window-to-wall ratios and shading; and skylights) are identified to evaluate performance. The variables are connected with parametric sliders (value expressed by a range of numbers despite a constant value), so that performance can be checked for different possible configurations. Rhinoceros, Grasshopper, ClimateStudio, Octopus, TT toolbox, and Energy plusTM software with plugins are used to conduct the optimization process. Genetic Algorithms are used to narrow down the optimization results and identify the best options that comply with the multi-objective goal. Predicted Percentage of Dissatisfaction (PPD) is also analyzed for the best options identified from the optimization process. The result shows the balanced option (best for both daylighting and energy) with changed materials satisfies the thermal comfort of users.

1. Introduction

Ready-made garment (RMG) factories in Bangladesh have been heavily criticized for their working conditions. More than 80 % of the export earnings of Bangladesh come from the RMG sector (Islam, 2021) and about four million people are involved in this industry. In the factories, workers are engaged in sewing, ironing, packing, tailoring, operating machines and other labor-intensive works. Due to the nature of their work and the heat generated from machinery, the indoor environment of the factories is often uncomfortable and workers suffer a range of health problems that affect the individual as well as the overall productivity of the factory. In RMG factories, along with other physical conditions, the quality of the luminous environment is affected by poor natural lighting systems and high internal heat gain from artificial lighting (Hossain & Ahmed, 2013). This creates an intolerably hot and uncomfortable working environment for the workers that is non-compliant with national and international standards. Since lighting directly affects visibility, light is critical to the productivity, safety and healthy working conditions of workers (Zohir & Majumder, 2008). Industrial workers spend more than 90 % of their lives in artificial luminous environments and in such conditions, natural light could work as medicine (Gligor, 2004). Different studies have shown that lighting is one of the biggest consumers of power in the RMG sector, accounting for around 21-35 % of the total

energy consumption (EAC, 2009). Much work has been done to reduce the power consumption of machinery in RMG factories; however, developments in the areas of lighting, heating and ventilation are limited (Godiawala et al., 2014).

Appropriate use of daylight and removing generated heat by effective natural and/or artificial ventilation systems can be an effective means to reduce energy consumption and excessive cooling load. With the appropriate use of technology, it is anticipated that the energy consumption in the building sector can be reduced to about 30 % to 80 % (Gupta, 2017). Due to current environmental concerns, energy saving has become the leading driving force in modern research (Bojic et al., 2013). Appropriate architectural design can reduce the energy consumption of heating or air conditioning systems significantly (Kalmár & Csiha, 2006). The EU energy policy in the buildings sector, including technical solutions and legal procedures, aims to improve the energy performance of buildings and guarantee human comfort (Tronchin & Tarabusi, 2013).

In recent times, to ensure workers' comfort and productivity, the construction of fully air-conditioned factory buildings with excessive artificial lighting has been gaining in popularity among owners and management of RMG factories in Bangladesh. Electricity-based carbon-intensive air conditioning and lighting systems can result in a significant amount of energy consumption. On the other hand, the use of daylight with passive or hybrid ventilation systems requires less energy to operate, while at the same time having less impact on the environment, carbon emissions and climate change. Using a case study approach based on a real RMG factory in Dhaka, this research presents a system for improving indoor lighting conditions and comfort by integrating passive strategies for the existing garment factories of Bangladesh. The research addresses the growing threat to worker health and productivity from the visual and heat stress that may be caused by climate change and seeks to identify sustainable passive strategies that will not add to the burden of greenhouse gas emissions.

2. Case Study

The case building is an 864-square-meter factory building with a pitched roof (Fig. 1). The building is north facing (Fig. 2: top) towards the access road. The roof is made of a metal sheet adjacent to a truss frame structure (Fig. 2: bottom). The north façade of the factory has two large gates (6 meters x 2.5 meters) made of steel. During working hours, these two gates remain closed for security purposes. So, for simulation modeling, the north façade of the base case was provided with no opening.

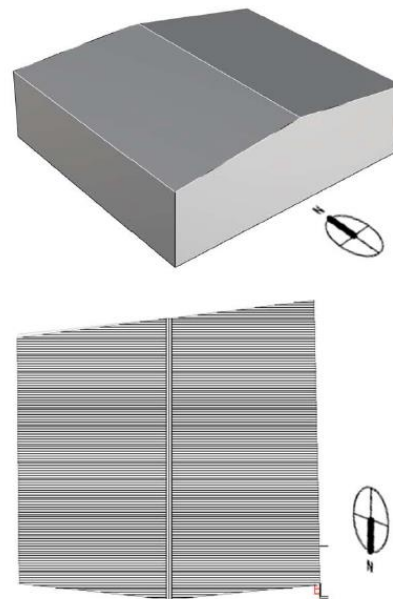


Fig. 1 – Rhinoceros model for case RMG factory (top) and top view of the roof (bottom)

A Kestrel 5400 pro instrument was installed inside the factory to measure air temperature, relative humidity (RH), wind speed, and black and wet bulb globe temperatures (Table 1). Three wireless tag loggers made by OnSolution were also placed at different locations inside the factory to measure temperature and RH. The collected data were cross-checked with the base case simulation modeling for validation.

3. Method

This study seeks to test and verify the effectiveness of optimization processes in the tropical climatic context, in this case, Bangladesh. Based on the

RMG factory described in Section 2, the internal conditions were optimized for the target parameters of daylighting and energy consumption. There are six main steps for the research, as explained below.



Fig. 2 – North side view of the case factory building (top), floor plan (middle), and inside view of the RMG factory (bottom) (pictures by Photographer Md M A R Joarder, 2020)

The first step is to select an RMG building for a case study. This research selected a single-storey RMG building constructed with steel and brick, located in northwest Dhaka (Fig. 2). The factory undertakes garment manufacture, from cutting through sewing and ironing to packing. A physical survey was conducted in the first step to measure the existing configuration and collect the climate data (Table 1) that is required for simulation analysis.

Table 1 – Indoor and outdoor mean maximum temperature (T_{max}) and mean minimum relative humidity (RH_{min}) between 08:00 and 18:00 on the days the factory was operating in 2021

	Indoor	Outdoor
January ($n=308$ hours over 28 days)		
T_{max} (°C)	28.6	24.5
RH_{min} (%)	44.2	50.3
March ($n=264$ hours over 24 days)		
T_{max} (°C)	29.6	33.3
RH_{min} (%)	59.9	38.8
September ($n=286$ hours over 26 days)		
T_{max} (°C)	30.1*	32.6
RH_{min} (%)	62.4*	64.3
All of 2021 ($n=3234$ hours over 294 days)		
T_{max} (°C)	30.9^	30.6
RH_{min} (%)	58.7^	55.9

*30 hours of missing data not included

^ 39 hours of missing data not included

The second step was to prepare the 3D model using the data collected during the physical survey. The simulation of the base case factory building was carried out at this step. Materials and other information for zones were transferred into simulation settings and Grasshopper scripts accordingly. In this script, the workflow could be divided into six parts. Part A was the components for developing the building geometry (floor, wall, roof, window, shading and skylight). The geometry was connected to components in Part B for energy and daylighting modeling. In this part, material selection for individual elements of the building, sensor grid settings for daylighting, zone settings, adiabatic and boundary condition settings were operated. The daylight model was connected to components in Part C for daylighting simulation. In this part, various simulation-related settings were identified (e.g., the number and name of the objectives and ClimateStudio Result [CSR] settings). Part D connected both the energy model from Part B and the daylighting simulation output from Part C for energy simulation. Part E was the components for optimization. Part F was the components for data output (Fang, 2017).

The third step was to run the optimization process for Option 1 (the best option for daylighting). Grasshopper script was prepared for modeling the case space with parametric design variables. Phe-

notype toggle in Octopus is connected with daylight performance batteries (LEED: Leadership in Energy and Environmental Design credit; sDA: Spatial Daylight Autonomy; ASE: Annual Sunlight Exposure; and Mean Illuminance) and energy performance batteries were skipped, as the best daylighting option was the target. As windows have a large-scale impact on daylighting and thermal comfort considering their size, orientation and shading configurations, as well as on the energy consumption of the building, it was thus necessary to optimize window design for maximum benefit (Aman, 2017).

The fourth step was to run the optimization process for Option 2 (the best option for energy). The overall procedure was similar to daylighting optimization. The difference was only in the optimization objective, which is Energy Use Intensity (EUI), and CO₂ emissions. Daylighting performance batteries were skipped here, as the best energy option is the target. Therefore, the Phenotype toggle in Octopus was connected with EUI and CO₂ only.

The fifth step was to run the optimization process for option 3 (the balanced option for daylight and energy both). In this step, three performance objectives (e.g., sDA, ASE and EUI) were identified to run the simulation. Octopus by default found the minimum value of each objective, so the objective to be maximized (sDA) should be multiplied by -1. Pareto Frontiers with the trade-off between each performance metric were found after the optimization process.

In the final (6th) step, Percentage of Mean Vote (PMV) and Predicted Percentage of Dissatisfaction (PPD), analyses were carried out to check thermal comfort inside the factory space. ClimateStudio and Grasshopper were used to run this analysis as well. Five simulations were run in this step (for Base case, Op1- Daylighting, Op2- Energy, Op3- Balanced, and Op4- Balanced and changed materials). Comparing the results of these five simulations, the best one complying with both the American Society of Heating, Refrigerating and Air-Conditioning Engineers (ASHRAE) standard and the Bangladeshi standard (BNBC, 2020) and which could provide thermal comfort inside the factory, was identified.

4. Simulation and Results


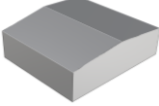
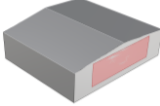

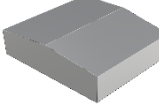
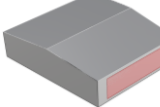

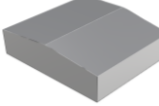
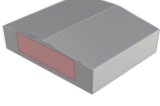

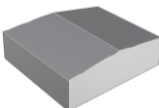
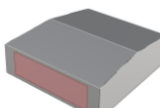

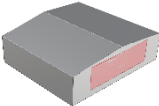
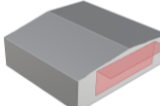

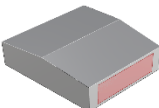
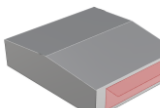

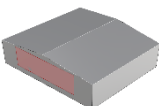
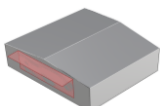

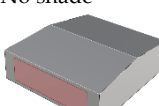
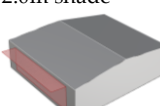

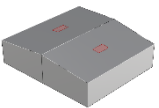
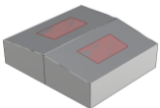
In this research, the percentage of windows and skylights, and depth of shading was explored for optimal daylighting and energy performance. There were no windows and shading on any of the façades of the factory building, and no skylight on the roof. For the modeling of the optimization process focusing on daylighting and energy, the placement of the doors and the interior partitions was not considered. The model was developed with Rhinoceros 7.1 (Fig. 1) and Grasshopper scripting. ClimateStudio 1.1 plugins were used for simulation. Existing data collected through factory visits were used for zone settings while simulations were conducted. There were 26 daylighting sensors evenly spaced at a height of 0.75 meters above the floor. Some building parameters were fixed throughout the optimization process: the height of the building from the ground to the edge of the pitched roof was 5 meters; windows were considered from 0 to 100% of the façade; areas of skylight were considered from 0 to 20% of the roof surface.

Building material details found during the physical survey were used in the model. To avoid excessive heat gain or heat loss from the skylight, an insulated translucent material was used as its glazing material. The material had a U-value of 0.45 W/(m² K). The reflectance of the ceiling, floor, interior, exterior walls, and shading were 0.8, 0.2, 0.5, 0.5, and 0.8 respectively. The windows had a transparent material with visible transmittance of 0.65. Skylights had a translucent material with a transmittance of 0.24. Nine independent design variables for the building geometry were analyzed: north, south, east and west windows to wall ratios [WWR] and shade; and Skylights. Table 2 shows the minimum (0 % for WWR, 0.0m for shade and 2 % for skylight) and maximum (100 % for WWR, 2.0 m for shade and 20 % for skylight) values of the variables and the ranges used during simulation analysis. The daylighting simulation output included sDA and ASE.

The energy simulation output Included annual heating, cooling, equipment and lighting energy loads. Since the equipment load stays the same for studied design options, it was not considered. The

energy optimization objective was to ensure the minimum total energy load. The total energy load was the sum of heating, cooling, and lighting loads. EUI was also calculated by dividing the total energy load by the occupied floor area of the factory building.

Table 2 – Design variables and ranges for simulation analysis

Variable	Minimum	Maximum
1 WWR-North 	 No windows	 Full-wall windows
2 WWR-East 	 No windows	 Full-wall windows
3 WWR-South 	 No windows	 Full-wall windows
4 WWR-West 	 No windows	 Full-wall windows
5 Shade Depth-North 	 No shade	 2.0m shade
6 Shade Depth-East 	 No shade	 2.0m shade
7 Shade Depth-South 	 No shade	 2.0m shade
8 Shade Depth-West 	 No shade	 2.0m shade
9 Skylight 	 2 %	 20 %

4.1 Base Case Modeling and Analysis

The first simulation was conducted for the base case, to understand the existing status of the building in terms of daylighting and energy performance. The model was prepared considering the exact dimensions of the building collected during the physical survey. The weather data file for Dhaka was used during the simulation process. The building was counted as air-conditioned and values of independent variables (windows, shading and skylight) were set to 0 (zero) representing the existing building. Simulation results for LEED credit, sDA, ASE, mean illuminance values, EUI and CO₂ emissions were 0, 0 %, 0 %, 0 lx, 223 kWh/(m² yr) and 198 kgCO_{2e}/(m² yr), respectively.

4.2 Optimization of Daylighting

The second simulation was conducted for the best daylighting results (Option 1). In this simulation, the population size was set to 20 and maximum generations were set to 10. In total, 200 iteration process were carried out to identify the best daylighting results. Pareto Front algorithm identified the best configurations among these combinations. Four daylighting performance objectives (LEED credits, sDA, ASE and mean illuminance) were set to run this optimization process. Table 3 shows the results of the simulation. LEED credit, sDA, ASE and mean illuminance values for the best daylighting case results are 3, 1 (100 %), 0.134 (13 %) and 1003 lx, respectively. In Fig. 3 (top), Pareto Front 3-dimensional graph shows the optimized results along with the Pareto Frontier (marked with a red circle).

4.3 Optimization of Energy

The third simulation was conducted to find the best energy consumption (Option 2). The process is similar to the prior simulation. The only difference is that two energy performance objectives (EUI and CO₂ emissions) were set to run this optimization. In Table 3, the third column presents the values of the independent variables that resulted from the optimization process and which were identified through the Pareto Front algorithm. The EUI and CO₂ emissions for the best energy case are

56 kWh/(m² yr) and 46 kgCO_{2e}/(m² yr), respectively. In Fig. 3 (middle), the Pareto Front 3-dimensional graph shows the studied iterations with the optimized one highlighted.

Table 3 – Optimization results for three different options

Design Variables	Op 1 (Day-lighting)	Op 2 (Energy)	Op 3 (Balanced)
WWR- North (%)	82.5	40	100
WWR-East (%)	43	4	10
WWR-South (%)	7.5	24	22.5
WWR-West (%)	80	34	10
Shading-North (m)	1.17	1.86	1.58
Shading-East (m)	1.72	0.95	1.04
Shading-South (m)	1.52	0.09	1.84
Shading-West (m)	0.32	0.39	1.01
Skylight (%)	23	10	7

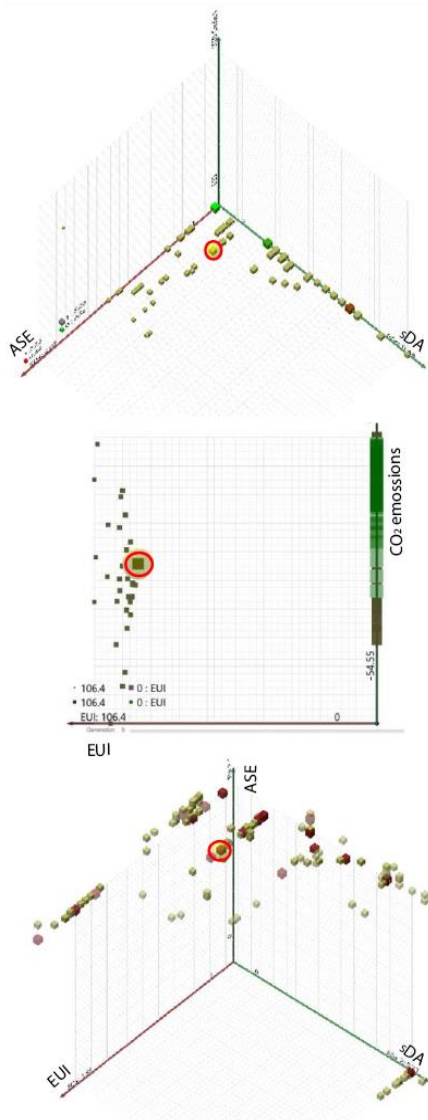


Fig. 3 – Pareto Front analysis for daylighting optimization (top), energy optimization (middle) and multi-objective optimization (bottom)

4.4 Optimization of Balanced Option

A Pareto optimization aims to find the trade-off front (ParetoFront) between multiple outcome objectives. The Octopus plugin handled the multi-objective optimization process using Pareto-Front algorithms (Aman et al., 2021). The fourth simulation was conducted for Option 3 (the balanced option for daylighting and energy combined). The simulation process was similar to the prior two simulations. Fig. 4 (top) shows the factory model while the optimization process of Op3 is running. Fig. 4 (bottom right) shows the ranges slider of nine variables in the Grasshopper script for this optimization. A large number of combinations are possible among these nine variables and within their ranges. Fig. 4 (bottom left) shows the values of six performance metrics (LEED credit, sDA, ASE, mean illuminance, EUI and CO₂ emissions) generated in this process. Later, three performance metrics (sDA, ASE and EUI) were considered for Pareto Front analysis to make the process simplified. The outcomes of the simulation studies are presented in Table 3 (fourth column, Op 3 Balanced; the values of design variables).

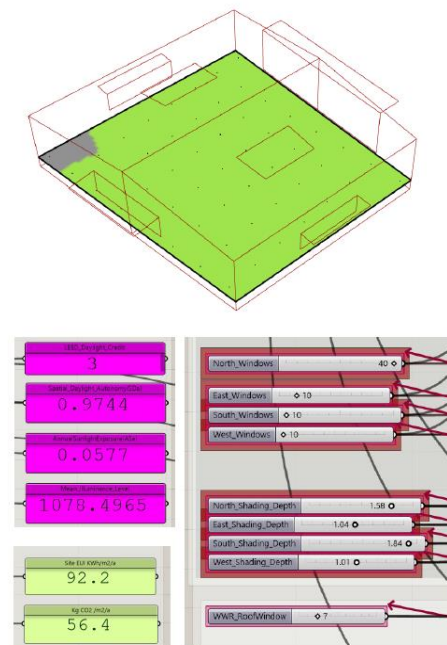


Fig. 4 – Rhinoceros model showing simulation process (top); results for six performance objectives appeared in Grasshopper script (bottom left); and Grasshopper slider for parametric design (bottom right)

In Fig. 3 (bottom), Pareto Front 3-dimensional graphs show different optimized results and locations (marked with a red circle) of the Pareto Frontier (the best one). sDA, ASE and EUI values for balanced option case are 0.90 (90 %), 0.09 (9 %) and 89 kWh/(m²yr), respectively.

Comparing the results of performance metrics for the base case (explained in Section 4.1) and the balanced option case reveals that the latter is performing effectively.

4.5 Thermal Comfort Analysis

By understanding the thermal behavior of the existing situation of factory buildings, owners can improve the indoor environment quality to increase their production (Sayem et al., 2011). The fifth simulation was conducted for analyzing the PPD. In this process, thermal comfort performance was checked for Base case, Op1 (daylighting), Op2 (energy), Op3 (balanced) and Op4 (balanced and changed materials). Design variables found in previous simulation results (presented in Table 3) were used in this study. In the base case, variables remain 0 (zero), as there were no windows, sunshades and skylights in reality. In Op4, variables were kept similar to Op3 (balanced), except for the changes of material for the roof and wall. 300 mm concrete, 80 mm insulation and 80 mm cement screed were used for the roof and walls. ClimateStudio's default script for spatial comfort analysis in the Grasshopper interface was used to run the PPD simulation. The building was considered non-AC during this simulation. Keeping the model static, the PPD analysis was performed by changing the values of design variables presented in Table 3.

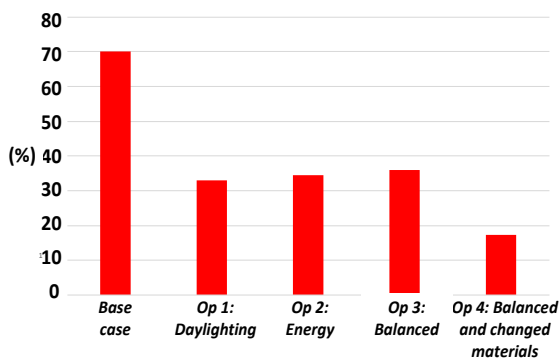


Fig. 5 – PPD results for the base case, daylighting, energy, balanced, and balanced and changed materials

In the case of Op4, in the Grasshopper script, roof and wall materials were changed from zone settings. Fig. 5 shows that the PPD value for the base case is 70 %, for Op1 32.9 %, for Op2 34.4 %, for Op3 35.9 % and for Op4 17.3 %. Although in ASHRAE standard below 10 % is recommended for thermal comfort, the value of 17.3 (below 20 %) for Op4 is also acceptable in the context of Bangladesh climate. The other 4 options do not comply with the ASHRAE standard and Bangladesh Standard (BNBC, 2020).

5. Conclusion

The global increase in demand for energy has generated pressure to save energy. Consequently, energy-efficient buildings are an important factor related to the energy issue (Jahangir et al., 2014). High-energy performance buildings can save primary energy and reduce CO₂ emissions. Optimization processes successfully present the ability to adapt to various design environments and provide design options with significant performance improvement. As a result, this method can be considered a valid approach (Fang, 2017). This research conducts three optimization processes and the results show that the configuration of the variables is changed in terms of Op1 (daylighting), Op2 (energy), and Op3 (balanced) (Table 3). The research recommends variables of Op3 (balanced) for RMG buildings in the context of Bangladesh, as it complies with both daylight and energy optimization. On the other hand, in the case of thermal comfort analysis, Op4 (balanced and changed materials) shows the best results among the options studied. In a nutshell, the features for RMG buildings in the climatic context of Bangladesh are: WWR-north 100 %, WWR-east 10 %, WWR-south 22.5 %, WWR-west 10 %, shade depth north- 1.35 m, shade depth east- 1.58 m, shade depth south- 1.63 m, shade depth west- 1.55 m, skylight- 10 %, roof and wall materials: 300 mm concrete, 80 mm insulation, and 80 mm cement screed performed the best among the options studied in terms of daylight penetration, energy consumption and providing thermal comfort. The features can be incorporated as strategies for sustainable RMG building design in Bangladesh.

Acknowledgement

This work is part of the “Managing heat stress among Bangladesh ready-made clothing industry workers” project funded by Wellcome under the Our Planet Our Health Programme. This work was carried out in the Department of Architecture, Bangladesh University of Engineering and Technology (BUET). The authors gratefully acknowledge the support and facilities provided by BUET.

Nomenclature

AC	Air Conditioning
ASE	Annual Sunlight Exposure
ASHRAE	American Society of Heating, Refrigerating and Air-Conditioning Engineers
CSR	ClimateStudio Results
EUI	Energy Use Intensity
LEED	Leadership in Energy and Environmental Design
PMV	Percentage of Mean Vote
PPD	Predicted Percentage of Dissatisfaction
RH	Relative Humidity
RMG	Ready-Made Garment
sDA	Spatial Daylight Autonomy

References

- Aman, J., N. Tabassum, J. Hopfenblatt, J. B. Kim, and M. O. Haque. 2021. "Optimizing Container Housing Units for Informal Settlements - A Parametric Simulation & Visualization Workflow for Architectural Resilience." 26th CAADRIA Conference, Hong Kong. 29 Mar - 1 Apr.
- Aman, J. 2017. "Impact of Windows for Daylighting on Thermal Comfort in Architecture Design Studios in Dhaka." 'Masters of Architecture' dissertation submitted to the Dept. of Architecture, BUET, Dhaka.
- Bojic, M., A. Patou-Parvedyb, and H. Boyer. 2013. "Optimization of thermal comfort in buildings through envelope design." 25th ECOS Conference, Perugia, Italy. 26-29th June.
- EAC. 2009. Energy Management Study on Abony Textile Limited and Abony Knitwear Limited, Hamayatpur, Savar, Dhaka. Energy Audit Cell, Ministry of Energy and Mineral Resources, BD.
- Fang, Y. 2017. "Optimization of Daylighting and Energy Performance Using Parametric Design, Simulation Modeling, and Genetic Algorithms." Ph.D. in Design, Graduate Faculty of North Carolina State University.
- Gligor, V. 2004. Luminous Environment and Productivity at Workplaces. Thesis (Licentiate). Espoo: Helsinki University of Technology, Finland.
- Godiawala, P., N. Anand, and J. M. Patel. 2014. "Sky lighting - A solution to reducing energy consumption in Apparel Sector." *International Journal of Scientific and Research Publications* 4(4).
- Gupta, M. 2017. "A path towards net-zero energy buildings." *International Journal of Research in Engineering & Technology (IJRET)* 5(2).
- Hossain, M. and K. S. Ahmed. 2013. "Illumination Conditions and Visual Comfort in Production Spaces of Ready-Made Garments Factories in Dhaka." *IACSIT International Journal of Engineering and Technology* 5(5).
- Islam, M. 2021. "Ready-made garments exports earning and its contribution to economic growth in Bangladesh." *GeoJournal*. 86 (2021).
- Jahangir, A, M. A. Islam, and B. K. Biswas. 2014. "Energy simulation to estimate building energy consumption using EnergyPlus." 3rd ICMIEE Conference. Khulna, Bangladesh. 26-27 Dec.
- Kalmár, F. and A. Csiha. 2006. "Interrelation between glazed surfaces, building structure and thermal comfort." 23rd PLEA conference, Geneva, Switzerland, 6-8 Sept.
- Sayem, A., H. Ahmad, and T Hayat. 2011. "Indoor thermal condition of factory building in Bangladesh." *Journal of Architecture and Built Environment* 38(2).
- Tronchin, L., and V. Tarabusi. 2013. "Energy Performance of Building and Thermal Comfort: a comparison. Recent Researches in Environmental and Geological Sciences." DIENCA-CIARM, University of Bologna, Italy.
- Zohir, S. C. and P. Majumder. 2008. "Garment Workers in Bangladesh: Economic, Social and Health Condition." Dhaka: Bangladesh Institute of Development Studies.

Transient Three-Dimensional CFD Modelling of Ceiling Fans: A Comparison Between Detailed and Simplified Models

Francesco Babich – Eurac Research, Italy – francesco.babich@eurac.edu

Akshit Gupta – Eurac Research, Italy – akshit.gupta@eurac.edu

Wilmer Pasut – Ca' Foscari University of Venice, Italy / Korea University – wilmer.pasut@unive.it

Abstract

Ceiling fans have been widely used for decades for providing thermal comfort in warm environments. They are an effective means of completely avoiding the use of energy-intensive air conditioning systems in milder environmental conditions and of reducing the use of such systems in more severe and hotter thermal environments. Ceiling fans can generate an immediate cooling effect on people, as they act on both sensible and latent heat exchange between the human body and the moved air. However, one of the major potential limitations of ceiling fans is that they generate non-uniform velocity profiles, and their effect is highly dependent on the mutual position between body and fan. Thus, it is essential to carefully evaluate the position in which they are installed to maximize their cooling effect where needed by people. CFD is a powerful technique for investigating the air velocity field generated by different ceiling fan configurations. Due to its high demand for computational power and the need for having stable models, previous studies proposed different approaches to model ceiling fans in CFD with some simplifications. As the available computational power increases, so does the possibility of creating more realistic models, but too little is known about when the benefits produced by more complex models are overtaken by their computational costs. The aim of this study was to compare the results obtained by using two approaches to include the ceiling fan into a CFD model, namely a detailed model of the geometry of the fan and a simplified implicit approach that emulates the effect of the fan only. The results illustrate that (a) both models capture the main regions of the air flow, (b) the implicit model provided considerably more accurate air speed values, (c) the computational time of the model with blades is one order of magnitude higher, and (d) fan geometry and meshing are the most critical issues in the model with blades.

1. Introduction

Ceiling fans have been widely used for decades for providing thermal comfort in warm environments. They are an effective means of completely avoiding the use of energy-intensive air conditioning systems in milder environmental conditions, and of reducing their usage in more severe and hotter thermal environments (Babich et al., 2017a; Pasut et al., 2014; Schiavon & Melikov, 2008). Ceiling fans can generate an immediate cooling effect on people, as they act on both sensible and latent heat exchanging between the human body and the moved air.

However, one of the major potential limitations of ceiling fans is that they generate non-uniform velocity profiles, and their effect is highly dependent on the mutual position between body and fan (Babich et al., 2021). Thus, it is essential to carefully evaluate the position in which they are installed to maximize their cooling effect where needed by people.

Computational fluid dynamics (CFD) is a powerful technique for investigating the air velocity field generated by different ceiling fan configurations. Due to its high demand for computational power and the need for having stable models, previous studies proposed different approaches to model ceiling fans in CFD with some simplifications (Babich et al., 2017b). As the available computational power increases, so does the possibility of creating more realistic models, but too little is known about when the benefits produced by more complex models are overtaken by their computational costs.

The aim of this study was to compare the results obtained by using two approaches to include the ceiling fan into a CFD model, namely a detailed model of the geometry of the fan and a simplified implicit approach that emulates the effect of the fan only.

2. Methodology

In this study, two identical set-ups were created in CFD apart from the ceiling fan. In the former, the fan was modeled as a ring to which a body force was applied, while in the latter the actual geometry of the blades was included. As a result, a moving mesh was used in the latter, while this was not needed in the former. Both models were validated with measured air velocity values.

2.1 Features Common to Both Models

In this study, the key features that are common to both models were taken from a CFD model originally developed for thermal comfort studies (Babich et al., 2017b).

The geometry comprises an environmental chamber in which only a 120-cm-diameter ceiling fan was installed (Fig. 1). 36 monitoring points were placed in the model (3 heights; 12 points per height distributed on each level as shown in Fig. 2) in the very same locations of the original measurements.

An unstructured mesh with ten prism layers (added adjacent to the walls to accurately model the boundary layer near surfaces) was adopted.

Transient simulations were performed to better model the real behavior of the ceiling fan. In the original model, 3-minute simulations were performed. In this study, the simulation time was reduced to 1-minute to decrease the computational effort. To ensure that this was not altering the model results, a preliminary test was performed. Using the original air speed values (available for each time step of the 3-minute simulation for all 36 point), the average air speed in each monitoring point was calculated for a set of 60 s intervals (from 0 s – 60 s to 110 s – 170 s). The results showed negligible variations for a study that aimed at comparing two types of ceiling fan CFD modelling. For most points, the ratio between standard deviation and mean (i.e., the mean of the means of each interval) values was equal to 4 % or less (for instance, in point “centre 1300”, the std is 0.06 m/s, the mean 2.05 m/s, and their ratio 2.9 %). Only at a very few points was this ratio higher than 10 %. However, all these points were at a higher level (70 cm or 130 cm above the floor) and far from the fan axis, and therefore in regions in which air speed values are considerably lower and less relevant.

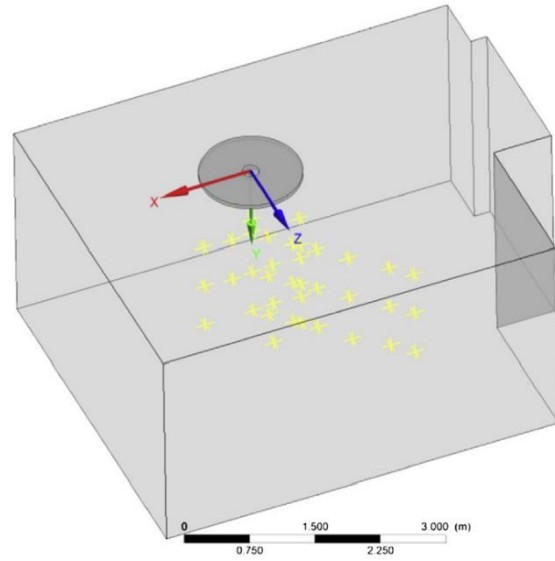


Fig. 1 – CFD model of the environmental chamber. In yellow, 36 monitoring points (Babich et al., 2017b)

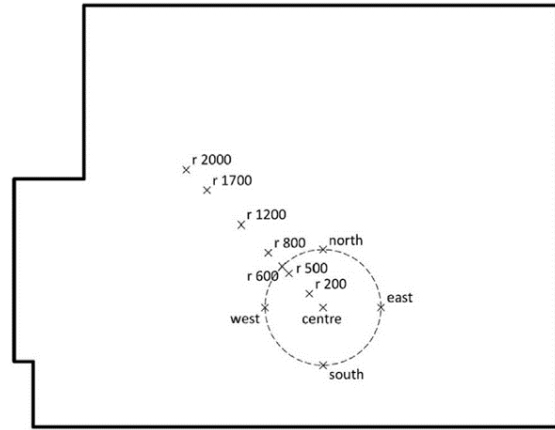


Fig. 2 – Plan view of the environmental chamber with the measurement locations (Babich et al., 2017b)

Convergence criteria were set equal to $1e-05$ for the RMS residuals, and an adaptive time step as a function of RMS Courant number was chosen, with the limit for the RMS Courant number set equal to 5. The SST (Shear Stress Transport) $k-\omega$ turbulence model was selected as it gave the most accurate results in the original study (best match with measurements).

All CFD simulations were performed with ANSYS CFX version 2021. For the mesh, ICEM CFD was used for its advanced capabilities. All simulations were performed using a workstation equipped with 16 GB RAM and a 6-core Intel Xeon Gold 6154 CPU.

2.2 Fan Implicit Model (Without Blades)

In this former model (Fig. 1), the ceiling fan was modeled as in the original study (Babich et al., 2017b). A ring with the same diameter and distance from the ceiling (30 cm) as the actual fan was created. At the centre of the ring, a cylindrical solid element was added to emulate the fact that, in a real ceiling fan, no air emanates from the centre. A momentum source defined by means of cylindrical components was applied to this ring: axial component $55 \text{ kg m}^{-2} \text{ s}^{-2}$ (push air downwards), theta component $8 \text{ kg m}^{-2} \text{ s}^{-2}$ (rotational movement), and radial component $0 \text{ kg m}^{-2} \text{ s}^{-2}$. This model led to a 1,933,004-element mesh.

2.3 Fan Explicit Model (With Blades)

In this second model (Fig. 3), the ceiling fan was modeled in more detail by implementing its three blades and central part. To enable the rotation of the fan, two domains were defined in the CFD model, namely a rotating domain (i.e., the cylindrical element shown in Fig. 3), which contained the fan, and a static domain (i.e., the remaining part of the room). One interface was used to link the two domains (lower and upper circles, and vertical side as shown in Fig. 3). In CFX, a “general connection” interface model and “transient rotor stator” were chosen. For mass and momentum, a “conservative interface flux” was used. The selected mesh connection method was “general grid interface” (GGI).

In this case, the model required a rotational velocity as an input, and this was set equal to 290 rpm, which was the corresponding rotational velocity for which the original model (Babich et al., 2017b) was developed. In this model, the total number of mesh elements is 2,088,669 (rotating domain = 217,150; remaining part of the room = 1,871,519).

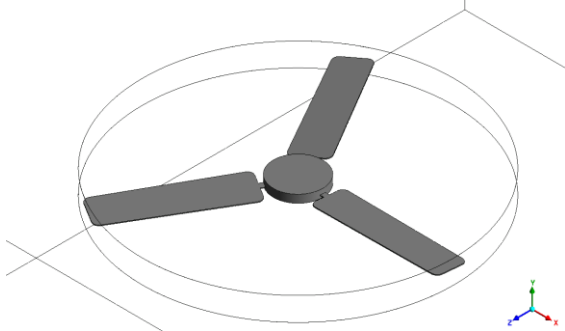


Fig. 3 – Ceiling fan with blades

3. Results

For both models, this section presents their capability of capturing the main regions of the air flow generated by the ceiling fan, the predicted air speed values, and the computational power required.

3.1 Regions of the Air Flow

Both modeling approaches capture the key qualitative features of the air flow generated by a ceiling fan (Fig. 4 and 5). In both cases, the main typical regions of the air flow can be identified (Jain et al., 2004; Wang et al., 2019), namely the region below the fan in which the highest speeds occur (excluding the small area immediately below the motor – also captured by both models), the regions near the floor and then the walls in which air (after having hit the floor) moves horizontally and then vertically to finally return to the blade areas, and lastly the remaining part of the room in which the lowest air speed values are usually recorded. In the region below the fan, like in previous studies (Babich et al., 2017b), the downward flow diverges with a variable half-cone angle depending on which time-step is analyzed.

However, by using the same scale (0.0 m/s to 2.0 m/s) to show the results of both models, it clearly appears that the absolute air speed values generated by the two modeling approaches are considerably different, the values obtained with the detailed model being significantly lower in almost all regions of the flow. This difference is particularly evident in the region below the fan in which the highest values are expected. On the other hand, there are no regions or other qualitative aspects of the flow that seem to be better captured by the detailed model.

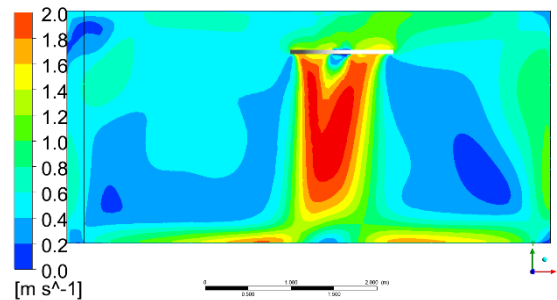


Fig. 4 – Air speed distribution - model without blades (scale from 0.0 m/s to 2.0 m/s)

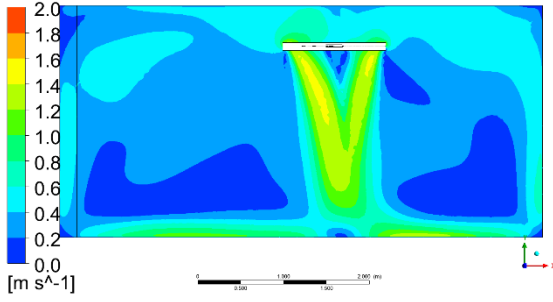


Fig. 5 – Air speed distribution - model with blades (scale from 0.0 m/s to 2.0 m/s)

3.2 Air Speed Values

Comparing the air speed values calculated by the two models and the measured values taken from previous studies (Babich et al., 2017b), in all 36 points the figures of the detailed model are considerably below the predictions of the implicit model (Fig. 6). Moreover, in most points, the output of the model without blades is much closer to the measured values than the predictions of the model with blades.

At the two higher levels (130 cm and 70 cm above the floor), the trend is very similar. Below the center of the fan and in the other points located in the region below the blades (r200 and r500), the air velocity obtained with the detailed model is approximately half the values generated by the implicit model, and the latter are usually in good agreement with measured values. Only in one (point r200 at 130 cm height) does the model without blades also underestimate the air speed, but it is still considerably closer to the measured value.

Focusing on the points that are more distant from the fan (r800 to r2000, i.e., 80 cm to 200 cm away from the fan rotational axis), air speed values are typically below 0.5 m/s, but even in this region the model with blades outperformed the one with blades by providing results that are closer the measurements.

Only in the points placed under the perimeter of the ceiling fan (which are r600, north, west, south and east) the trend is less clear. Both models show limited capability of capturing this region, which is characterized by rapid air speed variations. For the model without blades, this was already noted when it was originally developed (Babich et al., 2017b). On the other hand, modeling the blades did not lead to any noticeable improvement in this region of the flow.

At the lowest level (10 cm above the floor), the model without blades consistently underestimated the air speed values at all 12 points, and in none of them it proved to be superior to the model without blades.

Thus, overall, the model with blades did not lead to better results in any of the regions of the air flow, being considerably less accurate (i.e., less close to measured values) than the implicit model.

3.3 Computational Effort

The computational effort required to complete the simulations is considerably different (Table 1). Using exactly the same workstation and hardware-related settings, the total clock time of the model with blades is one order of magnitude higher than the total clock time of the model without blades. While the former simulation was completed in less than 4 hours, the latter required nearly 9 days.

Table 1 – Computational time

Model	Total clock time	Total clock time
Without blades	1.354e+04 s	3h 45m 40s
With blades	7.643e+05 s	8d 20h 18m 20s

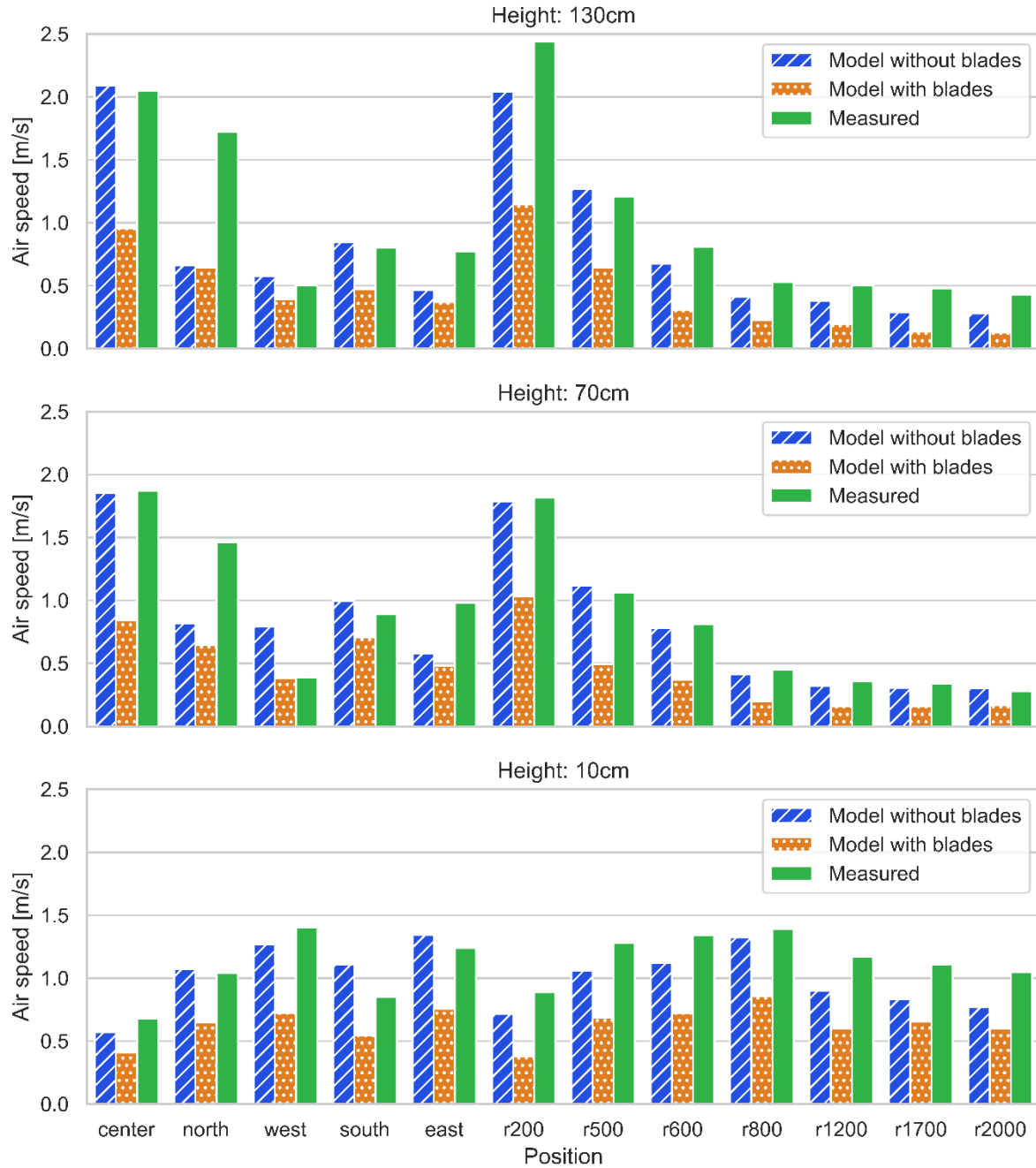


Fig. 6 – Simulated (60 s average) and measured (Babich et al., 2017b) air speed values

4. Discussion

The results of this study showed how the model without blades in which the ceiling fan is implicitly modeled by applying a body force to a cylinder provided more accurate air speed values in less than a tenth of the time, while qualitatively capturing all the main regions of the air flow. Thus, in this study, this modeling approach proved to be superior to a

more detailed approach by all aspects. Since the implicit model had previously been fully validated based on experimental data (Babich et al., 2017b), it was expected to be accurate. However, the considerably lower accuracy of the model with blades was less predictable. Therefore, questions arise as to why this happened, and if and when using a model with blades might be the best solution.

In this study, several key parameters were identical in both models. Both used the SST $k-\omega$ turbulence mode. For the implicit model, previous studies (Babich et al., 2017b) showed that this turbulence model led to the best agreement with measured values by testing several Reynolds Averaged Navier-Stokes (RANS) turbulence models. For the model with blades, although some tests could be performed, there are no evident reasons to think that the use of a different RANS model, such as the widely used Re-Normalisation Group (RNG) $k-\epsilon$, might significantly change the results. It might be also possible to explore the usability of other approaches to simulate the turbulence, such as large eddy simulation (LES). While the benefit (intended as better results) should be assessed, an increase in the computational time and in the set-up time would be certain.

Moreover, in both modeling approaches, an adaptive time step was set by using the same target, which is RMS Courant number equal to 5. For the turbulence model, also in this case there is no reason to assume that using a stricter target would considerably affect the results of the model with blades. However, the likelihood of a considerable increase in the computational time would be very high.

Focusing on the model with blades, the elements that are therefore more likely to explain the poor performances are the geometry of the fan, its meshing, and the interface between the two domains (rotating and stationary).

While in the implicit model the geometry is largely simplified (only dimensions of the total and central motor diameters are required), a considerably larger number of geometrical parameters are needed when the blades are modeled. If a computer-aided drafting (CAD) file is made available by the fan manufacturer, then the main effort is usually the cleaning of the geometry to remove all those small details that are required for production, but not CFD simulations, since they would be likely to increase the number of mesh elements and therefore also the computational time. However, an oversimplification might lead to inaccurate results.

On the other hand, if a CAD file is not made available, the geometry must be created by the modeler starting from the measurement taken on the actual fan. In this case, the accurate representation of the blades is usually the most difficult and time-consuming part (es-

pecially when there are multiple curvatures and variations of the profile). This is the approach used in this study. Further details could be added to try to improve the model predictions, but this is likely to increase the computational time, too.

Likewise, the use of a finer mesh in the rotating part might enhance the results. In this study, the minimum size of the surface mesh (on the fan surface) was 8 mm. This can be further reduced, and the overall meshing approach investigated in more detail. However, also in this case the computational time is likely to grow.

Focusing on the interface between the two domains, different settings might be evaluated, such as using three separate interfaces for the cylinder that encapsulates the fan to enable its rotation (upper circle, lower circle, and vertical side – Fig. 3). However, there are no evident reasons to expect considerably better results due to a change in the modeling of the domain interface only (ANSYS 2015).

Thus, fan geometry and meshing are likely to be the two most critical issues to be addressed to improve the capabilities of the model with blades. Although this study showed the higher accuracy and lower computational cost of an implicit ceiling fan model, its main limitation is the fact that each rotational speed requires different values for the momentum source, and the definition of the most appropriate values needs experimental data. The outcome might be a discrete set of momentum values (particularly useful for fans with a finite number of rotational speed levels) or a function that calculates the momentum values for any given rotational speed (more appropriate when direct current – DC – motors are used). On the other hand, an explicit CFD model of a ceiling fan uses the rotational speed as an input and therefore would not need experimental validation for multiple rotational speeds.

Thus, the main open question is whether it was better to develop an implicit model (the main effort is the creation of the experimental data) or to opt for an explicit model with blades (the main effort is on geometry and mesh implementation, and then on computational power). Assuming that measurements for different rotational speeds could be taken in one or two days, then the implicit model appears to be the best choice in most cases. However, especially if energy consumption for computing is not

considered, this might not be always the case (e.g., if a considerably high computational power such as a high-performance computing -HPC- cluster with hundreds of cores is available).

5. Conclusion

Ceiling fans are an effective means of completely avoiding the use of energy-intensive air conditioning systems in milder environmental conditions, and for reducing their usage in more severe and hotter thermal environments. CFD can be used to predict the air flow generated by ceiling fans, and therefore to better evaluate their capability of delivering comfort cooling.

The aim of this study was to compare the results obtained by using two approaches to include the ceiling fan into a CFD model, namely a detailed model of the geometry of the fan and a simplified implicit approach that emulates the effect of the fan only. The main findings of this study are as follows.

- both modeling approaches capture the key qualitative features of the air flow generated by a ceiling fan, and no relevant difference was noted.
- comparing the air speed values calculated by the two models and the measured values, the implicit model proved to be considerably more accurate. Especially in the regions of the flow in which the most elevated air speeds occur (such as below the fan), the measured figures and the values predicted by the implicit model were close, while the values obtained by the detailed model were much lower (half on the others in several points).
- using exactly the same workstation and hardware-related settings, the total clock time of the model with blades is one order of magnitude higher than the total clock time of the model without blades (less than 4 hours as opposed to nearly 9 days).
- fan geometry and meshing are likely to be the two most critical issues to be addressed to improve the capabilities of the model with blades. However, the use of a more detailed geometry and finer mesh would increase the computational time (and related energy consumption).
- the implicit model appears to be the best choice in most cases.

Considering that the main limitation of the implicit model is the fact that each rotational speed requires different values for the momentum source, and the definition of the most appropriate values needs experimental data, further work will focus on the geometry and meshing of the fan in the explicit model (in which the rotational speed is directly set).

Acknowledgement

The research presented in this paper was performed within H2020 Cultural-E project, which received funding from the European Union's Horizon 2020 research and innovation programme under grant agreement N. 870072.

References

- ANSYS. 2015. "CFX Solver Theory Guide." Canonsburg, PA, USA.
- Babich, F., M. Cook, D. Loveday, R. Rawal, and Y. Shukla. 2017a. "A New Methodological Approach for Estimating Energy Savings Due to Air Movement in Mixed Mode Buildings." In IBPSA.
- Babich, F., M. Cook, D. Loveday, R. Rawal, and Y. Shukla. 2017b. "Transient Three-Dimensional CFD Modelling of Ceiling Fans." *Building and Environment* 123: 37–49. doi: <https://doi.org/10.1016/j.buildenv.2017.06.039>
- Babich, F., W. Pasut, and A. Belleri. 2021. "The Use of Ceiling Fans in Reverse- Flow Mode for Comfort Cooling: Physiological Aspects and Relationship with International Standards." *ASHRAE Transactions* 127(2).
- Jain, A., R. R. Upadhyay, S. Chandra, M. Saini, and S. Kale. 2004. "Experimental Investigation of the Flow Field of a Ceiling Fan." In *Proceedings of the ASME Heat Transfer/Fluids Engineering Summer Conference* 2004, HT/FED 2004, 3:93–99. American Society of Mechanical Engineers. doi: <https://doi.org/10.1115/ht-fed2004-56226>
- Pasut, W., E. Arens, H. Zhang, and Y. Zhai. 2014. "Enabling Energy-Efficient Approaches to

- Thermal Comfort Using Room Air Motion." *Building and Environment* 79: 13–19. doi: <https://doi.org/10.1016/j.buildenv.2014.04.024>
- Schiavon, S., and A. K. Melikov. 2008. "Energy Saving and Improved Comfort by Increased Air Movement." *Energy and Buildings* 40(10): 1954–60. doi: <https://doi.org/10.1016/j.enbuild.2008.05.001>
- Wang, H., H. Zhang, X. Hu, M. Luo, G. Wang, X. Li, and Y. Zhu. 2019. "Measurement of Airflow Pattern Induced by Ceiling Fan with Quad-View Colour Sequence Particle Streak Velocimetry." *Building and Environment* 152: 122–34. doi: <https://doi.org/10.1016/j.buildenv.2019.02.015>

Intelligibility Prediction in Scholar Classrooms

Samantha Di Loreto – Università Politecnica delle Marche, Italy – s.diloreto@pm.univpm.it

Fabio Serpilli – Università Politecnica delle Marche, Italy – f.serpilli@univpm.it

Valter Lori – Università Politecnica delle Marche, Italy – v.lori@univpm.it

Costanzo Di Perna – Università Politecnica delle Marche, Italy – c.diperna@univpm.it

Abstract

In recent Italian Law, the DM 11/01/2017 about Environmental criteria, reference values for the acoustic indoor quality descriptors of public buildings are imposed. These reference values are in compliance with the national standards UNI 11532-1 and UNI 11532-2. Part two of the series standard, in particular, describes the procedures and gives limit values for the acoustic comfort descriptors for schools. Regarding schools, adequate acoustic comfort targets are required in terms of indoor noise level and acoustic quality. Indoor acoustic quality targets refer to reverberation time (RT), Clarity (C50) and/or speech intelligibility (STI). The limit values for these indoor acoustic quality parameters, established by the national standards, are related to the measurement methods results; however, it is necessary to use prediction methods to estimate these parameters during the design phase. The aim of this study is to verify the prediction method accuracy used to determine intelligibility score. The study was developed to model the existing calculation method of speech transmission index (STI) in Matlab software to determine the acoustic speech intelligibility in school classrooms. A school building located in central Italy, in the Marche Region, was taken as a case study. This research aims to determine a correlation factor between the results of predictions and measurement speech intelligibility methods.

1. Introduction

The theme of the acoustic comfort (ambient noise, sound insulation, reverberation time, speech intelligibility) in primary school classrooms, in secondary school classrooms, as well as in university classrooms, has been the focus of several studies all around the world (Sala & Viljanen, 1995; Zannin et al., 2009). High noise levels in classrooms cause students to tire early,

their cognitive abilities to decline, and they do not understand the content of the lessons. Excessive noise, too high reverberation, or the combined presence of both these effects in a classroom could reduce speech intelligibility, which is defined as the percentage of a message understood correctly.

The standard UNI EN ISO 9921 (UNI, 2004) specifies the requirements for the performance of speech communication and recommends the level of speech communication quality required for conveying comprehensive messages in several case studies. In (Pickett, 2005) many measurements of the intelligibility of speech were made to calculate the disturbance produced by different amounts of vocal force. The results of this case study show less than 5 % deterioration in intelligibility over the range, from a moderately low voice to a very loud voice (55 to 78 dB in a free field at one m from the lips). Other studies (Bradley et al., 1999; Yang & Bradley, 2009; Yang & Mak, 2018) have shown that speech intelligibility is influenced by reverberation time (RT), as well as by signal-to-noise ratios (SNR).

In (Choi, 2020), speech intelligibility tests were carried out in 12 university classrooms in Korea; the test results indicate that young adult listeners at university have a mean score of 95 % correct at a signal-to-noise ratio (SNR) value of +3 dB(A), which is a considerably lower SNR value than for the younger students in elementary schools. As a result, much attention to the development of effective objective indicators of quality and/or intelligibility are of particular interest, the measured parameters include reverberation time, early decay times, energy ratios, and STI values. The STI is a physical metric related to the intelligibility of speech degraded by additive noise and reverberation (Goldsworthy et al., 2004). Scientists nowadays consider the STI to be the parameter that best reflects the

intelligibility of speech (in a sound transmission system) (Steeneken & Houtgast, 1980). Consequently, the STI measure correlates well with subjective intelligibility scores for stimuli distorted by linear filtering, reverberation, and additive noise. Experiments in literature evaluate the effectiveness of the prevision method at predicting speech intelligibility.

In (Peters, 2020) the potential binaural effect of reducing reflection and reverberation was studied. These conditions create a reduction in intelligibility because echoes and strong discrete reflections, arriving late, lead directly to a wrong assessment when using the STI. Similarly, in (Schwerin & Paliwal, 2014) the STI approach was revisited and a variation was proposed which processes the modulation envelope in short-time segments, requiring only an assumption of quasi-stationarity (rather than the stationarity assumption of STI) of the modulation signal. Based on the tests in (Hongshan et al., 2020), the corresponding relation between STI and speech intelligibility in large spaces was modified, and a new rating threshold of STI was also proposed.

This paper aims to determine a correlation factor between the results of prediction and measurement speech intelligibility methods. The study was developed to model the existing calculation method of speech transmission index (STI) to determine the acoustic speech intelligibility in some classrooms at the Faculty of Engineering of the Università Politecnica delle Marche, Italy.

In this work, two sections are included. In the first, STI values are evaluated and calculated with the calculation method described in the annex L of BS EN 60268-16 (BSI, 2020). In the second, the result of the simulations is compared to the objective intelligibility measures in the same classes.

2. Material And Methods

2.1 Reference Values For Speech Transmission Index (STI)

The STI aims to objectively quantify speech intelligibility at a specific location in one environment when speech is produced through a normalized signal at another specific location in the same environment.

The STI index is based on the measurement of the Modulation Transfer Function (MTF). MTF quantifies the reduction in the modulation index of a test signal, de-

pending on the modulation frequency. For each modulation frequency, the MTF is determined by the ratio between the modulation index of the signal at the listener, m_0 , and the modulation index of the test signal, m_i . A family of MTF curves is determined, in which each curve is relative to each octave band of speech emission and is defined by the values that the modulation index reduction factor m assumes for each modulation frequency present in the envelope of a natural speech signal. For the STI index measurement, 7 octave bands, from 125 Hz to 8 kHz, and 14 modulation frequencies, between 0.63 Hz and 12.5 Hz at one-third octave intervals, are considered. The 98 (7×14) *m-values* are finally summarized in a single index, the STI, varying between 0 and 1, which represents the effect of the transmission system on intelligibility.

The STI quantifies the combined effect of background noise interference and reverberation on speech intelligibility reduction, with or without sound amplification systems.

The UNI EN ISO 9921 standard (UNI, 2004) establishes a relationship between STI value and their subjective assessment in terms of intelligibility for a normally hearing user. The values are shown in Table 1:

Table 1 – Relation between STI and Speech Intelligibility according to UNI EN ISO 9921:2004, Table F.1

Intelligibility rating	Sentence score %	STI
Excellent	100	> 0.75
Good	100	0.60 to 0.75
Fair	100	0.45 to 0.60
Poor	70 to 100	0.30 to 0.45
Bad	< 70	< 0.30

Another classification of speech intelligibility is provided in of BS EN 60268-16 (BSI, 2020); the standard defines qualification intervals for the levels of STI obtained, as shown in the following Fig. 1. The typical STI requirements for dedicated applications are also provided in Fig. 2.

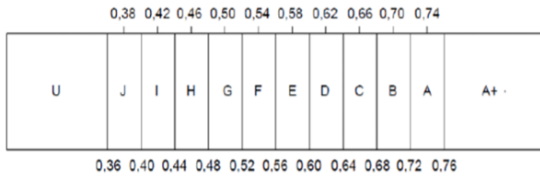


Fig. 1 – Qualification intervals for STI levels

Category	Nominal STI value	Type of message information	Examples of typical uses (for natural or reproduced voice)	Comment
A+	>0.76		Recording studios	Excellent intelligibility but rarely achievable in most environments
A	0.74	Complex messages, unfamiliar words	Theatres, speech auditoria, parliaments, courts, Assistive Hearing Systems (AHS)	High speech intelligibility
B	0.7	Complex messages, unfamiliar words		
C	0.66	Complex messages, unfamiliar words	Theatres, speech auditoria, teleconferencing, parliaments, courts	High speech intelligibility
D	0.62	Complex messages, familiar words	Lecture theatres, classrooms, concert halls	Good speech intelligibility
E	0.58	Complex messages, familiar context	Concert halls, modern churches	High quality PA systems
F	0.54	Complex messages, familiar context	PA systems in shopping malls, public buildings' offices, VA systems, cathedrals	Good quality PA systems
G	0.5	Complex messages, familiar context	Shopping malls, public buildings' offices, VA systems	Target value for VA systems
H	0.46	Simple messages, familiar words	VA and PA systems in difficult acoustic environments	Normal lower limit for VA systems
I	0.42	Simple messages, familiar context	VA and PA systems in very difficult spaces	
J	0.38		Not suitable for PA systems	
U	<0.36		Not suitable for PA systems	

Fig. 2 – Value for STI qualification bands and typical applications

There are two measurement methods for STI: the direct and indirect method. The direct method uses modulated (speech-like) test signals to directly measure the modulation transfer function. Typically modified Pink Noise with modulation frequencies was used. In this case, the measurement signal is either applied as an electric input to the system or through a “human speaker” loudspeaker to a microphone. The indirect method uses impulse response and forward energy integration (Schroeder integral) to derive the modulation transfer function. STI can be measured at the same time as other room acoustic parameters. This means that speech intelligibility will normally be measured using an omnidirectional speaker.

2.2 Room Descriptions and Measurements

The university building is in a suburban area of Ancona city, away from road traffic and other environmental noise sources. In addition, the classrooms are located at the rear of the building in relation to the access road. The external SPL during the daytime period is between 45 and 55 dB(A).

For the assessment of speech intelligibility, the AT2 classroom, belonging to the Engineering Faculty of the Marche Polytechnic University, was chosen as a case study. Classroom AT2 has a volume of 378 m³, an average height of 3 m and a base area of 126 m².

The classroom has a sound-absorbing acoustic ceiling,

wooden chairs, and tables. The windowed surface occupies 1/3 of the total surface of the concrete perimeter walls. Fig. 3 shows AT2 classroom, and the measurement positions, as required by UNI 11532-2 (UNI, 2020).

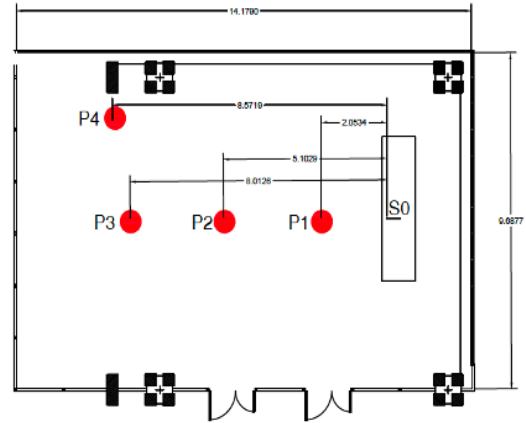


Fig. 3 – Plan of classroom AT2

The measurements in the classroom were done at four measurement points, chosen in compliance with UNI 11532 standard. Three positions were selected along the imaginary line traced on the longitudinal axis of the classroom, between the sound source and the back of the classroom, and a position was selected as representative of the most unfavorable listening condition (due to background noise, distance from the speaker, etc.). The STI measurements were derived from the impulse response measures and background noise measures with the indirect methodology proposed by BS EN 60268-16 (BSI, 2020).

Table 3 shows the results of STI for each measurement point and the STI mean value, without and with measurement uncertainty.

Table 3 – Value of STI for single point of measure, STI mean and STI mean with measurement uncertainty

STI (P1)	STI (P2)	STI (P3)	STI (P4)	STI mean
0.61	0.60	0.58	0.56	0.56
STI mean with measurement uncertainty		Speech quality in accordance with CEI EN 60268-16		
0.53		FAIR		

3. STI Prediction Using Indirect Method

Prediction of the STI of a sound system may be based on the MTF matrix that is calculated from the predicted room acoustic and electro-acoustic parameters and from the measured or estimated background noise levels, for each octave band contributing to the STI version chosen. The STI measure uses artificial signals (e.g., sinewave-modulated signals) as probe signals to assess the reduction in signal modulation in several frequency bands and for a range of modulation frequencies (0.6–12.5 Hz).

As requested in the reference standard, the speech spectrum at 1 meter in front of the mouth of a male speaker with the ambient noise spectrum reported in the Table H.1 of UNI EN ISO 9921:2004, see Table 4 and Table 5 was concatenated.

Table 4 – Speech spectrum at 1m in front of the mouth of a male speaker to UNI EN ISO 9921:2004, Table H.2

Octave band (Hz)	125	250	500	1000	2000	4000	8000
SPL@1m (dB)	62.9	62.9	59.2	53.2	47.2	41.2	35.2

Table 5 – Ambient noise spectrum according to UNI EN ISO 9921:2004, Table H.1

Octave band (Hz)	125	250	500	1000	2000	4000	8000
SPL@1m (dB)	41	43	50	53,2	47	42	39

The STI was calculated based on modulation transfer function (MTF) and the calculations used the method of Houtgast and Steeneken (1973).

In (UNI, 2020) for the calculation of the STI in classrooms without amplification system and with volumes > 250 m³, an emission signal at 1m in axis to the source equal to 70 dB is required. So, for the calculation of the predictive STI, the reference signal of the speech was increased by 10 dB.

The modulation transfer function of the transmission path may be quantified by comparing the ratio of the modulation depth at the output and input of the test signal, and it was written as Eq. (1):

$$m(fm) = \frac{|\int_0^\infty h(t)^2 e^{-j2\pi fm t} dt|}{\int_0^\infty h(t)^2 dt} \cdot [1 + 10^{\frac{SNR}{10}}]^{-1} \quad (1)$$

where:

- $m(fm)$ is the modulation transfer function of the transmission channel

- $h(t)$ is the impulse response of the transmission channel

- SNR is the signal-to-noise ratio in dB

Considering a diffuse reverberant field, the impulse response was written as Eq. (2):

$$h(t) = \frac{Q}{r^2} \cdot \delta(t) + \frac{13,8 Q}{r^2 T} e^{-\frac{13,8 t}{T}} \quad (2)$$

where:

- Q is the directivity factor for the sound source (talker)

- r is the talker-to-listener distance

- T is the reverberation time of the room space

The reverberation time was calculated with the method described in UNI EN 12354-6 (UNI, 2006), starting from the acoustic absorption of the room. The impulse response of the classroom was calculated in the four different positions of the room.

The standard UNI 11532-2:2020 in Paragraph 4.5 defines an optimal reverberation time, T_{ott} , corresponding with a conventional occupation of the environment equal to 80 % for categories A1, A2, A3, A4. The categories of the environment, in relation to the destined use, are reported in Table 6.

Table 6 – Categories of the environment in relation to the destined use according to UNI 11532-2:2020

CATEGORY	Activities in the environment	Methods of intervention
A1	Music	
A2	Spoken / conference	Objective achieved with integrated design of geometry, furniture, residual noise control
A3	Lesson / communication as speech and lecture	
A4	Special classroom lecture / communication	
A5	Sport	
A6	Areas and spaces not intended for learning and libraries	Objective achieved with sound absorption and residual noise control

The reference values for optimal reverberation time for A1-A4 categories are reported in Table 7.

Table 7 – Categories of the occupied environment in relation to the destined use according to UNI 11532-2:2020

CATEGORY	Occupied environment 80 %
A1	$T_{ott} = (0.45\text{Log}(V) + 0.07)$ ($30 \text{ m}^3 < V < 1000 \text{ m}^3$)
A2	$T_{ott} = (0.37\text{Log}(V) - 0.14)$ ($50 \text{ m}^3 < V < 5000 \text{ m}^3$)
A3	$T_{ott} = (0.32\text{Log}(V) - 0.17)$ ($30 \text{ m}^3 < V < 5000 \text{ m}^3$)
A4	$T_{ott} = (0.26\text{Log}(V) - 0.14)$ ($30 \text{ m}^3 < V < 500 \text{ m}^3$)

In Fig. 4, the graph of the simulated reverberation time vs measured reverberation time, for a conventional occupation of the environment equal to 80 %, is reported.

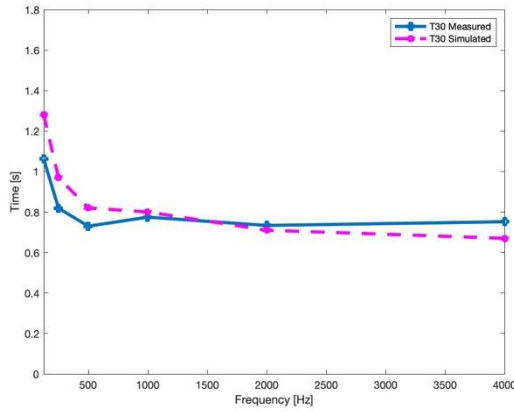


Fig. 4 – Reverberation time value in the octave bands between 125 Hz and 4000 Hz simulated (empty room) and measured

A constant MTF over the modulation frequencies indicates that speech intelligibility is mainly determined by background noise. A continuously decreasing MTF indicates an important influence of the reverberation and an MTF that decreases first and then increases again indicates the presence of an echo. Fig. 5 shows the result of the simulation of the modulation transfer function in the 7 octave bands calculated for P1.

The STI index can be finally obtained by using the weighted average method for the modulation transmission index on the considered octave bands Eq. (3):

$$STI = \sum_{k=1}^7 (a_k \times MTI_k) - \sum_{k=1}^6 \beta_k \times (MTI_k \times MTI_{k+1})^{1/2} \quad (3)$$

Where:

- α_k is the weight coefficient of octave band f_m
- β_k is the redundancy factor between octave band k and octave band $k + 1$.

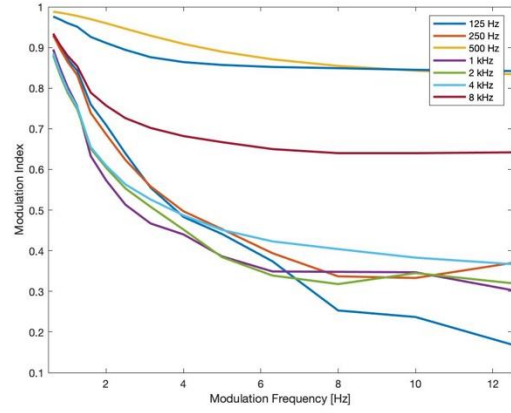


Fig. 5 – Modulation transmission ratio in the 7 octave bands

Table 8 shows the relationship between α_k , β_k and MTI_k to determine the STI for P1.

Table 8 – Result of the calculation for the P1

Frequency [Hz]	125	250	500	1000	2000	4000	8000
α_k male	0.085	0.127	0.230	0.233	0.309	0.224	0.173
Combined							
$MTI_k \times \alpha_k$	0.054	0.090	0.163	0.157	0.207	0.118	0.071
weighting							
β_k male	0.085	0.078	0.065	0.011	0.047	0.095	0.000
Combined							
$MTI_k \times \beta_k$	0.054	0.055	0.046	0.007	0.032	0.005	0.000
weighting							
sum α_k *	0.860						
MTI_k							
sum β_k *	0.244						
MTI_k							
STI (P1)	0.62						

The same calculation was carried out for all the positions and the STI simulation results are shown in Table 9.

Table 9 – Results of the calculation of STI for P1, P2, P3 P4 and STI mean

STI (P1)	STI (P2)	STI (P3)	STI (P4)	STI mean
0.62	0.55	0.53	0.53	0.55
STI mean with meas- urement uncertainty		Speech quality in accordance with CEI EN 60268-16		
0.53		FAIR		

4. Results

From the comparison between the results of STI obtained between measured and simulated values, it can be seen that the difference is very low. This attests that the predictive model turns out to be very effective to

ensure a good internal quality of the classrooms during the design phase.

In particular, the STI mean, simulated and measured, is equal and, in both cases, speech intelligibility is FAIR in accordance with the reference standard.

Considering the results of simulations and according to the background literature, a statistical analysis for the case study was carried out.

The proposed correlation model between the measurements of STI versus the simulations of STI is based on a polynomial function, according to the following Eq. 4.

$$y = ax^3 + bx^2 + cx + d \quad (4)$$

where y is the response variable and a, b, c, d represents partial correlation coefficients (coefficients with 95 % confidence bound).

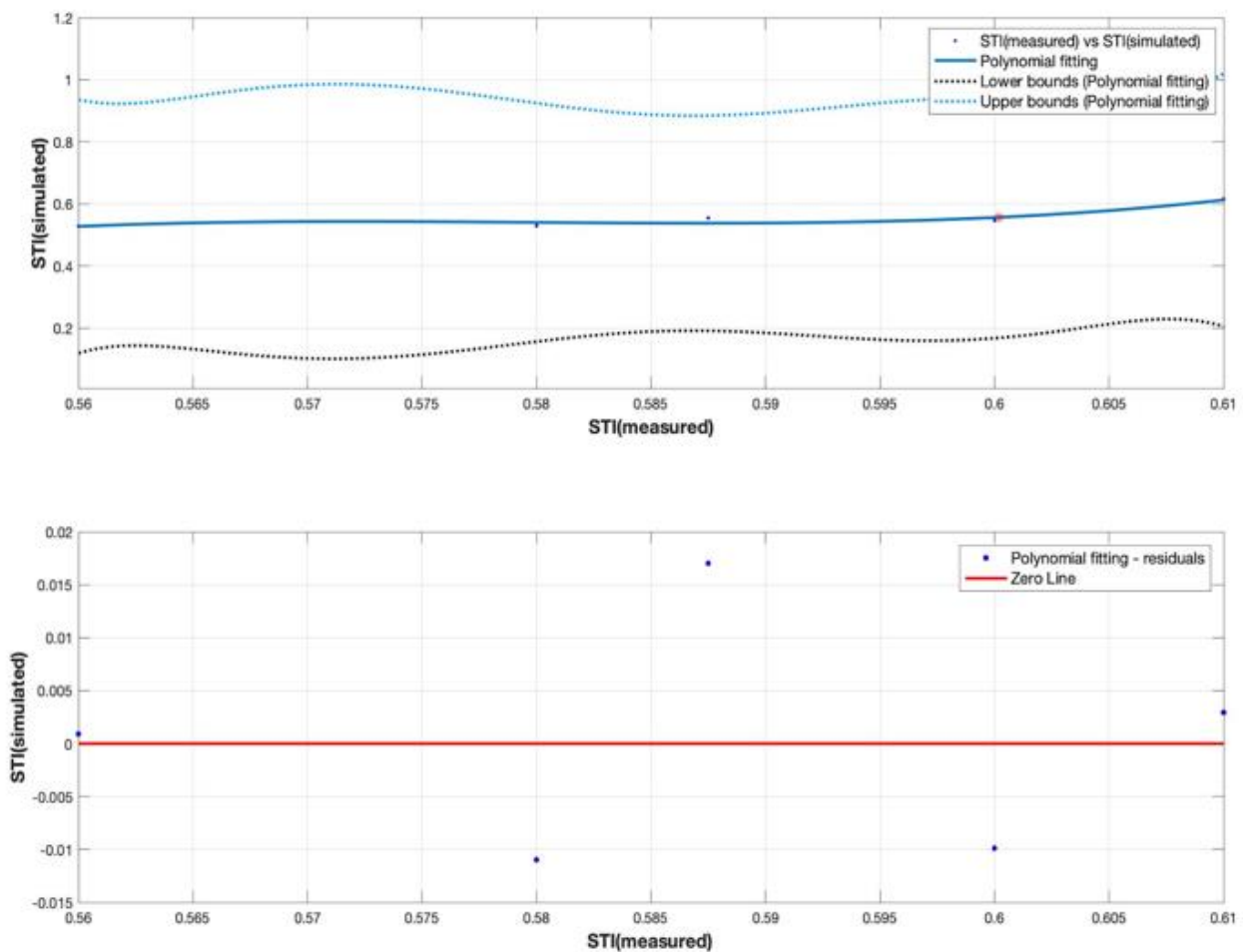
Fig. 6 – Best fit polynomial curve and residuals of the STI_m vs STI_p considered for each point of measure

Table 10 – Results of the polynomial regression

DFE	SSE	R ²	R	RMSE
1	5.18	0.89	0.60	0.02

The result of the correlation shows the statistical significance is indicated by the $R^2 = 0.89$ and this represents a good correlation between the variables (Fig. 6; Table 10).

5. Conclusions

This paper systematically provides the flow of STI indirect test method specified in BS EN 60268-16 and introduces in detail the calculation formula involved in the indirect method, with reference to Schroeder's Frequency analysis and therefore to the limits of validity of the sound equations of classical theory, associated with the simulation of the room.

The study highlighted that the one of the major problems when developing this type of prediction is represented by the error generated by a low signal-to-noise ratio. Therefore, the choice of the speech spectrum, as well as the residual noise setting, represents an important choice in order for overestimation errors of the STI not to be incurred.

Although the standard is clear in recommending standard spectra, a possible solution could be to simulate the environment impulse response using a commercial room acoustic software and enter, in the input phase, an environmental noise that could be representative of the acoustic scene of the room.

Nomenclature

Symbols

STI	Speech transmission index
IS	Intelligibility score
MTF	Modulation transfer function
SPL	Sound pressure level
STI _m	Speech transmission index (measured)
STI _p	Speech transmission index (predicted)

References

- Bradley, J. S., R. Reich, and S. G. Norcross. 1999. "On the combined effects of signal-to-noise ratio and room acoustics on speech intelligibility." *The Journal of the Acoustical Society of America* 106: 1820.
- BSI. 2020. BS EN 60268-16:2020. Sound system equipment - Objective rating of speech intelligibility by speech transmission index.
- Choi, Y.-J. 2020. "The intelligibility of speech in university classrooms during lectures." *Applied Acoustics* 162: 107211.
doi: <https://doi.org/10.1016/j.apacoust.2020.107211>
- Goldsworthy, R. L., and J. E. Greenberg. 2004. "Analysis of speech-based speech transmission index methods with implications for nonlinear operations." *The Journal of the Acoustical Society of America* 116: 3679.
- Hongshan, L., H. Ma, J. Kang, C. Wang. 2020. "The speech intelligibility and applicability of the speech transmission index in large spaces." *Applied Acoustics* 167: 107400. doi: <https://doi.org/10.1016/j.apacoust.2020.107400>
- Houtgast, T., and H. J. M. Steeneken. 1973. "The Modulation Transfer Function in Room Acoustics as a Predictor of Speech Intelligibility." *Acta Acustica united with Acustica*: 66-73.
- Peters, R. 2020. *Uncertainty in Acoustics*. Boca Raton: CRC Press.
- Pickett, J. M. 2005. "Effects of Vocal Force on the Intelligibility of Speech Sounds." *The Journal of the Acoustical Society of America* 28(902): 1956.
- Sala, E., and V. Viljanen. 1995. "Improvement of acoustic conditions for speech communication in classrooms." *Applied Acoustic* 45: 81-91. doi: [https://doi.org/10.1016/0003-682X\(94\)00035-T](https://doi.org/10.1016/0003-682X(94)00035-T)
- Schwerin, B., and K. Paliwal. 2014. "An improved speech transmission index for intelligibility prediction." *Speech Communication* 65: 9-19. doi: <https://doi.org/10.1016/j.specom.2014.05.003>
- Steeneken, H., and T. Houtgast. 1980. "A review of the MTF concept in room acoustics and its use for estimating speech intelligibility in auditoria." *The Journal of the Acoustical Society of America* 318-326.
- UNI. 2004. EN ISO 9921:2004. Assessments of speech communication.
- UNI. 2006. EN ISO 12354-6:2006. Building Acoustics - Estimation of acoustic performance of buildings from the performance of elements - Part 6: Sound absorption in enclosed spaces.

- UNI. 2020. UNI 11532-2:2020. Internal acoustical characteristics of confined spaces - Design methods and evaluation techniques - Part 2: Educational sector.
- Yang, D., and C. M. Mak. 2018. "An investigation of speech intelligibility for second language students in classrooms." *Applied Acoustic* 134: 54-149. doi: <https://doi.org/10.1016/j.apacoust.2018.01.003>
- Yang, W. Y., and J. S. Bradley. 2009. "Effects of room acoustics on the intelligibility of speech in classrooms for young children." *The Journal of the Acoustical Society of America* 125: 922-933.
- Zannin, P. H. T., D. Petri, and Z. Zwirnes. 2009. "Evaluation of the acoustic performance of classrooms in public schools." *Applied Acoustics* 70: 626-635. doi: <https://doi.org/10.1016/j.apacoust.2008.06.007>

Hybrid Heat Pump Systems: Is Predictive Control Worth Using?

Patricia Ercoli – Università Politecnica delle Marche, Italy – p.ercoli@pm.univpm.it

Alice Mugnini – Università Politecnica delle Marche, Italy – a.mugnini@univpm.it

Fabio Polonara – Università Politecnica delle Marche, Italy – f.polonara@univpm.it

Alessia Arteconi – Università Politecnica delle Marche, Italy; & KU Leuven, Belgium – a.artecni@univpm.it

Abstract

One of the possible solutions for renovating building heating systems is the use of hybrid systems, which consists of coupling heat pumps with traditional natural gas boilers. Hybrid Heat Pump systems are typically controlled to run the heat pump when the outside temperature is not too low, maintaining acceptable costs and good energy efficiency levels. However, when buildings also have a certain level of thermal inertia, proper management of the hybrid system can allow some flexibility. Especially in presence of non-programmable renewable sources, the control strategy can play an important role to maximize self-consumption.

The aim of this work is to assess the role of the control strategy in achieving this objective in relation to the cost reduction potential for energy bills. In particular, we investigate how much it is worth using an advanced control technique (e.g., a Model Predictive Control) compared to a Ruled Based Control to regulate the hybrid heating system of a residential building. The paper analyses a case study in which a building, equipped with Hybrid Heat Pump system assisted by photovoltaic panels serving a radiant floor, is controlled both through a Model Predictive and a designed Ruled Based Control. The objective of the controls is to minimize the energy bill for heating. The results are intended to assess whether the added complexity of the best performing model predictive control is justified by the magnitude of the performance increase that is obtained.

1. Introduction

In recent years, Heat Pumps (HPs) have seen an increase in their use in residential buildings. According to the International Energy Agency (IEA, 2021), as of 2015, there has been an upward trend in

HP sales within the European market, with an average annual growth rate of 12 %.

In the context of energy transition, HPs can offer a good solution for reducing energy consumption, as they give the possibility of using renewable energy sources such as aerothermal, geothermal and hydrothermal (Madonna et al., 2013), in addition to producing thermal energy through electricity (coming from the grid or produced on site).

The capability to correlate the thermal demand to electricity consumption is one of the most interesting aspects of HPs for unlocking the energy flexibility in buildings: the different levels of thermal inertia, which are already contained in buildings (thermal mass of the envelope or thermal storage devices), can be exploited to provide flexibility to the electricity grid.

One of the most frequently adopted solutions for exploiting the advantages of HPs, while maintaining acceptable costs and good levels of energy efficiency, are hybrid systems. In a Hybrid Heat Pump (HHP) system, the heat demand of the building is met by a HP coupled with a traditional boiler (EHI, 2020). This system is particularly useful in the presence of air-source HPs, since their performance depends heavily on the external climatic conditions. Although most HPs are installed in new constructions (IEA, 2021), hybrid systems present a good solution for home renovations (Dongellini et al., 2021). Indeed, in Italy, where the building stock is rather dated, the market of HHPs is one of the largest in the European Union, with about 7000 units sold in 2018 (EHI, 2020).

As for HP systems, a fundamental role is played by the control technique adopted also in HHP systems. To activate energy flexibility and optimize the ma-

nagement of sources, Model Predictive Controls (MPCs) are widespread. MPCs refer to an optimization problem to select the optimal set of control actions to minimize a given objective function at each time step.

There are many works available in the literature on the evaluation of the effectiveness of a MPC compared to a simpler Rule Based Control (RBC) for HPs. Fischer et al. (Fischer et al., 2017) have compared five different control methods, aimed at considering cases where the cost of electricity is constant, variable or cost-free in order to exploit self-consumption in a multi-family house equipped with an air-source HP supported by Photovoltaic (PV) panels and coupled to storage for domestic hot water. According to the authors, MPCs are more efficient than RBCs, with cost reductions of 6–16 % and 2–4 %, respectively. Zanetti et al. (2020) modeled an HHP, consisting of an air-to-water unit and a gas-fire boiler, assisted by PV panels and coupled to a water tank, serving a school supplied with floor heating. Comparing an RBC with an optimal control, from a thermal comfort point of view, the two controls provide similar results; regarding energy costs, the optimal control performs better as it allows savings of up to 20 % with an increase in self-consumption from 67 % (RBC) to almost 100 %. Ahmad et al. (Ahmad et al., 2013) have modeled a small house with an integrated HP via solar collector through a water tank for heating and hot water production. When compared to a simple RBC, the MPC was able to deliver savings of up to 9 %. From the comparison, the better performance of an optimized control is evident; however, as mentioned in (Fischer et al., 2017), its computational modeling and control fitting effort should be considered.

In this respect, this paper wants to analyze whether such advanced control techniques are worth using to control the heating system of a residential building according to a certain objective. In this regard, the paper proposes an analysis, in a simulation environment, of a case study in which a typical residential building subject to renovation, equipped with a HHP system assisted by PV panels and supplying a radiant floor, is controlled both through an MPC and a properly designed RBC. The main objective of the controls is to minimize the costs in

the electricity bill for heating.

2. Methodology

In order to assess the need for predictive control in an HHP system, the use of MPC and RBCs are compared in a residential building. In both cases, the controls aim to select the technology to be used (i.e., boiler or HP) to achieve economic savings, maximize the self-consumption of renewable sources and maintain thermal comfort. The comparison between MPC and RBC is carried out in a simulation environment. TRNSYS (TRNSYS 17, 2014) is selected to model the energy dynamics of the building. RBC is also modeled in TRNSYS, while MATLAB (MATLAB, 2014) is used for the MPC. The performance of RBC and MPC are evaluated by comparing the cost for satisfying the thermal demand of the building, the ability to maintain thermal comfort and the degree of exploitation of electricity produced by a PV plant installed on site. More details regarding the formulation of MPC and RBC are reported in the following subsections: subsection 2.1 describes the RBC, while in subsection 2.2 the formulation of MPC is explained.

2.1 Rule Based Control

RBC control is based on the determination of the external temperature (cut-off temperature) above which it is convenient to use the HP instead of the boiler. The cut-off temperature ($T_{\text{cut-off}}$) is determined through a comparison of the cost required to produce 1 kWh_{th}. For the HP, the cost is obtained considering the price of electricity withdrawal from the grid (c_e). To obtain the electrical energy absorbed by the HP, it was necessary to model the dependence of the COP on the temperatures of the air sources and the capacity ratio (CR). The model is based on the indications contained in EN 14825:2018 (CEN, 2018), starting from the performance map provided by the manufacturers. Since TRNSYS does not currently have a Type that allows modeling of a variable capacity HP, a new Type was developed by the authors, called Type 2701 (Ercoli et al., 2022). For the boiler, the cost of satisfying the heat demand is calculated by

multiplying the price of Natural Gas (c_{NG}) by its volume used. The latter is obtained by dividing the heat by the efficiency of the boiler (η_{BO}) and by the Higher Heating Value, HHV (condensing gas-fired boiler). Since also the availability of electricity from renewable sources is considered, two types of RBC were formulated: (i) base RBC (bRBC) and (ii) advanced RBC (aRBC). The bRBC is the simplest control where the switch between boiler and HP is determined only by $T_{cut-off}$. In addition, in the bRBC there is a thermostat that maintains the indoor air temperature (T_{air}) within a comfort range (2021 °C). On the other hand, the aRBC is set to force the HP to turn on regardless of $T_{cut-off}$ when a certain threshold of availability of PV is exceeded. It has been assumed as the minimum electrical power required for the minimum modulation of the HP (minimum CR of 0.3). To take advantage of the storage capacity of the heating system, the aRBC can exploit a wider comfort range (20 - 22 °C). However, in the absence of sufficient availability from PV, the HP and the boiler alternate their operation according to the set $T_{cut-off}$ and the thermostat is maintained within the 20 – 21 °C range.

2.2 Model Predictive Control

An MPC based on the system model was developed as an advanced control technique. The MPC can be divided into two parts: (i) the model of the system to be controlled and (ii) the optimizer. The system model (i) is responsible for forecasting the building's thermal demand. A lumped-parameter model based on the thermal-electricity analogy is used. Fig. 1 shows the structure of the resistances and capacitances (RC) network. It is composed of three thermal nodes. Each of them is represented by a capacitance (C) and a temperature (T). In particular, the thermal nodes represent the mass of the building envelope (C_e , T_e), the internal air (C_{air} , T_{air}) and the floor (C_f , T_f). The three thermal conductances K_{ea} , K_{fa} and K_{fg} model the heat flow between the three nodes, while the conductances K_w and K_{eo} model the heat flow between the external air (outdoor temperature, T_o) and T_{air} and T_e , respectively. The thermal flows entering the model are the solar gains (G_s) and the heating power provided by the heating system (Q_h). Since, as reported in Section 3,

the building is equipped with a radiant floor heating system, Q_h is directly applied to the thermal node of the floor (Fig. 1).

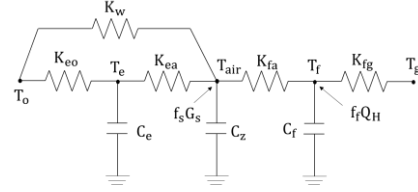


Fig. 1 – Third-order RC network building model

To obtain the numerical values of the parameters (C_e , C_{air} , C_f , K_{ea} , K_{fa} , K_{fg} , K_w , K_{eo} , f_f and f_s), the model was trained starting from the data obtained from the building simulation in TRNSYS (Root Mean Square Error of 0.16 °C in the training period involving the whole month of January).

With this structure, the model can be represented with a discrete state space formulation (Eq. 1 and 2):

$$\mathbf{X}(k+\Delta k) = \mathbf{A} \cdot \mathbf{X}(k) + \mathbf{B} \cdot \mathbf{U}(k) \quad (1)$$

$$\mathbf{Y}(k+\Delta k) = \mathbf{C} \cdot \mathbf{X}(k) + \mathbf{D} \cdot \mathbf{U}(k) \quad (2)$$

with the vector $\mathbf{X} = [T_{air} \ T_e \ T_f]^T$, which represents the state of the system at each timestep k (Δk is the time interval between two timesteps), $\mathbf{U} = [T_o \ Q_h \ G_s]^T$ the input vector and \mathbf{Y} the vector contains the output (T_{air}). \mathbf{A} , \mathbf{B} , \mathbf{C} and \mathbf{D} are time-invariant real matrices depending on the parameters of the system.

The model, therefore, can simulate the thermal dynamics of the building. At this point, the optimizer (ii) must select the best control actions of the HHP system to maintain the T_{air} within an accepted comfort range. As in the case of aRBC (subsection 2.1), also in this case a greater tolerance is granted to the thermostat (20 - 22 °C) to increase the exploitation of the thermal inertia of the building. The control actions to be set are the control signals for the HP and the boiler (1/0 control signals: $ctrl_{HP}$ and $ctrl_{BO}$). The objective of the optimization is to minimize the energy bill over a forecast period (FP). To do this, a Linear Programming optimization problem was formulated (Eq. 3, 4, 5, 6 and 7).

$$\begin{aligned} \text{minimize} \quad & \sum_k^{FP} \left(\frac{Q_{HP}(k)}{COP(k)} \cdot c_E(k) \right. \\ & \left. + \frac{Q_{BO}(k)}{\eta_{BO} \cdot HHV} \cdot c_{NG} \right) \end{aligned} \quad (3)$$

subject

$$\forall k = 1, \dots, FPT_{min} \leq T_{air}(k) \leq T_{max} \quad (4)$$

$$\forall k = 1, \dots, FP0 \leq Q_{HP}(k) \leq Q_{maxHP}(k) \quad (5)$$

$$\forall k = 1, \dots, FP0 \leq Q_{BO}(k) \leq Q_{maxBP} \quad (6)$$

$$\forall k = 1, \dots, FP Q_{BO}(k) + Q_{HP}(k) = Q_H(k) \quad (7)$$

Referring to Eq. 3, Q_{HP} and Q_{BO} are the thermal powers supplied by the HP and the boiler, respectively. These are the decision variables of the optimization problem. They can assume values between 0 and the maximum capacity of the HP (Q_{maxHP}) and the boiler (Q_{maxBO}), respectively. Eq. 4 contains the predictive model of the building. Eq. 5 and 6 set the boundary conditions for Q_{HP} and Q_{BO} . Finally, the constraint expressed by Eq. 7 is also inserted in order not to operate the HP and the boiler simultaneously (Q_H expresses the building load curve, Section 3). To incentivize the consumption of electricity produced by PV, a cost equal to 0 Eur kWh_e^{-1} is assigned to the electricity produced by PV. In general, Fig. 2 describes the dynamic behavior of the MPC. The MPC solves the optimization problem at each timestep k .

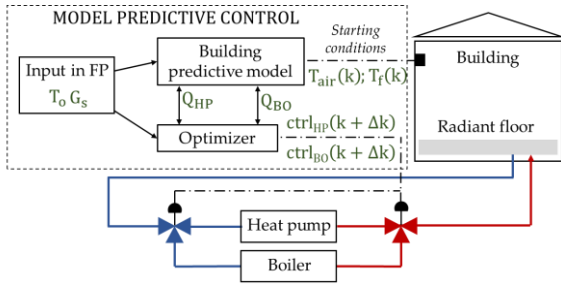


Fig. 2 – Schematic of the MPC

The actual temperatures (T_{air} and T_f) are passed as starting conditions to the MPC. Based on the receding horizon principle (Rawlings & Mayne, 2012), the MPC establishes the values of the control actions $ctrl_{HP}(k+\Delta k)$ and $ctrl_{BO}(k+\Delta k)$. These are derived from decision variables. Especially if $Q_{HP}(k+\Delta k)$ is greater than 0, $ctrl_{HP}(k+\Delta k)$ is 1, otherwise it is 0 (the same for $ctrl_{BO}$).

3. Case Study

A refurbishment for a residential building was considered as a case study. A single-family house whose construction characteristics refer to a period between 1991 and 2005 (Tabula Project (Corrado et al., 2014)) was chosen as an original building. The

building has a heated surface of 96 m^2 with a net heated volume of 299 m^3 . Table 1 contains the comparison between the thermal transmittances (U-values) of the original and the renovated building. Only the structures of the external walls and the windows were modified in the refurbishment (Table 1). In particular, the updated values were extrapolated from the most recent Italian regulation (DM, 2020).

Table 1 – U-values for renovated and original building

Building Status	Walls ($Wm^{-2}K^{-1}$)	Roof ($Wm^{-2}K^{-1}$)	Floor ($Wm^{-2}K^{-1}$)	Windows ($Wm^{-2}K^{-1}$)
Renovated	0.25	0.69	0.77	1.40
Original	0.59	0.69	0.77	1.70

For the simulations in TRNSYS, the climate file for a typical year of Ancona (43°37'N-13°31'E, Italy) was considered. Given an outdoor design temperature of -2 °C (UNI, 1976) and a T_{air} of 20 °C, the renovated building has a design peak load of 4.25 kW_{th} .

As mentioned, the heating system adopted in the renovated building is an HHP. It is composed of a modulating Air to Water Heat Pump (AWHP) and a condensing gas-fired boiler. To perform the study, commercial sizes of AWHP and boiler were taken as a baseline. For the HP, the operating characteristics were extrapolated from the data provided by a manufacturer. It presents a commercial size with 4.50 kW_{th} and 4.64 as COP, referred to an ambient temperature of 7 °C and a supply temperature of 35 °C. The boiler, on the other hand, has a capacity of 19 kW_{th} and an efficiency of 98 %, referred to the HHV (10.70 $kWh Sm^{-3}$).

As emission system, radiant floor heating was considered. The regulation of the heating system takes place with a compensation curve for the supply temperature (Fig. 3). The latter was calculated from the building load curve (Q_H) according to the T_o variation (Fig. 3).

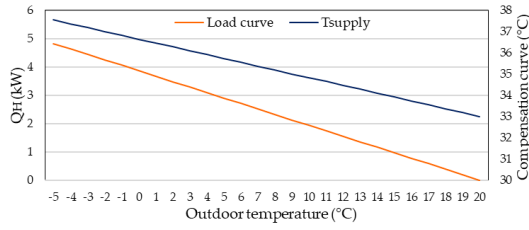


Fig. 3 – Building load curve (Q_H) and compensation curve

By applying the methodology described in Section 2.1 to the case study, the $T_{\text{cut-off}}$ obtained is 4 °C. This was achieved by considering a natural gas cost of 1.225 Eur Sm^{-3} and an electricity cost of 0.388 Eur kWh^{-1} (ENEL, 2022). The renovated building was also equipped with a PV system installed on site. The PV plant consists of 12 monocrystalline silicon panels for a nominal peak power of 3.80 kW_e .

4. Results

A reference period was selected to compare the performance of MPC and RBC, i.e., the first two weeks of January. The analysis of the results will first be presented for the two RBC controls (4.1), to then be extended to the case of MPC (4.2). Finally, in section 4.3, we will try to answer the original question: “Is it worth using predictive control?”.

4.1 Results for RBCs

The comparison between the internal air temperature trend in the case of bRBC and aRBC is shown in Figs. 4 and 5. In both bRBC and aRBC, there is a certain period in which the air temperature does not respect the thresholds set on the thermostat (Section 2.1). In the case of bRBC (Fig. 4), the air temperature drops below the minimum threshold (i.e., 20 °C) for the 2 % of the time (7 hours), reaching a minimum of 19.43 °C. From this point of view, better behavior is obtained with the aRBC. In fact, looking at Fig. 5, the air temperature assumes values lower than 20 °C for 1 hr and 30 mins (0.45 % of the time), reaching a minimum of 19.93 °C.

As for the upper temperature threshold, this is different between the two controls when PV is available. In fact, the aRBC can exploit the flexibility of the thermostat to increase PV self-consumption

and reach 22 °C. Comparing Fig. 4 and 5, it can be noted that there is a greater exploitation of the upper band granted to the thermostat in case of aRBC. Indeed, the average air temperature in case of bRBC is 20.47 °C, while it becomes 20.62 °C with the aRBC. Furthermore, with the aRBC, the air temperature exceeded the upper limit of 22 °C for a time of 2 hrs and 45 mins (about 0.82 % of the time) with a peak of 22.48 °C.

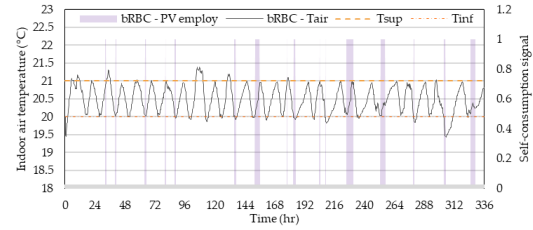


Fig. 4 – Internal air temperature (T_{air}) and self-consumption signals during basic RBC (bRBC) use

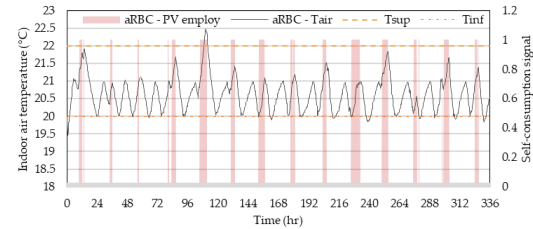


Fig. 5 – Internal air temperature (T_{air}) and self-consumption signals during advanced RBC (aRBC) use

Figs. 6 and 7 show the involvement of the single technologies (AWHP and boiler) in the case of the RBCs. From the comparison of Figs. 6 and 7, with bRBC, there is a higher utilization of the boiler and higher thermal demand peaks than in the case where the aRBC is used. In addition, from Fig. 7, there is an increase in AWHP utilization through use of the aRBC, since, as described in Section 2.1, the control is set to force the AWHP to turn on regardless of $T_{\text{cut-off}}$. In particular, the AWHP is found to be operating for 141 hrs and 45 mins through aRBC, 6.98 % more than bRBC. The boiler, on the other hand, works 7.17 % less during use of the aRBC than the basic one, for a total time of 61 hrs and 30 mins. Also, comparing Figs. 6 and 7, in addition to an increase of AWHP application, it is also possible to see a slight increase in the PV self-consumption by aRBC.

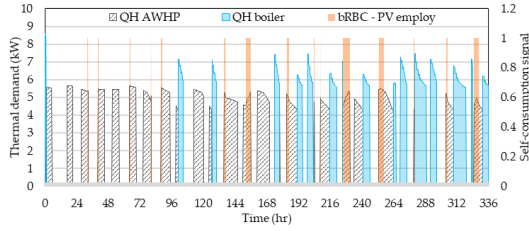


Fig. 6 – Thermal demand (Q_H) trends and self-consumption signals during bRBC use

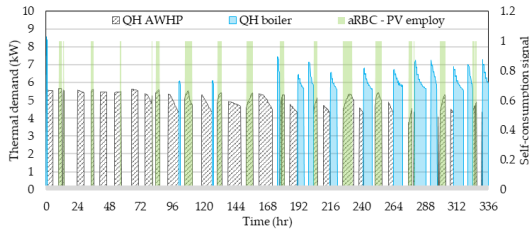


Fig. 7 – Thermal demand (Q_H) trends and self-consumption signals during aRBC use

The difference in utilization between the two RBCs can also be seen through the thermal demand via Fig. 8; from the comparison with the bRBC, the use of the aRBC involves an increase of the thermal demand of 6.46 % covered by the AWHP and a decrease of 7.18 % for the contribution of the boiler.

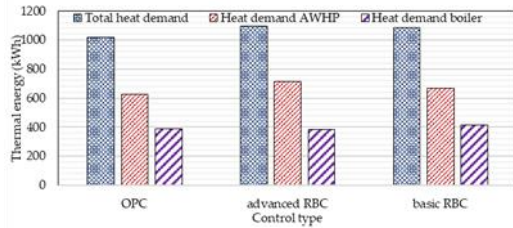


Fig. 8 – Thermal demand of the hybrid system, AWHP and boiler during the application of the three controls

The differences in terms of PV exploitation are also highlighted in Fig. 9, where the self-consumption of electric energy during advanced control is 6.43% higher than that through bRBC.

In terms of performance, the use of aRBC results in a slight reduction of 0.26 % in average COP, with a value of 4.21 compared with that of the bRBC of 4.22. Despite the slight decrease in average COP, the lower boiler utilization by the aRBC resulted in lower energy bill costs. From Fig. 10, a net saving is achieved through aRBC. In particular, the costs due to the boiler, which, compared with the case of the bRBC, decreased by 76.8 %.

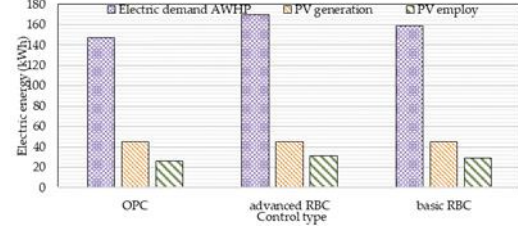


Fig. 9 – Electric consumption required by the AWHP, generated by the PV panels and self-consumed during the application of the three controls

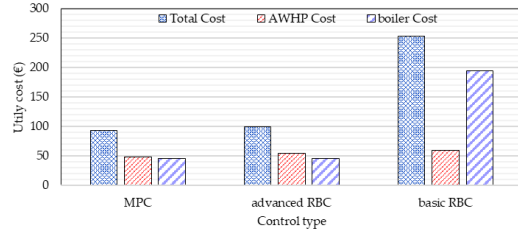


Fig. 10 – Cost due to use of hybrid system, AWHP and boiler during the application of the three types of control

4.2 Results for MPC

As with the two RBCs, Fig.11 shows the trend of the internal air temperature in the reference period for the MPC. It can be noted that the temperature fluctuates frequently around 20 °C with an average value of 20.11 °C. The MPC is able to maintain the air temperature within a narrower range of variation. Both violations towards the lower limit of the thermostat and towards the upper one are reduced in comparison with the RBCs. In fact, as can be seen in Fig. 11, the upper limit of 22 °C is not exceeded, and the air temperature reaches a peak of 21.4 °C.

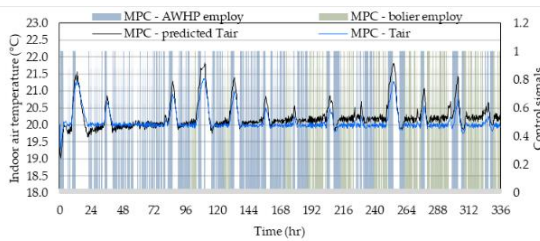


Fig. 11 – Calculated and predicted indoor temperature trends and AWHP and boiler usage signals during MPC application

In terms of running time, the use of the MPC leads to an overall reduction; both the AWHP and the boiler are used for less time, meaning 123 hr and 45 min and 58 hrs and 15 mins, respectively. Overall, there is a reduction in system utilization of less than 10.46 % compared with the aRBC and less than 8.43 % compared with the bRBC. Through Fig. 8, it

can be seen that the use of the MPC also leads to 7.19 % in thermal demand reduction due to the entire hybrid system compared with the aRBC. Even the AWHP provides a lower thermal demand of 11.82 %, probably due to its decreased use. In addition, this could lead to a reduction of the self-consumption, as shown in Fig. 10; in fact, compared with the aRBC there is a reduction of 17.33 % in self-consumption. Moreover, the AWHP, through the MPC, is able to provide better performance, with 4.26 as average COP, 0.94 % higher than the bRBC. Considering the energy costs, the MPC performs better than the RBCs, given the bill savings objective (Fig. 11). In fact, within a two-week reference period, the use of MPC, in the case study considered, resulted in savings of 63.27 % compared with bRBC and 5.93 % compared with aRBC.

4.3 Is It Worth Using Predictive Control?

The results shown in the previous sections showed that MPC achieved better performance in terms of cost savings and concerning the thermostat. On the other hand, the best performance regarding self-consumption of PV was obtained from the advanced RBC.

What is important to note is that, although the MPC is better at achieving the objective (e.g., cost reduction), modeling difficulties not present in RBC cases should be taken into account. In fact, the MPC being a model-based control, in the case of incorrect or missing data, there could be a wrong estimation of the thermal demand of the building and, consequently, incorrect decision making. Furthermore, the modeling and implementation difficulty that MPC requires compared with RBCs cannot be overlooked.

In the case studied, the advanced RBC turned out to be a good compromise; in fact, it was possible to achieve good savings over the basic RBC with less effort than the MPC. In particular, this was possible through: (i) a good estimation of the $T_{\text{cut-off}}$ (e.g. using the method described in section 2.1), (ii) forcing the AWHP to turn on during PV generation and (iii) the activation of the flexibility of thermostat. Indeed, it is possible to see in Fig. 12 how the $T_{\text{cut-off}}$ varies while using the MPC in com-

parison with the fixed 4 °C of RBCs. From the comparison, it can be seen that this transition temperature between the two generators was properly estimated through a comparison of the cost required to produce 1 kWh_{th} (section 2.1).

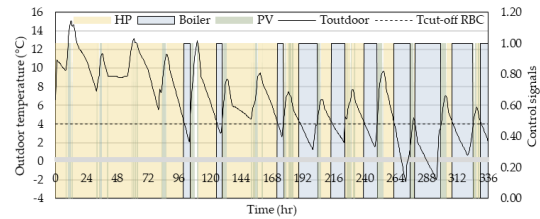


Fig. 12 – Variation of the outdoor temperature and AWHP and boiler use convenience signals based on cost

5. Conclusion

In this paper, we asked whether it is worth using a MPC to control a residential hybrid heating system with PV panels. To do this, a MPC was compared with two RBCs, one basic and one advanced.

From the results, the main conclusions can be summarized in the following points:

- The MPC is more effective in reducing the energy cost: a saving of 63.27 % was estimated in relation to the basic RBC and 5.93 % compared to advanced RBC.
- The advanced RBC allows a higher self-consumption of PV compared with MPC to be obtained (with the MPC a reduction in self-consumption of 17.33 % was achieved in comparison with advanced RBC).
- With the MPC there is no violation of the upper band of the thermostat – a phenomenon that occurs with the advanced RBC (0.82 % of the time, 2 hrs and 45 mins).

Although MPC has shown better performance than RBCs in terms of comfort and savings, its application for a system such as the one analysed should also consider the level of difficulty that its implementation requires. Through advanced RBC, it was possible to achieve good savings over the basic RBC but with less effort than the MPC, thus offering a good compromise between the two controls.

Despite good results from both MPC and advanced RBC, there were still unused amounts of self-

generated electrical power. One way to mitigate wasted electrical power could be to introduce additional integration devices to increase system flexibility and further exploit the building's storage capabilities. In this context, it might be interesting to further explore the comparison between different types of control.

References

- Ahmad, M. W., M. Eftekhari, T. Steffen and A.M. Danjuma. 2013. "Investigating the performance of a combined solar system with heat pump for houses" *Energy and Buildings* 63: 138-146. doi: <https://doi.org/10.1016/j.enbuild.2013.03.055>
- CEN (European Committee for Standardization). 2018. *EN 14825:2018. Air Conditioners, Liquid Chilling Packages and Heat Pumps, with Electrically Driven Compressors, for Space Heating and Cooling – Testing and Rating at Part Load Conditions and Calculation of Seasonal Performance*
- Corrado, V., I. Ballarini, and S. P. Corgnati. 2014. "Building Typology Brochure – Italy" EPISCOPE. Accessed January 10. <https://episcopes.eu/communication/download/>
- Dongellini, M., C. Naldi, and G. L. Morini. 2021. "Influence of sizing strategy and control rules on the energy saving potential of heat pump hybrid systems in a residential building" *Energy Conversion and Management* 235. doi: <https://doi.org/10.1016/j.enconman.2021.114022>.
- EHI (European Heating Industry). 2020. "Heating Market Report 2020" EHI. Accessed March 30. <https://ehi.eu/heating-market-report/heating-market-report-2020/>
- ENEL, 2022. www.enel.it/?ecid=paidsearch-google-alwayson_top_keyword-brand-enel_exact&gclid=EAlaIqObChMI5sa8hvaf9wIVBLLVCh0o4wDQEAAYASAAEgJAH_D_BwE&gclsrc=aw.ds
- Ercoli, P., A. Mugnini and A. Arteconi. 2022. github.com/diismunivpm/Type2701-for-TRNSYS.git
- Fischer, D., J. Bernhardt, H. Madani, and C. Wittwer. 2017. "Comparison of control approaches for variable speed air source heat pumps considering time variable electricity prices and PV." *Applied Energy* 204: 93-105. doi: <https://doi.org/10.1016/j.apenergy.2017.06.110>
- IEA - International Energy Agency. 2021. "Heat Pumps" IEA. Accessed March 21. <https://www.iea.org/reports/heat-pumps>
- Madonna, F., and F. Bazzocchi. 2013. "Annual performances of reversible air-to-water heat pumps in small residential buildings" *Energy and Buildings* 65: 299-309. doi: <https://doi.org/10.1016/j.enbuild.2013.06.016>.
- MATLAB - Matrix Laboratory. 2014. Version R2014a, MathWorks, Natick, Massachusetts, USA.
- Ministero dello sviluppo economico. 2020. "DECRETO 6 agosto 2020 - cd ECOBONUS (In Italian)" Ministero dello sviluppo economico. Accessed January 10. <https://www.gazzettaufficiale.it/eli/id/2020/10/05/20A05394/sg>
- Rawlings, J. B., and D. Q. Mayne. 2012. *Model Predictive Control: Theory and Design*. ISBN 9780975937709.
- TRNSYS 17 - Transient System Simulation Tool. 2014. Version 17.2, Solar Energy Laboratory, University of Wisconsin, Madison, USA.
- UNI (Italian National Agency for Unification). 1976. *UNI 5364:1976. Hot water heating systems. Rules for presentation of offer and for testing*.
- Zanetti, E., M. Aprile, D. Kum, R. Scoccia, and M. Motta. 2020. "Energy saving potentials of a photovoltaic assisted heat pump for hybrid building heating system via optimal control." *Journal of Building Engineering* 27. doi: <https://doi.org/10.1016/j.job.2019.100854>

The Acoustic Adaptation of the Aula Magna at the University of Bologna: Auditorium and Conference Hall Scenarios Simulated in the Main Nave of Santa Lucia's Church

Antonella Bevilacqua – University of Parma, Italy – antonella.bevilacqua@unipr.it

Ruoran Yan – University of Bologna, Italy – ruoran.yan2@unibo.it

Maria Cristina Tommasino – ENEA, Italy – cristina.tommasino@enea.it

Abstract

The main Auditorium of Bologna was created inside the original monastery built during the 16th century by the Jesuits. In the following century, the building was modified to become a Catholic church by the architect G. Rainaldi. After the French invasion led by Napoleon during the 18th century, the church was adapted to fulfil different uses. Nowadays, the main hall, composed of three naves but having audience seats in the central one only, is used for celebrations and civil events organized by the University of Bologna. Numerical simulations have been undertaken considering two different scenarios: acoustic adaptation to become an auditorium and to become a conference hall. The model representing the existing conditions has been calibrated on the measurements undertaken across the seating areas. The two scenarios simulated have been compared with the existing conditions of the Aula Magna: the outcomes highlight an improvement in speech comprehension across all the seating areas by achieving the optimal range of each acoustic parameter analyzed. A historical background has also been introduced to understand the adaptation of the original construction to the different room functions assigned throughout the centuries.

1. Introduction

Increased demand for the utilization of cultural heritage buildings has caused experts and scholars to study the existing historical patrimony (Vecco, 2010). On this basis, this paper deals with the acoustic simulations of two conditions that the old church of Santa Lucia could have: the adaptation to become an auditorium for classical music and to become a conference hall, both room functions in

line with academic activities run at the University (Dordevic, 2016). A digital model was utilised for the simulations after being calibrated with the measured values (Vorländer, 2007). The design project of the acoustic measures was digitally tested with the application of absorbing plaster on walls, installation of acoustic panels and addition of heavy curtains to close the main nave from the laterals. The results highlight a significant improvement in the outranges values related to the main acoustic parameters.

2. Historical Background

The main auditorium of the University of Bologna, the Aula Magna, was located inside Santa Lucia's church, and is now no longer in use. It was built during the 11th century, while the surrounding college buildings were erected in the 17th century.

During the 16th century, the original monastery became property of the Jesuits, and, on this occasion, the building was modified into a Catholic church by the architect G. Rainaldi (Wittkower et al., 1992). When the Jesuit order was suppressed by Pope Clement XIV, the church complex was transferred to the Barnabites at the end of the 16th century, and then turned into a military camp at the end of the 17th century. During the 18th century, under the French invasion led by Napoleon, the church was converted to fulfil different uses.

In the 1960s, the buildings were involved in a serious fire. From the 1970s to the 1980s, the restoration and modernization (Bettarello et al., 2010) project began to adapt the buildings to the needs of the

University of Bologna and finally opened to the public in 1988. At the end of the 20th century, Santa Lucia's church was also transformed into a university facility.



Fig. 1 – Internal view of the Aula Magna of Bologna

Nowadays, the Aula Magna is composed of three naves, having walls and ceilings decorated with transparent and hard plaster. The auditorium, with lightly upholstered seats in the central nave, is surrounded by wooden balconies, in place for the occasion of degree celebrations and civil events, as shown in Fig. 1.

3. Architectural Organization

The Aula Magna at the University of Bologna, whose current form can be traced back to 1843, has a total capacity of about 1000 seats. It consists of the main hallway and two high, wide, and solemn side passageways, with a total area of about 30000 m³, as shown in Fig. 2 and Fig. 3.

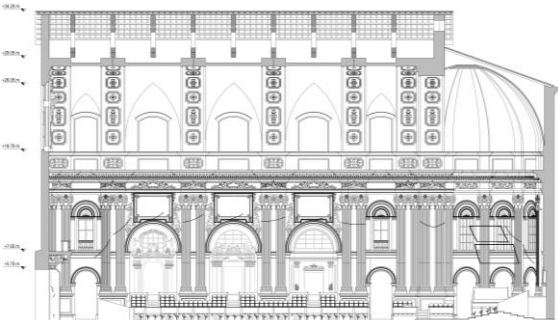


Fig. 2 – Longitudinal section of the Aula Magna of Bologna

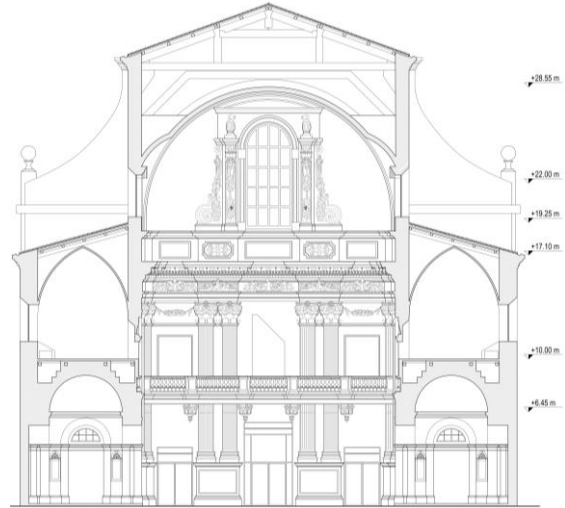


Fig. 3 – Transversal section of the Aula Magna of Bologna

The walls of the main hall are completely plastered, and the central area is decorated with stucco and is 10 to 15 m high. Wooden galleries and low padded seating platforms have been built on the sides of the nave, leaving full view of the auditorium.

3.1 Digital Model

From the architectural drawings, as well as for energy building and musical instruments simulation, (Fabbri et al., 2014; Farina et al., 1998; Manfren et al., 2019, 2021a, 2021b, and 2022; Tronchin, 2005) a digital model was realised to be composed of 3700 surface entities. The vault was realised with polyhedral geometry composed of 16 sides (Antlej, 2022). In a similar way, the apse was modeled by adopting the same methodology, as well as the capitals and the bases of the columns (Bettarello et al., 2021). As such, the model was exported in DXF format (Caniato et al., 2020a and 2020b), ready to be used within Ramsete software.

Attribution of the absorbing and scattering coefficients was carried out based on the acoustic measurements (Caniato et al., 2019), as indicated in Fig. 4.

In particular, the sound source and the receivers were placed in the same positions used during the survey (Caniato et al., 2021).

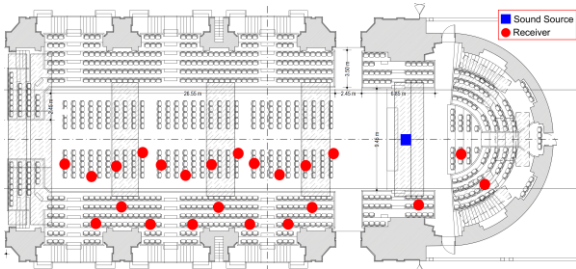


Fig. 4 – Equipment positions during the acoustic survey

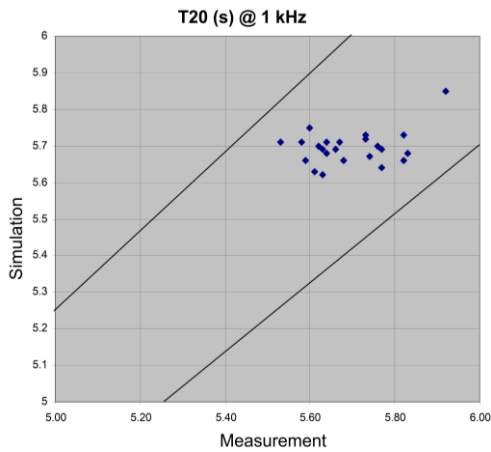


Fig. 5 – Reverberation Time (T_{20}) calibration between simulated and measured results of the existing conditions

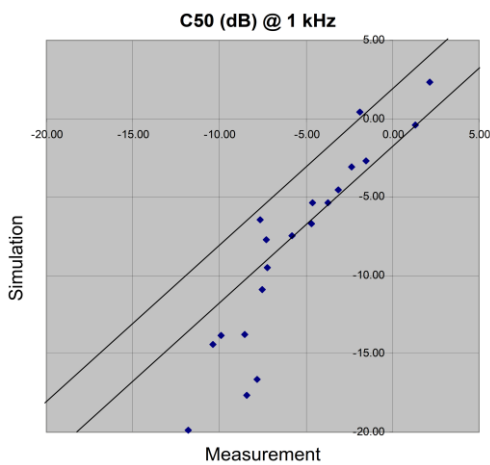


Fig. 6 – Clarity Index (C_{50}) calibration between simulated and measured results of the existing conditions

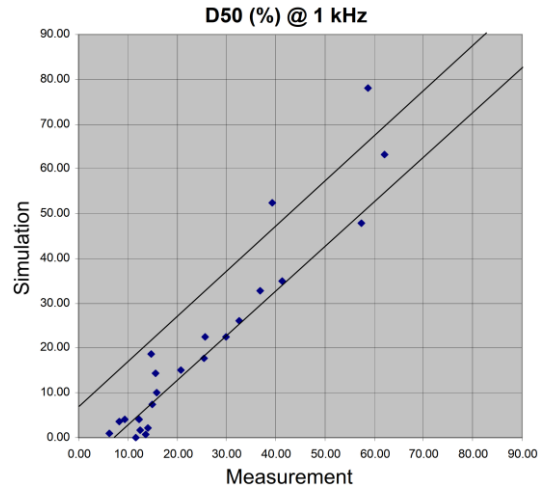


Fig. 7 – Definition (D_{50}) calibration between simulated and measured results of the existing conditions

The tuning process (Tronchin & Knight, 2016; Wang et al., 2004) was carried out upon the reverberation time (T_{20}), clarity index (C_{50}), and definition (D_{50}), as reported in Figs. 5, 6 and 7. The results simulated to be closer to the measured values should stand along the median line between the defined boundaries.

4. Acoustic Simulation

Two sets of simulations were carried out for the Aula Magna of Bologna, based on the functions that were attributed. The first set of simulations adapts the acoustics to auditorium functions, to be used for classical music, while the second set is more centred on speech intelligibility, since the purpose is to adapt the acoustics to suit a conference hall.

During the simulations of the auditorium, an omnidirectional sound source was placed in the location where the orchestra was intended to be located. Based on the room volume of the central nave of Santa Lucia's church being equal to 24000 m³, the optimal T_{20} value at 500 Hz should be around 2.8 s, as shown in Fig. 8.

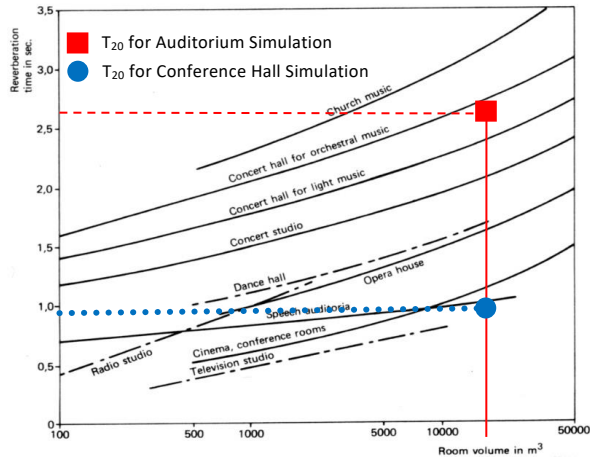


Fig. 8 – Optimal T₂₀ values at 500 Hz, based on room volume

When the simulations have the purpose of adapting the acoustics to suit a conference hall, the sound source was introduced in Ramsete by reproducing the characteristics of the human voice, in terms of spectrum, power, and directivity (Tronchin, 2005). In addition, the existing amplified system was also reproduced with further sound sources having the features of the loudspeakers in place. On this basis, the optimal T₂₀ value at 500 Hz for a room of such a volume size used as a conference hall should be around 1.1 s, as indicated in Fig. 8.

In both scenarios, the adopted acoustic measures involve the reduction of reverberation and an improvement in terms of speech intelligibility (Tronchin & Bevilacqua, 2022). Specifically, the measures consist of the following solutions:

- substitution of the standard plaster with an absorbing plaster, to be applied mainly to the surface area of the vault of the central nave;
- introduction of carpet along the corridors serving the seats;
- installation of heavy drapery to close off the lateral naves during conferences.

The application of the absorbing plaster was carried out on a surface area of 853 m², while the introduction of the reflecting panels covers a surface area of 331 m². Table 1 indicates the absorption coefficients of the materials listed above.

Table 1 – Absorption coefficients of the materials used for the project design

Material	Abs. Coeff. α - Octave Bands (Hz)					
	125	250	500	1k	2k	4k
Abs. plaster	0.23	0.30	0.59	0.64	0.67	0.082
Carpet	0.08	0.10	0.20	0.25	0.30	0.35
Drapery	0.08	0.29	0.44	0.50	0.40	0.35

4.1 Auditorium For Classical Music

Based on the acoustic measures being a common factor for the two scenarios, the simulation of the auditorium is focused on the insertion of reflecting panels to be installed above the area of the orchestra and above the stalls. The panels were designed to be in polycarbonate, with a transparency of 90 %, and suspended with steel wires hung to the existing beams. Fig. 9 and 10 show the configuration of the model for an auditorium.



Fig. 9 – Acoustic project design for the adaptation of Santa Lucia's church to an auditorium. Apse side



Fig. 10 – Acoustic project design for the adaptation of Santa Lucia's church to an auditorium. Entrance side

The reflecting panels were installed in such a way as to distribute the sound across the audience uniformly. The results of the conditions simulated for the auditorium scenario are shown in the acoustic maps highlighting the spatial distribution of the main parameters. Fig. 11 shows the T_{20} , while Fig. 12 reflects the results of C_{80} , simulated with and without the audience.

4.2 Conference Hall

The second set of simulations adapts the acoustics of the Aula Magna to a conference hall. The main difference compared with the other configuration consists of the use of heavy curtains and coconut fibres (Fabbri et al., 2021) to be kept closed during conferences to avoid disturbance from people walking in the lateral naves as well as to increase the absorbing surfaces that are useful for lowering the reverberation time (Tronchin et al., 2021a and 2021b). With the acoustic measures, the speech transmission index (STI) values are found to be more than 0.6, falling into a “good” category, as defined by the intelligibility rating according to ISO 9921 (Farina et al., 1998; Tronchin & Bevilacqua, 2021).

5. Results

The results are presented graphically with the plan distribution of the main acoustic parameters, by highlighting the difference between the existing conditions and the simulated environments, as indicated in Figs. 11 to 13. The simulated results shall be considered in unoccupied conditions.

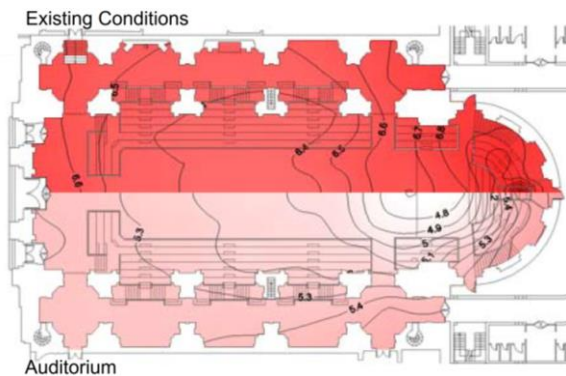


Fig. 11 – Spatial distribution of Reverberation Time (T_{20})

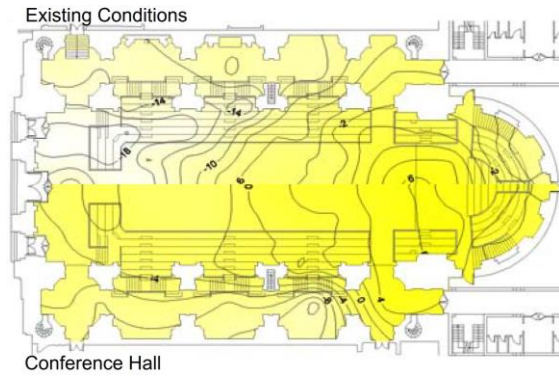


Fig. 12 – Spatial distribution of speech clarity index (C_{50})

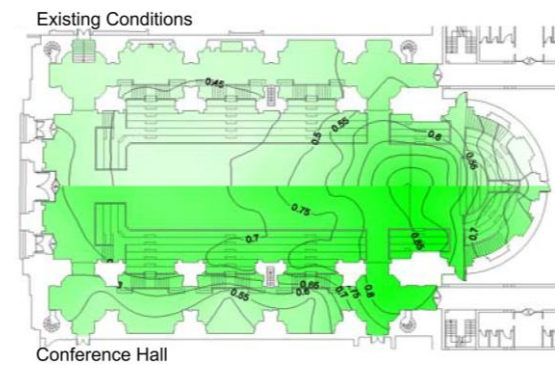


Fig. 13 – Spatial distribution of speech transmission index (STI)

Fig. 11 indicates that the T_{20} values decrease significantly with the introduction of the acoustic measures, passing from 8-9 s to 4.5 s. Such values result in greater uniformity across the plan layout (Mickaitis et al., 2021; Puglisi et al., 2021).

Fig. 12 shows the spatial distribution of the C_{50} values, improved to be within the optimal range as defined by the literature. The C_{50} values equal to -14 dB, especially at the back of the hall, were increased to up to 0 dB in the centre of the hall, and were more uniformly distributed (ISO, 2003; Jeon et al., 2009; Ortega & Rivera, 2012; Steeneken & Houtgast, 1980).

Fig. 13 shows the STI values to be around 0.7, which indicates a good rating. It should be noted that the results with full occupancy of the hall improve the simulated conditions even more, bringing the values closer and within the optimal range limits.

6. Conclusion

The application of the acoustic measures for the Aula Magna at the University of Bologna outlined by the design project has revealed an important benchmark achieved with the accuracy of the digital simulations. The installation of acoustic panels floating at different heights across the plan, along with the absorbing plaster to the vault and the curtains at the openings to the lateral naves, was considered the best option for a cultural heritage site of such historical value. In addition, the criteria of transparency for the suspended panels were assessed to leave the wide view of the indoor space intact as well as to filter the natural lights from the large windows. In summary, the outcomes of the simulated values compared with the existing conditions of the room outline a considerable improvement in speech comprehension, resulting in more appropriate functions assigned to the Aula Magna.

References

- Antleij, K. 2022. "Digital Heritage Interpretation of Modernist Modular Architecture: The K67 Kiosk." In: Bartolomei, C., A. Ippolito, S. H. T., Vizioli (eds) *Digital Modernism Heritage Lexicon*. https://doi.org/10.1007/978-3-030-76239-1_23
- Bettarello, F., P. Fausti, V. Baccan, and M. Caniato. 2010. "Impact Sound Pressure Level Performances of Basic Beam Floor Structures." *Building Acoustics* 17(3): 305-316. <https://doi.org/10.1260/1351-010X.17.4.305>
- Bettarello, F., M. Caniato, G. Scavuzzo, and A. Gasparella. 2021. "Indoor Acoustic Requirements for Autism-Friendly Spaces." *Applied Science* 11: 3942. <https://doi.org/10.3390/app11093942>
- Caniato, M., F. Bettarello, C. Schmid, P. Fausti. 2019. "The use of numerical models on service equipment noise prediction in heavyweight and lightweight timber buildings." *Building Acoustics* 26(1): 35-55. [Doi: https://doi.org/10.1177/1351010X18794523](https://doi.org/10.1177/1351010X18794523)
- Caniato, M., C. Schmid, and A. Gasparella. 2020a. "A comprehensive analysis of time influence on floating floors: Effects on acoustic performance and occupants' comfort." *Applied Acoustics* 166: 107339. [doi: https://doi.org/10.1016/j.apacoust.2020.107339](https://doi.org/10.1016/j.apacoust.2020.107339)
- Caniato, M., F. Bettarello, P. Bonfiglio, and A. Gasparella. 2020b. "Extensive Investigation of Multiphysics Approaches in Simulation of Complex Periodic Structures." *Applied Acoustics* 166:107356. [doi: https://doi.org/10.1016/j.apacoust.2020.107356](https://doi.org/10.1016/j.apacoust.2020.107356)
- Caniato, M., F. Bettarello, and A. Gasparella. 2021. "Indoor and outdoor noise changes due to the COVID-19 lockdown and their effects on individuals' expectations and preferences." *Scientific Reports* 11:16533. <https://doi.org/10.1038/s41598-021-96098-w>
- Dordevic, Z. 2016. "Intangible tangibility: Acoustical heritage in architecture". *Structural Integrity and Life* 16(1): 59-66.
- Fabbri, K, L. Tronchin, and V. Tarabusi. 2014. "Energy Retrofit and Economic Evaluation Priorities Applied at an Italian Case Study." *Energy Procedia* 45: 379-384. <https://doi.org/10.1016/j.egypro.2014.01.041>
- Fabbri, K., L. Tronchin, and F. Barbieri. 2021. "Coconut fibre insulators: The hygrothermal behaviour in the case of green roofs." *Construction and Building Materials* 266:1-9. <https://doi.org/10.1016/j.conbuildmat.2020.12102>
- Farina, A., A. Langhoff, and L. Tronchin. 1998. "Acoustic characterisation of "virtual" musical instruments: using MLS technique on ancient violins." *Journal Of New Music Research* 27(4): 359-379. [doi: https://doi.org/10.1080/09298219808570753](https://doi.org/10.1080/09298219808570753)
- ISO. 2003. ISO 9921:2003. *Ergonomics - Assessment of speech communication*.
- Jeon, J. Y., J. K. Ryu, Y. H. Kim, and S. Sato. 2009. "Influence of absorption properties of materials on the accuracy of simulated acoustical measures in 1:10 scale model test." *Applied Acoustics* 70(4): 615-25. <https://doi.org/10.1016/j.apacoust.2008.06.009>
- Manfren, M., B. Nastasi, E. A. Piana, and L. Tronchin. 2019. "On the link between energy performance of building and thermal comfort: An example." *AIP Conference Proceedings* 2123:1-9. [doi: https://doi.org/10.1063/1.5116993](https://doi.org/10.1063/1.5116993)

- Manfren, M., B. Nastasi, L. Tronchin, D. Groppi, D. A. Garcia. 2021a. "Techno-economic analysis and energy modelling as a key enablers for smart energy services and technologies in buildings." *Renewable and Sustainable Energy Reviews* 150:1-14.
<https://doi.org/10.1016/j.rser.2021.111490>
- Manfren, M., M. Sibilla, and L. Tronchin. 2021b. "Energy Modelling and Analytics in the Built Environment—A Review of Their Role for Energy Transitions in the Construction Sector." *Energies* 14:1-29.
<https://doi.org/10.3390/en14030679>
- Manfren, M., P. A. B. James, and L. Tronchin. 2022. "Data-driven building energy modelling – An analysis of the potential for generalisation through interpretable machine learning." *Renewable and Sustainable Energy Reviews* 167:1-13.
<https://doi.org/10.1016/j.rser.2022.112686>
- Mickaitis, M., A. Jagniatinskis, and B. Fiks. 2021. "Case study of acoustic comfort in conference room". *Proc. 27th International Congress of Sound & Vibration*.
- Ortega, G. V., and J. I. S. Rivera. 2012. "Acoustic study of Madrid auditorio nacional de musica: comparison between simulation and measurements." *41st International Congress and Exposition on Noise Control Engineering (INTER-NOISE 2012)*.
- Puglisi, G. E., A. Warzybok, A. Astolfi, and B. Kollmeier. 2021. "Effect of competitive acoustic environments on speech intelligibility". *Journal of Physics* 2069(1): 175180.
<https://doi.org/10.1088/1742-6596/2069/1/012162>
- Steeneken, H. J. M., and T. Houtgast. 1980. "A physical method for measuring speech-transmission quality." *Journal of Acoustic Society of America*, 67(1): 318-326.
- Tronchin, L. 2005. "Modal analysis and intensity of acoustic radiation of the kettledrum." *The Journal Of The Acoustical Society Of America* 117(2): 926-933.
<https://doi.org/10.1121/1.1828552>
- Tronchin, L., and D. J. Knight. 2016. "Revisiting Historic Buildings through the Senses. Visualising Aural and Obscured Aspects of San Vitale, Ravenna." *International Journal of Historical Archaeology* 20: 127-145.
<https://doi.org/10.1007/s10761-015-0325-2>
- Tronchin, L., and A. Bevilacqua. 2021. "Acoustic study of different sceneries at the São Carlos national theatre of Lisbon." *Applied Acoustics* 180:1-11.
<https://doi.org/10.1016/j.apacoust.2021.108102>
- Tronchin, L., F. Merli, and M. Manfren. 2021a. "On the acoustics of the Teatro 1763 in Bologna." *Applied Acoustics* 172: 1-9.
<https://doi.org/10.1016/j.apacoust.2020.107598>
- Tronchin, L., F. Merli, and M. Dolci. 2021b. "Virtual acoustic reconstruction of the Miners' Theatre in Idrija (Slovenia)." *Applied Acoustics* 172: 1-9.
<https://doi.org/10.1016/j.apacoust.2020.107595>
- Tronchin, L., and A. Bevilacqua. 2022. "Historically informed digital reconstruction of the Roman theatre of Verona. Unveiling the acoustics of the original shape." *Applied Acoustics* 185: 1-18.
<https://doi.org/10.1016/j.apacoust.2021.108409>
- Vecco, M. 2010. "A definition of Cultural Heritage: From the tangible to the intangible". *Journal of Cultural Heritage* 11: 321-324.
<https://doi.org/10.1016/j.culher.2010.01.006>
- Vorländer, M. 2007. "Fundamentals of Acoustics, Modelling, Simulation. Algorithms and Acoustic Virtual Reality".
- Wang, L. M., J. Rathsam, and S. R. Ryherd. 2004. "Interactions of model detail level and scattering coefficients in room acoustic computer simulation". *Proceeding International Symposium on Room Acoustics*.
- Wittkower, R., I. B. Jaffe, and M. Parizzi. 1992. "Architettura e arte dei Gesuiti". Electa.

Implementation and Calibration of a Model to Treat Naturally Ventilated Complex Fenestration Systems in TRNSYS

Ingrid Demanega – EURAC Research, Italy – ingrid.demanega@eurac.edu

Giovanni Gennaro – EURAC Research, Politecnico di Torino, Italy – giovanni.gennaro@eurac.edu

Giuseppe De Michele – EURAC Research, Italy – giuseppe.demichela@eurac.edu

Francesco Isaia – EURAC Research, Italy – francesco.isaia@eurac.edu

Fabio Favoino – Politecnico di Torino, Italy – fabio.favoino@polito.it

Stefano Avesani – EURAC Research, Italy – stefano.avesani@eurac.edu

Abstract

Adaptive façade systems offer the opportunity to improve building performance and user experience with their ability to adapt the façade configuration to the dynamic variability of the external environment. Nevertheless, the correct deployment of adaptive systems in real buildings is highly dependent on the ability to predict their performance. This is especially relevant in the case of Complex Fenestration Systems (CFS), which are characterized by a complex behavior both from a thermal and daylighting perspective. Often, such CFS are combined with airflow movement when the façade cavity is either mechanically or naturally ventilated, making the performance even more difficult to be characterized. The possibility to use building performance simulation tools to simulate the behavior of these systems integrated in a whole building is central for the proper use and the penetration on the market of these systems.

In this framework, a naturally ventilated window with integrated venetian blinds was modeled in TRNSYS and compared with a FEM-based 2D detailed model, developed in COMSOL Multiphysics. Type56_CFS solves thermal calculation and uses the Bidirectional Scattering Distribution Function for describing optical properties of the façade. This model requires the inlet mass flow rate, which was assessed thanks to an ad-hoc implementation of ISO 15099. The numerical modeling of the coupled heat transfer and fluid flow with COMSOL allowed the TRNSYS model to be calibrated.

The calibration was carried out by increasing the model complexity, focusing on the inlet ventilation flow rate parameter: (a) firstly, it was provided as an input to the Type56_CFS from the FEM-based simulation and then (b) it was calculated by the ISO 15099 internal model and provided to the Type56_CFS. Using this methodology, it was

possible to compare the ability of TRNSYS to simulate the thermal behavior of the naturally ventilated cavity against a FEM-based benchmark. Results show a difference of 5 % after the fine tuning of all TRNSYS-related parameters (40 % as un-calibrated starting value).

1. Introduction

Complex Fenestration Systems (CFS) can provide a valuable solution to lower the building energy needs by optimizing solar gains during winter, limiting them during the cooling season and reducing artificial lighting (Huckemann et al., 2010; Pomponi et al., 2016). In order to correctly implement these solutions, it is of crucial importance to predict their thermal and day-light behavior.

To this purpose, two main approaches can be used: on the one hand, FEM methods can be adopted to determine in a detailed way its thermal behavior, since all the system components and the relative thermo-physical properties are taken into account, along with the underlying thermo-physical phenomena (Dama et al., 2017; Li et al., 2017; Wang et al., 2016). As Jankovic and Goia (2021) stated, computational fluid dynamics methods are the most suitable tools for solving problems related to these systems. On the other hand, Building Energy Simulation (BES) tools implement simplified methodologies for taking into account the effect of such complex systems on the building scale and, in the case of open cavity fenestration systems, they are typically designed for modeling mechanically ventilated ones. The unavoidable approximations related

to the impossibility of fully considering the geometries and the detailed physical phenomena, however, strongly limit the modeling possibilities, especially when unconventional complex systems are considered. Catto Lucchino et al. (2021) used different BES tools to predict the behavior of a mechanically ventilated Double Skin Façade, and compared the results with measured data; the conclusions state that these tools can be acceptable for predicting an overall performance over a long period, but for short-term performance assessment the error is too large.

In this study, a CFS characterized by a naturally ventilated cavity with an integrated venetian blind was considered. Through a coupled heat transfer and fluid flow simulation with FEM-based calculation software, it is possible to fully capture the fenestration behavior at system scale, but great limitations are found if its impact on the building scale needs to be assessed. These limitations are particularly related to natural ventilation, which is always harder to predict compared with the mechanical ventilation (Wang et al., 2019). This paper hence aims at identifying the natural ventilation modeling limitations for CFS by comparing two calculation approaches (namely, concentrated-parameters and FEM-based models). To answer this research question, a custom simulation setup was built in TRNSYS 18 with the aim of modeling the naturally ventilated window with integrated venetian blinds and assessing its impact on the building scale. To allow this, a FEM-based 2D detailed model was developed in COMSOL Multiphysics with the purpose of obtaining the necessary data to support and calibrate the implementation of the proposed TRNSYS simulation setup.

2. Methodology

2.1 Case Study

In this study, a CFS consisting of a naturally ventilated window with integrated venetian blinds was studied. Fig. 1 shows how the window cavity is in direct connection with the external environment at the bottom and at the top part. A peculiarity is present in the shape of the external openings, which are

not continuous along the fenestration width, but interrupted by solid (closed) parts, as shown in Fig. 1. Additionally, the external openings are covered by a grille characterized by the ratio of blocked area to total area of 1/5. Furthermore, there is a second (internal) vent that is continuous along the fenestration width and characterized by a depth of 5 mm.

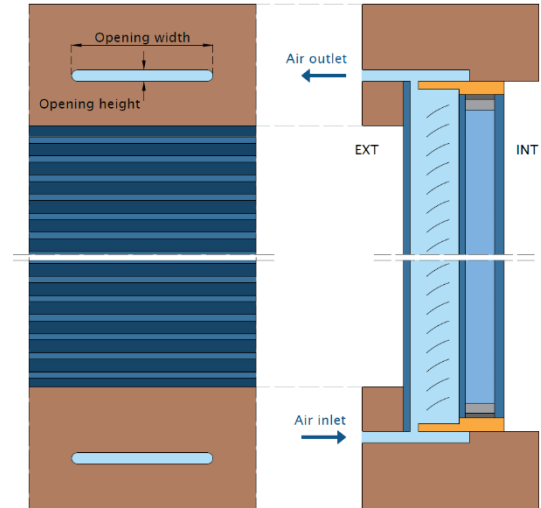


Fig. 1 – Scheme of the considered CFS: front view of a portion of the CFS (left) and vertical cross section (right)

The integrated venetian blind has a direct impact on the airflow and, therefore, on the cavity air temperature in terms of blind type and angles of the slats. In this study, the venetian blind was deployed with slat angles of 0°, 30° and 75° with respect to the horizontal plane. The external cavity (cavity 1) is composed of air, as it is in direct contact with the external environment, while the internal cavity (cavity 2) is filled with a gas mixture of 90 % argon and 10 % air. The external (1) and central (2) glasses are made of single float glass panes of 4mm, while the internal glass (3) is laminated and composed of two float glass panes of 3mm each and one PVB layer. On face 5 (exterior side of the interior glass pane) a low-emissivity coating is placed with an emissivity of 0.013. The geometrical properties of the CFS are listed in Table 1, while the thermal characteristics are reported in Table 2.

Table 1 – CFS geometric parameters

Symbol	Parameter	Value
dglass1-2	Glass 1-2 thickness	4 mm
dgap1	Cavity 1 width	30 mm
dgap2	Cavity 2 width	18 mm
dglass3	Glass 3 thickness	6 mm
w	Blind width	16 mm
α	Blind tilt	0°/30°/75°
H	Cavity height	1.33 m
open_w	Opening width	80mm
open_h	Opening height	7mm

Table 2 – CFS thermal parameters

Symbol	Unit	Blind	Glass1-2	Glass3	Frame
λ	W/m/K	100	1.0	0.65	0.12
c_p	J/kg/K	900	820	820	2700
ρ	kg/m ³	2700	2500	2500	532
ε_f	-	0.212	0.84	0.013	0.84
ε_b	-	0.489	0.84	0.84	0.84

2.2 Simulation workflow

The workflows adopted in the different modeling and simulation approaches of the CFS (FEM-based at system scale and using TRNSYS at building scale) are described in this chapter. The system scale simulation allowed an assessment of the system's performance in detail and temperature and airflow data to be gathered, later used to support the calibration of the TRNSYS model.

2.2.1 System scale simulation approach

The FEM-based software COMSOL Multiphysics (COMSOL n.d.) was used to compute the coupled heat transfer and fluid flow of the analysed CFS. To simplify the model and reduce computation time, the geometry of the CFS was reduced to a vertical cross section and modeled as a bi-dimensional domain. This assumption was supported by the statement of Pasut and De Carli (2012) describing that

the 3D modeling of a fenestration system does not provide a substantial improvement in the results, considering the additional complexity and computation time. The discretization of the domain occurred through the creation of a calculation grid (mesh). This latter was done dividing the geometry into various domains so that, according to the geometric and material characteristics, different types and sizes of the mesh could be adopted. To ensure that the solution is independent from the calculation grid, a mesh refinement study was carried out, and the thermal transmittance was used as control parameter. The final mesh is reported in Fig. 2.

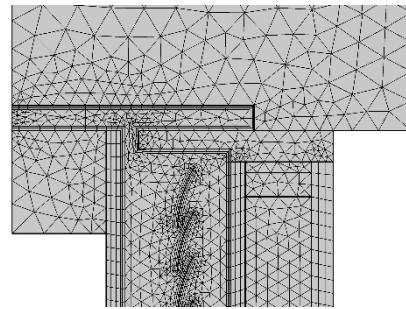


Fig. 2 – Final mesh of the Complex Fenestration System

The modeling of the short-wave radiation exchange due to solar irradiance was done outside the FEM model through a detailed optical calculation using Radiance (Ward, 1994). For each shading configuration, the Bidirectional Scattering Distribution Function (BSDF) was calculated and the solar absorption data for each glass pane and the shading system were derived. The share of incident solar radiation absorbed by each layer of the fenestration system was finally assigned as heat source to single domains within the FEM-based dynamic simulation (Demanega et al., 2020).

To model the natural ventilation through the open window cavity and the top and bottom vents, two additional domains representing the external ambient were added to the model. A relative pressure of 0 Pa was assigned to the top domain's boundaries and of $\frac{1}{2}\rho u^2$ to the bottom ones.

The presence of the grille on the vents was modeled as a pressure drop for a squared mesh described by the equation 1 (COMSOL n.d.), with a solidity σ_s (ratio of blocked area to total area of the screen) equal to 1/5.

$$K = 0.98 ((1 - \sigma_s)^{-2} - 1)^{1.09} \quad (1)$$

To account for the discontinuity of the external vertical opening, which is interrupted by solid (closed) parts along the fenestration width, this non-homogeneity was described analytically in the bi-dimensional FEM model through a localized pressure drop equation of the type $\Delta p = f(u)$, which was determined by means of a separate FEM CFD 3D model focussed only on the ventilation openings. The thermal boundary conditions were assigned in terms of convective and radiative heat flux on the internal and external glazing surfaces, while adiabatic conditions were assumed for the top and bottom boundaries. The simulation was run in a stationary regime and considered converged when the relative residuals of the continuity, momentum and energy equations were less than $10e-4$.

2.2.2 Building scale simulation approach

TRNSYS 18 was used as building dynamic energy simulation software to assess the impact of the CFS on the building scale. A single thermal zone with one window was modeled using the new version of the multi-zone building model Type 56 CFS. This in-built model enables a detailed CFS thermal simulation according to ISO 15099:2003 and uses the BSDF for describing the façade optical properties in the solar and visual band. This Type has been mainly meant to model mechanically ventilated gaps; indeed, it requires as input the inlet mass flow rate (together with its temperature), which is easily available from fan datasheets; however, in the case of naturally ventilated windows, this data is not known a priori because it is highly dependent on the cavity geometry and boundary conditions. For this reason, a Python-based script was implemented through TRNSYS Type 169, which calculated the inlet mass flow rate according to the ISO 15099. The air moves inside the cavity due to the stack effect, thus the velocity of the air gap depends on the driving pressure difference and the resistance of the openings. The airflow in the cavity is modeled as a pipe flow and the driving force of the flow is set equal to the total pressure loss, which takes into account Bernoulli's pressure loss, steady laminar flow and pressure loss due to the inlet and outlet openings. The resulting model exhibits an inter-

dependence between the air gap temperature and velocity and consequently an iterative calculation is performed until the relative convergence limit is less than 1 %.

2.2.3 Model calibration

Given the absence of measured data, the TRNSYS model was calibrated against the FEM one. To support this calibration, parametric simulations were performed with the FEM model considering all combinations of external air temperature ($T_{air,ext}$), internal air temperature ($T_{air,int}$) and solar irradiance (I_{sol}) listed in Table 3.

Table 3 – Boundary conditions for parametric simulations

$T_{air,ext}$ (°C)	0, 5, 10, 15, 25, 30, 35
$T_{air,int}$ (°C)	20, 24, 28
I_{sol} (W/m ²)	0, 250, 500, 750, 1000

COMSOL Multiphysics and TRNSYS 18 have two different approaches to simulate the thermal behavior of CFS. Therefore, to minimize these differences and to set the same boundary conditions, the following assumptions were used in the TRNSYS model: a single-zone “shoe-box” model was used as thermal zone, the surface temperatures of the walls were set equal to the indoor temperature and the view factor to the sky of the façade was set to 0.5 (as in the FEM-model).

To achieve steady-state conditions for every combination of the boundary conditions (as listed in Table 3), simulations were run for 100 hours while keeping fixed the values of $T_{air,ext}$, $T_{air,int}$ and I_{sol} . Results correspondent to the last timestep of each simulation were considered as the steady-state ones.

The ad-hoc TRNSYS Type was carried out by increasing the model complexity step by step, focusing on the inlet ventilation flow rate and the total heat flux.

In a first step, the mass flow rate resulting from the thermo-fluid dynamic simulation was provided as input to the TRNSYS type in order to tune the Type 56 CFS parameters and, in a second step, it was calculated by the Python-based Type 169 and provided as input to the TRNSYS building model. Comparing the outcomes of the two models at component level, it was possible to calibrate the natural flow rate Type, particularly focusing on the tuning

of the pressure loss factor along the window cavity, which takes into account the pressure losses caused by the ventilation openings (inlet and outlet), the squared mesh grille and the integrated venetian blinds. The ISO 15099 describes the pressure loss in the inlet and outlet openings through equation 2 and 3, and, in case of zero lateral opening area and equal top and bottom opening area, equation 4.

$$\Delta P_Z = \frac{1}{2} \rho v^2 (Z_{inl} + Z_{out}) \quad (2)$$

$$Z_{inl/out} = \left(\frac{A_s}{0.6 \cdot A_{eq,inl/out}} - 1 \right)^2 \quad (3)$$

$$A_{eq,inl/out} = A_{top/bot} + \frac{1}{4} A_h \quad (4)$$

Starting from these expressions, two calibration parameters were introduced in the formulation: the first parameter “ x ” 5 is used to calibrate the area of the openings in order to consider the effect of the discontinuity along the fenestration width of the ventilation openings, and the second parameter “ k ” 6 to tune the area of the holes of the venetian blinds.

$$A_{top/bot}^* = x \cdot A_{top/bot} \quad (5)$$

$$A_{eq,inl/out}^* = k \cdot \left(A_{top/bot}^* + \frac{1}{4} A_h \right) \quad (6)$$

Additionally, the pressure drop factor K was included in the total pressure loss equation 2, which becomes equation 7.

$$\Delta P_Z = \rho v^2 (Z_{inl/out} + K) \quad (7)$$

The parameters were varied parametrically one at a time: x between 0.1 and 10 and k between 0.1 and 1. The calibration procedure was divided into 2 steps: first, the opening parameter x was calibrated considering only the blind-up configuration, then the shading parameter k was calibrated keeping the x parameter fixed. In this way, the equation 4 becomes 8, forcing identical parameter values for all configurations.

$$A_{eq,inl/out}^* = k \cdot \left(x \cdot A_{top/bot}^* + \frac{1}{4} A_h \right) \quad (8)$$

The optimal values were chosen by minimizing two statistical indicators: the Root Mean Squared Error

(RMSE) (9) and the Mean Absolute Percentage Error (MAPE) (10), computed for the inlet mass flow rate and the total heat flux for all the cases considered.

$$RMSE = \frac{1}{N} \sqrt{\sum_{i=1}^N (x_{T,i} - x_{C,i})^2} \quad (9)$$

$$MAPE = \frac{1}{N} \sum_{i=1}^N \left| \frac{x_{T,i} - x_{C,i}}{x_{C,i}} \right| \cdot 100\% \quad (10)$$

In this way, the calibration was carried out both at component level (inlet flow rate) and at building level (contribute of the component on the thermal balance of the zone).

3. Results and Discussion

3.1 System Scale Results From COMSOL

The FEM-based simulation performed with COMSOL Multiphysics allowed the temperature, pressure, and velocity field over the fenestration system to be computed and the airflow rate and the total heat flux to be quantified in detail.

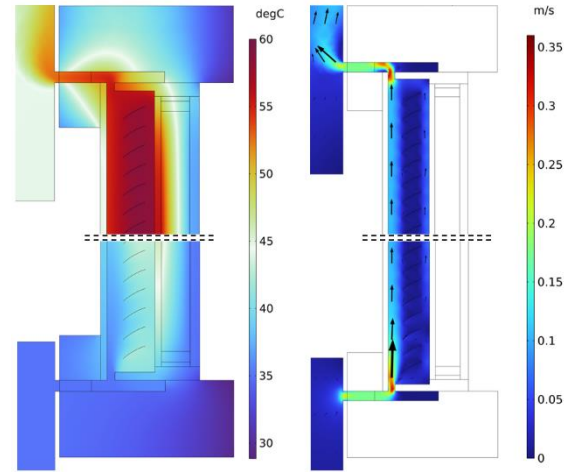


Fig. 3 – Temperature (left) and air velocity (right) distribution over the CFS, $T_{air,ext}=35^\circ\text{C}$, $T_{air,int} = 28^\circ\text{C}$, $I_{sol} = 500 \text{ W/m}^2$, blind tilt 30°

To showcase a possible temperature and air velocity distribution over the CFS with a blind tilt angle of 30° and warm summer conditions ($T_{air,ext} = 35^\circ\text{C}$, $T_{air,int} = 28^\circ\text{C}$, $I_{sol} = 500 \text{ W/m}^2$) an illustration of the spatial distribution of the two variables is shown in Fig. 3. It is possible to notice how buoyancy forces the warmer air to rise, resulting in a vertical

temperature gradient and leading to high temperatures in the upper part of the CFS, where 60 °C are reached.

3.2 Building Scale Results From TRN-SYS and Calibration Parameters

The FEM model outcomes were used to tune the two calibration parameters 5 and 6 of the Python-based Type 169. As mentioned before, only the blind-up dataset was used for the calibration of the x -parameter and focusing on the statistical indicators of the total heat flux, $x=0.5$ was found to be the optimal solution. Regarding the configuration with the shading system deployed, the x parameter was kept fixed to 0.5 and the parameter k was varied parametrically in order to identify the optimal value which minimizes the statistical indicators for the three blind tilt angles configuration. Fig. 5 shows the outcomes of the calibration procedure with blinds at 30° angle; models with $k = 0.3, 0.7$ and 1 were compared to the uncalibrated one ($x=1, k=1$). For each model, the COMSOL (x -axis) versus TRNSYS (y -axis) results are reported for inlet mass flow rate (a) and total heat flux (b). The scatter plots were clustered by the value of the incident solar irradiance, since it affects both the parameters analyzed. It should be noted that parameter k has a greater impact on the mass flow rate than on the total heat flux, because it directly determines the mass flow rate, which in turn influences the total heat flux. Since the flow rate and the total heat flux have different behaviors to the variation of parameter k , the value that minimizes the statistical indicators of the total heat flux was chosen as the optimal one. This assumption is related to the building scale model approach: the total heat flux of the CFS accounts directly for the contribution of the component on the thermal balance of the zone, therefore a greater weight to this parameter is given in the choice of the optimal value.

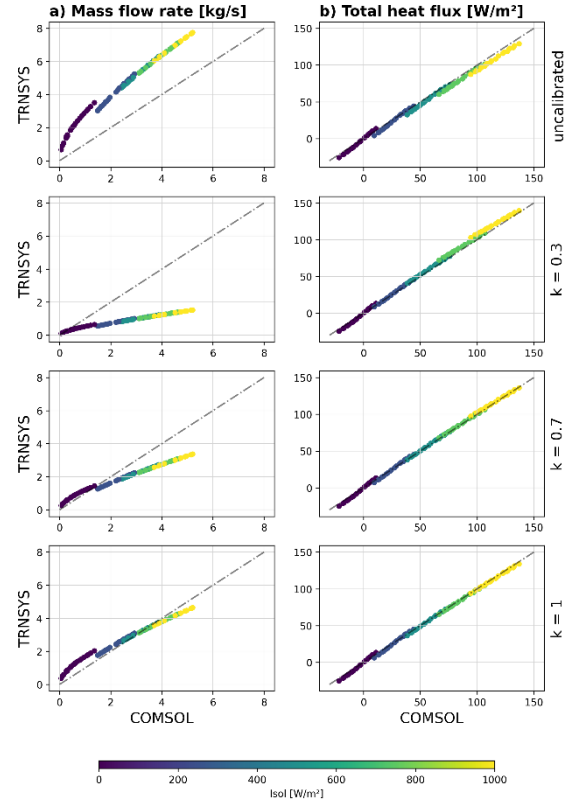


Fig. 4 – Inlet mass flow rate (a) and total heat flux (b) calibration outcomes for blind tilt 30°

The statistical indicator for total heat flux suggests that $k=0.7$ is the optimal solution, with a reduction of the statical errors of 67 % compared to the uncalibrated model ($x=1, k=1$). The same calibration procedure was repeated for the other 2 configurations. To avoid redundancy and for sake of brevity, Table 4 summarizes the results of the calibrated model compared to the uncalibrated one in terms of RMSE and MAPE indicators of inlet mass flow rate and total heat flux. A unique value of k parameter was chosen as optimal for all the configurations of the shading system, in order to avoid the need for changing the calibration values x and k for each blind tilt angle.

This, however, leads to a reduction of the model performance, especially with fully closed blinds. Nonetheless, by calibrating x and k parameters for the two extreme conditions (horizontal and fully closed) and one intermediate condition (30°), it can be assumed that the use of these values could be extended for the remaining configurations.

Table 4 – Comparison of RMSE (top) and MAPE (bottom)

Blind mode	Ventilation Type	Mass flow rate	Total heat flux
Blind up	final model	0.19 kg/s 13.2 %	3.12 W/m ² 5.6 %
	uncalibrated model	1.59 kg/s 100.8 %	3.74 W/m ² 6.7 %
Blind 0°	final model	0.39 kg/s 34.8 %	1.49 W/m ² 2.4 %
	uncalibrated model	2.41 kg/s 186.9 %	3.81 W/m ² 6.4 %
Blind 30°	final model	0.97 kg/s 37.9 %	1.58 W/m ² 1.3 %
	uncalibrated model	2.13 kg/s 125.5 %	4.74 W/m ² 5.8 %
Blind 75°	final model	0.98 kg/s 30.9 %	3.42 W/m ² 11.0 %
	uncalibrated model	1.67 kg/s 82.7 %	1.88 W/m ² 2.0 %

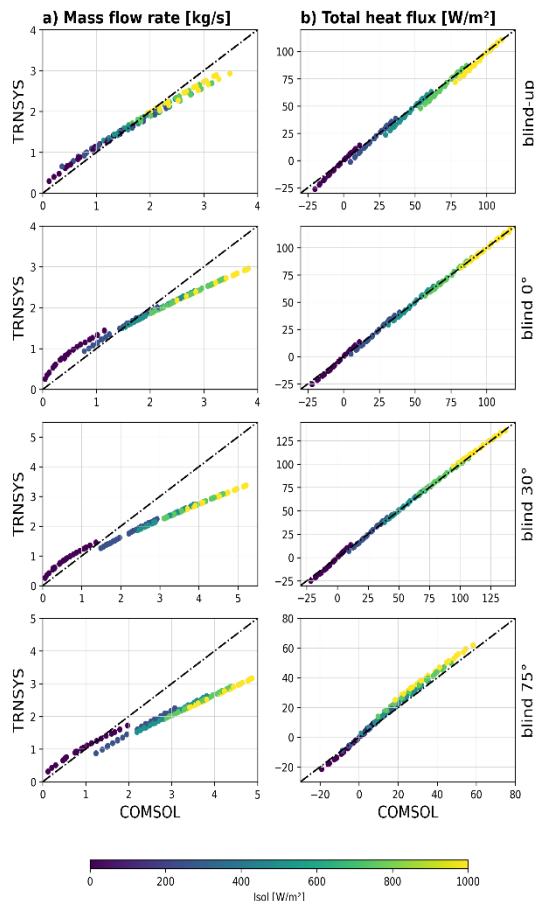


Fig. 5 – Inlet mass flow rate (a) and total heat flux (b) comparison for all blind configurations with the calibrated model

The calibration procedure resulted in a significant reduction of the RMSE in a range of 60 % (blind tilt 0°) to 66 % (blind tilt 30°) and in minimizing the MAPE (especially for blind tilt 0° and 30°). Finally, the comparisons with FEM results for the inlet mass flow rate and total heat flux are shown in Fig. 5 for all configurations. The TRNSYS model overestimates the inlet mass flow rate in the presence of low radiation (< 500 W/m²) and underestimates it in presence of high radiation.

4. Conclusions

To promote the implementation of CFS, it is crucial to enable a relatively simple yet reliable way of assessing their impact at building scale. In this paper, a novel workflow was implemented in one of the most widespread BES tools to assess the performance of a CFS in terms of heat fluxes and airflow rate. The results obtained through FEM simulations were used to calibrate the BES workflow and to assess the error of the calibrated BES tool. Results show a difference of 5 % of the total heat flux through the CFS after the fine-tuning of the ad-hoc Type parameter. The calibration was carried out focusing on the CFS contribution to the thermal balance zone to improve the BES tool's performance in predicting the thermal behavior of such complex components. Moreover, the ad-hoc type can be generalizable for modeling naturally ventilated windows with geometric features similar to the presented CFS (narrow cavity with small vents), since the calibration procedure was carried out by only varying the opening areas.

With this picture, it is possible to state that such workflows allow a consideration of the thermal behavior of CFS at building scale with an acceptable degree of uncertainty. This results in the great advantage of providing the possibility of assessing the impact of a CFS when there is still room for improvement and change in the design.

Acknowledgement

The research presented in this paper has been supported by the Cultural-E project. This project has received funding from the European Union's Horizon 2020 research and innovation program under grant agreement No 870072.

Nomenclature

Symbols

q	Specific heat flux (W/m ²)
h_c	Convective heat transfer coefficient (W/(m ² K))
T_{air}	Air temperature (°C)
T_{sf}	Surface temperature (°C)
σ	Stefan-Boltzmann constant (5.669x10 ⁻⁸ W/m ² /K ⁴)
ε	Thermal emissivity (-)
ε_f	Thermal emissivity front (-)
ε_b	Thermal emissivity back (-)
ρ	Mass density (kg/m ³)
u	Air velocity (m/s)
σ_s	Solidity (ratio of blocked area to total area of the screen)
K	Resistance coefficient (-)
λ	Thermal conductivity (W/m/K)
c_p	Specific heat capacity at constant pressure (J/kg/K)

References

- Catto Lucchino, E., A. Gelesz, K. Skeie, G. Gennaro, A. Reith, V. Serra, and F. Goia. 2021. "Modelling Double Skin Façades (DSFs) in Whole-Building Energy Simulation Tools: Validation and Inter-Software Comparison of a Mechanically Ventilated Single-Story DSF." *Building and Environment* 199. doi: <https://doi.org/10.1016/j.buildenv.2021.107906>
- COMSOL. n.d. "COMSOL Multiphysics® v. 5.6."
- COMSOL. n.d. "Screen Boundary Condition."
- Dama, A., D. Angeli, and O. Kalyanova Larsen. 2017. "Naturally Ventilated Double-Skin Façade in Modeling and Experiments." *Energy and Buildings* 144: 17–29. doi: <https://doi.org/10.1016/j.enbuild.2017.03.038>
- Demanega, I., G. de Michele, M. Hauer, S. Avesani, G. Pernigotto, and A. Gasparella. 2020. "Numerical and Experimental Characterization of the Thermal Behavior of Complex Fenestrations Systems under Dynamic Conditions." In *Proceedings of Building Simulation Applications 2019*, Bolzano, Italy.
- Huckemann, V., E. Kuchen, M. Leão, and É. F. T. B. Leão. 2010. "Empirical Thermal Comfort Evaluation of Single and Double Skin Façades." *Building and Environment* 45(4): 976–82. doi: <https://doi.org/10.1016/j.buildenv.2009.10.006>
- ISO. 2003. *ISO 15099 International Standard ISO 15099:2003. Thermal Performance of Windows, Doors and Shading Devices — Detailed Calculations*.
- Jankovic, A., and F. Goia. 2021. "Impact of Double Skin Facade Constructional Features on Heat Transfer and Fluid Dynamic Behaviour." *Building and Environment* 196: 107796. doi: <https://doi.org/10.1016/j.buildenv.2021.107796>
- Li, Y., J. Darkwa, and G. Kokogiannakis. 2017. "Heat Transfer Analysis of an Integrated Double Skin Façade and Phase Change Material Blind System." *Building and Environment* 125: 111–21. doi: <https://doi.org/10.1016/j.buildenv.2017.08.034>
- Pasut, W., and M. De Carli. 2012. "Evaluation of Various CFD Modelling Strategies in Predicting Airflow and Temperature in a Naturally Ventilated Double Skin Façade." *Applied Thermal Engineering* 37:267–74. doi: <https://doi.org/10.1016/j.applthermaleng.2011.11.028>
- Pomponi, F., P. A. E. Piroozfar, R. Southall, P. Ashton, and E. R. P. Farr. 2016. "Energy Performance of Double-Skin Façades in Temperate Climates: A Systematic Review and Meta-Analysis." *Renewable and Sustainable Energy Reviews* 54: 1525–36. doi: <https://doi.org/10.1016/j.rser.2015.10.075>
- Wang, Y., Y. Chen, and C. Li. 2019. "Airflow Modeling Based on Zonal Method for Natural Ventilated Double Skin Façade with Venetian Blinds." *Energy and Buildings* 191: 211–23. doi: <https://doi.org/10.1016/j.enbuild.2019.03.025>
- Wang, Y., Y. Chen, and J. Zhou. 2016. "Dynamic Modeling of the Ventilated Double Skin Façade in Hot Summer and Cold Winter Zone in China." *Building and Environment* 106:365–77. doi: <https://doi.org/10.1016/j.buildenv.2016.07.012>
- Ward, G. J. 1994. "The RADIANCE Lighting Simulation and Rendering System." *Proceedings of the 21st Annual Conference on Computer Graphics and Interactive Techniques, SIGGRAPH 1994* 459–72. <https://doi.org/10.1145/192161.192286>

Heat and Mass Transfer Modelling for Moisture-Related Risks in Walls Retrofitted by Timber Materials

Gianpiero Evola – University of Catania, Italy – gevola@unict.it

Alessandra Urso – University of Catania, Italy – alessandra.urso@phd.unict.it

Vincenzo Costanzo – University of Catania, Italy – vincenzo.costanzo@unict.it

Francesco Nocera – University of Catania, Italy – fnocera@unict.it

Luigi Marletta – University of Catania, Italy – luigi.marletta@unict.it

Abstract

The e-SAFE innovation project financed by the Horizon 2020 Programme and led by the University of Catania, is developing, testing and demonstrating an innovative combined energy-and-seismic renovation solution for Reinforced Concrete (RC) framed buildings based on the addition of Cross Laminated Timber (CLT) boards to the outer walls, in combination with wood-based insulation. In this paper, the proposed renovation solution (called e-CLT) is investigated in terms of moisture-related risks, i.e., the mold growth and the increase in heat losses due to Liquid Water Content (LWC) within building materials. To this aim, dynamic simulations are performed by means of Delphin 6.1, thus including combined heat and mass transfer (HAMT) due to water vapor migration and accumulation. The results show that, although there is no significant risk of mold growth in the e-CLT for climate conditions prevalent in Northern Italy, the moisture content within the materials implies an increase by about 10 % in the heat losses if compared with a dry wall. Furthermore, inaccurate material properties and boundary outdoor climate conditions can affect the reliability of the results: for this reason, a more appropriate hygrothermal characterization of materials is recommended, as well as the identification of suitable climate datasets, which, however, are not always available.

1. Introduction

Since around 80 % of the building stock in the European Union was built before 1990, i.e., before the enforcement of most EU regulations regarding the energy performance of buildings, it is apparent that deep renovation is a key challenge towards the decarbonization of the existing building stock.

In this framework, the e-SAFE innovation project financed by the Horizon 2020 Programme and led by the University of Catania, is developing, testing and demonstrating an innovative combined energy-and-seismic renovation solution for Reinforced Concrete (RC) framed buildings based on the addition of Cross Laminated Timber (CLT) boards to the outer walls, in combination with wood-based insulation. In this study, the proposed renovation solution (called e-CLT) is applied to a building with infill walls made of two leaves of lightweight concrete blocks with an intermediate air gap, a very common envelope solution in Italy for the residential buildings from the 1960s to the 1980s.

While the seismic performance ensured by the e-CLT solution is addressed in other studies, this paper aims to investigate moisture-related risks by means of Delphin 6.1 software, which allows transient simulations considering combined heat and moisture transport (HAMT). In fact, wood-based components are particularly prone to moisture storage due to their cellular structure, and – being wood an organic material – they are more sensitive to decay caused, e.g., by mold.

Preliminary investigations by means of Glaser's method revealed that, although the application of the e-CLT solution improves both thermal and hygrothermal behavior of the walls (Evola et al., 2021), interstitial condensation may occur in cold climates in case of high indoor humidity values (Costanzo et al., 2021a). A following study (Costanzo et al., 2021b) tested the e-CLT solution in three different climates in Italy, performing transient hygrothermal simulations and reaching similar conclusions: wood-based materials are likely exposed to mold

growth – although moderate – especially in colder climates.

Building on these previous research experiences, this paper focuses on the reliability of the results, which may be affected by inaccuracy of hygrothermal materials properties and climatic boundary conditions. To this aim, a literature review highlights the dispersion of the hygrothermal property values for wood, and the consequent effects on the simulation results. Moreover, the paper underlines the effects of using different weather datasets, such as a typical meteorological year (TMY) and a weather file available in the Delphin database for the same location. In particular, the simulations refer to Milan, a cold and humid climate in Northern Italy. Finally, moisture-related risks are investigated by looking not only at mold growth, but also at the increase in the heat transfer through the wall due to the liquid water content within building materials.

2. Methodology

The hygrothermal performance and the moisture-related risk of the e-CLT solution are investigated by means of dynamic finite element analyses performed in Delphin 6.1, a commercial program developed at University of Dresden.

The software allows the combined heat and moisture transport (HAMT) within porous building materials to be considered. To this aim, it requires hygrothermal material properties and functions (e.g., porosity, density, specific heat capacity, thermal conductivity, water vapor resistance factor, liquid conductivity, moisture storage curve), and indoor and outdoor climatic boundary conditions (e.g., temperature, relative humidity, driving rain, wind speed, wind direction, short and long wave radiation). The selection of appropriate material properties and climate data is a paramount issue due to their effect on the reliability of the results; for this reason, this paper pays particular attention to these issues, as highlighted in this Section.

2.1 Materials

The e-CLT solution is here applied to a typical Italian wall structure composed of (from internal to external side): cement plaster (20 mm), hollow concrete blocks with volcanic aggregates (80 mm), non-ventilated air cavity (100 mm), hollow concrete blocks with volcanic aggregates (120 mm) and cement plaster (30 mm).

As regards the e-CLT solution, this is composed of (from internal to external side): CLT (100 mm), low density wood fiber (60 mm), scarcely-ventilated air gap (20 mm) and a fiber cement cladding (12 mm). The proposed solution also includes a vapor-open foil ($s_d = 0.04$ m) to protect the insulation layer from the effect of wind-driven rain, applied to the external side of wood fiber. Materials are selected from the Delphin database; some properties have been modified according to technical sheets and standards in case of missing materials. Table 1 and Table 2 show the hygrothermal properties of the selected materials. In case of air gaps, the thermal conductivity is defined as an equivalent value calculated from the air gap thermal resistance.

Table 1 – Thermal properties of selected materials: “id” is the identification code on material database, (*) indicates modified properties

id	Material	ρ kg·m ⁻³	c_p J·kg ⁻¹ ·K ⁻¹	λ_{dry} W·m ⁻¹ ·K ⁻¹
242	Plaster	1390	850	0.75
508	Hollow blocks (80 mm)	845	1000	0.29*
15	Non-ventilated air gap	1.3	1050	0.56*
508	Hollow blocks (120 mm)	667*	1000	0.39*
712	CLT	450*	1843	0.12*
1762	Wood fiber	50*	1000	0.04
15	Scarcely-ventilated air gap	1.3	1050	0.22*
654	Fiber cement cladding	1160	1188	0.60*

Table 2 – Hygric properties of selected materials: “id” is the identification code on material database, (*) indicates modified properties

id	Material	μ -	A g·m ⁻² ·s ^{-0.5}	θ_{80} kg·m ⁻³	θ_{eff} kg·m ⁻³
242	Plaster	33	30	40.7	430.0
508	Hollow blocks (80 mm)	15	177	11.4	319.4
15	Non-ventilated air gap	1	-	-	-
508	Hollow blocks (120 mm)	15	177	11.4	319.4
712	CLT	186	2-5-12*	59.8	728.1
1762	Wood fiber	1.1	5	12.7	590.3
15	Scarcely-ventil. air gap	1	-	-	-
654	Fiber cement cladding	26	14	70.9	283.6

The hygrothermal characterization of the CLT requires a more detailed literature review, both because it is a missing material from the Delphin database, and because there are some discrepancies amongst the various sources surveyed. In particular, those parameters related to moisture transport, namely the water vapor resistance factor (μ -value) and the water uptake coefficient (A-value), show a high dispersion of their values. Thus, CLT is represented through the database material Spruce radial (id.: 712), experimentally tested by the Technical University of Dresden. However, since the manufacturing process can make CLT denser than the original wood (Lapage, 2012), density is replaced by the value supplied by manufacturers ($\rho = 450 \text{ kg}\cdot\text{m}^{-3}$), whereas dry thermal conductivity refers to EN ISO 10456 Standard (CEN, 2007a) ($\lambda = 0.12 \text{ W}\cdot\text{m}^{-1}\cdot\text{K}^{-1}$).

As regards moisture transport parameters, the glue between lumber boards in a CLT panel can affect the μ -value and A-value because it acts as a seal. Nevertheless, some studies show good agreement between CLT and transverse wood's hygric properties (AlSayegh, 2012; Lapage, 2012): Table 3 sums up experimental μ -value and A-value for softwoods and CLT, based on different species as reported in the literature. As shown in Table 3, moisture transport parameters depend firstly on species and fiber direction. The EN ISO 10456 Standard (CEN, 2007a) reports $\mu = 50$ for timber, i.e., the proposed resistance to vapour diffusion is about four times lower than spruce radial and ten times lower than spruce tangential as gathered from the Delphin database. However, if compared with literature values (AlSayegh, 2012; Kordiziel et al., 2020), the μ -value varies from 146 to 456 for softwoods and CLT boards made of softwood with transverse fiber direction. This means that μ -value of spruce radial ($\mu = 186$) can be assumed as a reliable value for simulations.

Coming to the A-value, this varies between $1.6 \text{ g}\cdot\text{m}^{-2}\cdot\text{s}^{-0.5}$ and $14 \text{ g}\cdot\text{m}^{-2}\cdot\text{s}^{-0.5}$ for transverse fiber direction. The wide range of values covered in the literature mainly depends on the preparation of test specimens. For instance, the presence of wood imperfections (e.g., checks, cracks, holes) could make wood more permeable to moisture, as confirmed by (Raina, 2021) by means of the visual evaluation of absorbed water from a surface with a small hole

during the water uptake test. For this reason, (Al-Sayegh, 2012) selected test specimens that are more representative of the material without checks, thus obtaining A-value = $1.9 - 2.0 \text{ g}\cdot\text{m}^{-2}\cdot\text{s}^{-0.5}$. In contrast, (Lapage, 2012) tested samples including “checks, cracks, pitch pockets and other deviations from ideal conditions”, and determined higher A-values ($4 - 14 \text{ g}\cdot\text{m}^{-2}\cdot\text{s}^{-0.5}$). The size of the sample can also affect the experimental results: indeed, small samples are likely to minimize the effects of checks and gaps in the boards (McClung et al., 2014). This could explain A-values ($2.1 - 2.8 \text{ g}\cdot\text{m}^{-2}\cdot\text{s}^{-0.5}$) found out by (Kordiziel et al., 2020), who used samples with smaller surface area than the minimum set in the Standard.

Table 3 – Softwoods and CLT features from literature (SPF: Spruce-Pine-Fir)

Source	Type	ρ $\text{kg}\cdot\text{m}^{-3}$	μ^* -	A $\text{g}\cdot\text{m}^{-2}\cdot\text{s}^{-0.5}$
Delphin database	Spruce (radial)	395	186	12
	Spruce (tangential)	395	488	5
	Spruce (longitudinal)	395	5	12
EN ISO 10456 (CEN, 2007a)	Timber	450	50	-
(Lapage, 2012)	CLT, Eastern SPF	486	-	4 - 7
	CLT, Western SPF	500	-	12
	CLT, European softwood	340	-	10 - 11
	CLT, Him-Fir	522	-	14
(Alsayegh, 2012)	CLT, Eastern SPF	370	328	2.0
	CLT, Western SPF	440	456	1.9
	CLT, European softwood	340	311	1.6
	CLT, Him-Fir	380	277	2.5
(Cho et al., 2019)	CLT	602	630	-
(Kordiziel et al., 2020)	CLT, SPF + Douglas Fir	423	-	2.5 - 2.8
	SPF without adhesive	426	146	2.8
	SPF with adhesive	426	168	2.4
(Raina, 2021)	CLT, European spruce	-	-	1.9 - 3.6
	CLT, European spruce - without covered edges	-	-	7 - 12
(Chang et al., 2020)	Larch (radial)	570	75	-
	Larch (tangential)	570	109	-
	Larch (longitudinal)	570	5	-
	CLT, larch and plywood	600	79	-

*dry cup, RH chamber = 50 %

Lastly, the sealing of edges could also influence test results. To this purpose, (Raina, 2021) tested various samples with and without sealed edges, demonstrating that the A-value can reach $12 \text{ g}\cdot\text{m}^{-2}\cdot\text{s}^{-0.5}$ due

to water absorbed from longitudinal fiber of the cut uncovered edges. Not surprisingly, the results are close to those reported by (Glass & Zelinka, 2010) for softwood in longitudinal direction ($10 - 16 \text{ g}\cdot\text{m}^{-2}\cdot\text{s}^{-0.5}$). In view of this, and considering A-values of 2 and $12 \text{ g}\cdot\text{m}^{-2}\cdot\text{s}^{-0.5}$ as reasonable extreme conditions, this paper assumes $5 \text{ g}\cdot\text{m}^{-2}\cdot\text{s}^{-0.5}$ as an intermediate value for spruce. However, simulations are repeated for other A-values to perform a sensitivity analysis.

2.2 Climate Boundary Conditions

The simulations are carried out for Milan (lat: 45° , long: 9° , altitude: 103 m) a cold and humid climate in Northern Italy. In order to assess the most appropriate available dataset for this location, the paper considers: i) the weather file from the Delphin database and ii) the TMY weather file from Linate (2004 – 2018) downloaded from the website (Climate.OneBuilding.org, 2022) (Fig. 1). In both cases, the investigated wall is oriented facing north, thus excluding the effect of direct solar radiation. For this reason, the plots in Fig. 1 only report the mean diffuse solar radiation.

Considering yearly mean values, the Delphin dataset shows 13 % higher diffuse solar radiation, but it appears colder (by 3°C on average), more humid (by 6 % on average) and rainier (by 20 % on average) than the Linate dataset. This suggests that it will more likely induce moisture-related risks. Nevertheless, the long wave sky radiation (LWR) data is missing in all Italian weather files within the Delphin database, which implies excluding long wave radiation exchange from the simulation, thus affecting the reliability of results. On the other hand, Linate TMY is not built *ad hoc* for hygrothermal simulations, i.e., it is not representative of the worst climate conditions from the point of view of moisture-related risks. The selection of the most appropriate dataset thus requires preliminary simulations, as discussed in Section 3.1.

The outside heat transfer coefficient and surface vapor diffusion coefficient are $25 \text{ W}\cdot\text{m}^{-2}\cdot\text{K}^{-1}$ and $7.5\cdot 10^{-8} \text{ m}\cdot\text{s}^{-1}$, respectively, while their indoor values are $8 \text{ W}\cdot\text{m}^{-2}\cdot\text{K}^{-1}$ and $2.5\cdot 10^{-8} \text{ m}\cdot\text{s}^{-1}$, respectively. The solar absorption coefficient is set to 0.6. The incident wind-driven rain (WDR) is calculated by Delphin

according to EN ISO 15927-3 Standard (CEN, 2009), using a splash coefficient of 0.7. In addition, a water source is assigned to the side of the insulation protected by the water-proof membrane, set equal to 1 % of the rain flux incident on external surface. This setting simulates rain leakage through the cladding.

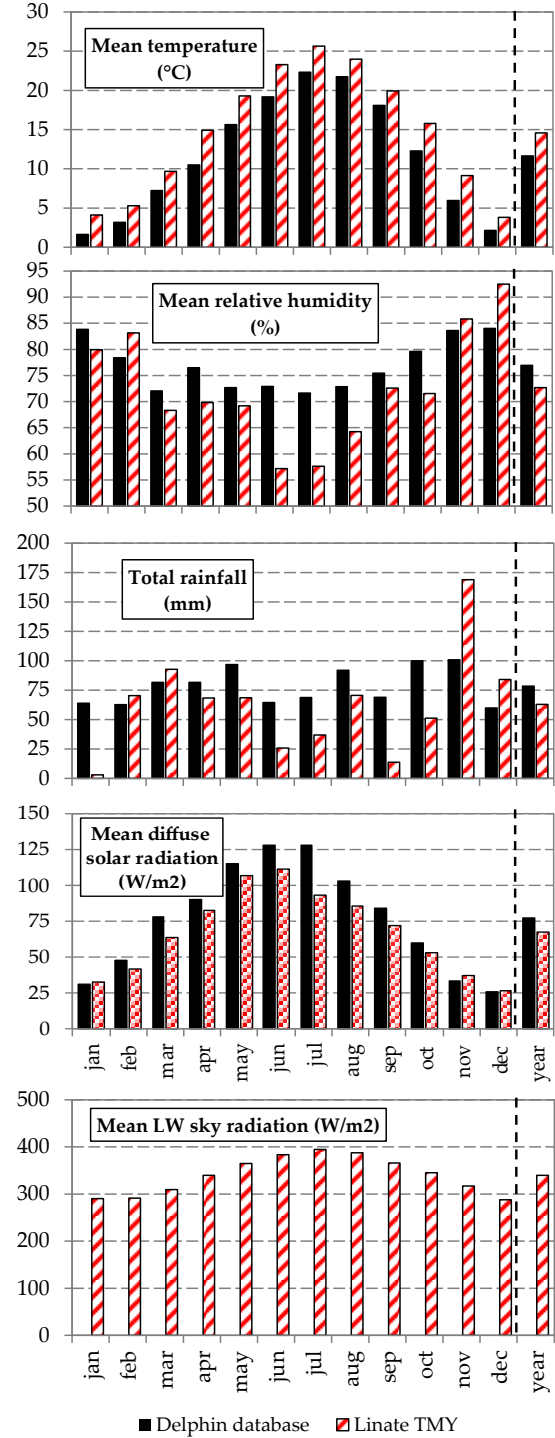


Fig. 1 – Comparison between weather data from Delphin Database and from a web service (Climate.OneBuilding.org, 2022)

On the other hand, the indoor conditions are set according to EN ISO 15026 Standard (CEN, 2007b). The standard offers a simplified approach to take the change in indoor temperature and relative humidity as a function of external conditions into account (Fig. 2). It is here relevant to highlight that moisture-related risks may also depend on the indoor conditions (Brambilla & Gasparri, 2020). This issue will be investigated in future studies.

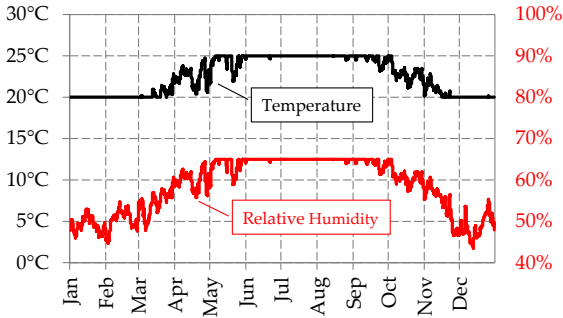


Fig. 2 – Indoor climate conditions as a function of outdoor temperature from Linat TMY, according to EN ISO 15026 (CEN, 2007b)

2.3 Initial Conditions

The simulations are performed over a 10-year-long period, in order to obtain stabilized behavior; the initial conditions correspond to 20 °C temperature and 80 % relative humidity for all materials.

2.4 Outputs

Moisture related-risks are evaluated for the e-CLT solution applied to the investigated existing wall by requesting as outputs from Delphin the time-dependent liquid water content (LWC) in both the CLT and the insulating material, as well as the temperature and relative humidity from which calculating the mold index (MI) by means of the tool PostProc 2.2.3.

In particular, the LWC ($\text{m}^3\cdot\text{m}^{-3}$) represents the volume fraction of liquid phase accumulated in the pores of the materials (Bauklimatik Dresden, 2022). Instead, according to the VTT model (Ojanen et al., 2010), MI measures the mold growth rate in a scale from 0 (no mold growth) to 6 (very heavy and tight mold growth); the authors also suggest that MI values above 3 are not acceptable. The model also considers the sensitivity of materials to mold growth: in this specific case, the CLT and the wood fiber are set as “sensitive”.

Further outputs are the mean conductive heat flux throughout the wall and the moisture-dependent thermal conductivity for each layer of the wall. They are required to assess the increase of thermal losses and U-value due to humidity within building materials.

More specifically, the moisture-dependent U-value ($\text{W}\cdot\text{m}^{-2}\cdot\text{K}^{-1}$) is calculated as follows:

$$U(\text{LWC}) = \left[\frac{1}{h_{0,e}} + \sum_{i=1}^n \frac{s_i}{\lambda_i(\text{LWC})} + \frac{1}{h_{0,i}} \right]^{-1} \quad (1)$$

where $h_{0,e}$ and $h_{0,i}$ are respectively the outside and inside heat transfer coefficient, previously defined, n is the number of layers and λ_i ($\text{W}\cdot\text{m}^{-1}\cdot\text{K}^{-1}$) is the moisture-dependent thermal conductivity of each layer, computed by Delphin as a function of LWC, given the dry thermal conductivity λ_{dry} (Vogelsang et al., 2013):

$$\lambda = \lambda(\text{LWC}) = \lambda_{\text{dry}} + 0.56 \cdot \text{LWC} \quad (2)$$

This study does not consider the influence of temperature on thermal conductivity, since Delphin does not include any built-in functions for the selected materials to this scope. However, by taking into account the conversion coefficients reported in Annex A of EN ISO 10456 Standard (CEN, 2007a), the maximum variation of λ within the range of temperatures occurring in this study would be around 3 % for the insulating material, and even less for the other materials.

3. Results And Discussion

3.1 The Role of the Weather Data

As mentioned above, the influence of weather data is preliminarily investigated. The main target is to understand which dataset is more appropriate, or implies more conservative results, in terms of moisture-related risk.

The simulations are repeated with i) weather data from the Delphin database, which does not include the LWR exchanges, ii) weather data from Linat TMY, with and without LWR exchanges. The results are reported in Fig. 3 and Fig. 4.

If looking at the results obtained using the weather file from the Delphin database (grey solid line in Figs. 3-4), the yearly mean LWC is $0.054 \text{ m}^3\cdot\text{m}^{-3}$ in

the external side of CLT and $0.012 \text{ m}^3\cdot\text{m}^{-3}$ in the external side of wood fiber. There is no risk of mold in both materials. Instead, the results from the simulations run with the TMY from Linate reveal that including LWR exchanges worsens the hygrothermal behavior of the e-CLT. In fact, using Linate TMY with LWR implies temperatures and relative humidity profiles respectively lower and higher than the case without LWR, which also means higher LWC and MI.

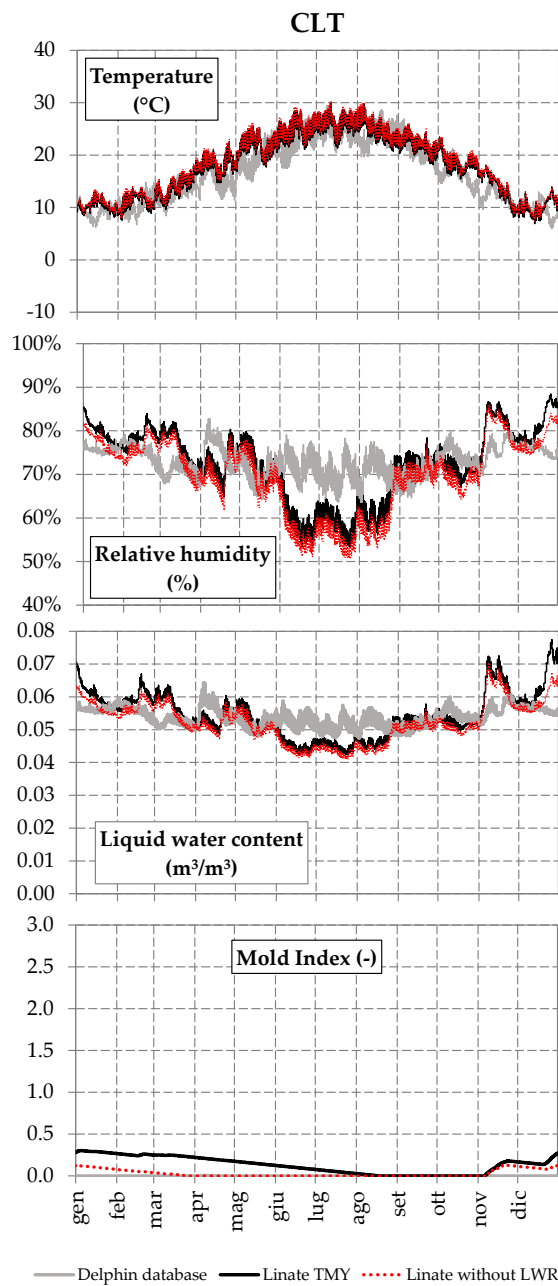


Fig. 3 – Comparison between simulations with weather data from Delphin database and from Linate TMY with/without LWR

In particular, the yearly mean LWC in the external side of both CLT and wood fiber increases by around 4 %. The risk of mold growth is higher in the wood fiber, for which the maximum MI is $2.17 - 0.27$ respectively taking and not taking into account LWR exchanges. Although the MI is still below the critical threshold, in the first case its values tend to increase over the years. This means that excluding the LWR exchanges, for instance by using the Italian weather files available in Delphin, can underestimate moisture-related risks.

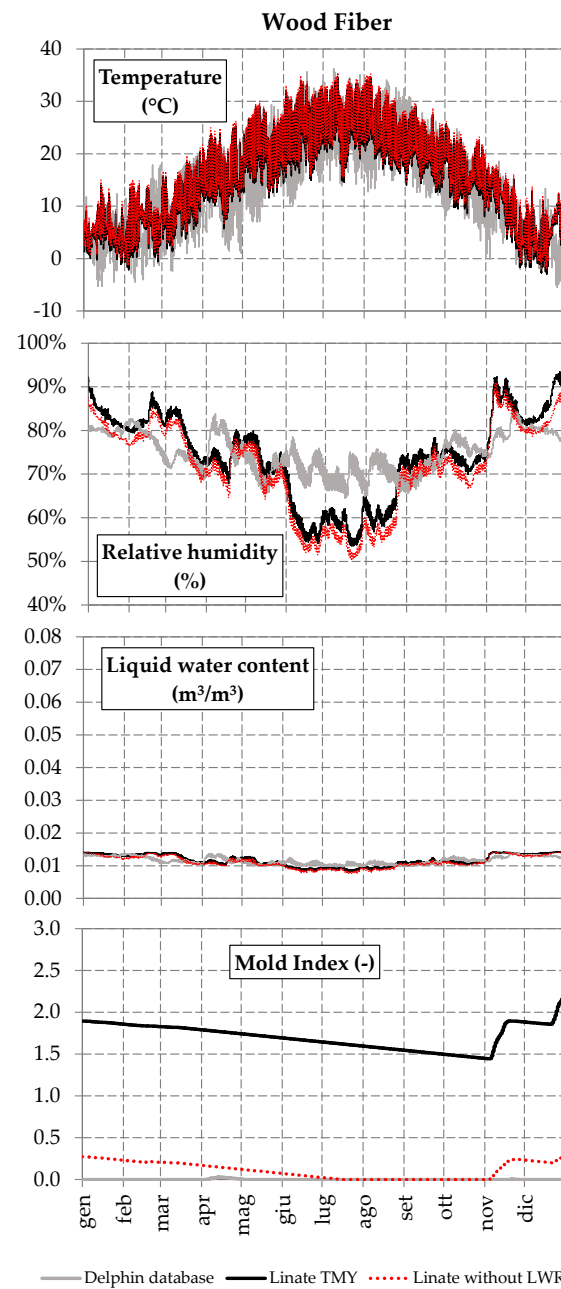


Fig. 4 – Comparison between simulations with weather data from Delphin database and Linate TMY with/without LWR

For this reason, the results discussed in the following sections refer to simulations performed with Linat TMY, even if this weather file is not built *ad hoc* for hygrothermal simulations. Future studies will rely on suitable extreme weather data for Milan, for instance created according to EN ISO 15026 (CEN, 2007b).

3.2 Humidity and Increased Heat Flux

In order to assess the increase in the heat losses due to LWC within building materials, the mean heat flux transferred through the wall is calculated considering thermal conductivity respectively dependent, or independent, on moisture content. Thus, simulations are repeated assuming for each material respectively Eq. 2 and Eq. 3.

$$\lambda = \lambda_{\text{dry}} \quad (3)$$

The results are reported in Fig. 5: not taking into account the variation in thermal conductivity due to moisture content within materials would underestimate heat losses by about 9.7 % on average. Similarly, the moisture-dependent yearly mean U-value ($U = 0.326 \text{ W} \cdot \text{m}^{-2} \cdot \text{K}^{-1}$) increases by 11.0 % with respect to the U-value in dry conditions ($U = 0.290 \text{ W} \cdot \text{m}^{-2} \cdot \text{K}^{-1}$).

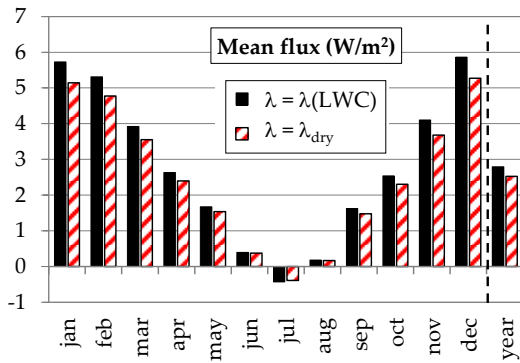


Fig. 5 – Monthly mean conductive heat flux: comparison between simulations taking and not taking into account moisture-dependent thermal conductivity

In a similar study, (Danovska et al., 2019) studied the impact of humidity and temperature on the thermal behavior of insulated timber walls for a series of Italian cities, and found out that the mean increase in heat losses – considering the actual thermal conductivity of materials – is below 6 % on average in Northern Italy locations and below 10 % in Southern Italy, the highest values pertaining to the most insulated wall structures. Finally, Fig. 6 suggests that the

monthly mean U-value of the wall retrofitted through the e-CLT solution can be linearly correlated with mean LWC of wood fiber with $R^2 = 0.99$. This means that the thermal performance of the e-CLT solution applied to the investigated wall decreases linearly with the amount of the LWC in the insulation layer.

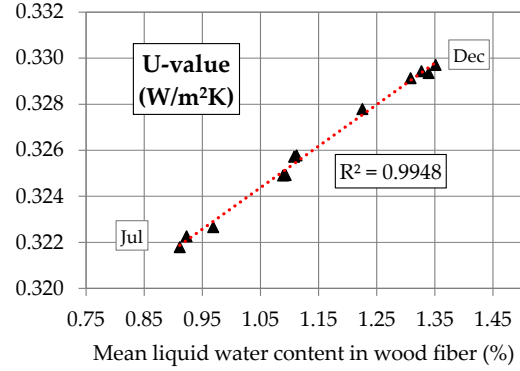


Fig. 6 – Moisture-dependent monthly mean U-value

3.3 The Water Uptake Coefficient

A sensitivity analysis is finally carried out to observe the CLT performance as a function of its A-value. The top plot in Fig. 7 shows the hourly profiles of mean LWC throughout the CLT, respectively with A-value = 2, 5 and 12 $\text{g} \cdot \text{m}^{-2} \cdot \text{s}^{-0.5}$ according to literature. In principle, higher A-values imply higher LWC during winter.

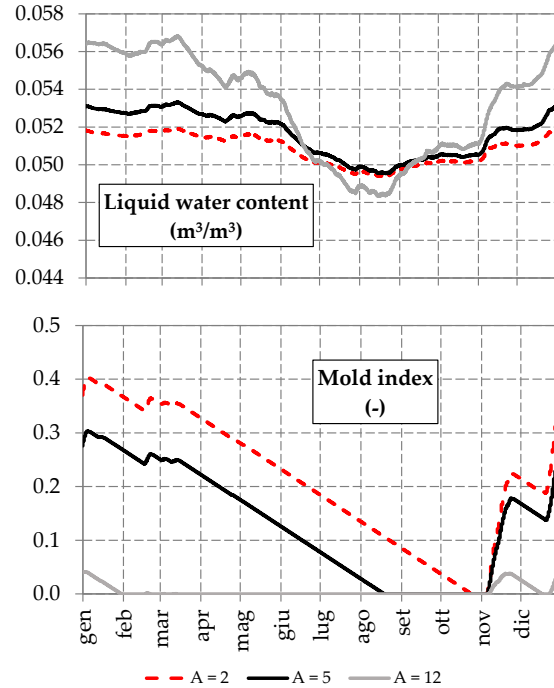


Fig. 7 – Influence of A-value on mean liquid water content and external face mold index. All values in legend are in $\text{g} \cdot \text{m}^{-2} \cdot \text{s}^{1/2}$

Overall, A-value does not significantly affect the e-CLT thermal performance: indeed, the yearly mean LWC ranges between $0.051 - 0.053 \text{ m}^3\cdot\text{m}^{-3}$, which does not imply variations in the heat losses. Finally, looking at the MI in the CLT (bottom plot of Fig. 7), the increase in A-value determines slightly higher mold growth risk. Indeed, in this case the moisture content between CLT and wood fiber is absorbed more rapidly towards the inner side. However, the risk is negligible ($\text{MI} < 0.4$).

4. Conclusion

In this study, the e-CLT building retrofit solution, applied to a typical existing Italian wall, is investigated in terms of moisture related risks, i.e., the mold growth and the increase in heat losses due to liquid water content within building materials. Moreover, this paper focuses on the role of weather data and of the water uptake coefficient of the CLT material on simulations. Since e-CLT is an innovative retrofit solution, this topic is not addressed in the literature except for some preliminary analyses carried out by the same authors (Costanzo et al., 2021b). With respect to the above-referenced study, the current research confirms that a moderate mold growth risk ($\text{MI} > 1$) can occur in a cold and humid Italian climate, while also discussing the role of CLT hygrothermal properties in greater detail. Furthermore, the reliability of the Italian weather files within the Delphin database is assessed in a systematic way.

The conclusions can be summed up as follows:

- excluding the long wave heat transfer from the simulation, for instance, when using Delphin database Italian weather files, leads to underestimate moisture-related risks;
- the inaccuracy on the A-value of CLT does not significantly impact on the LWC and MI;
- the increased heat losses due to LWC within building materials amount to around 10 %
- the monthly mean U-value is linearly dependent on LWC in the insulation layer, and on average can vary by around 11 % if compared to an equivalent dry wall.

The next steps of this research activity will investigate the hygrothermal behavior during extreme meteorological years, selected from long-term weather

acquisitions in different climate zones. In addition, further analyses are planned to better characterize hygrothermal properties of materials by means of experimental analyses.

Nomenclature

Symbols

A	water uptake coefficient ($\text{g}\cdot\text{m}^{-2}\cdot\text{s}^{-0.5}$)
CLT	cross laminated timber
c_p	specific heat capacity ($\text{J}\cdot\text{kg}^{-1}\cdot\text{K}^{-1}$)
HAMT	heat and moisture transport
λ	thermal conductivity ($\text{W}\cdot\text{m}^{-1}\cdot\text{K}^{-1}$)
λ_{dry}	dry thermal conductivity ($\text{W}\cdot\text{m}^{-1}\cdot\text{K}^{-1}$)
LWC	liquid water content ($\text{m}^3\cdot\text{m}^{-3}$)
LWR	long wave radiation
MI	mold index (-)
μ	water vapor resistance factor (-)
ρ	density ($\text{kg}\cdot\text{m}^{-3}$)
s_d	equivalent air layer thickness (m)
θ_{80}	moisture content at 80 % RH ($\text{kg}\cdot\text{m}^{-3}$)
θ_{eff}	effective saturation ($\text{kg}\cdot\text{m}^{-3}$)
U	thermal transmittance ($\text{W}\cdot\text{m}^{-2}\cdot\text{K}^{-1}$)
WDR	wind-driven rain

Acknowledgement

This paper was carried out within the framework of the “Energy and seismic affordable renovation solutions” (e-SAFE) project, which has received funding from the European Union’s Horizon 2020 research and innovation programme under grant agreement No. 893135. Neither the Executive Agency for Small-and-Medium-sized Enterprises (EASME) nor the European Commission is in any way responsible for any use that may be made of the information it contains. The activities are also partially funded by the University of Catania in the framework of the SIS-RENEW research project (Piano di incentivi per la Ricerca 2020–2022).

References

- AlSayegh, G. 2012. *Hygrothermal Properties of Cross Laminated Timber and Moisture Response of Wood at High Relative Humidity*. Ottawa, Ontario: Carleton University.

- Brambilla, A. and E. Gasparri. 2020. "Hygrothermal behaviour of emerging timber-based envelope technologies in Australia: A preliminary investigation on condensation and mould growth risk." *Journal of Cleaner Production* 276. doi: <https://doi.org/10.1016/j.jclepro.2020.124129>
- Bauklimatik Dresden. 2022. "Material Editor – Manual". Material Editor - Manual (bauklimatik-dresden.de). Accessed on March 15.
- CEN. 2007a. *EN ISO 10456:2007. Building materials and products, Hygrothermal properties, Tabulated design values and procedures for determining declared and design thermal values*. Brussels, Belgium.
- CEN. 2007b. *EN ISO 15026:2007. Hygrothermal performance of building components and building elements - Assessment of moisture transfer by numerical simulation*. Brussels, Belgium.
- CEN. 2009. *EN ISO 15127-3:2009. Hygrothermal performance of buildings - Calculation and presentation of climatic data - Part 3: Calculation of a driving rain index for vertical surfaces from hourly wind and rain data*. Brussels, Belgium.
- Chang, S. J., S. Wi, S. G. Kang, and S. Kim. 2020. "Moisture risk assessment of cross-laminated timber walls: Perspectives on climate conditions and water vapor resistance performance of building materials." *Building and Environment* 168. doi: <https://doi.org/10.1016/j.buildenv.2019.106502>
- Cho, H. M., S. Wi, S. J. Chang, and S. Kim. 2019. "Hygrothermal properties analysis of cross-laminated timber wall with internal and external insulation systems." *Journal of Cleaner Production* 231: 1353 - 1363. doi: [10.1016/j.jclepro.2019.05.197](https://doi.org/10.1016/j.jclepro.2019.05.197).
- Climate.OneBuilding.org.2022. https://www.climate.onebuilding.org/WMO_Region_6_Europe/ITA_Italy/index.htm. Accessed on March 17.
- Costanzo, V., G. Evola, A. Gagliano, L. Marletta, and F. Nocera. 2021a. "Hygrothermal Analysis of CLT-Based Retrofit Strategy of Existing Wall Assemblies According to EN 13788 Standard." *TECNICA ITALIANA - Italian Journal of Engineering Science* 65: 324 - 329. doi: <https://dx.doi.org/10.18280/ti-ijes.652-428>
- Costanzo, V., G. Evola, L. Marletta, and G. Roccella. 2021b. "Preliminary investigation on the transient hygrothermal analysis of a CLT-based retrofit solution for exterior walls." *Journal of Physics: Conference Series* 2042(1). doi: <https://doi.org/10.1088/1742-6596/2042/1/012142>
- Danovska, M., M. Libralato, G. Pernigotto, A. De Angelis, O. Saro, P. Baggio, and A. Gasparella. 2019. "Numerical and Experimental Study on the Impact of Humidity on the Thermal Behavior of Insulated Timber Walls." In *Proceedings of Building Simulation Applications BSA 2019*, 91 - 99. Bolzano.
- Evola, G., V. Costanzo, and L. Marletta. 2021. "Hygrothermal and Acoustic Performance of Two Innovative Envelope Renovation Solutions Developed in the e-SAFE Project." *Energies* 14(13). doi: <https://dx.doi.org/10.3390/en14134006>
- Glass, S. V., and S. L. Zelinka. 2010. "Chapter 4 - Moisture Relations and Physical Properties of Wood." In *General Technical Report FPL-GTR-190*. Madison, WI: U.S. Department of Agriculture, Forest Service, Forest Products Laboratory.
- Kordiziel, S., S. V. Glass, C. R. Boardman, R. A. Munson, S. L. Zelinka, S. Pei, and P. C. Tabares-Velasco. 2020. "Hygrothermal characterization and modeling of cross-laminated timber in the building envelope." *Building and Environment* 177. doi: <https://doi.org/10.1016/j.buildenv.2020.106866>
- Lapage, R. T. M. 2012. *Moisture Response of Wall Assemblies of Cross-Laminated Timber Construction in Cold Canadian Climates*. Waterloo, Ontario: University of Waterloo.
- McClung, R., H. Ge, J. Straube, and J. Wang. 2014. "Hygrothermal performance of cross-laminated timber wall assemblies with built-in moisture: field measurements and simulations." *Building and Environment* 71: 95-110. doi: <https://dx.doi.org/10.1016/j.buildenv.2013.09.008>
- Ojanen, T., H. Viitanen, R. Peuhkuri, K. Lähdesmäki, J. Vinha, and K. Salminen. 2010. "Mold growth modeling of building structures using sensitivity classes of materials." In *Proc. ASHRAE Conf. Buildings XI*, ASHRAE.
- Raina, L. 2021. *Capillary movement of water in a radial direction and moisture distribution in a cross-section of CLT panel*. Tallinn: Tallinn University of Technology.
- Vogelsang, S., H. Fechner, and A. Nicolai. 2013. "Delphin 6 Material File Specification, Version 6.0." *Technical Report*, Dresden, Germany: Institut für Bauklimatik Technische Universität Dresden.

Multi-Objective Optimization Of Thermo-Acoustic Comfort Of School Buildings

Daniele Colarossi – Università Politecnica Delle Marche, Italy – d.colarossi@pm.univpm.it

Samantha Di Loreto – Università Politecnica Delle Marche, Italy – s.diloreto@pm.univpm.it

Eleonora Tagliolini – Università Politecnica Delle Marche, Italy – e.tagliolini@pm.univpm.it

Paolo Principi – Università Politecnica Delle Marche, Italy – p.principi@univpm.it

Fabio Serpilli – Università Politecnica Delle Marche, Italy – f.serpilli@univpm.it

Abstract

The reduction of the environmental impact of the building sector is one of the top priorities in the “climate change challenge”. As the primary energy consumption of the building decreases, a high level of indoor comfort must be maintained. Both thermal parameters, lighting, acoustic level, and indoor air quality affect indoor comfort. These aspects are fundamental, especially in school buildings, where a good level of indoor comfort can help student to stay focused. This paper proposes a methodology for a combined optimization of the energetic and the acoustic performance of a school building. A case study, located in the center of Italy, was analyzed. Firstly, the thermal and acoustic performance was determined. Then a list of interventions was hypothesized and simulated, involving both the building envelope, the lighting and thermal plants. Normalized acoustic insulation of partitions between adjacent rooms, acoustic insulation of the façade and reverberation time were evaluated. The outdoor and ambient noise levels were based on the main characteristics of the façade (type and stratifications of opaque and transparent components, ventilation system, etc.). Results show that the optimal combination of interventions reduces the CO₂ emissions of 88.55 % and the global energy performance index of 85.2 %. The indoor sound pressure level due to traffic noise is reduced by 19 dB after acoustic insulation of the façade, while further treatments to indoor surfaces should be implemented to reduce internal reverberation time and to improve speech intelligibility. The combined optimization shows that the highest reduction of the global impact (89.2 %) is obtained by weighting 80 %/20 % the acoustic/thermal performance.

1. Introduction

Nowadays, the building sector accounts for around 40 % of total global energy consumption and more than 30 % of CO₂ emissions. To achieve net-zero carbon emissions by 2050, the International Energy Agency (IEA) estimates that the sector has to halve its emissions by 2030. In the EU, the situation is similar, with 36 % of CO₂ emissions from the building stock, of which the final energy consumption for heating and cooling is 50 %. Accordingly, improving the energy efficiency and fostering total decarbonization is an essential step towards renewal of the building stock. The current rate of renovation of public buildings ranges from 0.4 % and 1.2 % per year, while it should be around 3 %, as reported by the 2018/844/EU Directive.

In addition, a high level of indoor comfort is required. Indoor comfort is affected by several factors, such as thermal level (air temperature and humidity, air velocity and quality), lighting and acoustic quality. In school buildings, students spend many hours a day in the classroom. The correct environment can help students to be focused and energetic. Different strategies have been proposed to evaluate and optimize the performance of school buildings (MacNaughton et al., 2018), or energy audits (Wang et al., 2015). Díaz-López et al. (2022) identified the 24 best passive intervention strategies, analyzing research trends in 42 countries. Li et al. (2021) proposed a multi-objective optimization method based on the response surface method, where optimal design trade-offs between thermal comfort and energy demand are obtained. Omar et al. (2022) based their optimization on lighting and cooling plant

retrofitting, and on the integration of a photovoltaic plant to increase the share of renewable energy exploited. Results show a gain of renewable fraction of around 82 %. Gamarra et al. (2018) considered water consumption and carbon footprint, resulting in a life-cycle assessment.

Noise in schools derives from its original surrounding environment, which has turned from silent into very noisy over the years (Secchi et al., 2017). The specification regarding sound insulation properties and noise from equipment properties in Italy were defined in the D.P.C.M. 5/12/97. The recent Italian law D.M. 11/01/2017, recalls the Italian standard UNI 11367. According to these standards, new school buildings must guarantee a façade sound insulation of $D_{2m,nT,w} \geq 48$ dB, which is very restrictive. In UNI 11367, the limit value for the normalized acoustic insulation of partitions between adjacent rooms of the same unit was presented: basic performance, with $D_{nT,w} \geq 45$, and high performance, with $D_{nT,w} \geq 50$ dB. UNI 11367 also requires a Speech Transmission Index in classrooms higher than 0.60 and sets the optimum value of reverberation time (Tott) as average value between 500 and 1000 Hz for unoccupied classrooms (s). The limit values for the acoustic indoor room quality are also defined in the UNI 11532-1. In part 2 of the standard, the limit value for reverberation time, STI e/o C50, and sound pressure level for technologic systems installed inside the classroom are defined.

This paper presents a methodology for the thermo-acoustic optimization of an existing school building, based on combinations of interventions (Moazzen et al., 2020). A primary school building located in central Italy was taken as a case study. Firstly, the

current state of the building was analyzed using software to estimate the heating energy demand and acoustic performance. The analysis concerns both the design conditions and the dynamic consumption over a period of one year. Then, a list of interventions was hypothesized, involving both building envelope, the lighting system, the thermal plants and the acoustic parameters, to find out the optimal configuration. The novelty proposed is combined analysis, setting and optimizing weighting coefficients between thermal and acoustic performances.

2. Materials and Method

The methodology proposed consists of different steps:

- Identification of the case study building and determination of its properties and climatic conditions.
- Evaluation of energy and acoustic performance by software simulations.
- Proposal of interventions and combination of them.
- Simulation and index calculation.

The building chosen as reference case should be representative of the category of buildings under study, as regards the building geometry, energy performance for both envelope and plants, and climatic conditions. This way, the proposed model, once validated, can be easily applied to other buildings. In this paper, a primary school building has been chosen as reference case. Fig. 1 shows a real image of the building, while Fig. 2 shows the plan view.



Fig. 1 – Real image of the school building under study

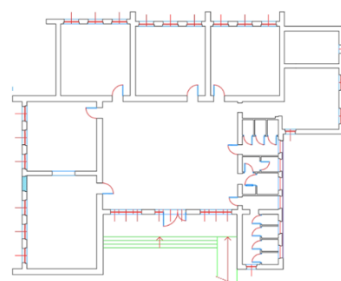


Fig. 2 – Plan view of the school building under study

The reference building presents a floor area of 350 m² and consists of 6 classrooms, with a net height of 3.25 m. The entrance hall has a sloped ceiling, average height 4.8 m. The occupancy has been hypothesized as typical of school buildings, namely on weekdays between 08.00 and 1700. According to the national standards, Italy is divided into six climatic zones, depending on the heating degree days. For each zone, there is a corresponding different annual heating period and number of hours of daily operation. In addition, a series of minimum U-values are provided for each zone. Central Italy, where the reference building is located, is involved in the “E” zone, which corresponds with a heating period from 15 October to 15 April. The specific location of the building presents a minimum temperature of -4 °C, as stated in the UNI 10349 standard. This data is required to calculate the energy performance of the building under the worst-case conditions. Then a dynamic hourly-based method is applied to provide the energy consumptions over a year. The first step for the energy performance calculation is the energy determination of the U-values of all vertical and horizontal, opaque and transparent structures. The U-value is a function of the thickness and type of each material of the stratification. The thermal conductivity is taken from the UNI 10351 standard for homogeneous materials and the UNI 10355 for heterogeneous ones. In the absence of reliable data, the U-value of opaque and transparent structures can be estimated as a function of the year of construction of the building. When data are collected, U-values can be determined. In Tables 1, 2, 3, 4 the stratifications and the thermal and acoustic performance of the opaque structures are presented.

Table 1 – Stratification of the front vertical facade

Total thickness [cm]				50
Surface mass [kg/m²]				1296
U-Value [W/(m² °C)]				2,02
Rw [dB]				54
Layer	Thickness [cm]	Thermal conductivity [W/(m °C)]	Density [kg/m ³]	
Gypsum plaster	2	0.35	1200	
Dolomite stone	48	1.8	2700	

Table 2 – Stratification of the external vertical wall

Total thickness [cm]				44
Surface mass [kg/m²]				560
U-Value [W/(m² °C)]				1.1
Rw [dB]				51
Layer	Thickness [cm]	Thermal conductivity [W/(m °C)]	Density [kg/m ³]	
Gypsum plaster	2	0.35	1200	
Perforated brick	40	1.8	2700	
Cement mortar	2	1.4	2000	

Table 3 – Stratification of the floor

Total thickness [cm]				32
Surface mass [kg/m²]				354
U-Value [W/(m² °C)]				1.64
Rw [dB]				52
Layer	Thickness [cm]	Thermal conductivity [W/(m °C)]	Density [kg/m ³]	
Ceramic tiles	2	1	2300	
Cement mortar	4	1.4	2000	
Floor brick	26	0.74	1185	

Table 4 – Stratification of the ceiling

Total thickness [cm]				24
Surface mass [kg/m²]				55
U-Value [W/(m² °C)]				0.20
Rw [dB]				48
Layer	Thickness [cm]	Thermal conductivity [W/(m °C)]	Density [kg/m ³]	
Wood panel	1.3	0.12	450	
BARRIER 100	0.1	0.35	950	
Rock wool	1.6	0.035	40	
Waterproofing	0.1	0.17	1200	
Air	5	0.32	1	
Roof tiles	1.5	1	2000	

The U-values of the transparent components range from 2.8 W/(m² °C), consisting of aluminum frame without thermal break and double glazing, to 5 W/(m² °C) for the oldest ones, consisting of metallic frame and single glazing.

Then the performance of the building was evaluated. Energetically, the building was modeled on MC4software, whose representation is shown in Fig. 3.

For the acoustic characterization of the unoccupied classrooms, forecast calculations were carried out according to the current technical regulations. These can be determined with the aid of performance and functional criteria. The forecast calculations and assessment methods are described in UNI 11532-2.

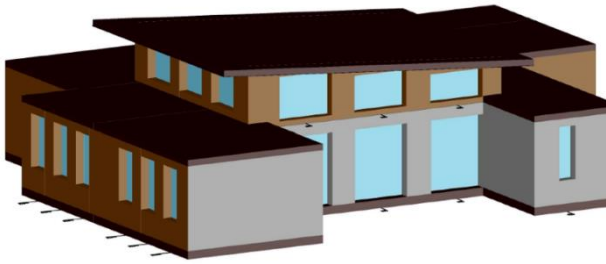


Fig. 3 - 3D model reconstruction for building simulation

The sound insulation performances of typical Italian classrooms were investigated in terms of indoor sound pressure level transmitted through the school façade, reverberation time and sound emitted by technological systems. The estimation of the indoor sound pressure level, L_2 , due to the sound from outdoor is obtained with Eq. (1), based on the ISO 12354-3.

$$L_2 = L_{1,2m} - D_{2m,nT} + 10 \log\left(\frac{T}{T_0}\right) \text{ [dB]} \quad (1)$$

where $L_{1,2m}$ is the outdoor sound pressure level 2 m in front of the façade (dB), $D_{2m,nT}$ is the standardized level difference of façade insulation, T is the reverberation time (s) and T_0 is the reference reverberation time (0.5 s).

The prediction method for calculating the Reverberation Time is described in EN 12354-6, while for the $L_{pu,c}$ index the reference standard is the EN 12354-5. Based on the energy efficiency interventions, the acoustic performance of the school has been calculated in parallel as the interventions varied.

A list of intervention has been hypothesized, involving both the building envelope and the thermal plant. Each specific building can require certain interventions. In this work general interventions are proposed, to remain valid in most of the cases. In Table 5 the interventions are listed.

Table 5 – List of interventions

Code	Intervention
GL1	Substitution of glazing
IN1	Insulation of vertical walls
IN2	Insulation of floor and addition of radiant heat floor
L1	Substitution of traditional lighting system with LED-based one
TP1	Substitution of traditional heat generator with heat pump
TP2	Introduction of a photovoltaic plant
TP3	Introduction of mechanic ventilation system

The substitution of glazing (GL1) allows a reduction of the U-value of the transparent components. Triple glass of thickness 5 mm with 12 mm of air gap has been chosen, with an aluminum frame and thermal break. The respective U-value turns out to be in the range 2.8 W/(m² K) and 5 W/(m² K), depending on the size of the window. The insulation of vertical walls (IN1) consists in the addition of a layer of thermal insulation, to increase the thermal resistance. An expanded polystyrene (EPS100) has been chosen, with a thermal conductivity of 0.035 W/m K and a density of 20 kg/m³. A layer of 12 cm, placed externally to the wall stratification, has been provided for the brick-based wall. The front façade instead, has been insulated with 6 cm of the same polystyrene but placed internally, to maintain the aesthetics of the faced stone. The U-value of the two walls becomes 0.2 and 0.5 W/(m² K), respectively.

The intervention on the lighting system (L1) consists in the replacement of traditional lamps with LED ones. The latter reduce the expense of electricity for lighting, considering that a traditional lamp produces 62 lm/W compared to 95 lm/W of a LED one. The number of LED lamps to be installed in each room (n) has been evaluated with the Eq. (2):

$$n = \frac{\phi_t}{m h \phi_l} \quad (2)$$

where ϕ_t is the luminous flux of the lamp, m is a coefficient of utilization in function of the shape of the lamp, h is the net height of the room and ϕ_l is the luminous flux on the target area.

The substitution of traditional heat generator for heat pump (TP1) increases the heat generation and

distribution efficiency by decreasing the working temperature of the water. In addition, this is a switch from natural gas to electricity. Consequently, the installation of a photovoltaic plant (TP2) is a fundamental step towards exploiting a local renewable energy source to cover the lighting and heat pump energy demand. The last intervention is the mechanical ventilation system (TP3), which improves the indoor air quality of the classrooms. The system is composed of a single machine, to be installed in each room, which provides an air ventilation rate proportional to the CO₂ percentage in the room. Then the single interventions were combined each other to maximize the energy performance of the building and the energy saving. Different scenarios, later called “packages”, have been simulated (Table 6).

Table 6 – Combination of interventions

Package	Building envelope		Lighting		Thermal plant		
P0	-	-	-	-	-	-	-
P1	GL1	-	-	-	-	-	-
P2	-	IN1	-	-	-	-	-
P3	GL1	IN1	-	-	-	-	-
P4	GL1	IN1	IN2	-	TP1	-	-
P5	GL1	IN1	IN2	L1	TP1	TP2	-
P6	GL1	IN1	IN2	L1	TP1	TP2	TP3

3. Results and Discussions

The parameters for the indoor conditions of the rooms were calculated separately for the thermal, acoustic and visual conditions. Energetically, the parameters are the global performance index and the CO₂ emitted. The first one, indicated with “EP_{gl,nren}” and expressed in kWh/m²yr, considers the amount of energy for the air conditioning over one year, normalized per meter square. This is a useful parameter for comparing different buildings. In addition, the index differentiates the fuel used, applying a higher coefficient for non-renewable ones and neglecting the share of local energy productions

from renewable sources. The CO₂ emitted considers the typology of fuel and its relative emissive factor, while for the electricity from the grid the factors are estimated based on the national energy mix. Results are shown in Fig. 4 and Fig. 5, for the global performance index and the CO₂ emitted, respectively. The reference case is characterized by a global performance index of 407.6 kWh/m² yr and 38037 kg of CO₂ emissions. Both parameters decrease, while the number of interventions increase. The best scenario allows a reduction of the CO₂ emissions of 88.5 %, 4354 kg, and the global performance index of 85.2 %, 60.3 kWh/m² yr.

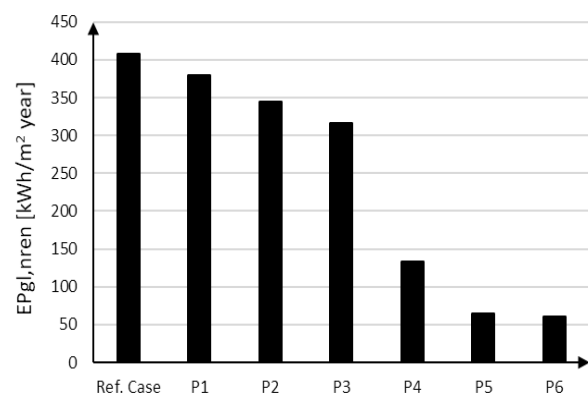
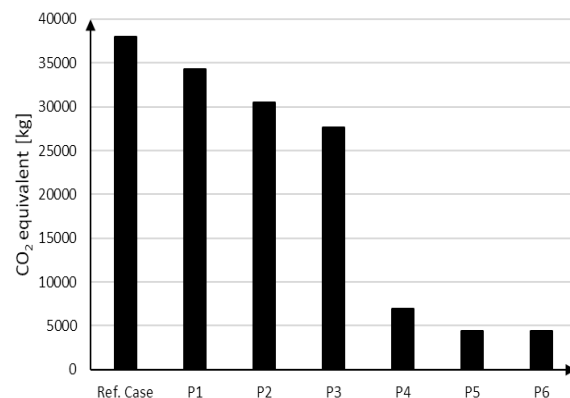


Fig. 4 – Global energy performance index for each scenario

Fig. 5 – CO₂ emissions for each scenario

The payback period (PB) was chosen as economic index. It provides information about the time necessary to recover the initial costs, by means of the annual energy saving of the improved scenario. The lower the PB is, the more the scenario becomes a priority. Table 7 summarizes the initial cost and the PB for each scenario analyzed. The best scenario turns out to be the combination of all interventions

except for the mechanical ventilation system, with a payback period of 13 years and 10 months.

Table 7 – Initial cost and payback period of the simulated scenarios

Intervention	Cost [€]	PB [years]
P1	27605	24 years 6 months
P2	37161	14 years 4 months
P3	64766	15 years 6 months
P4	217234	17 years 6 months
P5	283336	13 years 10 months
P6	303336	14 years 9 months

For the acoustic scenarios, results refer to the prediction values of façade sound insulation, to the reverberation time and to the calculated values of unoccupied indoor sound pressure level. Table 8 shows the average values of results of D2m,nT,w and DnT,w calculations for all classrooms, respectively. Results concerning corridors, gyms and closets were excluded from this analysis.

Table 8 – Acoustic performance ante and post operam

	Result	Limit value
Ante Operam Average	D2m,nT,w [dB]	D2m,nT,w [dB] D.P.C.M 5/12/97
	33	48
	DnT,w [dB] Between two classrooms	DnT,w [dB] high performance UNI 11367
	45	50
Post Operam Average	D2m,nT,w [dB]	D2m,nT,w D.P.C.M 5/12/97
	52	48
	DnT,w [dB] Between two classrooms	DnT,w high performance UNI 11367
	54	50

Schools with single-glazed windows have typically lower insulation performances. The improvement of acoustic performances is evident because of the better air thickness of the new windows and the insulation of vertical walls.

Fig. 6 shows the average reverberation time calculated in octave bands in all the classrooms.

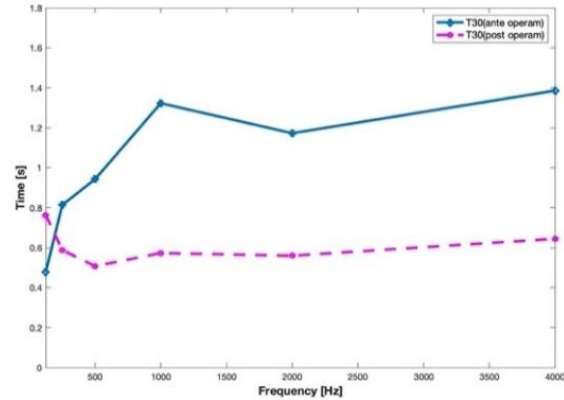


Fig. 6 – Reverberation time in pre (blue) and post operam (pink)

Reverberation time values averaged between the 500 Hz and 1 kHz octave bands, resulting in 1,02 s (ante operam) and 0,59 s (post operam).

The optimal value set by Italian law [16] is a function of the classroom volume. Averaging the volume of the examined classrooms (100 m³), the optimal average value is 0,47s.

For each façade, the outdoor noise levels (L_{1,2m}) were calculated. A weighted outdoor level equal to 60 dB (that is the maximum noise emissions level permitted by the law DCPM 14/11/97) was assumed. Results were compared to the limit values set by Italian legislation or by other relevant national or international references. The analysis of indoor SPL shows that, after the treatments of the façades, the main acoustic problem of the selected classrooms is the indoor reverberation time and it is not the noise from outdoor sources.

A subsequent statistical analysis was performed for the case study. The first correlation model is based on a multivariate regression between the representative thermal parameters and weighted on the non-renewable global energy performance index of the school (Fig. 7). The regression was calculated considering the results obtained by the seven scenarios.

The model is based on the following Eq. 4:

$$Model(x, y) = a + bx + cy + dx^2 + ey \quad (4)$$

where a, b, c, d, e represent the partial regression coefficients (with 95 % confidence bound).

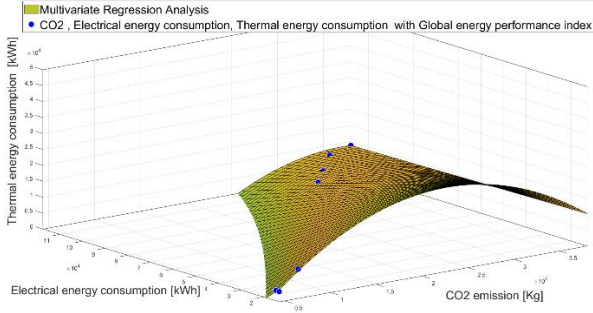


Fig. 7 – Multivariate regression (CO2 emission [kg], electrical energy consumption [kWh], thermal energy consumption [kWh] weighted on the global energy performance index). Several noteworthy results were: $R^2=0.99$, $R=0.97$, Dfe 2

The second correlation model aims to determine the impact of the acoustic and energetic interventions on processing costs. The model was defined as the weighted sum of the acoustic and thermal resulting parameter. The weights were assigned arbitrarily considering increasing weights to the acoustic performance and subsequently decreasing to the thermal one. The optimization model is represented by the following equation (Eq. 5):

$$opt = b \cdot \%EP_{gl,nren} + a \cdot \%RT + a \cdot \%SA \quad (5)$$

where $a = [0.2 \ 0.4 \ 0.6 \ 0.8]$, $b = [1-a]$, and the $EP_{gl,nren}$, RT (reverberation time (T30)) and SA (sound absorption) are expressed as percentages of saving compared to the reference case.

Results of the polynomial regression are shown in Fig. 8, while Table 9 summarizes the percentage of reduction of the global impact at the various weights.

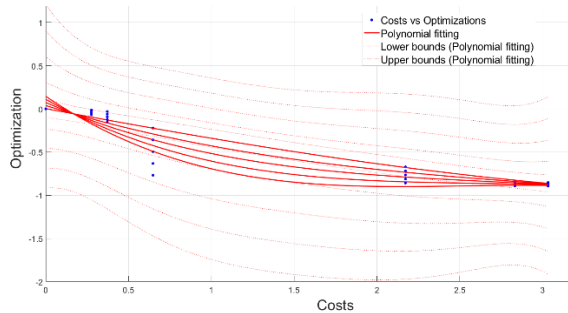


Fig. 8 – Results of linear regression between Thermal-Acoustic optimization and Costs (Euro). Several noteworthy results were: $R^2=0.85$, $R=0.70$, Dfe 3

Table 9 - Thermal-acoustic optimization vs costs of intervention at the different weights (w_0 , w_1 , w_2 , w_3 , w_4)

Intervention	w_0	w_1	w_2	w_3	w_4
P1	6.9%	5.6%	4.2%	2.8%	1.4%
P2	15.5%	12.3%	9.2%	6.1%	3.0%
P3	22.3%	35.9%	49.5%	63.2%	76.8%
P4	67.1%	71.8%	76.5%	81.1%	85.8%
P5	84.2%	85.4%	86.7%	87.9%	89.2%
P6	85.2%	86.2%	87.3%	88.3%	89.4%

4. Conclusions

This paper proposes a methodology for a combined optimization of the thermal and acoustic performance of a school building. A primary school building located in the center of Italy was chosen as case study. Firstly, the thermal and acoustic performance of the reference building were simulated. Then the proposed methodology was applied. A list of interventions was hypothesized, involving both the building envelope and the thermal and lighting plants. Different interventions were combined in packages, to optimize the overall performance of the building and to find the best scenario. Results show that the optimal scenario, combining all the interventions, reduces the CO₂ emission of 88.5 % (4354 kg, while it is 38037 kg for the reference case) and the global performance index of 85.2 % (60.3 kWh/m² yr, while it is 407.6 kWh/m² yr for the reference case). The acoustic treatment of façades, consisting of the replacement of windows and the insulation of vertical walls, produces good results in the abatement of indoor noise level (19 dB). The average reverberation time is reduced by about 0.40 s, which turns out to be a good result but still not compliant with the optimal time defined by the standards. However, the mechanical ventilation system negatively affects the intelligibility and, in general, the acoustic comfort in a classroom (Serpilli et al., 2022). Consequently, a combined plan between the façade refurbishment and the interior acoustic treatment of the classrooms is recommended. As regard the economic analysis, the best scenario turns out to be the combination of all interventions except for the mechanical ventilation system. This scenario returns the shortest payback period (13 years and 10

months). The combined optimization shows that the best scenario is obtained by weighting the acoustic performance 80 % and the thermal one 20 %, and ensures a global impact reduction of 89.2 %, compared with the reference case. Further research, under analysis, will be proposed extending the presented methodology to other school buildings, to validate the statistical approach and compare the results obtained.

References

- Díaz-López, C., A. Serrano-Jiménez, J. Lizana, E. López-García, M. Molina-Huelva, & Á. Barrios-Padura. 2022. "Passive action strategies in schools: A scientific mapping towards eco-efficiency in educational buildings". *Journal of Building Engineering* 45: 103598. doi: <https://doi.org/10.1016/j.jobe.2021.103598>
- D.P.C.M 5/12/97. Determinazione dei requisiti acustici passivi degli edifici.
- D.M. 11/01/2017. Criteri Ambientali minimi per l'affidamento di servizi di progettazione e lavori per la nuova costruzione, ristrutturazione e manutenzione di edifici pubblici.
- Gamarra, A. R., I. R. Istrate, I. Herrera, C. Lago, J. Lizana, & Y. Lechón. 2018. "Energy and water consumption and carbon footprint of school buildings in hot climate conditions. Results from life cycle assessment". *Journal of Cleaner Production* 195: 1326-1337. doi: <https://doi.org/10.1016/j.jclepro.2018.05.153>
- Li, Q., L. Zhang, L. Zhang, & X. Wu. 2021. „Optimizing energy efficiency and thermal comfort in building green retrofit". *Energy* 237: 121509. doi: <https://doi.org/10.1016/j.energy.2021.121509>
- MacNaughton, P., X. Cao, J. Buonocore, J. Cedeno-Laurent, J. Spengler, A. Bernstein, & J. Allen. 2018. "Energy savings, emission reductions, and health co-benefits of the green building movement". *J Expo Sci Environ Epidemiol* 28(307): 12. doi: <https://doi.org/10.1038/s41370-017-0014-9>
- Moazzen, N., T. Ashrafian, Z. Yilmaz, & M. E. Karagüler. 2020. « A multi-criteria approach to affordable energy-efficient retrofit of primary school buildings". *Applied Energy* 268: 115046. <https://doi.org/10.1016/j.apenergy.2020.115046>
- Omar, A. I., N. M. Khattab, & S. H. A. Aleem. 2022. "Optimal strategy for transition into net-zero energy in educational buildings: A case study in El-Shorouk City, Egypt." *Sustainable Energy Technologies and Assessments* 49: 101701. doi: <https://doi.org/10.1016/j.seta.2021.101701>
- Secchi, S., A. Astolfi, G. Calosso, D. Casini, G. Cellai, F. Scamoni, C. Scrosati & L. Shtrepi. 2017. "Effect of outdoor noise and façade sound insulation on indoor acoustic environment of Italian schools". *Applied Acoustics* 126: 120-130. doi: <https://doi.org/10.1016/j.apacoust.2017.05.023>
- Serpilli, F., S. Di Loreto, V. Lori, & C. Di Perna. 2022. "The impact of mechanical ventilation systems on acoustic quality in school environments. EPD sciences", 52nd A iCARR International Conference. doi: <https://doi.org/10.1051/e3sconf/202234305002>
- UNI 10349, 2016 "Riscaldamento e raffrescamento degli edifici-Dati climatici. Ente Nazionale Italiano Di Normazione
- UNI 10351, 2021—Building materials. Thermal conductivities and vapor permeabilities (in Italian: Materiali da costruzione. Conduttività termica e permeabilità al vapore)
- UNI 10355, 1994. Walls and floors—Thermal resistance values and calculation method
- UNI 11367, 2010. Acustica in edilizia – Classificazione acustica delle unità immobiliari – Procedura di valutazione e verifica in opera.
- UNI 11532-1, 2018. Caratterizzazione acustiche interne di ambienti confinati - Metodi di progettazione e tecniche di valutazione – Parte 1: requisiti generali.
- UNI 11532-2, 2020. Caratterizzazione acustiche interne di ambienti confinati - Metodi di progettazione e tecniche di valutazione – Parte 2: Settore scolastico.
- UNI EN ISO 12354-3, 2017. Building acoustics – Estimation of acoustic performance of buildings from the performance of elements - Part 3: Air-borne sound insulation against outdoor sound.
- UNI EN ISO 12354-5, 2009. Building acoustics - Estimation of acoustic performance of building from the performance of elements - Part 5: Sound levels due to the service equipment.

UNI EN ISO 12354-6, 2006. Building acoustics - Estimation of acoustic performance of buildings from the performance of elements - Part 6: Sound absorption in enclosed spaces.

Wang, Y., J. Kuckelkorn, F. Y. Zhao, D. Liu, A. Kirschbaum, & J. L. Zhan. 2015. „Evaluation on classroom thermal comfort and energy performance of passive school building by optimizing HVAC control systems“. *Building and Environment* 89: 86-106. doi: <https://doi.org/10.1016/j.buildenv.2015.02.023>

A Review on the FIVA-Project: Simulation-Assisted Development of Highly-Insulating Vacuum Glass Windows

Ulrich Pont – TU Wien, Austria – ulrich.pont@tuwien.ac.at

Peter Schober – Austrian Forest Products Research Society, Austria – p.schober@holzforschung.at

Magdalena Wölzl – TU Wien, Austria – Magdalena.woelzl@tuwien.ac.at

Matthias Schuss – TU Wien, Austria – Matthias.schuss@tuwien.ac.at

Jakob Haberl – Austrian Forest Products Research Society, Austria – j.haberl@holzforschung.at

Abstract

This contribution provides a review on research and development activities that have been conducted in the field of highly-insulating windows with vacuum glass. In a joint effort with the window-producing industry, different novel solutions for vacuumglass-equipped windows have been studied. Thereby, different methodological approaches have been deployed, including the construction of technology demonstrators, performance measurements on laboratory test sites, and numeric thermal bridge simulation. As a result, the project consortium succeeded in the development, construction, and exhibition to relevant stakeholders in the industry of four, innovative window prototypes. These windows not only employ vacuum glass products, but also in part provide new operation kinematics, motorization, and the implementation of automated ventilation positions. Moreover, the U-values of the windows could be approximated to be around or below $0.70 \text{ W}\cdot\text{m}^{-2}\cdot\text{K}^{-1}$ (i.e., U_{Win} -value) at pane thicknesses of less than a centimeter. The windows include turn windows to inside and outside, as well as a swing-operation window, and a window utilizing an offset- and slide-operation mechanism without visible railings. The contribution not only displays the final prototypes, but also highlights the methods and provides an outlook for future development in this area.

1. Introduction

1.1 Scope of the FIVA Project, Observations and Prerequisites

The present contribution highlights the methodology and results of a joint research effort conducted together with stakeholders of the window produc-

ing industry. The ultimate goal of this project, which was named FIVA (*Fensterprototypen mit integriertem Vakuumglas* – in English: Window prototypes that employ vacuum glass) was the development of vacuum-glazing-equipped windows that provide both a very good (thermal) insulating performance and a high degree of innovation in architectural appearance and operation. Moreover, that the resulting prototypes should fully prove their functionality, or in other words, a high TRL (technology readiness level) of the envisioned prototypes was an additional planned goal of the project.

The project's outline was built on and started based on a set of observations (O) and prerequisites (P):

O(b)servation)1: Although vacuum glass products finally arrived on the market after intensive research and development efforts by both industry and academia lasting close to a century (Zoller, 1913), there was little to no public and relevant research available about the utilization of such products in contemporary and past window constructions. **O2:** Companies in the window-producing sector agreed about the high potential of vacuum glass for window constructions, however, most companies were reluctant to pioneer vacuum-glazed window constructions. Moreover, there was little knowledge about the required changes to existing window/frame constructions amongst the relevant stakeholders. Furthermore, resentment against vacuum glass pertaining to the durability of the vacuum (and thus its thermal performance) in the products was reckoned. Given that, until 2020, vacuum glass products were not produced in

Europe, but majorly in South-East Asia, another threat was seen in the long delivery times in the case of the need for glass replacement. Moreover, while there have been multiple producers of multi-pane insulation glass, the number of vacuum glass producers was (and still is) limited. **O3:** Stakeholders in the glass-producing industry showed a certain ambivalence toward vacuum glass products. This was majorly because vacuum glass products show similar thermal performances to high-end triple glazing, but do feature one glass pane less (which would potentially have negative effects on feasibility and profit for glass producers). **O4:** Despite major efforts toward improvement of the performance of transparent envelope components, windows are still considered the weak spot in thermal envelopes, and are even considered to be responsible for a major share of building-related energy loss through the envelope. However, current highly-insulating windows are majorly triple-glazing windows coming with large system thickness and correspondingly heavy weight of the overall construction. Vacuum glass is considered to disrupt this situation.

Amongst the prerequisites for the FIVA project were the following: **P(requisite)1:** basic knowledge about the durability and thermal performance of different vacuum glass products was required. This was fulfilled due to the authors' previous research efforts into vacuum glass within the VIG-SYS-RENO project (Pont et al., 2018a). In this exploratory product, not only a wide range of tests pertaining to mechanics, thermal performance and acoustical performance of different glass products was conducted, but also basic challenges pertaining to the integration of vacuum glass into existing and new window frames were addressed. **P2:** A clear objective is required in the development process. While the integration of vacuum glass in existing (historically relevant) windows often needs to consider the upkeep of the appearance of the window (e.g., Kastenfenster / casement windows, compare (Pont et al., 2018b), new windows can be designed toward performance and operation optimization. Moreover, the specifics of vacuum glass (e.g., problematic thermal bridge along the edge seal) determine construction principles. As such, it was decided to design the win-

dows from scratch based on the specific requirements of the vacuum glass, rather than to adapt existing window constructions. **P3:** Subsequently, a set of innovative early-stage window designs (that consider the specifics of vacuum glass) was required. Such innovative and, in part, disruptive approaches to new windows were the result of another preliminary and exploratory research effort by the authors named MOTIVE (Pont et al., 2018c). **P4:** To start and successfully conduct the project, a strong consortium of academic partners and stakeholders from the relevant branches of industry was required who were open to new ideas and agreed upon close collaboration. This consortium consisted in the end of two academic and eight industrial partners (5 window-producing companies, 3 producers of different window constituents, namely fittings, seals, and vacuum glass). **P5:** To be able to explore the space of potential, innovative, high-performing vacuum glass windows, all partners were required to bring in their specific expertise and instruments. Simulation as a method specifically was deployed in the fields of operation kinematics of the innovative windows, and thermal performance assessment. For the latter, numeric thermal bridge simulation was deployed as instrument of choice.

1.2 Vacuum-Glazing Products

To understand the challenges connected with the integration of vacuum glass in windows, one needs to understand the technical specifications of vacuum glass. Vacuum glass products are regularly constituted of two planar, parallel glass panes. Between the glass panes, an interstitial space of rather small dimension (less than a millimeter) houses a grid of distance pillars. The axis-distance between the pillars is regularly between 20 and 40 mm. To close the interstitial space against the surroundings, a vacuum-tight edge seal is set up along the perimeter of both glass panes. Via an opening in one of glass panes, the interstitial space is then evacuated (leading to a high vacuum). The distance pillars mentioned maintain the parallel position of the glass panes, as otherwise the panes would be pushed together by the surrounding air pressure. Another important element is the so-

called getter. This is a highly reactive surface that filters/binds the remaining particles in the interstitial space. Due to the vacuum, heat transfer processes that require media are widely eliminated in the interstitial space (i.e., conduction and convection). Thereby, already rather slim systems (vacuum glass between 6 and 8 millimeters) provide excellent thermal insulation. However, the glass-edge seal, as well as the distance pillars, literally remain as connecting thermal bridges between the two glass panes and need to be considered in designing windows with vacuum glass. In a previous research effort (Pont & Mahdavi, 2017), the heat loss via conduction through the pillars was identified as noticeable but very small (majorly due to their limited physical dimensions). In contrast, the tight edge seal was identified as a major thermal bridge and needs to be covered / insulated as well as possible in window constructions. A sufficient glass edge-cover length can ensure this. Fig. 1 illustrates a schematic section through a (generic) vacuum glass product.

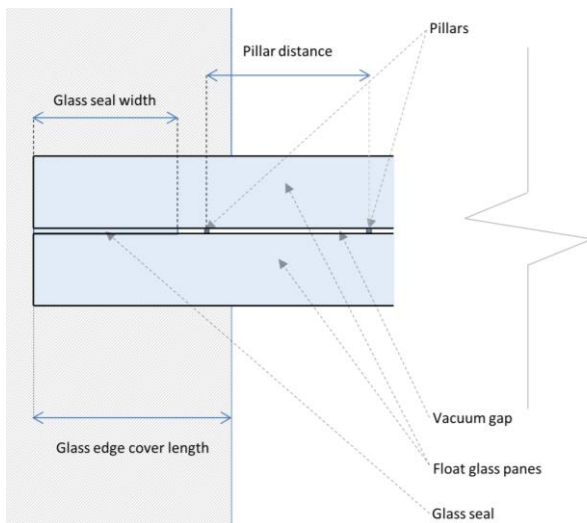


Fig. 1 – Schematic section through a generic vacuum glass product, including the relevant terminology (illustration by the authors)

2. Methodology

2.1 General R&D Efforts Within the Project

The development of new windows requires considerations from different backgrounds. Aspects such as the statics, weight, operation, acoustics, thermal performance, material, form and construc-

tion of frames, fittings, glass, seals, and many more need to be considered. To comply with these in part harsh requirements, the following strategy was deployed: in a first attempt, the major aspects to be worked upon were identified, including shifting certain aspects to post-project phases (as final product development done by the industry). Such aspects included production aspects, or the selection of the final components. Rather, the project team decided to work upon three major aspects: (a) The conception of specific window prototypes as such, which includes the operation/movement patterns and the principle architectural appearance. (b) The integration of motorized fittings for the specific window, preferably to be integrated in the fixed window frame (not into the moving part of the window). (c) The integration of the vacuum glass in the moveable wing of each of the windows under consideration of specific requirements of the vacuum glass, such as a well-dimensioned glass-edge seal cover. After setting up a decision fine-tuning of these aspects, an iterative development process started. Thereby, for each of the window prototypes, one of the industrial partners assumed responsibility for development, thus constructing the early prototypes and movement mock-ups, and conducting communicating/coordinating of geometry and semantic data means of their prototype with the consortium. The scientific partners, together with the industrial partners, were continuously developing and designing the corresponding windows. Thereby, one of their major responsibilities was to deliver proof of concept and proof of functionality results. A lot of iterative optimization characterized this later stage of the development. This workflow worked well and offered a lot of productive exploration of the space of possible solutions, mostly due to the many brainstorming and sketching meetings that were set up regularly.

2.2 Simulation and Thermal Performance Assessment

As already mentioned, one of the key tasks of the scientific partners in the project (namely the authors of this contribution) was to continuously assess the impact of design modifications on the thermal performance. To this end, we deployed

numeric thermal bridge simulation as matter of choice in assessing the critical thermal bridge situations along the window frames and highly conductive fitting parts. The tool we used was Antherm v. 10 (Antherm n.d.).

Moreover, the overall performance of the window in view of thermal transmittance was evaluated. Due to the non-off-the-shelf character of the windows, the equations from corresponding standards (i.e., EN ISO 10077 Parts 1 and 2 (EN10077 2017)) were found to be inappropriate for the purposes of vacuum glass windows, and thus slightly adapted. This majorly affected the U_{win} -equation, in which parts of the frame geometry that were supported with the highly-insulating vacuum glass were considered specific parts of reduced heat transfer in contrast to the otherwise rather weak performance of the frame.

Tables 1 and 2 illustrate both assumed conductivities and boundary conditions that were used for thermal performance assessment. Note that for encapsulated air and the vacuum gap replacement, Lambda-Values were considered, and that the colors in the table correspond with the materials in the illustrations in the Results section.

2.3 Subjective Assessment of Window Prototypes

To ensure that all relevant stakeholders accept new window constructions, it is not sufficient to just promise and provide excellent performance values. Rather, relevant stakeholders need to be convinced about aspects such as aesthetics, contemporaneity, innovation, feasibility of the construction, aspects of mounting, aspects of operation, and general acceptance amongst customers. To collect the opinion of domain experts and non-experts, we developed a short and easy-to-use questionnaire that encompassed these categories and allowed them to be graded (by the Austrian school grading system, starting from excellent to insufficient). Additionally, windows could be ranked by preference in the questionnaire, and additional comments could be written in the questionnaire.

Table 1 – Assumed thermal conductivities of materials and replace materials (vacuum gap, encapsulated air)















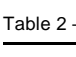


Color	Material	Conductivity [W.m ⁻¹ .K ⁻¹]
	Timber / Wood	0.11
	Steel	50
	Aluminium	200
	Compac Foam	0.031
	Insulation	0.041
	Seal(ing)	0.3
	Seal encapsuled	0.04
	Glass	1
	Plastic	0.2
	Masonry	0.45
	Purenite	0.096
	Plaster	0.7
	Silicone	0.35
	Vacuum	0.00000975
	Encapsulated Air	0.07

Table 2 – Boundary condition settings.

Colour	Boundary Condition	Rs (H,T) Value [m ² .K.W ⁻¹]
	Inside	0.13
	Outside	0.04

3. Results

3.1 Developed Window Prototypes

In the project, four different window prototypes were worked upon in depth and finally realized as full-scale functional mock-ups. These were:

- Turn window opening to inside (A): while adopting the traditional, established operation scheme of central Europe, the window provides a glass-inline-with-outer-perimeter appearance. Integration of external shading is easy, and the window operation is widely familiar to users.

- Turn window opening to outside (B): while not common in Central Europe anymore, windows that turn to the outside are familiar in Scandinavia. B comes with a rather reduced and thus aesthetically pleasing appearance.
- Swing window (C): adopting the principles of garage doors, this window provides a rather convenient way of storing the open wing above occupants' heads and thus allows spatial flexibility. The window was engineered to possess maximum flexibility and as few moving parts as possible.
- (Offset and) Sliding window (D): this window allows an offset movement to the outside for the purpose of ventilation. From this position, the window can be slid to one side on telescope railings, which remain totally invisible when the window is in its closed state.

All of the windows were equipped with electrical actuators, so that motorized operation could be realized. Thereby, automated operation in most cases covered the shift from fully closed to a ventilation position, while the classical full opening was still to be carried out manually (however, this has to be understood as a suggestion, both fully manual and fully motorized operation is possible in all four of the prototypes).

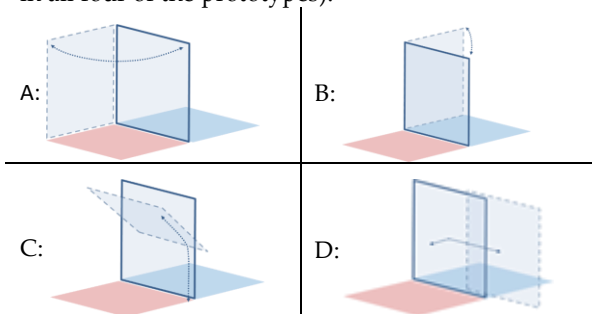


Fig. 2 – Opening/operation schemes of prototype A – D.

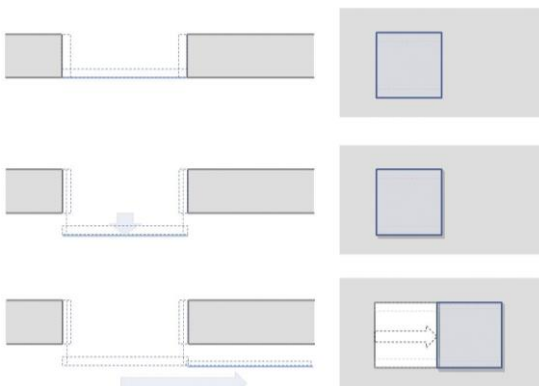


Fig. 3 – Conceptual view and section of prototype D



Fig. 4 – Opening/operation schemes of prototype A – D.

Fig. 2 illustrates the opening scheme of all four windows, while Fig. 3 provides some additional insight into prototype D. Fig. 4 shows photos of the finalized prototypes.

3.2 Performance Aspects of Developed Windows

A full documentation of the conducted thermal performance simulation efforts can be found in (Wölzl, 2019) and (Pont et al., 2020a). Exemplarily, Tables 3 to 6 illustrate some Key Performance Indicators (KPIs) of both the windows and the most crucial building construction joint, which is the lower connection between wall and window. The presented KPIs encompass U_{Win} -value, as well as f_{Rsi} -values and minimum surface temperature $\theta_{min,i}$. Note that the latter KPIs have been simulated assuming steady-state boundary temperatures (external temperature of $-10\text{ }^{\circ}\text{C}$, internal temperature $20\text{ }^{\circ}\text{C}$). The tables always provide the same structure: KPIs on top, followed by a false color image denoting the temperature distribution within the mentioned construction joint, and section through the same joint highlighting the assumed materials (compare Table 1 and 2).

Table 3 – Thermal Simulation of Window A

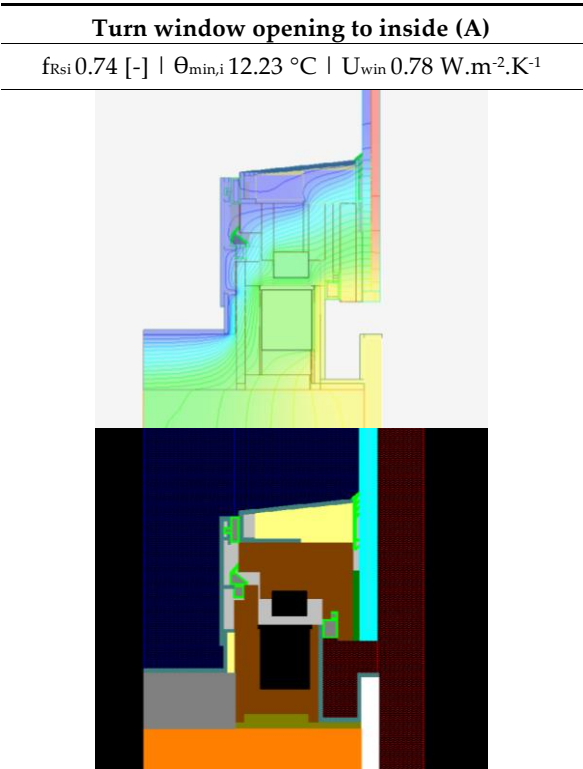


Table 5 – Thermal Simulation of Window C

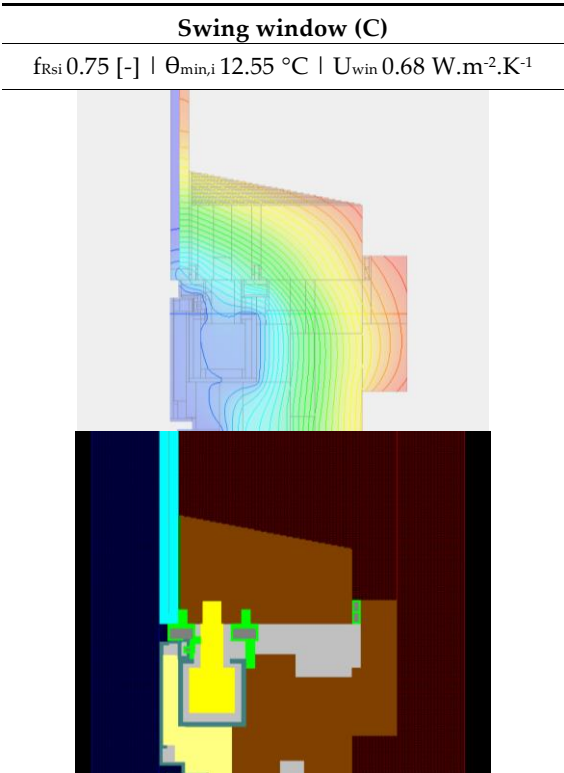


Table 4 – Thermal Simulation of Window B

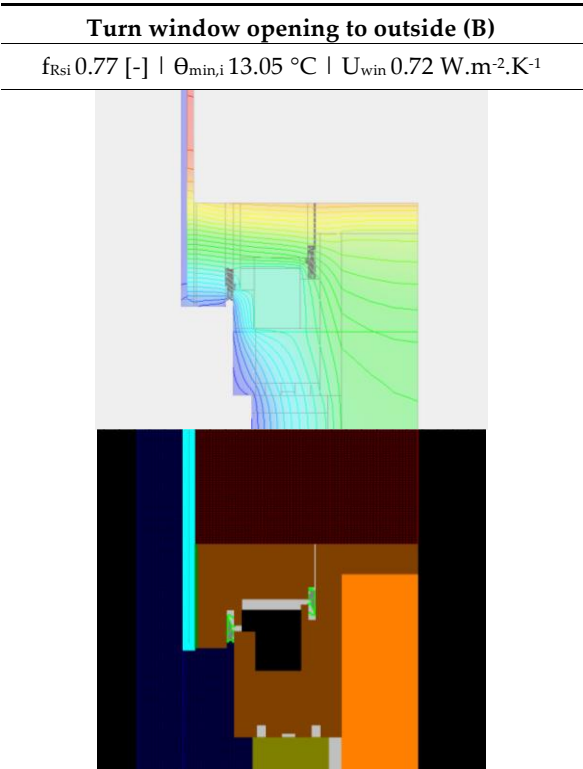
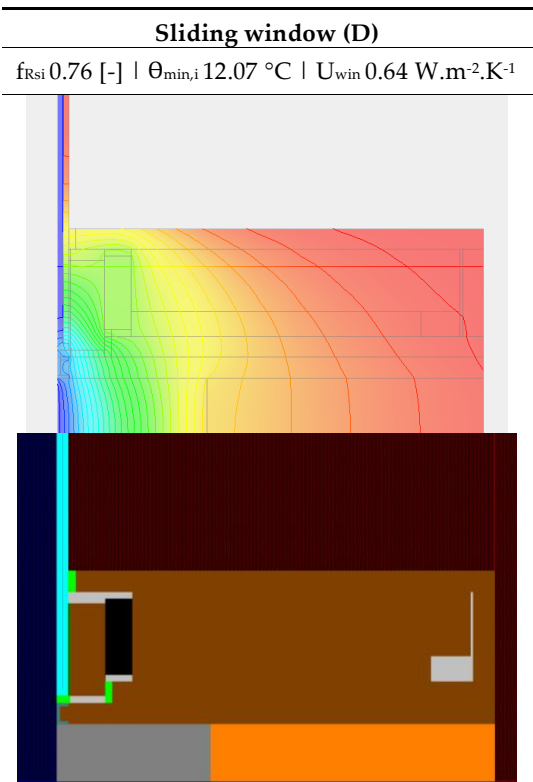


Table 6 – Thermal Simulation of Window D



Note that for all of these window prototypes, a vacuum glass pane of 8.15 mm thickness was assumed (U_g -value $0.7 \text{ W.m}^{-2}\text{.K}^{-1}$). The presented KPIs of all of the window prototypes well surpassed the minimum criteria for condensation risk assessment (which is a threshold f_{Rsi} -value of 0.71 following typical standards for opaque building constructions). Moreover, the U_{Win} -values that were reached are in the range of heavyduty triple glazing windows. Needless to say, the window constructions presented are featherweights in comparison with the triple-glazing windows mentioned.

3.3 Subjective Evaluation of Window Prototypes

The questionnaire-based evaluation of the prototypes was conducted during the FTT2020 (Fenster Türen Treff, 2020) in Salzburg, which is a trade fair and knowledge exchange event of the domain-relevant industry. All four window prototypes were exhibited there, and a talk about the project was held (Pont et al., 2020b). Fig. 5 shows the window prototypes in the exhibition. The grading results of the questionnaire are summarized in Table 7. Pertaining to the question as to which of the windows was preferred by the respondents, results showed that window D was favored, closely followed by A. This can be considered interesting, because these windows are fundamentally different: window D provides a disruptive new design with a very innovative and aesthetically attractive appearance and operation, and is thus far from what we see in most contemporary buildings. Prototype A, in contrast, is the contemporary adaptation of a well-established traditional window operation scheme. The rating by the domain experts thus hints at the fact that both tracks - disruptive change and continuing traditional technologies - need to be followed up.



Fig. 5 – Window prototypes exhibited during FTT2020 (Salzburg)

Table 7 – Domain experts' evaluation of the window prototypes (Austrian school grades: 1... excellent, 2... good, 3...average, 4... sufficient, 5...insufficient)

Criterion	A	B	C	D
Esthetics	1.7	2	2.4	1.2
Contemporaneity	1.8	2.4	2.6	1.6
Degree of innovation	2.1	2	2.2	1.2
Feasibility of the construction	1.8	2.4	2.6	2.1
Aspects of mounting	1.8	2.4	2.2	2.4
Aspects of operation	1.7	2.4	2.5	1.7
Acceptance amongst customers	1.9	2.4	3	1.8
Average	1.8	2.3	2.5	1.7

4. Conclusion and Future Research

The present contribution illustrated the outcome of a collaborative R&D effort which emphasized a set of interesting aspects:

- Shared projects between the building industry and academia can lead to disruptive developments in the AEC-context. Given the Paris climate goals and the rather slow innovation processes in the built environment, we are in urgent need of such fast-forward developments.
- The design of vacuum-glass-equipped windows should be carried out from scratch, even if traditional window operation concepts such as “turn-to-inside” are deployed. It is not feasible to simply take existing frame constructions and replace multi-pane insulation glass with vacuum glass, as such constructions cannot regularly fulfil the specific requirements of vacuum glass, such as a sufficient glass edge-cover length.
- While the window wing should be constructed around the vacuum glass, it seems wise to construct the fixed part of the window frame around the fittings system. As such, motorization of contemporary windows is facilitated, as no electricity needs to be interfaced to the moving part.

- Vacuum glass windows are capable of providing a very good performance in terms of thermal insulation at very slim (and thus lightweight) system thickness.

Needless to say, the prototypes presented are not yet available on the market and should be understood as “showcase” suggestions. Future R&D efforts shall address the development of specific parts (motorization and fittings) given that the elements used in FIVA were individually crafted. To become feasible, the motorization shall employ standard components and products. Moreover, the impact of vacuum glass and vacuum glass windows both on normative guidelines on windows and modeling in other (whole building) simulation tools has yet to be worked upon.

Acknowledgement

The project FIVA was generously funded by the Austrian Research Promotion Agency FFG (project-no. 867352). A set of partners contributed to the project, including domain experts of the window-producing companies Gaulhofer, Internorm, Katzbeck, Svoboda and Wick. Likewise, experts from the components industry contributed to the project, including Maco (fittings), ieb Eisele (sealings) and AGC Interpane (vacuum glass).

References

- AnTherm. n.d. <http://antherm.at/antherm/Waermebruecken.htm>
- CEN. 2017. *EN ISO 10077. 2017. EN ISO 10077-1:2017 Thermal performance of windows, doors and shutters — Calculation of thermal transmittance — Part 1: General; EN ISO 10077-2 Thermal performance of windows, doors and shutters — Calculation of thermal transmittance — Part 2: Numerical method for frames; International Standardization Institute.*
- Pont, U., and A. Mahdavi. 2017. "A comparison of the performance of two- and three-dimensional thermal bridge assessment for typical construction joints"; in: "Building Simulation Applications Proceedings", bu.press, 3. (2017), ISSN: 2531-6702; Paper ID 75, 8 pages.
- Pont, U., E. Heiduk, P. Schober, F. Romier, F. Dolezal, O. Proskurnina, M. Schuss, C. Sustr, H. Hohenstein, and A. Mahdavi. 2018a. „Sondierung von Fenstersystemen mit innovativen Gläsern, speziell Vakuum-Isoliergläsern, zur Gebäudesanierung“, Berichte aus Energie- und Umweltforschung 33/2018. Available via www.nachhaltigwirtschaften.at (last visit: March 2022)
- Pont, U., M. Schuss, P. Schober, P., and A. Mahdavi. 2018b. „Conception and Assessment of Technical Solutions for the Application of Vacuum Glazing in Contemporary Window Constructions“ in: "Proceedings of BauSim2018", A. Wagner, P. von Both et al. (ed.); (2018), Paper ID 1107, 8 pages.
- Pont, U., M. Schuss, A. Mahdavi, P. Schober, K. Hauer, and C. Lux. 2018c. „MOTIVE Modellierung, Optimierung und technische Integration von Vakuumglas-Elementen.“ Berichte aus Energie- und Umweltforschung 24/2018. Available via www.nachhaltigwirtschaften.at (last visit: March 2022)
- Pont, U., M. Wölzl, M. Schuss, A. Mahdavi, P. Schober, J. Haberl, and C. Lux. 2020a. „Fensterprototypen mit integriertem Vakuumglas – FIVA“. Berichte aus Energie- und Umweltforschung 47/2020. Available via www.nachhaltigwirtschaften.at (last visit: March 2022)
- Pont, U., P. Schober, M. Wölzl, M. Schuss, and J. Haberl. 2020b. „Das Morgenfenster - Entwicklung smarter und energieeffizienter Fensterprototypen" in: "Happy Birthday - Fenster-Türen-Treff 2020 - Tagungsband 5.-6. März 2020 Salzburg", Holzforschung Austria (ed.); (2020), ISBN: 978-3-9504488-8; 30 - 38.
- Wölzl, M. 2019. "Fensterkonstruktionen mit Vakuumglas: Simulationsbasierte Weiterentwicklung von innovativen Fensterkonstruktionen.", Master Thesis, TU Wien.
- Zoller, A. 1913. „Hohle Glasscheibe“. Patent-Nummer: No 387655., see: shorturl.at/lmEHO

Influence of Sound-Absorbing Ceiling on the Reverberation Time. Comparison Between Software and Calculation Method EN 12354-6

Nicola Granzotto – Free University of Bozen-Bolzano, Italy – nicolagranzotto74@gmail.com

Paolo Ruggeri – University IUAV of Venice, Italy – pruggeri@iuav.it

Fabio Peron – University IUAV of Venice, Italy – fperon@iuav.it

Marco Caniato – Free University of Bozen-Bolzano, Italy – marco.caniato@unibz.it

Andrea Gasparella – Free University of Bozen-Bolzano, Italy – andrea.gasparella@unibz.it

Abstract

The correct acoustic design of rooms such as classrooms, conference rooms and offices is of fundamental importance to ensure high speech intelligibility and to contain internal noise levels. The use of sound-absorbing ceilings alone is not always sufficient to guarantee adequate comfort, as the reflections between parallel walls could introduce unwanted phenomena such as flutter echo or the accentuation of modal resonances. One more issue is related to the use of Sabine or Eyring models, which could lead to an underestimation of the reverberation times. This article compares the reverberation time measured and simulated in two small rooms with (i) Sabine and Eyring models, (ii) two commercial simulation software and (iii) the EN 12354-6 standard method valid for rooms, with absorption not homogeneously distributed between the surfaces.

1. Introduction

Correct room acoustic design is of fundamental importance to increase comfort and speech intelligibility.

Many studies have been carried out regarding room acoustics optimization (Farina et al., 1998; Meissner, 2017; Nowoświat et al., 2016 and 2022; Prato et al., 2016; Tronchin et al., 2016, 2021a, 2021b, 2021c and 2022) and regarding acoustic building materials (Fabbri et al., 2021). The tools available to designers are simple equations, such as those of Sabine and Eyring or the EN 12354-6 standard or dedicated calculation software.

The Sabine and Eyring formulations are reliable under the following conditions:

- 1) diffuse sound field;
- 2) average absorption coefficient of the room less than 0.2;
- 3) homogeneous absorption.

Often in rooms such as offices, only the sound-absorbing ceiling is used both for cost and positioning reasons. In this case, the absorption is not homogeneous, since it is concentrated in just one part of the room. Thus, the Sabine and Eyring models may not provide reliable results.

To design rooms with non-homogeneous absorption, the calculation method described in EN 12354-6 Annex D can be used.

A further problem concerns the input data in the calculation software. The measurement of the absorption coefficient in the reverberation room, according to the ISO 354 standard, assumes a perfectly diffused sound field and the use of the Sabine formulation. Unfortunately, this is not possible in real laboratories, since these conditions are only ideal. Another problem of the measurement in a reverberant room is the presence of diffusers, which make the volume of the room lower than that actually used in the Sabine formula, with a consequent overestimation of the results (Scrosati et al., 2019).

On the other hand, methods such as normal incidence measurements according to ISO 10534-2 cannot be directly correlated with measurements carried out in a diffuse field in a reverberation room (Di Bella et al., 2019). The uncertainty of measurement of the absorption coefficient according to ISO 354 standard is also high (Scrosati et al., 2019 and 2020). This paper presents measurements made on two small, unfurnished offices with sound-absorbing ceilings and simulations carried out with simplified

formulations (Sabine, Eyring), EN 12354-6 calculation method and two dedicated room acoustic software packages.

2. Calculation Models

For the acoustic simulations the following models were compared:

- 1) equations of Sabine and Eyring;
- 2) calculation method EN 12354-6;
- 3) two different room acoustic simulation software.

The Sabine formula is:

$$T_{Sabine} = \frac{55.3 V}{c_0 A} \quad (1)$$

The equivalent absorption area A , considering only flat surfaces and not objects, is calculated with Eq. (2):

$$A = \sum_i \alpha_i S_i \quad (2)$$

Eyring equation is:

$$T_{Eyring} = \frac{55.3}{c_0} \frac{V}{-S \ln(1 - \alpha_m)} \quad (3)$$

The calculation method of EN 12354-6 (Annex D) for rooms with non-homogeneous absorption considers the following reverberation time (without the absorption of objects):

$$T_{est} = \frac{55.3V}{4c_0} \left(\frac{1}{A_x^*} + \frac{1}{A_y^*} + \frac{1}{A_z^*} + \frac{1}{A} \right) \geq T_{Sabine} \quad f \geq f_t = \frac{8.7c_0}{V^{1/3}} \quad (4)$$

$$T_{est} = \frac{55.3}{c_0} \frac{V}{A_{xyzd}^*} \quad f < f_t = \frac{8.7c_0}{V^{1/3}} \quad (5)$$

A_x^* , A_y^* , A_z^* , A^*_d are the effective sound absorption area for each sound field, while A_{xyzd}^* is the effective sound absorption area for the total field for low frequency ($f < f_t$).

The commercial software used are based on ray-tracing (A) and pyramid-tracing (B) techniques.

3. Case Studies

Two unfurnished rooms with an access floor with plan surfaces of 16.3 m² (Room 1) and 32.9 m² (Room 2) were examined. The walls are made of gypsum board and plastered concrete, the ceiling is

made with square rock wool panels, with dimensions of 600 mm x 600 mm. The windows equal in length to the façade are positioned 108 cm from the floor and have a height of 118 cm. The dimensions of the rooms are shown in Figs. 1, 2, 3 and 4.

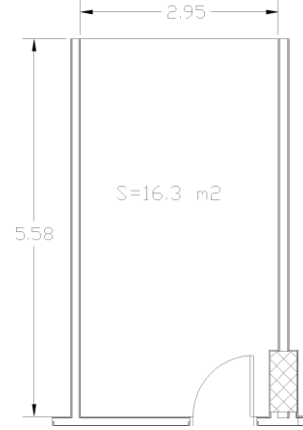


Fig. 1 – Room 1 plan

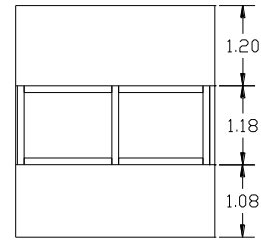


Fig. 2 – Room 1 Façade

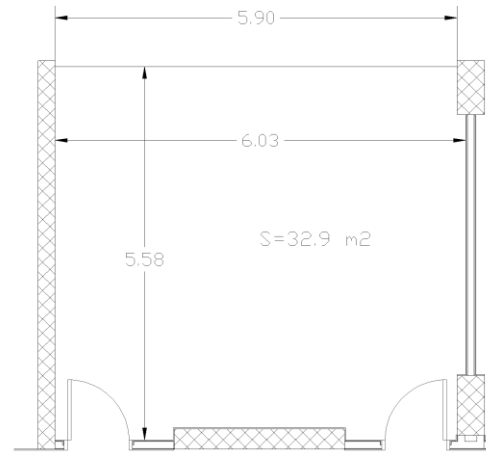


Fig. 3 – Room 2 plan

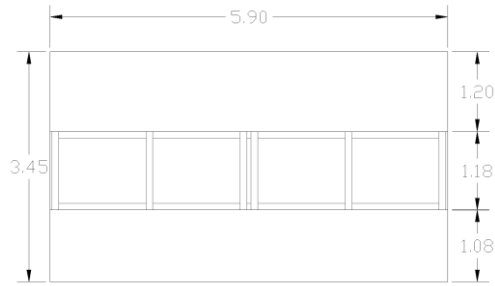


Fig. 4 – Room 2 Façade

The geometric characteristics of the rooms are shown in Table 1. The mean free path (MFP) calculated as Sabine, or obtained with the software, is also reported. It can be noted that the MFP obtained with the software is very similar to the ones obtained using the Sabine model.

Table 1 – Mean free path

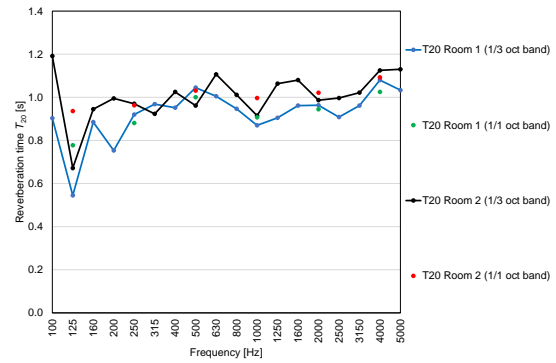
	Room 1	Room 2
V	56.2	113.5
S	91.5	147.2
$MFP=4V/S$	2.460	3.084
MFP-Software A	2.480	3.100
MFP-Software B	2.470	3.090

4. Reverberation Time Measurements

Reverberation time measurements T_{20} on the two offices (Room 1 and Room 2) were carried out to verify the reliability of the different calculation methods. Measurements were made with the interrupted noise method according to ISO 3382-2 standard.

In Room 1, one sound source position and three microphone positions were used, while in Room 2, two source positions and three microphone positions were used. Omnidirectional sound source was placed at 1.7 m height and a microphone was placed at 1.5 m height. Measurements were repeated twice for each source-microphone combination.

The results obtained are shown in Fig. 5.

Fig. 5 – Measured reverberation time T_{20} for Room 1 and Room 2 in 1/3 and 1/1 octave bands

It can be noted that the volume of room 1 is about half of the one of room 2, but the reverberation time is only slightly lower.

5. Acoustic Simulations

To verify the reliability of the different calculation methods, simulations of the reverberation time T_{20} were performed. 3D models were realized with two different types of room acoustic software, one based on ray-tracing and the other based on pyramid tracing. Models are reported in Figs. 6 - 9.

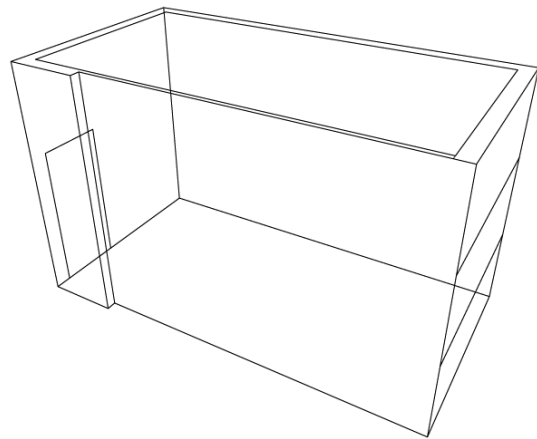


Fig. 6 – Room 1 - 3D simulation model - Software A

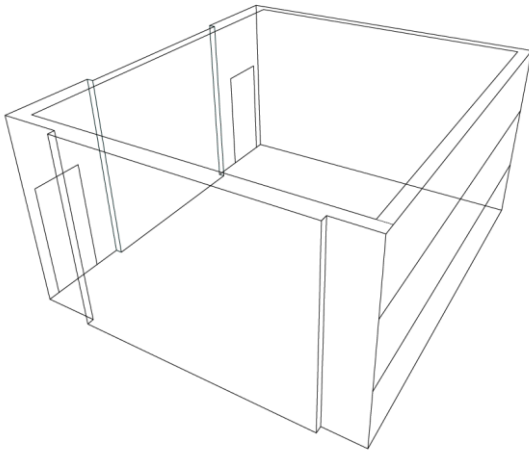


Fig. 7 – Room 2 - 3D simulation model - Software A

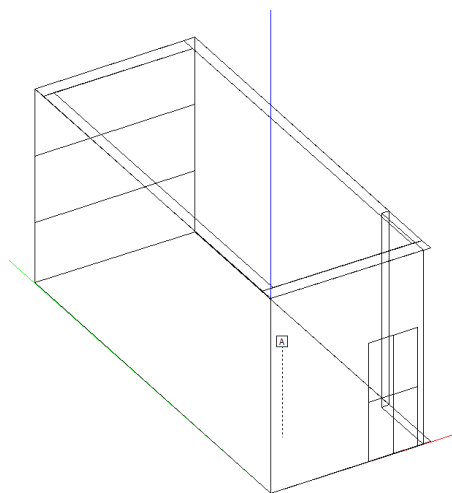


Fig. 8 – Room 1 - 3D simulation model - Software B

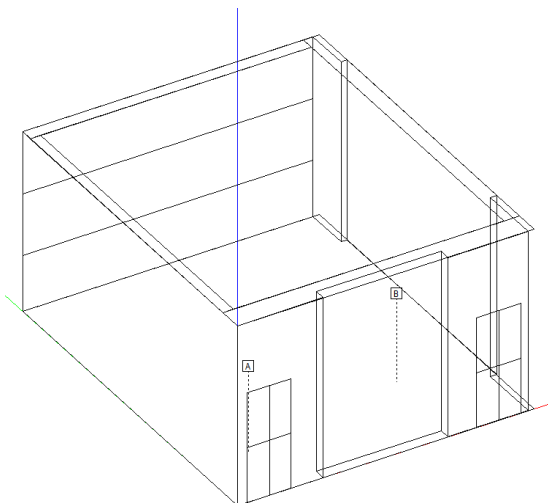


Fig. 9 – Room 2 - 3D simulation model - Software B

The acoustic absorption coefficients used are reported in Table 2.

Table 2 – Acoustic absorption coefficient

	125	250	500	1000	2000	4000
Ceiling	0.45	0.90	1.00	0.85	0.95	0.95
Plastered wall	0.02	0.03	0.03	0.04	0.05	0.07
Access floor	0.20	0.15	0.10	0.10	0.05	0.10
Gypsum board wall	0.15	0.10	0.06	0.04	0.04	0.05
Window	0.18	0.06	0.04	0.03	0.02	0.02
Door	0.14	0.10	0.06	0.08	0.10	0.10

6. Results and Discussion

The reverberation times obtained are shown in Fig. 10 (Room 1) and in Fig. 11 (Room 2). Some noise maps are shown in Fig. 12 (Room 1 - software B) and Fig. 13 (Room 2 - software B).

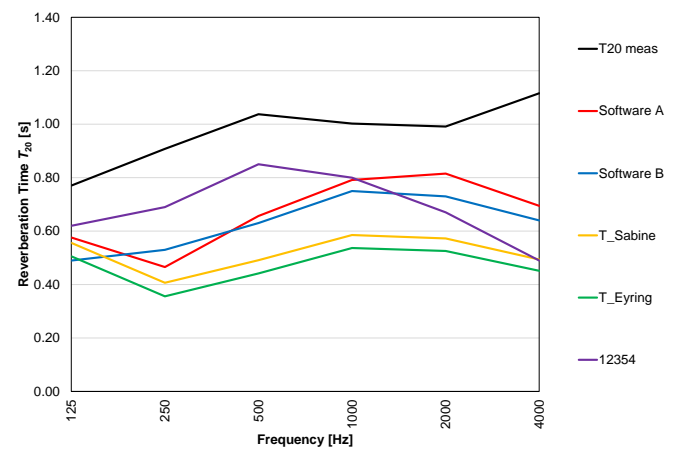


Fig. 10 – Measured and simulated reverberation time T_{20} (Room 1)

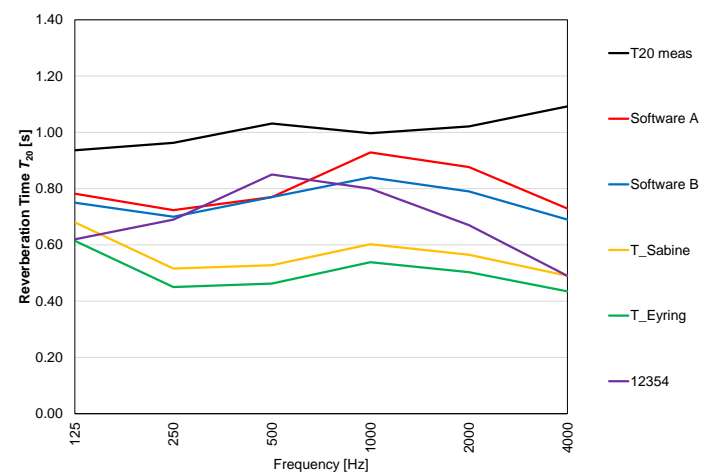


Fig. 11 – Measured and simulated reverberation time T_{20} (Room 2)

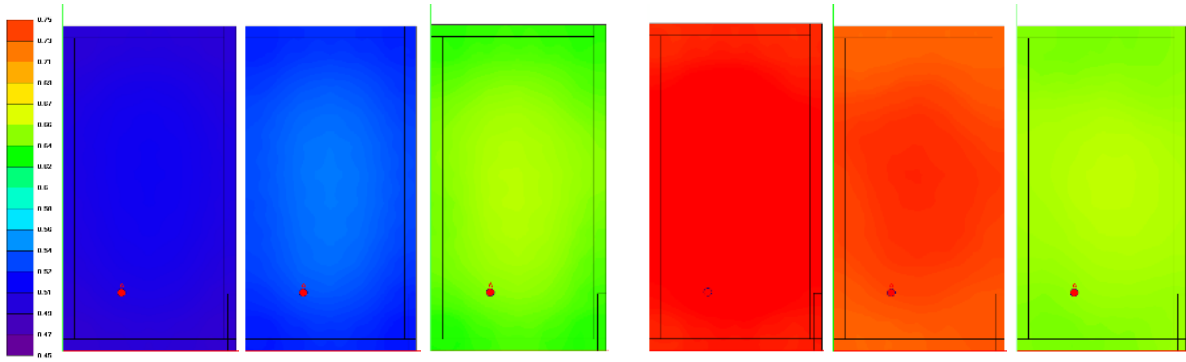


Fig. 12 – Reverberation time T_{20} simulation software B – Room 1 (125 Hz - 4000 Hz)

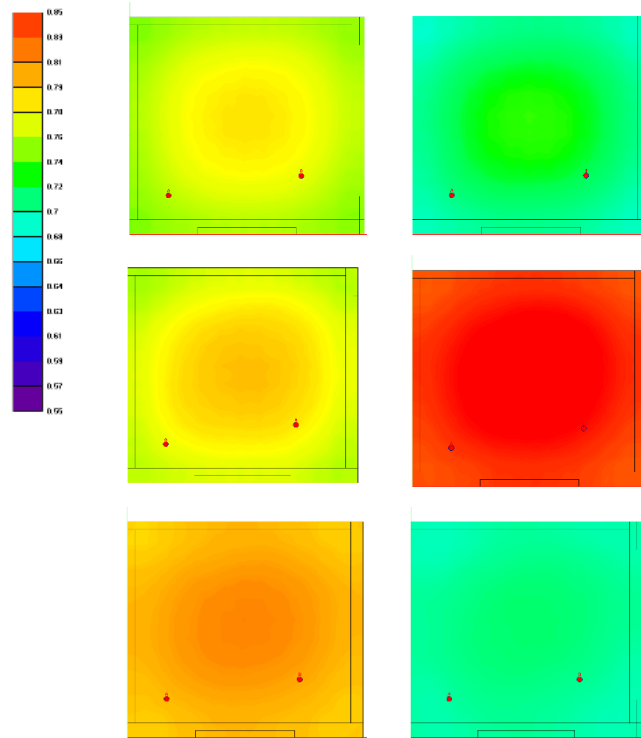


Fig. 13 – Reverberation time T_{20} simulation software B – Room 2 (125 Hz - 4000 Hz)

An underestimation of the simulated reverberation time compared to the measured one can be noted. In particular, the Sabine and Eyring formulas are not usable for rooms of this type. Accordingly, the simulated values obtained are about half of those measured (Farina, 1998). The results obtained with the EN 12354-6 model and with the calculation software are also lower than those measured, in particular, for room 1, the best estimate is represented by EN 12354-6 up to 1000 Hz and by software A over 1000 Hz. For room 2, the best estimate is represented by software A, as reported in Figs. 14 and 15.

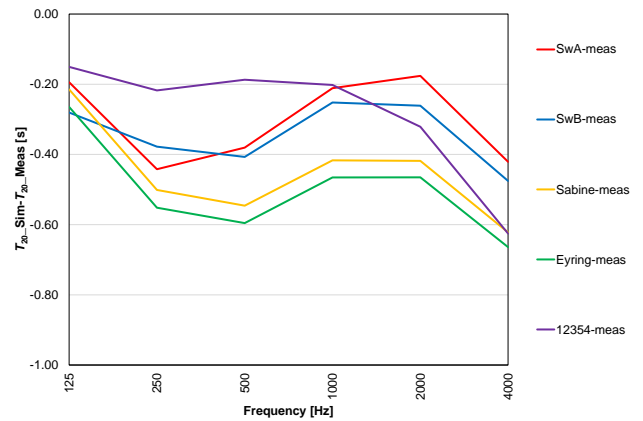


Fig. 14 – Difference between simulated and measured reverberation time T_{20} (Room 1)

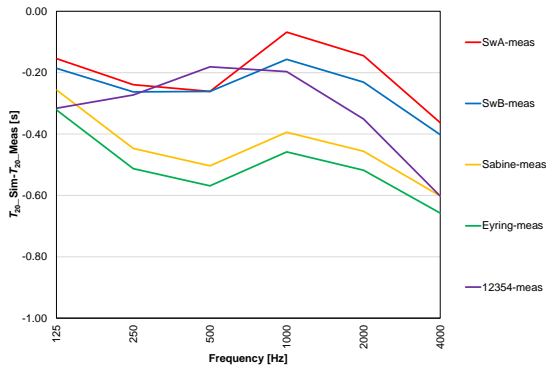


Fig. 15 – Difference between simulated and measured reverberation time T20 (Room 2)

This underestimation is due to an overestimation of the absorption coefficients obtained in the reverberation room according to ISO 354 standard. This is due to the not-perfectly-diffuse sound field and to the modification of the MFP, due to the diffusers hanging to the ceiling of the reverberation room, compared with the one predicted by the Sabine formula contained in the measurement method.

According to Scrosati et al. (2019), the MFP of their empty reverberation room changes from 3.853 m (without diffusers) to 3.377 m (with diffusers), while with specimen MFP varies from 3.750 m (without diffusers) to 3.295 m (with diffusers). The statistical value calculated for this reverberation room was 3.810 m. By modifying the Sabine formula of ISO 354 standard with the correct MFP specific for this reverberation room, the authors found an absorption coefficient about 20-23 % lower than the one measured according to ISO 354.

To better understand the phenomenon, the best fit acoustic absorption coefficients which best approximate the measured reverberation times were calculated both with software A and B. The results are shown in Fig. 16.

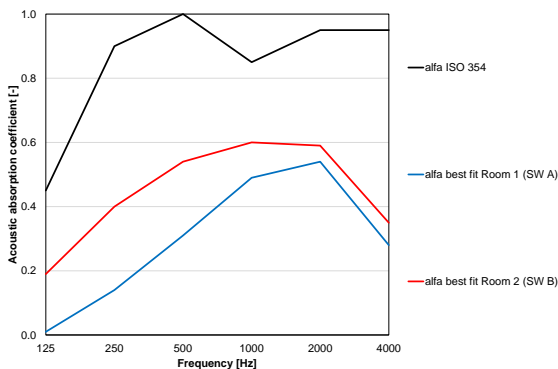


Fig. 16 – Best fit acoustic absorption coefficient

It can be noted that the best fit acoustic absorption coefficient is lower for room 1 than for room 2. This could be due to the different ceiling surface-to-total surface ratio (17.8 % for Room 1 and 22.8 % for Room 2). Furthermore, the ceiling angle of view concerning the sound source is 78° for Room 1 compared with 101° for Room 2 (Figs. 17 and 18) and differences could actually affect the real sound absorption.

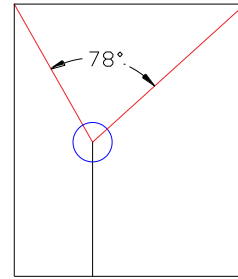


Fig. 17– Ceiling angle of view (Room 1)

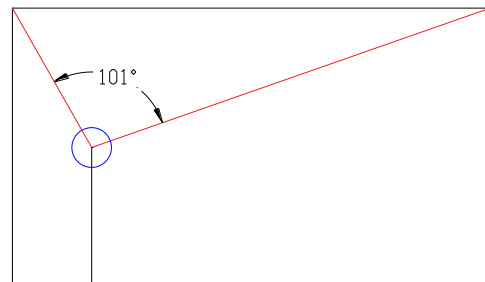


Fig. 18 – Ceiling angle of view (Room 2)

7. Conclusion

In this work, the acoustic simulation of the reverberation time of two small rooms with volumes of 56.2 m³ and 113.5 m³ was considered. These rooms feature sound-absorbing panels only on the ceiling. Therefore, they do not have a homogeneous surfaces absorption.

Simple equations such the Sabine and Eyring formulas, the EN 12354-6 standard model, and two dedicated calculation software were considered.

It was possible to note how all the computational models examined led to an underestimation of the reverberation time. In particular, since reverberation time values obtained with these methods are about half of those measured, the Sabine and Eyring models are not suitable for this type of room.

Better results were obtained using software based

on ray-tracing and pyramid-tracing and on the calculation model based on the EN 12354-6 standard. However, even in this case the reverberation time is underestimated.

A possible explanation of this phenomenon is the overestimation of the absorption coefficients obtained in the reverberation room, according to the ISO 354 standard, due to the not-perfectly-diffuse sound field and to the presence of the diffusers hanging from the ceiling. These do modify the effective volume of the reverberation room and the MFP compared with the one predicted by the Sabine formula.

It is therefore advisable to reduce the values of the acoustic absorption coefficients in the acoustic design.

Nomenclature

Symbols

T_{60}	Reverberation time (s)
V	Volume of the room (m^3)
A	Equivalent absorption area (m^2)
α	Acoustic absorption coefficient (m)
α_m	Mean acoustic absorption coefficient (m)
S	Surface (m^2)

Subscripts/Superscripts

i	i -th surface
-----	-----------------

References

- CEN (European Committee for Standardization). 2006. EN 12354-6:2006 Building acoustics - Estimation of acoustic performance of buildings from the performance of elements - Part 6: Sound absorption in enclosed spaces.
- Di Bella, A., N. Granzotto, P. Ruggeri and F. Peron. 2019. "Analysis of the acoustic absorption of fabrics in a diffuse sound field and for normal incidence." In: *Proceedings of the 26th International Congress on Sound and Vibration, ICSV 2019*. Toronto.
- Farina, A. A. Langhoff, and L. Tronchin. 1998. "Acoustic characterisation of "virtual" musical instruments: using MLS technique on ancient violins." *Journal Of New Music Research* 27(4):359-379. doi: <https://doi.org/10.1080/09298219808570753>
- Fabbri, K., L. Tronchin, and F. Barbieri. 2021. "Coconut fibre insulators: The hygrothermal behaviour in the case of green roofs." *Construction and Building Materials* 266: 1-9. doi: <https://doi.org/10.1016/j.conbuildmat.2020.121026>
- ISO. 1998. ISO 10534-2, Acoustics – Determination of sound absorption coefficient and impedance in impedance tubes – Part 2: Transfer-function method.
- ISO. 2003. ISO 354, Acoustics – Measurement of sound absorption in a reverberation room.
- ISO. 2008. ISO 3382-2, Acoustics – Measurement of room acoustic parameters – Part 2: Reverberation time in ordinary rooms.
- Meissner, M. 2017. "Acoustics of small rectangular rooms: Analytical and numerical determination of reverberation parameters." *Applied Acoustics* 120: 111-119. doi: <https://doi.org/10.1016/j.apacoust.2017.01.020>
- Nowoświat, A., M. Olechowska, and J. Ślusare. 2016. "Prediction of reverberation time using the residual minimization method." *Applied Acoustics* 106: 42-50. doi: <https://doi.org/10.1016/j.apacoust.2015.12.024>
- Nowoświat, A., and M. Olechowska. 2022. "Experimental Validation of the Model of Reverberation Time Prediction in a Room." *Buildings* 12(3): 347. doi: <https://doi.org/10.3390/buildings12030347>
- Prato, A., F. Casassa, and A. Schiavi. 2016. "Reverberation time measurements in non-diffuse acoustic field by the modal reverberation time." *Applied Acoustics* 110: 160-169. doi: <https://doi.org/10.1016/j.apacoust.2016.03.041>
- Scrosati, C., F. Scamoni, M. Depalma, and N. Granzotto. 2019. "On the diffusion of the sound field in a reverberation room." *Proceedings of the 26th International Congress on Sound and Vibration, ICSV 2019*.
- Scrosati, C., F. Martellotta, F. Pompoli, A. Schiavi, A. Prato, D. D'Orazio, M. Garai, N. Granzotto, A.

- Di Bella, F. Scamoni, M. Depalma, C. Marescotti, F. Serpilli, V. Lori, P. Nataletti, D. Annesi, A. Moschetto, R. Baruffa, G. De Napoli, F. D'Angelo, and S. Di Filippo. 2020. "Towards more reliable measurements of sound absorption coefficient in reverberation rooms: An Inter-Laboratory Test." *Applied Acoustics* 165: 107298. doi: <https://doi.org/10.1016/j.apacoust.2020.107298>
- Tronchin, L., and D. J. Knight. 2016. "Revisiting Historic Buildings through the Senses. Visualising Aural and Obscured Aspects of San Vitale, Ravenna." *International Journal of Historical Archeology* 20: 127-145. doi: <https://doi.org/10.1007/s10761-015-0325-2>
- Tronchin, L., and A. Bevilacqua. 2021a. "Acoustic study of different sceneries at the São Carlos national theatre of Lisbon." *Applied Acoustics* 180: 1-11. doi: <https://doi.org/10.1016/j.apacoust.2021.108102>
- Tronchin, L., F. Merli, and M. Dolci. 2021b. "Virtual acoustic reconstruction of the Miners' Theatre in Idrija (Slovenia)." *Applied Acoustics* 172: 1-9. doi: <https://doi.org/10.1016/j.apacoust.2020.107595>
- Tronchin, L. 2021c. "Variability of room acoustic parameters with thermo-hygrometric conditions." *Applied Acoustics* 177: 1-14. doi: <https://doi.org/10.1016/j.apacoust.2021.107933>
- Tronchin, L., and A. Bevilacqua. 2022. "Historically informed digital reconstruction of the Roman theatre of Verona. Unveiling the acoustics of the original shape." *Applied Acoustics* 185: 1-18. doi: <https://doi.org/10.1016/j.apacoust.2021.108409>

Simulation of Thermal and Acoustic Façade Insulation Starting From the Characteristics of the Individual Elements

Nicola Granzotto – Free University of Bozen-Bolzano, Italy – nicolagranzotto74@gmail.com

Paolo Ruggeri – IUAV, Italy – pruggeri@iuav.it

Fabio Peron – IUAV, Italy – fperon@iuav.it

Marco Caniato – Free University of Bozen-Bolzano, Italy – marco.caniato@unibz.it

Andrea Gasparella – Free University of Bozen-Bolzano, Italy – andrea.gasparella@unibz.it

Abstract

The thermal and acoustic insulation of individual building elements such as walls, windows and systems for roller shutters significantly affects the thermal and acoustic insulation of a building. This paper considers the acoustic and thermal performance of the individual elements evaluated in laboratory with simulation of both the façade sound reduction index and thermal transmittance of a typical room. The scope of this work is to verify if there are any correlations between acoustic and thermal performance; for this reason, 4 types of opaque wall, 3 window systems for roller shutters and 5 windows for a total of 60 façade configurations have been considered and combined.

1. Introduction

The correct acoustic and thermal design of a building is of fundamental importance for increasing indoor comfort.

Many studies have been carried out regarding acoustic and thermal comfort (Fabbri et al., 2014; Granzotto, 2021; Tronchin et al., 2018; Tronchin et al., 2021), façade acoustic insulation (Hua et al., 2021; Jagniatinskis et al., 2021) and thermal insulation (Theodosiou et al., 2019).

Other studies comparing acoustic and thermal characteristics of walls can be found (Di Bella et al., 2014; Di Bella et al., 2015). Sound insulation is one important factor for façade performance optimization. As an example, Ryu et al. (2010) proved that the sound insulation of a building façade influenced indoor annoyance due to transportation noise and the frequency content of intrusive noise.

For façade thermal insulation, Sierra-Peréz et al. (2016) demonstrated how an optimized combination of elements could affect indoor thermal perception.

In this work, the acoustic and thermal insulation of a façade has been considered, varying the performance of single elements. 4 walls, 3 shutter systems and 5 windows.

The acoustic performance was determined in a laboratory while the thermal performance was simulated from the thermal conductivity data, considering, in addition, linear thermal transmittance.

2. Calculation Models

The sound reduction index, R , of a building element is defined as:

$$R = 10 \lg \left(\frac{1}{\tau} \right) \quad (1)$$

The transmission coefficient τ is the ratio of the sound power, W_1 , which is incident on the test element to the sound power, W_2 , radiated by the test element to the other side.

R was measured in laboratory conditions according to the ISO 10140 (2021) series standard:

$$R = L_1 - L_2 + 10 \lg \left(\frac{S}{A} \right) \quad (2)$$

The composed sound reduction index, R_{tot} , was calculated as:

$$R_{\text{tot}} = 10 \lg \left(\frac{\sum_{i=1}^n S_i}{\sum_{i=1}^n 10^{(-R_i/10)} S_i} \right) \quad (3)$$

The weighted sound reduction index, R_w and the spectrum adaptation term for pink noise, C , and for traffic noise, C_{tr} , were calculated according to ISO 717-1 (2020). The thermal conductivity, λ , of materials such as rock wool, EPS and XPS is measured according to EN 12667 standard (2021), while the thermal transmittance, U , and the linear thermal transmittance, Ψ , were simulated by means of a FEM software according to ISO 10077-2 (2017) and ISO 10211 (2017) standards.

The composed thermal transmittance, U_{tot} , of the façade was obtained according to ISO 10077-1 (2017) with the following formula:

$$U_{\text{tot}} = \frac{\sum_{i=1}^n U_i S_i + \sum_{k=1}^m \Psi_k l_k}{\sum_{i=1}^n S_i} \quad (4)$$

3. Building Elements

The building elements considered are reported in Tables 1, 2 and 3.

Table 1 – Building elements - Walls

ID	Description
A	Aerated concrete blocks (350 kg/m ³ , 300 mm) lined with rock wool panels (45 mm) and gypsum board (12.5 mm).
B	Hollow brick plastered one side (250 mm) lined with rock wool panels (140 mm) and plaster (5 mm).
C	Hollow brick plastered one side (250 mm) lined with EPS panels (140 mm) and plaster (5 mm).
D	Aerated concrete blocks (300 kg/m ³ , 400 mm).

Table 2 – Building elements - Windows systems for roller shutters

ID	Description
a	Integrated windows system for roller shutter for window flush with the internal wall. $S=0.75 \text{ m}^2$.
b	Integrated windows system for roller shutter for window in the middle of the wall. $S=0.75 \text{ m}^2$.
c	Box for roller shutter suitable for building renovations. $S=0.45 \text{ m}^2$.

Table 3 – Building elements - Windows

ID	Description
1	One sash window with glass: 6 mm + 0.76 mm acoustic PVB + 6 mm / 16 mm Argon / 4 + 0.50 mm acoustic PVB + 4 mm.
2	One sash window with glass: 3 mm + 0.50 mm acoustic PVB + 3 mm / 15 mm Argon / 4 mm / 15 mm Argon / 3 mm + 0.50 mm acoustic PVB + 3 mm.
3	Two sash windows with glass: 4 mm + 0.76 mm acoustic PVB + 4 mm / 15 mm Argon / 4 mm / 15 mm Argon / 4 mm + 0.76 mm acoustic PVB + 4 mm.
4	One sash window with glass: 6 mm + 0.76 mm acoustic PVB + 6 mm / 12 mm Argon / 4 mm / 12 mm Argon / 4 mm + 0.76 mm acoustic PVB + 4 mm.
5	Two sash windows with glass: 3 + 0.38 PVB + 3 mm / 18 Argon / 4 + 0.50 mm acoustic PVB + 4 mm.

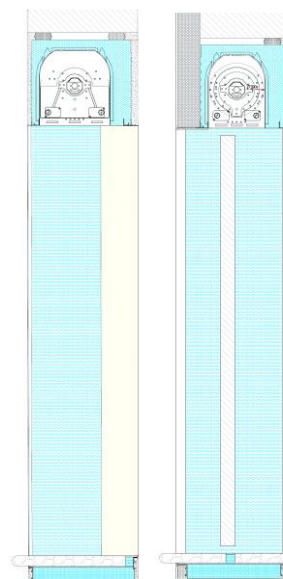


Fig. 1 – Window system for roller shutter “a” and “b”

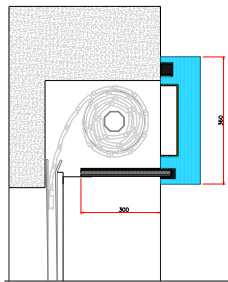


Fig. 2 – Window system for roller shutter “c”

Fig. 1 and 2 show the windows system for roller shutter used in the simulations. Window dimension was 1230 mm x 1480 mm, and wood frame thickness was 80 mm.

4. Acoustic Measurements and Thermal Simulations

The sound reduction index of the building elements was measured in the laboratory according to ISO 10140 (2021) series standard (Figs. 3, 4 and 5). The sound reduction index, R , of the building elements in the 1/3 octave frequency band is shown in Fig. 6. The weighted sound reduction and the thermal transmittance are shown in Table 4. The sound reduction index of the building elements in the 1/3 octave frequency band is shown in Fig. 6. The weighted sound reduction and the thermal transmittance are shown in Table 4. The thermal transmittance of the windows and window systems for roller shutters was simulated with FRAME SIMULATOR software. From the thermal profiles in Fig. 7, it is possible to consider the “a” box shutter as the one with the best performance followed by “b” and “c”.



Fig. 3 – Window – Laboratory test according to ISO 10140 (2021) series standard



Fig. 4 – Window system for roller shutter “a” – Laboratory test according to ISO 10140 (2021) series standard



Fig. 5 – Wall – Laboratory test according to ISO 10140 (2021) series standard

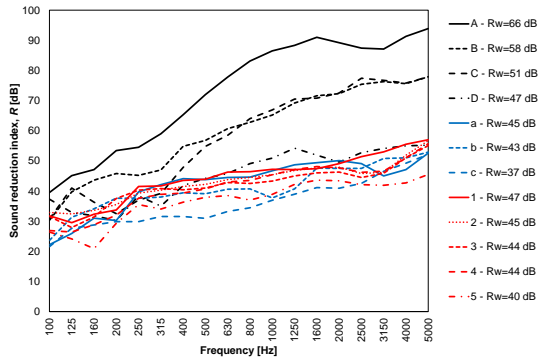


Fig. 6 – Sound reduction index of building elements in 1/3 octave bands

Table 4 – Building elements acoustic and thermal performance

Element	Type	$R_w(C;C_{tr})$	U
A	Wall	66(-2;-9)	0.201
B	Wall	58(-3;-9)	0.219
C	Wall	51(-2;-7)	0.193
D	Wall	47(-2;-6)	0.170
a	Shutter box	45(-2;-8)	0.385
b	Shutter box	44(-2;-5)	0.842
c	Shutter box	37(-1;-3)	1.061
1	Window	47(-2;-5)	1.200
2	Window	45 (-1;-3)	0.890
3	Window	44 (-1;-3)	1.100
4	Window	44(-1;-5)	0.890
5	Window	40(-2;-5)	1.300

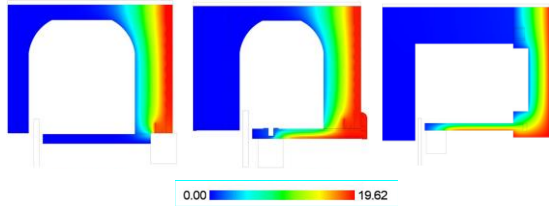


Fig. 7 – Temperature for windows system for roller shutter (left: “a”, center: “b”, right: “c”)

The linear thermal transmittances, Ψ , of the shutter-wall interface, wall-window interface and shutter-window interface were calculated with Finite Element Method software MOLD SIMULATOR, according to ISO 10211 (2017). Ψ_1 is the linear thermal transmittance for wall-shutter box, Ψ_2 is the linear thermal transmittance for wall-shutter-window, Ψ_3 is the linear thermal transmittance for shutter-window (Fig. 8 and Table 5).

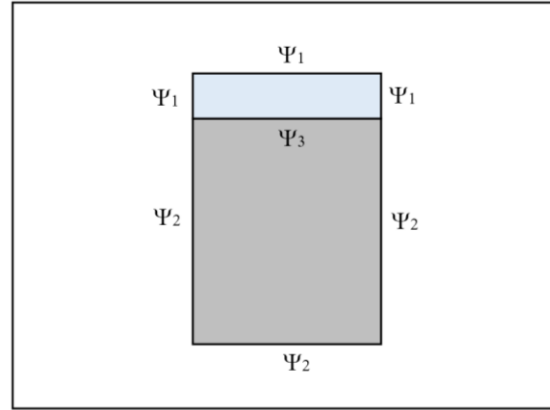


Fig. 8 – Linear thermal transmittance scheme

Table 5 – Building elements – Linear thermal transmittance

Configuration	Ψ_1	Ψ_2	Ψ_3
Aa	0.33	0.08	0.23
Ab	0.33	0.08	0.38
Ac	0.10	0.10	0.55
Ba	0.40	0.11	0.23
Bb	0.40	0.08	0.38
Bc	0.45	0.11	0.55
Ca	0.40	0.12	0.23
Cb	0.40	0.09	0.38
Cc	0.45	0.11	0.55
Da	0.33	0.08	0.23
Db	0.33	0.08	0.38
Dc	0.10	0.09	0.55

Figs. 9, 10 and 11 show some temperature examples of linear thermal transmittance simulations.

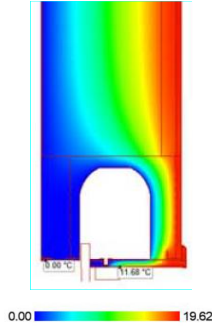


Fig. 9 – Example of ψ_1 simulation with MOLD software for "b" shutter box and wall "D"

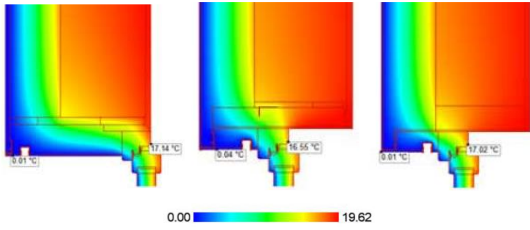


Fig. 10 – Example of ψ_2 simulation with MOLD software for "a", "b" and "c" shutter box (with Wall "B")

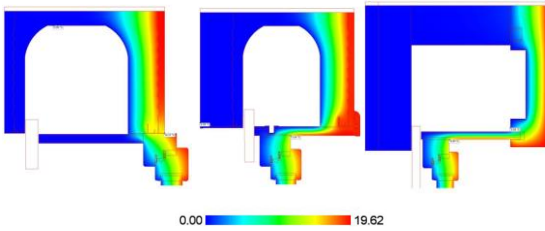


Fig. 11 – ψ_3 simulation with MOLD software for "a", "b" and "c" shutter box

5. Results

The acoustic and thermal insulation of a 2.7-m-high and 4-m-wide façade has been considered.

The composed weighted sound reduction index, R_w , vs composed thermal transmittance, U , is shown in Fig. 12.

The composed weighted sound reduction index, R_w+C_{tr} , vs composed thermal transmittance, U , is shown in Fig. 13. R_w+C_{tr} considers weighted sound reduction index in dB(A) for traffic noise.

The best configurations are located in the upper left quadrant.

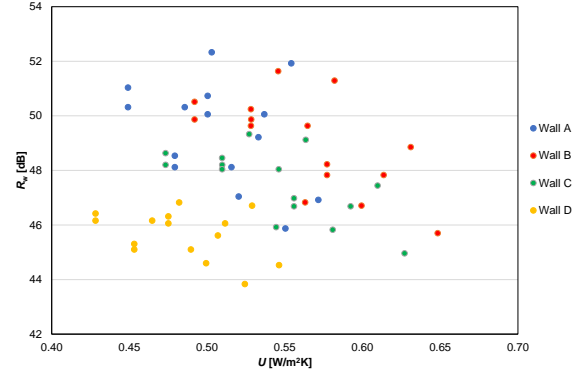


Fig. 12 – R_w vs U

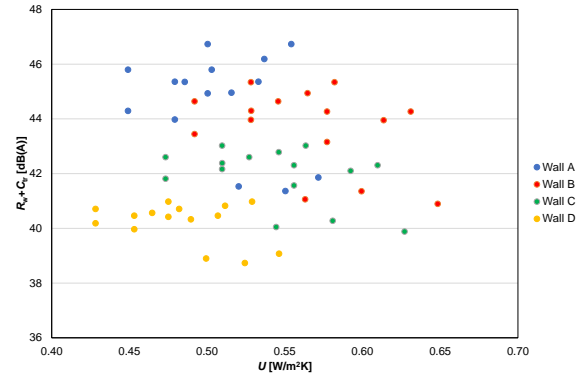


Fig. 13 – R_w+C_{tr} vs U

It can be noted that there are no correlations between acoustic and thermal performance at all. Indeed, poor correlations are obtained even considering single wall results.

For R_w :

- $R^2_{wall A}$ is 0.13;
- $R^2_{wall B}$ is 0.41;
- $R^2_{wall C}$ is 0.42;
- $R^2_{wall D}$ is 0.15.

For R_w+C_{tr} :

- $R^2_{wall A}$ is 0.09;
- $R^2_{wall B}$ is 0.16;
- $R^2_{wall C}$ is 0.18;
- $R^2_{wall D}$ is 0.14.

Fig. 14 shows the configurations examined as the thermal transmittance, U , decreases. In the same graph, the indices R_w and R_w+C_{tr} are indicated (dotted line indicates the calculated transmittance without considering the linear thermal transmittance).

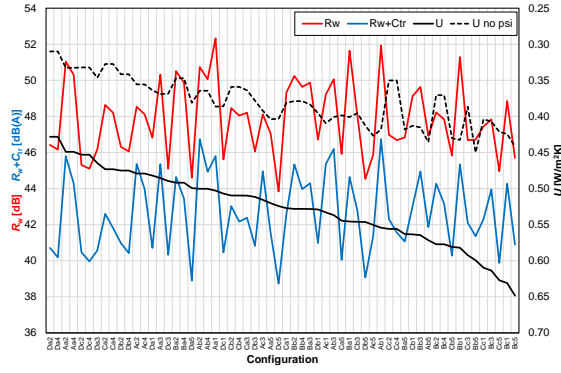


Fig. 14 – U vs R_w and U vs R_w+C_{tr}

Considering the variation in the performance of a single element (wall, window systems for roller shutters and window), it can be noted how the variations in the overall performance of the façade are different from an acoustic and thermal point of view (Fabbri et al., 2021; Tronchin, 2005). Interestingly, it can be noted that, if linear thermal transmittances are not considered, considerable errors are made ($\Delta U = 0.12\text{-}0.21 \text{ W}/(\text{m}^2\text{K})$).

Furthermore, it can be noted that the configurations with "D" wall are the best in terms of thermal insulation because of low U and reduced thermal bridges, while in terms of sound insulation they are not as effective as the other walls.

The configurations with shutter box type "c" provide good results even if the performances of this element are not optimal. This is due to the small surface of the element, which leads to a small overall influence.

It can be noted that the combination providing better acoustic and thermal performance is represented by the "Aa2" configuration.

In Figs. 15-23, the values of U , R_w , R_w+C_{tr} of the whole façade are reported and parametrically compared with the values of the walls (A, B, C and D), of the shutter boxes (a, b, and c) and of the windows (1, 2, 3, 4 and 5).

Configurations with the lowest value are indicated with a grey dashed line. In Fig. 15, it can be seen how wall A implies a lower value of U for the façade. This is due to the fact that wall A has a lower Ψ_2 value because of its composition (thermal insulating blocks). As regards the acoustic insulation, it can be noted that as the performance of the single element increases, the range of R_w and R_w+C_{tr} increases.

In Figs. 16 and 17, the overall acoustic performance is studied parametrically and compared to the wall ones. Interestingly, an important influence is assessed below 55 dB, while over this threshold no significant difference is found.

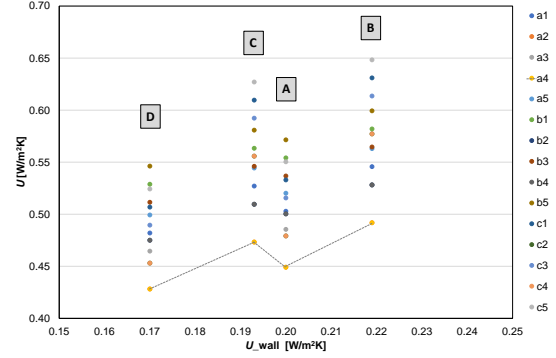


Fig. 15 – Overall U compared to the thermal transmittance of the wall (A, B, C and D), U_{wall}

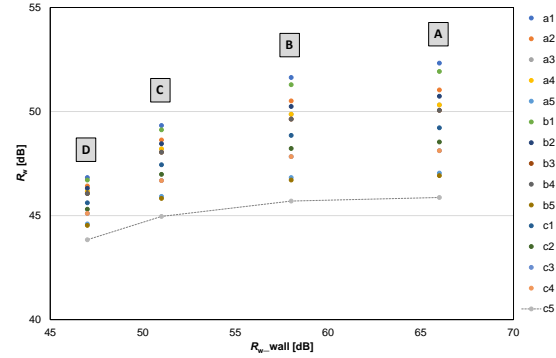


Fig. 16 – Overall R_w compared to the weighted sound reduction index of the wall (A, B, C and D), R_{w_wall}

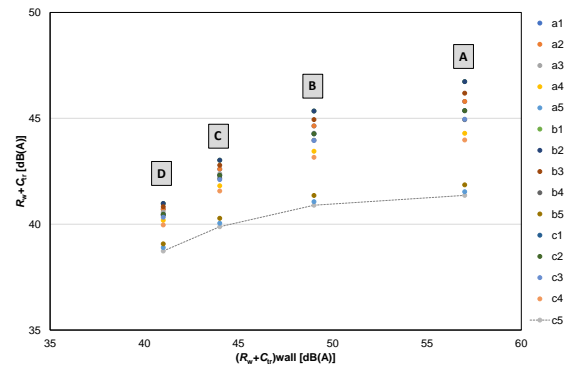


Fig. 17 – Overall R_w+C_{tr} compared to the weighted sound reduction index of the wall (A, B, C and D), $(R_w+C_{tr})_{\text{wall}}$

The influence of the shutter box transmittance is reported in Fig. 18. It is clear that shutters affect the final performance, but do not drive the overall final result because of their reduced area.

Moving on to the shutter box acoustic performances (Figs. 19-20), it can be seen that their influence affects overall results more when the wall provides high acoustic insulation.

The window parametric influence on overall results is depicted in Fig. 21.

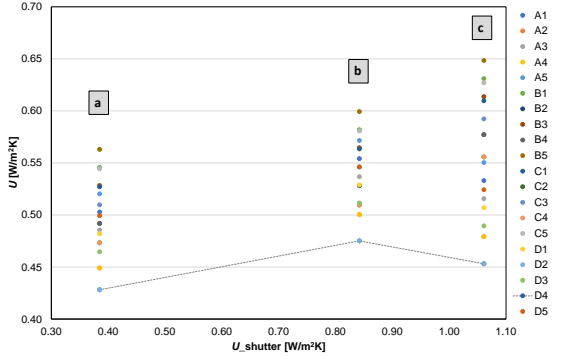


Fig. 18 – Overall U compared to the thermal transmittance of the shutter box, (a, b and c) U_{shutter}

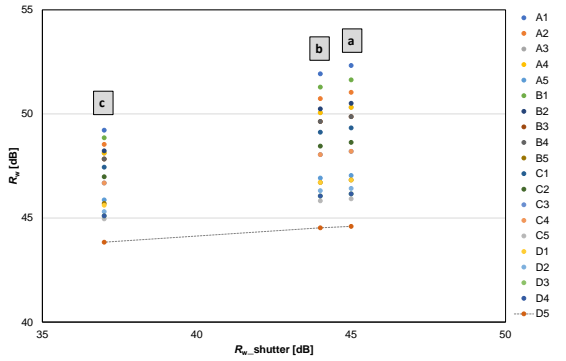


Fig. 19 – Overall R_w compared to the weighted sound reduction index of the shutter box (a, b and c), $R_{w_shutter}$

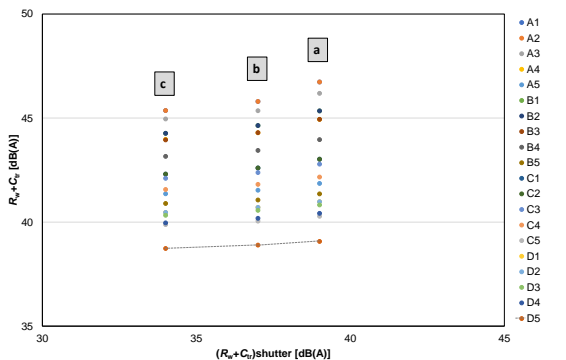


Fig. 20 – Overall $R_w + C_{tr}$ compared to the weighted sound reduction index of the shutter box (a, b and c), $(R_w + C_{tr})_{\text{shutter}}$

Here, it can be seen how, almost linearly, window thermal transmittances increase the overall final performances as expected because of their significant area.

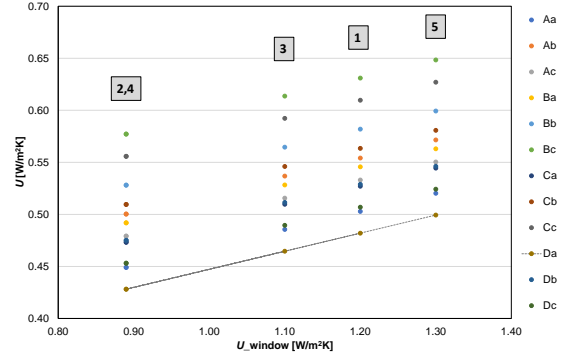


Fig. 21 – Overall U compared to the thermal transmittance of the window, (1, 2, 3, 4 and 5) U_{window}

When moving on to window acoustic parametric influence (Figs. 22-23), it can be highlighted that, when the sound insulation increases, the overall acoustic performance increases too. Again, this is due to window area, which is significant in the façades considered.

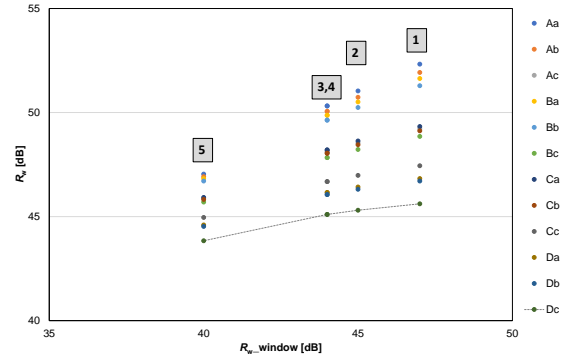


Fig. 22 – Overall R_w compared to the weighted sound reduction index of the window (1, 2, 3, 4 and 5), R_{w_window}

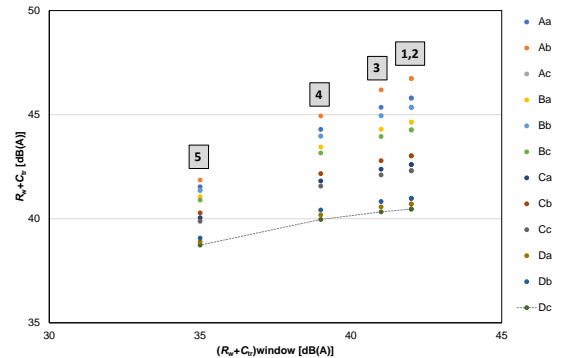


Fig. 23 – Overall $R_w + C_{tr}$ compared to the weighted sound reduction index of the window (1, 2, 3, 4 and 5), $(R_w + C_{tr})_{\text{window}}$

6. Conclusion

In this work, the acoustic and thermal insulation of 60 different combinations of façade elements was studied. 4 walls, 3 shutter systems and 5 windows were considered. It was possible to verify that there is no correlation between the overall final acoustic and thermal performances.

Some further considerations can be made:

- the best solutions from the thermal point of view are not the best ones from the acoustic point of view;
- the best combined thermal and acoustic performances are obtained using thermally insulating blocks (aerated concrete block) with internal lining and use of integrated window systems for roller shutters
- if linear thermal transmittance is not considered, considerable errors can be made ($\Delta U=0.12-0.21$ W/(m²K)).
- it can finally be pointed out how, from a thermal point of view, all three elements equally contribute to the final performance, while, regarding acoustic insulation, the wall and the windows play a more important role due to their more extended area.

Acknowledgement

This work was financed by the European Interreg BIGWOOD project, IT AT 1081 CUP: I54I18000300006.

Alpac S.r.l. and Punto Infissi S.r.l. are gratefully acknowledged for providing the acoustic and thermal data of their products.

References

- CEN (European Committee for Standardization). 2001. *EN 12667:2001 Thermal performance of building materials and products - Determination of thermal resistance by means of guarded hot plate and heat flow meter methods - Products of high and medium thermal resistance*.
- Di Bella, A., N. Granzotto and C. Pavarin. 2014. "Comparative analysis of thermal and acoustic performance of building elements." In: *Proceedings of Forum Acusticum 2014*.
- Di Bella, A., N. Granzotto, H. H. Elarga, G. Semprini, L. Barbaresi and C. Marinosci. 2015. "Balancing of thermal and acoustic insulation performances in building envelope design." In: *Proceedings of Inter-Noise 2015*. doi: <https://dx.doi.org/10.13140/RG.2.1.1435.9122>
- Fabbri, K., L. Tronchin and V. Tarabusi. 2014. "Energy Retrofit and Economic Evaluation Priorities Applied at an Italian Case Study." *Energy Procedia* 45:379-384. doi: <https://doi.org/10.1016/j.egypro.2014.01.041>
- Fabbri, K., L. Tronchin, and F. Barbieri. 2021. "Coconut fibre insulators: The hygrothermal behaviour in the case of green roofs." *Construction and building materials* 266:1-9. doi: 10.1016/j.conbuildmat.2020.121026
- Granzotto, N. 2021. "Optimization of Controlled Mechanical Ventilation Systems for Indoor Acoustic Comfort." *Designs* 5:48. doi: <https://doi.org/10.3390/designs5030048>
- Hua, Z., L. Maxit and L. Cheng. 2021. "Acoustic design and analyses of a double Skin Façade system." *Applied Acoustics* 173. doi: <https://doi.org/10.1016/j.apacoust.2020.107727>
- ISO (International Organization for Standardization). 2021. *ISO 10140-2:2021 Acoustics — Laboratory measurement of sound insulation of building elements — Part 2: Measurement of airborne sound insulation*.
- ISO (International Organization for Standardization). 2020. *ISO 717-1:2020 Acoustics — Rating of sound insulation in buildings and of building elements — Part 1: Airborne sound insulation*.
- ISO (International Organization for Standardization). 2017. *ISO 10077-1:2017 Thermal performance of windows, doors and shutters — Calculation of thermal transmittance — Part 1: General*.
- ISO (International Organization for Standardization). 2017. *ISO 10077-2:2017 Thermal performance of windows, doors and shutters — Calculation of thermal transmittance — Part 2: Numerical method for frames*.
- ISO (International Organization for Standardization). 2017. *ISO 10211:2017 Thermal bridges in building construction — Heat flows and surface temperatures — Detailed calculations*

- Jagniatinskas, A., B. Fiksa and M. Mickaitis. 2021. "Acoustic classification of building façades using statistical methods." *Applied Acoustics* 172. doi: <https://doi.org/10.1016/j.apacoust.2020.107653>
- Ryu, J. and H. Song. 2019. "Effect of building façade on indoor transportation noise annoyance in terms of frequency spectrum and expectation for sound insulation." *Applied Acoustics* 152: 21–30. doi: <https://doi.org/10.1016/j.apacoust.2019.03.020>
- Theodosiou, T., K. Tsikaloudaki, S. Tsoka, and P. Chastas. 2019. "Thermal bridging problems on advanced cladding systems and smart building facades." *Journal of Cleaner Production* 214: 62-69. doi: <https://doi.org/10.1016/j.jclepro.2018.12.286>
- Tronchin, L. 2005. "Modal analysis and intensity of acoustic radiation of the kettledrum." *The Journal Of The Acoustical Society Of America* 117(2):926-933. doi: <https://doi.org/10.1121/1.1828552>
- Tronchin, L., K. Fabbri and C. Bertolli. 2018. "Controlled Mechanical Ventilation in Buildings: A Comparison between Energy Use and Primary Energy among Twenty Different Devices." *Energies* 11:1-20. doi: <https://doi.org/10.3390/en11082123>
- Tronchin, L. 2021. "Variability of room acoustic parameters with thermo-hygrometric conditions." *Applied Acoustics* 177:1-14. doi: <https://doi.org/10.1016/j.apacoust.2021.107933>

Climate Change Impact on Historical Buildings: A Case Study Within the Interreg Ita-Slo Secap Project

Marco Manzan – University of Trieste, Italy – manzan@units.it

Amedeo Pezzi – University of Trieste, Italy – amedeopezzi@hotmail.com

Abstract

Climate change effects on human activities have become more and more evident in the last few decades and human society is looking for new solutions to deal with such consequences. One of the measures that can be developed to tackle this problem is the development of the Sustainable Energy and Climate Action Plans (SECAPs), aiming at reducing the mutual impact between human activities and climate at municipal level. To develop such policies, an extensive study of the building stock, of its current and future performances, and its possible improvements is fundamental. Therefore, an energy analysis for a historical building used as a museum and situated in Trieste, a location included in the Interreg ITA-SLO Secap Project, is carried on in this work. The building represents a challenging task due to its historical nature and architectural features. The current climate for Trieste was represented through a Test Reference Year that was then projected into the future using different climate models. The building was numerically modeled, highlighting its main structural and plant features and usage patterns. Future projections for the climate of Trieste showed a general increase in temperatures for all the studied models, leading to a forecasted decrease in heating gas consumption and an increase in electricity-cooling usage of the base building. Regarding the refurbishment interventions applicable in accordance with the preservation regulations, the results show an obtainable reduction of both gas and electricity consumption for every climatic condition considered. However, the interventions proved not to be economically feasible, showing a too-long simple economic return on the investment.

1. Introduction

In recent years climate change has proved to be an extremely influential parameter for consideration in the development of human society. Nowadays the scientific community has recognized the impact

of anthropogenic activities on global warming and climate in general (Cook et al., 2016). This is a mutual influence, since climate evolution is also affecting several sectors of human assets. In literature, many authors focused their studies on global warming effects on the building sector, showing that climate change has significant impacts on the energy consumption of buildings (Cui et al., 2017; Radhi, 2009; Wan et al., 2012). In fact, even if sometimes the projections show a reduced/minor impact of climate change in the short term for many aspects, significant variations are forecasted for long-term scenarios and should be considered within the design procedures. Generally, depending on climate type, a decrease in heating energy consumption and an increase in cooling energy consumption is forecast (Crawley, 2008).

Considering that, worldwide, the building sector accounts for a great part of total energy usage and of Greenhouse Gas emissions, it has become crucial for both mitigation and adaptation purposes to study and to reduce as much as possible the mutual interaction between this sector and climate evolution (Jentsch et al., 2008; Robert et al., 2012).

Many measures have been defined to tackle climate change on different scales, from global to local ones. About the former, the most well-known initiative is the Paris Agreement on Climate, aiming to limit global warming compared to the pre-industrial age to under 2 °C and pursuing efforts to limit it to 1.5 °C. It also aims to improve the capacity of countries and local governments to deal with the inevitable effects of climate change and support them in their efforts (Paris Agreement, 2015). Regarding local measures, one of the main ones is the evolution of the Sustainable Energy Action Plans, i.e., SEAPs, into Sustainable Energy and Climate Action Plans, i.e., SECAPs. These policies are draft-

ed at municipal level with the aim of reducing the impact of cities on the climate, and adapting them to the inevitable changes likely to happen in the future.

Because the municipalities are usually lacking the knowledge to develop these plans fully, different projects have been set up to support this process. One of these is the Interreg ITA-SLO Secap Project, aiming to stimulate the sustainable development of human activities within the cross-border territory composed of the metropolitan city of Venice, the Friuli Venezia Giulia region and the western part of Slovenia (Interreg, 2018).

The main aim of the project is to provide reliable bases and experiences that could help cities, both directly and indirectly, to reduce their environmental impact and develop suitable adaptation strategies to climate change. One of the main measures to achieve this objective is to reduce energy use in public and private buildings. In fact, in the European Union the building sector accounts for 26-28 % of the total energy usage (Borožan, 2018; Eurostat, 2020), and 19 % of Greenhouse Gas emissions (Eurostat, 2015). In Italy, this feature is even more relevant because of this sector accounting for about 31% of the total national energy consumption (Directorate-General for Energy, 2021). Regarding this, the municipalities developing their SECAPs normally focus their efforts on the building stock of their own property, accounting for a remarkable 46 % of the total of implemented policies (Palermo et al., 2020). In fact, this is the sector where they can intervene through a more systematic approach, having a full knowledge and control of their own buildings and equipment. Therefore, they can directly implement measures and monitor the results accurately.

Because of this situation, one of the main outputs developed in the Interreg ITA-SLO Secap Project and presented in this paper is the energy analysis of a building, representing a case study that municipalities could exploit when developing their SECAPs. The case study includes a dynamic energy simulation of the building-plant system, of its functioning in present and future climatic situations and the evaluation of the effects of its possible refurbishment improvements.

The building analysed for the case study is the Re-

voltella Museum of Trieste, a location included in the program area of the Project, and managed by the municipality itself. The choice fell on this building for several reasons. First, it is a historical building preserved by the regulations of the fine arts, a very common situation in Italy, where particular attention is required when dealing with refurbishment interventions (De Santoli, 2015). Because of this, the design solutions are limited and therefore it is of interest to highlight the effects of these restrictions on the analysis output. Moreover, the museum is a place of public utility, a category for which the government is allocating funds to improve energy efficiency. Finally, yet importantly, the municipality of Trieste openly stated a willingness to intervene in this particular building to improve its energy performance, therefore this will not be only a theoretical case study, but it will be effectively carried out.

2. Climate Change Modeling

The source data to represent the current climatic situation were detected between 1995 and 2019 by a meteorological station located less than 1 km away from the building analysed. Raw data were treated to assess their quality, fill the gaps and reject the periods having too-low data quality.

The actual climate for Trieste was represented through a Test Reference Year generated using the Finkelstein-Schfer statistic (Finkelstein et al., 1971). Climate change was modeled through five different Global-Regional circulation model couplings, assessed to be the most reliable for climate projections in the Friuli Venezia Giulia region, where Trieste is located, by the Regional Agency for Environment Protection, ARPA FVG:

- HadGEM2-ES RACMO22E;
- MPI-ESM-LR REMO2009;
- EC-EARTH CCLM4-8-17;
- EC-EARTH RACMO22E;
- EC-EARTH RCA4.

Before using them, the five models were calibrated through the quantile mapping method (Cannon et al., 2015) to better fit their outputs to the historical data detected for Trieste for a period common to both historical recordings and model outputs. This

allowed more reliable results for the future climate projections to be obtained. The corrected models were then applied to the RCP8.5 scenario, representing a situation where no relevant climate mitigation measures are implemented, therefore similar to the current global situation. The future timeframes considered in the analysis are 2021-2035 and 2036-2050 to represent climate evolution in the near future. Then, the mathematical morphing procedure (Belcher et al., 2005) was used to project the current TRY into the future considering these two periods.

Fig. 1 displays the Heating (a) and Cooling (b) Degree Days for Trieste for current and projected situations. It can be immediately noted that for all the climatic models considered an increase in temperature is forecast as it can be assessed by the decrease of the HDDs and the increase of CDDs. Moreover, it can be noted that climate warming will happen in both the timeframes considered, though with different magnitudes.

Among the projected situations, the one deriving from the HadGEM2-ES RACMO22E model proved to be the warmest one. This being the configuration that most differs from the actual climate, it was used as the future boundary condition for the building-plant analysis.

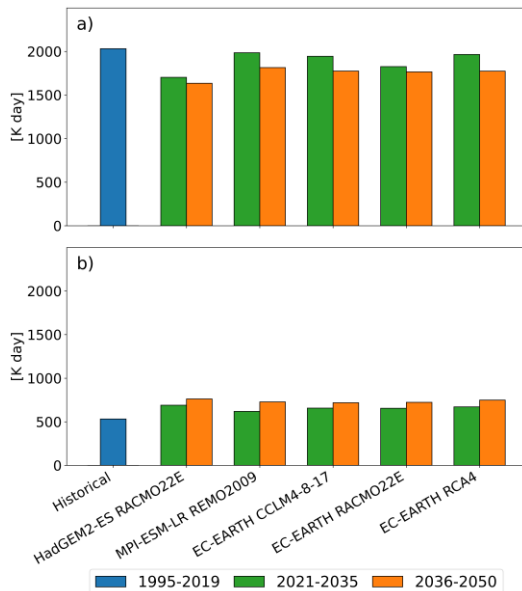


Fig. 1 - Heating (a) and Cooling (b) Degree Days of the historical and projected TRYs for Trieste

3. State-Of-The-Art Modeling

The geometry of the building was modeled using DesignBuilder software, the graphic interface of EnergyPlus calculation engine.

Fig. 2 shows the building within its urban context (a), and its model (b); the presence of the surrounding buildings inserted as elements of solar obstruction for a more accurate analysis can be appreciated in the model.

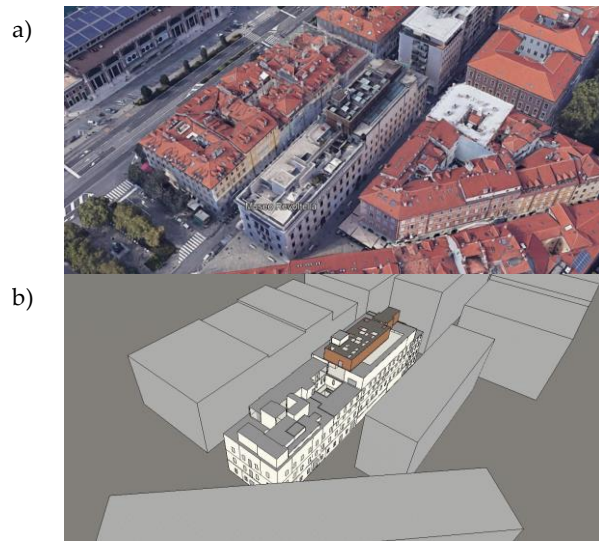


Fig. 2 – Revoltella Museum view (a) and numerical model (b)

To reduce the computational burden, the model was simplified by removing some internal partitions and unifying spaces sharing the same characteristics. Partitions were still considered as internal masses to correctly model the thermal inertia of the system. Fig. 3 presents as an example the spaces modeling for the second-last floor, with the internal masses added to ensure the correct thermal capacity of the building visible in blue.

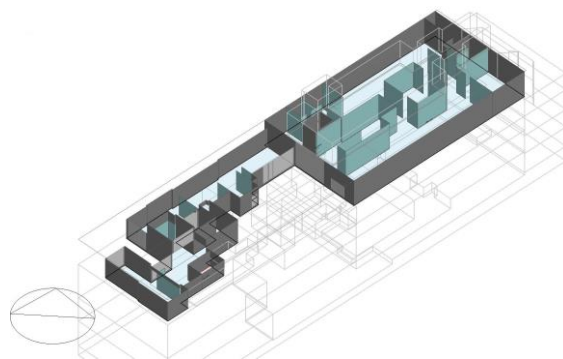


Fig. 3 – Internal spaces modeling for the second-last floor

In total, a building volume of 26,307 m³ was modeled. Envelope element stratigraphy was obtained through site inspections and data gathered from the municipality of Trieste. Table 1 reports the transmittance values for all opaque elements of the building.

Table 1 – Transmittance values of envelope opaque elements

Element	U [W/(m ² K)]
External walls	0.72
Earth retaining walls	1.20
Ground floor	0.41
Internal floor	1.94
Roof	1.77

Double-glazed windows with air-filled gap and wooden frame having transmittances of 3.21 W/(m² K) are present. The building also presents skylights having a transmittance of 5.59 W/(m² K).

Regarding the characteristics of the internal spaces and their use patterns, three main zones were identified for the typical floors and are reported in Fig. 4. Zone A is the historical residence museum and is architecturally preserved both internally and externally. Zone B hosts a modern art museum while zone C is intended for office use, and both are subject to preservation rules regarding only the façades.

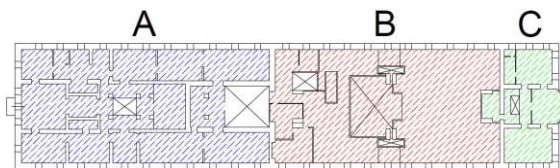


Fig. 4 – Building main zones: A (blue) – historical residence museum, B (red) – modern art museum, C (green) - offices

Because of this situation, internal gains due to illumination, people density and activity, as well as the features of the plant, vary between these three zones. Table 2 reports the principal features for every zone.

Table 2 – Building internal zones features and plant terminals

Parameter \ Zone	A	B	C
People density [people/m ²]	0.143	0.143	0.070
Lighting norm. power dens. [W/(m ² – 100 lx)]	6	6	4
Illuminance [lx]	200	200	300
Plant terminals [/]	Fan-coils	Fan-coils + CAV units	Radiators + VRF units

People density during the day was modified through a schedule following the typical occupation pattern detected during the opening time of the museum, 9 a.m. – 7 p.m., Tuesday excluded. People density in the office area was instead considered constant during the opening time, as well as lighting for all zones. People metabolic rates were fixed at 140 and 120 W/person for museum and office spaces respectively.

Regarding the plant, various terminals are used in this building, as can be deduced from Table 2; this is due to the different uses and working conditions of the building zones. In particular, only fan-coils are present in Zone A because of the preservation regulations limiting the possibilities in the historical internal spaces. Plant temperature set-points are 20 °C for heating and 25 °C for cooling respectively; humidity control is not present. Heating is available from October 15 to April 15, following the calendar of the Italian Climatic Zone E; cooling is always available. The former is working 14 hours per day, the maximum allowed from 7 a.m. to 9 p.m.; the latter is working during the opening time of the museum. Both are deactivated on Tuesday, the closing day of the museum. As it can also be noted by Table 2, the plant serving the building presents a complex configuration depending on the three main areas. The generators of zones A and B are gas-fired condensing boilers and a water chiller for heating and cooling purposes respectively. These generators serve both the fan-coils and the Air Handling Unit (AHU) for the functioning of the CAV system. Zone C generation is given by a dedicated gas-fired condensing boiler coupled with

VRF units for heating and cooling respectively. Finally, an evaporative cooling tower is present on the roof working with the chiller for summer season cooling.

In the analysis, the existing system was modeled as precisely as possible to determine the energy vectors involved in the most coherent way possible, also by exploiting the technical data sheets available for the boilers and the chiller. In addition to the synthetic data, the chiller performance was properly modeled as a function of the condenser and evaporator water temperatures. Through this, and to take the operation of the system in the different conditions into account, the correction curves for the nominal power and for the Energy Efficiency Ratio (EER) were obtained (UNI, 2018). In the same way, the efficiency and the nominal power of the gas-fired condensing boilers were parameterized according to the load and to the returning water temperature. Regarding the AHU, the cooling tower and the VRF units, their characteristics were hypothesized on the bases of the expected behavior of the whole plant and of historical consumption data. The whole audit process was carried out following what is reported in UNI CEI EN 16247-2 standard (UNI, 2014).

3.1 Model Calibration

To obtain reliable results, the state-of-the-art model has been calibrated through a comparison between its results and the historical recordings of gas and electricity consumption. Historical gas consumption data were available as an average for the years 2010-2012 and on a yearly basis for 2019 and 2020. The latter was characterized by the effects of the COVID-19 pandemic and therefore is not representative of the normal behaviour of the building. Year 2019 instead was not usable for the calibration due to the scarcity of climatic data detected by the meteorological station of Trieste, not allowing the execution of a yearly calibration simulation. Therefore, the mean gas consumption value for years 2010-2012 was used for the calibration. Regarding electricity, monthly consumption values for the years 2017-2020 were available. Year 2018 was chosen to calibrate the model because of the local meteorological station having good data quality for

that period. To perform the calibration, a special climatic file containing the 2010-2012 values for the winter season and 2018 values for the summer one was created. The calibration process led to some modifications regarding the envelope elements' transmittance, the internal gains due to people and lighting and the characteristics of the hypothesized elements of the plant. Because of these adjustments, the calibrated model achieved remarkable precision in reproducing the historical consumption recordings, as can be noted through Table 3. The calibrated model was the base to run the energy simulation with the different climatic conditions defined in Section 2 and to assess the effects of the refurbishment interventions described in the next section.

Table 3 – Model calibration results

Energy vectors consumption	Historical	Model	Model Error [%]
Gas [m ³]	56 056	52 458	-6.86
Electricity [kWh]	313 020	319 371	+2.03

4. Refurbishment Interventions

Given the preservation restrictions described in Section 3, the room for improvements to increase the energy performance of the building is very narrow. All the façades, windowed elements included, cannot be modified, and therefore it is not possible to massively intervene on the envelope. Moreover, zone A of the building is also internally protected, limiting the possibilities even further. Regarding the plant, most of its components are still pretty new, therefore solutions concerning this are not considered in this work. Because of this situation, three improvements were hypothesized for the analysed building:

- **A:** Internal insulation of walls pertaining to the modern art museum;
- **B:** Substitution of the existing skylights with new ones featuring solar control window panes;
- **C:** A combination of the previous two.

The internal insulation of the modern art museum

walls was carried out through the insertion of 10 cm of rock wool having a conductivity of 0.038 W/(m K), a density of 35 kg/m³ and specific heat of 840 J/(kg K), coupled with 2cm of plaster.

The skylights used in the second solution were composed of a PVC frame, of an external coated glass layer, 6 mm thick, having a reduced solar transmission value, 0.3622, a 16mm thick Argon-filled cavity and a standard clear glass layer 4 mm thick. This structure presented a transmittance of 1.554 W/(m² K) and the coated external layer aim was to reduce the solar heat gains during the summer season, therefore trying to reduce electricity consumption for cooling.

All three solutions were evaluated regarding their energy and economic aspects. The latter was considered in a simplified way by computing the simple return of the economic investment. Intervention costs were computed using the prices reported in the public regional administration price list “Prezzario Regionale dei Lavori Pubblici” (FVG Region, 2021). By using the reported prices of rock wool per square meter comprehensive of materials and manpower costs, applied to the surface to insulate, a cost of 409,264 € was computed for solution A. The same was done for skylight substitution, in this case considering the price per element and the number of elements to install, and a cost of 67,783 € was computed for solution B. The third solution cost is simply given by summing up the previous two, equal to 477,047 €.

5. Analysis Results

The energy dynamic analysis was first carried out for the state-of-the-art building using the current and the two future TRYs. The results, reported in Table 4, highlight a remarkable reduction of heating gas consumption, and an increase in electricity used for cooling and lighting. The variations compared to the current situation proved to be much more marked in the period 2021-2035 and then to slow down in 2036-2050.

This behavior is in line with the climatic projections, which foresee a slowdown of temperature rise in the second period, as can also

Table 4 – State-of-the-art simulation results

TRY	Gas use [m ³]	Electr. use [kWh]	Var. Gas [%]	Var. Electr. [%]
1995-2019	52,931	289,193	\	\
2021-2035	43,961	318,398	-16.95	+10.10
2036-2050	42,654	325,025	-19.42	+12.39

be noted by looking at the Degree Days reported in Fig. 1. It is then evident that the cooling component will become more influential in the energy consumption composition of this building.

Regarding the effects of the refurbishment interventions, reported in Table 5, the analysis highlighted a beneficial effect on both gas and electricity consumption.

Table 5 – Refurbishment effects for every climatic set

ID	Gas use [m ³]	Electr. use [kWh]	Var. Gas [%]	Var. Electr. [%]	Simple Return [years]
1995-2019 TRY					
SOTA	52,931	305,032	\	\	\
A	44,794	304,034	-15.37	-0.33	41
B	50,454	298,267	-4.68	-2.22	17
C	41,699	294,746	-21.22	-3.37	32
2021-2035 TRY					
SOTA	43,961	318,398	\	\	\
A	36,875	317,161	-16.12	-0.39	47
B	41,840	311,235	-4.82	-2.25	19
C	34,395	307,362	-21.76	-3.47	36
2036-2050 TRY					
SOTA	42,654	325,025	\	\	\
A	35,768	323,689	-16.14	-0.41	48
B	40,618	317,525	-4.77	-2.31	19
C	33,345	313,582	-21.82	-3.52	37

As can be seen in Table 5, the obtainable gas consumption reduction varies between 4 and 21 % compared with the state-of-the-art for every climatic set considered. The obtainable electricity consumption reduction is instead much smaller, between 0.3 and 3.5 %, mainly due to the reduced surface treated with the insertion of the new skylights. In general, the best reduction in energy consumption comes from solution C.

However, the economic analysis of these interventions highlighted that they are not economically convenient, showing too-long return times on investment, for every climatic set.

Therefore, coupling these actions with interventions on the plant should be considered. Considering that the generators were replaced a few years ago, and are therefore still functioning well, major interventions could rather focus on the distribution and emission parts of the plant, these being older and less efficient.

6. Conclusions

An energy audit was carried out for the Revoltella museum of Trieste. Great attention was placed on information gathering, this being a historical building featuring particular characteristics.

An evaluation of climate change effects has been carried out for the state-of-the-art building. The present climate was represented through a TRY that was then projected into the future by using different climate models applied to the RCP8.5 scenario. The results showed a steady increase in temperature for the near future, to year 2050, for every climatic model considered. By using the model giving the greatest rise in temperature, climate change effects were evaluated for the museum. Results showed that climate evolution will greatly influence the energy consumption of this building, leading to a decrease in gas consumption, up to 19 %, and an increase in electricity consumption, up to 12 %. Therefore, the municipality of Trieste, owner of the building, should start considering interventions on the building to adapt it to the incoming new working conditions.

In order to provide the municipality with a starting base for this purpose, some refurbishment inter-

ventions were modeled for the building for both the current and future climates. By considering the preservation restrictions to which the building is subject, internal insulation of walls and substitution of skylights were considered as feasible interventions. The analysis results showed that a good gas consumption decrease, between 4 and 21 %, would be obtainable for every climatic condition considered. Regarding electricity on the other hand, the beneficial effects would be much less evident, featuring a reduction of between 0.3 and 3.5 % of consumption. This minor effect on electricity is due to the possibility of intervening only on the skylights to reduce solar heat gains during the summer season, the windows on the façades not being replaceable due to the preservation rules. Regarding the economic aspect of the interventions, these did not prove to be economical, showing a too-long return time on investment for every climatic set considered.

Considering all the aspects that emerged from this work, it is strongly recommended for the municipality of Trieste to start designing adaptation measures to address the incoming changes in climate conditions. Results in fact highlighted that in the immediate future the focus of the building performance should be shifted gradually from heating to cooling functioning. That said, internal envelope insulation and skylight substitution proved to be good solutions for heating consumption reduction, but not so much for the cooling solution for every climatic set considered in this work. Therefore, these interventions should be coupled with others mainly pertaining to the plant, mainly focusing on distribution and emission components, given the relative novelty of the generators.

Acknowledgement

The authors wish to thank the municipality of Trieste for providing the valuable information used in this study and for giving access to the building analysed to carry out on-site inspections.

References

- Belcher, S., J. Hacker, and D. Powell. 2005. "Constructing design weather data for future climates". *Building Services Engineering Research and Technology* 26: 49-61. doi: <https://doi.org/10.1191/0143624405bt112oa>
- Borozan, D. 2018. "Decomposing the changes in European final energy consumption". *Energy Strategy Reviews* 22: 26-36. doi: <https://doi.org/10.1016/j.esr.2018.08.002>
- Cannon, A. J., S. R. Sobie, T. Q. Murdock. 2015. "Bias Correction of GCM Precipitation by Quantile Mapping: How Well Do Methods Preserve Changes in Quantiles and Extremes?". *Journal of Climate* 28: 6938-6959. doi: <https://doi.org/10.1175/JCLI-D-14-00754.1>
- Cook, J., N. Oreskes, P. T. Doran, W. R. L. Anderegg, B. Verheggen, E. W. Maibach, J. Stuart Carlton, et al. 2016. "Consensus on consensus: A synthesis of consensus estimates on human-caused global warming". *Environmental Research Letters* 11. doi: <http://dx.doi.org/10.1088/1748-9326/11/4/048002>
- Crawley, D. B. 2008. "Estimating the impacts of climate change and urbanization on building performance". *Journal of Building Performance Simulation* 1: 91-115. doi: <https://doi.org/10.1080/19401490802182079>
- Cui, Y., D. Yan, T. Hong, C. Xiao, X. Luo, and Q. Zhang. 2017. "Comparison of typical year and multiyear building simulations using a 55-year actual weather data set from China". *Applied Energy* 195: 890-904. doi: <https://doi.org/10.1016/j.apenergy.2017.03.113>
- De Santoli, L. 2015. "Guidelines on energy efficiency of cultural heritage". *Energy and Buildings* 86: 534-540. doi: <https://doi.org/10.1016/j.enbuild.2014.10.050>
- Directorate-General for Energy. 2021. *EU energy in figures - Statistical pocketbook 2021*. doi: <https://doi.org/10.2833/975418>
- Eurostat. 2020. *Energy data - 2020 edition*. <https://doi.org/10.2785/68334>
- Eurostat. 2015. *Eurostat Manual for air emission accounts - 2015 edition*. doi: <https://doi.org/10.2785/527552>
- Finkelstein, J.M., and R.E. Schafer. 1971. "Improved goodness of fit tests". *Biometrika* 58: 641-645. doi: <https://doi.org/10.1093/biomet/58.3.641>
- Friuli-Venezia Giulia Region. 2021. "Prezzario Regionale dei Lavori Pubblici", 2021. <https://www.regione.fvg.it/rafvfg/cms/RAFVG/infrastrutture-lavori-pubblici/lavori-pubblici/FOGLIA7/>
- Interreg ITA-SLO Secap Project 2018. Accessed March 20, 2022. <https://www.ita-slo.eu/en/secap>
- Jentsch, M. F., A. S. Bahaj, and P. A.B. James. 2008. "Climate change future proofing of buildings - Generation and assessment of building simulation weather files". *Energy and Buildings* 40: 2148-2168. doi: <https://doi.org/10.1016/j.enbuild.2008.06.005>
- Palermo, V., P. Bertoldi, M. Apostolou, A. Kona, and S. Rivas. 2020. "Assessment of climate change mitigation policies in 315 cities in the Covenant of Mayors initiative". *Sustainable Cities and Society* 60. doi: <https://doi.org/10.1016/j.scs.2020.102258>
- Paris Agreement 2015. Accessed March 17 2022. https://ec.europa.eu/clima/policies/international/negotiations/paris_en
- Radhi, H. 2009. "Evaluating the potential impact of global warming on the UAE residential buildings - A contribution to reduce the CO₂ emissions". *Building and Environment* 44: 2451-2462. doi: <https://doi.org/10.1016/j.buildenv.2009.04.006>
- Robert, A., and M. Kummert. 2012. "Designing net-zero energy buildings for the future climate, not for the past". *Building and Environment* 55: 150-158. doi: <https://doi.org/10.1016/j.buildenv.2011.12.014>
- UNI. 2014. *EN 16247-2: Energy audits - Part 2: Buildings*.
- UNI. 2018. *EN 14825: Air conditioners, liquid chilling packages and heat pumps, with electrically driven compressors, for space heating and cooling - Testing and rating at part load conditions and calculation of seasonal performance*.
- Wan, K. K.W., D. H.W. Li, W. Pan, and J. C. Lam. 2012. "Impact of climate change on building energy use in different climate zones and mitigation and adaptation implications". *Applied Energy* 97: 274-282. doi: <https://doi.org/10.1016/j.apenergy.2011.11.048>

Hourly Dynamic Calculation of the Primary Energy With Heat Pump Generation System (EN 15316-4-2): A Case Study in Italy

Giada Remia – Università Politecnica delle Marche, Italy – g.remia@pm.univpm.it

Serena Summa – Università Politecnica delle Marche, Italy – s.summa@univpm.it

Luca Tarabelli – Università Politecnica delle Marche, Italy – l.tarabelli@univpm.it

Costanzo Di Perna – Università Politecnica delle Marche, Italy – c.diperna@univpm.it

Abstract

With the aim of reducing greenhouse gas emissions, more and more heat pump generators are being used in the residential space heating sector to replace traditional condensing gas boilers. This paper discusses the application to an Italian case study of the new draft of EN 15316-4-2, which provides a methodology for the calculation of the energy performance of heat pump systems used for domestic hot water preparation or space heating purpose. The case study involves a two-storey residential building equipped with several modulating air-to-water heat pumps.

Two different daily profiles for heating were considered: continuous heating mode (heating system on 24 hours a day) and intermittent heating mode. Hourly building energy need for heating, calculated according to EN ISO 52016-1:2017, were used as input.

The seasonal coefficient of performance (SCOP) of heat pumps analysed with an intermittent profile are 45.77 % higher on average than those in continuous heating mode, even if, in the intermittent system configuration, there is always an amount of missing energy.

Finally, the results show that oversizing the heat pump leads to low SCOP and high non-renewable primary energy; while undersizing the heat pump leads to high SCOP but non-negligible missing energy values.

1. Introduction

The need to reduce greenhouse gas (GHG) emissions related to building energy production has led Europe to implement policies to reduce energy demand while promoting the use of renewable energy sources to replace fossil fuels.

Residential space heating is one of the sectors most

responsible for producing greenhouse gas; one of the most feasible solutions to decarbonise this sector is to electrify consumption by using heat pumps to replace gas boilers. (Famiglietti et al., 2021; Lin et al., 2021).

In the regulatory field, the European Committee for Standardisation (CEN) has approved a set of standards for the implementation of the EPBD (Energy Performance Building Directive) (European Parliament, 2018). These interconnected standards define calculation methodologies for the energy consumption and performance of buildings.

In this package of standards are EN ISO 52016-1:2017 (European Committee for Standardization, 2017) and the new draft of EN 15316-4-2 (European Committee for Standardization, 2018).

Specifically, EN ISO 52016-1 (European Committee for Standardization, 2017) introduces an hourly methodology for calculating the energy need for heating and cooling, while EN 15316-4 deals with the calculation of system energy requirements and system efficiencies according to the different types of generation system.

In the literature, different studies show how the use of the dynamic hourly method defined in UNI EN ISO 52016-1 (European Committee for Standardization, 2017) allows a more accurate assessment of energy needs than a semi-stationary model (Di Giuseppe et al., 2019; van Dijk, 2018) and how the hourly energy needs for heating calculated with the aforementioned standard is comparable with that obtained with TRNSYS (Summa et al., 2022; Zakula et al., 2021).

Regarding the application of the new draft of EN 15316-4-2, there are some studies concerning boilers (Mattarelli & Piva, 2014) and solar thermal

panels (Teodorescu & Vartires, 2016), but not heat pump systems.

To this purpose, this work aims to apply the calculation algorithm provided by the new draft of EN 15316-4-2 (European Committee for Standardization, 2018), concerning heat pump generation systems, on an Italian case study, using as input the hourly energy need for heating, calculated according to EN ISO 52016-1 (European Committee for Standardization, 2017).

2. Methods

2.1 EN ISO 52016-1:2017

The calculation algorithm of EN ISO 52016-1:2017 (European Committee for Standardization, 2017) provides the values of the following hourly parameters: indoor air temperature, mean radiant temperature, operative temperature, surface temperature of building elements and the energy needs for heating and cooling.

These parameters are determined for each thermal zone by providing input of climatic data defined on an hourly basis.

To determine the surface temperatures of the building elements and, consequently, all other parameters, the calculation algorithm provides the procedure for spatial discretization of the capacitive nodes and resistive layers of the opaque and transparent elements based on the thermoelectric analogy.

Transparent elements are discretized by two capacitive nodes and one resistive layer, and opaque elements by five capacitive nodes and four resistive layers.

2.2 EN ISO 15316-4-2

The calculation algorithm of the new draft of EN 15316-4-2 (European Committee for Standardization, 2018) provides as output the following hourly parameters: the total electrical energy, the energy from the cold source, the coefficient of performance (COP) of the heat pump, and the energy not supplied by the heat generator.

The algorithm also provides the amount of energy supplied by back-up systems (electrical resistance)

if the heat pump is not able to supply the required energy.

All these parameters are calculated separately for heating and domestic hot water.

The hourly profiles of outdoor temperature, indoor operative temperature, energy needs for heating, and domestic hot water, and the water flow temperature according to the system must be provided as input.

Finally, data concerning the heat pump must be entered, identifying its technology, the source and sink type.

The services the heat pump is used for, the presence of any back-up systems and its power and COP at full load, declared by the manufacturer, must also be specified.

3. Case Study

The case study is a two-storey residential building (Fig.1) with a bathroom, a storage room, a kitchen and a living room on the ground floor and two single rooms, a double room, a bathroom and a hallway on the first floor.

The stairwell and attic are unheated thermal zones. The net floor height is 2.70 m, while the net floor area is 129.64 m². The thermo-physical characteristics of the building elements are shown in Table 1.

Aiming at evaluating different climatic contexts, the case study focuses on three Italian locations: Milan, Rome and Palermo. The input hourly climate data were calculated according to UNI 10349 (Ente Nazionale Italiano di Unificazione, 2016). The analysis was carried out for the winter period in order to evaluate the behavior of the heat pump for the heating season only.

Two daily profiles for heating were considered, both with a set-point temperature of 20 °C: (i) the first ON 24h/24h and (ii) the second intermittent with a number of working hours equal to the maximum allowed by Presidential Decree 412/93 (Presidente della Repubblica, 1993) depending on the climatic zone considered (Tab.2).

As an evaluation of the operation of the only heat pump for heating is intended, the production of domestic hot water, the thermal storage and back-up heater have not been considered. Four modulat-

ing air-to-water heat pumps (AWHP) were analysed, with increasing powers of 2.3 kW, 4.6 kW, 5.8 kW and 8.3 kW, values declared according to UNI EN 14511-1:2018.

The hourly profile of water flow temperature for the heat pump was determined through a climatic curve as a function of the air outside temperature and the design temperature of the location considered. Furthermore, distribution, emission and regulation efficiency were not taken into account as assumptions.

4. Results

Using the hourly energy needs for heating calculated according to EN ISO 52016-1 (European Committee for Standardization, 2017) as input values, the electrical energy, the thermal energy from cold external source (air) and the COP of the heat pump per hour were determined using the new draft of EN 15316-4-2 EN 15316-4-2 (European Committee for Standardization, 2018).

Moreover, the primary renewable and non-renewable energy was calculated based on the energy sources used. The comparison between the different heat pumps was made using the SCOP, which is calculated as the ratio between the supplied energy and the respective electricity consumption during the heating season.

Fig. 2 shows how the SCOP are, on average, 45.77 % higher in the case of intermittent use of heating system than constant use.

Considering the four heat pumps used, switching from a constant to an intermittent profile, the average SCOP increase for Milan, Rome and Palermo is 20.10 %, 48.53 % and 68.67 %, respectively.

Considering the same heat pump and varying the daily heating profiles of the buildings analyzed, qualitatively the same pattern is observed for each location: (i) in the case of constant use, the load factor decreases to values of 0.30 or less, with consequent reduction of COP, which happens during the hours when heating energy need is reduced; (ii) in the intermittent mode, on the other hand, having a higher power demand for the heat pump, the load factor is higher, with a consequent higher COP.

For this reason, in the case of Rome and Palermo, where the number of hours the system is switched on is lower than in Milan, the average SCOP variation between intermittent and continuous use is higher.

Therefore, a more intermittent system implies a higher power demand in the first hours of operation and a limited number of hours with reduced load factors.

These two aspects result in higher seasonal COP in the intermittent regime than in the constant daily profile for heating.

In order to assess the different behavior of heat pumps, it is not sufficient to analyze only the SCOP. For this reason, it is also necessary to evaluate the possible presence of missing energy, i.e., not supplied by the heat pump ($Q_{H,gen,add}$).

This analysis was carried out for all the locations considered. Since the results obtained follow the same trend for each location, the decision to specifically analyze the results obtained for the coldest location, i.e., Milan, was made.

Table 3 shows the missing energy for each heat pump used and for the two daily profiles of the heating system considered. Moreover, the percentage of missing energy in relation to the energy required by the heat pump ($Q_{H,gen,out,req}$) and the percentage of hours when the missing energy is present compared to the heating period are listed.

Table 3 shows how, in the intermittent system configuration, there is always an amount of energy not supplied by the heat pump.

The SCOP are higher in the intermittent mode but, on the other hand, the heat pumps always return a higher missing energy than in the constant profile, where there is no missing energy, except for the smallest heat pump.

Table 3 also provides useful information for determining the correct heat pump size for the building analyzed. Results show how the AWHP 4.6 kW does not result in an amount of missing energy in the case of constant mode, while, for the intermittent profile, the energy not provided is equal to 2.76 % of the energy required for heating.

Moreover, AWHP 5.8 kW has a similar operation to the AWHP 4.6 kW for intermittent operation but would be oversized for constant daily profile use.

Oversizing or undersizing a heat pump has conse-

quences in terms of both primary energy and missing energy. An undersized heat pump (AWHP 2.3 kW) is characterized by a high SCOP (Fig. 2), but also by significant missing energy values (Table 3). An oversized heat pump (e.g., AWHP 8.3 kW) is characterized by a reduced SCOP, which is reflected in a higher primary energy, while not resulting in missing energy. In fact, Fig. 3 shows that the primary energy is higher in the case of the largest generator, i.e., AWHP 8.3 kW. Furthermore, the increase in primary energy leads to an increase of the non-renewable energy.

5. Conclusion

The new draft of EN 15316-4-2 (European Committee for Standardization, 2018), which provides a methodology for calculation of system energy requirements and system efficiencies for heat pump systems, has so far limited application in the literature. For this reason, in this paper the above-mentioned standard was tested by applying it to a residential building located in three different Italian cities and using the hourly energy need, calculated according to EN ISO 52016-1 (European Committee for Standardization, 2017), as input data.

This application shows that

- the use of an intermittent heating profile brings the heat pump to higher COP than a constant continuous heating mode;
- higher intermittency of the system implies a higher power demand in the first hours of operation and a limited number of hours with reduced load factors. These two aspects result in higher SCOP in the intermittent regime than in the constant on regime;
- in contrast, in the intermittent system configuration, an amount of energy not supplied by the heat pump is always present; this leads to an increase in non-renewable primary energy due to the need for an integrated back-up system (e.g., electrical resistance) or a second generator;
- undersizing the heat pump leads to high SCOP but non-negligible missing energy values.
- oversizing the heat pump leads to low SCOP and high non-renewable primary energy.

These results concern the case studies proposed and the methodologies associated with the standards used. The future development of this work will be to extend the calculation by considering an integrated back-up system (electrical resistance) and a storage system in order to assess their possible impact on the results.

Nomenclature

Symbols

COP	Coefficient of performance (-)
SCOP	Seasonal coefficient of performance (-)
M_s	Surface mass (kg/m ²)
U	Thermal transmittance (W/(m ² K))
Y_{IE}	Periodic thermal transmittance (W/(m ² K))
EP	Primary energy (kWh)
AWHP	Air-to-water heat pump

References

- Di Giuseppe, E., G. Ulpiani, S. Summa, L. Tarabelli, C. Di Perna, and M. D'Orazio. 2019. "Hourly dynamic and monthly semi-stationary calculation methods applied to nZEBs: Impacts on energy and comfort." *IOP Conference Series: Materials Science and Engineering* 609: 1–8. doi: <https://doi.org/10.1088/1757-899X/609/7/072008>
- Ente Nazionale Italiano di Unificazione. 2016. *UNI 10349-1:2016 - Riscaldamento e raffrescamento degli edifici - Dati climatici - Parte 1: Medie mensili per la valutazione della prestazione termo-energetica dell'edificio e metodi per ripartire l'irradianza solare nella frazione diretta e diffusa e per calcolare l'irradianza solare su di una superficie inclinata.*
- European Committee for Standardization. 2018. *EN 15316-4-2:2018 - Energy performance of buildings - Method for calculation of system energy requirements and system efficiencies - Part 4-2: Space heating generation systems, heat pump systems, Module M3-8-2, M8-8-2.*
- European Committee for Standardization. 2017. *EN ISO 52016-1:2017 - Energy performance of buildings — Energy needs for heating and cooling, internal temperatures and sensible and latent head*

- loads — Part 1: Calculation procedures Performance.
- European Parliament. 2018. "Directive (EU) 2018/844 of the European Parliament and of the Council of 30 May 2018 amending Directive 2010/31/EU on the energy performance of buildings and Directive 2012/27/EU on energy efficiency." *Official Journal of the European Union*.
- Famiglietti, J., T. Toppi, L. Pistocchini, R. Scoccia, and M. Motta. 2021. "A comparative environmental life cycle assessment between a condensing boiler and a gas driven absorption heat pump." *Science of the Total Environment* 762: 144392. <https://doi.org/10.1016/j.scitotenv.2020.144392>
- Lin, H., J. Clavreul, C. Jeandaux, J. Crawley, and I. Butnar. 2021. "Environmental life cycle assessment of heating systems in the UK: Comparative assessment of hybrid heat pumps vs. condensing gas boilers." *Energy and Buildings* 240: 110865. <https://doi.org/10.1016/j.enbuild.2021.110865>
- Mattarelli, A., and S. Piva. 2014. "EN 15316 Calculation Methods for the Generation Sub-system: The Influence of Input Data on the Results." *Energy Procedia* 45: 473–481. <https://doi.org/10.1016/j.egypro.2014.01.051>
- Presidente della Repubblica. 1993. *DECRETO DEL PRESIDENTE DELLA REPUBBLICA* 26 agosto 1993, n. 412. Italy.
- Summa, S., G. Remia, and C. Di Perna. 2022. "Comparative and Sensitivity Analysis of Numerical Methods for the Discretization of Opaque Structures and Parameters of Glass Components for EN ISO 52016-1." *Energies* 15. <https://doi.org/10.3390/en15031030>
- Teodorescu, D., and A. Vartires. 2016. "A Study of the Influence of Solar Panels Coupled with Thermal Systems for a Residential Building, by Applying Methods of Evaluation as EN 15316-4-3:2014 and TRANSOL." *Energy Procedia* 85: 530–538. <https://doi.org/10.1016/j.egypro.2015.12.240>
- van Dijk, D. 2018. "EPB standards: Why choose hourly calculation procedures?" *REHVA Journal*.
- Zakula, T., N. Badun, N. Ferdelji, and I. Ugrina. 2021. "Framework for the ISO 52016 standard accuracy prediction based on the in-depth sensitivity analysis." *Applied Energy* 298: 117089. <https://doi.org/10.1016/j.apenergy.2021.117089>

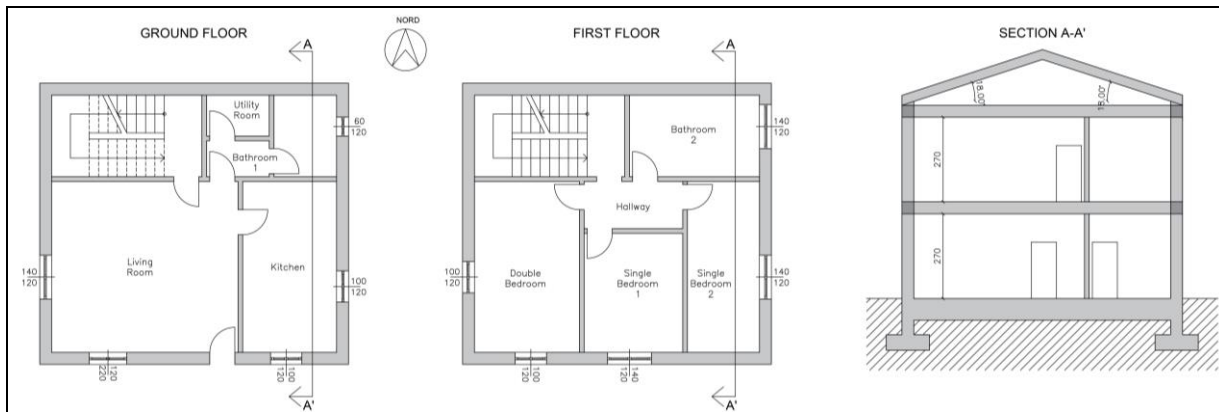


Fig. 1 – Plan view of the ground floor, first floor and section of the case study

Table 1 – Thermo-physical characteristics of the structures

Thermophysical Parameters		Milan	Rome	Palermo
External Wall	U [W/(m ² K)]	0.22	0.24	0.36
	M_s [kg/m ²]	227.80	228.86	274.85
	Y_{IE} [W/(m ² K)]	0.007	0.007	0.018
Ground Floor	U [W/(m ² K)]	0.25	0.27	0.35
	M_s [kg/m ²]	1370.60	1370.30	1369.40
	Y_{IE} [W/(m ² K)]	0.007	0.007	0.010
Sub-roofing Floor	U [W/(m ² K)]	0.24	0.27	0.37
	M_s [kg/m ²]	363.60	363.00	362.10
	Y_{IE} [W/(m ² K)]	0.038	0.028	0.064
Internal Floor	U [W/(m ² K)]	1.13	1.13	1.13
	M_s [kg/m ²]	111.60	111.60	111.60
	Y_{IE} [W/(m ² K)]	0.673	0.673	0.673
Roof	U [W/(m ² K)]	0.70	0.70	0.70
	M_s [kg/m ²]	427.20	427.20	427.20
	Y_{IE} [W/(m ² K)]	0.120	0.120	0.120
Internal Wall	U [W/(m ² K)]	0.35	0.35	0.35
	M_s [kg/m ²]	403.80	403.80	403.80
	Y_{IE} [W/(m ² K)]	0.039	0.039	0.039

Table 2 – Different daily profiles for heating system, according to the three thermal zone considered.

Climatic Zone	Time Intervals	Heating Period
Milan	6:00-12:00/17:00-23:00	15 October - 15 April
Rome	6:00-11:00/18:00-23:00	1 November - 15 April
Palermo	7:00-10:00/19:00-22:00	1 December - 31 March

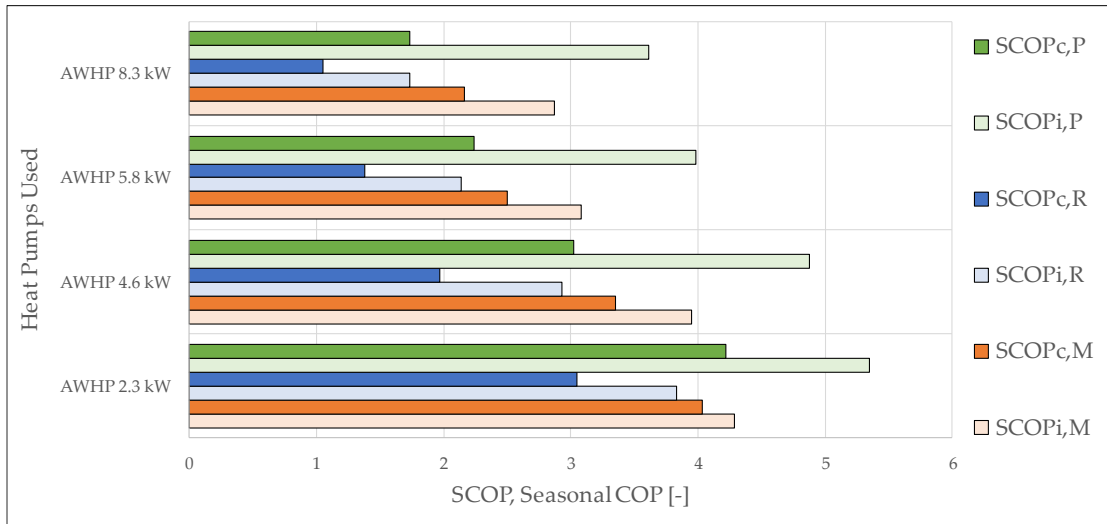


Fig. 2 – Seasonal COP for the three locations, two daily profiles for heating, four heat pumps: c/i:continuous/intermittent heating, P/R/M: Palermo, Rome, Milan

Table 3 – Energy not provided by the heat pump ($Q_{H,gen,add}$); percentage between energy not supplied and energy required for heating ($Q_{H,gen,add} / Q_{H,gen,out,req}$); percentage between the number of hours corresponding to missing energy and the total heating period ($h_{Q_{H,gen,add}} / h_{Q_{H,gen,out,req}}$)

Heat Pump	Milan					
	Intermittent Heating			Continuous Heating		
	$Q_{H,gen,add}$ [kWh]	$Q_{H,gen,add} / Q_{H,gen,out,req}$ [%]	$h_{Q_{H,gen,add}} / h_{Q_{H,gen,out,req}}$ [%]	$Q_{H,gen,add}$ [kWh]	$Q_{H,gen,add} / Q_{H,gen,out,req}$ [%]	$h_{Q_{H,gen,add}} / h_{Q_{H,gen,out,req}}$ [%]
AWHP 2.3 kW	641	18.62 %	30,29 %	18	0.51 %	5.20 %
AWHP 4.6 kW	95	2.76 %	3.72 %	0	0 %	0 %
AWHP 5.8 kW	75	2.17 %	3.19 %	0	0 %	0 %
AWHP 8.3 kW	1	0.04 %	0.33 %	0	0 %	0 %

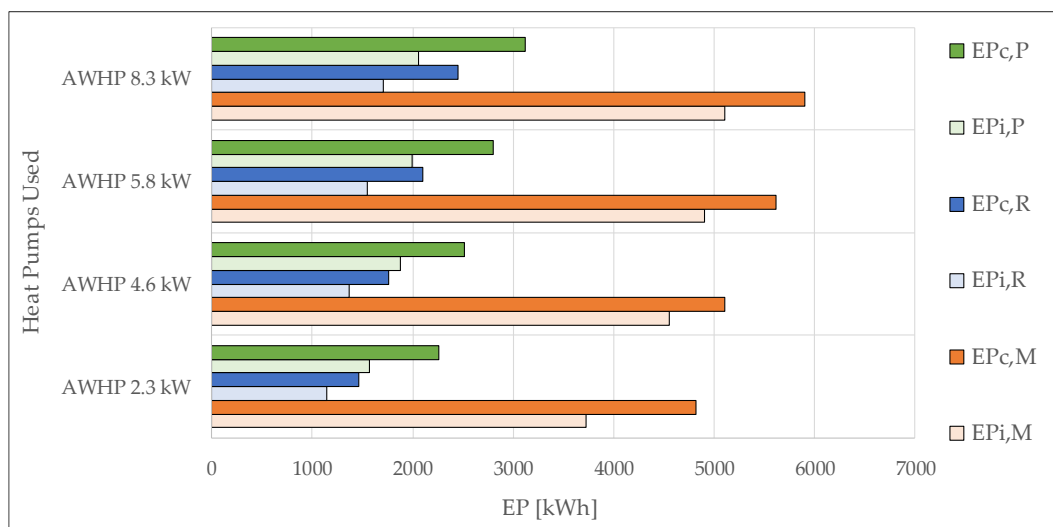


Fig. 3 – Primary energy for the three locations, two daily profiles for heatings, four heat pumps: c/i:continuous/intermittent heating, P/R/M: Palermo, Rome, Milan

A Project Focused on Sound Diffusion: The Acoustics of the Auditorium Yves St Laurent of Marrakech in Combination With its Innovative Architectural Design

Lamberto Tronchin – University of Bologna, Italy – lamberto.tronchin@unibo.it

Antonella Bevilacqua – University of Parma, Italy – antonella.bevilacqua@unipr.it

Ruoran Yan – University of Bologna, Italy – ruoran.yan2@unibo.it

Abstract

Yves St Laurent Auditorium was built at the core of Morocco as part of the museum that honors the French fashion designer. The interior and architectural design of the Auditorium evokes the colors and the materials typical of Marrakech, with bricks and wood being the primary structural resources of construction there. The shoebox envelope was modeled to accommodate ergonomically the select audience attending specific performances oriented towards fashion design. The sound diffusion was realized with the application of quadratic residue diffusers (QRD) installed on all the walls in a vertical configuration. These acoustic panels increase the phenomenon of sound scattering in all directions, making listening very warm and comfortable. This paper deals with the assessment of the main acoustic parameters gathered by the acoustic simulations of a digital model. The simulated values were compared with the optimal values of performing arts spaces of similar room volume.

1. Introduction

Auditoria have often been considered multi-purpose places thanks to their suitability for hosting conferences and musical performances (Bettarello et al., 2021). The challenges that architects and acousticians have to face are varied, going from interior design to materials selection based on geometrical characteristics, as well as for energy building and musical instruments simulation, (Fabbri et al., 2014; Manfren et al., 2021a, 2021b, and 2022; Tronchin et al., 2020) and lighting comfort for all the different events. The YSL Auditorium of Marrakech summarises all the aspects that a

design project finds as opportunities to extract the best architectural product from certain constraints. This paper deals with the acoustic simulations of the Yves St Laurent Auditorium based on different absorption coefficients assigned to different materials of the 3D models. The results of the simulated values were compared based on the main acoustic parameters.

2. Historical Background

Yves St Laurent Auditorium is located in the Saint Laurent Museum in Marrakesh, which was built in memory of the famous French fashion designer, Yves Saint Laurent (Sabbah, 2021; Vorländer, 2007) (www.museeyslmarakech.com/en/auditorium/).

The main purpose of the museum is to encourage cultural projects by displaying Yves Saint Laurent's masterpieces, and to preserve and disseminate his works in France and the rest of the world.

Fondation Pierre Bergé launched the Musée Yves Saint Laurent Paris project in 2017. However, this was not enough to show all the designer's artistic heritage, so they found another place to display Yves Saint Laurent's works.



Fig. 1 – Internal view of the Auditorium YSL of Marrakech

The Auditorium, jointly designed by the consulting experts of theatre projects and Ko architectural office studio (Sabbah, 2021), is located at the center of the museum with the aim of hosting conferences, screen shows, concerts, plays, films and other activities.

3. Architectural Characteristics

Seen from the outside, the entire building is composed of cubical shapes dressed in terracotta bricks as a reminder of the fabric of the local place, as shown in Fig. 1.

The auditorium was designed for a total capacity of 113 seats, with a total volume of 650 m³ and a high degree of flexibility, high acoustic quality and a lighting system capable of fulfilling a variety of activities (Sabbah, 2021). This multi-functionality is visible by the integration of a series of design elements with the technical tools to create a perfect experience for both performers and audience. The streamlined organization inside the auditorium is very logical and highly accessible. The adjustable sound-diffusing panels in the acoustic walls have excellent flexibility (for controlling reverberation time based on several different needs: natural or amplified musical shows, conference hall, or cinema screen (Tronchin, 2005; Tronchin et al., 2021a). Figs. 2 and 3 show the longitudinal section and the internal view of the auditorium, respectively.



Fig. 2 – Longitudinal section of Yves St Laurent Auditorium of Marrakech



Fig. 3 – Internal view of Yves St Laurent Auditorium of Marrakech

The ceiling of the auditorium is equipped with motorized wooden slats to regulate the sense of spaciousness based on the diffusing geometry that they can assume (Tronchin & Bevilacqua, 2022). The lateral walls are characterised by quadratic residue diffusers (QRDs), which contribute to the uniform distribution of the sound across the sitting area (Farina et al., 1998; Tronchin, 2021). The purpose of the diffusing panels is to spread uniformly sound energy in all directions and to reduce energy concentration and/or undesired reflections across the volume (Manfren et al., 2019). In the case of the QRDs, the reflections are spatially dependent and follow a numerical sequence provided by a uniform spatial Fourier transform (Tronchin et al., 2021b). The external envelope is composed of a double skin wall able to provide enough airborne sound insulation to stop intrusive noise (Bettarello et al., 2010).

4. Acoustic Simulation Setup

A digital model was created by using AutoCAD software (Caniato et al., 2020a and 2020b), where the 3D face entities were grouped based on type of material (Tronchin et al., 2020, 2021c; Vorländer, 2007). A view of the digital model is shown in Fig. 4.

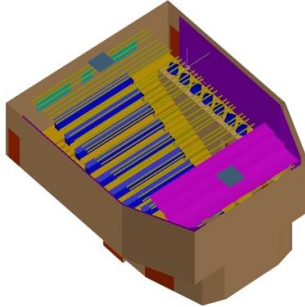


Fig. 4 – Digital model of Yves St Laurent Auditorium of Marrakech

The 3D model was exported in dxf format ready to be employed in the acoustic simulations. An omnidirectional sound source was placed on the stage, while 113 receivers were placed at different heights by homogeneously covering all area of the stalls. The simulation process was undertaken in two different steps: the first by applying the absorption coefficients as per the literature (Caniato et al., 2019; Farina et al., 1998; Tronchin & Bevilacqua, 2021; Tronchin & Farina, 1997), the second by calibrating the absorption coefficient based on experience of similar auditoria of comparable volume size. The difference between the two simulations is in the adjustment of the spectra related to the fabric, lowered by up to 0.6, and to the ceiling panels, lowered by up to 0.4.

5. Simulated Results

The main acoustic parameters were analysed by considering the bandwidth ranging from between 125 Hz and 8 kHz to be considered the average values of all the receivers.

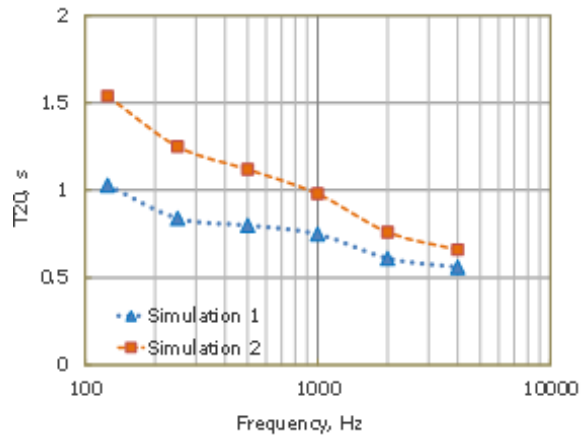


Fig. 5 – Simulated values of T_{20}

Fig. 5 indicates the simulated T_{20} values. The first simulation had absorption coefficients of the fabric close to 0.9, while the second one had absorption coefficients fluctuating around 0.3. Considering that the fabric covers a surface area equal to 58 m², it is considered the main determining factor of the T_{20} difference, highlighted especially at low frequencies (Wang et al., 2004).

Due to the multipurpose function assigned to this auditorium, intended to be suitable for both musical and conference events (Mickaitis et al., 2021; Tronchin & Knight, 2016), the overall T_{20} value of the two simulations was compared to the room volume, as indicated in Fig. 6.

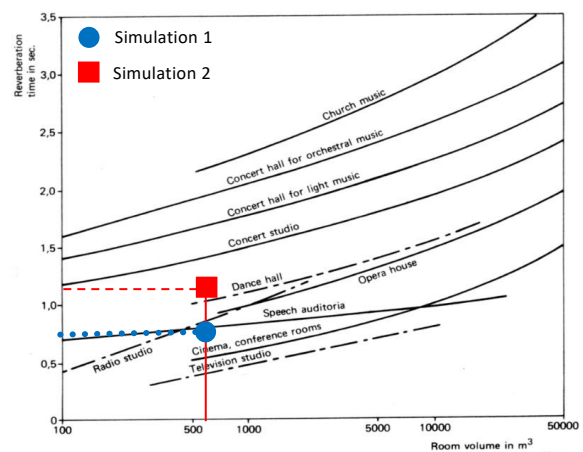


Fig. 6 – Optimal T_{20} values based on room volume

Fig. 6 highlights that the first simulation meet the criteria of a speech auditorium, while the second one turns out to be closer to a musical performance.

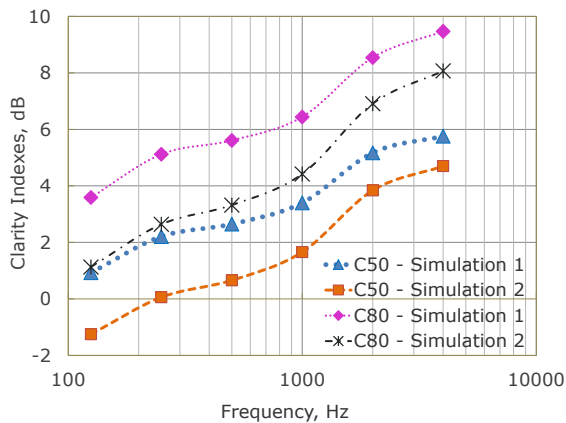


Fig. 7 – Simulated values of Clarity Indexes

Fig. 7 indicates the results of clarity indexes. In relation to speech (C_{50}), the values of the second simulations are within the optimal range ($-2 \text{ dB} < C < +2 \text{ dB}$) (Tronchin et al., 2020) for the octaves ranging from between 125 Hz and 1 kHz, while the higher frequencies are up to 4 dB above the upper range limit. In terms of music, (C_{80}), the results of both simulations were found to be up to 7 dB above the upper range limit across all the spectra.

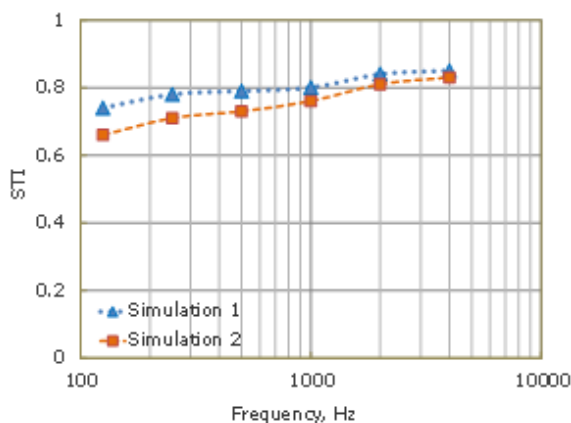


Fig. 8 – Simulated STI values

Fig. 8 shows the results related to speech comprehension. The simulated values of both simulations have been found to be above 0.6 for all octaves. This means that the overall result falls into a “good” category, even “excellent” at mid-high frequencies, as defined by the intelligibility rating according to ISO 9921.

6. Conclusion

This paper deals with two acoustic simulations of the YSL Auditorium of Marrakech. The contained room volume, allocating 113 seats, was designed with motorised wooden slats on the ceiling that can optimize the reverberation time based on the required functionality. The multipurpose hall, intended to be suitable for both speech and musical performances, also involves the design accuracy of the construction elements, like the side walls characterised by the QRD panels.

Two acoustic simulations were carried out by changing mainly the fabrics and the diffuser absorption coefficients. The difference between these is more evident at low frequencies for the T_{20} , while the clarity index for speech and music both proved to be up to 6 dB above the upper range limit, especially at mid-high frequencies. The STI values, found to be more than 0.65 across all the spectra, fall within the excellent category rating. Further research studies will deepen the investigation by comparing the simulated values with the on-site acoustic measurements (Caniato et al., 2021) in order to define the tuning process.

References

- Bettarello, F., P. Fausti, V. Baccan, and M. Caniato. 2010. “Impact Sound Pressure Level Performances of Basic Beam Floor Structures”. *Building Acoustics* 17(3): 305-316. doi: <https://doi.org/10.1260/1351-010X.17.4.305>
- Bettarello, F., M. Caniato, G. Scavuzzo, and A. Gasparella. 2021. “Indoor Acoustic Requirements for Autism-Friendly Spaces”. *Applied Science* 11: 3942. doi: <https://doi.org/10.3390/app11093942>
- Caniato, M., F. Bettarello, C. Schmid, and P. Fausti. 2019. “The use of numerical models on service equipment noise prediction in heavyweight and lightweight timber buildings”. *Building Acoustics* 26(1): 35-55. doi: <https://doi.org/10.1177/1351010X18794523>
- Caniato, M., F. Bettarello, P. Bonfiglio, and A. Gasparella. 2020a. “Extensive Investigation of Multiphysics Approaches in Simulation of

- Complex Periodic Structures". *Applied Acoustics* 166: 107356. doi: <https://doi.org/10.1016/j.apacoust.2020.107356>
- Caniato, M., C. Schmid, and A. Gasparella. 2020b. "A comprehensive analysis of time influence on floating floors: Effects on acoustic performance and occupants' comfort". *Applied Acoustics* 166: 107339. doi: <https://doi.org/10.1016/j.apacoust.2020.107339>
- Caniato, M., F. Bettarello, and A. Gasparella. 2021. "Indoor and outdoor noise changes due to the COVID-19 lockdown and their effects on individuals' expectations and preferences". *Scientific Reports* 11: 16533. doi: <https://doi.org/10.1038/s41598-021-96098-w>
- Fabbri, K., L. Tronchin, and V. Tarabusi. 2014. "Energy Retrofit and Economic Evaluation Priorities Applied at an Italian Case Study". *Energy Procedia* 45: 379-384. doi: <https://doi.org/10.1016/j.egypro.2014.01.041>
- Farina, A., A. Langhoff, and L. Tronchin. 1998. "Acoustic characterisation of "virtual" musical instruments: using MLS technique on ancient violins." *Journal Of New Music Research* 27(4): 359-379. doi: <https://doi.org/10.1080/09298219808570753>
- Manfren, M., B. Nastasi, E. A. Piana, and L. Tronchin. 2019. "On the link between energy performance of building and thermal comfort: An example". *AIP Conference Proceedings* 2123: 1-9. doi: <https://doi.org/10.1063/1.5116993>
- Manfren, M., B. Nastasi, L. Tronchin, D. Groppi, and D. A. Garcia. 2021a. "Techno-economic analysis and energy modelling as a key enablers for smart energy services and technologies in buildings". *Renewable and Sustainable Energy Reviews* 150: 1-14. doi: <https://doi.org/10.1016/j.rser.2021.111490>
- Manfren, M., M. Sibilla, and L. Tronchin. 2021b. "Energy Modelling and Analytics in the Built Environment—A Review of Their Role for Energy Transitions in the Construction Sector". *Energies* 14:1-29. doi: <https://doi.org/10.3390/en14030679>
- Manfren, M., P. A. B. James, and L. Tronchin. 2022. "Data-driven building energy modelling – An analysis of the potential for generalisation through interpretable machine learning". *Renewable and Sustainable Energy Reviews* 167: 1-13. doi: <https://doi.org/10.1016/j.rser.2022.112686>
- Mickaitis, M., A. Jagniatinskas, and B. Fiks. 2021. "Case study of acoustic comfort in conference room". *Proc. 27th International Congress of Sound & Vibration*.
- Sabbah, C. 2021. *Studio KO. Yves Saint Laurent Museum Marrakech*.
- Tronchin, L. 2005. "Modal analysis and intensity of acoustic radiation of the kettledrum." *The Journal Of The Acoustical Society Of America* 117(2): 926-933. doi: <https://doi.org/10.1121/1.1828552>
- Tronchin, L. 2021. "Variability of room acoustic parameters with thermo-hygrometric conditions." *Applied Acoustics* 177: 1-14. doi: <https://doi.org/10.1016/j.apacoust.2021.107933>
- Tronchin, L., and A. Bevilacqua. 2021. "Acoustic study of different sceneries at the São Carlos national theatre of Lisbon." *Applied Acoustics* 180: 1-11. doi: <https://doi.org/10.1016/j.apacoust.2021.108102>
- Tronchin, L., and A. Bevilacqua. 2022. "Historically informed digital reconstruction of the Roman theatre of Verona. Unveiling the acoustics of the original shape." *Applied Acoustics* 185: 1-18. doi: <https://doi.org/10.1016/j.apacoust.2021.108409>
- Tronchin, L., and A. Farina. 1997. "Acoustics of the former Teatro "La Fenice" in Venice." *Journal of the Audio Engineering Society* 45(12): 1051-1062.
- Tronchin, L., and D. J. Knight. 2016. "Revisiting Historic Buildings through the Senses. Visualising Aural and Obscured Aspects of San Vitale, Ravenna." *International Journal of Historical Archaeology* 20: 127-145. doi: <https://doi.org/10.1007/s10761-015-0325-2>
- Tronchin, L., F. Merli, M. Manfren, and B. Nastasi. 2020. "The sound diffusion in Italian Opera Houses: some examples." *Building Acoustics* 27(4): 333-355. doi: <https://doi.org/10.1177/1351010X20929216>
- Tronchin, L., F. Merli, and M. Manfren. 2021a. "On the acoustics of the Teatro 1763 in Bologna." *Applied Acoustics* 172: 1-9. doi: <https://doi.org/10.1016/j.apacoust.2020.107598>
- Tronchin, L., A. Farina, A. Bevilacqua, F. Merli,

- and P. Fiumana. 2021b. "Comparison failure and successful methodologies for diffusion measurements undertaken inside two different testing rooms." *Applied Sciences* 11: 10523. doi: <https://doi.org/10.3390/app112210523>
- Tronchin, L., F. Merli, and M. Dolci. 2021c. "Virtual acoustic reconstruction of the Miners' Theatre in Idrija (Slovenia)." *Applied Acoustics* 172: 1-9. doi: <https://doi.org/10.1016/j.apacoust.2020.107595>
- Vorländer, M. 2007. "Fundamentals of Acoustics, Modelling, Simulation. Algorithms and Acoustic Virtual Reality".
- Wang, L. M., J. Rathsam, and S. R. Ryherd. 2004. "Interactions of model detail level and scattering coefficients in room acoustic computer simulation." *Proc ISRA*. www.museeyslmarrakech.com/en/auditorium/. Accessed March 10, 2022.

On the Prints of Another Horseshoe-Shaped Historical Building: Acoustic Studies of the Bonci Theatre of Cesena

Antonella Bevilacqua – University of Parma, Italy – antonella.bevilacqua@unipr.it

Ruoran Yan – University of Bologna, Italy – ruoran.yan2@unibo.it

Abstract

The Bonci theatre in Cesena was built in 1846, becoming a stable public construction after a period when theatrical shows used to be privately performed inside aristocratic palaces. The architectural design, to be composed of 5 orders of balconies and the shape of the plan layout follow, in reduced dimensions, the Alla Scala theatre in Milan. Acoustic measurements were taken across the stalls and inside some selected boxes according to BS3382-1. The main acoustic parameters gathered by the measured values were compared with the acoustic simulations of a 3D model, which faithfully reproduces the Bonci theatre. The scope of this paper is the analysis of the acoustic behavior of the Bonci theatre, which can be used to calibrate a digital model before the executions of any acoustic simulations. This practice is fundamental for the accuracy of the results, which shall be carried out by comparing the measured with the calibrated values. A review of the historical background has been introduced to allow an appreciation of the architectural value of this cultural heritage.

1. Introduction

The acoustic discoveries of cultural heritage buildings have always been appreciated by the amateurs that experience these places on a regular basis. Additionally, this enriches the knowledge of experts and scholars focused on existing architectural patrimony of important value (Bettarello et al., 2021; Dordevic, 2016; Vecco, 2010). On this basis, this paper deals with the acoustic characteristics of Bonci theatre of Cesena, measured in line with the standard requirements outlined by ISO 3382 (Iannace & Ianniello, 2008; ISO, 2009; Tronchin et al., 2021a). The shape of the horseshoe plan layout is typical of a 19th century opera theatre character-

ised with four orders of balconies and a top gallery at the last level (Azzaroni et al., 1997; Battaglia et al., 1992; Iannace & Ianniello, 2008). The results highlight that the acoustic response of the Bonci theatre is suitable for both speech and music, which is what these building types were built for (Farina, 2007; Jordan, 1981; Tronchin et al., 2006). The acoustic parameters meet the criteria of a theatre having similar room volume. This analysis shall be considered as a preparatory study taken into account before any acoustic simulations are carried out upon a digital model.

2. Historical Background

Bonci theater in Cesena was formerly known as Spada theatre in the Aledossi Palace (Azzaroni et al., 1997; Iannace et al., 2019; Puglisi et al., 2021). In 1822, the community of Cesena wanted to purchase the noble theatre from the gonfalonier and build new walls and a solid public theatre (Iannace et al., 2000; Tronchin & Knight, 2016; Tronchin et al., 2020).

In 1842, the construction of Bonci theatre was planned under the supervision of the architect Ghinelli, but, due to financial difficulties, the project started the year after. In 1846, the main frame of the building, decoration, scene construction and furniture of the theater were completed (Battaglia et al., 1992).



Fig. 1 – Internal view of the Bonci theatre in Cesena

Bonci theater represents the paradigm of an Italian theater, with harmonious internal space organization, reflecting the perfect combination of functionality with aesthetics (Tronchin & Bevilacqua, 2022). The internal decorations show the characteristics of the neoclassical style, as indicated in Fig. 1. Bonci theater is characterized by four orders of balconies and a top gallery (*loggione*). The plan layout of the theater presents a horseshoe shape geometry. In particular, the final design opted for a total number of 23 boxes per balcony, to be 1.7 m wide at the parapet line.

The main hall is richly decorated, and the ceiling, with its allegorical representations, is embedded in a circular panel carved with gold-plated vine patterns. The walls of the main hall are treated with polished plaster, as shown in Fig. 2. The interior design of the boxes is also characterised by polished and stuccoed walls.



Fig. 2 – Decorations of the ceiling

Due to the existence of underground waterways, the foundation of the theater is built on wooden poles, which support a peripheral wall cage containing separated functional units and a large roof supported by huge trusses (Farina & Tronchin, 2000; Tronchin, 2021).

Nowadays, the theater is considered a real “machine” for the artistic shows that run throughout the year.

3. Architectural Organization

Bonci theater has a horseshoe-shaped plan layout, as shown in Fig. 3, having a total capacity of 930 seats, distributed as 364 in the stalls, 130 in the top gallery (*loggione*), and the rest across four orders of balconies composed of 25 boxes.

The surface area of the fly tower is a square of 24 m side having a height of 18 m and an inclination of 5 %. The proscenium arch is 12 m wide with a height of up to 7.8 m.

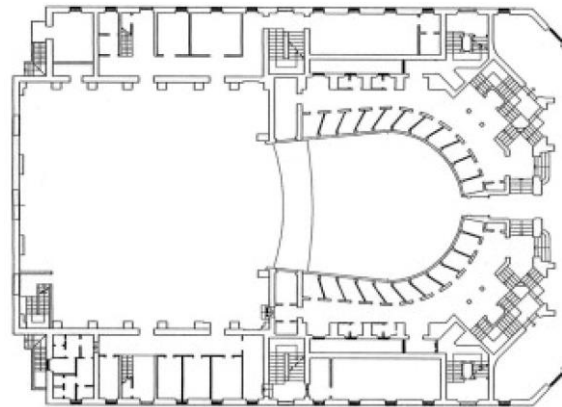


Fig. 3 – Plan layout of Bonci theater of Cesena

4. Acoustic Measurements

Acoustic measurements were carried out inside Bonci theater by using the following equipment:

- Equalised omnidirectional loudspeaker (Look Line);
- Binaural dummy head (Neumann KU-100);
- B-Format (Sennheiser Ambeo);

The sound source and the receivers were located across the stalls and in some selected boxes at different orders, as shown in Fig. 4.

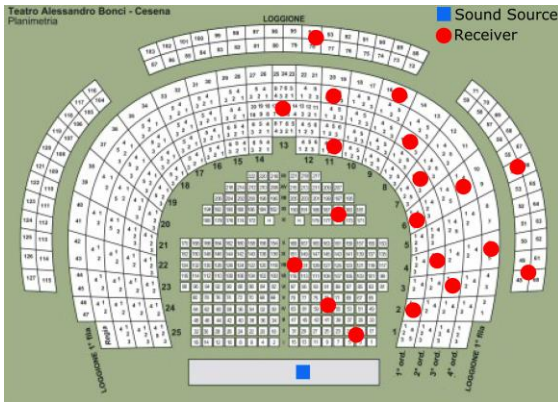


Fig. 4 – Equipment positions during the acoustic survey

The sound source was placed on the stage at a height of 1.4 m and the receivers were moved across the stalls and in the boxes by recording the Impulse Responses (IRs). The excitation signal (Bettarello et al., 2010) was the Exponential Sine Sweep (ESS) (Farina, 2007; Tronchin et al., 2021b), which was 15 s long, by covering a spectrum bandwidth ranging between 40 Hz and 20 kHz. The measurements were taken in unoccupied conditions.

5. Results

The recorded IRs were processed with the Aurora plugin, suitable for Audition 3.0, to gather the main acoustic parameters that are shown in Figs. 5 to 10 for the octave bands going from 125 Hz and 8 kHz.

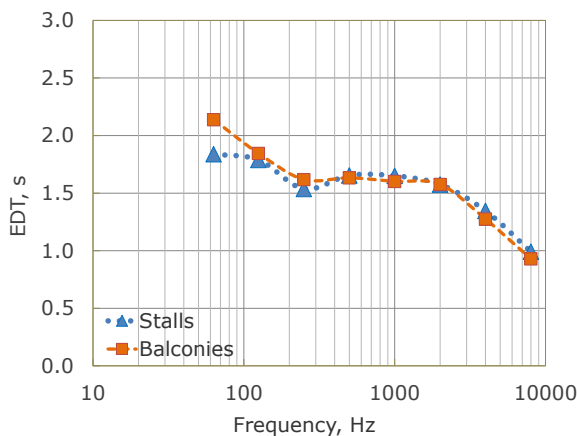


Fig. 5 – Measured values of Early Decay Time (EDT)

Fig. 5 shows the measured values of Early Decay Time (EDT), found to be very similar between

stalls and balconies. Between 250 Hz and 2 kHz, the values fluctuate around 1.6 s, while at lower frequencies the results rise to 2.2 s and at higher octaves the values drop to 1.0 s. The overall outcome is within the optimal range set for opera houses (Farina & Tronchin, 2005; Farina et al., 1998; Tronchin & Bevilacqua, 2021).

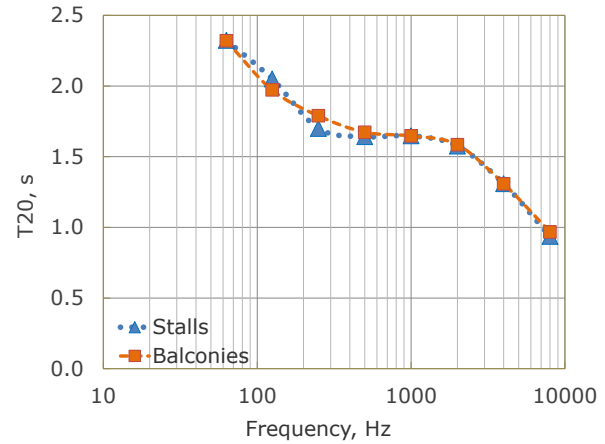


Fig. 6 – Measured values of reverberation time (T_{20})

Fig. 6 indicates that the averaged values of T_{20} are around 1.7 s at mid-frequencies, found to be very similar for stalls and balconies. This result meets the criteria of an opera house of such a volume size, as indicated in Fig. 7.

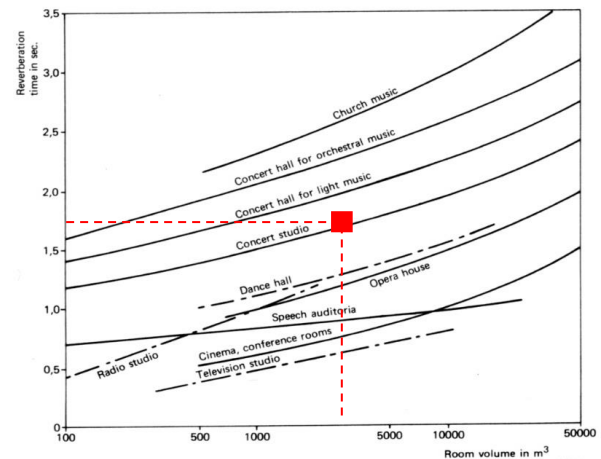


Fig. 7 – Optimal T_{20} values at 500 Hz, based on room volume

Fig. 8 shows the results of speech clarity index (C_{50}), found to be better in the stalls than on the balconies (Tronchin et al., 2006). The values in the stalls meet the optimal range (-2 dB to +2 dB) (ISO, 2003; Puglisi et al., 2021) for the mid-frequencies; the results of 63 Hz and 8 kHz are not included in the target set by the criteria. On the balconies, the

results are slightly below the lower range limit, except at 8 kHz, where the value is within the optimal range.

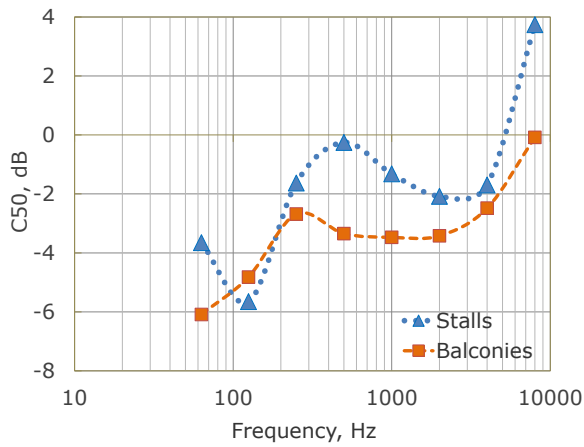


Fig. 8 – Measured values of speech clarity index (C_{50})

In terms of music, Fig. 9 indicates that the clarity index related to music (C_{80}) for both stalls and balconies was found to be within the optimal range for the mid octaves. This outcome highlights the suitability of Bonci theater for both opera and symphonic music (Beranek, 1962; Iannace et al., 2019; Tronchin, 2005).

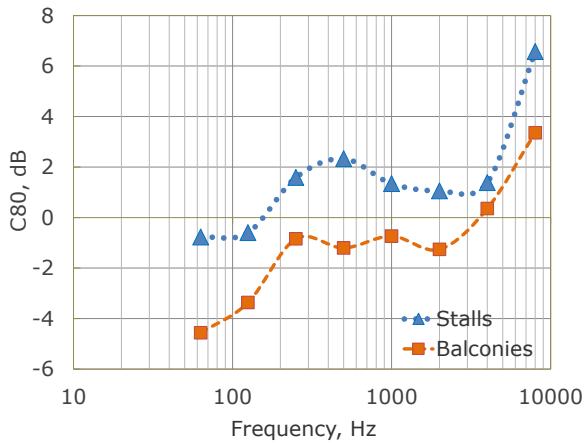


Fig. 9 – Measured values of music clarity index (C_{80})

The results related to definition (D_{50}) turned out to be 0.4 in the stalls and 0.3 on the balconies, as indicated in Fig. 10. This means that the definition is slightly better for music even if the overall outcome confirms what has been assessed for the other acoustic parameters (Iannace et al., 2000; Tronchin et al., 2020; Tronchin et al., 2021b).

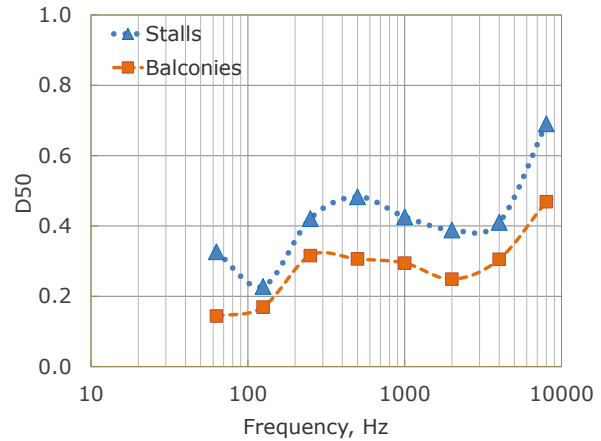


Fig. 10 – Measured values of D_{50}

6. Conclusion

The assessment of the acoustic measurements taken inside Bonci theater in Cesena outlines a good response regarding both speech and music. The best results were found at mid-frequencies, while a shortfall was found at the octaves below 125 Hz, and the results above 4 kHz were found to be slightly above the upper range limit. Based on the acoustic survey, future research studies will be focused on the acoustic simulations (Caniato et al., 2019 and 2020b) of a certain typology of scenery, with and without the audience, in order to highlight the differences of the acoustic parameters in stalls and balconies, as well as for energy building and musical instrument simulation (Fabbri et al., 2014; Manfredi et al., 2019, 2021a, 2021b and 2022; Tronchin et al., 2020). On the basis of this, this preparatory analysis would be of fundamental importance during the calibration process of the digital model (Caniato et al., 2020a), where the absorption coefficients would be applied to all the 3D elements.

References

- Azzaroni, G., F. Dell'Amore, P. G. Fabbri, R. Pieri, and A. Maraldi. 1997. *Un palcoscenico per Cesena. Storia del Teatro Comunale*. Il Ponte Vecchio, Cesena.
- Battaglia, F., M. Gradara, G. Conti, and G. Foschi. 1992. *Il Teatro Comunale Bonci e la Musica a Cesena*.
- Beraneck, L. 1962. *Music, acoustics and architecture*. Wiley: New York.
- Bettarello, F., P. Fausti, V. Baccan, and M. Caniato. 2010. "Impact Sound Pressure Level Performances of Basic Beam Floor Structures". *Building Acoustics* 17(3):305-316. doi: <https://doi.org/10.1260/1351-010X.17.4.305>
- Bettarello, F., M. Caniato, and A. Gasparella. 2021. "The Influence of Floor Layering on Airborne Sound Insulation and Impact Noise Reduction: A Study on Cross Laminated Timber (CLT) Structures". *Applied Science* 11(13): 5938. doi: <https://doi.org/10.3390/app11135938>
- Caniato, M., F. Bettarello, C. Schmid, and P. Fausti. 2019. "The use of numerical models on service equipment noise prediction in heavyweight and lightweight timber buildings". *Building Acoustics* 26(1): 35-55. doi: <https://doi.org/10.1177/1351010X18794523>
- Caniato, M., F. Bettarello, P. Bonfiglio, and A. Gasparella. 2020a. "Extensive Investigation of Multiphysics Approaches in Simulation of Complex Periodic Structures". *Applied Acoustics* 166: 107356. doi: <https://doi.org/10.1016/j.apacoust.2020.107356>
- Caniato, M., C. Schmid, and A. Gasparella. 2020b. "A comprehensive analysis of time influence on floating floors: Effects on acoustic performance and occupants' comfort". *Applied Acoustics* 166: 107339. doi: <https://doi.org/10.1016/j.apacoust.2020.107339>
- Dordevic, Z. 2016. "Intangible tangibility: Acoustical heritage in architecture." *Structural Integrity and Life* 6: 59-66.
- Fabbri, K., L. Tronchin, and V. Tarabusi. 2014. "Energy Retrofit and Economic Evaluation Priorities Applied at an Italian Case Study". *Energy Procedia* 45: 379-384. doi: <https://doi.org/10.1016/j.egypro.2014.01.041>
- Farina, A. 2007. "Advancements in impulse response measurements by sine sweeps." In *Proceedings of the 122nd AES Convention*.
- Farina, A., and L. Tronchin. 2000. "On the "virtual" reconstruction of sound quality of trumpets." *Acta Acustica united with Acustica* 86(4): 737-745.
- Farina, A., and L. Tronchin. 2005. "Measurements and reproduction of spatial sound characteristics of auditoria." *Acoustical Science and Technology* 26(2): 193-199. doi: <https://doi.org/10.1250/ast.26.193>
- Farina, A., A. Langhoff, and L. Tronchin. 1998. "Acoustic characterisation of "virtual" musical instruments: using MLS technique on ancient violins." *Journal Of New Music Research* 27(4): 359-379. doi: <https://dx.doi.org/10.1080/09298219808570753>
- Iannace, G., and E. Ianniello. 2008. "Sound-focusing effects in the plan of horse-shoe shaped opera theatres." In *Proceedings of European Conference on Noise Control*: 1639-1643.
- Iannace, G., C. Ianniello, L. Maffei, and R. Romano. 2000. "Objective measurement of the listening condition in the old Italian opera house Teatro di San Carlo." *Journal of Sound and Vibration* 232: 239-249. doi: <https://doi.org/10.1006/jsvi.1999.2696>
- Iannace, G., G. Ciaburro, A. Trematerra, and C. Foglia. 2019. "Acoustic correction of a renaissance period hall." *Canadian Acoustics* 47(2): 57-66.
- ISO. 2003. *ISO 9921:2003. Ergonomics - Assessment of speech communication*. Geneva, Switzerland.
- ISO. 2009. *ISO 3382-1:2009. Acoustics - Measurement of Room Acoustic Parameters; Part 1: Performance Spaces*. Geneva, Switzerland.
- Jordan, V. L. 1981. "A group of objective acoustical criteria for concert halls." *Applied Acoustics* 14: 253-266. doi: [https://doi.org/10.1016/0003-682X\(81\)90021-9](https://doi.org/10.1016/0003-682X(81)90021-9)
- Manfren, M., B. Nastasi, E. A. Piana, and L. Tronchin. 2019. "On the link between energy performance of building and thermal comfort: An example." *AIP Conference Proceedings* 2123: 1-9. doi: <https://doi.org/10.1063/1.5116993>
- Manfren, M., B. Nastasi, L. Tronchin, D. Groppi, and D. A. Garcia. 2021a. "Techno-economic analysis and energy modelling as a key

- enablers for smart energy services and technologies in buildings." *Renewable and Sustainable Energy Reviews* 150: 1-14. doi: <https://doi.org/10.1016/j.rser.2021.111490>
- Manfren, M., M. Sibilla, and L. Tronchin. 2021b. "Energy Modelling and Analytics in the Built Environment—A Review of Their Role for Energy Transitions in the Construction Sector." *Energies* 14: 1-29. doi: <https://doi.org/10.3390/en14030679>
- Manfren, M., P. A. B. James, and L. Tronchin. 2022. "Data-driven building energy modelling – An analysis of the potential for generalisation through interpretable machine learning". *Renewable and Sustainable Energy Reviews* 167: 1-13. doi: <https://doi.org/10.1016/j.rser.2022.112686>
- Puglisi, G. E., A. Warzybok, A. Astolfi, and B. Kollmeier. 2021. "Effect of competitive acoustic environments on speech intelligibility." *Journal of Physics* 2069(1): 175180. doi: <https://doi.org/10.1088/1742-6596/2069/1/012162>
- Tronchin, L. 2005. "Modal analysis and intensity of acoustic radiation of the kettledrum." *The Journal of the Acoustical Society of America* 117(2): 926-933. doi: <https://doi.org/10.1121/1.1828552>
- Tronchin, L. 2021. "Variability of room acoustic parameters with thermo-hygrometric conditions." *Applied Acoustics* 177: 1-14. doi: <https://doi.org/10.1016/j.apacoust.2021.107933>
- Tronchin, L., and A. Bevilacqua. 2021. "Acoustic study of different sceneries at the São Carlos national theatre of Lisbon." *Applied Acoustics* 180: 1-11. doi: <https://doi.org/10.1016/j.apacoust.2021.108102>
- Tronchin, L., and A. Bevilacqua. 2022. "Historically informed digital reconstruction of the Roman theatre of Verona. Unveiling the acoustics of the original shape." *Applied Acoustics* 185: 1-18. doi: <https://doi.org/10.1016/j.apacoust.2021.108409>
- Tronchin, L., and D. J. Knight. 2016. "Revisiting Historic Buildings through the Senses. Visualising Aural and Obscured Aspects of San Vitale, Ravenna." *International Journal of Historical Archaeology* 20: 127-145. doi: <https://doi.org/10.1007/s10761-015-0325-2>
- Tronchin, L., R. Shimokura, and V. Tarabusi. 2006. "Spatial sound characteristics in the Theatre Comunale in Bologna, Italy." In *Proceedings of the 9th Western Pacific Acoustics Conference (WESPAC)*, Seoul, Korea, June 26-28.
- Tronchin, L., F. Merli, M. Manfren, and B. Nastasi. 2020. "The sound diffusion in Italian Opera Houses: some examples." *Building Acoustics* 27(4): 333-355. doi: <https://doi.org/10.1177/1351010X20929216>
- Tronchin, L., F. Merli, and M. Manfren. 2021a. "On the acoustics of the Teatro 1763 in Bologna." *Applied Acoustics* 172: 107598. doi: <https://doi.org/10.1016/j.apacoust.2020.107598>
- Tronchin, L., F. Merli, and M. Dolci. 2021b. "Virtual acoustic reconstruction of the Miners' Theatre in Idrija (Slovenia)." *Applied Acoustics* 172: 1-9. doi: <https://doi.org/10.1016/j.apacoust.2020.107595>
- Vecco, M. 2010. "A definition of Cultural Heritage: From the tangible to the intangible." *Journal of Cultural Heritage* 11: 321-324. doi: <https://doi.org/10.1016/j.culher.2010.01.006>

Acoustic Discoveries of Another Masterpiece by Antonio Galli Bibiena: The Communal Theatre of Bologna

Antonella Bevilacqua – University of Parma, Italy – antonella.bevilacqua@unipr.it

Ruoran Yan – University of Bologna, Italy – ruoran.yan2@unibo.it

Abstract

The Communal Theater of Bologna was built in 1763, after a fire destroyed the previous Renaissance construction. The project was assigned to the architect Antonio Galli Bibiena, who belonged to a family of artists and scenographers. The interior design represents Baroque style, with its four orders of balconies surmounted by a top gallery. Acoustic measurements were carried out inside the theater in line with BS3382-1. The values measured were compared with the acoustic simulations of a digital model reproducing the shape and volume of this cultural heritage. The historical background of the building has been summarised to aid understanding of the construction development overseen by Antonio Galli Bibiena.

1. Introduction

The Communal Theater of Bologna, created by Antonio Galli Bibiena, was criticised at the beginning of the 18th century for being composed of a bell-shaped plan layout marking the main hall. This architectural choice was considered outside the traditional construction rules developed at that time, especially under the influence of Pierre Patte and his studies on the elliptical shapes of spaces for the performing arts. Nonetheless, the architect found a way to combine architectural finesse with a good acoustic response due to the specific materials employed on the finishes as well as to geometry very favourable to sound diffusion (Caniato et al., 2020; Fabbri et al., 2021; Tronchin & Farina, 1997).

The Communal Theater of Bologna was studied in depth during the 20th century, particularly after restoration work on the modification of the orchestra pit and of the initial part of the stage closer to

the audience damaged by a fire. Other work was completed on the structural frame of the boxes, on the main trusses of the roof and for the allocation of the electrical system. Fortunately, the interventions did not involve the acoustics, which represent one of the best masterpieces that Antonio Galli Bibiena left to post generations (Tronchin et al., 2021a and 2021b).

2. Historical Notes

The Communal Theater of Bologna was built in the location of the previous Malvezzi Theater, a wooden structure that burned down in 1745. In 1756, the City Council approved the proposal to build a new theater in Baroque style and assigned the project to the architect Antonio Galli Bibiena (Tronchin et al., 2020a, 2020b and 2020c). In 1763, the Communal Theater of Bologna was officially opened to the public.



Fig. 1 – Internal view of the Communal Theater of Bologna

Between 1818 and 1820, the theater underwent some restoration work, including the renovation of the dome, the reconstruction of the auditorium, and the stage. The second restoration campaign

took place between 1853 and 1854, when the architect C. Parmenani was responsible for the transformation work (Tronchin et al., 2020a, 2020b and 2020c). In 1865, the façade was restored along with some safety measures adopted in line with the new building regulations, as shown in Fig. 1.

In 1931, the theater experienced another fire, burning down the stage and the curtain, while many rooms survived. The restoration was completed in 1935 and, after than this event, the theater was closed again due to World War II, but it reopened in 1946 (Tronchin et al., 2006).

3. Architectural Description

The main hall of the Communal Theater of Bologna, completed in 1763, has a total capacity of 1176 seats distributed as 644 seats in the stalls and 532 seats on the elevated boxes. The preferred shape of a bell was designed by Galli Bibiena for the plan layout, having the axes measuring 22.4 m and 15.4 m (L, W), as shown in Fig. 2.

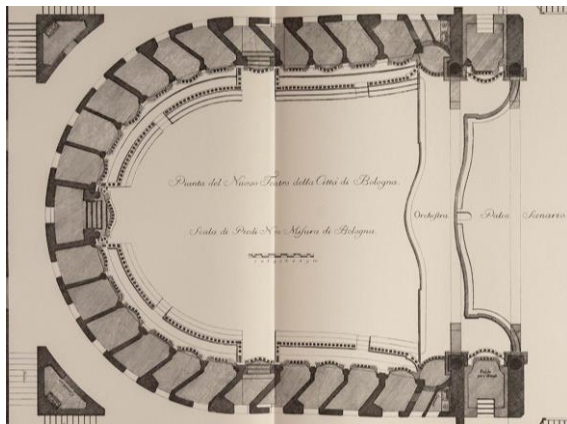


Fig. 2 – Plan layout of the Communal Theater of Bologna. Drawing by A. Galli Bibiena

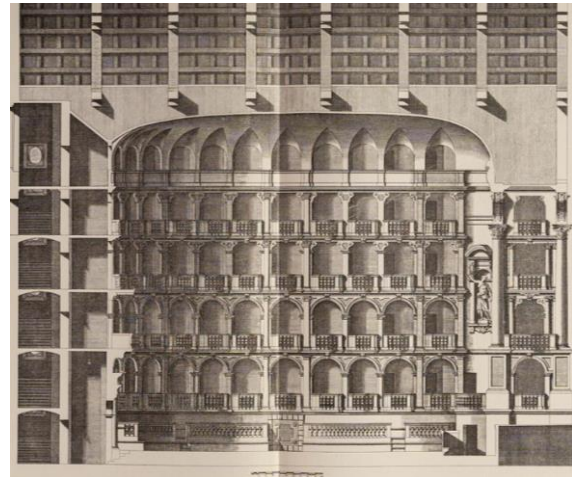


Fig. 3 – Longitudinal section of the Communal Theater of Bologna. Drawing by A. Galli Bibiena

The total height is about 16.9 m, which includes four orders of balconies surmounted by a gallery, as indicated in Fig. 3.

The architect also introduced a series of new constructive solutions, such as the use of load-bearing masonry rather than wooden frames (Amoruso, 2019).

However, these new schemes caused him serious slander, although it was proved that these innovations show excellent acoustic performance.



Fig. 4 – Wooden mechanical system located beneath the finish floor of the stalls

Beneath the floor of the main hall, a wooden mechanical system can regulate the height of the seating area, so to be at the same level as the stage, as shown in Fig. 4.

3.1 Digital Model

From the architectural drawings, a digital model was made, considering all the architectural elements and discarding the details of capitals and tiny decorations (Vorländer, 2011), as shown in Fig. 5. The layers represented in different colours were grouped based on the characteristics of the materials.

Thereafter, the model was exported in dxf format, ready to be used within Ramsete software (Farina, 1995). The attribution of the absorbing and scattering coefficients was carried out based on the acoustic measurements, as indicated in Fig. 6. The sound source and the receivers of the model were located in the same positions used for the survey (Caniato et al., 2021), in order to make the model calibration accurate (Manfren et al., 2020, 2021a and 2021b)

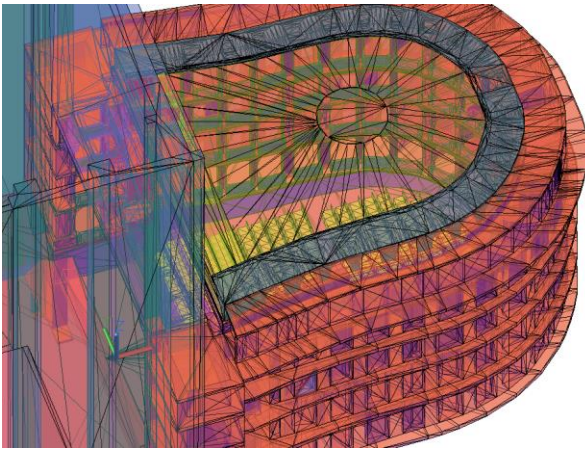


Fig. 5 – View of the 3D model

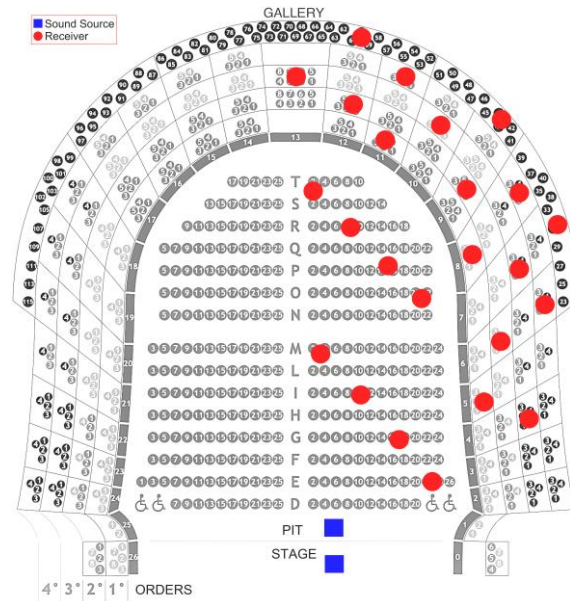


Fig. 6 – Scheme of the equipment positions during the acoustic survey

4. Acoustic Simulation

The acoustic simulations were carried out based on the absorption coefficients that were attributed by considering the materials inside the theater (Shtrepi, 2019). The simulations were calculated without any scenery on the stage, nor any audience; they faithfully represent the conditions found on site.

For the simulations, two omnidirectional sound sources were placed in the locations where they were positioned during the acoustic measurements (Iannace et al., 2000), in particular, on the stage and in the orchestra pit.

Figs. 7 to 11 show the main acoustic parameters for a bandwidth comprising a range of between 125 Hz and 8 kHz. The results shall be considered as the average of measured and simulated values related to stalls and balconies (Tronchin et al., 2021a and 2021b).

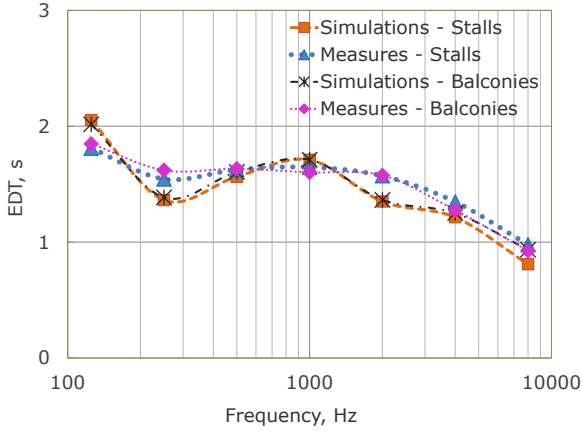


Fig. 7 – Measured and simulated values of EDT

Fig. 7 shows the comparison of the acoustic measurements and simulations of the EDT results. For this acoustic parameter, the difference between stalls and balconies is minimal across all the frequency bands. However, a drift between measurements and simulations does not exceed 5 % for the considered bandwidth (Caniato et al. 2019; Sakai et al., 2002).

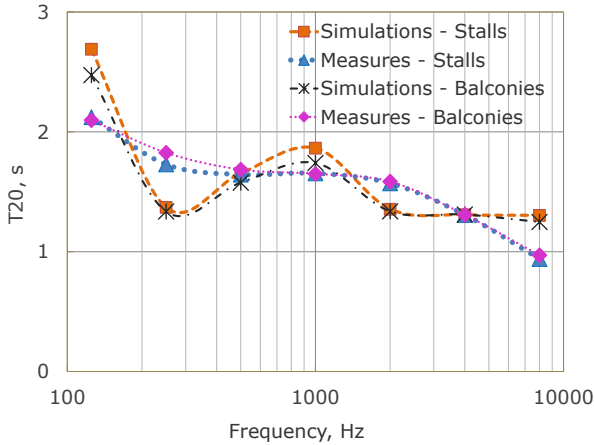
Fig. 8 – Measured and simulated values of T_{20}

Fig. 8 indicates that the T_{20} measured results around 1.8 s at mid-frequencies highlight a good reverberation time for a hall having a volume size equal to approximately 4,200 m³, and similar to other Italian opera theaters built in the same period (Vodola, 2019). The simulated values at 250 Hz and 2 kHz were calibrated to be up to 0.5 s away from the measured results; this was assessed along with the other acoustic parameters (Bettarello et al., 2021; Guarnaccia et al., 2019).

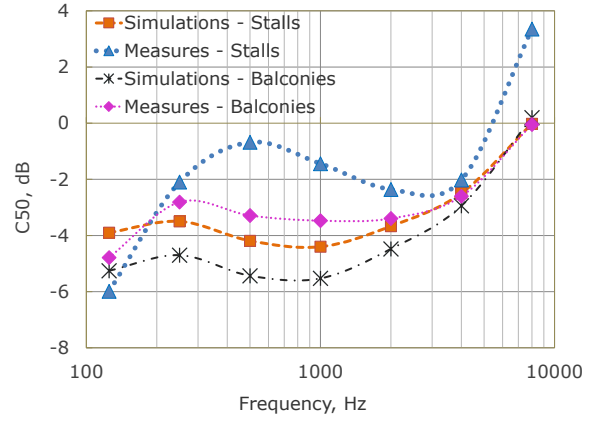
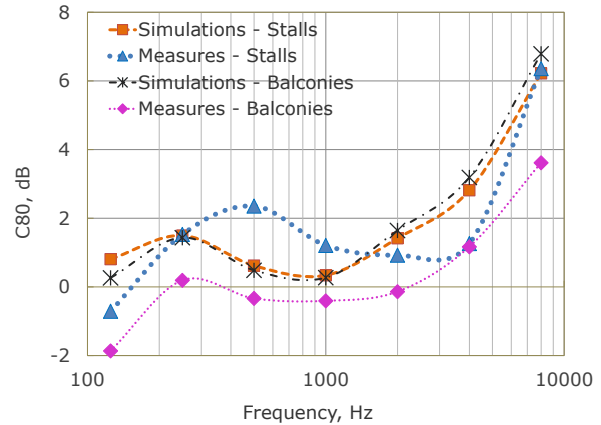
Fig. 9 – Measured and simulated values of C_{50}

Fig. 9 shows the results of the speech clarity index (C_{50}) to be between the optimal range (-2 dB and +2 dB) (Beranek, 1962) from 250 Hz onwards in relation to stalls, while the measured values in the balconies fall slightly below the lowest range limit, with the exception of 8 kHz being equal to 0 dB. The simulated values are shifted below the measurements of up to 2 dB for mid-frequency bands, while at 4 kHz the difference is minimised.

Fig. 10 – Measured and simulated values of C_{80}

In terms of music, the clarity index measured (C_{80}) falls within the optimal range (-2 dB and +2 dB) across all the frequency bands, with the exception of 8 kHz, where the values are up to 4 dB above the upper range limit. A difference of up to 2 dB was found between the measurements in the stalls and in the balconies, to be maximum at 500 Hz and negligible at 4 kHz. The difference in the simulated values between balconies and stalls is less, to approximately 1.5 dB at mid-octave and null at very high frequencies.

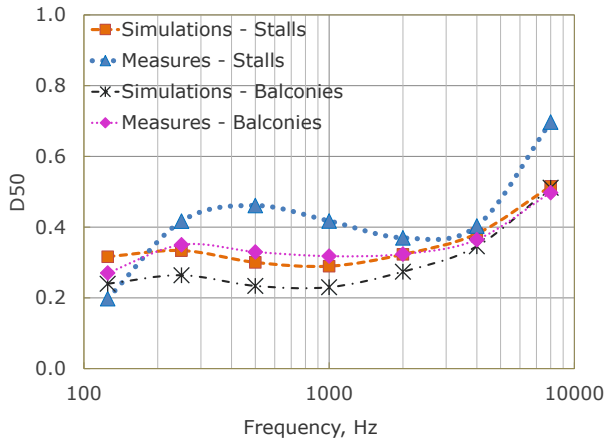


Fig. 11 – Measured and simulated values of D_{50}

Fig. 11 highlights that the measured values of definition (D_{50}) were found to be around 0.38 in the balconies and 0.42 across the stalls. This means that the acoustic response of the Communal Theater of Bologna is more suitable for music, with a shortfall at low frequency related to speech (Bettarello et al., 2010; Puglisi et al., 2021). The simulated values are shifted up to 1.5 below the trend lines related to balconies and stalls, despite the difference at high frequencies being negligible.

5. Conclusion

This paper deals with the acoustics of the Communal Theater of Bologna, one of the best architectural masterpieces designed by Antonio Galli Bibiena. The main acoustic parameters were analysed in comparison with the simulated results obtained by applying the absorbing and scattering coefficients to a digital model that faithfully reproduces the architectural composition of the theater. The results highlight an acoustic response suitable for both music and speech, while the simulated values were assessed to be within 5 % away from the values measured if averaged across all the spectrum bandwidth. The calibration process considered all the acoustic parameters as well as to be fruit of the authors' experience on acoustic simulations taken for similar room shapes.

References

- Amoruso, G. 2019. "The teatro of Bologna as a transformable space: drawing, geometry and invention in the study of the wooden model of the theatre by Antonio Galli Bibiena." *Lecture Notes in Civil Engineering* 24:375-394. doi: https://doi.org/10.1007/978-3-030-03676-8_13
- Beranek, L. 1962. *Music, Acoustics and Architecture*. John Wiley & Sons, Inc..
- Bettarello, F., P. Fausti, V. Baccan, and M. Caniato. 2010. "Impact Sound Pressure Level Performances of Basic Beam Floor Structures". *Building Acoustics* 17(3): 305-316. doi: <https://doi.org/10.1260/1351-010X.17.4.305>
- Bettarello, F., M. Caniato, G. Scavuzzo, and A. Gasparella. 2021. "Indoor Acoustic Requirements for Autism-Friendly Spaces". *Applied Science* 11: 3942. doi: <https://doi.org/10.3390/app11093942>
- Caniato, M., F. Bettarello, C. Schmid, and P. Fausti. 2019. "The use of numerical models on service equipment noise prediction in heavyweight and lightweight timber buildings". *Building Acoustics* 26(1): 35-55. doi: <https://doi.org/10.1177/1351010X18794523>
- Caniato, M., F. Bettarello, P. Bonfiglio, and A. Gasparella. 2020a. "Extensive Investigation of Multiphysics Approaches in Simulation of Complex Periodic Structures". *Applied Acoustics* 166: 107356. doi: <https://doi.org/10.1016/j.apacoust.2020.107356>
- Caniato, M., C. Schmid, and A. Gasparella. 2020b. "A comprehensive analysis of time influence on floating floors: Effects on acoustic performance and occupants' comfort". *Applied Acoustics* 166: 107339. doi: <https://doi.org/10.1016/j.apacoust.2020.107339>
- Caniato, M., F. Bettarello, and A. Gasparella. 2021. "Indoor and outdoor noise changes due to the COVID-19 lockdown and their effects on individuals' expectations and preferences". *Scientific Reports* 11: 16533. doi: <https://doi.org/10.1038/s41598-021-96098-w>
- Fabbri, K., L. Tronchin, and F. Barbieri. 2021. "Coconut fibre insulators: The hygrothermal behavior in the case of green roofs". *Construction and building materials* 266: 1-9. doi: <https://doi.org/10.1016/j.conbuildmat.2021.125888>

- <https://doi.org/10.1016/j.conbuildmat.2020.121026>
- Farina, A. 1995. "RAMSETE – a new pyramid tracer for medium and large-scale acoustic problems". In *Proceedings of Euro-Noise Conference*, Lyon, France.
- Guarnaccia, C., L. Tronchin, and M. Viscardi. 2019. "Special issue on modelling, simulation and data analysis in acoustical problems." *Applied Sciences* 9: 5261. doi: <https://doi.org/10.3390/app9235261>
- Iannace, G., C. Ianniello, L. Maffei, and R. Romano. 2000. "Objective measurement of the listening condition in the old Italian opera house Teatro di San Carlo." *Journal of Sound and Vibration*, 232(1): 239-249. doi: <https://doi.org/10.1006/jsvi.1999.2696>
- Manfren, M., B. Nastasi, E. A. Piana, and L. Tronchin. 2019. "On the link between energy performance of building and thermal comfort: An example". In *AIP Conference Proceedings* 2123: 1-9. doi: <https://doi.org/10.1063/1.5116993>
- Manfren, M., B. Nastasi, L. Tronchin, D. Groppi, and D. A. Garcia. 2021a. "Techno-economic analysis and energy modelling as a key enabler for smart energy services and technologies in buildings". *Renewable and sustainable energy reviews* 150: 1-14. doi: <https://doi.org/10.1016/j.rser.2021.111490>
- Manfren, M., M. Sibilla, and L. Tronchin. 2021b. "Energy Modelling and Analytics in the Built Environment—A Review of Their Role for Energy Transitions in the Construction Sector". *Energies* 14: 1-29. doi: <https://doi.org/10.3390/en14030679>
- Puglisi, G. E., A. Warzybok, A. Astolfi, and B. Kollmeier. 2021. "Effect of competitive acoustic environments on speech intelligibility." *Journal of Physics* 2069(1): 175180. doi: <https://doi.org/10.1088/1742-6596/2069/1/012162>
- Sakai, H., Y. Ando, N. Prodi, and R. Pompoli. 2002. "Temporal and spatial acoustical factors for listeners in the boxes of historical opera theatres." *Journal of Sound and Vibration*, 258(3): 527-547. doi: <https://doi.org/10.1006/jsvi.2002.5274>
- Shtrepi, L. 2019. "Investigation on the diffusive surface modeling detail in geometrical acoustics-based simulations." *Journal of Acoustic Society of America* 145(3): EL215–21. doi: <https://doi.org/10.1121/1.5092821>
- Tronchin, L., and A. Farina. 1997. "Acoustics of the former Teatro "La Fenice" in Venice." *Journal of the Audio Engineering Society* 45(12):1051-1062.
- Tronchin, L., R. Shimokura, and V. Tarabusi. 2006. "Spatial sound characteristics in the Theatre Comunale in Bologna, Italy". *Proceedings of the 9th Western Pacific Acoustics Conference (WESPAC)*, Seoul, Korea, June 26-28.
- Tronchin, L., M. Manfren, and V. Vodola. 2020a. "Sound characterization through intensity of acoustic radiation measurement: A study of persian musical instruments". *Applied Sciences* 10(2): 633. doi: <https://doi.org/10.3390/app10020633>
- Tronchin L., M. Manfren, and V. Vodola. 2020b. "The carabattola - vibroacoustical analysis and intensity of acoustic radiation (IAR)". *Applied Sciences* 10(2): 641. doi: <https://doi.org/10.3390/app10020641>
- Tronchin, L., F. Merli, M. Manfren, and B. Nastasi. 2020c. "The sound diffusion in Italian Opera Houses: some examples." *Building Acoustics*, 27(4): 333-355. doi: <https://doi.org/10.1177/1351010X20929216>
- Tronchin, L., F. Merli, and M. Dolci. 2021a. "Virtual acoustic reconstruction of the Miners' Theatre in Idrija (Slovenia)". *Applied Acoustics* 172: 1-9. doi: <https://doi.org/10.1016/j.apacoust.2020.107595>
- Tronchin, L., F. Merli, and M. Manfren. 2021b. "On the acoustics of the Teatro 1763 in Bologna." *Applied Acoustics* 172: 107598. doi: <https://doi.org/10.1016/j.apacoust.2020.107598>
- Vodola, V. 2019. "The renovation of the Teatro Nuovo in Spoleto: analysis of the acoustic quality of an Italian Opera House." *Journal of Physics Conference Series* 1351: 012013. doi: <https://doi.org/10.1088/1742-6596/1351/1/012013>
- Vorländer, M. 2011. "Models and algorithms for computer simulations in room acoustics." In *Proceedings of the International Seminar on Virtual Acoustics (ISVA)*, Valencia, Spain, November 24-25.

In Situ Measurement of Wall Thermal Properties: Parametric Investigation of the Heat Flow Methods Through Virtual Experiments Data

Andrea Alongi – Politecnico di Milano, Italy – andrea.alongi@polimi.it

Luca Sala – Politecnico di Milano, Italy – luca11.sala@mail.polimi.it

Adriana Angelotti – Politecnico di Milano, Italy – adriana.angelotti@polimi.it

Livio Mazzarella – Politecnico di Milano, Italy – livio.mazzarella@polimi.it

Abstract

Energy retrofit of existing buildings is based on the assessment of the starting performance of the envelope. The procedure to evaluate thermal conductance through in situ measurements is described in the technical standard ISO 9869-1:2014, which provides two alternative techniques to process collected data: the Average Method (AM) and the Dynamic Method (DM).

This work studies their effectiveness using virtual data from numerical simulations of three kinds of walls, performed using a Finite Difference model.

The AM always provides acceptable estimates in winter, with better outcomes when indoor heat flux is considered in every case except the highly insulated wall. Summer conditions do not lead to acceptable measurements, despite the fulfillment of the check required by the standard. The DM results show acceptable estimations of the thermal conductance in both climates, for most of the virtual samples considered, although critically depending on some parameters of the DM that are left to the user's discretion, without strict indications by the standard. This work highlights a possible approach for overcoming this issue, which requires deeper future investigation.

1. Introduction

To reduce the energy needs related to the existing building stock, great effort is oriented towards envelope renovation. As a first step in this direction, the thermal properties (thermal transmittance and conductance) of the existing building components are usually assessed through in situ measurements. To this purpose, the international technical standard ISO 9869-1:2014 describes the so-called Heat Flow

Meter method and two data processing techniques: the Average and the Dynamic Method.

Within the dedicated literature there is a wide variety of results (Atsonios et al., 2017; Gaspar et al., 2018; Lucchi et al., 2017). This is possibly due to the diversity of wall typologies investigated and boundary conditions occurring. Moreover, even when different walls are studied in the same work (Atsonios et al., 2017), experimental measurements are not performed at the same time.

To overcome the limitations inherent with experimental approaches, this work analyzes the efficacy of the Average and the Dynamic Method in finding the wall conductance by using virtual wall samples with different known properties, simulated through a Finite Difference model with controlled and repeatable boundary conditions. Moreover, these analyses are also aimed at looking for supplementary criteria concerning some key parameters of each methodology.

2. Methods and Materials

In this paper the Average and the Dynamic methods of analysis suggested by ISO 9869-1:2014 are applied to virtual data obtained through virtual Heat Flow Meter experiments i.e., heat transfer numerical simulations on wall components. The purpose of the data analysis is to derive the “experimental” thermal conductance, that in this case can be compared with the exactly known true value. In this section the experimental and data processing approaches by the standard are briefly illustrated. Secondly, the

numerical model for heat transfer across the wall is described and the three virtual walls and boundary conditions provided.

2.1 The HFM Method According to the Standard

The in situ estimation of the thermal conductance is based on the monitoring of the indoor and outdoor surface temperatures (T_{si} and T_{se} respectively) of a given wall, along with the heat flux density (φ) at one of these surfaces. More precisely, the ISO 9869-1:2014 suggests sampling this quantity at the indoor surface, due to a generally greater stability.

Data processing is then performed according to two possible techniques, the Average Method (AM) and the Dynamic Method (DM).

The sampling period is suggested as being at least 72 h, but it can be longer if required. This parameter is subject of discussion later in this work. As far as sampling frequency is concerned, it can be around $0.5 \div 1$ h for the AM, while for the DM no explicit indication is provided. However, in this work the sampling frequency is significantly increased, reducing the sampling interval to 5 minutes to allow more accurate estimations.

2.1.1 The Average Method

According to the AM approach, the overall thermal conductance Λ of the building envelope component is progressively evaluated while the measurement itself is ongoing, through the following equation:

$$\Lambda = \frac{\sum_{i=1}^n \varphi_i}{\sum_{i=1}^n (T_{si,i} - T_{se,i})} \quad (1)$$

where φ_i , $T_{si,i}$ and $T_{se,i}$ are heat flux density [Wm^{-2}], indoor and outdoor surface temperature [$^{\circ}\text{C}$] respectively at the i -th sampling moment (with $i = 1 \div N$). Both summations in Eq. 1 progress with time and their ratio should reach a stable value that approximates the real thermal conductance of the investigated component. This approach is based on the steady state assumption. For this reason, the standard suggests performing the sampling in winter periods, when outdoor conditions are more stable and larger heat flow densities usually occur. For elements with an expected thermal capacity lower than $20 \text{ kJ m}^{-2} \text{K}^{-1}$, only data acquired during the nights should be used. The standard also provides three conditions for good estimation, i.e.:

- the test should last more than 72 h;
- the deviation between the result at the end of the test and the value reached 24 h before should be within ± 5 %;
- the deviation between the results obtained considering the first 2/3 and the last 2/3 of the test duration should be within ± 5 %.

In this work the constraint on the overall test duration is not strictly considered in order to investigate how much the sampling period can be reduced while maintaining an acceptable outcome of the procedure. At the same time, the other two conditions are always checked. Moreover, the standard suggests either the use of a thermal mass factor correction or the implementation of the DM whenever the change in internal energy of the wall is more than 5 % of the heat passing through the wall during the test. Since it is not clearly explained how this condition should be assessed and this work deals with the DM anyway, no thermal mass factor correction is considered.

2.1.2 The Dynamic Method

This second processing technique is suggested as a way of estimating the steady-state properties of a building element starting from highly variable temperatures and heat fluxes and is applied at the end of their acquisition. It is based on the solution of the Fourier equation through the Laplace transformation method (Ahvenainen et al., 1980):

$$\begin{aligned} \varphi_i = & \Lambda(T_{si,i} - T_{se,i}) + \\ & + K_1 T'_{si,i} - K_2 T'_{se,i} + \\ & + \sum_n P_n \sum_{j=i-p}^{i-1} T_{si,j} (1 - \beta_n) \beta_n (i - j) + \\ & + \sum_n Q_n \sum_{j=i-p}^{i-1} T_{se,j} (1 - \beta_n) \beta_n (i - j) \end{aligned} \quad (2)$$

where $T'_{si,i}$ and $T'_{se,i}$ are the surface temperature time derivatives [K s^{-1}] at the i -th sampling moment (approximated using the incremental ratio referred to the sampling interval Δt), K_1 , K_2 , P_n and Q_n are unknown dynamic characteristics of the wall that depend on the n -th time constant τ_n (also unknown). Even though the number of time constants should be theoretically infinite, a limited number m (generally from 1 to 3) is adequate to correctly describe the system behaviour. Finally, β_n is defined as:

$$\beta_n = e^{-\Delta t / \tau_n} \quad (3)$$

Once the m time constants are initialized, the $(2m+3)$ unknowns are iteratively calculated optimizing the τ_n , through the minimisation of the square deviation between the measured and the estimated (φ^*) heat flux densities:

$$S^2 = \sum (\varphi_i - \varphi_i^*)^2 \quad (4)$$

The sums over the index j in Eq. 2 are the approximation of the integration process and are performed over a supplementary subset of p data, with $p = M - N$ and M the number of data triplets (φ_i , $T_{si,i}$, and $T_{se,i}$) that are actually used in the estimation of φ^* , as shown in Fig. 1.

Therefore, the user is expected to choose the number of time constants m (and their starting value for the iteration process) and M . While the standard provides some indications about the former, the latter is left to the user's experience (the only constraint is $M > 2m+3$). No univocal criterion is provided to assess the quality of the estimation and, ultimately, of the thermal conductance Λ achieved: the technical standard reports only an equation to calculate the confidence interval I for the estimated Λ (see ISO 9869-1:2014), stating that whenever I is lower than 5 % of the estimated conductance, the latter is generally close to the real value.

As far as the DM is concerned, this work aims at:

- assessing its effectiveness for different wall kinds, both in winter and summer conditions;
- evaluating the sensitivity of the outcomes on the number and the initial values of the time constants considered;
- evaluating the sensitivity of the method to the parameter M , possibly finding useful indications for the user.

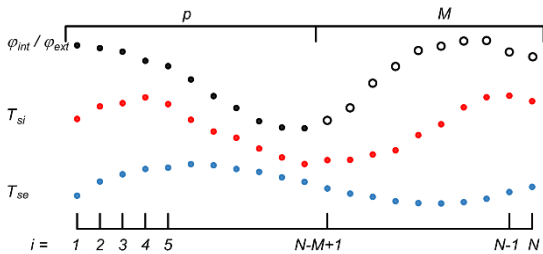


Fig. 1 – data utilization representation for the DM, with indication of p and M

2.2 The Numerical Model

In this work virtual experiments are performed

using a one-dimensional Finite Difference model based on the one presented and validated in (Alongi et al., 2021). For a given k -th layer of the wall ($k = 1 \div K$), the discretized version of the Fourier equation is:

$$\frac{T_i^{j+1} - T_i^j}{\Delta t} = \alpha_k \frac{T_{i+1}^{j+1} - 2T_i^{j+1} + T_{i-1}^{j+1}}{\Delta x^2} \quad (5)$$

where α_k is the thermal diffusivity, T_i is the temperature at the i -th node ($i = 1 \div N_{FD}$) and at the j -th timestamp ($j = 1 \div M_{FD}$), Δx and Δt are the space and time discretization respectively. The numerical model uses a central difference scheme for the spatial derivative and a fully implicit representation of the time variation.

Third type boundary conditions are imposed at both edges of the domain, along with an imposed heat flux at the outdoor surface to take into account solar radiation, while temperature and heat flux continuity is imposed at the interface between adjacent layers. In all simulations performed, a structured grid is considered, with a constant step $\Delta x = 0.001$ m (which in (Alongi et al., 2021) is suggested as a good compromise between accuracy and computational cost), and the timestep Δt is set equal to 300 s.

The main outcomes of the simulations used by both the AM and the DM are the surface temperature trends, along with the corresponding heat flux densities. For the latter, the three-points formulation is chosen as in (Alongi et al., 2021):

$$\varphi_{ext}^j = -\lambda_1 \frac{3T_3^j - 4T_2^j + T_1^j}{2\Delta x} \quad (6)$$

$$\varphi_{int}^j = -\lambda_K \frac{3T_{N_{DF}}^j - 4T_{N_{DF}-1}^j + T_{N_{DF}-2}^j}{2\Delta x} \quad (7)$$

where φ_{ext} and φ_{int} are the heat flux densities at the outer and the inner edges of the domain, respectively, both positive when directed inward.

2.3 The Virtual Samples

The effectiveness of the two methods is evaluated on three walls with different thermophysical properties, used as virtual samples: a light and well insulated dry wall (W1); a heavy wall (W2); an externally insulated wall (W3). Layer sequences and material thermal properties are reported in Table 1 (density ρ , thermal conductivity λ , specific heat c and thickness s), along with the following reference quantities, calculated as follows:

- thermal conductance

$$\Lambda_{ref} = \left(\sum R_{cd,i} + \sum R_{cav,j} \right)^{-1} \quad (8)$$

- Specific heat capacity per unit area

$$C_{ref} = \sum (\rho_i \cdot c_i \cdot s_i) \quad (9)$$

- time constant

$$\tau_{ref} = \sum (R_{cd,i} \cdot C_i) \quad (10)$$

where C_i [$\text{J} \cdot \text{m}^{-2} \cdot \text{K}^{-1}$] and $R_{cd,i}$ [$\text{m}^2 \cdot \text{K} \cdot \text{W}^{-1}$] are the heat capacity per unit surface and the conductive resistance, respectively, of the i -th solid layer, $R_{cav,j}$ is the convective-radiative resistance of the j -th gap. It can be noticed that for all the walls C_{ref} is larger than $20 \text{ kJ m}^{-2} \text{K}^{-1}$.

Table 1 – names and main properties of the virtual samples

	ρ [kgm^{-3}]	λ [$\text{Wm}^{-1}\text{K}^{-1}$]	c [$\text{Jkg}^{-1}\text{K}^{-1}$]	s [m]
<i>W1 - light and insulated wall</i>				
sandwich	230	0.532	1500	0.04
rock wool	70	0.033	1030	0.2
air gap	-	-	-	0.055
rock wool	40	0.035	1030	0.04
$\Lambda_{ref} = 0.134 \text{ Wm}^{-2}\text{K}^{-1}$ $C_{ref} = 30 \text{ kJm}^{-2}\text{K}^{-1}$ $\tau_{ref} = 0.54 \text{ d}$				
<i>W2 - heavy wall</i>				
plaster	1800	0.9	1000	0.03
brick wall	1800	0.787	1000	0.425
plaster	1400	0.7	1000	0.02
$\Lambda_{ref} = 1.661 \text{ Wm}^{-2}\text{K}^{-1}$ $C_{ref} = 847 \text{ kJm}^{-2}\text{K}^{-1}$ $\tau_{ref} = 5.00 \text{ d}$				
<i>W3 - externally insulated wall</i>				
plaster	1300	0.3	840	0.03
rock wool	120	0.035	1030	0.06
hollow bricks	1000	0.163	1000	0.3
plaster	1400	0.7	1000	0.02
$\Lambda_{ref} = 0.271 \text{ Wm}^{-2}\text{K}^{-1}$ $C_{ref} = 368 \text{ kJm}^{-2}\text{K}^{-1}$ $\tau_{ref} = 6.50 \text{ d}$				

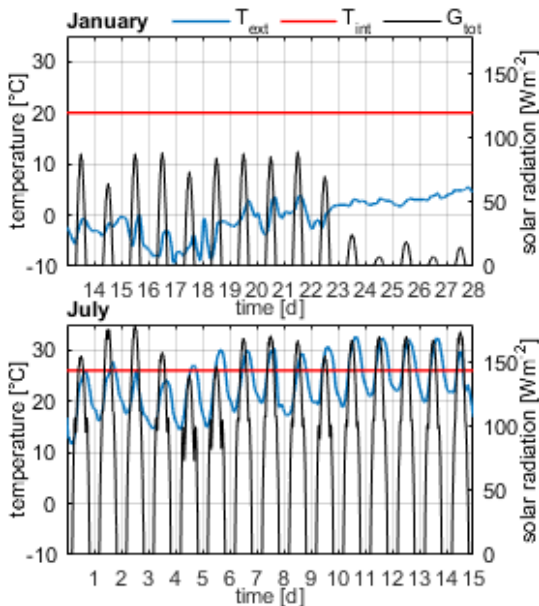


Fig. 2 – Indoor and outdoor boundary conditions for the two 14-day periods considered

As boundary conditions, two alternative indoor constant values for operative temperatures are considered: 20°C in winter (from October 15th to April 15th) and 26°C in summer (the rest of the year). Daily variations are neglected, limiting fluctuations to those caused by the outdoor conditions, which are based on the Typical Meteorological Year for Milan-Linate (Italy). More in detail, both external operative temperature and total solar radiation on a vertical surface facing North are used. Finally, even though the whole year is simulated, only the two most relevant 14-day periods are considered: from the 14th to the 28th of January for winter and from the 1st to the 15th of July for summer (Fig. 2).

3. Results And Discussion

The simulations provide the trends of the surface temperatures and the heat fluxes for each wall. For the sake of brevity, Fig. 3 shows only the results for W1 as an example, while Table 2 reports the main performance of each virtual sample (average, minimum and maximum for every quantity).

During the winter period, the three walls show stable thermal conditions, with indoor-outdoor temperature differences constant in sign. Heat flux densities, however, feature higher oscillations on the outer boundaries, with several sign inversions for all walls except W1. A more stable behavior can be observed on the indoor side (no sign inversions), with heat flux density always below 1 W m^{-2} for W1. Greater instability can be observed during the summer period, with multiple sign changes for both temperature difference and heat fluxes. These virtual measurements are then used to estimate Λ .

3.1 The Average Method Results

This method has been applied for each wall to the two complete 14-day periods, starting the average process at the beginning of each time window and considering the indoor and outdoor heat flux densities alternatively. Fig. 4 shows the conductance curves obtained in both periods for each wall investigated. The time needed to achieve a reliable estimation is actually the minimum time period

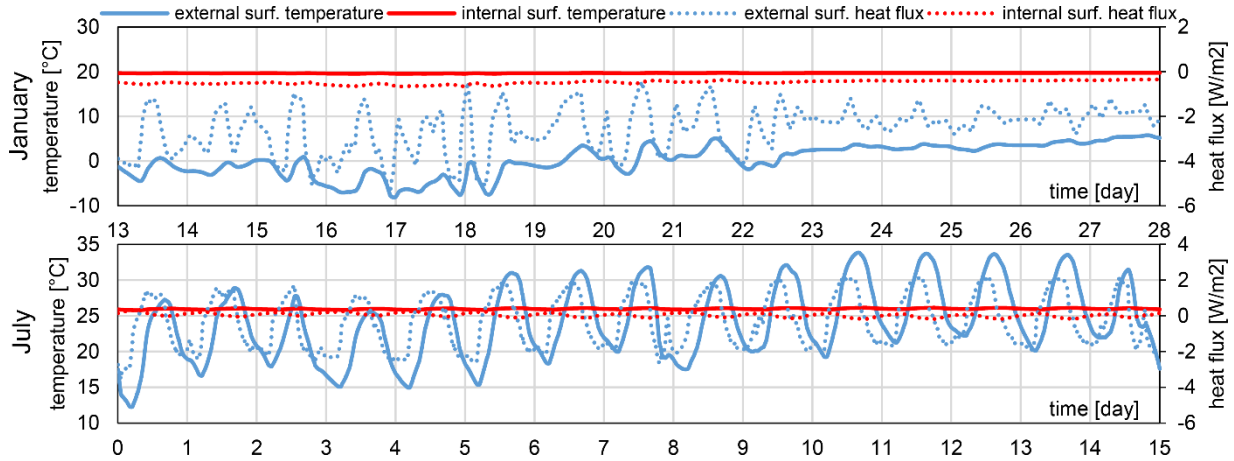


Fig. 3 – Simulation results (indoor and outdoor temperature and heat flux density fluctuations) for the W1 virtual sample

Table 2 – Average, minimum and maximum indoor and outdoor surface temperatures and heat flux densities for each virtual sample

		W1				W2				W3			
		T_{se}	T_{si}	ϕ_{ext}	ϕ_{int}	T_{se}	T_{si}	ϕ_{ext}	ϕ_{int}	T_{se}	T_{si}	ϕ_{ext}	ϕ_{int}
		[°C]	[°C]	[Wm ⁻²]	[Wm ⁻²]	[°C]	[°C]	[Wm ⁻²]	[Wm ⁻²]	[°C]	[°C]	[Wm ⁻²]	[Wm ⁻²]
Jan.	av.	0.23	19.67	-2.55	-0.48	0.58	16.48	-25.15	-27.14	-0.23	19.29	-5.04	-5.49
	min	-8.15	19.54	-5.40	-0.66	-6.63	15.69	-79.90	-33.22	-8.79	19.16	-26.31	-6.45
	max	5.78	19.76	-0.45	-0.35	5.92	17.26	28.72	-21.10	5.48	19.42	24.54	-4.44
July	av	24.12	25.97	-0.30	0.04	24.13	25.64	-2.29	2.77	24.06	25.92	-0.47	0.60
	min	12.23	25.78	-3.54	-0.18	14.31	25.01	-94.45	-2.26	12.05	25.83	-38.56	-0.24
	max	33.84	26.12	2.18	0.32	32.26	26.29	63.20	7.66	33.90	26.03	27.15	1.32

required to fulfil the constraints provided by the ISO 9869-1:2014. The main results for each wall are reported in Table 3, where *n.a.* means that for a given condition it was not possible to satisfy the standard constraints within the 14-day period. It is possible to observe that acceptable outcomes (i.e., up to 5 % accuracy) can be achieved for every wall in the winter conditions minimum period required by the standard, provided that the proper heat flow density is chosen. In general, while both W2 and W3 feature acceptable outcomes with both heat flux densities, with an improvement when the indoor one is considered, for W1 only ϕ_{ext} provides accurate results, while ϕ_{int} leads to an unacceptable value of Λ . This is possibly due to the small values of the indoor heat flux density, as a consequence of the high insulation level. Table 3 also shows that increasing the evaluation period up to 14 days does not lead to a significant improvement, as the corresponding estimated conductance Λ_{14} shows.

As far as the summer conditions are concerned, the constraints of the standard are never met for W2 and W3, while 5 days are needed for W1. However, despite satisfying the constraints given by the ISO 9869-1:2014 for W1, estimations based on the indoor

heat flux density lead to an unacceptable value of the thermal conductance ($\sim 82\%$), while with ϕ_{ext} , Λ never stabilizes around an asymptotic value (Fig. 3). This oscillatory trend is also present in W2 and W3, wherever the heat flux is measured. These analyses show that the indications provided by the standard are only partially effective: first of all, a stable heat flux is not enough to achieve a reliable estimate of the thermal conductance, but it needs to be above a threshold (even the -6 to -4 W m⁻² observed for W3 seem to suffice); more reliable outcomes are achieved with highly insulated walls when ϕ_{ext} is used. Moreover, the constraints in the standard only deal with the apparent stability of the thermal conductance estimate and can be misleading in some cases, like what happens for W1 either considering ϕ in the winter period or both heat flux densities in the summer period. Thus, the calculations required by the standard must be supported by a critical evaluation of the outcome and a visual inspection of the thermal conductance trend during the whole period.

3.2 The Dynamic Method Results

The DM has been tested on each wall considering several time windows within the two simulated periods to evaluate the shorter time needed to achieve a reliable estimation. A first sensitivity analysis demonstrated that the number of time constant has little effect on the outcomes. Thus, only one time constant is considered ($m = 1$), to reduce computational costs. Fig. 5 shows the thermal conductance and the square deviation achieved with the shorter data set, among the several investigated, used for each wall and each climate, both as function of M . Moreover, conductance trends feature the confidence interval (coloured areas), calculated as indicated by the ISO 9869-1:2014.

Outcomes for W1 are similar to those achieved with the AM: despite the better stability, φ_{int} does not

provide acceptable results, while better agreement between estimated and reference Λ is obtained using φ_{ext} . Moreover, winter conditions lead to more stable results, while summer ones show a great dependence on M . In both seasons two days are enough to achieve acceptable results (Table 3).

As far as W2 is concerned, better outcomes are achieved using the heat flux density at the indoor surface both in January and in July, with a greater stability observable in the winter period (Table 3), when two days of data are enough. Indeed, the summer period needs a three-day data set and leads to a trend with a great dependence on the M parameter and, therefore, is more difficult to interpret. Finally, W3 seems to be more difficult to investigate:

Table 3 – Main outcomes of the AM and the DM for the three virtual samples and the two periods investigated

			W1				W2				W3				
			January		July		January		July		January		July		
			int	ext	int	ext	int	ext	int	ext	int	ext	int	ext	
AM	t	$[d]$	3	3	5	5	3	5	n.a.	n.a.	3	5	n.a.	n.a.	
	Λ	$[W/(m^2K)]$	0.024	0.139	0.024	0.145	1.609	1.826	n.a.	n.a.	0.258	0.305	n.a.	n.a.	
	err.		-81.9%	3.7%	-82.0%	8.4%	-3.1%	10.0%	n.a.	n.a.	-4.5%	13.1%	n.a.	n.a.	
	Λ_{14}	$[W/(m^2K)]$	0.025	0.131	0.023	0.163	1.707	1.582	1.833	1.520	0.282	0.258	0.321	0.250	
	err.	$[\%]$	-81.7%	-2.0%	-82.5%	21.8%	2.8%	-4.7%	10.4%	-8.4%	4.3%	-4.4%	18.9%	-7.4%	
DM	best case	t	$[d]$	2	2	2	2	2	2	3	3	3	3	6	6
		N	$[-]$	575	575	575	575	575	575	863	863	863	863	1727	1727
		Λ	$[W/(m^2K)]$	0.029	0.134	0.027	0.133	1.663	1.656	1.518	2.057	0.259	0.271	0.227	0.350
		err.	$[\%]$	-78.2%	0.0%	-79.8%	-0.5%	0.2%	-0.3%	-8.6%	23.9%	-4.2%	0.5%	-15.9%	29.6%
		τ_1	$[d]$	0.85	0.12	0.63	0.13	0.48	0.01	0.07	0.08	0.24	0.01	0.17	0.16
	S^2_{loc}	M	$[-]$	86	466	76	446	296	326	786	796	726	736	1606	1636
		Λ	$[W/(m^2K)]$	0.025	0.136	0.025	0.133	1.620	1.746	1.499	2.234	0.254	0.285	0.227	0.455
		err.	$[\%]$	-81.7%	1.3%	-81.6%	-0.5%	-2.4%	5.2%	-9.7%	34.6%	-5.8%	5.5%	-15.9%	68.6%
		M	$[-]$	416	536	436	446	506	526	796	816	806	846	1606	1456

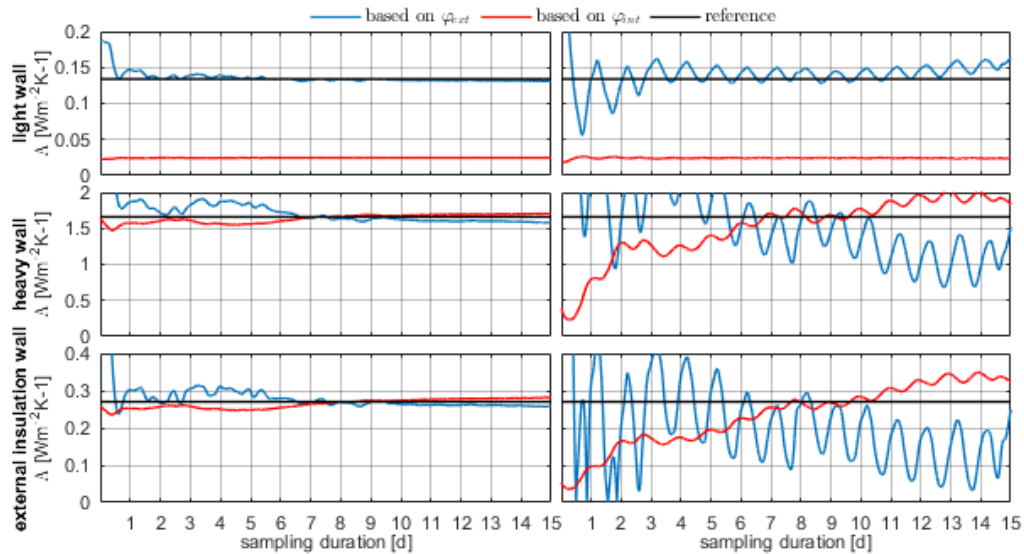


Fig. 4 – Outcomes of the AM: progressive estimate of Λ for the three walls in January and July, considering φ_{ext} and φ_{int}

three days of data are needed in winter to achieve an acceptable result, for both indoor and outdoor heat flux densities, while in summer several time frames have been considered (1 to 14 days) without success (the six-day one is shown in Fig. 5).

In general, the interpretation of the outcomes of each analysis is not straightforward: the sensitivity to M is great in several cases and the lack of clear indications by the ISO 9869-1:2014 may be an issue in a real implementation of this method, since the reference thermal conductance to validate the estimations is usually unknown. Moreover, the indication on the value of the confidence interval

mentioned previously does not provide any guidance: the fulfilment of this criterion, shown in Fig. 5 as horizontal coloured bars in the S^2 graphs, occurs for many values of M , even when the discrepancy between reference and estimated thermal conductance is unacceptable. Also, the post-fitting value of the time constant does not provide any indication about the reliability of the results: τ_1 in the best conductance estimates shown in Table 3 (grouped under *best case*) differs significantly from the respective lumped capacity reference τ_{ref} (Eq. 10), suggesting that it is not possible to assign this physical meaning to τ_1 .

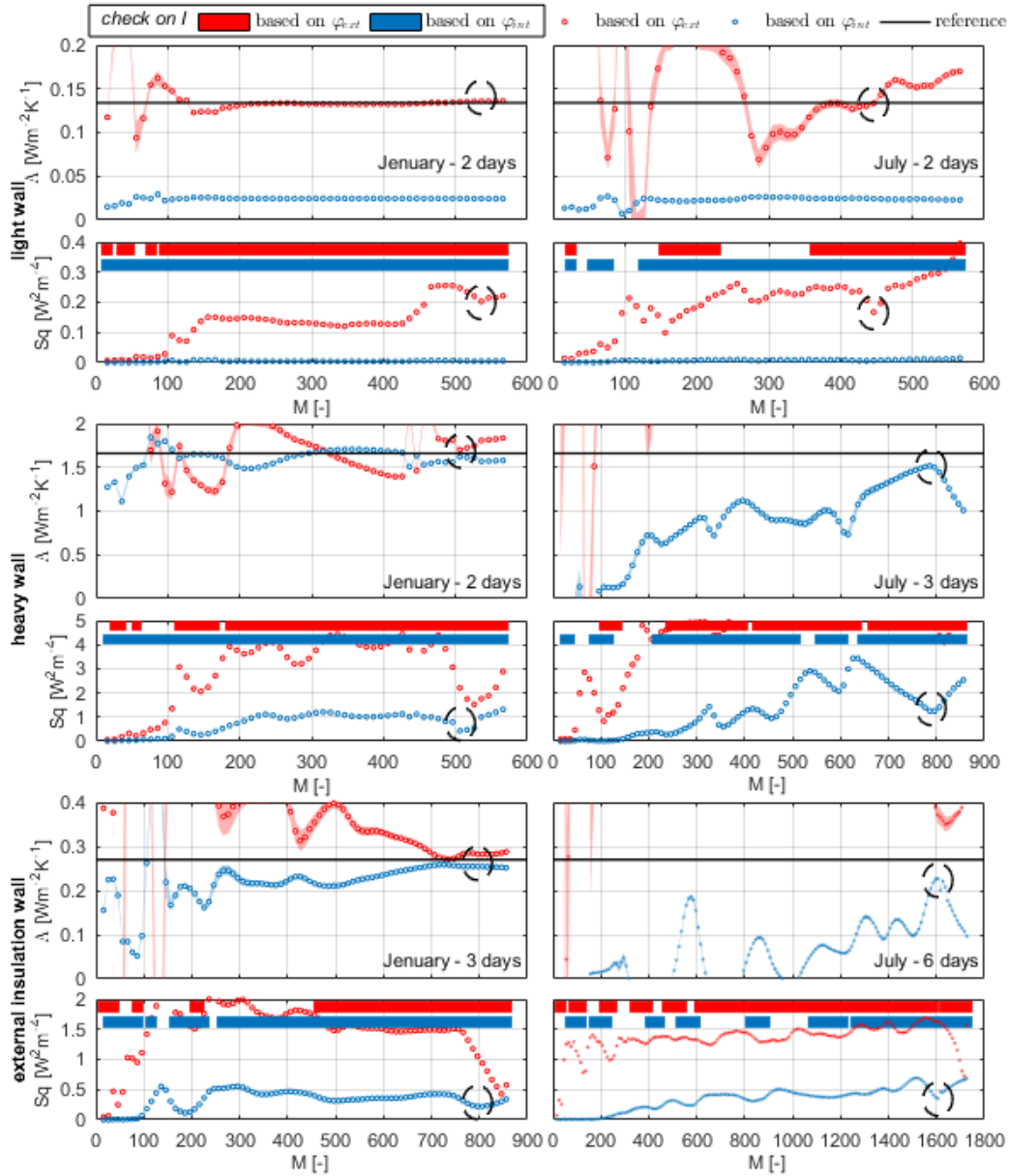


Fig. 5 – Outcomes of the DM: estimate of Δ and S^2 as function of M for the three walls in January and July, considering ϕ_{ext} and ϕ_{int}

To identify the most accurate estimate of Λ , a possible indication might come from the S^2 trend as function of M : good outcomes are indeed achieved for values of M greater than $N/2$ and corresponding to the last local minimum of S^2 (highlighted by dashed circles in Fig. 5 and grouped in Table 3 as $S^2_{loc\ min}$). This behaviour has been observed in several other cases, when different time frames have been considered. Therefore, it suggests that a technician should perform a sensitivity analysis on M and evaluate the outcomes using the S^2 trend as described above. Yet, this observation only suggests a possible line of investigation: this approach will need further analyses to provide a mathematical explanation and verify its repeatability.

4. Conclusions

This work investigates the accuracy of the post processing techniques provided by the ISO 9869-1:2014 by means of numerical simulations on three virtual wall samples, and focuses on two 14-day periods in January and July.

The analyses on the AM show that the best period to implement this technique is winter, in agreement with the standard. However, even though the latter suggests considering the heat flux density at the surface where it is more stable, it has been proven that a proper amplitude of the signal is more important than stability when dealing with highly insulated walls. Moreover, the criteria included in the standard can be misleading at times, as observed for W1, either in summer or, if φ_{int} is considered, in winter. Thus, a careful analysis of the conductance trend with time is needed to verify convergence to a stable and reasonable value.

As far as the DM is concerned, it generally leads to acceptable outcomes with acquisition periods shorter than the AM in winter, and summer measurements can be used too. W1 shows the same behavior described above, providing acceptable Λ only when the outdoor heat flux is considered in both periods. Results for both W2 and W3 are less sensitive to the choice between φ_{int} and φ_{ext} in winter, while in summer only the indoor one is useful for W2 and no reasonable outcome is obtained for W3 for every timespan considered. Dealing now with

the parameters of the method, while the number and the initial values of the time constants do not affect the final outcomes, great sensitivity on M is observed, which makes the results difficult to interpret when the method is applied, as expected, to a wall with unknown properties.

However, there is a correspondence between an acceptable thermal conductance value and the local minimum of the S^2 for M near to N . This finding will need further investigations in order for it to be confirmed and formally systematized.

References

- Ahvenainen, S., E. Kokko, and A. Aittomaki. 1980. "Thermal conductance of wall-structures" Report 54. Espoo: Technical Research Centre of Finland, Laboratory of Heating and Ventilating.
- Alongi, A., A. Angelotti, and L. Mazzarella. 2021. "A numerical model to simulate the dynamic performance of Breathing Walls". *Journal of Building Performance Simulation* 14 (2): 155-180. doi: <https://doi.org/10.1080/19401493.2020.1868578>
- Atsonios, I. A., I. D. Mandilaras, D. A. Kontogeorgos, and M. A. Founti. 2017. "A comparative assessment of the standardized methods for the in-situ measurement of the thermal resistance of building walls." *Energy and Buildings* 154: 198-206. doi: <https://doi.org/10.1016/j.enbuild.2017.08.064>
- Gaspar, K., M. Casals, and M. Gangoellis. 2018. "In situ measurement of façades with a low U-value: avoiding deviations." *Energy and Buildings* 170: 61-73. doi: <https://doi.org/10.1016/j.enbuild.2018.04.012>
- International Standard. 2014. ISO 9869-1:2014 - Thermal insulation — Building elements — In-situ measurement of thermal resistance and thermal transmittance — Part 1: Heat flow meter method.
- Lucchi, E. 2017. "Thermal transmittance of historical stone masonries: a comparison among standard, calculated and measured data." *Energy and Buildings* 151: 393-405. doi: <https://doi.org/10.1016/j.enbuild.2017.07.002>

Investigating the Performance of Different Window Opening Styles for Single-Sided Wind-Driven Natural Ventilation Using CFD Simulations

Akshit Gupta – Eurac Research, Italy – akshit.gupta@eurac.edu

Annamaria Belleri – Eurac Research, Italy – annamaria.belleri@eurac.edu

Francesco Babich – Eurac Research, Italy – francesco.babich@eurac.edu

Abstract

Natural ventilation can be an effective means of providing healthy and comfortable indoor environments while minimizing energy consumption. However, the use of diverse types of windows and control strategies usually leads to different indoor local thermal conditions. Previous studies have focused on indicators of ventilation effectiveness, but too little is known about the spatial variations of thermal comfort generated by different window opening styles. CFD is a powerful numerical modeling technique to compare the air distribution within a room, and therefore to evaluate the performances of different type of window in terms of delivered thermal comfort and indoor air quality (including local effects). Thus, the aim of this research is to investigate the effectiveness of diverse type of window, such as bottom-hung, horizontal pivot and top-hung fan-light for single-sided wind-driven natural ventilation. In this study, two wind speeds and two wind-window angles were investigated, for two weather conditions typical for the region of South Tyrol, Italy. In this study, thermal comfort was evaluated based on standards EN ISO 7730 and ASHRAE Standard 55. Using transient RANS CFD simulations, the performance of different window configurations for the different boundary conditions were numerically evaluated. The boundary conditions, geometrical simplifications, grid-independence tests, discretization, and basic principles for a transient simulation were chosen based on previous studies and then tested to ensure the correct modelling of a wind-driven natural ventilation flow. The results show 25 %-200 % higher incoming air-flow when the wind enters at an acute angle as compared with perpendicular wind. Furthermore, the horizontal-pivot window reports a 39 % higher incoming airflow when compared with bottom-hung window style, while the draught risk in winter conditions was similar for both.

1. Introduction

Across the world, buildings are a big consumer of energy. In the EU alone, buildings account for 40 % of our energy consumption and 36 % of greenhouse gas emissions (European Commission 2020). The energy in buildings is largely used for heating, ventilation, and air conditioning (HVAC) in order to achieve the necessary air changes and provide a good quality of indoor environment (Zhong et al., 2022). To reduce dependence on fossil fuels, Natural Ventilation (NV) is being widely recognised as an effective means of delivering fresh air and comfort cooling in buildings, but the performance depends greatly on design (Nomura & Hiyama, 2017; Zhong et al., 2022). A well-designed NV system can ensure removal of indoor contaminants, provide thermal comfort and occupant control at a much lower cost compared with a mechanical ventilation system (Belleri et al., 2014; Gupta et al., 2021; Zhong et al., 2022). Designing a NV strategy depends on several factors, such as opening styles, arrangement of the opening, indoor-outdoor condition, wind condition, among others (Wang et al., 2017; Zhong et al., 2022). A building's architectural arrangement is a crucial factor in incorporating a suitable NV strategy in a room. In many cases, such as residential buildings, hostels, and dormitories, openings are possible only on one side of the room, thus falling under the single-sided ventilation category (Gupta et al., 2021). Many studies in the past have focused on the performance of ventilation for single-side natural ventilation for different window configurations, but not so much on the thermal comfort aspects. This study focuses on providing a deeper understanding of efficiently using a CFD simulation tool to replicate wind-driven single-sided NV flow and

choosing different window opening styles based on parameters of ventilation effectiveness and thermal comfort, as per EN-ISO 7730, for draught risk calculations and parameters of thermal discomfort in winter conditions; and the American Society of Heating, Refrigerating and Air-Conditioning Engineers (ASHRAE) Standard 55, for thermal comfort parameters in summer conditions.

In the subsequent sections, the three different window opening types are discussed for wind-driven single-sided natural ventilation flow to evaluate parameters of ventilation effectiveness and thermal comfort for different boundary conditions and geometrical simplifications for high quality CFD simulations.

2. Methodology

A CFD study was conducted for different window configurations to evaluate the flow rates based on different internal-external pressure differences. In this section, the model configuration and geometrical assumptions considered for the CFD analysis are presented, followed by the parameters considered for comparing the performance of different window types.

2.1 Geometric Model and Discretization

In natural ventilation flows, the airflow through an opening is affected by several factors, such as the opening configuration, indoor-outdoor temperature difference, heat sources, room geometry, wind speed, direction, among others.

The geometry of one of the two test chambers of Eurac Research's Façade System Interaction Lab is used for the internal domain (8 m x 4 m x 3 m). To replicate outdoor conditions, an external domain of the size 48 m x 36 m x 12 m is used. It should be noted that the computational domains (Fig. 1) for carrying out the CFD simulations were modeled based on the conclusions of Wang et al. (2018) and Gupta et al. (2021), to accurately replicate the physics of a single-sided wind driven flow, while keeping the computational time within a reasonable range. The resulting blockage ratio of this domain size is 2.8 %, which is below the recommended

limits of 3 % (Blocken, 2015). This ensures a large enough domain for correct development of the air-flow (Liu & Niu, 2016).

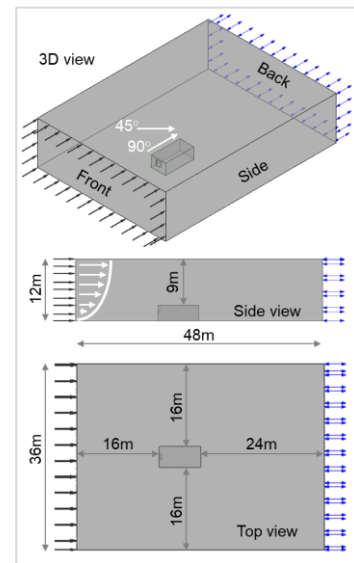


Fig. 1 – CFD model of the domains

For better flexibility, domain discretization is carried out using an unstructured meshing technique, and the mesh is finest at critical points, such as the opening, less coarse for the internal chamber and coarse for the external domain. The meshing technique, as well as the conclusions of the grid independence study inside the chamber, follow the methodology of Gupta et al. (2021). The three different window configurations considered in this study were chosen after a preliminary market analysis (Gupta et al., 2021). Fig. 2 shows the 3 window types and their opening areas. Type_1 (6° open) and Type_2 (20° open) cases have an overall area of 1190 x 1450 mm, and Type_3 (20° open) top-hung fanlight has a top area of 1190 x 450 mm, with a fixed bottom glazed area.

2.2 Basic CFD Principles

The CFD software used a parallel, implicitly coupled multigrid solver. The simulation period was 120 seconds, in transient condition, using steady-state solution for initialisation. An adaptive time-step was used, varying between 10 and 0.5 seconds, as a function of root-mean-square (RMS) courant number of 5, to keep under the residual target within 20 coefficient loops (Babich et al., 2017;

Gupta et al., 2021). A thermal energy transfer is considered, and, since the fluid is air, a Newtonian fluid, Boussinesq approximation was used to consider the buoyancy effects caused due to variations in air density, and was applied by setting up the reference buoyancy temperature equal to the glass temperature (ANSYS Inc., 2013; Babich et al., 2017; Gupta et al., 2021; Wang et al., 2018). The convergence criteria for the RMS residuals was 1e-05 and a conservation target was 0.01 (Babich et al., 2017; Gupta et al., 2021). The Reynolds-averaged Navier–Stokes (RANS) model and SST (Shear Stress Transport) k- ω turbulence model were selected to effectively solve the airflow characteristics (ANSYS Inc. 2013; Gupta et al., 2021; Babich et al., 2017; Zhong et al., 2022). All the simulations were performed with Ansys CFX 2021, and meshing with Ansys ICEM, on a work-station of 16 GB RAM and a 6-core Intel Xenon Gold 6154 CPU.

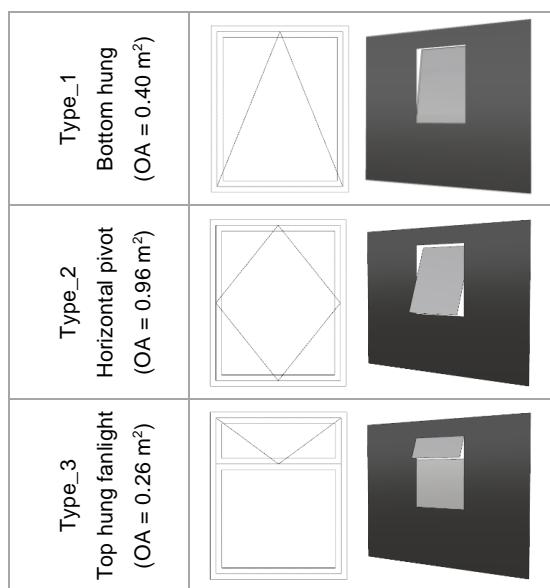


Fig. 2 – Window configurations (OA = opening area)

2.3 Boundary Conditions

Two weather conditions representing typical winter and summer conditions, with internal–external temperature of 20 °C – 10 °C and 30 °C – 25 °C, were considered. Table 1 shows the boundary conditions and temperatures for each domain.

The glass temperature was set to an approximate average of the two domains and is also used as the reference buoyancy temperature as well. The wind force is applied at the front face of the external

domain as an inlet condition, and the wind speed is defined based on the power law, as per Eq. 1:

$$u = u_{\text{ref}} \cdot \alpha \cdot (y/y_{\text{ref}})^{\gamma} \quad (1)$$

where u is the wind speed at y height on the surface, and u_{ref} is the reference velocity of 1 m/s, at a reference height of y_{ref} (equal to the Lab height 5 m), as shown in Fig. 1 (side view), and parameters $\alpha=1$, $\gamma=0.143$ refer to a terrain with few trees or small buildings (Wang et al., 2018; Yi et al., 2019).

Table 1 – Boundary conditions and temperatures (air/surface)

Location	Boundary Condition	Temperature	
		Winter	Summer
(a) Chamber Air		20 °C	30 °C
Wall surfaces	No-slip	20 °C	30 °C
Ceiling surface	No-slip	20 °C	30 °C
Floor surface	No-slip	23 °C	30 °C
Window Glass	No-slip	14 °C	28 °C
(b) External Domain Air		10 °C	25 °C
Top surface	Free slip	10 °C	25 °C
Front surface	Inlet	10 °C	25 °C
Ground surface	No-slip	10 °C	25 °C
Side surfaces	Free slip	10 °C	25 °C
Back surface	0Pa opening	10 °C	25 °C
Window Glass	No-slip	14 °C	28 °C

Two wind speeds (1 m/s and 2 m/s), and two wind angles (90°-wind coming perpendicular to the window from the front, and 45°) were chosen for this study, as representative conditions of the region of South Tyrol, Italy. For the wind angle of 45°, the inner domain was rotated for the CFD simulations, as represented in Fig. 1 (3D view), while the external domain remains the same.

2.4 Performance Parameters

The main parameters of ventilation effectiveness and thermal comfort, to compare the performance of different windows, are based on a previous study on buoyancy-driven single sided NV flow (Gupta et al., 2021):

1. Temperature profile – the temperature contour at the vertical plane in the middle of the room.
2. Velocity field – the velocity fields at the same vertical plane in the middle of the room.
3. Incoming airflow rate (Q) – the airflow rate entering the room through the window.

4. Mean Age of Air (MAA) – average time the air entering a building through an opening takes to reach a specific point in the zone (Zhong et al., 2022). It is calculated locally at every point in space, as a scalar quantity in the CFD solver (Gupta et al., 2021).
5. Air changes per hour (ACH) – the total number of times the air inside a space is completely replaced in one hour, as per the Eq. 2:

$$ACH = (Q / V) * 3600 \quad (2)$$
 where Q is the incoming airflow rate (m³/s), and V is the total volume (m³).
6. Effective penetration depth – the longitudinal distance traveled by the air entering from the inlet inside the room. This indicator represents the effective ventilating ability of NV and is an important parameter for single-side ventilated spaces (Zhou et al., 2021). For the context of this study, a maximum length of 8 m is considered.
7. Discharge coefficient (C_d) – this is a function of volume flow rate and pressure difference for a fluid flowing through an opening. It is calculated by rearranging the orifice equation (Yi et al., 2019).

$$C_d = Q / A \cdot \sqrt{\rho/2\Delta p} \quad (3)$$
 where Q is the airflow rate entering the opening (m³/s), A is the opening area (m²), ρ is the air density in the room (kg/m³) and Δp is the difference between the pressure at the opening area and in the room (Pa).
8. Temperature stratification – the difference in temperature along different planes based on EN ISO 7730 and ASHRAE Standard 55, in order to estimate the local thermal discomfort: (a) vertical air temperature difference between the head level (1.8 m from the floor for standing, and 1.1 m from the floor for sitting position) and ankles (0.1 m from floor), and (b) temperature difference at distances 0.5 m, 1 m, 1.5 m and 2 m from the window.
9. Draught risk (DR) – the discomfort caused in winter due to draught is calculated using Eq. 4 (Section 6.2 EN ISO 7730-2005):

$$DR = (34 - t_a) \cdot (v_a - 0.05)^{0.62} (0.37 \cdot v_a \cdot T_u + 3.14) \quad (4)$$
 where t_a is the local air temperature (°C), v_a is the local mean air velocity (m/s), and T_u is the local turbulence intensity (%).

10. Mean air velocity at different heights – the average air velocity at 1.8 m, 1.1 m, and 0.1 m distance above the floor. Based on EN ISO 7730, the effects on the perceived air temperature due to variations in air velocity is evaluated.
11. Mean air velocity near surfaces – this helps to compare the convective heat transfer which is enhanced due to the fluid motion near the surface. Predicting the air velocity near surfaces can be very complicated, but using CFD it can be computed. The air velocity is averaged at a plane 5 cm away from each surface.

3. Results And Discussion

Based on the performance parameters listed in Section 2.4, the results are discussed in this section.

1. Temperature distribution – in Fig. 3 the thermal profiles are presented at the vertical plane in the middle of the room for the wind at a 90° angle. The focus is laid on the inner chamber, without showing the entire external domain. The air enters inside differently according to the different window opening styles and modifies the indoor environment differently. A greater drive of buoyancy is seen at 1 m/s speed, where the colder outdoor wind enters from the lower parts of the window, such as the winter case for Type_1 and Type_2. On the contrary, for 2 m/s wind, the colder wind from outside is dominant and enters through the upper portions. Type_2 shows higher inflow and lower indoor temperatures. In winter conditions, the reduction in the mean indoor temperature for Type_1 at 2 m/s is only 0.6 % higher than the reduction achieved at 1 m/s, whereas for Type_2 this difference is 6.3 %. While in summer, the reduction for Type_1 is only 1.1 %, and for Type_2 is 12.2 %. Type_3 shows a much lower incoming airflow, higher indoor temperature, and a more homogeneous distribution due to low opening area. Up until the part to which the wind penetrates, the profiles are similar to the thermal profiles at the central plane of Wang et al. (2018).

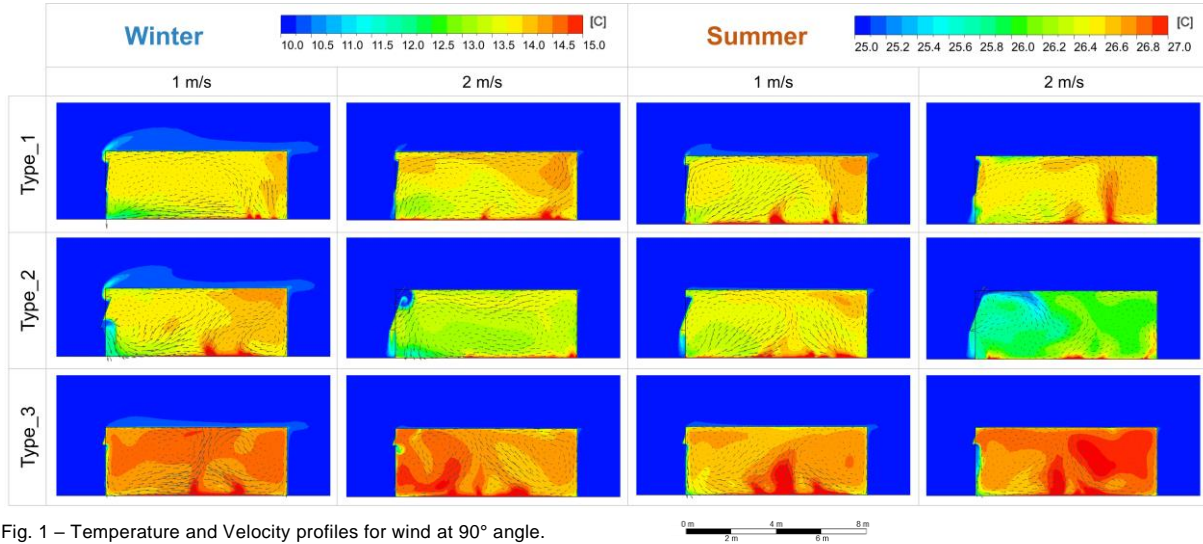


Fig. 1 – Temperature and Velocity profiles for wind at 90° angle.

2. Velocity fields – the velocity profile in the inner chamber, for wind at a 90° angle, are shown in Fig. 3. In the winter case, at lower speed, the buoyant forces are dominant, due to high temperature differences. For Type_3, the buoyancy forces are always dominant due to the geometrical configuration of the window, which does not allow the wind to directly enter inside, and the cold air can be seen entering the lower part and immediately falling. Similar fields for these types of windows can be noticed in the results obtained by Wang et al. (2018), but a direct comparison is not possible due to different opening sizes.
3. Incoming airflow rate (Q) – as shown in Fig. 4 (a), Q varies largely by the opening types, wind angle and wind speed, and not due to the indoor-outdoor temperature conditions tested. Q for summer and winter conditions do not vary more than 20 %, except for Type_2 for 1 m/s

wind at a 90° angle when Q in summer conditions is 33 % less than in winter conditions. Based on wind speed, Q for 2 m/s wind is always higher than Q for 1 m/s wind, with the minimum difference of 44 % for Type_1 for wind at 45° in winter, up to a maximum of 342 % higher rate for Type_2 for wind at 90° in summer. Based on the angle of wind, Q is always higher for wind at a 45° angle, with a difference of 25 % for Type_1 for 2 m/s wind in summer, up to 210 % for Type_3 for 2 m/s wind in winter and both speeds in summer. This is due to the geometrical advantage of wind coming at an angle and entering indirectly.

4. Mean Age of Air (MAA) – as shown in Fig. 4 (b), for the same wind speed and angle, MAA in summer is higher than in winter conditions, because the air changes are slower for lower temperature differences in the summer case, except for Type_2 for 2 m/s wind at a 90° angle where MAA in summer is 17 % lower than in

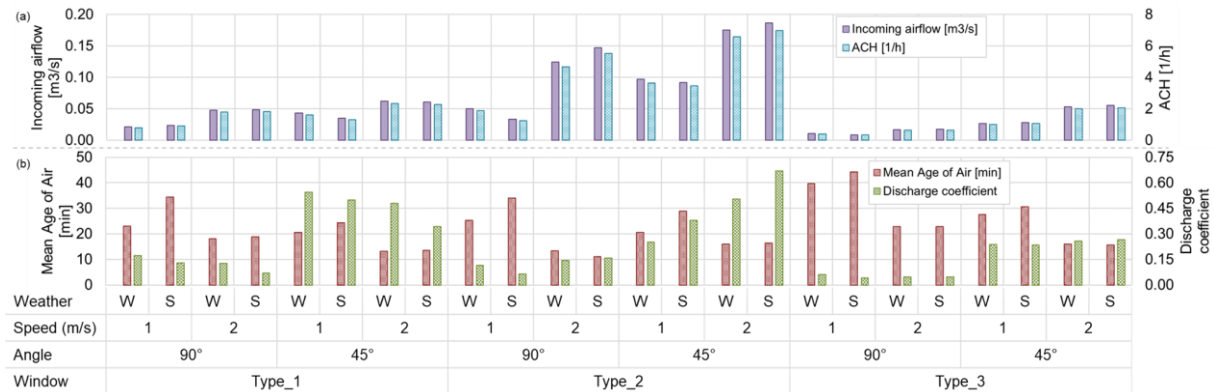


Fig. 2 – Results for (a) incoming airflow and air changes per hour (ACH); (b) mean age of air and discharge coefficient. [W=winter, S=summer]

winter conditions. Based on the wind speed, MAA for 2 m/s is always lower than for 1 m/s wind, from 22 % lower for Type_1 for wind at 90° in winter, as well as for Type_2 for wind at 45° in winter, up to 67 % lower for Type_2 for wind at a 90° angle in summer, due to the corresponding lower Q. For the same wind speed and temperature, MAA for wind at 45° is lower than wind at a 90° angle, except for Type_2 for 2 m/s wind in both weathers.

5. Air changes per hour (ACH) – trends for ACH are observed similar to Q. On comparison with previous studies, ACH for Type_2 shows consistent behavior on increasing wind speed, as well as the range of ACH being consistent for the two wind speeds (Wang et al., 2018).
6. Effective penetration depth – as visible in the velocity profile at the vertical plane in the middle of the room, shown in Fig. 3, it can be observed that the effective penetration depth in all cases varies for each window type, as the influence of the incoming air is different.
7. Discharge coefficient (C_d) – shown in Fig. 4 (b), the C_d of the same type of window varies largely with temperature, wind speed and wind angle, as concluded by previous studies (Heiselberg et al., 2001; Karava et al., 2004; Yi et al., 2019). Based on the wind speed, Type_1 always shows a low C_d for 2 m/s speed, whereas the other Type_2 shows a high C_d at 2 m/s wind. This is due to the geometrical structure of the window opening. Based on the wind angle, C_d is always higher for wind at a 45° angle, with a minimum difference of 118 % for Type_2 for 1 m/s wind in winter, up to 500 % higher for Type_2 for 2 m/s wind in summer. The variation of C_d with wind angle is consistent with the conclusions of Yi et al. (2019), and is due to decreased resistance, as also noticed with the incoming airflow rate.
8. Temperature stratification – the temperature differences at different heights and distances from the window are represented in Fig. 6 (a). More stratification is noticed in winter, due to higher indoor-outdoor temperature difference. The maximum differences at the horizontal and vertical planes are seen for Type_2 in winter for 2 m/s wind at a 90° angle, whereas in the

summer cases, the overall differences are quite low. This shows a good level of air mixing inside the chamber. The temperature differences between head level (1.1 m) and ankles (0.1 m) are in accordance with Category A of ISO 7730, since it is always lower than 2 °C in all cases (Section A.3 EN ISO 7730-2005), and in accordance with ASHRAE 55 (Section 5.3 ASHRAE Standard 55-2017).

9. Draught risk (DR) – Fig. 5 shows the DR and mean indoor temperatures in winter. The maximum DR of 15.8 % is observed for Type_2 at 2 m/s wind at a 45° angle. For the same wind angle, DR is always observed as higher for wind speed 2 m/s, up to 29 % higher for Type_2 for wind at a 90° angle, due to higher mean air velocity indoors. Based on wind angle, DR is always higher for wind at a 45° angle. The thermal environment lies in Category B of the ISO 7730, since DR lies between 10-20 % (Section A.1 EN ISO 7730-2005).
10. Mean air velocity at different heights – as represented in Fig. 6 (b), higher velocity of air is observed at the lowest level of 0.1 m, because of colder air entering and flowing downwards. Based on the ISO 7730, for occupancy similar to office spaces, the maximum mean air velocity lies in Category B for both winter and summer cases (Section A.4 EN ISO 7730-2005).
11. Mean air velocity near surfaces – as per Fig. 6 (b), air velocity is higher near the floor surface and lowest near the ceiling. A maximum of 0.21 m/s is observed near the sidewall for Type_1 for 2 m/s wind at a 45° angle. Due to higher velocity at the floor, a heat source near the floor could be a good option for promoting convective heat transfer, as it is enhanced due to the fluid motion near the surface.

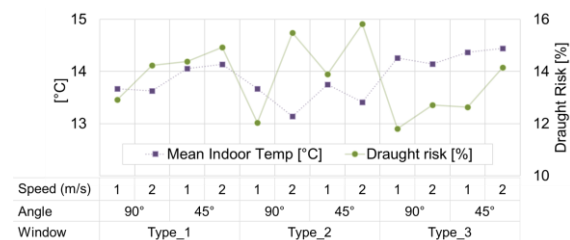


Fig. 5 – Draught risk and mean indoor temperatures in winter for the different window types in different weather conditions

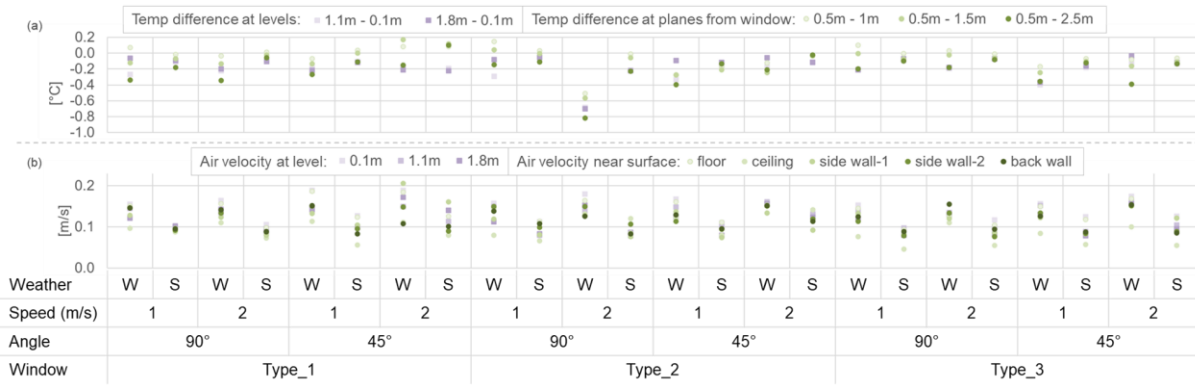


Fig. 6 – Results showing (a) temperature differences at various levels, and (b) air velocity. [W=winter, S=summer]

4. Conclusion

The aim of this study was to investigate the effectiveness of different types of windows for single-sided wind-driven natural ventilation using CFD simulations. A methodology of geometrical modeling of a one-room zone, which is a common condition for student dormitories and many residential apartments with openings only on one side, was studied. The model considered was tested for three different window configurations, two weather conditions, two wind speeds and two different wind angles. The performance of the windows was tested for its ventilation performance, as well as thermal comfort.

It was observed that the ventilation performance is sensitive to the ambient conditions, but for the different opening configurations this sensitivity varies. At low wind speed (1 m/s), the buoyant forces dominate, whereas at higher wind speed (2 m/s), the wind pressure becomes dominant and air enters from the upper portions of the windows. Based on wind speed, for 2 m/s wind, the incoming airflow and air changes per hour are always higher, whereas the mean age of air is always lower when compared with 1 m/s wind. Based on wind angle, for the wind at a 45° angle, the airflow and the air changes per hour are always higher, whereas the mean age of air is generally lower when compared with wind at 90° to the window. The mean age of air in summer is generally higher than in winter, because the air changes are slower for lower temperature differences in the summer case.

The discharge coefficient is dependent on various factors, and the traditional concept of a unique

constant discharge coefficient is not suitable, as the value obtained in the cases modeled was generally below the recommended value of 0.6, which can overestimate the natural ventilation performance. Type_2 (horizontal pivot) shows an increase in discharge coefficient for increasing wind speed, whereas Type_1 (bottom-hung) shows inverse behavior. Based on the wind angle, the discharge coefficient is always higher for wind at a 45° angle. For Type_2 (horizontal pivot) window, higher differences of temperature at different vertical and horizontal places were observed. Based on wind speed, the draught risk is higher for 2 m/s wind, and, based on wind angle, it is higher for wind at a 45° angle. The air velocities are generally high at lower heights, which can promote convective heat transfer.

Therefore, for different window configurations, the aspects of local weather conditions, such as wind speed, angle, indoor-outdoor temperature, should be carefully considered by the designers to better determine ventilation performance and the natural ventilation strategy for each context.

Acknowledgement

The research presented in this paper is supported by funding from the European Regional Development Fund POR FESR 2014-2020 of the Province of Bolzano, under Project number 1116, NEW-AIR: Nuovo approccio per una qualità degli ambienti interni energeticamente efficiente: ricerca e aziende fanno sistema in Alto Adige (English: New approach for an energy efficient IEQ: research and firms systemizing cooperation in South Tyrol).

References

- ANSYS Inc. 2013. "ANSYS CFX Solver Modeling Guide 15.0."
- Babich, F., M. Cook, D. Loveday, R. Rawal, and Y. Shukla. 2017. "Transient Three-Dimensional CFD Modelling of Ceiling Fans." *Building and Environment* 123: 37–49. doi: <https://doi.org/10.1016/J.BUILDENV.2017.06.039>
- Belleri, A., R. Lollini, and S. M. Dutton. 2014. "Natural Ventilation Design: An Analysis of Predicted and Measured Performance." *Building and Environment* 81: 123–38. doi: <https://doi.org/10.1016/J.BUILDENV.2014.06.009>
- Blocken, B. 2015. "Computational Fluid Dynamics for Urban Physics: Importance, Scales, Possibilities, Limitations and Ten Tips and Tricks towards Accurate and Reliable Simulations." *Building and Environment* 91: 219–45. doi: <https://doi.org/10.1016/J.BUILDENV.2015.02.015>
- European Commission. 2020. "Energy Efficiency in Buildings." February 17. https://ec.europa.eu/info/news/focus-energy-efficiency-buildings-2020-lut-17_en
- Gupta, A., A. Belleri, and F. Babich. 2021. "Evaluating the Performance of Different Window Opening Styles for Single-Sided Buoyancy-Driven Natural Ventilation Using CFD Simulations." In *Proceedings of Building Simulation 2021 Conference*. Bruges, Belgium.
- Heiselberg, P., K. Svidt, and P. V. Nielsen. 2001. "Characteristics of Airflow from Open Windows." *Building and Environment* 36(7): 859–69. doi: [https://doi.org/10.1016/S0360-1323\(01\)00012-9](https://doi.org/10.1016/S0360-1323(01)00012-9)
- Karava, P., T. Stathopoulos, and A. K. Athienitis. 2004. "Wind Driven Flow through Openings-A Review of Discharge Coefficients." *International Journal of Ventilation* 3(3). doi: <https://doi.org/10.1080/14733315.2004.11683920>
- Liu, J., and J. Niu. 2016. "CFD Simulation of the Wind Environment around an Isolated High-Rise Building: An Evaluation of SRANS, LES and DES Models." *Building and Environment* 96: 91–106. <https://doi.org/10.1016/J.BUILDENV.2015.11.007>
- Nomura, M., and K. Hiyama. 2017. "A Review: Natural Ventilation Performance of Office Buildings in Japan." *Renewable and Sustainable Energy Reviews* 74: 746–54. doi: <https://doi.org/10.1016/J.RSER.2017.02.083>
- Wang, J., S. Wang, T. Zhang, and F. Battaglia. 2017. "Assessment of Single-Sided Natural Ventilation Driven by Buoyancy Forces through Variable Window Configurations." *Energy and Buildings* 139: 762–79. doi: <https://doi.org/10.1016/J.ENBUILD.2017.01.070>
- Wang, J., T. Zhang, S. Wang, and F. Battaglia. 2018. "Numerical Investigation of Single-Sided Natural Ventilation Driven by Buoyancy and Wind through Variable Window Configurations." *Energy and Buildings* 168: 147–64. doi: <https://doi.org/10.1016/J.ENBUILD.2018.03.015>
- Yi, Q., X. Wang, G. Zhang, H. Li, D. Janke, and T. Amon. 2019. "Assessing Effects of Wind Speed and Wind Direction on Discharge Coefficient of Sidewall Opening in a Dairy Building Model – A Numerical Study." *Computers and Electronics in Agriculture* 162: 235–45. doi: <https://doi.org/10.1016/J.COMPAG.2019.04.016>
- Zhong, H.Y., Y. Sun, J. Shang, F.P. Qian, F.Y. Zhao, H. Kikumoto, C. Jimenez-Bescos, and X. Liu. 2022. "Single-Sided Natural Ventilation in Buildings: A Critical Literature Review." *Building and Environment* 212: 108797. doi: <https://doi.org/10.1016/J.BUILDENV.2022.108797>
- Zhou, J., Y. Hua, Y. Xiao, C. Ye, and W. Yang. 2021. "Analysis of Ventilation Efficiency and Effective Ventilation Flow Rate for Wind-Driven Single-Sided Ventilation Buildings." *Aerosol and Air Quality Research* 21(5): 200383. doi: <https://doi.org/10.4209/AAQR.200383>

The Management of the Energy Performance Simulation of a Complex Building Portfolio. The Case of the School Building Asset of an Italian Municipality

Claudia Bo – Politecnico di Milano, Italy – claudia.bo@polimi.it

Enrico De Angelis – Politecnico di Milano, Italy – enrico.deangelis@polimi.it

Andrea Augello – Politecnico di Milano, Italy – andrea.augello@polimi.it

Abstract

This paper aims at presenting a methodology for the management of multiple energy simulations of complex building assets. The educational buildings of the Milan municipality have been chosen as case studies: several retrofit strategies are tested on hundreds of buildings, evaluating their feasibility and calculating the potential energy savings. The results, obtained with dynamic simulations using SketchUp and the “Intelligent Community Design (iCD)” plugin, are then compared with a static calculation implemented on a regional scale in Lombardy. Besides, a methodology for the collection of the input parameters is proposed, based on the combination of data coming from several sources.

1. Introduction

Due to the increasing risks derived from global warming, proved to be caused by human activities, a dramatic reduction of the greenhouse gas emissions in the atmosphere will be crucial in the near future (Pörtner et al., 2022). The built environment plays a dominant role, since it is one of the largest sources of direct and indirect greenhouse gas emissions (36 %, in Europe) and the share (40 %, *ibid.*) of energy consumption. In this framework, urban areas play a fundamental role and are deeply involved in meeting the main decarbonization objectives. Educational buildings account for a small percentage of built stock (about 4 % of the European one, in terms of net floor area, and even less, about 3 %, in terms of energy consumption, due to their short time use, (Re Cecconi, 2020)), but they represent a critical asset, in particular in Italy (we can refer to the periodic reports edited by Legambiente and the

most recent one in particular, Legambiente 2021), because of their age, their maintenance needs and, in general, their social role. Unfortunately, a precise understanding of the energy and carbon footprint of the built asset is rare and often unreliable (this is particularly true for the Italian educational building asset; the Legambiente 2021 report, for example, mentions that the energy-rated buildings are less than ¼ of the total). Data – when easily available – report consumptions only as averages and even their physical description is often unreliable (but improving, see the MIUR OpenData). As a consequence, energy retrofit strategies are usually referred to as one or more “typical” buildings or “archetypes”, representatives of the average energy need of the asset and the average retrofit potentials, without defining the real priorities of the asset. This approach is investigated by Mohammadizazi et al. (2021), who estimated the energy performances of the commercial building stock in Pittsburgh by analyzing twenty building archetypes with a dynamic tool, i.e., EnergyPlus. The same methodology was applied by Caputo et al. (2013), who proposed the estimation of the energy consumption of residential and commercial buildings in Milan, analyzing 56 archetypes different in geometry, construction period, and function. Also, in this case, they use a dynamic tool, i.e., EnergyPlus, whose results were later validated and compared with the energy consumptions reported in the SIRENA (Sistema Informativo Regionale Energia Ambiente) database. Another dynamic tool, i.e., DOE-2.2, was adopted by Krarti et al. (2020) to analyze 54 building archetypes and assess the energy and non-energy benefits in investing in retrofitting existing residential building stock in

Saudi Arabia. Other authors prefer to assess the energy performances of building archetypes using steady-state methods, using Microsoft Excel (Tuominen et al., 2014) or national energy certification software (Dascalaki et al., 2016). Other methods used for the energy analysis of building archetypes are based on the EN ISO 13790 (Yang et al., 2020; Yang et al., 2022) or multiple regression analysis (Wong et al., 2019). Bottom-up approaches without building archetypes were studied by Costanzo et al. (2019) and Wang et al. (2018). Costanzo et al. (2019) developed a bottom-up engineering approach applied to the Yuzhong District of Chongqing municipality in China, based on EnergyPlus with the Urban Modeling Interface. Similarly, Wang et al. (2018) analyzed the energy demand and the retrofitting potential for three Swiss residential districts of Zurich and Zerne, adopting a bottom-up approach without building archetypes based on EnergyPlus. Other bottom-up approaches investigated are based on statistical methods, e.g., multiple linear regression techniques, as proposed by Mastrucci et al. (2014), Torabi Moghadam et al. (2018), and de Rubeis et al. (2021). These methods can predict the energy consumption on a large scale with reduced computational time and without the need for complex input data as with the physics-based models. The advantages of physical models and data-driven methods are combined and investigated by Li & Yao (2021) and Zygmunt & Gawin (2021), who proposed hybrid approaches based on building archetypes with machine learning and artificial neural network models, respectively. Other analysis methods are based on the energy performance certificates available, as demonstrated by Hjortling et al. (2017) and Gangolells et al. (2016), who respectively mapped the energy performances of existing Swedish and Spanish buildings.

This paper presents a methodology for the assessment of energy retrofit scenarios applied to Italian educational buildings. The energy performances of the school buildings belonging to the Milan municipality were assessed with both dynamic and steady-state tools, testing the effect of three retrofit strategies. The research allowed us to evaluate the energy consumption innovatively; it eliminates the concept of the archetype: the whole urban area of Milan was modeled, assessing the energy perfor-

mances of each school building. Furthermore, it gave us a clear idea about the available database open sources, cross-checking of the input data, mainly about the buildings' geometry and envelope/plant properties, thus increasing the model reliability and finding a compromise when data were missing.

2. Methodology

2.1 Data Sources and Reliability

This paragraph describes the primary data sources of the modelled school buildings and their related uncertainties. The geometrical models are based on geographic information system (GIS) data, which were later compared with AutoCAD drawings; the buildings' characteristics are obtained from several data sources, such as European projects, national open data, energy performances certificates, etc.

GIS data: OpenStreetMap and Lombardy geographical data

OpenStreetMap (OSM), a crowd-sourcing editable world map, is currently the biggest freely available geodata platform; it provides different kinds of open data, such as building footprints, function, name, height, etc. These maps are based on polylines created with GPS tracks, satellite photos, and various data provided by local governments or volunteers. However, OSM contains two main levels of errors: a systematic one due to the uncertainty of the GIS data, and a casual error, i.e., an unpredictable error due to the inaccuracy of users themselves; besides, for many buildings, we observed an additional lack of information, for example, related to the height of the buildings, which was not consistent with the real values. To overcome these uncertainties, the GIS database of the Lombardy region and the city of Milan was analyzed, visualizing their metadata (shapefile, JSON or CSV format, raster data) on the software QGIS.

AutoCAD drawings

The plans, sections, and elevations for about 20 school buildings, provided as AutoCAD files by the Municipality of Milan, have been analyzed to validate the geometrical information reported in the other data sources.

IEE TABULA project database

The Intelligent Energy Europe Tabula project, published in May 2012 and updated in July 2014, assesses the energy performances of the existing Italian residential buildings, predicting the impact of retrofit measures on both building envelope and plants. This project is chosen as a reference since it contains useful information about the building envelope components: according to the period of construction, it provides a general description of its typical construction elements with their related thermal performances.

Ministero dell'istruzione, dell'università e della ricerca (MIUR) open data

The Italian ministry of education, university, and research provide open data about the whole Italian school asset. For each Italian school, represented by a unique building code, data about location, total areas, and volumes, number of floors, typology of installed plants, year of construction, etc. is provided.

Energy Performance Certificates

The Energy Performance Certificates (EPCs) of the Lombardy region provide more detailed information about the school building asset: heated surfaces and volumes, typology of installed plants, electricity and gas consumptions, envelope thermal transmittances, primary energy consumptions, etc. However, these data are not available for all school buildings, since they refer only to the Italian schools having certified energy performances. Besides, another limitation of these data is related to the certified building unit: in many cases, the energy certificate is provided only for a part of the entire school building, and therefore, in these cases, the data are not representative of the whole building.

EnergyPlus Weather data

The chosen weather data come from the World Meteorological Organization Region and Country and is referred to as a Typical Meteorological Year based on the Milano Malpensa climate. Due to the distance between the airport weather station and the city center, a source of uncertainty arises, since the weather file does not consider the urban heat island effect, which could determine an increased air temperature for several parts of the city.

2.2 Calculation Methods

Two calculation methodologies were chosen: a dynamic one, based on the simulation tool “Intelligent Community Design (iCD)” and applied to 277 educational buildings in Milan, and a steady-state one, based on the UNI/TS 11300-1 and applied to 1036 educational buildings of Lombardy. The first one is a plug-in to SketchUp, a 3D master planning modeling tool able to perform energy analysis scalable from individual buildings up to entire cities. It could be used for both new interventions and retrofit projects, assessing: the heating and cooling energy consumption, the effects of retrofit strategies on the overall performances (i.e., addition of insulation to the building envelope, replacement of the HVAC systems, etc.), energy produced with renewable sources, accessibility to transport and amenities, total building water consumption, etc. The building geometries can be drawn manually on SketchUp or imported from the OpenStreetMap database; all the other characteristics of the buildings can be later assigned by choosing from lists of predefined values. The applied steady-state method is a simplification of the procedure described in the UNI/TS11300-1 standard, and it aims at calculating the final and primary energies according to the following equations:

$$Q_U = (Q_L - \eta Q_G) / \epsilon_P \quad (1)$$

$$EP_H = Q_U \cdot fp_{nren} \quad (2)$$

For the steady-state calculations, the following hypothesis was assumed: an average air change per hour of 0.4 was considered for each school building, without any heat recovery; the transmission losses were calculated starting from the average envelope thermal transmittances, calculated as weighted values. Concerning the total gains, intended as the sum of internal and solar gains, reference was made to the UNI 10349 for the climatic data and the UNI/TS 11300-1 for the applied average internal gains, equal to 4 W/m²; besides, a boiler efficiency of 0.83 was assumed to consider the possible losses of the building's systems. In the end, a primary energy conversion of 1.05 was used to estimate the primary energy, choosing natural gas as the primary energy source.

2.3 The Building Geometrical Model

Starting from the OpenStreetMap database, the volumes of all the buildings in Milan were modeled. However, the chosen database contains uncertainties and inaccuracies, mainly linked to the footprint area and height of the buildings: for this reason, the geometry of about 20 educational buildings was later checked and compared with detailed AutoCAD drawings; the rest of the school buildings were instead checked with the data, even if approximate, provided by Google Earth, since no architectural drawings were available for those buildings. The geometric GIS data of different layers are metadata containing technical information and are identified by alphanumeric codes. The school's name or its unique identification code is the link between the geometric and the envelope information. Three actions were performed to achieve the input data needed for the steady-state calculations, based on "Scuole Lombardia", "A020101" and "corpo edificato massima estensione" layers:

- 1) Filtration in Mapshaper Console: the volumetric unit who have "servizio pubblico - istruzione - sede scuola" were considered.
- 2) Data Process in Qgis: NN Join Plugin, based on the shorter distance, linked the school's name with the geometry.
- 3) Data transformation: the surface to volume ratio (S/V) was calculated for all the Lombardy schools based on the procedure proposed by Vicentini and Mutani (2012).

Moreover, the calculated volumes of the buildings were used as reference to check the ones provided by MIUR open data.

2.4 The Building Technological Model

The Lombardy Region Database and MIUR provide very useful but generic information, giving a general description of the building envelope (e.g., "double glazing" or "single glazing" as information for the windows). On the contrary, the Certificazione Energetica degli Edifici (CENED) data provide more specific information that could be, however, as stated in the previous paragraph, related to a small portion of the school buildings modeled. For this reason, the envelope properties were estimated starting from the IEE TABULA project database,

assigning the material properties according to the buildings' year of construction. The chosen thermal properties are shown in Table 1.

Table 1 – Envelope thermal transmittance [$\text{W/m}^2\text{K}$] according to the construction year of the buildings (dynamic and steady-state models)

	?-1975	1976-1990	1991-2005	After 2006
Roof	2.02	1.05	0.68	0.3
Ext. wall	1.74	0.79	0.6	0.34
Int. floor	2.28	0.93	0.65	0.36
Windows	5.23	3.17		2.3
Ground floor	0.79	0.79	0.79	0.79
Int. wall	1.06	0.76 - 0.59		

However, not all the building characteristics were defined using the previously cited sources of data, due to their limitations in terms of information provided. For example, the window to wall ratios (WWR), i.e., the ratio between glazed and opaque envelopes was estimated using Google Earth, calculating these quantities for 49 school buildings. Consequently, the calculated average WWR of 23 % was applied to all 277 school buildings.

2.5 The Building Plant Model

A "central heating radiators" system was applied to all the school buildings as HVAC system; no cooling system is considered. The technical data of the modeled building plants of the dynamic analysis, taken from the iCD database, are summarized in Table 2.

Table 2 – Building system characteristics (dynamic model)

SCOP [kW/kW]	0.83
Heating setpoint [$^{\circ}\text{C}$]	20
SEER [kW/kW]	-
Cooling setpoint [$^{\circ}\text{C}$]	-
Auxiliary energy [W/m^2]	0.95
Ventilation heat recovery [%]	-
Air supply [$\text{l}/(\text{s}\cdot\text{m}^2)$]	0.27
Infiltration rate [ach]	0.167
Domestic Hot Water efficiency [%]	0.5
Average Cold Water temperature [$^{\circ}\text{C}$]	10
Average Hot Water temperature [$^{\circ}\text{C}$]	60

2.6 The Building Usage Model

iCD contains several predefined usage profiles, specific for each building typology and human activity. The internal gains are thus assigned to the model, selecting, among the available ones, the usage

profiles defined as “School or University”, which are summarized in Table 3 and plotted in Fig. 1 along with the building system schedules.

Table 3 – Applied internal gains (dynamic model)

Daily average internal gains [W/m ²]			Average people density [m ² /pers]
People	Lighting	Appliances	
4	3.4	4	6.8

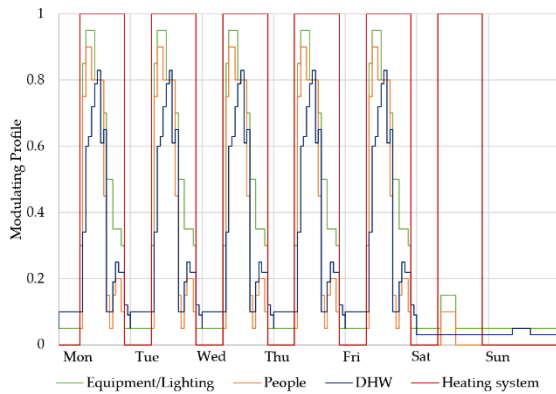


Fig. 1 – Weekly schedules of internal gains and plants (dynamic model)

3. Results and Discussion

3.1 Energy Consumption

The dynamic simulation for all 277 buildings was performed on iCD, analyzing the energy consumption concerning the following: domestic hot water production, auxiliary energy, heating system, equipment, and lighting. These results are plotted in Fig. 2, which summarizes the energy consumption of the school asset as average values. The results show that the highest consumptions, i.e., 69 % of the total, are due to the heating system, probably due to the high heat losses through the envelope and the low efficiency of the installed systems. Therefore, the average total energy of 179.9 kWh/m² is obtained, of which 123.4 kWh/m² are due to heating consumption. This value is consistent with the Italian average heating consumption, estimated equal to 115 kWh/m² (Dias Pereira et al., 2014). Starting from the baseline results, three retrofit scenarios are tested:

- 1) S1: Replacement of the external windows with double glazing with a thermal transmittance equal to 1.4 W/(m² K)

- 2) S2: Installation of 10 cm of thermal insulation on the external side of external walls and roof. Fiberglass with a thermal conductivity of 0.034 W/(m K) is chosen for the external walls, while a glass wool panel with thermal conductivity of 0.037 W/(m K) is proposed for the roof.
- 3) S3: Replacement of the existing boiler with a heat pump with a COP equal to 3.5

The averages and frequencies of the total energy consumption are reported and compared in Fig. 2 and Fig. 3. The replacement of the windows (S1) determines a reduction of the heat losses by transmission, thanks to the reduced thermal transmittance values; in this way, it is possible to reduce the average heating energy consumption, going from 123.4 kWh/m² to 105.7 kWh/m². This solution is optimal for buildings with several floors and a restricted footprint area because the most significant slice of dispersion area will be due to the external area of the wall also influenced by the WWR. The results of the S2 scenario demonstrate the importance of having a well-insulated envelope: we registered a further decrease in the average heating consumption, which arrives at 74.7 kWh/m². Certainly, this solution is more effective than the S1 scenario, due to the larger area of the opaque envelopes. The best results are obtained with the S3 scenario: the replacement of the heat generator determines a reduction of 87 % of the average heating consumption compared with the baseline configuration, decreasing the heating need to 16.5 kWh/m².

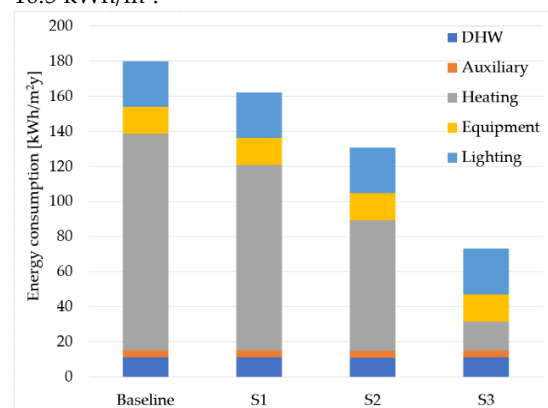


Fig. 2 – Comparison of the average energy consumption

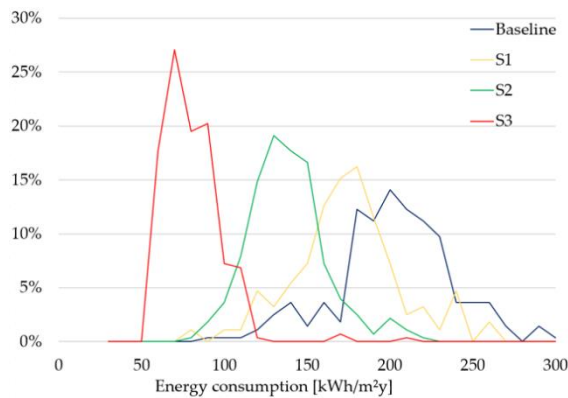


Fig. 3 – Frequency distribution of the total energy consumption

Furthermore, the heating consumption of the school buildings in Lombardy was calculated with a steady-state method: however, to compare these results with those coming from the dynamic model, the initial sample of 1036 schools was reduced to 144 buildings, i.e., the number of buildings common for both steady-state and dynamic models. Comparing the frequencies of several ranges of heating consumption (Fig. 4), we notice that the results of the dynamic calculation do not exceed 240 kWh/m², while for the steady-state model we register energy consumption even higher than 340 kWh/m². Besides, using the dynamic tool, more than half of the school buildings in Milan are characterized by a heating consumption lower than 140 kWh/m²; on the contrary, with the steady-state tools, they reach 240 kWh/m². Therefore, significant differences between the results compared are presented, which seems higher for the steady-state method. This difference could be related to the methodology itself, highlighting the advantages of dynamic simulation tools, or to the input data and assumptions.

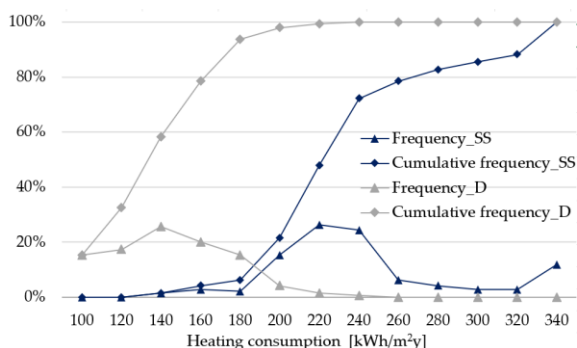


Fig. 4 – Frequency distribution for the steady-state (SS) and dynamic (D) heating consumption

3.2 Limitations and Open Questions

The main limitation of the present methodology concerns the input data needed: several sources have been used to define the buildings' geometries, envelope performances, usage profiles, etc., which might not be consistent with the actual buildings' characteristics. Therefore, the results reported should be compared with measured energy consumption, thus improving and validating the proposed methodology.

4. Conclusion

This paper proposes a methodology for the assessment of the energy performances of urban areas. The educational building asset of Milan was chosen as a case study, calculating its energy consumption with a dynamic tool and obtaining results close to the ones proposed by other authors (e.g., Dias Pereira et al., 2014). Three retrofit strategies were proposed and their effect was assessed: the best results were obtained by replacing the existing heat generators with heat pumps, decreasing the average heating consumption by about 87 % compared to the baseline one. Furthermore, the results obtained with the dynamic tool were compared with steady-state calculations analysing a sample of 144 educational buildings: we registered higher energy consumption with the steady-state method, which could be related to the methodology itself or the different input and sources of data. Hence, future investigations will improve and validate the proposed methodology by comparing the obtained results with actual measured energy consumption.

Acknowledgments

We wish to thank the ICL consultancy team and, in particular, Mario Favalli Ragusini, Fergus Ross, and Valeria Ferrando for their support with the Intelligent Communities Lifecycle ICL software.

Nomenclature

Symbols

ε	Efficiency (-)
η	Utilization factor (-)
EP	Primary energy (kWh)
fp	Primary energy conversion factor (-)
Q	Energy (kWh)

Subscripts/Superscripts

G	Gains
H	Heating
L	Losses
nren	Non-renewable
P	Plants
U	Useful

References

- Caputo, P., G. Costa, and S. Ferrari. 2013. "A supporting method for defining energy strategies in the building sector at urban scale". *Energy Policy* 55: 261-270. doi: <http://dx.doi.org/10.1016/j.enpol.2012.12.006>
- Certificazione ENergetica degli EDifici (CENED). Accessed on April 15. <https://www.cened.it/>
- Costanzo, V., R. Yao, X. Li, M. Liu, and B. Li. 2019. "Urban building energy model: Database development, validation, and application for commercial building stock." *Cities* 95. doi: <https://doi.org/10.1016/j.cities.2019.102467>
- Dascalaki, E. G., C. A. Balaras, S. Kontoyiannidis, and K. G. Droutsas. 2016. "Modeling energy refurbishment scenarios for the Hellenic residential building stock towards the 2020 & 2030 targets". *Energy and Buildings* 132: 74-90. doi: <http://dx.doi.org/10.1016/j.enbuild.2016.06.003>
- de Rubeis, T., L. Giacchetti, D. Paoletti, and D. Ambrosini. 2021. "Building energy performance analysis at urban scale: A supporting tool for energy strategies and urban building energy rating identification". *Sustainable Cities and Society* 7: 74. doi: <https://doi.org/10.1016/j.scs.2021.103220>
- Dias Pereira, L., D. Raimondo, S. P. Corgnati, and M. G. da Silva. 2014. "Energy consumption in schools – A review paper." *Renewable and Sustainable Energy Reviews* 40: 911-922. doi: <http://dx.doi.org/10.1016/j.rser.2014.08.010>
- EnergyPlus. Accessed on May 16. <https://energyplus.net/>
- Gangolells, M., M. Casals, N. Forcada, M. Macarulla, and E. Cuerva. 2016. "Energy mapping of existing building stock in Spain". *Journal of Cleaner Production* 112: 3895-3904. doi: <http://dx.doi.org/10.1016/j.jclepro.2015.05.105>
- Geoportale della Regione Lombardia. Accessed on August 5. <https://www.geoportale.regione.lombardia.it/>
- Hjortling, C., F. Bjork, M. Berg, and T. af Klintberg. 2017. "Energy mapping of existing building stock in Sweden – Analysis of data from Energy Performance Certificates". *Energy and Buildings* 153: 341-355. doi: <http://dx.doi.org/10.1016/j.enbuild.2017.06.073>
- Intelligent Energy Europe Project TABULA. Accessed on July 18. <https://episcopes.eu/welcome/>
- Krarti, M., M. Aldubyan, and E. Williams. 2020. "Residential building stock model for evaluating energy retrofit programs in Saudi Arabia". *Energy* 195. doi: <https://doi.org/10.1016/j.energy.2020.116980>
- Li, X., and R. Yao. 2021. "Modelling heating and cooling energy demand for building stock using a hybrid approach". *Energy and Buildings* 235. doi: <https://doi.org/10.1016/j.enbuild.2021.110740>
- Mastrucci, A., O. Baume, F. Stazi, and U. Leopold. 2014. "Estimating energy savings for the residential building stock of an entire city: A GIS-based statistical downscaling approach applied to Rotterdam". *Energy and Buildings* 75: 358-367. doi: <http://dx.doi.org/10.1016/j.enbuild.2014.02.032>
- Ministero dell'istruzione, dell'università e della ricerca. Accessed on April 7. <https://dati.istruzione.it/opendata/opendata/>
- Mohammadizazi, R., S. Copeland, and M. M. Bilec. 2021. "Urban building energy model: Database development, validation, and application for commercial building stock." *Energy and Buildings* 248. doi: <https://doi.org/10.1016/j.enbuild.2021.111175>

- Pörtner, H.-O., et al. 2022. *Climate Change 2022: Impacts, Adaptation and Vulnerability. Contribution of Working Group II to the Sixth Assessment Report of the Intergovernmental Panel on Climate Change*. doi: <https://doi.org/10.1017/9781009325844.002>
- OpenStreetMap. Accessed on March 15. <https://www.openstreetmap.org/>
- Re Cecconi, F., L. C. Tagliabue, N. Moretti, E. De Angelis, A. G. Mainini, and S. Maltese. 2019. "Energy retrofit potential evaluation: The Regione Lombardia school building asset", in: Della Torre, S., M. Bocciarelli, L. Daglio, R. Neri (2019), *Buildings for Education, A Multidisciplinary Overview of The Design of School Buildings*. doi: https://doi.org/10.1007/978-3-030-33687-5_27
- Torabi Moghadam, S., J. Toniolo, G. Mutani, and P. Lombardi. 2018. "A GIS-statistical approach for assessing built environment energy use at urban scale". *Sustainable Cities and Society* 37: 70-84. doi: <https://doi.org/10.1016/j.scs.2017.10.002>
- Tuominen, P., R. Holopainen, L. Eskola, J. Jokisalo, and M. Airaksinen. 2014. "Calculation method and tool for assessing energy consumption in the building stock." *Building and Environment* 75: 153–160. doi: <http://dx.doi.org/10.1016/j.buildenv.2014.02.001>
- Vicentini, G., and G. Mutani. 2012. "L'analisi del fabbisogno di energia elettrica e termica del parco edilizio esistente attraverso un sistema informativo geografico open source". *GFOSS-DAY 2012 - Fifth Italian conference on geographic free software and open geodata*.
- Wang, D., J. Landolt, G. Mavromatidis, K. Orehounig, and J. Carmeliet. 2018. "CESAR: A bottom-up building stock modelling tool for Switzerland to address sustainable energy transformation strategies". *Energy and Buildings* 169: 9-26. doi: <https://doi.org/10.1016/j.enbuild.2018.03.020>
- Wong, I. L., E. Kruger, A. C. M. Loper, and F. K. Mori. 2019. "Classification and energy analysis of bank building stock: A case study in Curitiba, Brazil". *Journal of Building Engineering* 23: 259-269. doi: <https://doi.org/10.1016/j.jobbe.2019.02.003>
- Yang, X., M. Hu, A. Tukker, C. Zhang, T. Huo, and B. Steubing. 2022. "A bottom-up dynamic building stock model for residential energy transition: A case study for the Netherlands". *Applied Energy* 306: 118060. doi: <https://doi.org/10.1016/j.apenergy.2021.118060>
- Yang, X., M. Hu, N. Heeren, C. Zhang, T. Verhagen, A. Tukker, and B. Steubing. 2020. "A combined GIS-archetype approach to model residential space heating energy: A case study for the Netherlands including validation". *Applied Energy* 280. doi: <https://doi.org/10.1016/j.apenergy.2020.115953>
- Zygmunt, M., and D. Gawin. 2021. "Application of Artificial Neural Networks in the Urban Building Energy Modelling of Polish Residential Building Stock". *Energies* 14(24): 8285. doi: <https://doi.org/10.3390/en14248285>

Hourly-Simplified Calculation to Identify Cost-Optimal Energy Performance Requirements for the Italian Building Stock

Matteo Piro – Politecnico di Torino, Italy – matteo.piro@polito.it

Franz Bianco Mauthe Degerfeld – Politecnico di Torino, Italy – franz.bianco@polito.it

Giovanna De Luca – Politecnico di Torino, Italy – giovanna.deluca@polito.it

Ilaria Ballarini – Politecnico di Torino, Italy – ilaria.ballarini@polito.it

Vincenzo Corrado – Politecnico di Torino, Italy – vincenzo.corrado@polito.it

Abstract

The 2010/31/EU Directive established a comparative methodology framework to determine minimum energy performance requirements based on a cost-optimal approach. This research investigates the cost-optimal outcomes resulting from the application of the monthly quasi-steady state method (UNI/TS 11300-1) and the simplified hourly dynamic model (EN ISO 52016-1), both aimed at determining the thermal energy needs for space heating and cooling. The technical building systems have been modelled by means of a monthly steady-state method, in agreement with the UNI/TS 11300 series. The global cost has been calculated from a financial perspective according to EN 15459-1. The proposed methodology has been applied to two buildings that differ in their climatic zone, construction period, and intended use. For this purpose, a single-family house located in Palermo and an office building sited in Milan have been assessed. To investigate the deviations between the two energy models, the results in terms of packages of energy efficiency measures and global cost have been compared.

1. Introduction

1.1 The Comparative Methodology Framework and the *EP* Assessment

The Commission Delegated Regulation No. 244/2012 (European Commission, 2012a), which supplements European Directive 2010/31/EU (European Commission, 2010a), specifies a comparative methodology framework and prescribes Member States to define minimum energy performance requirements for buildings to achieve “cost-optimal levels”, i.e., the lowest global cost (GC)

during the building lifecycle. Moreover, the European Directive requires the Member States to update the applied methodology regularly. The Guidelines accompanying Commission Delegated Regulation No. 244/2012 (European Commission, 2012b) established three different applicable calculation methods to determine the building energy needs: monthly quasi-steady state, simple hourly, or fully dynamic approach. In Italy, the deployed comparative methodology, described by Corrado et al. (2018), provides for performing the calculations through a monthly quasi-steady state method, according to the UNI/TS 11300 series (UNI, 2010-2019).

Recently, the mandate of the European Commission M480 (European Commission, 2010b), aimed at developing a new harmonized package of EPB directives, has conceived the EN ISO 52016-1 standard (CEN, 2017b). Italy is finalizing its National Annex (NA) of EN ISO 52016-1 (CTI, 2021), providing some main improvements that are related to: a) a new discretization approach of opaque building components (Mazzarella et al., 2020); b) a more accurate method to determine the solar heat gains and the longwave radiation heat exchange with the sky vault; c) the introduction of a weighting factor for the *g*-value calculation that accounts for incident angle dependency on direct and diffuse solar irradiance.

1.2 Aim of the Research

This work is part of a study carried out in collaboration with the Italian National Agency for New Technologies, Energy and Sustainable Economic

Development (ENEA; Corrado et al., 2021); it investigates the employment of the simplified dynamic hourly model, introduced by EN ISO 52016-1, for determining the minimum energy performance requirements to achieve the cost-optimal level. For this work, two representative case studies (a single-family house located in Palermo and an office building sited in Milan) have been selected between twenty-six buildings and have been simulated to upload the comparative methodology. These results have been compared, in terms of the optimal set of energy efficiency measures (EEMs) and global cost, with those derived from the application of the monthly quasi-steady state method, carried out in accordance with the UNI/TS 11300-1 (UNI, 2014) calculation procedures.

2. Methodology

The EPBD recast establishes the comparative methodology framework to set out the minimum energy performance requirements for new buildings and existing buildings undergoing a major renovation. This approach requires Member States to:

- a) identify an adequate number of real and/or 'virtual' residential and non-residential reference buildings, representative of the national building stock,
- b) define energy efficiency measures for the refurbishment of the building envelope and the technical building systems for each reference building, also detecting technologies that exploit renewable energy sources,
- c) calculate the primary energy demand deriving from the application of different packages of energy efficiency measures for each identified reference building,
- d) calculate the global cost associated with the different building energy renovation scenarios,
- e) derive the cost-optimal level for each reference building that minimises the global cost value.

2.1 Thermal Energy Needs Calculation Models

The calculation tool used in Corrado et al. (2018) has been updated for the sake of the present study to determine the thermal energy needs for space heating and cooling according to the EN ISO 52016-1 simplified hourly method (Corrado et al., 2021). For consistency with the quasi-steady state UNI/TS 11300-1 calculation method, some of the improved calculation options introduced by the Italian NA have been implemented, namely the hourly variations of the sky temperature and of the total solar energy transmittance of the glazed components. In the NA, the sky temperature is determined by means of the formulation presented in UNI/TS 11300-1, and it depends on the external vapor pressure. Moreover, the solar gains through windows are determined with a weighting factor for the g -value. The correction factor is formulated as a function of the solar angle, exposure, and glazing type. While in the quasi-steady method, the values are determined for each month through a tabular approach, in the Italian NA the properties are defined on an hourly basis.

2.2 The Cost-Optimal Approach

The cost-optimization procedure employed in this work is a single-objective optimization approach that applies discrete energy efficiency options (EEOs) one at a time to obtain a new partial optimized building for each step of the calculation. The full procedure is described in Corrado et al. (2014) and is based on the methodology proposed by Christensen et al. (2006). In particular, the identification of the cost-optimal level has been performed by applying at the same time more EEMs in an iterative procedure, to exploit the synergy effects of different measures. For each step of the calculation, the algorithm identifies a new renovation scenario, associated with a combination of EEMs, and calculates both the primary energy demand and the global cost. If the subsequent package of energy efficiency measures results in a lower GC, then the procedure sets a new partial optimum. The optimization proceeds until the package of EEMs that determines the lowest global cost is found.

Starting from a reference set of EEMs, the optimiza-

tion procedure will test the different EEOs until the energy efficiency package of measures that guarantees the minimum global cost is found.

The energy efficiencies of the technical building subsystems have been evaluated considering the UNI/TS 11300 series monthly steady-state method. The investment costs of EEMs have been derived from DEI (2017). Then, the global cost has been calculated according to EN 15459-1 (CEN, 2017a), considering a lifespan of 30 years and the financial perspective, i.e., analysing the mere evaluation of the private investment. In the assessment, a real interest rate of 4% has been assumed. Moreover, the cost-optimality approach, being a comparative methodology for the determination of the GC, neglects the same cost categories repeated for several measures (safety costs, ancillary charges, etc.), and the cost items on building materials whose installation does not have an impact on the energy performance of the building.

3. Application

3.1 Case Studies

In the present work, the reference buildings have been assumed to be located in two different Italian climatic zones (Palermo and Milan), and two construction periods have been considered (an existing building, built in the period 1977-90, and a new building). Two different intended uses have been assumed: residential and non-residential.

The single-family house sited in Palermo was selected from the IEE-TABULA project (*Typology Approach for Building Stock Energy Assessment*; Loga et al., 2012), while the office located in Milan was derived from the survey of Margiotto & Puglisi (2009). Both buildings present a reinforced concrete structure, with reinforced concrete and hollow brick slabs. Brick masonry cavity walls for the single-family house and hollow brick masonry walls for the office have been assumed, respectively. The upper slabs face the external environment, while the bottom floor is adjacent to an unconditioned zone (cellar). Table 1 reports the main geometrical characteristics.

In its current state, the single-family house, located in Palermo, presents single-glazed windows with-

out external solar shading devices installed. The residential house is equipped with a heat generator for space heating and domestic hot water, and a multi-split system for space cooling (see Table 2).

Table 1 – Geometrical characteristics of the case studies

	Residential/Existing bldg/Palermo	Office/New bldg/Milan
V_g [m ³]	725	6100
A_t [m ²]	199	1519
A_{env} / V_g [m ⁻¹]	0,72	0,35
A_w [m ²]	25	434
no. storeys	2	4

3.2 Energy Efficiency Measures

Sixteen categories of EEMs have been defined, considering up to five different energy efficiency options for each EEM, characterised by increasing levels of performance. The EEMs are classified into three different groups according to their application field: a) the thermal insulation of the building fabric (i.e., opaque and transparent building envelope components) and installation of solar shading devices; b) the replacement of technical building systems components (i.e., heating, cooling, and domestic hot water generators, ventilation, and lighting systems); c) the installation of renewable energy plants. The considered number of EEOs is variable depending on both the reference building and the specific EEM. In Table 2, the thermo-physical parameters and costs associated with each EEO are reported per each EEM.

3.3 Consistency Options

As introduced, the cost-optimal packages of energy efficiency measures determined by means of the monthly and the simplified hourly dynamic methods respectively are compared in the present work. To make the results of the two calculation methods comparable, some consistency options have been considered:

- Typical Meteorological Years (TMY) elaborated by the Italian Thermo-technical Committee (CTI, 2015) have been adopted in both calculation methodologies,
- diversity factors for energy calculation on an hourly basis have been introduced to eval-

Table 2 – EEOs per EEMs for residential and non-residential buildings

EEMs		Residential/Existing bldg/Palermo					Office/New bldg/Milan				
		EEOs					EEOs				
		1 (*)	2	3	4	5	1	2	3	4	5
External wall thermal insulation	U_{wl} [W m ⁻² K ⁻¹]	-	0,54	0,45	0,40	0,26	1,50	0,36	0,30	0,26	0,17
	c_{eli} [€ m ⁻²]	-	79	83	85	96	-	58	62	66	80
or Cavity wall thermal insulation	U_{wl} [W m ⁻² K ⁻¹]	1,10	0,37	-	-	-					
	c_{eli} [€ m ⁻²]	-	21	-	-	-					
Roof thermal insulation	$U_{fl,up}$ [W m ⁻² K ⁻¹]	2,16	0,41	0,34	0,32	0,26	1,50	0,30	0,25	0,22	0,18
	c_{eli} [€ m ⁻²]	-	45	50	52	59	-	40	45	48	55
Floor thermal insulation	$U_{fl,lw}$ [W m ⁻² K ⁻¹]	0,78	0,58	0,48	0,42	0,28	1,50	0,36	0,30	0,26	0,17
	c_{eli} [€ m ⁻²]	-	9	9	9	12	-	12	14	16	26
Windows	U_w [W m ⁻² K ⁻¹]	4,90	3,80	3,20	3,00	1,60	5,00	2,20	1,80	1,40	1,10
	c_{eli} [€ m ⁻²]	-	300	306	346	624	200	365	379	388	391
Solar shading devices	F or M (**)/ τ_{sh} [-]	-	F /	M /	-	-	F /	M /	-	-	-
	c_{eli} [€ m ⁻²]	-	0,20	0,20	-	-	0,20	0,20	-	-	-
Chiller	EER [-]	2,35	3,30	-	-	-	3,30	-	-	-	-
	C [k€]	-	3,77	-	-	-	71,90	-	-	-	-
plus Heat generator for space heating	COP [-]	-	3,70	4,10	-	-					
	c [€ kW ⁻¹]	-	451	493	-	-					
plus Heat generator for domestic hot water	$\eta_{w,gn}$ [-]	-	0,93	1,00	-	-					
	c [€ kW ⁻¹]	-	210	629	-	-					
or Combined heat generator for space heating and domestic hot water	$\eta_{H+W,gn}$ [-]	0,73	0,93	1,00	-	-	0,93	1,05	-	-	-
	c [€ kW ⁻¹]	-	264	209	-	-	179	124	-	-	-
or Heat pump for space heating, domestic hot water, and space cooling	COP [-] and EER [-]	-	4,10 3,50	-	-	-	3,00 2,80	3,50 3,20	-	-	-
	c [€ kW ⁻¹]	-	967	-	-	-	329	372	-	-	-
Thermal solar system	A_{coll} [m ²]	-	1	2	3	-	2	4	6	8	10
	c_{coll} [k€ m ⁻²]	-	1,40	1,40	1,40	-	1,40	1,40	1,20	1,00	0,80
Photovoltaic system	W_p [kW]	-	1,36	1,70	2,04	-	8,80	11,00	13,20	-	-
	c [k€ kW ⁻¹]	-	1,50	1,50	1,50	-	1,25	1,25	1,25	-	-
Heat recovery ventilation system	η_{ru} [-]						0,60	0,70	0,90	-	-
	C [k€]						3,79	9,76	17,67	-	-
Space heating control sub-system	$\eta_{H,rg}$ [-]	0,78÷ 0,89	0,94	0,98	0,99	-	0,94	0,98	0,99	-	-
	C [€]	-	52	288	90	-	358	1.075	394	-	-
Lighting system	P_n [W m ⁻²]						6,00	6,00			
	Fo [-]						1,00	0,80	-	-	-
	Fc (Fd) [-]						1,00	0,90			
	ct [€ m ⁻²]						24	30	-	-	-

(*) For the existing building the first column represents the current state

(**) F = fixed louveres, M = mobile louveres

uate the temporal distribution of the internal heat gains, in accordance with EN 16798-1 (CEN, 2019),

- c) in the simplified hourly model, the mass of the internal horizontal partitions has been associated with the internal node of the conduction model. Moreover, the specific heat capacity of air and furniture has been neglected.

4. Results

The results of the optimization procedure are presented in terms of the overall non-renewable energy performance ($EP_{gl,nren}$) vs. the global cost in Fig. 2 and Fig. 1 for the single-family house and the office building respectively. Both partial optimum and the cost-optimal points, calculated on a monthly and hourly basis, are shown. Moreover, Table 3 specifies the cost optimal EEMs packages for each reference building and for the two calculation methods (monthly and hourly).

The comparative analysis shows slight differences between the global costs and the cost-optimal package of energy efficiency measures. In light of the comparison between the two case studies and the two calculation methodologies, GC and $EP_{gl,nren}$ of the cost-optimal levels present negligible deviations. The $EP_{gl,nren}$ deviation of the hourly cost-optimal level with respect to the monthly one is equal to 11% and -3% for the single-family house and the office respectively. For both buildings, from the global cost view, the relative variation of the global cost is close to 1%. The cost-optimal combination of EEMs varies between the two calculation models, as highlighted in Table 3 (coloured cells). For both buildings, a different level of thermal insulation of the bottom floor in the cost-optimal EEMs is displayed when applying a different calculation model. More evident variations occur for the single-family house, in which different levels of the EEOs for the solar shading devices and the photovoltaic system are reported.

Primarily, deviations in the results can be ascribed to major differences in the calculation methods, such as the deployment of a different model for the heat conduction assessment in every building component and the approach to determine the heat

transfer through unconditioned zones. From the optimal package of EEMs view, although the determination of the thermal energy needs for space heating and cooling is strictly related to the building fabric energy performance, this does not necessarily imply that the EEOs of the technical building system cannot vary between the two calculation methods. In fact, the energy cost, which is a term of the global cost calculation, is directly influenced by the building energy needs. Moreover, most of the sensitivity in the EEO variation is related to the measures with the minimal difference cost as a consequence of the energy efficiency increase. A significant example that describes this phenomenon is represented by the floor thermal insulation (see Table 3).

5. Conclusion

The comparative methodology applied in 2018 to identify the cost-optimal minimum energy performance requirements for the Italian building stock has been updated with the new simplified hourly model specified by EN ISO 52016-1 and by its National Annex. In the present work, the outcomes of the comparative analysis for a single-family house located in Palermo and for an office building situated in Milan have been presented. For each building, the cost-optimal energy efficiency measures resulting from the calculation of the thermal energy needs for space heating and cooling both on a monthly basis (UNI/TS 11300-1) and on an hourly basis (EN ISO 52016-1) have been assessed and compared. The outcomes, which are presented in terms of the cost-optimal package of EEMs and global cost, do not lead to significant differences under application of a different calculation method.

Future works will provide an update of the cost-optimal methodology to assess the technical building system performance on an hourly basis.

Table 3 – Optimal EEM packages resulting from different calculation methods, for residential and non-residential buildings

EEM		Optimal EEO		Optimal EEO	
		Residential/Existing bldg/Palermo		Office/New bldg/Milan	
		Monthly method	Hourly method	Monthly method	Hourly method
External wall thermal insulation <i>or</i> cavity wall thermal insulation	$U_{wl} [W m^{-2}K^{-1}]$	-	-	0,36	0,36
		1,10	1,10		
Roof thermal insulation	$U_{fl,up} [W m^{-2}K^{-1}]$	0,41	0,41	0,30	0,30
Floor thermal insulation	$U_{fl,lw} [W m^{-2}K^{-1}]$	0,28	0,78	0,30	0,36
Windows	$U_w [W m^{-2}K^{-1}]$	4,90	4,90	1,10	1,10
Solar shading devices	F <i>or</i> M (%) / $\tau_{sh} [-]$	F / 0,20	M / 0,20	M / 0,20	M / 0,20
Chiller	EER [-]	2,35	2,35	-	-
<i>plus</i> Heat generator for space heating	COP [-]	-	-		
<i>plus</i> Heat generator for domestic hot water	$\eta_{w,gn} [-]$	-	-		
<i>or</i> Combined heat generator for space heating and domestic hot water	$\eta_{H+W,gn} [-]$	1,00	1,00	-	-
<i>or</i> Heat pump for space heating, domestic hot water, and space cooling	COP [-]	-	-	3,50	3,50
	EER [-]	-	-	3,20	3,20
Thermal solar system	$A_{coll} [m^2]$	absent	absent	2,00	2,00
Photovoltaic system	$W_p [kW]$	1,36	2,04	13,20	13,20
Heat recovery ventilation system	$\eta_{ru} [-]$			0,60	0,60
Space heating control sub-system	$\eta_{H,rg} [-]$	0,99	0,99	0,99	0,99
	$P_n [W m^{-2}]$			6,00	6,00
Lighting system	Fo [-]			0,80	0,80
	Fc (Fd) [-]			0,90	0,90

(*) F = fixed louvres, M = mobile louvres

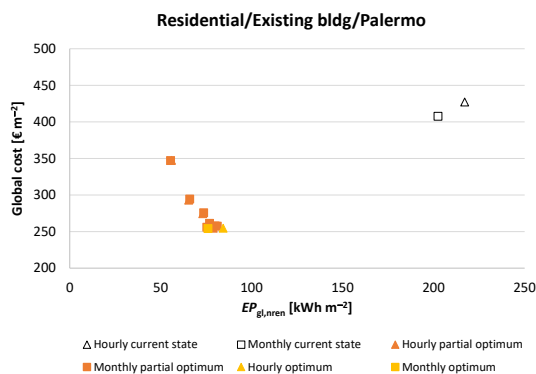


Fig. 1 – Cost-optimal level for the single-family house

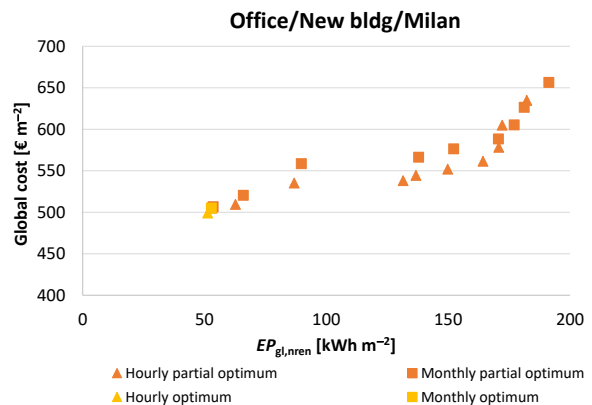


Fig. 2 – Cost-optimal level for the office building

Acknowledgement

This work is part of research supported by the Italian National Agency for New Technologies, Energy and Sustainable Economic Development (ENEA), regarding the application of the simplified hourly calculation model (UNI EN ISO 52016-1) and the update of methodology for calculating cost-optimal levels of energy performance.

For the research, a tool developed by the EPB Center and made available within a cooperation agreement with the Department of Energy “Galileo Ferraris” of the Politecnico di Torino was implemented.

Nomenclature

Symbols

A	area (m^2)
C	cost (€)
c	specific cost (€ m^{-2}) or (€ kW^{-1})
COP	coefficient of performance (-)
EER	energy efficiency ratio (-)
EP	energy performance indicator (kWh m^{-2})
F	factor (-)
P	lighting power density (W m^{-2})
U	thermal transmittance ($\text{W m}^{-2}\text{K}^{-1}$)
V	volume (m^3)
W	peak power (kW)
η	efficiency (-)
τ	coefficient of transmission (-)

Subscripts/Superscripts

C	constant illuminance
$coll$	solar collector
D	daylight dependency
eli	building element
env	building envelope
f	net floor
fl, lw	lower floor
fl, up	upper floor
g	gross
gl	overall
gn	generation sub-system
H	space heating

n	number of luminaires in the zone
$nren$	non-renewable
O	occupancy dependency
p	peak
rg	control sub-system
ru	heat recovery unit
sh	shading
W	domestic hot water
w	window
wl	wall

References

- Christensen, C., R. Anderson, S. Horowitz, A. Courtney, and J. Spencer, 2006. *BEoptTM Software for Building Energy Optimization: Features and Capabilities*. Golden, Colorado (USA): U.S. Dep. of Energy, National Renewable Energy Laboratory. <https://www.nrel.gov/docs/fy06osti/39929.pdf>
- Corrado, V., I. Ballarini, F. Bianco Mauthe Degerfeld, and M. Piro, 2021. “Aggiornamento della metodologia di calcolo dei livelli ottimali di prestazione energetica in funzione dei costi”. Rome: Agenzia Nazionale per le Nuove Tecnologie, l’Energia e lo Sviluppo Economico Sostenibile (ENEA). ENEA. In print.
- Corrado, V., I. Ballarini, G. De Luca, and E. Primo, 2018. “Aggiornamento della metodologia comparativa per la determinazione dei livelli ottimali di prestazione energetica negli edifici”. Report RdS/2017/141. Rome: Agenzia Nazionale per le Nuove Tecnologie, l’Energia e lo Sviluppo Economico Sostenibile (ENEA). ENEA. https://www.enea.it/it/Ricerca_sviluppo/documenti/ricerca-di-sistema-elettrico/adp-mise-enea-2015-2017/edifici-nzeb/report-2017/rds-par2017-141.pdf
- Corrado, V., I. Ballarini, and S. Paduos, 2014. “Assessment of cost-optimal energy performance requirements for the Italian residential building stock”. *Energy Procedia* **45**: 443–452. doi: <https://doi.org/10.1016/j.egypro.2014.01.048>
- EPB Center. 2019. “Demo (EN) ISO 52016-1 (energy needs heating and cooling, internal

- temperatures and loads)". Accessed June 1, 2021. <https://epb.center/support/documents/demo-en-iso-52016-1>
- European Commission. 2010a. "Directive 2010/31/EU of 19 May 2010 on the energy performance of buildings (recast)". *Official Journal of the European Union*, 19 May 2010.
- European Commission. 2010b. "M/480 EN: Mandate to CEN, CENELEC and ETSI for the elaboration and adoption of standards for a methodology calculating the integrated energy performance of buildings and promoting the energy efficiency of buildings, in accordance with the terms set in the recast of the directive on the energy performance of buildings (2010/31/EU)". 14 December 2010.
- European Commission. 2012a. "Commission delegated regulation (EU) No 244/2012 of 16 January 2012 supplementing Directive 2010/31/EU of the European Parliament and of the Council on the energy performance of buildings by establishing a comparative methodology framework for calculating cost-optimal levels of minimum energy performance requirements for buildings and buildings elements". *Official Journal of the European Union*, 16 January 2012.
- European Commission. 2012b. "Guidelines accompanying Commission Delegated Regulation (EU) No 244/2012 of 16 January 2012 supplementing Directive 2010/31/EU of the European Parliament and of the Council on the energy performance of buildings by establishing a comparative methodology framework for calculating cost-optimal levels of minimum energy performance requirements for buildings and building elements". *Official Journal of the European Union*, 19 April 2012.
- European Committee for Standardization (CEN). 2017a. *EN 15459-1: Energy performance of buildings - Economic evaluation procedure for energy systems in buildings - Part 1: Calculation procedures, Module M1-14*. CEN: Brussels, Belgium.
- European Committee for Standardisation (CEN). 2017b. *EN ISO 52016-1: Energy Performance of Buildings – Energy Needs for Heating and Cooling, Internal Temperature and Sensible and Latent Heat Loads. Part 1: Calculation procedures (ISO 52016-1:2017)*. CEN: Brussels, Belgium.
- European Committee for Standardization (CEN). 2019. *EN 16798-1: Energy performance of buildings. Ventilation for buildings. Indoor environmental input parameters for design and assessment of energy performance of energy performance of buildings addressing indoor air quality, thermal environment, lighting and acoustics. Module M1-6*. CEN: Brussels, Belgium.
- Italian Organisation for Standardisation (UNI). 2010-2019. *UNI/TS 11300 (series): Energy performance of buildings*. UNI: Milan, Italy.
- Italian Organisation for Standardisation (UNI). 2014. *UNI/TS 11300-1: Energy performance of buildings - Part 1: Evaluation of energy need for space heating and cooling*. UNI: Milan, Italy.
- Italian Thermo-technical Committee (CTI). 2015. "Typical Meteorological Year (2015)". Accessed June 1, 2021. <https://try.cti2000.it>.
- Italian Thermo-technical Committee (CTI). 2021. *Documento n. 020200134, Bozza di Appendice Nazionale UNI EN ISO 52016-1*. CTI: Milan, Italy.
- Loga, T., N. Diefenbach, B. Stein, 2012. "Typology Approach for Building Stock Energy Assessment. Main Results of the TABULA Project". Institut Wohnen und Umwelt GmbH: Darmstadt, Germany. <https://doi.org/10.1016/j.enbuild.2016.06.094>
- Margiotta, M., and G. Puglisi, 2009. "Caratterizzazione del parco edilizio nazionale. Determinazione dell'edificio tipo per uso ufficio". Report RdS/2009/164. Rome: Agenzia Nazionale per le Nuove Tecnologie, l'Energia e lo Sviluppo Economico Sostenibile (ENEA). https://www.enea.it/it/Ricerca_sviluppo/documenti/ricerca-di-sistema-elettrico/condizionamento/rse164.pdf
- Mazzarella, L., R. Scoccia, P. Colombo, and M. Motta, 2020. "Improvement to EN ISO 52016-1:2017 hourly heat transfer through a wall assessment: the Italian National Annex". *Energy and Buildings* **210**: 109758. Doi: <https://doi.org/10.1016/j.enbuild.2020.109758>
- Tipografia del Genio Civile (DEI). 2017. "Prezzi informativi dell'edilizia". DEI: Rome, Italy.

A Novel Methodology for Risk Assessment of Airborne Transmission due to Covid-19 in University Classrooms

Giulia Lamberti – University of Pisa, Italy – giulia.lamberti@phd.unipi.it

Roberto Rugani – University of Pisa, Italy – roberto.rugani@phd.unipi.it

Fabio Fantozzi – University of Pisa, Italy – fabio.fantozzi@unipi.it

Abstract

The Covid-19 pandemic revolutionized the way of designing buildings, which should be created to improve health conditions and limit the spread of contagion. Among these, schools certainly need special attention. To improve indoor conditions, the first step of this study was conducted by simulating three classrooms having different ventilation strategies, using a CFD analysis. Then the infection probability was calculated using the Gammaitoni-Nucci model to analyse the risk in the classrooms according to different ventilation and building characteristics. The study showed the need for providing adequate ventilation to ensure healthy conditions for the students. Furthermore, the infection probability was calculated considering non-uniform environments, which can result from various air distributions in the classroom due to local non-uniformities. The configuration obtained from the CFD analysis was then compared to the standard condition, which considers the classrooms as uniform environments. This allows an understanding of the effective conditions to which students are exposed and to comprehend whether the classical models do not risk underestimating the infection probability. This study provides a new methodology for airborne transmission risk assessment in non-homogeneous environments and supports designers with a new tool to evaluate HVAC systems layout and classroom operation.

1. Introduction

The importance of providing Indoor Environmental Quality (IEQ) in buildings has been always a necessity for enhancing people's health and well-being (Lamberti, 2020), especially in educational buildings, where students can improve their learning abilities (Bluyssen, 2016; Lamberti et al., 2021). This issue became even more evident after the

Covid-19 outbreak, when improving IEQ to guarantee occupants' health became a priority, both during normal and critical operations (Awada et al., 2021). This new awareness led building practitioners to focus on the aspect of Indoor Air Quality (IAQ) (Awada et al., 2022). Overall, there was a tendency to rethink building design strategies (Megahed & Ghoneim, 2021) to prepare buildings for post-pandemic architecture.

Since airborne transmission was recognized as a possible route of infection (Morawska et al., 2020), researchers focused on the relationship between ventilation rate and infection risk. Indeed, ventilation can be an important preventive measure to reduce infection probability, even if most existing ventilation standards are comfort-based and not sufficient to control the risk (Ding et al., 2022). For this reason, studies that relate the ventilation rate and infection probability have been carried out considering diverse building types (Dai & Zhao, 2020). The most used models for assessing these relationships are the well-established Wells-Riley (Riley & Nardell, 1989) and the Gammaitoni-Nucci (Gammaitoni & Nucci, 1997) models. In this scenario, educational buildings present particularly critical situations, as students spend a consistent amount of time indoors (Lamberti et al., 2020) and are in close contact with other occupants. Thus, the infection risk was often analyzed in these types of buildings (Pavilonis et al., 2021; Fantozzi et al., 2022) to ensure healthy conditions for students.

However, these models assume that the air in the indoor environment is uniformly distributed, which is not necessarily true. Indeed, there is the possibility of underestimating infection risk if, in some locations of the room, the ventilation rate is below the assumed uniform value. This fact may

have negative consequences on students' health, especially if the infection probability is underestimated in the positions occupied by their desks. Building simulation and CFD analysis, which have often been used to evaluate various aspects of IEQ (Rugani et al., 2021) and validated on the real conditions encountered in classrooms (Fantozzi et al., 2021), are valid tools for analyzing the distribution patterns of the air in the rooms. In fact, CFD simulations were recently used to minimize Covid-19 spread (Ascione et al., 2021).

The aim of this paper is, then, to analyze the air patterns through a CFD analysis using university classrooms with different room characteristics, occupancy, and operation mode as a case study. This analysis will provide important information regarding the estimation of infection risk considering the classrooms as non-uniform spaces and validation of the models predicting infection risk. Furthermore, an innovative methodology for enhancing classroom management and improving the health conditions of the students is proposed.

2. Methodology

2.1 The Case Study

In this study, the classroom environments were studied as a non-homogeneous space, investigating the infection probability from an individual-oriented perspective. Three different classrooms at the School of Engineering of the University of Pisa were simulated, which present three different HVAC configurations. The three classrooms are located in different buildings: the first is under construction and will be equipped with a VRF system with a mechanical air exchange ventilation system (Class A), the second was built in 2006 and is air-conditioned by an air-to-air heat pump with ceiling fan coil distribution (Class B); the latter was built in 1930 and has a traditional hydronic radiator system (Class C).

Table 1 shows the characteristics of the three classrooms studied. Ideal manikins were placed in the stalls to study the infection risk that the users are actually exposed to.

Several points mainly corresponding to students' positions were identified.

Table 1 – Characteristics of the classrooms

Class	Surface [m ²]	Volume [m ³]	Occupancy	Ventilation rate [m ³ /h]
Class A	130	390	129	3250
Class B	131	468	130	1000
Class C	70	182	49	370

2.2 Simulation of the Classrooms and Infection Probability

The three classrooms were analyzed by means of a 3D CFD analysis, using Autocad CFD. CFD decomposes the environment of a zone into a large number of control volumes and can provide a detailed description of the airflow by solving the Navier-Stroke's equations. CFD was used with the Finite Volume Method (FMV) approach, as it can perform detailed computation on heat transfer and air-flow simulation. The standard k-ε turbulence model was used for air turbulence due to its accuracy in predicting indoor airflows (Hughes et al., 2012).

Classes A, B, and C were modeled and simulated in two different scenarios: one lesson on a summer day and on a winter day. The boundary conditions were set as the output of a Building Energy Simulation (BES) campaign carried out using the well-known EnergyPlus software with a Typical Mean Year weather file. The room investigated and all adjacent classrooms were modeled as different thermal zones. An airflow network was used to simulate internal air movements, aimed at assessing the effective boundary conditions, i.e., mainly wall surface temperatures, for CFD analysis. The aim was to obtain the local value of the Local Mean Age (LMA) and the air velocity at the previously identified points of the environment.

The infection probability in the classroom was calculated using the well-established Gammaitoni-Nucci model (Gammaitoni & Nucci, 1997), which relates the ventilation rate to the infection probability. First, P was calculated considering the air distribution in the classroom uniform using the values from Table 1, then the infection probability was evaluated for the different zones that were established in the different classrooms, obtaining the Air

Changes per Hour for each zone from the simulated local mean age. The ACH for each zone corresponded to the position occupied by the students to assess their actual condition. The number of infectors was considered equal to 2 % of the total number of occupants.

3. Results

3.1 Local Mean Age

From the LMA, obtained from the CFD simulation, it was possible to derive the ventilation rate, so the Air Changes per Hour (ACH) were assumed for each zone, considering summer (yellow) and the winter (light blue) conditions (Fig. 1). The dashed line represents the ACH assumed for the simulations, which was considered uniform in the entire classroom ($ACH_{uniform}$), and is calculated from the ventilation rate given in Table 1.

Fig. 1 shows that the most favorable conditions can be encountered in Class A, which presents the highest ACH, both considering the $ACH_{uniform}$ and the single zones. On the other hand, the most critical conditions are in Class C, which is the naturally ventilated classroom, and whose ventilation was poorer both during summer and winter conditions. From the simulation of summer and winter conditions, it can be noticed that, for Class A, the winter scenario was generally less critical than the summer one, while, for Class B, the trend was the opposite. In general, mechanically ventilated classrooms present better indoor conditions, with higher values of ACH. It can be immediately noticed that the $ACH_{uniform}$ remains lower in each case than the ACH obtained in the different zones, which is a good indicator that assuming this parameter for

the calculation of the infection probability does not lead to underestimation of the risk. The ventilation rate in the different zones of the classroom tends to be higher than the one assumed if the air distribution of the room is considered uniform. This tendency is particularly evident in the mechanically ventilated classrooms (Class A and B), while it is less clear for the naturally ventilated ones (Class C). This fact shows that, in the naturally ventilated classroom, the air distribution tended to be more uniform and closer to the value assumed for $ACH_{uniform}$, probably also due to the reduced volumetric dimensions of Class C.

3.2 Calculation of the Infection Probability for the Different Classrooms

The infection probability for five hours of exposure was then calculated using the Gammaitoni-Nucci model for Classes A, B, and C (Fig. 2). Five hours of exposure were considered, as they are the most critical representative period in which students may remain in a classroom. Two typical activities that can be performed in classrooms were reported: the infector breathing and the infector speaking while the occupants are resting. The winter scenario was chosen for the analysis and Fig. 2 reports the infection probability calculated in the case that the air distribution in the classroom is considered uniform (continuous line), for the zone with the lowest ACH ("worst condition", dashed line) and the zone with the highest ACH ("best condition", dotted line). This allows a comparison of the results of the different conditions in classrooms, as all the other zones will be included between the best and the worst conditions for each class.

It can be noticed that, for all the classrooms, the in-

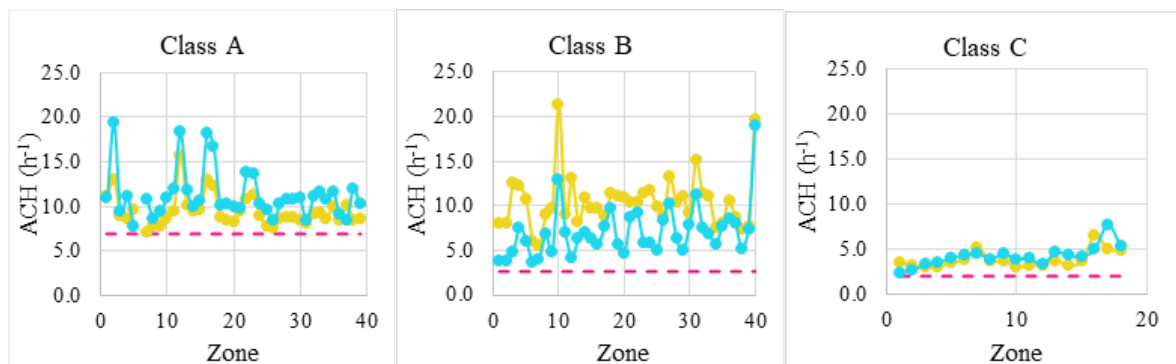


Fig. 1 – ACH obtained for each zone in the three classrooms for summer (yellow) and winter (light blue) conditions. The dashed line represents the ACH assumed for the entire classroom.

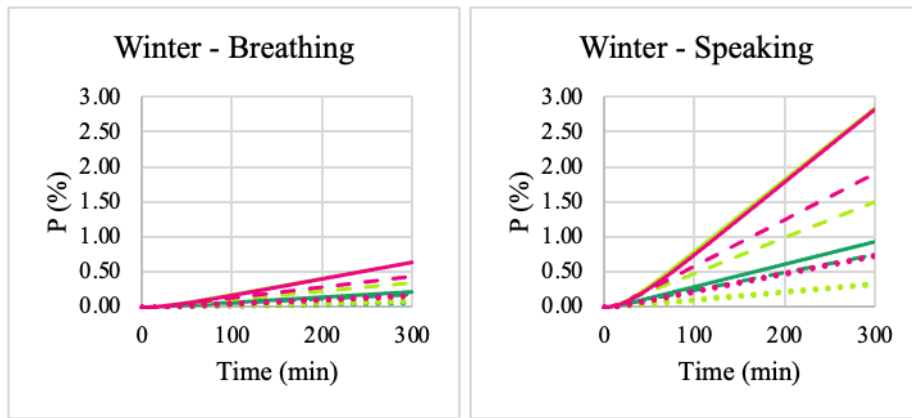


Fig. 2 – Infection probability for 5 hours of exposure in the three classrooms considered. Classes A, B, C are represented by the green, yellow, and red colors, respectively. The continuous line shows the uniform case, the dashed line the worst, and the dotted line the best condition

fection probability for the worst and the best conditions remained below the one calculated considering the $ACH_{uniform}$. This means that using the typical conditions assumed in infection risk models, namely the hypothesis of well-mixed air distribution, there is no risk of underestimating infection probability. On the contrary, the ventilation required to reduce infection probability can lead to an increased demand for ventilation, which may affect energy costs.

Fig. 2 shows that the most critical cases are represented by Classes B and C, due to the reduced ventilation. Furthermore, results show a high influence of the infector's activity on the infection probability. Indeed, the infection probability remains below 1 % for all the classrooms if the infector is only breathing, considering the five hours of exposure. On the contrary, if the infector is speaking, P exceeds 1 % after about 140 minutes in Class C and 200 minutes in Class B, considering the most critical zone (dashed line). On the contrary, Class A reports the most favorable conditions, where the critical infection probability of 1 % is never exceeded for all the scenarios and in five hours of exposure, showing the importance of providing adequate ventilation in educational buildings. Indeed, correct ventilation design can have a consistent influence on the maintenance of healthy indoor conditions. The infection probability calculated for the best condition (dotted line) shows that some positions are particularly favorable for maintaining the health of the occupants, which suggests that the students should favor certain locations in the class over more risky ones.

Since the real challenge is to design buildings that are healthy and comfortable for everyone, in the design phase it is necessary to consider the most critical scenario, which is represented by the activity of speaking. In this case, for Classes B and C, the threshold infection probability is soon exceeded, and preventive measures, such as increasing the ventilation rate, reducing the number of occupants, or including breaks during the duration of the lecture, are needed.

3.2.1 Relation between the ACH and infection probability in different classrooms

The relation between ventilation rate, expressed by the ACH, and infection probability was analyzed for different classrooms for the activity of speaking, as shown in Fig. 3. The exposures of one and five hours were considered, as they represent the minimum and the maximum time that students usually spend in university classrooms. The activity of speaking was chosen, as it represents the most critical scenario that can be probably encountered in university classrooms.

Regarding ventilation, Class A presents the most uniform conditions, as can be noticed by the range in which the ACH was varying. Classes B and C are less uniform, as they present Air Changes per Hour varying between about 5 h^{-1} and 25 h^{-1} . Non-uniformity in classroom ventilation can lead to different exposures to the infection risk, which means that some locations are less favorable than others. There is then the need for avoiding students being exposed to unhealthy conditions and, therefore, for providing indications on the correct management of university classrooms.

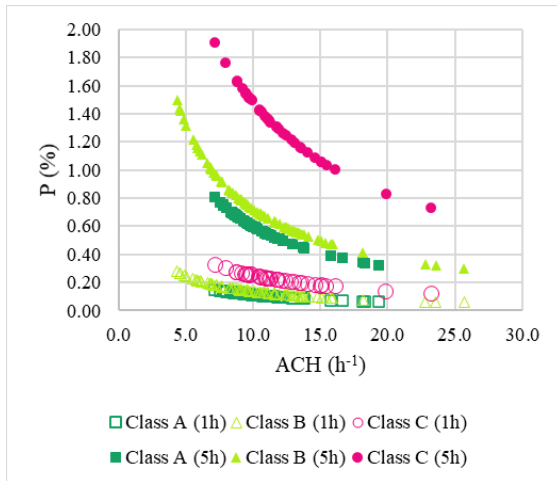


Fig. 3 – Relation between the infection probability for 1 and 5 hours of exposure and the ACH in the three classrooms considered with an infector speaking.

Concerning exposure time, for one hour of exposure, infection probability remains below the threshold value of 1 % for all the classrooms, while, for five hours, only Class A remains below this limit. This implies that, for long exposures, not all the locations should be occupied, but only the ones with acceptable risk values, or that breaks should be guaranteed to reduce infection probability.

Also noteworthy is the fact that there are some differences in the relationship between the ACH and infection probability considering the characteristics of different classrooms. Indeed, despite Class A and B presenting a higher occupation and therefore a higher number of possible infectors, the reduced room volume of Class C largely influences infection probability, as the curve of this class is much higher. The difference between the classrooms is particularly evident for long exposures, as can be noticed in Fig. 3.

4. Discussion

To assess the relationship between ventilation rate and infection probability, the models that are commonly used adopt the hypothesis that ventilation is uniformly distributed in all the locations in the room. However, from the previous results obtained from CFD simulations, it can be noticed that the local mean age of the air, and therefore the ventilation rate, may vary greatly between different posi-

tions. In this paper, mechanically and naturally ventilated university classrooms were analyzed to understand how different ventilation strategies, building characteristics, and occupancy can influence indoor infection probability. The crucial point is that the risk must not be underestimated by considering the air in the space to be uniformly distributed.

For this reason, the deviation between infection probability in the different zones (P_{zone}) and infection probability calculated considering ventilation uniform in all the classrooms ($P_{uniform}$) was calculated. Table 2 reports the minimum and maximum deviation for the three classes for the activity of speaking. The choice of infection probability for speaking is related to the fact that it is the most critical and common condition that can be encountered in university classrooms.

The deviation was calculated as the maximum difference between the effective infection probability in the zone and the one calculated considering the ventilation uniformly distributed in the environment. The negative sign in the deviation is associated with the fact that the $P_{uniform}$ was higher than the P_{zone} for all the zones of the classrooms, even in the case of the ventilation rate being the lowest, thus their difference is negative. This means that there is no risk of underestimating the infection probability by using uniform air distribution in the classroom, which is a fundamental issue if the health and the safety of the students are to be guaranteed.

Table 2 – Minimum and maximum deviation for the three classes for the activity of speaking

Class	Season	Minimum deviation	Maximum deviation
Class A	Summer	-0.11	-0.53
Class A	Winter	-0.17	-0.58
Class B	Summer	-1.79	-2.55
Class B	Winter	-1.35	-2.51
Class C	Summer	-1.20	-2.00
Class C	Winter	-0.92	-2.10

This result shows that, in certain cases, the effective infection probability P_{zone} was much lower than the $P_{uniform}$, especially for Classes B and C. Therefore, even if some differences occur, these results demonstrate that assuming the air to be

are found for lower exposures. This division enables more efficient management of classrooms favoring student health. For example, it is possible to recommend certain positions in the classroom depending on the probability of infection, especially if room capacity is not at the maximum.

The extreme cases are Class A, which remains totally below the critical probability of 1 %, and Class C, with a probability above 1 % in practically every position. In the latter case, it is necessary to find solutions that do not involve the positioning of students, since there are no areas of lower risk.

The case of Class B is interesting, since it presents a great variety of situations within it. The best area is in the middle, near the ventilation system, and at the back where there are windows (albeit closed). The side at the back of the classroom furthest from the windows is more critical, although this is not a problem, since this area is a corridor that is not usually occupied by students.

In conclusion, this methodology allows for the efficient management of university spaces, favoring the health of the occupants.

5. Conclusion

The importance of guaranteeing safe and healthy conditions in classrooms has become increasingly relevant, especially after the Covid-19 pandemic. However, the impact of adequate ventilation on students' health and productivity has always been a crucial point for researchers and building designers. Indeed, there is a necessity to provide sufficient air changes to enhance indoor air quality.

In this scenario, to assess the conditions of health indoors, infection probability has been often associated with ventilation rate, using predictive models that assume that air distribution in the room is uniform. However, it can be noticed that, in several cases, classrooms do not present uniform conditions due to the positioning of the ventilation systems or the window or door openings. It is necessary to verify that these non-uniformities do not lead to an underestimation of the infection risk, compromising students' health. With a CFD model, it was possible to simulate different scenarios using university classrooms that presented diverse

building characteristics and operation modes as a case study. Results indicate that the less critical situation can be found in mechanically ventilated classrooms, which provide adequate ventilation for the duration of exposure. Furthermore, results show that these models can be applied, despite the different conditions that can be encountered in classrooms, as the assumption of uniform distribution of the air tends to be pro-safety with no risk of underestimating infection probability.

Furthermore, division into equal-risk zones allows for intelligent management of the classroom, which permits students' positioning according to the most favorable conditions indoors, improving their health. Moreover, the new methodology has an important practical application, since it is possible to optimize the HVAC system position in the design phase.

References

- Ascione, F., R.F. De Masi, M. Mastellone, and G.P. Vanoli. 2021. "The Design of Safe Classrooms of Educational Buildings for Facing Contagions and Transmission of Diseases: A Novel Approach Combining Audits, Calibrated Energy Models, Building Performance (BPS) and Computational Fluid Dynamic (CFD) Simulations." *Energy and Buildings* 230: 110533. <https://doi.org/10.1016/j.enbuild.2020.110533>
- Awada, M., B. Becerik-Gerber, S. H. Zheng O'Neill, et al. 2021. "Ten Questions Concerning Occupant Health in Buildings during Normal Operations and Extreme Events Including the COVID-19 Pandemic." *Building and Environment* 188: 107480. doi: <https://doi.org/10.1016/j.buildenv.2020.107480>
- Awada, M., B. Becerik-Gerber, E. White, et al. 2022. "Occupant Health in Buildings: Impact of the COVID-19 Pandemic on the Opinions of Building Professionals and Implications on Research." *Building and Environment* 207: 108440. doi: <https://doi.org/10.1016/j.buildenv.2021.108440>
- Bluyssen, P. M. 2016. "Health, Comfort and Performance of Children in Classrooms – New Directions for Research." *Indoor and Built*

- Environment* 26(8): 1040–50. doi: <https://doi.org/10.1177/1420326X16661866>
- Dai, H., and B. Zhao. 2020. "Association of the Infection Probability of COVID-19 with Ventilation Rates in Confined Spaces." *Building Simulation* 13(6): 1321–27. doi: <https://doi.org/10.1007/s12273-020-0703-5>
- Ding, E., D. Zhang, and P. M. Bluyssen. 2022. "Ventilation Regimes of School Classrooms against Airborne Transmission of Infectious Respiratory Droplets: A Review." *Building and Environment* 207: 108484. doi: <https://doi.org/10.1016/j.buildenv.2021.108484>
- Fantozzi, F., G. Lamberti, F. Leccese, and G. Salvadori. 2022. "Monitoring CO2 Concentration to Control the Infection Probability Due to Airborne Transmission in Naturally Ventilated University Classrooms." *Architectural Science Review*: 11-13. doi: <https://doi.org/10.1080/00038628.2022.2080637>
- Fantozzi, F., G. Lamberti, and R. Rugani. 2021. "Thermal Comfort in University Classrooms: Analysis of Simulated and Real Conditions." In *2021 IEEE International Conference (EEEIC/ I&CPS Europe)*. Bari, Italy. doi: <https://doi.org/10.1109/EEEIC/ICPSEurope51590.2021.9584490>
- Gammaitoni, L., and M. C. Nucci. 1997. "Using a Mathematical Model to Evaluate the Efficacy of TB Control Measures." *Emerging Infectious Diseases* 3: 335–42. doi: <https://doi.org/10.3201/eid0303.970310>
- Hughes, B. R., J. K. Calautit, and S. A. Ghani. 2012. "The Development of Commercial Wind Towers for Natural Ventilation: A Review." *Applied Energy* 92: 606–27. doi: <https://doi.org/10.1016/j.apenergy.2011.11.066>
- Lamberti, G. 2020. "Thermal Comfort in the Built Environment: Current Solutions and Future Expectations." In *2020 IEEE International Conference (EEEIC / I&CPS Europe)*, 1–6. doi: <https://doi.org/10.1109/EEEIC/ICPSEurope49358.2020.9160558>
- Lamberti, G., F. Fantozzi, and G. Salvadori. 2020. 'Thermal Comfort in Educational Buildings: Future Directions Regarding the Impact of Environmental Conditions on Students' Health and Performance'. In *2020 IEEE International Conference (EEEIC/I&CPS Europe)*. doi: <https://doi.org/10.1109/EEEIC/ICPSEurope49358.2020.9160680>
- Lamberti, G., G. Salvadori, F. Leccese, F. Fantozzi, and P. M. Bluyssen. 2021. "Advancement on Thermal Comfort in Educational Buildings: Current Issues and Way Forward." *Sustainability* 13(18). doi: <https://doi.org/10.3390/su131810315>
- Megahed, N. A., and E. M. Ghoneim. 2021. "Indoor Air Quality: Rethinking Rules of Building Design Strategies in Post-Pandemic Architecture." *Environmental Research* 193: 110471. doi: <https://doi.org/10.1016/j.envres.2020.110471>
- Morawska, L., J. W. Tang, W. Bahnfleth, et al. 2020. "How Can Airborne Transmission of COVID-19 Indoors Be Minimised?." *Environment International* 142: 105832. doi: <https://doi.org/10.1016/j.envint.2020.105832>
- Pavilonis, B., A. M. Ierardi, L. Levine, F. Mirer, and E. A. Kelvin. 2021. "Estimating Aerosol Transmission Risk of SARS-CoV-2 in New York City Public Schools during Reopening." *Environmental Research* 195: 110805. doi: <https://doi.org/10.1016/j.envres.2021.110805>
- Riley, R. L., and E. A. Nardell. 1989. "Clearing the Air: The Theory and Application of Ultraviolet Air Disinfection." *The American review of respiratory disease* 139(5): 1286–1294. <https://doi.org/10.1164/ajrccm/139.5.1286>
- Rugani, R., M. Picco, M. Marengo, and F. Fantozzi. 2021. "Can PCS Help Us Save Energy? Initial Assessment Using Dynamic Energy and CFD Analyses." In *2021 IEEE International Conference (EEEIC/I&CPS Europe)*. doi: <https://doi.org/10.1109/EEEIC/ICPSEurope51590.2021.9584694>

Integrated Approach to Assess the Energy and Environmental Payback Time of Buildings Refurbishment: A Case Study

Marta Roncone – Roma Tre University, Roma, Italy – marta.roncone@uniroma3.it

Francesco Asdrubali – Roma Tre University, Roma, Italy – francesco.asdrubali@uniroma3.it

Gianluca Grazieschi – EURAC, Bolzano, Roma, Italy – gianluca.grazieschi@eurac.edu

Chiara Tonelli – Roma Tre University, Roma, Italy – chiara.tonelli@uniroma3.it

Abstract

The design of nZEB buildings, as well as the implementation of retrofit interventions in existing structures, are essential tools for reducing energy consumption in buildings and increasing decarbonization of the building sector. To describe the effectiveness of a retrofit intervention, in addition to the analysis of the benefits in terms of costs and energy savings, an environmental analysis should also be performed, introducing various indicators, such as energy and environmental payback times. In this article, we considered a residential building located in Montemarcello (Liguria, North-west of Italy) that had been subjected to a refurbishment and an expansion, with the aim of evaluating the energy and carbon savings achievable due to the interventions carried out. The life cycle analysis approach was applied to calculate the environmental payback times. The main purpose of this work is the application of an integrated approach to assess the economic, energetic and environmental convenience of retrofit interventions during the entire life cycle of the building, underlining the importance of considering LCA and environmental aspects to achieve decarbonisation of the construction sector. The results show that energy and environmental payback times are lower than the useful life of the building and of its components, and that LCA proves to be a strategic methodology for studying the problems deriving from global warming and energy supply in the building sector.

1. Introduction

It is well known that the construction sector is nowadays one of the most energy-intensive, and that, in Europe, it is responsible for about 40 % of final energy consumption and 36 % of greenhouse gas emissions, representing about one third of EU energy-

related emissions (European Commission, 2020). These emissions arise partly from the direct use of energy from fossil fuels in buildings and partly from the indirect emissions due to the generation of electricity used in buildings.

Although the EU's total greenhouse gas emissions from buildings decreased significantly by 29 % over the period 2005-2019 (EEA, 2021), Member States' emissions should continue declining in the future in order to achieve the EU climate change policy goals. Indeed, to achieve the overall EU target of a 55 % reduction in emissions by 2030, the construction sector would need to reduce its emissions by 60 % (EEA, 2021). For this to happen, the current energy renewal rate of building stock must greatly increase. In this context, to reduce energy consumption and to increase the decarbonisation of the construction sector, the design of nearly Zero Energy Buildings - nZEB (European Parliament and Council, 2010), as well as the implementation of retrofit interventions on existing structures or the selection of materials and building elements with low environmental impact are essential actions to be undertaken. Concerning the embodied burdens, different literature works have already shown that certification with Environmental Product Declarations – EPD (CEN, 2019) – can help in the determination of the environmental performance of building materials, such as insulation (Grazieschi et al., 2021) and windows (Asdrubali et al., 2021).

The implementation of retrofit interventions on existing structures is of additional importance.

However, in order to identify the most efficient and sustainable retrofit intervention, in addition to an assessment in terms of economic benefits, environmental and energy analyses must also be

considered, using appropriate indicators, such as environmental and energy payback times (Asdrubali et al., 2019; Asdrubali & Grazieschi, 2020).

Most of the scientific literature reviewed (Ardente et al., 2011; Webb, 2017) focuses on the evaluation of retrofit interventions of existing buildings or on the energy and environmental performances of new constructions. This work presents, on the other hand, a combined intervention that is characterized by the retrofitting of an existing house that involves a new add-on part. These typologies of retrofit interventions, sometimes referred as parasite architecture (Rinaldi et al., 2021), nowadays represent one of the possible architectural solutions for increasing living spaces, indoor comfort conditions and, if necessary, reducing energy consumption (Assimakopoulos et al., 2020).

In particular, a residential building located in Montemarcello (Liguria, North-west of Italy) subjected to a renovation and construction of an extension was considered, evaluating the energy and carbon savings due to the interventions and applying the life cycle analysis (LCA) to calculate the environmental payback times.

Therefore, this work presents the application of an integrated approach for estimating the environmental convenience of some structural and energy redevelopment interventions during the entire life cycle of the building.

The paper is organized as follows: Section 2 describes the materials and methodologies used in this work for the life cycle, energy and economic analysis of the pre- and post-energy requalification study building; in Section 3, the case study is presented; in Sections 4 and 5, the results of the study are reported and discussed, respectively, while in Section 6, conclusions are provided.

2. Materials and Methods

2.1 LCA and Dynamic Energy Simulation

Life Cycle Analysis (LCA) is a methodology that aims at determining the overall environmental impacts of a product or a service during the entirety of its life stages. This analysis addresses a comprehensive evaluation so that it is able to detect burden

shifting or a trade-off between life cycle phases or between different categories of environmental impact.

The methodology is standardized at international level by ISO 14040 (ISO, 2006) and 14044 (ISO, 2006). These two standards give a general overview of the phases that every LCA study should follow, defining a framework that is not characterized by a rigid temporal order, but which permits a shift from one phase to another also in reverse order when there is the need for updating or revising the assumptions previously made. The LCA phases individuated by the ISO standards are: goal and scope definition, life cycle inventory (LCI), life cycle impact assessment (LCIA), results reporting and sensitivity analysis.

The LCA application is very useful for identifying the most effective scenario in building retrofit interventions, also starting from the early design stage when there is the need to choose the solution that minimizes the cumulative environmental impacts during the whole life cycle of the construction.

In this work, the aim of the study was to compare the environmental impacts of a building, chosen as a case study, which was subjected to an energy retrofit intervention that also includes an extension of its useful volume, thus a new part. The life cycle environmental burdens of the ex-ante scenario and of the retrofitted solution were compared to confirm the environmental benefit deriving from the intervention proposed.

The functional unit that was chosen for the comparison was equal to the gross internal area of the building. The boundaries of the analysis included the raw material supply (A1), the transportation to the fabrication site (A2), the manufacturing process (A3), the transportation to the construction site (A4), the replacement of materials and components after their useful service lives (B4), the operational energy uses (B6) and, finally, the end-of-life stages (C1-C4).

The “cradle-to-grave” approach is so adopted for the analysis, excluding some stages that are considered negligible for the scopes of the evaluation (see Fig. 1 for more details).

LCA Phases															Benefits and Loads beyond the System Boundary				
Product Stage			Construction process		Use							End of Life							
Cradle to gate			Gate to site																
Cradle to site					Cradle to grave														
A1	A2	A3	A4	A5	B1	B2	B3	B4	B5	B6	B7	C1	C2	C3	C4	D			
Raw Materials Supply		Transport	Manufacturing	Transport	Construction and installation	Use/application	Maintenance	Repair	Replacement	Refurbishment	Operational Energy	Operational Water	De-Construction/ Demolition	Transport	Waste Processing	Disposal	Reuse		
																Recovery			
																Recycling			
																Exported Energy			

Fig. 1 – Building life cycle stages and related system boundaries - modified from PCR (Wiklund, 2019)

The environmental impacts determined employing the SimaPro software (PRé Sustainability, 2022) were the primary energy non-renewable requirement (PENR), calculated from the Cumulative Energy Demand (Frischknecht et al., 2015) single issue indicator, and the IPCC Global Warming Potential – GWP 100y (IPCC, 2007). Ecoinvent database (ecoinvent, 2021) was used as the background source of data.

The operational energy requirements were evaluated through a dynamic simulation of the building using the EnergyPlus code implemented in DesignBuilder environment (DesignBuilder Software Ltd., 2022).

The assumptions that were made for the development of the LCA are detailed in the following bullet points:

- The useful life of the building (after the intervention) was considered equal to 50 and 100 years, as recommended by the Product Category Rules (Wiklund, 2019) for the compilation of buildings Environmental Product Declarations and other LCA studies (Asdrubali et al., 2019; Asdrubali and Grazieschi, 2020; Blengini and Carlo, 2010). A 100-year lifespan is quite a long time-frame but it permits consideration of the long service life that interventions undertaken with good construction quality generally have.
- The analysis was performed for a rough building, thus external spaces, technical rooms, internal furniture, potable water grids, sewage grids, electrical plants, and any swimming pools were not considered in the evaluation, which was limited to the external envelope, to the internal walls and to energy systems. The consumption of water, DHW, electricity for lighting and household appliances was also excluded.

- Only heating and cooling energy requirements were accounted for in the analysis.
- A complete substitution of the components after their service life was foreseen without fractioning their environmental impacts in case of maintenance of the functionality after the end-of-life of the building.
- Load-bearing structures were supposed to have a service life of 100 years; secondary constructions and insulating materials were supposed to have a duration of 50 years, while for windows it was 35 years; energy systems and plants were modeled with a 20-year life span.
- The transportations means were supposed to be 16-ton trucks (diesel-fueled), while the transportation distance was always considered equal to 60 km.
- Construction and demolition waste material was considered but excavated soils (about 600 m³) were not accounted for in the evaluation.

2.1 Energy and Carbon Payback Times

The energy and carbon payback time are the two indicators that were considered to describe the effectiveness of the interventions proposed from an energetic and environmental point of view. These two indicators were calculated only for the retrofit intervention of the existing building and for the combined solution. which also includes the realization of the new extension: in fact, the evaluation for the new part was not possible because no ex-ante baseline scenario could be individuated.

The Energy Payback Time (EPBT) is the ratio between the difference of Embodied Energy (EE), after and before the retrofit, and the annual saved energy due to the retrofiting (see Eq. 1).

$$EPBT = \frac{EE_{A1-A4} + EE_{B1-B4} + EE_{C1-C4}}{E_{sav}} \quad (1)$$

The Carbon Payback Time (CPBT) is the ratio between the difference in Embodied Carbon, after and before the retrofit, and the annual carbon reduction due to the retrofiting (see Eq. 2).

$$CPBT = \frac{GWP_{A1-A4} + GWP_{B1-B4} + GWP_{C1-C4}}{GWP_{sav}} \quad (2)$$

The numerators of equations (1) and (2) represent the energy consumptions and the CO₂ emissions due to the construction of the system (stages A1-A4,

B1-B4 and C1-C4) and E_{sav} and GWP_{sav} are the annual reductions of PENR consumption and CO₂ emission due to the system operation, respectively.

3. Case Study

The residential complex under study is located in Montemarcello, in the Liguria region (Italy). The building is in a countryside area (226 m a.s.l.) and was built around the year 1930.

According to Italian legislation, the climatic zone of the property is C (on a scale from A to F, where A corresponds to the hottest places and F to the coldest), with a value in degree days between 1400 and 2100 (President of Italian Republic, 1993).

The building was subject to redevelopment and expansion interventions with the aim of ensuring an adequate level of internal environmental well-being and the containment of the consumption of energy and environmental resources. Fig. 2 shows the structural demolition and reconstruction interventions carried out on the property.

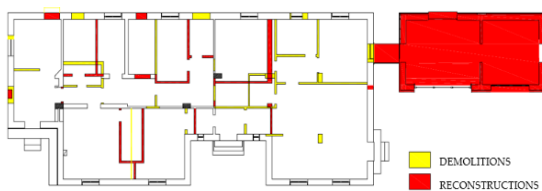


Fig. 2 - Demolitions and reconstructions conducted on the study building for the refurbishment and expansion of the building

The ante operam building, with an area of 211 m², consisted mainly of a brick-cement structure with single-glazed wooden windows. The heated space was separated from the roof by an accessible, unventilated and uninsulated attic, while the roof, also not insulated, was made of a brick-cement structure with tile cladding. The floor slab was raised above the ground level on a dry and damp air space. Instead, the infill walls are of the empty box type with a 10 cm thick air gap. Regarding the heating system, this consisted of 2 natural gas boilers with a nominal power of 24.4 kW and heat input between 12.5 and 27.1 kW. The emission system consisted of a radiant floor with copper pipes embedded in a cement screed directly laid on the brick-cement floor, for an

overall average thickness determined by means of a span, including the tiles, of 11 cm. Finally, the regulation system included the room thermostat.

The interventions carried out on the building consisted of a major energy renovation, since the intervention involved more than 50 % of the dispersant envelope (Italian Ministry of Economic Development, 2015) and consisted of: the insulation of the floors, the insulation of the walls, the replacement of fixtures, the reduction of thermal bridges, the replacement of the thermal system, the integration of the summer cooling system, the dehumidification of the air during the winter and summer with heat recovery, and finally the remote management of the heating system.

Fig. 3 illustrates some elevations of the building ante operam, inter operam and post operam.

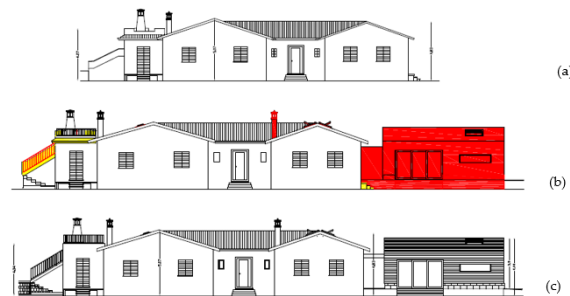


Fig. 3 - Prospects of the studio building ante operam (a), inter operam (b) and post operam (c)

The redeveloped building has a total area of 255 m², including an extension structure of 44 m². In the energy efficiency project, much importance was given to the insulation of the building envelope. In particular, windows with a transmittance between 1.1 and 1.5 W/(m²K) (< 2.0 W/(m²K) of limit value (Italian Ministry of Economic Development, 2015)) and glazed components with a transmittance between 1.332 and 1.687 W/(m²K) were installed. Finally, opaque elements with overall values lower than 0.42 W/(m²K) were obtained, as prescribed by the legislation in force in Italy on the minimum requirements about energy efficiency in buildings (Italian Ministry of Economic Development, 2015). While the toilets are to be heated with towel-warmer radiators, the heating system of the redeveloped building is of the low-temperature type with radiant floor panels. This system is also capable of cooling in the summer.

The older system was based on a traditional boiler fed by natural gas, with radiators as terminal units and split air-to-air heat pumps for summer cooling. Before the retrofit, the control system was characterized by an on-off thermostat installed in the living room, while after the retrofit each room was also equipped with its own thermostat in order to manage and differentiate the temperature independently.

The central heating and cooling system involves the use of a 500-liter boiler (technical water) and an integrated solar thermal circuit, designed to be combined with a single phase heat pump of 10.6 kW.

4. Results

The results showed that the application of energy efficiency measures can bring significant savings in terms of operational non-renewable primary energy consumption and GHG emissions. In particular, the retrofitting of the existing building permitted a reduction of the non-renewable primary energy demand for heating and cooling of 62 % to be obtained, increasing the coverage of renewable energy (see Fig. 4). The overall intervention, on the other hand, produced a reduction of the non-renewable energy demand equal to 60 % if compared with the ante operam situation.

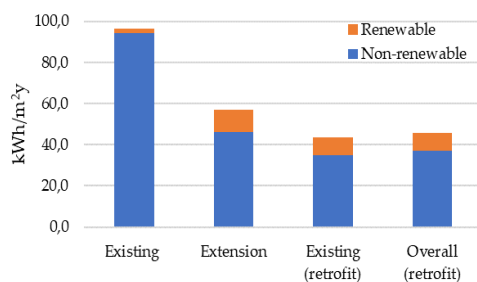


Fig. 4 – Overall annual energy consumptions per square meter for the different scenarios considered (operational energy)

The effort in reducing the operational non-renewable energy demand, however, caused an increase in the embodied impacts due to the introduction of new materials and energy systems. Tables 1, 2 and 3 show the PENR and GWP that characterize the extension, the retrofitted building

and the overall combined intervention (composed of the requalification of the existing part and the addition of the new volume).

Table 1 – PENR and GWP of the new extension

LCA stage	PENR (kWh/m²y)	GWP (kg CO ₂ eq/m²y)
A1-A3	21.3	5.78
A4	1.3	0.28
B1-B4	17.0	3.90
B6	41.7	7.90
C1-C4	1.9	1.70

Table 2 – PENR and GWP of the existing part after the retrofit

LCA stage	PENR (kWh/m²y)	GWP (kg CO ₂ eq/m²y)
A1-A3	12.0	2.73
A4	0.3	0.07
B1-B4	12.0	2.51
B6	35.0	6.70
C1-C4	0.4	0.42

Table 3 – PENR and GWP of the overall intervention: retrofit of the existing building and new extension

LCA stage	PENR (kWh/m²y)	GWP (kg CO ₂ eq/m²y)
A1-A3	13.6	3.26
A4	0.5	0.11
B1-B4	12.9	2.75
B6 (post)	36.9	7.04
C1-C4	0.7	0.64

The increase in embedded impacts was relevant and cannot be discarded. Considering the existing construction, for example, the retrofit produces an increment of about 25 kWh/(m²y) in the embedded PENR that corresponds to 26 % of the initial operational non-renewable energy requirement. Looking at the results for the new extension (Table 1), the embodied components (stages A1-A4 and B1-B4) account for 47 % of the total PENR and 57 % of the life cycle GWP of the building. Moreover, if we consider a building lifespan equal to 50 years, the percentage incidence of the embodied components reaches 57 % and 68 % of the life cycle PENR and GWP, respectively, becoming the most important sources of environmental impact.

Fig. 5 displays the overall non-renewable life cycle energy of the scenarios analysed versus its operational component. As can be noted, the increment of the embodied impacts is beneficial, since it is followed by a reduction of the overall life cycle non-renewable primary energy of the building. The calculation of the energy and environmental payback times (see Table 4) confirmed the environmental advantages of the intervention, showing values that are much lower than the useful life of the building (50 or 100 years are both considered) and of its components.

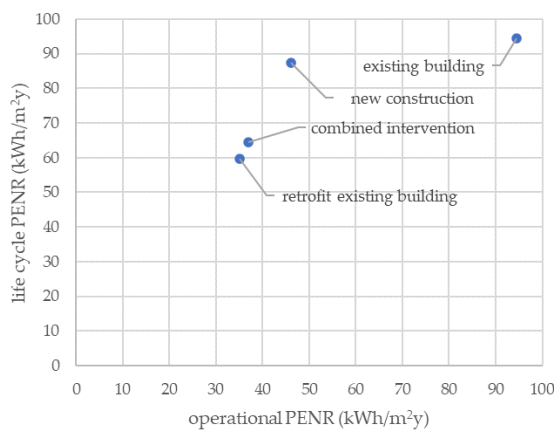


Fig. 5 – Life Cycle-PENR versus operational PENR for the existing building and for the interventions supposed

Table 4 – Payback times of the overall intervention

	Payback (months) 100-year life span	Payback (months) 50-year life span
retrofit existing part		
PENR	5	6
GWP	3	4
combined intervention		
PENR	6	8
GWP	4	6

5. Discussion

The analysis showed that the most sustainable intervention resulted in the energy requalification of the existing part. The addition of the extension results, on the other hand, is a much less competitive solution in the whole life cycle if compared with the retrofit of the old part: the interventions related to

the extension, in fact, have a higher PENR in the entire life cycle. This result depends on different aspects:

1. The operational energy requirements of the old construction after the retrofit are lower than the ones of the new built volume. This is linked with the higher S/V ratio and with the higher window-to-wall ratio of the extension.
2. The retrofit definitely involves a lower embodied energy and carbon because only the roof is completely re-built, while external walls and foundations are conserved.
3. The retrofit implies a higher production of construction and demolition waste, but the management of this waste has relatively low environmental impact. In particular, the demolition waste generated was composed of 46.8 tons of mineral materials, 226 kg of metal waste (ferrous material), 361 kg of glass waste and 720 kg of wood waste.

The overall combined intervention is mainly affected by the retrofit of the existing part, albeit still slightly higher than the one concerning only the redevelopment of the existing building. However, it is characterized by life cycle environmental performances that are still very interesting, even if slightly higher than the ones of the most sustainable solution (namely retrofitting only the existing building): the calculation of the payback times for the overall intervention shows that they are much lower than the service lives of the installed construction materials and components and it confirms the environmental benefit and the compatibility of the solution.

6. Conclusions

The energy and structural refurbishment of existing buildings implies the selection of a series of strategies and solutions.

In order to identify the most sustainable ones from an environmental point of view, it is necessary to take into consideration an integrated approach that also considers the environmental impacts in terms of the energy and carbon that are incorporated in the building materials and components.

In this study, a residential building subject to an energy retrofit, a structural intervention and an

extension was analyzed. The energy consumptions of the building were simulated in an EnergyPlus environment, while the overall LCA was performed employing an ecoinvent life cycle database.

Therefore, using the PENR, GWP, EPBT and CPBT indicators, the results for the new construction, for the existing building after and before the retrofit and for the combined intervention were compared. The results are in accordance with other literature studies regarding single buildings with a residential function. In particular, as already shown by other works (Asdrubali & Grazieschi, 2020; Blengini & Carlo, 2010), the operational PENR can be significantly reduced (from 94 to 35 kWh/(m²y) in our case study) if an adequate combination of passive and active solutions is designed and implemented. Consequently, in such low energy solutions, the embodied impacts can represent a very significant part of the total impact, even more than 50 %.

The adoption of a life cycle approach therefore proved to be very useful for the evaluation of the overall environmental burdens. It permitted detection of the burden shifting between the operational and production stages that characterizes the energy retrofit interventions or the construction of new energy-efficient buildings. Moreover, the study made it possible to understand the heaviest interventions and the most impacting phases from an energetic and environmental point of view, while underlining that the energy and environmental payback times are much lower than the useful life of the building and its components. Also in this case, the outcomes obtained agree with the results of other literature works (Ardente et al., 2011; Asdrubali et al., 2019). The trade-off turns out to be only temporary, while environmental benefits are obtainable in the long term.

The new add-on volume, which represents the most peculiar aspect of the retrofit intervention, increased the energy requirement and the environmental burdens of the building, also delaying the payback times of the intervention. That is mainly linked to the fact that the two parts were not integrated, but conceived of as separate units. A higher integration between the two could have been more interesting from the environmental perspective, particularly if the add-on volume had contributed to the reduction of the energy requirement of the existing part.

References

- Ardente, F., M. Beccali, M. Cellura, and M. Mistretta. 2011. "Energy and environmental benefits in public buildings as a result of retrofit actions." *Renewable and Sustainable Energy Reviews* 15: 460–470.
<https://doi.org/10.1016/j.rser.2010.09.022>
- Asdrubali, F., I. Ballarini, V. Corrado, L. Evangelisti, G. Grazieschi, and C. Guattari. 2019. "Energy and environmental payback times for an NZEB retrofit". *Building and Environment* 147: 461-472.
doi: <https://doi.org/10.1016/j.buildenv.2018.10.047>
- Asdrubali, F., and G. Grazieschi. 2020. "Life cycle assessment of energy efficient buildings." *Energy Reports* 6 (8): 270-285. doi: <https://doi.org/10.1016/j.egyr.2020.11.144>
- Asdrubali, F., M. Roncone, and G. Grazieschi. 2021. "Embodied energy and embodied GWP of windows: A critical review." *Energies* 14 (13). doi: <https://doi.org/10.3390/en14133788>
- Assimakopoulos, M. N., R. F. de Masi, A. Fotopoulou, D. Papadaki, S. Ruggiero, G. Semprini, and G. P. Vanoli. 2020. "Holistic approach for energy retrofit with volumetric add-ons toward nZEB target: Case study of a dormitory in Athens." *Energy and Buildings* 207. doi: <https://doi.org/10.1016/j.enbuild.2019.109630>
- Blengini, G.A, and T. Di Carlo. 2010. "The changing role of life cycle phases, subsystems and materials in the LCA of low energy buildings". *Energy and Buildings* 42 (6): 869-880. doi: <https://doi.org/10.1016/j.enbuild.2009.12.009>
- CEN. 2019. EN 15804-2019 - Sustainability of Construction Works. Environmental Product Declarations, Core Rules for the Product Category of Construction Products. Bruxelles, Belgium.
- DesignBuilder Software Ltd. 2022. "DesignBuilder." Accessed on January 16. <https://designbuilder.co.uk/>
- Ecoinvent. 2021. "ecoinvent Database." Accessed on February 8. <https://ecoinvent.org/>
- EEA. 2021. "Greenhouse gas emissions from energy use in buildings in Europe." Accessed May 20. <https://www.eea.europa.eu/data-and->

- maps/indicators/greenhouse-gas-emissions-from-energy/assessment
- European Commission – Department of Energy. 2020. “Energy efficiency in buildings.” Accessed on 29 October 2021. https://ec.europa.eu/info/news/focus-energy-efficiency-buildings-2020-lut-17_en
- European Parliament and Council of the European Union. 2010. “Directive 2010/31/EU of the European Parliament and of the Council of 19 May 2010 on the energy performance of buildings.” Accessed on 29 October 2021. <https://eur-lex.europa.eu/legal-content/EN/TXT/?uri=celex%3A32010L0031>
- Frischknecht, R., F. Wyss, S.B. Knöpfel, T. Lützkendorf and M. Balouktsi. 2015. “Cumulative energy demand in LCA: the energy harvested approach.” *The International Journal of Life Cycle Assessment* 20: 957–969. doi: <https://doi.org/10.1007/s11367-015-0897-4>
- Grazieschi, G., F. Asdrubali, and G. Thomas. 2021. “Embodied energy and carbon of building insulating materials: A critical review.” *Cleaner Environmental Systems* 2. doi: <https://doi.org/10.1016/j.cesys.2021.100032>
- Intergovernmental Panel on Climate Change (IPCC). 2007. “Fourth Assessment Report.” Accessed on January 11. <https://www.ipcc.ch/assessment-report/ar4/>
- International Organization for Standardization. 2006. ISO 14040:2006 Environmental management — Life cycle assessment — Principles and framework. Geneva, Switzerland.
- International Organization for Standardization. 2006. ISO 14044:2006 Environmental management — life cycle assessment — Requirements and guidelines. Geneva, Switzerland.
- Italian Ministry of Economic Development. 2015. Ministry Decree of 26 June 2015 “Applicazione delle metodologie di calcolo delle prestazioni energetiche e definizione delle prescrizioni e dei requisiti minimi degli edifici”. Accessed on 29 October 2021. <https://www.gazzettaufficiale.it/eli/id/2015/07/15/15A05198/sg>
- PRé Sustainability. 2022. LCA software for informed change-makers. Accessed on January 11. <https://simapro.com/>
- President of the Italian Republic. 1993. Decree of 26 August 1993 n. 412 “Regolamento recante norme per la progettazione, l’installazione, l’esercizio e la manutenzione degli impianti termici degli edifici ai fini del contenimento dei consumi di energia”. Accessed on 4 December 2021. <https://www.gazzettaufficiale.it/eli/id/1993/10/14/093G0451/sg>
- Rinaldi, S., G. Frunzio, M. Guadagnuolo, L. Di Gennaro, and L. Massaro. 2021. “A sustainable material for sustainable architecture: wood in parasite architecture.” In *Congresso Internacional Sobre Patologia e Reabilitação Das Construções, Universidade Federal do Ceará*, 481–488. doi: <https://doi.org/10.4322/CINPAR.2021.061>
- Webb, A. L.. 2017. “Energy retrofits in historic and traditional buildings: A review of problems and methods.” *Renewable and Sustainable Energy Reviews* 77: 748–759. doi: <https://doi.org/10.1016/j.rser.2017.01.145>
- Wiklund, U. 2019. Product Category Rules for Buildings - version 2.01. Accessed on January 11. <https://portal.environdec.com/>

Comparison Between Measured and Calculated Values in Relation to Noise From Wind Turbines

Antonella Bevilacqua –University of Parma, Italy - antonella.bevilacqua@unipr.it

Gino Iannace - University of Campania “Luigi Vanvitelli”, Italy - gino.iannace@unicampania.it

Ilaria Lombardi - University of Campania “Luigi Vanvitelli”, Italy - ilaria.lombardi@unicampania.it

Amelia Trematerra - University of Campania “Luigi Vanvitelli”, Italy - amelia.trematerra@unicampania.it

Abstract

The noise from wind turbines is generally assessed according to ISO 9613 in order to preserve the internal noise levels of the nearest sensitive receptors. Following the standard requirements, the wind turbines are considered point sources with an attenuation decay equal to 6 dB by doubling the distance. These indications should be taking into account also the air absorption at different octave bands and the gradient effects due to outdoor environmental conditions. This paper deals with the comparison of some acoustic measurements carried out in Campania (Italy) with the theoretic outcomes obtained in line with the standard ISO 9613. Different types of wind turbines have been assessed, based on a variety of power supply, distance between source and receiver and gradient of wind speed and direction. The surveys have been undertaken inside the nearest sensitive receptors with the conditions of open windows. The results highlight a drift between results, where the calculated are found to be lower than the measured-on site, underestimating the real environmental conditions.

1. Introduction

Wind energy contributes significantly to reducing the use of fossil fuels in the production of electricity, having the benefit of little surface area of occupation. The first wind towers built for the transformation of wind energy into electricity occurred in the United States during 1950s and thereafter it spread rapidly during the 1970s, following the fossil energy crises. Nowadays, wind energy is the most competitive renewable energy source to produce electricity, contributing to both limiting the use of fossil fuels and reducing the effects of atmospheric pollution. Therefore, it is considered a

growing business market. The uprising growth at global scale can be translated in numbers as summarised in Table 1.

Table 1 – Global growth of wind power in the last decades

Time	Wind Tower Production (MW)
1996	6100
2001	24000
2017	540000

The areas with the most significant increase are Asia (China and India), Europe (especially France, Spain and Germany) and the United States. In Italy the first wind towers were built in 1990. Based on the geographical morphology, Italy has a significant number of sites suitable for the productivity of wind power, especially in the south and on the islands, where strong winds are dominant. Many wind farms have been built nearby existing residential properties, rising nuisance concerns for the occupants living in the surrounding areas (Sardaro et al., 2019; Shaheen et al., 2016). Noise emission by the operation of wind turbines is potentially causing sleep disturbance and other disease, depending on time of exposure and level of noise. According to the World Health Organization (WHO), limits from nuisance have been established in relation to night-time period (Guillemette & Larsen, 2012). In particular, thresholds of 40 dB(A) for outdoor areas and 30 dB(A) within bedrooms are considered the recommended limits to avoid sleep disturbance which may be potentially causing distress and having negative impact on health (Raman et al., 2016).

Specifically, the noise coming from wind turbines is due to both the effects of air interaction during the blades rotation and the systems inside the nacelle (Wagner et al., 2012). As such, the components of the generated noise are the following (Zajamsek et al., 2014):

- Airborne emission due to the blades' rotation, characterised by a broadband spectrum; and
- Structural-borne emission produced by the electro-mechanical pieces, like the generator, turning over-gear, cooling systems and other components).

Based on a comparison between the two, the levels of the second type of noise are lower than the first one (Bowdler et al., 2011; Burton et al., 2001). By calculating predictions according to ISO 9613 (ISO) the wind turbines are considered as point sources, and the major contribution of the total sound energy is considered to be issued by the gearbox. Generally, the higher the electric power production, the higher the sound pressure levels emitted by a wind tower. By detailing the noise at the gear box, a variation of sound levels is generated whereas the blade crosses the pole during the rotation. This variation can be defined as an amplitude modulation and is one of the most important factors of annoyance since the human hearing is more sensitive to impulsive than steady (or tonal) noise (Doolan et al., 2012; Rogers et al., 2006; Van den Berg, 2004). When compared to other noise sources (e.g. aircraft, railways, etc.) the degree of annoyance of noise from wind turbines is consistent (Pedersen et al., 2004; Waye & Öhrström, 2002).

This paper deals with the acoustic measurements of noise generated by wind turbines of different power supply undertaken inside sensitive residential properties; the measured results have been compared with the outcomes of the numerical predictions calculated in accordance with ISO 9613 (ISO, 2006). The two main scenarios (with the noise source on and off) have been compared with each other and with the predictions carried out by model simulations (Krijgsveld et al., 2009; Ladenburg, 2009; Lee et al., 2011; Shepherd et al., 2011; Voicescu et al., 2016).

2. Sound Propagation Based On Simulated Predictions

The assessment of the acoustic impact generated by the operation of wind turbines is one of the concerns considered since the design phase. The predictions herein calculated have been assessed according to ISO 9613-2 (ISO, 2006; Wszolek et al., 2019), which considers the sound emission as a point source: a numerical model that can match the reality if the receiver is located at a large distance from the source. For the determination of environmental noise levels, the standard ISO 9613-2 provides a theoretical method to evaluate the sound attenuation based on free field conditions. The calculation of the equivalent continuous sound pressure level (L_{Aeq}) is summarized in equation (1).

$$L_p = L_w + D_{i\theta} - A_{div} - A_{atm} - A_{gr} - A_{bar} - A_{misc} \quad (1)$$

where:

- L_p : sound pressure level, dB(A),
- L_w : sound power level, dB(A),
- $D_{i\theta}$: directivity factor,
- A_{div} : attenuation due to geometric divergence,
- A_{atm} : attenuation due to atmospheric absorption,
- A_{gr} : attenuation due to the ground effect,
- A_{bar} : attenuation due to any barrier,
- A_{misc} : attenuation due to foliage, industrial sites, housing.

By simplifying equation (1) and considering the geometric divergence only, the sound pressure level becomes as indicated in equation (2).

$$L_p = L_w - A_{div} \quad (2)$$

where A_{div} is calculated according to UNI ISO 9613-2, which is given in equation (3).

$$A_{div} = 20 \log(d) + 11 \quad (3)$$

where d is the distance between the sound source and the receiver. In line with the ISO 9613 (ISO, 2006), the sound pressure level at the nearest sensitive locations shall include the attenuation effect of the open window, or the difference between the sound levels measured outdoor and inside the building.

3. Acoustic Measurements

The acoustic measurements were carried out with a First-Class sound level meter LXT1 Larson Davis. The equipment was calibrated before and after the survey and no drift in calibration was noted. Sets of 5-minute were made at the 3-hour long term attended measurement locations, identified inside the nearest sensitive receptors. The measurements recorded overall A-weighted L_{eq} and L_{95} sound pressure levels, with the time averaging constant set to 'Fast' (Ciaburro et al., 2021). The sound level meter was installed on a tripod at a height of 1.4 m from the finish floor and a minimum of 2 m from any vertical surface. The acoustic measurements were carried out under the condition of having open window. The noise levels have been recorded for wind turbines in operation and out of any activity, in order to assess, under the same wind speed condition, the noise contribution from the wind farms in operation against the background noise levels without any activity running (Iannace, 2016; Iannace et al., 2019a; Trematerra & Iannace, 2017).

3.1 First Case Study

The first measurement campaign has been conducted in autumn, with a relative humidity equal to 50 %, a temperature around 10 °C, and a wind speed averaging between 8 m/s and 10 m/s, from South-West direction (Iannace et al., 2019a; Iannace et al., 2019b). With wind towers provided with 3.0 MW power supply. The rotation speed is about 12 rpm. The microphone was installed in a room having dimensions of 2 × 3 × 3 m (W, L, H). Given the different orientation, the wind turbines were operating singularly during the survey, such that each contribution has been calculated singularly (Iannace et al., 2020). The measured equivalent sound pressure levels at the receiving positions have been summarized in Table 2.

Table 2 – Measured results related to the first case study

Activity of Wind Towers	L_{eq} (dBA)	L_{95} (dBA)	Average wind speed (m/s)
On	45	39	8 - 9
Off	35	31	9 - 10
On	52	48	10 - 11
On	43	36	9 - 10

Table 2 indicates that the noisiest condition occurs when the wind speed fluctuates around 10-11 m/s; in this case the equivalent sound pressure level is equal to $L_{eq} = 52$ dB(A). With similar wind speed conditions (9-10 m/s), when the wind turbines are off, the background noise level drops to $L_{eq} = 35$ dB(A), up to 17 dB below. By comparing the sound pressure levels measured at the nearest sensitive receptor and the predictions as outlined by the standard requirements, it is possible to calculate the sound pressure level for each distance of the three towers from the receiver. Considering the distance of each wind tower equal to 450 m, 650 m, and 950 m, that a nominal power of each wind turbine is 3.0 MW (equivalent to $L_W = 104$ dB(A)), the predicted sound pressure levels emitted by a wind turbine according to ISO 9613 are summarised in Table 3. A total predicted equivalent sound pressure level at the receiver location would be equivalent to $L_p = 42$ dB(A). Additionally, the effect of the open window shall be counted to be around 4-5 dB. Therefore, the sound level inside the sensitive receptor is equal to $L_p = 37$ -38 dB(A), meaning that the regulation underestimates the overall value if compared with the measured results.

Table 3 – Predicted noise levels according to ISO 9613. First case study

Distance of the Towers from Receiver	A_{div} values (dBA)	L_p values (dBA)
450	64	40
650	67	37
950	71	33

3.2 Second Case Study

This second acoustic survey deals with wind towers provided with 60 kW power supply. The tower is located about 250 m from the nearest sensitive receptor, and it is composed of a 40 m high pole and three blades. The rotation speed is about 30 rpm. The rotation is discontinuous because it depends on instantaneous wind speed, that therefore generates an intermittent noise. The measured equivalent sound pressure levels at the receiving positions have been summarized in Table 4.

Table 4 – Measured results related to the second case study

Activity of Wind Towers	L_{eq} (dBA)	L_{95} (dBA)	Average wind speed (m/s)
On	45	40	8 - 9
Off	32	33	8 - 9
On	48	46	11 - 12
On	50	47	12 - 15
On	41	38	7 - 8

When the wind turbine is not in operation, the background noise level measured inside the sensitive receptor is equal to $L_{eq} = 32$ dB(A), while results of the wind farm in operation is between $L_{eq} = 41$ dB(A) and $L_{eq} = 50$ dB(A). Considering the theoretical methodology based on ISO 9613 standard, with a distance equal to 250 m, the sound attenuation indicated in equation (4) is the following.

$$A_{div} = 20 \log(250) + 11 = 59 \text{ dB(A)} \quad (4)$$

The nominal power of the wind turbine is 60 kW (equivalent to $L_W = 100$ dB(A)); as such, the predicted sound pressure levels emitted by a wind turbine considered a point source in accordance with ISO 9613 is given in equation (5).

$$L_p = 100 - 59 = 41 \text{ dB(A)} \quad (5)$$

By applying a further attenuation for the open window equal to 4 dB, the predicted noise levels is $L_p = 37$ dB(A). For this second case study, the meth-

odology outlined by the standard underestimates effective noise level and highlights a difference of up to 13 dB between the maximum measured results and the calculated value.

3.3 Third Case Study

The third acoustic survey has been performed inside a sensitive receptor that is 250 m distant from the wind towers. With wind towers provided with 1.0 MW power supply. A South-West wind direction has been recorded to have a speed of approximately 8-9 m/s. The rotation speed of these blades is equal to 15 rpm. The measured equivalent sound pressure levels at the receiving positions have been summarized in Table 5.

Table 5 – Measured results related to the third case study

Activity of Wind Towers	L_{eq} (dBA)	L_{95} (dBA)	Average wind speed (m/s)
On	45	31	8 - 9
Off	33	31	8 - 9

Table 5 indicates that when the wind turbine is in operation the equivalent sound pressure levels measured inside the sensitive receptor is equal to $L_{Aeq} = 45$ dB(A), with a difference of 12 dB by considering the quiet condition (i.e., background noise level). Considering the theoretical methodology based on ISO 9613 standard, with a distance equal to 250 m, the sound attenuation is similar to what calculated in equation (4) to be equal to $A_{div} = 59$ dB(A). The nominal power of this wind turbine is 1.0 MW, which is equivalent to $L_W = 104$ dB(A). Based on these values, the predicted sound pressure level emitted by a wind turbine considered a point source in accordance with ISO 9613 is given in equation (6).

$$L_p = 104 - 59 = 45 \text{ dB(A)} \quad (6)$$

By applying a further attenuation for the open window equal to 4 dB, the predicted noise levels is $L_p = 41$ dB(A). Similarly, this third case study highlights an underestimation of the predicted calcula-

tions of 4 dB compared to the measured value.

3.4 Fourth Case Study

The fourth acoustic survey has been performed inside the nearest sensitive receptor located 200 m from the wind farm. With wind towers provided with 1.0 MW power supply. The North wind direction has been recorded to have a speed equal to 15 m/s. The rotation speed for this wind turbines is equal to 15 rpm. The acoustic measurements were performed by placing the microphone in a room facing the wind turbines, with the window open. The measured equivalent sound pressure levels at the receiving positions have been summarized in Table 6 (Berardi et al., 2020).

Table 6 – Measured results related to the fourth case study

Activity of Wind Towers	L_{eq} (dBA)	L_{95} (dBA)	Average wind speed (m/s)
On	52	49	15
Off	44	40	15

Table 6 indicates that when the wind turbine is in operation the equivalent sound pressure levels measured inside the sensitive receptor is equal to $L_{Aeq} = 52$ dB(A), with a difference of 8 dB by considering the quiet condition (i.e., background noise level). Considering the theoretical methodology based on ISO 9613 standard, with a distance equal to 200 m, the sound attenuation expressed in equation (7) is given as follows.

$$A_{div} = 20 \log(200) + 11 = 57 \text{ dB(A)} \quad (7)$$

Having a nominal power of 1.0 MW, which is equivalent to $L_W = 104$ dB(A) the predicted noise levels based on theoretical concepts is given in equation (8).

$$L_p = 104 - 57 = 47 \text{ dB(A)} \quad (8)$$

With the open window attenuation, the final predicted noise level emitted by the wind turbine is equal to $L_p = 43$ dB(A). On this basis, it has been

demonstrated that a difference of 9 dB has been found between measured and estimated values.

3.5 Fifth Case Study

The fifth acoustic survey has been performed inside the nearest sensitive receptor located 450 m from the wind farm. With wind towers provided with 1.0 MW power supply. The North wind direction has been recorded to have a speed around 6-8 m/s. The rotation speed of the blades is equal to 11 rpm. The acoustic measurements were performed by placing the microphone in a room facing the wind turbines, with the window open. The measured equivalent sound pressure levels at the receiving positions have been summarized in Table 7.

Table 7 – Measured results related to the fourth case study

Activity of Wind Towers	L_{eq} (dBA)	L_{95} (dBA)	Average wind speed (m/s)
On	40	37	6 - 8
Off	35	31	6 - 8

Table 7 indicates that when the wind turbine is in operation the equivalent sound pressure levels measured inside the sensitive receptor is equal to $L_{Aeq} = 40$ dB(A), with a difference of 5 dB by considering the background noise level. Considering the theoretical methodology based on ISO 9613 standard, with a distance equal to 450 m, the sound attenuation expressed in equation (9) is given as follows.

$$A_{div} = 20 \log(450) + 11 = 64 \text{ dB(A)} \quad (9)$$

Given the nominal power produced by the sound source equal to $L_W = 104$ dB(A) the theoretical sound pressure level emitted by a wind turbine according to ISO 9613 is summarised in equation (10).

$$L_p = 104 - 64 = 40 \text{ dB(A)} \quad (10)$$

With the additional open window attenuation, the

final predicted noise level emitted by the wind turbine is equal to $L_p = 36$ dB(A). On this basis, it has been demonstrated that a difference of 4 dB has been found between measured and estimated values.

4. Discussion

Different campaigns of measurements have been carried out inside sensitive receptors near to the wind farms. The nominal power of the wind turbine varied from 60 kW, 1.0 MW to 3.0 MW. The surveys were carried out in rooms having similar volume size and with the window open, with the microphone directly facing the sound sources. This paper has demonstrated that the difference between measured results and predicted values calculated in accordance with ISO 9613 is consistent, to be up to 13 dB. From the five case studies it has been shown how the predicted values are lower than the measured results therefore underestimating the effective impact that the wind farms have on the sensitive receptors. The effects of the disturbance due to the noise perceived inside the houses is a function of the difference in the noise level measured when the wind turbine is off or in operation. If from the analysis of the acoustic measurements between the sound source switched off or in operation, a difference is detected then we are in the presence of a disturbing noise, that is generates annoyance. It may happen that for wind speeds above 15 m/s the wind noise covers the noise emitted by the wind turbines, in this condition the noise emitted by the wind turbines is not perceived by the people living inside the houses, but this is a condition limit that happens a few times.

5. Conclusions

The theoretical assessment of the noise propagation from wind turbines in operation has been performed in accordance with the ISO 9613 standard requirements. The predictions are based on the simulation of a wind turbine as a point source and on the open window attenuation. The variety of

case studies, characterised by different distance between source and receiver, has demonstrated that the predictions underestimate the effective noise levels of the wind farms as they have been measured on site. One of the main factors that the regulation shall take into account is the wear of the rotating elements that is cause of an increase of noise levels compared to the initial assessment carried out in laboratory conditions, before the wind farms are installed. This outcome highlights the limits of the existing regulation (ISO 9613) that shall be implemented with further considerations in order to produce results to be close to the acoustic measurements.

References

- Berardi, U., G. Iannace, G. Ciaburro, D. D'Orazio, and A. Trematerra. 2020. "Mini-Wind Turbine Noise Measured Inside Near-by Houses". *Canadian Acoustics* 48(3): 18-20.
- Bowdler, D., and L. Leventhall. 2011. *Wind turbine noise*, Multi-science Publishing Co. Ltd.
- Burton, T., D. Sharpe, N. Jenkins, and E. Bossanyi. 2001. *Wind energy handbook* (Vol. 2). New York: Wiley.
- Ciaburro, G., G. Iannace, V. Puyana-Romero, and A. Trematerra. 2021. "Machine learning-based tools for wind turbine acoustic monitoring". *Applied Sciences* 11(142) doi: <https://doi.org/10.3390/app11146488>
- Doolan, C. J., D. J. Moreau, and L. A. Brooks. 2012. "Wind turbine noise mechanisms and some concepts for its control". *Acoustics Australia* 40(1): 7-13.
- Guillemette, M., and J. K. Larsen. 2002. "Post development experiments to detect anthropogenic disturbances: the case of sea ducks and wind parks". *Ecological Applications* 12: 868-877.
- Iannace, G. 2016. "Effects of noise from wind turbines inside home". *Wind Engineering* 40(1): 25-30. doi: <https://doi.org/10.1177/0309524X15624339>
- Iannace, G., U. Berardi, G. Ciaburro, and A. Trematerra. 2019. "Wind turbines noise measurements inside homes". In *Proc. of INTER-NOISE and NOISE-CON* 259(7): 2845-2854.

- Iannace, G., G. Ciaburro, and A. Trematerra. 2019. "Wind turbine noise prediction using random forest regression". *Machines* 7(4): 69. doi: <https://doi.org/10.3390/machines7040069>
- Iannace, G., Berardi, U., Ciaburro, G., Trematerra, A., 2019. Wind turbines noise measurements inside homes. In *proc. of Internoise Conference*, Madrid.
- Iannace, G., G. Ciaburro, and A. Trematerra. 2020. "Using neural networks to detect wind turbine functioning conditions". *International Journal of Automation and Smart Technology* 10(1): 145-152. doi: <https://doi.org/10.5875/ausmt.v10i1.2225>
- ISO. 1996. *ISO 9613-2: 1996, Acoustics - Attenuation of sound during propagation outdoors*.
- Krijgsveld, K. L., K. Akershoek, F. Schenk, F. Dijk, and S. Dirksen. 2009. "Collision risk of birds with modern large wind turbines". *Ardea* 97(3), 357-366.
- Ladenburg, J. 2009. "Visual impact assessment of offshore wind farms and prior experience". *Applied Energy* 86(3): 380-387.
- Lee, S, K. Kim, W. Choi, and S. Lee. 2011. "Annoyance caused by amplitude modulation of wind turbine noise". *Noise Control Engineering Journal* 59(1): 38-46
- Pedersen, E., and K. P. Waye. 2004. "Perception and annoyance due to wind turbine noise - a dose – response relationship". *Journal of Acoustical Society of America* 116(6): 3460 – 3470.
- Raman, G., R. C. Ramachandran, and M. R. Aldeman. 2016. "A review of wind turbine noise measurements and regulations". *Wind engineering* 40(4): 319-342.
- Rogers, A. L., J. F. Manwell, and S. Wright. 2006. *Wind turbine acoustic noise*. Renewable Energy Research Laboratory, Amherst: University of Massachusetts.
- Sardaro, R., N. Faccilongo, and L. Roselli. 2019. "Wind farms, farmland occupation and compensation: Evidences from landowners' preferences through a stated choice survey in Italy". *Energy Policy* 133: 110885.
- Shaheen, M., and M. Z. Khan. 2016. "A method of data mining for selection of site for wind turbines". *Renewable and Sustainable Energy Reviews* 55: 1225-1233.
- Shepherd, D., D. McBride, D. Welch, K. N. Dirks, and E. M. Hill. 2011. "Evaluating the impact of wind turbine noise on health-related quality of life". *Noise and Health* 13(54): 333.
- Trematerra, A., and G. Iannace. 2017. "Wind turbines acoustic measurements". In *AIP Conference Proceedings* 1859(1): 020001.
- Van den Berg, G. P. 2004. "Effects of the wind profile at night on wind turbine sound". *Journal of sound and vibration* 277(4-5): 955-970.
- Voicescu, S. A., D. S. Michaud, K. Feder, L. Marro, J. Than, M. Guay, A. Denning, T. Bower, F. van den Berg, N. Broner, and E. Lavigne. 2016. "Estimating annoyance to calculated wind turbine shadow flicker is improved when variables associated with wind turbine noise exposure are considered". *The Journal of the Acoustical Society of America* 139(3): 1480-1492.
- Wagner, S., R. Bareiss, and G. Guidati. 2012. *Wind turbine noise*. Springer Science & Business Media.
- Waye, K. P., and E. Öhrström. 2002. "Psycho-acoustic characters of relevance for annoyance of wind turbine noise". *Journal of sound and vibration* 250(1): 65-73.
- Wszolek, T., B. Stępień, and D. Mleczko. 2019. "Comparison of ISO 9613-2 and CNOSSOS-EU methods in noise modelling of a large industrial plant". In *Proc. of INTER-NOISE*.
- Zajamsek, B., D. J. Moreau, and C. J. Doolan. 2014. "Characterizing noise and annoyance in homes near a wind farm". *Acoustics Australia* 42(1): 14-19.

Thermo-Hygrometric Comfort Analysis in a Real Public Conference Room to Support a Digital-Twin Targeted to Parametric Investigations

Roberto Bruno – University of Calabria, Italy – roberto.bruno@unical.it

Piero Bevilacqua – University of Calabria, Italy – piero.bevilacqua@unical.it

Daniela Cirone – University of Calabria, Italy – daniela.cirone@unical.it

Natale Arcuri – University of Calabria, Italy – natale.arcuri@unical.it

Abstract

In this paper, the efficient use of a building-plant system in terms of thermal comfort conditions for a real conference room was verified in the summer by its digital twin. A DesignBuilder model was calibrated by experimental data concerning the indoor air temperature, average radiant temperature, relative humidity and CO₂ concentration. Different situations for people's well-being were studied by varying emitter typology, control strategies, subjective parameters and internal loads. The EMS tool was used to simulate high-level control strategies. It was found that radiant ceilings in continuous operation could promote situations of undercooling, whereas a predicted plant operation is appropriate with intermittent functioning. People's metabolism affects comfort conditions more than internal loads, determining an increase of about 3 degrees in indoor air and mean radiant temperature. Inlet temperature variations in fan coils modify comfort conditions marginally. However, these emitters interact worse with internal loads than radiant ceilings. Aside from the Fanger PMV, discomfort indices following EN 15251 were also evaluated. However, in prevision of the implementation of predictive control strategies, the degree hour approach is not recommended because it does not consider clothing resistance properly.

1. Introduction

Recent studies confirm how the implications of thermal comfort in human activities are increasingly relevant, from energy management to ensuring energy efficiency, up to contexts linked to environmental impact and economy (Abdelrahman et al., 2022). People, indeed, spend up to 90 % of their lives in buildings, therefore proper management of

indoor spaces is required, also to have a positive impact on people's productivity (Asadi et al., 2017). Recently, targeted investigations have shown that, beyond the subjective parameters involved in ISO 7730, a sort of dependence on gender, age, lighting, CO₂ concentration and noise occurs (Crosby & Rysanek, 2021). However, also the more updated thermal comfort models produce accuracy in results of less than 33 % when compared with measured data (Li et al., 2018). In the light of this, the procedures based on the development of a tuned digital twin of the building plant systems could improve the reliability of the result. Moreover, predictive control strategies can be developed to attain simultaneously well-being and energy savings when significant parameters change dynamically. Despite the elevated potential, also to favor the intuitive visualizations of the monitored data in appropriate dashboards, digital twins have rarely been studied for thermal comfort evaluation. A vector-based spatial model, called Build2Vec, for predicting spatial-temporal occupants' indoor environmental preferences was studied in (Abdelrahman et al., 2022), showing a 14 %-28 % accuracy improvement. In (Zhang et al., 2022) a web-based digital twin platform combined with IoT allowed real-time control of the relative humidity level of underground heritage sites to promote preservation to be achieved. A system architecture for the live PMV/PPD calculation based on ASHRAE 55 and enrichment of BIM-based representations of building spaces in virtual reality environments, with live IoT-enabled monitoring data, was proposed in (Shahinmoghdam et al., 2021). In this paper, referring to a real conference room lo-

cated at the University of Calabria, experimental data of indoor air temperature, relative humidity, CO₂ concentration and mean radiant temperature were used to calibrate the digital twin developed in the DesignBuilder environment (DesignBuilder Software Ltd, 2018), a user interface based on an EnergyPlus engine (Berkeley et al., 2019). In this study, the model was employed to determine the influence of different parameters on thermal comfort indices. This work is targeted for the successive implementation of predictive control strategies that assure appropriate thermal comfort conditions in transient regimes. So, the real-time monitoring associated with IoT will be able to intervene by apposite actuators in order to maintain comfort indices within a suitable range.

2. Materials and Methods

Indoor microclimatic measurements were carried out from 11 on 19 July 2019 to 11 on 22 July 2019 using the BABUC control unit (*LSI - Babuc System*, 2022). The aim was to obtain experimental data necessary for validating a dynamic model in DesignBuilder and then proceed to further parametric analyses. In Figure 1, the conference room monitored is shown in blue. The variables strictly related to people, such as metabolism and clothing thermal resistance, were changed related to the different seasons following UNI EN ISO 9920 (Italian Unification Institution, 2009). Environmental parameters refer to the UNI EN ISO 7726 (Italian Unification Institution, 2001).

2.1 The Building-Plant System

The experimental site is located at the University of Calabria (Southern Italy, 39°19'58"80N - 16°11'6"72 E) with typical Mediterranean climatic conditions, defined as subtype CSa following the Köppen climate classification (Peel et al., 2007).

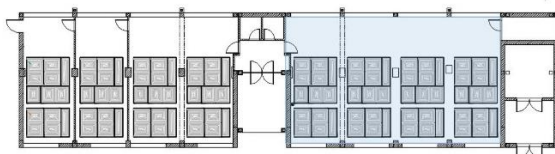


Fig. 1 – Ground floor plane and highlighted monitored area

Table 1 – Layers of the vertical walls

Layer	T [m]	TC [W m ⁻¹ K ⁻¹]	SH [J kg ⁻¹ K ⁻¹]	D [kg m ⁻³]
Plaster	0.02	0.900	800	1400
Hollow brick	0.30	0.157	1000	1250
Plaster	0.02	0.900	800	1400

Table 2 – Layers of the ground floor

Layer	T [m]	TC [W m ⁻¹ K ⁻¹]	SH [J kg ⁻¹ K ⁻¹]	D [kg m ⁻³]
Tiles	0.005	1	1000	2000
Light concr.	0.050	2	800	900
EPS	0.090	0.035	800	55
Stru. element	0.140	2.2	1000	2600

Table 3 – Layers of the ceiling deck

Layer	T [m]	TC [W m ⁻¹ K ⁻¹]	SH [J kg ⁻¹ K ⁻¹]	D [kg m ⁻³]
Tiles	0.005	1	1000	2000
Light concr.	0.050	2	800	900
EPS	0.090	0.035	800	55
Stru. element	0.140	2.2	1000	2600
Plaster	0.020	0.9	800	1400

The structure is made of reinforced concrete with transparent surfaces located in the South and North. Stratigraphies of vertical and horizontal opaque walls are listed from Tab. 1 to Tab. 3 with thickness (T), Thermal conductivity (TC), Specific heat (SH) and density (D), all derived from material datasheets.

Highly efficient technological solutions were implemented inside the building, with a control system capable of optimizing renewable energy resources. Two air-water heat pumps in master/slave functioning with a rated thermal power of 5 kW and cooling capacity of 3.8 kW each, connected with a 4 kW_p PV generator, provided heating and cooling by an 800-litre storage tank, configured as a sui-generis electrical storage system to manage PV surpluses. A cogenerative biomass boiler with a Stirling engine (14 kW of thermal power, 1 kW of electric load) was used as an integration system. Emitters consisted of radiant ceilings in mineral fibre, thermally decoupled from the structure, installed in a false ceiling, with an active radiant surface of 124.8 m² distributed in eight independent sectors (see Fig. 1). The main novelty lay in the

management of the experimental set-up: while integrating different systems and devices, the system carries out checks on a single decision-making level to rationalize and manage resources in the best possible way by creating an electrical island grid-independent.

2.2 Measurement System

The BABUC instrument line consists of an assembly of instruments, sensors, accessories and software programs for acquisition, display, storage and processing purposes. Different sensors adopting different physical principles can be connected simultaneously to BABUC, and those employed are listed in Tab. 4. All the probes were positioned in the centre of the conference room.

2.3 Simulation Model

DesignBuilder is based on an EnergyPlus calculation engine and allows for managing the degree of detail with which it intends to set envelope and technological aspects, internal loads, occupancy scenarios, clothing and others.

Climatic data were provided by an *.epw file on an hourly basis using the real values acquired by the weather stations located at the University of Calabria (external air temperature, relative humidity, atmospheric pressure, global horizontal irradiation, beam and diffuse components). Schedules were set for light activity with a metabolism of 1.2 met and a summer clothing factor of 0.5 clo. Air infiltration was set following EN 12831 and it was evaluated as a discriminating element for the calibration of the model. On the other hand, natural ventilation was neglected.

Table 4 – Probes employed for room monitoring

Code	Probe	Measured parameter
BSU102	Psychrometer	Dry bulb temperature (°C)
		Wet Bulb Temperature (°C)
		Relative Humidity (%)
		Dew point temperature (°C)
		Enthalpy (J)
BST131	Globe Thermometer	Globe temperature (°C)
		Mean radiant temperature (°C)
BSO103.1	CO ₂ sensor	CO ₂ concentration (ppm)
BSR001	Lux meter	Illuminance (lux)

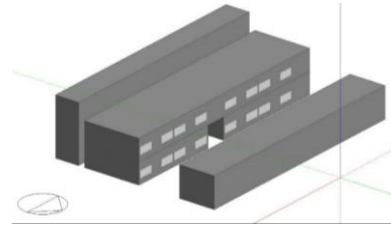


Fig. 2 – Reference building model in DesignBuilder

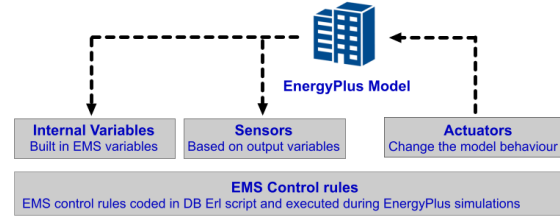


Fig. 3 – Scheme of operation of an EMS control

The HVAC system assumed an ideal setting with unlimited power to attain a setpoint of 22 °C. An EMS (Energy Management System) was employed to carry out an advanced control of the CO₂ concentration. This tool is one of the high-level control methods available in EnergyPlus. An EMS script can access a wide variety of “sensor” data to direct various types of control actions. The EMS uses the concept of sensors to obtain information from elsewhere to use in control calculations. Actuators determine changes in the model and these commands will be used in future studies for the evolution of the model and for the control of air flows to control CO₂ levels by adding control logic following the scheme of Fig. 3

3. Results

3.1 Experimental Data and Validation

The microclimatic surveys for the validation of the model were carried out considering the presence of nine people on 19 July from 14:00 to 18:30 and on 20 July from 9:00 to 14:00, following the real occupation profile. Calibration was carried out by considering closed windows and non-activated shading devices. In order to tune the results, in the model the specific heat and the density of the layers (from Tab. 1 to Tab. 3), the infiltration flow rate and the optical properties of the transparent surfaces were varied. After a fair number of attempts, the temperature profiles of the indoor air matched,

with a slight temporal shift between the experimental and modeled trends (imperfect tuning of the building thermal mass), as depicted in Fig. 4. This aspect is more evident with the indoor mean radiant temperature (Fig. 6). Instruments do not record variations of the relative humidity in the presence of occupants, while the simulation returns a sudden increase (Fig. 5). It can be assumed that real ventilation produces a considerable lowering of humidity ratio in the indoor environment, without affecting the indoor relative humidity. A good match can be observed also for the CO₂ concentration (Fig. 7). Validation was analytically confirmed by statistical indices: mean square error (RMSE), mean bias error (MBE) and correlation factor “r”, listed in Tab. 5. It can be appreciated, as temperature and CO₂ concentration are met quite well; relative humidity is slightly underestimated, as indicated by the negative MBE value.

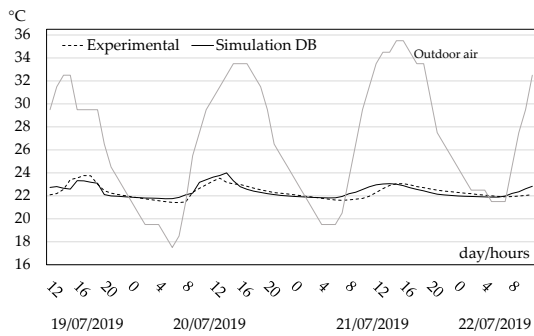


Fig. 4 – Experimental and modeled indoor air temperature

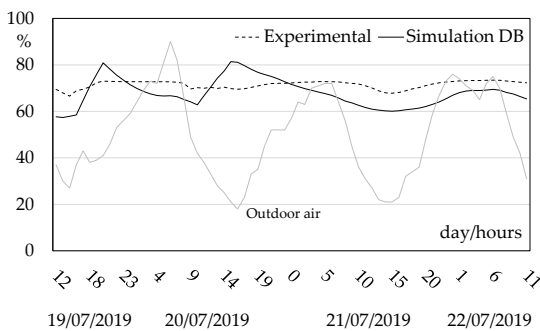


Fig. 5 – Experimental and modeled indoor relative humidity

Table 5 – Some statistical indices for the validation procedure

	RMSE	r	MBE
Indoor air temperature	0.37	0.8	0.00004
Relative humidity	6.61	0.41	-0.00068
Mean radiant temperature	0.48	0.66	0.00014
CO ₂	272.17	0.92	-0.00170

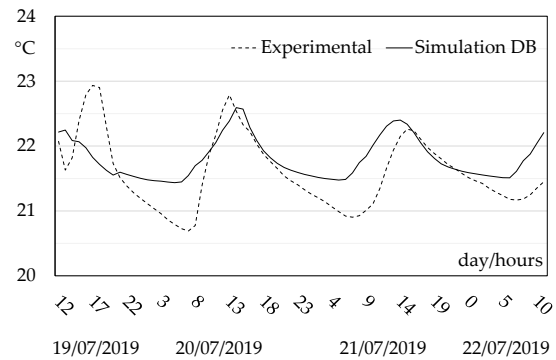
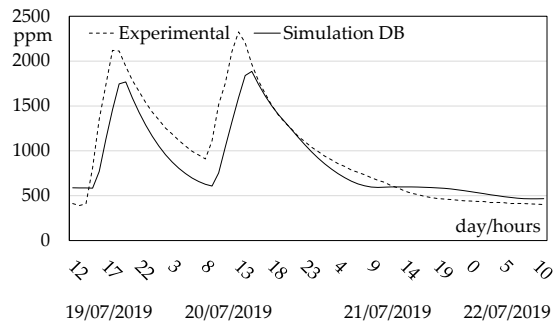


Fig. 6 – Experimental and modeled mean radiant temperature

Fig. 7 – Experimental and modeled indoor CO₂ concentration

3.2 Thermal Comfort Evaluation

After validation, the model results were used to proceed with parametric studies for thermal comfort evaluation inside the conference room. Initially, the use of fan-coils and radiant ceilings (both installed in the conference room, with fan-coils provided mainly for dehumidification purposes) and the variation of the inlet temperature was considered by referring to the whole month of July and 9 to 18 users from Monday to Friday (with an hour and a half of lunch break from 13:00 to 14:30). Lightings (dimming LED system with 5 W of electric power each) were scheduled with the same profile relating to user presence. The cases listed in Tab. 6 were considered.

Table 6 – Cases considered for the thermal comfort evaluation

	Emitter	Cooling time	Clothing/ Metabolism
Case 1	Radiant ceiling 15 °C	7-18 Mo- Fr	0.5 clo/1.2 me
Case 2	Radiant ceiling 15 °C	24h Mo- Fr	0.5 clo/1.2 me
Case 3	Fan coil 15 °C	7-18 Mo- Fr	0.5 clo/1.2 me
Case 4	Fan coil 7 °C	7-18 Mo- Fr	0.5 clo/1.2 me

Regarding the plant operation, two modes were envisaged: the first follows the occupation profile starting one hour earlier. The second mode provides continuous functioning for weekdays to overcome the issues related to the inertia of the radiant ceilings. The Fanger PMV, the Pierce PMV SET, the PMV ET and the operative temperature, as described in the EN 15251 standard, were determined. For the latter, assuming a category II, an operative temperature range is recommended in summer at $23 \div 26$ °C. The Degree Hours criterion, which defines the time during which the operative temperature exceeds the comfort range by the weight factor w_t , was also calculated. It can be noticed that a continuous functioning regime of radiant ceilings allows for the best result (-5.03 °C/month), followed by the intermittent functioning ($+119.4$ °C/month), whereas fan-coils always involve a worsening of the operative temperature due to the prevalent convective exchange inside the indoor environment (422.11 and 324.08 °C/month, respectively, for Cases 3 and 4). The daily average comfort indexes obtained by DesignBuilder confirmed Case 2 as the situation that allows for achieving values falling within the comfort range with the greatest frequency, while fan coils produce marked overheating conditions.

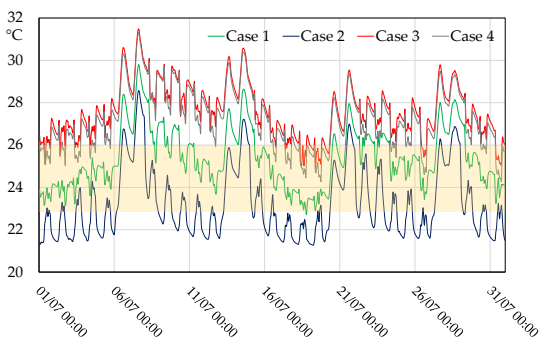


Fig. 8 – Operative temperature in July for the cases considered

Case 2 often guarantees thermal neutrality, but sometimes also a slight undercooling, confirmed both by the w_t index and by the Fanger PMV, whereas the other indices denote a position closer to a slightly warm condition. In Case 1, a slight overheating is detected, meaning that a proper activation in advance is needed to attain adequate comfort. Fan coils supplied at 7 °C guarantee better comfort conditions than Case 4. However, similar comfort indices were obtained, meaning that the inlet temperature is not suitable for regulating thermal comfort when these emitters are employed.

3.3 Parametric Studies

For cases 1, 2 and 4, the role of some parameters on the thermal comfort conditions was evaluated. Case 3 was not considered because it produced the worst scenario. The situation VAR1 involves an increase of internal loads by adding 10 computers supplying 100 Watts each of sensible load. VAR2, instead, considers an increase in 10 people supplying 2 met, whereas in VAR3, a change in clothing insulation to 0.72 clo was implemented. Table 7 highlights how the three situations affect the operative temperature values in Case 1. An evident similarity was detected between the base case and VAR 3, because the indoor air and the mean radiant temperature are the same by changing the clothing thermal resistance. Conversely, a considerable increase was observed in VAR 1 and VAR 2. In particular, 10 people supplying 2 met led to an indoor air temperature growth of 3.6 °C, and the average radiant temperature increased up to 3.4 °C. The weight factor w_t increases in VAR 1 and VAR 2, with the latter affecting results more than the addition of 10 computers (2 met per person for a body area of 1.8 m² corresponds approximately to 200 W following Dubois). It can be appreciated that the mean and maximum temperatures slightly vary, the minimum temperature is almost constant, whereas the degree hour criterion shows considerable worsening with people's metabolism increase.

Table 7 – Operative temperatures with variations in Case1

Base Case	VAR 1	VAR 2	VAR 3
Mean = 25.4 °C	Mean = 26 °C	Mean = 26.9 °C	Mean = 25.5 °C
Max = 29.8 °C	Max = 30 °C	Max = 30.7 °C	Max = 29.8 °C
Min = 22.8 °C	Min = 23.4 °C	Min = 23.6 °C	Min = 22.7 °C
$w_i = 119.4$	$w_i = 179.43$	$w_i = 347.57$	$w_i = 119$
°C/month	°C/month	°C/month	°C/month

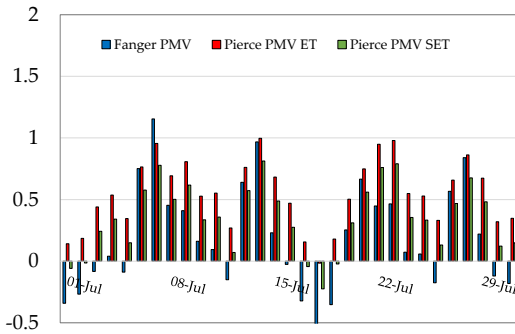


Fig. 9 – Some comfort indices for July 2012, Case 1-base case

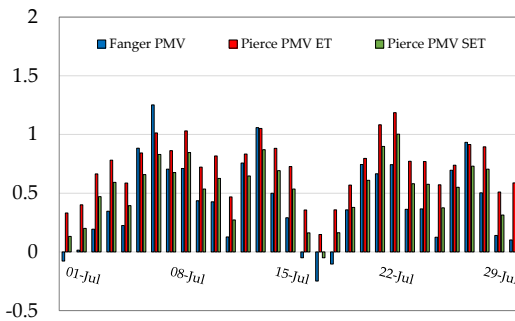


Fig. 10 – Some comfort indices for July 2012, Case 1-VAR1

It can be appreciated that, in the base case, the mean daily Fanger PMV allows for remaining frequently in the desirable range $-0.5/+0.5$, whereas both Pierce PMV ET and PMV SET produce a situation with slight overheating. In particular, the latter are majorly affected by people's metabolism increase, therefore the use of these indices has to be evaluated carefully because it is more sensitive than Fanger PMV. In accordance with the w_i index, the PMV also records the greatest discomfort in VAR 2. For VAR 3, on the other hand, the PMV indices highlight an exceeding of the comfort threshold, nevertheless offering more consistency than the w_i index.

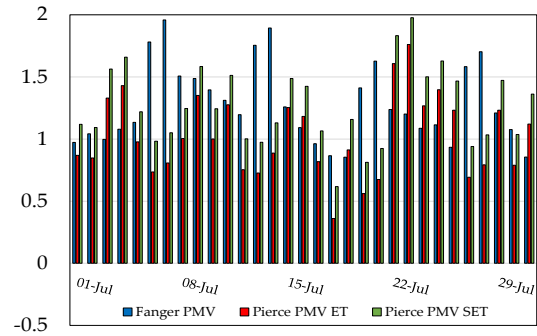


Fig. 11 – Some comfort indices for July 2012, Case 1-VAR2

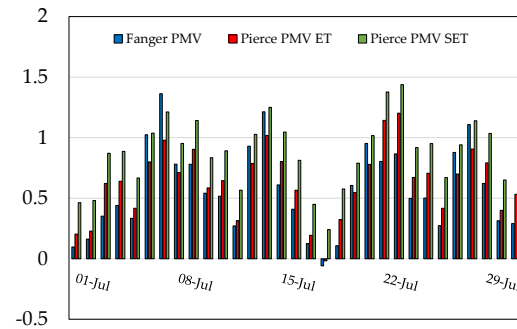


Fig. 12 – Some comfort indices for July 2012, Case 1-VAR3

Case 2 produces similar results to those obtained for case 1. The addition of internal loads and clothing resistance growth determined a Fanger PMV less than 1 with VAR 1 and VAR 3. VAR 2 produced a slightly warm thermal zone with PMV up to 1.5. This result shows that a continuous operation of the radiant ceiling system can guarantee proper thermal comfort conditions when people's activity level is high, so control systems must intervene to limit cooling loads by acting, for instance, on the shading device of the transparent surfaces. Furthermore, even in this case, in the situation of VAR 3, the w_i value fails to return the discomfort increase. On the other hand, all the indices confirm VAR 2 as the situation that causes the greatest discomfort. Nevertheless, the functioning of the radiant ceilings 24 hours per workday allows for more easily meeting the comfort range than an intermittent functioning, but with obvious energy repercussions.

Table 8 – w_i index determined with Case 2 in different situations

Base Case	VAR 1	VAR 2	VAR 3
$w_i = -5.03$	$w_i = 45.87$	$w_i = 61.94$	$w_i = -5.03$

Passing to fan-coils (case 4), again operative temperatures remain almost the same with VAR 3. Unlike the other two previous cases, VAR 2 produced a slight increase. Conversely, VAR 1 determined a significant increase (Figure 13 and Table 9). Indeed, PCs were set mainly as a radiative load (which in the previous cases is instantaneously removed from radiant ceilings), whereas metabolism is prevalently a convective load. This means that fan-coils interact in a worse manner to contrast the endogenous loads. Similarly, regarding the w_i index, the operative temperature increases more with the presence of PCs and not with people's metabolism, and, again, the increase in clothing resistance does not affect its value.

Table 9 – Operative temperatures with variations in Case 4

Base Case	VAR 1	VAR 2	VAR 3
Mean = 27.2 °C	Mean = 28.8 °C	Mean = 27.5 °C	Mean = 27.2 °C
Max = 31.3 °C	Max = 31.8 °C	Max = 31.5 °C	Max = 31.3 °C
Min = 24.3 °C	Min = 24.7 °C	Min = 24.4 °C	Min = 24.3 °C
$w_i = 324.08$	$w_i = 418.45$	$w_i = 331.05$	$w_i = 324.08$
°C/month	°C/month	°C/month	°C/month

As for Case 1, in Figure 14 and Figure 15, the average daily values concerning the comfort indices are displayed for the base case and VAR 1. It can be noticed that the variant records significant discomfort compared with the base case. In accordance with the w_i index, the PMV indices record the greatest discomfort in VAR 2, even if the PMV is more sensitive to the increase in met than the other indices. These results are in line with radiant ceilings. However, it is highlighted that thermal comfort conditions are more difficult to control in presence of fan coils.

4. Conclusions

Thermal comfort conditions were analyzed by a digital twin for a conference room located in South Italy. This allows, in successive steps, for the implementation of predictive control strategies to apply by IoT for preserving thermal comfort conditions, without exceeding energy consumption, by acting on envelope and cooling plant.

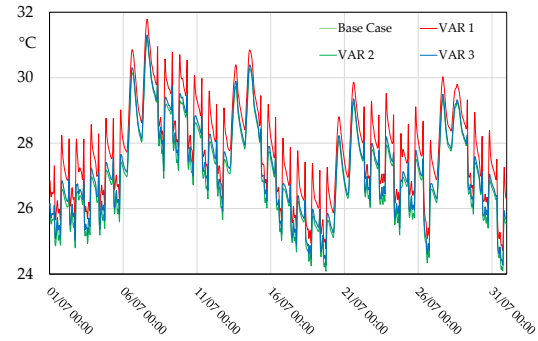


Fig. 13 – Operative temperatures in Case 4 with variants

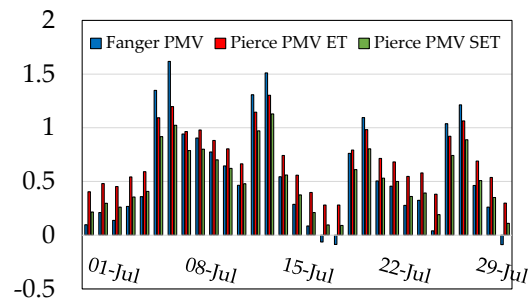


Fig. 14 – Some comfort indices for July 2012, Case 4-base case

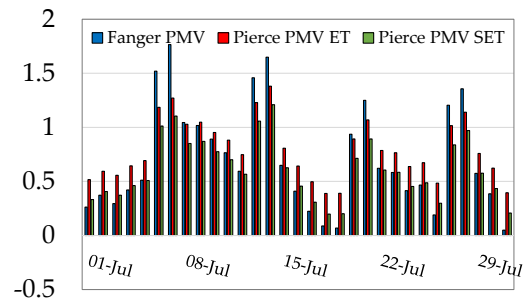


Fig. 15 – Some comfort indices for July 2012, Case 4- VAR 1

A DesignBuilder model was validated by statistical indices calculated starting from experimental data of the indoor microclimatic parameters. Analyses referred to the degree hours criterion (EN 15251) and the Fanger and Pierce comfort indices.

The latter agree with the results of the degree hours criterion. However, when clothing resistance has to be considered is not indicated. Radiant ceilings in a continuous regime offer more days in which the average comfort remains within the range of -0.5 and +0.5. Nevertheless, the risk of zone undercooling occurs. Intermittent functioning produces appreciable comfort conditions only when plant activation is planned in advance. In a parametric study, the Fanger PMV denoted negligible variations, while, conversely, wider deviances were observed for Pierce PMV ET and PMV SET,

which are more sensitive. In particular, with the modification of clothing resistance, the degree hours criterion fails and only Fanger and Pierce comfort indices provide accuracy. In these situations, the Fanger PMV varies from -0.5 to -0.05 with intermittent functioning, and from -0.79 to -0.29 in continuous operation. The same index varies from -0.09 to 0.31, assuming fan coils supplied at 15 °C. The variation of the inlet temperature in fan coils does not modify the comfort indices noticeably. The variation of internal loads and people's metabolism shows a considerable increase both in the w_f coefficient and in the other comfort indices. The slight undercooling detected by the Fanger PMV in the continuous operation of radiant ceilings can be easily overcome by increasing internal gains. The increase in people's metabolism produces overheating both with the Fanger PMV and the Pierce PMV. Therefore, the activation of solar shadings is recommended. Fan coils are more difficult to manage because they are ineffective against removing radiative loads instantaneously, so a predictive control is highly recommended for these emitters.

References

- Abdelrahman, M. M., A. Chong, and C. Miller. 2022. "Personal thermal comfort models using digital twins: Preference prediction with BIM-extracted spatial-temporal proximity data from Build2Vec." *Building and Environment* 207. doi: <https://doi.org/10.1016/j.buildenv.2021.108532>
- Asadi, I., M. Mahyuddin, and P. Shafigh. 2017. "A review on indoor environmental quality (IEQ) and energy consumption in building based on occupant behavior." *Facilities* 35: 684–695. doi: <https://doi.org/10.1108/F-06-2016-0062>
- Berkeley, L. et al. EnergyPlus Essentials. 2019. Available online: <https://energyplus.net/documentation>
- Crosby, S., and A. Rysanek. 2021. "Correlations between thermal satisfaction and non-thermal conditions of indoor environmental quality: Bayesian inference of a field study of o_ces." *Journal of Building Engineering* 35. doi: <https://doi.org/10.1016/j.jobbe.2020.102051>
- DesignBuilder Software Ltd. 2018. *User manual of the software Design Builder 6*.
- Italian Unification Institution. 2001. UNI 7726. *Ergonomia Degli Ambienti Termici - Strumenti per La Misurazione Delle Grandezze Fisiche*.
- Italian Unification Institution. 2009. UNI 9920. *Ergonomia Dell Ambiente Termico - Valutazione Dell Isolamento Termico e Della Resistenza Evaporativa Dell Abbigliamento*.
- Li, H., S. Wang, and H. Cheung. 2018. "Sensitivity analysis of design parameters and optimal design for zero/low energy buildings in subtropical regions." *Applied Energy* 228: 1280–1291. doi: <https://doi.org/10.1016/j.apenergy.2018.07.023>
- LSI – Babuc. 2022. <https://www.lsi-lastem.com>
- Peel, M. C., B. L. Finlayson, and T. A. McMahon. 2007. "Updated world map of the Köppen-Geiger climate classification." *Hydrology*. doi: <https://doi.org/10.5194/hess-11-1633-2007>
- Shahinmoghdam, M., W. Natephra, and A. Motamedi. 2021. "BIM- and IoT-based virtual reality tool for real-time thermal comfort assessment in building enclosures." *Building and Environment* 199. doi: <https://doi.org/10.1016/j.buildenv.2021.107905>
- Zhang, H. H., L. Kwok, H. Luo, J. C. Tong, J. C. Cheng. 2022. "Automatic relative humidity optimization in underground heritage sites through ventilation system based on digital twins." *Building and Environment* 216. doi: <https://doi.org/10.1016/j.buildenv.2022.108999>

Validation of Energy Simulations of a Sustainable Wooden House in a Mediterranean Climate

Piero Bevilacqua – University of Calabria, Italy – piero.bevilacqua@unical.it

Roberto Bruno – University of Calabria, Italy – roberto.bruno@unical.it

Daniela Cirone – University of Calabria, Italy – daniela.cirone@unical.it

Stefania Perrella – University of Calabria, Italy – stefania.perrella@unical.it

Natalia Shushunova – Moscow State University of Civil Engineering, Russia – nshushun@gmail.com

Natale Arcuri – University of Calabria, Italy – natale.arcuri@unical.it

Abstract

Wood has become an appealing solution in the building sector compared with traditional materials such as stone, steel, concrete, and brick for several reasons: it is more sustainable, it provides good thermal properties, and allows for fast construction processes in dry-assembled applications. However, wooden buildings in the Mediterranean area are still not very widespread, mainly due to social prejudices about their resistance to seismic events and doubts concerning durability and fire resistance. The paper focuses on the validation of an energy model of a sustainable wooden building that is the prototype of a research project aiming at producing advancement in the development of residential settlement models with solutions to implement in new single or multi-story buildings. The single-family building is located in the province of Cosenza (South Italy). The building was equipped with a monitoring system for the acquisition of quantities of interest for thermal analysis and was subject to an experimental campaign conducted in the summer of 2021. The building was then modeled in the TRNSYS environment accounting for the detailed modeling of solar radiation. Simulations were performed in free-floating conditions, allowing the thermal model to be validated. Then, further energy simulation allowed an evaluation of the thermal performances of building in different Italian localities, allowing the viability of wood solution in a Mediterranean climate to be demonstrated.

1. Introduction

Sustainability has become a major concern nowadays where worldwide policies aim at achieving

the sustainable development of society, with minimal depletion of material and energy (Shushunova et al., 2020). The building sector is an important field where lots of efforts have been made to reduce the energy consumption associated with annual operation and enhance the sustainability of construction (Korol et al., 2018). Wood has been used in the past as the main construction element, especially in cold climates (Arumägi & Kalamees, 2014), but then disregarded in favor of materials such as steel, concrete, and brick rendered more available by the strong industrialization of manufacturing.

Recently, wood has been rediscovered thanks to its appealing characteristics (Slávik et al., 2019) since it is recyclable, reusable, and naturally renewable. Moreover, it has excellent strength-to-weight ratios, thermal insulating and acoustical properties (Caniato et al., 2022) that make it appropriate for different kinds of applications in buildings (Asdrubali et al., 2017). A comparison of the sustainability impacts of both wood- and concrete-based building materials (Žemaitis et al., 2021) shows that that glue-laminated timber and sawn timber value chains have more positive sustainability impacts, especially when referred to environmental indicators. The study also highlighted the socio-economic advantage of wood, which could increase the competitiveness of the regions and contributes to their sustainable development.

Despite the growth and numerous advantages of timber construction, the global scale of multi-story timber construction is still relatively low (Leskovar & Premrov, 2021) compared to reinforced concrete

and steel construction. One of the reasons lies in the complexity of their design, whereby the architectural design, the selection of a suitable structural system, and the energy efficiency concept heavily depend on the specific features of the location, particularly climate conditions, wind exposure, and seismic hazard. An interesting construction solution combining a timber frame with a precise layout of cross-laminated timber panels for a multi-story building has been proposed (Bruno et al., 2019). Such a building was capable of attaining both seismic safety and nZEB requirements.

An experimental research study on a wooden frame house was conducted in France to better understand hygrothermal phenomena, and to allow the validation of numerical models for heat, air, and moisture transfers in wooden frame buildings (Piot et al., 2011). Another study in France focused on the desorption and adsorption behavior of exotic wood, then modeled heat and mass transfer through a wooden wall (Simo-Tagne et al., 2021). This paper focuses on the energy performance of a single-story wooden building in the Mediterranean area. The prototype was built as part of a research project aiming at producing advancement in the development of residential settlement models. A monitoring campaign was conducted in the summer and the thermal model developed in TRNSYS environment was validated thanks to the experimental data. Finally, a series of simulations showed the thermal behavior and winter and summer energy consumption of the proposed building in different Italian localities.

2. Methodology

2.1 The Building Prototype

The demonstrator is a single-family building, classified as a single-story /insulated house, located in Zumpano, a town in the province of Cosenza (South Italy), in the climatic zone D with 1647 degree-days. The building is the output of a regional research project and has a gross surface area of 96 m² including the patios on the main front and back, and an inter-floor height of 2.70 m. The building presents a platform frame constructive system.

The project aims at proposing innovative modular solutions for buildings that can be easily assembled and disassembled providing flexibility in the creation of new spaces, and with the use of sustainable materials for their construction.



Fig. 1 – Prototype building of the project Sweethome

The massive employment of wood confers characteristics of celerity of construction and ultimately pushes toward the development of a local production chain of wooden elements, given the abundance of woods in the Calabria. The thermal properties of the layers of the vertical opaque elements are reported in Table 1.

Table 1 – Thermal properties and layers of the opaque vertical envelope

Material	S [cm]	λ [W m ⁻¹ K ⁻¹]	ρ [kg m ⁻³]	c_p [kJ kg ⁻¹ K ⁻¹]
Rock Wool	5	0.035	78	1.03
OSB panel	1.5	0.130	650	1.7
Wood beams +Mineral wool	12	0.192*	105	1.3
OSB panel	1.5	0.130	650	1.7
Air	5	0.28	1.23	1
OSB panel	1.5	0.130	650	1.7
Plasterboard panel	1.2	0.210	816	1

* equivalent thermal conductivity

The resultant thermal transmittance is 0.23 W/(m² K), due to the high presence of thermal insulation. The wall facing North presents an additional layer of fir wood, mainly for aesthetic appearance. The ground floor has 6 cm of EPS insulation, reaching an overall U-value of 0.24 W m⁻² K⁻¹. The roof cover has the same value.

Different types of windows were employed in the prototype. In the main room, the East façade has a double-glazed window with lamellar chestnut frames and a U-value of $1.73 \text{ W m}^{-2} \text{ K}^{-1}$, whereas the North and South façades have a glazed window with PVC frame with a U-value of $1.47 \text{ W m}^{-2} \text{ K}^{-1}$ and $1.68 \text{ W m}^{-2} \text{ K}^{-1}$, respectively.

2.2 The Experimental Campaign

In order to assess the thermal performance of the proposed solution, a monitoring campaign was performed in the summer of the year 2021. Several thermo-hygrometric quantities have been monitored with the help of a conspicuous number of sensors and probes. In particular, only the central room of the building was monitored, since it has the largest area, and is the most representative space of the house.

Data logger M-log from LSI LASTEM was placed in the middle of the room to measure:

- Air temperature
- Relative humidity
- Air velocity
- Wet-bulb temperature
- Mean radiant temperature

The psychrometer measures the dry bulb temperature with a Pt100 class 1/3 and an accuracy of $0.10 \text{ }^{\circ}\text{C}$ at $0 \text{ }^{\circ}\text{C}$. The relative humidity is measured with an accuracy of 2 %.

Furthermore, a series of Resistance Thermal Detectors were placed in correspondence with each opaque and glazed surface to measure the internal surface temperature of each wall and window. In particular, 4-wire Pt100 sensors class 1/3 with an accuracy of $0.10 \text{ }^{\circ}\text{C}$ at $0 \text{ }^{\circ}\text{C}$ were employed. Such data were acquired by a datalogger Hioki LR8400-20.



Fig. 2 – Sensors and instruments installed in the central room of the building prototype

A further thermohygrometer DELTAOHM HD2101.2 was placed outdoors behind the main entrance, covered by the external patio to avoid direct exposition to solar radiation, to measure external temperature and relative humidity. The probe used is the HP474AC R with an accuracy of $\pm 1.5 \text{ \%}$ ($0 \dots 90 \text{ \% RH}$) for relative humidity and $\pm 0.3 \text{ }^{\circ}\text{C}$ for temperature. The datalogger has an internal memory allowing the storage of data that can be successively downloaded to a pc.

2.3 The Simulation Model

The simulation model of the building prototype was developed in a TRNSYS 18 environment. This well-known software allows for dynamic energy simulation of buildings and energy systems in general. The 3D model of the building was realized in Sketchup with the TRNSYS 3D plug-in allowing for a detailed geometry representation. To increase the accuracy of the model and account for the effect of shadings and overhangs, the detailed model for beam radiation and diffuse radiation was set for calculation in TRNBUILD. Likewise, a detailed approach was chosen for the longwave radiation exchange. Internal and external heat transfer coefficients were set to $11 \text{ kJ h}^{-1} \text{ m}^{-2} \text{ K}^{-1}$ and $64 \text{ kJ h}^{-1} \text{ m}^{-2} \text{ K}^{-1}$ respectively. The solar absorption coefficient was set to 0.14 for external white surfaces and 0.75 for the north one with a wooden finish. For windows, the g value was assumed to be 0.62 for the window on the north façade and 0.66 for all other windows.

Since during the monitoring campaign there were

no internal loads in the building, the thermal gains were set to 0.

Furthermore, because of the careful construction of the building with a high degree of air tightness, it was possible to exclude infiltration through the envelope.

Type 9 was used to provide hourly data on solar radiation, dry bulb temperature, and relative humidity. Type 16g was then used to evaluate irradiation on different tilted surfaces; Type 69b and 33e were used to evaluate the sky temperature and finally Type 77 provided the ground temperature at different depths.

3. Results and Discussion

The validation of the model was performed with data acquired from 01/06/2021 to 16/06/2021 when the building was operating in a free-floating regime. The main quantity considered for validation was the internal air temperature of the zone. The values of simulated and measured temperature are reported in Fig. 3.

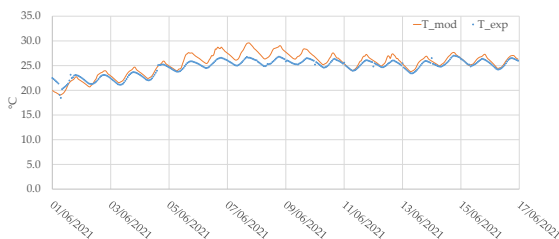


Fig. 3 – Trends of simulated and experimental internal air temperature in the free-floating regime for the period 01/06/2021 – 16/06/2021

The model showed an excellent capability for predicting the internal air temperature variations. Some differences can be observed in the central days of Fig. 3, which are mainly attributed to uncertainty in the values of solar radiation employed for simulation and because of some deviances in the prediction of the temperature of some internal surfaces. Overall, the performance was fairly satisfactory, with an average difference between predicted and measured temperatures of -0.74°C . The results are further confirmed by Fig. 4, which reports the simulated versus the measured temperature. As can be observed, the data are well aligned

along the bisector and a global correlation coefficient R^2 of 0.9683 can be obtained.

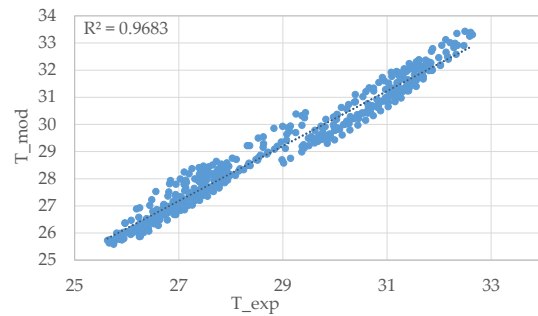


Fig. 4 – Simulated versus experimental internal air temperature in the period 01/06/2021 – 16/06/2021

3.1 Thermal Performance of the Prototype Building

In order to obtain more detailed information on the energy performance of the prototype building in different climatic conditions, a series of subsequent simulations have been performed. To describe more realistically the operation of the building, internal gain according to the Italian reference UNI EN TS 11300 was defined and set in the building model. In particular, for the main room of the building, a daily profile as in Fig. 5 was defined, with a maximum load of 20 W m^{-2} .

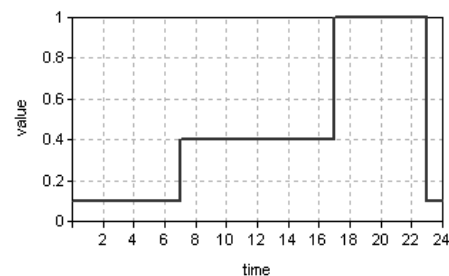


Fig. 5 – Internal gain profile for the main room of the building

Simulations were then performed in different Italian cities, each one representative of a different climatic zone. The heating setpoint temperature was set to 20°C , whereas the cooling one was set to 26°C .

In the warm locality of Palermo, with an average yearly temperature of 18.60°C and global solar horizontal radiation of 1662 kWh m^{-2} , the results are reported in Fig. 6.

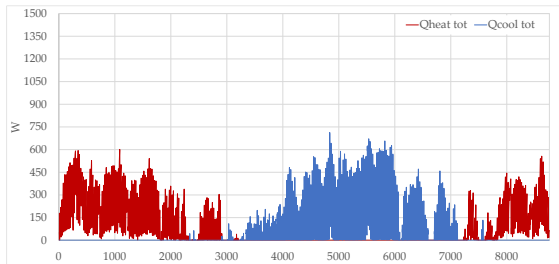


Fig. 6 – Heating and cooling load for the locality of Palermo

The annual energy consumption amounts to 668 kWh for heating and 514 kWh for cooling.

In the milder location of Rome with an average yearly temperature of 15.5 °C and a global solar horizontal radiation of 1559 kWh m⁻², the results are reported in Fig. 7.

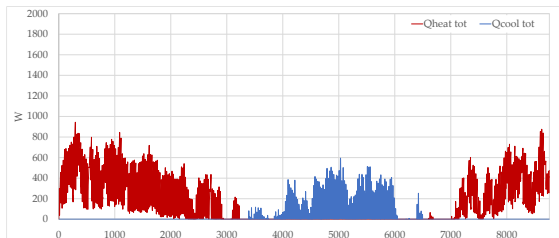


Fig. 7 – Heating and cooling load for the locality of Rome

The annual energy consumption amounts to 1430 kWh for heating and 270 kWh for cooling.

In the colder locality of Bolzano with an average yearly temperature of 12.1 °C and a global solar horizontal radiation of 1250 kWh m⁻², the results are reported in Fig. 8.

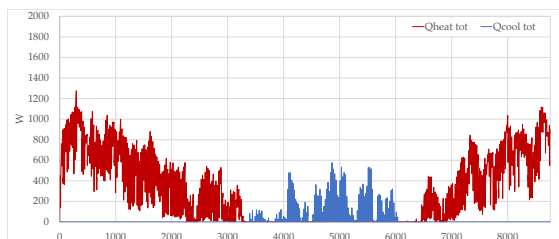


Fig. 8 – Heating and cooling load for the locality of Bolzano

The annual energy consumption amounts to 2563 kWh for heating and 178 kWh for cooling.

4. Conclusion

Recently, the use of wood in building construction has increased noticeably since it is recognized that wood is an environmentally friendly material and

can contribute to the achievement of sustainable development goals. However, the rate of these construction solutions is still low compared to reinforced concrete and steel constructions, mainly because the selection of a suitable structural system and the energy efficiency strongly depend on the specific location and in particular climate conditions and seismic hazards. The paper presents the validation of the energy model of a single-storey wooden building in the Mediterranean area. The building was equipped with a complete monitoring and data acquisition system, and an experimental campaign was conducted in the summer of 2021. The energy model of the building was developed in TRNSYS environment and was validated thanks to the experimental data acquired. With reference to the internal air temperature of the main room of the building, a correlation index R^2 of 0.9683 was obtained for a simulation period of 17 consecutive days.

Then the model was employed to evaluate the energy consumption of the building in winter and summer conditions in different climatic localities in Italy.

The results showed the limited energy needs of the building. Heating requirements ranged from 668 kWh in Palermo to 2563 kWh in Bolzano. In the same two cities, the cooling requirements amounted to 514 kWh and 178 kWh.

Acknowledgment

The paper was partly supported by Regione Calabria POR CALABRIA FERS FSE 2014-2020 ASSE I – promozione della ricerca e dell'innovazione through the grant of project SWEET HOME - Sustainable Wooden and Energy Efficient HOuse in the Mediterranean. CUP J18C17000600006

References

- Arumägi, E., and T. Kalamees. 2014. "Analysis of energy economic renovation for historic wooden apartment buildings in cold climates." *Applied Energy* 115: 540-548. doi: <https://doi.org/10.1016/j.apenergy.2013.10.041>

- Asdrubali, F., B. Ferracuti, L. Lombardi, C. Guattari, L. Evangelisti, and G. Grazieschi. 2017. "A review of structural, thermo-physical, acoustical, and environmental properties of wooden materials for building applications." *Building and Environment* 114: 307–332. doi: <https://doi.org/10.1016/J.BUILDENV.2016.12.033>
- Bruno, R., P. Bevilacqua, T. Cuconati, and N. Arcuri. 2019. "Energy evaluations of an innovative multi-storey wooden near Zero Energy Building designed for Mediterranean areas." *Applied Energy* 238: 929–941. doi: <https://doi.org/10.1016/j.apenergy.2018.12.035>
- Caniato, M., A. Gasparella, F. Bettarello, A. Santoni, P. Fausti, N. Granzotto, F. X. Bécot, F. Chevillotte, L. Jaouen, G. Borello, O. Robin, and N. Atalla. 2022. "A reliability study concerning the acoustic simulations of timber elements for buildings." *Construction and Building Materials* 315: 125765. doi: <https://doi.org/10.1016/J.CONBUILDMAT.2021.125765>
- Korol, S., N. Shushunova, and T. Shushunova. 2018. "Indicators of the resource efficiency development in Russia", in: MATEC Web of Conferences. doi: <https://doi.org/10.1051/matecconf/201819305075>
- Leskovar, V. Ž., and M. Premrov. 2021. "A Review of Architectural and Structural Design Typologies of Multi-Storey Timber Buildings in Europe." *Forests* 12(6): 757. doi: <https://doi.org/10.3390/F12060757>
- Piot, A., M. Wołoszyn, J. Brau, and C. Abele. 2011. "Experimental wooden frame house for the validation of whole building heat and moisture transfer numerical models." *Energy and Buildings* 43: 1322–1328. doi: <https://doi.org/10.1016/J.ENBUILD.2011.01.008>
- Shushunova, T., N. Shushunova, E. Pervova, R. Dernov, and K. Nazarova. 2020. "Tendencies of the green construction in Russia." *IOP Conference Series: Materials Science and Engineering* 960. doi: <https://doi.org/10.1088/1757-899X/960/4/042022>
- Simo-Tagne, M., R. Remond, R. Kharchi, L. Bennamoun, M. C. Ndukwu, and Y. Rogaume. 2021. "Modeling, numerical simulation and validation of the hygrothermal transfer through a wooden building wall in Nancy, France." *Thermal Science and Engineering Progress* 22: 100808. doi: <https://doi.org/10.1016/J.TSEP.2020.100808>
- Slávik, R., M. Čekon, and J. Štefaňák. 2019. "A Nondestructive Indirect Approach to Long-Term Wood Moisture Monitoring Based on Electrical Methods." *Materials* 12(15): 2373. doi: <https://doi.org/10.3390/MA12152373>
- Žemaitis, P., E. Linkevičius, M. Aleinikovas, and D. Tuomasjukka. 2021. "Sustainability impact assessment of glue laminated timber and concrete-based building materials production chains – A Lithuanian case study." *Journal of Cleaner Production* 321: 129005. doi: <https://doi.org/10.1016/J.JCLEPRO.2021.129005>

Thermal and Acoustic Simulation of a Technical Enclosure for High Voltage Control Equipment

Edoardo A. Piana – University of Brescia, Italy – edoardo.piana@unibs.it

Somayan Basu – University of Brescia, Italy – s.basu@unibs.it

Francesco Palone – TERN Rete Italia SpA, Italy – francesco.palone@terna.it

Simone Sacco – TERN Rete Italia SpA, Italy – simone.sacco@terna.it

Roberto Spezie – TERN Rete Italia SpA, Italy – roberto.spezie@terna.it

Abstract

The development of the electric power grid addresses the needs deriving from the growing use of renewable sources and from the dispatching flexibility required by mobility electrification. New infrastructures to control the grid parameters and configuration are also being installed in the urban environment, and the relative equipment must generally be enclosed in technical rooms to prevent unauthorised access. Such enclosures must fulfil two conflicting requirements: on the one hand, they must be closed enough to reduce the potentially disturbing noise emitted by the inner equipment, and, on the other hand, they must feature openings for natural ventilation, as high-voltage elements may get damaged due to overheating. Therefore, cooling and sound insulation aspects must be properly integrated during the design phase, keeping an eye on other potential issues, such as condensation. This paper presents a possible strategy of dual acoustic and thermal simulation applied to the design of a new high-voltage control system that allows the expensive technical equipment to be safeguarded while reducing the risk of noise annoyance.

1. Introduction

As detailed in the Electricity Ten Year Statement (Leslie, 2021), with the growing requirement of having smart electric distribution grids capable of adapting to the different needs of the users, transmission system operators (TSO) are developing new solutions with the aim of achieving a remotely operated fast re-configuration of the power grid (Chen et al., 2016). The expansion of green power and the refurbishment of old plants able to with-

stand the shortage of natural gas have shown the importance of voltage regulation and reactive power compensation (Leborgne & Stypulkowski, 2017). This situation overlaps with the increasing demand for electricity due to the development of electric vehicles and the ever-growing expansion of air conditioning systems. The need for having a flexible distribution network is even more important in the light of the recent developments related to the international situation.

In many cases, the devices used to re-configure or control the power grid are better integrated into the distribution system if they are placed close to the users, and then in the proximity of residential areas (Cohen et al., 2014). Since these devices are based on mechanisms that, under certain circumstances, can produce noise (Piana et al., 2018), it is important to control the sound emitted by the installations. For TSO it is not possible to decrease the noise emissions through a better design of the source itself. The next step is to work on the structures through the implementation of sound insulating shelters containing the noise sources and the related control systems. One drawback of this type of solution is that, in order to avoid damage due to overheating, the thermal power generated by the current flowing through the conductors must be properly dissipated. A sensible solution to avoid adding further noise sources is the use of natural ventilation (Izadyar et al., 2020). If the shelter is properly designed, the ventilation openings will be responsible for the main noise contributions in the surroundings.

These must be large enough to allow a certain air mass flow and, at the same time, small enough to

prevent noise spreading in the neighborhood. For this reason, an accurate thermal and acoustic design of the shelter is necessary. The goal of the present article is to give the reader an idea of the procedure that can be adopted to design the openings necessary to guarantee a sufficient degree of cooling to the high-voltage-control equipment contained in the enclosure, assuring, at the same time, that the noise produced by the devices is compatible with the limits applied to very quiet areas. The amount of heat dissipated by the openings can be improved by using conductive materials (Neri & Pilotelli, 2019; Neri et al., 2020).

The study will be carried out through two different types of simulation software: the first one to predict the indoor thermal conditions and the second one to assess the acoustic impact of the installation. The structure of the article is as follows. Section 2 briefly gives the geometric, thermal, and acoustic parameters needed for the simulations. Section 3 describes the thermal model implemented in EnergyPlus. In Section 4 the outcomes of the thermal simulations in terms of opening dimensions will be used to assess the sound pressure level distribution around the shelter using Ramsete. Finally, Section 5 will draw the conclusions.

2. Materials and Methods

The shelter considered in the present study consists of a single volume having dimensions $7 \times 7 \times 6 \text{ m}^3$. The size has been specifically chosen by the

TSO research and development team so that it can contain all the devices needed to implement the remotely controlled system and all the related auxiliary components, maintaining at the same time a suitable occupation of public land. Due to safety reasons, the main volume must be kept apart from undesired accesses of people and animals. For this reason, the walls and the roof must be made of solid materials. Moreover, the structures must be strong enough to withstand natural events (wind, rain, and snow). For aesthetic reasons, the main volume will be enclosed in a buffer of panels acting as a second skin with camouflage purposes. If properly selected, such panels can also behave as a sound barrier. The distance of the second skin from the main volume is about 500 mm. After a discussion with the technical team responsible for the structural design, it was decided that the panels selected for the main structure can be standard sound-insulating sandwich panels made of two external 1 mm thick steel laminates and a 300 mm gap filled with 70 kg/m^3 stone wool. The aesthetic panels can be selected from a wide range of solutions. For the purposes of the present study, their mass per unit area is of importance since they must behave as sound barriers. For this reason, it was decided that the mass per unit area of such panels must be higher than 30 kg/m^2 .

The sound source placed inside the shelter is represented by a set of mechanical switches generating impulsive noise (Fig. 1).

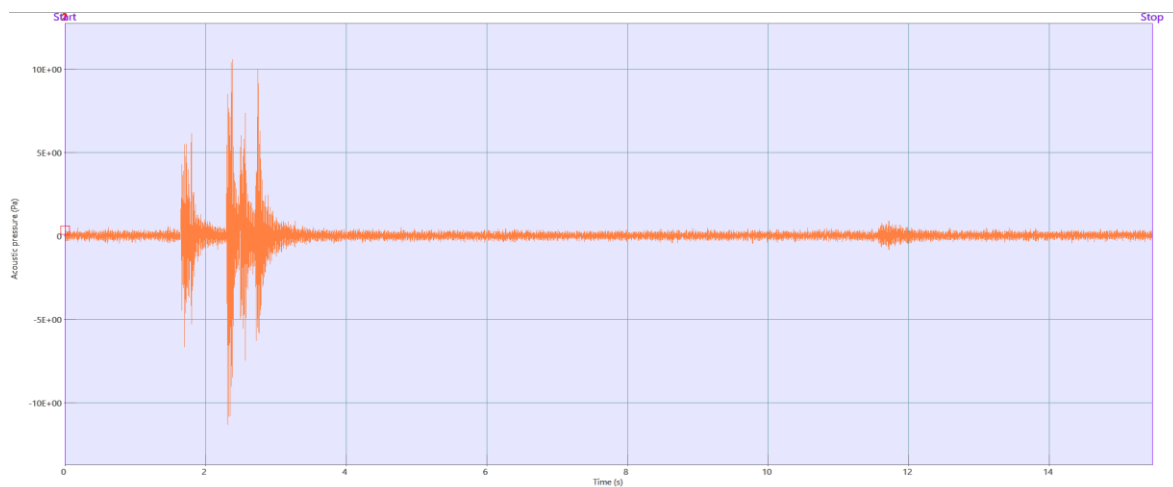


Fig. 1 – Recording of the pressure signal measured at 2 m distance from the switch

The average sound pressure level measured at 2 m distance from one of these switches is reported in Fig. 2. The overall sound energy level due to the single event, according to the international standard ISO 3744 (ISO, 2010), is equal to 114 dB(A) *re* 1pW. It is interesting to note that most of the sound pressure level encompasses between 250 Hz and 20 kHz. This means that, since the sound insulation in the low frequency range is usually dominated by the mass-per-unit area, the required value of this parameter for the panels surrounding the noise sources does not need to be extremely high.

Concerning the thermal simulations, the main parameter to be considered is the thermal power, which needs to be dissipated inside the volume. The current generates heat due to the joule effect. This contribution can be computed once the electric current running through the switching apparatus, the length of the conductors and their resistance known. From a first evaluation of the current (900 A) and of the resistance and length of the conductors, a total thermal power of 4 kW caused by the joule effect can be estimated. In addition, the control and anti-dew systems placed inside the shelter add a further 2 kW to the thermal load, bringing the total amount of thermal power to be dissipated at 6 kW. To prevent damage to the electrical systems, the average temperature inside the volume must be kept below 40 °C.

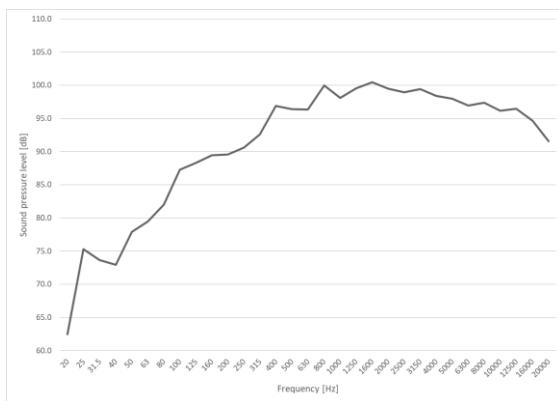


Fig. 2 – Average sound pressure level measured at 2 m distance from the switch

Since the decision was made to use a natural ventilation system, the amount of heat dissipated depends on the dimensions of the openings and on the external air temperature.

It is known that a fluid possesses a density which

decreases with its temperature. If a fluid is less dense than the surrounding one, it tends to shift upwards, generating a convective motion. The two openings of the shelter must be located in such a way that the cold air flowing through the inlet is heated when passing through the volume. The density reduction due to heating generates a convective motion towards the higher part of the shelter, where the air can exit the volume through the outlet. Hence, it is necessary to place the outlet in a position which simplifies the discharge of the warm air. In the simulations, the inlet and the outlet does not have initial mean flow assigned and the pressure is assumed to be atmospheric. Concerning the walls, they are assumed to be rigid but not adiabatic. From this point of view, it is important to find suitable materials possessing both thermal and acoustic properties, as stated by (D'Amore et al., 2020) and (Caniato et al., 2017). The region where the shelter is located is very important. For the purposes of the present study, the thermal simulations were made considering the shelter located in Brescia, northern Italy. The meteorological data of this location, such as the wind speed, the wind direction and the solar gain were given as an input to EnergyPlus.

3. Thermal Simulations

The thermal simulations were carried out using EnergyPlus. A first drawing of the shelter was made in Sketchup. After the work of Correia et al. (2020), and a section of the openings equal to 3 x 1 m² to guarantee at least 20 air volume changes each hour was chosen. To exploit the chimney effect due to the different density of the air inside the shelter volume, the two openings (inlet and outlet) have a height difference of 4 m. For the purpose of properly considering the thermal transmittance of the walls, these were virtually assembled in EnergyPlus according to the description given in Section 2 and using the characteristics of the materials shown in Table 1.

The total transmittance for the entire envelope of the main volume is 0.377 W/(m² K).

Table 1 – Materials used for the walls of the shelter

Material	Thickness [mm]	Density [kg/m ³]	Thermal conductivity [W/(m K)]
Steel plate	1	8000	52
Mineral wool	98	70	0.04
Steel plate	1	7800	52

The thermal load acting on the shelter can be divided into two contributions: the internal thermal load (6 kW distributed on the floor of the main volume) and the solar gain. A reasonably accurate way of simulating the heat source within the volume is to let the heat enter the volume through its floor. This can be considered a reasonable assumption because the components which dissipate heat are located close to the bottom of the shelter. The heat source can be assumed to be a uniformly distributed 122.5 W/m² heat flux, for a total amount to 6 kW.

The solar gain is automatically taken into account by EnergyPlus once the location of the construction is selected as an input.

In the case at hand, the shelter is considered as being situated in Brescia. In this way, EnergyPlus can also consider the average external air temperature, the solar gain and wind speed/direction. These parameters represent the boundary conditions of the simulation. The dataset used encompasses a one-year span, so that the outputs can cover both winter and summer times.

EnergyPlus can give a large number of parameters as outputs. For the present work, the most interesting ones are the average temperature inside the volume, the temperature of the walls and the mass flow rate of the air through the openings. Fig. 3 shows a plot of the mean radiant temperature (black line), the mean air temperature inside the volume (blue line) and the outdoor air temperature (cyan line). In Fig. 4, the mass flow rate of the air running through the openings is given. Fig. 3 and Fig. 4 are yearly-based plots. They can give a reasonable projection of what happens during one “average” year as a function of the meteorological conditions and of the solar gain. It is interesting to

note that such simulations give temperatures that are always between -8 °C and 40 °C. This last value represents the limit fixed for the overheating protection of the devices. The natural ventilation of the volume is then able to assure that the temperature is kept below the limit with a certain safety margin, which can be assumed as 4 °C.

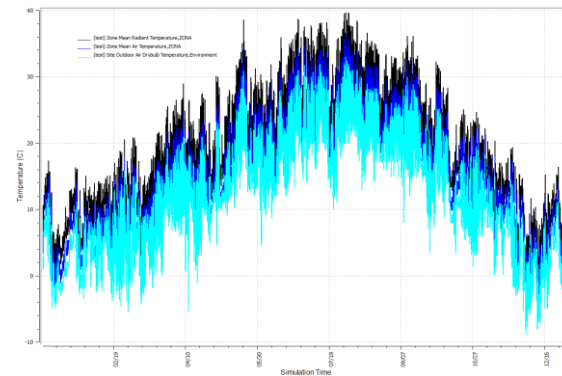


Fig. 3 – Average temperature of the air inside the technical volume of the shelter

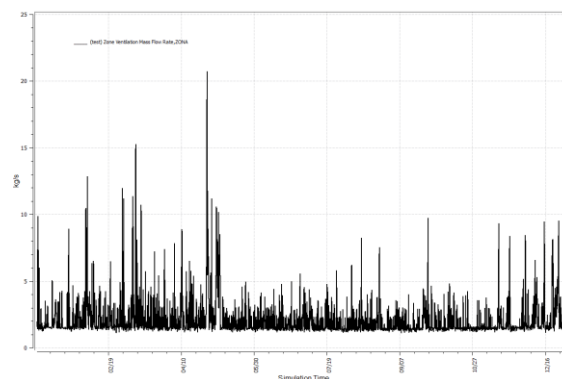


Fig. 4 – Mass flow rate of the air through the openings

Of course, the simulation run assuming a certain location, thus the results cannot be extended to any other possible construction site. The situation can be very different in other contexts like, for example, southern Italy. In this case, a new thermal simulation can be easily made using the specific meteorological dataset of the location chosen as final installation site. In case the proposed dimension of the opening is not sufficient, it can be easily increased, or, in extreme cases, a ventilation system can be added to ensure proper cooling. In the latter case, the noise contribution of the fan must be considered as an additional contribution to the acoustic simulations.

4. Acoustic Simulations

Once the thermal simulation gives feasible results, suggesting a reasonable dimension for the openings, it is possible to run the acoustic simulation to check the sound pressure level distribution around the shelter. The use of acoustic simulation on thin structures was already proved to be effective (Caniato et al., 2020). The simulations were carried out using Ramsete, a software specifically developed for the simulation of the acoustic quality of rooms (Tronchin, 2013), which is also capable of performing the calculation of the noise spreading outdoors (Farina, 2000). One of the characteristics of this software is that it can take sound absorption, sound insulation and the diffraction of the structures into account. This means that the second skin represented by the lightweight panels can be properly represented both in terms of its sound reduction index and diffraction effect. In this sense, the position of the openings is extremely important since the effectiveness of a sound barrier depends on the additional path of the sound wave compared to the direct path. The inlet is placed close to the ground and has an area of $3 \times 1 \text{ m}^2$. The outlet placed on the opposite vertical face of the shelter has the same area, and its lower side is at 4 m from the ground. The walls of the shelter have the sound absorption coefficient and the sound reduction index reported in Fig. 5.

	31 Hz	63 Hz	125 Hz	250 Hz	500 Hz	1 kHz	2 kHz	4 kHz	8 kHz	16 kHz
α	0.092	0.137	0.277	0.608	0.855	0.840	0.794	0.741	0.679	0.639
R	11.0	17.0	23.4	25.6	30.4	26.6	38.2	44.0	50.0	56.0

Fig. 5 – Sound absorption coefficient α and sound reduction index R – shelter walls

The choice of the material for the aesthetic lightweight panels surrounding the shelter was made by architects. The material chosen for these panels is Perspex. The sound-absorption coefficient and the sound-reduction index of the Perspex panels is shown in Fig. 6.

	31 Hz	63 Hz	125 Hz	250 Hz	500 Hz	1 kHz	2 kHz	4 kHz	8 kHz	16 kHz
α	0.040	0.070	0.050	0.030	0.020	0.020	0.030	0.020	0.010	0.010
R	16.0	14.0	18.0	24.0	30.0	36.0	42.0	40.0	48.0	56.0

Fig. 6 – Sound absorption coefficient α and sound reduction index R – aesthetic walls (Perspex glass)

Fig. 7 shows a 3D sketch of the acoustic model imported in Ramsete. The model can give the sound pressure level distribution of the sound emitted by the installation as an output. This means that the sound pressure level computed by Ramsete represents only the contribution of the source placed in the shelter, without the contribution of the background noise. According to Italian legislation (Italian Parliament, 1995), the allowed “Emission Level” in built-up areas depends on the destination of the area itself and on the time of day. Considering the daytime (6-22) and the nighttime (22-6), the emission level limits are summarized in Table 2. Looking at Table 2 and given the intention of installing the shelter in residential areas, it is sensible to design the shelter so that the limits for Class II during the nighttime (40 dB(A)) are fulfilled. Since the final installation site is not known in advance, satisfying the limits for Class I (35 dB(A)) is still a goal that, if possible, represents an optimal achievement for the project.

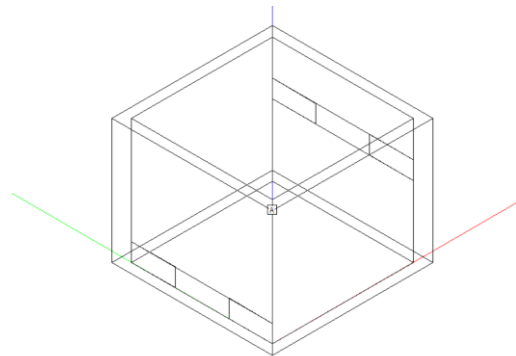


Fig. 7 – Sketch of the acoustic model

Fig. 8 and Fig. 9 show the sound pressure level computed by Ramsete on a horizontal grid of receivers placed at 2 m one from the other, at a height of 1.5 m from the ground and on the vertical mid-section of the shelter, up to a height of 16 m. The sound pressure level inside the shelter is very high and reaches values close to 97 dB(A).

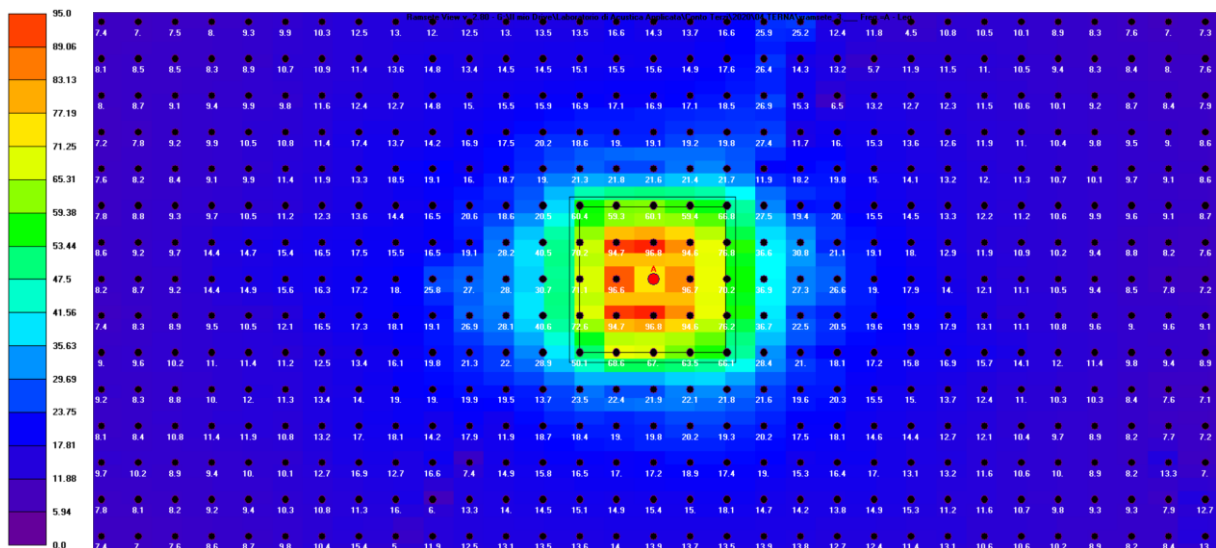


Fig. 8 – Sound pressure level distribution around the shelter – site map

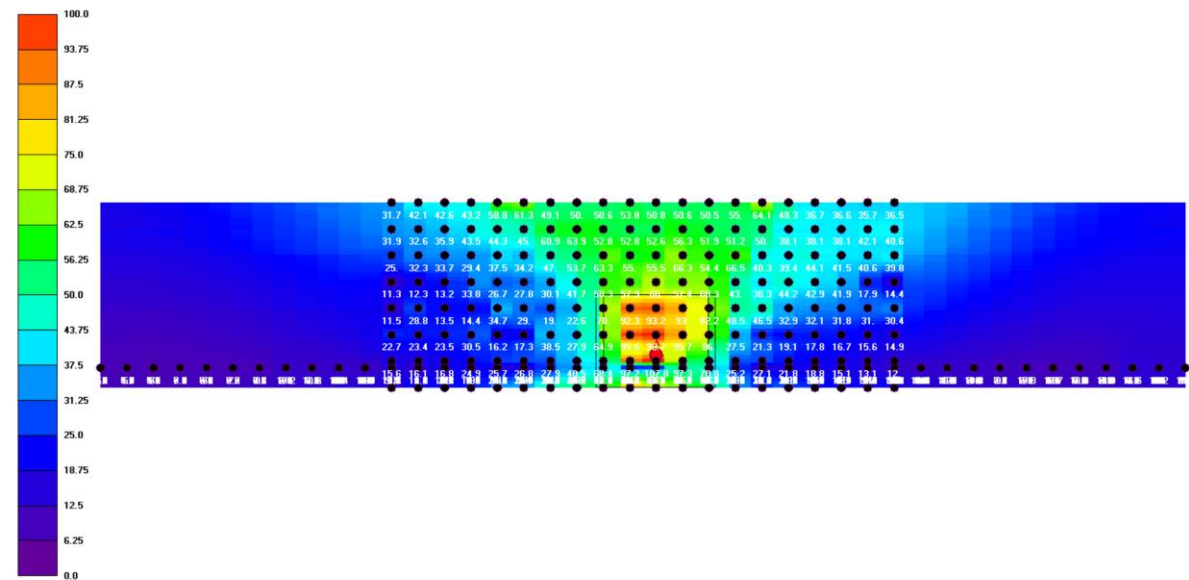


Fig. 9 – Sound pressure level distribution around the shelter – vertical section

Table 2 – Emission level limits

Area destination	Daytime [dB(A)]	Nighttime [dB(A)]
I - Sensitive	45	35
II - Residential	50	40
III - Mixed	55	45
IV - Intense activity	60	50
V - Industrial	65	55
VI – Excl. industrial	65	65

It is important to note that, for keeping sound pressure level as low as possible, the inner side of the shelter walls must feature a certain sound absorption. From Fig. 9 it can be noted also that the sound pressure level in the gap between the shelter and the aesthetic panels depends on the position considered. If a point in front of the opening placed closer to the ground is selected, then the sound pressure level is near 76 dB(A), while on the side where the opening is at 4 m from the ground the sound pressure level is around 72 dB(A). The other two sides of the shelter are characterized by sound pressure levels around 60 dB(A). The result is that,

beyond the aesthetic panel, the sound pressure level is more than acceptable.

Looking at the zones characterized by the higher sound pressure levels, the values at different distances are reported in Table 3.

The sound pressure level values reported in Table 3 show that the sound emission of the shelter is compatible with the limits of Class I starting from 10 m from the wall featuring the air outlet, which is the one giving the highest sound pressure level values. Since it can be expected that no buildings can be erected at a distance lower than 30 m from the shelter, the result achieved allows full compatibility of the installation with the built environment also in the case of the class featuring the lowest emission limits.

Table 3 – Sound pressure levels at different distances from the walls [dB(A)]

Distance [m]	Inlet side	Outlet side
5	30	37
10	19	26
20	10	15

5. Conclusions

A flexible distribution grid, capable of being configured in real time depending on the needs of the customers, is becoming an important point for transmission system operators. This capability has strong advantages when discontinuous green power technologies or loads are integrated in the transmission line. TERN Rete Italia is working to develop a set of remotely operated systems allowing a fast reconfiguration of the distribution grid. Since the devices used for the reconfiguration can emit noise and the system is more effective if placed in close vicinity of the users, the acoustic compatibility of this solution with the residential areas is crucial. Nonetheless, assuring acoustic compatibility requires the noisy devices to be enclosed in a shelter having sufficient sound insulation and, at the same time, the capability of allowing a certain cooling of the high voltage systems contained in it.

The present paper presented the thermal and acoustic simulations used to verify the compatibility of the system with the noise limits proposed by Italian legislation for a residential area. The study started with the dimensioning of the openings required for cooling the shelter volume. To avoid additional sound sources, reliance on only natural ventilation was chosen. The simulations were carried out using EnergyPlus and considering the solar gain as well as the temperature distribution outdoors across the entire year. As a result, the dimensions and the position of the openings required for a proper cooling were set. The next step was to check the noise emission of the entire installation. The sound power level of the devices to be placed in the shelter was derived from experimental measurements. Using Ramsete software and properly selecting the materials for the walls and the roof of the shelter, it was possible to run the simulations necessary to predict the noise emissions. A big advantage derived from the choice of the architects to improve the visual impact of the installation by placing four “aesthetic walls” around the shelter. Such structures, from an acoustic point of view, act as noise barriers, shielding the sound spreading from the ventilation openings.

Merging the results of the thermal simulations with the results of the acoustic simulations, it was possible to predict the full compatibility of the installation with the limits of Italian legislation for residential areas. Moreover, the sound emissions are so low that compatibility is assured also for sensitive areas featuring the lowest emission limits allowed by Italian legislation.

References

- Caniato, M., F. Bettarello, P. Bonfiglio, and A. Gasparella. 2020. “Extensive Investigation of Multiphysics Approaches in Simulation of Complex Periodic Structures”. *Applied Acoustics* 166. doi: <https://doi.org/10.1016/j.apacoust.2020.107356>
- Caniato, M., F. Bettarello, A. Ferluga, L. Marsich, C. Schmid, and P. Fausti. 2017. “Thermal and acoustic performance expectations on timber buildings.” *Building Acoustics* 24(4): 219–37. doi: <https://doi.org/10.1177/1351010X17740477>

- Chen, L., H. Y. Li, S. Cox, and K. Bailey. 2016. "Ancillary Service for Transmission Systems by Tap Stagger Operation in Distribution Networks." *IEEE Transactions on Power Delivery* 31(4): 1701–9. doi: <https://doi.org/10.1109/TPWRD.2015.2504599>
- Cohen, J. J., J. Reichl, and M. Schmidthaler. 2014. "Refocussing research efforts on the public acceptance of energy infrastructure: A critical review." *Energy* 76: 4–9. doi: <https://doi.org/10.1016/j.energy.2013.12.056>
- Correia, A., L. Ferreira, P. Coimbra, and A. de Almeida. 2020. "Impacts of Automated Natural Ventilation in the Temperature and Humidity of a Distribution Transformer Room." In *Proceedings of 2020 IEEE 14th International Conference on Compatibility, Power Electronics and Power Engineering (CPE-POWERENG)*, Setubal, Portugal. doi: <https://doi.org/10.1109/CPE-POWERENG48600.2020.9161687>
- D'Amore, G. K. O., F. Mauro, A. Marinò, M. Caniato, and J. Kašpar. 2020. "Towards the Use of Novel Materials in Shipbuilding: Assessing Thermal Performances of Fire-Doors by Self-Consistent Numerical Modelling." *Applied Sciences* 10(17). doi: <https://doi.org/10.3390/APP10175736>
- Farina, A. 2000. "Validation of the pyramid tracing algorithm for sound propagation outdoors: Comparison with experimental measurements and with the ISO-DIS 9613 standards." *Advances in engineering software* 31(4): 241–50. doi: [https://doi.org/10.1016/S0965-9978\(99\)00053-8](https://doi.org/10.1016/S0965-9978(99)00053-8)
- Farina, A. "Ramsete Home Page". Last accessed in December 2019. <http://www.ramsete.com/>
- ISO. 2010. *ISO 3744:2010 -- Acoustics -- Determination of Sound Power Levels and Sound Energy Levels of Noise Sources Using Sound Pressure -- Engineering Methods for an Essentially Free Field over a Reflecting Plane*.
- Italian Parliament. 1995. *Legge 26/10/1995, n. 447 -- Legge quadro sull'inquinamento acustico (Law 26/10/1997, n. 447 -- Framework law on environmental noise, in Italian)*.
- Izadyar, N., W. Miller, B. Rismanchi, and V. Garcia-Hansen. 2020. "Impacts of Façade Openings' Geometry on Natural Ventilation and Occupants' Perception: A Review." *Building and Environment* 170: 106613. doi: <https://doi.org/10.1016/j.buildenv.2019.106613>
- Neri, M., and M. Pilotelli. 2019. "Device for limiting the temperature at chimney-roof penetration in very critical chimney operating conditions." *Fire Technology*, 55(6): 1937-1965. doi: 10.1007/s10694-019-00837-5
- Neri, M., P. Leppanen, M. Alanen, D. Luscietti, S. Bani, and M. Pilotelli. 2020. "Effects of the coupling of insulating and conductive materials to limit the temperature at chimney-roof penetration." *Fire Technology*, 56(4): 1655-1680. doi: 10.1007/s10694-020-00947-5
- Leborgne, R. C., and Y. S. Stypulkowski. 2017. "Optimal Reactive Power Compensation in Weak Grids with Insertion of Wind and Solar Sources." In *Proceedings of 2017 Brazilian Power Electronics Conference (COBEP)*, Juiz de Fora, Brazil. doi: <https://doi.org/10.1109/COBEP.2017.8257362>
- Leslie, J. 2021. «ETYS 2021».
- Piana, E. A., F. Bignucolo, A. Donini, and R. Spezie. 2018. "Maintenance of a high-voltage overhead transmission line: Sustainability and noise impact assessment." *Sustainability* 10(2). doi: <https://doi.org/10.3390/su10020491>
- Tronchin, L. 2013. "Francesco Milizia (1725-1798) and the Acoustics of His Teatro Ideale (1773)." *Acta Acustica United with Acustica* 99(1): 91–97. doi: <https://doi.org/10.3813/AAA.918592>

Investigating the Role of Humidity on Indoor Wellness in Vernacular and Conventional Building Typologies

Suchi Priyadarshani – Indian Institute of Science, Bangalore, India – suchip@iisc.ac.in

Roshan R Rao – Indian Institute of Science, Bangalore, India – roshanrao@iisc.ac.in

Monto Mani – Indian Institute of Science, Bangalore, India – montoman@iisc.ac.in

Daniel Maskell – University of Bath, United Kingdom – D.Maskell@bath.ac.uk

Abstract

Moisture in air is essential for human life. It drives all physiological processes and determines occupant wellness. As a crucial parameter of Indoor Environmental Quality (IEQ), it is regulated by building typology and its constituent materials. Besides affecting heating and cooling energy requirements, indoor moisture also determines occupants' comfort and health.

Occupant comfort, commonly referred to as thermal comfort, is paramount for building and indoor environment design. Currently available building simulation tools majorly incorporate temperature-related comfort models like PMV, PPD, and adaptive thermal models. In conjunction with temperature, indoor moisture levels impact occupants' skin-related and respiratory comfort, resulting in health issues such as skin irritation, allergies, respiratory infections, asthma, etc. Humidity has not been adequately dealt with in comfort studies. This study proposes a novel computational approach derived from an existing model to explain and assess humidity-related comfort in buildings. The study also involves real-time monitoring of indoor-outdoor temperature and humidity and occupant comfort-votes.

The hygroscopic properties of building materials impact the regulation of indoor moisture, thereby impacting occupant comfort and health. This article examines humidity-related comfort aspects between conventional and vernacular building typologies. Results from the simulation have been used to explain the comfort votes obtained from an on-field survey of occupants. Skin temperature and wettedness derived through energy balance between the human skin and the indoor air parameters can be used as an indicator to assess skin-related comfort in indoor environments.

Comfort is an essential indicator of wellness in an indoor environment. Clarity on approaches to evaluate different aspects of comfort attributed to building materials is

crucial for built environment design for occupant wellness. Incorporating humidity-associated comfort parameters in building simulation tools could be beneficial in selecting materials for building design to cater to varying functionalities and health co-morbidities.

1. Introduction

Moisture is omnipresent and fundamental to life. The human body comprises 70 % water. Water balance between the surrounding air and the human body is essential for life. Human beings spend 90 % of their time indoors. Indoor surfaces (building envelope) determine the Indoor Air Quality (IAQ), impacting occupant comfort and health (al Horr et al., 2016; Petty, 2017). Indoor air is the connecting link between the building typology (and materials used) and the occupant. Moisture in the air is a critical determinant of IAQ. Indoor air moisture (as affected by building typology due to heat and moisture transport mechanisms) determines the occupant's thermo-physiological balance, thereby determining comfort. Unregulated (high/low) moisture is generally considered detrimental to health.

Majorly, simulation-based indoor comfort analysis accounts for thermal comfort using indices like PDD (Predicted Percentage of Dissatisfied) and PMV (Predicted Mean Vote). Thermal comfort is determined majorly by environmental (air temperature, relative humidity, wind velocity, and radiation) and personal (metabolism and clothing) factors. Heat-Stress indices like WBGT (Wet-Bulb Globe Temperature) Index, Oxford index, and Effective Temperature are used for varied applications other than indoor comfort like sports, clothing design etc.

Numerous empirical studies have also indicated the impact of (de Dear et al., 1991; de Dear et al., 2015; Jokl, 2002; Kong et al., 2019; Parsons, 2003; van Hoof et al., 2010) indoor humidity on thermal comfort. While humidity is also accepted as a significant determinant of skin-related and respiratory comfort (Wolkoff & Kjærgaard, 2007); it has not been dealt with explicitly. Tools for evaluating skin-related or respiratory comfort due to changing indoor air parameters are not incorporated in commonly used building simulation softwares.

Vernacular (earth-based materials) and conventional (standardized bricks and RCC) buildings in Jamgoria village, Jharkhand (India), situated in composite climate zone, were monitored (Priyadashani et al., 2021a) for indoor air parameters. This study revealed a significant moderation of indoor RH exhibited by vernacular building typology. The variations in humidity seen in different building typologies provided clear grounds for understanding the humidity-related comfort parameters of occupants with varying indoor environments. Thus, further extension of this study (Priyadarshani et al., 2021b) was carried out to record the response of occupants to skin and respiratory comfort throughout the year in both the building typologies. Skin acts as the interface with the *indoor air moisture* and can be witnessed as wettedness/dryness. The aims of this work are:

1. To compute diurnal/seasonal variations of skin temperature (T_{sk}) and wettedness (w) in vernacular and conventional dwellings using an energy balance-based simulation approach.
2. To explain the changing skin-related comfort votes (oily/very-dry skin) of occupants in vernacular and conventional dwellings using computed T_{sk} and w .

2. Applied Approach and Methods

2.1 Energy Balance of the Human Body (Core-Skin-Indoor Air)

Simulation-based analysis was done to derive the skin wettedness and temperature corresponding to diurnally/seasonally varying indoor temperature and RH in conventional and vernacular building

typologies. The Gagge 2-node model, validated for occupants in indoor environments (Atmaca & Yigit, 2006), was used to represent the energy balance between the human body and indoor air. Factors concerning ethnicity and regional stereotypes were not examined. The model considers 16 cylindrical segments (see Fig. 1) representing different human body parts, each comprising two nodes (core and skin).

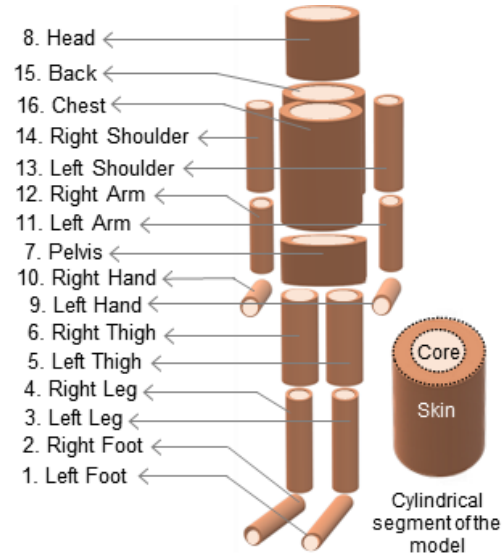


Fig. 1 – Description of segments of the human body in Gagge-2 Core, 16 segment model

Indoor temperature and RH data obtained from real-time monitoring of vernacular and conventional building typologies were used as input parameters for the model. The energy balance between the core and the skin for each segment was expressed as:

$$S_{cr}(i) = M - W[C_{res}(i) + E_{res}(i)] - Q_{cr,sk}(i) \quad (1)$$

$$S_{sk}(i) = Q_{cr,sk}(i) - [C(i) + R(i) + E_{sk}(i)] \quad (2)$$

Here, $C_{res}(i) + E_{res}(i)$ correspond to the respiration at the core of the chest segment.

The rate of change of internal energy in the core and the skin layers is given by:

$$S_{cr}(i) = \frac{[1 - \alpha(i)]m(i)c_{p,b} \left[\frac{dt_{cr}(i)}{d\theta} \right]}{A(i)} \quad (3)$$

$$S_{sk}(i) = \frac{\alpha(i)m(i)c_{p,b} \left[\frac{dt_{sk}(i)}{d\theta} \right]}{A(i)} \quad (4)$$

Heat losses from each segment, and exchange from the core to the skin (and vice versa) within the segment are given by:

$$C(i) + R(i) = \frac{[t_{sk}(i) - t_o]}{R_t(i)} \quad (5)$$

$$C_{res}(i) + R_{res}(i) = [(0.0014)M(34 - t_o)] + [(0.0173)M(5.87 - p_{wv,a})] \quad (6)$$

$$E_{sk}(i) = w(i) \frac{[p_{sk,s}(i) - p_{wv,a}]}{R_{e,t}(i)} \quad (7)$$

$$Q_{cr,sk}(i) = [K + c_{p,bl}m_{bl}(i)][t_{cr}(i) - t_{sk}(i)] \quad (8)$$

For the analysis, air temperature [t_o] was assumed to be the same as operative temperature. RH recorded on-field was used to calculate the partial pressure of ambient air [$p_{wv,a}$]. The total thermal resistance [R_t] and evaporative resistance [$R_{e,t}$] were computed for single-layer, 1.2 mm-thick cotton weave cloth for each body segment using Equations 9 and 10, respectively. Head, left foot, right foot, left hand, and right-hand segments were considered unclothed.

$$R_t(i) = R_a(i) + [R_f(i) + R_{al}(i)] \quad (9)$$

$$R_{e,t}(i) = R_{e,a}(i) + [R_{e,f}(i) + R_{e,al}(i)] \quad (10)$$

Segment-wise convective heat transfer coefficients were obtained from (de Dear et al., 1997). Metabolic heat loss [M] and heat loss due to external work [W] was taken as 60 and 30 W/m², respectively.

2.2 Aggregated Comfort Survey

A questionnaire-based field survey was conducted using an aggregated comfort survey approach (Shastry et al., 2016). 62 occupants living in conventional (Total=32, M=18 and F=14) and vernacular (Total=30, M=13 and F=17) building typologies, aged between 20-56 years, were interviewed. The survey was conducted when the subjects were indoors and not involved in any exhaustive physical activity. Their comfort votes (thermal, respiratory, and skin-related) and health symptoms were recorded for each month of the year. Indoor Air Quality (IAQ) is determined by the constituents of the indoor air (water vapor, carbon dioxide, volatile organic

compounds etc.); however, in this study, only indoor air humidity-related skin stickiness/dryness was examined. Also, their clothing, activity (standing, walking, sleeping, lying down), environmental temperature, and RH during the interview were recorded.

3. Results and Discussions

The comfort votes of the occupants (Thermal, Skin-related, and Respiratory) for all the months are shown in Fig. 2. There is a close relation between thermal comfort and the skin-related (IAQ) comfort votes of occupants, suggesting that the occupants felt that their skin was stickier/oilier during warmer months. During the colder months, occupants experienced dry skin. However, the response varied within the building typologies. The response of occupants in vernacular dwellings is more consistent than that of the occupants of conventional buildings. Comfort votes of occupants represents their expectations from the built environment, reflecting adaptive strategies. Skin-related comfort/discomfort is often manifested as a change in thermal comfort vote, making it challenging to discern.

Occupants report neutral respiratory comfort mostly, other than the cold winter months when the Humidity Ratio (HR) of the air goes low. Low HR values can cause serious difficulty in respiration due to inefficient nasal mucociliary clearance, especially in the elderly. As regulated by the building material and anthropogenic factors, the humidity of the indoor air is responsible for maintaining the homeostasis of the human airways (Hugentobler, 2021). Even though the average daily humidity ratio was higher than that suggested by ASHRAE for comfort, i.e., 0.012 kg-wv/kg-da in both the building typologies, a deficit was observed from the saturated (trachea) airway HR of 0.041kg-wv/kg-da (at saturated core temperature 36.7 °C), more so in the winter months. The humidity ratio in the conventional building remains lower than in the vernacular building throughout the year. Also, as illustrated in Fig. 3 and Fig. 4, the diurnal variation of the moisture deficit remains very high in the conventional room, especially when the HR of outdoor air is low in the winters (see Fig. 4).

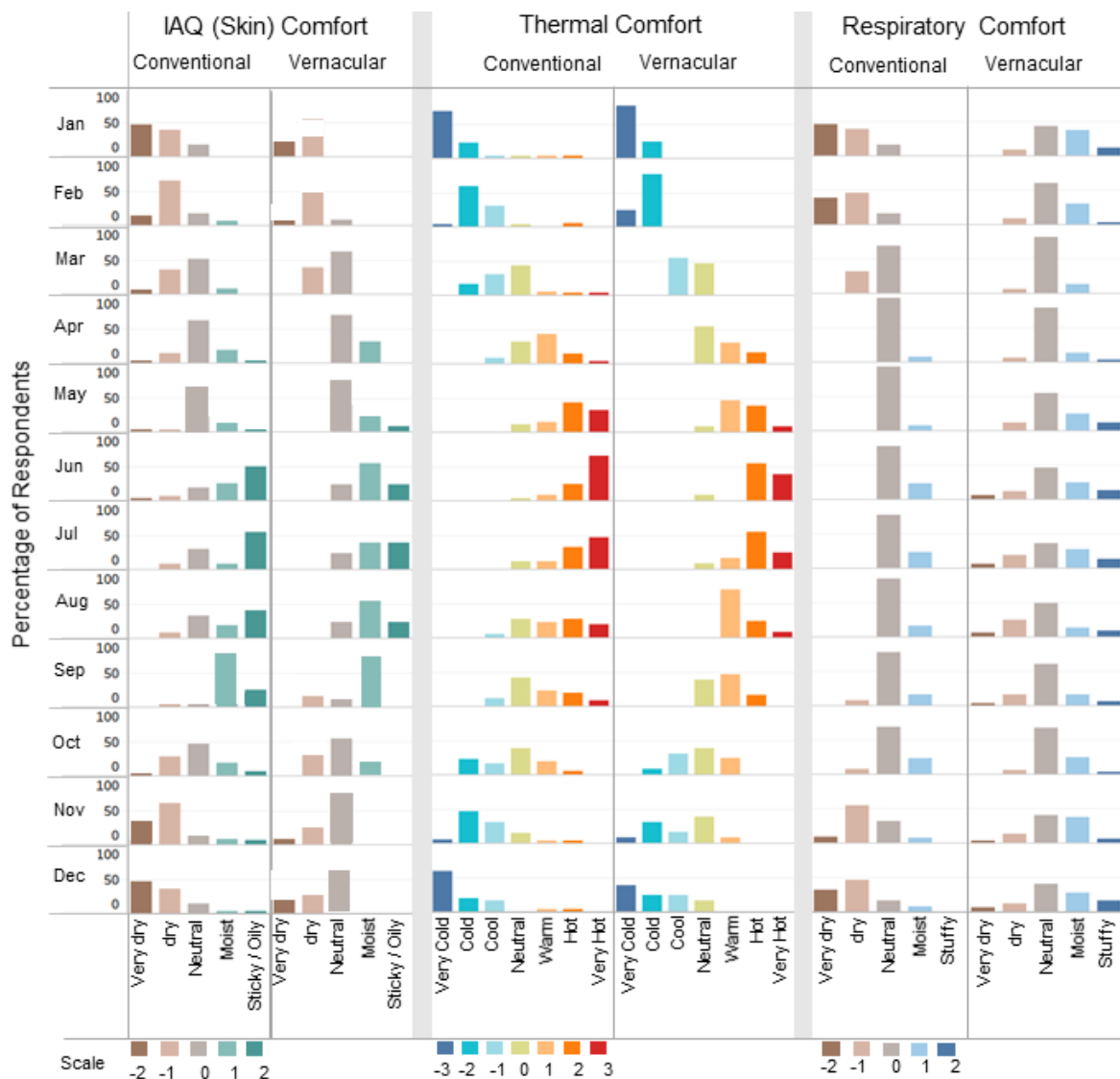


Fig. 2 – Aggregated Comfort Votes of occupants

The equilibrium (heat and mass) between the skin and the indoor air is associated with heat loss or gain by the human body, leading to thermal comfort perception. The local changes in the skin's temperature due to the heat loss/gain to attain equilibrium leads to skin-related discomfort.

In this article, skin temperature and wettedness, computed using the Gagge-2 core model, were used to understand the interaction of skin with indoor air. The system of differential equations for energy balance was solved using an iterative approach until the difference between two consecutive skin temperature values was less than 10^{-8} °Celsius. Convergence of the model was ensured in the entire range of temperature and humidity conditions recorded during the field study.

The trends of Mean Skin Temperature (MT_{sk}), Evaporative heat loss (E_{sk}), and skin wettedness (w) of occupants in different buildings (and outdoors) for four typical seasons, Spring (March), Summer (May), Monsoon (September), and Winter (November) are shown in Figs. 5, 6 and 7, respectively. During September, the average MT_{sk} variation is close to the neutral MT_{sk} ; occupants report feeling hot and humid. The corresponding E_{sk} is lower, with higher values of w . This implies that the evaporative losses are restricted in the humid months from the skin causing sweat accumulation on the skin surface, resulting in the occupants feeling sticky. In November, when the occupants feel cold and dry, the variation in average MT_{sk} is the highest, implying more deviation from the neutral MT_{sk} . However,

even though the MT_{sk} is lower than the neutral, and the human body needs to gain heat, E_{sk} is higher, and the skin is still losing energy. This negative response of the skin is due to active perspiration from the skin (high HR) into the outdoor air (low HR) to attain mass equilibrium, further cooling the skin. This loss of moisture leads to skin dryness.

In May, even though the MT_{sk} , E_{sk} , and w remain the highest, the skin-related (IAQ) comfort vote remains close to neutral. High E_{sk} and moderate w have a cooling effect on the skin, promoting the lowering of skin temperature to the neutral MT_{sk} .

The building clusters in the survey locality are designed to accommodate open, closed, and semi-open spaces (courtyard/verandah). Transitions from outdoor/semi-outdoor to indoors are inevitable for daily activities. Thermoregulation on the skin's surface is perturbed in this transition.

Human skin tries to maintain a balance through active perspiration, leading to a spontaneous skin temperature change. These variations in the skin temperature and wettedness due to environmental air parameters can cause dryness.

In Fig. 8 and Fig. 9, the computed skin temperatures of each body segment in the courtyard (outdoors), vernacular room, and conventional room at different times of the day are illustrated. The indoor environmental parameters in the vernacular buildings are very close to the outdoor environment on the low humidity cold days, implying lowered discomfort. It may be noted that some segments reach MT_{sk} as high as 40°C , which may not occur in reality. The calculated MT_{sk} indicates an equilibrium temperature between the skin and the indoor air. However, the skin responds instantaneously with indoor air temperature/RH perturbation, not necessarily after the equilibrium is reached.

Nonetheless, the temperatures illustrated are valid for understanding the stress that human skin may undergo. Also, the thermal stress on the skin in the courtyard, conventional and vernacular rooms is contrasted.

The change in temperature and RH outdoors diurnally also changes skin parameters. Vernacular indoor environments are regulated, moderating the thermal exchanges between the human body and the indoor air throughout the day.

Other reported health outcomes like colds, coughs,

headaches, etc., need further scrutiny for their association with Indoor Environmental Quality (IEQ). Also, the present humidity-related comfort standards need to be validated for their applicability given the varying building typologies, acclimatization, personal habits, and occupants' preferences.

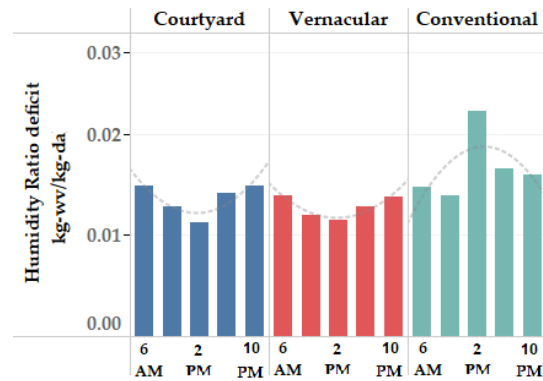


Fig. 3 – HR deficit on highest outdoor humidity day (23 Sept 2020)

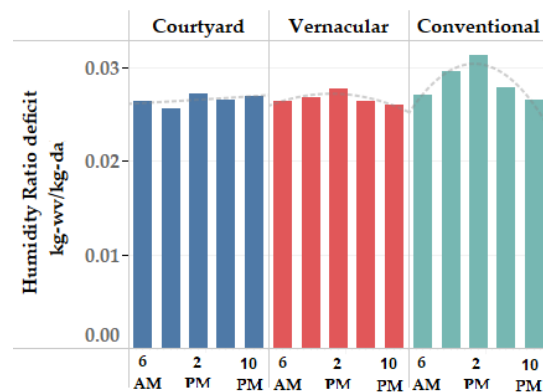


Fig. 4 – HR deficit on lowest outdoor humidity day (4 Nov 2020)

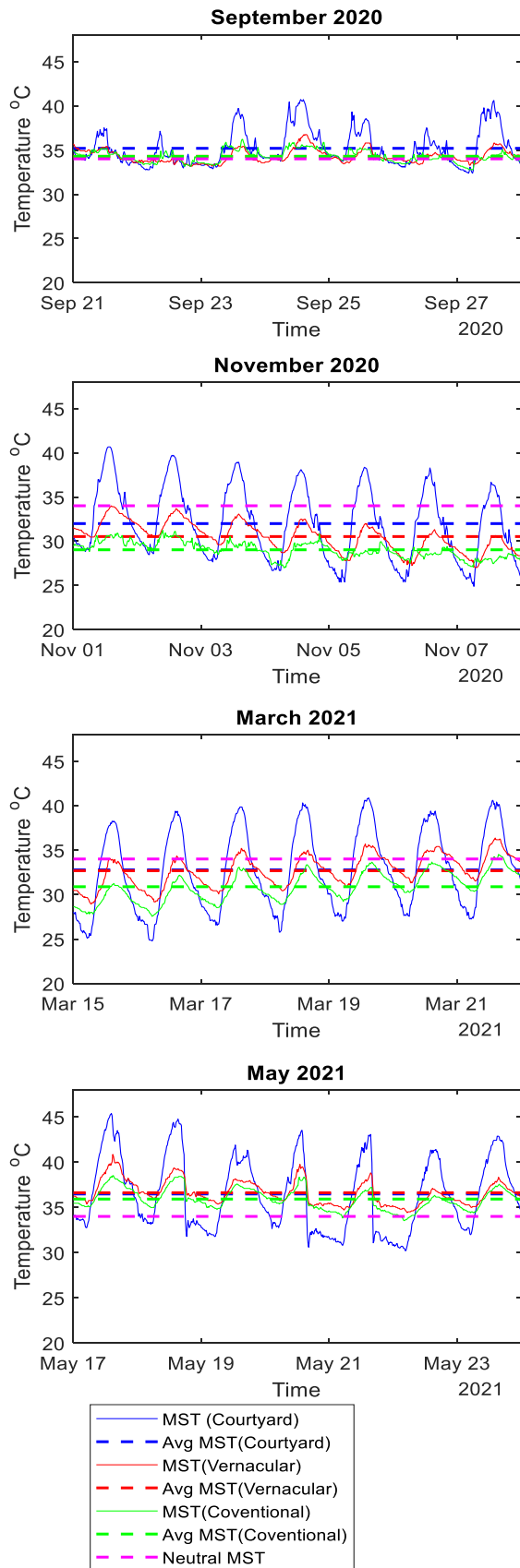


Fig. 5 – Seasonal variations of Mean Skin Temperature in Courtyard, Vernacular and Conventional Rooms

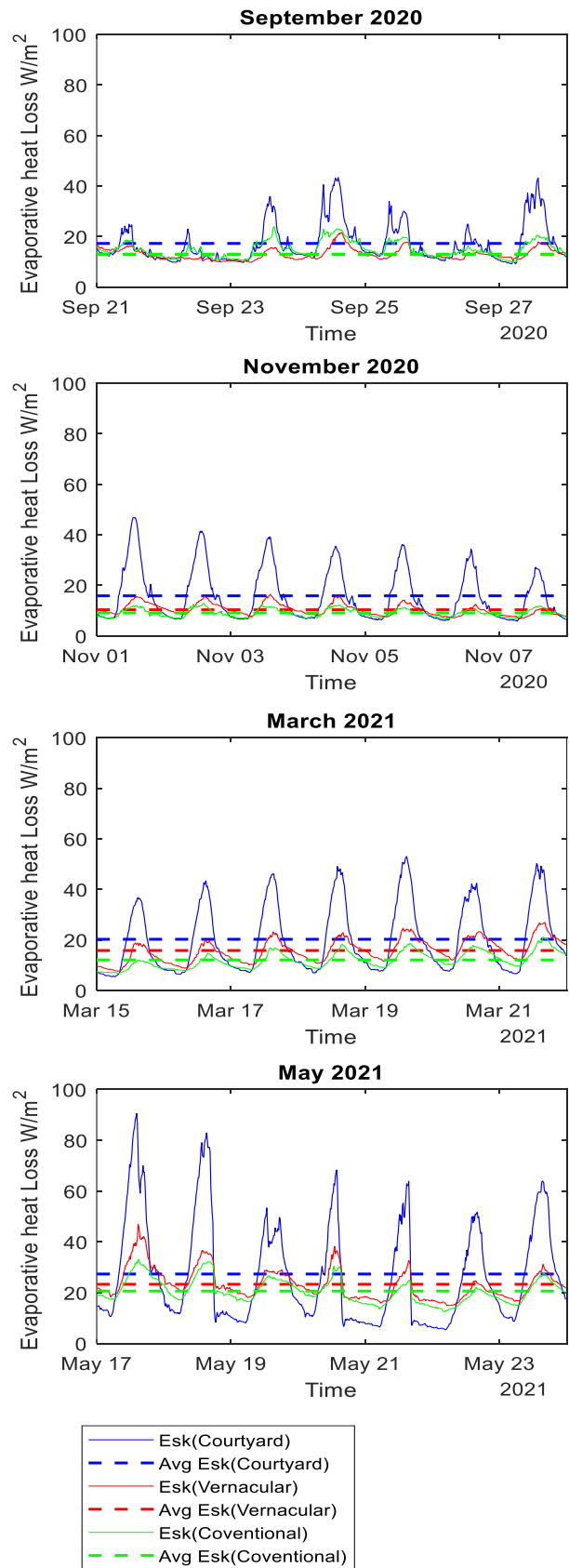


Fig. 6 – Seasonal variations of Evaporative heat loss in Courtyard, Vernacular and Conventional Rooms

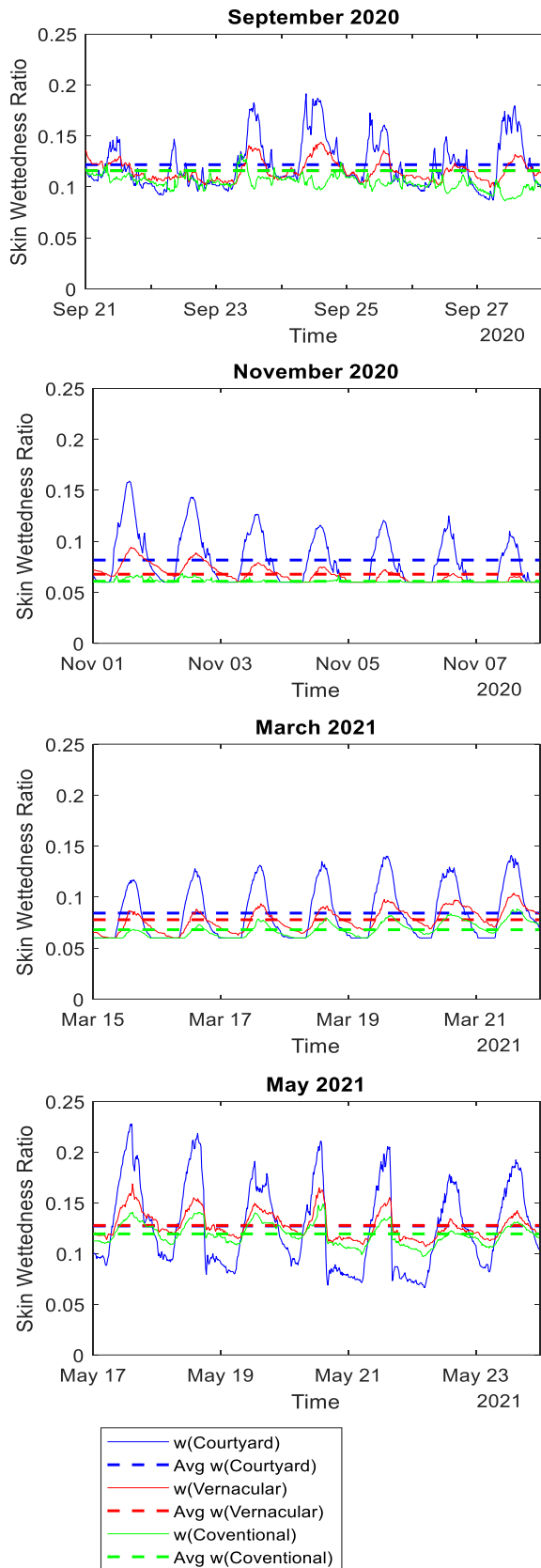


Fig. 7 – Seasonal variations of skin wettedness in courtyard, vernacular and conventional rooms

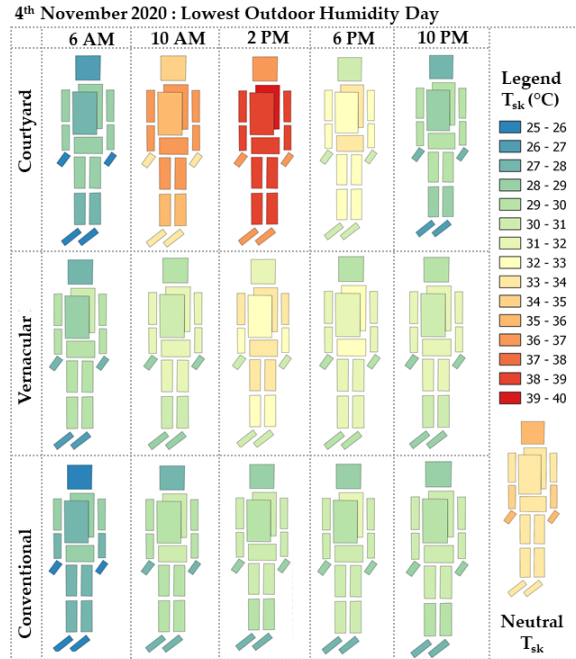


Fig. 8 – Variation of skin temperatures diurnally in the courtyard, vernacular dwelling, and conventional dwelling on lowest outdoor humidity day (4 Nov 2020)

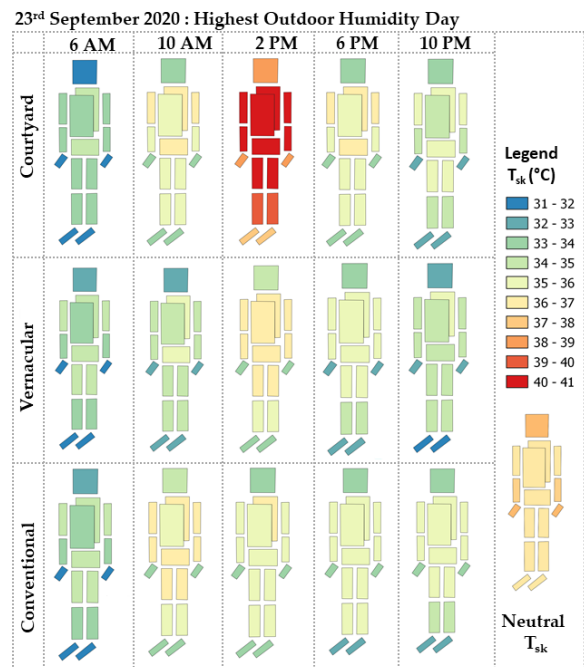


Fig. 9 – Variation of skin temperatures diurnally in the courtyard, vernacular dwelling, and conventional dwelling on highest outdoor humidity day (23 Sept 2020)

4. Conclusion

This study attempts to explain the impact of varying indoor RH in vernacular and conventional building typologies on humidity-related comfort and health outcomes. It involves real-time monitoring and a computational approach. Skin temperature and wettedness were computed corresponding to real-time indoor conditions in vernacular and conventional buildings based on the energy balance between the skin and indoor air. Humidity is an essential determinant of thermal, respiratory, and skin-related comfort, determining everyday habits like clothing, use of cosmetics etc., water intake etc. thereby impacting health. Although the current building simulation tools incorporate examination of thermal comfort associated with humidity, skin and respiratory comfort are not explicitly examined. Integration of this approach in building simulation tools could improve understanding into occupants' skin and respiratory comfort. The results show that building typology (materials) is vital in enhancing humidity-related IEQ parameters. Vernacular dwelling was more conducive to occupants' comfort and health in this study. Vernacular dwellings are earth-based and carry a lower carbon/ecological footprint. There is immense scope for occupant wellness in their adoption in modern buildings.

Acknowledgment

This study was supported by Prime Minister's Research Fellowship at the Indian Institute of Science and the British Academy's Wellbeing achieved from Earthen Residence (WAFER) project (UWB190086).

Nomenclature

Symbols

A	Surface Area (m^2)
$c_{p,b}$	Constant pressure specific heat of tissue ($kJ/(kg\ K)$)
$c_{p,bl}$	Constant pressure specific heat of blood ($kJ/(kg\ K)$)
C	Convective heat transfer (W/m^2)
C_{res}	Sensible heat loss due to respiration (W/m^2)

E_{res}	Evaporative heat loss due to respiration (W/m^2)
E_{sk}	Evaporative heat loss from the skin (W/m^2)
HR	Humidity Ratio ($kg\text{-}wv/kg\text{-}da$)
i	Body segment (dimensionless)
K	Effective conductance between core and skin ($W/(m^2K)$)
m	Mass (kg)
m_{bl}	Blood flow (core-skin) ($kg/(m^2s)$)
M	Metabolic heat production (W/m^2)
$p_{sk,s}$	Partial pressure of saturated water vapor at skin temperature (kPa)
$p_{wv,a}$	Partial pressure of water vapor in the air (kPa)
$Q_{cr,sk}$	Heat flow from core to skin (W/m^2)
R	Radiative heat transfer (W/m^2)
R_a	Thermal resistance of outer air layer (m^2C/W)
R_{al}	Thermal resistance of intermediate air layer (m^2C/W)
$R_{e,a}$	Evaporative resistance of outer air layer (m^2kPa/W)
$R_{e,al}$	Evaporative resistance of intermediate air layer (m^2kPa/W)
$R_{e,f}$	Evaporative resistance of fabric layer (m^2kPa/W)
$R_{e,t}$	Total evaporative resistance (m^2kPa/W)
R_t	Total thermal resistance (m^2C/W)
S_{cr}	Heat storage in the core (W/m^2)
S_{sk}	Heat storage in the skin (W/m^2)
t_o	Air temperature ($^{\circ}C$)
t_{cr}	Core temperature ($^{\circ}C$)
$t_{cr,n}$	Neutral core temperature ($^{\circ}C$)
t_{sk}	Skin temperature ($^{\circ}C$)
$t_{sk,n}$	Neutral skin temperature ($^{\circ}C$)
w	Skin wettedness ratio (dimensionless)
W	Heat due to external work (W/m^2)
α	Body mass fraction at the skin (dimensionless)
θ	Time (s)

References

- al Horr, Y., M. Arif, A. Kaushik, A. Mazroei, M. Katafygiotou, and E. Elsarrag. 2016. "Occupant Productivity and Office Indoor Environment Quality: A Review of the Literature". *Building and Environment* 105: 369–89. doi: <https://doi.org/10.1016/j.buildenv.2016.06.001>
- Atmaca, I., and A. Yigit. 2006. "Predicting the Effect of Relative Humidity on Skin Temperature and Skin Wettedness". *Journal of Thermal Biology* 31(5): 442–52. doi: <https://doi.org/10.1016/j.jtherbio.2006.03.003>
- de Dear, R. J., K. G. Leow, and S. C. Foo. 1991. "Thermal Comfort in the Humid Tropics: Field Experiments in Air Conditioned and Naturally Ventilated Buildings in Singapore". *International Journal of Biometeorology* 34(4): 259–65. doi: <https://doi.org/10.1007/BF01041840>
- de Dear, R. J., E. Arens, Z. Hui, and M. Oguro. 1997. "Convective and Radiative Heat Transfer Coefficients for Individual Human Body Segments". *International Journal of Biometeorology* 40(3): 141–56. doi: <https://doi.org/10.1007/s004840050035>
- de Dear, R. J., J. Kim, C. Candido, and M. Deuble. 2015. "Adaptive Thermal Comfort in Australian School Classrooms". *Building Research and Information* 43(3): 383–98. doi: <https://doi.org/10.1080/09613218.2015.991627>
- Hugentobler, W. 2021. "Mucociliary Clearance Is Humidity Dependent-Contrary to Common Belief". *Proceedings of the 17th International Healthy Buildings Conference*: 66–69.
- Jokl, M. V. 2002. "Thermal Comfort and Optimum Humidity". *Acta Polytechnica* 42(1): 12–24.
- Kong, D., H. Liu, Y. Wu, B. Li, S. Wei, and M. Yuan. 2019. "Effects of Indoor Humidity on Building Occupants' Thermal Comfort and Evidence in Terms of Climate Adaptation". *Building and Environment* 155: 298–307. doi: <https://doi.org/10.1016/j.buildenv.2019.02.039>
- Parsons, K. C. 2003. "Human Thermal Environments: The Effect of Hot, Moderate and Cold Environments on Human Health". *Comfort and Performance*: 262–294.
- Petty, S. E. 2017. *Indoor Environmental Quality, Forensic Engineering: Damage Assessments for Residential and Commercial Structures*. doi: <https://doi.org/10.1201/b14052>
- Priyadarshani, S., M. Mani, and D. Maskell. 2021a. "Discerning Relative Humidity Trends in Vernacular and Conventional Building Typologies for Occupant Health". *Proceedings of the 17th International Healthy Buildings Conference*: 587–98.
- Priyadarshani, S., M. Mani, and D. Maskell. 2021b. "Influence of Building Typology on Indoor Humidity Regulation". *REHVA Journal* 6: 48–52.
- Shastri, V., M. Mani, and R. Tenorio. 2016. "Evaluating Thermal Comfort and Building Climatic Response in Warm-Humid Climates for Vernacular Dwellings in Suggenhalli (India)". *Architectural Science Review* 59(1): 12–26. doi: <https://doi.org/10.1080/00038628.2014.971701>
- van Hoof, J., M. Mazej, and J. L. M. Hensen. 2010. "Thermal Comfort: Research and Practice". *Frontiers in Bioscience* 15(2): 765–88. doi: <https://doi.org/10.2741/3645>
- Wolkoff, P., and S. K. Kjærgaard. 2007. "The Dichotomy of Relative Humidity on Indoor Air Quality". *Environment International* 33(6): 850–57. doi: <https://doi.org/10.1016/j.envint.2007.04.004>

An Investigation Into Thermal Performance of Buildings Built Using Upcycled End-Of-Life Photovoltaic Panels

Roshan R Rao – Indian Institute of Science, India – roshanrao@iisc.ac.in

Suchi Priyadarshani – Indian Institute of Science, India – suchip@iisc.ac.in

Monto Mani – Indian Institute of Science, India – monto@iisc.ac.in

Abstract

End-of-Life, or discarded, Solar Photovoltaic panels are rising in huge numbers every year throughout the world. This is of grave concern as the environmentally safe handling of EoL-PV is not yet established fully. We propose a novel approach to upcycle End-of-Life (EoL)-PV as a building material that can extend the life of PV by another 2~3 decades. PV panels are a multi-layered laminate of different materials. In the course of environmental exposure and use, degradation induces variation in the optical properties of EoL-PV. Variations in thermal properties have not been explicitly examined, which has a bearing on the thermal performance of a building when integrated as a building material. This work studies the influence of the thermal conductivity and solar transmittance of PV panels on the surface temperatures using a steady-state energy balance model. Also, through the whole building simulation, the implications on the mean radiant temperature and the heating/cooling load of the building by using EoL PV compared to a new PV are understood. Other factors, like the area of PV to wall ratio, seasonal changes, and climate zone are found to play a role in the relative changes in the MRT and Heating/Cooling Load attributed to EoL-PV integration in buildings.

1. Introduction

Solar Photovoltaic (PV) installations are growing exponentially worldwide, leaving behind a massive pile of PV waste after its decommissioning. By 2050, cumulative PV waste would be 60~78 million tons (IEA-PVPS and IRENA, 2016). Currently, most PV panels end up in shredders and/or landfills, contaminating and disrupting our ecosystem. We propose a novel approach to upcycle End-of-Life (EoL)-PV as a building material that can extend the life of PV by another 2~3 decades. On another note, the num-

ber of people living in slums or informal settlements is over 1 billion, with 80 % in Eastern and South-Eastern Asia, sub-Saharan Africa and Central and Southern Asia. About 3 billion people will require adequate and affordable housing by 2030 (United Nations, 2021).

EoL-PV panels are a low-cost alternate durable option as a building material, and this approach promotes planetary wellness by offsetting the use of conventional materials and preventing toxic elements in PV entering the ecosystem. On using PV panels as a building façade, the occupants are exposed to the backsheet of the PV panel. Backsheet chalking (presence of white coloured powder on the backsheet) is commonly observed in field degraded PV. In a few cases, it has been investigated and discovered to be TiO_2 (Gebhardt et al., 2018), and usage of such PV panels in buildings exposes the occupants to such powders. Also, the release of fluorine from the backsheet has been examined at high temperatures ($> 300^\circ\text{C}$) (Danz et al., 2019). The release of fluorine at room temperature or the nature of the impact of chalking on occupants has not been understood. Studies involving any emissions from PV backsheet (due to cracking, chalking, burns, etc.) and its negative impact on occupants is essential.

PV panels are laminate of different materials. A typical PV panel configuration is Glass / EVA / Cell / EVA / Backsheet and layers of anti-reflective coating subject to the manufacturer. A commonly observed degradation mode in PV is EVA (ethylene vinyl acetate) discoloration, which occurs due to acetic acid formation (Pern & Czanderna, 1992). Also, the adhesion strength of the EVA (primarily used as an adhesive layer in panels) is compromised in aged PV (Desai et al., 2022), which could lead to delamination of PV panels. A change in vinyl acetate (VA)

content has been reported in the aged PV panel (Desai et al., 2022). VA content change can imply a change in the thermal conductivity of the EVA (Jia and Zhang, 2022) layer in the PV panel. Also, due to discoloration of the EVA layer, optical transmittance is reported to have dropped (Desai et al., 2020; Jeong et al., 2013). Due to the inherent nature of PV panels being composed of multiple layers of different materials, unlike a homogenous panel, physical and chemical changes in any layer impact the optical and thermal properties of the bulk material. Our preliminary investigations include understanding the influence of physical degradation on optical and thermal transmittance of EoL-PV (aged) and its influence on the building's thermal performance and indoor thermal comfort. A steady-state energy balance model is used to understand the effect of changes in optical and thermal properties on PV surface temperatures. When PV panels are integrated as a building elements, multiple other factors influence the thermal performance of the building. Hence, a whole building simulation is performed using Design Builder software with EoL-PV integrated with the building.

2. Methodology

2.1 Energy Balance Model

An optical model considering the interaction of light through multiple layers of PV is used to calculate the spectral transmittance, reflectance and absorptance of the PV panel at each layer (Lu & Yao, 2007). The heat transfer modes among the layers considered are shown in Fig. 1. The transmittance, reflectance, and absorptivity of n (number of layers) layers of the PV panel are calculated using the multi-layered optical model developed (Lu & Yao, 2007).

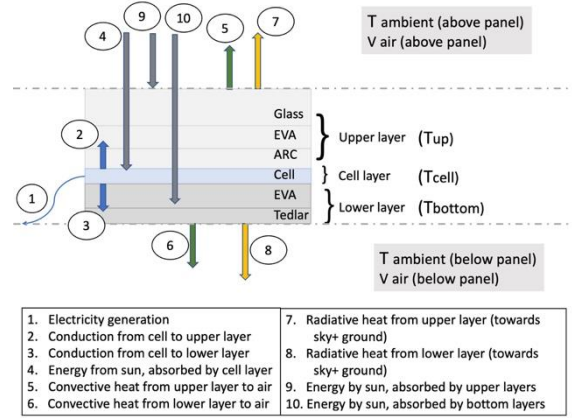


Fig. 1 - Heat transfer modes at different layers of a typical PV module

A steady-state energy balance model for PV panel is used, which considers the heat transfer through multiple layers of PV panel (Glass, EVA, ARC, Si-cell, EVA, Tedlar). The angle between the sun and the normal to PV panel is calculated using the following equations

$$a = (\sin \phi \cdot \sin \delta \cdot \cos \beta) - (\cos \phi \cdot \sin \delta \cdot \cos \gamma_m \cdot \sin \beta) \quad (1)$$

$$b = (\sin \phi \cdot \cos \delta \cdot \cos \gamma_m \cdot \sin \beta) + (\cos \phi \cdot \cos \delta \cdot \cos \beta) \quad (2)$$

$$c = (\cos \delta \cdot \sin \gamma_m \cdot \sin \beta) \quad (3)$$

$$\theta = \cos(a + b \cos \omega + c \sin \omega) \quad (4)$$

Electricity generated depends on the net radiation transmitted through the first three layers and the efficiency of the solar cell (Zarei & Abdolzadeh, 2016). The rate of energy absorption by a Solar cell depends on the absorptivity of the cell layer.

$$q_4 = \int_0^\infty A_{cell}(\lambda) \cdot g(\lambda) d\lambda \quad (5)$$

$$q_1 = \eta_{electricity} \int_0^\infty \tau_u(\lambda) \cdot g(\lambda) d\lambda \quad (6)$$

Bi-directional (towards the upper and lower layers) conduction from the cell depends on the temperature differences and the thermal conductivity of the corresponding layers (Zarei & Abdolzadeh, 2016).

$$q_{2,3} = \frac{T_{cell} - T_{u,b}}{R_{u,b}} \quad (7)$$

Convective heat transfer occurs at the top layers-air interface, and the bottom layers-air interface is a function of the temperature difference and heat transfer co-efficient. The heat transfer coefficient approximations are adapted from (Zarei & Abdolzadeh, 2016).

$$q_{5,6} = h_{u,b} \cdot (T_{u,b} - T_{air-film\ u,b}) \quad (8)$$

Radiative heat transfer between the top layers-sky, top layers-ground and bottom layers-sky, bottom layers-ground is a function of view factor and temperature difference (Zarei & Abdolzadeh, 2016).

$$q_7 = \varepsilon_u \sigma F_{u,sky,ground} (T_u^4 - T_{sky,ground}^4) \quad (9)$$

$$q_8 = \varepsilon_b \sigma F_{b,sky,ground} (T_b^4 - T_{sky,ground}^4) \quad (10)$$

$$q_{9,10} = \int_0^\infty A_{u,b}(\lambda, \theta) \cdot g(\lambda) d\lambda \quad (11)$$

The above system of equations was solved for top, bottom, and cell temperatures through an iterative approach. The thickness of Glass, EVA, Cell and Backsheet is in the range of 3~4 mm, 0.4~0.5 mm, 0.2~0.4 mm, and 0.1~0.35 mm, respectively.

The thermal conductivity of Glass, EVA, Cell and Backsheet are in the range of 0.98 – 1.8 W/(m K), 0.23~0.35 W/(m K), 148~150 W/(m K), and 0.2~0.36 W/(m K), respectively (Chamkha & Selimefendgil, 2018; Hammami et al., 2017; Lee et al., 2008; Popovici et al., 2016; Sahli et al., 2018; Syafiqah et al., 2019). The thickness and thermal conductivity used as a base case in the steady-state model: glass (3 mm, 0.98 W/(m K)), EVA (0.5 mm, 0.35 W/(m K)), cell (0.4 mm, 148 W/(m K)), back sheet (0.1 mm, 0.2 W/(m K)).

To understand the influence of the thermal conductivity of each layer on the surface temperatures, thermal conductivity values were varied from -100 % ~ +200 % of the base-case values.

2.2 Design Builder Model

A whole building simulation has been performed for the modified BESTEST case 600FF (Design-Builder v6.1 with EnergyPlus v 8.9, 2021) model (a block of 6 m X 8 m and height of 2.7 m) (Fig. 2). PV panels have been integrated in the buildings as Glazing integrated Photovoltaics. PV panels are applied to substitute for the walls and roof and not over the existing wall or roof. The properties of the PV (250 Wp typical crystalline Silicon PV panel): (a) front and back emissivity is 0.8, infrared transmittance is 0.2, inside and outside reflectance (solar and visible) is 0.1, and the thermal conductivity, solar transmittance is varied in the range tabulate in Table 1. The PV panels are not connected to any power

sources in the simulation and are only considered a building material. Simulations are performed for varying PV area in the wall (varied as window-to-wall ratio in the Design Builder) for two cases, 25 % and 75 %. Multiple scenarios of PV integration in all four walls and roof are considered. The wall (without PV) is the 'BESTEST Lightweight Wall', which has a concrete cast (dense) with a thickness of 0.1m (see Fig. 2). The floor construction is 'BESTEST Ground Floor', which has a thickness of 0.225 m and a U value of 0.039 W/(m² K). The roof (without PV) is 'BESTEST Roof' with a U value of 0.319 W/(m² K) and thickness of 0.1 m. The simulation is performed with an occupancy density of 0.04 people/m² and no furniture/furnishings in the building. The BESTEST building being simulated is a block with a heating and cooling setpoint temperatures of 20 °C and 26 °C, respectively. India has varied climate zones, and simulations are performed for five representative cities corresponding to five climate zones (Table 2).

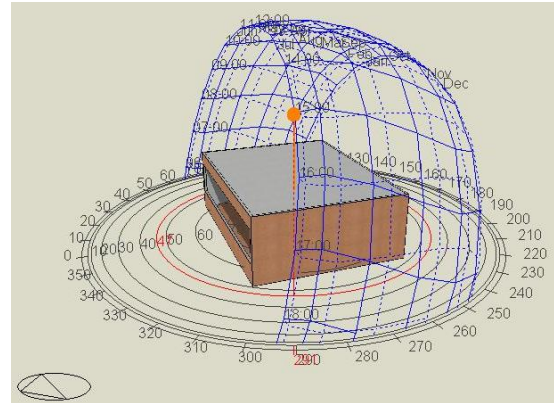


Fig. 2 – Design Builder model (600FF) modified by integrating PV in all the walls and roof

The thermal conductivity of the EVA layer varies due to the variation in the % VA content. An empirical relation has been proposed (Jia et al., 2022) to describe the relationship between thermal conductivity and % VA content.

With ageing, a maximum change in VA content in EVA was seen, with an increase from 18.1 % to 21.9 % (Desai et al., 2022). This is estimated to cause a drop in thermal conductivity of EVA and the bulk of PV panels. But this does not explain any changes in the bulk thermal conductivity. There are possibilities of reduction in the thickness (Hu et al., 2016; Jahn, 2018) of the back sheet due to weathering, and

this can cause the bulk thermal conductivity to rise. Hence, there is a possibility that the bulk thermal conductivity may get altered depending on the combination and severity of multiple degradation modes. To accurately quantify the change in thickness, thermal conductivity of the individual layers and bulk properties associated with aged PV panels (EoL-PV) requires sophisticated measurements. To broadly understand the impact of such a change at the building level, we have varied the bulk thermal conductivity (equivalent thermal conductivity of a PV panel including all the layers) and solar transmittance of the PV panels in 5 steps each. A total of 25 scenario combinations of PV panel have been considered for whole building simulations (Table 1).

Table 1 – Range of Thermal conductivity and Solar Transmittance values. Corresponding SHGC and U-value of all the possible combinations

Parameter	Range	Steps
Thermal Conductivity	0.1 ~ 2.8 W/(m K)	0.7 W/(m K)
Solar Transmittance	0.1 % ~ 16 %	4 %
SHGC (calculated)	0.271 ~ 0.408	-
U- Value (calculated)	4.763 ~ 5.782 W/(m ² K)	-

Table 2 – The representative cities selected for each climate zone in India

Climate Zone	City	Lat/Long (°North / °East)	Mean Daily Temp (°C) (min ~ max)
Temperate	Bangalore	12.97 / 77.58	15.0 ~ 33.9
Composite	Lucknow	26.75 / 80.88	7.3 ~ 40.3
Warm-Humid	Kolkata	22.65 / 88.45	13.7 ~ 35.7
Hot-Dry	Ahmedabad	23.07 / 72.63	13.1 ~ 41.4
Cold	Shillong	25.58 / 91.89	4.4 ~ 24.0

To allow for a comparative assessment between an EoL PV panel and a new panel, the new panel has been considered to have a thermal conductivity of 0.7 W/(m K) and 8 % solar transmission. Mean

Radiant Temperature (used as a heat index to indicate thermal comfort) and Heating/Cooling loads resulting from 25 combinations of PV panels have been analyzed. Simulations are performed to understand the influence of PV covered area to wall area ratio, the direction of the envelope on which the PV panels are integrated and Climate zone.

3. Results and Discussion

When the thermal conductivity of the glass layer is varied from -100 % to 200 % of its reference value (0.9 W/(m K)), the top layer's thermal resistance increases exponentially with the decrease in the thermal conductivity of glass. The increase in the thermal resistance in the top layer causes a drop in the rate of conduction heat transfer between cell and top layer. This causes a reduction in the top layer energy, as the radiation absorption by the top layer is unaffected by the change in the thermal conductivity of the glass. The decrease in the top layer energy is associated with the reduction in the top layer temperature. As the energy balance between energy into the cell and out of the cell has to be maintained at the steady-state, the conduction heat transfer between cell-bottom layer increases. This causes the bottom layer energy to increase and results in the rise in temperature of the bottom layer (Fig. 3). Each layer's thermal conductivity variation impacts the PV panel's bulk thermal conductivity (equivalent thermal conductivity). The PV panel's bulk thermal conductivity (equivalent thermal conductivity) was varied to understand the bottom surface temperature variation, as this is the surface that will interact with the indoor air when integrated in the building. A surface temperature calculation is made for the scenario where the PV panel is horizontal, and solar radiation of 900 W/m² is incident on the PV panel (Fig. 4). Further, in the whole building simulation, the degradation of PV was parameterized as a variation in solar transmittance (τ) and thermal conductivity (k) (equivalent thermal conductivity) of PV. The different scenarios of PV are compared with the base case of PV, and only relative changes in MRT and Heating Cooling load with respect to the base case is reported throughout.

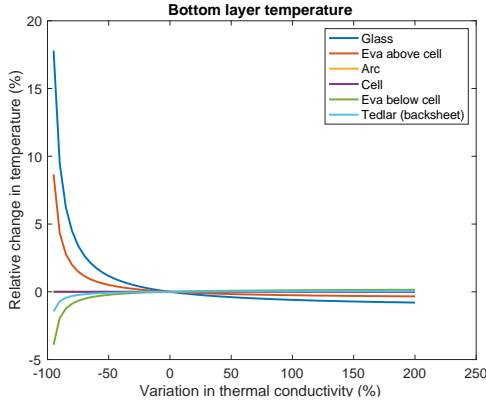


Fig. 3 – Bottom surface temperature variation with variation in the thermal conductivity of each layer of PV module

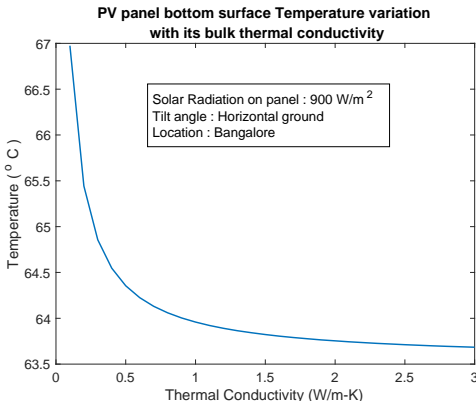


Fig. 4 – PV bottom surface temperature variation with the bulk thermal conductivity of PV panel (equivalent thermal conductivity of PV panel)

PV was integrated in the roof, and a typical summer week simulation revealed that, as the solar transmittance drops, there is about 2 % and 15 % drop in the relative change in Mean Radiant Temperature (MRT) and Heating Cooling load, respectively (Fig. 5). We understand from the literature that there are higher chances of solar transmittance drop due to EVA degradation, glass degradation, etc. The maximum and minimum relative changes in MRT and Heating Cooling load occur at maximum and minimum solar transmittance conditions. A typical summer week and winter week are compared for the maximum and minimum relative changes. Fig. 6 shows that the ranges of relative changes are broadened during winter, indicating that the external temperature has a role in indoor and MRT changes.

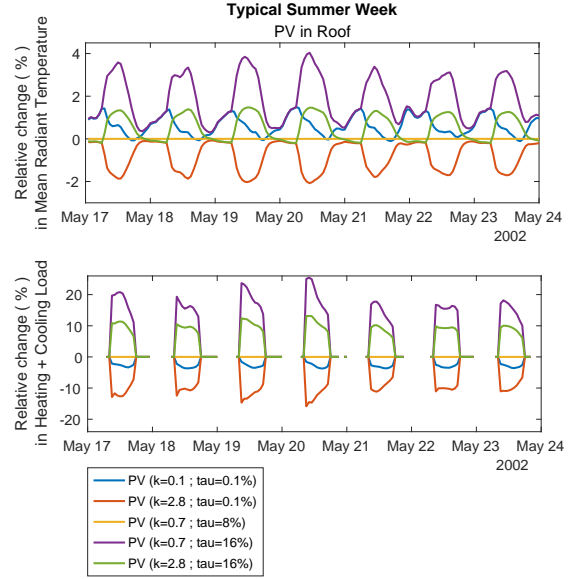


Fig. 5 – Relative change (%) in the Mean Radiant Temperature and Heating+Cooling Load for a typical summer week in Bangalore

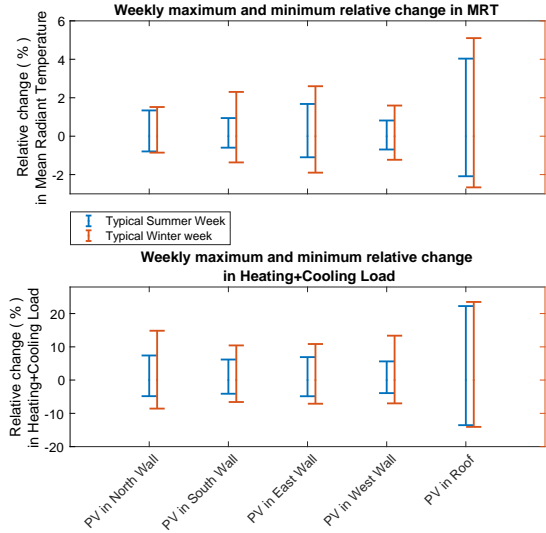


Fig. 6 – Weekly maximum and minimum relative change in MRT and Heating+Cooling Load when PV is integrated in North wall, South wall, East wall, West wall and Roof

The relative changes in MRT and Heating Cooling load variation with thermal conductivity of PV are investigated with a simulation of PV in the roof for a summer month (Fig. 7). The trend is similar to the trend observed using the steady-state energy balance model at the PV panel level (Fig. 4). The area ratio of PV to the wall also magnifies the range of minimum and maximum relative changes in the MRT and Heating Cooling load (Fig. 8).

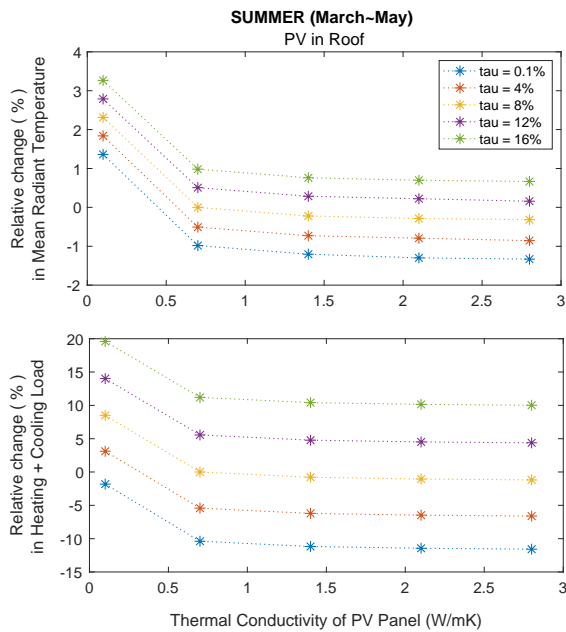


Fig. 7 – Influence of Solar Transmittance and Thermal Conductivity on the Relative change in MRT and Heating+Cooling Load

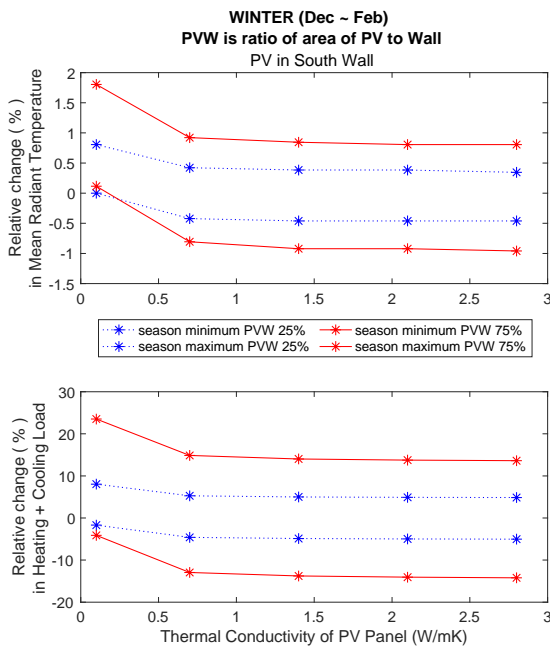


Fig. 8 – Influence of ratio of PV area-to-wall area on minimum and maximum relative changes in annual mean MRT and heating/cooling load

Annual mean MRT and Heating Cooling loads are calculated based on simulations run for all the days of the year. Such a simulation was performed to compare the relative changes in different climate zones and the location of application of PV in a building.

Annual Minimum relative change (%) in MRT					
Bangalore	-0.3824	-0.5977	-0.5568	-0.5241	-1.453
Ahmedabad	-0.2911	-0.5626	-0.5306	-0.4654	-1.388
Lucknow	-0.346	-0.6282	-0.522	-0.5281	-1.44
Kolkata	-0.2579	-0.5005	-0.3276	-0.4323	-1.112
Shillong	-0.823	-0.3065	-0.8039	-1.087	-1.963
	North	South	East	West	Roof
Annual Maximum relative change (%) in MRT					
Bangalore	0.9178	1.121	0.928	0.9734	3.702
Ahmedabad	0.5459	0.8439	0.7075	0.6445	3.311
Lucknow	0.7305	1.109	0.8949	0.8299	3.567
Kolkata	0.5158	0.7508	0.5461	0.6844	2.813
Shillong	1.875	0.6567	1.697	1.914	5.207
	North	South	East	West	Roof

Fig. 9 – Minimum and Maximum relative changes in annual mean MRT for different cities and PV application location in building

Fig. 9 and Fig. 10 tabulate the relative changes in the annual mean MRT and Heating Cooling load for different cities and the location in the building where PV is applied. The application of EoL PV on the roof seems to be more beneficiary in terms of reduction in MRT and Heating Cooling load. This could be possible due to the larger area exposed to the sun for longer hours than the walls.

4. Conclusion

This work has discussed a novel approach to up-cycle EoL PV panels into building applications. The bottom surface temperature of PV rises when the thermal conductivity of the PV panel reduces. Specifically, glass layer's thermal conductivity variation has a dominant impact on temperature variation due to its thickness. Furthermore, whole building simulations also confirm the exponential temperature variation of mean radiant temperature with thermal conductivity. Our simulation indicates a drop of about 2 % in MRT and close to 13 % in Heating Cooling load due to the loss in solar transmittance and thermal conductivity of PV. The reduction of solar transmittance due to EVA degradation is widely reported in the literature, making it favorable for EoL PV in building applications. The application of EoL PV on the roof seems to be more beneficiary in terms of reduction in MRT and Heating Cooling load.

Annual Minimum relative change (%) in Heating+Cooling Load					
Bangalore	-4.822	-5.822	-5.513	-5.548	-12.74
Ahmedabad	-2.421	-4.049	-3.715	-3.549	-10.72
Lucknow	-2.556	-4.552	-3.955	-3.636	-10.49
Kolkata	-2.285	-3.614	-2.678	-3.492	-9.435
Shillong	-3.985	-6.761	-4.157	-6.04	-9.586
	North	South	East	West	Roof
Annual Maximum relative change (%) in Heating+Cooling Load					
Bangalore	8.45	9.813	8.929	8.675	22.02
Ahmedabad	2.999	5.694	5.116	4.625	18.27
Lucknow	3.181	6.675	5.514	4.862	17.68
Kolkata	3.166	5.135	3.683	4.65	15.83
Shillong	3.856	11.32	5.961	9.765	14.91
	North	South	East	West	Roof
	PV location				

Fig. 10 – Minimum and Maximum relative changes in annual mean Heating Cooling load for different cities and PV application location in building

The benefit is achieved in the case of lower solar transmittance conditions, which also implies lesser daylight entry into the building. The implication of this on the marginal rise in electricity consumption for artificial lighting is the scope of further study. There is no significant difference in the magnitude of relative changes in MRT or Heating Cooling loads at different climate zones. At this point, it can be argued that application of EoL PV has the potential to be used as a building material in general and provide better thermal performance at the same time. A more detailed understanding of the variations of optical and thermal properties due to different degradation modes permits us to speculate on the possible implication of EoL-PV applications in buildings more accurately.

Nomenclature

Symbols

$A_{cell,u,b}$	Absorptivity (cell, upper or bottom layers)
$F_{b,sky,ground}$	View Factor (bottom layer - sky or bottom layer - ground)
$F_{u,sky,ground}$	View Factor (upper layer - sky or upper layer - ground)
$h_{u,b}$	Convective heat transfer coefficient (W/m ² K) (upper or bottom layers)
$R_{u,b}$	Resistance in conduction (K/W) (upper or bottom layer)

$T_{air-film\ u,b}$	Temperature (°C) (air film upper or bottom layers)
$T_{cell,u,b}$	Temperature (°C) (cell, upper or bottom layer)
$T_{sky,ground}$	Temperature (°C) (sky or ground)
$\eta_{electricity}$	PV conversion efficiency
$\tau_{u,b}$	Transmittivity (upper or bottom layers)
ϕ	Latitude
g	Solar radiation (W/m ²) incident on PV panel
τ	Solar Transmittance
β	Tilt angle (degrees from horizontal)
δ	Declination angle (degrees)
θ	Inclination angle (degrees) between sun and normal to PV panel
ω	Hour angle (degrees)

References

- Chamkha, A. J. and F. Selimefendigil. 2018. "Numerical Analysis for Thermal Performance of a Photovoltaic Thermal Solar Collector with SiO₂-Water Nanofluid". *Applied Sciences* 8(11). doi: <https://doi.org/10.3390/app8112223>
- Danz, P., V. Aryan, E. Möhle, and N. Nowara. 2019. "Experimental Study on Fluorine Release from Photovoltaic Backsheet Materials Containing PVF and PVDF during Pyrolysis and Incineration in a Technical Lab-Scale Reactor at Various Temperatures". *Toxics* 7(47).
- Desai, U., B. K. Sharma, A. Singh, and A. Singh. 2020. "Enhancement of Resistance against Damp Heat Aging through Compositional Change in PV Encapsulant Poly (Ethylene-Co-Vinyl Acetate)". *Solar Energy* 211: 674–82. doi: <https://doi.org/10.1016/j.solener.2020.09.083>
- Desai, U., B. Kumar Sharma, A. Singh, and A. Singh. 2022. "A Comparison of Evolution of Adhesion Mechanisms and Strength Post Damp-Heat Aging for a Range of VA Content in EVA Encapsulant with Photovoltaic Backsheet". *Solar Energy* 231: 908–20. doi: <https://doi.org/10.1016/j.solener.2021.12.031>
- DesignBuilder v6.1 with EnergyPlus v 8.9, ANSI/ASHRAE Standard 140-2017 Building

- Thermal Envelope and Fabric Load Tests - Validation Report, 2021.
- Gebhardt, P., L. P. Bauermann, and D. Philipp. 2018. "Backsheet Chalking - Theoretical Background and Relation to Backsheet Cracking and Insulation Failures". In *35th European PV Solar Energy Conference and Exhibition*.
- Hammami, M., S. Torretti, F. Grimaccia, and G. Grandi. 2017. "Thermal and Performance Analysis of a Photovoltaic Module with an Integrated Energy Storage System". *Applied Sciences* 7(11). doi: <https://doi.org/10.3390/app7111107>
- Hu, H., W. M. Wang, O. Fu, A. Bradley, T. Felder, W. Gambogi, and T. J. Trout. 2016. "Typical Photovoltaic Backsheet Failure Mode Analysis under Different Climates in China". *SNEC International Photovoltaic Power Generation Conference*.
- IEA-PVPS and IRENA. 2016. *End-of-Life Management: Solar Photovoltaic Panels*.
- Jahn, U. 2018. *Methoden Zur Fehlererkennung Bei PV-Modulen Und Anlagen-Qualitaetssicherung Im Feld*, pp. 1–22.
- Jeong, J. S., and N. Park. 2013. "Field Discoloration Analysis and UV/Temperature Accelerated Degradation Test of EVA for PV". *2013 IEEE 39th Photovoltaic Specialists Conference (PVSC)*.
- Jia, Y. and J. Zhang. 2020. "Thermal Conductivity of Ethylene-Vinyl Acetate Copolymers with Different Vinyl Acetate Contents Dependent on Temperature and Crystallinity". *Thermochimica Acta* 708:179141. doi: <https://doi.org/10.1016/j.tca.2021.179141>
- Lee, B., J. Z. Liu, B. Sun, C. Y. Shen, and G. C. Dai. 2008. "Thermally Conductive and Electrically Insulating EVA Composite Encapsulant for Solar Photovoltaic (PV) Cell". *Express Polymer Letters* 2(5): 357–63. doi: <https://doi.org/10.3144/expresspolymlett.2008.42>
- Lu, Z. H., and Q. Yao. 2007. "Energy Analysis of Silicon Solar Cell Modules Based on an Optical Model for Arbitrary Layers". *Solar Energy* 81: 636–47, 2007. doi: <https://doi.org/10.1016/j.solener.2006.08.014>
- Pern, F. J., and A. W. Czanderna. 1992. "Characterization of Ethylene Vinyl Acetate (EVA) Encapsulant: Effects of Thermal Processing and Weathering Degradation on Its Discoloration". *Solar Energy Materials and Solar Cells* 25(1–2): 3–23, 1992. doi: [https://doi.org/10.1016/0927-0248\(92\)90013-F](https://doi.org/10.1016/0927-0248(92)90013-F)
- Popovici, C. G., S. V. Hudişteanu, T. D. Mateescu, and N. C. Cherecheş. 2016. "Efficiency Improvement of Photovoltaic Panels by Using Air Cooled Heat Sinks". *Energy Procedia* 85: 425–32. doi: <https://doi.org/10.1016/j.egypro.2015.12.223>
- Sahli, M., J. P. de Magalhaes Correia, S. Ahzi, and S. Touchal. 2018. "Thermomechanical Investigation of PV Panels Behaviour under NOCT Conditions". *Proceedings of 2017 International Renewable and Sustainable Energy Conference, IRSEC 2017*. doi: <https://doi.org/10.1109/IRSEC.2017.8477292>
- Syafiqah, Z., N. Amin, M. Irwanto, W. Z. Leow, and A. R. Amelia. 2019. "Thermal and Electrical Study for PV Panel with Cooling System". *Indonesian Journal of Electrical Engineering and Computer Science* 17(2): 941–49, 2019. doi: <http://doi.org/10.11591/ijeecs.v7.i2.pp492-499>
- United Nations. 2021. *Make Cities and Human Settlements Inclusive, Safe, Resilient and Sustainable*.
- Zarei, T., and M. Abdolzadeh. 2016. "Optical and Thermal Simulations of Photovoltaic Modules with and Without Sun Tracking System". *Journal of Solar Energy Engineering* 138(1): 1–12. doi: <https://doi.org/10.1115/1.4031684>

Determining the Energy Benefits from Passive Solar Design Integration through the Sensitivity Analysis of Different Case Studies

Giacomo Cillari – University of Pisa, Italy – giacomo.cillari@phd.unipi.it

Alessandro Franco – University of Pisa, Italy – alessandro.franco@unipi.it

Fabio Fantozzi – University of Pisa, Italy – fabio.fantozzi@unipi.it

Abstract

The increasing energy demand of our buildings is putting stress on the building systems and energy grids in terms of need for efficiency improvements. The maximization of the overall performance requires a multidisciplinary approach towards seeking innovative solutions to help reduce the building loads. In terms of efficient energy planning, the building design phase has often been often disregarded or looked at from a single point of view. In this case, research places its attention either on the performance of the opaque or transparent envelope to define optimization criteria. A comprehensive analysis of the impact of different passive solutions on the energy demand of buildings with different uses is the core of the present paper. The main goal is to define design guidelines for the integration of simple to complex passive configurations into the building design to help reduce the heating demand by better exploiting solar radiation. The paper gathers data from 384 simulations, on different test buildings, with the permutation of various design parameters, including window-to-wall ratio, wall heat transfer coefficient and heat capacity. Simulations were run in two different locations, typical of southern and northern Italian climate conditions, for both residential and office use. After the best solutions according to the heating or total energy performance over a nominal year were highlighted, the guidelines were applied to a case study. The aim is to determine a methodology to properly integrate passive solutions on the basis of energy performance. This performance, indeed, constitutes a trade-off of the potential of passive systems to understand when it can be profitable to integrate these. The building analyzed, a cohousing project still in the design phase, showed that 10 to 16 % of the total energy demand can be saved. The energy saving is reached by simply integrating and declining the passive configuration suggested with marginal modifications to the initial design.

1. Introduction

The impact of the residential sector share on global energy consumption is known to be relevant. Therefore, practice has increasingly paid attention to energy conservation and efficiency strategies, use of efficient building plants and, recently, integration of renewable energy systems (RES). Among the latter, photovoltaic and solar thermal technologies have spread all over the market as the most user-friendly RES to integrate into buildings (O'Shaughnessy et al., 2018), but proper sizing and management of these systems is crucial to avoid wasting the energy produced (Cillari et al., 2021a and 2021b). From the perspective of nearly-zero-energy buildings (Albayyaa et al., 2019), the rational use of available sources must be further increased. Solar energy being one of the most suitable for exploitation in the building sector, the design of the building envelope must take into account the impact of an integrated passive solar system (Bajcinovci & Jerliu, 2016). to maximize the potential benefits,. Even if passively exploiting green and renewable energy, such as solar radiation, can be regarded to as a relevant advantage in the application of these solutions, their integration, especially in modern buildings, has been limited to a few, broad projects, due to the prediction of the final performance being hard to estimate. The prediction of passive solar potential on a suburban scale may help the performance of neighborhood design and find the optimal starting configuration (Nault et al., 2017). The energy behavior of the passive solar design, however, is influenced by many different factors, either intrinsic or extrinsic to the design, from latitude and orientation to specific solution details, such as cavity depth (Cillari et al.,

2021a and 2021b). Various optimization techniques and objective functions can be used to improve the behavior of solar passive design due to its multi-disciplinary nature, as it can positively affect heating, cooling, lighting and ventilation demand (Stevanović, 2013).

Based on the operational characteristic of each solution, such as adaptability, overheating sensitivity and estimated cost, a schematic view of different suggested solutions has been already proposed (Cillari et al., 2020). The present work deals with the modeling of the integration of different passive solar solutions and evaluation of the related energy results achievable. The purpose is to define a methodological approach for the integration of such solutions based on the trade-off regarding their energy performance. To deal with different affecting parameters, a permutation of the most impactful factors was implemented, as described in Methodology, Section 2. Section 3 presents the results and discussion of both general investigation and case study. Finally, conclusions are drawn in Section 4.

2. Methodology

Passive strategies are usually divided, according to the relative position of the solar collector, the thermal mass and the indoor environment, into direct gain systems, indirect systems, and isolated gain systems (Givoni, 1991). In the first category, we have wide windows systems, shading systems and solar paintings, while indirect gain systems include the most complex configurations, such as roof pond, massive and Trombe walls. The last class consists of sunspaces and Barra-Costantini systems. In order to develop a comprehensive analysis of passive solar design, four different solutions were analysed, namely *direct gain systems*, *Trombe walls*, *direct sunspaces* and *nanopainting*, which can affect cooling savings. The present investigation is based on a sensitivity analysis of these passive configurations through an extensive dynamic energy simulation with the software EnergyPlus™. Simulations are based on two different climate conditions and building destinations: residential and office buildings in location 1, Palermo,

and location 2, Bolzano. The two climatic contexts are defined by an average annual solar irradiation of 1673 kWh/m² and 1218 kWh/m² respectively, with an average air temperature of 18.8 °C and 13.7 °C. Maximum, minimum and average monthly temperature and average monthly global horizontal solar radiation are shown for the two locations in Fig. 1. The three orientations were investigated. Lightweight and heavyweight structures were considered for the simulation, with average heat capacity per unit area values using 30-cm-thick concrete and wooden structures as a reference.

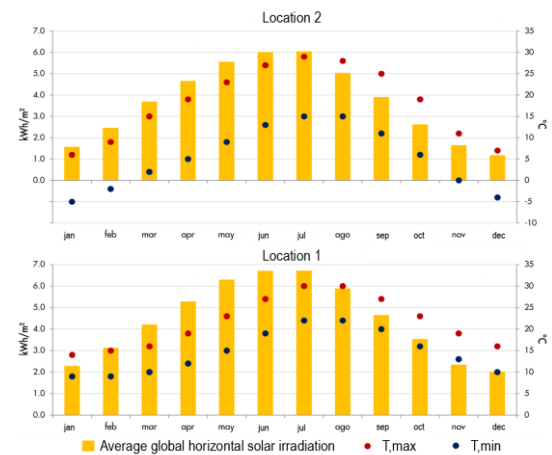


Fig. 1 – Temperature and radiation for location 1 and 2

The direct gain systems simulation consists of the increase of the reference window-to-wall ratio (WWR), according to Table 1, as with glass U-values. The Trombe wall was simulated as a detached thermal zone, with different constructions for the heat capacity and the WWR of the outer glass collector values of Table 1. Within the air cavity of the zone, for the modeling of the Trombe Wall, the ISO 15099 correlation, as validated by (Ellis, 2003), was adopted. For the summer period, the following equation was used to model the thermal chimney behavior of the opened air cavity:

$$Q = C_d A_o \sqrt{[2 * (T_{fo} - T_r) / (T_r) * g L] / (1 + A_{rt})^2} \quad (1)$$

$$A_{rt} = A_o / A_i \quad (2)$$

where C_d is the discharge coefficient, A_o and A_i are the cross-sectional areas of air channel outlet and inlet, respectively, T_{fo} is the outlet air temperature,

T_r is the room air temperature and L is the total length of the thermal chimney. The sunspace was simulated as a detached sunspace, thus in a different thermal zone, with a local airflow network. Walls and roof are completely glazed; the floor construction is the same of the main building. Finally, nanopainting characteristics were included in the outer plaster layer of the wall, according to reflexivity and emissivity parameters of Table 1. For each passive solution analysed, the simulation included all the permutation of the two values of each parameter. To manage the results, an alphanumeric code was adopted based on the acronyms in brackets showed in Table 1. The simulated building, with average heat transmittance coefficients given in Table 2, has a surface-to-volume ratio of 0.715 over 77.44 m².

The sensitivity analysis of the parameters listed with relative ranges of variation in Table 1 provides results based on the mutual effects of common design factors already investigated in previous research separately, such as orientation (Morrissey et al., 2011), glass U-value (Nielsen et al., 2001) and thermal mass (Albayyaa et al., 2019).

As the objective is to gain potential energy savings during the heating season, the simulation is set accordingly. The blinds activate in winter to reduce night losses, and in the summer period, when the solar radiation on the windows rises over 250 W/m². Natural ventilation was added in summer, reproducing full opening of the windows in daytime during building occupation. The aim and novelty of the analysis is to provide not an optimization method, but a preliminary optimized set of parameters for specific solutions. Through the application to a case study, the scope is to determine an energy-related trade-off for the possible application of such passive solutions providing designers with a starting set of design parameters to investigate the benefits of integrating passive solutions in their projects. A multi-objective approach, including comfort indexes to modify system set points according to an adaptive approach, will be explored in future work.

Table 1 – Acronyms of the alphanumeric code

Category	Acronyms	Characteristics/Value
Building reference	B1	
Building destination	R	Residential
	O	Office
Location	L1	Palermo
	L2	Bolzano
Passive solution	DG	Direct gains
	TW	Trombe wall
	SS	Sunspace
	NP	Nanopainting
Orientation	E	East
	W	West
	S	South
Window to Wall Ratio (WWR)	<i>first parameter</i>	0.2 – 0.6
Glass U-value [W/m ² K]	<i>second parameter</i>	0.8 - 2.3/1.0*
Heat capacity per unit area [kJ/m ² K]	<i>third parameter (TS1-TS2)</i>	160-800
Reflectivity	<i>fourth parameter</i>	0.1 – 0.9
Emissivity	<i>fifth parameter</i>	0.1 – 0.9

*limit in North Italy

Table 2 – Heat transfer coefficients of building constructions

Construction	U-value [W/(m ² K)]
Roof	2.2
Floor	2
Wall	1.26

3. Discussion of the Results

3.1 Passive Solar Design Guidelines

On the basis of Table 1, four reference cases can be detected, based on location and building use: Table 3 shows the related energy demand.

Table 3 – Energy demand of the reference cases

CODE ID	Heating demand [kWh]	Cooling demand [kWh]	Total demand [kWh]
B1_R_L1	961	1671	2632
B1_O_L1	977	1896	2873
B1_R_L2	4494	391	4885
B1_O_L2	2854	436	3290

It can be noticed that a slight difference occurs in terms of destination for L1, larger in L2. In this section, the best results of each specific simulated solution from the sensitivity analysis in terms of heating and global energy saving are introduced. **Direct gain** systems show the highest performance in residential applications and close to the highest in offices. From Fig. 2 it is clear how south can be seen as the best orientation option, with more thermal mass needed in the northern areas. **Trombe wall** systems perform slightly better than direct gains in offices, with a still-high share of energy saving in residential buildings. Fig. 3 highlights how south-bound systems are still the best choice, with heavyweight structures generally preferred, to limit nighttime losses and prevent excessive heat transfer from the air cavity. **Sunspace** best configurations still include south, with one west-bound configuration, as in the previous cases. In this scenario, the heavyweight system is preferred due to the high amount of solar radiation to dispose of. As described by Fig. 4, they perform better in residential applications, thanks to the delay guaranteed by the thermal mass. **Nanopainting**, in Fig. 5 shows very low shares for heating performance, while they mainly impact on the cooling load.

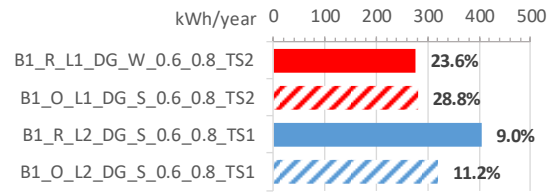


Fig. 2 – Best direct gain configurations

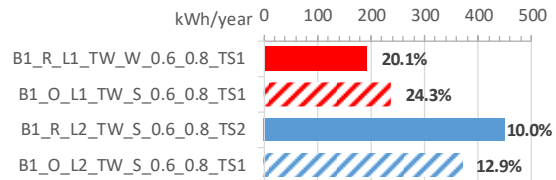


Fig. 3 – Best Trombe wall configurations

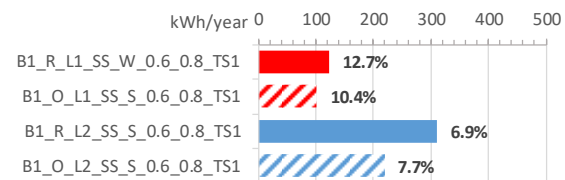


Fig. 4 – Best sunspaces configurations

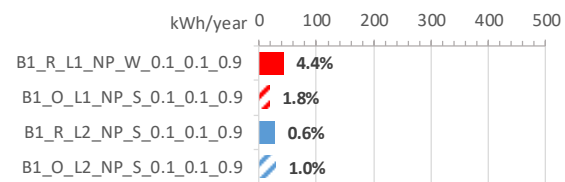


Fig. 5 – Best nanopainting configurations

South orientation proved to be the best solution, as described in Fig. 6, with west in second place, performing better than east in order to get heat late in the afternoon when people are back home. Almost all the configurations prefer 0.6 and 0.8 as WWR and glass U-value. It is worth noting that direct gain systems are the suggested solution for Palermo, while Trombe walls should be preferred in Bolzano.

Finally, Table 4 shows the best configuration for the four base case scenarios in terms of heating performance, while Table 5 shows the code of the passive solar design configurations that perform better in terms of total energy saving.

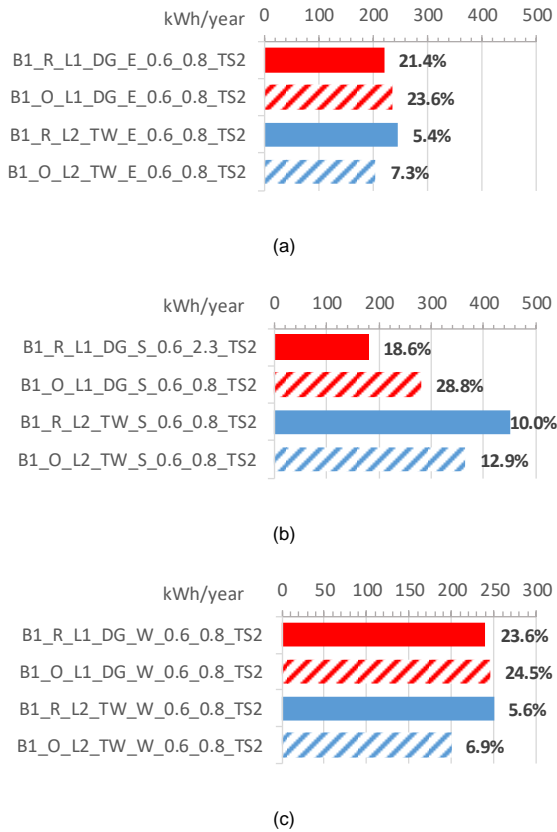


Fig. 6 – Best east (a), south (b) and west (c) bound configurations

Table 4 – Best configuration for heating energy savings

CODE ID	Heating	Cooling	Total
	[%]	[%]	[%]
B1_R_L1_DG_W_0.6_0.8_TS2	-23.6	+120.3	+67.8
B1_O_L1_DG_S_0.6_0.8_TS2	-28.8	+64.3	+32.6
B1_R_L2_TW_S_0.6_0.8_TS2	-10	+33.2	-6.6
B1_O_L2_TW_S_0.6_0.8_TS2	-12.9	+20.6	-8.5

Table 5 – Best configuration for total energy savings

CODE ID	Heating	Cooling	Total
	[%]	[%]	[%]
B1_R_L1_NP_W_0.1_0.9_0.9	+1.8	-2.5	-0.9
B1_O_L1_TW_S_0.2_0.8_TS2	-11.3	+3.3	-1.7
B1_R_L2_TW_S_0.6_0.8_TS2	-10	+33.2	-6.6
B1_O_L2_TW_S_0.6_0.8_TS2	-12.9	+20.6	-8.5

In Palermo, L1, the high solar irradiation leads to an increase of the cooling loads, which, as a result, generates an increment in the total energy loads. In Table 5, total energy savings are achieved as long as they are low. This is mainly due to the simulation set, as it focuses on the heating performance, with no optimized shading system for the summer period. However, for Bolzano (L2), the best heating configurations correspond to the best in total energy savings, between 6-8 %. The solution is Trombe Wall, with a high WWR and a low heat transfer coefficient. Direct gain configurations are the best passive heating systems for Palermo (L1), but can even double the cooling demand. In terms of total performance, nanopainting and Trombe walls slightly reduce the total demand even in a hot climate with a short heating season. As in previous cases, south-bound solutions are the most useful ones, with west limited to the residential case in location 1.

3.2 Optimization of the Case Study

The analysis of the case study allows a generalization of the approach to the previous solutions. The test case demonstrates the benchmark of the potential savings achievable through passive systems. The trade-off between passive and active solutions depends on the energy benefit the building can obtain, which is related to the climatic conditions, the kind and use of buildings, and the behavior of the occupants. The case analyzed is a co-housing project located in central Italy. Fig. 7 provides a schematic view. The building is a part of a master-plan for the development of 16 blocks. Developed on 4 floors, 180 m² each, the building hosts a co-working space and standardized flats for families. Each flat consists of a wide living space, a private terrace, one bathroom and two bedrooms, for a total of 78 m². The approach to the case study started from the application of the configuration suggested by the analysis previously described. Starting from the simulation of the base case, reference loads were identified, with an overall demand of 30.11 MWh per year. Fig. 8 shows the results of the cumulative application of suggested solutions in terms of energy savings. The case study took place in the center of Italy, Pisa, defined by L3: the cli-

matic conditions, 14.8 °C average air temperature and 1500 kWh/m² of annual solar irradiation, fall between the two locations previously analyzed. The solution applied, taken from L1 results, will then be linearized according to both series of results. Firstly, direct gains on the west façade were integrated: the increase of the WWR led to 7.8 % heating energy saving. However, the cooling load increased to 16.5 %, causing the total demand to rise around 6 %. Looking at the orientation solutions in Fig. 8, east appears to be the second-most efficient for residential application. Direct gain systems are thus simulated on the east façade, with a close heating performance and a slightly lower cooling increase compared to west orientation. In the third step, the increase in the WWR was split between the two façades to better exploit solar radiation early in the morning and late in the afternoon - basically when passive heating is needed by the house occupants. To reduce the cost of the intervention, the increase in the WWR is compensated for by moving out the windows from the north-facing façade.

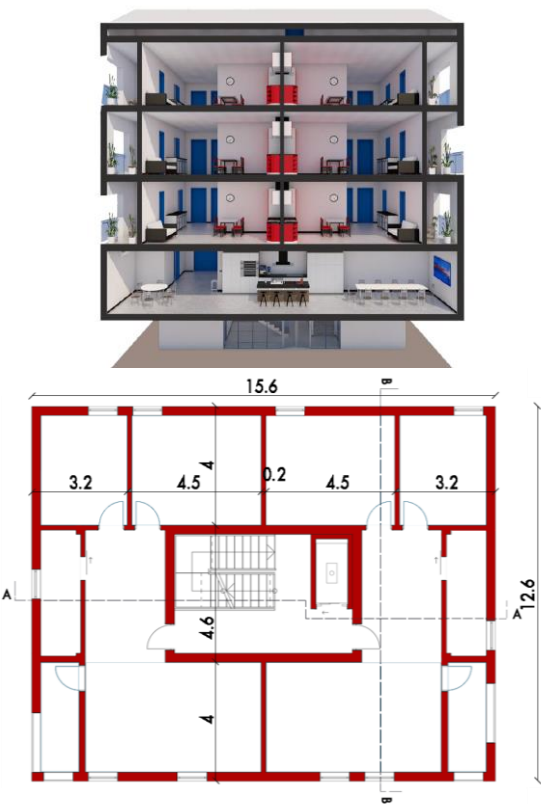


Fig. 7 – Schematic section of the building

This results in a higher heating performance, with an increase of the total demand, due to the cooling demand, being almost imperceptible. To reduce the cooling load, the best configurations in terms of total energy, in Table 5, were applied in step 4, starting with nanopainting. The cooling load is drastically reduced, 8 % compared to the base case, and finally energy saving is achieved in a total basis, even if the improvement in the heating performance is halved. Step 5 includes the optimization of summer shading, to further reduce the cooling load, -23.6 %. Finally, in step 6, sunspaces were implemented. This configuration was included due to the specific design of the building, whose terraces can be easily closed. Sunspace management system is optimized to get passive heating in winter, and assure natural ventilation through opening in summer. Shading system is implemented too. The result is a 14.3 % reduction in heating energy demand, 18.4 % in cooling and a total energy saving of 16.7 %.

Fig. 9 shows the changes in the building design. By moving additional windows from the north façade, the cost of the intervention is low, while the modular rhythm of the façades is preserved.

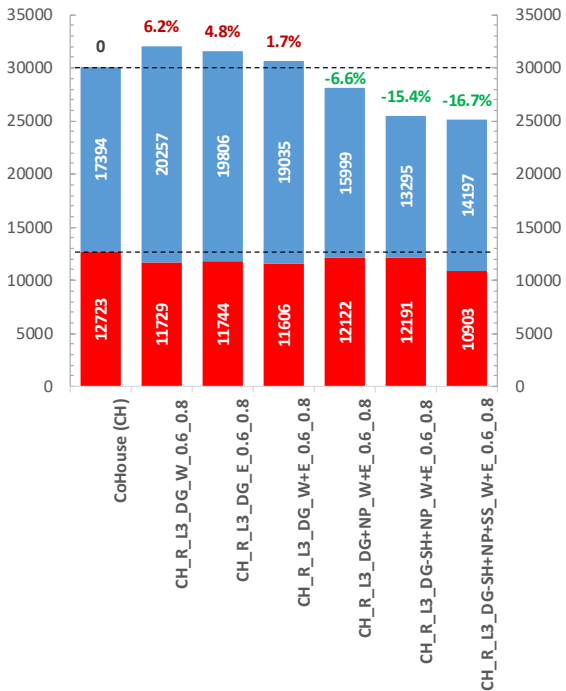


Fig. 8 – Heating, cooling and total energy saving of the case study design steps

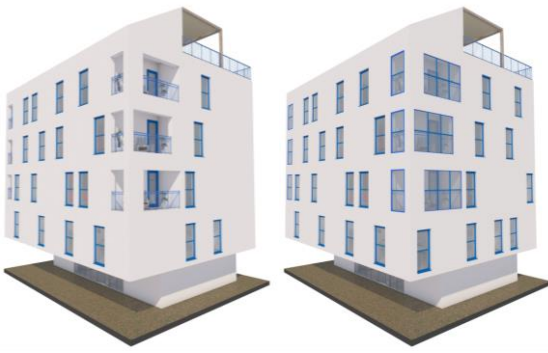


Fig. 9 – Starting (left) and final (right) project design

While nanopainting has no influence on the overall architectural design, the integration of sunspaces in the terrace does have a minimal impact, limited to the winter time. The test case confirms the limits of complex passive configurations in terms of energy benefits and management, to balance passive heating with cooling request. The integration of wide direct systems or sunspaces led to relative savings in the heating demand, but their counter effect on the cooling load unbalanced their effect on the overall consumption. More simple solutions, such as shading systems and nanopainting, on the other hand, proved to perform equally. The use of nanopainting, with its impact on the cooling demand, and the integration of a properly set shading system brings a reduction of the overall demand, allowing for a higher degree management of the passive heating load. Being easier to integrate, in technical and economic terms, their trade-off makes them more appealing for building application.

4. Conclusion

Passive solar design strategies are a tool for reducing building energy demand by exploiting solar energy. High heating energy savings can be passively achieved by simply optimizing the building design through the integration of passive solar solutions. The focus on the energy performance of the different passive configurations analyzed allowed the most proficient solutions in terms of both passive heating and energy saving for office and residential buildings in two different climates to be determined. The sensitivity analysis was

based on both extrinsic and intrinsic factors, such as building use, location, WWR and glass U-value. The present work aims to address the lack of guidelines or suggested solutions and a methodology for a rational application of such configurations in different kinds of buildings. The purpose is to define an analysis to determine the possible energy-related trade-off for simple to complex passive configurations. A general methodology for the application and integration of the configuration during the design step of a new building was proposed through the analysis of a case study. The analysis moves from the solutions suggested by the general investigation to the integration of elements due to the specific building design:

- marginal savings can be achieved by simply applying the suggested solution for passive heating (direct gains, -7 % of the heating demand)
- the integration of the suggested solution in terms of total energy saving reduces the cooling load (nanopainting, -7 % of the demand)
- the optimization of the shading system helps to prevent the overheating risk in summer (optimized shading system, -15 % of the demand)
- finally, building specific solutions boost the performance (sunspaces, -14 % of the heating demand, -16 % of the total demand).

The results are achieved by minimizing two relevant factors for the promotion of passive solar design integration: impact on the building design, and thus architectural interferences, and the cost of interventions. A relevant element for a widespread application of passive solar design, which this paper attempts to address, is the development of design guidelines. The results of the present analysis can be generally applied as preliminary suggested parameters for the integration of passive systems in the Italian climate, by properly scaling values according to local climate conditions. To generalize the application of these guidelines, the trade-off of the application of passive solutions must be addressed. As seen by the test case, simple kinds of passive measures, such as nanopainting and shading, have a comparable performance on the demand of the building: with easier integration and lower cost, their trade-off suggests a wider application when compared with complex solutions. Fur-

ther analysis must be carried out to take into account the effect of climate-related parameters, such as solar radiation, and local economy factors on the trade-off of these systems. Cost analysis and comfort models should be integrated into the sensitivity analysis.

Acknowledgement

The authors acknowledge Alessio Bardelli for his work within the framework of his Master's Thesis.

Nomenclature

Symbols

A	cross-sectional area (m^2)
Ar	aspect ratio of the cavity
C	discharge coefficient
g	gravity acceleration (m/s^2)
L	length of the chimney (m)
Q	air flow rate (m^3/s)
T	temperature (K)

Subscripts/Superscripts

d	discharge
fo	outlet air
i	inlet
o	outlet
r	room air
rt	ratio

References

- Albayyaa, H., D. Hagare, and S. Saha. 2019. "Energy conservation in residential buildings by incorporating Passive Solar and Energy Efficiency Design Strategies and higher thermal mass." *Energy and Buildings* 182: 205–213. doi: <https://doi.org/10.1016/j.enbuild.2018.09.036>
- Bajcinovci, B., and F. Jerliu. 2016. "Achieving Energy Efficiency in Accordance with Bioclimatic Architecture Principles." *Environmental and Climate Technologies* 18(1): 54–63. doi: <https://doi.org/10.1515/rtuect-2016-0013>
- Cillari, G., F. Fantozzi, and A. Franco. 2020. "Passive solar systems for buildings: performance indicators analysis and guidelines for the design." *E3S Web of Conferences* 197: 02008. doi: <https://doi.org/10.1051/e3sconf/202019702008>
- Cillari, G., F. Fantozzi, and A. Franco. 2021a. "Passive Solar Solutions for Buildings: Criteria and Guidelines for a Synergistic Design." *Applied Sciences* 11(1): 376. doi: <https://doi.org/10.3390/app11010376>
- Cillari, G., A. Franco, and F. Fantozzi. 2021b. "Sizing strategies of photovoltaic systems in nZEB schemes to maximize the self-consumption share." *Energy Reports* 7. doi: <https://doi.org/10.1016/j.egy.2021.09.117>
- Ellis, P. G. 2003. "Development and validation of the unvented Trombe wall model in EnergyPlus." Master Degree Thesis, University of Illinois.
- Givoni, B. 1991. "Characteristics, design implications, and applicability of passive solar heating systems for buildings." *Solar Energy* 47(6): 425–435. doi: [https://doi.org/10.1016/0038-092X\(91\)90110-I](https://doi.org/10.1016/0038-092X(91)90110-I)
- Morrissey, J., T. Moore, and R. E. Horne. 2011. "Affordable passive solar design in a temperate climate: An experiment in residential building orientation." *Renewable Energy* 36(2): 568–577. doi: <https://doi.org/10.1016/j.renene.2010.08.013>
- Nault, E., P. Moonen, E. Rey, et al. 2017. "Predictive models for assessing the passive solar and daylight potential of neighborhood designs: A comparative proof-of-concept study." *Building and Environment* 116: 1–16. doi: <https://doi.org/10.1016/j.buildenv.2017.01.018>
- Nielsen, T. R., K. Duer, and S. Svendsen. 2001. "Energy performance of glazings and windows." *Solar Energy* 69: 137–143. doi: [https://doi.org/10.1016/S0038-092X\(01\)00062-7](https://doi.org/10.1016/S0038-092X(01)00062-7)
- O'Shaughnessy, E., D. Cutler, K. Ardani, et al. 2018. "Solar plus: Optimization of distributed solar PV through battery storage and dispatchable load in residential buildings." *Applied Energy* 213: 11–21. doi: <https://doi.org/10.1016/j.apenergy.2017.12.118>
- Stevanović, S. 2013. "Optimization of passive solar design strategies: A review." *Renewable and Sustainable Energy Reviews* 25: 177–196. doi: <https://doi.org/10.1016/j.rser.2013.04.028>

A Novel Personal Comfort System: A Radiant Desk With a Loop Heat Pipe

Roberto Rugani – University of Pisa, Italy – roberto.rugani@phd.unipi.it

Marco Bernagozzi – University of Brighton, United Kingdom – M.Bernagozzi3@brighton.ac.uk

Marco Picco – University of Brighton, United Kingdom – M.Picco@brighton.ac.uk

Giacomo Salvadori – University of Pisa, Italy – giacomo.salvadori@unipi.it

Fabio Fantozzi – University of Pisa, Italy – fabio.fantozzi@unipi.it

Abstract

This study is the second step toward the development and prototyping of a Personal Comfort System for tertiary sector working environments. The entire industrial sector, and, in particular, offices, have seen changes in working habits, with a large increase in smart working also due to prevention of COVID infection. The chance to partialize the HVAC system and maintain rooms in an under-conditioned state is the obligatory way towards reducing energy waste, providing each workstation with an independent system that guarantees the operator's comfort conditions. The goal of the second step presented in this work was to size and optimize the radiating desk, with the aim of testing an experimental demonstrator. A LHP was chosen to bring heat from the source to the desk, decoupling the heat generation and heat distribution system, without the need for additional parasitic power consumption or moving parts, adding to the innovation of the proposed design. The ergonomic optimization of the surface and its power reduction did not affect its ability to improve localized comfort, since the operators' conditions move from a slightly cold to a neutral situation. Moreover, no discomfort due to vertical temperature differences or radiant asymmetries were found. Therefore, the next research step will lead to prototype creation and its analyses, conducted in a climatic room to test if the distribution system can satisfy comfort thermal requirements with probes as well as real users.

1. Introduction

Reducing energy consumption is a current issue, made increasingly stringent with the progress of the 21st century (Allouhi et al., 2015; Almasri & Alshitawi, 2022). The total energy consumption

associated with HVAC services (heating, ventilation, and air conditioning) in buildings accounts for 40 % of total energy consumption in Europe and 36 % of greenhouse gas emissions (EU. Buildings, 2020).

New methods of building design and HVAC systems are becoming increasingly popular, yet people still often complain of thermal discomfort (Fantozzi et al., 2020; Ortiz et al., 2017), and inadequate attention is paid to reducing energy waste (Carmenate et al., 2016; Li et al., 2019). Moreover, buildings do not meet the regulations' modest goal of having no more than 20 % unsatisfied occupants, primarily due to building over-conditioning and occupants' inability to adjust the environment individually to meet their personal needs (Brager et al., 2015).

The importance of providing Indoor Environmental Quality (IEQ) is widely recognised (Lamberti, 2020), especially in the work-place, where not only personal well-being increases productivity (Greenberger et al., 1989; Rocca et al., 2020), but it also makes up the greatest component towards dissatisfaction (Frontczak et al., 2012; Huizenga et al., 2006). The IEQ is defined by many interacting factors (Bluyssen, 2020), among which thermal comfort is the most significant on the perception of environmental quality and the energy consumption associated with IEQ achievement (Lamberti, 2020). As the individual differences based on age, gender, or body fat content show, thermal comfort is not only a simple function of the thermal environment, but it is also influenced by a whole set of individual factors. Thermal neutrality is considered to provide the best comfort, but this does not respect individual preferences (Fantozzi et al., 2021; van Hoof, 2008).

Personal ability to thermoregulate oneself plays a key role in this process (de Dear et al., 2013). Therefore, the local microenvironment needs to become personalized to fit the preferences of everyone.

Individually oriented new approaches are under development in this emerging research area, to evaluate the average zone thermal comfort metrics. For instance, a personal comfort model predicts individuals' thermal comfort responses, instead of the average response of a large population with an improved comfort predictive power compared to conventional models (PMV, Adaptive) (Kim et al., 2018).

A noteworthy model is the Berkeley Comfort Model, which predicts the sensation for each local body part with input data related to skin temperature (Huizenga et al., 2001); a physical measurement campaign or a thermophysiological computer program that treats the body as multiple segments would be needed to simulate this data (Zhang et al., 2010a; Zhang et al., 2010b). Thermal sensation and comfort for local body parts vary greatly and affect thermal sensation and comfort perceived for the whole body (Arens et al., 2006a). In a cool environment, hands and feet feel colder than other body parts, and feet are the major sources of discomfort (Arens et al., 2006b; Zhang et al., 2010c). In the tests performed by Arens et al, people perceived neutral conditions as "comfortable", but the "very comfortable" rating was achieved only in the asymmetric or transient environment conditions, which can be achieved through local Personal Comfort Systems (PCS), defined as systems that heat and cool individuals without affecting the environments of surrounding occupants (Arens et al., 2006a).

PCSs play an important role in this landscape with the target of conditioning only the "personal" microclimate rather than the volume of the entire building, in contrast to traditional HVAC systems (Kalaamani et al., 2020).

PCSs provide a series of benefits to indoor environments, like ensuring comfort conditions (Tsuzuki et al., 1999; Warthmann et al., 2018; Zhang et al., 2010) and reducing energy waste (Godithi et al., 2019; Shahzad et al., 2018; Zhang et al., 2015). They can provide comfort conditions with an environment temperature as low as 15 °C (Vesely & Zeiler, 2014). Zhang et al. found that there are several benefits to providing personal control over an environmental

feature capable of providing a local pleasurable sensation (Zhang et al., 2010c).

The present study is the second step of a research study aimed at prototyping a radiant-conductive system to guarantee microclimatic comfort conditions in open-space offices, transferring heat directly to the person (Rugani et al., 2021). Furthermore, reducing air movement will bring about the additional benefit of reducing the movement of pollutants and micro-particulates.

The global COVID-19 pandemic has increased cases of smart-working, often causing office staff presence to be significantly lowered. The direct consequence was seen in the wasted energy needed to air-condition entire offices where most desks remained empty (Jiang et al., 2021). PCSs can provide microclimatic comfort for operators, and the possibility of reducing the setpoint temperatures of the primary HVAC system would lead to a drastic reduction in energy losses (Rugani et al., 2021). The trend is generally to rethink design strategies as a result of the pandemic (Megahed & Ghoneim, 2021), rethinking buildings both from a spatial point of view, but also in terms of HVAC systems.

Therefore, the prototyping of a bespoke radiant surface embedded in a desk and the study of the comfort conditions that this can provide is the objective of the research. In this second research step, the preparatory analyses were carried out considering a Loop Heat Pipe (LHP) as the thermal vector from the heat source and the radiant plate. LHPs are a passive devices, whose heat transfer and fluid motions are ensured by cycles of evaporation and condensation of a working fluid. Hence the lack of need for pumps or additional energy sources for their operation makes up their great scientific interest.

2. Method

2.1 Overview

The aim of the study is to prototype and optimise a Personal Comfort System (PCS). In the previous phase, the PCS was conceived and studied as a complete radiant desk, analysing the comfort provided to the user according to the potential energy savings in offices (Rugani et al., 2021).

Two possibilities were identified for transferring heat to the desk - via a hydronic system and via an electric infrared surface. The objective of the current research is the sizing of the hydronic one, with the application of a Loop Heat Pipe. It allows the parasitic energy consumption of the pump for a standard hydronic system to be saved and a plug-in desk, versatile and easily interfaced with the energy sources, with no moving parts and no risk of failure to be created.

The analysis consisted of a first phase of the LHP condenser sizing, i.e., the radiant plate to be placed in the desk, simulating it in the operating conditions. Several condensers designed were studied to find the most efficient one. Meanwhile, CFD analysis with a similar methodology to the previous study by the Authors was conducted, simulated in two different heating system configurations: heating with standard setpoint and underconditioned state with local PCS.

2.2 LHP Design

LHPs have been widely implemented in space applications and thermal management, for which they were first created in the early 70s. They are a two-phase passive heat exchanger, able to transfer heat over several meters without the need for moving parts or any additional energy for its functioning. This would reduce power consumption and the noise in using a hydraulic active system, the complexity, and the risk of failure, hence increasing the overall system efficiency. LHPs work thanks to the cyclic evaporation/condensation processes of a working fluid, whose motion is ensured by a positive pressure gradient arising in a porous structure, due to capillarity (Maydanik, 2005). LHPs have been extensively studied in recent years in several applications, like aircraft (Pagnoni et al., 2021) and electric vehicle thermal management (Bernagozzi et al., 2021), solar water heating (Wang & Yang, 2014), and electronics cooling (Domiciano et al., 2022).

The LHP has the function of transferring heat from the source (evaporator) to the radiating desk (condenser). Its sizing was performed thanks to a validated Lumped Parameter Model (LPM) code validated by Bernagozzi et al. (2018). The power of the system was chosen according to the previous

analysis performed. Compared with the first study, the power range was reduced because the radiating surface was optimized, according to an ergonomic study about the user's position. Values aligned with those previously identified by Mao et al. (2017), who provided the desk with a palm warmer with a power consumption of 26 W at steady state (typical surface temperature of 35 °C).

Fig. 1 shows the condenser, which represents the heating plate, located in the desk. Fig. 2 shows the desk section with the embedded condenser of the LHP. This will be a small diameter meandering pipe where condensation of the working fluid takes place, ensuring a constant temperature profile along the radiating surface, ultimately increasing the individual's feeling of comfort.

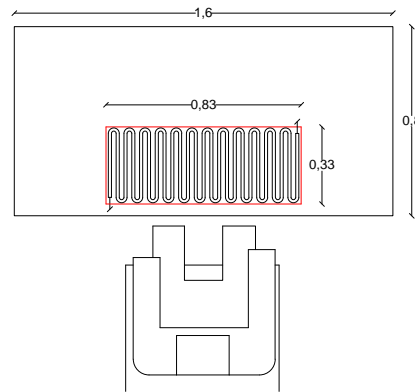


Fig. 1 – Example of a desk configuration, with the heating plate facing the user

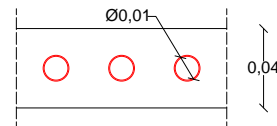


Fig. 2 – Desk section

2.3 CFD Modeling

A CFD analysis was conducted using Autocad CFD software. The purpose was to obtain the local environmental conditions on an ideal manikin placed on a chair in front of the desk. Solving the Navier-Stokes equations allowed an assessment of the local comfort conditions and the convective and radiant energy contributions of the PCS, which are impossible to evaluate with a Building Energy Simulation (BES).

CFD models have been widely adopted as effective tool for natural ventilation simulations, while BES is more stable with the heat transfer between solid and

fluid (Zhang et al., 2013). Moreover, the effect of air mixing considerably affects the zone temperatures. Thus, CFD analysis is the most suitable option for assessing the temperature variation (Jones et al., 2020; Salimi & Hammad, 2020).

Following the previous methodology, two configurations were studied: heating with standard set-point (21 °C), and PCS in an under-conditioned environment (17 °C).

The CFD simulations aimed at evaluating the size and shape of the condenser in ensuring user comfort. Thus, this phase was conducted in parallel with the calculation of the LHP system.

2.4 Comfort Assessments

To determine thermal comfort, several models were developed. Most of the research conducted on the assessment of comfort conditions were based on Fanger's thermal model and the calculation of the two indices: the Predicted Mean Vote (PMV) and the Predicted Percentage of Dissatisfied (PPD) (ISO 7730:2005 2005).

Individual-oriented models, such as the Berkeley Comfort Model, while more effective at predicting local response, require experimental data on a physical person. Although Fanger's indexes were created for the evaluation of general comfort, several studies demonstrated its ability to compare thermal comfort from different setups (Orosa Jose, 2010; Shahzad et al., 2018; Zhang et al., 2015).

To compare the case study results to the previous analysis (Rugani et al., 2021) and to the research conducted by Shahzad et al. (2018), the applied conditions are those shown in Table 1.

Table 1 – Comfort evaluation parameters for Fanger's model

Humidity (RH)	30%
Metabolic rate (MET)	1
Clothing insulation (CLO)	0.7

Furthermore, two local models based on environmental data were applied (ASHRAE, 2021): discomfort due to vertical temperature difference (1), and discomfort due to radiant asymmetry (2-3). Also, specific standards on heating radiant systems such as EN ISO 11855 (ISO, 2021) indicate following the

previous models for local discomfort evaluation.

$$PD = 100 / (1 + \exp(5.76 - 0.856 \cdot \Delta t_{a,v})) \quad (1)$$

$$PD = 100 / (1 + \exp(6.61 - 0.345 \cdot \Delta t_{pr})) \quad (2)$$

$$PD = 100 / (1 + \exp(9.93 - 0.50 \cdot \Delta t_{pr})) \quad (3)$$

Where PD is the Percentage Dissatisfied and Δt are the temperature differences in each case.

The limits prescribed by the regulations are applied, with particular attention to temperature differences. The vertical temperature gradient between head and feet is prescribed as 3 °C/m by ASHRAE 55 (ASHRAE 2020) and ISO 7730 (ISO 7730:2005 2005). Nevertheless, Liu et al. (2020) found that vertical temperature gradient changes with thermal sensation votes and could be increased to 5 °C/m when the subject is thermally neutral.

3. Results

Different heating inputs were provided to the LHP evaporator to achieve the optimum desk surface temperature of 36 °C, namely 15 W, 20 W, 25 W, and 30 W. Moreover, several working fluids were investigated for the LHP: water, acetone, ethanol, R1233, and Novec649. Finally, tubes of various sizes were tested, with internal radius of 4, 5, and 6 mm.

Figs. 3, 4, and 5 show the superficial temperature variation of the desk as a function of the working fluid, the heating power, and the pipes dimension.

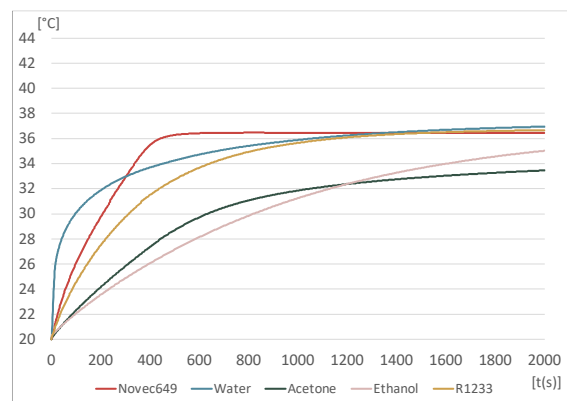


Fig. 3 – Radiant surface temperature of the desk as a function of the liquid in the LHP loop, with a power of 20W and an internal radius of 6 mm

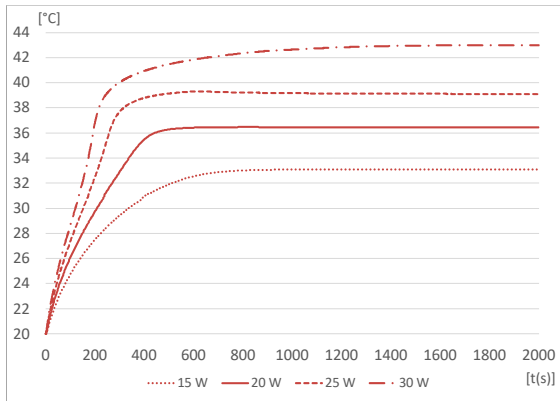


Fig. 4 – Radiant surface temperature of the desk as a function of the power applied to the evaporator, Novec649 in the loop and an internal radius of 6 mm

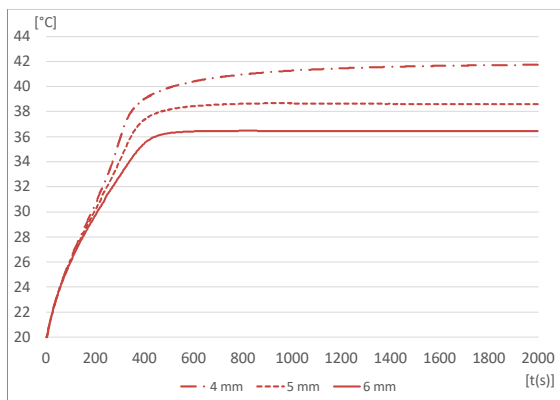


Fig. 5 – Radiant surface temperature of the desk as a function of the pipes dimension, Novec649 in the loop and a power of 20W

The CFD results allowed the overall comfort situation (Fig. 6) and the temperature distributions around the workers to be studied (Fig. 7).

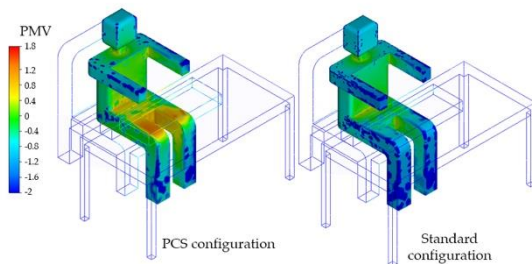


Fig. 6 – PMV distribution at each point of the environment

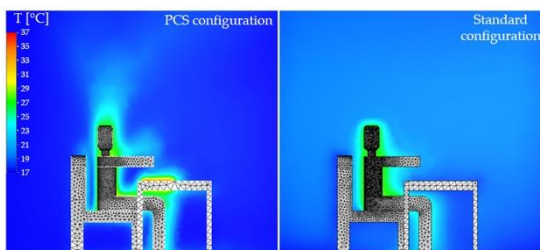


Fig. 7 – Temperature distribution at each point of the environment

4. Discussion

The coupling of CFD and LHP sizing calculations allowed optimization of the heating plate, i.e., the LHP condenser, with the aim of creating a real prototype.

Sizing results showed that the most efficient working fluid was the heat transfer fluid Novec™ 649, produced by 3M™, as it condensed earlier than other liquids and allowed the system to be operative in the shortest time. Interestingly, in the design configuration, 20 W was the power that allows the desired desk surface temperature to be reached, associated with pipes whose inner radius was 6 mm. This low value of power opens up different avenues on heat recovery, for instance, suggesting the use of the waste heat from the electronic components present on the desk, e.g., laptop.

The CFD results show an alignment with those of the first step of the research (Rugani et al., 2021). Although the heating surface area was reduced to 0.27 m², as well as the power delivered, the general comfort situation was not affected. The ergonomic study prior to prototyping thus succeeded in optimizing the panel while maintaining its ability to ensure local comfort (Table 2).

Table 2 – Localized results of CFD analyses

	PCS		Standard	
	PMV	PPD	PMV	PPD
Face	-0.06	5	-0.27	7
Torso	0.11	5	-0.42	9
Knee	0.23	6	-0.47	10

A further step conducted in this analysis phase was to verify the compliance of local discomfort models for vertical air temperature difference and radiant asymmetry. There are no major temperature differences between the ankles and the head, as the surface heats in both directions. The PD value is below 1. Likewise, vertical radiant asymmetry discomfort from cold ceilings hardly exceeds PD value 1. On the other hand, if the radiating desk were located near a cold wall, the discomfort from radiant asymmetry could lead to a PD value of 2 with a temperature difference of 8 °C, which in any case is lower than the 10 °C indicated as the standard limit.

5. Conclusion

Today's society demands quality and comfort, especially in the workplace. This study aims to increase comfort and satisfaction with the thermal microclimate in large offices.

The global pandemic has accentuated smart working. Thus, the possibility of being able to partialize thermal systems and to locally heat and cool only occupied workstations is a winning strategy for reducing energy waste.

A first step of this research was conducted to analyze the thermal comfort provided by a radiant desk combined with the associated energy savings. The goal of the second step presented in this work was to size and optimize the radiating desk, with the aim of testing an experimental demonstrator.

A LHP was chosen to bring heat from the source to the serpentine on the horizontal table. Its sizing was performed thanks to a validated Lumped Parameter Model (LPM). 20 W was the power that allows reaching the desired desk surface temperature, associated with pipes whose inner radius was 6 mm. The CFD results confirmed the ability of the PCS to ensure comfortable conditions even at sub-comfort room temperatures, moving to a neutral situation with PMV value near to 0 (face -0.06, torso 0.11, knee 0.23), thus reducing energy losses from heating entire rooms, such as open space offices, recently left almost empty due to the increase in smart working. The ergonomic optimisation of the surface and its power reduction did not affect its ability to improve localised comfort. Moreover, no discomfort due to vertical temperature differences or radiant asymmetries was found, with PD below 1 and temperature gradients not exceeding regulatory limits.

Summarizing, the contribution of this work is two-fold: firstly, the improvement of the individual's comfort by the adoption of microclimatic comfort; secondly, the system allows an increase in the efficiency of the building's HVAC system, reducing energy consumption and moving a few steps in the net-zero direction.

Future research developments include the comparison of this hydronic desk with a similar electrically powered desk. The reason for this analysis is to conduct an exergetic comparison by contrasting the quality of energy with the versatility and efficiency

of systems to ensure local comfort and reduce energy consumption.

Moreover, analyses will be conducted in a climatic room to test that the distribution system can satisfy comfort thermal requirements with probes, as well as real users. Additionally, The CFD model will be rebuilt and validated with ANSYS Fluent software.

References

- Allouhi, A., Y. el Fouih, T. Kousksou, A. Jamil, Y. Zeraoui, and Y. Mourad. 2015. "Energy Consumption and Efficiency in Buildings: Current Status and Future Trends." *Journal of Cleaner Production* 109: 118–130. <https://doi.org/10.1016/j.jclepro.2015.05.139>
- Almasri, R. A., and M. S. Alshitawi. 2022. "Electricity Consumption Indicators and Energy Efficiency in Residential Buildings in GCC Countries: Extensive Review." *Energy and Buildings* 255: 111664. <https://doi.org/10.1016/j.enbuild.2021.111664>
- Arens, E., H. Zhang, and C. Huizenga. 2006a. "Partial- and Whole-Body Thermal Sensation and Comfort - Part II: Non-Uniform Environmental Conditions." *Journal of Thermal Biology* 31:60–66. doi: <https://doi.org/10.1016/j.jtherbio.2005.11.027>
- Arens, E., H. Zhang, and C. Huizenga. 2006b. "Partial- and Whole-Body Thermal Sensation and Comfort - Part I: Uniform Environmental Conditions." *Journal of Thermal Biology* 31:53–59. doi: <https://doi.org/10.1016/j.jtherbio.2005.11.028>
- ASHRAE. 2020. *ANSI/ASHRAE Standard 55: 'Thermal Environmental Conditions for Human Occupancy.'*
- ASHRAE. 2021. *Handbook of Fundamentals.*
- Bernagozzi, M., S. Charmer, A. Georgoulas, I. Malavasi, N. Michè, and M. Marengo. 2018. "Lumped Parameter Network Simulation of a Loop Heat Pipe for Energy Management Systems in Full Electric Vehicles." *Applied Thermal Engineering* 141: 617–629. doi: <https://doi.org/10.1016/j.applthermaleng.2018.06.013>
- Bernagozzi, M., A. Georgoulas, N. Miché, C. Rouaud, and M. Marengo. 2021. "Novel Battery

- Thermal Management System for Electric Vehicles with a Loop Heat Pipe and Graphite Sheet Inserts." *Applied Thermal Engineering* 194: 117061. doi: <https://doi.org/10.1016/j.applthermaleng.2021.117061>
- Bluyssen, P. M. 2020. "Towards an Integrated Analysis of the Indoor Environmental Factors and Its Effects on Occupants." *Intelligent Buildings International* 12(3): 199–207. doi: <https://doi.org/10.1080/17508975.2019.1599318>
- Brager, G., H. Zhang, and E. Arens. 2015. "Evolving Opportunities for Providing Thermal Comfort." *Building Research & Information* 43(3): 274–287. doi: <https://doi.org/10.1080/09613218.2015.993536>
- Carmenate, T., P. Inyim, N. Pachekar, G. Chauhan, L. Bobadilla, M. Batouli, and A. Mostafavi. 2016. "Modeling Occupant-Building-Appliance Interaction for Energy Waste Analysis." *Procedia Engineering* 145: 42–49. doi: <https://doi.org/10.1016/j.proeng.2016.04.012>
- de Dear, R. J., T. Akimoto, E. A. Arens, G. Brager, C. Candido, K. W. D. Cheong, B. Li, et al. 2013. "Progress in Thermal Comfort Research over the Last Twenty Years." *Indoor Air* 23(6): 442–461. doi: <https://doi.org/10.1111/ina.12046>
- Domiciano, K. G., L. Krambeck, J. P. M. Flórez, and M. B. H. Mantelli. 2022. "Thin Diffusion Bonded Flat Loop Heat Pipes for Electronics: Fabrication, Modelling and Testing." *Energy Conversion and Management* 255: 115329. doi: <https://doi.org/10.1016/j.enconman.2022.115329>
- EU. Buildings. 2020. "Energy Performance of Buildings Directive." https://ec.europa.eu/energy/topics/energy-efficiency/energy-efficient-buildings/energy-performance-buildings-directive_en
- Fantozzi, F., G. Lamberti, F. Leccese, and G. Salvadori. 2020. "The Indoor Thermal Environment in Fencing Halls: Assessment of the Environmental Conditions Through an Objective and Subjective Approach." *Advances in Physical, Social & Occupational Ergonomics*, edited by W. Karwowski, R. S. Goonetilleke, S. Xiong, R. H. M. Goossens, and A. Murata, 223–229. Cham: Springer International Publishing.
- Fantozzi, F., G. Lamberti, and R. Rugani. 2021. "Thermal Comfort in University Classrooms: Analysis of Simulated and Real Conditions." 2021 IEEE (EEEIC / I&CPS Europe). Bari. doi: <https://doi.org/10.1109/EEEIC/ICPSEurope51590.2021.9584490>
- Frontczak, M., S. Schiavon, J. Goins, E. Arens, H. Zhang, and P. Wargocki. 2012. "Quantitative Relationships between Occupant Satisfaction and Satisfaction Aspects of Indoor Environmental Quality and Building Design." *Indoor Air* 22(2): 119–131. doi: <https://doi.org/10.1111/j.1600-0668.2011.00745.x>
- Godithi, S. B., E. Sachdeva, V. Garg, R. Brown, C. Kohler, and R. Rawal. 2019. "A Review of Advances for Thermal and Visual Comfort Controls in Personal Environmental Control (PEC) Systems." *Intelligent Buildings International* 11 (2): 75–104. <https://doi.org/10.1080/17508975.2018.1543179>
- Greenberger, D. B., S. Strasser, L. L. Cummings, and R. B. Dunham. 1989. "The Impact of Personal Control on Performance and Satisfaction." *Organizational Behavior and Human Decision Processes* 43(1): 29–51. [https://doi.org/10.1016/0749-5978\(89\)90056-3](https://doi.org/10.1016/0749-5978(89)90056-3)
- Huizenga, C., S. Abbaszadeh, L. Zagreus, and E. Arens. 2006. "Air Quality and Thermal Comfort in Office Buildings: Results of a Large Indoor Environmental Quality Survey." *Proceedings of Healthy Buildings 2006*, Lisbon, Vol. III, 393–397.
- Huizenga, C., H. Zhang, and E. Arens. 2001. "A Model of Human Physiology and Comfort for Assessing Complex Thermal Environments." *Building and Environment* 36. doi: [https://doi.org/10.1016/S0360-1323\(00\)00061-5](https://doi.org/10.1016/S0360-1323(00)00061-5)
- ISO. 2021. *ISO 11855-1:2021, 'Building Environment Design — Embedded Radiant Heating and Cooling Systems. Part 1: Definitions, Symbols, and Comfort Criteria.'*
- ISO. 2005. *ISO 7730:2005. 2005. Ergonomics of the Thermal Environment -- Analytical Determination and Interpretation of Thermal Comfort Using Calculation of the PMV and PPD Indices and Local Thermal Comfort Criteria.*
- Jiang, P., Y. van Fan, and J. J. Klemeš. 2021. "Impacts of COVID-19 on Energy Demand and Consumption: Challenges, Lessons and Emerging Opportunities." *Applied Energy* 285.

- doi:
<https://doi.org/10.1016/j.apenergy.2021.116441>
- Jones, N. L., I. Chaires, and A. Goehring. 2020. "Detailed Thermal Comfort Analysis from Preliminary to Final Design." *Proceedings of Building Simulation 2019: 16th Conference of IBPSA* 16: 2675–2682. doi: <https://doi.org/10.26868/25222708.2019.210875>
- Kalaimani, R., M. Jain, S. Keshav, and C. Rosenberg. 2020. "On the Interaction between Personal Comfort Systems and Centralized HVAC Systems in Office Buildings." *Advances in Building Energy Research* 14(1): 129–157. doi: <https://doi.org/10.1080/17512549.2018.1505654>
- Kim, J., S. Schiavon, and G. Brager. 2018. "Personal Comfort Models – A New Paradigm in Thermal Comfort for Occupant-Centric Environmental Control." *Building and Environment* 132: 114–124. doi: <https://doi.org/10.1016/j.buildenv.2018.01.023>
- Lamberti, G. 2020. "Thermal Comfort in the Built Environment: Current Solutions and Future Expectations." *Proceedings - 2020 IEEE, IEEEIC / I and CPS Europe 2020*. doi: <https://doi.org/10.1109/IEEEIC/ICPSEurope49358.2020.9160558>
- Li, J., K. Panchabikesan, Z. Yu, F. Haghighat, M. el Mankibi, and D. Corgier. 2019. "Systematic Data Mining-Based Framework to Discover Potential Energy Waste Patterns in Residential Buildings." *Energy and Buildings* 199: 562–578. doi: <https://doi.org/10.1016/j.enbuild.2019.07.032>
- Liu, S., Z. Wang, S. Schiavon, Y. He, M. Luo, H. Zhang, and E. Arens. 2020. "Predicted Percentage Dissatisfied with Vertical Temperature Gradient." *Energy and Buildings* 220. doi: <https://doi.org/10.1016/j.enbuild.2020.110085>
- Mao, N., D. Pan, Z. Li, Y. Xu, M. Song, and Sh. Deng. 2017. "A Numerical Study on Influences of Building Envelope Heat Gain on Operating Performances of a Bed-Based Task/Ambient Air Conditioning (TAC) System in Energy Saving and Thermal Comfort." *Applied Energy* 192: 213–221. doi: <https://doi.org/10.1016/j.apenergy.2017.02.027>
- Maydanik, Y. F. 2005. "Loop Heat Pipes." *Applied Thermal Engineering* 25(5): 635–657. doi: <https://doi.org/10.1016/j.applthermaleng.2004.07.010>
- Megahed, N. A., and E. M. Ghoneim. 2021. "Indoor Air Quality: Rethinking Rules of Building Design Strategies in Post-Pandemic Architecture." *Environmental Research* 193: 110471. doi: <https://doi.org/10.1016/j.envres.2020.110471>
- Orosa Jose, J. A. 2010. "A Review of General and Local Thermal Comfort Models for Controlling Indoor Ambiences." *Air Quality* 1966. doi: <https://doi.org/10.5772/9763>
- Ortiz, M. A., S. R. Kurvers, and P. M. Bluysen. 2017. "A Review of Comfort, Health, and Energy Use: Understanding Daily Energy Use and Wellbeing for the Development of a New Approach to Study Comfort." *Energy and Buildings* 152: 323–335. doi: <https://doi.org/10.1016/j.enbuild.2017.07.060>
- Pagnoni, F., V. Ayel, Y. Bertin, J. Coulloux, and M. Zebian. 2021. "Loop Heat Pipe for Thermal Management of Aircraft Engine Equipment." *Journal of Thermophysics and Heat Transfer* 35(2): 323–334. doi: <https://doi.org/10.2514/1.T6049>
- Rocca, M., F. Leccese, and G. Salvadori. 2020. "Health and Well-Being in Indoor Work Environments: Features of an Expert Assessment Campaign in an Italian University Hospital." *Proceedings - 2020 IEEE, IEEEIC / I and CPS Europe 2020*, 0–5. doi: <https://doi.org/10.1109/IEEEIC/ICPSEurope49358.2020.9160493>
- Rugani, R., M. Picco, G. Salvadori, M. Marengo, and F. Fantozzi. 2021. "Can PCS Help Us Save Energy? Initial Assessment Using Dynamic Energy and CFD Analyses." *2021 IEEE (IEEEIC / I&CPS Europe), Bari, Italy*.
- Salimi, S., and A. Hammad. 2020. "Optimizing Energy Consumption and Occupants Comfort in Open-Plan Offices Using Local Control Based on Occupancy Dynamic Data." *Building and Environment* 176: 106818. doi: <https://doi.org/10.1016/j.buildenv.2020.106818>
- Shahzad, S., J. Kaiser Calautit, K. Calautit, B. Hughes, and A. I. Aquino. 2018. "Advanced Personal Comfort System (APCS) for the Workplace: A Review and Case Study." *Energy*

- and *Buildings* 173: 689–709.
<https://doi.org/10.1016/j.enbuild.2018.02.008>
- Tsuzuki, K., E. Arens, F. Bauman, and D. Wyon. 1999. "Individual Thermal Comfort Control with Desk-Mounted and Floor-Mounted Task/Ambient Conditioning (TAC) Systems." *Indoor Air* 99, August 8-13, Edinburgh, UK.
- van Hoof, J. 2008. "Forty Years of Fanger's Model of Thermal Comfort: Comfort for All?" *Indoor Air* 18(3): 182–201.
<https://doi.org/10.1111/j.1600-0668.2007.00516.x>
- Veselý, M., and W. Zeiler. 2014. "Personalized Conditioning and Its Impact on Thermal Comfort and Energy Performance - A Review." *Renewable and Sustainable Energy Reviews* 34: 401–408. <https://doi.org/10.1016/j.rser.2014.03.024>
- Wang, Z., and W. Yang. 2014. "A Review on Loop Heat Pipe for Use in Solar Water Heating." *Energy and Buildings* 79: 143–154.
<https://doi.org/10.1016/j.enbuild.2014.04.051>
- Warthmann, A., D. Wölki, H. Metzmacher, and C. van Treeck. 2018. "Personal Climatization Systems-a Review on Existing and Upcoming Concepts." *Applied Sciences* 9(1).
<https://doi.org/10.3390/app9010035>
- Zhang, H., E. Arens, C. Huizenga, and T. Han. 2010a. "Thermal Sensation and Comfort Models for Non-Uniform and Transient Environments: Part I: Local Sensation of Individual Body Parts." *Building and Environment* 45(2): 380–388.
<https://doi.org/10.1016/j.buildenv.2009.06.018>
- Zhang, H., E. Arens, C. Huizenga, and T. Han. 2010b. "Thermal Sensation and Comfort Models for Non-Uniform and Transient Environments, Part II: Local Comfort of Individual Body Parts." *Building and Environment* 45(2): 389–398.
<https://doi.org/10.1016/j.buildenv.2009.06.015>
- Zhang, H., E. Arens, C. Huizenga, and T. Han. 2010c. "Thermal Sensation and Comfort Models for Non-Uniform and Transient Environments, Part III: Whole-Body Sensation and Comfort." *Building and Environment* 45(2): 399–410.
<https://doi.org/10.1016/j.buildenv.2009.06.020>
- Zhang, H., E. Arens, D. E. Kim, E. Buchberger, F. Bauman, and C. Huizenga. 2010. "Comfort, Perceived Air Quality, and Work Performance in a Low-Power Task-Ambient Conditioning System." *Building and Environment* 45(1): 29–39.
<https://doi.org/10.1016/j.buildenv.2009.02.016>
- Zhang, H., E. Arens, and Y. Zhai. 2015. "A Review of the Corrective Power of Personal Comfort Systems in Non-Neutral Ambient Environments." *Building and Environment* 91: 15–41.
<https://doi.org/10.1016/j.buildenv.2015.03.013>
- Zhang, R., K. P. Lam, S. Yao, and Y. Zhang. 2013. "Coupled EnergyPlus and Computational Fluid Dynamics Simulation for Natural Ventilation." *Building and Environment* 68: 100–113.
<https://doi.org/10.1016/j.buildenv.2013.04.002>

Energy Signature Modeling Towards Digital Twins – Lessons Learned From a Case Study With TRV and GAHP Technologies

Massimiliano Manfren – ENEA, Italy – M.Manfren@soton.ac.uk

Maria Cristina Tommasino – ENEA, Italy – cristina.tommasino@enea.it

Lamberto Tronchin – University of Bologna, Italy – lamberto.tronchin@unibo.it

Abstract

In building refurbishment projects, efficient technologies such as heat pumps are increasingly being used as a substitute for conventional technologies such as condensing boilers, with the aim of reducing carbon emissions and determining operational energy and cost savings. Measured building performance, however, often reveals a significant gap between the predicted energy use (design stage) and actual energy use (operation stage). For this reason, a scalable energy signature modeling approach is presented in this paper to verify building energy performance from measured data. Regression models are built with data at multiple temporal resolutions (monthly and daily) and are used to verify the performance improvement due to smart heating controllers (TRV) and Gas Absorption Heat Pumps (GAHP). The capabilities of energy signature analysis are enhanced by including additional variables in the modeling process and by running the models as “digital twins” with a rolling horizon of 15 days of data. Finally, a regression model for GAHP technology is developed to validate the results measured in the monitoring process in a comparative way. The case study chosen is Hale Court sheltered housing, located in the city of Portsmouth (UK). The results obtained are used to illustrate possible extensions of the use of energy signature modeling, highlighting implications for energy management and innovative building technologies development.

1. Introduction

The necessity of achieving high energy efficiency targets while maintaining an adequate level of services in the building stock is one of the topics driving the built environment today. Innovative heating technologies are part of this research and Gas Absorption Heat Pump (GAHP) can be used as an

alternative to conventional and condensing boilers. Additionally, smart heating controllers, such as Smart TRVs (Thermostatic Radiator Valves) are often reported as a promising technology, even if this depends on multiple factors and, in particular, operational patterns and user behavior (Manfren et al., 2021a, 2021b and 2022; Tronchin et al., 2018).

The case study of Hale Court, considering intervention in the North Block allows testing of the new methodology in question. In particular, the area was monitored before and after the retrofit intervention – namely, first with the installation of Smart TRVs (Thermostatic Radiator Valves) and then with the installation of Gas Absorption Heat Pumps (GAHPs). The monitored data are split into three periods: explicitly before retrofit, after the installation of TRVs and after the installation of GAHPs and plant room upgrade. The performance before retrofit represents for us the baseline for evaluation. Data are summarized and aggregated at different time scales (monthly and daily), energy signatures are calculated from energy metering data and piecewise linear regression models are fitted for the different monitoring periods to enable performance comparison. Finally, the savings monitored are compared to the ones calculated by a regression model of GAHP performance

2. Methods

First of all, the methods used in this research are aimed at giving primarily a reliable assessment of the actual impact of different technologies in terms of efficiency. For this reason, the regression-based approaches proposed by state-of-the-art Measurement and Verification (M&V) protocols such as ASHRAE 14 (ASHRAE, 2014), Efficiency Value

Organization (EVO, 2003), Federal Energy Management Program (FEMP, 2008), frequently indicated with the term M&V 2.0 (Gallagher et al., 2018), are included. This is crucial because of the necessity of performing an initial screening analysis before proceeding with more in-depth evaluations. Technical state-of-the-art standardization was used as a basis and some innovative elements were introduced. The starting point is a regression-based analysis of energy signatures (i.e., average power in a certain interval of analysis).

Sample models for the whole-building approach (ASHRAE 14:2014 Measurement of Energy, Demand, and Water Savings) are used:

- mean, or one-parameter model, (electricity);
- two-parameter model;
- three-parameter heating model (similar to a variable-base degree-day VBDD model for heating);
- three-parameter cooling model (VBDD for cooling);
- four-parameter heating model;
- four-parameter cooling model;
- five-parameter model.

Energy signature regression is proposed in standardization as a way of “normalizing” energy performance with respect to the main influencing factors - outdoor air temperature in this case. Models can then be used to track performance in time (Manfren et al., 2019 and 2021b).

3. Case Study

Hale Court is a sheltered housing development run by Portsmouth City Council, built in 1984. Hale Court consists of 80 flats with a mix of studio flats, 1 bedroom-, 2 bedroom- and 3-bedroom-flats.

As part of the EU Horizon 2020 project THERMOSS), Smart Thermostatic Radiator Valves were installed and the heating system plant room was refurbished with the installation of Gas Absorption Heat Pumps (GAHP). A monitoring system was set-up to enable detailed building energy performance analysis.

The proposed refurbishment of the heating system for the North Block plant room involves: (1) keeping the existing gas boilers (2) removal of the water heaters (3) addition of a 3-GAHP cascade (4) incorporation of thermal storage and (5) reconfiguration of the piping layout.

Table 1 – Characteristics of the thermal systems

HEAT GENERATORS	
Gas Boilers x2	REMEHA GAS 110 Eco
Capacity	115 kW (per boiler)
Boiler design Temperature	80 °C
Typology	Condensing
Gas Absorption Heat Pump	GHP AWO 38 Three appliance cascade
Thermal power output A7W50	114.9 kW
Gas Utilization Efficiency A7W50	1.52
Natural gas power input A7W50	75.6 kW
Max. heating water flow temperature	65 °C
Permissible Ambient Temperature	-20 to +40 °C

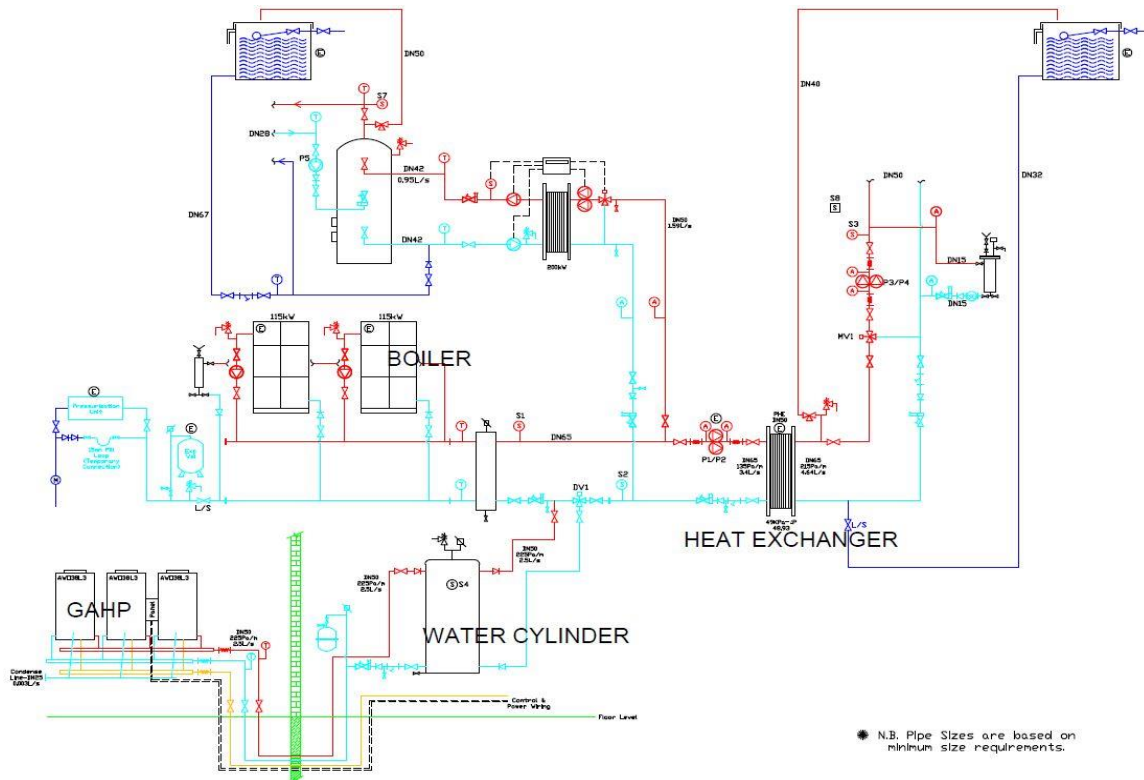


Fig. 1 – Technological scheme of the case study – Hale Court

4. Results and Discussion

Energy signature analysis of natural gas and electricity requires using piecewise linear regression for Hale Court, North Block.

The two models for natural gas demand signature (three-parameter heating model) and electricity signature are in the boundaries fixed by the ASHRAE 14:2014 guidelines.

Table 2 – Results of analysis for natural gas demand signature

Period	Energy indicator		Statistical indicator				
	Energy Measured (M)	Energy Predicted (P)	Relative differences	R ²	MAPE	NMBE	Cv(RMSE)
1	293464	299273	-1.98	93.0	14.3	1.98	11.9
2	93466	93544	-0.08	91.1	15.9	0.08	12.2
3	242586	243004	-0.17	88.3	13.9	0.17	13.3

The energy demand reduction regression model of GAHP performance shows a reduction of 20 %.

Table 3 shows the energy demand reduction using a prediction model, with standard weather and normalized occupant behavior.

Table 3 – Reductions

Period	Description	Overall reduction	Relative reduction
1	Before retrofit	0 (baseline)	-
2	TRVs installation	7.2 %	0 (baseline)
3	GAHPs and plant room upgrade	25.8 %	20.0 %

In order to characterize GAHP performance, we need to consider the *GUE* (Gas Utilization Efficiency), which is the parameter describing its thermal conversion efficiency. *GUE* is defined as the ratio between the delivered thermal energy and the fuel energy (and substantially similar to the COP for an electric heat pump).

Prediction of thermal power output P_{th} and *GUE* in full load conditions as a function of outdoor air temperature and supply water temperature used multivariate regression.

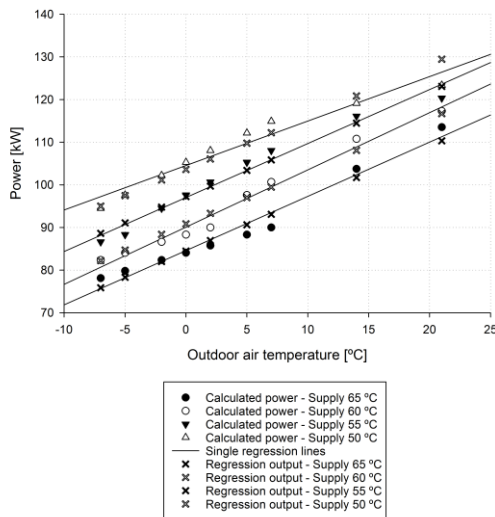


Fig. 2 – Thermal power output as a function of outdoor air temperature

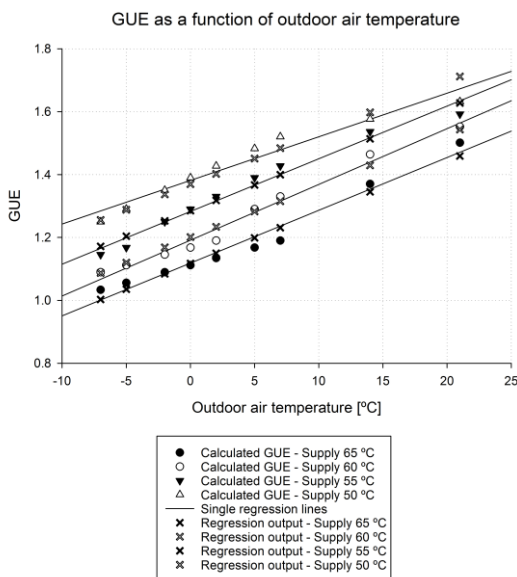


Fig. 3 – GUE as a function of outdoor air temperature

5. Conclusions

Energy signature modeling is a powerful tool for a first screening using monthly data. GAHP performance linearization enables the estimation of performance variability (P_{th} , GUE) as a function of outdoor air and supply temperatures and the calculation of part-load performance. Feedback from data analysis can help to improve management and control of GAHP.

Further research concerns application to daily and hourly data, to derived daily and hourly energy signature analysis and performance tracking:

1. Calculation of part-load performance ratio for GAHP using the regression model as reference.
2. Analysis of average thermo-physical properties of building to support detailed energy model calibration.

References

- ASHRAE. 2014. *ASHRAE Guideline 14-2014: Measurement of Energy, Demand, and Water Savings*. American Society of Heating, Refrigerating and Air-Conditioning Engineers: Atlanta, GA, USA.
- EVO. 2003. *IPMVP New Construction Subcommittee. International Performance Measurement & Verification Protocol: Concepts and Option for Determining Energy Savings*. In *New Construction, Volume III; Efficiency Valuation Organization (EVO)*: Washington, DC, USA.
- FEMP. 2008. *Federal Energy Management Program, M&V Guidelines: Measurement and Verification for Federal Energy Projects Version 3.0*. U.S. Department of Energy Federal Energy Management Program.
- Gallagher C. V., K. Leahy, P. O'Donovan, K. Bruton, and D. T. J. O'Sullivan. 2018. "Development and application of a machine learning supported methodology for measurement and verification (M&V) 2.0." *Energy and Building* 167: 8–22. doi: <https://doi.org/10.1016/j.enbuild.2018.02.023>
- Manfren, M., B. Nastasi, E. A. Piana, and L. Tronchin. 2019. "On the link between energy performance of building and thermal comfort: An example." *AIP Conference Proceedings* 2123: 1-9. doi: <https://doi.org/10.1063/1.5116993>
- Manfren, M., B. Nastasi, L. Tronchin, D. Groppi, and D. A. Garcia. 2021a. "Techno-economic analysis and energy modelling as a key enablers for smart energy services and technologies in buildings". *Renewable and Sustainable Energy Reviews* 150: 1-14. doi: <https://doi.org/10.1016/j.rser.2021.111490>
- Manfren, M., M. Sibilla, and L. Tronchin. 2021b. "Energy Modelling and Analytics in the Built Environment—A Review of Their Role for Energy Transitions in the Construction Sector."

Energies 14: 1-29- doi:

<https://doi.org/10.3390/en14030679>

Manfren, M., P. A. B. James, and L. Tronchin. 2022.
“Data-driven building energy modelling – An
analysis of the potential for generalisation
through interpretable machine learning”.
Renewable and Sustainable Energy Reviews 167: 1-
13. <https://doi.org/10.1016/j.rser.2022.112686>

Tronchin, L., K. Fabbri, and C. Bertolli. 2018.

“Controlled Mechanical Ventilation in
Buildings: A Comparison between Energy Use
and Primary Energy among Twenty Different
Devices.” *Energies* 11: 1-20, doi:
<https://doi.org/10.3390/en11082123>

The Amintore Galli Theatre in Rimini: A Dataset of Building Simulation Tools for its Acoustic Design

Antonella Bevilacqua – University of Parma, Italy – antonella.bevilacqua@unipr.it

Massimiliano Manfren – University of Southampton, UK – M.Manfren@soton.ac.uk

Maria Cristina Tommasino – ENEA, Italy – cristina.tommasino@enea.it

Ruoran Yan – University of Bologna, Italy – ruoran.yan2@unibo.it

Lamberto Tronchin – University of Bologna, Italy – lamberto.tronchin@unibo.it

Abstract

The Amintore Galli theater in Rimini re-opened in 2018, after more than 60 years of inactivity. Its acoustics have been studied in depth, starting in 2009 until the re-opening of the theater. This paper analyses the following different steps of the acoustic design of the Opera House: the analysis of the acoustics of similar other theaters, the design of the acoustics of the new main hall, the analysis of the acoustic characteristics of the diffusing panels in the theater, and the acoustic design of other rooms, including the rehearsal room. Moreover, this paper reports some of the most relevant results of the acoustic surveys conducted after the re-opening, comparing the values of some acoustic parameters obtained after the simulation processes, and the values of the same parameters during the final validation of the theater.

1. Introduction

The acoustic studies of Italian opera theater houses have been improved in their accuracy by the development of new generation technology (Farina et al., 1998; Tronchin, 2005 and 2021; Tronchin & Bevilacqua, 2021 and 2022; Tronchin & Knight, 2016; Tronchin et al., 2020a, 2020b, 2021a and 2021b). An acoustic survey was undertaken inside Galli theater of Rimini in order to show the acoustic parameters as required by the regulations (ISO 3382-1). Furthermore, a multichannel spherical array microphone was employed to add value to this acoustic investigation by illustrating the impulse response (IR) through an overlay video. The outcomes of this additional provision were recorded with some snaps related to different moments of

the IR decay. The authors of this paper also outline a brief history of Galli theater of Rimini, including a description of the architectural features that characterize this important opera house.

2. Historical Background

The theater was originally named "Teatro Nuovo" (The New Theater), and the project began in 1841, overseen by architect Luigi Poletti. The theater distinguished itself from other theaters in the same period, showing the innovative style of memorial architecture of classical architecture (Toyota, 2020). The theater was built between 1843 and 1856, and the project was delivered to Pietro Bellini, the Rimini contractor. The cost of the theater was mostly covered by the aristocracy. The theater officially opened in 1857. It was renamed Teatro Vittorio Emanuele II in 1859 (Toyota, 2020).

In 1916-1923, the ceiling of the theater was damaged and cracked in an earthquake. In addition to the necessary repair of the historical structure, it was also equipped with an electrical system (Toyota, 2020). Subsequently, the architect Gaspare Rastelli completed the Ridotto and upper Gallery of the theater with neoclassical elements different from Poletti (Toyota, 2020).

In 1943, the theater was almost completely destroyed by bombing during World War II. At the same time, the theater was looted after becoming a military camp, and the best furniture in the theater was robbed. In 1947, it was officially renamed with its current name in memory of the great composer, Amintore Galli.

Since 1948, any decision on the restoration of the theater was repeatedly postponed because Rimini, a town of Roman origin, contained a lot of Roman relics. Part of the reconstruction of Amintore Galli theater began in 1997, and, in 2010, under the auspices of the municipal authorities, adhering to the concept of being as faithful to the original design as possible while respecting the safety rules, the theater began to be fully rebuilt. After a long period of restoration work, Amintore Galli theater reopened in 2018.



Fig. 1 – Internal view of the Galli theater of Rimini

The main hall of Galli theater could host more than 700 people. All these seats are distributed as 268 seats in the stalls, and 324 seats on the three orders of boxes and 108 seats in the gallery. The dimensions of the main axes of the horseshoe shape plan are 22 m and 16 m [L, W], which are crowned by three orders of balconies, surmounted by a gallery having a capacity of 108 seats. The total height of the main hall is 20 m. The floor of the stalls is composed of oak planks, slightly inclined (2 %) towards the stage.

The restoration works in Galli theater had previously also included the restoration of the main foyer of the theater, and also other rooms, including the “ballet room”, located just beyond the roof, on top of the foyer.

3. Architectural Organization

The main hall of Amintore Galli theater, completed in 1856, is a traditional horseshoe plan, with a total capacity of 700 seats, of which 268 seats are distributed in the stalls, 324 seats are distributed in the elevated box, and 108 seats in the gallery. The main hall is 22 m, 16 m and 20 m [L, W, H],

crowned by a three-order balcony, with a gallery at the top that can accommodate 108 seats. The floor of the stalls is slightly inclined towards the stage, composed of oak planks, as shown in Fig. 2.

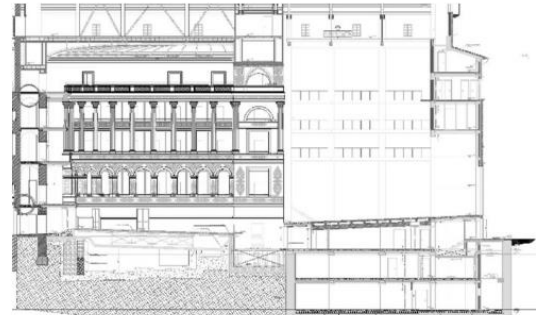


Fig. 2 – Longitudinal section of Amintore Galli Theater

After a period of long repair, the main hall still retains the original historical appearance dominated by ivory and gold. The floor and ceiling have been reinforced, and the decorations and painting have been restored (Toyota, 2020), as shown in Fig. 3. Further, pomegranate red has been used on seats and for the upholstery of the boxes.



Fig. 3 – Reliefs have been restored

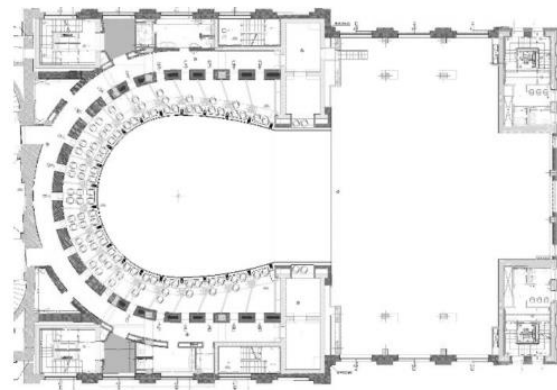


Fig. 4 – Plan layout of the main hall

The total area of the stage is 358 m² and the proscenium arch is 13 m large and 17 m high, the stage inclined by 2 %. The orchestra pit is 5.5 m deep and 12 m wide. Fig. 4 shows the horseshoe-shaped layout of the main hall.

Table 1 summarizes the architectural features of Amintore Galli theater.

Table 1 - Architectural characteristics of Amintore Galli theater

Description	Features
Type of plan layout	Horseshoe box
Total volume (m ³)	14420
Total capacity (no. of seats)	700
Stage dimension (m) [L × W]	30 × 16
Inclination of stage floor (%)	2 %
Inclination of stalls area (%)	2 %
Volume of the flytower (m ³)	8640
Volume of the main hall (m ³)	5780



Fig. 5 – View of the main hall of Teatro Galli of Rimini

Elaborate decoration is installed all around the main hall, with floor finishings, seats, upholstery and the walls of the boxes, having a pomegranate red color. Other dominant colors are ivory and gold, used on the wooden decorations.

The acoustics of Teatro Galli have been studied since 2010, when a specific 3D model was created in order to determine the future sound distribution in the main hall. Fig. 6 reports the numeric model of the theater.

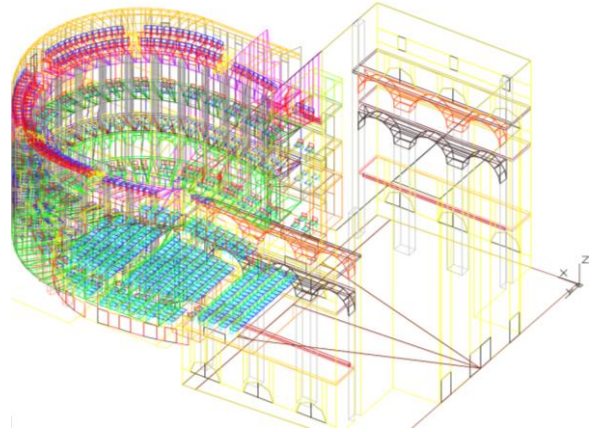


Fig. 6 – 3D numeric model of Teatro Galli

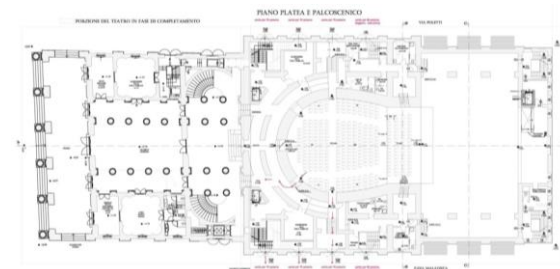


Fig. 7 – Plan layout of Teatro Galli of Rimini

4. Acoustic Surveys

Inside Galli theater, several acoustic measurements were taken during different steps of the reconstruction of the theater, and compared with the simulation conducted during the acoustic design. At the same time, thermo-hygrometric parameters were also taken into consideration, since the variation of the acoustic parameters with thermo-hygrometric conditions are relevant. The acoustic survey was carried out with the following equipment:

1. Equalised omnidirectional loudspeaker (Look Line);
2. Binaural dummy head (Neumann KU-100);
3. B-Format (Sennheiser Ambeo);
4. Omnidirectional microphone (Bruel&Kjaer);
5. 32-channel spherical array (Mh Acoustic em32 Eigenmike®);
6. Ricoh Theta V 360 camera
7. Personal Computer connected to the loudspeaker and all the receivers.

Fig. 8 reports a screenshot of two impulse responses, measured in the stalls and in the box.



Fig. 8 – Impulse responses measured in the stalls (n 2) and box (2nd order (n 12))

Fig. 9 reposts the comparison for reverberation time T_{30} obtained after reconstruction with the same parameter simulated in 2010.

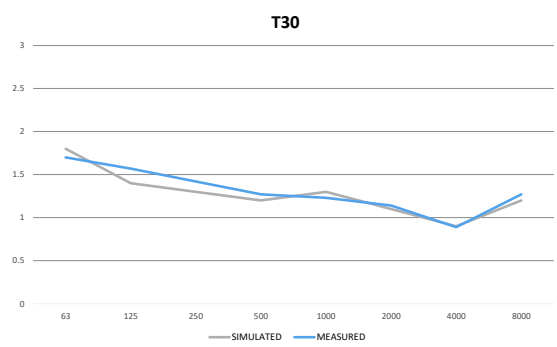


Fig. 9 – Reverberation time measured after reconstruction compared with the values obtained during the acoustic design in 2010

The sound source was located 1.4 m from the stage floor, while the receivers were positioned at a height of 1.2 m on stalls and boxes. The excitation signal emitted by the sound source was the Exponential Sine Sweep (ESS), having a duration of 15 s at a uniform sound pressure level for the between 40 Hz and 20 kHz range. The measurements were undertaken in unoccupied conditions and without any scenery or acoustic chamber mounted. Fig. 10 and Fig. 11 show the measurement positions of sound source and receivers placed across the sitting areas.

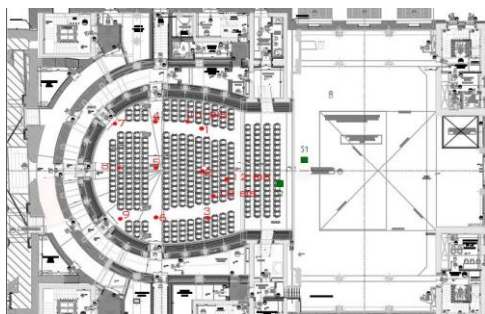


Fig. 10 – Scheme of the equipment location during the acoustic measurements in the stalls of Teatro Galli of Rimini



Fig. 11 – One of the surveys conducted in Teatro Galli in Rimini

5. Results

5.1 Traditional Parameters

The recorded ESS signals were processed by using the Aurora plugin suitable for Audition 3.0. Different acoustic parameters defined by the international standards ISO 3382-1 were analyzed and commented on. To be included are reverberation time (T_{20}), early decay time (EDT), clarity indexes (C_{80} and C_{50}), definition (D_{50}) and strength (G). The main acoustic parameters are reported in the octave bands between 125 Hz and 4 kHz, considered as the average results of all the measurement positions.

Fig. 12 and Fig. 14 show the graphs of the measurements of the main acoustic parameters. Fig. 13 shows the frequency response of the EDT and T_{20} parameters. If optimal values of EDT for concert halls are considered to range between 1.8 and 2.6 s, as defined by the literature, this target was not achieved by the measured values related to the selected bandwidth. However, if compared with several other opera houses, the results for Teatro Galli are much better than the others.

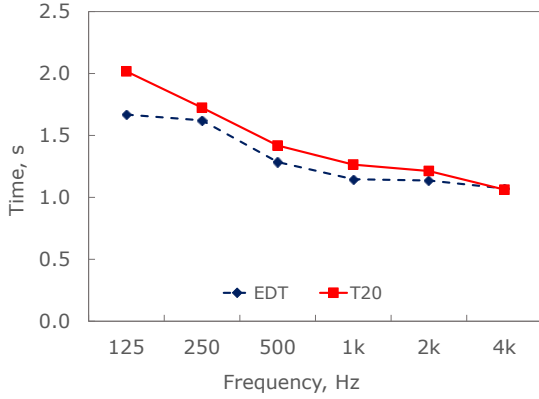


Fig. 12 – Measured results of clarity indexes (C50 and C80)

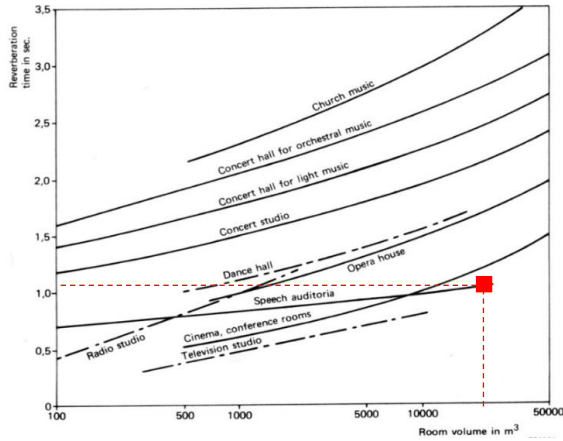


Fig. 13 – Optimum reverberation time values in function of room volume

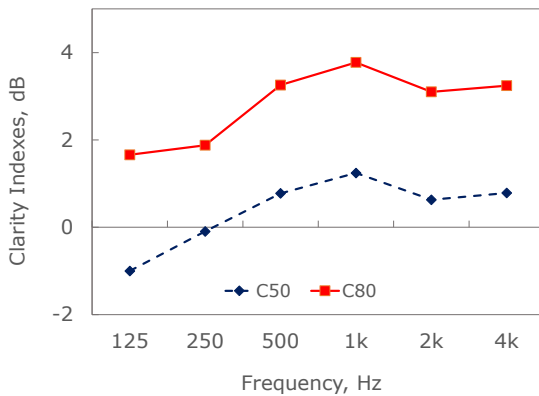


Fig. 14 – Measured results of clarity indexes (C50 and C80)

Following the research studies by Reichardt, the optimum values for the speech clarity index (C_{50}) would be ≥ 0 dB. In Teatro Galli, this parameter floats between +1 and +4 dB, at low and high frequency bands, respectively. Based on the results of Fig. 14, the good response of C_{50} was achieved at frequencies higher than 500 Hz. However, the shortfall at low frequencies found to be slightly

below the lowest range limit is not to be interpreted as a negative result.

5.2 Acoustic Analysis of 3D Sound Maps

The employment of the spherical array microphone (i.e., em32 Eigenmike®) allowed the authors to elaborate sound maps obtained for each source-receiver combination. These maps were created by a video-overlay that reproduces the recorded IR. This different data analysis is obtained by a combination of the omnidirectional sound source, the multichannel microphone (i.e., em32 Eigenmike®) and the panoramic camera (i.e., Rico Teta V, capturing a 360° image herein represented in an equirectangular view). The 32 microphone signals were processed by extracting 122 high-directivity virtual microphones (with 8th order cardioid setup) with the addition of the Spatial PCM Sampling (SPS). By using this methodology, it was possible to encode the direction of arrival of all the sound rays, including the direct sound and the reflections occurring after hitting any surface.

The colors shown in the map overlay range between red tinge (indicating the high level of sound energy) and blue-violet shades (representing a poor energy sound wave). Fig. 15 shows an illustration of the outcomes.

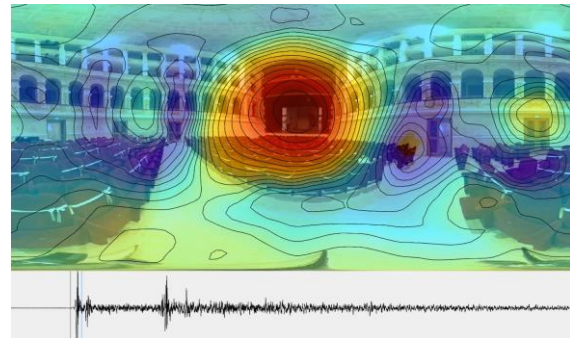


Fig. 15 – Acoustic map showing direct sound arriving to the receiver placed in the stalls

Fig. 15 shows the late reflections hitting the ceiling surface area. As per the above discussion, the overlay videoclip allows the surface areas that contribute toward creating the early and late reflections to be visualized. The bar at the bottom of the image indicates the flow time of the IR.

6. Conclusions

This paper deals with the representation of the acoustic results obtained by the survey undertaken in the Teatro Galli in Rimini. Measurements were conducted by using an omnidirectional sound source and four types of microphones.

Overall, the results obtained from the measurement campaign showed that the theater has a good response for speech performance, with some difficulties at low frequencies in terms of strength, which requires the singers to put more effort into the bass tones. In terms of music, the theater turns out to be slightly dry compared to opera houses of similar volume size.

This acoustic study was extended to analyze the specific trajectory of the sound waves during the IR. The capabilities of the multi-channel spherical microphone (i.e., em32 Eigenmike®) allowed the authors to render 3D sound maps, obtained for each source-receiver combination. Such maps indicate the direction of arrival of the sound rays and their intensity, contributing to understanding the specific role of the specific construction elements interacting with the sound waves.

References

- Farina, A., A. Langhoff, and L. Tronchin. 1998. "Acoustic characterisation of "virtual" musical instruments: using MLS technique on ancient violins." *Journal Of New Music Research* 27(4): 359-379. doi: <https://doi.org/10.1080/09298219808570753>
- Toyota, Y. 2020. *Concert Halls by Nagata Acoustics: Thirty Years of Acoustical Design for Music Venues and Vineyard-Style Auditoria*.
- Tronchin, L. 2005. "Modal analysis and intensity of acoustic radiation of the kettledrum." *The Journal Of The Acoustical Society Of America* 117(2): 926-933. doi: <https://doi.org/10.1121/1.1828552>
- Tronchin, L. 2021. "Variability of room acoustic parameters with thermo-hygrometric conditions." *Applied Acoustics* 177: 1-14. doi: <https://10.1016/j.apacoust.2021.107933>
- Tronchin, L., & A. Bevilacqua. 2021. "Acoustic study of different sceneries at the São Carlos national theatre of Lisbon." *Applied Acoustics* 180: 1-11. doi: <https://doi.org/10.1016/j.apacoust.2021.108102>
- Tronchin, L., and A. Bevilacqua. 2022. "Historically informed digital reconstruction of the Roman theatre of Verona. Unveiling the acoustics of the original shape." *Applied Acoustics* 185: 1-18. doi: <https://doi.org/10.1016/j.apacoust.2021.108409>
- Tronchin, L., and D. J. Knight. 2016. "Revisiting Historic Buildings through the Senses. Visualising Aural and Obscured Aspects of San Vitale, Ravenna." *International Journal of Historical Archaeology* 20: 127-145. doi: <https://doi.org/10.1007/s10761-015-0325-2>
- Tronchin, L., M. Manfren, and V. Vodola. 2020a. "The carabattola - vibroacoustical analysis and intensity of acoustic radiation (IAR)". *Applied Sciences* 10(2): 641. doi: <https://doi.org/10.3390/app10020641>
- Tronchin, L., M. Manfren, and V. Vodola. 2020b. "Sound characterization through intensity of acoustic radiation measurement: A study of persian musical instruments". *Applied Sciences* 10(2), 633. doi: <https://doi.org/10.3390/app10020633>
- Tronchin, L., F. Merli, and M. Dolci. 2021a. "Virtual acoustic reconstruction of the Miners' Theatre in Idrija (Slovenia)." *Applied Acoustics* 172: 1-9. doi: <https://doi.org/10.1016/j.apacoust.2020.107595>
- Tronchin, L., F. Merli, and M. Manfren. 2021b. "On the acoustics of the Teatro 1763 in Bologna." *Applied Acoustics* 172: 1-9. doi: <https://doi.org/10.1016/j.apacoust.2020.107598>

Data-Driven Building Energy Modelling – Generalisation Potential of Energy Signatures Through Interpretable Machine Learning

Massimiliano Manfren – University of Southampton, UK – M.Manfren@soton.ac.uk

Maria Cristina Tommasino – ENEA, Italy – cristina.tommasino@enea.it

Lamberto Tronchin – University of Bologna, Italy – lamberto.tronchin@unibo.it

Abstract

Building energy modeling based on data-driven techniques has been demonstrated to be effective in a variety of situations. However, the question about its limits in terms of generalization is still open. The ability of a machine-learning model to adapt to previously unseen data and function satisfactorily is known as generalization. Apart from that, while machine-learning techniques are incredibly effective, interpretability is required for a "human-in-the-loop" approach to be successful. This study develops and tests a flexible regression-based approach applied to monitored energy data on a Passive House building. The formulation employs dummy (binary) variables as a piecewise linearization method, with the procedures for producing them explicitly stated to ensure interpretability. The results are described using statistical indicators and a graphic technique that allows for comparison across levels in the building systems. Finally, suggestions are provided for further steps toward generalization in data-driven techniques for energy in buildings.

1. Introduction

Data-driven building energy modeling methods that use machine-learning techniques have been shown to be useful in a variety of applications (Hong et al., 2020), from design (Westermann & Evins, 2019) to operation (Manfren et al., 2020). As a result, they have the potential to become a key tool for accelerating the ongoing process of building stock decarbonisation (Norton et al., 2021; Tronchin, & Knight, 2016) as well as an integral part of innovative services and technologies (Farina et al., 1998; Manfren et al., 2021a). However, the question of whether data-driven approaches can be generalized is still being debated.

The ability of a machine-learning model to adapt to previously unknown data and perform reasonably well, given specified performance criteria, is referred to as generalization. A simple example of generalization is a model trained on building energy consumption data over a period of time and then used to estimate energy consumption during a successive period of time. This is the counterfactual approach used in Measurement and Verification (M&V) protocols, which uses statistical indicators as model acceptability criteria during the calibration phase. A more ambitious form of generalization would be that of using data-driven methods on energy modeling problems involving sets of building with homogeneous characteristics. Using data-driven methods on energy modeling problems involving different sets of buildings with relatively similar characteristics would be a more ambitious type of generalisation.

In this research, we use regression models trained and tested on building energy signatures as a tool for addressing the generalization problem. In fact, methods based on energy signature (ISO, 2013) (i.e., energy divided by the number of operating hours in the time interval of the analysis, corresponding to an average power) are scalable (temporally and spatially) (Manfren et al., 2021b; Tronchin, 2021; Tronchin et al., 2018), can work with unstructured data (using clustering) (Pistore et al., 2019; Westermann et al., 2020) and provide results that are weather normalized (Fazeli et al., 2016). Additionally, energy signatures can be scaled according to the building's size (Pistore et al., 2019; Tronchin et al., 2016), to produce a performance comparison that is independent of the size. Further, regression-based approaches are considered interpretable machine learning techniques (ISO, 2020) because it is possible

to predict how the model output will change in response to a change in input data or algorithmic parameters (i.e., the rationale behind model output and the algorithmic logic can be easily understood in human terms) (Fabbri et al., 2014 and 2021). In this study, we employ this technique to analyze monitored data from a Passive House building in the Province of Forlì-Cesena in northern Italy, with the goal of improving formulations at the state of the art while also considering generalization and interpretability issues (Tronchin, 2005 and 2021).

2. Methods

The regression model proposed in this research is a reformulation of the variable-based degree-days regression, originally proposed by Kissock et al. (2003) in their Inverse Modeling Toolkit (IMT), which has been included in ASHRAE 14:2014 (ASHRAE, 2014) and has been evolving steadily with different algorithmic formulations. Essentially, interpretable regression-based methods can be based on general piecewise linearization methods (Lin et al., 2013) and use dummy (binary variables) to handle non-linearities. Model formulation and calibration criteria are reported hereafter (Tronchin et al., 2021a and 2021b).

2.1 Model Formulation

Separate sub-models (heating, base load and cooling), indicated in Table 1, are combined into a single model (which is the sum of the individual sub-models) by introducing additional variables (dummy, 0-1 binary variables) to the original datasets using rules, indicated in Table 2. The binary variables multiply the original variables and act as interaction terms. Two types of models are tested, type 1 and type 2. In the first case, the independent variable is outdoor air temperature, while, in the second case, the independent variables are outdoor air temperature and total solar radiation on horizontal surface. The dependent variables are the energy signatures calculated from the monitored data described in Section 3.

The rules provided hereafter in Table 2 can be applied both manually and in an automated way to the

dataset, for example, using ranges of balance-point temperature (change-points) for heating and cooling (Manfren et al., 2019).

Table 1 – Regression model formulation

Mode Demand	Sub-models
Type 1	Heating $q_h = a_0(X_h) + a_1(X_h\theta_e) + \varepsilon_h$ (1)
	Base load $q_b = b_0(X_b) + b_1(X_b\theta_e) + \varepsilon_b$ (2)
	Cooling $q_c = c_0(X_c) + c_1(X_c\theta_e) + \varepsilon_c$ (3)
Type 2	Heating $q_h = a_0(X_h) + a_1(X_h\theta_e) + a_2(X_hI_{sol}) + \varepsilon_h$ (4)
	Base load $q_b = b_0(X_b) + b_1(X_b\theta_e) + b_2(X_bI_{sol}) + \varepsilon_b$ (5)
	Cooling $q_c = c_0(X_c) + c_1(X_c\theta_e) + c_2(X_cI_{sol}) + \varepsilon_c$ (6)

Table 2 – Rules for dummy variable creation

Rule	Description	Variables
1	If the energy demand is greater than 0 for the corresponding sub-model (e.g., heating, cooling or base load), then the dummy variable is equal to 1.	X_h , X_b , X_c
2	If the outdoor air temperature is lower than balance point temperature for heating (i.e., heating base temperature), the dummy variable for heating is equal to 1.	X_h
3	If the outdoor air temperature is greater than balance point temperature for cooling (i.e., cooling base temperature), the dummy variable for cooling is equal to 1.	X_c
4	All the dummy variables (that partition heating, cooling and base load demands) should be coherent with the schedules of operation for building services (i.e., months of heating and cooling system operation).	X_h , X_b , X_c
5	The dummy variables for base load are assumed to be 1 in all the months (i.e., electricity and hot water demand are always present).	X_b

2.2 Model Calibration Criteria

Following the indications proposed by state-of-the-art Measurement and Verification (M&V) protocols, such as ASHRAE 14:2014 (ASHRAE, 2014), Efficiency Value Organization (EVO) IPMVP (EVO,

2003), and Federal Energy Management Program (FEMP) (FEMP, 2008), the thresholds of acceptability for regression models as calibrated with monthly data are reported in Table 3.

Table 3 – Model calibration criteria

Data interval	Metric	ASHRAE Guidelines 14	IPMVP	FEMP
Monthly	NMBE	±5	±20	±5
	Cv(RMSE)	15	-	15

3. Case Study

The case study is Passive House building, located in the northern Italian province of Forlì-Cesena; the essential building data are reported in Table 4.

The building was monitored for three years and electric and thermal demand data were split by end use, as indicated in Table 5.

The modeling workflow pursued to test the models reported in Table 1 incrementally is set out in the following steps:

1. Initial training, year 1, 2.
2. Testing, year 3 (model created in step 1).
3. Retraining, year 1, 2 and 3.

The results obtained are reported hereafter in Section 4.

Table 4 – Building design data

Group	Type	Unit	Design
Geometry	Gross volume	m ³	1557
	Net volume	m ³	1231
	Heat loss surface area	m ²	847
	Net floor area	m ²	444
	Glazed area/total wall area ratio	%	22.5
	Surface/volume ratio	1/m	0.54
Envelope	U value external walls	W/(m ² K)	0.18
	U value roof	W/(m ² K)	0.17
	U value transparent components	W/(m ² K)	0.83
HVAC and DHW	Ground-source heat pump (GSHP) -	kW	8.4
	Brine/Water Heat Pump (B0/W35)*		
	Borehole heat exchanger (2 double U boreholes)	m	100
On-site energy production	Building Integrated Photovoltaic (BIPV) - Polycrystalline silicon	kW _p	9.2
	Solar thermal - Glazed flat plate collector	m ²	4.32
	Domestic hot water storage	m ³	0.74

* EN 14511 test condition in heating mode, brine at 0 °C and water 35 °C with supply-return temperature difference $\Delta t = 10$ °C.

Table 5 – Dataset used for modeling

Data	Enduse	Interval	Monitoring period
Electric	Total	Monthly	3 years
	HVAC, DHW	Monthly	3 years
	Appliances and lighting	Monthly	3 years
Thermal energy	Heating	Monthly	3 years
	Cooling	Monthly	3 years

4. Results and Discussion

In this section, the results of the model training and testing process are reported, indicating both numerical results represented by statistical indicators (Table 3) and visualization of energy signatures for the different models fitted.

4.1 Numerical Results of Regression Models

The results obtained are split with respect to the two types of models considered, namely type 1 and type 2.

4.1.1 Model Type 1

It can be clearly seen that model type 1, after 2 years, obtains values for the indicators *NMBE* and *Cv(RMSE)* that make them acceptable as calibrated (Table 3), with the exception of electricity demand for HVAC and DHW and thermal demand for cooling. In these cases, the values are higher than 15 % for *Cv(RMSE)* but lower than 20 %.

Table 6 – Model type 1 – Initial training (year 1 and 2)

Data	End-use	<i>EN(M)</i>	<i>EN(P)</i>	<i>R</i> ²	<i>NMBE</i>	<i>Cv(RMSE)</i>
		kWh	kWh	%	%	%
Electric	Total	23812	23510	84.77	-1.27	12.59
	HVAC, DHW	8611	8499	91.05	-1.30	17.99
	Appliances	15201	15202	70.27	0.01	10.12
Thermal	Heating	17761	17757	98.05	-0.03	8.87
	Cooling	5054	5004	93.50	-0.99	16.45

The model trained for the period indicated in Table 6 (first 2 years) is then tested for the third year of monitoring. In this case, we can see how, for model type 1, the statistical indicators in the testing phase are larger (i.e., the model performance is lower in terms of goodness of fit).

Table 7 – Model type 1 – Testing (year 3)

Data	End-use	<i>EN(M)</i>	<i>EN(P)</i>	<i>R</i> ²	<i>NMBE</i>	<i>Cv(RMSE)</i>
		kWh	kWh	%	%	%
Electric	Total	11318	10167	65.37	-10.17	20.15
	HVAC, DHW	3659	3181	90.78	-13.07	20.76
	Appliances	7659	7013	26.83	-8.44	22.13
Thermal	Heating	6029	5460	85.28	-9.53	21.17
	Cooling	1784	1841	63.23	3.19	20.21

Finally, models are retrained with the entire 3-year dataset, obtaining results that are slightly better compared to the ones presented in Table 6, but not largely different.

Table 8 – Model type 1 – Retraining (year 1, 2 and 3)

Data	End-use	<i>EN(M)</i>	<i>EN(P)</i>	<i>R</i> ²	<i>NMBE</i>	<i>Cv(RMSE)</i>
		kWh	kWh	%	%	%
Electric	Total	35130	34819	84.41	-0.88	12.12
	HVAC, DHW	12270	12139	91.23	-1.07	17.35
	Appliances	22860	22868	67.34	0.04	10.56
Thermal	Heating	23790	23795	95.91	0.02	12.42
	Cooling	6838	6735	90.91	-1.51	17.77

4.1.2 Model Type 2

The same workflow presented for model type 1 in Section 4.1.1 is repeated here for model type 2. The results are reported in Tables 9, 10 and 11, respectively. In this case, we can see a moderate improvement for the model training (Table 9) and retraining (Table 11), but a much better performance of the models in the testing phase (Table 10). In general, model type 2 performs better than type 1.

Table 9 – Model type 2 – Initial training (year 1 and 2)

Data	End-use	$EN(M)$	$EN(P)$	R^2	$NMBE$	$Cv(RMSE)$
		kWh	kWh	%	%	%
Electric	Total	23812	23518	88.36	-1.23	11.05
	HVAC, DHW	8611	8534	91.74	-0.90	17.16
	Appliances	15201	15204	82.19	0.02	7.84
Thermal	Heating	17761	17759	98.95	-0.01	6.50
	Cooling	5054	5229	93.54	3.46	18.34

Table 10 – Model type 2 – Testing (year 3)

Data	End-use	$EN(M)$	$EN(P)$	R^2	$NMBE$	$Cv(RMSE)$
		kWh	kWh	%	%	%
Electric	Total	11318	10551	85.96	-6.78	12.53
	HVAC, DHW	3659	3248	91.75	-11.24	18.80
	Appliances	7659	7329	66.66	-4.30	12.04
Thermal	Heating	6029	5828	94.13	-3.59	13.52
	Cooling	1784	1964	85.58	10.10	16.66

Table 11 – Model type 2 – Retraining (year 1, 2 and 3)

Data	End-use	$EN(M)$	$EN(P)$	R^2	$NMBE$	$Cv(RMSE)$
		kWh	kWh	%	%	%
Electric	Total	35130	34847	89.75	-0.81	10.16
	HVAC, DHW	12270	12200	92.41	-0.57	16.56
	Appliances	22860	22870	84.05	0.05	7.60
Thermal	Heating	23790	23798	98.32	0.03	7.96
	Cooling	6838	7002	91.61	2.39	17.04

4.2 Energy Signature Visualization

In this section, energy signatures are visualized for both electric and thermal data and divided by end use. Section 4.2.1 focuses on electricity data, while Section 4.2.2 focuses on thermal data.

4.2.1 Energy Signatures – Electricity

The energy signature shapes shown in Fig. 1 for total electricity, Fig. 2 for electricity for HVAC and DHW, Fig. 3 for appliances and lighting, are substantially similar to a 5p or nearly 4p model according to the classification proposed by ASHRAE14:2014. The charts are used to compare models type 1 and 2 at multiple levels in the building

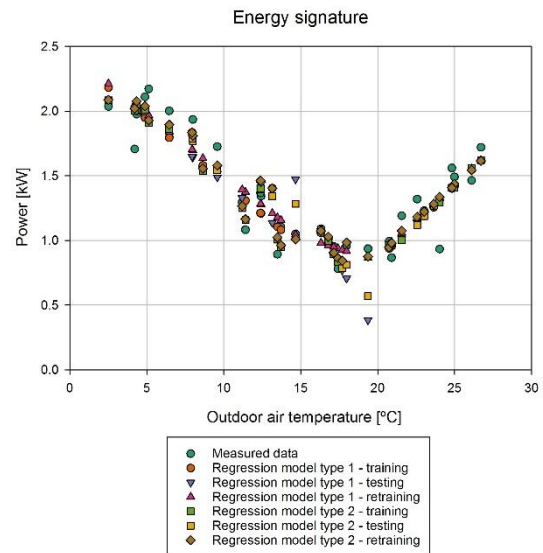


Fig. 1 – Energy signatures, measured data and regression models types 1 and 2 – Total electricity

The spread of data around the trend line is quite limited in Fig. 1 (total electricity) and Fig. 2 (electricity for HVAC and DHW), while it is more pronounced for Fig. 3 (appliances and lighting). In the latter, there is a lower temperature dependence (steepness of the trend line), compared to the other cases. However, the dependence is actually on daylight hours, which are correlated to temperature (lower temperatures correspond to winter condition where daylight hours are less and electric consumption for lighting is higher) and on the actual operation pattern, whose variability also determines the larger spread of values.

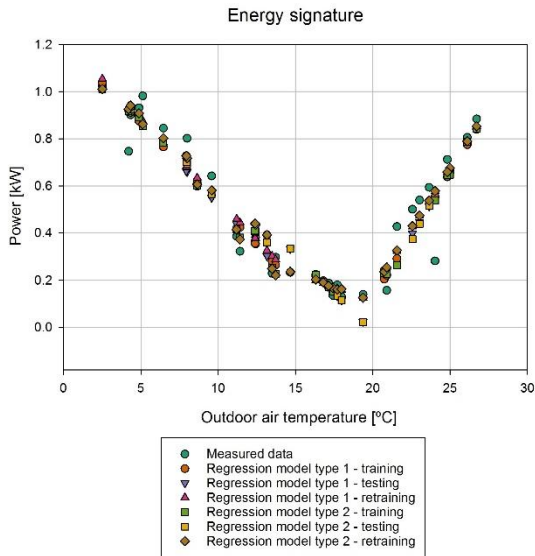


Fig. 2 – Energy signatures, measured data and regression models types 1 and 2 – Electricity for HVAC and DHW

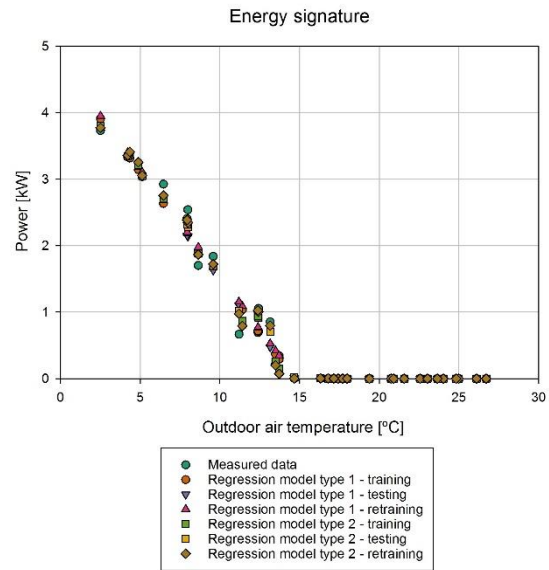


Fig. 4 – Energy signatures, measured data and regression models types 1 and 2 – Thermal energy for heating

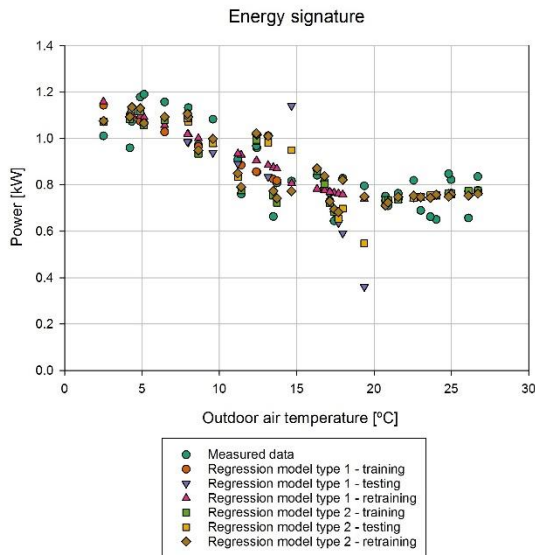


Fig. 3 – Energy signatures, measured data and regression models types 1 and 2 – Electricity for appliances and lighting

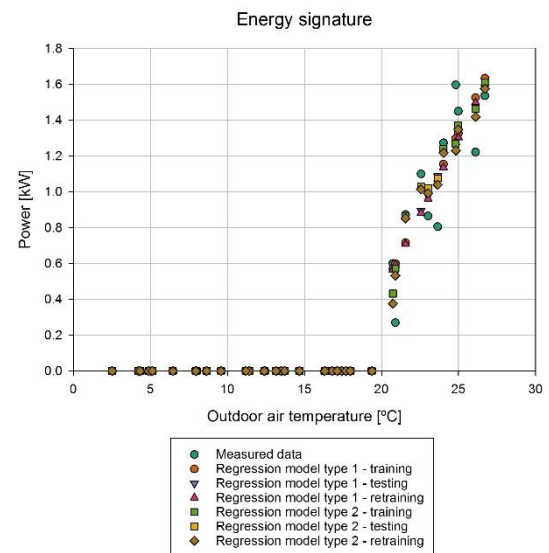


Fig. 5 – Energy signatures, measured data and regression models types 1 and 2 – Thermal energy for cooling

4.2.2 Energy Signatures – Thermal Energy

The energy signature shapes shown in Fig. 4 for thermal demand for heating and in Fig. 5 for thermal demand for cooling are essentially similar to a 3p model according to the classification proposed by ASHRAE14:2014. There are clearly some months when the technical systems do not produce either heating or cooling. Finally, it is possible to identify graphically, in an approximated way, the balance-point temperature for heating and cooling, around 14 °C and 19 °C, respectively.

5. Conclusion

Machine learning-based building energy modeling techniques have proved to be effective in a range of applications. However, problems such as generalization and interpretability must be considered in order to enable the widespread adoption of these techniques. A piecewise linear regression model (interpretable) was proposed to analyze monitored data from a Passive House building, located in the northern Italian province of Forlì-Cesena. The

building was monitored for three years, and this technique requires at least two years of monthly interval data to be used effectively. Nonetheless, the formulation provided is quite simple and flexible; the visualization of energy signatures can also help understanding the actual spread of data around the trend line, which represent outdoor air temperature dependence.

Further efforts involving the categorization of building data according to archetypes could be considered to address the generalization issue effectively. Finally, interpretability is extremely relevant because of the necessity to promote a “human-in-the-loop” approach when using machine learning tools and the transparent link between regression model formulation and other analytical techniques at the state-of-the-art could represent an interesting research area from the perspective of future studies (Tronchin et al., 2020a and 2020b).

Nomenclature

Symbol	Quantity	Unit
a_0, b_0, c_0	regression coefficients, intercept	kW
a_1, b_1, c_1	regression coefficients, temperature dependence term	kW/K
a_2, b_2, c_2	regression coefficients, solar radiation dependence term	m ²
$Cv(RMSE)$	coefficient of variation of RMSE	-
$EN(M)$	measured energy	kWh
$EN(P)$	predicted energy	kWh
I_{sol}	total solar radiation on horizontal surface (direct and diffuse) average hourly value on monthly base	kW/m ²
$NMBE$	normalized mean bias error (expressed in percentage)	-
q^h	energy signature heating	kW
q^b	energy signature base load	kW

q^c	energy signature cooling	kW
R^2	determination coefficient (expressed in percentage)	-
X_h	dummy variable (binary 0-1) heating	-
X_b	dummy variable (binary 0-1) base load	-
X_c	dummy variable (binary 0-1) cooling	-
θ_e	outdoor air temperature	°C
ε_h	error term heating	kW
ε_b	error term base load	kW
ε_c	error term cooling	kW

References

- ASHRAE. 2014. *ASHRAE Guideline 14-2014: Measurement of Energy, Demand, and Water Savings*. American Society of Heating, Refrigerating and Air-Conditioning Engineers: Atlanta, GA, US.
- EVO. 2003. *IPMVP New Construction Subcommittee. International Performance Measurement & Verification Protocol: Concepts and Option for Determining Energy Savings in New Construction, Volume III*. Efficiency Valuation Organization (EVO): Washington, DC, US.
- Fabbri, K., L. Tronchin, and V. Tarabusi. 2014. “Energy Retrofit and Economic Evaluation Priorities Applied at an Italian Case Study”. *Energy Procedia* 45: 379-384. doi: 10.1016/j.egypro.2014.01.041.
- Fabbri, K., L. Tronchin, and F. Barbieri. 2021. “Cocunut fibre insulators: The hygrothermal behaviour in the case of green roofs”. *Construction and Building Materials* 266: 1-9. doi: 10.1016/j.conbuildmat.2020.121026.
- Farina, A., L. Langhoff, and L. Tronchin. 1998. “Acoustic characterisation of “virtual” musical instruments: using MLS technique on ancient violins”. *Journal of new music research* 27(4): 359-379.

- Fazeli, R., M. Ruth, and B. Davidsdottir. 2016. "Temperature Response Functions for Residential Energy Demand – A Review of Models." *Urban Climate* 15: 45–59. doi: <https://doi.org/https://doi.org/10.1016/j.uclim.2016.01.001>
- FEMP. 2008. *FEMP. Federal Energy Management Program, M&V Guidelines: Measurement and Verification for Federal Energy Projects Version 3.0*. U.S. Department of Energy Federal Energy Management Program: Washington, DC, US.
- Hong, T., Z. Wang, X. Luo, & W. Zhang. 2020. "State-of-the-Art on Research and Applications of Machine Learning in the Building Life Cycle." *Energy and Buildings* 212: 109831. doi: <https://doi.org/https://doi.org/10.1016/j.enbuild.2020.109831>
- ISO. 2013. *ISO 16346:2013, Energy Performance of Buildings – Assessment of Overall Energy Performance*.
- ISO. 2020. *ISO/IEC TR 29119-11:2020(En) Software and Systems Engineering – Software Testing – Part 11: Guidelines on the Testing of AI-Based Systems*.
- Kissock, J. K., J. S. Haberl, and D. E. Claridge. 2003. "Inverse Modeling Toolkit: Numerical Algorithms." *ASHRAE Transactions* 109: 425.
- Lin, M.-H., J. Gunnar Carlsson, D. Ge, J. Shi, and J.-F. Tsai. 2013. "A Review of Piecewise Linearization Methods." *Mathematical Problems in Engineering* 2013: 101376. <https://doi.org/10.1155/2013/101376>
- Manfren, M., B. Nastasi, E. A. Piana, and L. Tronchin. 2019. "On the link between energy performance of building and thermal comfort: An example". In *AIP Conference Proceedings* 2123: 1-9. doi: <https://doi.org/10.1063/1.5116993>
- Manfren, M., B. Nastasi, and L. Tronchin. 2020. "Linking Design and Operation Phase Energy Performance Analysis Through Regression-Based Approaches." *Frontiers in Energy Research* 8: 288. doi: <https://doi.org/10.3389/fenrg.2020.557649>
- Manfren, M., B. Nastasi, L. Tronchin, D. Groppi, and D. Astiaso Garcia. 2021a. "Techno-Economic Analysis and Energy Modelling as a Key Enablers for Smart Energy Services and Technologies in Buildings." *Renewable and Sustainable Energy Reviews* 150: 111490. doi: <https://doi.org/https://doi.org/10.1016/j.rser.2021.111490>
- Manfren, M., M. Sibilla, and L. Tronchin. 2021b. "Energy Modelling and Analytics in the Built Environment—A Review of Their Role for Energy Transitions in the Construction Sector." *Energies* 14(3): 679. doi: <https://doi.org/10.3390/en14030679>
- Norton, B., W. B. Gillett, and F. Koninx. 2021. "Decarbonising Buildings in Europe: A Briefing Paper." *Proceedings of the Institution of Civil Engineers - Energy* 174(4): 147-155. doi: <https://doi.org/10.1680/jener.21.00088>
- Pistore, L., G. Pernigotto, F. Cappelletti, A. Gasparella, and P. Romagnoni. 2019. "A Stepwise Approach Integrating Feature Selection, Regression Techniques and Cluster Analysis to Identify Primary Retrofit Interventions on Large Stocks of Buildings." *Sustainable Cities and Society* 47: 101438. doi: <https://doi.org/https://doi.org/10.1016/j.scs.2019.101438>
- Tronchin, L., M. Manfren, and L. C. Tagliabue. 2016. "Optimization of Building Energy Performance by Means of Multi-Scale Analysis – Lessons Learned from Case Studies." *Sustainable Cities and Society* 27: 296–306. doi: <https://doi.org/https://doi.org/10.1016/j.scs.2015.11.003>
- Tronchin, L. 2005. "Modal analysis and intensity of acoustic radiation of the kettledrum". *The Journal of the Acoustical Society of America* 117(2): 926-933. doi: <https://doi.org/10.1121/1.1828552>.
- Tronchin, L. 2021. "Variability of room acoustic parameters with thermo-hygrometric conditions". *Applied Acoustics* 177: 1-14. doi: <https://doi.org/10.1016/j.apacoust.2021.107933>
- Tronchin, L., K. Fabbri, and C. Bertolli. 2018. "Controlled Mechanical Ventilation in Buildings: A Comparison between Energy Use and Primary Energy among Twenty Different Devices". *Energies* 11: 1-20. doi: <https://doi.org/10.3390/en11082123>
- Tronchin, L., and D. J. Knight. 2016. "Revisiting Historic Buildings through the Senses. Visualising Aural and Obscured Aspects of San Vitale, Ravenna". *International Journal of*

- Historical Archaeology* 20: 127-145. doi: <https://doi.org/10.1007/s10761-015-0325-2>
- Tronchin, L., M. Manfren, and V. Vodola. 2020a. "The carabattola - vibroacoustical analysis and intensity of acoustic radiation (IAR)". *Applied Sciences* 10(2): 641. doi: <https://doi.org/10.3390/app10020641>
- Tronchin, L., M. Manfren, and V. Vodola. 2020b. "Sound characterization through intensity of acoustic radiation measurement: A study of persian musical instruments". *Applied Sciences* 10(2): 633. doi: <https://doi.org/10.3390/app10020633>
- Tronchin, L., F. Merli, and M. Manfren. 2021a. "On the acoustics of the Teatro 1763 in Bologna". *Applied Acoustics* 172: 1-9. doi: <https://doi.org/10.1016/j.apacoust.2020.107598>
- Tronchin, L., F. Merli, and M. Dolci. 2021b. "Virtual acoustic reconstruction of the Miners' Theatre in Idrija (Slovenia)". *Applied Acoustics* 172: 1-9. doi: <https://doi.org/10.1016/j.apacoust.2020.107595>
- Westermann, P., C. Deb, A. Schlueter, and R. Evins. 2020. "Unsupervised Learning of Energy Signatures to Identify the Heating System and Building Type Using Smart Meter Data." *Applied Energy* 264: 114715. doi: <https://doi.org/https://doi.org/10.1016/j.apenergy.2020.114715>
- Westermann, P., and R. Evins. 2019. "Surrogate Modelling for Sustainable Building Design – A Review." *Energy and Buildings* 198: 170–86. doi: <https://doi.org/https://doi.org/10.1016/j.enbuild.2019.05.057>

Estimated Versus Actual Heating Energy Use of Residential Buildings

Matthias Schuss – TU Wien, Vienna, Austria – matthias.schuss@tuwien.ac.at

Martin Fleischhacker – Vienna, Austria – martin2fleischhacker@gmail.com

Ardeshir Mahdavi – TU Wien, Vienna, Austria – amahdavi@tuwien.ac.at

Abstract

The energy demand of buildings plays an important role with regard to energy conservation objectives as well as reduction of greenhouse gas emission. The well-established building energy certificates provide essential information concerning the thermal quality and resulting energy demands of buildings in general. Hence, related Austrian regulations and standards specify a demand-orientated calculation method based on construction and material data together with standardized usage profiles, as well as a location-related weather data set. This method is also applied in the case of existing buildings, which differs from some other European countries, where certificates represent real energy usage and provide a comparison with similar buildings in terms of construction period and usage. However, it is not guaranteed that an energy demand certificate according to Austrian standards is able to represent the actual energy use of existing buildings, a circumstance that is typically referred to as ‘energy performance gap’. In this context, we conducted a comprehensive comparison of real energy consumption and the certificate-based energy demand predictions for a number of buildings located in and around the city of Vienna, Austria. Specifically, 15 residential building complexes with nearly 1400 units were selected, involving a large variety of building construction dates and their thermal quality. The buildings were analyzed in detail based on historic energy consumption data from 2011 to 2017. The paper provides an overview of the real energy performance together with a detailed analysis of the discrepancies between actual energy use and certificate-based estimations. Generally speaking, the buildings with a higher energy standard and lower demand displayed higher discrepancies (expressed in terms of relative deviations) than older buildings with higher energy demand.

1. Introduction

Over the past decades, increasing efforts have been made to reduce energy consumption in all sectors. The building sector requires an average of 40 % of the total energy demand of the European Union (EU, 2010). Great saving potentials were identified for buildings and this resulted in extensive energy efficiency measures. As a result, not only new buildings are now better insulated, but also the existing building stock is to be significantly improved with necessary thermal retrofitting measures. Other additional tools for higher energy efficiency are better building systems that could contribute to further reduction of the energy requirements of the buildings. But how effective are these measures and how much can energy consumption actually be reduced?

In Austria, the Energy Performance Certificate Submission Act of 2012 mandates the following: "... the obligation of the seller or inventor to present and hand over an energy certificate to the buyer or existing customer when selling or in-stocking a building or object of use, as well as the obligation to provide certain indicators on the energy quality of the building ...)" (EAVG, 2012).

The basic idea of an energy certificate lies in the possibility of verifiability of the energy demand and better estimation of running costs. Furthermore, this is expected to influence the market prices according to the thermal quality and the predicted future energy needs and costs. Hence, an energy certificate should not be merely a project description with vague information about the energy demand and thermal quality to fulfil the requirements defined by law. Rather, it should act as a purchase or sales argument and should motivate owners to improve the energy performance. In this context, the present contribution examines the validity of energy

certificates based on information from a set of building complexes.

2. Method

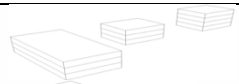

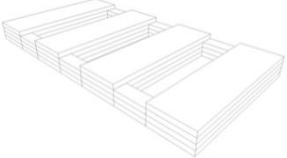
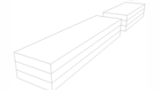

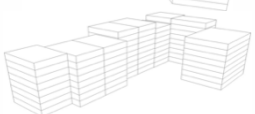
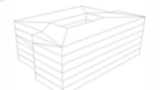
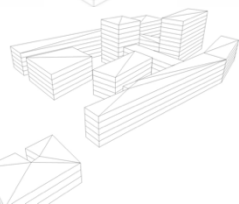
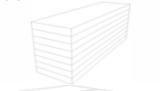


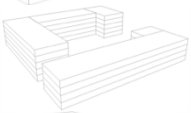
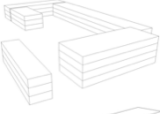
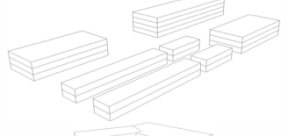

Recorded energy usage data of nearly 1400 apartments over a period of seven years (2011 to 2017) was analyzed with focus on the verifiability of the energy demand as entailed in the building energy certificates. To this end, energy consumption data from annual accounting bills were collected and compared with certificates to assess differences between the predicted and the real energy usage both at the building complex level and at the level of individual units. An initial quality check of the available data showed that 12 complexes with a total of 1043 units could be used for a detailed comparison between the estimated heating demands and the real energy usage.

3. Used Building Sampling

The building sample consists of a total of 15 complexes with nearly 1400 units, as shown in Table 1. From the schematic drawings of the cubature, it is the fact that the sampling includes different types of building complexes with single buildings as well as blocks of attached buildings may be seen. The buildings are mainly located in the city of Vienna (see Fig. 1). Buildings referred to as BH and KF are close to near to the border of the Vienna municipality, whereas AS is near Wiener Neustadt (approximately 45 km from Vienna).

Table 2 shows the variety of the buildings in terms of construction and size. Detailed information about the number of units, the building class, the heated and total area, as well as the ratio of volume and area are also included in the overview. The buildings are sorted from high to low energy demand with energy labels from C to A+. Buildings with limited data that show accounting units (relative dimensionless fraction of energy use) instead of kWh in the reporting bills are marked in red.

Table 1 – Overview of building sample, including the object code, number of units, and illustration of cubature

Object	Units/flats	Cubature
AL	28	
JB	46	
ZS	231	
UZ	23	
FM	47	
DP	148	
RA	41	
KE	324	
VG	52	
AS	45	
AB	108	
KT	90	
KF	47	
BH	73	
KW	45	

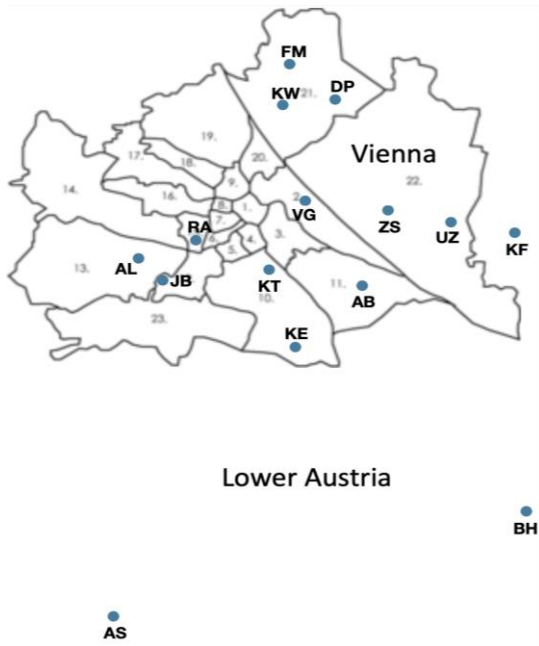


Fig. 1 – Location of the analyzed building complexes

The energy class variety of the analyzed 15 complexes included buildings from C to A++ in a range of 11 to 57 kWh/(m² a) as mentioned in Table 2 and illustrated in Fig. 2.

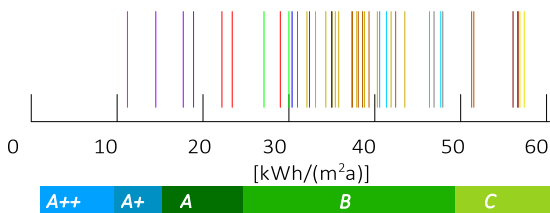


Fig. 2 – Distribution of certificate-based heating demand prediction and the building energy efficiency label from the analyzed building complexes

4. Heating Degree Days and Data Normalization

The calculation of the building energy certificate values depends on the location and its climate conditions and shows a strong dependence on the magnitude of local heating degree days (HDD). Standardized values for the different climate regions and altitudes of buildings in Austria are specified in the related OIB-RL6 regulation (OIB, 2015). The values of heating degree days are calculated as the difference between the room air temperature, which is specified as 20 °C, and the outside temperature, if it

is below 12 °C. When calculating the number of heating degree days in a year, all days with daily average outside temperatures below 12 °C are specified as heating days and are considered in the calculation.

The general trend for calculated annual heating degree days for Vienna (Fig. 2), based on real temperature data from the public weather station at “Hohe Warte” (ZAMG, 2018), shows, with 2295.1 K d, the lowest value of heating degree days for 2014 and the highest value of 2940.4 K d for 2015. The mean value of 2720.4 K d is significantly lower than the standard defined value (3355 K d) for “Wien Döbling” as documented in the OIB-RL6 regulation. Hence, the recorded energy usage of the sample buildings could be expected to be significantly lower for these years when compared with the values in the certificates. The analyzed weather data showed, for the study period (2011 to 2017), approximately 19 percent lower heating degree days for Vienna.

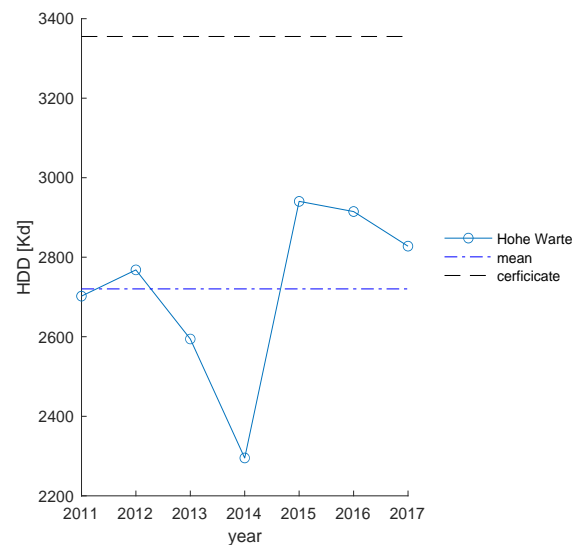


Fig. 3 – Heating degree days for the years 2011 to 2017 based on measurements from the ZAMG weather station (“Hohe Warte”) in Vienna

In the following analysis, an HDD-normalization of the data was performed with a yearly factor considering the HDD-difference, and increases the yearly energy usage accordingly. Due to the proximity to Vienna (same climate zone), a separate evaluation of heating degree days in Lower Austria was not considered.

5. Results of Energy Usage Evaluation

In total, 15 residential building complexes with nearly 1400 units were evaluated on the basis of energy consumption data over a period of seven years (2011-2017). For twelve of the complexes with nearly 1050 units, a detailed comparison between the heating demand displayed in the certificate and the recorded heating energy usage was performed with a detailed discussion of the variety. The remaining three other complexes with data showing cost profiles as accounting units are limited in their analyzing possibilities and resulted in an analysis of the variation only.

5.1 Total Energy Consumption for Heating, Ventilation and Hot Water Production

The trends of the total annual energy consumption for heating, ventilation and hot water production (Fig. 4) shows, as expected, a general correlation with the variation of the real heating degree days as presented before.

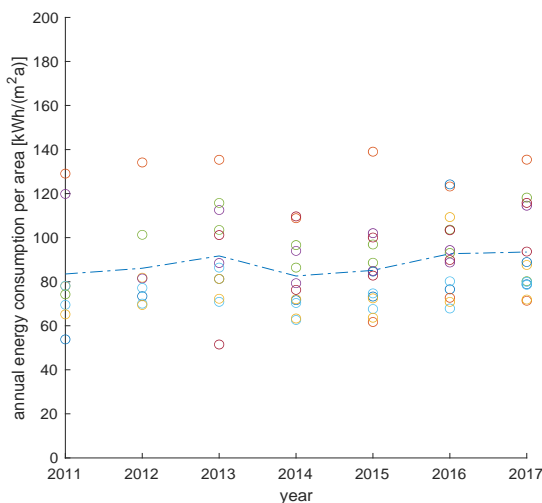


Fig. 4 – Total annual energy consumption for heating, ventilation, and hot water production recorded in the years 2011 to 2017

Fig. 5 illustrates the variation of annual total energy usage for the years 2011 to 2017. As expected, some of the complexes (KE and KF) show a much higher variation than the others. This could be partly explained with energy partly used for hot water preparation, which generally does not depend on the heating degree days, but depends rather on user behavior.

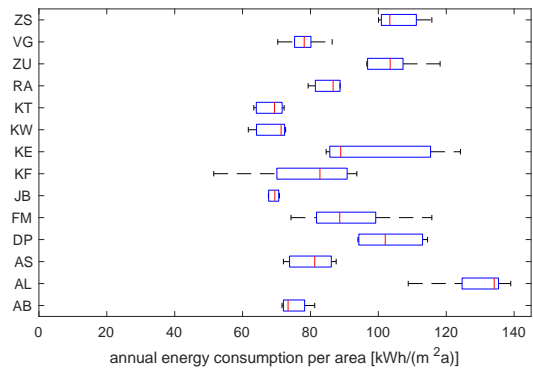


Fig. 5 – Distribution of the total annual energy consumption for heating, ventilation, and hot water production recorded in the years 2011 to 2017

5.2 Energy Demand vs Real Energy Consumption Used for Room Heating

A detailed comparison of the certificate-based energy demand for heating and the real measurements from the year 2011 to 2017 recorded by individual submeters for each unit was possible for 12 of the 15 complexes. An initial comparison of HDD-normalized annual average energy usage for heating (40 buildings and 1043 units) showed much higher usage than expected (Fig. 6). Note that not even a single building in the sample was performing equally or better than estimated in the certificate. A more detailed evaluation of the data was carried out to identify possible tendencies in relation to the building class in the certificate. Fig. 7 shows the variation of the annual HDD-normalized energy usage for heating sorted from high (at the top) to low heating energy demands (marked with blue X in the plot).

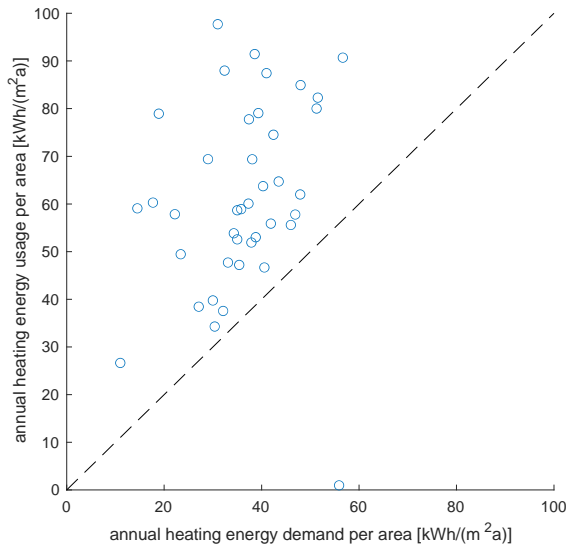


Fig. 6 – Annual certificate-based energy demand versus average annual HDD-normalized energy usage for heating recorded in the years 2011 to 2017

It may be seen that not all instances have a similar variety over time, suggesting a possible role of other influencing parameters other than the outside temperature and the related HDD influence.

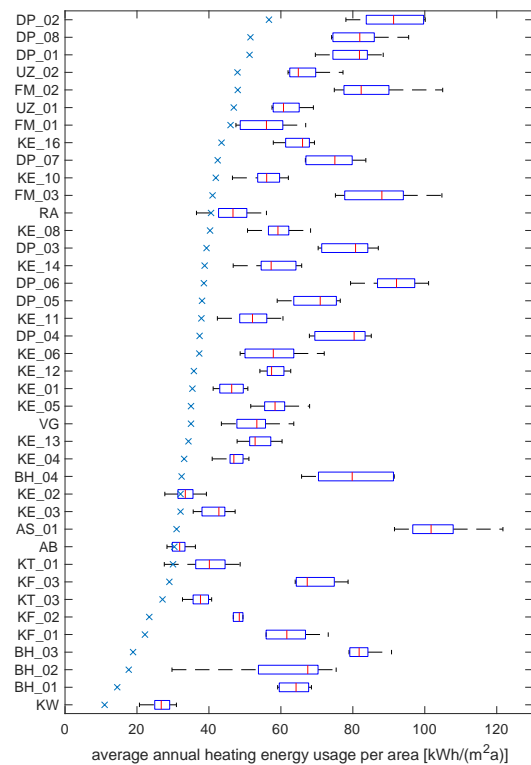


Fig. 7 – Distribution of building average (2011 to 2017) HDD-normalized annual heating energy usage together with the certificate-based heating demand (marked with a blue x)

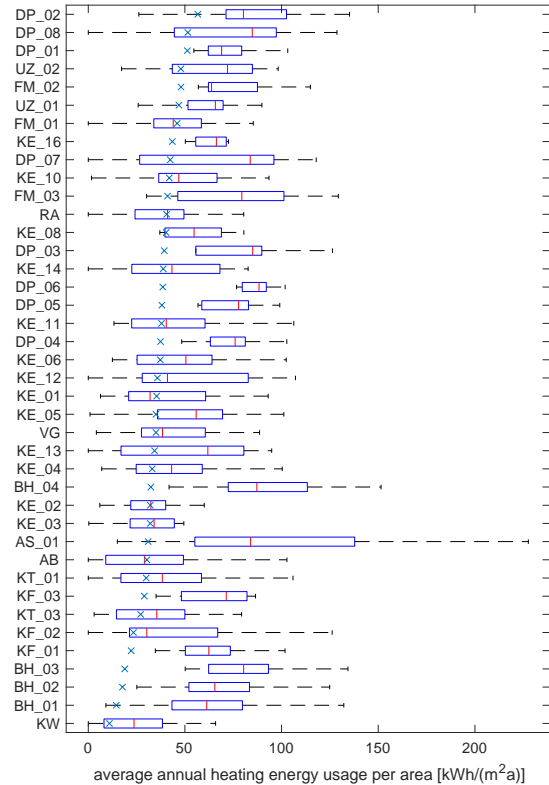


Fig. 8 – Distribution of units' HDD-normalized annual heating energy usage in the year 2016 together with the certificate-based heating demand (marked with a blue x)

Especially in the high-rated buildings (according to certificates), such as AS_01, KF_03, KF_01, BH_03, BH_02 and BH_01, rather high measured energy use values can be observed. A closer look into the variation of the units' HDD-normalized annual heating energy usage was carried out for the year 2016 and is presented in Fig. 7. It may be seen that the variation between the units is very large and could be thought of as having been caused by the occupants' influence. Again, high-ranked buildings display a wide variation. The buildings KW, BH_01, BH_02, BH_03, and BH_04 with a controlled ventilation system show much higher and wider distributed values than expected. These buildings were designed as passive houses. Hence, it could have been expected that the ventilation system would significantly reduce the heating energy use. For three complexes and the respective 9 buildings, a detailed comparison was not possible, but the variation of the energy usage documented with the related accounting units of the annual bills was analyzed in a similar way as above. Fig. 9 shows a similar variety of the units' HDD-normalized annual heating energy usage in groups of

accounting units for each sampling object as for the rest of the building sample.

The main task of the study was to examine the validity of energy certificates and to evaluate how future energy usage and running costs can be predicted. The recorded data of the real energy usage in the years 2011 to 2017 for sampled buildings suggest that the real energy usage for heating is significantly higher.

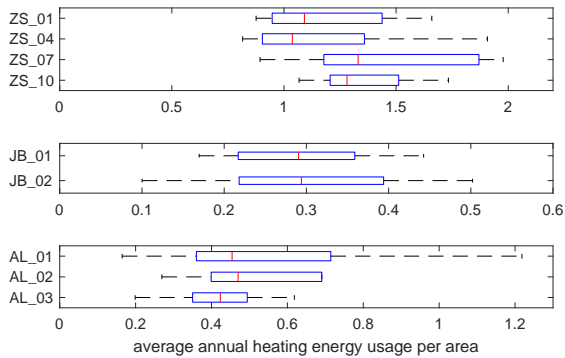


Fig. 9 – Distribution of units' HDD-normalized annual heating energy usage for buildings with heating usage data in accounting units only in the year 2016

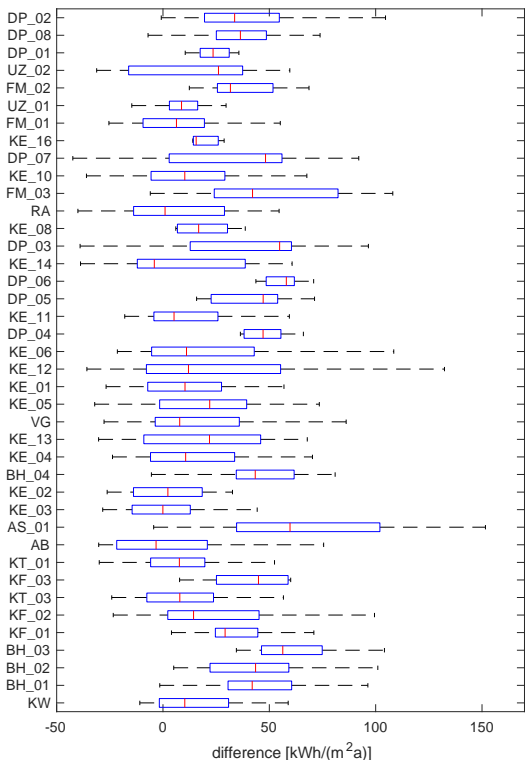


Fig. 10 – Difference distribution of unit average (2011 to 2017) HDD-normalized annual heating energy usage and the certificate-based heating demand

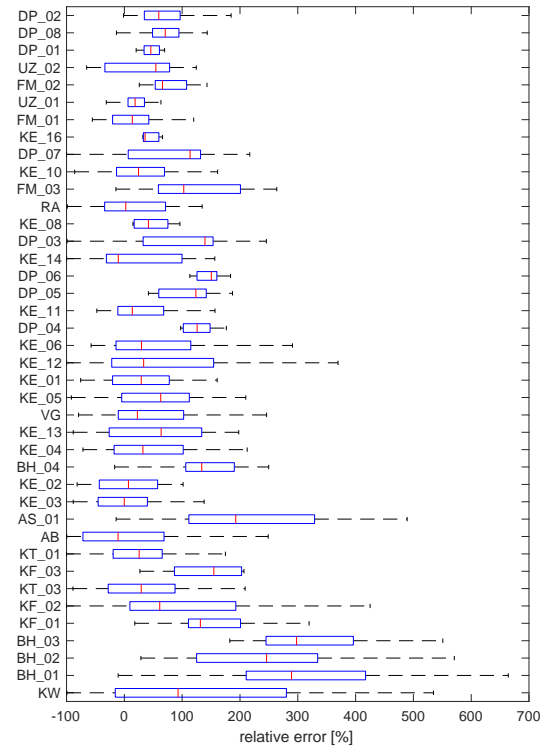


Fig. 11 – Relative error distribution of unit average (2011 to 2017) HDD-normalized annual heating energy usage and the certificate-based heating demand

Fig. 10 illustrates this for example with overview of the unit average (2011 to 2017) HDD-normalized annual heating energy usage and the certificate-based heating demand. It is clearly visible that especially the higher rated buildings at the bottom show similar or, in some cases higher, differences to the predicted heating demand. The unsatisfactory performance of those buildings is even more visible in the calculation of a relative error to the heating demand, as illustrated in Fig. 11.

6. Conclusion

The evaluation of energy consumption data (years 2011 to 2017) from 15 residential building complexes with nearly 1400 units facilitated an examination of the reliability of energy certificates in view of the prediction of building future energy use and related costs. The available data showed much higher energy consumption when compared with the values in energy certificates. This could be shown for the total energy use for heating, domestic hot water, and ventilation in cases with controlled ventilation,

as well as for the heating energy usage itself.

Buildings with higher thermal standards showed in relative terms a larger energy performance gap when compared with buildings with lower energy certificate ratings. This may be a consequence of the high potential for the influence of building occupants in total energy use.

Acknowledgement

This contribution was only possible with support by EBG Hausverwaltung and the provision of the building description documents of the residential properties examined. In addition, the accounting companies concerned, ISTA and TECHEM, facilitated this study with the preparation and provision of the detailed billing data.

References

- EU. 2010 "Directive 2010/31/EU". European Union L 153/13 18.6.2010
- EAVG 2012. „Bundesgesetz über die Pflicht zur Vorlage eines Energieausweises beim Verkauf und bei der In-Bestand-Gabe von Gebäuden und Nutzungsobjekten BGBl. I Nr. 27/2012
- OIB. 2015. "OIB-Richtlinie 6: Energieeinsparung und Wärmeschutz". Österreichisches Institut für Bautechnik. OIB-330.6-009/15.
- ZAMG. 2018. „Tagesauswertung Lufttemperatur Wien Hohe Warte, 2011-2017". Zentralanstalt für Meteorologie und Geodynamik. Accessed 25.09.2018.
<https://www.zamg.ac.at/cms/de/klima/klimauebersichten/jahrbuch>

Polyamide Waste Thermal and Acoustic Properties: Experimental and Numerical Investigation on Possible Reuse for Indoor Comfort Improvement

Manuela Neri – University of Brescia, Italy – manuela.neri@unibs.it

Eva Cuerva – Universitat Politècnica de Catalunya, Italy – eva.cuerva@upc.edu

Alfredo Zabaleta – Universitat Politècnica de Catalunya, Spain – alfredo.guardo-zabaleta@upc.edu

Pablo Pujadas – Universitat Politècnica de Catalunya; Spain – pablo.pujadas@upc.edu

Elisa Levi – University of Brescia; Italy – elisa.levi@unibs.it

Ondrej Sikula – Brno University of Technology, Czech Republic – sikula.o@vutbr.cz

Abstract

Referring to the circular economy model, end-of-life household materials (EoLHM), such as packaging and clothes, could be converted into building elements with thermal and acoustic properties; for example, they could be converted into panels to be installed indoors for building refurbishment. Given the high availability almost anywhere, panels made of EoLHM would represent an alternative to commercial insulating materials that, even though relatively cheap, cannot be afforded by disadvantaged people. This paper presents a multidisciplinary analysis aimed at the characterization of polyamide 6.6, obtained as a waste from the production of non-surgical face masks. The research focuses on the thermal and acoustic properties of the material. The properties have been determined experimentally through the guarded hot plate method and the impedance tube technique. Then, the influence of the panel's position on the indoor operative temperature and the reverberation time has been analyzed through numerical simulations. Results show that, from the thermal and acoustic point of view, this waste is suitable for the realization of building panels, and the performance depends on the density and the thickness of the material. However, aspects such as fire resistance and the containment of the material need further investigation.

1. Introduction

Living in dwellings characterized by inadequate indoor temperature and poor air quality is called “energy poverty”, a condition affecting 1 in 3 Eu-

ropeans, and linked to 100000 premature deaths each year (European Parliament and Council of the European Union, 2018; González-Eguino, 2015). People living in disadvantaged contexts cannot refurbish their dwellings because of the relatively high price of commercial insulating materials. By 2030, the United Nations aim to make cities inclusive, safe, resilient, and sustainable, and to promote the circular economy model (Carnemolla et al., 2021; United Nations, 2015).

An alternative to commercial insulating materials is insulating elements realized by reusing end-of-life household materials (EoLHM) such as packaging and clothes. In the literature, several studies investigated the properties of EoLHM, but a comprehensive and systematic analysis is still missing (Drochytka et al., 2017; Ibrahim & Meawad, 2018; Kudzal et al., 2018; Mansour & Ali, 2015; Neri et al., 2021a and 2021b; Secchi et al., 2015).

The aim of this paper is the thermal and acoustic characterization of polyamide 6.6 waste (henceforth polyamide) obtained from the production of non-surgical face masks. Firstly, polyamide's thermal and acoustic properties have been determined experimentally. Then, the improvement of the building's indoor condition due to the installation of panels made of polyamide has been assessed through numerical simulations. These panels are intended installed indoors to allow for easy and fast building refurbishment interventions and also by unskilled people.

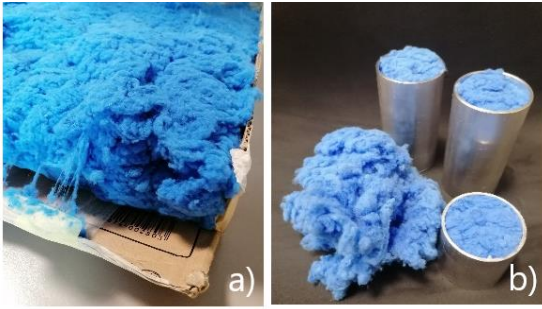


Fig. 1 – Test specimens for the thermal test a), and for acoustic tests b). For the thermal test, the material has been confined in a cardboard case. For the acoustic tests, the material in the samples was contained between two glass tissue discs to ensure that the front surface was normal to the axis of the tube

Indoor comfort embraces several aspects, such as thermal and acoustic comfort, which are the two aspects analyzed in this paper. Under steady-state conditions, heat transfer through a wall is described by the relationship:

$$q = A \cdot \Delta T / (\Sigma (s/\lambda)) \quad (1)$$

where q is the heat flux through the wall, A , s , λ are the surface, thickness, and thermal conductivity of the wall. ΔT is the difference in temperature measured on the panel surfaces. Conversely, under unsteady conditions, the heat flux q depends also on the wall heat capacity and position of the layers. In this study, the thermal conductivity of samples realized with polyamide at different densities has been measured employing the hot plate method with the guard ring.

When dealing with indoor acoustic comfort, one of the aspects to be evaluated is the reverberation time TR , which is related to the indoor sound quality in terms of echo effect and, consequently, vocal message intelligibility. Optimal TR values depend on the ambient intended use, and reference values are specified in the UNI 11367 (UNI, 2010). TR is the time lapse in which the sound energy density decreases by 60 dB. It is determined by suddenly switching off a sound source and measuring the sound energy level variation. TR can be estimated according to the Sabins formula:

$$TR = 0.16 V/S \quad (2)$$

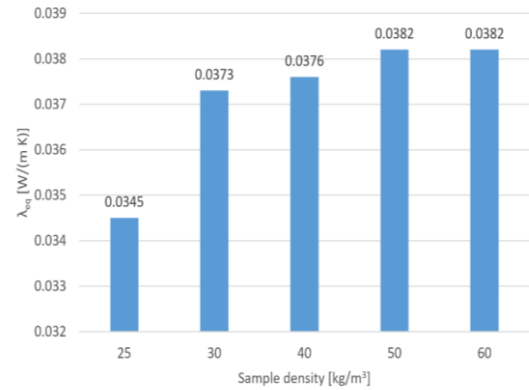


Fig. 2 – Measured equivalent thermal conductivity of polyamide

where V is the volume of the room, and S is the room sound absorption. The term S is defined as $S = \Sigma(\alpha \cdot A)$, where A is the surface extension, and α is the sound absorption coefficient of the room surfaces.

The sound energy balance on a surface impinged by sound power leads to:

$$1 = \eta + \tau + \alpha \quad (3)$$

where η is the sound reflection coefficient, τ is the sound transmission coefficient, and α is the sound absorption coefficient.

Generally, for porous material such as the one investigated in this paper, the higher the density, the lower α , while the greater the thickness, the higher α . The sound absorption coefficient for a hard-backed element is defined as:

$$\alpha = 1 - |TL|^2 \quad (4)$$

where TL is the sound transmission loss, that is generally determined experimentally and is a function of τ according to:

$$TL = 10 \cdot \log_{10}(1/\tau) \quad (5)$$

In this paper, the sound absorption coefficient α and transmission loss TL have been determined by means of the impedance tube technique. This technique is suitable for R&D analysis but considers only waves that impinge the sample surface normally.

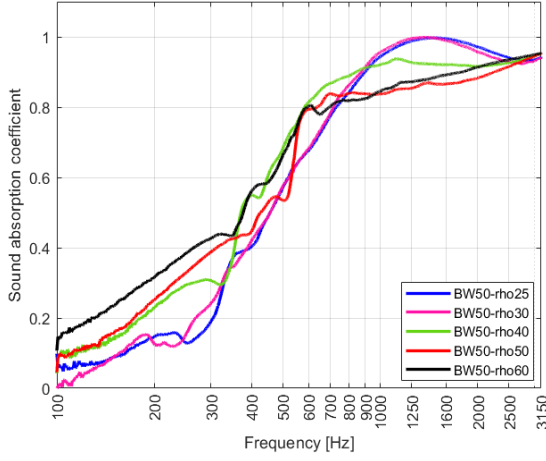


Fig. 3 – Sound absorption coefficient of the 50-mm-thick samples

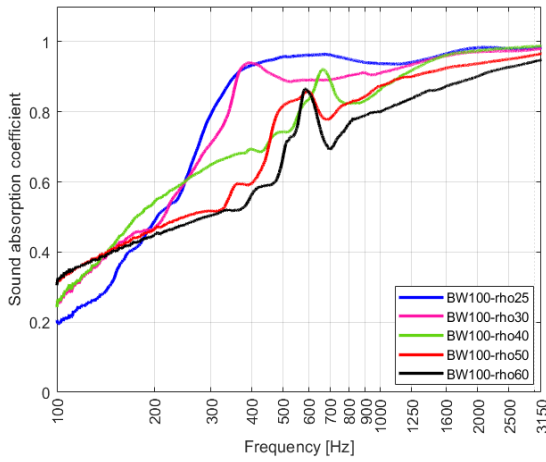


Fig. 4 – Sound absorption coefficient of the 100-mm-thick samples

2. Experimental Campaign

Since polyamide is a soft and porous material (see Fig. 1), its density depends on the packing degree, which is an important aspect in view of panel self-realization. To evaluate this aspect, the equivalent thermal conductivity λ_{eq} as a function of the density has been determined through the guarded hot plate method.

The test consisted in measuring the heat flow q obtained under a predefined temperature difference ΔT , and λ_{eq} is determined as:

$$\lambda_{eq} = (q \cdot s) / (A \cdot \Delta T) \quad (6)$$

where A and s are the surface and thickness of the same. Results are shown in Fig. 2.

Samples of different densities have been realized and tested in the impedance tube apparatus to de-

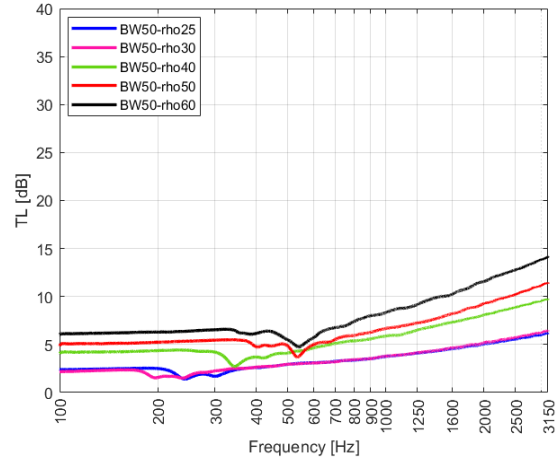


Fig. 5 – Sound transmission loss of the 50-mm-thick samples

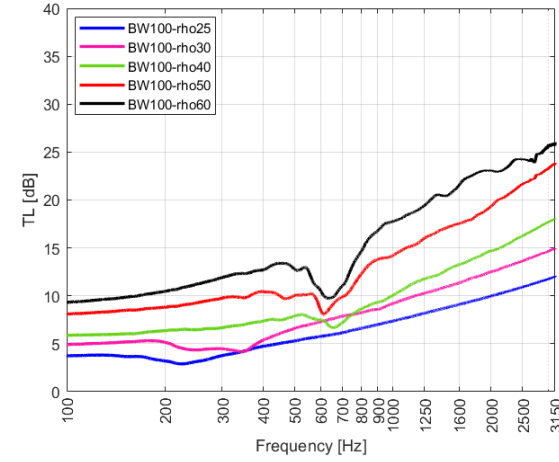


Fig. 6 – Sound transmission loss of the 100-mm-thick samples

termine the polyamide sound absorption coefficient α , and the sound transmission loss TL . The test apparatus consists of two tubes 4.6 cm in diameter connected to a test sample holder. Two microphones are placed on either side of the specimen (45 mm from each other). A source emitting a pink noise is placed at one end of the tube. A multi-channel Fast Fourier Transform (FFT) analyzer acquires the signals captured by the microphones. The pressure and particle velocity of the travelling and reflected waves are determined by a MATLAB script implemented according to the E2611 ASTM standard (ASTM E2611, 2019). To assess the influence of the specimen's thickness, samples 50-mm and 100-mm thick have been realized and tested. The frequency range is between 100 Hz and 3150 Hz, according to the characteristics of the test apparatus.



Fig. 7 – The real case study, a classroom in the Raval neighbourhood in Barcelona: **a)** façade, **b)** interior with furniture, **c)** view from the balcony, and **d)** view of the opposite building

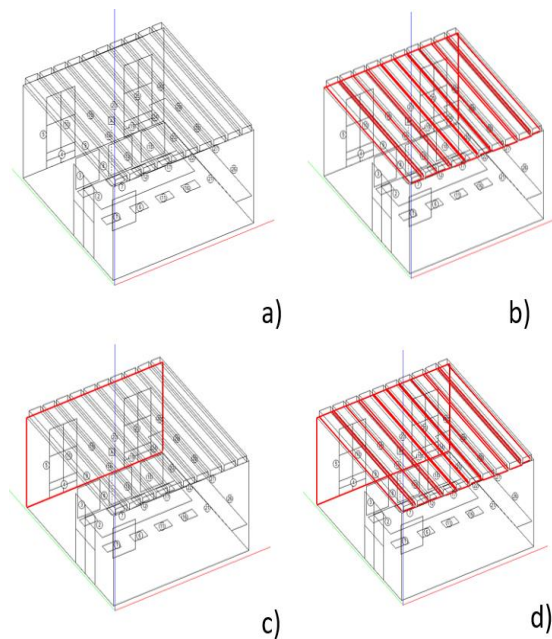


Fig. 8 – Scenarios considered in the numerical analysis: **a)** current configuration without panels (*Case00*), **b)** panels installed on the ceiling (*Case01*), **c)** panels installed indoors on the façade (*Case02*), **d)** panels installed indoors on both the façade and the ceiling (*Case03*)

Table 1 – Wall layers set in the numerical model defined with Energy+

Structure	Layer 1	Layer 2	Layer 3	Layer 4
Roof	T	XPS	HR	P
Internal wall	P	DIW	P	
Facade	P	DIW	P	
Basement	CLS_B	CLS_S	CLSM	T
Floor	P	HF	CLSM	T
Ceiling	T	CLSM	HF	P

Table 2 – Material properties set in the numerical model defined with Energy+

Material	s [m]	λ [W/(m K)]	ρ [kg/m ³]	c [kJ/(kg K)]
Plaster	0.015	0.8	1600	1
Hollow bricks_R	0.5	0.24	800	1
Hollow bricks_F	0.3	0.24	800	1
CLS_S	0.1	0.9	1800	0.88
Dolomite_IW	0.15	1.75	2872	0.91
XPS	0.08	0.035	30	1.5
Tiles	0.01	0.208	530	1
CLS_M	0.05	1.1	1000	0.88
Dolomite_F	0.35	1.75	2872	0.91
CLS_B	0.3	2.4	2400	1

The lower and the upper working frequencies are determined according to:

$$f_u < 0.586 \cdot c_{air} / d \quad (7)$$

$$d < 0.586 \cdot c_{air} / f_u \quad (8)$$

where c_{air} is the sound speed in the tube, and d is the tube diameter. Results are shown in Fig. 3 - 6.

3. Numerical Simulations

To assess how the panel made of polyamide and installed indoors on the walls and the ceiling affects indoor conditions, an acoustic and a thermal numerical model were set. Two open-source software solutions, Energy+ and Ramsete, were used.

In the numerical simulations, the panel is 10-cm thick, made of polyamide at 25 kg/m³ confined between two glass veil layers.

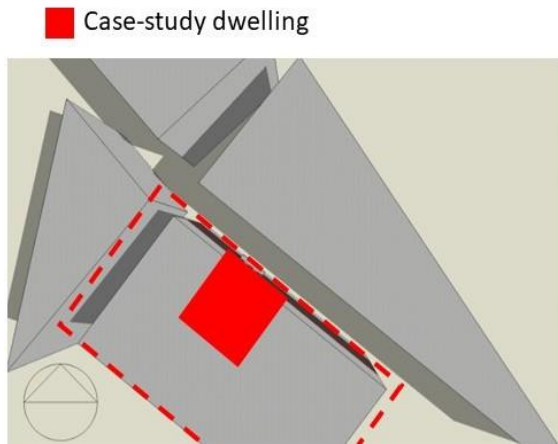


Fig. 9 – Model defined in Energy+. The building is modelled as a single thermal zone which includes another thermal zone related to the classroom. The other buildings participate in the shading effect

The models represent a classroom in the Raval neighborhood in Barcelona (see Fig. 7), where thermal and acoustic measurements were taken. The classroom is on the second floor of a building and is 5.1 x 5.8 x 3.0 m in dimension. The façade is 17 m² with two windows 2.6 x 1.1 m in dimensions. The ceiling is a typical Catalan structure with 30-cm-wide vaults. In the acoustic model (see Fig. 8), also the furniture is modeled, as it may affect the sound wave reflection and, in turn, the reverberation time. Materials properties are listed in Tab. 1 and Tab. 2: some properties have been hypothesized, while the building owner provided others. The material vapor diffusion factor equal to 180 was chosen. The polyamide vapor diffusion factor equal to 1.254 according to CIBSE Guide A (CIBSE, 2015) was chosen. The occupancy level is 0.38 persons/m², and air natural infiltration is considered.

Numerical simulations were performed for different scenarios in which the panel's position varied according to Fig. 8. Scenario *Case00* is representative of the current configuration without panels. In contrast, panels are installed in the other scenarios: the panels are placed in the ceiling vaults in *Case01*, on the façade in *Case02*, and on both the ceiling and façade in *Case03*. The wall surface covered with panels varies according to the scenario: 29 m² for *Case01*, 17 m² for *Case02*, and 47 m² for *Case03*.

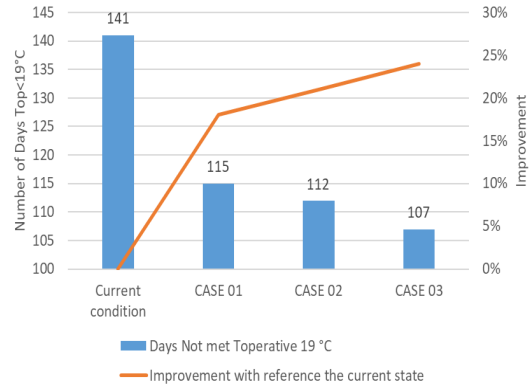


Fig 10 – Number of days when the indoor temperature is lower than 19°C, and improvement of the indoor operative temperature as a function of the panels' position. The panels are intended installed indoors

The model defined in Energy+ includes the building where the classroom is located (considered as two thermal zones) and the surrounding buildings that contribute to shading (see Fig.9). Results in Fig. 10 show the number of days when the indoor temperature is lower than 19 °C, and a heating system would be necessary to maintain an adequate indoor temperature.

Ramsete software is based on the Pyramid Tracing algorithm, and it can analyze problems in large enclosures or outdoors. It considers specular reflections over sound-absorbing surfaces. In the acoustic model, an omnidirectional sound speaker and 30 sound receivers uniformly distributed in the room have been set. In the acoustic analysis, polyamide is considered confined between two layers of glass veil - a very light material that does not affect the thermal and acoustic properties of the panel. Material-sound-absorbing coefficients are reported in Tab. 3, and they have been selected from the database of the software. For polyamide experimental data presented in this paper has been used.

In the classroom, acoustic tests were performed according to the ISO 16283-3:2016 standard (ISO 16283:2016) through the loudspeaker method. The indoor sound pressure level was measured by a sound pressure meter LD-831-C fulfilling the standard IEC 60942 (IEC 60942:2017). Experimental data were used to verify whether the numerical model can predict the acoustic conditions in the

classroom correctly. Measured and estimated reverberation time TR are shown in Fig. 11, while the reverberation time estimated for the different panels' positions is reported in Fig. 12.

Table 3 – Sound absorption coefficients α of the materials set in the numerical model defined with Ramsete. Polyamide sound absorption coefficients relate to incident sound waves only

Material	31 Hz	63 Hz	125 Hz	250 Hz	500 Hz	1 kHz	2 kHz	4 kHz
Plaster (walls)	0.01	0.01	0.01	0.01	0.01	0.02	0.02	0.02
Window - slightly open	0.4	0.8	0.8	0.8	0.8	0.8	0.9	0.99
Glass (windows)	0.21	0.42	0.35	0.25	0.18	0.12	0.07	0.04
Floor	0.02	0.03	0.03	0.03	0.04	0.04	0.04	0.04
Wood (window)	0.06	0.12	0.17	0.2	0.21	0.22	0.18	0.12
Painted wood (ceiling)	0.06	0.11	0.11	0.12	0.12	0.12	0.1	0.1
Plaster on wood (ceiling)	0.02	0.03	0.04	0.05	0.06	0.07	0.07	0.06
Chairs	0.08	0.1	0.15	0.74	0.82	0.9	0.9	0.78
Polyam.- 25 kg/m ³ - 10 cm	0.03	0.1	0.26	0.62	0.96	0.94	0.98	0.9

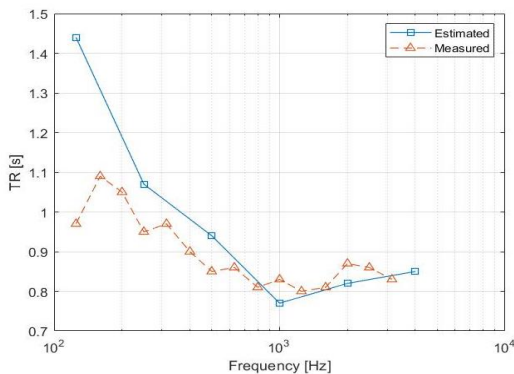


Fig. 11 – Comparison between estimated and measured reverberation time TR in the test case in Barcelona

4. Discussion

Through the analysis of experimental and numerical data, an assessment of whether polyamide is suitable for the realization of panels destined for building refurbishment was performed.

4.1 Experimental Results

Fig. 2 shows the measured equivalent thermal conductivity of polyamide as a function of density.

Density does not affect the material's thermal properties significantly, and measured values are comparable to those of commercial insulation materials such as mineral wool. However, the best performance was shown by the lightest panel.

According to Fig. 3 and Fig. 4, density affects the material's acoustic properties in the low-middle frequency range. The typical trend for porous materials, with low values at low frequencies and high values in the high-frequency range, is detected. According to Fig. 3, lower sound absorption coefficients are measured for higher density values; indeed, compact wool behaves as a stiff spring that reflects the sound energy. Fig. 4 refers to samples 10-cm thick and shows an overall performance improvement in the low-frequency region for all the tested samples thanks to the greater thickness. Fig. 5 and Fig. 6 show the sound transmission loss TL results. In Fig. 5, all five samples feature a similar trend, and higher panel density entails lower TL : high-density samples reflect the sound energy backwards, thus reducing the sound transmitted component.

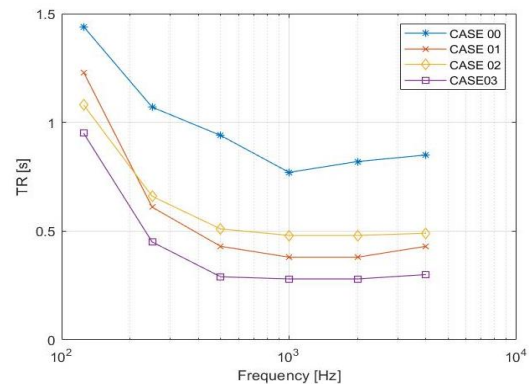


Fig. 12 – Reverberation time TR estimated in the different scenarios for the test case in Barcelona

In Fig. 6, the sound absorption performance is better throughout the entire frequency range thanks to the sample thickness of 100 mm, and the five plots are more distant from each other.

4.2 Numerical Results

As regards the numerical analysis, Fig. 10 shows that the presence of panels installed indoors improves the operative temperature. The number of days when the indoor operative temperature is

lower than 19 °C decreases depending on the panel position. When considering panels installed only on a surface, i.e., *CASE01* and *CASE02*, the best condition is represented by the panel installed on the façade; indeed, this is the only wall facing the external environment. The more significant improvement belongs to scenario *CASE03* with panels installed on both the façade and the ceiling, and this is an expected result since a wider surface is treated. However, a weak point is possible water condensation in the wall, and this requires the installation of a vapor barrier.

As the numerical and measured results in Fig. 11 are comparable, the numerical model defined in Ramsete can be used to design interventions for improving indoor acoustic comfort. Fig. 12 shows that when the panels are installed indoors, *TR* is lower than 0.62 s, which corresponds to the optimal reverberation time for environments destined for speech and sports activities suggested by the UNI 11367 (UNI, 2010). The greatest improvement is detected between 200 and 1200 Hz, where *TR* reduces by 0.5 s. Results are comparable for *CASE01* and *CASE02*, but panels installed on the ceiling are more effective at low frequency, while the panel on the internal surface of the façade is more effective in the middle-high frequency range. The best improvement is detected for *CASE03*, with panels installed both on walls and ceiling, and it is coherent with the theory. However, sound-absorption improvement is expected when considering polyamide properties for diffuse sound, but this data is obtainable only by tests performed in the sound reverberation room.

5. Conclusion

The study investigated experimentally and numerically the thermal and acoustic properties of polyamide 6.6. Experimental results have shown that polyamide has interesting properties, which are comparable to commercial insulating materials. Therefore, it could be used for realizing building elements. Results show that density influences sound properties significantly: low-density panels show better thermal insulation (λ_{eq} between 0.034 and 0.0382 W/(m K)) and sound insulation properties (α higher

than 0.9 for frequency higher than 400 Hz), while high-density panels show better sound insulation properties which depend also on thickness.

Numerical results show that the panels when installed indoors on the walls and ceiling increase the indoor operative temperature in winter and reduce the reverberation time. Therefore, this material is suitable for building thermal and acoustic refurbishment. However, further analysis is needed to evaluate the thermal performance in summer, sound performance related to the diffuse sound field, material containment, and fire resistance.

Acknowledgement

The contribution has been supported by TAČR NCK CAMEB nr. TN01000056/06, and by the Department of Mechanical and Industrial Engineering of the University of Brescia through the MetATer PRD project.

Nomenclature

<i>A</i>	surface (m ²)
<i>c</i>	specific heat (J/(kg K))
<i>c_{air}</i>	sound speed in air (m/s)
<i>d</i>	distance between microphones (m)
<i>f_l</i>	lower working frequency (Hz)
FFT	Fast Fourier Transform
<i>f_u</i>	upper working frequency (Hz)
<i>q</i>	heat flux (W)
<i>R</i>	thermal resistance (m ² K/W)
<i>s</i>	thickness (m)
<i>S</i>	total absorption surface (m ²)
<i>T</i>	temperature (°C)
<i>TL</i>	sound transmission loss (-)
<i>Top</i>	indoor operative temperature (°C)
<i>TR</i>	reverberation time (s)
<i>V</i>	volume (m ³)
α	sound absorption coefficient (-)
λ	thermal conductivity (W/(m K))
λ_{eq}	equivalent thermal conductivity (W/(m K))
η	sound reflection coefficient (-)
ρ	density (kg/m ³)
τ	sound transmission coefficient (-)

References

- ASTM. 2019. "ASTM E2611 Standard Test Method for Normal Incidence Determination of Porous Material Acoustical Properties Based on the Transfer Matrix Method."
- BSI. 2016. "BS EN ISO 16283-3:2016 Acoustics — Field measurement of sound insulation in buildings and of building elements — Part 3: Façade sound insulation."
- Carnemolla, P; S. Robinson, and K. Lay. 2021. "Towards inclusive cities and social sustainability: A scoping review of initiatives to support the inclusion of people with intellectual disability in civic and social activities." *City, Culture and Society* 25: 100398. doi: <https://doi.org/10.1016/j.ccs.2021.100398>
- CIBSE. 2015. "CIBSE - Guide A - Environmental design."
- Drochytka, R., M. Dvorakova, and J. Hodna. 2017. "Performance Evaluation and Research of Alternative Thermal Insulation Based on Waste Polyester Fibers." *Procedia Engineering* 195: 236–243. doi: <https://doi.org/10.1016/j.proeng.2017.04.549>
- González-Eguino, M. 2015. "Energy poverty: An overview." *Renewable and Sustainable Energy Reviews* 47: 377–385. doi: <https://doi.org/10.1016/j.rser.2015.03.013>
- Ibrahim, S., and A. Meawad. 2018. "Assessment of waste packaging glass bottles as supplementary cementitious materials." *Construction and Building Materials* 182: 451–458. doi: <https://doi.org/10.1016/j.conbuildmat.2018.06.119>
- IEC. 2017. "IEC 60942:2017 - Electroacoustics – Sound calibrators"
- Kudzal, A., S. Pliestic, D. Filipovic, I. Kovacev, K. Copek, Z. Janjecic, and D. Bedekovic. 2018. "Mechanical properties of ten-egg boxes made of different materials." *Journal of Food Science and Technology* 55: 1325–1330. doi: <https://doi.org/10.1007/s13197-018-3043-z>
- Mansour, A., and S. Ali. 2015. "Reusing waste plastic bottles as an alternative sustainable building material." *Energy for Sustainable Development* 24: 79–85. doi: <https://doi.org/10.1016/j.esd.2014.11.001>
- Neri, M., M. Pilotelli, M. Traversi, E. Levi, E. A. Piana, M. Bannò, E. Cuerva, P. Pujadas, and A. Guardo. 2021a. "Conversion of end-of-life household materials into building insulating low-cost solutions for the development of vulnerable contexts: Review and outlook towards a circular and sustainable economy." *Sustainability* 13(8): 4397. doi: <https://doi.org/10.3390/su13084397>
- Neri, M., E. Levi, E. Cuerva, F. Pardo-Bosch, A. G. Zabaleta, and P. Pujadas. 2021b. "Sound absorbing and insulating low-cost panels from end-of-life household materials for the development of vulnerable contexts in circular economy perspective." *Applied Sciences* 11(12): 5372. doi: <https://doi.org/10.3390/app11125372>
- Polyamide 6.6 characteristics. Available at <https://designerdata.nl/materials/plastics/thermo-plastics/polyamide-6.6>. Accessed on the 15th of April 2022.
- Secchi, S., F. Asdrubali, G. Cellai, E. Nannipieri, A. Rotili, and I. Vannucchi. 2015. "Experimental and environmental analysis of new sound-absorbing and insulating elements in recycled cardboard." *Journal of Building Engineering* 5: 1–12. doi: <https://doi.org/10.1016/j.jobe.2015.10.005>
- United Nations. 2015. "Transforming Our World: The 2030 Agenda for Sustainable Development."
- UNI. 2010. "UNI 11367:2010 Acoustic classification of building units - procedure for evaluation and verification in situ."

Assessment of Demand-Side Management on the Performance of a Single-Dwelling Mechanical Ventilation Plus Radiant Floor System

Paolo Bonato – Eurac Research, Italy – paolo.bonato@eurac.edu

Anton Soppelsa – Eurac Research, Italy – anton.soppelsa@eurac.edu

Marta Avantaggiato – Eurotherm, Italy – marta.avantaggiato@eurotherm.info

Roberto Fedrizzi – Eurac Research, Italy – roberto.fedrizzi@eurac.edu

Abstract

This paper focuses on the profitability of demand-side management strategies developed for a single-dwelling mechanical ventilation plus radiant floor system. Energy savings and comfort indicators are quantified for a number of control options, including demand-controlled ventilation and temperature setbacks. The assessment is based on numerical energy simulations conducted in TRNSYS for the climate of Bolzano (Italy). To perform the simulations, numerical models of the energy system and the reference dwelling were developed. Based on the analysed climate and building, it was found that demand-side management strategies can have a significant impact on the energy consumption and time distribution of energy loads: demand control ventilation allows the achievement of consistent energy savings in the electrical consumption of the fans (up to 37 %), whereas the use of an adaptive dehumidification setpoint can lead to savings within the range of 10 % in summer electrical consumption. The use of non-occupancy temperature setbacks does not show a significant impact on the annual thermal demand, although the time pattern of the loads is considerably affected, with a cascade effect on the performance of the air-to-water heat pump. The use of the climatic curve parameters at the generator allows an improvement of the electrical performance of the heat pump, increasing the SCOP of more than 20 %.

1. Introduction

The smart management of heating, ventilation and air conditioning systems is an active area of research, as new controls are developed to reduce energy consumption and improve occupant hygro-

thermal comfort. Innovative solutions are moving on from simple strategies, providing an excess of ventilation to deal with poor or no information available on occupation, to providing just enough ventilation to fulfil comfort needs, thus avoiding waste of thermal and electric energy. This trend is favored by the availability of incrementally cheaper sensors and control hardware (Araújo et al., 2020), allowing for a detailed monitoring of the operation conditions and control of system components.

This paper investigates the impact of different control strategies on the performance of a single-dwelling mechanical ventilation and radiant floor system in the context of multi-family houses in Bolzano (Italy). Although a vast literature already exists on the topic of optimization of HVAC operational parameters (Gholamzadehmir et al., 2020; Selmats et al., 2020), this paper aims to contribute by providing a fresh perspective, since:

- it focuses on management strategies that could be easily adopted by using sensors and control hardware already on the market;
- it focuses on the growing sector of renovated buildings, where the use of mechanical ventilation and heat pumps is becoming a wide-spread solution;
- the impact of single-control choices are analysed considering not only the energy domain, but also IAQ and thermal comfort;
- the performances of a real ventilation unit are measured in the laboratory and used to calibrate the numerical model to provide more reliable results.

This study was performed as part of the FESR project NewAir, which hosted the development of an innovative mechanical ventilation unit with dehumidification.

2. Methodology

To assess the energy and comfort signatures of the controls presented in the following, annual energy numerical simulations were performed with dynamic energy simulation software (TRNSYS (Klein et al., 1979)), coupled with a plug-in (TRNFLOW) modeling airflows and pollutant transport. Numerical models are elaborated accordingly after the following steps:

- Development of the thermal model of a renovated flat including a heat-pump-based energy system and radiant floors;
- Development and calibration of the numerical model of a ventilation based on the performance of a prototype tested in the laboratory.

Concerning Key Performance Indicators, the impact of single control strategies is assessed based on a set of indicators, which are (I) heat pump thermal energy generation, (II) heat pump electricity consumption, (III) electricity consumption of fans and refrigerant cycle in the ventilation unit, (IV) overheating / undercooling for thermal comfort and (V) occupancy hours distribution by CO₂ concentration classes according to (EN 16798-1, 2019).

Table 1 – CO₂ concentration thresholds for IAQ (EN 16798-1, 2019)

Class	Living room [ppm]	Bedroom [ppm]
1	< 950	< 780
2	950 < CO ₂ < 1200	780 < CO ₂ < 950
3	1200 < CO ₂ < 1750	950 < CO ₂ < 1250
4	> 1750	> 1250

2.1 Reference Thermal Zone

The dwelling studied in this work is located in a multi-family house in Bolzano (Italy) and has a heated floor area equal to about 68 m². The apartment is divided into a living room, two bedrooms, a kitchen, a bathroom and a corridor. The thermal model of the dwelling is divided into six different thermal zones (one per room), each

containing an air node. Table 2 lists the main parameters of such a model. The occupancy profile is developed based on a three-state model: a person can be “away” or “at home and sleeping” or “at home and active”. Depending on the occupancy status, different generation rates for internal gains (metabolism, use of appliances and lighting) and CO₂ emission are considered.

Table 2 – Thermal model parameters

Properties of building assemblies		
Glass, g-value	0.63	-
Glass, U-value	0.81	W/(m ² K)
Window frame, U-value	0.93	W/(m ² K)
External walls, U-value	0.35	W/(m ² K)
Ventilation and infiltrations		
Design ventilation rate	0.75	ach
Infiltration rate at 50 Pa	1.5	ach
Internal gains and occupancy rate		
Occupants “home and active” (1.2 met (SIA, 2015)), latent gains	0.0153	g/s/pers
Occupants “home and active” (1.2 met (SIA, 2015)), sensible gains	76	W/pers
Appliances installed power (standby consumption: 10 %) (SIA, 2015)	10	W/m ²
Lighting installed power (SIA, 2015)	2.7	W/m ²
Crowding index	0.044	pers/m ²
Full occupancy	3	pers
Thermostat settings		
Air temperature - Space heating	21	°C
Air temperature - Space cooling	25	°C
CO ₂ transport model		
CO ₂ generation, occupants “home and active” (based on (Persily & De Jonge, 2017))	0.009039	g/s/pers
CO ₂ generation, occupants “home and sleeping” (based on (Persily & De Jonge, 2017))	0.007123	g/s/pers
Outdoor CO ₂ concentration	400	ppm
Radiant floors		
Winter performance (room at 20 °C, water inlet at 30 °C, DT = 5 K)	36	W/m ²
Summer performance (room at 26 °C, water inlet at 16 °C, DT = 5 K)	30	W/m ²
Air-to-water heat pump		
COP (A7/W35)	4.17	-
EER (A35/W7)	3.02	-

The energy system is based on a 3 kW air-to-water reversible heat pump, which is able to work at partial loads in the range of 40-100 % compressor

speed. For the sake of simplicity, it is assumed that domestic hot water is prepared with an additional heat generator. The heat pump numerical model is based on the performance map of a commercial product, including multiple air temperatures, water temperatures and compressor speeds. The space heating and cooling network is composed of the heat pump, a small thermal buffer and a radiant floor system. It is assumed that the thermal plant is activated without any restriction on the time of the day, and that the heating season spans the 1st of October to the 15th of April. It is assumed that sensors are installed in all rooms, except for the corridor and bathroom, to monitor temperature, humidity and CO₂ level. The radiant floor works both in heating and cooling working modes. The water loops in living room and bedrooms are managed based on the local temperature measures, whereas the ones in the kitchen and bathroom are controlled based on the living room temperature reading and can provide only heating. The supply temperature to the radiant floors is regulated based on the climatic curves shown in Fig. 1, whereas the water flow rate is governed in each loop by on-off valves activated when the air temperature thresholds are exceeded.

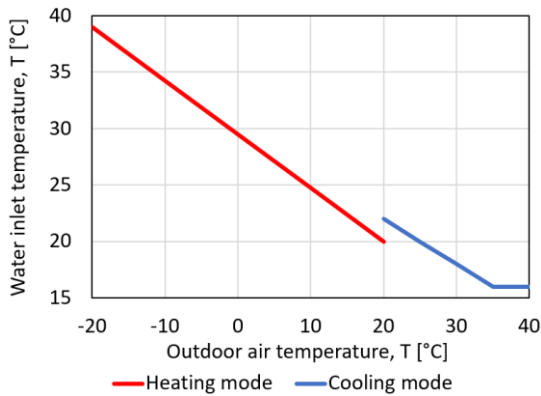


Fig. 1 – Climatic curves applied to the radiant floor system

An annual dataset of climate data was generated from the Meteonorm database for the locality of Bolzano (Italy). This dataset contains hourly values of climatic variables, such as convective air temperature and humidity, solar irradiation and intensity of wind for a typical meteorological year.

2.2 Mechanical Ventilation Unit

In the FESR project “NewAir”, a single-dwelling mechanical ventilation unit was developed to supply fresh air, provide dehumidification during summertime and support the distribution of space heating/cooling thermal power. This unit is double flow and integrates a high-efficiency heat recovery unit, a water-to-air heat exchanger, as well as a refrigerant cycle that is used for dehumidification. In more detail, the condenser and the evaporator of the refrigerant cycle are crossed by the supply airflow and a pre-cooling coil is also activated whenever dehumidification is required. Two dampers regulate the heat recovery bypass and the amount of indoor air that is circulated.

The numerical model of the ventilation unit consists of multiple TRNSYS Types, each simulating an energy component of the ventilation unit. Selected parameters were tuned to replicate the performance of the ventilation unit developed in the NewAir project as closely as possible. More specifically, the data sources for the calibration process were:

- Laboratory measures for (1) external pressure - airflow rate - electrical consumption curves, (2) thermal efficiency of the bypass to the heat recovery and (3) dehumidification capacity;
- Online calculators and datasheets from manufacturers for the thermal performances of heat recovery and water coil.

Table 3 lists the maximum airflow rates and the fan consumption in different working modes, derived assuming external pressure losses equal to 100 Pa at 200 m³/h.

Table 3 – Working modes of the ventilation unit

Working mode	Fresh air [m ³ /h]	Circulated air [m ³ /h]	Supply air [m ³ /h]	Fan cons. [W]
Renewal	140	-	140	110
Circulation	-	200	200	75
Renewal and circulation	100	100	200	124

The ventilation unit is connected to the different indoor spaces by three separate aeraulic networks (supply air, return air and air circulation air), as shown in Fig. 2. The airflow is split among living room and bedrooms based on the floor area.

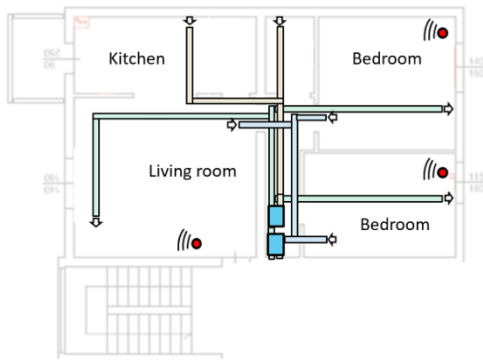


Fig. 2 – Schematic of the aeraulic networks in the apartment. Return air in orange, supply air in green, air circulation in blue

2.3 Demand-Side Management

The demand-side management of energy systems aims at optimizing the use of energy by acting on the consumption picture, that is, on energy use, energy quality or load time-patterns. In the context of a single-dwelling mechanical ventilation plus radiant floor system, this study quantifies the effects of the following control management strategies designed to reduce energy waste:

- Implementation of demand-controlled ventilation (DCV) (Emmerich & Persily, 2001), that is, the modulation of the fresh air intake to meet the ventilation demand of the zone. In this work, multiple options are compared: (1) occupancy-based DCV strategy, where the control hardware is reactive to human presence through, for example, PIR sensors or geofencing, and triggers air renewal at nominal airflow rate when the apartment is occupied; (2) CO₂-based DCV strategy, where the fresh air intake is modulated based on the CO₂ concentration. In this case, the system can work in on-off mode based on a single hysteresis, but could also implement a multistep or a proportional control. In the case of multiple CO₂ sensors, the most critical reading is considered for the fresh airflow calculations. Fig. 4 shows the selected CO₂-based DCV strategies and the related CO₂ thresholds, which were identified based on (EN 16798-1, 2019) limits for IAQ Category I.
- Use of moving thresholds to trigger the dehumidification function of the ventilation unit during the cooling season. A constant relative humidity threshold is a common way of managing dehu-

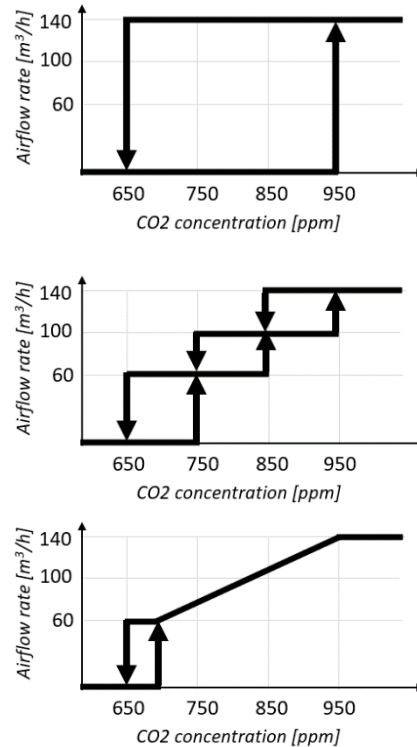


Fig. 3 – CO₂-based DCV with on-off hysteresis (top), multistep modulation (middle) and proportional modulation (bottom)

midification units, but an alternative solution could be dividing the goals of guaranteeing comfort conditions to occupants and avoiding condensation over the radiant floors. To assess such a strategy, a comparison is performed between a baseline scenario (constant setpoint equal to 55 % relative humidity) and an advanced scenario where multiple movable thresholds are implemented: (1) a limit of 60 % relative humidity and 12 g/kg absolute humidity is applied when the dwelling is occupied to guarantee acceptable comfort (Class II comfort according to (EN 16798-1, 2019)); (2) a limit in absolute humidity is applied to avoid condensation based on the working conditions of the radiant floors (i.e., temperature at the inlet of the radiant system). When multiple criteria apply at the same time, the strictest threshold is considered.

- Use of moving thermostat temperature setpoints. A 2 K setback is applied to the air temperature thresholds in two separate circumstances, that is, when the apartment is not occupied (non-occupancy setback) or between 23:00 and 06:00 (night setback). To demonstrate, Fig. 4 shows the air temperature setpoints for a single day.



Fig. 4 – Temperature setpoints with non-occupancy setbacks (top) and night setbacks (bottom)

- The implementation of the climatic curve parameters directly to the heat pump rather than to the radiant collectors during wintertime is to produce heat at the required temperature and to avoid a pointless reduction in the heat quality with thermostatic valves. The efficiency of heat pumps is indeed correlated to the temperature level of the water in the condenser, with higher Coefficients of Performance (COPs) at lower water temperatures.

3. Results and Discussion

This section presents the numerical results of the energy simulations divided by analyzed strategy.

3.1 Demand-Controlled Ventilation

Several DCV strategies are compared with a baseline where air renewal is always active. Table 4 reports the numerical results for different scenarios. The air quality is medium-high in all simulated cases. Slightly worse results are found for DCV strategies based on CO₂ concentration, but also in this case, C1 and C2 categories are vastly more populated than C3 and C4. Space heating and cooling thermal demands show limited variations, with higher heating demand and lower cooling demand at higher air change rates. During wintertime, the effect of the additional heat losses due to overventilation is indeed limited by the high-efficiency heat recovery unit. During summertime, higher air change rate may provide at times some benefit in removing the excess heat from indoor

spaces, thus reducing the active cooling load. A more evident impact is registered on dehumidification, since the removal of indoor-generated humidity is also influenced by the hygienic air change. DCV strategies are indeed linked to an increase in the consumption of the refrigerant cycle in the range of 11 % to 20 % with respect to the baseline. The electrical consumption of the fans is reduced in the range of -17 % to -38 % in the DCV scenarios, as a result of the lower air volumes exchanged throughout the year. The best-performing DCV strategies are the ones based on CO₂ concentration, since CO₂ generation is dependent on the number and the activity of occupants and thus the air change can be more sharply adapted to the effective demand for air change. Among CO₂-based strategies, no significant difference is found between multistep and proportional control, whereas the on-off strategy is outperformed, as it cannot modulate the airflow and thus is less flexible than the others. Neither overheating nor undercooling issues are found in any of the tested scenarios. The annual HVAC electrical consumption is reduced by DCV between -6 % and -13 % compared with the baseline, but it has to be noted that the advantages of such strategies may vary significantly depending on the occupancy patterns of spaces (IEA, 1997).

Table 4 – Numerical results for scenarios (1) baseline, (2) DCV based on occupancy, (3) DCV CO₂ based with on-off hysteresis, (4) multistep modulation and (5) proportional modulation

	Annual energy demand						CO ₂ classes			
	Q _{heat} kWh	Q _{cool} kWh	W _{fan} kWh	W _{rf} kWh	W _{hp} kWh	W _{tot} kWh	C1 %	C2 %	C3 %	C4 %
1	3333	1515	942	186	1425	2553	44	40	16	0
2	3333	1519	778	207	1423	2408	44	40	17	0
3	3320	1547	674	233	1424	2331	40	42	18	0
4	3316	1535	587	229	1417	2232	38	42	20	0
5	3318	1529	591	224	1416	2231	38	43	19	0

3.2 Moving Thresholds for Dehumidification

Fig. 5 shows the numerical results of the energy simulations for the cooling season: the use of mobile thresholds is compared with a baseline with a constant humidity setpoint equal to 55 % relative humidity. As may be seen, the use of moving thresholds allows the achievement of significant energy savings (about -13 % total electrical consumption). The

impact is not limited to the refrigerant cycle consumption (-40 %), but extends to fan consumption (-4 %) and active cooling demand (-9 %).

The active dehumidification triggers the “renewal and circulation” mode of the ventilation unit, which provides higher airflow rates to maximise the dehumidification effect, but also increases the fan consumption. Dehumidification is also linked to the active cooling load, since before entering the refrigerant cycle, the supply airflow is pre-cooled by a water coil as described above, thus generating a thermal load for the heat pump. The lower electrical consumption of refrigerant cycle, fan and heat pump points to a less frequent use of active dehumidification. No significant difference is found in terms of air quality and thermal comfort. It has to be noted that the working conditions of the radiant floor, and thus the humidity threshold for active dehumidification, will depend on the intensity of the cooling load. In this sense, more challenging conditions for the radiant floor during summertime will represent a smaller possibility of achieving savings by using a movable setpoint.

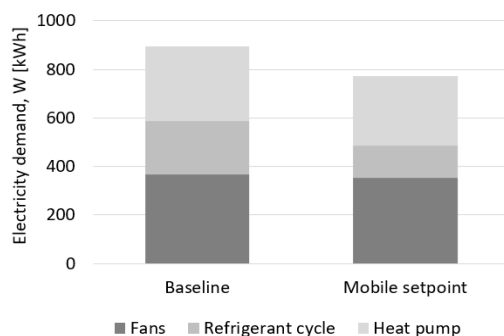


Fig. 5 – Electrical consumption during the cooling season

3.3 Non-Occupancy and Night Temperature Setback

The use of temperature setbacks is assessed by comparing a baseline scenario where the setpoints remain unvaried to the use of a 2 K setback during non-occupancy periods or during night-time. In the non-occupancy scenario, the setback is applied every time the dwelling is empty, which is equal to about 19 % percent of the year, or 1680 hours/year, divided into events that are mostly 1 to 4 hours long for the studied occupancy schedule. The night setback is applied for about 29 % of the year, or 2555 hours/year, in events that are each 7 hours long.

Fig. 6 and Fig. 7 show the monthly thermal energy demand and the percentage variation of heat performance indicators SCOP and SEER with respect to the baseline. As may be seen, the use of the temperature setback leads only to a limited reduction of the thermal demand (in the range of -1 % to -5 % on an annual basis), likely due to the fact that the setback is applied only for limited periods (especially in the non-occupancy scenario) and the thermal losses of the building are minimized by fair envelope properties and low ventilation/infiltration heat losses. The annual electricity consumption of the heat pump is reduced by a factor of -3 % in the non-occupancy setback scenario, and -12 % in the night setback scenario. This is only partially connected to the reduction of the thermal load, since the performance of the heat pump is also affected by the setbacks, as shown in Fig. 6. More specifically, the use of non-occupancy setbacks leads to better SEER during summertime, whereas the use of the night setback leads to higher SCOPs in winter and lower SEERs in summer.

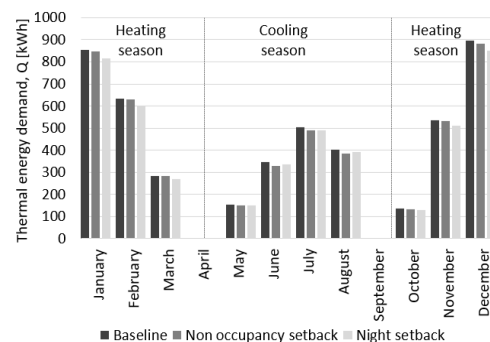


Fig. 6 – Monthly thermal energy demand

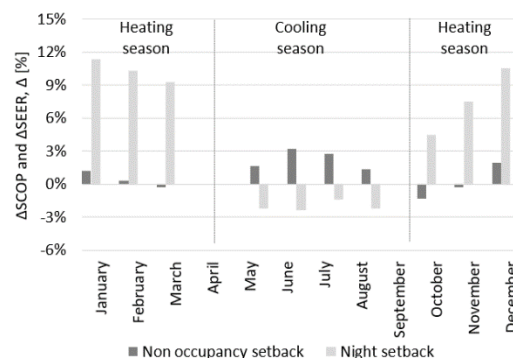


Fig. 7 – SCOP and SEER variation in setback scenarios

To better understand the underlying causes, the hourly daily averages of the thermal energy produced by the heat pump in heating and cooling are

shown in Fig. 8 for the months of January and July. Even though the thermal loads do not significantly vary in absolute terms, as discussed above, the use of setbacks causes a massive impact on the time patterns of thermal energy generation. In the non-occupancy setback scenario, the load profile tends to differ from the baseline during the daytime when occupants are mostly away and a peak in energy demand is registered at around 18-20 h around the time when the dwelling is be occupied again.

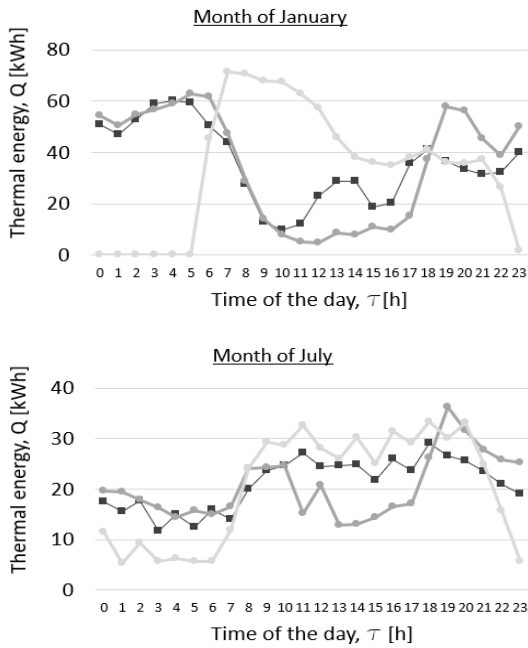


Fig. 8 – Hourly averages of heat pump energy generation

As expected, the use of night setback leads to lower thermal loads during the night, but most of the energy is then delivered during the daytime. The variation of the time patterns for energy generation has quite a significant effect on the air-to-water heat pump performances, since the external air temperature varies throughout the day, with generally higher temperatures during the day (better COPs and worse EERs) and lower temperatures during the night (lower COPs and higher EERs). Thermal comfort is maintained at all times, although it is found that, when setbacks are applied, air heating/cooling is called on to support the radiant floor, which has a slower response to changing temperature setpoints due to the thermal capacity of the screed.

3.4 Implementation of Climatic Curve at the Generator

A baseline scenario, where the heat pump produces warm water at 40 °C and a thermostatic valve controls the inlet temperature to the radiant floors, is compared with an advanced scenario, where the climatic curve is implemented directly at the heat pump to avoid depreciation of the heat quality.

Table 5 – Performances in baseline and advanced scenarios

Description	Q_{heat} kWh	W_{hp} kWh	SCOP -	Δ %
Baseline	3315	1150	2.88	-
Advanced	3226	863	3.74	23 %

As shown in Table 5, the thermal load in the baseline is higher, mostly due to the more intense thermal losses from the water distribution system (about +100 kWh/y). It is also found that applying the climatic curve at the generator leads to a significant improvement in the electrical performances of the heat pump, with a SCOP increasing from 2.9 to 3.7, about +23 % percentage improvement. This is due to the better working conditions of the heat pump, which is not required to produce water at 40 °C, but can profit from a lower-temperature energy demand. It is, however, remarked that state-of-the-art heat pumps can usually offer some form of climatic control. In this case, the simulation results simply reflect the importance of selecting the most appropriate climatic curve based on type of terminals and energy performance of the dwelling to avoid energy waste.

4. Conclusions

This paper presents a study on the performance of different demand-side management strategies applied to a ventilation system plus radiant floor system in the climate of Bolzano.

Based on the analyzed building and climate, the implementation of DCV strategies shows good potential for reducing the electrical consumption of fans (up to -38 %) without worsening the indoor air quality. Space heating and cooling thermal demand are not significantly affected, whereas a moderate impact is registered on dehumidification. It is found

that the use of moving setpoints could be a valid strategy to adapt the operation of the dehumidification system to the dehumidification load and reduce the summer energy consumption (-10 % for the studied conditions). The use of non-occupancy or night setbacks does not lead to significantly different annual energy demands, but a considerable impact is found on the time distribution of the thermal loads, with a cascade effect on the performance of the heat pump. More specifically, night setbacks allow the thermal loads to be shifted to the daytime, with a positive effect on the winter performances of the heat pump and a negative effect in summer. Finally, the implementation of a climatic curve at heat pump level allows the achievement of lower heat losses from the distribution system and a significant improvement in the heat pump performance. Overall, it was found that air change, thermal load and dehumidification are interconnected: changes in the control strategies looking at one domain at the time may lead to suboptimal solutions. In addition, it was found that the performance of the heat pump is massively influenced by the controls of the heating/cooling emission system and that there are options for load shifting that could be synergically exploited by photovoltaics. Far-reaching integrated control logics that can better capture the overall impact of single-control choices to reach one or multiple goals are to be implemented to achieve significant energy savings, while preserving optimal comfort conditions. Future studies will focus on the use of Model Predictive Control (MPC) based on forecasted weather conditions and dwelling loads.

Acknowledgement

The research presented in this paper is supported by funding from the European Regional Development Fund, through the operational programme POR FESR 2014-2020 of the Province of Bolzano, under the project number FESR 1116, named: NEW-AIR - Nuovo approccio per una qualità degli ambienti interni energeticamente efficiente: ricerca e aziende fanno sistema in Alto Adige.

Nomenclature

Symbols

HVAC	Heating, Ventilation and Conditioning
IAQ	Indoor Air Quality
Q	Thermal energy demand, [kWh]
SCOP	Seasonal Coefficient of Performance, [-]
SEER	Seasonal Energy Efficiency Ratio, [-]
W	Electricity consumption, [kWh]

Subscripts/Superscripts

cool	referred to cooling energy
fan	referred to the fans
heat	referred to heating energy
hp	referred to the heat pump system
rf	referred to refrigerant cycle

References

- Araújo, T., L. Silva, and A. Moreira. 2020. "Evaluation of Low-Cost Sensors for Weather and Carbon Dioxide Monitoring in Internet of Things Context." *Internet of Things* 1(2): 286-308. <https://doi.org/10.3390/iot1020017>
- CEN. 2019. *EN 16798-1. 2019. Energy performance of buildings - Ventilation for buildings - Part 1.*
- Emmerich, S., and A. K. Persily. 2001. "State-of-the-art Review of CO₂ Demand Controlled Ventilation Technology and Application." *NISTIR 6729*.
- Gholamzadehmir, M., C. Del Pero, S. Buffa, R. Fedrizzi, and N. Aste. 2020. "Adaptive-predictive control strategy for HVAC systems in smart buildings - A review." *Sustainable Cities and Society* 65. <https://doi.org/10.1016/j.scs.2020.102480>
- IEA, International Energy Agency. 1997. "A summary of IEA Annex 18 - Demand Controlled Ventilation Systems"
- Klein, S. A., et al. 1979. "TRNSYS 17, transient system simulation program." University of Wisconsin, WI, USA, www.trnsys.com
- Persily, A., and L. De Jonge. 2017. "Carbon dioxide generation rates for building occupants." *Indoor air* 27(5): 868-879. <https://doi.org/10.1111/ina.12383>
- Selmat, H., M. F. Haniff, Z. M. Sharif, S. M. Attaran, F. M. Sakri, and M. Al'Hapis Bin Abdul Razak. 2020. "Review on HVAC System Optimization Towards Energy Saving Building Operation." *International Energy Journal* 20(3): 345-358.
- SIA. 2015. *SIA 2024: Raumnutzungsdaten für die Energie- und Gebäudetechnik.*

Passive Design Strategies for the Improvement of Summer Indoor Comfort Conditions in Lightweight Steel-Framed Buildings

Nicola Callegaro – University of Trento, Italy – nicola.callegaro@unitn.it

Max Wieser – University of Trento, Italy – max.wieser@unitn.it

Giovanni Manzini – Cogi S.r.l, Italy – lorenzo.manzini@cogi.info

Ivan Kharlamov – Altai State University, Russia – kharlamov-1948@mail.ru

Rossano Albatici – University of Trento, Italy – rossano.albatici@unitn.it

Abstract

The market for lightweight construction systems is growing rapidly due to their potential in terms of prefabrication, ease of transportation and assembly. However, given their thermophysical properties, these types of structures present a limited thermal capacity that may reduce their performance in terms of comfort and energy consumption during the hot seasons. The present paper, through a series of computational fluid dynamics (CFD) simulations, offers a numerical assessment of the performance of an existing lightweight steel-framed building selected as a case study. The data required to perform the simulations are collected with a deep monitoring campaign and the building is analysed in its current state (actual conditions of use) and after the application of simulated passive cooling strategies. The role of natural ventilation, both day and night, is explored by investigating different opening/closing configurations of external windows and internal doors. Moreover, the positive effects of surface thermal mass and shading systems are numerically validated. The results, although limited to a specific context of analysis, show that, with appropriate adaptation strategies, even in lightweight buildings, occupants can achieve adequate levels of comfort, thus reducing the need for cooling. A combined and weighted use of passive solutions results in a reduction of about 3 °C in the average daily indoor temperature. Ventilation at night and solar shading during the day make a steel-framed building as comfortable as a massive one, both with regard to the internal surface temperature of the building components and to the discomfort indices. Changing the mass of the interior cladding of a wall, ceiling or floor, for example, from plasterboard to cement board, is another effective cooling strategy.

1. Introduction

Reducing costs, increasing speed, and minimizing risks have always been the main objectives of the construction industry. Buildings are therefore increasingly made up of standardized and performance-guaranteed components, both considering the systems and the envelope. The market for lightweight steel-framed building systems (LSF) has thus greatly increased over the last few decades, especially in low-rise residential buildings. Several advantages have driven their spread: ease and speed of on-site installation, low weight combined with high mechanical strength, large potential for recycling and reuse, easy prefabrication, flexibility of use for different architectural retrofit purposes, economy in transportation and handling, resistance to moisture and insect attack (Soares et al., 2017).

However, lightweight structures, particularly steel-framed ones, can contribute towards reducing building energy and indoor comfort performance during hot seasons (Lomas & Porritt, 2016) due to steel's high thermal conductivity and lightness (Santos, 2017). This represents a significant challenge, since with the increase in average annual temperature and the continuous growth of electricity demand, particularly of the residential sector, summer air conditioning has had a very significant influence on the overall energy consumption of buildings (Santamouris, 2016).

However, the use of additional thermal mass and high values of internal areal heat capacity can minimize peak heating and cooling loads in lightweight buildings (Di Perna et al., 2011; Kuczyński & Staszczuk, 2020; Rodrigues et al., 2013), especial-

ly when coupled with natural or mechanical ventilation (Yang & Li, 2008). CFD simulation is considered the most valuable tool for designing, verifying, and predicting the indoor thermal comfort level in relation to these aspects. Through this type of simulation, Mora-Pérez et al. (2017) explain the benefits of combined use of mechanical and natural ventilation to maximize comfort and reduce energy consumption. Much attention is often paid to the influence of the specific building component. Deng et al. (2017) discuss in depth the impact of window length, aspect ratio, height above the ground, window opening angle and fly screen porosity on the airflow pattern inside residential buildings. Aryal and Leephakpreeda (2015) emphasize how interior partitions significantly change perceived thermal comfort and the resulting energy consumption for heating and cooling, while Hajdukiewicz et al. (2013) focus on highly-glazed façades in meeting rooms. Few articles simultaneously address different cooling passive strategies through CFD simulation, and the study of lightweight structures, such as steel-framed, is still limited in this field.

In this paper we investigate the effectiveness of lightweight steel-framed structures to ensure, through the implementation of passive design and use strategies, high levels of indoor comfort during the hot season. Through CFD simulation, the paper explores the ways in which natural ventilation, wall heat capacity and external shadings can reduce indoor temperatures and improve comfort. Different windows and door opening/closing patterns are compared at (a) different external wind speeds and (b) the ability of windows shadings to mitigate temperature peaks is evaluated. The behavior of (c) different wall surface claddings with changed weight is also investigated and, finally, a comparison (d) is made between the starting lightweight structure (steel-frame with external insulation), the same structure with the implementation of the aforementioned passive strategies, an insulated reinforced concrete massive structure and an insulated brick structure. Simulations are performed on a case study built in 2018 in Barnaul (RU), southwestern Siberia, and monitored for two years. The continental climate of the area has a high seasonal temperature range with lows of -35°C in winter and highs of $+35^{\circ}\text{C}$ in the hot sea-

son. The summer behavior of the building was examined, taking into account these particular extreme environmental conditions which, however, due to climate change, will also be increasingly common in less severe climates (IPCC, 2021).

2. Materials and Methods

In this section, the case study, methodology and simulation tools, as well as the parameters monitored, are presented. In addition, the characteristics and the boundary conditions of the simulation model, the different passive strategies implemented, and the output variables analysed in Section 3 are described in depth.

2.1 The Case Study

The case study is a single-storey residential building realized, as regards the structural design, with panels made of cold-bent steel profiles (Fig. 1a-1b). The building is about 80 square meters and is divided into entrance, living room-kitchen, bathroom, boiler room and two bedrooms (Fig. 2). An insulated ceiling divides the living space from the pitched roof, made of sandwich panels. The heating system is powered by gas condensation boiler, and a controlled mechanical ventilation ensures the indoor-outdoor air exchange.



Fig. 1 – The building during (a) and at the end of the construction phase (b). Picture by Giovanni Manzini, 2019

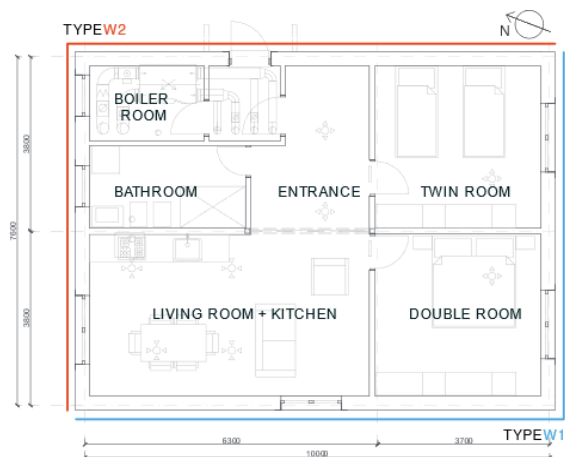


Fig. 2 – Horizontal section of the building

Table 1 – Thermophysical properties of the wall W1

Layers (int. to ext.)	s [cm]	λ [W/(m K)]	ρ [kg/m ³]	c [J/(kg K)]
Plasterboard	2.5	0.2	800	836.8
Insulated Counter-Wall	7	0.072	101.24	1024.3
Glass wool	8	0.035	35	1030
Plasterboard	1.25	0.2	800	836.8
SteelMAX® Structure + insulation	10	0.067	143.78	1022.6
Cement board	1.25	0.35	1150	836.8

Table 2 – Thermophysical properties of the wall W2

Layers (int. to ext.)	s [cm]	λ [W/(m K)]	ρ [kg/m ³]	c [J/(kg K)]
Plasterboard	2.5	0.2	800	836.8
Insulated Counter- Wall	5	0.068	101.2	1024.2
Glass wool	5	0.035	35	1030
Plasterboard	1.25	0.2	800	836.8
SteelMAX® Structure + insulation	10	0.067	143.78	1022.6
Cement board	1.25	0.35	1150	836.8
EPS insulation	5	0.038	21	1260

The building has two different external walls (Tables 1-2, Fig. 2) to test in-situ, through monitoring data, the energy performance of two akin solutions. Table 3 describes the thermal properties of the main building components.

The building is equipped with energy and environmental sensors to monitor its behavior 24 hours a day. The monitored parameters are:

- temperature, relative humidity, and CO₂ of all indoor environments.
- surface and internal temperatures of walls, ceiling, floor.
- inlet and outlet temperature of the controlled mechanical ventilation machine.
- energy consumption.
- external environmental conditions (temperature, humidity, wind speed and direction, solar radiation).

The data monitored provided the necessary information to set the boundary conditions for the simulation model.

2.2 The Simulation Model

Computational fluid dynamics (CFD) is a branch of fluid mechanics that analyses and solves problems involving fluid flows using numerical analysis and data structures (Lomax et al., 2013). CFD analysis involves the simultaneous calculation of temperature and velocity domains, flows and pressures, considering the interaction between these variables. The great advantage of this type of simulation, compared to simplified empirical formulae, is the three-dimensional representation of the results. Properly setting the calculation grid and cell size, which have a significant impact on the calculation time and memory demands, as well as on the accuracy of the results, is a key prerequisite for the robustness of the CFD simulation. The minimum size of the cells is determined according to the specific problem to be analysed: for this case study, the volume of a single calculation cell is 8 cm³ (2x2x2 cm). The number of cells also depends on the calculation domain. In order to include the effect of wind, which is essential for assessing the benefits of natural ventilation, a larger calculation domain than the building envelope is required, which may lead to a higher calculation effort.

Table 3 – Thermal properties of the building components

	W1 Walls	W2 Walls	Ceiling	Ground floor
Thickness [cm]	30	30	43	45
Thermal transmittance [W/m ² K]	0.194	0.186	0.27	0.31
Decrement factor [-]	0.59	0.32	0.07	-
Time lag [h]	6.68	8.8	14.2	-
Internal areal heat capacity [kJ/m ² K]	22.4	20.9	38.2	-
Periodic thermal transmittance [W/m ² K]	0.114	0.06	0.019	-

The domain must be large enough not to bias the result and is typically expressed as a function of the building size. In accordance with Etheridge (2011), the following domains have been evaluated:

- Domain A: this coincides with the internal surface of the envelope. Boundary conditions at the inlets and outlets must be specified to run the simulation
- Domain B: external domain. The supply flow rate is determined as part of the simulation for this type of domain, which has dimensions that are normally twice those of the envelope. This means that the boundary conditions are different, and problems of convergence can arise.
- Domain C: the external flow to the inlet is included in the calculation. This requires extending the domain by an order of magnitude larger than the envelope.
- Domain D (used in the calculation): CFD boundary conditions for internal flows are generated using CFD data for the external flow.

Domain type D used in the case study simulation is a volume of 260 m³ (10.3x7.8x3.25 m) with boundaries that coincide with the internal walls. Based on a calculation previously carried out with an enlarged domain (type C: size of the domain is five times the size of the building), CFD allows wind velocity and air pressure along the building surface

to be calculated. This choice reduces computational effort and, at the same time, enables the wind effects to be adequately considered. As regards the turbulence model for the calculation, the k-epsilon model was applied. The simulation model is built in Flovent®, proprietary software from Mentor Graphics®. For any other specifications regarding the methodology or the theory underlying the calculation, please refer to (Mentor Graphics Corporation, 2018).

2.3 Cooling Passive Strategies

2.3.1 Daytime natural ventilation

The transient simulation investigated the daily behavior of the building to the variation of the external climatic conditions, by focusing the analysis on the 48 hottest hours of the summer (3rd-4th of July). The set time step is 1 hour. Several monitor points were defined at different heights and in different rooms. The initial boundary conditions were set according to the data measured on site (Tab. 4). At first, an average wind velocity of 1.3 m/s in a north-westerly to south-easterly direction was considered, equal to the average wind speed measured in situ on that day. Then, extreme conditions of no wind and strong wind (0 and 5 m/s) were set to verify the reliability of the results and the magnitude of the wind.

Table 4 – Simulation boundary conditions

	Min	Max	Mean
Hourly outdoor temperature [°C] (see also Fig. 7c)	13.6	32.2	23.1
Solar radiation [W/m ²] (at 12.30 PM)		873	
Starting indoor temperature [°C]		25	

Several combinations are simulated (Tab. 5) with different window opening/closing schemes (Fig. 3). The daytime period is considered to start at 4 AM and end at 9 AM. In this case, it was considered that night ventilation was not feasible for other reasons (e.g., safety, noise, security).

Table 5 – Daytime natural ventilation: simulation cases

Sim.	Int. doors	Awning Windows	Hopper Windows	Wind
0	Closed	-	-	-
D10	Closed	-	F1, F2, F4, F5, F6	1.3 m/s
D11	Closed	-	F1, F2, F4, F5, F6	0 m/s
D12	Closed	-	F1, F2, F4, F5, F6	5 m/s
D13	Opened	-	F1, F2, F4, F5, F6	1.3 m/s
D14	Opened	-	F1, F2, F4, F5, F6	0 m/s
D15	Opened	-	F1, F2, F4, F5, F6	5 m/s
D20	Closed	F1, F2, F4	F5, F6	1.3 m/s
D21	Closed	F1, F2, F4	F5, F6	0 m/s
D22	Closed	F1, F2, F4	F5, F6	5 m/s
D23	Opened	F1, F2, F4	F5, F6	1.3 m/s
D24	Opened	F1, F2, F4	F5, F6	0 m/s
D25	Opened	F1, F2, F4	F5, F6	5 m/s



Fig. 3 – Windows nomenclature (a). Awning window example (b); hopper window example (c).

<https://blog.jonnew.com/assets/windows/types.jpg>

For this and all simulations described in the next subsections, the output control variables are:

- Indoor temperature
- Internal wall surface temperature
- Predicted mean vote (PMV) (UNI, 2006)
- Predicted Percentage of Dissatisfied (PPD) (UNI, 2006)

Regarding PMV and PPD, to facilitate the calculation, some conditions were assumed to be constants:

- standing activity (1.2 met).
- summer clothing (0.5 clo).
- a relative humidity of 50 %.

The focus of the research was the thermal performance of the building. No acoustic and/or lighting comfort requirements were considered.

2.3.2 Nighttime cooling ventilation

The reduction of surface temperature of the walls, floor, and roof as a result of opening windows at night was explored by running a dynamic simulation. The role of various external window and internal door closing/opening techniques was examined. The night period is considered to start at 9 PM and end at 4 AM. The boundary conditions for temperature and solar radiation are the same as those shown in Table 4. The different combinations are listed in Table 6.

Table 6 – Nighttime cooling ventilation: simulation cases

Sim.	Int. doors	Awning Windows	Hopper Windows	Wind
0	Closed	-	-	-
N10	Closed	-	F1, F2, F4, F5, F6	0.5 m/s
N11	Closed	-	F1, F2, F4, F5, F6	0 m/s
N12	Closed	-	F1, F2, F4, F5, F6	5 m/s
N13	Opened	-	F1, F2, F4, F5, F6	0.5 m/s
N14	Opened	-	F1, F2, F4, F5, F6	0 m/s
N15	Opened	-	F1, F2, F4, F5, F6	5 m/s
N20	Closed	F1, F2, F4	F5, F6	0.5 m/s
N21	Closed	F1, F2, F4	F5, F6	0 m/s
N22	Closed	F1, F2, F4	F5, F6	5 m/s
N23	Opened	F1, F2, F4	F5, F6	0.5 m/s
N24	Opened	F1, F2, F4	F5, F6	0 m/s
N25	Opened	F1, F2, F4	F5, F6	5 m/s

2.3.3 Influence of thermal mass

To evaluate the effect of the surface thermal mass (UNI, 2017), three different simulations were carried out by varying the internal finishing layer, from plasterboard to cement board to plaster (Table 7).

- Sim n° 0: original case study.
- Sim n° M1: the internal plasterboard is replaced by 2 panels of cement board.

- Sim n° M2: the internal plasterboard is replaced by 3 panels of cement board.
- Sim n° M3: the internal plasterboard is replaced by 2cm of plaster (the air layer in the ceiling is thus eliminated).

The reduction of the surface temperature of the walls, floor, and roof due to the material replacement was studied, as well as the comfort (PMV/PPD) and the reduction of the internal temperature peaks during the day. The dynamic analysis was carried out on two days with conditions similar to those shown in Table 4. The effects were evaluated on the second day of the analysis.

Table 7 – Thermal mass influence: simulation cases

Sim.	Internal areal heat capacity [kJ/(m²K)]		
	North Walls	South Walls	Ceiling
0	20.9	22.4	38.2
M1	33	34.6	43.9
M2	42.2	43.6	49.8
M3	33.3	34.3	52.2

2.3.4 Final comparison

The best cases from the previous 3 analyses were combined to obtain a best practice (case a). This was compared with the original building (case b) and with the same building modifying the load-bearing structure from insulated steel-frame ($\lambda=0.58$ W/(m K), $\rho=100$ kg/m³) to reinforced concrete ($\lambda=1.4$ W/(m K), $\rho=2300$ kg/m³ - case c) to brick ($\lambda=0.35$ W/(m K), $\rho=700$ kg/m³ - case d). A further comparison was made by optimizing "case i" by adding windows external shading (case e). This was simulated by reducing the solar heat gain coefficient of window glass by 85 % when the windows are closed.

3. Results and Discussion

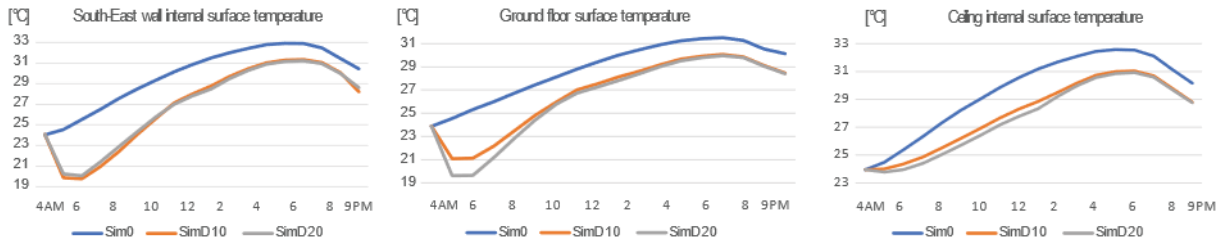
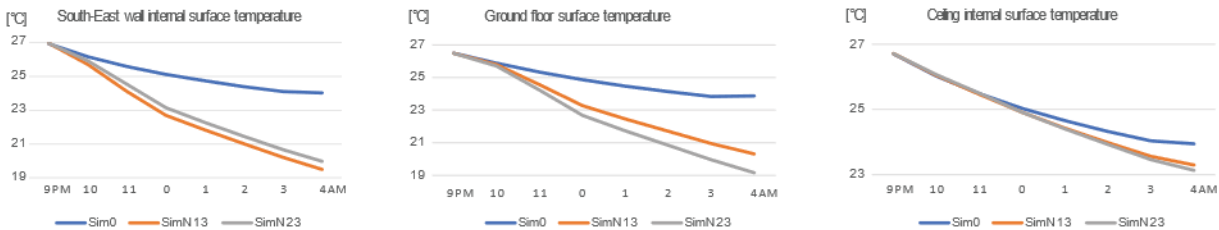
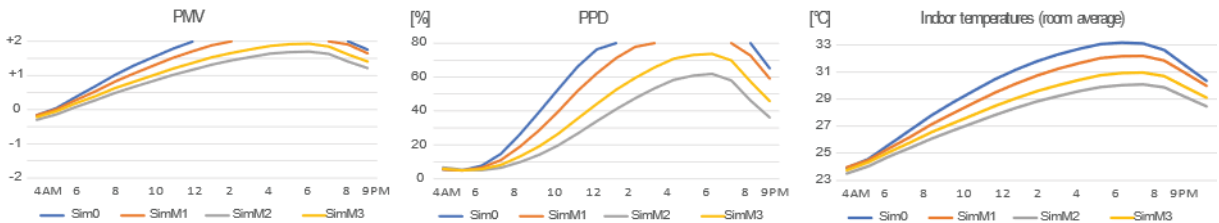
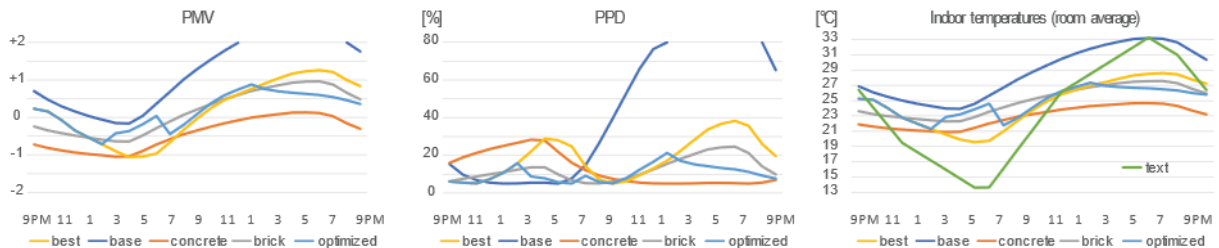
As regards natural daytime ventilation, with reference to the simulations from D10 to D15 shown in Table 5, the most cooled surfaces are the floor (massive element), followed by the leeward external walls, the internal partitions and, finally, the

windward walls and the roof (Fig. 4). The cooling rate is similar for the different configurations. In simulation D15 (strong wind and open internal doors), the greatest benefits are found in terms of reduction of indoor temperature and surface temperature (about 3 °C), but the indoor air velocities lead to unacceptable levels of discomfort. The considerations are similar for simulations D20 to D25 (awning windows). It is worth noting that the results are very dependent on the boundary conditions and are mainly useful for comparison. Simulations D10 and D20, which are, in Fig. 4, compared with the base case, reveal that a proper window opening strategy during the daytime, with appropriate outdoor environmental conditions, can reduce the daily average surface temperature of the building components by approximately 2 °C during a typical summer day.

In the case of nighttime natural ventilation combined with an accurate opening strategy for windows and internal doors, it is possible to reduce the temperature of the internal surfaces of the building by up to 7 °C (Fig. 5). Different natural ventilation strategies lead to different results. The analysis shows that cross ventilation, enabled by the opening of the inner doors, produces a 1 °C reduction in the internal temperature compared with single side ventilation. The combination of curtains and hopper windows (SimN23) is most effective in cooling the air volume near the floor area (Fig. 5), which could positively affect comfort conditions of a person lying at rest.

As regards the analysis performed by modifying the wall and roof cladding surfaces (Fig. 6), it can be stated that:

- in the M1 case study, with the replacement of plasterboard by cement board, the reduction of the average internal temperature is about 1°C during the daytime
- the 3 fibrocement panels(M2), which are, in any case, not easy to install from a technical point of view, so were considered only as a theoretical comparison, would guarantee a temperature reduction of 3 °C, with excellent benefits also in terms of PMV and PPD


 Fig. 4 – Daytime natural ventilation simulations results: internal surface temperatures of different building components (4th of July)

 Fig. 5 – Nighttime natural ventilation simulations results: internal surface temperatures of different building components (4th of July)

 Fig. 6 – Thermal mass simulations results: PMV (a), PPD (b) and indoor temperature (c) trends (4th of July)

 Fig. 7 – Final comparison results: PMV (a), PPD (b) and temperature (c) trends (3rd-4th of July)

- plaster would certainly be more efficient than plasterboard (M3), with a reduction of about 2.2 °C in the average internal temperature.

This positive effect also affects internal surface temperatures for all building components, thus increasing the indoor mean radiant temperature. Therefore, in the M2 case, the percentage reduction of PPD is over 20 %.

Fig. 7 compares data from the on-site monitoring system (base) with simulations described in Section 2.3.4. Massive/Solid constructions (concrete and brick) prove to be effective in softening outdoor temperature peaks, as noted in the literature. However, the combination of multiple passive cooling

strategies (best), including a well-planned window opening strategy and heavier interior surface cladding materials, can positively reduce the risk of overheating even in steel-framed constructions.

The "optimized" case, which simulates the presence of a shading system through the reduction of the window solar heat gain coefficient, demonstrates how it is possible to achieve a more-than-acceptable level of comfort in light structures even in summer. Please note that the plots in Fig. 7 represent a 24-hour zoom on a simulation conducted over multiple days. For this reason, the initial indoor temperature conditions do not reflect those described in Table 4.

2. Conclusion

This work, starting from the monitoring of a real case study, provides a numerical evaluation of the indoor thermal comfort achieved in residential buildings during summer by applying passive cooling strategies. The focus is on lightweight steel-framed buildings, where, as the literature has frequently highlighted, overheating is still a big issue. Different strategies were tested through CFD simulations: from natural day and night ventilation to the implementation of different interior surface finishing materials, from different window opening configurations to external shading systems.

Based on the achieved results the paper confirms that:

- it is possible to adjust the nighttime discomfort level (too cold or too hot temperatures) by natural ventilation. It is necessary to find a compromise between the need to cool the envelope components and the internal ambient temperature, which strongly depend on the strategy adopted and, more generally, on the external temperature, wind speed and direction. Acoustic and lighting comfort issues should also be considered.
- the most effective strategy to regulate the daytime discomfort level is to shade window surfaces.
- daytime ventilation, in the analyzed conditions, produce limited effects. It is highly influenced by outdoor environmental condition trends, solar radiation, and sun exposure.
- by simply replacing the internal surface layer, without modifying the load-bearing structure, the internal areal heat capacity of the walls can be increased with positive effects on thermal comfort.

In this paper, monitoring data were exclusively used to set the boundary conditions for the simulation model. In the future, the implemented monitoring system will make it feasible to compare simulation findings with on-site measurements, calibrate the model, and put the recommended strategies into practice, involving building users. Further analysis will be required to evaluate the achieved results at different times of the year and with other building types.

Acknowledgement

This work was realized within the IsolMAX project funded by Cogi Srl - Italy and supported by the Operative Program FESR 2014-2020 of the Autonomous Province of Trento. The authors would like to thank the architect Basilio Guerra of Enerconsult Srl – Brescia (Italy) for his valuable contribution towards the monitoring campaign, and to remember the surveyor Mario Guidotti, head of the project, who recently passed away.

References

- Aryal, P., and T. Leephakpreeda. 2015. "CFD Analysis on Thermal Comfort and Energy Consumption Effected by Partitions in Air-Conditioned Building." *Energy Procedia* 79: 183–188. doi: <https://doi.org/10.1016/J.EGYPRO.2015.11.459>
- Deng, X., P. Cooper, Z. Ma, and G. Kokogiannakis. 2017. "Numerical analysis of indoor thermal comfort in a cross-ventilated space with top-hung windows." *Energy Procedia* 121: 222–229. doi: <https://doi.org/10.1016/J.EGYPRO.2017.08.021>
- Di Perna, C., F. Stazi, A. U. Casalena, and M. D'Orazio. 2011. "Influence of the internal inertia of the building envelope on summertime comfort in buildings with high internal heat loads." *Energy and Buildings* 43(1): 200–206. doi: <https://doi.org/10.1016/J.ENBUILD.2010.09.007>
- Etheridge, D. 2011. *Natural Ventilation of Buildings: Theory, Measurement and Design*. Wiley.
- Hajdukiewicz, M., M. Geron, and M. M. Keane. 2013. "Calibrated CFD simulation to evaluate thermal comfort in a highly-glazed naturally ventilated room." *Building and Environment* 70: 73–89. doi: <https://doi.org/10.1016/J.BUILDENV.2013.08.020>
- IPCC. 2021. *Climate Change 2021: The Physical Science Basis. Contribution of Working Group I to the Sixth Assessment Report of the Intergovernmental Panel on Climate Change*. Cambridge University Press.

- Kuczyński, T., and A. Staszczuk. 2020. "Experimental study of the influence of thermal mass on thermal comfort and cooling energy demand in residential buildings." *Energy* 195: 116984. doi: <https://doi.org/10.1016/J.ENERGY.2020.116984>
- Lomas, K. J., and S. M. Porritt. 2016. "Overheating in buildings: lessons from research." *Building Research & Information* 45(1–2): 1–18. doi: <https://doi.org/10.1080/09613218.2017.1256136>
- Lomax, H., T. H. Pulliam, and D. W. Zingg. 2013. *Fundamentals of Computational Fluid Dynamics*. Springer Berlin Heidelberg.
- Mentor Graphics Corporation. 2018. *FloVENT® Background Theory Reference Guide v.12.2*. www.mentor.com
- Mora-Pérez, M., I. Guillen-Guillamón, P. A. López-Jiménez. 2017. "A CFD study for evaluating the effects of natural ventilation on indoor comfort conditions." *AIMS Environmental Science* 4(2): 289–309. doi: <https://doi.org/10.3934/ENVIRONSCI.2017.2.289>
- Rodrigues, L. T., M. Gillott, and D. Tetlow. 2013. "Summer overheating potential in a low-energy steel frame house in future climate scenarios." *Sustainable Cities and Society* 7: 1–15. doi: <https://doi.org/10.1016/J.SCS.2012.03.004>
- Santamouris, M. 2016. "Cooling the buildings – past, present and future." *Energy and Buildings* 128: 617–638. doi: <https://doi.org/10.1016/J.ENBUILD.2016.07.034>
- Santos, P. 2017. "Energy Efficiency of Lightweight Steel-Framed Buildings." *Energy Efficient Buildings*. doi: <https://doi.org/10.5772/66136>
- Soares, N., P. Santos, H. Gervásio, J. J. Costa, and L. Simões da Silva. 2017. "Energy efficiency and thermal performance of lightweight steel-framed (LSF) construction: A review." *Renewable and Sustainable Energy Reviews* 78, 194–209. doi: <https://doi.org/10.1016/J.RSER.2017.04.066>
- UNI. 2017. *UNI EN ISO 13786:2017 - Thermal performance of building components - Dynamic thermal characteristics - Calculation methods*.
- UNI. 2006. *UNI EN ISO 7730:2006 - Ergonomics of the thermal environment - Analytical determination and interpretation of thermal comfort using calculation of the PMV and PPD indices and local thermal comfort criteria*.
- Yang, L., and Y. Li. 2008. "Cooling load reduction by using thermal mass and night ventilation." *Energy and Buildings* 40(11): 2052–2058. doi: <https://doi.org/10.1016/J.ENBUILD.2008.05.014>

Energetic Optimisation of the Domestic Hot Water System in a Residential Building by Means of Dynamic Simulations

Paolo Valdiserri – University of Bologna, Italy – paolo.valdiserri@unibo.it

Aminhossein Jahanbin – University of Bologna, Italy – aminhossein.jahanbin@unibo.it

Giovanni Semprini – University of Bologna, Italy – giovanni.semprini@unibo.it

Abstract

The present study deals with the energetic optimisation of Domestic Hot Water (DHW) system in a residential building located in Catania, Italy. Each dwelling is equipped with a specific decentralised tank with an internal heat exchanger which is connected to a 2-pipe hot water network system for tank charging. The technical water is produced by an Electrical Heat Pump (EHP) coupled to a central storage tank. The energy performance analysis of the DHW model is evaluated by means of dynamic simulations under three different scenarios of charging the decentralised storage tanks by circulating pump unit: Pump activated during daytime, activated twice a day, and activated three times per day. The results obtained allow an evaluation of the DHW consumption profile, temperature variation in central storage and decentralised tanks, and the annual electrical/thermal energy analysis. The results indicate that the activation of the circulating pump during the day leads to an achievement of the highest amount of thermal energy, as well as having minimum temperature oscillation in both central storage and decentralised tanks. However, these advantages are at the cost of consuming much more electrical energy by the heat pump and up to 29 % higher emissions of CO₂. The best scenario in terms of energy-saving and CO₂ emission is the case in which the circulating pump works twice a day, consuming annually 5,832 kWh less electrical energy, compared to the case of an activated pump during the day.

1. Introduction

In recent years, research on the reduction of energy use in buildings has focused primarily on the reduction of space heating/cooling and ventilation needs. At the same time, present knowledge and understanding of energy use for Domestic Hot Water (DHW) production seem to be insufficient.

The energy used for DHW production currently accounts for approximately 15–40% of the total energy needed in dwellings, and this proportion is likely to be augmented as the energy used for space heating keeps decreasing. Studies available in the literature indicate that the energy efficiency of DHW systems is surprisingly low and that a significant amount of heat is lost from the hot water before it reaches the draw-off points (Pomianowski et al., 2020). The efficiency of the DHW production and distribution varies to a significant extent from case to case due to the large scattering of key parameters in the system, such as plumbing layout, insulation level of pipework, pipe dimension and location, size of storage tank, and time-dependency of DHW consumption profile (Lutz, 2005; Marini et al., 2015; Valdiserri, 2018).

Space heating and DHW production in existing buildings require water at high temperatures (50–70 °C). Traditional 1st generation gas boilers or district heating networks generally have low efficiency and require high primary energy consumption. Furthermore, a higher thermal loss occurs in traditional DHW centralised systems of large buildings where, typically, a recirculating network from the central storage tank to individual dwellings works at high temperatures 24 hours/day. Nowadays, heat pumps are widely used for space heating purposes in buildings thanks to the high Coefficient of Performance (COP), and for the possibility of utilising renewable energy sources. Meanwhile, storage systems play an important role in order to reduce peak energy demand and increase the efficiency of whole production systems.

For these reasons, the concept developed in the e-

SAFE project (Evola et al., 2021) appoints a central role to heat storage systems, in order to develop innovative technologies that enable effective integration and communication in heating/cooling as well as domestic hot water production. The e-SAFE project defines a control strategy that ensures the supply of hot water produced by the heat pump to individual apartments, optimising the direct use of the electricity produced by the on-site PV system during daytime periods.

In this context, the present study aims to evaluate the energy performance of the proposed model for DHW in the e-SAFE project under three different scenarios of charging the decentralised tanks by circulating pump unit: activated pump during daytime, activated twice a day, and activated three times per day. In order to find the best strategy, by means of dynamic simulations, the DHW consumption profile, technical water flow rate, and annual thermal and electrical energy consumptions are analyzed within three different charging periods. The findings of the present study are expected to provide an insight for the energetic optimisation of DHW systems.

2. DHW System Description

In the e-SAFE project, a specific system for producing DHW was designed for a residential building of 10 dwellings (5 floors) with 32 persons, located in Catania, Italy. As shown in Fig.1, each dwelling is equipped with a specific decentralised wall-mounted tank with an internal heating coil (heat exchanger) which is connected to a 2-pipe hot water network system for tank charging. The technical water is produced by an Electrical Heat Pump (EHP) coupled to a central storage tank. The technical water is supplied to decentralised tanks via the circulating pump unit.

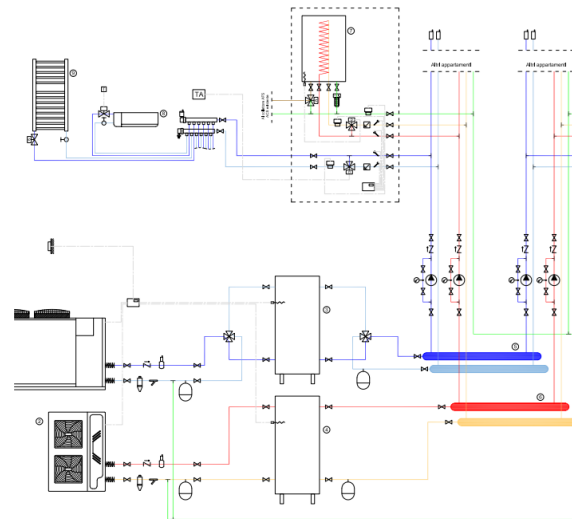


Fig. 1 – Layout of the proposed model for DHW system (the heating/cooling system is not considered in this paper)

The distribution network can be used only for the charging of DHW storage tanks or, in some contexts, can work at low temperature for heating purposes. In both cases, the network (2-pipe water loop) works at high temperature only during charging periods for few hours a day, resulting in lower heat losses in the piping network compared with traditional centralised DHW production, where a recirculating loop at high temperature works 24 hours/day.

3. Dynamic Simulation Model

The energy performance of DHW network is investigated by means of a dynamic simulation model implemented through TRNSYS software. The central storage tank (Type 60g) has a volume of 1500 l, height of 2.4 m and loss coefficient of 0.7 W/(m²K), with a temperature set point of 65 °C. Each apartment was equipped with a plug-and-play decentralised hot water storage system (wall-mounted) with a volume of 140 l. The decentralised tank (Type 534-coiled) consisted of two inlet and two outlet flow ports; on one side, an inlet port for the aqueduct and an outlet port for the DHW; on the other side, an inlet and outlet for the technical water flowing through the heat exchanger. The coiled heat exchanger inside the tank with tube diameter of 0.025 m and loss coefficient of 1.4 W/(m²K) had a total length of 17.8 m with coil diameter and coil pitch equal to 0.145 m and 0.35

m, respectively. The temperature setpoint for the decentralised tank was equal to 55 °C. An ON/OFF controller (Type 2) was employed for both central storage and decentralised tanks in order to regulate the setpoint temperatures in the range of ± 2.5 °C.

The technical water is supplied to the decentralised tanks by two circulating pumps (Type 743), i.e., each pump for five apartments, with the power of 200 W and a constant mass flow rate of 300 kg/h. The energy performance of the DHW model was evaluated under three different scenarios for charging the decentralised tank by circulating pump unit, namely activated pump during the daytime, activated twice a day, and activated three times per day. Table 1 reports the time slots in which the circulating pump is activated.

Table 1 – Operational time slots of the circulating pump

	1 Slot (Continuous)	2 Slots	3 Slots
Operational time slots of pump	06 – 22	08 – 10 & 15 – 18	06 – 08 & 15 – 17 & 20 – 22

The domestic hot water needs were regulated on the basis of the number of people in each apartment, the mean seasonal consumption, and the daily (hourly) consumption profile. In order to model the DHW consumption, a MATLAB code was developed and linked to the TRNSYS model by introducing a NORMRND function, i.e., random samples from a normal (Gaussian) distribution, in order to simulate the daily DHW consumption similar to the real condition.

The MATLAB code reads the number of residents in each apartment from the TRNSYS, and then, at each time step, returns a value as a consumption, simulated on the basis of seasonal and daily (hourly) profile. According to the literature data, the mean daily DHW consumption for each person was considered equal to 45 l, varying slightly in each season. Furthermore, in the daily consumption profile, it was assumed that peaks of the daily consumption profile occur in the early morning between 06 and 10 (45 % of total daily consumption) as well as in the evening between 18 and 22 (25 % of total daily consumption).

4. Results and Discussion

The profile of hot water consumption during a day for three different apartments is illustrated in Fig. 2. The selected apartments are those with the minimum, intermediate and maximum number of residents, namely 1, 3, and 5 persons. It is evident from the figure that peak consumption in each apartment is in the early morning and evening, as described in the previous section. While the peak consumption rate in the apartment with 5 persons reaches 53.9 kg/h, it hardly exceeds 9.5 kg/h in the apartment with 1 person. The trend of DHW request shows the role of virtual user, namely the MATLAB code, in random consumption of DHW in predefined ranges, on the basis of number of persons and daily profile slots. Elaboration of the annual consumption for each apartment implies that the mean daily consumption of hot water for apartments with 1, 3 and 5 person(s) is equal to 43.9, 135.7 and 217.4 l (kg), respectively.

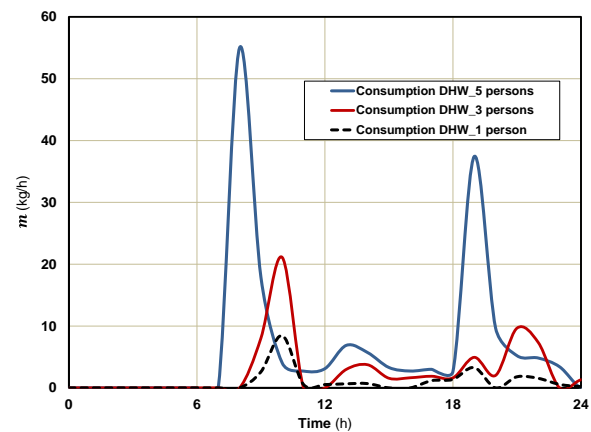


Fig. 2 – The profile of daily hot water consumption in three apartments with 1, 3 and 5 residents

The daily variation in temperature of the central storage and decentralised tank triggered by consuming hot water for different operational time slots is demonstrated in Fig. 3. The considered decentralised tank here is that of the apartment with intermediate number of residents, namely 3 persons. The figure shows that the temperature of decentralised tank increases versus set-point (57.5 °C) in defined working hours of the circulating pump, which feeds the hot water from central storage into the heat exchanger of decentralised tank, and as soon as it discharges the hot water by users (see Fig. 2), its temperature starts to decrease.

It is evident from the figure that reducing the working hours of the circulating pump results in more drastic oscillating in temperature of both central storage and decentralised tank. However, this variation in central storage is less significant compared with the internal tank. While the tank temperature in daytime activated mode (1 slot) does not drop below 37 °C, it reaches 20 °C and 29 °C in 2 and 3 operational time slots, respectively.

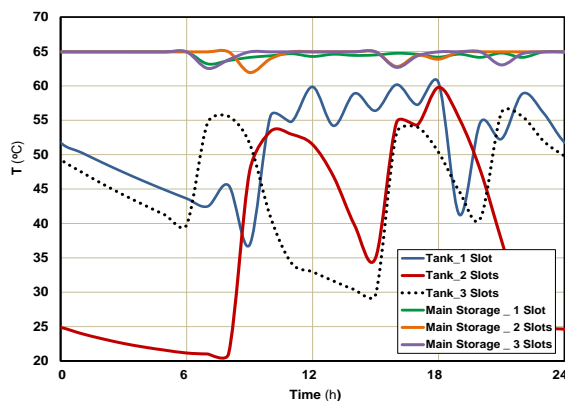


Fig. 3 – The temperature variation in central (main) storage and decentralised tank (of a dwelling with 3 persons) for different activation times of the circulating pump

A comparison between the results of Figs. 2 and 3 allows two points to be concluded. A short activation time of the circulating pump causes the risk of having a low-temperature DHW when there is a request out of operational time slots, particularly for apartments with larger number of residents. Another issue to be addressed is the advantage of matching the activation time of the circulating pump with hours in which there is the peak of DHW consumption, according to the profiles in Fig. 2.

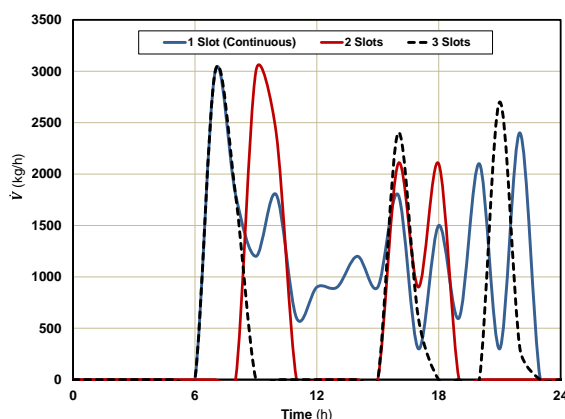


Fig. 4 – Daily total mass flow rate of technical water for different activation times of the circulating pump

Fig. 4 shows the daily total mass flow rate of technical water circulating from the central storage to each apartment's tank, for different working time slots. The figure shows that the flow rate of technical water during the early morning period reaches the highest rate, namely 3000 kg/h, in all operational time slots, implying the hot water demand by all apartments (Fig. 2). Moreover, the figure indicates that, when the circulating pump is in daily activated mode, namely available on request between 06 and 22 h, the flow rate of technical water does not reach zero during the day, due to receiving the hot water request by at least an apartment. On the other hand, the mass flow rate of technical water for 2 and 3 slots daily charging is mostly equal to zero, except for pre-defined working hours. A comparison between results shows that the total daily mass flow rate of technical water in continuous mode (1 slot) is up to two times higher than that in 2 times activated per day. Indeed, the possibility of charging tanks during the day (1 slot) leads to maintaining the temperature of tanks and, consequently, the DHW as high as possible. Nonetheless, it is shown in the following that this higher temperature will be at the cost of consuming much higher electrical energy, as well as the emission of CO₂.

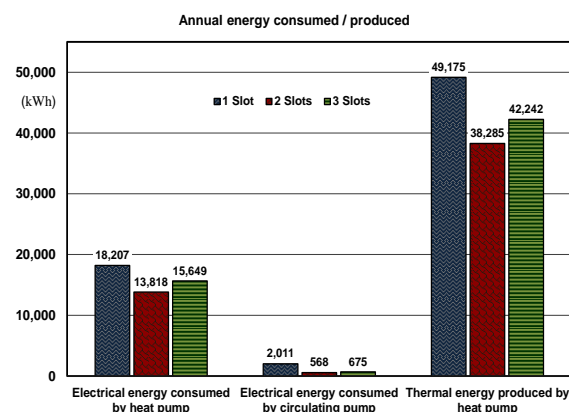


Fig. 5 – A comparison between annual energy consumed/produced in various activation time slots of the circulating pump

The charts in Fig. 5 compare the annual amount of electrical energy consumed by the heat pump and circulating pump, as well as the thermal energy produced by the heat pump for different operational time slots of the pump. The figure shows that employing a continuous daytime operation of

circulating pump (1 slot) leads to much higher electrical energy consumption of both the heat pump and circulating pump, compared with 2 and 3 slot operations; the total electrical energy consumed by the continuous operation is 5,832 and 3,894 kWh higher than that in 2 and 3 time slot operations, respectively. On the other hand, when the circulating pump is activated during the day (1 slot), the heat pump produces annually about 50,000 kWh thermal energy for DHW production, which is far higher than other scenarios.

Table 2 – A comparison between annual electrical consumption, mean COP of heat pump and CO₂ emission for different activation time slots of the circulating pump

	1 Slot	2 Slots	3 Slots
Total electrical energy consumed (kWh)	20218	14386	16324
Mean annual COP	2.69	2.77	2.71
CO₂ emission (kg)	9098.1	6473.5	7345.7

Table 2 reports values of the total electrical energy consumed, mean annual COP of heat pump, and amount of CO₂ emission by different scenarios considered for charging the tanks. The table shows that the mean annual COP of the heat pump is slightly improved when the internal tanks charge only two times per day. Considering the mean value of 0.45 kg emission of CO₂ for producing 1 kW of electricity, according to the literature data, the continuous charging of tanks (1 slot) causes 9098 kg emission of CO₂, which is 29 % and 19 % larger than 2- and 3-times charging modes.

5. Conclusions

In the present study, the energetic optimisation of the Domestic Hot Water (DHW) in a residential building was investigated by means of a dynamic simulation model developed in TRNSYS software linked to a MATLAB code. In the proposed model for the DHW system, the technical water was produced by an Electrical Heat Pump (EHP) coupled to a central storage tank. Each dwelling was equipped with a specific decentralised tank with an internal heat exchanger, which was connected to a 2-pipe hot water network system for

tank charging. The energy performance of the DHW model was evaluated under three different scenarios for charging internal tanks by circulating pump unit, namely activated pump during daytime, twice a day, and three times per day.

The results obtained by dynamic simulations allowed an evaluation of the DHW consumption, temperature variation in central storage and internal tanks, the flow rate of technical water, and annual electrical/thermal energy consumption analysis. The results showed that employing the daily activated circulating pump has the advantage of achieving the highest amount of thermal energy, as well as having minimum temperature oscillation in both central storage and decentralised tanks. However, these advantages were at the cost of consuming much more electrical energy and up to 29 % higher emission of CO₂. The best scenario in terms of energy saving and CO₂ emission was when the circulating pump was working twice a day consuming annually 5,832 kWh less electrical energy compared to when the pump was activated during the day.

Acknowledgement

This paper was carried out in the framework of the "Energy and seismic affordable renovation solutions" (e-SAFE) project, which received funding from the European Union's Horizon 2020 research and innovation programme under grant agreement No. 893135.

References

- Evola, G., G. Margani., V Costanzo, C Tardo, E. M. Marino, G Semprini, R. Tomasi, C. Halmdienst, and B. Voortman. 2021. "The e-SAFE energy and seismic renovation solutions for the European building stock: Main features and requirements." *Journal of Physics: Conference Series* 2069(1): 012224. doi: <https://doi.org/10.1088/1742-6596/2069/1/012224>
- Lutz, J. 2005. *Estimating Energy and Water Losses in Residential Hot Water Distribution Systems*. Lawrence Berkeley National Laboratory.

- Marini, D., R. Buswell, and C. Hopfe. 2015. "Estimating waste heat from domestic hot water systems in UK dwellings." In *Proceedings of Building Simulation 2015*, Hyderabad, India. <https://doi.org/10.1111/hex.12279>
- Pomianowski, M. Z., H. Johra, A. Marszal-Pomianowska, and C. Zhang. 2020. "Sustainable and energy-efficient domestic hot water systems: A review." *Renewable and Sustainable Energy Reviews* 128: 109900. doi: <https://doi.org/10.1016/j.rser.2020.109900>
- Valdiserri, P. 2018. "Evaluation and control of thermal losses and solar fraction in a hot water solar system." *International Journal of Low-Carbon Technologies* 13(3): 260–265. doi: <https://doi.org/10.1093/ijlct/cty025>

Assessing the Climate Resilience of Passive Cooling Solutions for Italian Residential Buildings

Mamak P.Tootkaboni – Politecnico di Torino, Italy – mamak.ptootkaboni@polito.it

Ilaria Ballarini – Politecnico di Torino, Italy – ilaria.ballarini@polito.it

Vincenzo Corrado – Politecnico di Torino, Italy – vincenzo.corrado@polito.it

Abstract

One of the most significant repercussions of greenhouse gas concentration increase has been the global rise in temperature, resulting in drastic changes in the climate. According to this background, buildings are not only contributing to climate change, but they are also being affected by it, as climate change will raise the risk of overheating and cooling demand in buildings. Therefore, assessing and communicating resilient cooling and overheating protection solutions is inexorable. This paper aims to analyse the energy efficiency and climate resiliency of three passive cooling solutions for Italian residential buildings in future climates. Simulations have been performed using EnergyPlus for the pre-retrofitted condition (without insulation and conventional heating and cooling systems) and the retrofitted building (with insulation and a reversible heat pump for heating and cooling). Results show that buildings will be subject to an increase in cooling loads, electrical energy consumption for cooling, and overheating risk due to climate change. The ultra-selective double-glazed window is found to be more climate-resilient in comparison with roller blind and cool roof tiles. Besides, combining these three cooling technologies can guarantee the best future energy performance for each period. However, the overheating risk during the power outage still exists, especially for the post-retrofitted building. These findings have significant implications for understanding how analyzing multiple factors is essential to guarantee the climate resilience of cooling systems in a holistic way.

1. Introduction

Each of the last four decades since 1980 has been successively warmer than the preceding decade. According to the latest Assessment Report (6th A.R.) of the Intergovernmental Panel on Climate

Change (IPCC), the concentration of greenhouse gases (GHG) in the atmosphere has continued to increase since 2011 (measurements in IPCC 5th A.R.) (Masson-Delmotte et al., 2021). Considering the fact that global CO₂ emissions from the building sector increased by 50 % from 1990 to 2019, making it the main contributor to GHG emissions, its impact on intensifying climate change is undeniable (Cabeza et al., 2022). Furthermore, climate change is already impacting many weather and climate extremes in all world regions. Due to methodological advances and new data sets, evidence of observed changes in climate-related hazards, such as heatwaves, has increased since the 5th A.R. (Symon, 2013). In this case, buildings are not only responsible for climate change but are highly affected by it. Accordingly, many published studies worldwide suggest a shift in building energy performance due to the impacts of climate change. For instance, Wan et al. (2012) analysed the heating and cooling energy use of an office building in different Chinese cities and reported an increase in cooling energy consumption of up to 24.2 %, implying a shift towards higher electricity demand. In the U.S. context, Shen (2017) demonstrated a rise in cooling energy use and a drop in heating energy use for office and residential buildings in four American cities. In addition, the inconsistency of energy use in residential buildings located in cold and hot regions of the U.S. is expected to decrease due to the impact of climate change. In Canada, an increase in cooling demand by up to 126 % and a decrease in heating demand by up to 33 % were predicted for several urban regions by Berardi & Jafarpur (2020).

Besides the expected changes in energy needs, the overheating risk will also become a challenge in the future. For example, in southern regions of the U.K., overheating is expected to create a cooling problem for a third of the year, as Peacock et al. (2010) suggested. In the same vein, Dino & Akgül (2019) examined a typical mid-rise residential building in four different cities in Turkey, and found that inhabitants would experience overheating, particularly in naturally ventilated houses. In addition, other studies demonstrated that such changes in energy needs, and overheating risk are also predicted for retrofitted and energy-efficient buildings. In other words, due to the changing climate, meeting nearly zero-energy building (NZEB) requirements may not necessarily guarantee the energy performance and indoor environmental quality of buildings in the future. For example, as Tabatabaei Sameni et al. (2015) suggested, thermal discomfort during the cooling season is foreseen for 72 % of analysed social housing flats – built to Passivhaus standards – due to the impact of climate change. Attia & Gobin (2020) looked at a Belgian reference example of the NZEB and found that there would be overheating up to +43.5 % at the end of the century. In another study, Da Guarda et al. (2020) examined the influence of climate change on zero-energy buildings in 2020 (2011 to 2040), 2050 (2041 to 2070), and 2080 (2071 to 2100). It has been proved that energy consumption will rise, so further dimensioning of renewable energy installations is required to achieve zero net energy balance. Taken together, these studies suggest that to maintain energy efficiency, sustainability, and climate resilience of buildings over time, an assessment of the performance of energy-efficient buildings using future weather data is essential.

This paper is a part of research carried out in collaboration with the International Energy Agency (IEA) Energy in Buildings and Communities Programme (E.B.C) Annex 80 "Resilient Cooling of Buildings". This project develops, assesses, and communicates strategies for resilient cooling and overheating protection (Annex 80 IEA EBC, 2018). After creating reliable future weather data for Rome, the resilience of three passive cooling technologies was investigated using thermal comfort and energy performance metrics to assess and de-

velop the adaptation and mitigation framework on a regional scale.

2. Materials and Methods

2.1 Generation of Future Weather Data

In synergy with the IEA-Annex 80 Weather Data Task Group, future typical meteorological years were created for Rome during the first step.

For this purpose, Regional Climate Models (GERICS-REMO 2015, MPI-M-MPI-ESM-LR) from Euro-CORDEX on a 0.11° grid in rotative coordinates (equivalent to a 12.5 km grid) were used. In detail, G.C.M.s (Global Climate Models) are mathematical models for forecasting climate change providing information on a global scale with a spatial resolution of 150–600 km (Symon, 2013). Since climate change effects and related weather extremes at the local level will not be considered using these models, they are not appropriate for energy simulations on the building scale. Therefore, it is necessary to downscale the models to applicable spatial (less than 100 km) and temporal resolution (less than monthly value). The dynamical technique employs regional climate models (R.C.M.s) to obtain finer spatial and temporal climate information; this is one of the downscaling methodologies. R.C.M.s can better capture the geographical and temporal variability of the local climate and provide physically consistent datasets (Soares et al., 2012). As mentioned above, this study employs the GERICS-REMO-2015 as the R.C.M. In addition, since being well-supported by the IPCC report on climate model evaluation (Flato et al., 2014), the MPI-M-MPI-ESM-LR is the study's driving model. Besides, the data source is the EURO-CORDEX entry point through the Earth System Grid Federation (ESGF) for the Europe domain on a 0.11° grid, in rotative coordinates (equivalent to a 12.5 km grid). NetCDF4, which is a file format for storing multi-dimensional scientific data, is the accessible format for this source. The hourly climatic data for Rome Fiumicino airport was extracted using the Cordex Data Extractor program, which enables the discovery of the data point on the grid closest to the

specified latitude and longitude. These climatic data were extracted by adapting the RCP 8.5 (Representative Concentration Pathway) scenario from IPCC 5th A.R. for the 2041-2060 (2050s) and 2081-2100 (2080s) periods. These scenarios were the latest available projections of future climate at the time of the study.

Accordingly, the EN ISO 15927-4 (2005) methodology was applied to construct the future typical meteorological year from the 20 years of climatic data. This international standard addresses the selection of appropriate meteorological data for the assessment of the long-term mean energy use for heating and cooling. Twelve Best Months were picked by comparing the Cumulative Distribution Function of the single and reference years using the Finkelstein-Schafer (F.S.) statistics (Finkelstein & Schafer, 1971). This method was selected for this study because it includes the global solar irradiance, relative humidity, dry-bulb air temperature, and wind speed. The best representative 12 months were then employed to construct the T.M.Y. Historical (2001-2020), future medium-term (2041-2060), and future long-term (2081-2100) are the T.M.Y.s referred to in this study. Despite not being adjusted for bias, the results are reliable; since a relative comparison is applied in this study, and for confronting different technologies, this kind of future weather data is acceptable.

2.2 Cooling Strategies

In IEA EBC Annex 80, four categories of cooling strategies were created according to their approaches to cooling people or the indoor environment. They include strategies aimed at: a) reducing heat gains to indoor environments and people indoors, b) removing sensitive heat from indoor environments, c) enhancing personal comfort apart from cooling whole spaces, and d) removing latent heat from indoor environments.

For the present analysis, three cooling solutions were selected from the first category: ultra-selective double-glazed window, external roller blind, and cool roof tiles.

The ultra-selective double-glazed window is a static technology that incorporates low thermal-infrared emittance (low-E) coatings with spectral con-

trol to reduce the window heat loss (U -value $\leq 1.8 \text{ W/(m}^2 \text{ K)}$) and solar heat gain ($g \leq 30 \%$), while admitting most daylight ($\tau_v > 60 \%$). The external roller blind is a dynamic technology with a low solar transmittance ($\tau_s < 15 \%$) that strongly reduces the solar heat gain due to its external position and can be controlled to optimise both thermal and visual comfort and energy demands for heating, cooling and lighting. Cool roof tiles are a static technology that reduces net radiative heat gain at the envelope (solar + thermal infrared radiation) thanks to the high solar reflectance ($\rho_s > 0.30$ for pitched roofs, $\rho_s > 0.65$ for flat roofs).

2.3 Calculation Methods and Performance Indicators

The following three key performance indicators (KPIs) were used for the performance assessment of the selected cooling solutions:

- HE [%], i.e., hours of exceedance, which are the number of hours during June, July, and August in which the operative temperature of the zone is greater than the upper limit temperature,
- $EP_{C,nd}$ [kWh/m²], which is the thermal energy need for space cooling in June, July, and August,
- $E_{el,C}$ [kWh/m²], which is the electrical energy consumption (from the grid) for cooling in June, July, and August.

The above indicators were chosen from the list of KPIs officially adopted in IEA EBC Annex 80 to represent the summer performance of the building according to the following criteria: a) thermal discomfort in free-floating conditions (absence of cooling or power outage) or in case of power shortage, b) thermal performance of the fabric in cooling operation, and c) energy performance of the building (including HVAC system) in cooling operation.

All the adopted indicators are based on international standards. HE accounts for the number of weighted hours exceeding the acceptable range of the indoor operative temperature. For free-floating conditions, the adaptive comfort method is assumed according to the Annex-H of EN ISO 7730, 2005. $EP_{C,nd}$ reflects the basic energy

needs of the building in ideal thermal conditions (uniform and ideally controlled indoor temperature) without interaction with specific technical building systems (EN ISO 52016-1, 2017). $E_{el,C}$ represents the energy delivered to the building for cooling by adding the effect of the energy losses of the cooling system (EN ISO 52000-1, 2017).

2.4 Case Study

With the aim of extending the research outcomes on a broader territorial scale, the case study was selected to be representative of a specific category, i.e., the Italian single-family house built in the period 1946-1960 (Ballarini et al., 2014). Among the Italian existing building categories, the one selected presents the lowest energy performance due to its highest shape factor and uninsulated envelope components (Ballarini et al., 2017). In a recent study (Tootkaboni et al., 2021), this type of building was found to be more sensitive to climate change due to its high shape factor. According to the IEE-TABULA project (Corrado et al., 2012), the building selected is an "archetype" (Fig.1), which means that it is characterised by average dimensional properties (gross heated volume, shape factor, conditioned net floor area, number of floors, number of apartments) of a representative building sample according to statistical analysis.

The main geometric data of the analysed archetype are listed in Table 1. The thermo-physical features of the building envelope components are provided in Table 2, assuming the building type both in the original pre-retrofit situation and in the retrofitted state. This double condition allows an assessment of the effect of the passive cooling strategies both on low energy-efficiency buildings and on already insulated buildings. The U -values of the envelope components in the pre-retrofit state refer to typical technologies of the construction period (solid brick masonry and single-glazing windows). The retrofitted state presents components insulated in accordance with the notional reference building for the climatic zone of Rome, as expressed by the Italian energy regulations (M.D 26 June, 2015), which also represents the nearly zero-energy building target. The post-retrofit windows present a low-E double-glazing. In addition, while the original building is

not equipped with solar shading devices, these are provided for in the retrofitted building (external wooden Venetian blinds).

As far as the technical building systems are concerned, the building in the pre-retrofit state is equipped with a gas standard boiler and radiators for space heating and a split system for space cooling. In the post-retrofit phase, both heating and cooling are provided by a reversible air-to-water heat pump with fan coils as heat emitters.



Fig. 1 – Archetype of the Italian single-family house built in the period 1946-1960 (Corrado et al., 2012)

Table 1 – Geometric data of the case study

Parameter	Value
Conditioned gross volume, V_g [m ³]	584
Conditioned net floor area, A_{fl} [m ²]	162
Shape factor, A_{env}/V_g [m ⁻¹]	0,73
Window-to-wall ratio, WWR [-]	0,09
Number of floors [-]	2
Number of apartments [-]	1

Table 2 – Thermo-physical parameters of the envelope components

Component	Parameter	Pre-retrofit	Post-retrofit
External wall	U [W·m ⁻² K ⁻¹]	1.48	0.29
	U [W·m ⁻² K ⁻¹]	1.65	0.26
Roof	α_s [-]	0.75	0.75
	ρ_s [-]	0.25	0.25
Bottom floor	U [W·m ⁻² K ⁻¹]	2.00	0.29
Windows	U [W·m ⁻² K ⁻¹]	4.9	1.30
	U [W·m ⁻² K ⁻¹]	5.7	1.20
Glazing	g [-]	0.85	0.59
	τ_v [-]	0,90	0,80
	τ_s [-]	N/A	0,40
Shading	ρ_s [-]	N/A	0,12

The energy performance of the case study was assessed considering the behavior of a standard user. Hourly profiles of internal heat gains, which include occupants, electric lighting and appliances, and ventilation airflow rates were assumed in accordance with the Italian National Annex draft of the EN 16798-1 technical standard (2020).

A continuous operation mode of the technical building systems was adopted, considering heating and cooling temperature set-points equal to 20 °C and 26 °C, respectively. The heating season is included in the period from 1st November up to 15th April, while the cooling period was assumed for the months of June, July, and August. The operation of the solar shading devices was set in the function of a threshold value of the incident solar irradiance (300 W/m²), in accordance with UNI/TS 11300-1 (2014).

3. Results and Discussion

The results obtained from the simulations are shown in Figs. 2 to 7. The first two refer to the thermal energy need for space cooling ($EP_{C,nd}$) during the months of June, July, and August in 2020, 2050, and 2080. Besides, Figs. 4 and 5 represent the electrical energy consumption (from the grid) for cooling ($E_{el,C}$) during the same period. An increase of up to 75 % for the pre-retrofitted and 35 % for the post-retrofitted case is shown in $EP_{C,nd}$ over time due to climate change. Furthermore, the increase in $E_{el,C}$ is up to 80 % for the pre-retrofitted and 30 % for the post-retrofitted building. For post-retrofitted building, the variations of $EP_{C,nd}$ and $E_{el,C}$ are less than the pre-retrofitted one. It can be argued that the post retrofitted building is less sensitive to the effects of climate change.

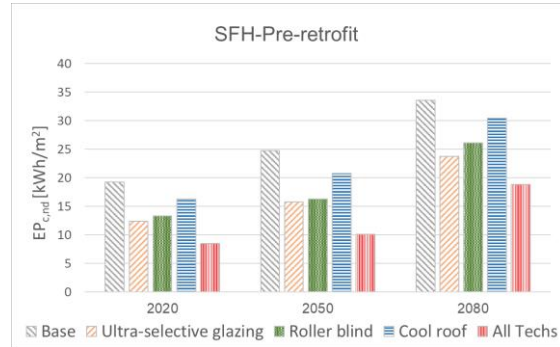


Fig. 2 – Thermal energy need for space cooling (June/July/August) in 2020, 2050, and 2080 for pre-retrofit building



Fig. 3 – Thermal energy need for space cooling (June/July/August) in 2020, 2050, and 2080 for post-retrofit building

The reduction in the $EP_{C,nd}$ and $E_{el,C}$ caused by either of the cooling solutions is more significant in the pre-retrofitted building. In addition, it is shown that the most effective one is ultra-selective glazing in both conditions. The cool roof has a minor effect, as the building has a pitched roof with an attic. This effect is negligible for the electrical energy consumption in the post-retrofitted building in all three periods. If all cooling solutions are applied, the $EP_{C,nd}$ and $E_{el,C}$ can be reduced to the degree that in 2080 they are almost the same as the present base case. This result is valid for both building conditions.

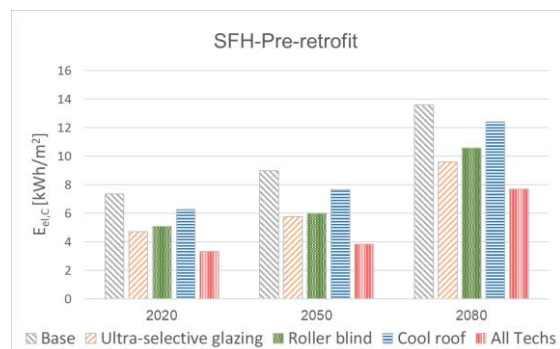


Fig. 4 – Electrical energy consumption (from the grid) for cooling (June/July/August) in 2020, 2050, and 2080 for pre-retrofit building

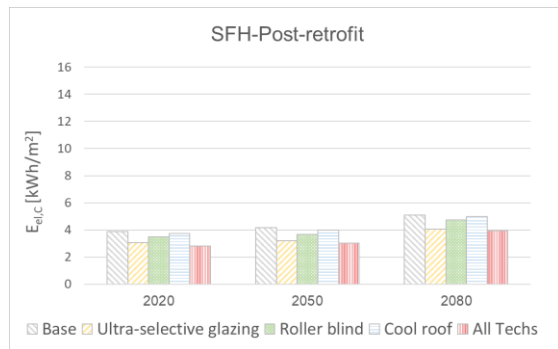


Fig. 5 – Electrical energy consumption (from the grid) for cooling (June/July/August) in 2020, 2050, and 2080 for post-retrofit building

As mentioned earlier, when it comes to the impact of climate change on buildings, it is necessary to take the overheating risk into account. For this purpose, by running free-floating simulations, weighted hours of exceedance for June, July, and August in 2020, 2050, and 2080 are calculated and presented in Figs. 6 and 7. Results report that the weighted hours of exceedance increase due to climate change in both conditions. However, in the post-retrofitted building, occupants will experience overheating equal to 5328 hours in the future scenarios, while this amount reaches a maximum of 2628 hours for the pre-retrofitted building in 2080. This result is due to the unwanted effect of insulation that causes a heat trap in the building in a free-floating regime. The results also show that the cooling solutions can reduce weighted exceedance hours. For the pre-retrofitted building, the effect of ultra-selective glazing and roller blind is almost the same and significantly higher than the cool roof. For post-retrofitted case, ultra-selective glazing has the most significant effect. The effect of the roller blind is diminished in this case since the post-retrofitted building was equipped with a Venetian blind in the base case. By applying all the cooling solutions, weighted hours of exceedance are reduced significantly for both cases. However, the weighted hours of exceedance in the pre-retrofitted building for the worst-case scenario (2080) equal 700 hours, which is much less than the post-retrofitted case (2600 h).

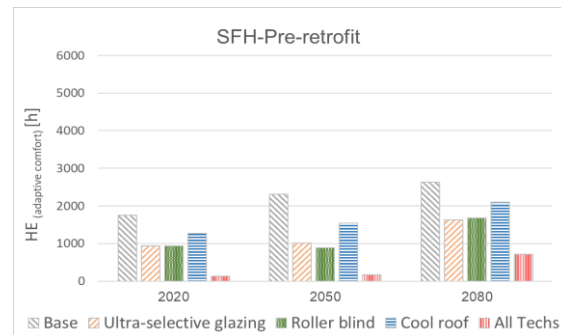


Fig. 6 – Weighted hours of exceedance (June/July/August) in 2020, 2050, and 2080 for pre-retrofit building, in free-floating condition



Fig. 7 – Weighted hours of exceedance (June/July/August) in 2020, 2050, and 2080 for post-retrofit building, in free-floating condition

4. Conclusion

The present research aimed to examine the climate resilience of three passive cooling solutions regarding the future performance of Italian residential buildings. To achieve this aim, the impact of the ultra-selective double-glazed window, external roller blind, and cool roof tiles was investigated on the thermal comfort and energy performance of an Italian single-family house built in 1946-1960. Two building conditions (pre-and post-retrofitted) and three periods (2020, 2050, and 2080) were considered. The current study results indicate that, among selected solutions, the ultra-selective double-glazed window has the most significant impact on reducing the effect of climate change on thermal energy needs for space cooling, electrical energy consumption from the grid for cooling, and weighted hours of exceedance in free-floating condition. The findings of this research also revealed that applying all three cooling solutions mentioned could significantly develop

the energy performance of the buildings, so that in the worst-case future scenario (2080), the energy performance will be almost the same as the base case in 2020. This improvement is more considerable for the post-retrofitted building. However, in the absence of electrical energy (free-floating condition), although studied cooling solutions help to reduce the overheating, the risk is still present, specifically for the post-retrofitted building. These findings shed new light on the trade-off between energy efficiency and climate resiliency. In this case, it is necessary to identify cooling solutions that help to mitigate climate change and foster adaptation to it, to ensure both sustainability and climate resilience for the built environment.

Nomenclature

Symbols

A	Area (m^2)
E	Energy consumption (kWh/m^2)
EP	Energy performance (kWh/m^2)
HE	Hours of exceedance (h)
U	Thermal transmittance ($\text{W}/(\text{m}^2\cdot\text{K})$)
V	Volume (m^3)
g	Total solar energy transmittance (solar factor) (–)
τ	Transmittance (%)
ρ	Reflectance (%)

Subscripts/Superscripts

C	Space cooling
el	Electrical energy
env	Envelope
fl	Floor
g	Gross
nd	Need
s	Solar
v	Visible

References

- Annex 80 IEA EBC. 2018. "IEA EBC Annex on Resilient Cooling for Residential and Small Commercial Buildings" .Draft Annex Text, pp. 1–13.
- Attia, S., and C. Gobin. 2020. "Climate Change Effects on Belgian Households: A Case Study of a Nearly Zero Energy Building." *Energies* 13(20): 5357. doi: <https://doi.org/10.3390/en13205357>
- Ballarini, I., S. P. Corgnati, and V. Corrado. 2014. "Use of reference buildings to assess the energy saving potentials of the residential building stock: The experience of TABULA project." *Energy policy* 68: 273–284. doi: <https://doi.org/10.1016/j.enpol.2014.01.027>
- Ballarini, I., V. Corrado, F. Madonna, S. Paduos and F. Ravasio. 2017. "Energy refurbishment of the Italian residential building stock: energy and cost analysis through the application of the building typology." *Energy Policy* 105: 148–160. doi: <https://doi.org/10.1016/j.enpol.2017.02.026>
- Berardi, U., and P. Jafarpur. 2020. "Assessing the Impact of Climate Change on Building Heating and Cooling Energy Demand in Canada." *Renewable and Sustainable Energy Reviews* 121: 109681. doi: <https://doi.org/10.1016/j.rser.2019.109681>
- Cabeza, L. F., Q. Bai, P. Bertoldi, J. Kihila, A. F. P. Lucena, É. Mata, S. Mirasgedis, A. Novikova, Y. Saheb, P. Berrill, L. R. Caldas, M. Chàfer, S. Hu, R. Khosla, W. Lamb, D. Várez, J. Wanemark, and J. Keenan. 2022. "Climate Change 2022, Mitigation of Climate Change. Working Group III contribution to the Sixth Assessment Report of the Intergovernmental Panel on Climate Change." *Climate Change*. <https://www.ipcc.ch/report/sixth-assessment-report-working-group-3/>
- Comitato Termotecnico Italiano. 2020. Technical Commission 241, Doc. (181) Italian National Annex of the EN 16798-1 Technical Standard (Working Draft for Internal Use).
- Corrado, V., I. Ballarini, and S. P. Corgnati. 2012. National scientific report on the TABULA activities in Italy. Dipartimento di Energetica, Gruppo di Ricerca TEBE, Politecnico di Torino, Torino, Italy. https://episcopo.eu/fileadmin/tabula/public/docs/scientific/IT_TABULA_ScientificReport_POLITO.pdf
- Da Guarda, E. L. A., R. M. A. Domingos, S. H. M. Jorge, L. C. Durante, J. C. M. Sanches, M. Leao, and I. J. A. Callejas. 2020. "The influence of

- climate change on renewable energy systems designed to achieve zero energy buildings in the present: A case study in the Brazilian Savannah." *Sustainable Cities and Society* 52: 101843. doi: <https://doi.org/10.1016/j.scs.2019.101843>
- Dino, I. G., and C. M. Akgül. 2019. "Impact of Climate Change on the Existing Residential Building Stock in Turkey: An Analysis on Energy Use, Greenhouse Gas Emissions and Occupant Comfort." *Renewable Energy* 141: 828-846. doi: <https://doi.org/10.1016/j.renene.2019.03.150>
- Ente Italiano di Normazione. 2014. *UNI/TS 11300-1. 2014. Energy Performance of Buildings Part 1: Evaluation of Energy Need for Space Heating and Cooling* (in Italian). UNI, Milan, Italy.
- European Committee for Standardization. 2005. *EN ISO 7730:2005. Ergonomics of the thermal environment - Analytical determination and interpretation of thermal comfort using calculation of the PMV and PPD indices and local thermal comfort criteria. Annex-H: Long-term evaluation of the general thermal comfort conditions*.
- European Committee for Standardization. 2017. *EN ISO 52016-1:2017. Energy performance of buildings -Energy needs for heating and cooling, internal temperatures and sensible and latent heat loads - Part 1: Calculation procedures, 52016-1*.
- European Committee for Standardization. 2017. *EN ISO 52000-1:2017. Energy performance of buildings -Overarching EPB assessment -Part 1: General framework and procedures, 52000-1*.
- Finkelstein, J. M., and R. E. Schafer. 1971. "Improved goodness-of-fit tests." *Biometrika* 58(3): 641-645. doi: <https://doi.org/10.1093/biomet/58.3.641>
- Flato, G., J. Marotzke, B. Abiodun, P. Braconnot, S. C. Chou, W. Collins, and M. Rummukainen. 2014. "Evaluation of Climate Models. In Climate Change 2013: The Physical Science Basis. Contribution of Working Group I to the Fifth Assessment Report of the Intergovernmental Panel on Climate Change." Cambridge University Press 741-866. doi: <https://doi.org/10.1017/CBO9781107415324.020>
- Italian Ministry of Economic Development. 2015. Italian Ministerial Decree 26th June 2015. "Application of energy performance calculation methodologies and specification of prescriptions and minimum requirements."
- Masson-Delmotte, V., P. Zhai, A. Pirani, S. L. Connors, C. Péan, S. Berger, N. Caud, Y. Chen, L. Goldfarb, M. I. Gomis, M. Huang, K. Leitzell, E. Lonnoy, J. B. R. Matthews, T. K. Maycock, T. Waterfield, O. Yelekçi, R. Yu, and B. Zhou. 2021. "Summary for Policymakers. The Physical Science Basis. Contribution of Working Group I to the Sixth Assessment Report of the Intergovernmental Panel on Climate Change." *Climate Change*.
- Peacock, A. D., D. P. Jenkins, and D. Kane. 2010. "Investigating the Potential of Overheating in UK Dwellings as a Consequence of Extant Climate Change." *Energy Policy* 38(7): 3277-3288. doi: <https://doi.org/10.1016/j.enpol.2010.01.021>.
- Shen, P. 2017. "Impacts of Climate Change on U.S. Building Energy Use by Using Downscaled Hourly Future Weather Data." *Energy and Buildings* 134: 61-70. doi: <https://doi.org/10.1016/j.enbuild.2016.09.028>
- Soares, P. M., R. M. Cardoso, P. Miranda, J. de Medeiros, M. Belo-Pereira, and F. Espirito-Santo. 2012. "WRF high resolution dynamical downscaling of ERA-Interim for Portugal." *Climate dynamics* 39(9): 2497-2522. doi: <https://doi.org/10.1007/s00382-012-1315-2>
- Symon, C. 2013. "Climate Change: Action, Trends and Implications for Business." The IPCC's Fifth Assessment Report.
- Sameni, S. M. T., M. Gaterell, A. Montazami, and A. Ahmed. 2015. "Overheating Investigation in UK Social Housing Flats Built to the Passivhaus Standard." *Building and Environment* 92: 222-235. doi: <https://doi.org/10.1016/j.buildenv.2015.03.030>
- Tootkaboni, M. P., I. Ballarini, and V. Corrado. 2021. "Analysing the future energy performance of residential buildings in the most populated Italian climatic zone: A study of climate change impacts." *Energy Reports* 7: 8548-8560. doi: <https://doi.org/10.1016/j.egyr.2021.04.012>
- Wan, K. K., D. H. Li, W. Pan, and J. C. Lam. 2012. "Impact of climate change on building energy use in different climate zones and mitigation and adaptation implications." *Applied Energy* 97: 274-282. doi: <https://doi.org/10.1016/j.apenergy.2011.11.048>

Ventilation of Residential Buildings in Alpine Region: A Comparison Between Natural, Mechanical, and Mixed-Mode Strategies

Francesca Avella – Eurac Research, Italy – francesca.avella@eurac.edu

Paolo Bonato – Eurac Research, Italy – paolo.bonato@eurac.edu

Annamaria Belleri – Eurac Research, Italy – annamaria.belleri@eurac.edu

Francesco Babich – Eurac Research, Italy – francesco.babich@eurac.edu

Abstract

Many studies have shown how controlled natural ventilation has multiple benefits on the health of people and the buildings in terms of indoor air quality (IAQ) and thermal comfort, as well as on the energy consumption of the building.

However, unfavorable outdoor environmental conditions can limit the use of solely natural ventilation and, for this reason, it is often necessary to resort to mixed-mode ventilation.

The aim of this research is to demonstrate the potential of mixed-mode ventilation strategies in comparison with the performance of controlled natural ventilation and mechanical ventilation applied separately, in the context of a dwelling located in a multi-family house in Bolzano (Italy) during the summer season.

Dynamic simulations were performed, developing a room-by-room coupled thermal and airflow model of the dwelling in TRNSYS and TRNFLOW to characterize its thermal behavior and the natural airflows.

The study analyzes and compares three different scenarios: (1) only controlled natural ventilation (CNV), (2) only mechanical ventilation (MVT), (3) a combination of the two (mixed ventilation strategies, MIX).

In this work, the controlled natural ventilation strategies are designed with a twofold aim, which is (a) to improve the indoor thermal comfort, reducing the overheating risk thanks to ventilative cooling, and (b) to improve IAQ by removing indoor airborne pollutants coming from indoor sources.

The first results show that (a) CNV effectively reduces the overheating risk, also achieving excellent IAQ levels; (b) MVT allows acceptable IAQ conditions and good water vapor removal, while overheating could become an issue in terms of duration and intensity. In addition, there is the electricity consumption associated with MVT; (c) in most cases, mixed ventilation provides excellent perfor-

mance in terms of IAQ and thermal comfort, compared with the former strategies. Overheating is well managed, and the electrical consumption of MVT is limited.

1. Introduction

Many studies have shown how controlled natural ventilation has multiple benefits on the health of people and buildings in terms of indoor air quality (IAQ) and thermal comfort, as well as on the energy consumption of the building (Belleri et al., 2021; Schulze & Eicker, 2013; Schulze et al., 2018). It also has architectural benefits, as it does not require space for duct network to distribute the air within the building, leaving free use of floor-to-ceiling height (CIBSE, 2005). Furthermore, measures to enhance daylight (such as limited penetration depth and increased floor-to-ceiling height) also favor the use of natural ventilation (Carrilho da Graça & Linden, 2016).

However, unfavorable outdoor environmental conditions can limit the use of solely natural ventilation and, for this reason, it is often necessary to resort to hybrid ventilation systems (Ezzeldin & Rees, 2013; Salcido et al., 2016a), or so-called mixed-mode ventilation. There are many studies that have shown the benefits of combining controlled natural ventilation and mechanical ventilation in terms of indoor environment conditions (Arata & Kawakubo, 2022; Hamdy & Mauro, 2019; Kim & de Dear, 2021; Salcido et al., 2016b), but too little is known about the potential of these strategies applied in the South Tyrolean climate context (northern Italy). These strategies must not only be designed with the aim of maximizing IAQ and

thermal comfort while reducing energy consumption, but should also take into account the climatic conditions, the typological aspects of the building stock and the habits of the occupants.

The aim of this research is to estimate the potential of mixed-mode ventilation strategies in comparison with the performance of controlled natural ventilation and mechanical ventilation applied separately, in the context of a dwelling located in a multi-family house in Bolzano (Italy) during the summer season.

2. Methodology

The case study building presented in this paper consists of a dwelling located in a multi-family house in Bolzano (Italy). It has a net floor area of 54 m² and is occupied by 3 tenants. The model consists of five thermal zones, one for each room of the apartment, i.e., two bedrooms, a living room/kitchen, a bathroom and a small central corridor. Each room, except bathroom and corridor, has only one window. The living area faces south, while the sleeping area faces south and east.

Dynamic simulations and the related analysis were performed, developing a room-by-room coupled thermal and airflow model of the dwelling in TRNSYS and TRNFLOW to characterize its thermal behavior and natural airflows.

We applied the schedules for occupancy, lighting, and electric equipment reported in Wilson et al., 2014, assuming that four occupants are living in the apartment. The total heat gains related to occupants, as well as the CO₂ generation rates, were calculated according to typical metabolic heat generation for domestic activities, namely 1.2 met for occupants in the living area, and 1 met for occupants in the sleeping area. Lighting power density was assumed to be equal to 2.7 W/m². When the rooms are occupied, lights are switched on if beam radiation on the room window surface is below 140 W/m². Electrical equipment power density was assumed to be equal to 8 W/m². If occupants are “sleeping” or “absent”, internal loads are considered equal to 2 W/m² (20 % of total installed power); if occupants are “active”, internal loads are considered equal to 6 W/m² (60 % of total installed

power, considering a coincidence factor of 0.6). Solar shadings are activated if the zone air temperature is above 24 °C and incident solar radiation on the window is above 140 W/m².

The infiltration and ventilation airflows are calculated through the multizone airflow network model coupled to the thermal model through TRNFLOW. The airflow network model includes cracks along the window perimeter and openings at each window and internal door. Fig. 1 also reports a scheme of the airflow network with air nodes, flow paths and flow links. The flow coefficients of the cracks were set in order to have an overall envelope air tightness equal to 0.6 h⁻¹ at 50 Pa. No cooling system is considered, but natural ventilation can be activated to provide for ventilative cooling over the warm season. A dual-flow ventilation unit uses supply and return fans to bring fresh air from outside into the living room and bedrooms, and exhausts stale air from the bathroom and kitchen. The ventilation unit is equipped with a high-efficiency passive heat exchanger that allows ventilation thermal losses to be minimized. The heat exchanger can also be bypassed. Each simulation was performed with a timestep of 15 min over the warm season (from May to September). The weather data was generated by Meteonorm using extreme hourly values over a 10-year weather time series for the city of Bolzano. This study analyzes and compares three different scenarios in the climate conditions of Bolzano: (1) only controlled natural ventilation (CNV), (2) only mechanical ventilation (MVT), (3) a combination of the two (mixed ventilation strategies, MIX).

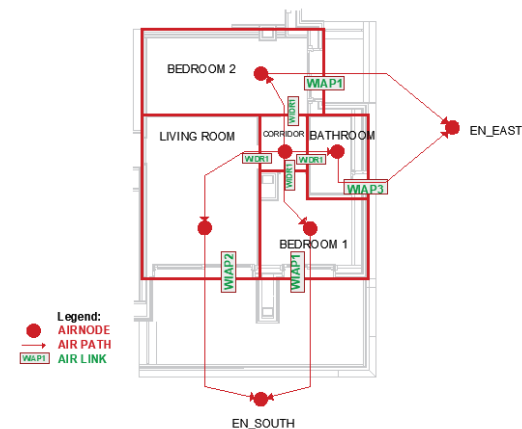


Fig. 1 – Reference building plan, thermal zones, airflow network

2.1 Controlled Natural Ventilation

CNV strategies are designed with a twofold aim, which is (a) to improve the indoor thermal comfort reducing the overheating risk thanks to ventilative cooling, and (b) to improve IAQ by removing indoor airborne pollutants coming from indoor sources.

Two CNV strategies are implemented: a) the single-sided ventilation strategy (CNV-SN) controls the opening and closing of the windows in individual rooms of the apartment independently of the other rooms, while the cross-ventilation strategy (CNV-CR) simultaneously controls multiple rooms. In a real-building application, the opening or closing of the windows could be automated by the application of actuators whose action is guided by algorithms which, based on the internal and external environmental conditions, identify the optimal opening level. The opening or closing of windows is represented in the model by an opening factor, which is a value of between 0 and 1. 0 means total closure and 1 full opening of the window (an opening factor of 0.2 indicates, for instance, a bottom hung window opening) (Table 1). All doors between rooms are assumed to stay half-opened all the time. In order to find the most suitable natural ventilation strategy, internal and external environmental conditions, such as internal temperature and CO₂ concentration, outdoor temperature and relative humidity, are considered in the analysis (Table 2).

Table 1 – Range of window opening factor

Output	Description	Value
WIN_LR	Living room window opening factor	0-1 ¹
WIN_BR1	Single bedroom window opening factor	0-1
WIN_BR2	Double bedroom window opening factor	0-1

¹ In this study 0.2 is considered because of the vasistas opening mode

Table 2 - Controlled natural ventilation input

Input	Description	Unit of measurement
TAIR_EXT	Convective outside air temperature	°C
HR_EXT	Relative humidity of the outside air	%
TAIR_LR	Convective air temperature in the living room	°C
TAIR_BR1	Convective air temperature in the single bedroom	°C
TAIR_BR2	Convective air temperature in the double bedroom	°C
CO ₂ _LR	CO ₂ concentration in the living room	ppm
CO ₂ _BR1	CO ₂ concentration in the single bedroom	ppm
CO ₂ _BR2	CO ₂ concentration in the double bedroom	ppm

Table 3 – Control parameters for the activation of controlled natural ventilation

Parameter	Description	Default Value
TAIR_EXT _{min}	Minimum outdoor temperature	16 °C
HR_EXT _{max}	Minimum relative humidity	85 %
TAIR _{cmf}	Convective air temperature for the activation of CNV	25 °C
CO ₂ _LR _{min}	CO ₂ concentration limit in the living room	750 ppm
CO ₂ _BR1 _{min}	CO ₂ concentration limit in the single bedroom	1000 ppm
CO ₂ _BR2 _{min}	CO ₂ concentration limit in the double bedroom	1000 ppm

Assuming that the apartment is equipped with measurement points of the parameters shown in Table 2, these are compared with the threshold values shown in Table 3.

In Table 4, the control signals are listed, defined as Booleans calculated with logic functions of measured data, control parameters or a combination of other control signals.

Table 4 – Control signals of controlled natural ventilation

Signal	Logic function
Y_SN	SN=1-0
Y_CR	CR=1-0
A	TAIR_EXT > TAIR_EXTmin
R	HR_EXT < HR_EXTmax
G_ZONE	TAIR_EXT < TAIR_ZONE
F_ZONE	TAIR_ZONE > TAIR _{cmf}
E_ZONE	CO ₂ _ZONE > CO ₂ _min ²
H	MIN(F_LR+F_BR1+F_BR2,1)
L	MIN(G_LR+G_BR1+G_BR2,1)

In Fig. 7 and Fig. 8 the processes that led to the activation of CNV-SN and CNV-CR are summarized. In particular, the activation of the CNV is regulated according to the external environmental conditions (external temperature greater than 16 °C and relative humidity less than 85 %).

2.2 Mechanical Ventilation

A CO₂-based demand-controlled ventilation strategy (DCV) is applied to trigger the operation of the mechanical ventilation unit, which considers the CO₂ concentration threshold value greater than 200 ppm compared with those designed for the activation of the CNV.

More detailed information is reported in Table 5.

Table 5 – MVT properties

Air flow rate per occ [m ³ /h]	Specific fan pow. [Wh/m ³] ³	Heat rec. eff	Free cooling mode ON
36	0.28	70 %	TAIR_EXH ⁴ > 23.5 °C TAIR_EXT < TAIR_ZONE TAIR_EXT > 16 °C

2.3 Mixed-Mode Ventilation

Mixed-mode ventilation allows the use of CNV and MVT. There are no conditions imposed a priori on the alternative or simultaneous use of the two ventilation techniques, but the control logic settings of both systems prioritize the use of natural ventilation when the outdoor conditions are acceptable. The activation of CNV occurs after an increase of indoor temperature above the reference comfort temperature or for hygienic ventilation needs, while mechanical ventilation intervenes only when the CO₂ concentration exceeds the threshold and natural ventilation is not effective in providing hygienic ventilation rates. In fact, the pollutant concentration thresholds defined for the activation of controlled natural ventilation and mechanical ventilation are different, with lower threshold values for the activation of CNV. From this perspective, it will be possible to encourage the use of natural ventilation compared with mechanical ventilation, reducing electrical consumption. The performance indicators considered in the analysis of the results are summarized in Table 6 and refer to IAQ, thermal comfort and electricity consumption for MVT.

3. Results and Discussion

The study examines and compares three different scenarios: (1) only CNV, (2) only MVT, (3) a combination of the two (mixed ventilation strategies).

³ 'SIA-Shop Produkt - 'SIA 2024 / 2015 D - Raumnutzungsdaten Für Energie- Und Gebäudetechnik (Normenwerk => Architekt).'" n.d. Accessed March 31, 2022. <http://shop.sia.ch/normenwerk/architekt/sia/2024/d/2015/D/Product>.

⁴ TAIR_EXH = exhaust air temperature

² It refers to CO₂_LRmin - CO₂_BR1min - CO₂_BR2min

Table 6 – Performance indicators

Symbol	Unit of measurement	Description
N _{on}	h	No. of hours of activation of the CNV and MVT strategies
D _{op}	h	Avg duration of window opening
N _{att}	No	No. of actv. of the window actuators
W _{MVT}	kWh	Electricity consumed by the MVT
W _{MIX-SN}	kWh	Electricity consumed by the MIX-SN
W _{MIX-CR}	kWh	Electricity consumed by the MVT-CN
OH _h	%	% of occ. hours T _{air} >26 °C (Nicol, 2013)
OH _i	K	Avg. intensity OH during occ. hours
CO ₂ , C ₁₋₄	%	% of occ. hours CO ₂ (cat I-IV) ⁵
HR, C ₁₋₄	%	% of occ. hours HR (cat I-IV) ⁶

The results of the simulation model are analyzed in terms of IAQ, thermal comfort and electricity consumption connected to ventilation. Fig. 2 shows the average distribution of occupied hours of the three thermal zones (living room, single bedroom, double bedroom) in the four categories of environmental quality (“CEN/TR 16798-2:2019 Energy Performance of Buildings - Ventilation for Buildings - Part 2: Interpretation of the Requirements in EN 16798-1 - Indoor Environmental Input Parameters for Design and Assessment of Energy Performance of Buildings Addressing Indo” 2019) defined by concentration of CO₂ in the thermal zones during the summer period (May-September). As regards

CNV, it guarantees excellent levels of IAQ in terms of CO₂ concentration for the greatest number of hours (55 % of occupied hours fall into category I), while, for the remaining part of the time, the IAQ falls in category IV (where Category I corresponds to a high level of expectation, Category II to a medium level). This is probably due to the fact that the activation of the CNV is regulated according to the external environmental conditions (external temperature and relative humidity, see Fig. 7 and Fig. 8), which, if they were not favorable, would not allow the opening of the windows for the correct hygienic replacement.

The optimal results are those obtained from the use of mixed-mode ventilation strategies, able to exploit the potential of natural ventilation strategies and to use MVT as a backup if the activation of natural ventilation is not convenient.

Compared to CNV, MVT guarantees a greater number of occupied hours in which the CO₂ concentration level corresponds to the one required by categories I and II of indoor environmental quality (IEQ).

Focusing on controlled and mixed-mode natural ventilation strategies, Fig. 3 shows the distribution of the activation hours of the strategies in the living room for the summer season by type of ventilation.

Only with controlled natural ventilation strategies are the windows open for about 60 % of the summer hours, while for about 40 % of the hours natural ventilation cannot be activated, despite the need for ventilation, because of unfavorable outdoor conditions. In the case of mixed ventilation, this eventuality is considerably reduced to about 15 % of the total summer hours, thanks to the contribution of mechanical ventilation, which is active for about 30 % of the hours. It is also observed that the number of hours in which both natural and mechanical ventilation are active is very low (about 2 % of the hours).

⁵ CO₂ categories were defined according to EN16798-1 Annex B assuming 400ppm as the average outdoor concentration (“EN 16798-1:2019 Energy Performance of Buildings - Ventilation for Buildings - Part 1: Indoor Environmental Input Parameters for Design and Assessment of Energy Performance of Buildings Addressing Indoor Air Quality, Thermal Environment, Lighting and Acous” 2019)

⁶ relative humidity cat. were defined according to EN16798-1 Table I.11

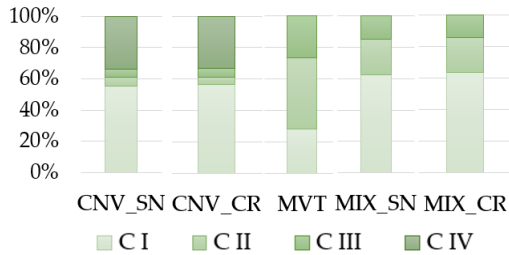


Fig. 2 – Distribution of IAQ categories (C I–C IV) for the CO₂ concentration during the occupied hours considering the five ventilation strategies during the summer period (May–September)

Even if the two control systems do not communicate with each other, their control prevents their simultaneous activation, allowing the two types of ventilation to alternate with each other. In addition, Fig. 4 shows the influence that outdoor temperature and humidity conditions (see Table 3) have on the activation of CNV strategies. As the figure shows, the outdoor temperature is the most critical parameter (higher than 70 % of hours during the summer period), when the outside temperatures are lower and, during the night, they can drop below 16 °C. In general, no significant improvement occurs by activating the CNV-CR strategy, probably due to the fact that air mixing within the apartment was ensured by an open door all the time. As regards the hygrometric results, Fig. 5 shows the distribution of the relative humidity in the four categories of environmental quality during the occupied hours considering all the ventilation scenarios.

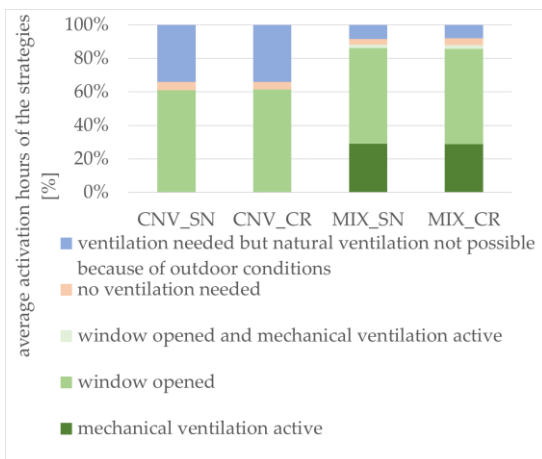


Fig. 3 – Average activation hours of the strategies in the LR during the summer period

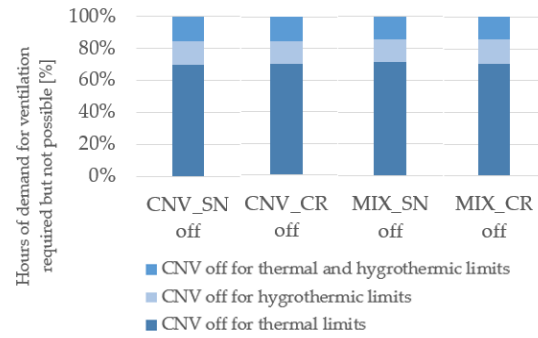


Fig. 4 – LR % of hours in which it is not possible to take advantage of CNV due to the thermal and hygrometric limits imposed on its activation [%]

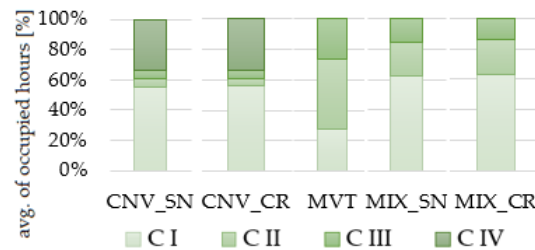


Fig. 5 – Distribution of hygrometric categories (C I – C IV) for the relative humidity assessed during the occupied hours considering the five ventilation strategies during the summer period

In all scenarios, most of the occupied hours fall into category I or II, i.e., with a relative humidity of between 25 % and 60 %. Only the MVT scenario guarantees better results, probably due to the fact that the air intake with MVT is localized in the rooms where there is the greatest generation of water vapor. A percentage of hours greater than 0 % falls into categories III–IV, assuming that unfavorable external conditions do not allow the opening of the windows.

As regard overheating, the graph in Fig. 6 shows the average percentage of occupied hours with overheating risk (reference temperature equal to 26 °C) and the average intensity. As the figure shows, the highest overheating occurs in the MVT case with monthly average overheating hours of 80 % and monthly average intensity of 2.7 °C.

The higher overheating rate in the MVT case is probably due to (1) the presence of the heat recovery unit, which has an undesirable recovery effect even in free cooling mode, (2) the limited air flows moved by the ventilation and finally (3) the lack of forced ventilation control dedicated to ventilative cooling. The scenarios with CNV and MIX strategies show a lower overheating rate, even if lower

percentages of monthly average overheating hours and monthly average overheating intensity are noted in the second case.

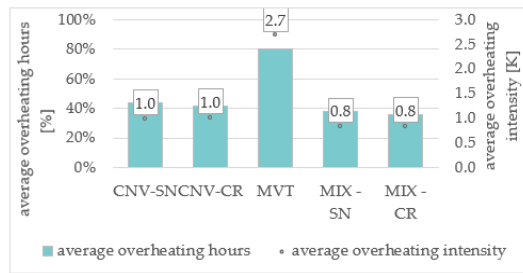


Fig. 6 – Average overheating hours and overheating intensity across all the model zones

As regards electricity consumption, with MVT only this is equal to 75 kWh, MIX-SN to 35 kWh and MIX-CR to 34 kWh. MIX therefore allows a saving of approximately 40 kWh of electricity to be achieved, which corresponds approximately to a reduction of 54 % of electricity consumption for ventilation compared with the case of MVT only. In the case of CNV, during the cooling season, it is relatively lower than MVT, since the only energy use is for opening and closing the windows.

4. Conclusion

The aim of this research is to demonstrate the potential of mixed-mode ventilation strategies in comparison with the performance of CNV and MVT (without free-cooling option) applied separately, in the context of a dwelling located in a multi-family house in Bolzano (Italy) during the summer season.

This study analyzes and compares three different scenarios in the climate conditions of Bolzano during the cooling season: (1) only CNV, (2) only MVT, (3) a combination of the two (mixed-mode ventilation strategies).

The main results show that CNV and MIX allow a reduction in the overheating risk and an excellent level of IAQ to be achieved, although inadequate outdoor conditions may prevent window opening. MVT allows acceptable IAQ and humidity levels. However, overheating can occur up to 80 % of the time over the summer period due to: (1) the presence of the heat recovery unit, which has an unde-

sirable recovery effect, even in free cooling mode, (2) the limited amount of air flows moved by the ventilation machine and (3) the lack of a forced ventilation control for the ventilative cooling. MIX provides excellent performance in terms of IAQ and overheating control, compared to the former strategies. The lower use of MVT makes it possible to achieve a saving of approximately 40 kWh of electricity for the summer season, which corresponds approximately to a reduction of 54 % of electricity consumption for ventilation compared with the case of MVT only. As shown in the system activation trends, the greater use of natural ventilation corresponds with less frequent use of mechanical ventilation, with a very reduced number of hours of simultaneous activation of the two (approximately 2 % of the total hours).

More in-depth analyses will be carried out on overheating to compare strategies in summer conditions, through an adaptive analysis of thermal comfort.

Acknowledgement

This research is supported by funding from the European Regional Development Fund, operational programme POR FESR 2014-2020 of the Province of Bolzano, project number FESR 1116: NEW-AIR - Nuovo approccio per una qualità degli ambienti interni energeticamente efficienti: ricerca e aziende fanno sistema in Alto Adige.

References

- Arata, S., and S. Kawakubo. 2022. "Study on Productivity of Office Workers and Power Consumption of Air Conditioners in a Mixed-Mode Ventilation Building during Springtime." *Building and Environment* 214: 108923.
- Belleri, A., F. Avella, and F. Babich. 2021. "The Impact Of Controlled Natural Ventilation In Residential Buildings." *Roomvent* 2020.
- Carrilho da Graça, G., and P. Linden. 2016. "Ten Questions about Natural Ventilation of Non-Domestic Buildings." *Building and Environment* 107: 263–73.
<https://doi.org/10.1016/J.BUILDENV.2016.08.007>

- CEN. 2019a. CEN/TR 16798-2:2019 *Energy Performance of Buildings - Ventilation for Buildings - Part 2: Interpretation of the Requirements in EN 16798-1 - Indoor Environmental Input Parameters for Design and Assessment of Energy Performance of Buildings Addressing Indo.*
- CEN. 2019b. EN 16798-1:2019 *Energy Performance of Buildings - Ventilation for Buildings - Part 1: Indoor Environmental Input Parameters for Design and Assessment of Energy Performance of Buildings Addressing Indoor Air Quality, Thermal Environment, Lighting and Acoustics.*
- CIBSE. 2005. "CIBSE Applications Manual AM10." *Cibse Am10*, 70.
- Ezzeldin, S., and S. J. Rees. 2013. "The Potential for Office Buildings with Mixed-Mode Ventilation and Low Energy Cooling Systems in Arid Climates." *Energy and Buildings* 65: 368–81. doi: <https://doi.org/10.1016/j.enbuild.2013.06.004>
- Hamdy, M., and G. M. Mauro. 2019. "Optimizing Hybrid Ventilation Control Strategies Toward Zero-Cooling Energy Building." *Frontiers in Built Environment* 5. doi: <https://doi.org/10.3389/fbuil.2019.00097>
- Kim, J., and R. de Dear. 2021. "Is Mixed-Mode Ventilation a Comfortable Low-Energy Solution? A Literature Review." *Building and Environment* 205: 108215. <https://doi.org/10.1016/J.BUILDENV.2021.108215>
- Nicol, F. 2013. *The Limits of Thermal Comfort: Avoiding Overheating in European Buildings.* London: CIBSE.

<https://www.cibse.org/knowledge/knowledge-items/detail?id=a0q20000008I7f5AAC>

- Salcido, J.C., A. A. Raheem, and R. R. A. Issa. 2016a. "From Simulation to Monitoring: Evaluating the Potential of Mixed-Mode Ventilation (MMV) Systems for Integrating Natural Ventilation in Office Buildings through a Comprehensive Literature Review." *Energy and Buildings* 127: 1008–18. doi: <https://doi.org/10.1016/j.enbuild.2016.06.054>
- Salcido, J.C., A. A. Raheem, and R. R. A. Issa. 2016b. "From Simulation to Monitoring: Evaluating the Potential of Mixed-Mode Ventilation (MMV) Systems for Integrating Natural Ventilation in Office Buildings through a Comprehensive Literature Review." *Energy and Buildings* 127: 1008–18. doi: <https://doi.org/10.1016/J.ENBUILD.2016.06.054>
- Schulze, T., and U. Eicker. 2013. "Controlled Natural Ventilation for Energy Efficient Buildings." *Energy and Buildings* 56: 221–32. doi: <https://doi.org/10.1016/J.ENBUILD.2012.07.044>
- Schulze, T., D. Gürlich, and U. Eicker. 2018. "Performance Assessment of Controlled Natural Ventilation for Air Quality Control and Passive Cooling in Existing and New Office Type Buildings." *Energy and Buildings* 172: 265–78. doi: <https://doi.org/10.1016/J.ENBUILD.2018.03.023>
- Wilson, E., C. E. Metzger, S. Horowitz, and R. Hendron. 2014. "2014 Building America House Simulation Protocols." www.nrel.gov/publications

Appendix

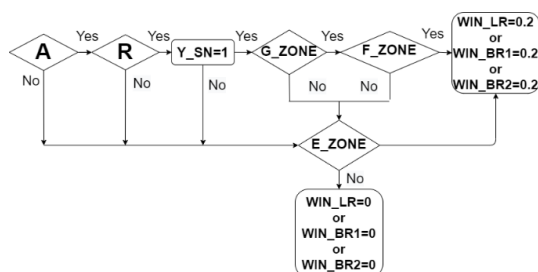


Fig. 7 – CNV-SN

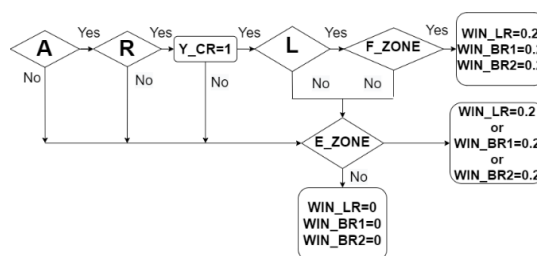


Fig. 8 – CNV-CR

A Comparison Among Three Whole-Building Dynamic Simulation Software and their Applicability to the Indoor Climate Modelling of Historical Buildings

Francesca Frasca – Sapienza University of Rome, Italy – f.frasca@uniroma1.it

Elena Verticchio – Sapienza University of Rome, Italy – elena.verticchio@uniroma1.it

Michele Libralato – University of Udine, Italy – michele.libralato@uniud.it

Paola D'Agaro – University of Udine, Italy – paola.dagaro@uniud.it

Giovanni Cortella – University of Udine, Italy – giovanni.cortella@uniud.it

Anna Maria Siani – Sapienza University of Rome, Italy – annamaria.siani@uniroma1.it

Cristina Cornaro – Università degli Studi di Roma “Tor Vergata”, Italy – cornaro@uniroma2.it

Abstract

Building energy simulations are important for assessing the performance of buildings and for designing solutions aimed at reducing energy consumption and carbon emissions. Many software tools perform these simulations, focusing on systems operations and energy losses and gains. When it comes to modelling historical buildings, the simulations could be also used to estimate the risk of damage and decay processes. This paper presents preliminary results based on twelve standardised exercises of increasing complexity for the comparison of microclimate simulations modelled through three whole-building hygrothermal dynamic simulation (BDS) software tools, specifically IDA ICE, WUFI PLUS and ENERGY PLUS. Different to the testing procedures already available, this research focused on the physical variables that are relevant for conservation of historical buildings (i.e., temperature (T) and relative humidity (RH)). Starting from Common Exercise 0 (CE0), seven simulations were customised to capture differences in T values. Then, five building models were specifically conceived to consider some typical features of Historical Buildings (HB0): small window size, heavyweight structures, low insulation of roofs, large volume and free-floating conditions. In the case of CE0, good agreement was found in the simulation of indoor T. In addition, detailed windows reduced the discrepancy in T results compared with the use of simplified windows. In the case of HB0, small windows slightly affected the microclimate simulations regardless of the number of transparent elements and their position. RH variability was driven only by T, as the partial water vapor pressure was affected only by infiltrations through the building. To conclude, the comparison allowed a

highlighting of some critical points due to different model implementations, such as weather file timestamp interpretation, window models or irradiation calculations. HB0 models could be used for software and model comparisons, new software testing and training activities.

1. Introduction

Whole-building dynamic simulation (BDS) has been extensively applied over the last decades to study the energy performance of new and existing buildings. BDS can be used as a tool to identify measures aimed at reducing energy consumption and greenhouse gas emissions, as required by the Green Deal to be climate neutral in 2050. In the case of historical buildings, which account for a relevant portion of the total amount of energy consumption (Filippi, 2015) and are part of the cultural heritage, designing efficient and cautious interventions to accomplish the Green Deal goals is a complex matter. In addition, since humidity plays a key role in the different deterioration phenomena affecting materials (making the choice of unique critical thresholds challenging (EN 16893:2018)), simulation can identify the conservation risks of materials triggered by indoor climate conditions (Akkurt et al., 2020; Frasca et al., 2021).

In this context, it was demonstrated that the hygrothermal modeling through BDS can be used advantageously to design solutions for minimizing the energy demand whilst keeping the risk of deterior-

ration low. However, whole set of BDS software needs to accurately model the time behavior of the key hygrothermal variables (e.g., temperature and relative humidity) responsible for degradation on a short and long-term scale. Several commercial BDS software tools are available for hygrothermal modeling. However, since they are based on different numerical methods and parameterizations to solve physical equations, discrepancies may occur in the simulation of indoor climate conditions when the same building is modeled using different BDS software. For this reason, it is worth estimating to what extent the variability among the outputs from different BDS software can affect decision-making on energy (e.g., setup of HVAC systems (Nicolai et al., 2021; Tarantino, 2020)) and conservation issues in real applications (e.g., estimation of climate-induced conservation risks (Frasca et al., 2021; Libralato et al., 2021a)). This evaluation is important, as it offers the chance to provide comparable indoor climate projections regardless of the BDS software in use. This aspect plays a key role when it comes to assessing the impact of the ongoing climate change on material conservation (Campisi & Colajanni, 2021) and the effectiveness of materials for retrofitting/strengthening historical structures. In such a way, the BDS becomes a powerful approach to be applied with the aim of contributing towards meeting global 2030 Sustainable Development Goals (SDGs) in the historical building sector (e.g., definition of adaptation pathways and mitigation strategies against climate change).

This study aimed to compare three commercial whole-BDS software tools (namely EnergyPlus, IDA Indoor Climate and Energy (ICE) and WUFI Plus) frequently validated and commonly used in research activities for the indoor climate modeling of historical buildings (to cite but a few Angelotti et al., 2019; Frasca et al., 2018; Gori et al., 2021; Libralato et al., 2021b). The comparison, based on standardised exercises, was not conceived to identify the most suitable tools for historical buildings modeling, but rather to evaluate the effect on simulations due to the differences in interfaces and modeling approaches. In this contribution, indoor humidity balance considered only the water vapor in/exfiltration through the envelope, to limit the initial uncertainties related to heat and moisture transfer through walls. Further investigations on this topic will be the subject of future studies.

2. Materials and Methods

According to ANSI/ASHRAE 140 Standard, there are three ways to evaluate the accuracy of BDS software tool: empirical validation (comparison with measured data), analytical verification (comparison with a known analytical solution) and comparative testing (the software is compared with itself or to other programs). In this paper, we adopted the comparative testing to estimate the differences among the three BDS software tools. Comparison among BDS software was conceived

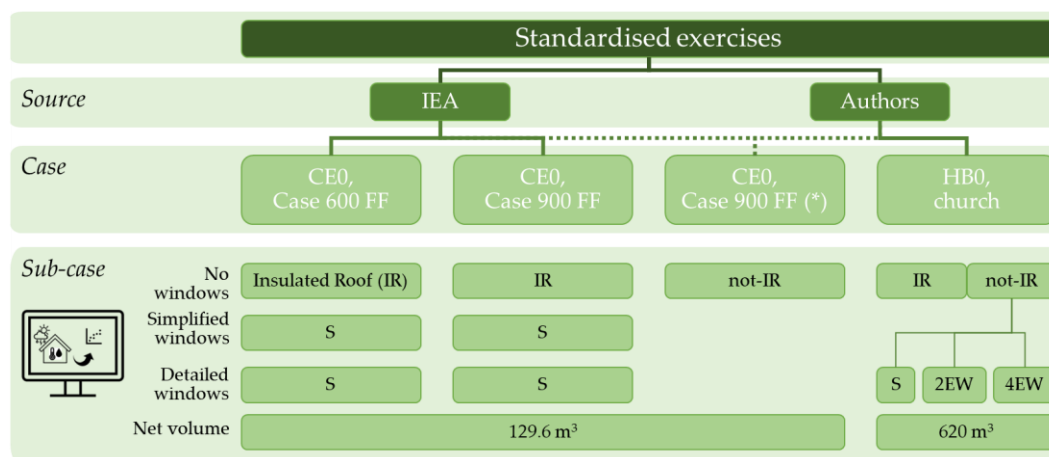


Fig. 1 – Set of simulations based on standardised exercises for the comparative assessment of commercial whole-building dynamic simulation software. CE0: Common Exercise 0; HB0: Historical Building 0; IR: insulated roof; not-IR: not-insulated roof; S: south façade; E: east façade; W: west façade; 2: two windows; 4: four windows

following the schema in Fig. 1. The simulation set consisted of twelve standardised exercises that considered both the BESTEST (Building Energy Simulation TEST) Common Exercise 0 (hereafter called CE0), developed in the framework of the International Energy Agency (IEA), and a historical building (HB0) proposed by the authors. CE0 included seven sub-cases aimed at studying both the influence on simulations of detailed/simplified south-oriented windows as well as the role of a flat insulated/not-insulated roof. HB0, on the other hand, included five sub-cases with a sloping insulated/not-insulated roof and an increasing number of differently oriented windows (South, East-West).

All simulations were run with an initialization period of 31 days and a weather file of data having time steps of 1 hour. All simulations covered one calendar year.

In this study, *.EPW files were used for the weather file. Energy Plus uses the “next hour interpolation scheme”, assigning the 1:00 time stamp to the average of the weather file values at hour 0:00 and 1:00. IDA ICE interprets the weather file, assigning the value around the time stamp (average value measured between 30 minutes before and after the time stamp) and the results are reported as the average of the hour preceding the output time stamp. WUFI Plus uses the *.EPW file provided by the user, as it is, starting from hour 01:00 (first observation) and automatically converting radiation and rain (the latter is not included in simulations within this research) in order to consider these loads in accordance with the orientation and the inclination of the individual building component.

IDA ICE climate calculations were based on the “BDFwall” thermal model using a finite differences algorithm of a multi-layer component including wind-dependent bidirectional heat and moisture transport through leaks.

WUFI Plus performed thermal calculations including methods for wind-dependent heat transfer on external surfaces and moisture balance due to in/exfiltration.

In Energy Plus, the heat balance algorithm used is the “Conduction Finite Difference” algorithm, based on the finite difference method. The surface convection algorithm for the external surfaces is

the “DOE-2” algorithm, wind-dependent and based on measurements, while for the internal surfaces, constant convection coefficients are used.

In all simulations, a constant air infiltration was set, meaning that no wind-driven air and vapor infiltrations were considered.

2.1 BESTEST Developed in the Framework Of IEA Annex

The CE0 exercise was used to investigate differences in free-floating (FF) simulations among the three BDS software for both lightweight (Case 600) and heavyweight (Case 900) buildings, using the weather at the site of Denver-Stapleton. The FF cases were chosen, as in most historical buildings, active climate control systems are not used. The common exercise adopted was slightly modified to study the features of the BDS software in the simulation of indoor temperature through cases at increasing complexity. All features were retrieved from the Publications and Work Reports available online for the IEA Annex 41 (Rode & Woloszyn, 2007). The influence of solar radiation incident on opaque and transparent surfaces was evaluated modeling the building firstly without windows and, then with windows on the southern façade ($U\text{-value} = 3.0 \text{ W}\cdot\text{m}^{-2}\cdot\text{K}^{-1}$; hemispherical SHGC = 0.686). Specifically, windows were modeled using both simplified and detailed models available in the BDS software to estimate the influence of the input parameters on the indoor temperature. Windows models differ from the number of input parameters that users can set. In addition, we decided to modify Case 900 FF by replacing the original roof with a not-insulated roof. This case, renamed Case 900 FF (*), was conceived to understand the influence on indoor temperature simulations of not-insulated roof in heavyweight structures (i.e., typical features in historical buildings).

2.2 Standardised Exercise for Historical Building (HB0)

A new standardised exercise for historical buildings (HB0) was proposed by the authors, starting from the average features extracted from the literature on the topic (Akkurt et al., 2020) and from the Italian technical report UNI/TR 11552:2014. All the

cases are considered in free-floating conditions, without internal gains (occupants and other devices) in accordance with CE0.

Fig. 2 shows the 3D geometry of the HB0 model used in the tested sub-cases. Table 1 summarizes some features of the opaque elements in HB0. The simulations are performed using the IWEK weather file for Rome.

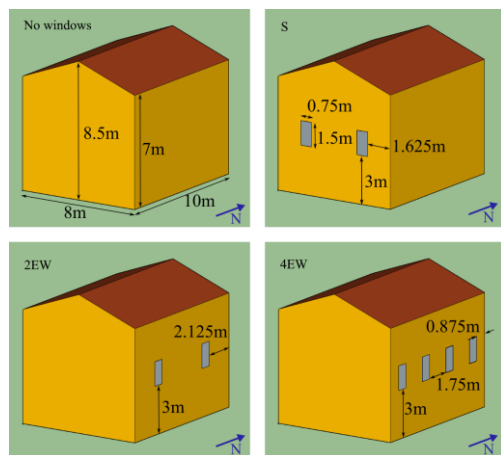


Fig. 2 – 3D sketch of the standardised exercise HB0 used to compare commercial whole-building dynamic simulation software in case of a historical building. Net floor area = 80 m²; net volume = 620 m³

U-value of the floor is extremely low in accordance with the BESTest and to avoid the effect of ground modeling on the indoor climate simulation. Windows were modeled as single pane glass with a total transparent area of 0.75×1.5 m² without frame and a U-value of 5.5 W·m⁻²·K⁻¹. Five sub-cases were modeled (Fig. 2):

- no transparent elements and insulated roof (hereafter called IR);
- no transparent elements and not-insulated roof (not-IR);
- two windows on south façade (2S);
- two windows on both east and west façades (2EW);
- four windows on both east and west façades (4EW).

The air infiltrations were set to a constant air change of 0.7 h⁻¹, i.e., an average infiltration rate in historical churches (Akkurt et al., 2020). In addition, solar emissivity and absorption of internal/external opaque surfaces were set equal to 0.9 and 0.6, respectively.

2.3 Statistical Analysis

The average of the maximum semi-dispersion (Δ_{max} , i.e., the mean half spread between the smallest and largest number over the simulation period) was used as a synthetic index to compare the variability of hourly microclimate values (i.e., temperature and relative humidity) resulting from the annual simulations modeled by the three BDS software tools. As no reference has been defined so far to estimate agreement between simulations run by different BDS software tools, we decided to use the threshold suggested in (Frasca et al., 2021; Rajčić et al., 2018) for the accuracy assessment of the hygro-thermal simulations with respect to microclimate observations: high agreement, if data are within ± 1 °C for T and ± 5 % for RH, good agreement, if data are within ± 3 °C for T and ± 10 % for RH, and poor agreement, if data are beyond ± 3 °C for T and ± 10 % for RH.

Table 1 – Summary of thermo-physical properties of opaque elements in HB0

Building component	Area	U-value	Thermal mass
Unit	[m ²]	[W·m ⁻² ·K ⁻¹]	[kJ·m ⁻² ·K ⁻¹]
External walls	264	0.67	1184
Roof	88	2.48	255
Floor	80	0.04	112

In the case of CE0, the daily evolution of indoor and outdoor temperatures was plotted to assess agreement at a short-term time scale among the three BDS software tools on the coldest and the hottest days of the year of the weather file, respectively.

In the case of HB0, a 3-by-3 matrix of plots was used to analyse the differences in the microclimate outcomes (temperature and partial water vapor pressure). The scatter plots in the matrix allowed a comparison of the outputs between pairs of BDS software (*inter-comparison*). Along the matrix diagonal, stair plots were displayed to study the influence of different HB0 configurations on the microclimate variables within the same BDS software (*intra-comparison*).

3. Results

3.1 BESTEST in IEA Annex (CE0)

Table 2 shows that:

- in the case without windows, temperature simulations were in good agreement both in light- and heavyweight structures;
- the highest variability is associated with the simulations of Case 600 FF with simplified windows;
- the use of detailed windows allowed a reduction in dispersion among simulated indoor T values from 1.4-2.2 °C to 0.9-1.8 °C.

Table 2 – Summary of the maximum semi-dispersion (Δ_{max}) of the hourly temperature values modeled by the three BDS software tools in case of CE0 in free-floating conditions

Case	No windows	Simplified windows	Detailed windows
Case 600 FF	1.0	2.2	1.8
Case 900 FF	0.7	1.4	0.9
Case 900 FF (*)	1.1	-	-

In addition, for both Case 600 FF and Case 900 FF with detailed windows, the modeled minimum annual temperature values (i.e., when the impact of solar radiation is limited) were in accordance with the reference ranges reported in (Rode & Woloszyn, 2007).

On the other hand, lower agreement was observed with the reference ranges in terms of the average and maximum annual temperature values, due to differences in the calculation of solar gains through windows. The first source of discrepancy in the time series of the results is different interpretation of the weather file (WF) due to the different conversion of the time stamp to specific points in time used by the BDS software.

As an example, Figs. 3 and 4 show that the weather file temperatures considered by each software (WF series) have a time shift of at least one hour.

The discrepancy in the WF series influences the simulation of indoor temperatures. Indeed, although highly correlated, T peaks modeled by WUFI Plus and Energy Plus models showed a one-hour delay compared with IDA ICE. This behavior

is also affected by differences in the calculation of the wind-driven coefficients of convection and radiation heat transfer, as described in Section 2.

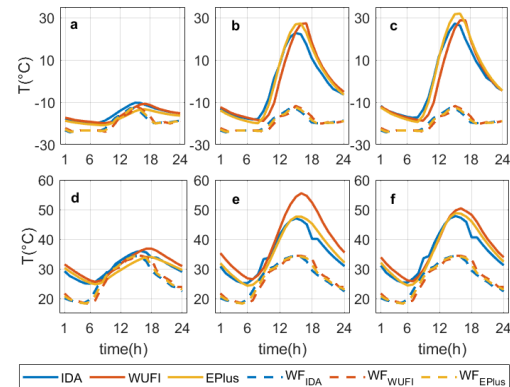


Fig. 3 – Time evolution of temperature on the coldest day (upper panels) and the warmest day (lower panels) in Case 600 FF without windows (a, d), with simplified windows (b, e) and with detailed windows (c, f). The WF series indicates the weather file temperature considered by the software

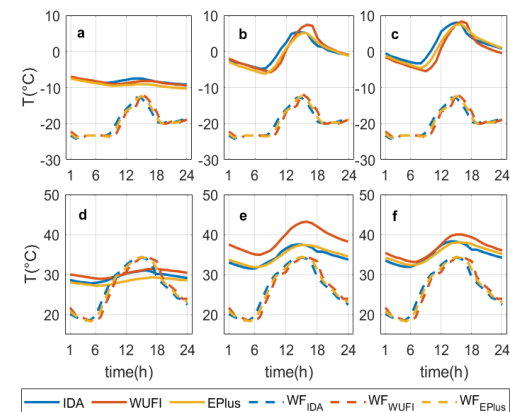


Fig. 4 – Time evolution of temperature on the coldest day (upper panels) and the warmest day (lower panels) in Case 900 FF without windows (a, d), with simplified windows (b, e) and with detailed windows (c, f). The WF series indicate the weather file temperature considered by the software

Moreover, the three BDS software tools calculate the resulting solar radiation incident on surfaces differently, leading to a different indoor heat balance due to the solar net radiative balance. For example, Energy Plus and IDA ICE use the Perez model, but with a different set of coefficients. This effect was evident when comparing the intensity of T peaks in the case of simplified windows models, which seem to be differently reproducing the transparent surface behavior in both Case 600 FF (Fig. 3) and Case 900 FF (Fig. 4).

3.2 Standardised Exercise for Historical Building (HB0)

In the case of HB0, simulations were run using detailed windows.

The values of total annual incident solar radiation on opaque surfaces (walls and roof) were compared to better interpret whether some of the differences in T simulations were ascribable to this contribution (Fig. 5). The smallest differences can be seen for the east side of the roof, as well as for east and west façades. However, specific implementations of the combination of direct and diffuse solar radiation result in different solar gains at each opaque surface. For example, in WUFI Plus, the total annual incident solar radiation is higher on north and lower on south façades than those of the other two BDS software tools. In addition, in IDA ICE, the total annual incident solar radiation on the west side roof is higher not only than that of the other two BDS software but also than that of the east side roof.

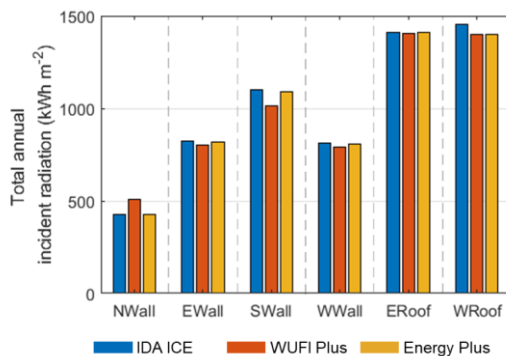


Fig. 5 – Total irradiance incident on opaque elements modeled by the three BDS software for each HB0 case

It was found that T and RH simulations resulting from the three BDS software tools showed good agreement with Δ_{\max} ranging between 0.9-1.5 °C for T and 4.9-6.1 % for RH (Table 3).

T simulations modeled by WUFI Plus were on average higher (up to 2 °C) than those modeled by IDA ICE and Energy Plus. For the sake of brevity, only the minimum values were plotted in Fig. 6 as differences in Δ_{\max} , for average and maximum values are negligible.

Table 3 – Summary of the maximum semi-dispersion (Δ_{\max}) of the hourly temperature (T) and relative humidity (RH) values modelled by the three BDS software in case of HB0 in free-floating conditions

Sub-case	Code	T (°C)	RH (%)
no windows			
insulated roof	HB0_0	0.9	4.1
not-insulated roof	HB0_1	1.5	6.1
two S-windows	HB0_2S	1.4	5.6
two E-W- windows	HB0_2EW	1.4	5.6
four E-W- windows	HB0_4EW	1.4	5.3

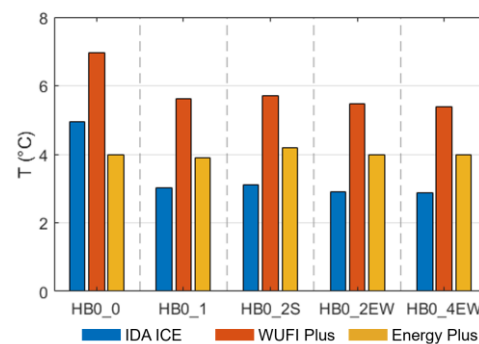


Fig. 6 – Annual minimum temperature values (T) modeled by the three BDS software for each HB0 case

As HB0 differed from Case 900 FF (*) only for the building net volume (Fig. 1), we can assume that differences among the three software tools can be mainly ascribable to the amount of air mass in the calculation. Fig. 7 shows a matrix plot that allows a comprehensive assessment of the differences among HB0 sub-cases (*BDS intra-comparison*, i.e., stair plots along diagonal matrix with the frequency distribution) and among BDS software (*inter-comparison*, scatter plots of paired BDS software). Looking at the stair plots, transparent elements did not strongly affect T distributions within the same BDS software. In addition, simulations performed by Energy Plus were not sensitive to the insulation on the roof (HB0_0 and HB0_1), as no significant difference in annual T values and distributions was detected (on the contrary, IDA ICE and WUFI Plus simulated lower T values in HB0_0 than those in HB0_1 due to the lower heat transmittance of the roof). Looking at the scatter plots, T simulations resulting from IDA ICE and Energy Plus are scat-

tered around the bisectrix (dashed grey line in Fig. 6), whereas T values simulated by WUFI Plus were usually above the bisectrix in all the sub-cases. If we compare T simulations of WUFI Plus and Energy Plus, it is evident that they were more in agreement in HB0_0 than in the other sub-cases, where T by WUFI Plus were higher than those by Energy Plus. This might be due to differences in the convective heat transfer coefficient in vertical upward flow.

Regarding RH simulations (Table 3), Δ_{\max} ranged from between 4.1 % (HB0_0) and 6.1 % (HB0_1), showing good agreement among BDS software. To study the indoor humidity conditions without dependence on T , the partial water vapor pressure (e_v) values were compared in the matrix plot (Fig. 6). Since e_v did not change from one sub-case to another, the differences in RH values were driven only by the difference in T , meaning that moisture exchanges occurred only by infiltration. Although BDS software were able to similarly simu-

4. Conclusion

In this paper, a new set of benchmarks for historical building models was presented and used with three BDS software tools with the aim of evaluating the effect on indoor climate simulations related to the differences in their modeling approaches. The benchmarks are designed to represent the characteristics of historical buildings and consist of twelve standardised models, seven of them being a variation of the BESTEST Common Exercise 0 (CE0), while the others are a variation of a single zone historical building (HB0), proposed by the authors. All the buildings are considered in the free-floating condition, without internal gains (occupants and other devices). The results of the comparison of IDA ICE, WUFI Plus and Energy Plus were presented, showing how the benchmark could be used to identify the differences between software.

The variables considered for the comparison are the ones of interest for the conservation of histori-

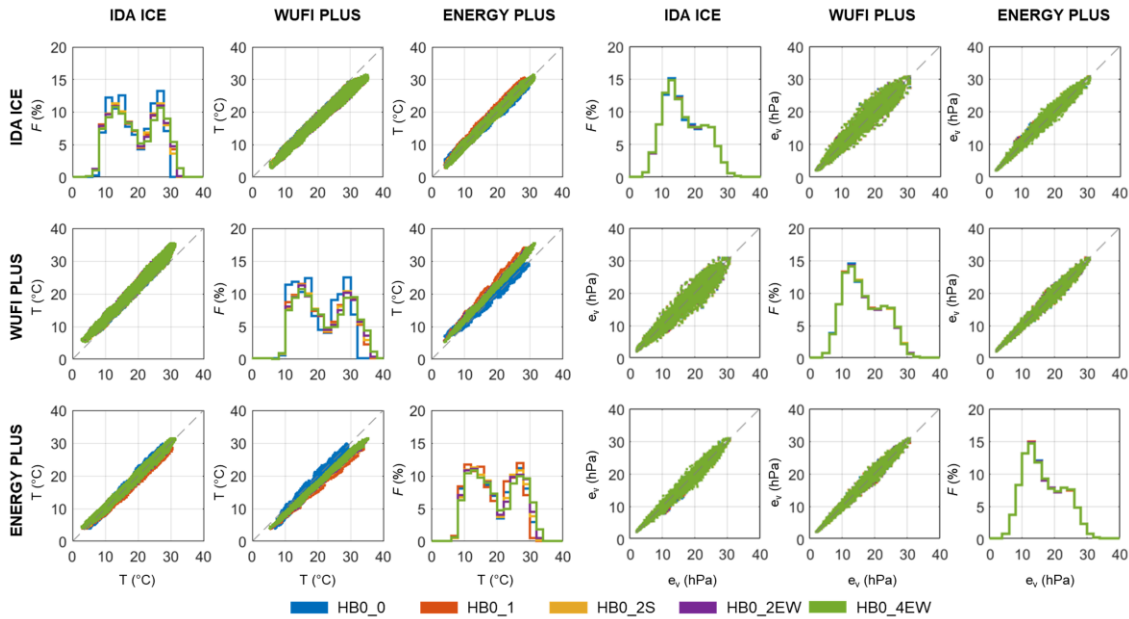


Fig. 7 – Matrix plots of temperature (T) and partial water vapor pressure (e_v) modeled by the BDS software for each HB0 case. Stair plots along the diagonal show the frequency distribution (F)

late water vapor saturated conditions, IDA ICE and Energy Plus modeled a higher frequency of saturation conditions (for the sake of brevity, RH plots are not shown).

cal buildings, such as indoor air temperature and relative humidity. Incident solar irradiation is also considered for its relevance in the calculations. The maximum semi-dispersion between the time series is used to evaluate the differences between the simulations. Because of their relevance, the time

series of the temperatures of the coldest and the hottest day of the year are compared.

When the benchmark comparison is performed on the three software tools, the results highlighted the differences in the software models and implementations:

- the comparison among the temperature simulations in the case of CE0 showed good agreement in the sub-case without windows both in light- (Case 600 FF) and heavyweight structures (Case 900 FF);
- the addition of the windows increased the variability among the results, with the highest dispersion associated with the Case 600 FF with simplified windows and the lowest with the Case 900 FF with detailed windows;
- in the case of HB0, the annual minimum values of temperature simulated by the BDS software showed low agreement. In general, T simulations modelled by WUFI Plus were on average higher than those modelled by IDA ICE and Energy Plus. These differences are probably ascribable to the amount of air mass considered in the calculation.
- some discrepancies found in the modeled incident solar radiation might have been caused by the different implementations in the BDS software of the combination of direct and diffuse solar radiation resulting in different solar gains at each opaque surface.

These preliminary results provided a basis for two potential future research lines:

- a more detailed comparison of the BDS software, including models of simultaneous heat and moisture transfer through walls, would require an in-depth study of the hygrothermal properties of historical building materials, including also simplified models (Zu et al., 2020);
- a software-independent procedure for the calibration of a hygrothermal model of a historical building should be defined using indoor temperature and relative humidity observations collected in a real context.

Both these research lines could lead to a better interpretation of the energy and indoor climate scenarios through hygrothermal simulation and an increased awareness of the confidence of calibration in the case of historical buildings (Frasca et al., 2019).

Acknowledgement

Frasca F. and Libralato M. acknowledge fellowship funding from MUR (Ministero dell'Università e della Ricerca) under PON "Ricerca e Innovazione" 2014-2020 (D.M. 1062/2021). The research leading to these results has also received funding from the MIUR of Italy within the framework of the PRIN2017 project "The energy flexibility of enhanced heat pumps for the next generation of sustainable buildings (FLEXHEAT)", grant 2017KAAECT. Frasca F. and Siani A.M. thank for the financial support of the conference fee the CollectionCare project (European Union's Horizon 2020 research and innovation programme under grant agreement No 814624).

Nomenclature

Acronyms

BDS	Building Dynamic Simulation
CE0	Common Exercise 0
E	East
e_v	Partial water vapor pressure
HB0	Historical Building 0
IEA	International Energy Agency
IR	Insulated Roof
N	North
S	South
SHGC	Solar Heat Gain Coefficient
U-value	Thermal transmittance
W	West

References

- Akkurt, G. G., N. Aste, J. Borderon, A. Buda, M. Calzolari, D. Chung, V. Costanzo, et al. 2020. "Dynamic Thermal and Hygrometric Simulation of Historical Buildings: Critical Factors and Possible Solutions." *Renewable and Sustainable Energy Reviews* 118: 109509. doi: <https://doi.org/10.1016/j.rser.2019.109509>
- Angelotti, A., M. Ballabio, L. Mazzarella, C. Cornaro, G. Parente, F. Frasca, A. Prada, et al. 2019. "Dynamic Simulation of Existing Buildings: Considerations on the Model Calibration." *Building Simulation Conference*

- Proceedings* 6: 4165–72. doi:
<https://doi.org/10.26868/25222708.2019.210439>
- ASHARE. 2007. *ANSI/ASHRAE Standard 140: Standard Method of Test for the Evaluation of Building Energy Analysis Computer Programs*. Atlanta: American Society of Heating, Refrigerating and Air-Conditioning Engineers.
- Campisi, T., and S. Colajanni. 2021. “Technological Performances Upgrading and Rehabilitation of Building Heritage inside the Historic Centre of Palermo.” *IOP Conference Series: Earth and Environmental Science* 863(1). doi:
<https://doi.org/10.1088/1755-1315/863/1/012004>
- CEN. 2018. *EN 16893:2018. Conservation of cultural heritage - Specifications for location, construction and modification of buildings or rooms intended for the storage or use of heritage collections*. European Committee for Standardization (CEN), Brussels, Belgium.
- Filippi, M. 2015. “Remarks on the Green Retrofitting of Historic Buildings in Italy.” *Energy and Buildings* 95: 15–22. doi:
<https://doi.org/10.1016/j.enbuild.2014.11.001>
- Frasca, F., C. Cornaro, and A. M. Siani. 2018. “Performance Assessment of a Heat and Moisture Dynamic Simulation Model in IDA ICE by the Comparison with WUFI Plus.” *In IOP Conference Series: Materials Science and Engineering*. doi:
<https://doi.org/10.1088/1757-899X/364/1/012024>
- Frasca, F., E. Verticchio, C. Cornaro, and A. M. Siani. 2019. “Optimising Conservation of Artworks, Energy Performance and Thermal Comfort Combining Hygrothermal Dynamic Simulation and On-Site Measurements in Historic Buildings.” *In Proceedings of the 16th IBPSA Conference*: 2856–63.
- Frasca, F., E. Verticchio, C. Cornaro, and A. M. Siani. 2021. “Performance Assessment of Hygrothermal Modelling for Diagnostics and Conservation in an Italian Historical Church.” *Building and Environment* 193: 107672. doi:
<https://doi.org/10.1016/j.buildenv.2021.107672>
- Gori, V., S. Efthymiopoulos, X. Tian, J. Dong, and V. Marincioni. 2021. “Assessing the Role of Simulation Tool Selection for the Evaluation of Heat and Moisture Balance in Historic Buildings.” *IOP Conference Series: Earth and Environmental Science* 863 (1). doi:
<https://doi.org/10.1088/1755-1315/863/1/012050>
- Libralato, M., A. De Angelis, O. Saro, M. Qin, and C. Rode. 2021a. “Effects of Considering Moisture Hysteresis on Wood Decay Risk Simulations of Building Envelopes.” *Journal of Building Engineering* 42: 102444. doi:
<https://doi.org/10.1016/j.jobbe.2021.102444>
- Libralato, M., A. De Angelis, G. Tornello, O. Saro, P. D’agaro, and G. Cortella. 2021b. “Evaluation of Multiyear Weather Data Effects on Hygrothermal Building Energy Simulations Using Wufi Plus.” *Energies* 14(21). doi:
<https://doi.org/10.3390/en14217157>
- Nicolai, A., S. Hirth, and M. Madjidi. 2021. “SimQuality. A Novel Test Suite for Dynamic Building Energy Simulation Tools.” *Proceedings of Building Simulation 2021*. doi:
<https://doi.org/10.13140/RG.2.2.27833.90725>
- Rajčić, V., A. Skender, and D. Damjanović. 2018. “An Innovative Methodology of Assessing the Climate Change Impact on Cultural Heritage.” *International Journal of Architectural Heritage* 12 (1): 21–35. doi:
<https://doi.org/10.1080/15583058.2017.1354094>
- Rode, C., and M. Woloszyn. 2007. “Whole-Building Hygrothermal Modeling in IEA Annex 41.” *Proceedings of the 10th ASHRAE conference on Thermal Performance of the Exterior Envelopes of Whole Buildings*.
- Tarantino, S. 2020. “Accuracy of Code Compliant Design-Stage Building Energy Performance Simulation Models.” *Advancements in Civil Engineering & Technology* 4 (2): 1–17. doi:
<https://doi.org/10.31031/acet.2020.04.000581>
- UNI. 2014. *UNI/TR 11552:2014 Standard. Opaque Envelope Components of Buildings - Thermo-Physical Parameters*.
- Zu, K., M. Qin, C. Rode, and M. Libralato. 2020. “Development of a Moisture Buffer Value Model (MBM) for Indoor Moisture Prediction.” *Applied Thermal Engineering* 171: 115096. doi:
<https://doi.org/10.1016/j.applthermaleng.2020.115096>

QGIS-Based Tools to Evaluate Air Flow Rate by Natural Ventilation in Buildings at Urban Scale

Silvia Santantonio – Politecnico di Torino, Italy – silvia.santantonio@polito.it

Guglielmina Mutani – Politecnico di Torino, Italy – guglielmina.mutani@polito.it

Abstract

Urban-scale evaluations of aerodynamic and morphological parameters allow correction of the wind speed within the urban boundary layer, as the wind profile is strongly influenced by the presence of roughness elements. This can have important implications for defining urban strategies for the reduction of buildings' energy consumption and the improvement of air quality and liveability of outdoor spaces. Among the current models for assessing the air flow rate by natural ventilation in buildings at urban scale, this study aims to define a GIS-based methodology, using existing databases and an open source QGIS plug-in. From a digital surface elevation dataset, and considering prevalent wind directions, the displacement height (z_d) was determined. The wind speed was corrected, applying the logarithmic or turbulent laws of wind profile, respectively, above and below z_d . This method could determine the spatial distribution of wind speed, considering each building façade characteristics and its surroundings. Resulting wind pressure on windward and leeward façades drives the air flow rate inside the buildings. Further developments of this work will improve the air flow modelling in buildings with other tools for applications at urban scale.

1. Introduction

Understanding and modeling the urban local wind environment has been a focus of attention for many researchers, especially in high density urban areas. Here, the heterogeneity of urban morphology, due to the presence of different type of roughness elements, strongly influences local wind performance (Peng et al., 2019). Studying air flow properties has important implications for urban design in terms of energy consumption, outdoor thermal comfort, and air quality, and building energy performance for

space heating and cooling (Suszanowicz, 2018). Relations between urban morphology and wind flow can be assessed with different methods: i) field measurements, whose high time and cost limitations mean that they are not suitable for large scale studies; ii) wind tunnel experiments, which constitute the reference dataset, despite operating costs and application limits; iii), Computational Fluid Dynamic (CFD) numerical modellings with high computational requirements (Buccolieri & Hang, 2019); iv) parametric models, mainly based on wind tunnel test or CFD simulations, having a good cost-benefit ratio but limited application field; v) Geographical Information System (GIS) and remote sensing techniques that retrieve roughness parameters based on interactions with buildings' geometries at city-scale, especially at mesoscale (Wong et al., 2010). Into the last group fits the place-based methodology presented in this work: a flexible integration of physical laws of wind phenomena and local characteristics of the urban context, based on the open-source software QGIS and existing databases, already used by urban planners. The study is part of broader research that aims to implement an hourly GIS-based engineering model to assess the energy consumption for the space heating and cooling of residential buildings at urban and district scales (Mutani & Todeschi, 2020; Mutani et al., 2022). The implementation concerns the monthly and hourly detail definition of number of air change per hour (ach) that influences thermal loads by natural ventilation in the building's thermal energy balance, considering the air flow rate for infiltration caused by wind-driven effects. The wind pressure generated on a building façade is evaluated as a function of the vertical and horizontal distribution of wind speed, starting from the characterization of roughness and

built environment characteristics. After a brief description of natural wind profiles in urban areas, this work aims to present some QGIS tools currently available to assess the urban wind field and its relationship with roughness parameters, applying the methodology to a case study.

2. Physical Laws of Wind Profiles

The wind phenomenon is influenced by the surface roughness of the ground and other objects (i.e., buildings, vegetation) that create obstacles to the undisturbed flow. A wind profile is associated with different environmental contexts (i.e., urban, sub-urban, rural areas), describing mathematically the mean wind speed (U_z) as a function of height (z) from the ground. Reference heights individuate boundary layers that limit air flow zones in which different physical laws can be applied.

2.1 Boundary Layers and Heights

In this work, reference was made to an older bibliography for defining wind phenomena, and to a more recent one for applying physical laws. Considering the horizontal scale of wind influence, three scale of interest exist (Oke, 2004): i) the *mesoscale*, where weather and climate are influenced by the whole city; ii) the *local scale*, where landscape features or topography are considered; iii) the *microscale*, where variations occur over very short distances, causing great airflow perturbations around roughness elements. Regarding the vertical scale of wind influence, relevant boundary layers and heights are defined:

- Atmospheric Boundary Layer (ABL)

In the ABL, or Planetary Boundary Layer, which extends up to 1-2 km (Z_{ABL} in Fig.1), the undisturbed wind flow present in upper layers is progressively slowed down due to friction with the ground and roughness elements. In the case of smooth soils (i.e., rural areas) the wind speed reaches upper layers values more quickly than urban areas.

- Urban Boundary Layer (UBL)

The UBL identifies the part of the ABL influenced by the presence of a large city. It is divided into:

Mixed Layer (ML), whose upper limits coincide with the height of UBL (Z_i in Fig.1), and Surface Layer (SL) whose depth is about a tenth of UBL ($Z_{i/10}$ in Fig.1), and which, in turn, is divided into two.

- Internal Sub-Layer (ISL)

In the upper layer of SL, the flow is free of individual wakes associated with roughness elements, and wind can be assumed as a constant flux with a laminar, horizontally homogeneous flow ($Re < 2000$). Here, the wind log law can be applied to determine average wind speed (U_z).

- Roughness Sub-Layer (RSL)

This extends from ground level to the blending height Z_{RSL} (Fig. 1), where effects of individual roughness elements are visible. Airflow perturbation caused by individual surface and obstacles persists for a certain distance until it is mixed with the effect of turbulent eddies. Blending distance depends on the magnitude of the effect, the wind velocity, and the stability of the flux. Minimum $Z_{RSL} = 2 \cdot Z_H$ is suggested by observations in dense urban settings (Oke, 2004); it can vary with density, staggering, and heights of objects.

- Urban Canopy Layer (UCL)

This is equivalent to the mean height Z_H (Fig. 1) of the main roughness elements. To overcome the frictional effect of surface roughness elements, the wind flux loses its momentum: turbulent flows are generated near the surfaces ($Re > 4000$). Lower wind speed can occur, and turbulent models are required to calculate wind velocity inside urban canyons.

2.2 Aerodynamic Roughness Parameters

At local and micro scale, in the air zone where the flow is free from roughness-element turbulent wakes, two aerodynamic parameters are used to describe the wind speed profile influenced by surface roughness elements (Fig. 1):

- Zero-plane displacement height (z_d)

It is intended as a new “ground level” from which the wind profile originates, after the wind passes over high-density buildings (Lv et al., 2022), and it is used for setting a base for the application of the wind log law (Oke, 2004). According to (Abubaker et al., 2018), it is the depth of still air trapped among the roughness elements.

- Roughness length (z_0)

This is the height above Z_a at which wind velocity becomes zero when the logarithmic wind profile is applied and represents the size of the eddies produced from wind moving over a rough surface (Abubaker et al., 2018). It depends on turbulence intensity and, therefore, on the surface drag.

In urban areas, three flow regimes were classified when aerodynamic parameters are morphometrically determined (Oke, 2004): i) *isolated flow*, where buildings are individual wake generators; ii) *wake interference flow*, where wakes reinforce each other as space between buildings is close; iii) *skimming flow*, where main flow skips over the top of the great density of buildings. The wake interference regime is the one in which the greatest roughness activity can be generated. The building density (λ_p) is very important in cities, where the high variability of roughness height can cause complex surface morphology and turbulent wakes that are challenging to assess.

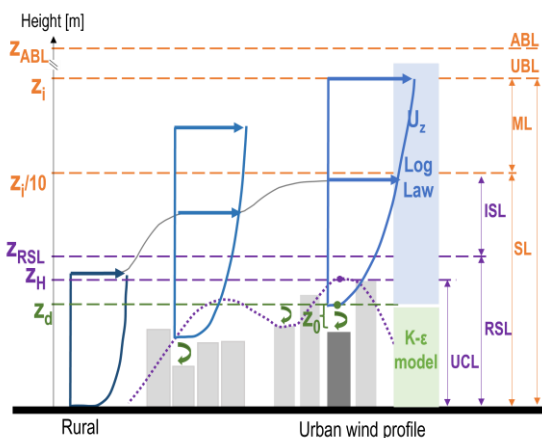


Fig. 1 – Boundary layers and their reference height (y axis) at mesoscale (in orange) and local scale (in purple)

2.3 Wind Profiles Laws at District Scale

In this work, two methods were compared to determine the wind speed (U_z), from measured U_{ref} at reference height (z_{ref}): the *Cp methodology* and *z_d methodology*, whose procedures are schematized in Fig. 2. U_{ref} need to be adjusted considering the wind incident angle (Eq. 1, in Fig. 2) and objects and terrain roughness of the context. For wind fluxes that occur above the displacement height z_d , two wind profiles can be applied.

The power law wind profile is based on empirical assumption for mesoscale application for large heights ($30 \text{ m} < z < 300 \text{ m}$), but it is less accurate when close to the ground. It can be determined according to Eq. 2 (Fig. 2), where V_z is the wind speed at height z [m·s⁻¹], $V_{\text{ref,corr}}$ is the adjusted reference wind speed [m·s⁻¹] at height z_{ref} , z_{UBL} is the height of the UBL [m], and α the terrain roughness coefficient (wind speed profile exponent) [-]. The last two parameters refer to tabular data, determined through empirical assumptions from real measurements or wind tunnel tests. Several references exist in the literature, including the unified terrain roughness categories given by (Choi, 2009). Table 1 reports typical values for roughness parameters for the most used terrain categories.

Table 1 – Referenced roughness parameters for terrain typology

Terrain roughness type	Z _{UBL} [m]	ν [-]	Z ₀ [m]	Z _d [m]
Level surfaces, grass land	250	0.10	-	-
Flat open country	280	0.14	0.03	0.0
Rolling/level surfaces	300	0.22	0.1	0.0
Heterogeneous surface	330	0.28	-	-
Low density suburban areas	390	0.34	0.5	0.7 _{ZH}
Mid-high density urban areas	450	0.40	1.0	0.8 _{ZH}
Very high density city areas	510	0.45	> 2.0	0.8 _{ZH}

The logarithmic law wind profile allows an approximation of the wind profile at lower boundary condition ($z \leq 200\text{m}$). Its lower limit of application at urban local scale is identified by z_0 and z_d , according to the logarithmic function of Eq. 3 (Fig. 2), where U_z is the wind speed [$\text{m}\cdot\text{s}^{-1}$] at height z , $U_{\text{ref,corr}}$ is the corrected wind speed at height z_{ref} , z_d is the zero-plane displacement height [m], and z_0 is the roughness length [m]. At microscale, inside the urban canopy layer, where turbulent fluxes occur at a height z lower than displacement height z_d , the log-law is not valid and turbulent models should be applied. The k-epsilon (k- ϵ) model is the most common model in CFD analyses for simulating the mean flow characteristics for turbulent flow conditions. It belongs to the Reynolds-averaged Navier Stokes (RANS) models that represent an optimal compromise between accuracy and efficiency for microclimate studies in urban environments (Javanroodi et al., 2022).

2.4 Wind Flow at Building Local Scale

Natural ventilation in buildings is driven by pressure differences on building façades by two forces: the stack (or buoyancy) effect and the wind-driven effect. This work focuses on the latter, while in future works, buoyancy will be considered in a multi-zones airflow model to assess ventilation loads in buildings. Wind generates positive pressure and negative pressure on windward and leeward façades, respectively. The surface pressure (P_s , P_v) can be calculated according to Eq.4 or Eq.5 (Fig. 2), respectively, with C_p and z_d methodology, where ρ is air density [$\text{kg}\cdot\text{m}^{-3}$], V_z (power law) and U_z (log-law) are the adjusted wind speed [$\text{m}\cdot\text{s}^{-1}$] and C_p is the pressure coefficient [-]. It is a non-dimensional coefficient estimated according to i) real scale measurements, ii) wind tunnel tests, iii) CFD and iv) parametric models, among which there is *Cpcalc+* software (Chiesa & Grosso, 2019), whose input data are listed in Table 2. Even if the power law application determines a vertical variation of wind velocity at the local urban scale, the C_p allows the distribution of wind speed horizontally and vertically at the scale of interesting points on a building façade with respect to the windward and leeward façade dimensions; it also considers building geometry and orientation, urban density, and roughness characteristic of the surrounding environment. The algorithm used in *Cpcalc+* is based on experimental wind tunnel tests results, considering different typical buildings and urban contexts (e.g., Fracastoro et al., 2001). Limitations of the software concern the scale of the application field (suitable at building scale, not at district-urban scale), and the application range of some parameters, especially the relative building height and the aspect ratios ($0.5 \leq \text{FAR} \leq 4$ and $0.5 \leq \text{SAR} \leq 2$).

Table 2 – Input data required by *Cpcalc+* software (<https://iris.polito.it/handle/11583/2579969>)

Climate data			
Wind speed		Wind direction	
Urban parameter			
Plan Area Density	Surroundings building height	Wind profile exponent	
Building Characteristic			
Frontal/Side Aspect Ratio (FAR/SAR)	Building dimension	Building azimuth	Roof slope

2.5 Place-Based Tools and Plug-Ins for Wind Analysis at Urban Scale

In this paragraph, GIS-based tools and a plug-in to assess wind at urban scale are described.

SAGA GIS software presents some useful tools for wind correction at the mesoscale, to consider terrain influence on observed meteorological conditions. In the *Climate and Weather* section, the *Wind Effect Correction* tool allows the scaling factor of the wind effect in determining ABL conditions (e.g., precipitation, cloudiness) to be calibrated. In the *Terrain analysis - Morphometry* section, the *Wind Effect* tool classifies wind exposed and shades area through a dimensionless index, considering terrain elevation and specifying wind data; these tools were created for topo-climatic wind assessments. Existing methods to determine the aerodynamic parameters at urban scale can be grouped into three main classes: i) *reference-based values from field observations*, which provide a wide range of values whose application in complex and heterogenous urban areas has some limitations; ii) *anemometric methods* requiring experimental campaigns, applicable on a limited and non-replicable scale; iii) *morphometric methods* based on the relationships between aerodynamic parameters and roughness elements geometry, described through urban morphological parameters, already used both at mesoscale (Darmanto et al., 2017) and local scale (Badach et al., 2020). This work aims to present z_d methodology (Fig. 2), determining z_d and z_0 using the open-source QGIS plug-in Urban Multi-scale Environmental Predictor (UMEP), version 1.6.1 (Lindberg et al. 2016). Among the pre-processing tools, there are the *Urban Morphology- Morphometric Calculator (Grid)* and *(Point)*, which only differ in the geometry of the calculation area. Both calculate five morphometric parameters (Table 3, Fig. 3) based on digital surface models (DSM) to calculate the two aerodynamic parameters according to six different methods (Table 4). The required input data are three separate raster files (*geoTIFF*) with the same pixel resolution: DSM, digital elevation model (DEM, only ground elevation), and roughness elements elevation, calculated with the QGIS *Raster calculator tool*, by subtracting the other two rasters (DSM-DEM).

	Cp method	z_d method
Software:	CpCalc+	QGIS UMEP plug-in
Input data:	Wind speed (U_{ref}) from a reference height (z_{ref}) of the weather station	
Uref adjustment – wind incident angle (θ)	Eq. 1) $U_{ref,corr} = U_{ref} \cdot \cos(\theta)$	θ wind incident angle normal to the windward building facade
Uref adjustment – terrain and object roughness correction:	Power law wind profile Eq. 2) $V_z = U_{ref,corr} \cdot \left(\frac{z_{UBL,ref}}{z_{ref}} \right)^{V_{ref}} \cdot \left(\frac{z}{z_{UBL}} \right)^{V_z}$ <div> $\left. \begin{array}{l} \text{Tabular data} \\ \text{Mesoscale} \end{array} \right\}$ </div>	Log law wind profile Eq. 3) $U_z = U_{ref,corr} \cdot \left[\frac{\ln\left(\frac{z - z_d}{z_0}\right)}{\ln\left(\frac{z_{ref} - z_d}{z_0}\right)} \right]$ <div> $\left. \begin{array}{l} z_d - \text{GIS plug-in} \\ z_0 - \text{Local scale} \end{array} \right\}$ </div>
	vertical distribution for each z_n	horizontal distribution for each z_n <i>Uz from correlations of CFD results</i>
Pressure coefficient (Cp) calculation:	vertical and horizontal distribution on building facades (from CpCalc+)	
Surface pressure :	Eq. 4) $P_s [Pa] = \frac{1}{2} \cdot \rho \cdot U_z^2 \cdot C_p$	Eq. 5) $P_v [Pa] = \frac{1}{2} \cdot \rho \cdot U_z^2$
Limits of the methodology:	<ul style="list-style-type: none"> • Roughness correction at mesoscale (wide scale) • Roughness correction from tabular data (wide range values) • Application range of some parameters based on experimental tests (0.5 ≤ FAR ≤ 4 and 0.5 ≤ SAR ≤ 2, building height) • Building scale application not suitable for district scale 	<ul style="list-style-type: none"> • Results accuracy strongly affected by the radius of calculation area and size of grid cells (no unified standard for selecting area) • Horizontal distribution of wind speed variation only for heights greater than Z_d (above canopy layer)

Fig. 2 – Comparison between the C_p and z_d methodologies for the assessment of surface pressure generated by the wind flow

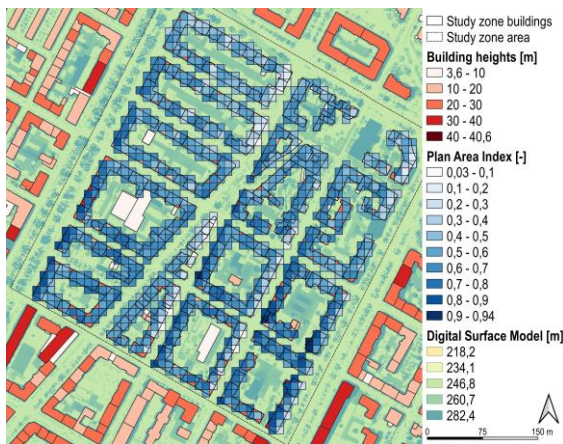


Fig. 3 – Plan area index (λ_p) within its range (0-1) for a squared cell grid, considering building heights in a selected area

The main setting concerns the extension of the calculation area that will be considered to determine the morphological and aerodynamic parameters, indicating the radius length from the selected point or the centroid of each grid cell. There are no unified standards for the size of calculation area, though it greatly affects the accuracy of results (Lv et al., 2022). In addition, it is possible to specify the wind direction (in degrees, from north - clockwise). The five morphometric parameters calculated in UMEP correspond to some of the most frequently used urban parameters in the urban planning research field; Table 3 reports their definitions. The morphological and aerodynamic parameters can vary according to the analyzed wind direction, allowing more precise results of z_d and z_0 , considering the variability of the roughness surfaces (Oke, 2004).

Table 3 – Urban parameters defined in QGIS-UMEP tool

Urban parameter	Unit	Formula
Plan Area Index	[-]	$\lambda_p = (\sum_{i=1}^n A_{pi}) / A_T$
Frontal Area Index	[-]	$\lambda_f = (\sum_{i=1}^n A_{fi}) / A_T$
Mean Height	[m]	$Z_H = (\sum_{i=1}^n H_i) / n$
Maximum Height	[m]	$Z_{Hmax} = \text{Max} (H_i)$
Height variability	[m]	$Z_{Hstd} = \sqrt{\frac{1}{n} \sum_{i=1}^n (H_i - Z_H)^2}$

The UMEP tool calculates the aerodynamic roughness parameters (z_d , z_0) by applying six different morphometric methods (Kent et al., 2017). For each method, Table 4 reports urban parameters used in the calculation: plan area density (λ_p), frontal area ratio (λ_t), average (z_H) and maximum (z_{Hmax}) buildings height and height variability (z_{Hstd}). In this work, the Kanda method was used (Kanda et al., 2013), as it is more suitable in dense, city-center districts, due to the importance of considering roughness elements' height heterogeneity. The flow chart in Fig. 4 summarizes the *z_d methodology* used to determine the aerodynamic parameters and the proper wind profile with the QGIS UMEP plug-in.

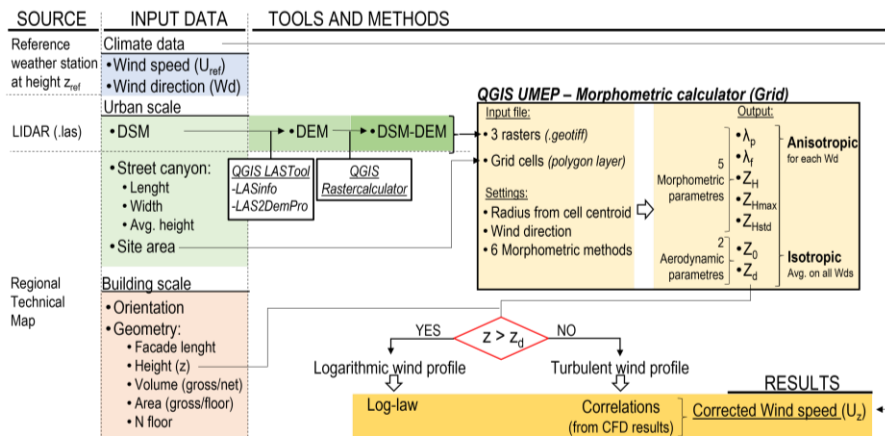
Fig.4 – Flow chart of the z_d methodology based on QGIS-UMEP tools

Table 4 – Morphometric methods included in the UMEP plug-in

Method	Urban Parameter				
	λ_p	λ_f	Z_H	Z_{Hmax}	Z_{Hstd}
Rule of thumb			X		
Raupach		X	X		
Bottema	X	X	X		
Macdonald	X	X	X		
Millward-Hopkins	X	X	X		X
Kanda	X	X	X	X	X

3. Application of the UMEP Tool at District Scale in Turin

The place-based methodology was applied to a central district in the city of Turin (Italy). For an in-depth analysis of case study zone (200 m x 200 m) selection criteria and characteristics, refer to (Mutani et al., 2021). The local monthly prevalent wind is from North-NorthEast and West-SouthWest, with a mean velocity of 1.4 m/s. Table 5 shows main the urban parameters calculated in QGIS to describe the case study area.

Table 5 – Morphological and roughness characteristic of the area

Urban parameter	Unit	Study area
Built Coverage Ratio (BCR)	[-]	0.33
Plan Area Density (PAD)	[-]	1.66
Volume Area Ratio (VAR)	[-]	0.30
Surrounding buildings' height	[m]	19.5
Height of boundary layer (z_{UBL})	[m]	450
Wind speed profile exponent (ν)	[-]	0.4
Short urban canyon (L/H)	[m]	≤ 3
Long urban canyon (L/H)	[m]	> 5

For the UMEP tool application, a grid vector polygon was created, with a 5-m-squared grid, and results were assigned to grid cells and related buildings. Three raster files were created, starting from a 1-m resolution surface elevation dataset (DSM). From the centroid of each cell of the grid, a 300m radius study area was set, obtaining, for each cell, 12 different results of morphological and aerodynamic parameters, for 12 wind directions.

4. Results and Discussion

The UMEP tool results are the *anisotropic* and *isotropic* output: the first gives values for each wind direction, the second reports mean values of all wind directions. Fig. 5 shows the isotropic results of the displacement height z_d for the case study zone. The anisotropic results of z_d consider the two prevalent wind directions (N-NE, Fig.6a and W-SW, Fig.6b). Results were assessed at the building scale. According to building heights (z) and floor numbers, for each floor, the wind speed was adjusted applying the log law (if $z > z_d$) or the turbulent motion equation (if $z \leq z_d$). Buildings were classified into those with logarithmic and turbulent wind profile, or only turbulent profile (red and blue points, in Fig. 6a-b, respectively). Figs. 6a-6b show that the buildings for which the log law is valid are those located in urban canyons oriented parallel to the prevailing wind direction. In this work, the wind speed above z_d was calculated applying the log law equation (Eq.3, in Fig.2), while below z_d , it was calculated based on correlations

found from the CFD model results (Javanroodi et al., 2022). Reference was made to a case study with similar urban morphological characteristics (Table 5); linear and exponential correlations were determined for short and long canyons (Fig. 7).

A block of buildings (red rectangle, Fig. 6a) well exposed to the N-NE wind, was selected to assess the surface pressure generated by the wind on the windward façade of buildings, comparing results of the two different methodologies (Fig. 2). Wind speed was corrected applying the power law (C_p method) and log law (z_d method), at three representative heights for each building in the block (first floor- z_1 , average floor- z_2 , top floor- z_3) and 30 points on windward block façade (i.e., 1-30).

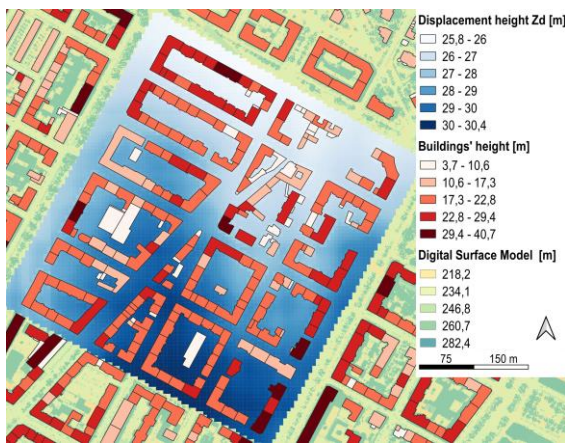


Fig. 5 – Isotropic result of the displacement height z_d [m].

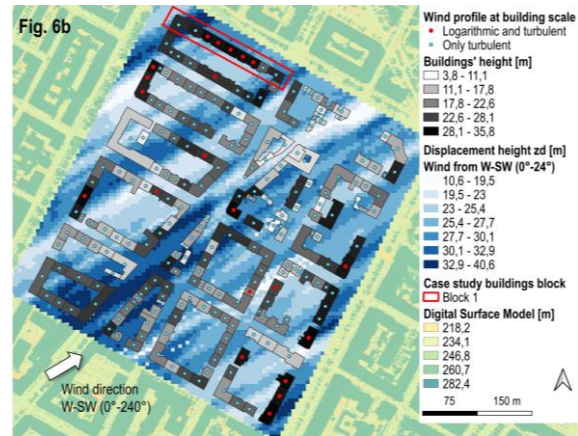
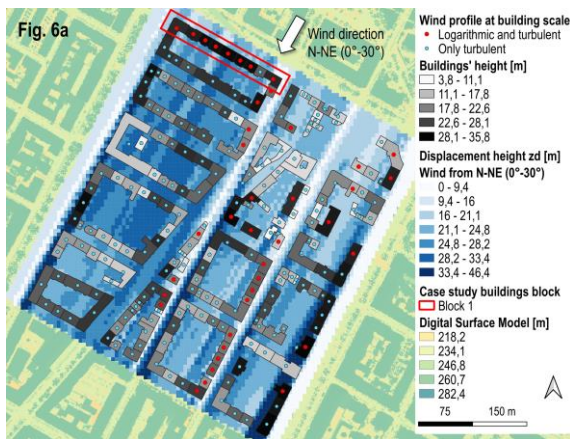


Fig. 6 a,b – Anisotropic result of displacement height z_d , for wind direction N-NE (a) and W-SW (b)

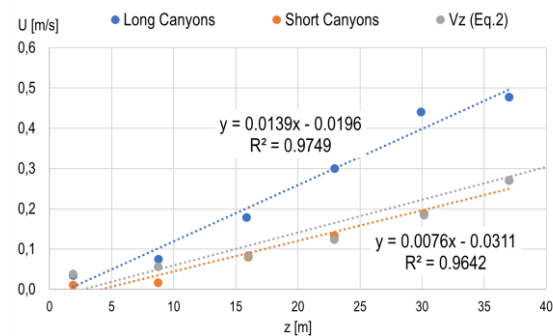


Fig. 7 – Correlations for long (blue) and short (orange) canyons

To horizontally distribute the wind speed along the windward façade, C_p was calculated with the $C_{p\text{calc}}$; in the z_d method, a value of z_d and z_0 was determined for each cell of the grid, obtaining a different wind velocity for each cell spatially distributed in front of the façades. Considering the three heights of building, Fig. 8 shows results of the surface pressure P_s and P_v , calculated with C_p -method and z_d -method, respectively.

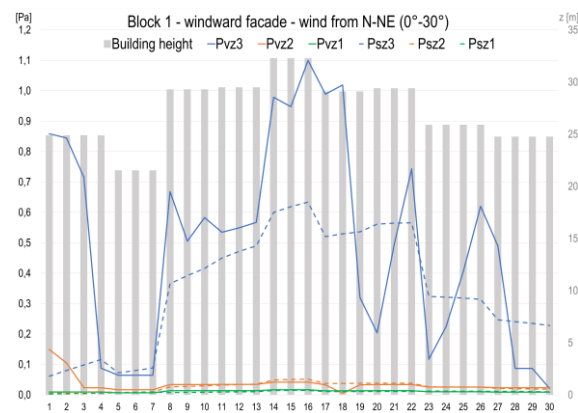


Fig. 8 – Surface pressure calculated with the c_p method (P_s , dotted lines) and the z_d method (P_v , continuous line)

It can be noticed that, for the height z_3 (blue line), above z_d , results of *z_d-method* are more precise than the *cp-method* one when describing variations that occur on façades and that are mainly due to the wind wakes generated from surrounding buildings. The main limit of the *cp-method* concerns its range of application, since the analyzed block exceeds the aspect ratio range ($FAR > 4$). For heights (z_1, z_2), below z_d , surface pressures are very low in both methods, due to the reduced wind speed inside the canyon (Fig. 8).

5. Conclusion and Further Development

This study aims to determine the variation in wind speed at local scale as a function of roughness elements and their effects on the urban context. The model's place-based approach, based on accessible databases and open-source software (QGIS), is applied at neighbourhood scale and it is adaptable to other contexts and urban scales. The methodology presented determines heights of boundary canopy layer (z_d, z_0) to apply the proper wind profile law, in relation to building heights. If compared to the *Cp method*, it can assess horizontal wind speed distribution along building façades, and to calculate surface pressure driving the air flow rate inside buildings. This aspect can be further investigated thanks to the flexibility of GIS place-based methodology. In fact, the novelty of this work lies in the possibility of adapting and integrating new or already existing software into QGIS, in the attempt to calculate the natural ventilation loads with a lumped model for all buildings at urban scale. A recent upgrade of the *CpCalc+* algorithm in a Python script (Chiesa & Grosso, 2019), constitutes an interesting opportunity for methodology implementation. Therefore, different scenarios can be investigated, including exploiting the GIS tool to retrieve all input data at urban scale necessary for *Cp* calculations, or directly integrating the *CpCalc+* algorithm into a dedicated QGIS plug-in. A simplified parametric model to evaluate wind flows around buildings at urban scale is essential for supporting urban planning in increasing buildings' energy performance and liveability of urban environments.

References

- Abubaker, A., I. Kostić, and O. Kostić. 2018. "Numerical modelling of velocity profile parameters of the atmospheric boundary layer simulated in wind tunnels". *IOP CS: Materials Science and Engineering* 393: 012025. doi: <https://doi.org/10.1088/1757-899X/393/1/012025>
- Badach, J., D. Voordeckers, L. Nyka, and M. Van Acker. 2020. "A framework for Air Quality Management Zones - Useful GIS-based tool for urban planning: Case studies in Antwerp and Gdańsk". *Building Environment* 174: 106743. doi: <https://doi.org/10.1016/j.buildenv.2020.106743>
- Buccolieri, R., and J. Hang. 2019. "Recent Advances in Urban Ventilation Assessment and Flow Modelling". *Atmosphere* 10(3). doi: <https://doi.org/10.3390/atmos10030144>
- Chiesa, G., and M. Grosso. 2019. "Python-based calculation tool of wind-pressure coefficients on building envelopes". *JPCS* 1343(1): 012132. doi: <https://doi.org/10.1088/1742-6596/1343/1/012132>
- Choi, E., 2009. "Proposal for Unified Terrain Categories Exposures Velocity Profiles". In 7th APCWE, Vol. VII.
- Darmanto, N. S., A. C. G. Varquez, and M. Kanda. 2017. "Urban roughness parameters estimation from globally available datasets for mesoscale modeling in megacities". *Urban Climate* 21: 243–261. doi: <https://doi.org/10.1016/j.uclim.2017.07.001>
- Fracastoro, G. V., G. Mutani, M. Perino. 2001. "A simple tool to assess the feasibility of hybrid ventilation systems". In 4th IAQVEC, Vol. III: 1421-1429, Hunan (China). ISBN:962-442-190-0
- Javanroodi, K., V. M. Nik, M. G. Giometto, and J.-L. Scartezzini, 2022. "Combining computational fluid dynamics and neural networks to characterize microclimate extremes: Learning the complex interactions between meso-climate and urban morphology". *STE* 829: 154223. doi: <https://doi.org/10.1016/j.scitotenv.2022.154223>
- Kanda, M., A. Inagaki, T. Miyamoto, M. Gryschka, and S. Raasch 2013. "A New Aerodynamic Parametrization for Real Urban Surfaces". *BLM* 148(2): 357–377. doi: <https://doi.org/10.1007/s10546-013-9818-x>
- Kent, C. W., et al., 2017. "Evaluation of Urban Local-Scale Aerodynamic Parameters: Implications for the Vertical Profile of Wind Speed and for Source Areas". *BLM* 164(2): 183–213. doi: <https://doi.org/10.1007/s10546-017-0248-z>
- Lindberg, F., et al., 2018. "Urban Multi-scale Environmental Predictor (UMEP): An integrated tool for city-based climate services". *Environmental Modelling & Software* 99: 70–87. doi: <https://doi.org/10.1016/j.envsoft.2017.09.020>
- Lv, G., et al., 2022. "An urban-scale method for building roofs available wind resource evaluation based on aerodynamic parameters of urban sublayer surfaces". *Sustainable Cities and Society* 80: 103790. doi: <https://doi.org/10.1016/j.scs.2022.103790>
- Mutani, G., and V. Todeschi. 2020. "Building energy modeling at neighborhood scale". *EE* 13 (7): 1353–1386. doi: <https://doi.org/10.1007/s12053-020-09882-4>
- Mutani, G., S. Santantonio, and V. Todeschi, 2021. "Evaluation of ventilation loads in buildings energy modelling at urban scale". In 2021 IEEE 4th CANDO-EPE 37–42. doi: <https://doi.org/10.1109/CANDO-EPE54223.2021.9667547>
- Mutani, G., S. Santantonio, and V. Todeschi, 2022. "Urban-Scale energy models: the relationship between cooling energy demand and urban form". *JPCS 38th UIT*, 2021, Gaeta (Italy).
- Oke, T. 2004. "Initial guidance to obtain representative meteorological observations at urban sites. Instruments and observing methods". World Meteorological Organization/TD 1250-81
- Peng, Y., Z. Gao, R. Buccolieri, and W. Ding. 2019. "An Investigation of the Quantitative Correlation between Urban Morphology Parameters and Outdoor Ventilation Efficiency Indices". *Atmosphere* 10(1). doi: <https://doi.org/10.3390/atmos10010033>
- Suszanowicz, D. 2018. "Optimisation of Heat Loss through Ventilation for Residential Buildings". *Atmosphere* 9(3). doi: <https://doi.org/10.3390/atmos9030095>
- Wong, M., et al. 2010. "GIS techniques for mapping urban ventilation, using frontal area index and least cost path analysis". *IAPRSS* 38(2):586-591.

Modeling Energy Consumption in a Single-Family House in South Tyrol: Comparison Between Hemp Concrete and Clay Bricks

Silvia Ricciuti – Eurac Research, Italy – silvia.ricciuti@eurac.edu

Irene Lara-Ibeas – Eurac Research, Italy – irene.laraibeas@eurac.edu

Annamaria Belleri – Eurac Research, Italy – annamaria.belleri@eurac.edu

Francesco Babich – Eurac Research, Italy – francesco.babich@eurac.edu

Abstract

The built environment generates nearly 40 % of annual global CO₂ emissions. To reduce these emissions, alternative materials able to store CO₂ have started to be used in the construction sector. In the case of hemp concrete, part of this storage occurs during its service life leading to a potential decrease of indoor CO₂ levels. Assuming that CO₂ is used to control ventilation rates in certain buildings, the use of this material might lead to lower ventilation requirements and, thus, reduced energy consumption. The aim of this work was to develop an energy model including the CO₂ sequestration capability of hemp concrete to estimate the potential energy savings derived from its use in a typical residential building in South Tyrol with CO₂-based demand controlled ventilation. This result was later compared with the energy consumption of the same building made of clay bricks and the influence of air infiltration on indoor CO₂ levels was also evaluated. The results obtained from the simulations showed that indoor CO₂ levels were always lower in the hemp concrete buildings compared to the building made of clay bricks. However, in hemp concrete buildings with high air infiltration rates, the effect of the CO₂ absorption by the hemp concrete wall might be negligible. The energy required for the mechanical ventilation to maintain the CO₂ levels under the 1200 ppm threshold was estimated to be 0.28, 0.02 and 0.01 kWh/(m² yr), for the clay brick with low infiltration, hemp concrete houses with low and high air infiltration, respectively. Therefore, the operation of hemp concrete buildings with CO₂-based demand-controlled ventilation may have a slightly lower energy consumption as well as environmental impact than the equivalent clay brick buildings.

1. Introduction

The revised Energy Performance of building directive (EPBD) is reinforcing the need to reduce the energy consumption of buildings with the vision of a decarbonized building stock by 2050. Achieving zero emissions from the existing building stock will require not only increasing energy efficiency and generating 100 % renewable energy, but also reducing the emissions associated with the manufacture of the construction materials, the so-called embodied carbon emissions. Therefore, the construction sector plays a critical role in fighting climate change and a significant shift is required towards the use of more eco-friendly and sustainable materials to meet the European climate-neutral targets. In this context, hemp concrete has been recently adopted as an innovative solution by the building industry to reduce emissions, as this material stores more than 90 % of the carbon dioxide (CO₂) emitted during its production (Jami et al., 2019). Part of this storage occurs during its service life leading to a decrease of indoor CO₂ levels. Given this feature, the use of this material in buildings with CO₂-based demand-controlled ventilation might lead to lower ventilation requirements and a potential reduction of the energy consumption of the building.

Several studies have been conducted to characterize the CO₂ sequestration potential of hemp concrete (Arehart et al., 2020; Jami et al., 2016), most of them being focused on the assessment of its carbon footprint through Life Cycle Assessment (Pretot et al., 2014). However, the influence of CO₂ storage capacity of hemp concrete on the energy consumption of a building made with this material has not been explored so far. Thus, the aim of this research was to

develop an energy model including CO₂ absorption by hemp concrete to estimate the energy savings achievable in a hemp concrete residential building with CO₂-based demand-controlled ventilation and compare them with the energy consumption of the same building made of clay bricks.

2. Methodology

In this study, dynamic thermal simulations were used to evaluate the performance of hemp-based constructions. The thermal transmittance of a hemp concrete wall was calculated based on the data provided by the manufacturer, and experimental measurements were conducted to estimate CO₂ absorption rate of a hemp concrete wall. Then, these experimental data were included in a building energy model created using EnergyPlus to estimate the energy consumption of a hemp concrete building with CO₂-based demand-controlled ventilation. The same model was used to estimate the energy consumption of an identical house made of clay bricks for comparison.

2.1 Modeling

2.1.1 Reference Building

The case study building is representative of typical new single-family houses in the South Tyrol region (northern Italy). This building was chosen as a result of the analysis of a building stock in a valley in South Tyrol obtained from the TABULA project¹ and the guidelines and database of the local energy certification agency called Agenzia per l'Energia Alto Adige-CasaClima.

The case-study building was modeled and simulated with EnergyPlus 9.3.0 (US Department of Energy's (DOE), USA). Each simulation was performed over an entire reference year using an hourly timestep. For the simulations, the city of Bolzano (capital of South Tyrol) was selected and the corresponding weather file was taken from the energy plus weather platform (<https://energyplus.net/weather>).

2.1.2 Geometry And Construction Type

The geometry of a building has a major impact on the efficiency of the building. In particular, the volume-to-surface ratio determines the relative heat loss on the thermal envelope. In order to partially reduce the heat losses, the building was assumed to be a semi-detached house, as illustrated in Fig. 1. The opaque components of the building are listed in Table 2. These elements were taken from a freely available catalogue (dataholz.eu) which is a catalogue of wood and wood-based materials, building materials, components and component connections for timber construction covering thermal, acoustic, fire and ecological performance levels, released by accredited testing institutes or accepted research institutions.

The case-study building consists of 9 thermal zones: one living room, two bathrooms, three bedrooms and one studio. The building has a net floor area of 124 m² and a floor-to-ceiling height of 2.7 m. The east façade was assumed to be adjacent to another similar building (adiabatic).

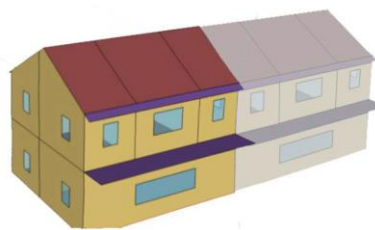


Fig. 1 – Reference case-study building

For the external walls, two typologies were simulated:

- A supporting structure of wood, filled with clay bricks and an external insulation (see Table 1)
- A supporting structure of wood, filled with hemp bricks (see Table 2).

2.1.3 Internal Gains, Heating And Ventilation


The internal gains, heating and ventilation systems were modeled as in previous work (Babich et al., 2020). The key points are as follows:

Schedules for occupancy, lighting and electric equipment set according to the 2014 Building America House Simulation Protocol (Wilson et al., 2014) were applied, as this protocol considers

¹ <https://episcopo.eu/iee-project/tabula/>

disaggregated schedules for living room and bedrooms, as well as for weekdays and weekends.

Table 1 – Brick wall stratigraphy

n.	Material	S [m]	λ [W/(m K)]	P [kg/m³]	c [J/(kg K)]	
1	External Plaster	0.015	0.7	1400	1000	
2	Insulation	0.16	0.04	18	1450	
3	Clay Brick	0.3	0.22	930	1450	
4	Interior Plaster	0.015	0.7	1400	1000	
Total thickness = 0.49 m U-value = 0.18 W/(m² K)						

The total number of occupants in the house was assumed as being equal to four. Based on typical metabolic heat generation for domestic activities (ASHRAE, 2009), the heat gains related to the occupancy were assumed to be 126 W for a standing relaxed person and 72 W for seated person.

The amount of carbon dioxide generated by a person depends on their activity level. In this model, the activity for the occupants of the living room was assumed to be equal to 1 met (i.e., seated quiet person) and 0.7 met for people occupying the bedroom (i.e., sleeping person). Based on these activity levels, the rate of CO₂ generation was calculated according to Eq. 2 (ASHRAE, 2009):

$$G_{CO_2} = G_{O_2} * RQ = \frac{0.00276 * A_D * M}{(0.23 * RQ + 0.77)} * RQ \quad (1)$$

Where G_{CO_2} is a CO₂ generation rate per person (L/s); A_D is the Dubois area (m²); RQ is the respiratory quotient (-); and M is the metabolic rate (met). The heating setpoint was set to 20 °C during the day and a constant setback of 18 °C during the night. The heating system was modeled as an ideal system with infinite heating capacity that supplied conditioned air to the zone, meeting all the load requirement and consuming no energy.

To guarantee acceptable indoor air quality, pollutants must remain below a certain threshold. In this study, only CO₂ was considered and a CO₂ threshold

value of 1200 ppm was selected for the activation of the mechanical ventilation based on category 2 (i.e., normal level of expectation, which is the suggested level for residential buildings) of the standard EN 16798-1:2019.

The reference building was intended to represent a typical new residential building of the South Tyrol region. According to the local legislation, air tightness of $n_{50} = 1.5 \text{ h}^{-1}$ was selected to meet the requirements of CasaClima A and B standard. Additionally, a value of $n_{50} = 3 \text{ h}^{-1}$ was also simulated to investigate the relevance of the air tightness on the CO₂ absorption capacity of hemp concrete walls.

2.1.4 Carbon Dioxide Sequestration

To model contaminant levels in EnergyPlus, the ZoneAirContaminantBalance object is commonly used. It can be used also to model CO₂ levels, although carbon dioxide is not considered an indoor contaminant. In this object, the outdoor CO₂ concentration was assumed to be equal to 400 ppm. The carbon dioxide sequestration capability of hemp concrete was modeled using a ZoneContaminantSourceAndSink:Carbondioxide object. This object allows the input of carbon dioxide sources or sinks in a zone. To model the hemp concrete walls as a sink, a value of -1 for the design carbon generation rate (m³/s) was set for each room. The design value is modified by the schedule, which was defined based on the experimental measurements conducted in the hemp concrete prototype house.

2.2 Thermal Transmittance Calculation

The thermal transmittance (U value) defines the ability of an element of structure to transmit heat under steady-state conditions (Willoughby, 2002). It is a measure of the quantity of heat that will flow through a given element subjected to a temperature difference on its external surfaces. The measurement of transmittance allows an estimate of the thermal conduction characteristics of vertical and horizontal opaque closures, which are necessary for calculating the heating requirements of buildings and, consequently, energy demands.

The composition of the hemp concrete façade investigated in this work is presented in Table 2. The wall was composed of an external plaster, two rows of hemp bricks of 24 cm each and an internal plaster.

Hemp bricks were composed of a mixture of hemp shives and a lime binder.

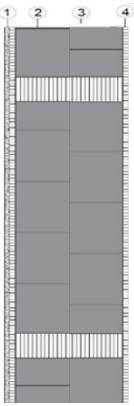
The thermal transmittance of a wall was estimated according to the standard UNI EN ISO 6946:2008 based on the thermal transmittance of the different elements of the wall provided by the manufacturer. Knowing the thickness (s_i) and the conductivity (λ_i) of each layer, it is possible to calculate its thermal resistance and then the thermal transmittance (see Eq. 1) of the wall.

$$U = \frac{1}{R} = \frac{1}{R_{si} + \frac{s_i}{\lambda_i} + \frac{s_n}{\lambda_n} + \frac{1}{C} + R_{se}} \quad (2)$$

Where R_{si} is the internal surface resistance, R_{se} is the external surface resistance and R the total thermal resistance of the wall.

Table 2 – Stratigraphy of the analysed wall

n.	Material	S [m]	λ [W/(m K)]	ρ [kg/m ³]	C [J/(kg K)]
1	External Plaster	0.020	0.7	1400	1000
2	Hemp brick	0.24	0.07	330	1700
3	Hemp brick	0.24	0.07	330	1700
4	Plaster	0.020	0.7	1400	1000
Total thickness = 0.40 m					
U-value = 0.18 W/(m ² K)					



2.3 CO₂ Monitoring

To estimate the CO₂ absorption rate of hemp concrete, CO₂ levels were monitored in a prototype house (see Fig. 2). The interior of the prototype house consisted of a wooden floor and ceiling and hemp concrete walls, whereas the façade was made of wood. In this house, two CO₂ sensors (K30, CO₂ meter, USA) were installed one inside and another outside the house to continuously monitor CO₂ levels from July to October 2021.

Outdoor air is an additional source of CO₂, therefore, the outdoor air supply entering the prototype house should be considered in order to estimate the

CO₂ absorption rate of hemp concrete. A blower door test was conducted to determine the number of air exchanges per hour in the prototype house.



Fig. 2 - Prototype house made of hemp concrete and wood

3. Results And Discussion

3.1 Thermal Transmittance

The thermal transmittance calculated according to UNI EN ISO 6946:2008 was equal to 0.18 W/(m² K). This value is lower than the required thermal transmittance by the National standard (Ministero Dello Sviluppo Economico, 2015), which is set at 0.26 W/(m² K) for new buildings in climate zone E, indicating that hemp concrete has high insulation properties.

The same thermal transmittance value was obtained for the modeled clay brick wall, thus the energy consumption related to the heating requirements is expected to be similar in both buildings. However, it is important to mention that the hemp brick wall does not have any thermal insulation layer and hence a lower variety of raw materials is needed for its manufacture. In the case of clay bricks, an insulation layer is required to meet the national standards for new buildings in terms of thermal transmittance. Therefore, besides the energy consumption and CO₂ emissions associated with the manufacturing process of the bricks, an additional amount of resources is needed for the manufacture of the insulation layer, which may potentially increase the environmental impact of the building construction.

3.2 CO₂ Absorption Rate

To estimate the CO₂ absorption rate, the CO₂ levels measured inside the prototype house were analyzed

and the air exchange rate of house was determined. The air exchange rate (n_{50}) per hour in the prototype house determined by the blower door test under a pressure difference of 50 Pa was found to be 7.22 h^{-1} . However, it is important to mention that this value represents the number of air exchanges at a pressure difference of 50 Pa when, at ambient pressure levels, this difference is approximately between 1 and 4 Pa. Therefore, the air exchange rate at 1 Pa was estimated from the air exchange rate at 50 Pa to be equal to 0.57 h^{-1} using the equations proposed in ASHRAE Handbook of Fundamentals.

The CO_2 levels inside the prototype house were analyzed and a repetitive daily pattern was identified over the different weeks of the monitoring campaign as illustrated in Fig. 3. During the morning, the indoor CO_2 concentration was closer to the ambient levels ($\sim 400 \text{ ppm}$) and slightly higher ($500\text{--}750 \text{ ppm}$) when occupants were inside the house. Every evening, when the occupants were gone and the house was closed, CO_2 levels sharply decreased down to $50\text{--}100 \text{ ppm}$. As can be seen in the figure, the upper part of the CO_2 concentration curve is linear, but the lower part has the shape of an exponential function indicating that steady-state concentration was reached overnight.

During the monitoring campaign, the different linear intervals (from 400 to $50\text{--}100 \text{ ppm}$) of the CO_2 level decreases were analyzed and an average CO_2 concentration variation of -103.2 ppm/h was estimated. This concentration variation was the result of two processes: i) addition of CO_2 coming from the outdoor air due the infiltration in the building and ii) CO_2 absorption by hemp concrete.

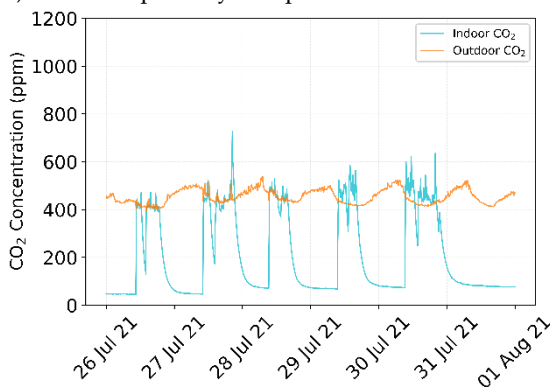


Fig. 3 - CO_2 levels measured inside and outside the prototype

Thus, considering an outdoor CO_2 level of $\sim 400 \text{ ppm}$, an air exchange per hour at 1 Pa of 0.57 h^{-1} , and assuming steady-state conditions in a ventilated space with a uniform CO_2 concentration the average CO_2 absorption rate of hemp concrete was estimated to be equal to 331.2 ppm/h .

3.3 Indoor CO_2 Levels

The simulation was run for the three investigated house configurations. The CO_2 concentrations obtained over a day in the living room are presented in Fig. 4. As it was the most crowded room, the living room was selected to illustrate the effect of hemp concrete walls on indoor CO_2 concentrations. Due to the CO_2 sequestration capability of hemp concrete, the CO_2 levels in the houses made with this material were always lower than in the brick house. Comparing the two hemp concrete houses, the CO_2 trends are very similar, most of the time the levels being slightly lower in the house with a lower infiltration rate. Interestingly, between 8 pm and 3 am, the CO_2 levels were lower in the hemp concrete house with $n_{50} = 3 \text{ h}^{-1}$ than in the one with $n_{50} = 1.5 \text{ h}^{-1}$. This fact might be explained by the higher infiltration rate, which allowed a faster air renewal and thus contributed to the dilution of the indoor CO_2 concentrations.

According to the results obtained, hemp concrete walls might influence indoor CO_2 levels, however, the impact of this absorptive property on the indoor CO_2 levels strongly depends on the air infiltration rate. In buildings with infiltration rates higher than 3 h^{-1} , the CO_2 sequestered by the hemp wall might be negligible, as the rate of air renewal is much higher than the absorption rate and thus the indoor CO_2 is evacuated before it can be absorbed by the wall.

3.4 Energy consumption

The energy consumption was estimated for the three house configurations investigated. The main sources of energy consumption were the district heating and the mechanical ventilation. As expected, the energy consumption associated with the heating is very similar for the hemp concrete and the clay brick buildings with a low infiltration rate (see

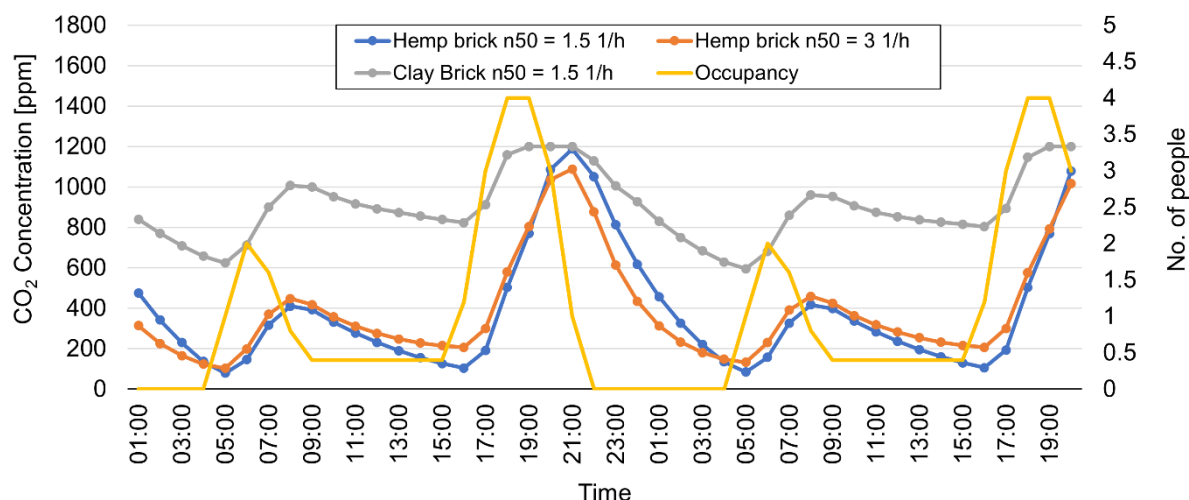


Fig. 4 - CO₂ concentration in the living room of the three investigated configurations

Table 3), as these walls have similar thermal properties. In the case of the hemp concrete building with higher infiltration rate, the energy consumption significantly increased due to the heat losses resulting from the faster air renewal. On the other hand, the energy required to run the mechanical ventilation and maintain the CO₂ levels under the 1200 ppm threshold was estimated to be 0.28, 0.02 and 0.01 kWh/(m² yr), for the clay brick and the hemp concrete houses with low and high air infiltration, respectively. In this case, as clay bricks are not able to sequester CO₂, a great difference was observed between the house made of this material and the ones made of hemp concrete, regardless of the air infiltration. However, even if the difference is remarkable, the absolute value is relatively small and might not have a significant impact on the overall energy consumption of the building.

Nonetheless, the energy consumption should be evaluated in context. An increase in the energy consumption also means an increment in greenhouse emissions. To uniformly express the climate impact of different greenhouse gases, the CO₂ equivalent unit is commonly used.

In Italy, the CO₂ emission factors used to convert from energy data to CO₂ equivalents are defined and regularly updated by the Italian National Energy Efficiency Agency ENEA (Agenzia Nazionale Efficienza Energetica). These factors depend on the primary source used to generate electricity and the generation efficiency.

Table 3 - Final energy and mechanical ventilation needed for three different configurations

	Thermal Energy Demand [kWh/(m ² yr)]	Energy Needs for Mechanical Ventilation [kWh/(m ² yr)]
Hemp brick n ₅₀ = 1.5 h ⁻¹	29.55	0.02
Clay brick n ₅₀ = 1.5 h ⁻¹	31.25	0.28
Hemp brick n ₅₀ = 3 h ⁻¹	46.75	0.01

In Bolzano, there is a district heating plant that provides heating from waste incineration. For this type of energy generation, the CO₂ emission factor is 0.17 kgCO_{2,eq}/kWh_{fin}. Conversely, the mechanical ventilation requires electrical energy and the CO₂ emission factor for this conversion is equal to 0.46 kgCO_{2,eq}/kWh_{fin} (Istituto Superiore per la Protezione e la Ricerca Ambientale, 2021). Based on these factors, the associated greenhouse emissions were calculated in CO₂ equivalents. As shown in Fig. 5, the emissions produced by the hemp concrete house with lower air infiltration are 8 % and 58 % lower than the ones associated with the clay brick house and the hemp concrete house with higher air

infiltration, respectively. These results indicate that the operation of hemp concrete buildings with CO₂-based demand-controlled ventilation may have a slightly smaller environmental impact than its clay brick counterparts.

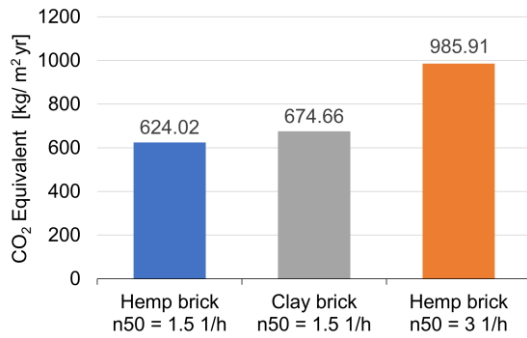


Fig. 5 - CO₂ equivalent emissions for the three different house configurations

4. Conclusion

The research presented in this paper aimed to develop an energy model including the CO₂ absorption by hemp concrete to estimate the potential energy savings achievable in a hemp concrete residential building with CO₂-based demand controlled ventilation and compare them with the energy consumption of the same building made of clay bricks. The key findings are:

- Indoor CO₂ levels in hemp concrete buildings are lower than in clay brick buildings due to the CO₂ sequestration capability of hemp concrete.
- In hemp concrete buildings with high air infiltration rates, the effect of the CO₂ absorption by the hemp concrete wall may be negligible.
- Regardless of the air infiltration, there is a significant difference in the electrical energy required to run the mechanical ventilation and maintain the CO₂ levels under the 1200 ppm threshold between hemp concrete and clay brick houses.
- The operation of hemp concrete buildings with CO₂-based demand-controlled ventilation may have a slightly lower environmental impact than the equivalent clay brick buildings.

4.1 Limitations And Future Work

Estimation of CO₂ absorption rate strongly depends on the temperature, the relative humidity and composition of the hemp concrete. In this study, only one type of hemp concrete was investigated, thus the results obtained can only be considered for hemp concretes with comparable composition. Moreover, CO₂ measurements in the prototype house were conducted from July to October. The data collected during those months were averaged to estimate an average CO₂ absorption rate. However, this time interval does not represent the full year and seasonal variability (i.e., low temperatures during winter) could potentially affect the CO₂ absorption rate. Therefore, the CO₂ absorption rate averaged over the entire year might be slightly different from the estimated value. More studies in which CO₂ is monitored over a longer period including all seasons of the year are needed in order to accurately determine the CO₂ absorption rate of hemp concrete.

Acknowledgement

The research leading to these results has received funding from the European Regional Development Fund POR FESR 2014–2020 of the Province of Bolzano, under Project number 1161, TinyFOP, Tiny FOP MOB - nachhaltige Realexperimente im Bausektor der Zukunft (Tiny FOP MOB - sustainable real-world experiments in the construction sector of the future).

Nomenclature

Symbols

s	Thickness (m)
λ	Thermal Conductivity (W/(m K))
ρ	Density (kg/m ³)
C	Specific heat (J/(kg K))
U	Thermal transmittance (W/(m ² K))
U_g	Thermal transmittance of glass (W/(m ² K))
U_f	Thermal transmittance of window frame (W/(m ² K))

References

- Arehart, J. H., W. S. Nelson, and W. V. Srubar. 2020. "On the Theoretical Carbon Storage and Carbon Sequestration Potential of Hempcrete." *Journal of Cleaner Production* 266: 121846. doi: <https://doi.org/10.1016/j.jclepro.2020.121846>
- ASHRAE. 2009. *ASHRAE Handbook: Fundamentals*. American Society of Heating, Refrigeration and Air-Conditioning Engineers.
- Babich, F., I. Demanega, F. Avella, and A. Belleri. 2020. "Low Polluting Building Materials and Ventilation for Good Air Quality in Residential Buildings: A Cost-Benefit Study." *Atmosphere* 11(1): 102. doi: <https://doi.org/10.3390/atmos11010102>
- Istituto Superiore per la Protezione e la Ricerca Ambientale. 2021. "Indicatori di efficienza e decarbonizzazione del sistema energetico nazionale e del settore elettrico."
- Jami, T., S. R. Karade, and L. P. Singh. 2019. "A Review of the Properties of Hemp Concrete for Green Building Applications." *Journal of Cleaner Production* 239: 117852. doi: <https://doi.org/10.1016/j.jclepro.2019.117852>
- Jami, T., D. Rawtani, and Y. K. Agrawal. 2016. "Hemp Concrete: Carbon-Negative Construction." *Emerging Materials Research* 5(2): 240–47. doi: <https://doi.org/10.1680/jemmr.16.00122>
- Ministero Dello Sviluppo Economico. 2015. "Decreto Interministeriale 26 Giugno 2015-Applicazione Delle Metodologie Di Calcolo Delle Prestazioni Energetiche e Definizione Delle Prescrizioni e Dei Requisiti Minimi Degli Edifici."
- Pretot, S., F. Collet, and C. Garnier. 2014. "Life Cycle Assessment of a Hemp Concrete Wall: Impact of Thickness and Coating." *Building and Environment* 72: 223–31. doi: <https://doi.org/10.1016/j.buildenv.2013.11.010>
- Willoughby, J. 2002. "30 - Insulation." In *Plant Engineer's Reference Book (Second Edition)*, edited by D. A. Snow, 30–31. Oxford: Butterworth-Heinemann. doi: <https://doi.org/10.1016/B978-075064452-5/50085-7>
- Wilson, E, C Engebrecht Metzger, S Horowitz, and R Hendron. 2014. "2014 Building America House Simulation Protocols." National Renewable Energy Laboratory.

A Fully Automated and Scalable Approach for Indoor Temperature Forecasting in Buildings Using Artificial Neural Networks

Jakob Bjørnskov – University of Southern Denmark, Denmark – jabj@mmmi.sdu.dk

Muhyiddine Jradi – University of Southern Denmark, Denmark – mjr@mmmi.sdu.dk

Christian Veje – University of Southern Denmark, Denmark – veje@mmmi.sdu.dk

Abstract

Improving the performance of buildings is a core pillar to attaining future energy and environmental goals in different countries, considering that the building sector is a major contributor in terms of both energy consumption and carbon emissions. These ambitious goals and the call for smarter, energy-efficient, and flexible buildings have called for innovative and scalable energy and indoor thermal comfort modeling and prediction approaches. This work presents a fully automated and scalable solution using Artificial Neural Networks to forecast indoor room temperatures in buildings. A case study of an 8500 m² university building in Denmark was considered for testing and evaluating the proposed approach. An extensive dataset was constructed with sensor data from 76 rooms that contain both readings on indoor temperature, CO₂ concentrations, and actuating signals on radiator valves and dampers, as well as outdoor ambient conditions. Using this dataset, a well-performing architecture is identified, which provides accurate temperature predictions in the various rooms of the building for prediction horizons of 24 hours.

1. Introduction

Buildings are widely regarded as one of the major contributing sectors in terms of both energy consumption and CO₂ emissions. Furthermore, future energy systems with high fractions of Renewable Energy Sources (RES) depend on high demand-side flexibility. Therefore, there is a clear need for increasing not only the performance but also the flexibility of buildings. However, to achieve feasible and intelligent operation strategies for both cost minimization and flexibility services implementation without compromising the indoor

comfort levels of buildings, reliable and accurate forecasting of building indoor thermal behavior is vital. In terms of indoor temperature forecasting, Artificial Neural Network (ANN) models have shown great potential in capturing the dynamics with high prediction accuracy (Alawadi, et al., 2022). In addition, these models can also be easily adapted and scaled up to different building cases. This work presents an ANN-based approach that requires no prior specifications for the modeled building and can achieve accurate indoor temperature predictions for long prediction horizons of 24 hours or more. The models developed generalize well enough to be used for scenario planning and what-if analyses, e.g., to test the impact of custom setpoint and shading schedules on indoor temperature.

2. Case Definition

The building under consideration in this work is an 8500 m² highly energy-efficient university building from 2015. It is located in Denmark, and it primarily consists of space types such as classrooms, study zones, corridors, and offices. In each of these spaces, indoor air temperature T and CO₂ concentration C are measured through installed sensors. In addition, each space contains space heaters of specific capacities with equipped mechanical valves that control the water massflow. The position of these valves $u_v \in [0,1]$ is managed centrally by the Building Management System (BMS) with $u_v = 0$ meaning fully closed with no massflow and $u_v = 1$ meaning fully open with maximum massflow. The supply water temperature is kept constant at approximately 60 °C.

The building is also equipped with a weather station that measures outdoor air temperature T_o , longwave solar irradiance Φ_L , shortwave solar irradiance Φ_s , and wind speed. The supply air temperature set-point is constant, at either 21-22 °C, depending on each space. The supply and exhaust airflows are controlled in each space by the supply and exhaust damper positions $u_d \in [0,1]$, with $u_d = 0$ meaning fully closed with no airflow, and $u_d = 1$ meaning fully open with maximum airflow. These damper positions are also managed through the BMS with Demand Controlled Ventilation (DCV), aiming at keeping the measured CO₂ concentration below 600 ppm. Finally, each space is also equipped with shades that are controlled by the BMS through a position parameter $u_{sh} \in [0,1]$, with $u_{sh} = 0$ meaning fully exposed with no shading, and $u_{sh} = 1$ meaning fully enclosed with maximum shading. The shades are controlled based on outdoor and indoor illuminance with a safety roll-up mechanism that sets $u_{sh} = 0$ at wind speeds higher than 15 m/s.

3. Methodology

3.1 Model Architecture

This work makes use of a specific type of ANNs called Recurrent Neural Networks (RNN) to model the transient temperature dynamics of a room. Specifically, Long Short-Term Memory (LSTM) networks were chosen due to their numerous demonstrations of adaptability and robustness in time-series black-box modeling, including indoor environment modeling (Fang et al., 2021; Mtibaa et al., 2020). LSTM models are a specific kind of RNN that were originally developed to deal with the vanishing and exploding gradient problem of traditional RNN models. A detailed explanation of the LSTM model is provided in the references (Hochreiter & Schmidhuber, 1997; Van Houdt et al., 2020).

To properly account for all phenomena that can significantly influence the energy balance of the room, it is very important to choose appropriate dynamic inputs for the model. In this work, the inputs are determined by considering the following energy transfer mechanisms:

- *Heat transfer by conduction through external surfaces* is considered by including indoor air temperature T , and outdoor temperature T_o as input.
- *Heat transfer by radiation* is considered by including longwave solar irradiance Φ_L , shortwave solar irradiance Φ_s , and the position of the shades u_{sh} in the model input.
- *Internal heat gains through occupancy* are included indirectly by including measured CO₂ concentration C , and damper position u_d . These inputs can, to a certain extent, represent occupancy due to the direct correlation between CO₂ concentration, ventilation airflow, and occupancy presence (Franco & Leccese, 2020).
- *Heat added by the space heater* is considered by adding the measured valve position u_v as input, which represents the water massflow. The supply water temperature is constant and does not therefore contribute as input.
- *Heat transfer by ventilation* is considered by adding the supply and exhaust damper positions u_d as inputs, which represent the airflow rates. The supply air temperature is constant and therefore does not contribute as input.

The model architecture is seen in Fig. 1 with inputs and outputs of the model. As shown, the model consists of two sequential LSTM models, A and B. All previously mentioned weather and sensor inputs from the previous timestep are fed to LSTM A. In addition, the LSTM also receives the cell state vector $c_{A,t-1} \in \mathbb{R}^n$ and hidden state vector $h_{A,t-1} \in [-1,1]^n$, where n is a hyperparameter that determines the size of these vectors. These two state vectors are an integral part of LSTM models, which essentially dictate the state of the system modeled during a given timestep. LSTM A outputs $c_{A,t}$ and $h_{A,t}$, which represents the updated state vectors.

LSTM B has $n = 1$ and is only given three inputs, the cell state $c_{B,t-1} \in \mathbb{R}$, the hidden state $h_{B,t-1} \in [-1,1]$, and the hidden state vector $h_{A,t}$. LSTM B outputs $c_{B,t}$ and $h_{B,t}$, which represent the updated state vectors of LSTM B. The training task is then to find an optimal set of parameters in LSTM A and B to minimize the error between $h_{B,t}$ and the chosen prediction target over multiple sequences of data.

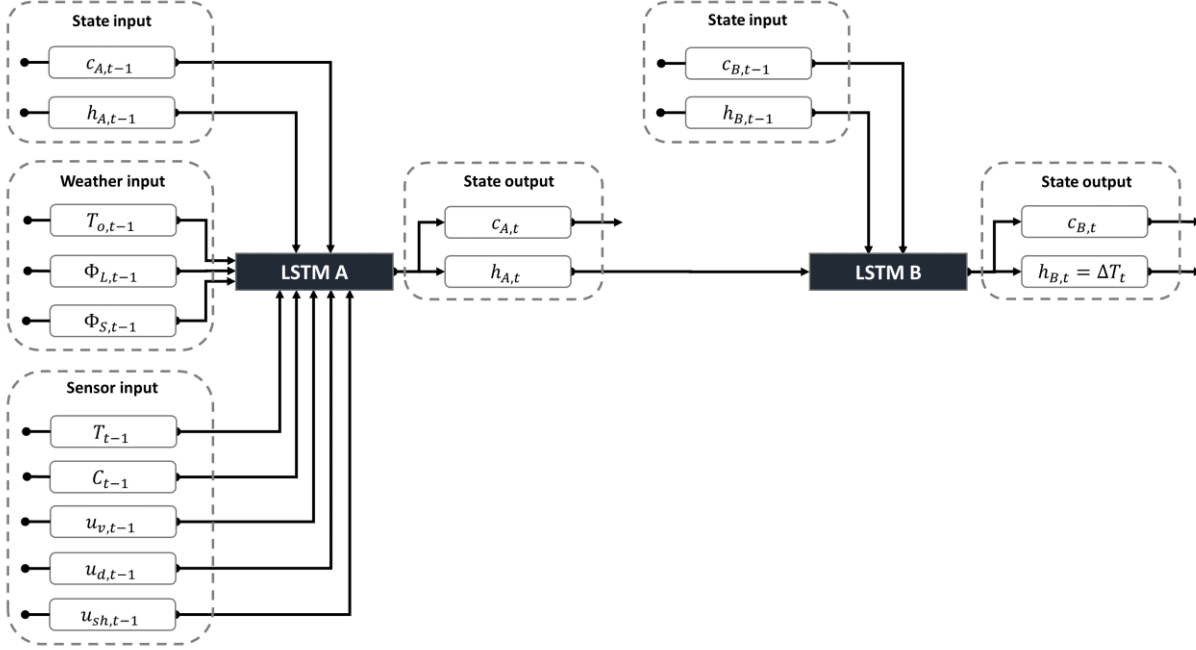


Fig. 1 – Model architecture with inputs and outputs of the sequential LSTM models, A and B

In the studies reviewed, the prediction target of the learning algorithms employed was indoor temperature in all cases. During initial testing, it was found that this configuration yielded good prediction results when testing with historical data as input. However, it was found that the models generalized poorly when fed with custom inputs instead of historical data, e.g., when using the model for setpoint control, as shown later in Section 4.2. When collecting operational data from a building, the actuation signals, e.g., valve positions, are typically directly correlated with indoor temperature through a thermostat with a simple control law, e.g., in the form of a Proportional (P) or Proportional Integral (PI) controller. Therefore, if the prediction target is temperature, the model will likely overfit the specific mode of operation that is reflected in the historical data used to train and test the model. We hypothesize that the model essentially learns to map the inverse control law of the thermostat instead of the actual thermal physics of the room. In this work, we are proposing that the model should predict the indoor temperature change ΔT instead of the actual temperature value, as this disrupts the direct correlation that is otherwise present between input and output.

3.2 Data Preprocessing

The dataset was constructed with all the weather and sensor readings introduced for 76 rooms in the case study building at a 10- minute interval for two years spanning January 1st 2018 to December 31st 2019. The raw data were pretreated and validated to ensure that proper and clean data were used. Following this, all inputs were min-max scaled between -1 and 1. After preparing the dataset, 24-hour sequences of 144 timesteps with no missing data were selected to form a collection of sequences for each space. In Fig. 2, the distribution of data sequences available among spaces is shown monthly. As shown, the number of sequences varies between rooms. The month with the most data is January, with a median of about 6000 sequences, while the month with the least data is August, with a median of about 3000 sequences.

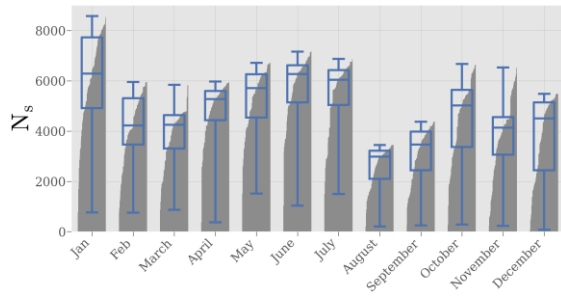


Fig. 2 – Number of sequences available per space for each month

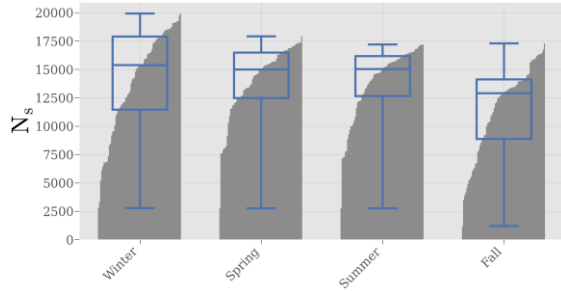


Fig. 3 – Number of sequences available per space for each season

In Fig. 3, the distribution is shown on a seasonal level. Here, the dataset generally appears to be more balanced with less variation. Hence, it is expected that the constructed datasets have enough diversity to cover most of the seasonal variance in the operation and thermal dynamics of the building.

3.3 Training and Testing Method

After preprocessing, the data is split into training, validation, and testing data sets with the splits [2/3, 1/6, 1/6], respectively. These data splits were carefully designed to ensure no overlap between sequences in the three data sets, while ensuring that seasonal and monthly variations are reflected in each dataset. For training, the machine-learning library Pytorch was used with Stochastic Gradient Descent (SDG) as optimizer, a momentum of 0.9, a batch size of 32, and a learning rate of 10^{-1} . The size n of cell state c_A and hidden state h_A was set to 20 for all space models.

During training, the model loss was evaluated on the validation dataset and saved at every 64th gradient update. At every 3000th gradient update, a copy of the model was saved, along with an average of the last 100 validation loss evaluations. After 100,000 gradient updates, the model with the lowest saved validation loss was selected. If the model had

not converged after 100,000 gradient updates, the procedure was repeated up until 400,000 gradient updates. This approach was used to train models for all 76 spaces. To properly test the trained space models, two modes of operation were presented.

The first mode was aimed at assessing the prediction accuracy of the space models given historic inputs. Here, the developed models were employed in a closed-loop configuration, as shown in Fig. 4, where future temperature predictions were based on past predictions. Perfect forecasting was assumed by feeding historical data for all weather and sensor inputs, except for the indoor temperature.

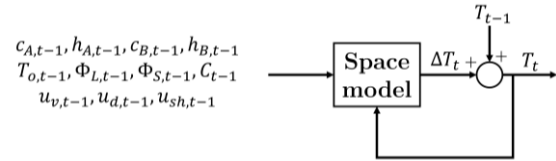


Fig. 4 – Closed-loop configuration designed to forecast indoor temperature for an arbitrary number of timesteps

The model then, for each timestep, predicted the temperature change to obtain the indoor temperature of the next time step, which was fed back to the model. This could be repeated as long as historical inputs were available. By repeating this for all timesteps in a simulation period, the produced temperature profile could then be compared with the actual measured temperature profile of the room to assess the prediction accuracy of the space model.

The second mode of operation was aimed at testing whether the developed space models generalize well enough to provide reasonable predictions under unseen operational conditions. Here, custom inputs were thus be fed to the model to observe the response. This was a very important property that made it possible to use the model for testing different operational strategies or what-if scenarios and their influence on indoor comfort in a safe environment.

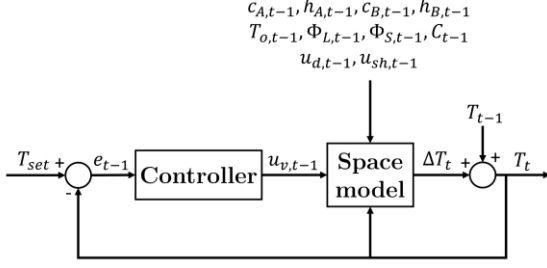


Fig. 5 – Closed-loop configuration designed for temperature set-point control through the valve position of the space heater

In this work, two model inputs were considered for this purpose; u_v and u_{sh} . In one simulation, the space heater valve position input u_v was constructed by implementing the space models in a closed-loop configuration for temperature setpoint control, as shown in Fig. 5. Here, all inputs were historical except for u_v and temperature T . The implemented controller was a simple proportional controller that each timestep scales the input signal $u_{v,t-1}$ proportionally to the error $e_{t-1} = T_{set} - T_{t-1}$, where T_{set} was the temperature setpoint in the room. In another simulation, the shades position input u_{sh} was constructed by implementing a simple predetermined schedule that operates based on the time of the day. All inputs except for u_{sh} and T were thus historical.

4. Results and Discussion

4.1 Quantitative Performance Assessment

First, the quantitative model performance was evaluated by using the first mode of operation as described in Section 3.3. Here, the Mean Absolute Error (MAE) between measured indoor temperature and predicted temperature was calculated for each space model across all 24-hour sequences in the test dataset. Fig. 6 shows the performance of each trained space model. Specifically, it shows the relationship between MAE, Standard Deviation of prediction targets $\sigma(\Delta T)$, and number of sequences N_s . The three marked space models were used for a qualitative performance assessment in Section 4.2. As seen in the figure, most of the space models (~86 %) achieve MAE values below 0.5 °C, which is lower than the required measurement accuracy of temperature sensors of ± 0.5 °C (ISO, 1998).

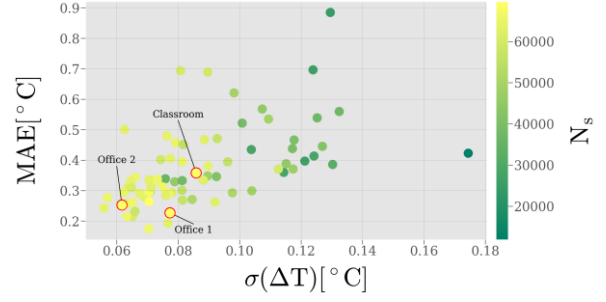


Fig. 6 – Relationship between Mean Absolute Error MAE, Standard Deviation of prediction targets $\sigma(\Delta T)$, and number of sequences N_s . The three space models chosen for qualitative assessment are marked

The best performing space model represents an office with $N_s = 66297$ and $MAE = 0.17$, while the worst performing model is of a classroom with $N_s = 24210$ and $MAE = 0.88$. As seen from the colormap in Fig. 6, there seems to be a negative correlation between the prediction error and the number of sequences available, agreeing with the general notion in machine-learning, that more data yields lower prediction error and better model generalization. Therefore, it is expected that the poor-performing space models could attain similar performance with more data. Furthermore, there seems to be a positive correlation between prediction error and the variation observed for the prediction target ΔT . This means that the prediction error will be higher for datasets that have a more fluctuating temperature profile. This is to be expected, as a fluctuating indoor temperature is generally harder to predict than a steady temperature.

4.2 Qualitative Performance Assessment And Applications

To provide a qualitative performance assessment of the models developed, three case study spaces were selected, one classroom and two offices, as also marked in Fig. 6. For each of these space models, a winter period and a summer period of 24 hours were chosen to evaluate how the space models perform under different ambient conditions. The models were first simulated for these periods using the first mode of operation, as explained in Section 3.3.

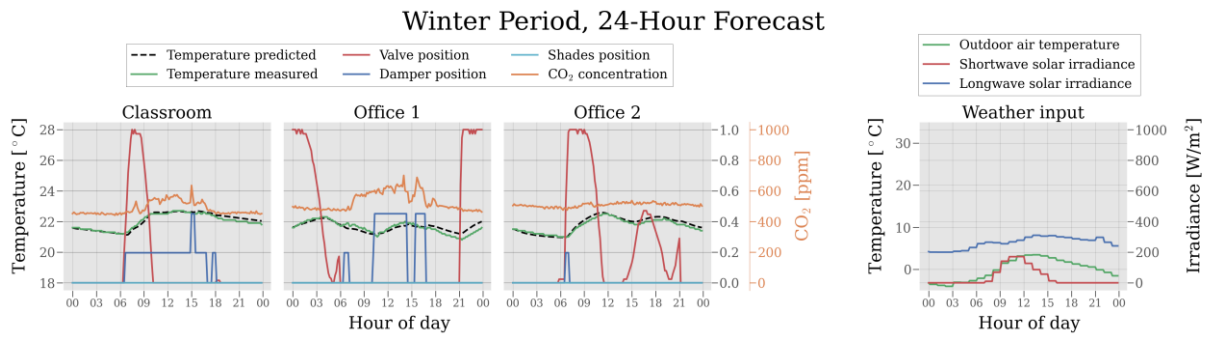


Fig. 7 – 24-hour temperature forecast in a winter month compared with actual measured temperature. The weather input is shown on the plot furthest to the right, while the individual inputs for the three selected space models are shown on the plots to the left

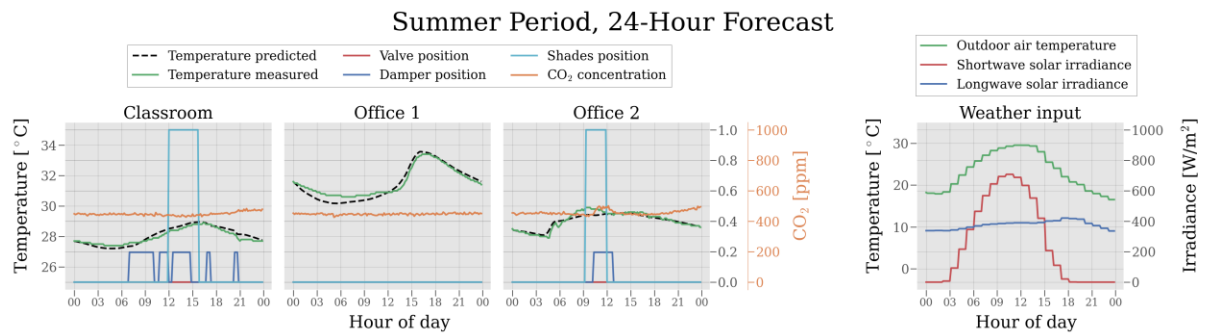


Fig. 8 – 24-hour temperature forecast in a summer month compared with actual measured temperature. The weather input is shown on the plot furthest to the right, while the individual inputs for the three selected space models are shown on the plots to the left

For the winter simulation, the results are shown in Fig. 7, with the weather inputs in the plot furthest to the right, while the results for each of the three chosen rooms can be seen on the left. As seen, all three space models accurately predict the indoor temperature, although Office 1 seems to slightly overestimate the temperature during the last 6 hours. The space heater valve position has a clear significance in all three spaces, where the general trend is that $u_v = 0$ results in decreasing room temperature, while $u_v > 0$ results in increasing room temperature. The models are also able to account for heat gains and heat losses associated with occupancy and ventilation. This is mostly seen in the Classroom and Office 1 in the period from 09:00 to 15:00, where the CO₂ concentration rises above 600 ppm and the dampers are positioned at around 50 %. Here, the model correctly predicts that the indoor temperature increases, although the space heater is not in operation. The shades are all rolled up ($u_{sh} = 0$) as they have no desirable effect during winter. Moving to the simulation results for the summer period, the results are shown in Fig. 8. The weather data inputs are again seen on the plot furthest to the

right, where the ambient temperature and irradiance levels are much higher compared with the winter period. As seen, this has a significant impact on the predicted and actual temperatures in the three spaces, especially for Office 1, where temperatures are above 30 °C during the whole 24 hour-period. The cause for large differences in both shape and peaks of the temperature profiles was different orientation, shading, and geometrical properties of the spaces. As seen, all three space models have learned to correctly account for these properties and provide accurate predictions for all 24 hours, although Office 1 slightly underestimates the temperature during the first 12 hours of the period. From the CO₂ levels, which have a very constant profile of around 450 ppm, the occupancy appears to be close to zero. However, this is expected during July and August, where the students are on summer leave. The shades are, to some extent, utilized in the Classroom and Office 2. However, it is expected that the high temperatures could be mitigated even more, by increasing the duration of the shades being rolled down ($u_{sh} = 1$). This will be investigated further in the following analysis.

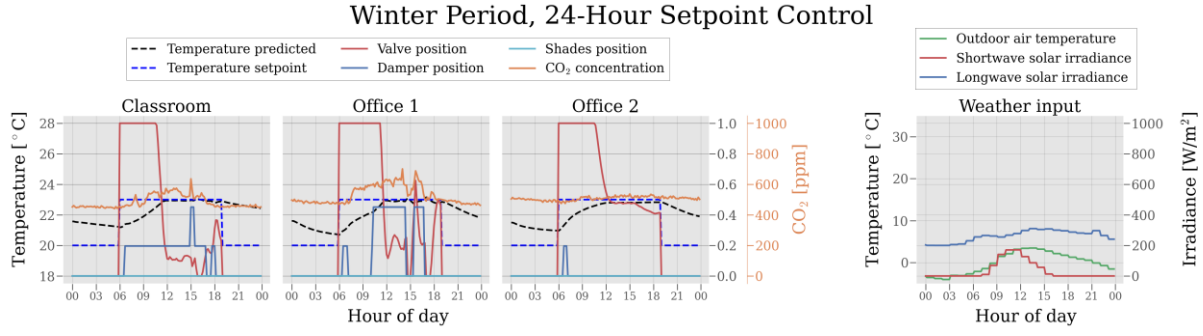


Fig. 9 – 24-hour setpoint control in a winter month. The weather input is shown on the plot furthest to the right, while the individual inputs for the three selected space models are shown on the plots to the left along with the predicted temperature and the setpoint

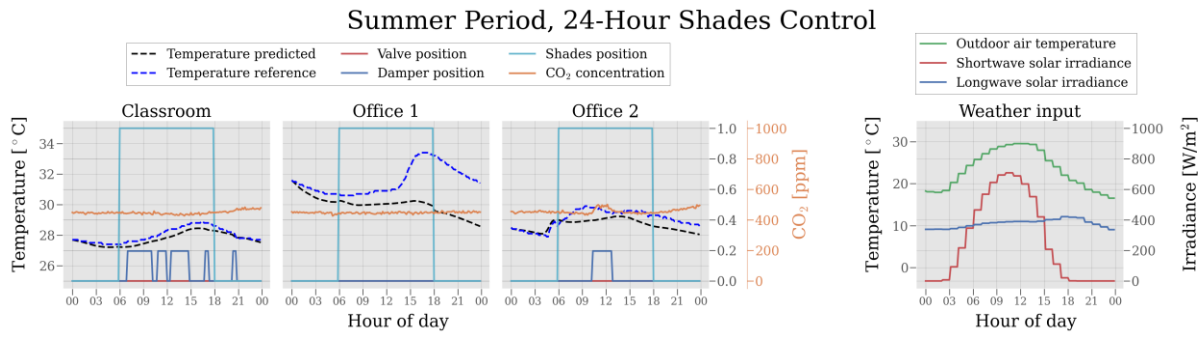


Fig. 10 – 24-hour shades control in a summer month. The weather input is shown on the plot furthest to the right, while the individual inputs for the three selected space models are shown on the plots to the left along with the predicted temperature. The original measured temperature in this period is shown as a reference

As just demonstrated, the models perform well when predicting temperatures under historical conditions. However, to demonstrate the applicability of the models, the second mode of operation, as presented in Section 3.3, was employed. The temperature setpoint control was implemented for the same winter period as shown in Fig. 7, while the shades control was implemented for the same summer period as shown in Fig. 8.

The results for the temperature setpoint control are shown in Fig. 9. As seen, the setpoint was varied, depending on the time of day. From 06:00 to 18:00, the setpoint was 23 °C, while from 18:00 to 06:00, the setpoint was 20 °C. The controller adapted to these setpoint signals by varying the valve position accordingly. For all three spaces, the valve was closed during the night, where the temperature was allowed to decrease. At 06:00, when the setpoint was raised to 23 °C, the valve was opened, and the indoor temperature increased until around 12:00, where the indoor temperature in all three rooms reached the specified setpoint. At this point, the

valve position was operated between 0 and 1 in an attempt to keep the indoor temperature at the setpoint. For Office 2, it was noticed that the temperature and valve position profile was smoother compared to the Classroom and Office 1, which had small fluctuations in temperature. However, as seen, the Classroom and Office 1 also had more disturbances in the form of varying CO₂ levels and ventilation airflows. Despite these disturbances, the simple controllers managed to keep the temperature at 23 °C in all three space models until 18:00, where the setpoint was again decreased to 20 °C. Here, the valve was again shut, and the temperature started to decrease.

Moving on to shades control during the summer period, the results are shown in Fig. 10. Here, the shades were rolled down ($u_{sh} = 1$) from 06:00 to 18:00 and rolled up ($u_{sh} = 0$) from 18:00 to 06:00. This had a significant effect on the predicted indoor temperature when compared with the original measured temperature (temperature reference), where the duration of shading was very limited. The

effect was very clear for Office 1, where the peak at 17:00 shifted from around 33 °C to 30 °C. The Classroom and Office 2 also had a reduced temperature response, although not as significant as Office 1.

5. Conclusion

In this work, a fully automated and scalable approach for temperature forecasting in buildings was presented and assessed. The presented method relied on ANNs in the form of two sequential LSTM models to predict temperature change within a room, given weather data and sensor inputs such as space heater valve positions, damper positions, shades positions, and CO₂ concentration. Hence, the developed approach needed no prior information about the building such as geometry, material properties, design data, etc.

The methodology developed was implemented considering 76 rooms of an 8500 m² university building in Denmark with 86 % of the rooms achieving a Mean Squared Error of less than 0.5 for 24-hour forecasting. The difference in prediction performance between space models was explained by differences in the amount of data available. However, more work is needed to identify more robust criteria concerning the amount, type, and quality of data that is needed to obtain accurate space models. The applicability of the models was demonstrated by implementing three selected models in a closed-loop setpoint control configuration for a 24-hour winter period. Additionally, different shading schedules were also explored to show their impact during a 24-hour summer period.

In line with the emerging initiatives toward digitalization of the building sector, building digital twins has promising technical and economic impacts. In this context, a fully scalable and automated energy modeling approach is vital, so that these twins can provide a robust, generic, and effective solution for various applications in the building sector. The modeling approach proposed in this study serves as a core for future building digital twin development and could be used as a backbone for various automated services, including performance monitoring, scenario assessment, and operational management.

Acknowledgement

This work was carried out under the ‘Twin4Build: A holistic Digital Twin platform for decision-making support over the whole building life cycle’ project, funded by the Danish Energy Agency under the Energy Technology Development and Demonstration Program (EUDP), ID number: 64021-1009.

References

- Alawadi, S., D. Mera, M. Fernández-Delgado, F. Alkhabbas, C. M. Olsson, and P. Davidsson. 2022. “A comparison of machine learning algorithms for forecasting indoor temperature in smart buildings.” *Energy Systems* 13: 689–705. doi: <https://doi.org/10.1007/s12667-020-00376-x>
- Fang, Z., N. Crimier, L. Scanu, A. Midelet, A. Alyafi,, and B. Delinchant. 2021. “Multi-zone indoor temperature prediction with LSTM-based sequence to sequence model.” *Energy and Buildings* 245: 111053. doi: <https://doi.org/10.1016/j.enbuild.2021.111053>
- Franco, A., and F. Leccese. 2020. “Measurement of CO₂ concentration for occupancy estimation in educational buildings with energy efficiency purposes.” *Journal of Building Engineering* 32: 101714. doi: <https://doi.org/10.1016/j.jobee.2020.101714>
- Hochreiter, S., and J. Schmidhuber. 1997. “Long Short-term Memory.” *Neural computation* 9(8): 1735-1780.
- ISO. 1998. *ISO 7726 - Ergonomics of the Thermal Environment - Instruments for Measuring Physical Quantities*.
- Mtibaa, F., K.-K. Nguyen, M. Azam, A. Papachristou, J.-S. Venne, and M. Cheriet. 2020. “LSTM-based indoor air temperature prediction framework for HVAC systems in smart buildings.” *Neural Computing and Applications* 32: 17569–17585. doi: <https://doi.org/10.1007/s00521-020-04926-3>
- Van Houdt, G., C. Mosquera, and G. Nápoles. 2020. “A Review on the Long Short-Term Memory Model.” *Artificial Intelligence Review* 53(8): 5929-5955. doi: <https://doi.org/10.1007/s10462-020-09838-1>

Effects of Different Moisture Sorption Curves on Hygrothermal Simulations of Timber Buildings

Michele Libralato – University of Udine, Italy – michele.libralato@uniud.it

Maja Danovska – Free University of Bozen-Bolzano, Italy – maja.danovska@natec.unibz.it

Giovanni Pernigotto – Free University of Bozen-Bolzano, Italy – giovanni.pernigotto@unibz.it

Andrea Gasparella – Free University of Bozen-Bolzano, Italy – andrea.gasparella@unibz.it

Paolo Baggio – University of Trento, Italy – paolo.baggio@unitn.it

Paola D'Agaro – University of Udine, Italy – paola.dagaro@uniud.it

Giovanni Cortella – University of Udine, Italy – giovanni.cortella@uniud.it

Abstract

Building energy simulations are a key tool in designing high performance buildings capable of facing the future challenges and in helping emission reduction targets to be met. Currently, thermal properties of materials used in most building energy simulations are assumed to be constant and not dependent on moisture content and temperature. Heat and moisture dynamic transfer models allow a simulation of building envelope performance considering thermal resistance reduction due to moisture effects. These models are generally considered more accurate than the heat transfer models, and they could be used to simulate the heat transfer (increased by water vapor storage) and the moisture buffering effect on the indoor environment. For the simulation to be performed, hygrothermal material properties should be known as functions of moisture content. Nevertheless, hygrothermal material properties are rarely available and correlations from the literature have to be used. In this study, the moisture storage curves of CLT, OSB and two types of wood fibre insulation have been measured with a dynamic vapor sorption analyser. The other hygrothermal properties are estimated from values measured in previous studies or taken from the literature. The simulations of two small single room buildings in four Italian locations are performed with the software EnergyPlus, considering an ideal HVAC system, to calculate the heating and cooling needs of the building. The HAMT (heat and moisture transfer) module of EnergyPlus is used. With the results presented in this study, it is possible to evaluate how an approximated curve affects the results of a whole-building simulation in terms of wall average water content, indoor air relative humidity and heating/cooling loads.

1. Introduction

The energy required for heating and cooling buildings is a large fraction of the total consumption and therefore of greenhouse gas emissions. These emissions need to be reduced as soon as possible and Building Energy Simulation (*BES*) methods are essential for designing high performance buildings and predicting their energy needs. Researchers and practitioners are using dynamic detailed building energy models that consider the transient behavior of the building envelope and of the *HVAC* systems to minimize the carbon emissions and reduce the energy demands during both heating and cooling seasons. When the building envelopes are composed of porous materials, water vapor diffusion plays a significant role in heat transfer. The main effect on the materials is the increase of the value of thermal conductivity, which results in larger heat losses during the heating season and larger heat gains during the cooling one (Danovska et al., 2020a and 2020b). Using the appropriate software, it is possible to model whole buildings using heat, air and moisture transfer models (*HAMT*) for the building envelope, calculating the effects of moisture diffusion and storage in building materials (Libralato et al., 2021a and 2021b), as well as the moisture buffering effect on the air conditions of the thermal zones (Zu et al., 2020). 17 *BES* tools based on *HAMT* models (including EnergyPlus) are presented in Woloszyn and Rode (2008), defining a benchmarking process included in IEA EBCS Annex 41. All these models require advanced

hygrothermal material characterizations, which are possible with time-consuming testing activities. The thermal and hygroscopic properties of the materials have to be tested at different temperatures and moisture contents, often requiring months of conditioning in climatic chambers (depending on the size of the samples).

This research is focused on the comparison between Moisture Sorption Curves (*MSCs*) interpolation models (Fig. 1), commonly used for timber materials when few Equilibrium Moisture Content (*EMC*) values are available. The study is based on the *MSCs* of four wood-based materials, measured at the Thermal Systems Laboratory of the University of Udine, and the thermal conductivity of three of the same set of materials, previously measured at different moisture contents and temperatures at the Building Physics Laboratory of the Free University of Bozen-Bolzano (Danovska et al., 2020a and 2020b).

First, the points of the moisture curve are measured using a Dynamic Vapor Sorption (*DVS*) analyser. Then, a piece-wise linear curve is developed to represent a *MSC* starting from the measured points. At this stage, using only three *EMC* points from the measured ones, three commonly used *MSC* models are adopted to interpolate the values. Finally, two small single-zone buildings are simulated in four locations, using the 4 *MSC* modeling approaches and comparing the results. The simulation tool used is EnergyPlus (version 9.5).

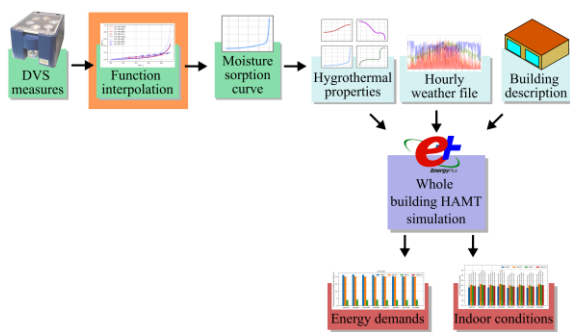


Fig. 1 – Study procedure scheme. In this study the effects of the choice of the function interpolation of *MSC* are quantified in terms of energy demands and indoor air conditions

The effect of *HAMT* models on *BES* energy consumption results has been already studied in the literature (Yang et al., 2015), finding differences of 5-10 % from the thermal simulations. The aim of

this comparison is to assess to what extent an approximated sorption curve can alter the results of a whole-building hygrothermal simulation. Indeed, little information exists in the literature on the influence of different *MSCs* on *BES*.

The topic of the effects of *MSC* has been mainly tackled when considering moisture hysteresis in *HAMT* wall simulations for moisture-related risk analysis or for moisture buffering evaluations (Berger et al., 2020; Libralato et al., 2021a; Scheffler, 2008), comparing the effects of including hysteresis sorption models in the material sorption process. In this paper, hysteresis will not be considered, since EnergyPlus cannot model moisture hysteresis, but the adsorption and desorption curves of the materials will be taken into account separately.

2. Material Characterization

To perform heat and moisture transfer transient simulations, knowledge of several hygro-thermal material properties is required. In this study, the *MSCs* and thermal conductivities are obtained from measurements, while heat capacity and vapor permeability is taken from the literature. The study is limited to the hygroscopic range (under 95 % *RH*).

The *MSCs* of four materials were measured using the Proumid VSORP basic *DVS* analyser (Fig. 2). The instrument was set to perform gravimetric tests of the five samples every 20 minutes in a small climatic chamber with controlled dry bulb air temperature (*T*) and relative humidity (*RH*). *T* and *RH* being kept constant, and the samples are weighed until they reach equilibrium conditions. This procedure is performed automatically for every point of the *MSCs*. The environment was set to 23 °C and the relative humidity was set sequentially to 0 %, 30 %, 40 %, 50 %, 60 %, 70 %, 80 %, 90 %, 80 %, 70 %, 60 % and 50 % *RH*. The air *RH* is kept constant until the equilibrium condition is met by all the samples. The equilibrium condition is set to a mass change lower than 0.01 % in 350 minutes. The balance resolution is 0.1 mg. The whole test lasted approximately 42 days for a total of 12 *EMC* points.

The measurement procedure used differs from the standard ISO 12571 (CEN, 2021) on the following points:

- the sample's mass shall be at least of 10 g, and 100 mm x 100 mm if the material has a density lower than 300 kg/m³. Smaller samples can be used but it should be demonstrated that the result will not be affected;
- three samples shall be tested for each material;
- the equilibrium is reached when three consecutive weights, made 24 h apart, differ less than 0.1 % of the total mass;
- the starting point for the desorption curve should be at least 95 % RH.

Using the DVS analyser in place of the standard procedure removes the error caused by moving the sample from the controlled air environment to the scale, and reduces the time required by the test.

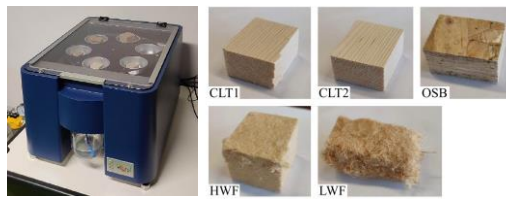


Fig. 2 – Experimental device (Vsorp Basic dynamic vapor sorption analyser) and studied samples of wood-based materials

The materials studied (Fig. 2) are spruce timber (used for Crossed Laminated Timber (CLT) panels), Orientated Standard Board (OSB), Low-density Wood Fibre (LWF) and High-density Wood Fibre (HWF). Since the instrument can measure 5 samples at the same time, two samples of CLT are tested and the MSCs used in the simulations is obtained averaging the two values.

The dry weight, volume, and free saturation moisture content of the samples are presented in Table 1. The dry weight is obtained after conditioning the samples at 0 % RH at 23 °C. The free saturation moisture contents of the five samples are obtained from the weight of the samples submerged in water until the weight variation is under the 0.1 %. A scale with 0.01 g resolution is used. The results of the sorption analysis are presented in Fig. 3. The EMCs of the five samples for the adsorption process are measured starting from the dry state up to the 90 % RH, and for the desorption process, starting at 90 % RH and back to 50 % RH.

Table 1 – Sample description

Sample ID	Dry weight [mg]	Volume [mm ³]	Sat. M.C. [mg]
CLT1	7577.0	14570	13270
CLT2	7094.2	15850	14740
OSB	8632.1	18045	19890
LWF	2449.5	47740	41410
HWF	8654.5	80686	46390

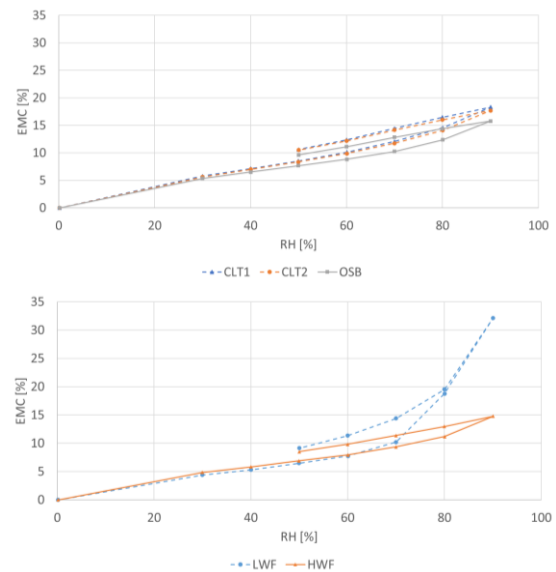


Fig. 3 – Adsorption and desorption curves measured for the five samples

2.1 Other Hygrothermal Properties

The thermal conductivity and specific heat values of the materials are taken from (Danovska et al., 2022), except for the OSB values which are obtained from the correlation reported in (Vololonorina et al., 2014) at 25 °C. The values of thermal conductivity are measured at different moisture contents and temperatures, but for this paper only the values at 20 °C with different moisture contents are considered. As an overall description of the materials, the hygrothermal properties are presented in Table 2. The values of permeability μ_{dry} and specific heat c_{dry} of the dry materials are taken from (Carbonari, 2010), except for OSB, which is from (Igaz et al., 2017).

Table 2 – Hygrothermal properties of the materials

Material	λ_{dry} [W m ⁻¹ K ⁻¹]	ρ_{bulk} [kg m ⁻³]	c_{dry} [J kg ⁻¹ K ⁻¹]	μ_{dry} [-]
CLT	0.104	467	1380	34
OSB	0.096	478	1287	46
LWF	0.039	51	2100	6
HWF	0.048	107	1380	6

The values of density ρ_{bulk} are calculated from Table 1. The values of μ used in the models are dependent on the moisture content and are described by linear piecewise functions connecting the values presented in (Vololonorina et al., 2014). The values of the vapor resistance factor at 0 % RH, μ_{dry} are presented in Table 2.

2.2 Moisture Sorption Curve Functions

In this study, four types of MSC interpolation are compared:

- 1 - Piecewise linear function (PLF)
- 2 - Brunauer–Emmett–Teller model (BET)
- 3 - Guggenheim-Anderson-de Boer model (GAB)
- 4 - Modified BET (B80)

The PLF case is obtained from the list of measured points. The interpolated EMC are calculated between the known points with a linear interpolation. The BET and the GAB model isotherm functions are considered in the form described in (Thybring et al., 2021) and they are used to obtain a correlation for the MSCs from three points of the measured EMC values series using the parabolic form presented also in (Thybring et al., 2021). The B80 modified BET model is presented in (Künzel, 1995) and it is used in the WUFI software family to define the unknown MSCs. The parameters of the B80 curve are defined by the EMC at 80 % RH and by the free water saturation point, set at 100 % RH, therefore it is the only function in this study that includes information on the over-hygroscopic range. The analytical curves obtained are used to define the sorption curve in EnergyPlus in the hygroscopic range for both adsorption and desorption curves. Fitting the values of EMC is commonly done when only few measured EMC are available. Therefore, to perform this situation, 3 EMC values

are used to calculate the functions' parameters. The GAB and BET adsorption curves are fitted to the EMC values of 30 %, 50 % and 80 % RH, while the desorption curves are fitted to the 50 %, 70 % and 80 % RH points.

3. Simulations

To perform a simple comparison a modified version of the BESTEST Common Exercise 600 (Fig. 4) is used as test building (ANSI/ASHRAE, 2017).

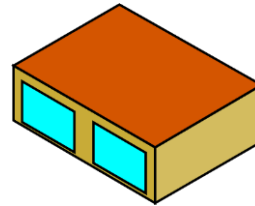


Fig. 4 – The BESTEST 600 geometrical model is used for the simulations. The model is a single room building with two large windows facing South

To evaluate the effects of the variation of the MSCs, the Heat Balance Algorithm is set to the Combined Heat and Moisture Finite Element model. Then the materials' MSCs are defined with 22 points (EnergyPlus allows a maximum of 25 points). The 22-point definition of the MSCs GAB, BET and B80 is obtained from this subdivision of the RH range: every 10 % RH up to the 70 % RH, while from 72 % RH to 96 % every 2 %; the last point of the moisture curve is set at 100 % RH to the free water saturation point. The liquid conduction coefficients are set to 0 to avoid the over-hygroscopic moisture transport. Constant infiltration is set to 0.5 ACH and the internal sensible heat gains are set (as the BESTEST case) constantly to 200 W (60 % radiative, 40 % convective, 0 % latent). The weather files used are the ASHRAE IWEC (International Weather for Energy Calculation) files for the locations of Milan, Rome, Palermo and Venice. Annual average T , RH and total solar horizontal irradiation I_G of the weather files are presented in Table 3. The initial water content for every material is set to the EMC value correspondent to the 50 % RH value of the adsorption PLF MSC.

Table 3 – Weather files: average temperature and relative humidity, and total solar horizontal irradiation

Location	T [°C]	RH [%]	I_G [MWh/m ²]
Milan	11.8	75	1.29
Palermo	18.8	74	1.69
Rome	15.8	78	1.46
Venice	13.2	77	1.15

Two construction types are set as external vertical walls (yellow walls in Fig.4): a *CLT* wall and a frame wall, while the floor and the roof constructions are the same for both cases. The build-ups of the two walls are described in Table 4.

Table 4 – Wall types

Wall type	Material layers	d [cm]
<i>CLT</i> wall $U = 0.26 \text{ W/(m}^2\text{K)}$	<i>OSB</i> (external layer)	2
	<i>LWF</i>	10
	<i>CLT</i>	10
Frame wall $U = 0.37 \text{ W/(m}^2\text{K)}$	<i>OSB</i> (external layer)	2
	<i>HWF</i>	10
	<i>OSB</i>	2
Floor and Roof $U = 0.31 \text{ W/(m}^2\text{K)}$	Barrier (external layer)	-
	<i>HWF</i>	10
	<i>LT</i>	10

A vapor barrier ($S_d = 1500 \text{ m}$), not defined in the BESTEST, is added on the external side of the floor and of the roof, to remove the influence of the ground and of the roof. The floor external surface is set as adiabatic. An ideal heating and cooling system is set to maintain the internal temperatures between 20 °C and 27 °C, without air humidity control, and the heating and cooling demand is calculated. There are six warmup days required by EnergyPlus to reach convergence not reported in the results.

4. Results

In this section, first the *MSC* fitted curves are compared with the measured *PLF* curves, then the effects of using different *MSCs* in EnergyPlus *HAMT* whole building simulations are presented.

4.1 Fitting Evaluation

The curves fit the experimental points differently: from Fig. 5 it could be observed that the *GAB* model tends to follow the measured points, but it does not increase the *EMC* values after 90 % *RH*. Differently, the *BET* and *B80* curves always have lower *EMC* for values of *RH* lower than 80 %.

On one hand, the *B80* function is constrained at the *EMC* for 80 % *RH* and at 100 % *RH* and overestimates the values at 90 % *RH*. On the other hand, the *BET* curves overestimate also the 80 % *RH*. It should be also noted that the *LWF* adsorption *GAB* curve is above the desorption curve after the 80 % *RH*, being the only case where the *GAB* curve shows high moisture contents in the higher *RH* values.

Depending on the *RH* range used in the simulations, the material will have different moisture contents. In the cases studied, the room air *RH* is calculated to be between 30 % and 60 %, therefore, the representativeness is evaluated only up to 70 %. To evaluate the goodness-of-fit, the difference (in terms of moisture content) between the curves (*BES*, *GAB* and *B80*) and the *EMC* measured points (*PLF*) is calculated for each measured point of the desorption and adsorption curves, up to 70 %. The average of the differences is presented in Fig. 6. The *GAB* curves are the closest to the measured points, except for the *LWF* curve. The *BET* and *B80* curves have higher differences, therefore larger differences are expected in the simulation results. Despite the constraint at 80 % *RH*, the *B80* curves have larger average distances from the measured points.

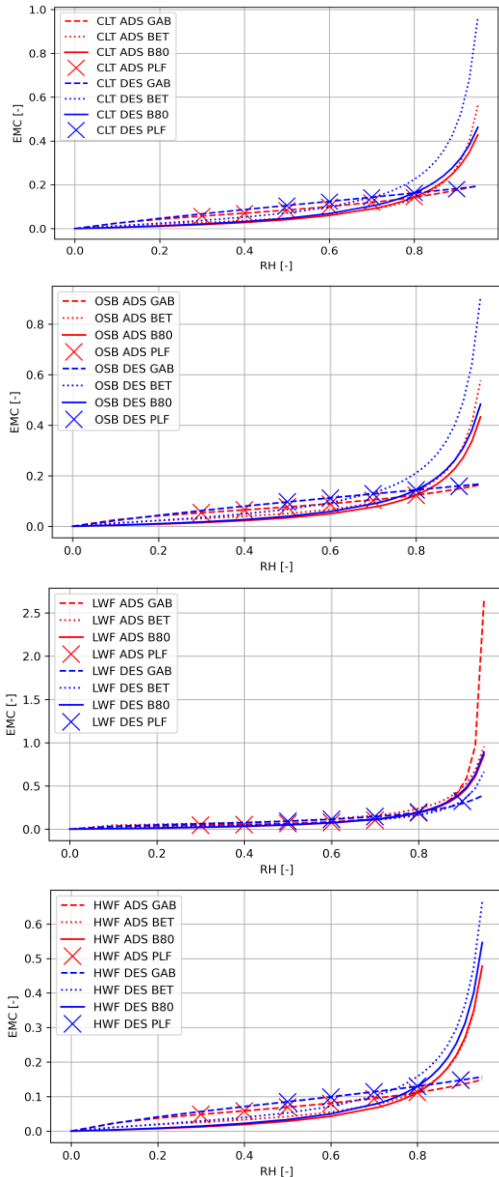


Fig. 5 – Measured (PLF) adsorption and desorption curves, BET, GAB and B80 (adsorption and desorption) curves for the four considered materials

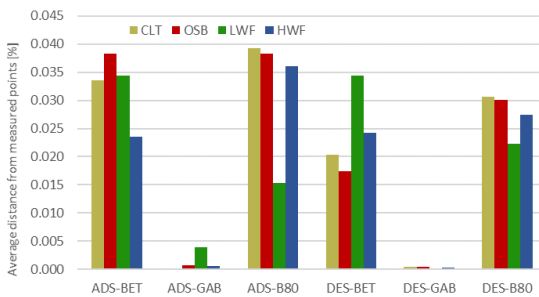


Fig. 6 –Absolute average distance from measured points of the MSCs considered. The differences are expressed in percentage mass/mass and the points from 0 % to 70 % RH are considered

4.2 Simulations

The results of the simulations follow the expectations of the differences presented in Fig. 6. The hourly values (Fig. 7) show that the moisture contents calculated with the measured curves are almost overlapping the values obtained using the GAB curve for both adsorption and desorption. The other results follow the order of the CLT sorption curves: ADS-B80, DES-B80, then ADS-BET and DES-BET, ADS-GAB and ADS-PLF (whose line is covered by the ADS-GAB), and, finally, DES-GAB and DES-PLF.

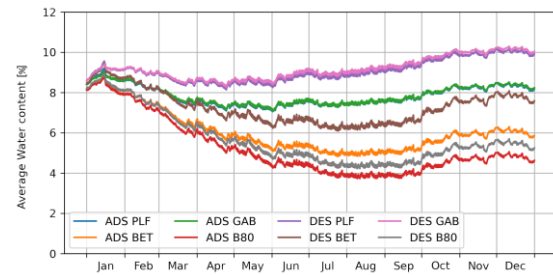


Fig. 7 – Hourly average water content of 1 m² of the North-facing wall for the CLT wall building simulation in the Milan weather file. The visualised values start after the 6-day warm-up period and are expressed in %kg_{water}/kg_{dry}

In Fig. 8, the annual mean values are reported for both wall typologies and for all the other climates considered. The relative positions of the MSCs seen in Fig. 6 are confirmed. Similar results with similar values are obtained for the Frame wall case (not reported here). When considering the heating and cooling demands, the simulations with MSCs with higher EMC values are expected to have larger values of energy needs, and lower energy needs for lower EMC, since the thermal conductivity is dependent on the moisture content of materials. Moreover, also the effects of latent heat transfer should be expected, especially when the effect of initial moisture content is present.

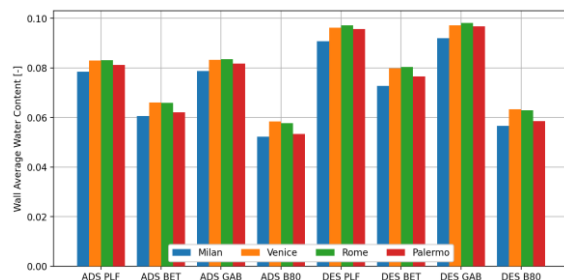


Fig. 8 – Annual mean water content of 1 m² of the North-facing wall for the CLT wall building simulation in the Milan weather file

Heating and cooling demands are also influenced by the latent loads due to the walls drying or adsorbing air moisture to reach *EMC*; this resulted in larger heating loads for the simulations with *MSCs* with lower *EMC* values and vice versa. The differences among the loads of the studied cases are the combination of the effect of the conductivity reduction and the effect of latent loads provided by the moisture migration from the walls. The results for the adsorption and desorption curves are presented as annual energy demands in Table 4 (*CLT* wall) and Table 5 (frame wall). In most of the cases, the energy demands values are higher for the adsorption curve results, except for the *CLT* cooling demands of Venice, Rome and Palermo, and the heating demands in Milan.

Table 4 – Annual heating and cooling demands calculated for the *CLT* wall with the adsorption and desorption *PLF MSC*

Location	Heating demand [kWh/(m ² yr)]		Cooling demand [kWh/(m ² yr)]	
	<i>ADS</i>	<i>DES</i>	<i>ADS</i>	<i>DES</i>
Milan	21.77	21.80	32.40	32.32
Venice	20.98	20.75	27.75	27.77
Rome	4.19	4.05	40.16	40.19
Palermo	0.17	0.16	56.45	56.61

Table 5 – Annual heating and cooling demands calculated for the frame wall with the adsorption and desorption *PLF MSC*

Location	Heating demand [kWh/(m ² yr)]		Cooling demand [kWh/(m ² yr)]	
	<i>ADS</i>	<i>DES</i>	<i>ADS</i>	<i>DES</i>
Milan	28.22	27.95	33.54	33.28
Venice	26.05	25.80	28.11	27.89
Rome	7.52	7.34	40.48	40.19
Palermo	0.69	0.65	56.03	55.90

The desorption curves have higher moisture contents, and this is expected to lead to higher demands, caused by higher thermal conductivity values of the envelope materials. However, when the

loads due to the drying process are larger, the resulting effect is the opposite. The charts in Fig. 9 show the deviation from the adsorption and desorption results obtained using *MSC* fitting curves. In these charts the difference for the adsorption and desorption fitting curves is calculated from the results of the adsorption and desorption *PLF* curves, respectively. The calculated differences for the heating demands are all below 1.2 kWh/m², with Milan *CLT ADS-BET* having the highest corresponding to a deviation of 5 % from the *PLF* values. The higher relative deviations are found for Palermo *CLT DES-B80* (38 % of 0.16 kWh/(m² yr)) due to the very low heating loads. The cooling loads differences are below 1 kWh/m² (e.g., for Milan frame wall *DES-B80*), which is also the maximum relative difference (2.5 %). As expected, in every case, the *GAB* model produces the lowest differences, while the *B80* the largest. The negative values of the *CLT* wall cooling demands are caused by the drying process due to the initial moisture contents of the walls. To verify this, multi-year simulations have been performed (removing the dependence on the initial moisture content), obtaining positive differences in the last year of the simulations.

The effect of the *MSCs* on the internal environment for the *CLT* wall case is presented in Fig. 10. While the internal temperature values are controlled by the ideal heating and cooling system, the relative humidity is influenced by the constant air infiltration and by the moisture buffering effect of the building materials on the internal environment. The results show that the *MSCs* compared can also have an influence on the annual average moisture content. The variation due to the *MSC* of the average value is less than 2 % *RH*, while the maximum values have variations up to 4 % *RH*. The minimum annual average values are found for the *CLT ADS-B80* case (e.g., 41.3 % *RH* in Milan), while the maximum is found for *CLT DES-GAB* (e.g., 43.0 % *RH* in Milan). The *ADS* simulations have 1 % *RH* higher values than the respective *DES* simulations, and the *BET* and *B80* have higher values than *PLF* and *GAB*. Sorption curves with lower *EMC* obtained lower wall moisture contents (Fig. 8) and higher air *RH* values.

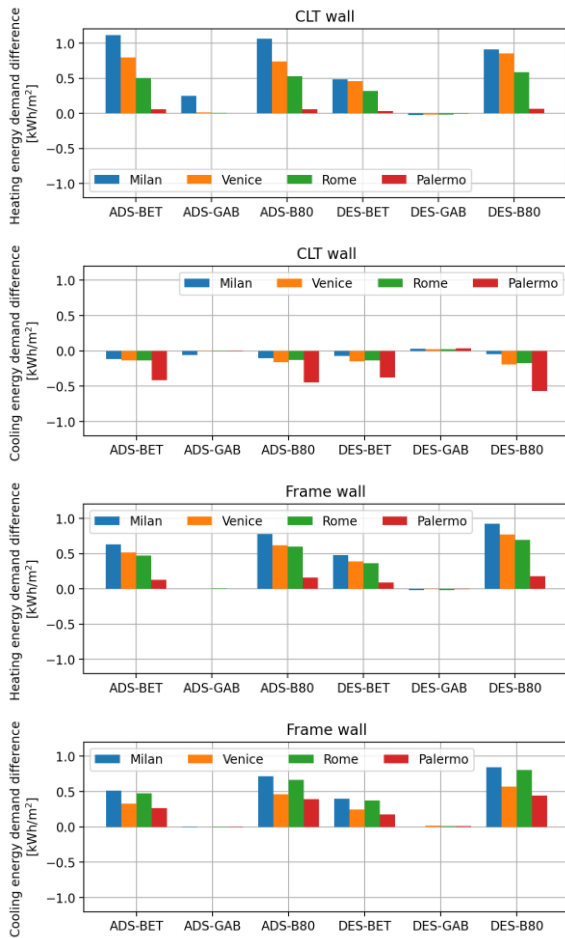


Fig. 9 Annual heating and cooling demands deviations. The differences of the ADS and DES fitting curves are calculated from the respective ADS and DES PLF curves (Table 5)

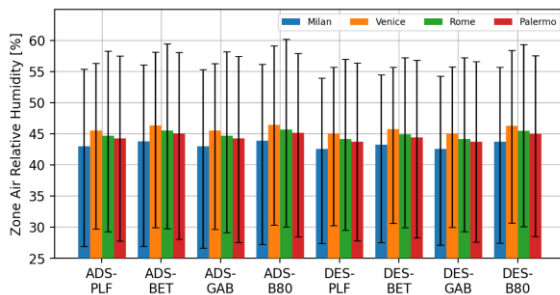


Fig. 10 – Annual average indoor air RH calculated with different MSCs at different locations. The error bars indicate the annual hourly maximum and minimum RH values

5. Conclusions

In this preliminary research the moisture adsorption and desorption curves of four wood-based building materials have been measured with a DVS analyser. The measured values have been com-

pared with three commonly used fitting functions based on different MSC models. 64 simulations of a small building have been performed, with two different envelopes composed of the materials analysed, in four Italian locations, for four MSC fitting curves, for both adsorption and desorption curves. The simulations have been performed with the software EnergyPlus considering moisture dependent hygrothermal material properties. The effects of every fitting function on the results of the simulation have been quantified in terms of heating and cooling annual demands, moisture content in walls and air relative humidity. The main findings are:

- The GAB function represents better the measured EMC in the hygroscopic range.
- For the studied cases, using the BET and B80 functions in hygrothermal building energy simulations caused errors in the heating demand up to 1.2 kWh/(m² yr) (case of CLT simulation in Milan, with 5 % difference from the same PLF case) and 1 kWh/(m² yr) in cooling demands (Milan frame wall DES-B80, with 5 % difference from the same PLF case).
- When considering the internal annual average air relative humidity, the influence of the fitting function is found to be of 2 % RH, and of 4 % RH on the annual maximum values.

In conclusion, the differences are of a small order, and could be of interest when high precision results are required (for example, with high performance buildings, in risk evaluations, or in model calibration procedures). The desorption curves, as expected, led to the calculation of higher moisture contents and internal relative humidity values, and should be preferred to adsorption curves when conservative simulations are needed.

Further research is required to increase the accessibility of hygrothermal simulations. Future work will focus on extending the analysis on the other hygrothermal material properties and on the over-hygroscopic range, considering the effects of rain and extreme weather conditions. Occupants' comfort parameters and multi-year results will also be considered.

Acknowledgement

The research leading to these results has also received funding from the MIUR of Italy within the framework of the PRIN2017 project «The energy flexibility of enhanced heat pumps for the next generation of sustainable buildings (FLEXHEAT)», grant 2017KAAECT.

Libralato M. acknowledges fellowship funding from MUR (Ministero dell'Università e della Ricerca) under PON «Ricerca e Innovazione» 2014-2020 (D.M. 1062/2021).

This research was partially funded by the project «Klimahouse and Energy Production», in the framework of the programmatic-financial agreement with the Autonomous Province of Bozen-Bolzano of Research Capacity Building.

Nomenclature

Symbols

c_{dry}	Specific heat capacity ($J \cdot kg^{-1} K^{-1}$)
λ_{dry}	Thermal conductivity ($W \cdot m^{-1} K^{-1}$)
μ_{dry}	Water vapor resistance factor (-)
ρ_{bulk}	Density ($kg \cdot m^{-3}$)
U	Air-to-air thermal transmittance ($W \cdot m^{-2} K^{-1}$)

Abbreviations

ADS	Adsorption
B80	BET model with 80 % RH constraint
BES	Building Energy Simulation
BET	Brunauer–Emmett–Teller model
CLT	Cross-Laminated Timber
DES	Desorption
DVS	Dynamic Vapor Sorption analyser
EMC	Equilibrium Moisture Content
GAB	Guggenheim-Anderson-deBoer model
HAMT	Heat Air and Moisture Transfer
HWF	High-density Wood Fibre
LWF	Low-density Wood Fibre
MSC	Moisture Sorption curve
OSB	Oriented Strand Board
PLF	Piecewise Linear Function
RH	Relative Humidity

References

- ANSI/ASHRAE. 2017. “Standard Method of Test for the Evaluation of Building Energy Analysis Computer Programs (ANSI/ASHRAE Standard 140).”
- Berger J., T. Busser, T. Colinart, and D. Dutykh. 2020. “Critical assessment of a new mathematical model for hysteresis effects on heat and mass transfer in porous building material.” *International Journal of Thermal Sciences* 151: 106275. doi: <https://doi.org/10.1016/j.ijthermalsci.2020.106275>
- Carbonari, A. 2010. “Proprietà materiali edilizi.” Lecture notes. Accessed on December 1, 2021 <http://www.iuav.it/Ateneo1/docenti/architettura/docenti-st/Carbonari/-materiali-1/ciaSA-06-0/proprmat.pdf>
- CEN. 2021. EN ISO 12571:2021 – *Hygrothermal performance of building materials and products - Determination of hygroscopic sorption properties*. European Committee for Standardization.
- Danovska, M., G. Pernigotto, P. Baggio, and A. Gasparella. 2022. “Simulation uncertainty in heat transfer across timber building components in the Italian climates: the role of thermal conductivity”. *Energy and Buildings* 268: 112190. doi: <https://doi.org/10.1016/j.enbuild.2022.112190>
- Danovska, M., G. Pernigotto, M. Baratieri, P. Baggio, and G. Gasparella. 2020a. “Influence of moisture content, temperature and absorbed solar radiation on the thermal performance of a spruce XLAM wall in the Italian climates.” *Journal of Physics: Conference Series, 37th UIT Heat Transfer Conference*. doi: <https://doi.org/10.1088/1742-6596/1599/1/012028>
- Danovska, M., M. Libralato, G. Pernigotto, A. De Angelis, O. Saro, P. Baggio, and A. Gasparella. 2020b. “Numerical and experimental study on the impact of humidity on the thermal behavior of insulated timber walls.” *Proceedings of Building Simulation Applications BSA 2019*. doi: <https://doi.org/10.13124/9788860461766>
- EnergyPlus. 2021. “Weather Data.” National Renewable Energy Laboratory (NREL). Accessed Dec 1, <https://energyplus.net/weather>

- Igaz, R., L. Krišťák, L. Ružiak, M. Gajtanska and M. Kučerka. 2017. "Thermophysical properties of OSB boards versus equilibrium moisture content." *BioResources* 12(4): 8106-8118.
- Künzel, H.M. 1995. "Simultaneous heat and moisture transport in building components: One- and two-dimensional calculation using simple parameters." Fraunhofer-Institut für Bauphysik
- Libralato, M., A. De Angelis, O. Saro, M. Qin, and C. Rode. 2021a. "Effects of considering moisture hysteresis on wood decay risk simulations of building envelopes." *Journal of Building Engineering* 42: 102444 doi: <https://doi.org/10.1016/j.jobe.2021.102444>
- Libralato, M., A. De Angelis, G. Tornello, O. Saro, P. D'Agaro, and G. Cortella. 2021b. "Evaluation of Multiyear Weather Data Effects on Hygrothermal Building Energy Simulations Using WUFI Plus." *Energies*. doi: <https://doi.org/10.3390/en14217157>
- Scheffler, G. A. 2008. "Validation of hygrothermal material modelling under consideration of the hysteresis of moisture storage." PhD Thesis. Dresden University of Technology.
- Thybring, E. E., C. R. Boardman, S. L. Zelinka, and S. V. Glass. 2021 "Common sorption isotherm models are not physically valid for water in wood." *Colloids and Surfaces A: Physicochemical and Engineering Aspects* 627: 127214. doi: <https://doi.org/10.1016/j.colsurfa.2021.127214>
- Vololonorina, O., M. Coutand, and B. Perrin. 2014. "Characterization of hygrothermal properties of wood-based products – Impact of moisture content and temperature." *Construction and Building Materials* 63: 223–233. doi: <https://doi.org/10.1016/j.conbuildmat.2014.04.014>
- Woloszyn, M., and C. Rode. 2008. "Tools for performance simulation of heat, air and moisture conditions of whole buildings." *Building Simulation* 1: 5–24. doi: <https://doi.org/10.1007/s12273-008-8106-z>
- Yang, J., H. Fu, and M. Qin. 2015. "Evaluation of Different Thermal Models in EnergyPlus for Calculating Moisture Effects on Building Energy Consumption in Different Climate Conditions" *Procedia Engineering* 121: 1635-1641 doi: <https://doi.org/10.1016/j.proeng.2015.09.194>
- Zu, K., M. Qin, C. Rode, and M. Libralato. 2020. "Development of a moisture buffer value model (MBM) for indoor moisture prediction." *Applied Thermal Engineering* 171: 115096 doi: <https://doi.org/10.1016/j.applthermaleng.2020.115096>

Energy Performance Evaluation and Economical Analysis by Means of Simulation Activities for a Renovated Building Reaching Different Nzeb Definitions Targets

Riccardo Gazzin – EURAC Research, Italy – riccardo.gazzin@eurac.edu

Jennifer Adami – EURAC Research, Italy – jennifer.adami@eurac.edu

Mattia Dallapiccola – EURAC Research, Italy – mattia.dallapiccola@eurac.edu

Davide Brandolini – EURAC Research, Italy – davide.brandolini@eurac.edu

Miren Juaristi Gutierrez – EURAC Research, Italy – miren.juaristigutierrez@eurac.edu

Diego Tamburrini – EURAC Research, Italy – diego.tamburrini@eurac.edu

Paolo Bonato – EURAC Research, Italy – paolo.bonato@eurac.edu

Martino Gubert – EURAC Research, Italy – martino.gubert@eurac.edu

Stefano Avesani – EURAC Research, Italy – stefano.avesani@eurac.edu

Abstract

The nZEB target is increasingly becoming one of the main objectives in building renovation, but a unique nearly-Zero Energy Building definition is not explicitly available in the 31/2010 EU directive, the so-called “Energy performance of buildings directive”. Nevertheless, the technical implementation of the nearly-Zero Energy Building concept into defined constraints and requisites is a determining factor for the consequences of energy-economic performance. In fact, in the renovation process of a building, different technical requirements lead to different design solutions that affect investment and operative costs, as well as energy performance. Through an optimization process based on dynamic simulations for energy and economic performance assessment, a comparison between different approaches for the nZEB building retrofit for a demo-case building has been performed. First, an energy target which is stricter than the nZEB standard is examined. In particular, the so-called “Positive Energy Building” approach, consisting of the design of a building that produces more energy than it consumes in the overall year, is evaluated. Then, the results of the Positive Energy Building target are compared to a nearly-Zero Energy Building approach in which self-sufficiency is promoted, instead of the energy production/consumption balance. Also, the nearly-Zero Energy Building target promoted by the Italian legislation has been evaluated, comparing the result of a plausible implementation with the other more stringent approaches. The simulation work has been aimed at comparing significant Key Performance Indexes, regarding both energetical

and economical aspects. In particular, initial investment costs, expected net present value of the investment after 25 years and energy performance indexes have been evaluated. The discussion demonstrates that, according to the assumptions adopted for the investment and energy costs, the Positive Energy Building target is excessively economically inconvenient for a renovation intervention of this type. Moreover, designers should prioritize the self-sufficiency of the building energy system with respect to the production/consumption yearly ratio. Finally, the discussion demonstrates that a renovation design in accordance with the Italian nearly-Zero Energy Building target is economically sustainable but the PV system size to meet the minimum requirements could be non-optimal.

1. Introduction

1.1 Background

To achieve the goal of a strong reduction of building-related CO₂ emissions for the next decades in the EU, a significant contribution must come from acting on the existing residential building stock renovation. The target of nearly-Zero Energy Buildings (nZEB) for new buildings has been set by the EU Commission with the 31/2010 EU directive, the “Energy performance of buildings directive” (EPBD). Nevertheless, a unique approach for the definition of the technical requirements has not been defined,

since each country should take charge of the implementation of the directive (D'Agostino et al., 2021). The nZEB as target performance also applies to major building renovation since 2021. Moreover, building deep retrofit is one of the key actions capable of decarbonizing the building sector to meet global targets to address climate change (D'Agostino et al., 2017). Reaching nZEB targets when renovating a building allows a greater reduction in fossil energy savings and greenhouse gas emissions compared with a traditional retrofit intervention (Holopainen et al., 2016). In the literature, cost-optimum calculations have been performed to identify which renovation interventions lead to the best economic benefits while meeting the nZEB target (Zangheri et al., 2018). Nevertheless, the renovation rate in Europe is around 1 % (A Renovation Wave for Europe, 2020) - still quite below the target of 2 %. In this framework, the trend of a prefabricated and industrialised retrofit is attracting more and more attention thanks to a set of research projects (D'Oca et al., 2018) and bottom-up national initiatives (e.g. EnergieSprong, ...). Prefabricated solutions could allow an increase of the annual renovation rate of the European building stock, also thanks to the integration of different functions and technologies in the same element (Pernetti et al., 2021; Pinotti, 2020).

After the introduction of the nZEB target, Positive Energy Buildings (PEBs) are somehow considered as the next phase for building sector sustainability. The requirements in terms of energy consumption efficiency are the same as the nZEB target, but a reinforcement of the building energy production is expected. Barriers and challenges in the Positive Energy Building implementation have been investigated by Ala-Juusela et al. (2021). PEBs also allow a significant contribution to the energy support of the local neighborhood, the so-called Positive Energy Neighborhood. Good et al. (2017), analysed this topic, highlighting its challenges and opportunities.

1.2 Italian Framework for nZEB Buildings

In the Italian framework, the implementation of the EU directive for nZEB buildings has been carried out by the "Decreto ministeriale 26/06/2015". In both cases of new construction or renovation, the decree

requires that the project building is compared with a reference building.

The reference building is a fictitious building that has identical geometrical shape (same volume, floor areas, envelope surfaces etc.), climatic conditions, orientation, destination of use and surrounding situation. The differences from the project building lie in the thermal characteristics of the envelope and in the energy system characteristics. These values are reported in specific tables.

A series of indexes that indicate the quality of the envelope and the efficiency of the energy system are calculated both for the project building and the reference building. Then, a comparison is made to assess whether the building can be considered as nZEB or not, considering the reference building as the minimum standard to be achieved by the project case.

Specifically, the previously mentioned indexes are:

- H'_T , which is the overall average coefficient of heat transfer by transmission
- $A_{sol,est}/A_{sup\ utile}$, which is the so-called equivalent summer solar area per useful area unit
- Solar transmission factor, also considering the shadings
- Thermal inertia properties, such as superficial mass (M_s) and periodic thermal transmittance (Y_{IE})
- Thermal transmittance of the internal partition walls and of the outward-facing structures of non-air-conditioned rooms.
- Useful thermal performance indexes for heating ($E_{PH,nd}$) and cooling ($E_{PC,nd}$)
- Energy performance indices for winter space heating (E_{PH}) and summer space cooling (E_{PC}) and overall building performance, in non-renewable and total primary energy (E_{Pgi})
- Seasonal average efficiency of the system for winter space heating (η_H), summer space cooling (η_C) and domestic hot water production (η_w).

In addition, the building must accomplish some requirements in terms of renewable energy production. These requisites are reported in the "Allegato 3, DLgs 3 marzo 2011 n. 28". The building must guarantee:

- production of electrical energy by means of systems from renewable sources (mandatory installed on or inside the building or in its out-buildings) with a power measured in kW calculated according to the following formula:

$$P = \frac{1}{k} \cdot S [kW]$$

where:

S is the floor area of the building at ground level, measured in m²; k is a coefficient that takes the value K = 50 m²/kW if the application for the authorization is submitted after 1 January 2017.

- Contemporary coverage, by means of renewable energy sources, of the 50 % of the domestic hot water, space heating and cooling demand, and the 50 % of domestic hot water. In case the building is public, these percentages must be increased by 10 %.

1.3 Aim and Research Objective

The ambitious target of nZEB to be achieved by a prefabricated solutions approach for the renovation of a building is still lacking a technical feasibility analysis. In other words, from the literature it is still not clear which technical features of a retrofit action are compliant with the nZEB definition. Moreover, a techno-economic comparison between different nZEB definitions to be achieved with prefabricated technologies has not been performed. Such research questions are national-dependent and will be discussed in this paper for a case study in Italy. The case study is a residential building undergoing an innovative renovation process. The renovation intervention consists of the installation of prefabricated multifunctional envelope modules (façade and roof) that might integrate the following available technologies depending on needs: building-integrated photovoltaic or solar thermal panels (BIPV and BIST), mechanical ventilation machine units and green façade modules. Coloured BIPV panels are taken into consideration to optimize the building integration from an aesthetic point of view.

For the support activities in the preliminary design phase, dynamic simulations have been performed to examine the relationship between possible different renovation scenarios and the fulfilment of the nZEB definitions. In particular, a preliminary design of

the BIPV system, with the possibility of integrating a Battery Energy Storage System (BESS), has been carried out.

The whole analysis aims at investigating how different renovation building scenarios – all targeting the nZEB level, perform from a techno-economic point of view.

2. Methodology

The building to be renovated is located in Greve in Chianti (Florence), and consists of two heated floors, with four apartments overall. The renovation aims to convert the building energy system into a full-electric system, producing electricity on-site to cover the energy demand. The heating and cooling services are set to be provided by an electric air-to-air heat pump, which will be, at least partially, fed by the BIPV system.

To achieve the goal of evaluating different renovation scenarios and their impacts in terms of nZEB definitions, energy performance and costs, the following methodology has been defined. First, the target scenarios have been defined:

- Scenario 1, based on the Positive Energy Building (PEB) target d1, for which the building produces more energy than it consumes in a yearly balance. As a consequence, the BIPV system has been sized to cover more than 100 % of the building's electric demand.
- Scenario 2 assumes that the system has to guarantee a level of self-sufficiency equal to the one resulting in Scenario 1 while minimizing the cost per kWh produced (Levelized Cost Of Electricity, LCOE). It means the BIPV system is optimized in a way that a specified portion of the energy demand is covered by self-produced electricity, also considering the support of a battery storage system.
- Scenario 3 assumes that the system has to guarantee self-sufficiency equal to 30 %, i.e., a typical value achieved in residential applications (McKenna et al., 2017).
- Scenario 4 aims to meet the Italian nZEB target described in Section 1.2. Unlike in the previous scenarios, here the PV configuration is an input of the BIPV optimization tool, which is used in

simulation mode, and the building electric load is not taken into account for the sizing of the components. In particular, the PV nominal power is the result of a previous calculation (UNI/TS 11300 and “Allegato 3 del D. Lgs. 28/2011”), aimed at ensuring the minimum compliance with the Italian regulation; the PV module position is determined considering the most irradiated building surfaces, i.e., in this case, the south-facing roof pitch.

These scenarios are summarized in Table 1.

Table 1 - nZEB scenarios for the simulations

Scenario	nZEB approach	Energy target
1 st scenario	Zero Energy Building	Energy produced is equal to energy consumed in a yearly balance
2 nd scenario	Prioritization of self-sufficiency	Same self-sufficiency of the 1 st scenario, but the Levelized Cost of Electricity is minimized
3 rd scenario	Prioritization of self-sufficiency	Self-sufficiency is lower than in 2 nd scenario, Levelized Cost of Electricity is still minimized
4 th scenario	Italian nZEB standard	Requirements of the “Allegato 3 del D. Lgs. 28/2011” and other technical requisites

Then, the final Key Performance Indicators to compare the renovation scenarios against been defined as the following:

- Initial investment costs for the BIPV system (including the battery cost)
- Expected NPV (Net Present Value) after 25 years
- Self-sufficiency (i.e., the portion of building demand directly covered by self-consumed PV electricity)

- Self-consumption (i.e., the portion of PV-produced electricity directly consumed or stored in the building)
- Annual cumulative production – consumption rate

The electrical energy demand for the different renovated building scenarios has been calculated with an energy dynamic model (TRNSYS). After that, the electrical demand curve is considered as input in a “BIPV optimization tool”, able to find optimal BIPV-battery configurations to meet the previously described requirement scenarios. The outcomes of the optimization are processed and evaluated in terms of energy and economic performance through the set of KPIs that have been previously described. Hence, the solutions suggested for the BIPV and battery system design are compared. Considerations regarding different nZEB approaches and requisites are also reported.

2.1 Electrical Energy Demand Calculation

For the purposes of this work, the dynamic energy modeling tool TRNSYS (Thermal Energy System Specialists) has been used to model and simulate the building thermal behavior, calculating the space heating and cooling energy demands, the indoor thermal comfort and the electrical energy consumption needed by the heating/cooling and ventilation systems (plug loads are not considered). The required input data are reported in Table 2. Specifically, a 3D model is produced to represent the geometry of the building (Fig. 1). Information regarding the actual thermal characteristics of the envelope, as well as the ones related to the energy system are retrieved from a previous building energy audit. The characteristics of the existing building are then crossed with the planned renovation project, defining the future building energy model. In fact, the thermal transmittance of the envelope-renovated portion is updated to the designed conditions and the new Heating, Ventilation and Cooling (HVAC) system is implemented, using a heat pump TRNSYS type developed at Eurac Research. This type has been developed as a grey-box model, in which the generated heat and the electrical consumption are

determined by developed algorithms out of performance maps provided by manufacturers. Generated heat and electrical consumption of the heat pump are calculated as a function of boundary conditions. After the boundary conditions of the simulation are set, together with the expected building occupants' behavior and the expected internal gains (SIA 2024:2015), the total electrical energy demand is calculated.

Table 2 - Input for the TRNSYS model

Input data	Source
Geometry of the building	SketchUp 3D model
Thermal properties of the building envelope	Energy audit report; thermal characteristics of the prefabricated panels and new windows
HVACS characteristics	Properties of the system that is expected to be installed during the renovation process; heat pump performance is simulated with a black-box model developed by EURAC Research
Boundary weather conditions	Typical meteorological year (TMY) of the building location
Occupancy schedule and internal gains	SIA 2024:2015

Simulating the behavior of the building in hourly time-steps, the electrical energy consumption is calculated in TRNSYS. This electricity curve is later used as input in the "BIPV optimization tool".

2.2 BIPV Optimization

For the BIPV system optimization, a Python-based tool (EnergyMatching) (Lovati et al., 2019) has been used.

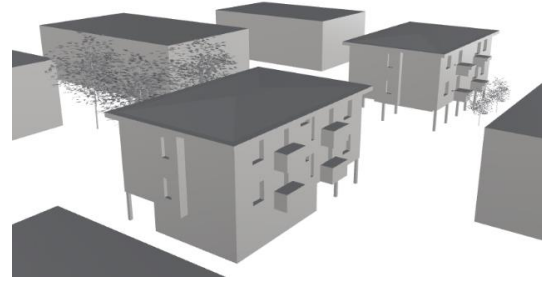


Fig. 1 - 3D model of the building case study

This has been developed by Eurac Research to support designers and other professionals who want to integrate a photovoltaic system in buildings or districts. The tool is based on a direct search algorithm applied to a minimization/maximization problem, which can be constrained or unconstrained, depending on the target function selected (minimization of the Levelized Cost of Electricity, Maximization of the Net Present Value, etc.). As a solution, it suggests the optimal BIPV configuration, i.e., how many PV modules and where to integrate them over the building envelope (on roofs, façades, shading devices, balustrades, etc.). It can also suggest including an electric storage system to increase the ratio of self-consumed energy. The BIPV configurations are optimized according to the specificities of the cases (building geometry, local weather, surrounding shade, unitary costs of the system and current benefits to produce electricity, sold or self-consumed), also considering how much energy is indeed needed by the building throughout the day and the seasons. Moreover, different target functions can be assigned to the tool, to achieve energy, economic and/or environment-related goals. Based on hourly time-step calculations that allow evaluation of the energy fluxes between the photovoltaic system, the battery, the load and the grid, the tool can provide a set of KPIs showing the expected performance of the photovoltaic system, from energy, economic and environmental points of view. Further information and details on the BIPV optimization tool calculation model are available in (EnergyMatching, 2022).

The assumptions and input data for the BIPV-BESS optimization are reported in Table 3. It has to be noted that the technology prices are higher than benchmark on-the-market PV modules because it refers to aesthetically appealing glass-glass BIPV

modules able to comply with the requirements of façade integration also in culturally preserved urban contexts.

Table 3 - Assumptions and input data for BIPV optimization

Price of electricity bought from the grid	0.215	[€/kWh]
Price of electricity sold to the grid	0.05	[€/kWh]
BIPV module efficiency	0.13	[%]
BIPV cost	2800	[€/kWp]
BESS cost	800	[€/kWh]

3. Results Analysis and Discussion

The results obtained for the four renovation scenarios considered are shown in Table 4 and discussed case-by-case in this section.

Table 4 - Results of BIPV optimization tool in the four scenarios

Scenarios	1	2	3	4
Suggested PV capacity [kWp]	15.7	11	5.4	4.4
Suggested electric storage capacity [kWh]	0	3.4	0	0
Investment costs [€]	44045	33533	14976	12333
Expected NPV after 25 years [€]	-18018	-10034	-60	571
Self-sufficiency [%]	48	48	30	27
Self-consumption [%]	46	66	86	91
Annual cumulative ratio production/consumption	1.03	0.73	0.36	0.29

Scenario 1: considering the design target of a ratio production/consumption (on a yearly basis) higher than one, the photovoltaic nominal power suggested by the BIPV optimization tool is the highest among the scenarios considered and is equal to 15.7 kWp. On the contrary, the electric storage capacity is 0 kWh, since it does not contribute towards achieving the design target. From an economic point of view, this solution is the less cost-effective, from both the investment and NPV perspective.

Scenario 2: results obtained show the same performance in terms of self-sufficiency as Scenario 1 (because it has been set as optimisation target for this scenario) but with lower investment costs and a better NPV, due to the presence of a battery storage. As the suggested PV capacity is lower, the annual ratio production/consumption decreases to 0.73.

Scenario 3: in this scenario, the annual cumulative ratio production/consumption is lower compared with Scenario 1 and 2 (below 0.4) but the investment payback is achieved during the system lifetime of 25 years considered. Self-sufficiency is only 30 %, meaning that the BIPV system contributes less compared with the previously described scenarios to cover the electricity demands of the building.

Scenario 4 achieves similar results in terms of annual balance and self-sufficiency compared with the ones obtained in Scenario 3.

The best BIPV configuration obtained for Scenario 1 turns out to be less cost-effective than the ones obtained with the other approaches from both the investment and NPV perspective.

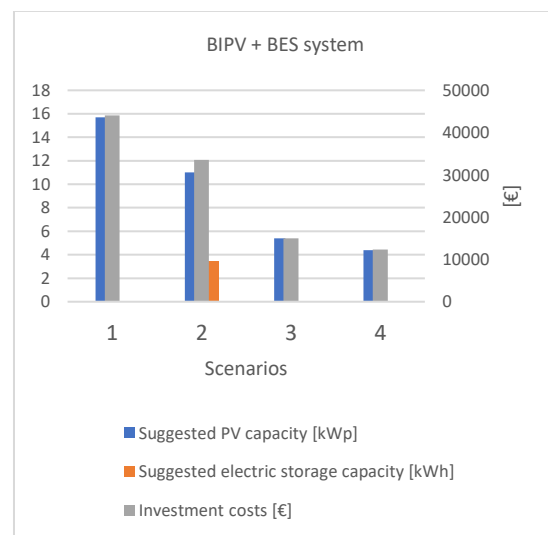


Fig. 2 - BIPV and BESS characteristics

Moreover, considering that the only design constraint is obtaining the target yearly energy production, the electric storage capacity is equal to 0, at the cost of a low self-consumption (46 %), as seen in

Fig. 3. On the contrary, results obtained for Scenario 2 confirm that the same self-sufficiency can be achieved by installing a more balanced system. This is confirmed by the self-consumption index (SC), which is increased to 66 % by decreasing the nominal power of the photovoltaic system and favoring the installation of an electric energy storage (3.4 kWh), as seen in Fig. 2. Also from an economic point of view, Scenario 2 can be considered a better approach, since the investment costs are decreased by 24 % and the NPV also improves. Due to the lower nominal power installed, the ratio consumption/production decreases to 0.73, meaning that, on an annual basis, the building does not produce the same electrical energy that is consumed.

Regarding Scenario 3, the annual cumulative ratio of production/consumption decreases significantly (below 0.4) but the payback of the system is achieved after 25 years. This is caused by the fact that a small system is installed and no battery is needed to meet the energy target. This is confirmed by the high value of self-consumption (86 %), meaning that most of the energy produced is directly self-consumed by the building. However, high values of self-consumption and low values of self-sufficiency mean that the system covers only a small fraction of the total energy consumption even if most of the energy produced is self-consumed. This usually indicates that the system is slightly undersized compared with the building energy consumption.

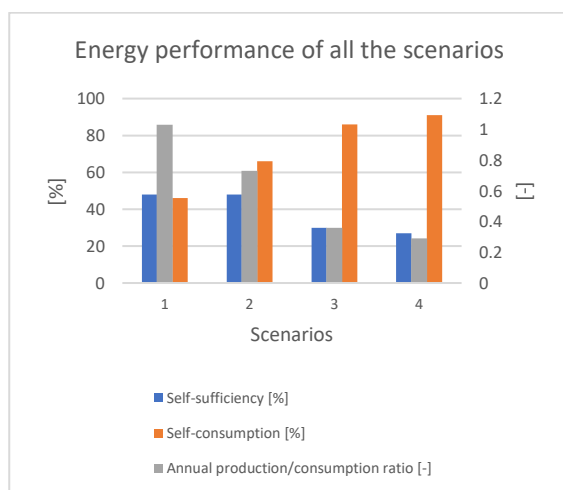


Fig. 3 - Self-sufficiency and self-consumption for the scenarios considered

For Scenario 4, the system was not optimized to obtain a specific target but designed to respect the Italian regulation for the installation of photovoltaic panels in nZEB buildings. Results obtained are similar to the ones obtained for Scenario 3 and the same considerations can be applied. However, the main limitation of this approach is that it suggests reasonable solutions only for a limited number of cases. In fact, as discussed in the paperwork by Lovati et al. (2020), the same photovoltaic nominal power is suggested for a fixed building gross area and it does not depend on the building floors (and as a consequence on the building energy consumption).

Numerical results can change if investment costs or if the price of electricity are different. There are important aesthetic advantages to the selected BIPV panels, but they lead to higher investment costs and lower efficiency compared with standard solutions. This means that the payback time of the investment is also longer.

All the analyzed have proved to be compliant with the nZEB Italian definition, which is the minimum required by law. Nevertheless, actual foreseen energy performances are very different among the scenarios and underline relevant discrepancies in the energy behavior. In particular, Scenario 1 can be called “yearly zero energy balance”, but requires the electric grid to perform the electric energy exchange and is the most expensive in terms of initial investment with the longest payback time. Scenario 2 can be considered a “low grid dependency” nZEB target. In fact, it prioritizes self-sufficiency, which considers the energy produced in situ, which is directly consumed (or stored) without exchange with the grid. This approach presents better economic results if compared with Scenario 1, having lower investment costs and shorter payback time. Decreasing the self-sufficiency target, in Scenario 3, the economic KPIs are improved and the Italian nZEB requisites are still accomplished.

4. Conclusions

Observing the results of the dynamic simulations, which assess the expected energy and economic consequences of renovating a building according to different nZEB approach targets, it is possible to assert that the implementation choice of the nZEB definition has a strong impact. Since the European guidelines are not very well defined in terms of technical requisites and energy performance targets, each EU Country has decision space to set its own technical requirements for the nearly-Zero Energy Building assessment. Because of the elevated number of factors that occur in the energy sector, identifying an optimal nZEB definition is not simple. Nevertheless, the authors consider that the renovation design for a nearly-Zero Energy Building should lead to an energy-efficient building, capable of supplying its own energy demands through the implementation of economically and environmentally sustainable solutions.

The simulation outcomes indicate that prioritizing the energy production/consumption yearly balance, having as the Positive Energy Building target as an objective, could lead to an oversized system in terms of energy generation and, consequently, to an excessive investment cost compared with the economic benefits over time. On the other hand, prioritizing the self-sufficiency of the building energy system could lead to the design of more balanced systems and a significant improvement in the energy and economic KPIs.

The current Italian nZEB target, which has also been examined, seems to be economically sustainable for this specific case-study, but it could lead to not-optimal designs in case of multi-floor buildings.

Prioritizing the self-sufficiency target instead of the yearly ratio production/consumption will become particularly relevant and crucial in the next years, when subsidies such as net billing and net metering will be abolished in many European countries. In this view, the results presented in this article should be considered when the requirements for the PEB and nZEB standards are updated.

The fluctuations of the electricity price and the increase of the cost of raw materials could have an impact on the results. It would be interesting to carry out further research regarding the impact of cost

variability on the analysis considerations performed.

This paper is part of the research activities of the INFINITE project, funded by the European Union's Horizon 2020 research and innovation programme under grant agreement No 958397.

References

- Ala-Juusela, M., H. u. Rehman, M. Hukkalainen, and F. Reda. 2021. "Positive Energy Building Definition with the Framework, Elements and Challenges of the Concept". *Energies* 14(19): 6260. doi: <https://doi.org/10.3390/en14196260>
- Communication from the Commission to the European parliament, the council, the European economic and social committee and the committee of the regions, "A Renovation Wave for Europe - greening our buildings, creating jobs, improving lives", 2020
- D'Agostino, D., S. Tsemekidi Tzeiranaki, P. Zangheri, and P. Bertoldi. 2021. "Assessing Nearly Zero Energy Buildings (NZEBs) development in Europe" *Energy Strategy Reviews* 36: 100680. doi: <https://doi.org/10.1016/j.esr.2021.100680>
- D'Agostino, D., P. Zangheri, and L. Castellazzi. 2017. "Towards Nearly Zero Energy Buildings in Europe: A Focus on Retrofit in Non-Residential Buildings". *Energies* 10(1): 117. doi: <https://doi.org/10.3390/en10010117>
- DIRECTIVE 2010/31/EU - Energy performance of buildings directive. "Directive 2010/31/EU of the European Parliament and of the Council of 19 May 2010 on the energy performance of buildings". EU commission. 2010.
- D'Oca, S., A. Ferrante, C. Ferrer, R. Perneti, A. Gralka, R. Sebastian, and P. Op 't Veld. 2018. "Technical, Financial, and Social Barriers and Challenges in Deep Building Renovation: Integration of Lessons Learned from the H2020 Cluster Projects". *Buildings* 8(12): 174. doi: <https://doi.org/10.3390/buildings8120174>
- Energy Matching website. 2022. "Results". Energy Matching. Accessed April 5, 2022. <https://www.energymatching.eu/results/?page=2>

- Good, N., E. A. Martínez Ceseña, P. Mancarella, A. Monti, D. Pesch, and K.A. Ellis. 2017. *Barriers, Challenges, and Recommendations Related to Development of Energy Positive Neighborhoods and Smart Energy Districts. Energy Positive Neighborhoods and Smart Energy Districts: Methods, Tools, and Experiences from the Field.* Elsevier BV. pp. 251-274. doi: <https://doi.org/10.1016/B978-0-12-809951-3.00008-9>
- Holopainen, R., A. Milandru, H. Ahvenniemi and T. Häkkinen. 2016. "Feasibility Studies of Energy Retrofits – Case Studies of Nearly Zero-energy Building Renovation". *Energy Procedia* 96: 146-157. doi: <https://doi.org/10.1016/j.egypro.2016.09.116>
- Lovati, M., M. Dallapiccola, J. Adami, P. Bonato, X. Zhang, and D. Moser. 2020. "Design of a residential photovoltaic system: the impact of the demand profile and the normative framework". *Renewable Energy* 160: 1458-1467. doi: <https://doi.org/10.1016/j.renene.2020.07.153>
- Lovati, M., G. Salvalai, G. Fratus, L. Maturi, R. Albatici, and D. Moser. 2019. "New method for the early design of BIPV with electric storage: A case study in northern Italy". *Sustainable Cities and Society* 48: 101400. doi: <https://doi.org/10.1016/j.scs.2018.12.028>
- McKenna, R., E. Merkel, and W. Fichtner. 2017. "Energy autonomy in residential buildings: A techno-economic model-based analysis of the scale effects". *Applied Energy* 189: 800-815. doi: <https://doi.org/10.1016/j.apenergy.2016.03.062>
- Pernetti, R., R. Pinotti, and R. Lollini. 2021. "Repository of Deep Renovation Packages Based on Industrialized Solutions: Definition and Application". *Sustainability* 13(11): 6412. doi: <https://doi.org/10.3390/su13116412>
- Pinotti, R. 2020. *Timber Prefabricated Multifunctional Facade: Approaches and Methods for a Feasibility Analysis, System Design and Testing*, PhD Thesis, Free University of Bozen-Bolzano, Italy.
- Swiss society of engineers and architects. Raumnutzungsdaten für Energie- und Gebäudetechnik. SIA 2024:2015.
- TRNSYS Software website. 2022. Thermal Energy System Specialists. Accessed 5 April, 2022. <http://www.trnsys.com/index.html>
- Zangheri, P., R. Armani, M. Pietrobon and L. Pagliano. 2018. "Identification of cost-optimal and NZEB refurbishment levels for representative climates and building typologies across Europe". *Energy Efficiency* 11: 337–369. doi: <https://doi.org/10.1007/s12053-017-9566-8>

Preliminary CFD Parametric Simulations of Low- and Medium-Density Urban Layouts

Ritesh Wankhade – Free University of Bozen-Bolzano, Italy – riteshnarendra.wankhade@natec.unibz.it

Giovanni Pernigotto – Free University of Bozen-Bolzano, Italy – giovanni.pernigotto@unibz.it

Michele Larcher – Free University of Bozen-Bolzano, Italy – michele.larcher@unibz.it

Abstract

Most existing cities were not designed to exploit wind and air displacement phenomena to ensure pollutant dilution and enhance the effectiveness of natural ventilation of the built environment. Although this problem is well known in the literature, the majority of previous studies focused on real case studies or on parametric layouts often characterized by high-rise buildings, which are not typical for most Italian and European cities. In this framework, the goal of this research was to perform a preliminary CFD parametric study on street canyons with low- and medium-rise buildings, focusing on the different parameters impacting outdoor air displacement in an urban layout. Seven different configurations of street canyon were simulated with ANSYS Fluent, focusing on the air displacement around a low-, medium- or high-rise target building, located at the beginning, at the end, or in the middle of the street canyon, respectively. The velocity and pressure contour plots were analysed to understand the behavior of airflow around the buildings in the different configurations, discussing in such a way the natural ventilation potential.

1. Introduction

Advances in technology and facilities available in urban cities have caused rapid urbanization, leading to the transfer of the population from rural to urban areas in search of new opportunities. The United Nations estimates that, by the year 2030, 60 % of the population will live in urban areas with at least half a million inhabitants (United Nations, 2018). Compared to the current situation, this phenomenon will generate demand for the construction of new homes and buildings. As a result, concerns about urban environmental and human health issues, such as air quality, natural outdoor ventilation, and dilution of pollutants in the built

environment will grow (Li et al., 2020). If not properly managed, these urbanization trends will bring increased urban density, with limited spaces among buildings (e.g., parks, parking lots, trees, etc.). This will further reduce air flows coming from surrounding areas, affecting air quality and pollutant dilution (Li et al., 2020; Song et al., 2018).

For this reason, there are many studies that have been conducted on the phenomena of urban ventilation and effectiveness of natural ventilation in cities. In particular, several studies focused on the impact of different urban parameters on natural ventilation, working on generic layouts, real city layouts, or both. Guo et al. (2015) selected a typical urban area in Dalian, China, to perform a comparative and simulative analysis about air displacement due to wind using CFD tools. King et al. (2017) presented a relationship between incident angle and ventilation rate, using an isolated cube and an array of irregular cubes representing generic buildings. Peng et al. (2017) ran CFD simulations of ten identical buildings forming a street canyon to investigate wind-driven natural ventilation and pollutant diffusion at pedestrian level.

When working with building layouts, there are some aspects to consider, such as the space between buildings, the size of buildings, doors and windows, and the width of the streets adjacent to them. These parameters are useful for understanding the relationship between buildings, cities, and natural ventilation potential. Some of the important parameters are, for instance, building height, building density BD (Ding & Lam, 2019), floor area ratio FAR , building site coverage BSC , and street aspect ratio AR_{street} (Yang et al., 2020). Park et al. (2020) and Cheng et al. (2009) investigated the flow characteristics around step-up street canyons and ventilation performance with different aspect ratios using

CFD. Peng et al. (2019) used the floor area ratio and the building site coverage to find the correlation between urban morphological parameters and ventilation performance. By keeping the floor area ratio constant and changing the building site coverage, they established nine idealized building configurations to find the correlation between these urban morphological parameters and ventilation performance. Street canyons and their size can also influence natural ventilation performance. For example, Yang et al. (2020) and Chatzimichailidis et al. (2019) underlined the importance of the street canyon aspect ratio characterizing indoor and outdoor ventilation and flow patterns.

As observed in the literature, CFD simulations have been used to compare and discuss in more detail the results obtained from experiments. For instance, Padilla-Marcos et al. (2017) performed their simulation with Ansys Fluent for a generic building layout, with the aim of studying ways to increase natural ventilation potential in buildings. However, the majority of these studies, and, in particular, those which evaluate natural ventilation in street canyons, primarily focus on high-density or populated cities. As an example, Yuan and Ng (2012) examined the pedestrian-level natural ventilation performance in the context of a regular street grid in the high urban density of Mong Kok in Hong Kong.

Despite the variety of research, most of this has paid particular attention only to high-rise buildings, with limited investigation into low-density cities and low or medium-rise buildings, which are more representative and typical of several countries in the European Union, such as Italy. Therefore, the aim of this study was to perform a preliminary CFD parametric analysis for low or medium-rise buildings, focusing on the different parameters impacting outdoor air displacement in this kind of urban layout, and to discuss if there is a potential for natural ventilation of buildings, considering relative height and position in a street canyon.

2. Methodology

2.1 Generic Urban Buildings Layout

In this work, a generic street canyon layout was chosen. The shape of each building considered is cuboidal with a cross-section equal to 20 m x 20 m. Each floor of the building has a gross height of 4 m, assuming the internal room height of 2.8 m. The height of the high, medium, and low-rise target buildings are 36 m, 24 m, and 12 m, respectively. 10 buildings are positioned in a 5 x 2 rectangular array, where the target building, i.e., the object of the investigation, can be in the front corner, in the middle of the side, or in the rear corner. Different to other studies in the literature (Ding & Lam, 2019; Ramponi et al., 2015), the distances between adjacent buildings along the street canyon are modeled as significantly less than the street's width, i.e., 5 m distance against 20 m of street width. Figs. 1 to 4 show the different configurations of the building arrangements.

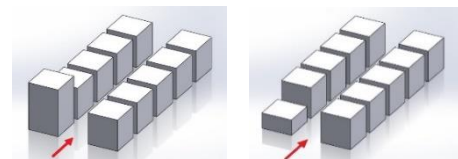


Fig. 1 – High-rise and low-rise building at corner (windward)

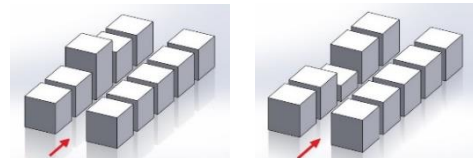


Fig. 2 – High-rise and low-rise building at side

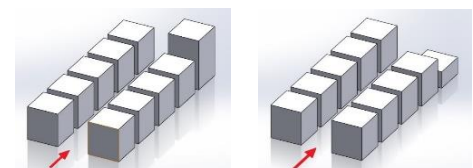


Fig. 3 – High-rise and low-rise building at corner (leeward)

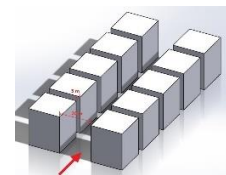


Fig. 4 – Buildings with same height

2.2 CFD Simulation

2.2.1 Computational Domain

The Ansys Fluent 19.0 simulation tool was used to simulate the cases mentioned in Section 2.1. The building geometries were drawn at full scale in Solidworks 2018 and then exported to Ansys Fluent. The computational domain size was based on previous examples from the literature, such as (Ding & Lam, 2019) and (Park et al., 2020). Following the examples of (Ding and Lam, 2019), the computational domain was set with a downstream length of eight times the building height (H) $8H$, an upstream length of $4H$, a lateral length of $4H$ on both sides of the buildings, and a height of $4H$. As a whole, the CFD domain size was set to 1560 m x 1020 m x 300 m (respectively, length, width, and height). The distance between the windward surface of the domain and the first building walls was equal to 450 m; both lateral distances between the surface of the domain and the walls of the building were 480 m; and the distance between the leeward surface of the domain and the wall surface of the rear building was equal to 930 m.

2.2.2 Meshing

Before setting up and running the CFD simulation, it was necessary to create a mesh. Following the literature (King et al., 2017), it was decided to use the hexahedral mesh for the entire domain in order to keep the resolution scheme simple. Fine meshing was applied on the buildings' walls in order to accurately capture the flow around them. The number of elements for the generic building layout cases ranged from 3 to 5.2 million.

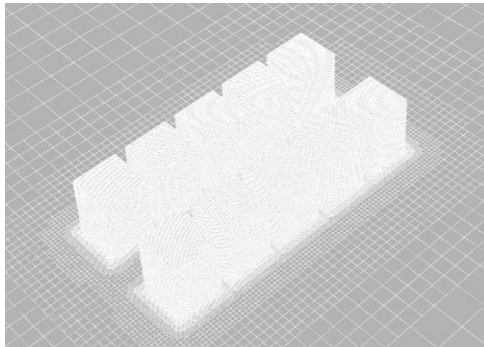


Fig. 5 – Mesh representation of generic building layout

2.2.3 Boundary Conditions and Numerical Setup

Choosing an appropriate boundary condition is an important step in CFD simulations. The windward surface of the domain was considered as the velocity inlet, and the lateral surfaces, the top surface, and the leeward surface of the domain as the pressure outlet. The velocity profile ($u(z)$) of inlet, the turbulent kinetic energy profile (k) and turbulent dissipation rate profile (ϵ) were calculated in agreement with the following equations (King et al., 2017):

$$u(z) = \frac{u^*}{\kappa} \ln \left(\frac{z+z_0}{z_0} \right) \quad (1)$$

$$k = \frac{u^{*2}}{\sqrt{C_\mu}} \quad (2)$$

$$\epsilon = \frac{u^{*3}}{\kappa(z+z_0)} \quad (3)$$

where u^* , z , z_0 are friction velocity (m/s), height coordinate (m), and roughness length (m), respectively. κ (≈ 0.41) and C_μ (≈ 0.09) are von Karman constant and a model constant, respectively. Referring to the meteorological data of Bolzano (typical year according to the Comitato Termotecnico Italiano), an average wind velocity of 1 m/s was chosen.

Reynolds-averaged Navier-Stokes (RANS) and Large Eddy Simulation (LES) are the most commonly used turbulence models for urban ventilation assessment. The accuracy of the LES turbulence model is higher than the RANS turbulence models, but it is also more expensive compared with the computational cost of the RANS turbulence models (Peng et al., 2019). RANS turbulence models are appropriate because of their simplicity, reasonable ventilation assessment results and less expensive computing power (Padilla-Marcos et al., 2017; Peng et al., 2019). The standard $k-\epsilon$ turbulence model was used. The standard $k-\epsilon$ model is a semi-empirical model based on model transport equations for the turbulence kinetic energy (k) and its dissipation rate (ϵ). The governing equations that were solved during the simulation in case standard $k-\epsilon$ turbulence model are the following:

$$\frac{\partial}{\partial t} (\rho k) + \frac{\partial}{\partial x_i} (\rho k u_i) = \frac{\partial}{\partial x_j} \left[\left(\mu + \frac{\mu_t}{\sigma_k} \right) \frac{\partial k}{\partial x_j} \right] + G_k - \rho \epsilon - Y_M \quad (4)$$

$$\frac{\partial}{\partial t} (\rho \epsilon) + \frac{\partial}{\partial x_i} (\rho \epsilon u_i) = \frac{\partial}{\partial x_j} \left[\left(\mu + \frac{\mu_t}{\sigma_\epsilon} \right) \frac{\partial \epsilon}{\partial x_j} \right] + C_{1\epsilon} \frac{\epsilon}{k} G_k - C_{2\epsilon} \rho \frac{\epsilon^2}{k} \quad (5)$$

$$\mu_t = \rho C_\mu \frac{k^2}{\epsilon} \quad (6)$$

In these equations, G_k represents the generation of turbulence kinetic energy due to the mean velocity gradients. Y_M represents the contribution of the fluctuating dilatation in compressible turbulence to the overall dissipation rate. $C_{1\varepsilon}$ ($=1.44$), $C_{2\varepsilon}$ ($=1.92$) and μ_t ($=0.09$) are constants. σ_k ($=1.0$) and σ_ε ($=1.3$) are the turbulent Prandtl numbers for k and ε , respectively.

The pressure-velocity coupling used was SIMPLE, with final second order spatial discretization methods for pressure, momentum, turbulent kinetic energy (k), and turbulent dissipation rate (ε). The convergence criteria were set to 1×10^{-6} for all the residuals.

The simulation was initialized with the first order spatial discretization parameters and default under-relaxation factors ($URFs$) until the residuals' stabilization. Once the residual stability was achieved, the spatial discretization parameters were changed to second order upwind and the $URFs$ to 0.15 for pressure and 0.4 for density, body forces, momentum, turbulent kinetic energy (k), turbulent dissipation rate (ε) and turbulent viscosity (μ_t).

3. Results and Discussions

The simulation results are presented as a function of geometry and position of the buildings, distinguishing cases with the same height, low and high-rise building cases (at side, corner windward, and corner leeward).

Due to the different shapes and sizes of the buildings, there was a variation in the magnitudes of the different parameters under consideration. There was also a change in flow direction at various points due to buildings, which caused a change in magnitude. The variations in the parameters' magnitudes help in understanding the feasibility of airflow and natural ventilation around buildings and street canyons. As specified in Section 2.1, the height of each floor of the building was 4 m. The reference plane for the analysis was set at 1.5 m above the ground of each floor. The airflow velocities and the corresponding static pressures at different locations in the reference planes can be viewed in the contour plots.

3.1 Contour Plot Presentation of the Cases

Fig. 6 shows the static pressure contour developed around the buildings due to airflow. The change in pressure gradient can be noticed from the first buildings (left in the figure) to the last buildings (right in the figure). As the first buildings are directly facing the incoming airflow, there is a maximum pressure on the walls facing the airflow and then it gradually decreases.

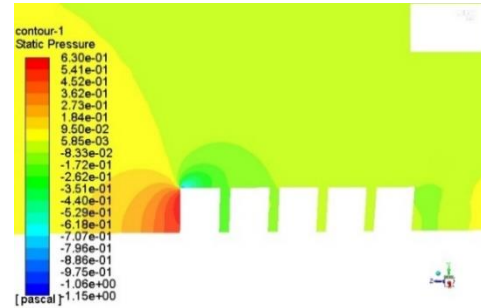


Fig. 6 – Static pressure contour for buildings with same height

Fig. 7 presents the contour plot of velocity around the reference plane on the side. The street aspect ratio (AR_{street}) for the case of buildings with the same height is 1.2 and the aspect ratio ($AR_{building\ gap}$), considering the gap between the buildings, is 4.8, which greatly affects the airflow behavior and natural ventilation around the buildings.

$$AR_{street} = \frac{H_{target\ building}}{Street\ width} \quad (7)$$

$$AR_{building\ gap} = \frac{H_{target\ building}}{Gap\ between\ buildings} \quad (8)$$

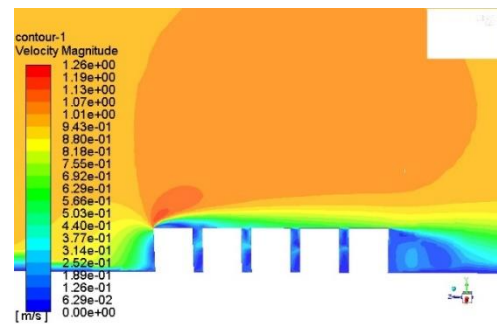


Fig. 7 – Velocity contour for buildings with same height

As mentioned in the literature, there are three main flow regimes: isolated roughness flow regime (IRF , $AR < 0.1-0.125$), wake interference flow regime (WIF , $0.1 < AR < 0.67$) and skimming flow regime with one main vortex (SF , $0.67 < AR < 1.67$) (Yang, et al., 2020).

However, in the configuration with buildings with same height, the $AR_{building\ gap}$ is 4.8, i.e., much higher than the skimming flow regime case. Indeed, two vortices with low intensity can be observed in the gaps between the buildings (Figure 8).

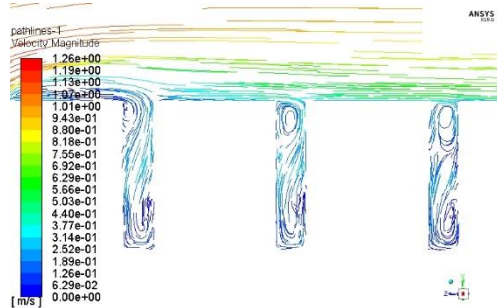


Fig. 8 – Velocity path lines for buildings with same height (side view)

The cases of high-rise and low-rise buildings represent the step-up and step-down canyon cases (Li et al., 2020; Park et al., 2020). The $AR_{building\ gap}$ for high-rise and low-rise buildings is 7.2 and 2.4, respectively. Depending on the location of the high-rise and low-rise buildings, step-up and step-down canyons were decided.

The pressure contours for different cases of high-rise and low-rise buildings indicate that there is a similar trend in the pressure distribution for different buildings configurations, as mentioned at the beginning of this section. This can be seen from Figures 9 to 14 for the high-rise building cases.

Figs. 15 to 20 represent velocity contour plots for low and high building cases. Great variation in the velocity magnitude can be seen near building walls and around buildings, as illustrated by the velocity contour plots illustrate. In addition, as previously mentioned, there is an occurrence of vortices in the gap between buildings which assist airflow around buildings. Flow has been diverted due to buildings being obstacles and there is a recirculation of the airflow at the top of the buildings. This also an essential condition to have an airflow around buildings and, in turn, suitable for natural ventilation around and inside the buildings.

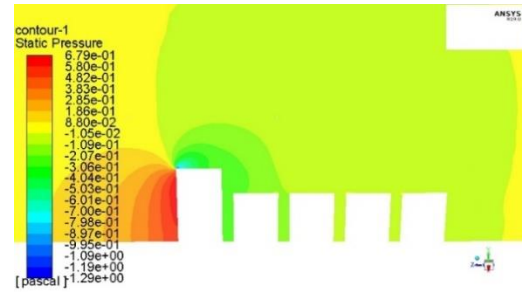


Fig. 9 – Pressure contour plot for high-rise building at windward position

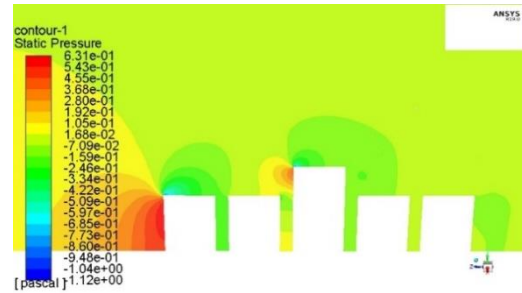


Fig. 10 – Pressure contour plot for high-rise building at center-side position

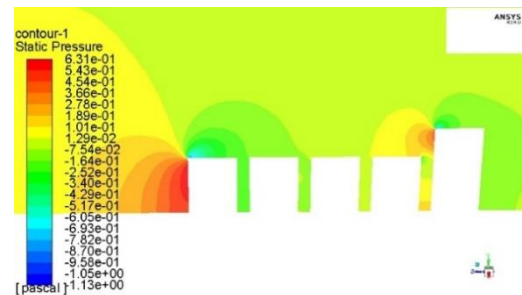


Fig. 11 – Pressure contour plot for high-rise building at leeward position

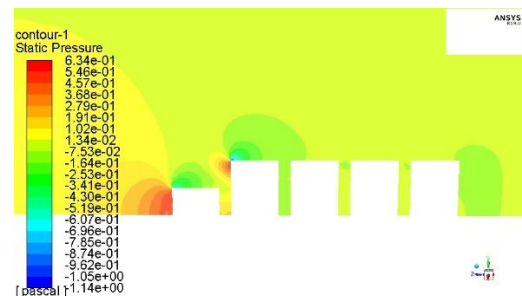


Fig. 12 – Pressure contour plot for low-rise building at windward position

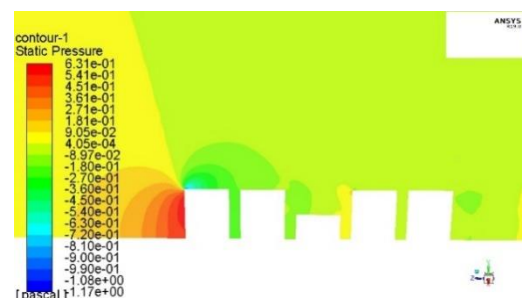


Fig. 13 – Pressure contour plot for low-rise building at center-side position

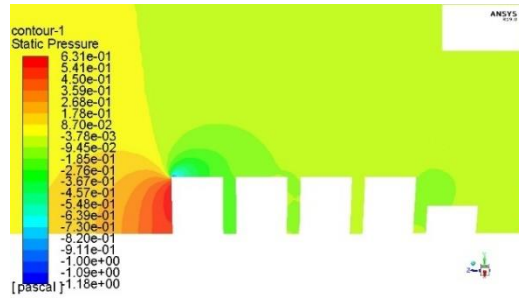


Fig. 14 – Pressure contour plot for low-rise building at leeward position

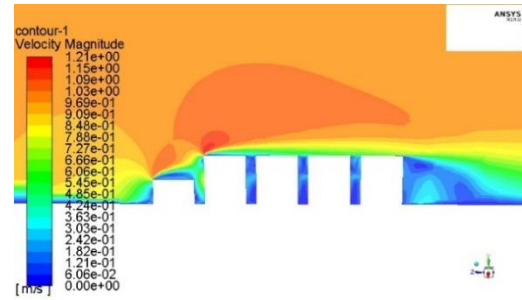


Fig. 18 – Velocity contour plot for low-rise building at windward position

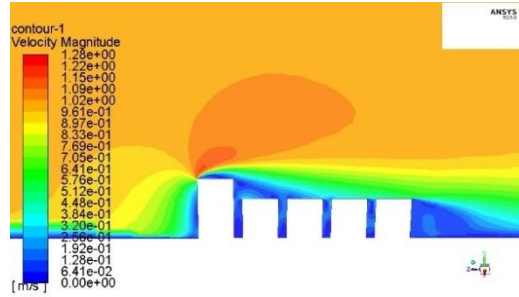


Fig. 15 – Velocity contour plot for high-rise building at windward position

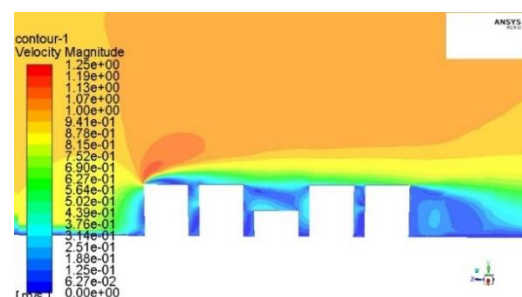


Fig. 19 – Velocity contour plot for low-rise building at center-side position

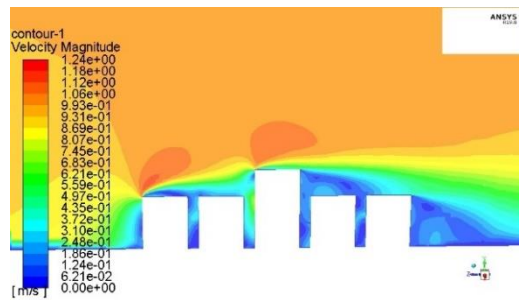


Fig. 16 – Velocity contour plot for high-rise building at center-side position

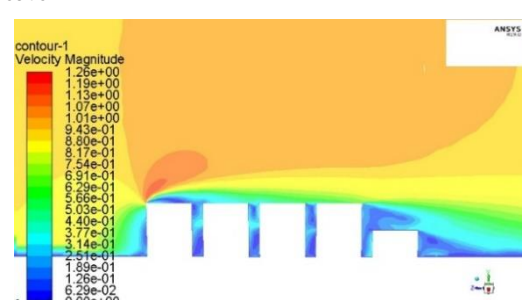


Fig. 20 – Velocity contour plot for low-rise building at leeward position

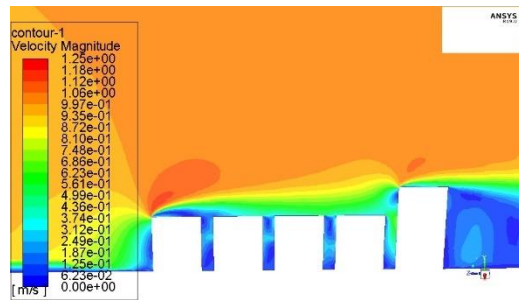


Fig. 17 – Velocity contour plot for high-rise building at leeward position

3.2 Graphical Representation of the Cases

The graphs in Figs. 21 to 24 illustrate the velocity and pressure plots determined at different heights at a distance of 1 m from the walls of the building facing the street. The vertical distance represented in the graphs is a normalized vertical distance, calculated as the ratio of the vertical distance of the point measured from the ground ($Y_{position}$) to the height of the target building (H). Similar criteria are set for the normalized velocity, which is the ratio of the velocity at the corresponding point (V_{mag}) to the reference velocity (V_{ref}) of 1 m/s.

It can be observed from Figs. 21 and 22 that the graphs for the high-rise buildings ($AR_{street,high-rise,1} = 1.8$, $AR_{street,high-rise,2} = 1.2$) in the center and leeward positions have a similar trend, while that is not true in case of the building in the windward position,

characterized by higher airflow velocities and pressures. This suggests higher potential of exploitation of natural solutions for the ventilation of the indoor environments of that building.

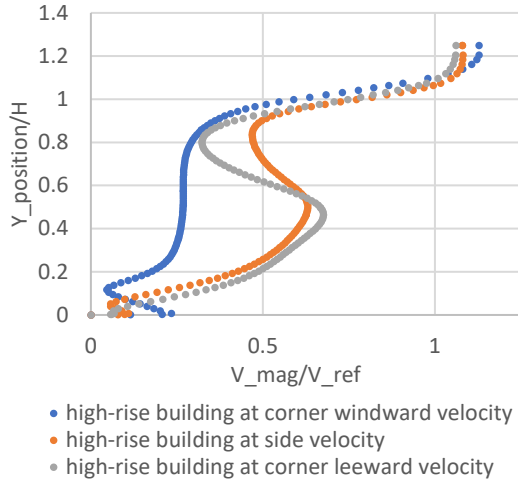


Fig. 21 – Velocity plot for high-rise buildings (1m from the wall facing the street)

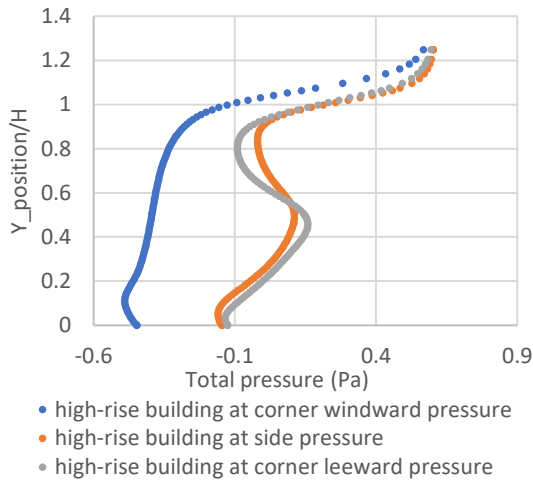


Fig. 22 – Total pressure plot for high-rise buildings (1m from the wall facing the street)

In the case of low-rise buildings ($AR_{street,low-rise,1} = 0.6$, $AR_{street,low-rise,2} = 1.2$) (Fig. 23 and 24), similar trends can be observed, with an increase in velocity and pressure magnitudes along the vertical distance of the target building. Low-rise windward buildings do not follow the same path as the other two low-rise building cases.

In the windward cases of both high- and low-rise buildings, the first buildings experience the decrease in velocity and pressure at ground floor level. This occurs because these buildings are directly facing the wind flow, which causes air recirculation (as it can be noticed from Figs. 15 to 20), resulting in the decreased velocity and pressure.

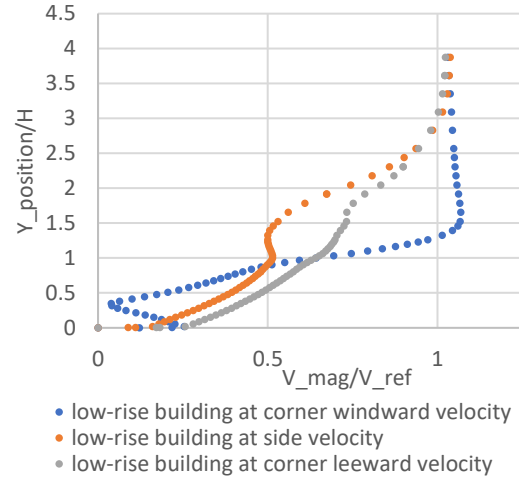


Fig. 23 – Velocity plot for low-rise buildings (1m from the wall facing the street)

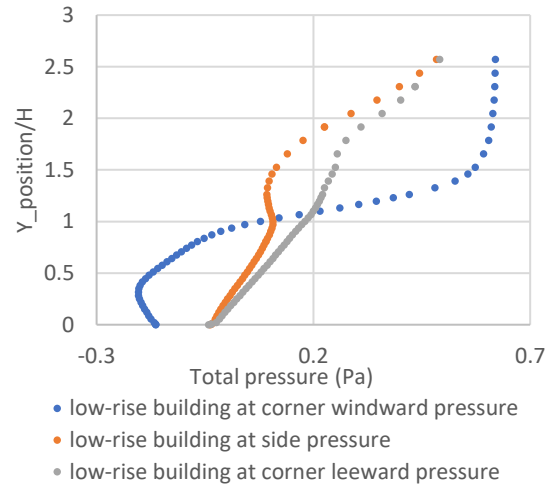


Fig. 24 – Total pressure plot for low-rise buildings (1m from the wall facing the street)

4. Conclusion

This work is a preliminary parametric CFD study about the behavior of airflow around the buildings in different configurations. The analysis focused on the generic building layout of street canyons, considering same-height buildings and different types of target building (high-rise, low-rise). Seven configurations were evaluated, each time focusing on the air displacement around a target building, located respectively at the beginning, at the end, or in the middle of the street canyon, and a case of same height building layout. Pressure and velocity variations were analyzed at different floors of the building façade, also with the help of CFD contour plots.

We observed that, considering the higher aspect ratio of the gaps between buildings in comparison with that of the street canyon, vortices can be easily generated, inducing a recirculation that could facilitate the exploitation of natural ventilation solutions at the different floors of the target building. From the contour and graphic results, it can also be stated that specific building configurations and building positions (e.g., high-rise and low-rise building at the center and the leeward position in the street canyon) show higher potential for exploiting natural solutions for the ventilation of the indoor environments. On the contrary, the buildings in a windward position show a poorer performance.

Further developments of this preliminary research will address validation and generalization of the findings. First, the obtained results will be verified and validated against small-scale experimental tests. Then, multiple configurations of street canyons will be simulated, with the goal of developing a set of rules and simplified correlations useful to engineers, architects, and urban planners to discuss natural ventilation potential from the early stages of new building design or retrofitting of the existing ones.

References

- Chatzimichailidis, A. E., C. D. Argyropoulos, M. J. Assael, and K. E. Kakosimos. 2019. "Implicit Definition of Flow Patterns in Street Canyons—Recirculation Zone—Using Exploratory Quantitative and Qualitative Methods." *Atmosphere* 10(12): 794. doi: <https://doi.org/10.3390/atmos10120794>
- Cheng, W. C., C.-H. Liu, and D. Y. C. Leung. 2009. "On the comparison of the ventilation performance of street canyons of different aspect ratios and Richardson number." *Building Simulation* 2 (1): 53-61. doi: <https://doi.org/10.1007/S12273-008-8332-4>
- CTI. 2016. Comitato Termotecnico Italiano Energia e Ambiente. www.cti2000.it
- Ding, C., and K. P. Lam. 2019. "Data-driven model for cross ventilation potential in high-density cities based on coupled CFD simulation and machine learning." *Building and Environment* 165: 106394. doi: <https://doi.org/10.1016/j.buildenv.2019.106394>
- Guo, F., Y. Fan, and H. Zhang. 2015. "Natural Ventilation Performance in a High Density Urban Area Based on CFD Numerical Simulations in Dalian." In *Proceedings of ICUC9 - 9th International Conference on Urban Climate jointly with 12th Symposium on the Urban Environment*.
- King, M.-F., H. L. Gough, C. Halios, J. F. Barlow, A. Robertson, R. Hoxey, and C. J. Noakes. 2017. "Investigating the influence of neighbouring structures on natural ventilation potential of a full-scale cubical building using time-dependent CFD." *Journal of Wind Engineering and Industrial Aerodynamics* 169: 265-279. doi: <https://doi.org/10.1016/j.jweia.2017.07.020>
- Li, Z., T. Shi, Y. Wu, H. Zhang, Y.-H. Juan, T. Ming, and N. Zhou. 2020. "Effect of traffic tidal flow on pollutant dispersion in various street canyons and corresponding mitigation strategies." *Energy and Built Environment* 1(3): 242-253. doi: <https://doi.org/10.1016/j.enbenv.2020.02.002>
- Padilla-Marcos, M. Á., A. Meiss, and J. Feijó-Muñoz. 2017. "Proposal for a simplified CFD procedure for obtaining patterns of the age of air in outdoor spaces for the natural ventilation of buildings." *Energies* 10(9): 1252. doi: <https://doi.org/10.3390/en10091252>
- Park, S.-J., J.-J. Kim, W. Choi, E.-R. Kim, C.-K. Song, and E. R. Pardyjak. 2020. "Flow Characteristics Around Step Up Street Canyons with Various Building Aspect Ratios." *Boundary-Layer Meteorology* 174(3): 411-431. doi: <https://doi.org/10.1007/s10546-019-00494-9>
- Peng, Y., X. Ma, F. Zhao, C. Liu, and S. Mei. 2017. "Wind driven natural ventilation and pollutant dispersion in the dense street canyons: Wind Opening Percentage and its effects." *Procedia Engineering* 205: 415-422. doi: <https://doi.org/10.1016/j.proeng.2017.10.392>
- Peng, Y., Z. Gao, R. Buccolieri, and W. Ding. 2019. "An Investigation of the Quantitative Correlation between Urban Morphology Parameters and Outdoor Ventilation Efficiency Indices." *Atmosphere* 10(1): 33. doi: <https://doi.org/10.3390/atmos10010033>
- Ramponi, R., B. Blocken, L. B. de Coo, and W. D. Janssen. 2015. "CFD simulation of outdoor

- ventilation of generic urban configurations with different urban densities and equal and unequal street widths." *Building and Environment* 92: 152-166. doi: <https://doi.org/10.1016/j.buildenv.2015.04.018>
- Song, J., S. Fan, W. Lin, L. Mottet, H. Woodward, Davies M. Wykes, R. Arcucci, et al. 2018. "Natural ventilation in cities: the implications of fluid mechanics." *Building Research and Information* 46(8): 809-828. doi: <https://doi.org/10.1080/09613218.2018.1468158>
- United Nations. 2018. "The World's Cities in 2018." https://www.un.org/en/events/citiesday/assets/pdf/the_worlds_cities_in_2018_data_booklet.pdf
- Yang, X., Y. Zhang, J. Hang, Y. Lin, M. Mattsson, M. Sandberg, M. Zhang, and K. Wang. 2020. "Integrated assessment of indoor and outdoor ventilation in street canyons with naturally-ventilated buildings by various ventilation indexes." *Building and Environment* 169: 106528. doi: <https://doi.org/10.1016/j.buildenv.2019.106528>
- Yuan, C., and E. Ng. 2012. "Building porosity for better urban ventilation in high-density cities - A computational parametric study." *Building and Environment* 50: 176-189. doi: <https://doi.org/10.1016/j.buildenv.2011.10.023>

Smart Sensors and Auditory Sensitivity: Acoustic Optimization of Dedicated Spaces for Autistic Individuals

Federica Bettarello – University of Trieste, Italy – fbettarello@units.it

Marco Caniato – Free University of Bozen-Bolzano, Italy – marco.caniato@unibz.it

Arianna Marzi – Free University of Bozen-Bolzano, Italy – arianna.marzi@natec.unibz.it

Giuseppina Scavuzzo – University of Trieste, Italy – gscavuzzo@units.it

Andrea Gasparella – Free University of Bozen-Bolzano, Italy – andrea.gasparella@unibz.it

Abstract

This work deals with the design of an indoor environment dedicated to autistic individuals, who may suffer from hypersensitivity to acoustic stimuli. Specifically, in this volume customized pieces of furniture are included, containing smart sensors, designed to help people with cognitive deficits to live an independent life. Among the indoor comfort aspects, the acoustic requirements have been investigated, in order to guarantee both the optimal functioning of the acoustic sensors and the acoustic occupants' well-being. The optimal indoor acoustic levels are based on a literature review. Measurements are performed in order to calibrate a 3D acoustic model. Then diverse scenarios are analysed, and an optimized configuration is proposed and realized. The model is then validated with the final acoustic measurements, which confirm the designed results.

1. Introduction

Many autistic individuals show particular sensitivity to noise disturbance, both indoors and outdoors, often to a greater extent than neurotypical people, thus exhibiting acoustic hypersensitivity (American Psychiatric Association, 2013).

In a recent study conducted in Canada involving 168 families with an autistic child (3-16 years old) 87 % of the respondents reported that their children were very sensitive to noise (Nagib & Williams, 2018). Specific studies carried out on school environments (Tronchin et al., 2018) with autistic children have shown that the application of interventions aimed at reducing noise coming from outside the classroom (from corridors, or neighbor-

ing classrooms), have permitted them to reduce behavioral temperaments (self-stimulatory behavior), such as obsessive behavior, specific for each child, including head-banging, biting their hands and rocking (Kanakri et al., 2017). These results are also confirmed by the first analysis of the SENSHome Interreg Project research, which features an investigation of Italian and Austrian families. In this case too, acoustics were found to be the greatest source of stress for autistic people and their relatives and caregivers. Many papers, institutional programs, manuals and documents related to acoustic individuals explained that acoustics are of paramount importance when designing dedicated spaces (Ahrentzen & Steele, 2015; Braddock & Rowell, 2011; Mostafa, 2014).

For all these reasons, during the construction and setting up of an environment dedicated to a full-scale reproduction of living environments for autistic people and their families, the acoustic aspect was analysed beforehand and verified on site. Specifically, the SENSHome environment is located inside the Building Physics Laboratory at the Free University of Bolzano. It hosts the furniture specifically designed for autistic people by the University of Trieste and integrated with the smart sensors system that make up the early warning system, specifically developed for the SENSHome project.

2. Setting Up The SENSHome Laboratory

As formerly pointed out, the determination of acoustic quality parameters is of paramount im-

portance (Tronchin, 2021). The reverberation time R_t , clarity C_{50} and definition D_{50} for environments dedicated to autistic people are the most commonly used parameters to qualify an indoor environment both for indoor comfort and for the use of microphone sensors (Griesinger, 2013; Marshall, 1994; Tsilfidis, 2013). These factors were then considered as reference for the acoustic optimisation of this environment.



Fig. 1 – Starting conditions of the building physics laboratory at UNIBZ

The interior design included a frame structure of vertical wooden panels and some fake windows covered with a white acoustic-transparent membrane (Fig. 2). Featuring this configuration, the space included three areas: an entrance, a kitchen and a living room (quiet space). Each area is then filled with furniture specifically designed for the project (Fig. 3).



Fig. 2 – Interior covering provided in the laboratory for the preparation of the SENSHome scenario. Vertical wooden panels

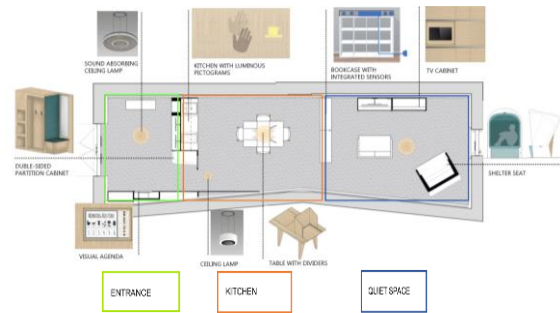


Fig. 3 – Layout of the internal distribution of spaces and location of various pieces of furniture

From an acoustic point of view, it was possible to act directly at the design phase, considering the issues related to indoor acoustic comfort described. Going into detail, many elements of the designed furniture were implemented with sound-absorbing materials (Fabbri et al., 2021) or systems. In particular, the coverings of the entrance furniture (Fig. 4a) and the quiet place armchair (refuge space, Fig. 4b) were produced using soft, sound-absorbing materials, (specifically a polyurethane foam), featuring a thickness of 5 cm.

Interestingly, inside the refuge space, both the high performance of the sound-absorbing interior coating and the huge presence of exposed surface area permitted a very special acoustic field for those sitting inside. This was highly appreciated by the autistic individuals, who liked this special feature of the refuge space, lying inside it many times and for significant time spans.

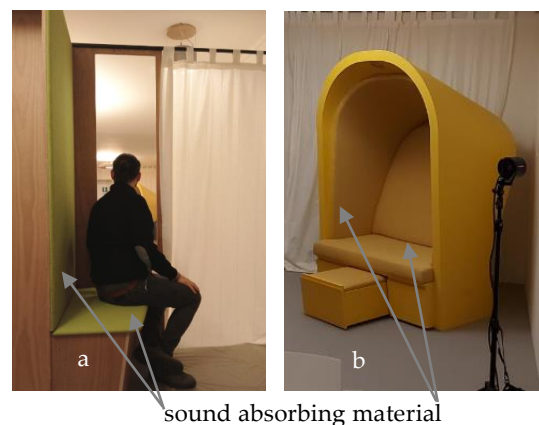


Fig. 4 – a) entrance furniture with sound-absorbing coating; b) dedicated armchair (refuge space) with sound absorbing coating

Another piece of furniture which included sound-absorbing characteristics is the kitchen table. It is equipped with special panels, which could be used to separate every single person sitting around it. Indeed, some autistic individuals cannot stand someone else's food or smell. For this reason, the panels include active carbon layers and sound-absorbing elements. This provides a customized local environment where an individual can experience her/his own personal requirements, but still maintain a social breakfast/lunch/dinner. In Fig. 5, the panels are shown. It is possible to detect the perforated internal surface, where both odors and noise could enter and be absorbed.

Moving onto the suspended ceiling lamps, 4 elements were included. Specifically, a round-shaped wood panel was used and filled with microphone sensors, LED strips and sound-absorbing polyurethane foam, 7 cm thick. The lamps are 65 cm in diameter and suspended where the highest noise levels are supposed to be. Accordingly, one was suspended over the lunch table (Fig. 5), another one over the sofa where the television is seen, a third one in the entrance where people gather before entering and the last one over the kitchen space.



Fig. 5 – Detail of the kitchen table with sound-absorbing dividers and ceiling lamps with sound-absorbing coating

In addition, between the wooden frame of the casing and the cladding, a hollow space is left to be filled with sound-absorbing panels, usable to reduce internal reverberation (Fig. 6).



Fig. 6 – Detail of the suspended sound-absorbing panels layered between the wooden structure and beyond the acoustic-transparent membrane

The sound-absorbing foam used to cover furniture complements and the sound-absorbing panels on the wall are characterized by the frequency sound absorption coefficients reported in Figs. 7 and 8. It is possible to notice how the two selected layers are characterized by a very good acoustic performance.

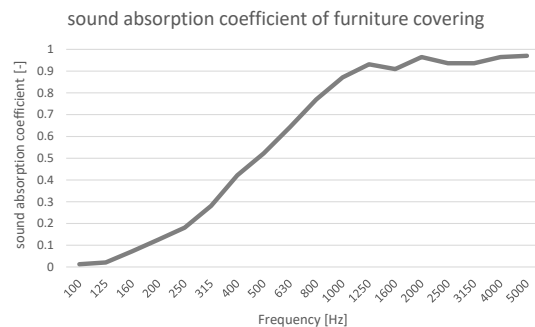


Fig. 7 - Sound absorption coefficient frequency trend of the cover furniture

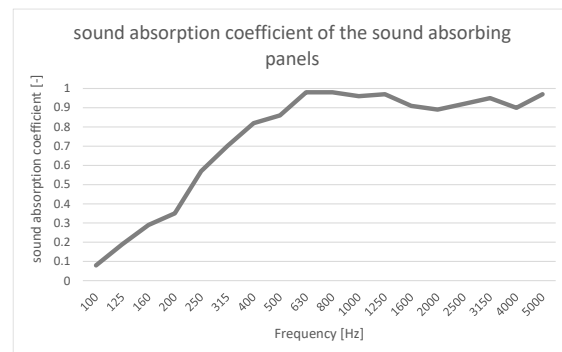


Fig. 8 - Sound absorption coefficient frequency trend of the internal panels

The main aim of the acoustic analysis was to obtain an indoor average reverberation value of between 0.5 and 0.7 s (Griesinger, 2013; Marshall, 1994; Tsilfidis, 2013). These values represent the right compromise for the achievement of optimal conditions both for the use of the environment by autistic people and for the use of the microphone sensors.

3. Acoustic Analysis of Various Scenarios

Since it is acknowledged that acoustic models should be calibrated using reverberation time (Karjalainen & Järveläinen, 2001; Suárez et al., 2005; Tronchin, 2005), only this parameter was considered in the following dissertation.

The general criteria of the ISO 3382-1 were considered when performing acoustic measurements. The microphone height was 1.6 m, while the source height was 1.9 m in all cases (Tronchin et al., 2021). The measurement was set by placing the source in 2 different positions and the 8 receivers all along the void space (Tronchin & Bevilacqua, 2022). The source played a sinusoidal sine sweep having a frequency of between 50 Hz and 12000 Hz and a duration of 20 seconds (Tronchin & Knight, 2016). Measurements were performed in an unoccupied configuration.

The average reverberation time of the laboratory in the empty condition was measured and was 3.5 s. The average was computed considering the range 500 Hz – 1000 Hz – 2000 Hz. Since the aim is to obtain an average reverberation time on the same frequency range of 0.5-0.7 seconds (Griesinger, 2013; Marshall, 1994; Tsilfidis, 2013), some actions should be considered.

Therefore, the correct amount of sound-absorbing panels had to be calculated in order to achieve the target reverberation values. For the acoustic optimisation of the laboratory environment, it was necessary to provide a quantity of sound-absorbing materials of approx. 45 m² (i.e., an amount equal to 22.5 % of the total reflective surface of the room). Figs. 8-10 show the virtual models of the three configurations of the laboratory analyzed: i) empty, ii)

with furniture and iii) with furniture and sound-absorbing panels.

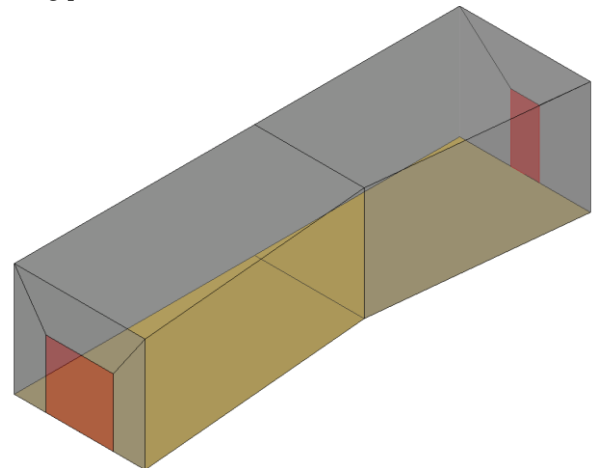


Fig. 8 – Virtual model of the laboratory: configuration i) empty

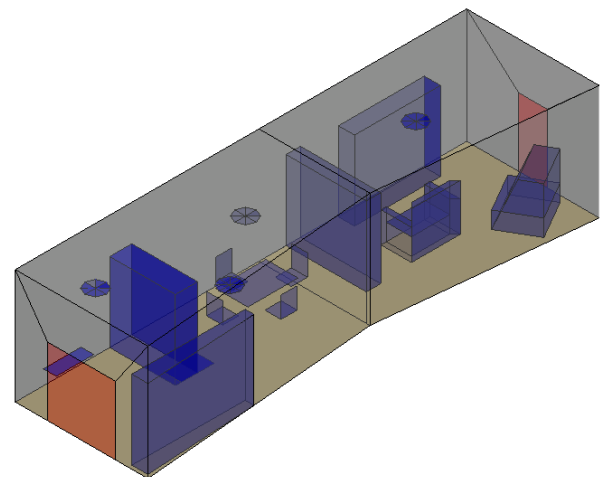


Fig. 9 – Virtual model of the laboratory: configuration ii) with furniture

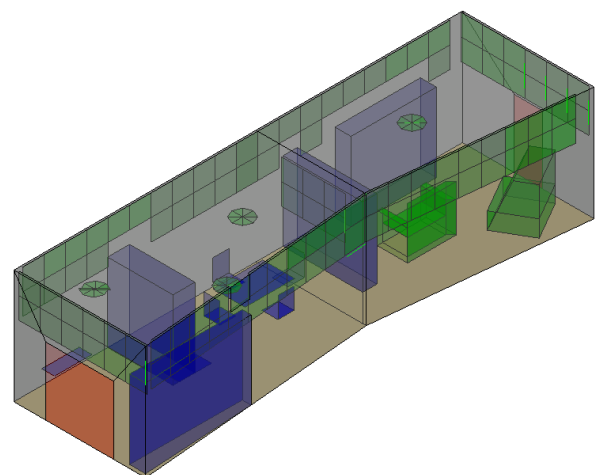


Fig. 10 – Virtual model of the laboratory: configuration iii) with furniture and sound-absorbing panels

In Table 1, we can see that, for the empty scenario, the simulation provides good results compared to the measured ones. In Fig. 11, the indoor sound field simulated at 1000 Hz is represented. It is interesting to notice how its distribution it is almost symmetrical. Since the calibration is positive, it is possible to proceed with the other two scenarios reported in Figs. 9 and 10.

Table 1 – Calculated averaged reverberation time for different scenarios

Lab configuration	Scenario (i)	Scenario (ii)	Scenario (iii)
Average reverberation time [s]	3.49	1.49	0.61

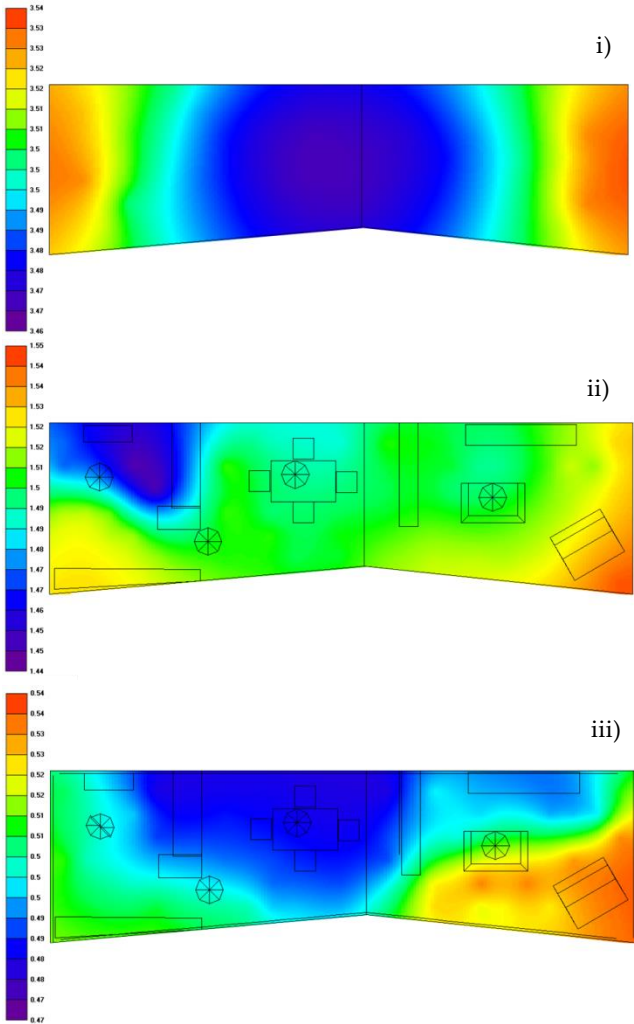


Fig. 11 – spatial reverberation time distribution for different scenarios: i) empty room, ii) furnished room and iii) furnished room with sound absorbing panels. Frequency plot: 1000 Hz

In Table 1, the average reverberation time values are reported, while in Figs. 12 and 13 the average reverberation time values at 1000 Hz are reported, for the analysed configurations.

4. Model Validation

The validation of the 3D model was developed when the SENSHome laboratory (scenario iii) had been set up (Fig. 12).



Fig. 12 – Two views of the SENSHome environment

The results obtained in terms of reverberation time agree strongly with the simulated ones. Indeed, the measured average reverberation time value is 0.63 seconds. Fig. 13 shows the frequency trend of measured results.

These values permit the next phase of the SENSHome laboratory to proceed, which concerns testing of the operation of the microphone sensors and the validation of the SENSHome scenario by hosting autistic individuals and their families and

caregivers within it. This will permit an understanding of the effectiveness of the indoor sound field designed.

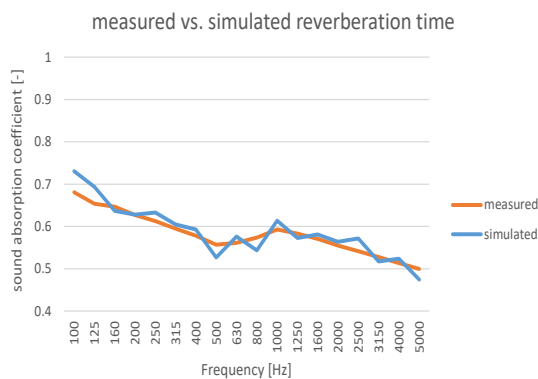


Fig. 13 – Reverberation time frequency trend of furnished room with sound-absorbing panels: in situ measurements

5. Conclusion

Acoustics are an indoor comfort aspect of paramount importance, especially for autistic people featuring auditory hypersensitivity. Taking care of the sound field of indoor environments could mean creating hospitable and non-discouraging living conditions. Using a robust procedure to design the SENSHome environment by means of measurements, 3D acoustic simulation and final validation also permitted the reverberation time of different scenarios to be optimised. This was also aimed at creating the best operating conditions for the microphone sensors that are part of the smart system included in the SENSHome environment. The acoustic properties of the sound-absorbing coverings were investigated. This led to the calculation of the surface area of the sound-absorbing panels to be used. The final measurements performed in the SENSHome environment built permitted an assessment of the effectiveness of the design developed. Future developments include validation of the microphone sensor operation conditions and of the internal acoustic quality perceived by autistic individuals, their relatives and caregivers.

Acknowledgement

This study was supported by the Interreg Italy-Austria project "SENSHome" ITAT 1088 CUP: I54I18000310006.

References

- Ahrentzen, S., and K. Steele. 2015. *At Home with Autism. Designing Housing for the spectrum.* Bristol University Press.
- Braddock, G., and J. Rowell. 2011. *Making Homes that Work: A Resource Guide for Families Living with Autism Spectrum Disorder and Co-occurring Behaviors* (p. 81). Creative Housing Solutions, Rowell Brokaw Architects.
- Fabbri, K., L. Tronchin, and F. Barbieri. 2021. "Coconut fibre insulators: The hygrothermal behaviour in the case of green roofs". *Construction and building materials* 266: 1-9. doi: 10.1016/j.conbuildmat.2020.121026
- Griesinger, D. 2013. "Physiologically based measures for clarity and engagement." *International Symposium on Room Acoustics.*
- ISO. 2009. ISO 3382-1: 2009 Acoustics — Measurement of room acoustic parameters — Part 1: Performance spaces.
- Kanakri, S. M., M. Shepley, J. W. Varni, and L. G. Tassinary. 2017. "Noise and autism spectrum disorder in children: An exploratory survey." *Research in Developmental Disabilities* 63: 85–94. doi: <https://doi.org/10.1016/j.ridd.2017.02.004>
- Karjalainen, M., and H. Järveläinen. 2001. "More about this reverberation science: Perceptually good late reverberance." *The 111th Convention of the Audio Engineering Society.*
- Marshall, L. G. 1994. "An acoustics measurement program for evaluating auditoriums based on the early/late sound energy ratio." *The Journal of the Acoustical Society of America* 96: 2251- 2261.
- Mostafa, M. 2014. "Architecture for Autism: Autism ASPECTSS™ in School Design." *International Journal of Architectural Research* 8(1)
- Nagib, W., and A. Williams. 2018. "Creating therapeutic landscapes at home: The experiences of families of children with autism." *Health and Place* 52: 46-54. doi:

- <https://doi.org/10.1016/j.healthplace.2018.05.001>
- Suárez, R., J. J. Sendra, J. Navarro, and A. L. León. 2005. "The sound of the cathedral-mosque of Córdoba." *Journal of Cultural Heritage* 6: 307–12. doi: <https://doi.org/10.1016/j.culher.2005.03.005>
- Tronchin, L. 2005. "Modal analysis and intensity of acoustic radiation of the kettledrum". *The journal of the acoustical society of America* 117(2): 926-933: doi: <https://doi.org/10.1121/1.1828552>
- Tronchin, L. 2021. "Variability of room acoustic parameters with thermo-hygrometric conditions". *Applied acoustics* 177: 1-14. doi: <https://doi.org/10.1016/j.apacoust.2021.107933>
- Tronchin, L., and A. Bevilacqua. 2022. "Historically informed digital reconstruction of the Roman theatre of Verona. Unveiling the acoustics of the original shape". *Applied acoustics* 185: 1-18. doi: <https://doi.org/10.1016/j.apacoust.2021.108409>
- Tronchin, L., and D. J. Knight. 2016. "Revisiting Historic Buildings through the Senses. Visualising Aural and Obscured Aspects of San Vitale, Ravenna". *International journal of historical archaeology* 20: 127-145. doi: <https://doi.org/10.1007/s10761-015-0325-2>
- Tronchin, L., K. Fabbri, and C. Bertolli. 2018. "Controlled Mechanical Ventilation in Buildings: A Comparison between Energy Use and Primary Energy among Twenty Different Devices". *Energies* 11: 1-20. doi: <https://doi.org/10.3390/en11082123>
- Tronchin, L., F. Merli, and M. Dolci. 2021. „Virtual acoustic reconstruction of the Miners' Theatre in Idrija (Slovenia)". *Applied acoustics* 172: 1-9. doi: <https://doi.org/10.1016/j.apacoust.2020.107595>
- Tsilfidis, A., I. Mporas, J. Mourjopoulos, and N. Fakotakis. 2013. "Automatic speech recognition performance in different room acoustic environments with and without dereverberation preprocessing." *Computer Speech & Language* 27(1): 380-395. doi: <https://doi.org/10.1016/j.csl.2012.07.004>

Simulation Application for the Assessment of the Energy Performance of a Building Renovated Using I-BEST System (Innovative Building Envelope through Smart Technology)

Cristina Carpino – University of Calabria, Italy – cristina.carpino@unical.it

Mario Maiolo – University of Calabria, Italy – mario.maiolo@unical.it

Patrizia Piro – University of Calabria, Italy – patrizia.piro@unical.it

Roberto Bruno – University of Calabria, Italy – roberto.bruno@unical.it

Natale Arcuri – University of Calabria, Italy – natale.arcuri@unical.it

Abstract

Energy renovation of existing buildings represents a fundamental action for achieving the objectives aimed at overcoming the climate crisis. However, several difficulties are encountered in building refurbishment. Among these are the high costs and long construction times, the invasiveness of interventions, which often prevent the usability of the building, and the impossibility of providing maintenance and verifying degradation of the underlying layers of the envelope. Regarding the systems, retrofit often causes substantial alterations to the building aesthetics, affecting its original character and defacing the surrounding environment. Furthermore, the integration of renewable sources is often hard to implement. The I-BEST system (Innovative Building Envelope through Smart Technology) is an innovative multifunction façade system for the redevelopment of the existing building stock, which aims to overcome these limits by offering a valid response to the growing demand for building “recladding”. The system consists of sliding, modular and multi-functional panels, supported by a metal and light load-bearing structure fixed on the external wall and spaced from it to create a suitable cavity for containing plant ducts. The purpose of the present work is to evaluate, through dynamic simulation, the energy performance of a building renovated with the I-BEST system.

1. Introduction

Based on the Green Deal objectives, the European Union (EU) will have to achieve zero climate impact by 2050 (EU Commission). In the energy tran-

sition, a significant role is played by decarbonisation of the building stock, which accounts for 36 % of EU CO₂ emissions (United Nations Environment Programme, 2021). The European Commission has outlined a long-term restructuring strategy, using primarily the principle of energy efficiency, as well as evaluating the use of renewable energy. Consistently, each Member State has developed an Integrated National Plan for Energy and Climate to support the renovation of existing residential and non-residential buildings, both public and private, into nearly zero energy buildings, promoting cost-effective strategies. The renovation of buildings, which should take place at an average rate of 3 % per year, will make it possible to progressively increase the EU’s energy independence, considering that each percentage point of increase in energy savings corresponds to a reduction in gas imports of 2.6 % (Directive (EU) 2018/844). In addition to energy inefficiency, existing buildings frequently show physical and formal degradation, which significantly alters the quality of the urban environment. Renovation actions often entail a series of problems that make it difficult to implement restructuring plans. The most common problems include: high costs and long construction times; the invasiveness of the interventions that usually require occupancy and work activities to be suspended; in the case of the application of external thermal insulation, the impossibility of periodic maintenance of the underlying elements and the inability to identify any cracks caused by earthquakes; the difficulty of integrating systems for the

production of energy from renewable sources; in the hypothesis of replacing the heating and cooling systems, the presence of pipes on the external façades that disfigure the appearance of the building. A potential solution to the aforementioned problems consists of the renovation of the building through systems that involve the application of a second skin from the outside. This technical solution has been proposed and analysed in various forms, characterized by different configurations and operating principles, and which have different effects on the energy performance of the buildings that they are applied to (Pomponi et al., 2016; Shameri et al., 2011). Generally, in the literature, the addition of a second layer on the external surface of the walls is defined as a “double skin” or, more properly when speaking of interventions on existing buildings, “recladding”, meaning a coating with elements that can also be opaque. As stated by (Alberto et al., 2017), the double-skin system is strongly influenced by climatic conditions and the location of the building. The authors of this study developed a parametric analysis based on numerical simulation to evaluate the impact on the building's energy performance, of geometry, airflow path, cavity depth, openings area and type of glazing. The results showed that the most efficient solution leads to a 30 % saving in energy demand in a temperate climate and that the orientation of the façade (North or South) produces a difference in the results of 40 %. (Hamza, 2008) explored the possibilities of using the double façade in a hot and arid climate; in particular, the cooling loads were compared for a single skin base case against three possible changes to the physical properties of the external layer of the double skin façade. The simulation results showed that a reflective double façade can achieve higher energy savings than a reflective single façade. The research conducted by (Blanco et al., 2016) concerned the evaluation and optimization of perforated metal sheet double skin façades for a case study in Spain. Through simulation, the influence of different configurations on heating, cooling and artificial lighting loads was evaluated, and a methodology aimed at the optimization of design sustainability based on minimum energy consumption was developed. (Jankovic & Goia, 2021) presented a literature re-

view on experimental and numerical studies of double-skin façades that investigates and evaluates the cause-and-effect connection between the construction characteristics and the thermo-physical phenomena occurring in the system. Simple links between construction properties and performance have been identified, but only when one parameter is analyzed at a time. However, the authors highlighted that the complex interaction between multiple variables is rarely investigated. The study developed by (Tao et al., 2021) proposes two new analytical models to determine the ventilation rate inside naturally ventilated double façades, depending on various factors and using simple inputs. An adjustable double-skin façade mock-up placed into a climate simulator was used by (Jankovic et al., 2022), to investigate different double-skin façade configurations in combination with a wide range of boundary conditions. The authors provided an overview of several methods based on different types of experimental investigations with various levels of complexity to assess how different constructive features and boundary conditions affect the performance of double-skin façades. Recently, more advanced double-skin façade solutions have been tested. For example, (Alqaed, 2022) examined the use of different types of façades (simple façade, double-skin façade and double-skin façade filled with phase changing materials) based on different climatic conditions in Saudi Arabia. The results proved that the use of phase change materials in the double skin façade significantly reduces the energy demand for both heating and cooling. (Pérez et al., 2021) focused on the development of a method for creating the 3D characterization of an experimental double-skin green façade, using LiDAR technologies. The proposed methodology enabled the 3D reconstruction of the green façade's outer envelope, also allowing an evaluation of the temperature reduction obtainable on the external surface of the building and providing a 3D object to be used in Building Information Modeling (BIM).

In the present study, an innovative double-façade model, designed for the renovation of existing buildings, is presented and its effectiveness in reducing the heating energy demand is evaluated for a selected case study, with reference to Mediterra-

near climatic conditions. The proposed system differs from the solutions currently available and discussed in the literature because: a) the façade is made up of opaque panels; b) the cavity of the double envelope is not ventilated; c) the system is multifunctional, in the sense that it is possible to adapt the cladding panels to different functions, according to the specific needs of the case in hand.

2. Methodology

2.1 Description of the I-BEST System (Innovative Building Envelope through Smart Technology)

I-BEST (Innovative Building Envelope through Smart Technology) is an innovative multifunction façade system developed for the refurbishment of existing buildings. This system is designed to implement integrated energy efficiency both in envelope and plant performance. Using the I-BEST system, in fact, it is possible to do the following: improve the energy efficiency of the building; enhance the aesthetic quality of the building and therefore of the surrounding urban environment; avoid the degradation phenomena affecting the materials of the building envelope; implement non-invasive interventions for the occupants of the building, who can continue to use the interior even during the renovation works. The I-BEST technology consists of a system of sliding, modular and multifunctional panels, supported by a metal and light load-bearing structure, which is fixed to the existing building from the outside, without structurally weighing on it. The application of the double skin creates a cavity that can be used to install plant ducts (air conditioning, electrical, water systems and the collection and drainage of rainwater). The design solution meets the growing demand from the recladding sector, which requires the replacement of façades, claddings and openings of aged buildings with new, modern, functional and high-performance components. Furthermore, the system offers a high potential in the construction market, thanks to its modularity, adaptability to different building types, and replicability in various climatic contexts, while maintaining low costs

and reduced construction times. The main strength of the I-BEST system is its high flexibility. The multifunctional module-panels, in fact, can be used as a simple coating (also customizable on the surface), or they can include a layer of thermal insulation that varies according to the climate, incorporate solar modules for the production of renewable energy, integrate layers with vegetation to create green surfaces.

2.2 Presentation of the Case Study

For the evaluation of the I-BEST performance, its application to a building identified as a case study is considered. The building is part of the residential centre of the University of Calabria Campus. The location is characterized by a Mediterranean climate. The building consists of two adjacent blocks, slightly staggered in plan and two floors high. Each block includes two residential units, one on the ground floor and one on the first floor, with a net surface area of about 65.5 m². Overall, the building includes four apartments, with a total net area of 262.0 m². Fig. 1 shows the floor plan of the building. As regards the construction characteristics of the building, the external walls are made with a double layer of perforated bricks and a central cavity with thermal insulation, with thermal transmittance of 0.52 W/(m² K). Fig. 2 depicts the detailed stratigraphy of the external wall. The roof is flat, not insulated, with thermal transmittance equal to 1.35 W/(m² K).

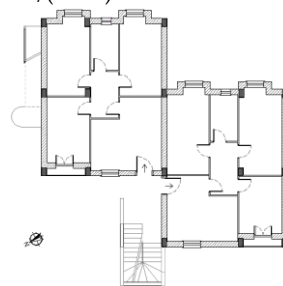


Fig. 1 – Floor plan of the case study building

The ground floor slab, also not insulated, is characterized by a U value of 1.55 W/(m² K). The windows have single glazing ($U_{\text{glass}}=5.7$ W/(m² K) and aluminum frames without thermal break ($U_{\text{frame}}=5.9$ W/(m² K)). Each apartment is equipped with a gas boiler for heating and DHW production.

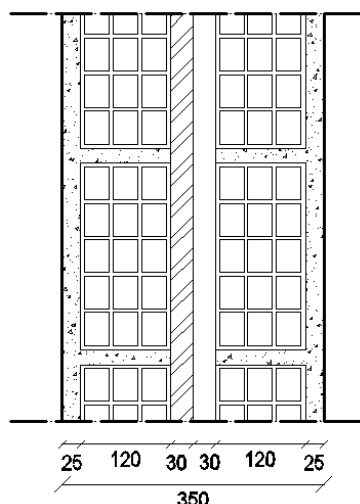


Fig. 2 – Stratigraphy of the external wall before renovation

2.3 Calculation Assumptions

In order to conduct a preliminary analysis, the energy model of the building was created using DesignBuilder software (DesignBuilder Software Ltd), a graphical interface of EnergyPlus (Energy Plus). The model was used to perform dynamic simulations and evaluate the effect of the introduction of the I-BEST system in the building, estimating the energy demand for heating before and after the installation of the double façade. The building was actually selected as a test building for the research project within which the innovative I-BEST system was developed, and it will therefore be renovated through the installation of the I-BEST modules on the external façades, in order to experimentally evaluate the performance of the proposed system. In this study, the effectiveness of the I-BEST system is evaluated exclusively by simulation and is limited to the analysis of the solution relating to the use of the I-BEST panel containing a layer of thermal insulation. Future studies will be aimed at exploring the effect produced by other solutions associated with the multi-functionality of the panel (integration of solar panels and green surfaces). Fig. 3 shows the stratigraphy of the external wall following the application of the I-BEST modules. Assuming the non-ventilated cavity, the thermal transmittance of the wall after the energy renovation with I-BEST is equal to $0.20 \text{ W}/(\text{m}^2 \text{ K})$, complying with the minimum requirements set by law (D.M. 26 June 2015).

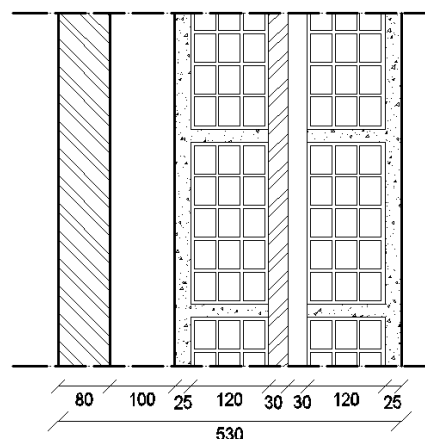


Fig. 2 – Stratigraphy of the external wall after renovation with the I-BEST system

Hourly weather data provided by the Italian Thermotechnical Committee (CTI - Comitato Termotecnico Italiano) were used in the simulation. The location is classified within the climatic zone D (D.P.R. 412/93), with the heating period running from 1 November to 15 April. The heating setpoint temperature is set at 20°C . Since no specific information on the occupancy is available, the internal gains have been quantified following the standard (UNI/TS 11300-1) and amount to $5.68 \text{ W}/\text{m}^2$. Similarly, the natural ventilation rate has been estimated based on technical specification (UNI/TS 11300-1) and is equal to 0.3 ach. Dynamic simulation was conducted on an hourly basis in order to predict the thermal needs for heating and the primary energy required by the building at the current state and after the I-BEST renovation.

3. Results and Discussion

Fig. 3 shows the thermal heating requirement on a monthly basis, at present and after renovation with the I-BEST system. The results refer exclusively to the intervention on the external walls, in order to evaluate the impact of the proposed double façade system. For the purposes of this study, no other envelope efficiency measures were considered that would in any case be required to meet regulatory constraints (e.g., insulation of the roof and ground floor slab, replacement of the windows).

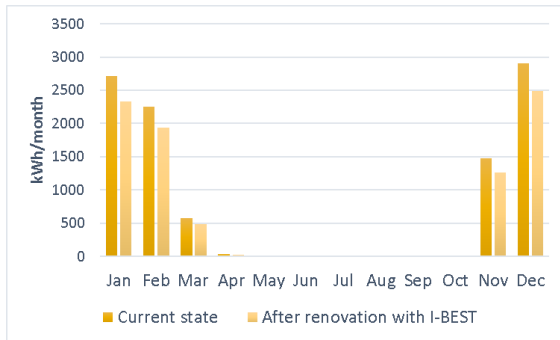


Fig. 3 – Thermal requirements for heating of the case study building before and after the renovation with I-BEST system

The installation of the I-BEST panels, including an appropriate layer of thermal insulation, allows a reduction in the monthly thermal requirement for heating varying from 14.0 % to 16.4 % to be obtained. Considering the whole heating season, the energy needs decrease from 38.08 kWh/(m²year) to 32.58 kWh/(m²year). The improvement in the energy performance of the external walls is also evident in the internal air temperature. Fig. 4 and Fig. 5 show the average daily air temperature corresponding to the coldest day of the year based on the weather file used, that is, February 2. On this day, the lowest outdoor air temperature occurs, equal to -2.8 °C.

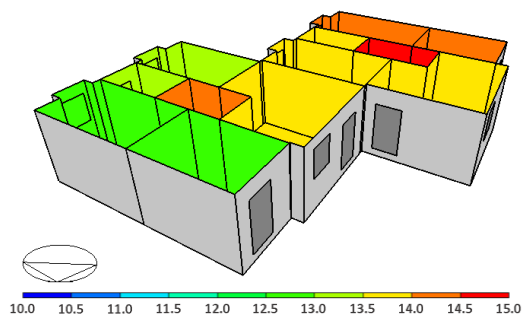


Fig. 4 – Average daily internal air temperature before renovation (free-floating simulation carried out for the coldest day of the year)

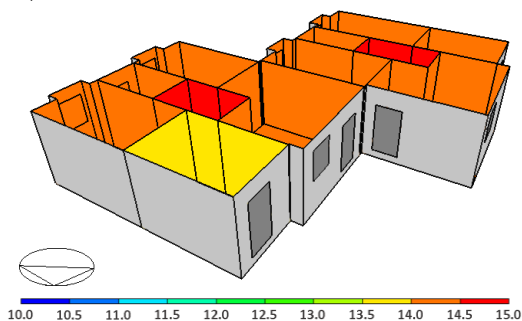


Fig. 5 – Average daily internal air temperature after renovation with I-BEST system (free-floating simulation carried out for the coldest day of the year)

The simulation is carried out in free-floating conditions, thus without considering the activation of the heating system. Therefore, the performance represented in the figures refers to the passive behavior of the envelope and only considers the energy efficiency measure applied on the external walls. The results are displayed based on a color graphic scale and are represented as an example for the ground floor of the building. From the figures, it can be noted that the use of the I-BEST modules produces an increase in the internal air temperature in all the areas of the housing units analyzed. This effect is due to the decrease in the thermal transmittance of the external walls after the addition of the I-BEST panels.

The assembly of the panels on the external façades allows a non-ventilated cavity, which acts as a thermal buffer between the internal and external environment, to be obtained. In fact, inside this cavity, the temperature values are higher than the external air temperature, creating a transition zone capable of mitigating heat dispersion. Fig. 6 shows the temperature trend for the coldest day (February 2), in free-floating operation. In particular, the external air temperature, the internal air temperature and the air temperature inside the cavity are displayed in the graph, with reference to a room on the ground floor.

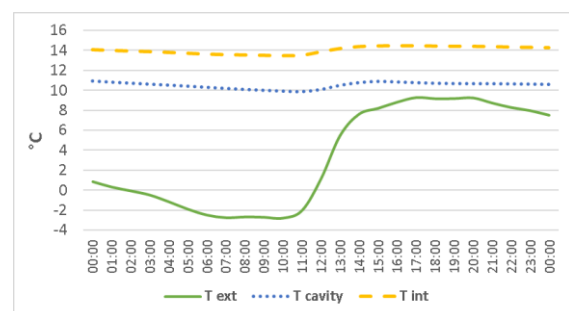


Fig. 6 – Hourly trend of the air temperature (external, internal and inside the cavity) obtained from simulation conducted in free-floating conditions for the coldest day of the year

However, the greatest potential of the I-BEST solution derives from the fact that it is an "integrated" renovation system which, in addition to improving the performance of the building envelope, allows renovation of the heating plant to be carried out easily and economically. The unvented cavity created by the installation of the double façade, in

fact, can be used to conveniently place the pipes of the heating system. Consequently, it is possible to assume the replacement of the existing heating plant consisting of gas boilers and radiators, with a more efficient system including an air-water heat pump ($SCOP=3.5$) supplying fan coils. Furthermore, this solution would also allow cooling in the summer. Thanks to the I-BEST technology, the new heating plant can be fitted quickly, without demolition work and excavations for the passage of the pipes, and without interfering with the use of the internal environment. At present, a gas supply of 11703 kWh is required. Considering the integrated restructuring of the envelope and heating plant, which involves the installation of the I-BEST system and the replacement of the boilers with an electric heat pump, electricity consumption of 2439 kWh is predicted.

To make a comparison, the energy supplied is converted into primary energy using the non-renewable primary energy conversion factors provided by the law (D. M. 26 Giugno 2015). Fig. 7 presents the monthly values of primary energy demand before and after renovation. A saving of 61 % is achieved for the heating season, with a reduction from 46.90 kWh/(m²year) to 18.15 kWh/(m²year).

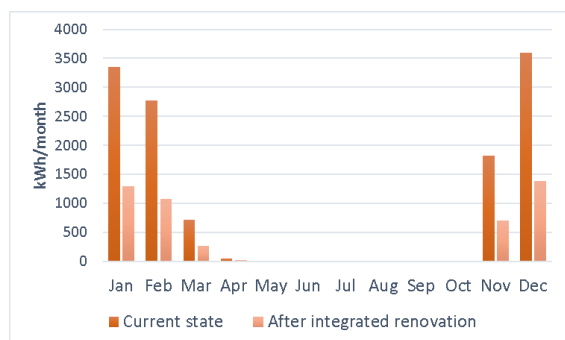


Fig. 7 – Comparison between the monthly primary energy demand for heating before and after integrated renovation, involving the installation of the I-BEST double façade and heat pump system

4. Conclusions

The analysis presented in this work concerned the evaluation using dynamic energy simulation of the energy performances offered by an innovative building renovation system, consisting of sliding

and multifunctional modular panels (I-BEST system). The proposed technology allows for the creation of a double façade by realizing a non-ventilated cavity, which can be used to set up the pipes of the plants. This makes it possible to operate an integrated renovation of the building envelope and heating system in a short time, without demolition work and reducing costs. Since the I-BEST system is designed for the combined renovation of the heating system and external walls, its affordability is particularly evident when the following conditions occur: the need to install, complete or renovate the air conditioning system; the need to place scaffolding on public land to implement the work aimed at the thermal insulation of the envelope. In the first case, it would be very expensive to operate inside the house to build the air conditioning system, as this involves the demolition and reconstruction of the tracks where the pipes pass. With reference to the second hypothesis, the municipal charges to be paid for the occupation of public land are high, and a faster operation, such as that allowed by the I-BEST system can bring significant savings.

The modular and multifunction panels confer high flexibility to the system, in terms of adaptation to different contexts and functions performed (simple cladding, thermal insulation, solar façade, and green surfaces). In particular, the analysis developed in this study focused on the evaluation of the configuration designed for thermal insulation. A building was selected as a case study and the energy saving achievable following the integrated renovation was assessed, involving the application of the I-BEST system and the replacement of the heating plant. The results showed that the use of the I-BEST double façade allows for a reduction in the heating requirement of about 14 %. The enhanced performance of the walls allows an improvement of the internal conditions with regard to the passive behaviour of the envelope to be obtained, resulting in an increase in the internal air temperature. Considering the refurbishment of the heating system through the installation of a heat pump, it is possible to achieve a saving of 61 % in terms of primary energy. Future studies will be aimed at extending the analysis to evaluate the effect of the I-BEST technology also in the cooling period and to

explore the other possible alternative configurations of the I-BEST system (solar façade and green façade). Moreover, the implementation of the system on the building selected as test-case for the research project will also allow experimental analyses to be performed.

Acknowledgement

The study was developed as part of the I-BEST (Innovative Building Envelope through Smart Technology) Research Project funded by the PON Mise (Ministry of Economic Development) - H2020 program.

Identification number F/050234/01-0-2/X32

References

- Alberto, A., N. M. M. Ramos, and R. M. S. F. Almeida. 2017. "Parametric Study of Double-Skin Façades Performance in Mild Climate Countries." *Journal of Building Engineering* 12: 87–98. doi: <https://doi.org/10.1016/j.jobee.2017.05.013>
- Alqaed, S. 2022. "Effect of Annual Solar Radiation on Simple Façade, Double-Skin Façade and Double-Skin Façade Filled with Phase Change Materials for Saving Energy." *Sustainable Energy Technologies and Assessments* 51: 101928. doi: <https://doi.org/10.1016/j.seta.2021.101928>
- Blanco, J. M., A. Buruaga, E. Rojí, J. Cuadrado, and B. Pelaz. 2016. "Energy Assessment and Optimization of Perforated Metal Sheet Double Skin Façades through Design Builder; A Case Study in Spain." *Energy and Buildings* 111: 326–36. doi: <https://doi.org/10.1016/j.enbuild.2015.11.053>
- CTI - Comitato Termotecnico Italiano <https://www.Cti2000.It/> (Accessed on 13 July 2021).
- DesignBuilder Software Ltd, DesignBuilder Version 6, (2020). <http://www.Designbuilder.Co.Uk> (accessed on 13 July 2021).
- EnergyPlus. n.d. <https://energyplus.net/> (last access on 18 January 2022).
- European Commission. EU Commission European Green Deal."
- <https://ec.europa.eu/info/strategy/priorities-2019-2024/european-green-deal/>
- European Parliament And Council. 2018. "Directive (Eu) 2018/844 of the European Parliament and of the Council of 30 May 2018 Amending Directive 2010/31/EU on the Energy Performance of Buildings and Directive 2012/27/EU on Energy Efficiency."
- Hamza, N.. 2008. "Double versus Single Skin Façades in Hot Arid Areas." *Energy and Buildings* 40(3): 240–48. doi: <https://doi.org/10.1016/j.enbuild.2007.02.025>
- Italian Government. 2015. D. M. 26 Giugno 2015 'Applicazione Delle Metodologie Di Calcolo Delle Prestazioni Energetiche e Definizione Delle Prescrizioni e Dei Requisiti Minimi Degli Edifici'.
- Jankovic, A., and F. Goia. 2021. "Impact of Double Skin Façade Constructional Features on Heat Transfer and Fluid Dynamic Behaviour." *Building and Environment* 196: 107796. doi: <https://doi.org/10.1016/j.buildenv.2021.107796>
- Jankovic, A., M. S. Siddiqui, and F. Goia. 2022. "Laboratory Testbed and Methods for Flexible Characterization of Thermal and Fluid Dynamic Behaviour of Double Skin Façades." *Building and Environment* 210: 108700. doi: <https://doi.org/10.1016/j.buildenv.2021.108700>
- Pérez, G., A. Escolà, J. R. Rosell-Polo, J. Coma, R. Arasanz, B. Marrero, L. F. Cabeza, and E. Gregorio. 2021. "3D Characterization of a Boston Ivy Double-Skin Green Building Façade Using a LiDAR System." *Building and Environment* 206. doi: <https://doi.org/10.1016/j.buildenv.2021.108320>
- Pomponi, F., P. A.E. Piroozfar, R. Southall, P. Ashton, and E. R.P. Farr. 2016. "Energy Performance of Double-Skin Façades in Temperate Climates: A Systematic Review and Meta-Analysis." *Renewable and Sustainable Energy Reviews* 54: 1525–36. doi: <https://doi.org/10.1016/j.rser.2015.10.075>
- President of the Italian Republic. 1993. D.P.R. 412/93 'Regolamento Recante La Progettazione, l'installazione, l'esercizio e La Manutenzione Degli Impianti Termici Degli Edifici Ai Fini Del Contenimento Dei Consumi Di Energia, in Attuazione Dell'art. 4, Comma 4, Della L. 9 Gennaio 1991, n. 10.'

- Shameri, M. A., M. A. Alghoul, K. Sopian, M. Fauzi M. Zain, and O. Elayeb. 2011. "Perspectives of Double Skin Façade Systems in Buildings and Energy Saving." *Renewable and Sustainable Energy Reviews* 15(3): 1468–75. doi: <https://doi.org/10.1016/j.rser.2010.10.016>
- Tao, Y., X. Fang, M. Yit Lin Chew, L. Zhang, J. Tu, and L. Shi. 2021. "Predicting Airflow in Naturally Ventilated Double-Skin Façades: Theoretical Analysis and Modelling." *Renewable Energy* 179: 1940–54. doi: <https://doi.org/10.1016/j.renene.2021.07.135>
- UNI. 2014. *UNI/TS 11300–1. Building Energy Performance – Part 1: Evaluation of the Energy Need for Space Heating and Cooling* (in Italian).
- United Nations Environment Programme. 2021. *Global Status Report for Buildings 2021*, Available at <https://Globalabc.Org/Resources/Publications/2021-Global-Status-Report-Buildings-and-Construction> (Last Access on 30/11/2021).

Modeling Occupants' Behavior to Improve the Building Performance Simulation of Classrooms

Federica Morandi – Free University of Bozen-Bolzano, Italy – federica.morandi@unibz.it

Julian Donges – Free University of Bozen-Bolzano, Italy – julian.donges@natec.unibz.it

Ilaria Pittana – IUAV University of Venice, Italy – ilaria.pittana@iuav.it

Alessandro Prada – University of Trento, Italy – alessandro.prada@unitn.it

Francesca Cappelletti – IUAV University of Venice, Italy – francesca.cappelletti@iuav.it

Andrea Gasparella – Free University of Bozen-Bolzano, Italy – andrea.gasparella@unibz.it

Abstract

Window operation in naturally ventilated classrooms is the only strategy for achieving proper air change rates. The modeling of the ventilation rate based on the window state implies knowledge of the window opening angle to evaluate the net exchange area. Nonetheless, the sensors most used to monitor window opening state are contact sensors, which allow only a binary state (i.e., open/close) to be devised. This work aims to investigate the effect that window opening information has on ventilation rates and building performance simulation by comparing the case in which window opening is described by the opening angle to the condition in which it is described as a binary I/O variable. A measurement campaign was conducted on six classrooms in a secondary school in Morlupo, Rome. Temperature, CO₂ concentration and relative humidity were monitored in the six classes, while temperature and relative humidity were monitored outdoors. During school time, a few students per class were asked to report information concerning the number of occupants and the opening state of windows and shutters on a discrete scale. From the data collected, an equivalent opening area was calculated, accounting for the combined opening of windows and shutters, being therefore representative of the net exchange area. Based on the original dataset, a second dataset was generated by considering binary window opening information both for windows and shutters. The two datasets were used, together with environmental data, to train behavioral models that were then fed into a building energy simulation model. The results of the simulations show that the simplified dataset causes an overestimation of the air changes and of the building energy need.

1. Introduction

Occupant behavior is commonly recognized as an influential factor when seeking explanations for the difference between the predicted performance of a building and its actual performance in post-occupancy conditions, the so-called performance gap (Shi et al., 2019).

Though most of the literature on occupant behavior focuses on residential and office buildings (Franceschini et al., 2022), the importance of studying people's behavior in educational buildings stems from the findings of the extensive literature regarding the role that ventilation plays in students' concentration, health, and performance (Bakó-Biró et al., 2012; Haverinen-Shaughnessy et al., 2015).

The drivers for human interaction with the envelope should be sought in a multi-domain approach. For instance, operating the shutters might be a consequence of glare or of direct solar radiation, and window operation might be triggered by air quality concerns, thermal comfort, or noise protection (Delzendeh et al., 2017). However, the drivers that are mostly used in occupant behavior modeling relate to the thermal and indoor air quality domains (Dai et al., 2020).

The interaction between occupants and the envelope is particularly relevant in naturally ventilated buildings, where window operation directly impacts on ventilation rates and, consequently, on indoor temperature, air quality, and finally on the building energy demand. In such buildings, the ventilation rate can be estimated from the indoor

and outdoor environmental conditions and the net exchange area (EN 16798), which can be derived by the combined state of windows and shutters.

Many sensors and technologies are available to detect the window state. The ones that are most often deployed, which are relatively cheap and require low implementation effort, are contact sensors, which report a binary status (Belafi et al., 2018; Naspi et al., 2018; Park et al., 2019). Nonetheless, monitoring the opening angle besides the state might be relevant, as different opening angles determine different net exchange areas. Window opening angle can be monitored, among other methods, using accelerometers (Andersen et al., 2013), by implementing image recognition algorithms (Sun et al., 2022), or assessed through the administration of questionnaires (Kim et al., 2019).

2. Aim And Method

In this paper, a naturally ventilated school building is used as a case study to develop behavioral models devoted to window opening to be used in building performance simulations. In particular, the focus is on the impact of detailed models able to predict the window opening angle as opposed to simpler binary models. The research question is: **To which extent does detailed information on window state affect the building energy demand compared to an I/O information?**

The methodology adopted to address such question can be summarized by the following steps:

1. **Collection of experimental data.** A measurement campaign was carried out in six classrooms of a high school in Morlupo, Rome. Environmental parameters were monitored and detailed information on the state of windows and roller shutters was reported by the students.
2. **Modeling occupant behaviour.** Data were pre-processed by calculating an equivalent opening area that takes into consideration the opening of the sashes and of the roller shutters. Then, a second dataset was created by attributing a binary status to sashes and shutters, i.e., simulating the dataset that would have been collected if contact sensors were used.

Two behavioral models were trained on the two datasets based on classification trees, algorithms that split the data into branches based on impurity criteria and assign, following the tree-like structure built upon predictor variables, the probability of falling within a specific class of the response variable.

3. **Simulation of building performance.** Energy modeling of a reference building was carried out using the two different behavioral models to evaluate the effects of window state information on the ventilation rate, and the overall energy performance.

In the analysis proposed, only thermal and indoor air quality environmental variables are accounted for (air temperature, relative humidity, and CO₂ concentration), as these can be predicted by means of building energy simulations.

3. The Measurement Campaign

The measurement campaign took place between January and May 2022, for a total of 17 weeks. Six classrooms were involved in the reporting activities. Students participated in a training program organized jointly by the universities involved in the project and the high school.

The layout of the monitored classrooms is depicted in Fig. 1 and Fig. 2. The floor surface of each classroom is 50 m² approx. Classrooms are equipped with three two-sash windows and roller shutters.

The indoor environmental conditions were monitored using HoBO MX 1102 loggers (T, RH, CO₂ concentration), which were fixed on the walls, while outdoor conditions were monitored using a HOBO U23-001A data logger (T, RH). Data acquisition was carried out with a 10-min time resolution. During the lecture, students were provided with printed spreadsheets in which they were asked to write down the condition of the room and the time at which any change in state occurred. The parameters that were monitored are:

- State of each window sash (0-0.5-1)
- State of each shutter (0-0.25-0.5-0.75-1)
- State of the door (0-1)
- Number of people in the classroom
- State of the lights (0-0.5-1).

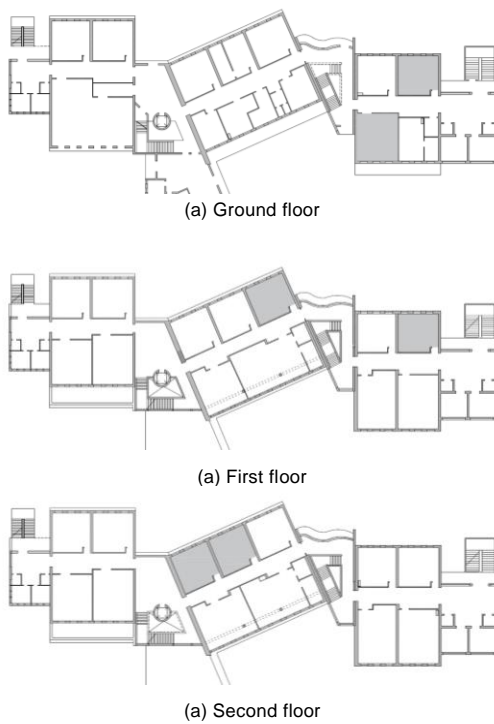


Fig. 1 – Floor plans of the IIS "Margherita Hack" in Morlupo, Rome, with indication of the classrooms involved in the project (in gray color)



Fig. 2 – Internal view of one of the classrooms that participated in the project

Fig. 3 represents the physical meaning attributed to the values that represent the state of windows and shutters. Besides the state of these elements, students also had to report the motivation that led to the interaction with the environment, by choosing from a set of pre-determined questions, and to indicate whether the request for change came from a student or from the teacher.

Each classroom managed the organization of the data collection in a different manner. Students built shifts so that each component (e.g., windows,

lights, shutters, etc) was controlled by one person at a time, to ease the work and not to distract them

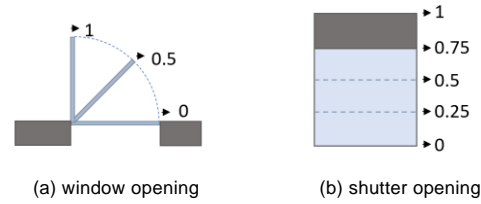


Fig. 3 – Options available for the reporting of sashes (a) and shutters (b) status

too much from their lesson.

After these paper-based sheets were collected, they were transferred to a digital archive in which the state was reported per each time step at which an environmental measure was available, i.e., every other 10 minutes.

4. Results

4.1 Data Pre-Processing

Data were filtered by presence, to exclude data that referred to unoccupied periods from the evaluation. Only complete datasets were included in this analysis, i.e., data was excluded from the selection, when even just the state of one sash was not reported.

Starting from the information on window and shutters status, an equivalent opening area was calculated by computing, for each window, the average opening of the two sashes and by multiplying that value by the opening of the shutter. In this manner, a situation in which window sashes are open and the shutter is closed would be represented by a null equivalent opening area. This dataset will be referred to in the following as "case 1".

From the original dataset, another equivalent opening area was calculated by considering that window sashes and shutters could only assume 1/0 values. In the case of windows, values of 0.5 were then converted into 1, while in the case of shutters, values of 0.25-0.5 and 0.75 were converted into 1. Then, the equivalent opening area was calculated again, following the procedure described above. This second dataset, referred to in the following as "case 2", is characterized by a less continuous distribution of values.

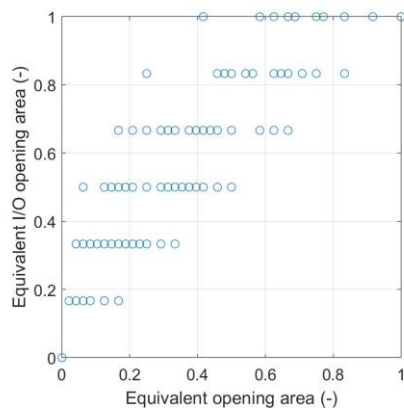


Fig. 4 – Equivalent opening areas calculated from the original dataset (case 1, x-axis) and from the modified dataset (case 2, y-axis)

The scatter plot of the equivalent opening areas calculated for case 1 and case 2 is reported in Fig. 4. The levels of equivalent opening area that are determined by the 1/0 discretization are clearly visible. As expected, in case 2 the equivalent opening area is much larger compared with the actual opening area.

4.2 Modeling Occupant Behavior

The two pre-processed datasets were then used to train behavioral models based on decision trees. To improve prediction accuracy, bagged tree classifiers were used. The equivalent opening area, binned at 25 % intervals, was assumed as the response variable, and the following predictors were used as input variables: indoor temperature, relative humidity and CO₂ concentration, outdoor temperature, and relative humidity. It is specified that the classes are very unbalanced, with a great number of occurrences related to the “closed” condition (0), and that no occurrence is found at fully open (1). This relates to the way the equivalent opening area is defined, as it is a multiplication between average opening of the window and of the shutters (which are hardly ever totally closed).

The importance of the predictors in estimating the models is reported in Fig. 5. The outdoor temperature has significant impact on both models, followed by indoor temperature and relative humidity. Outdoor humidity ranks the lowest predictor in terms of importance.

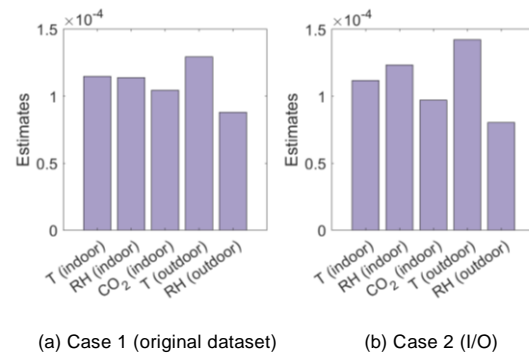


Fig. 5 – Importance of the predictors of the behavioral models

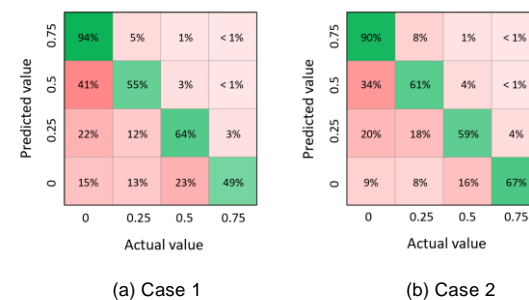


Fig. 6 – Confusion matrices of the behavioral models trained

The accuracy of the models is 81.9 % and 76.5 % for case 1 (original dataset) and case 2 (I/O dataset), respectively. The confusion matrices of the two trained models are reported in Fig. 6. Green diagonals show that most of the classes are correctly identified.

The relevant share of incorrect classifications displayed in the lower left part of the diagrams indicates a tendency of both models to underestimate the equivalent opening area.

4.3 Building Performance Simulations

The trained models were nested in the energy simulation of a school building located in Milan. The building consisted of two classrooms with a total surface of 100 m² and 3 m high, recalling the dimensions of the classrooms in which the training dataset was collected.

The typical reference year developed in (Pernigotto et al., 2014) was used. By looping TRNSYS with Matlab, the decision tree was used as a black box that, for each time step, would read the values of the predictors (i.e., indoor temperature, relative humidity and CO₂ concentration, and the outdoor temperature and relative humidity) and attribute a class to the response variable (i.e., equivalent open-

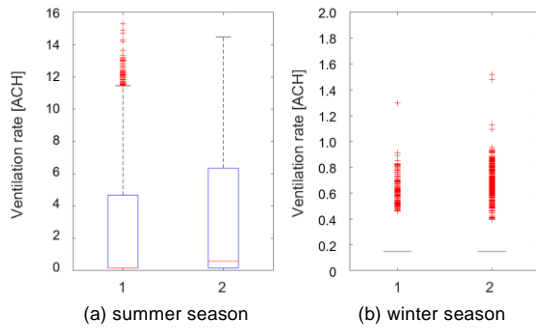


Fig. 7 – Ventilation rate in the summer (a) and winter (b) season for case 1 and case 2

ing area) based on a probabilistic approach. The information on window opening area was then used to estimate the ventilation rate based on the EN 16798 approach. A constant infiltration rate of 0.15 ACH was assumed in addition to natural ventilation to determine the overall air change rate.

All building characteristics were left unvaried in the two models (e.g., occupancy profiles, envelope characteristics, outdoor climate, etc), the different results generated by the twin simulations solely ascribable to the behavioral model called.

Fig. 7 provides a qualitative overview of the seasonal Air Changes per Hour (ACH) returned by the simulations. In the heating season (15th October-15th April), ventilation is governed by infiltration (almost no window opening). In summer, conversely, higher ventilation rates are predicted and differences among the two models arise – the number of air changes per hour being sensitively greater for case 2.

By summing up the ACH on a seasonal basis for case 1 and case 2 (Fig. 8), data displays a difference in ACH of 33 % in the summer season and a difference of 13 % in the winter season - case 2 leading to an overestimation of the ventilation rate in both cases.

Since air change rate related to infiltration is known (0.15 ACH), by data filtering it is possible to distinguish when the air change is related to infiltration or to window operation. These data are presented in Fig. 9, where the number of times in which ventilation could be attributed to infiltration or ventilation is represented as a percentage related to all observations. In case 2 (I/O opening), ventilation is generally triggered by window opening for a greater number of times compared to case 1.

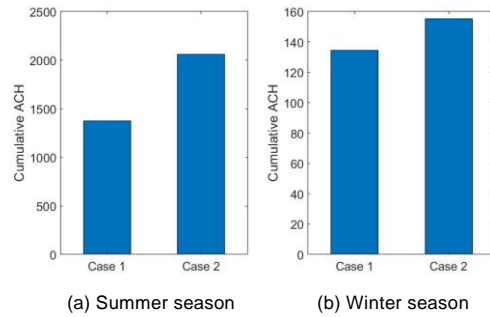


Fig. 8 – Cumulative ACH calculated over the summer (a) and winter (b) season for case 1 and case 2

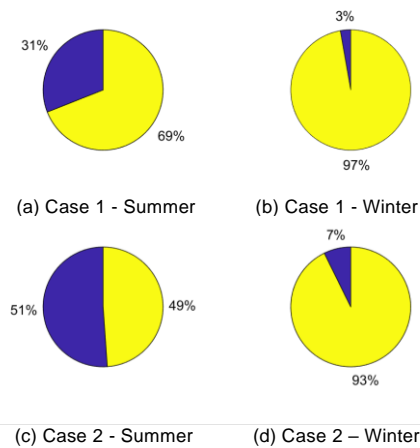


Fig. 9 – Share of ventilation rates occurrences related to window opening (in purple) and to infiltration (in yellow)

This effect is magnified in the summer season (51 % of occurrences related to window opening in case 2 vs 31 % in case 1).

This qualitative analysis might suffer from a bias related to the effectiveness of the window operation in the two models: in case 2, does the model predict fewer window openings because the air exchange is more effective?

The different estimates in ventilation rates affect the energy performance of the building. The energy demand in the winter season in case 1 corresponds to 1.93 MWh, while in case 2 it is 2.04 MWh, therefore indicating a 5 % increase in energy demand for case 2 in relation to case 1.

5. Discussion

The analysis carried out so far shows that there is a sensitive variation in the estimate of the air change rate when the actual window opening angle is

used. In relation to the individual steps of the method proposed, some points call for further comments:

- **Experiment bound.** Occupant behavior should be dealt with as a multi-domain-driven mechanism, as multiple factors contribute to determining the interaction of individuals with the envelope. In the present study, the environmental parameters considered refer to the thermal and air quality comfort domains, through the measurement of indoor and outdoor temperature and relative humidity, and indoor CO₂ concentration. This choice was made based on the consideration that these are the features that can be controlled in building performance simulations. Multi-domain simulation would allow for a proper integration of factors.
- **Data collection.** The information of window status was reported by students and is therefore subject to accuracy issues. Errors in reporting the window and shutter states should be random (one might forget to report a window opening as well as a window closing), and therefore it might contribute to the data noisiness. In any case, this should not affect the outcome of the present study, as a comparison is proposed between the two subsets, one of which is generated based on the other. Conversely, the accuracy of data reporting might affect the accuracy of the behavioral models trained. For this reason, some of the classrooms analyzed in the present study were equipped with a device to monitor the window opening angle; data will be used in further work to test the reliability of the data reported by students.
- **Behavioral models.** The behavioral models trained show high accuracy (82 % and 76 %, respectively), but the share of false negatives is not homogeneous among classes and shows a tendency of both models to underestimate the equivalent exchange area. That might be related to the fact that samples are unbalanced. Furthermore, an extension of the original dataset both in terms of monitored states and of environmental conditions would improve the model accuracy.

- **Building performance simulation.** The results of building performance simulations show a sensitive decrease in ventilation rate when actual opening angles are considered. For the case study analyzed, this translates into an underestimate of building energy consumption by 5 %. The magnitude of this effect might be biased by building, weather and systems-related factors and will be addressed in future work.

6. Conclusion

The research aimed at understanding the impact that window opening modeling has on energy performance simulation. An experimental campaign was carried out in which environmental parameters and the detailed states of windows and shutters were monitored. Two behavioral models were trained to account for I/O opening information and the discrete dataset.

Energy performance simulations show that ventilation rate is strongly affected by the detail with which the window opening information is provided. A I/O discretization would, in general, lead to an overestimate of the ventilation rate and of the overall energy demand of the building.

Future work will concern the improvement of behavioral models, the evaluation of the uncertainty brought by behavioral models into energy simulation, the evaluation of the reliability of the data reported by the students, and the inclusion of monitoring parameters affecting the other domains of comfort as drivers for the window opening.

Acknowledgement

The authors thankfully acknowledge Davide Michetti, Sonia Sgavicchia and Silvia D'Isidoro for their support for the project, Eleonora Righi for her support in the management of the experimental data of the monitoring campaign, and the students of Margherita Hack High School in Morlupo (classes 2D, 3B, 3C, 3D, 4A, 4B) for their active participation and dedication to the project.

References

- Andersen, R., V. Fabi, J. Toftum, S. P. Corngnati, and B. W. Olesen. 2013. "Window opening behaviour modelled from measurements in Danish dwellings." *Building and Environment* 69: 101-113. doi: <https://doi.org/10.1016/j.buildenv.2013.07.005>
- Bakó-Biró, Zs., D. J. Clements-Croome, N. Kochhar, H. B. Awbi, and M. J. Williams. 2012. "Ventilation rates in schools and pupils' performance." *Building and Environment* 48: 215-223. doi: <https://doi.org/10.1016/j.buildenv.2011.08.018>
- Belafi, Z. D., F. Naspi, M. Arnesano, A. Reith and G. M. Revel. 2018. "Investigation on window opening and closing behavior in schools through measurements and surveys: A case study in Budapest." *Building and Environment* 143:523–531. doi: <https://doi.org/10.1016/j.buildenv.2018.07.022>
- CEN. 2017. EN 16798-7:2017. *Energy performance of buildings - Ventilation for buildings - Part 7: Calculation methods for the determination of air flow rates in buildings including infiltration*. CEN, Brussels, 2017.
- Dai, X., J. Liu, and X. Zhang. 2020. "A review of studies applying machine learning models to predict occupancy and window-opening behaviours in smart buildings." *Energy and Buildings* 223: 110159. doi: <https://doi.org/10.1016/j.enbuild.2020.110159>
- Delzendeh, E., S. Wu, A. Lee, and Y. Zhou. 2017. "The impact of occupants' behaviours on building energy analysis: A research review." *Renewable and Sustainable Energy Reviews* 80: 1061-1071. doi: <https://doi.org/10.1016/j.rser.2017.05.264>
- Franceschini, P. B., and L. Oliveira Neves. 2022. "A critical review on occupant behaviour modelling for building performance simulation of naturally ventilated school buildings and potential changes due to the COVID-19 pandemic." *Energy and Buildings* 258: 111831. doi: <https://doi.org/10.1016/j.enbuild.2022.111831>
- Haverinen-Shaughnessy, U., R. J. Shaughnessy, E. C. Cole, O. Toyinbo, D. J. Moschandreas, 2015. "An assessment of indoor environmental quality in schools and its association with health and performance." *Building and Environment* 93(1): 35-40. doi: <https://doi.org/10.1016/j.buildenv.2015.03.006>
- Kim, A., S. Wang, J. E. Kim, and D. Reed. 2019. "Indoor/outdoor environmental parameters and window-opening behavior: A structural equation modeling analysis." *Buildings* 9:94. doi: <https://doi.org/10.3390/buildings9040094>
- MATLAB(R2019a). Natick, Massachusetts: The MathWorks Inc.
- Naspi, F., M. Arnesano, L. Zampetti, F. Stazi, G. M. Revel and M. D'Orazio. 2018. "Experimental study on occupants' interaction with windows and lights in Mediterranean offices during the non-heating season." *Building and Environment* 127: 221–238. doi: <https://doi.org/10.1016/j.buildenv.2017.11.009>
- Park, J., and C. S. Choi. 2019. "Modeling occupant behavior of the manual control of windows in residential buildings." *Indoor Air* 29(2): 242–251. doi: <https://doi.org/10.1111/ina.12522>
- Pernigotto, G., A. Prada, D. Cóstola, A. Gasparella, J. L. M. Hensen. 2014. "Multi-year and reference year weather data for building energy labelling in north Italy climates." *Energy and Buildings* 72: 62–72. doi: <https://doi.org/10.1016/j.enbuild.2013.12.012>
- Shi, X., B. Si, J. Zhao, Z. Tian, C. Wang, X. Jin, and X. Zhou. 2019. "Magnitude, Causes, and Solutions of the Performance Gap of Buildings: A Review." *Sustainability* 11: 937. doi: <https://doi.org/10.3390/su11030937>
- Sun, C., X. Guo, T. Zhao, and Y. Han. 2022. "Real-time detection method of window opening behavior using deep learning-based image recognition in severe cold regions." *Energy and Buildings* 268: 112196. doi: <https://doi.org/10.1016/j.enbuild.2022.112196>
- TRNSYS 18.02, Solar energy laboratory. A transient systems simulation program.

Modeling and Measurements in Natural Ventilation of Massive Buildings: A Case Study

Francesco Asdrubali – Roma Tre University, Italy – francesco.asdrubali@uniroma3.it

Luca Evangelisti – Roma Tre University, Italy – luca.evangelisti@uniroma3.it

Claudia Guattari – Roma Tre University, Italy – claudia.guattari@uniroma3.it

Marta Roncone – Roma Tre University, Italy – marta.roncone@uniroma3.it

Lucia Fontana – Roma Tre University, Italy – lucia.fontana@uniroma3.it

Ginevra Salerno – Roma Tre University, Italy – ginevra.salerno@uniroma3.it

Chiara Tonelli – Roma Tre University, Italy – chiara.tonelli@uniroma3.it

Valeria Vitale – Roma Tre University, Italy – valeria.vitale@uniroma3.it

Abstract

Numerical simulations are widely used to evaluate the thermal comfort and energy savings in the retrofit of historic buildings. In most cases, however, no detailed data are available on the materials and stratigraphy of the building envelopes, and on-site measurements can be expensive and time consuming.

The present work uses as a case study a university building characterized by a high thermal capacity in the city of Rome to verify whether the use of natural ventilation can be a practice of use in order to guarantee energy saving and natural comfort.

To this end, in the summer of 2020, an experimental campaign was carried out aimed at acquiring thermofluidometric measurements through the vertical walls, the air temperature inside and outside the analyzed environment and the air velocity. Measurements were conducted under three different usage protocols, including night ventilation and 24-hour continuous ventilation.

These measurements made it possible to identify the thermophysical characteristics of a wall considered "equivalent" to the real wall, allowing the realization of thermofluidodynamic computational models. In particular, in the study, 3 different stratigraphies were considered and compared, corresponding in the first case to the equivalent wall, in the second to that available from the Comsol software library, and, finally, in the third and last case, from literature data (Tabula project) for the building typology analyzed.

From the analysis, it emerged that the 3 groups of parameters do not have a significant impact in terms of variation of internal comfort, confirming the reliability of the use of the literature values for these types of modeling.

1. Introduction

Several findings in the literature highlight the significance of the aspects related to the indoor climatic control and the energy efficiency of historical buildings (Bay et al., 2016).

Natural ventilation of buildings is a good practice for the air quality of living and working environments and the well-being of the occupants. One of the significant effects of an adequate air change is the contribution given to the reduction of gas levels in buildings. The systems that are usually applied in heritage buildings are forced air coils and radiators based on hot water, since the initial investment is quite low compared with other solutions, and they have a short response time to cool/heat large volumes of indoor air. These two plant typologies adapt very well to the specific occupancy patterns and can be employed either discontinuously, targeting occupant thermal comfort satisfaction for a brief period of time, or uninterruptedly, to maintain constant hygrothermal conditions benefitting from the building's thermal mass (Bay et al. 2016; Bencs et al., 2007; Bratasz et al., 2007).

In buildings which are not designed to guarantee an adequate number of air changes, the ventilation obtained through the opening of windows does not allow high indoor thermal comfort level to be maintained, which inevitably returns within a few hours to levels similar to those present before ventilation.

An alternative to the ventilation obtained by simply opening windows can be obtained by equipping the building with an active ventilation system, obtained by means of ducts and aspirators that ensure an exchange of air between the external and internal environment.

This system guarantees greater continuity in the ventilation of the environment, not being linked to manual intervention, and can be carried out uninterrupted or cadenced over 24 hours, limiting the inconvenience of not being able to be used in the presence of wind. However, it should be emphasized that the use of active ventilation must be suitably sized, in order to avoid possible negative effects of a different nature.

In the presence of natural ventilation and high thermal masses, the use of passive and hybrid strategies based on natural ventilation and nocturnal thermal mass precooling can be crucial in terms of internal comfort and energy saving.

The aim of this work, taking as a case study a university building characterized by a high thermal capacity in the city of Rome, is to show the potential of CFD numerical models for quantifying the cooling effects and internal thermal comfort, analyzing different sets of thermophysical parameters assigned to the high thermal mass walls.

2. Material And Methods

This work presents a 2D model of Pavilion 2B (Fig. 1) of the *Ex-Mattatoio* (former abattoir) (Ersch, 1891) in Rome, built using Computational Fluid Dynamics (CFD) software based on the finite element method (FEM). The transient simulations, as explained in a previous work (Vitale & Salerno, 2017), take the temporal variations and the interactions between internal and external thermal conditions into account, with the aim of evaluating different usage profiles and estimating the effects of

passive cooling in the presence of natural ventilation and high thermal masses.

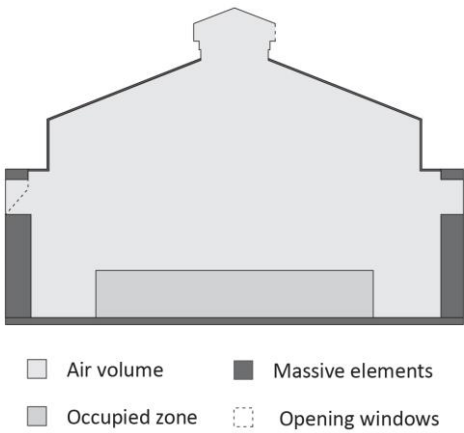


Fig. 1 – Cross section of the Pavilion 2B

The simulations were set up according to the following criteria:

- considering the variations in external conditions (temperature and solar radiation);
- without the use of HVAC systems;
- without occupancy load.

All simulations were carried out in three different usage profiles:

- with nocturnal and diurnal ventilation (24hV);
- with only nocturnal ventilation (10hV);
- without natural ventilation (Nov).

In addition to the three usage profiles, a parametric study was conducted using in each simulation three different sets of thermophysical parameters assigned for the wall (Table 1), determined as follows:

- COM: values from COMSOL Multiphysics library and literature (old simulations);
- SOS: values calculated with measured data and equivalent wall model;
- TAB: values from Tabula library, a report on Italian Building Typology realized by Turin Polytechnic as part of a European project and including the thermophysical characteristics of the most common building types in Italy from the 20th century onwards (Tabula project).

Table 1 – Thermophysical properties of the walls used for the simulations

Set	Thermal conductivity λ	Heat capacity c	Density ρ
Unit	[W/(m·K)]	[J/(kg·K)]	[kg/m ³]
COM	0,81	1512	1800
SOS	0,68	1200	2200
TAB	0,64	840	1681

In particular, Figs. 2 and 3 illustrate the plan of the pavilion selected for the experimentation (Fig. 2) and the measurement scheme of the instruments used for the acquisition of experimental data in the study room (Fig. 3) (Insula Architettura e Ingegneria), respectively.

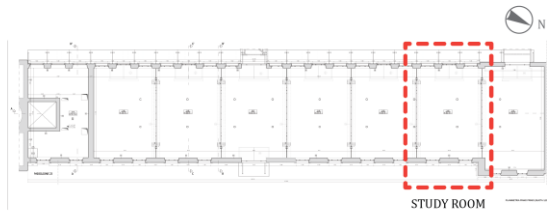


Fig. 2 – Plan of the pavilion analyzed with the delimitation of the study room

The experimental campaign took place in summer, in the period from 28 July 2020 to 7 September 2020, with the aim of acquiring data on the surface temperatures inside and outside the study wall, the heat flow through the wall, the temperatures of the air both inside and outside the study room, at the speed of the internal air (by placing a microclimatic control unit in the central position of the study room), and finally the surface temperature of the floor in the area near the microclimatic control unit. The uncertainty related to the measurement performed on the case study is equal to $\pm 10\%$ (Evangelisti et al., 2022).

The data recorded allowed the study room to be characterized from a thermal point of view and made it possible to evaluate the equivalent thermal properties of the multilayer wall under study by coupling the simulations conducted with COMSOL Multiphysics software (COMSOL) on the experimental measurements (Evangelisti et al., 2022). By

assimilating the multilayer wall to an "equivalent homogeneous wall" (Evangelisti et al., 2018.), thanks to a methodology already applied in several literature studies, its "equivalent thermophysical properties" were determined, thus obtaining a further set of data called "SOS" (Evangelisti et al., 2018; Gori et al., 2016).

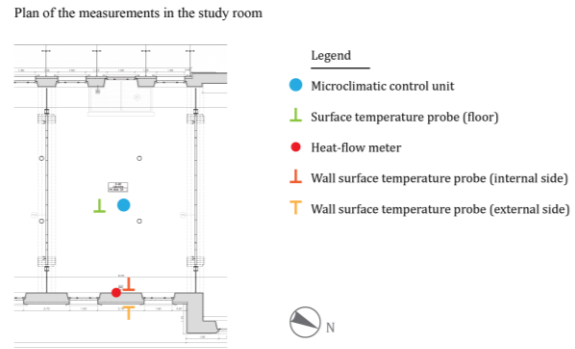


Fig. 3 – Plan of the study room with the measurement scheme of the instruments used in the experimental campaign

The main objective of this work is to show the potential of CFD numerical models for quantifying the incidence of different thermophysical characteristics on internal thermal comfort conditions in buildings with high inertia wall in different natural ventilation scenarios.

Figs. 4 and 5 show the air temperature trend (considering the average in the potentially occupied zone), the mean radiant temperature and the operative temperature for the three thermophysical sets with nocturnal and diurnal ventilation (24hV).

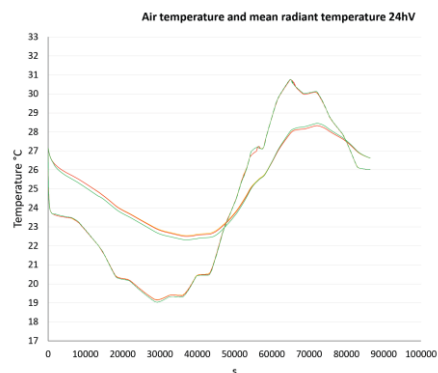


Fig. 4 – Air temperature and mean radiant temperature with diurnal and nocturnal ventilation (24hV)

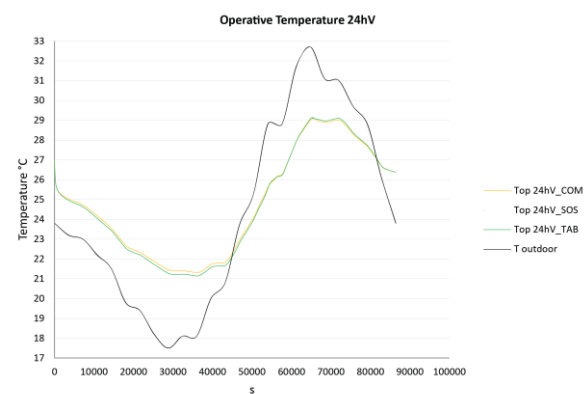


Fig. 5 – Operative temperature with diurnal and nocturnal ventilation (24hV)

In Figs. 6 and 7, the results for the three thermo-physical sets with only nocturnal ventilation (10hV) are shown.

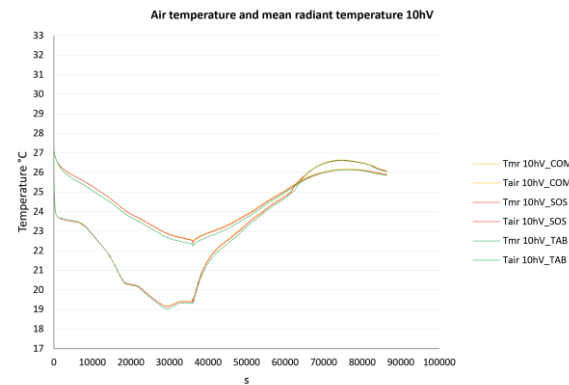


Fig. 6 – Air temperature and mean radiant temperature with only nocturnal ventilation (10hV)

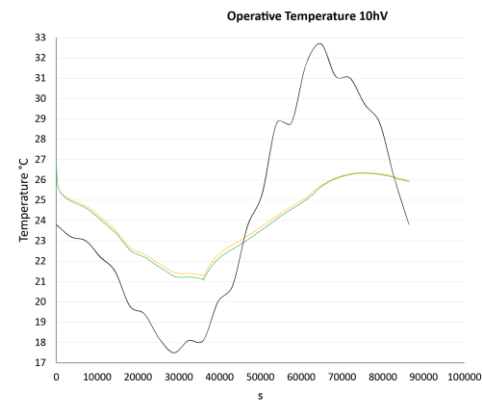


Fig. 7 – Operative temperature with only nocturnal ventilation (10hV)

In Figs. 8 and 9, the results for the three thermo-physical sets without ventilation (NoV) are shown.

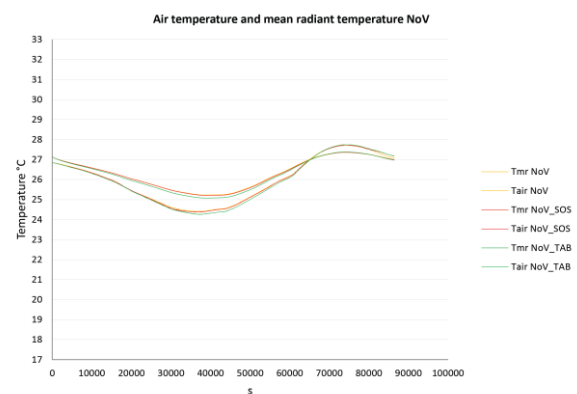


Fig. 8 – Air temperature and mean radiant temperature without ventilation (NoV)

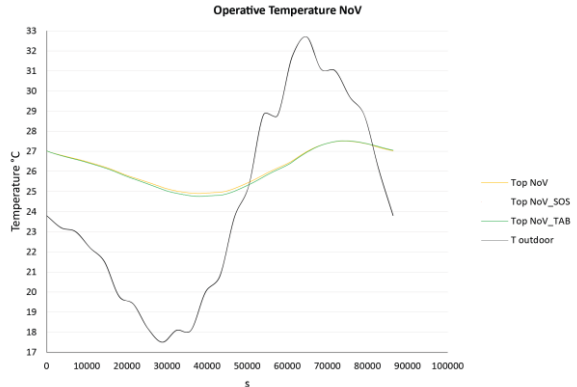


Fig. 9 – Operative temperature without ventilation (NoV)

Finally, Figs. 10, 11 and 12 show, for each ventilation scenario, the differences found between the results of the simulations, using the three sets of thermophysical parameters. The figures show the maximum, minimum and average difference of the mean radiant temperature (Tmr), the air temperature in the potentially occupied zone (Tair), and the operative temperature (Top).

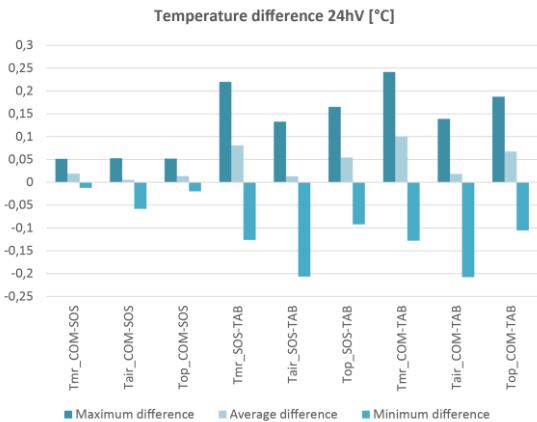


Fig. 10 – Temperature difference between thermophysical parameters sets with diurnal and nocturnal ventilation (24hV)

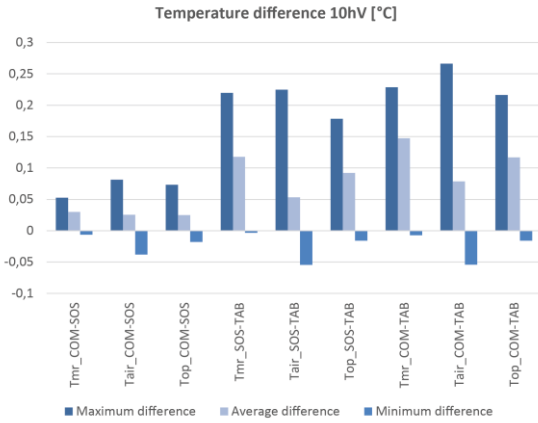


Fig. 11 – Temperature difference with only nocturnal ventilation (10hV)

By comparing temperature differences, we deduce that, in the three cases, although the parameter sets are different, their impact on internal condition is not so incisive.

It is interesting to note that the COM and SOS sets have more similar trends than the TAB set. Since the COM and SOS sets have more similar values of heat capacity while the SOS and TAB sets have more similar values of conductivity, it can be deduced that, in buildings with high thermal inertia under natural ventilation scenarios, the heat capacity value of the walls has a greater impact, in terms of internal comfort, than the thermal conductivity.

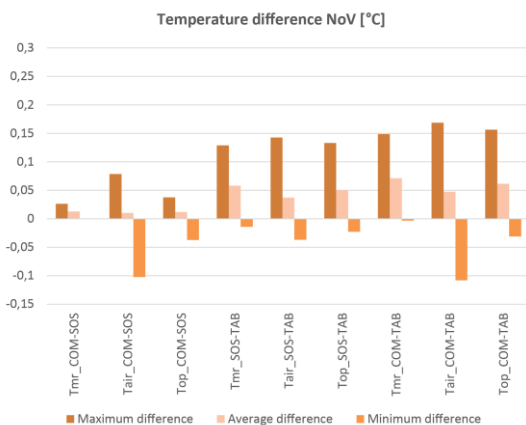


Fig. 12 – Temperature difference without ventilation (NoV)

This concept is reinforced by the fact that the NoV profile (without ventilation) is the one that reports the lowest differences between the three sets of thermophysical parameters.

3. Conclusions

In buildings characterized by high thermal masses, employing passive and hybrid strategies based on natural ventilation and nocturnal thermal mass precooling can be a critical issue for internal comfort and energy saving. With the aim of verifying whether the use of natural ventilation can be a practice of use to achieve energy saving and natural comfort, this work took a university building (in the city of Rome) characterized by high thermal capacity as a case study.

Different CFD numerical models were carried out to quantify the cooling effects and internal thermal comfort of different thermophysical parameters assigned to the walls and different natural ventilation scenarios (both nocturnal and diurnal).

It is worth noting that, when comparing the temperature differences among the three cases analyzed, although they have different thermophysical parameters, their impact on internal condition is not significant. Starting from the characteristics of the parameters sets considered, it can be observed that the internal comfort of buildings characterized by high thermal inertia, under natural ventilation conditions, are more influenced by the heat capacity value than by the thermal conductivity.

References

- Bay, E., A. Martínez-Molina, I. Tort-Ausina, S. Cho, and J. L. Vivancos. 2016. "Energy Efficiency and Thermal Comfort in Historic Buildings: A Review". *Energy and Buildings* 61: 70-85. doi: <https://doi.org/10.1016/j.rser.2016.03.018>
- Bencs, L., Z. Spolnik, D. Limpens-Neilen, H. L. Schellen, B. A. H. G. Jütte, and R. Van Grieken. 2007. "Comparison of hot-air and low-radiant pews heating systems on the distribution and transport of gaseous air pollutants in the mountain church of Rocca Pietore from artwork conservation points of view". *Journal of Cultural Heritage* 8: 264-271. doi: <https://doi.org/10.1016/j.culher.2007.05.001>
- Bratasz, Ł., R. Kozłowski, D. Camuffo, and E. Pagan. 2007. "Impact of indoor heating on painted wood monitoring the altar piece in the

- church of santa maria Maddalena in rocca pietore, Italy". *Studies in Conservation* 52(3): 199–210. doi: <https://doi.org/10.1179/sic.2007.52.3.199>
- COMSOL, Multiphysics 4.4, <http://www.comsol.com>
- Ersoch, G. *Roma: il mattatoio e mercato del bestiame costruiti dal comune negli anni 1888-1891: descrizione e disegni, con progetto e direzione di Gioacchino Ersoch, Roma, 1891.*
- Evangelisti, L., R. De Lieto Vollaro, and F. Asdrubali. 2022. "On the equivalent thermo-physical properties for modeling building walls with unknown stratigraphy". *Energy* 238: 121679. doi: <https://doi.org/10.1016/j.energy.2021.121679>
- Evangelisti, L., C. Guattari, and F. Asdrubali. 2018. "Influence of heating systems on thermal transmittance evaluations: Simulations, experimental measurements and data post-processing". *Energy and Buildings* 168: 180-190. doi: <https://doi.org/10.1016/j.enbuild.2018.03.032>
- Evangelisti, L., C. Guattari, P. Gori, and F. Asdrubali. 2018. "Assessment of equivalent thermal properties of multilayer building walls coupling simulations and experimental measurements". *Building and Environment* 127: 77–85. doi: <https://doi.org/10.1016/j.buildenv.2017.10.038>
- Evangelisti, L., A. Scorza, R. De Lieto Vollaro, and S. A. Sciuto. 2022. "Comparison between Heat Flow Meter (HFM) and Thermometric (THM) Method for Building Wall Thermal Characterization: Latest Advances and Critical Review". *Sustainability* 14(2): 693. doi: <https://doi.org/10.3390/su14020693>
- Gori, P., C. Guattari, L. Evangelisti, and F. Asdrubali. 2016. "Design criteria for improving insulation effectiveness of multilayer walls". *International Journal of Heat and Mass Transfer* 103: 349 – 3591. doi: <https://doi.org/10.1016/j.ijheatmasstransfer.2016.07.077>
- Insula Architettura e Ingegneria, "Ex-Mattatoio al Testaccio, Roma, riconversione del Padiglione 2B in aulee universitarie", The Plan Webzine - Search engine for architecture. Available at: <http://www.theplan.it/webzine/architettura-italiana/ex-mattatoio-al-testaccio-roma>
- Tabula, https://episcopo.eu/fileadmin/tabula/public/docs/brochure/IT_TABULA_TypologyBrochure
- Vitale, V., and G. Salerno. 2017. "A numerical prediction of the passive cooling effects on thermal comfort for a historical building in Rome". *Energy and Buildings* 157: 1-10. doi: <https://doi.org/10.1016/j.enbuild.2017.06.049>

Calibration of the Energy Simulation Model of a Library with a Meta-Model-Based Optimization Approach

Maja Danovska – University of Trento, Italy – maja.danovska@unitn.it

Alessandro Prada – University of Trento, Italy – alessandro.prada@unitn.it

Paolo Baggio – University of Trento, Italy – paolo.baggio@unitn.it

Abstract

Building simulations play a fundamental role both in applications like the design of new constructions and the optimization of building operation and control. This is quite relevant in the current energy framework, in which the energy consumption of buildings has increased over past decades. The reliability of the results' model does not depend only on the model itself, like the mathematical expression or the resolution process, but it is also related to the uncertainty that those parameters involve. This can cause discrepancies between the simulated and the real behavior of the building, causing a deviation from the expected one of the performance of a building. Hence, the calibration procedure of the model is a necessary process which allows more accurate results to be obtained and predictions that are closer to the real behavior of the building to be made, minimizing the discrepancy between predicted and actual performance by changing the values of the simulation parameters. When it comes to calibration of simulation models, many approaches are available in the literature, comprising manual and iterative ones, graphic comparative procedures, techniques based on specific tests, and many others. Among all possible approaches, optimization-based calibration is the most widely adopted in model calibration. However, this approach, which is usually based on evolutionary algorithms, has the disadvantage that it requires many expensive simulations to be run, especially when the number of parameters to be calibrated is high. This issue can be overcome by a preliminary sensitivity analysis that reduces the number of parameters to be calibrated and by an efficient optimization algorithm. For this reason, this work proposes a framework based on a sensitivity analysis designed to identify the most significant parameters separately on the energy budgets and other monitored environmental variables. The proposed calibration procedure is based on functional approximation models, which greatly increases the efficiency of the

optimization algorithm. The case study is a university library placed in the municipality of Trento, Italy. The building was monitored in terms of indoor carbon dioxide, indoor temperature, and relative humidity. Results show how successful the proposed approach is in reducing the computational time required for calibration, especially when considering models with a high degree of complexity.

1. Introduction

Energy demand from buildings is still considered a significant share of the global energy consumptions, i.e., 36 % of the total energy demand (Santamouris & Vasilakopoulou, 2021). This means that measures in this sector must be taken to considerably reduce overall energy consumption. In this context, dynamic simulations of buildings are an extremely powerful tool, which can help in achieving such goals, not only from the point of view of assessing the energy efficiency of new constructions, but also for optimizing building operation and control. Nevertheless, dynamic and detailed models require a high number of both input data and parameters for describing the whole system. As reviewed by Chong et al. (2021), the building model requires input data which describe the physical model. If not directly measured or known, as in the case of new constructions, parameters must be assumed by the user. This assumption procedure brings uncertainty that has an unavoidable impact on the simulation output. Authors such as Karlsson et al. (2007), Scofield (2009) and Turner & Frankel (2008) reported how simulation results can differ significantly from monitored data. Hence, to adopt energy models that are as accu-

rate as possible, calibration procedures are becoming increasingly fundamental and are an unavoidable step in building simulation for closely matching simulated building behavior to reality (Coakley et al., 2014). When it comes to calibration of simulation models, many approaches are available in the literature, comprising manual and iterative ones, graphical comparative procedures, techniques based on specific tests and many others (Chong et al., 2021). Among all possible approaches, the optimization-based calibration is the most widely adopted in model calibration. However, this approach, which is usually based on evolutionary algorithms, has the disadvantage that it requires many expensive simulations to be run, especially when the number of parameters to be calibrated is high, as in detailed models. This issue can be overcome by a preliminary sensitivity analysis that reduces the number of parameters to be calibrated, and by an efficient optimization algorithm.

Thus, this research work proposes a framework based on a sensitivity analysis designed to identify the most significant parameters separately on the energy budgets, other monitored environmental variables and, after that, considering all the variables together. Then, a calibration procedure is performed based on functional approximation models, which greatly increases the efficiency of the optimization algorithm. The Root Mean Square Error (RMSE) was chosen as statistical indicator to be minimized, instead of the monitored variables. The case study is a university library located in the municipality of Trento, Italy. The building is constantly monitored in terms of indoor temperature ($^{\circ}\text{C}$), relative humidity (%) and indoor carbon dioxide (ppm). The results show how successful the proposed approach is in reducing the computational time required for calibration, especially when considering models with a high degree of complexity.

2. Methodology

2.1 Monitored Case Study

To test the proposed calibration procedure, a real building was considered, specifically, a university library placed in Mesiano ($46^{\circ} 3' \text{ N}$, $11^{\circ} 8' \text{ N}$), municipality of Trento, Italy.



Fig. 1 – Case study: University library BUM, University of Trento, Trento (Italy). The building was opened in 2021. Picture retrieved from <http://www.weberwinterle.com>

The construction was built in 2020, and it has a total floor area of 1533 m^2 . It is a three-storey building composed of an underground basement, used as an archive and technical room, and two upper floors connected by internal stairs, where rooms are mainly used as offices and lecture halls. The generation system is composed of two heat pumps, one air-to-water and a ground source one. The hydronic heating/cooling system is based on a radiant floor panel system for the two upper floors, and a fan-coil system for the basement. The building is supplied with an air mechanical ventilation system coupled with an Air Handling Unit AHU, except for the basement.

Sensors are installed all over the library with the aim of monitoring the indoor conditions in terms of temperature T , relative humidity RH , and levels of CO_2 in each ambient. Additional sensors are also placed on the plant side (i.e., heat pump system and the Air Handling Unit). Since its construction, the building has been constantly monitored by means of the *Schneider Building Automation Server*. Fig. 2 shows the positions of the data loggers in the library. Red sensors record indoor temperature and relative humidity, and CO_2 levels, while the green ones only record the temperature. Data were recorded with time steps of 15 min. Table 1 lists the different sensors and the names of the different

zones.



Fig. 2 – Sensor locations with their identification numbers

Table 1 – Sensor list and their positioning

Sensor	Monitored quantity	Zone	Floor
1	T, RH, CO ₂	Reading hall vs. Stairs	1 st
2	T, RH, CO ₂	Reading hall vs. Office	1 st
3	T, RH, CO ₂	Wardrobe	1 st
4	T, RH, CO ₂	Architecture hall	1 st
5	T, RH, CO ₂	Reading hall vs. Offices	GF
6	T, RH, CO ₂	Reading hall vs. Toilets	GF
7	T, RH, CO ₂	Architecture hall	GF
8	T, RH, CO ₂	Conference room	GF
9	T, RH, CO ₂	Archive	B
10	T	Office	1 st
11	T	Meeting room	GF
12	T	Office 1	GF
13	T	Office 2	GF

2.2 Building Simulation Model

TRNSYS® (v18) software was adopted to model the building's performance.

At first, the geometry of the model was created through the TRNBUILD application in the SketchUp environment (<https://www.sketchup.com/it>), and then it was imported into the program through Multizone Building Modeling (*Type56*), where each thermal zone (35 in total) was defined in this subroutine, thermo-physical properties of materials adopted in the opaque components, glazing properties and so on were defined. In particular, those data were retrieved from technical datasheets of the construction company.

Weather data, in terms of external total solar radiation (W m^{-2}), external air temperature ($^{\circ}\text{C}$), external air relative humidity (%) and wind speed (m s^{-1}), were taken from the weather station at Trento Laste (<https://www.meteotrentino.it>) with time steps of 1 h.

Solar radiation for each external tilted surface was modeled with the Perez Model (Perez et al., 1990) through *Type16*. The ground temperature was modeled with *Type77*. The external convective heat transfer coefficient h_{ce} was defined according to the Standard EN ISO 6946:2017 (CEN, 2017). Air infiltrations were calculated in accordance with the empirical method suggested by the ASHRAE K₁, K₂ and K₃ model (ASHRAE Handbook, 1989). Since the building is a new one, coefficients can be assumed equal to $K_1 = 0.1$, $K_2 = 0.011$ and $K_3 = 0.034$ (for tight constructions).

The light power density was taken from technical documentations and differentiated for each thermal zone. Three levels were considered, which are 20, 15 and 10 W m^{-2} , of which 60 % was accounted as thermal gain directly affecting the air node thermal balance. As regards thermal gains generated by the equipment, 7, 5 and 4 W m^{-2} power density levels were considered according to the ASHRAE Handbook (ASHRAE, 1989).

Schedules of lights, as well as of the external shading devices, were imported from an external file through *Type9*. These data come from the monitoring, since the building is also equipped with sensors giving information about the state of the lighting power in percentage terms and percentage value of the window shadings.

Since detailed occupancy schedules were not available, occupancy was assumed to follow Eq. (1).

$$occupancy_i = \max people_i \cdot Schedule_i \quad (1)$$

The maximum number of people for each thermal zone was obtained with the help of on-site inspection by counting the number of available chairs, while the schedule of the reading hall, a value ranging from 0 to 1, was determined by analyzing the weekly occupancy rate supplied by Google (see Fig. 3) and available because of globalization. As regards offices, a different schedule was considered.

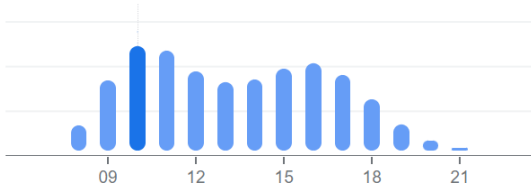


Fig. 3 – Example of occupancy rate of the library adopted as schedule for the reading hall. Profile retrieved from Google. Values range from 0 to 1. X-axis shows the time in hours

The Air Handling Unit was modeled as a black box, taking as input the monitored air temperature T_{supply} and relative humidity RH_{supply} of the supply air. In this way, composing devices were neglected. In the period monitored, the unit was working in *all-air* configuration due to COVID restrictions, thus no air recirculation was performed, and air was taken completely from the outside. Data about the supply air were passed through *Type9*. The air volume flow rate VFR introduced in each ventilated zone was defined as:

$$VFR = VFR_{\text{design}} \cdot \text{Schedule}_{\text{VENT}} \cdot R_{\text{gVENT}} \quad (2)$$

where the design volume flow rate was taken from technical documentations, and the AHU schedule (expressed from 0 to 1) and the regulation of the supply ventilator expressed in percentage terms were retrieved from monitored data (through *Type9*).

The Radiant panels, adopted for both heating and cooling, were modeled through *Type1231 – Radiator* (TESS Libs 17 – HVAC Library Mathematical Reference). The general expression of the specific thermal output for a general radiator was characterized for the radiant floor system by setting a value of 1 for the exponent linked to the difference between surface temperature and air temperature. And a value of 0.2 was considered for calculating the altitude correction factor. Inlet water temperature to the radiant floor system was taken from monitored data (*Type9*) and the water mass flow rate expressed in kg hr^{-1} was defined as the product of the design water flow rate for each zone (retrieved from technical documentation) and the monitored signal relative to the functioning of the radiant floor system in that zone.

The evolution profiles of CO_2 concentrations were simulated as well. The levels of CO_2 in a room de-

pend on the occupancy rate in that volume, the ventilation rate, and on the infiltrations. The model considered for the evolution in time of the indoor concentration accounts for the maximum value, at each time step, between the outdoor carbon dioxide $\text{CO}_{2,\text{ext}}$, considered equal to 400 ppm, and the expression in Eq. (3).

$$\begin{aligned} \text{CO}_{2[i,m]} = & \text{CO}_{2[i,m-1]} + \{ \text{INF} \cdot (\text{CO}_{2,\text{ext}} - \text{CO}_{2[i,m-1]}) + \dots \\ & \dots + VFR_i/V_i \cdot (\text{CO}_{2,\text{ext}} - \text{CO}_{2[i,m-1]}) + \dots \\ & \dots + (k_{\text{gen}} \cdot 10^6 \cdot \text{occupancy})/V_i \} \cdot \Delta t \end{aligned} \quad (3)$$

The generation term is equal to $0.017568 \text{ m}^3 \text{ hr}^{-1} \text{ person}^{-1}$. The three terms correspond to the infiltrations, ventilation system and the occupancy, respectively.

Beyond the thermal and the occupancy balance, also the moisture one was implemented by considering the moisture production of the people according to the ASHRAE Handbook (ASHRAE, 2017), where two different levels of activity were set, both sedentary and active.

2.3 Sensitivity Analysis

To identify the most dominant parameters affecting the model's outputs, a preliminary sensitivity analysis was performed. In particular, the methodology adopted is the one proposed by Sohier et al. (2014), which is a modified version of the qualitative *Morris method*, in which the significance threshold depends on the parameter with the highest elementary factor. This modification showed improvements in the estimation of the factors' impact with respect to the original one. The sensitivity analysis was applied separately to the three balances, and in particular:

- (i) at first, on the thermal balance, by considering as objective function the RMSE for the indoor temperature T .
- (ii) second, on the humidity balance, by considering the RMSE for the indoor absolute humidity x .
- (iii) at the end, on the CO_2 balance, by considering the RMSE for the CO_2 concentration levels.

For each case, every parameter taken into consideration was varied in a specific range, then simula-

tions were run and the magnitude of the variation of the Root Mean Square Error RMSE, expressed in Eq. (4), was assessed.

$$RMSE_i = \sqrt{\frac{\sum_{m=1}^N (y_{i,m}^{mis} - y_{i,m}^{sim})^2}{N - 1}} \quad (4)$$

In particular, the *RMSE* relative to the individual variable, i.e., temperature, relative humidity, and CO₂ concentration, was calculated for each monitored zone and then averaged using the corresponding volume. The method was implemented in the MATLAB® environment, which allowed automatic link to the software TRNSYS.

2.4 Calibration Process

After the preliminary parameter screening, the calibration procedure was addressed. In particular, a meta-models-based optimization approach was adopted, which is described and discussed in detail in the work of Prada et al. (2018). Meta-models are, substantially, surrogate models that emulate building dynamics. Hence, instead of optimizing the initial building simulation code directly, an explicit expression of the code is constructed starting from the building simulation results and used together with the Genetic Algorithm *GA* for the optimization procedure. The main advantage of such meta-models is to filter out the variable domain regions with no eligible Pareto solutions, as stated by Prada et al. (2018). In particular, in this research, the surrogate model implemented is called Multivariate Adaptive Regression Splines (*MARS*) meta-model and it is based on piecewise cubic splines, which are adopted to approximate the cost function.

Such an approach aims at overcoming some issues related to the commonly adopted evolutionary algorithms, whose procedure is extremely time-consuming. The calibration was based on three monitored quantities, which are, firstly, the indoor air temperature of each zone, secondly, the absolute humidity for each ambient, except those related to sensors 10 to 13 (see Fig. 2) and, thirdly, regarding the CO₂ variable, all zones equipped with

a CO₂ sensor were considered, except for the conference room and the basement (i.e., sensors 8 and 9), where the random component of the occupancy schedule was extremely significant and, thus, neglected. The objective function set for minimization is the RMSE (Eq. 4), defined separately for each monitored quantity, i.e., temperature, absolute humidity and CO₂, and normalized considering the initial case. Simulations were run considering a time-step of 15 min and a period from the 6th of November 2011 to the 12th of November 2011 (heating period). As for the sensitivity analysis, the procedure was implemented in the MATLAB® environment, which allowed an automatic link to the software TRNSYS.

3. Results and Discussion

In this section, results of the sensitivity analysis, as well as of the calibration procedure, are shown and discussed together. For instance, Table 2 shows the dominant parameters most affecting the model's output as a result of the sensitivity analysis. In particular, for each parameter, the magnitude of the influence (i.e., with numbers from 1 to 12) on each balance of temperature, of absolute humidity and of the CO₂ is specified. The term N/A is adopted when the model is not sensitive to that parameter. The parameters most influencing the temperature variable are mainly related to material properties, i.e., specific heat capacity, infiltration rates and gains related to lights and equipment. However, gains related to occupancy and the volume flow rate of the ventilation system also have an impact on the temperature's output, as seen in Table 2. In terms of absolute humidity, the parameters affecting the balance the most are the occupancy rates and the volume flow rates of the environments where the ventilation system is installed. The same stands for the CO₂ balance, considering, in addition, the effect of the external levels of CO₂. Since parameters from no. 1 to no. 7 affect only the temperature, their calibration was performed only on the thermal balance and by considering a single objective function based on the indoor air temperature. On the other hand, the other parameters from no. 8 – 15 that have an influence either on absolute

humidity, CO₂ or both, were adjusted according to a two-objective function calibration, based on such variables. In this way, the calibration procedure was decoupled. As regards parameters related to occupancy rate and volume flow rates, which influence not only the absolute humidity and CO₂, but also the temperature (e.g., no. 8, 9, 10, 12 and 13), these were accounted for in the two-objective function calibration, since they are more dominant on such balances than on the thermal one. Once parameters no. 8, 9, 10, 12 and 13 were calibrated, they were changed in the thermal balance, and the calibration of the temperature was performed. Table 2 shows the calibration ranges of each parameter, where a variation of $\pm 20\%$ from the initial value was considered.

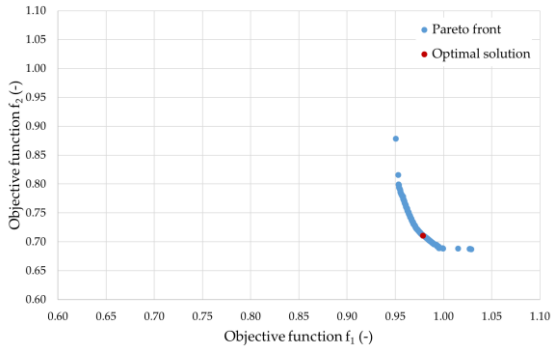


Fig. 4 – Pareto front (blue data) with the combinations of the objective functions f_1 and f_2 related to the absolute humidity AU (kg kg⁻¹) and CO₂ (ppm), respectively. The optimal solution is highlighted in red

Fig. 4 shows results of the optimization-based calibration on the absolute humidity and the CO₂, as combinations of the objective functions f_1 and f_2 expressed as the ratio between the current RMSE and the RMSE related to the initial case, both for the AU and the CO₂, respectively (see Eq. 5).

$$f_{1 \text{ or } 2} = \frac{RMSE_{AU \text{ or } CO_2}}{RMSE_{0_{AU \text{ or } CO_2}}} \quad (5)$$

Results are placed on the Pareto front, as depicted in blue. By assessing the minimum distance of each solution from the origin, the optimal solution was selected and highlighted in red, as shown in Fig. 4. In particular, with this solution, only the CO₂ concentration was improved, instead of the absolute humidity, for instance, $f_1 = 0.98$ and $f_2 = 0.71$ (improvements equal to 2 % and 9 % compared with

the initial case, respectively). This is because the prediction of humidity in environments was modeled with a simplified approach, which neglects some mechanisms like moisture buffering due to the building's opaque components. The values of the calibrated parameters related to this optimal solution are summarized in Table 2 from no. 8 to no. 15. Besides values of occupancy and volume flow rates of the ventilation system, the parameter which shows remarkable change with respect to the initial case is the external CO₂ concentration, which was not measured but assumed, and whose value influences the indoor CO₂ balance to a great extent, according to Eq. (3).

Results of the calibration on the thermal balance are reported in Table 2 from parameters no. 1 to 7, which refer to the minimum value of the objective function as expressed in Eq. 5, but only in terms of temperature. The obtained temperature objective function was equal to 0.90, which means a 10 % improvement compared with the initial case. In particular, parameters related to air infiltrations slightly decrease from the initial values, confirming the hypothesis of a highly airtight building, typical of new constructions.

Table 3 shows the computational effort of each calibration procedure (in h), the percentage improvement of the model with respect to the initial case expressed as $1 - f$ and the calibration accuracy in terms of RMSE for each variable. In particular, three cases were reported: the initial one, the case after the decoupled calibration composed of *Cal 1* and *Cal 2*, which considered the joined AU and CO₂, and T, respectively. And, at the end, a third case based on a standard calibration procedure (*Cal 3*) taken only as a comparison. Specifically, the calibration considered all parameters of Table 2 and three objective functions for every variable implemented together. The computational time necessary for the decoupled calibration is about 32 h considering both *Cal 1* and *Cal 2*. Clearly, *Cal 1* is remarkably more time-consuming than *Cal 2* (i.e., 30.8 h vs 1.2 h) because of the two objective functions. The improvement obtained after the decoupled procedure with respect to the initial case is 2 % for the absolute humidity, 29 % for the CO₂ and 10 % for the temperature. In terms of RMSE, it can be noticed that the variations with the initial case

are limited especially in terms of temperature and absolute humidity prediction. A more marked reduction in the RMSE(CO₂) is evident, i.e., from 88.3 ppm to 61.6 ppm. This is because the model was already robust at the beginning thanks to the reliability of the input data and parameters - a typical condition of new constructions. As regards the

standard case, results in Table 3 show that the calibration procedure requires about 9 % more time than the decoupled case (i.e., 35 h vs 32 h) to get a comparable accuracy, or even slightly lower, when considering the CO₂ prediction. As before, the improvement is not greatly higher than the initial case because of the goodness of the initial model.

Table 2 – Parameters which influence the most the models' output obtained from the sensitivity analysis

Category	No.	Parameter	T	AU	CO2	Values range	Calibrated value
Material properties	1	c reinforced concrete [kJ kg ⁻¹ K ⁻¹]	3 rd	N/A	N/A	[0.704-1.056]	1.03
	2	c concrete - heated floor [kJ kg ⁻¹ K ⁻¹]	11 th	N/A	N/A	[0.704-1.056]	0.95
Infiltration rate	3	$K1 - INF [-]$	5 th	N/A	N/A	[0.08-0.12]	0.08
	4	$K2 - INF [-]$	2 nd	N/A	N/A	[0.088-0.0132]	0.009
Gains from lights and equipment	5	Light power density -1 st level [kJ hr ⁻¹ m ⁻²]	1 st	N/A	N/A	[58-86]	59
	6	Light power density - 2 nd level [kJ hr ⁻¹ m ⁻²]	9 th	N/A	N/A	[43-65]	63
	7	Equipment power density - 1 st level [kJ hr ⁻¹ m ⁻²]	8 th	N/A	N/A	[20-30]	20
Gains from people	8	Max PPL Reading hall vs. Stairs 1 st [-]	4 th	2 nd	2 nd	[50-74]	70
	9	Max PPL Reading hall vs. Offices 1 st [-]	6 th	1 st	N/A	[6-10]	6
	10	Max PPL Reading hall vs. Offices GF [-]	12 th	4 th	N/A	[26-30]	26
	11	Max PPL Reading hall vs. Toilet GF [-]	N/A	N/A	3 rd	[32-48]	32
Ventilation	12	VFR Reading hall vs. Stairs 1 st [m3 hr ⁻¹]	7 th	3 rd	N/A	[888-1332]	1024
	13	VFR Reading hall vs. Offices GF [m3 hr ⁻¹]	10 th	5 th	5 th	[435-653]	645
	14	VFR Reading hall vs. Toilet GF [m3 hr ⁻¹]	N/A	N/A	4 th	[544-816]	773
External environmental conditions	15	CO _{2, ext} [ppm]	N/A	N/A	1 st	[200-600]	514

Table 3 – Computational time, improvement and accuracy of the decoupled and standard calibration approach

	Initial case	Decoupled		Standard
		Cal 1	Cal 2	Cal 3
Calibration Time*	-	30.8 h	1.2 h	35 h
Improvement 1- <i>f</i>	-	2 % (AU)	29 % (CO ₂)	10 % (T)
RMSE _T	0.6 °C	0.6 °C		0.6 °C
RMSE _{AU}	0.3 g kg ⁻¹	0.3 g kg ⁻¹		0.3 g kg ⁻¹
RMSE _{CO2}	88.3 ppm	61.6 ppm		63.6 ppm

* Processor: AMD Ryzen 9 5950X 16-Core – 3.40 GHz; Installed RAM: 32.0 GB.

4. Conclusions

In this work, a calibration of an energy simulation model based on the meta-model optimization approach was tested on a real case study. The methodology comprised a first sensitivity analysis designed to identify the most significant parameters on the energy budgets and other monitored environmental variables separately. Then, a calibration procedure based on functional approximation models was applied separately on the monitored variables, which are temperature, humidity and CO₂. The case study is a university library placed in the municipality of Trento, Italy. The building was monitored in terms of indoor carbon dioxide, indoor temperature, and relative humidity. Results show how the decoupled approach increases the efficiency of the optimization algorithm, especially in energy simulation codes with a high degree of complexity, thus with a high number of parameters. For instance, to obtain the same, or even slightly greater, accuracy than a standard calibration approach, the computational time required for this decoupled calibration is 9 % less than a standard approach, where no differentiation among monitored variables is performed. Hence, the adoption of the MARS model in calibration procedures of building simulation models can provide a contribution towards the optimization of both building refurbishment design, as well as building operation and control.

Nomenclature

Symbols

ACH	Air Changes per Hour (h ⁻¹)
AHU	Air Handling Unit
B	Basement
c	Specific heat capacity (kJ kg ⁻¹ K ⁻¹)
CO ₂	Carbon Dioxide (ppm)
Δt	Simulation time step (hr)
GA	Genetic Algorithm
GF	Ground Floor
H/C	Heating/Cooling
h _{ce}	External convective heat transfer coefficient (kJ hr ⁻¹ m ⁻² K ⁻¹)
INF	Infiltration rate (h ⁻¹)

λ	Thermal conductivity (W m ⁻¹ K ⁻¹)
N	Number of simulation time steps
k _{gen}	Generation rate (m ³ hr ⁻¹ person ⁻¹)
PPL	People
Rg	Regulation
RH	Relative Humidity (%)
RMSE	Root Mean Square Error
T	Indoor air temperature (°C)
X	Absolute humidity (kg kg ⁻¹)
Y	Variable (either T, RH or CO ₂)
VFR	Volume Flow Rate (m ³ hr ⁻¹)

Subscripts/Superscripts

ext	External
i	Of the i th thermal zone
mis	Measured
m	Of the current time step (-)
m-1	Of the previous time step (-)
sim	Simulated
supply	Of the supply air of the AHU
VENT	Of the supply ventilator

Acknowledgments

This research was funded by MIUR – the Italian Ministry of Education, Universities and Research (PRIN 2017) grant number 2017KAAECT in the framework of FLEXHEAT project “The energy FLEXibility of enhanced HEAT pumps for the next generation of sustainable buildings”.

References

- ASHRAE. 1989. *Handbook of Fundamentals: Ventilation and Infiltration*, Chapter 22.
- ASHRAE. 2017. *Handbook Fundamentals, Nonresidential cooling and heating load calculations*, Chapter 18: 18.1-18.62.
- Chong, A., Y. Gu, and H. Jia. 2021. “Calibrating building energy simulation models: A review of the basics to guide future work.” *Energy and Buildings* 253: 111533. doi: <https://doi.org/10.1016/j.enbuild.2021.111533>
- Coakley, D., P. Raftery, and M. Keane. 2014. “A review of methods to match building energy

- simulation models to measured data." *Renewable and Sustainable Energy Reviews* 37: 123-141. doi: <https://doi.org/10.1016/j.rser.2014.05.007>
- CEN European committee for Standardization. 2017. EN 6946. *Building components and building elements — Thermal resistance and thermal transmittance — Calculation methods*.
- Karlsson, F., P. Rohdin, and M.-L. Persson. 2007. "Measured and predicted energy demand of a low energy building: important aspects when using Building Energy Simulation." *Building Services Engineering Research and Technology* 28(3): 223–235. doi: <https://doi.org/10.1177/0143624407077393>
- Perez, R., P. Ineichen, R. Seals, J. Michalsky, and P. Stewart. 1990. "Modeling daylight availability and irradiance components from direct and global irradiance." *Solar Energy* 44:271–89. doi: [https://doi.org/10.1016/0038-092X\(90\)90055-H](https://doi.org/10.1016/0038-092X(90)90055-H)
- Prada, A., A. Gasparella, and P. Baggio. 2018. "On the performance of meta-models in building design optimization." *Applied Energy* 225: 814-826. doi: <https://doi.org/10.1016/j.apenergy.2018.04.129>
- Santamouris, M., and K. Vasilakopoulou. 2021. "Present and future energy consumption of buildings: Challenges and opportunities towards decarbonization." *e-Prime-Advances in Electrical Engineering, Electronics and Energy* 1: 100002. doi: <https://doi.org/10.1016/j.prime.2021.100002>
- Scofield, J. H. 2009. "Do LEED-certified buildings save energy? Not really..." *Energy and Buildings* 41(12): 1386-1390. doi: <https://doi.org/10.1016/j.enbuild.2009.08.006>
- Sohier, H., J.-P. Farges, and H. Piet-Lahanier. 2014. "Improvement of the Representativity of the Morris Method for Air-Launch-to-Orbit Separation." In *IFAC Proceedings Volumes* 47(3): 7954-7959. doi: <https://doi.org/10.3182/20140824-6-ZA-1003.01968>
- TESS Libs 17 – HVAC Library Mathematical Reference. Available online: <http://www.trnsys.com/tess-libraries/>
- Turner, C., and M. Frankel. 2008. *Energy performance of LEED for new construction buildings*. New Buildings Institute, Washington, DC, US.

Development of a Detailed Model of Hybrid System Composed by Air-to-Water Heat Pump and Boiler

Erica Roccatello – University of Trento Italy – Erica.Roccatello@unitn.it

Alessandro Prada – University of Trento Italy – Alessandro.Prada@unitn.it

Marco Baratieri – Free University of Bozen-Bolzano, Italy – Marco.Baratieri@unibz.it

Paolo Baggio – University of Trento Italy – Paolo.Baggio@unitn.it

Abstract

Air-to-water heat pumps are one of the most promising and increasingly widespread solutions, despite some intrinsic drawbacks, such as their poor efficiency at low ambient temperatures and at high sink temperatures, e.g., in domestic hot water production. In this context, hybrid heat pump systems combining air-to-water heat pumps and boilers (HSs) have been proposed on the market, especially for the renovation of existing buildings, where high supply water temperatures are typically required. Even though HSs are off-the-shelf technology, the topic has recently gained interest in research. HSs consist of two generators, which must be designed with an integrated approach from the start. However, the performance improvement hinges on the availability of a detailed model able to accurately predict the HS performance. Most of the studies available in the literature use models based on performance maps that are not suitable for HS design. This study presents a new detailed model of a hybrid system, developed in the MATLAB environment. The model adopts a quasi-physical representation of the heat pump cycle and condensing boiler. The boiler model thermodynamically simulates the combustion process, using the Cantera solver and the Gri-Mech properties. The heat pump model simulates the thermodynamic cycle, using refrigerant properties obtained from Cool-Prop libraries. A detailed model for each main component of the system is developed. Component models are combined, thus allowing the user to consider the influence of single components or construction parameters on the overall HS performance. Individual component models were validated against software or performance data provided by manufacturers. The validation proved that the models of the single components can reproduce performance with high accuracy. Therefore, the model can be used for future studies involving HS design, to analyze the influence of construction choices on overall system efficiency.

1. Introduction

Hybrid systems (HSs) can be a promising solution for increasing the efficiency of heating systems, particularly for existing buildings that do not have as high levels of insulation as new buildings (Roccatello et al., 2022).

The way the two generators (boiler and heat pump) are combined is crucial for system efficiency. Therefore, the HS, consisting of two generators, must be designed with an integrated approach from the start. A detailed model of the system would be needed to study and develop a HS. This would allow the design of the individual components of the system to be optimized for their combination, to maximize the efficiency of the hybrid system under the chosen operating conditions.

Previous studies on the topic developed a HS model and used it to compare system performance with other solutions, e.g., monovalent systems with heat pump or boiler. Klein et al. (2014) applied a model of HS for simulating a building with different insulation levels, using TRNSYS software. They used a model of the hybrid system based on performance maps. Di Perna et al. (2015) adopted an experimentally derived HS model, for the comparison of HS performance with that of boiler or electric heaters. Bagarella et al. (2016) conducted simulations using TRNSYS to discuss the distribution between heat pump and boiler operation based on outdoor temperature. The HP model is based on the combination of performance map data for each component, while the evaporator was modeled using finned coil evaporator design software, which allows for estimation of the frost formation process on the evaporator. The boiler model ap-

plies numerical correlations for determination of the efficiency. Dongellini et al. (2021) analyzed the primary energy consumption due to the HS with different heat pump sizes. The model of the HS is based on performance data provided by manufacturers. Li & Du (2018) compared different hybrid system configurations by simulating system performance under certain operating conditions. They adopted a model based on performance maps for the heat pump, and an average efficiency for the boiler. Park et al. (2014) developed a detailed HP model, based on individual models of system components, and a boiler model based on experimental correlations.

The literature review shows that most of the hybrid system models are based on performance maps. These models, as already discussed, are well suited for application to building simulations, as they provide the real-life behavior of components already available on the market. However, they are not suitable to be used for a new design of the system itself, but rather to analyze the performance of a given system over a certain period of time.

The goal of the present work is to develop a semi-physical model of a HS. The model is primarily based on the physical laws describing the processes occurring in the individual components of the system.

The modeling involved the main components of the heat generators. The models of the individual components were combined into the overall model of the single generator. The HP and boiler models can be retrieved as subroutines from the overall HS model, which contains the hybrid system logic.

The heat pump and boiler model development are based on the currently most adopted systems in HSs. The heat pump considered for modeling is a modulating heat pump, equipped with a plate heat exchanger (HX) for the condenser, and a finned-coil HX for the evaporator. The boiler considered is a condensing, modulating, natural gas-fired boiler.

2. Methodology

The HS model consists of the logic that manages the interaction with the heating system – i.e., it determines whether a generator should operate and calculates the system setpoint – and decides which generator to operate based on the chosen control strategy. For a more detailed description of the logic of the HS model, the reader can refer to Roccatello et al. (2022). This paper presents a different type of HS model, in which the subroutines containing the heat pump and boiler models are not based on performance maps, but on semi-physical models of components. The generator models are developed as the union of the system components. The heat pump model is the combination of the component models of the air-refrigerant and water-refrigerant heat exchangers (evaporator and condenser), compressor, and expansion valve. The boiler is modeled as the union of the combustion chamber and the flue gas-water HX. Figs. 1 and 2 show the schematic of the heat pump and boiler models, respectively.

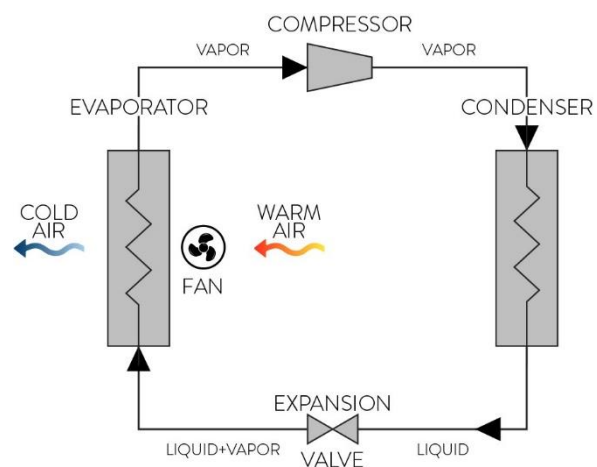


Fig. 1 – Schematic of heat pump model

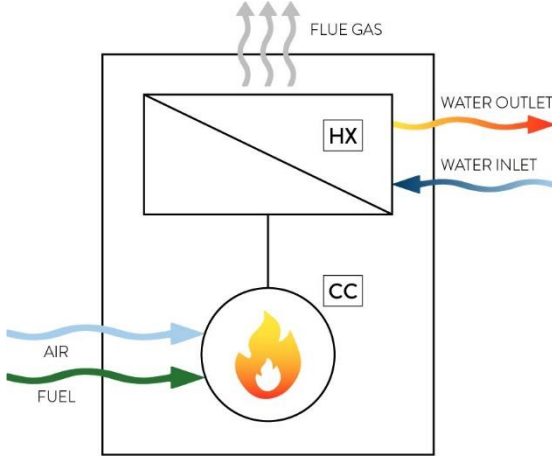


Fig. 2 – Schematic of boiler model

The following sections describe how the component models were developed, and subsequently combined, to generate the boiler and heat pump models.

2.1 Heat Pump Model

2.1.1 Condenser model

In this section, the heat transfer between refrigerant and water is modeled. The refrigerant exiting the compressor exchanges heat with water and undergoes condensation and subcooling. An example of a heat pump refrigerant cycle on a pressure/enthalpy diagram is shown in Fig. 3, in which the condensation process is highlighted.

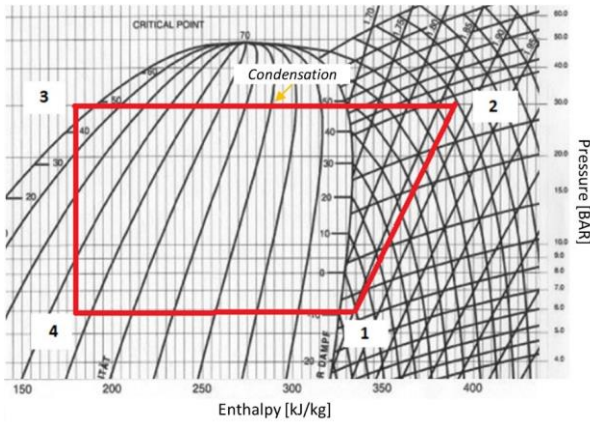


Fig. 3 – Condensation process represented on a pressure/enthalpy diagram

The condenser model refers to a plate HX, which is the most used type of exchanger for residential size heat pump systems.

Initially, a first guess of the value of the condensation temperature is estimated. The heat of conden-

sation (Q_{cond}) can be calculated using the following equation, which considers the enthalpy state of the refrigerant entering and leaving the condenser.

$$Q_{cond} = m_{ref}(h_2 - h_3) \quad (1)$$

Subsequently, heat transfer correlations are implemented for determination of the global heat transfer coefficient (Bergman et al., 2017). The equation for the calculation of the global heat transfer coefficient of the condenser (U_c) is reported here below:

$$U_c = \frac{1}{\frac{1}{h_c} + \frac{1}{h_w}} \quad (2)$$

in which h_c is the heat transfer coefficient of refrigerant, and h_w is the water heat transfer coefficient in the condenser. The calculation of h_w is performed according to the following equation:

$$h_w = \frac{k_{wt} Nu_{wc}}{D_c} \quad (3)$$

D_c represents the hydraulic diameter, while Nu_{wc} is calculated according to the following equation:

$$Nu_{wc} = C_{wc} (Re_{wc})^{wn} (Pr_{wc})^{\frac{1}{3}} \quad (4)$$

in which:

- Re_{wc} and Pr_{wc} : Reynolds and Prandtl number
- μ_{wc} : viscosity of the water

The values of C_{wc} and wn are evaluated as follows:

$$C_{wc} = \begin{cases} 0.718 & Re_{wc} \leq 10 \\ 0.348 & Re_{wc} > 10 \end{cases} \quad (5)$$

$$wn = \begin{cases} 0.349 & Re_{wc} \leq 10 \\ 0.663 & Re_{wc} > 10 \end{cases} \quad (6)$$

The refrigerant heat transfer coefficient (h_c) is evaluated in a different way when the refrigerant is the vapor phase and when it is in the condensation phase. In the first case it is calculated as:

$$h_{sc} = \frac{k_{sc} Nu_{sc}}{D_c} \quad (7)$$

in which k_{sc} represents the thermal conductivity of refrigerant.

In the condensation process, the heat transfer coefficient of the refrigerant (h_{tc}) is calculated as follows:

$$h_{tc} = \frac{k_{tc} Nu_{tc}}{D_c} \quad (8)$$

in which k_{tc} is the thermal conductivity of the refrigerant and Nu_{tc} is calculated according to the following equation:

$$Nu_{tc} = 0.0125 \left(Re_{tc} \sqrt{\frac{\rho_{cl}}{\rho_{cv}}} \right)^{0.9} \left(\frac{x_c}{1-x_c} \right)^{0.1x_c+0.8} Pr_{cl}^{0.63} \quad (9)$$

- Re_{tc} is the Reynolds number of the refrigerant during condensation
- ρ_{cl} and ρ_{cv} are the refrigerant density of liquid and vapor
- x_c is the vapor quality
- Pr_{cl} is the Prandtl number of the refrigerant in the liquid-phase.

Finally, the calculation of the heat exchanged between the fluids in the condenser (Q_{cond}) is expressed by the equation:

$$Q_{cond} = U_c A_c \Delta T_c \quad (10)$$

where ΔT_c is the mean temperature difference between water and refrigerant, U_c the global heat transfer coefficient and A_c the condenser heat transfer area. The equation allows the adjustment of the value previously assumed for the condensation temperature.

2.1.2 Expansion valve

The process that the fluid undergoes after exiting the condenser is modeled as an isenthalpic expansion (Fig. 4). Hence, the following equation is obtained, which provides the input enthalpy conditions for the refrigerant evaporation phase.

$$h_3 = h_4 \quad (11)$$

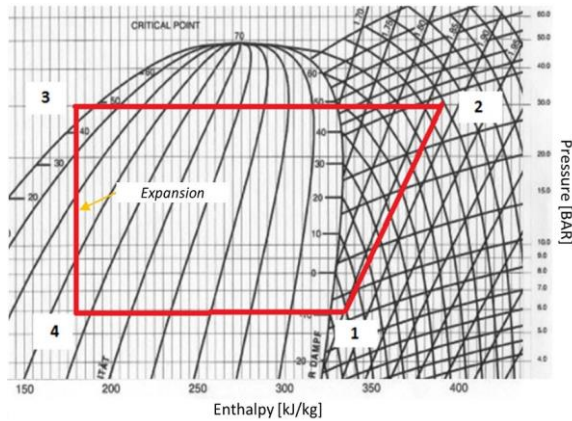


Fig. 4 – Expansion process represented on a pressure/enthalpy diagram

2.1.3 Evaporator

This section describes the modeling of heat transfer between air and refrigerant. The refrigerant pro-

cess through the evaporator is shown in Fig. 5, on the pressure/enthalpy diagram. In the heat exchanger, the refrigerant undergoes an evaporation and a superheating. The type of HX considered is a finned-coil HX, which is widely used in air source heat pumps.

Initially, a first-guess value of evaporation temperature is assumed, which allows estimation of the heat exchanged during the evaporation process (Q_{ev}), hence the enthalpy difference between the outlet state and the inlet state at the evaporator. Referring to the diagram in Fig. 5, this can be expressed by the following equation:

$$Q_{ev} = m_{ref} (h_1 - h_4) \quad (12)$$

where m_{ref} represents the refrigerant mass flow rate.

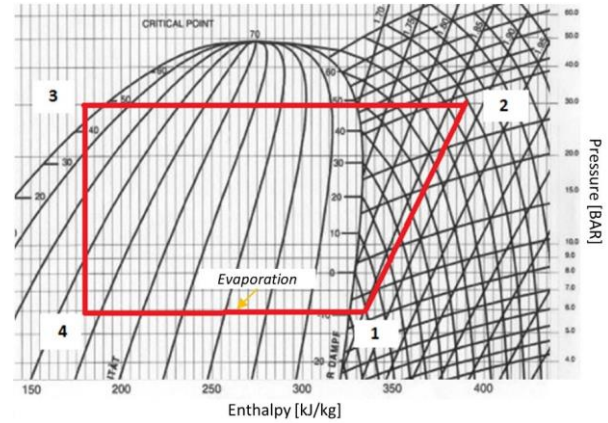


Fig. 5 – Evaporation process represented on a pressure/enthalpy diagram

Subsequently, the heat transfer correlations are implemented for the determination of the global heat transfer coefficient (Bergman et al., 2017).

h_a represents the air-side heat transfer coefficient:

$$h_a = \frac{j_a \rho_a u_m c_a}{Pr_a^{2/3}} \quad (13)$$

in which:

- ρ_a is the density of the air
- c_a is the specific heat of the air
- j_a is the heat transmission factor
- u_m is the maximum wind speed
- Pr_a is the Prandtl number of the air

j_a is calculated according to the following equation:

$$j_a = 0.0014 + 0.2618 Re_a^{-0.4} \left(\frac{A_{af}}{A_a} \right)^{-0.15} \quad (14)$$

in which:

- Re_a is the Reynolds number

- A_{at}/A_a is the ratio between the surface area of the tubes with and without fins.

The maximum wind speed (u_m) is calculated by Eqn. (15):

$$u_m = u_f \frac{s_h s_v}{(s_h - D_{te})(d_1 - d_2)} \quad (15)$$

where:

- u_f is the fan wind speed
- s_h is the tube spacings in the horizontal direction
- s_v is the tube spacings in the vertical direction
- D_{te} is the diameter of the tubes
- d_1 is the are the thickness of the fins
- d_2 is the spacing of the fins.

After that, the refrigerant heat transfer coefficient (h_e) is calculated. The value of the refrigerant heat transfer coefficient differs if the refrigerant is in the evaporation or in the superheating phase.

The refrigerant heat transfer coefficient in the superheating phase (h_{se}) is calculated as follows:

$$h_{se} = \frac{k_{se} Nu_{se}}{D_{te}} \quad (16)$$

in which k_{se} is the refrigerant thermal conductivity.

$[Nu]_{se}$ is calculated as:

$$Nu_{se} = \frac{(f_{se}/8) Re_{se} Pr_{se}}{1.07 + 1.27 \left(\frac{f_{se}}{8} \right)^{0.5} (Pr_{se}^{1/3} - 1)} \quad (17)$$

in which Re_{se} and Pr_{se} are the refrigerant Reynolds and Prandtl number, and f_{se} is the friction coefficient, calculated according to the equation:

$$f_{se} = (1.82 \ln Re_{se} - 1.64)^{-2} \quad (18)$$

The heat transfer coefficient of the refrigerant in the condensation phase is calculated according to the following equation:

$$h_{te} = h_{el} \left\{ \left[(1 - x_e) + 1.2 x_e^{0.4} (1 - x_e)^{0.01} \left(\frac{\rho_{el}}{\rho_{ev}} \right)^{0.37} \right]^{-2.2} + \left[\frac{h_{ev}}{h_{el}} x_e^{0.01} (1 + 8(1 - x_e)^{0.7} \left(\frac{\rho_{el}}{\rho_{ev}} \right)^{0.67} \right]^{-2} \right\}^{-0.5} \quad (19)$$

where:

- h_{el} is the heat transfer coefficient of the refrigerant liquid-phase
- h_{ev} is the heat transfer coefficient of the refrigerant vapor-phase
- ρ_{el} is the density of the refrigerant liquid-phase
- ρ_{ev} is the density of the refrigerant vapor-phase
- x_e is the vapor quality of the refrigerant.

Thus, the calculation of the evaporator global heat transfer coefficient (U_e) is performed according to the following equation:

$$U_e = \frac{1}{\frac{1}{h_e} + \frac{1}{h_a}} \quad (20)$$

Finally, the calculation of the heat exchanged between the fluids in the evaporator (Q_e) is expressed by the equation:

$$Q_{ev} = U_e A_e \Delta T_e \quad (21)$$

where ΔT_e is the mean temperature difference between air and refrigerant and A_e the evaporator heat transfer area.

2.1.4 Compressor

Given the geometric and operational complexity of the component, the compressor was modeled using performance data provided by the manufacturers, to avoid great inaccuracy of the heat pump model. The compressor model adopts polynomial correlations, which allow for the estimation of the refrigerant mass flow rate and compressor power input, as a function of suction and discharge pressure, which correspond to the evaporating and condensing pressures in the heat pump model, if neglecting pressure drops.

In addition, the polynomial correlations are a function of the compressor frequency, i.e., they allow for the modeling of a variable-speed compressor, and thus for the development of a modulating heat pump model.

The correlations used in the model are reported here below (Copeland Select Software). The variable X represents either the refrigerant mass flow rate or the compressor power input. S and D are the evaporating and condensing temperatures, respectively, expressed in °C, while $C0 - C9$ are the specific coefficients for the compressor provided by the manufacturer.

$$X = C0 + C1*S + C2*D + C3*S^2 + C4*S*D + C5*D^2 + C6*S^3 + C7*D*S^2 + C8*S*D^2 + C9*D^3 \quad (22)$$

2.1.5 Model development

The flow chart in Fig. 6 describes the rationale of the heat pump model. At the beginning, initial values of the evaporating and condensing temperatures are guessed. Based on these values, the com-

pressor model estimates the refrigerant mass flow rate and power input. These values are used as inputs by the condenser model, which estimates the heat exchanged in the condenser and adjusts the value of the condensing temperature. Similarly, the evaporator model allows for the adjustment of the first guess evaporating temperature value through an iterative procedure. Finally, the outputs of the model, i.e., heating capacity and power input, are released, allowing for the COP calculation.

2.2 Boiler Model

The boiler was modelled by subdividing the system into its major components, namely combustion chamber (CC) and HX.

The model of the CC is based on a thermodynamic equilibrium simulation of the combustion process carried out using the Cantera solver (Cantera). The inputs to the combustion chamber model are the fuel mass flow rate and air mass flow rate (or excess air). Through the modeling of the combustion process, the adiabatic flame temperature is calculated, i.e., the temperature that the gas mixture would ideally reach in the absence of heat loss. The model considers the heat losses of the combustion chamber ($Q_{\text{loss_cc}}$), based on information provided by the manufacturer. The outputs of the combustion chamber model are the temperature and mass flow rate of the flue gas.

These values are used as input for the model of the water-flue gas HX. An exchanger with unitary efficiency was considered, which is a good approximation, given the very high efficiency in recovering flue gas heat in the heat exchange process.

The value of flue gas outlet temperature determines whether condensation of water vapor in the flue gas occurs. If the flue gas outlet temperature is lower than the dew point, the condensation heat is recovered and transferred to the water. The logic adopted in the boiler model development is shown in Fig. 7.

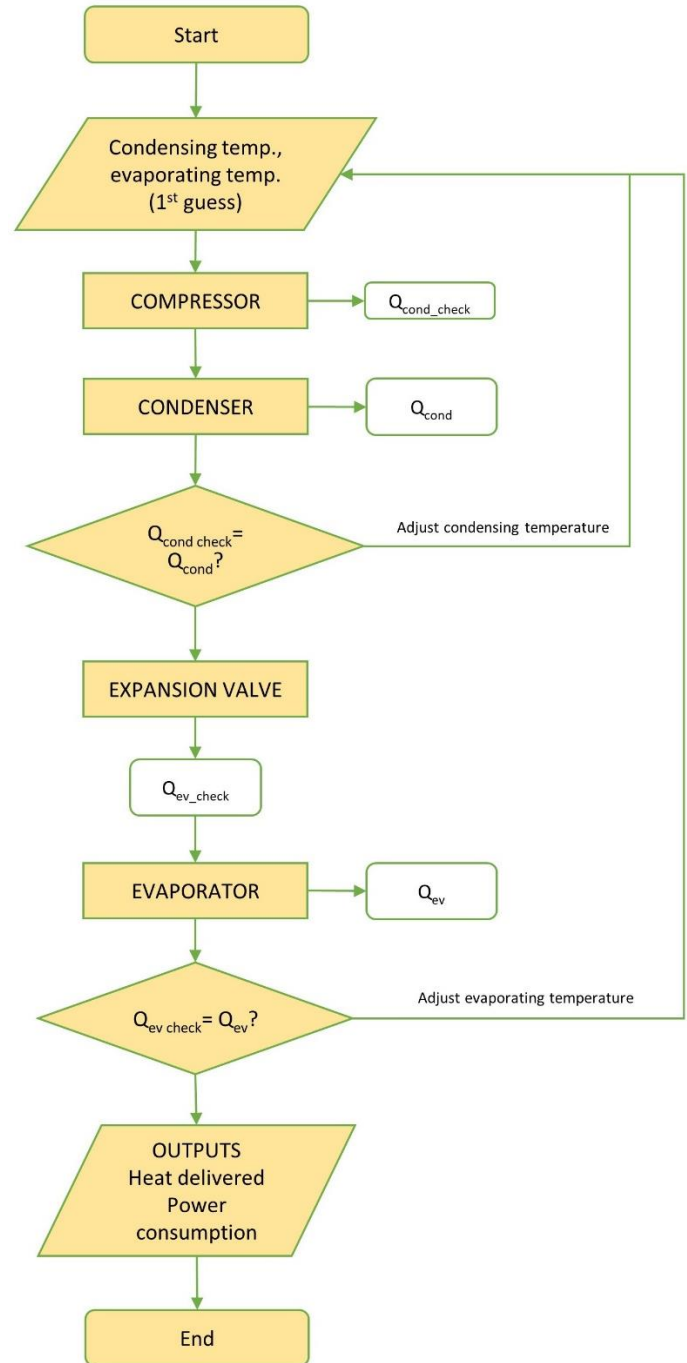


Fig. 6 – Heat pump model logic

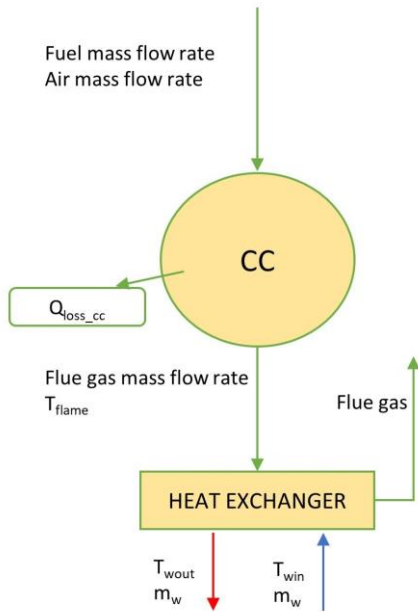


Fig. 7 – Boiler model logic

2.3 Model Validation

For the heat pump, validation of the HX models is presented, the compressor model being based on performance maps. The validation of the condenser model was carried out using the selection software provided by SWEP (SSP G8-SWEP), which provides the geometric parameters of the heat exchangers and allows the exchanged capacity to be evaluated by setting the operating conditions as input to the software.

The validation of the evaporator model was performed using performance data from a finned-coil HX obtained from NIST software (EVAP-COND). The software receives as input the geometric parameters and operating conditions and calculates the system performance in terms of exchanged capacity.

The validation of the boiler model was carried out using the data of heating capacity provided by the manufacturer, as a function of the fuel mass flow rate and water entering and leaving temperature.

3. Results And Discussion

In this section, the results of the validation of the component models are presented.

3.1 Condenser Model Validation

For a given heat exchanger, SWEP software returns the exchanged heating load by entering the operating condition data. The HX geometry and operating conditions are given as input to the model, which determines the overall heat transfer coefficient and heat load. Tables 1 and 2 show the geometrical and operating parameters related to the validation test carried out. Table 3 shows the results related to the heat exchanged between the fluids in the condenser obtained from the manufacturer's software and estimated using the model. It can be observed that the relative error in the estimate of the heat load is less than 5 %.

Table 1 – Input geometrical parameters used for validation test of plate heat exchanger model

Geometric parameters		
Total heat transfer area	m ²	1.57
Refrigerant channel volume	dm ³	0.0313
Water channel volume	dm ³	0.0301
Number of plates	units	58
Height	mm	324
Length	mm	94
Width	mm	90.7

Table 2 – Input operating parameters used for validation test of plate heat exchanger model

Operating parameters		
Operating parameters	°C	50
Condensing temperature	°C	56.2
Subcooling	°C	2
Condenser inlet temperature	°C	80
Refrigerant mass flow rate	kg/s	0.059
Water mass flow rate	kg/s	0.458

Table 3 – Heat load values provided by manufacturer and calculated by the model, and relative error, for validation test on plate heat exchanger model

Validation results		
Manufacturer's heat load	kW	9.6
Model heat load	kW	10.0
Relative error	%	4.7

3.2 Evaporator Model Validation

The model validation of the evaporator was performed, using EVAP-COND software, for a given finned-coil HX geometry. The heat exchanged between the two fluids calculated by the software was compared with the exchanged heat estimated by the model. The data for the finned-coil HX geometry considered for the validation are shown in Table 4 and the operating parameters used in the validation are reported in Table 5.

Table 4 – Evaporator geometric parameters

Geometric parameters		
Number of tubes	units	16
Number of rows	units	3
Tube length	mm	454
Inner diameter	mm	9.22
Outer diameter	mm	10.01
Tube pitch	mm	25.40
Depth row pitch	mm	22.23
Front area	mm	0.188
Heat transfer area	mm	3.8
Fin data		
Thickness	mm	0.2032
Pitch	mm	2.004

Table 5 – Evaporator operating parameters

Operating parameters		
Volumetric air flow rate	m ³ /min	30
Evaporating temperature	°C	0
Superheating	°C	4.1
Air inlet temperature	°C	15
Inlet vapor quality	-	0.2
refrigerant mass flow rate	kg/h	0.0345

The results of the validation are shown in Table 6. The test shows a relative error below 10 % for the estimation of the heat exchanged between water and refrigerant in the evaporator.

Table 6 – Results of model validation

Validation results		
EVAP-COND heat load	kW	6.0
Model heat load	kW	6.5
Relative error	%	7.0

3.3 Boiler Model Validation

For the validation of the boiler model, the performance data of a commercial model of boiler manufactured by the Immergas S.p.A company were considered, for which certified performance data are available. These data show the useful heating capacity produced by the boiler as a function of fuel mass flow rate and water inlet and outlet temperatures. The manufacturer also indicates the value of excess air used by the boiler.

The model receives the fuel mass flow rate, excess air, return temperature, and water flow rate as inputs, and estimates the useful power delivered to the water. The validation was performed considering the conditions of inlet water at 30 °C and outlet water at 50 °C. In this case, water vapor condensation in the flue gas occurs. Validation was performed for fuel mass flow rates varying from min-

imum to maximum. The operating conditions used for validation are summarized in Table 7. The graph in Fig. 8 shows the results of the validation. It can be observed that the maximum relative error on the estimate of the useful boiler heating capacity does not exceed 10 % for each value of fuel mass flow rate.

Table 7 – Operating conditions for boiler model validation

Operating conditions		
Inlet water temperature	°C	30
Outlet water temperature	°C	50
Fuel mass flow rate (max-min)	kg/h	3.69–0.43

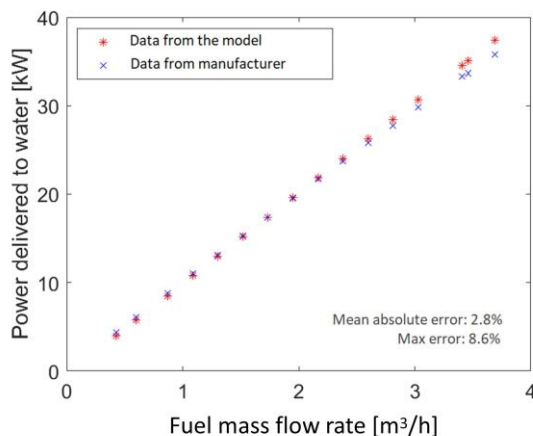


Fig. 8 – Validation results for the boiler model

3.4 Discussion

Regarding the validation of the heat pump components, the results presented show that the component models developed according to physical laws give results which are in line with the performance values declared by the manufacturers. Similarly, the validation of the boiler model showed how the physical model replicates with good accuracy the performance data provided by the manufacturer. The heat pump and boiler models described can be used as subroutines of an overall HS model. Thus, this new model can be used to evaluate the influence that the choice of certain system components, or certain construction parameters, has on the overall efficiency of the hybrid system.

4. Conclusions

This paper presents the development of a new quasi-physical model of a hybrid system, based on the combination of the models of the individual components of the system. These models are based on physical laws, except for the compressor model, because of the high geometrical complexity of the component and the risk of introducing large errors by approximating its behavior with an analytical model.

For the heat pump, the evaporator and condenser model were developed using heat transfer correlations, which model the heat exchange between air and refrigerant, and water and refrigerant. The compressor model, on the other hand, is based on performance data provided by the manufacturers. The process occurring in the expansion valve is modeled as an isenthalpic expansion.

The boiler model is divided into a model of the combustion chamber and a model of the heat exchanger between flue gas and water. The combustion chamber model is based on the thermodynamic equilibrium simulation of the combustion process carried out using the Cantera solver.

After that, the validation of the models of the system components was presented, which provided results with acceptable accuracy to qualitatively estimate the behavior of a hybrid system.

Therefore, the model can be used for the detailed study of a hybrid system, and especially in the design process of the system itself. It will be possible to analyze the influence of the choice of certain components or construction parameters on the overall efficiency of the hybrid system.

Acknowledgement

This research was funded by the MIUR-Italian Ministry of Education, Universities and Research (PRIN 2017) grant number 2017KAAECT within the framework of FLEXHEAT project “The energy FLEXibility of enhanced HEAT pumps for the next generation of sustainable buildings”.

Nomenclature

CC	Combustion chamber
HS	Hybrid system
HX	Heat exchanger
$Q_{\text{loss_cc}}$	Heat losses in the combustion chamber
Q_{cond}	Heat exchanged in the condenser
Q_{ev}	Heat exchanged in the evaporator
m_{ref}	Refrigerant mass flow rate
m_w	Water mass flow rate
T_{win}	Inlet water temperature
T_{wout}	Outlet water temperature
T_{flame}	Temperature of flue gas exiting the combustion chamber

References

- Bagarella, G., R. Lazzarin, and M. Noro. 2016. "Annual simulation, energy and economic analysis of hybrid heat pump systems for residential buildings." *Applied Thermal Engineering* 99: 485–494. doi: <https://doi.org/10.1016/j.applthermaleng.2016.01.089>
- Bergman, T. L., A. Lavine, and F. P. Incropera, Fundamentals of heat and mass transfer. 2017.
- Cantera. [Online]. Available: <https://cantera.org/> [Accessed: 01-Feb-2022].
- Copeland Select Software | Emerson IT. [Online]. Available: <https://climate.emerson.com/en-it/tools-resources/copeland-select-software> [Accessed: 01-Feb-2022].
- Di Perna, C., G. Magri, G. Giuliani, and G. Serenelli. 2015. "Experimental assessment and dynamic analysis of a hybrid generator composed of an air source heat pump coupled with a condensing gas boiler in a residential building." *Applied Thermal Engineering* 76: 86–97. doi: <https://doi.org/10.1016/j.applthermaleng.2014.10.007>
- Dongellini, M., C. Naldi, and G. L. Morini. 2021. "Influence of sizing strategy and control rules on the energy saving potential of heat pump hybrid systems in a residential building." *Energy Conversion and Management* 235: 114022. doi: <https://doi.org/10.1016/j.enconman.2021.114022>
- EVAP-COND, Version 5.0 | NIST. [Online]. Available: <https://www.nist.gov/services-resources/software/evap-cond-version-50> [Accessed: 01-Feb-2022].
- Klein, K., K. Huchtemann, and D. Müller. 2014. "Numerical study on hybrid heat pump systems in existing buildings." *Energy and Buildings* 69: 193–201. doi: <https://doi.org/10.1016/j.enbuild.2013.10.032>
- Li, G., and Y. Du. 2018. "Performance integration and economic benefits of new control strategies for heat pump-gas fired water heater hybrid system." *Applied Energy* 232: 101–118. doi: <https://doi.org/10.1016/j.apenergy.2018.09.065>
- Park, H., K. Hwan Nam, G. Hyun Jang, and M. Soo Kim. 2014. "Performance investigation of heat pump-gas fired water heater hybrid system and its economic feasibility study." *Energy and Buildings* 80: 480–489. doi: <https://doi.org/10.1016/j.enbuild.2014.05.052>
- Roccatello, E., A. Prada, P. Baggio, and M. Baratieri. 2022. "Analysis of the Influence of Control Strategy and Heating Loads on the Performance of Hybrid Heat Pump Systems for Residential Buildings." *Energies* 15(3). doi: <https://doi.org/10.3390/en15030732>
- SSP G8 - SWEP. [Online]. Available: <https://www.swep.net/support/ssp-calculation-software/ssp-g8/> [Accessed: 01-Feb-2022].

The Role of Ventilation in Indoor Spaces During the Covid-19 Pandemic: Comprehensive Analysis of ASHRAE Standard 62.1

Giovanni Francesco Giuzio – Università degli studi di Napoli Federico II, Italy – giovannifrancesco.giuzio@unina.it

Giovanni Barone – Università degli studi di Napoli Federico II, Italy – giovanni.barone@unina.it

Annamaria Buonomano – Università degli studi di Napoli Federico II, Italy – annamaria.buonomano@unina.it

Gianluca Del Papa – Università degli studi di Napoli Federico II, Italy – gianluca.delpapa@unina.it

Cesare Forzano – Università degli studi di Napoli Federico II, Italy – cesare.forzano@unina.it

Adolfo Palombo – Università degli studi di Napoli Federico II, Italy – adolfo.palombo@unina.it

Giuseppe Russo – Università degli studi di Napoli Federico II, Italy – giuseppe.russo9@unina.it

Abstract

The spread of COVID-19 has significantly increased attention focused on the air quality of indoor environments. All major international health organizations (e.g., World Health Organization, etc.) recognize the importance of ventilation in enclosed spaces in reducing pathogen concentrations and fighting the Corona virus, or future pandemics. In this context, the roadmap to ensure safer and healthier indoor environments, by also guaranteeing an adequate comfort level, involves the implementation of several measures leading to a not-negligible increase in buildings' energy consumption. Within this framework, the present paper aims to analyze the adequacy of the current Indoor Air Quality (IAQ) standards requirements, and to assess the impact of IAQ improving measures on end-use energy profiles to ensure occupants' comfort. Specifically, a dynamic simulation approach is adopted to estimate, for each building space typology defined by ASHRAE 62.1, both air contaminant concentration and zone energy consumption. Specifically, the risk to occupants of contracting the COVID-19 virus was assessed for different scenarios using a modified Wells-Riley model. The study confirms the urgent need for enhancing ventilation in enclosed spaces to exit the health emergency caused by COVID-19. In addition, the paper provides quantitative data on the resulting operating costs of HVAC systems.

1. Introduction

The diffusion of general pollutants, viruses, bio effluents, etc. in the indoor environment is kept under control by the ventilation system, whose key role is largely recognized and investigated in the scientific community (Emmerich et al., 2013; Risbeck et al. 2021; Shrubsole et al., 2019). Still, higher attention and interest has increased around this topic since the Covid-19 outbreak (Faulkner et al., 2021; Pan et al., 2021; Sun & Zhai, 2020; Zheng et al., 2021) and the vital need for reducing the infection risk (Agarwal et al., 2021; Li & Tang, 2021) by supplying outdoor air in adequate quantities (Guo et al., 2021; Sha et al., 2021). In this context, the aim of the present work is to analyze the existing connection between SARS-CoV-2 contagion risk and the fresh air rates per person, targeting a proposal of different solutions to reduce the contagion risk by also evaluating their energy impact to maintain adequate occupant comfort regarding indoor air quality and healthy conditions in indoor spaces (Castaldo et al., 2018).

Several studies in the literature investigate the risk of contagion of COVID-19 with increased mechanical ventilation in the indoor environment, such as classrooms (Schibuola & Tambani, 2021a; Xu et al., 2021), offices (Sha et al., 2021; Srivastava et al., 2021; Pavilonis et al., 2021), universities (Mokhtari & Jahangir, 2021), restaurants (Li et al., 2021), and hospitals (Li & Tang, 2021) etc. Among the works

stating the usefulness of adopting increased outdoor air ventilation rates in reducing the Covid-19 contagion risk, it is very difficult to find works quantitatively assessing the related energy impact, with the only exception of works reported in Balocco & Leoncini (2020) and Schibuola & Tambani (2021b). This is a large gap, given the great influence of ventilation systems on building energy demands. In addition, there is a lack of manuscripts investigating the Covid-19 contagion risk in a comprehensive way by assessing the analysis for a large group of space types, whereas it is more common to find works focusing on a specific case study. Such a lack implies the impossibility of determining unique design criteria and defining guidelines.

The aim of the present work is to fill the gap in knowledge identified above. Specifically, the Wells-Riley model (Miller et al., 2021; Riley et al., 1978), largely adopted in the literature to evaluate Covid-19 contagion risk, was implemented in a purpose-developed Matlab routine. By means of this tool, aiming at filling the lack of works examining a wide range of building types, all the building categories presented in the ANSI/ASHRAE Standard 62.1-2019 were studied by considering, for each space type, the related crowding indexes, the occupancy schedules, and the outdoor air ventilation rates suggested by the standard. By doing so, it was possible to assess Covid-19 contagion risk in the case of the presence of infected people for each of the investigated building typologies, as a function of diverse pivotal parameters (exposure time to virus, typology of the facial mask worn, etc.). To reduce the Covid-19 contagion risk associated with the investigated scenarios, and with the aim of providing useful insights and design criteria for ventilation system, higher outdoor air flow rates were tested by assessing their effect in terms of infection probability. Finally, by exploiting a dynamic simulation model, purposely developed by means of a Building Energy Modeling (BEM) approach, the energy implications of the proposed ventilation strategies were assessed. The mentioned analyses are presented in detail hereinafter.

2. Method and Mathematical Model

In the present paragraph, the method adopted to carry out the previously mentioned analyses is described. Specifically, in Fig. 1, a schematic diagram of the adopted workflow is presented. Specifically, to perform a parametric analysis of several building categories, a Matlab routine capable of both simulating energy performance of the examined room and assessing the probability of infection of the occupants was purposely developed. As shown in Fig. 1, the Matlab script is intended to manage either the inputs and outputs of the detailed simulation model of the building room or the infection risk calculation model.

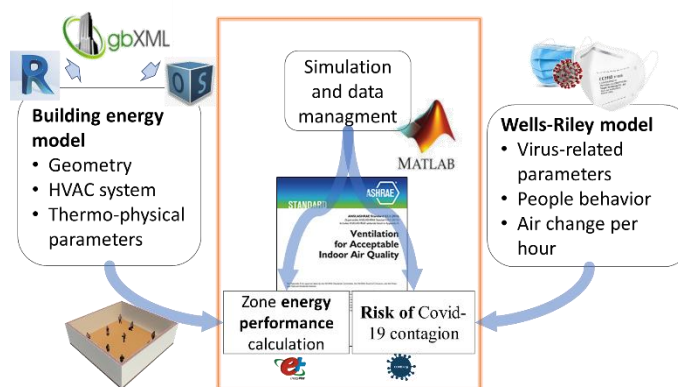


Fig. 1 - Schematic workflow of the methodology adopted (authors' illustration)

The building energy simulation relies on three different tools: Autodesk Revit, OpenStudio, and Energy Plus. Specifically, in Autodesk Revit, the building 3D model is developed in detail, by including building elements, as well as thermal zone data. The building model is then exported, by exploiting gbXML file, into OpenStudio suite, which is an energy-modeling software built on the EnergyPlus engine. At the same time, the assessment of Covid-19 contagion risk, for the same building and operating condition is also performed. This is conducted into a purposely developed Matlab subroutine, based on the Wells-Riley model. Both the energy consumption and Covid-19 contagion risk assessment methods will be described in detail in the following.

2.1 Building Energy Model

The energy model resulted in a well-mixed air single-zone building equipped with an ideal air loads systems capable of providing the exact thermal energy required to keep the temperature setpoints. An HVAC system like this also guarantees the minimum outdoor airflow rate (V_{bz} , breathing-zone ventilation), specified by means of Eq. (1), which depends on the number of people in the zone (N), the outdoor airflow rate per person (R_p), the net area of the zone (A_z), and the corresponding outdoor airflow rate required for unit of zone area (R_a).

$$V_{bz} = R_p \cdot N + R_a \cdot A_z \quad (1)$$

Furthermore, the influence of people, lighting and electrical equipment on the heat balance algorithm is accounted for by means of characteristic heat gain parameters, such as sensible and latent heat fraction per person ($g_{s,p}$ and $g_{l,p}$, W/person), lighting power load intensity (g_l , W/m²) and electrical equipment power load intensity (g_{ee} , W/m²). Appropriate schedules complete the model, taking into account the actual operating regime of the buildings under investigation. It is worth noticing that the ventilation rate necessary to ensure adequate IAQ is one of the key multi-physics factors that influences the occupants' comfort in indoor spaces; in this regard, complete multi-physics and multi-domain analysis aim at assessing thermo-hygrometric comfort, visual comfort, healthy conditions, and air quality.

2.2 Modified Wells-Riley Model

In order to assess the Covid-19 contagion risk, the Wells-Riley model (Miller et al., 2021; Peng & Jimenez, 2021; Peng et al., 2022; Riley et al., 1978) was adopted. This model is based on a standard aerosol Wells-Riley infection model, opportunely modified to consider the hypothesis of well mixed air volume. Following this model, the Covid-19 infection probability P can be expressed as:

$$P = 1 - e^{-n} \quad (2)$$

where n represents the inhaled "quanta", which is the concentration of infectious doses of the virus which are inhaled by a person. Note that a quanta is defined as the dose necessary to cause an infection in 63 % of the persons susceptible. The Covid-19 infection probability expressed by Eq. (2) is valid

under certain hypothesis: i) the quanta emission rate from the infectious individual is constant, ii) no prior quanta are in the investigated environment, iii) the quanta aerosol is evenly distributed in the environment, iv) close-proximity infection is neglected. The number of quanta inhaled by a person is calculated as follow:

$$n = q_c \cdot b_r \cdot D \cdot (1 - \eta_{wm} \cdot \eta_{in}) \quad (3)$$

where η_{in} is the mean filtration efficiency of the face mask for inhalation, η_{wm} is the percentage of people wearing a facemask, D is the exposure time to the virus, b_r is the breathing rate, and q_c is the average quanta concentrations.

3. Case Study

The Wells-Riley model was adopted to investigate the effectiveness, in relation to Covid-19 contagion risk, of the ventilation rates proposed by ANSI/ASHRAE Standard 62.1-2019. To perform this analysis, a generic room (Fig. 2) characterized by a walkable area of 100 m² (10 m x 10 m), with a height of 3 m, for a total volume of 300 m³, was considered. It is worth noticing that the investigated room was assumed as to be located in the core of a generic building. Consequently, all the walls were modeled as adiabatic. Note that such a hypothesis was made to provide results that were as little case-specific as possible, and take into account the sole effect of ventilation and internal heat gains on energy performance.

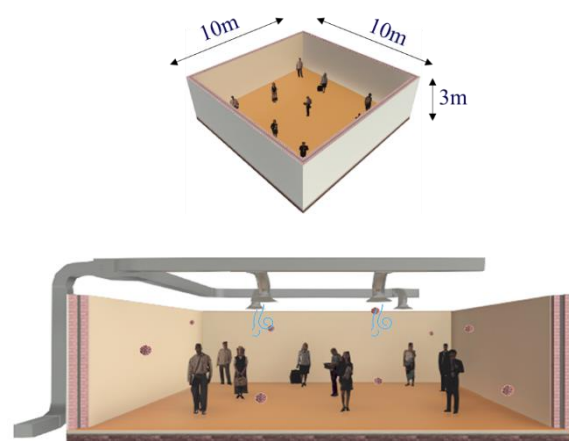


Fig. 2 – Investigated room

The investigated room was considered as alternatively belonging to all the 109 occupancy categories reported in the ANSI/ASHRAE Standard 62.1-2019, by taking into account the related outdoor air rates and occupancy density values. The 109 space typologies were grouped following the ANSI/ASHRAE Standard 62.1-2019, into 11 categories. The minimum and maximum outdoor air rates and occupancy density occurring within the group are reported in Table 1.

Note that the values reported in Table 1 represent the range limits of each building category group. However, each of the 109 spaces presented in the ANSI/ASHRAE Standard 62.1-2019 were simulated individually. For further details, please refer to the standard (ASHRAE, 2019). For each of the considered spaces, the Covid-19 contagion risk resulting from the adoption of the outdoor air ventilation rates suggested by the standard (calculated by means of Eq. 1) was assessed.

Table 1 – Outdoor ventilation rates, and occupant density for all the investigated categories

Occupancy Category	People Outdoor Air Rate		Area Outdoor Air Rate		Occupant Density	
	[L/s person]		[L/s person]		[persons/100m ²]	
	min	max	min	max	min	max
Animal Facilities	5	5	0.6	0.9	20	20
Correctional Facilities	2.5	3.8	0.3	0.6	15	50
Educational Facilities	2.5	5	0.3	0.9	10	100
Food and Beverage	2.5	3.8	0.3	0.9	2	100
Hotels, Motels, Resorts	2.5	3.8	0.3	0.6	10	120
Miscellaneous Spaces	2	5	0	0.9	0	100
Office Buildings	2.5	2.5	0.6	0.12	2	60
Outpatient Health Care	2.5	10	0.3	2.4	5	50
Public Assembly	2.5	3.8	0.3	0.6	10	150
Retail	3.8	10	0.3	2.4	7	150
Sports, Entertainment	3.8	10	0.3	2.4	7	150

The quanta exhalation rates, namely ER, used to evaluate the infection risk were gathered from the reference (Schibuola & Tambani, 2021a). Furthermore, in order to investigate diverse scenarios, five pivotal parameters were supposed to be variable as follows: i) three different Covid-19 variants were alternatively considered. The variant choice affects the quanta emission rate by means of a correction factor Q_{var} . Specifically, the three investigated

variants are: original variant ($Q_{var} = 1$), Delta ($Q_{var} = 2$); and Omicron ($Q_{var} = 2.5$) (Burki, 2022; Campbell et al., 2021); ii) three different exposure times (D) were considered: 1 hour, 2 hours, 6 hours; iii) three different face mask scenarios, affecting inhalation and exhalation efficiency: no mask scenario, all people wearing surgical masks scenario, and all people wearing FFP2 masks scenario.

3.1 Proposed Solutions

The previously described case study, adopting the outdoor ventilation rates suggested by the ANSI/ASHRAE Standard 62.1-2019, was considered as Reference System (RS). To reduce Covid-19 contagion risk, the convenience of using increased outdoor air ventilation rates was investigated. Specifically, ventilation rates augmented three and ten times (Proposed System 1 – PS1, and Proposed System 2 – PS2, respectively) higher than those suggested by the standard were considered and tested. These values, which might seem quite high compared to those adopted in the case of RS, were selected in accordance with the data found in the existing literature, referenced in the literature review section. It should be considered that, as expected, the proposed outdoor rates will imply a substantial increase of the energy consumption for space heating and cooling due to the augmented ventilation loads. For this reason, both PS1 and PS2 systems were also tested by additionally considering a sensible heat recovery device equipped to reduce the ventilation load. The selected sensible heat recovery device is a commercial device with an average heat recovery efficiency equal to 75 %, and nominal pressure drops ranging from 100 to 300 Pa (depending on the elaborated airflow rate). Table 2 lists all the investigated systems.

Table 2 – Investigated case studies

System	Outdoor Ventilation Rates	Heat Recovery
RS	ANSI/ASHRAE Standard 62.1-2019	No
PS1	Ventilation x3	No
PS1.1	Ventilation x3	Yes
PS2	Ventilation x10	No
PS2.1	Ventilation x10	Yes

3.2 Energy Analysis

To assess the energy consumption associated with the selected ventilation strategies (both RS and proposed systems), the ANSI/ASHRAE Standard 90.1-2016 was taken into account for the following data: i) occupancy scheduling; ii) lighting load density and scheduling; iii) machinery load density and scheduling; iv) indoor air setpoints. Specifically, each of the investigated occupancy category spaces (see Table 1) was simulated by considering the corresponding values of the above-reported parameters. Concerning the HVAC system, the considered room space heating and cooling is ensured by an air source HPC (heat pump/chiller), sized on the maximum load, with a variable COP (Barone et al., 2016 and 2020). The energy consumption resulting from the conducted analysis is affected substantially by the climate zone, due to the different outdoor air temperature (it is worth noticing that the room is placed in the core of a conditioned building, so no transmission load is considered). Thus, aiming at assessing the energy impact of the proposed ventilation strategies for diverse climates, three different European weather zones were considered as representative of hot, mild, and cold weather (see Table 3).

Table 3 - Investigated weather zones

Climate	HDD	CDD	ISR
	[K d]		[kWh/(m ³ y)]
Almeria	763	982	1664
Rome	1475	730	1529
Berlin	3394	262	1001

4. Result and Discussion

In this paragraph, the results of the analyses carried out are provided. Specifically, the Covid-19 results will be presented first, then the energy implications will be discussed.

4.1 Covid-19 Analysis

In this section, the results of the Covid-19 analysis, in term of contagion probability, are presented. Specifically, in Fig. 3, the Covid-19 contagion risk is reported for all the occupancy categories investigated, in the case of two different face mask scenarios (no

mask, on the left, surgical mask on the right), and in the case of three different exposure times (one hour in blue, two hours in red, and six hours in yellow). Note that the FFP2 mask results are not presented, since in this case the resulting Covid-19 contagion risk was already remarkably low. Numerical results obtained (probability of infection) are reported as boxplots in Fig. 3. Specifically, the distribution of the set of data, the minimum and maximum values (whiskers), as well as the 1st and 3rd quartiles (boxes), and the median are depicted for each of the occupancy category groups.

The infection probability, in case of people not wearing a mask and for an exposure time of one hour, almost always turns out to be higher than 1 % (considered in the literature as a “safe” value), while remaining quite close to it. Higher risk occurs in the case of 2 hours, with infection probability rising to 4 %. Finally, the highest infection probability in the case of no masks worn is obtained for 6 hours of exposure time, with contagion risk values rising to 12-14 %

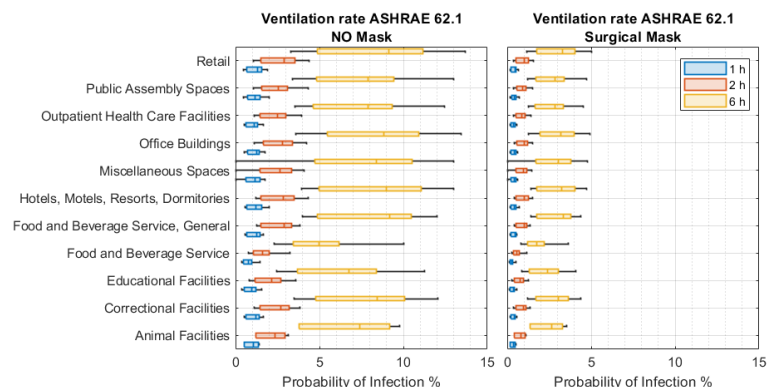


Fig. 3 – Covid-19 infection probability for all the investigated case studies (standard ventilation)

By using surgical masks (right-hand diagram in Fig. 3, it is possible to notice that, in the case of both 1 hour and 2 hours of exposure time, the infection probability is almost always below the 1 % value. Nevertheless, in the case of 6 hours, the risk is still higher than the threshold value. The reported results show that the ventilation rates suggested by the ANSI/ASHRAE Standard 62.1-2019 are adequate to control the Covid-19 contagion risk only in the case of all the occupants wearing an FFP2 mask, whereas a higher risk occurs in the case of surgical masks, and no mask worn. To reduce the estimated

contagion risk, the ventilation rates suggested by the standard were augmented 3 times, and the related contagion risk results are shown in Fig. 4. Here, it is possible to notice that, in the case of the no mask scenario, the contagion risk in the case of 1 hour exposure time is almost always below 1 %, ensuring occupant safety. Also, the contagion risks relative to 2 hours of attendance time drop. However, many cases return infection probabilities still higher than the safe threshold. The contagion risk connected to six hours exposure time is also reduced regarding the standard ventilation base case. Still, very high values are reached. A different situation occurs in the case of surgical masks worn. In this case, both 1 hour and 2 hours' exposure time return contagion risks lower than 1 %, whereas the 6-hour case returns a contagion risk higher than the safe threshold, but remarkably reduced compared with the base case.

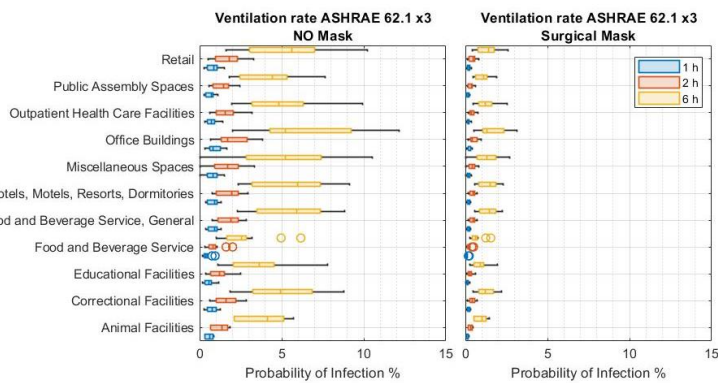


Fig. 4 – Covid-19 infection probability for all the investigated case studies (x3 ventilation)

In order to further reduce the contagion risk, ten-times-increased standard ventilation was also tested, and the related results are reported in Fig. 5. Here, it is possible to notice that, in the case of surgical mask worn, the contagion risk probability is lower than the threshold value for almost all the investigated scenarios and exposure times. On the contrary, in the case of no masks worn, one and two-hours residency time turns out to be still safe. It is worth noticing that the absolute values shown in the previously reported figures are subject to uncertainty. This is mainly due to the adopted number of quanta, whose value is still under discussion in the scientific community. For this reason, relative results are also presented.

Specifically, the average relative contagion risk reduction, for all the mask configurations and exposure time, is presented in Fig. 6. From the figure it is possible to notice that, beside the absolute contagion risk value, the contagion risk percentage reduction ranges from 30 to 50 % in the case of x3 ventilation, and from 65 to 80 % in the case of x10 ventilation. Such results help in understanding the great effect that outdoor ventilation rates have on Covid-19 contagion risk reduction.

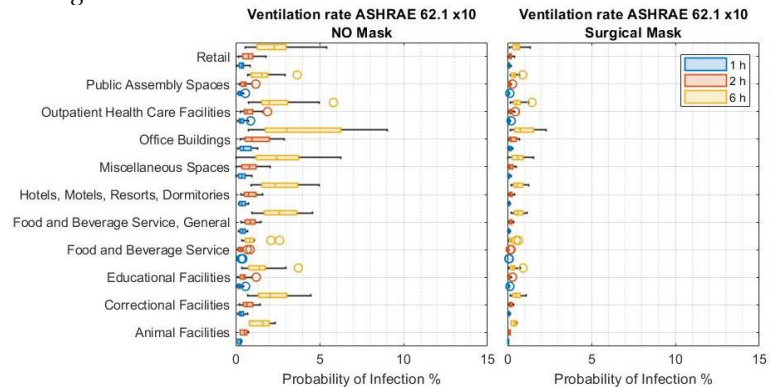


Fig. 5 – Covid-19 infection probability for all the investigated case studies (x10 ventilation)

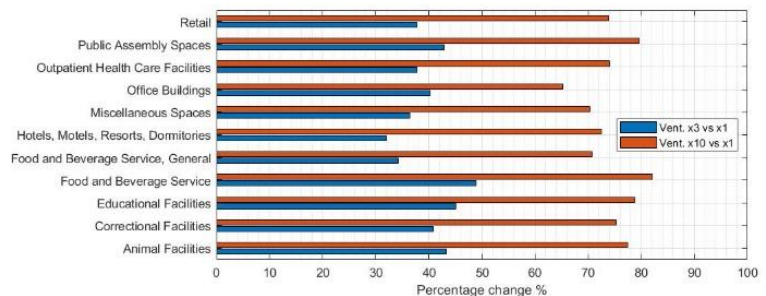


Fig. 6 – Average relative contagion risk reduction for all the face mask configurations

The higher ventilation rates proposed also entail a much higher dilution of indoor pollutants and lower level of carbon dioxide within the spaces. The indoor air quality significantly improves, so that the required comfort level by the occupants can be fully satisfied with the proposed ventilation rates (ASHRAE 62.1 x3 and ASHRAE 62.1 x10) as demonstrated by Fig. 7. The figure refers to an auditorium seating area with high occupancy (about 150 people). With the current standard (ASHRAE 62.1), the CO₂ concentration rises to 1800 ppm, leading to a discomfort level perceived by the occupants due to poor air. In contrast, both the proposed ventilation rates adopted to reduce the Covid contagion risk

keep the CO₂ concentration within the acceptable range suggested by OSHA (Occupation Health & Safety Administration) for well ventilated indoor spaces.

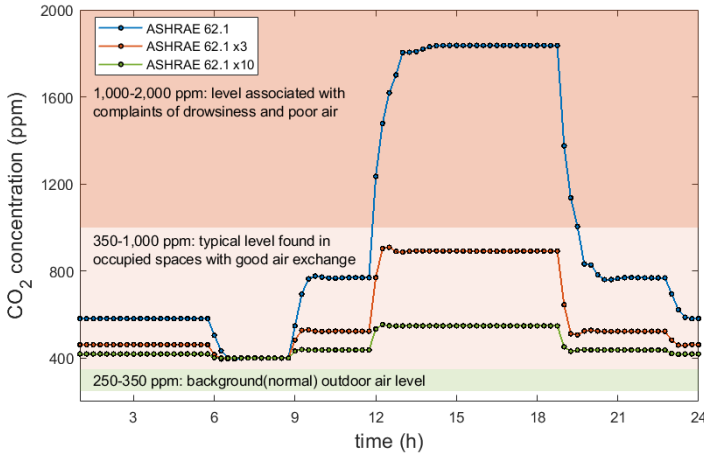


Fig. 7 – CO₂ concentration in the auditorium space and related comfort range for occupants

4.2 Energy Analysis

The previously described ventilation strategies, while reducing Covid-19 contagion risk, also increase the energy consumption of the building for space heating and cooling due to the augmented ventilation load. Furthermore, more air treated leads to higher handling costs. As an example of this increase, the space heating thermal energy demand for representative space typologies (selected from each category) are presented in Fig. 8 in the case of the building located in Berlin. From the figure, as expected, it is possible to notice that the adoption of x3 (PS1) and x10 (PS2) ventilation flow rates (red and light blue bars) always implies a remarkably higher energy demand compared with the RS scenario (blue bar). Different results are, on the other hand, achieved in the case of adoption of Heat Recovery (HR) device (orange – PS1.1 - and green – PS2.1 - bars in Fig. 8). Here, it is possible to notice that the energy demand increase is remarkably lower than those occurring without the HR adoption. It worth noticing that, in some cases, the PS1.1 energy demand (orange bars) is comparable with the RS one (blue bars).

Similar outcomes can be detected in the case of the thermal energy demand for space cooling, as shown in Fig. 9, where the results in the case of the building located in Almeria are presented. Nevertheless, by

analyzing Fig. 9, it is possible to notice that, in the case of x3 ventilation, lower energy demands for space cooling are obtained also without HR (PS1 - orange bars). Such an occurrence is due to the free cooling effect played, in some cases, by the augmented flow rate. The same effect is not noticeable in the case of x10 ventilation (PS2 – light blue bars), since the positive effects connected with the free cooling are overwhelmed by the negative ones occurring in the other hours. However, it worth noticing that the overall weight of cooling need increase is remarkably lower than that of heating (the y-axis scale of Fig. 9 is different to that of Fig. 8). In addition, also the benefits of the HR are lower due to lower temperature difference between the outdoor air and the zone temperature during the summer season.

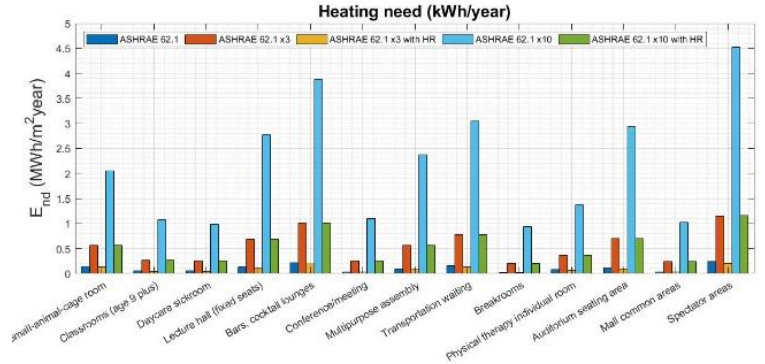


Fig. 8 – Space heating needs for all the case studies investigated for the building located in Berlin

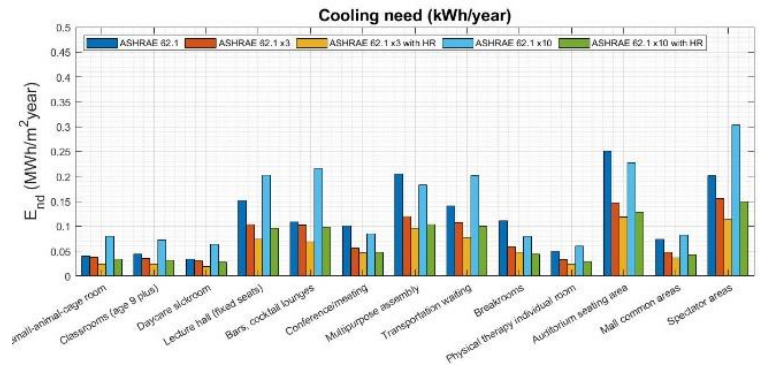


Fig. 9 – Space cooling needs for all the case studies investigated for the building located in Almeria

The thermal energy demand variations presented in Fig. 8 and Fig. 9 imply a variation of the considered room electricity consumption. Specifically, in Fig. 10, the distribution of electricity consumption is presented for all the investigated case studies. It is

worth noticing that, differently to Fig. 8 and Fig. 9, which report only the influence of the diverse ventilation strategies on the space heating and cooling thermal energy demand, the electricity results presented in Fig. 10 also take the electricity consumption of the fans into account. Referring to the median values of the set of data in Fig. 10, as expected, the adoption of PS1 (red boxes) and PS2 (purple boxes) systems always presents higher electricity demand vs the RS (blue boxes).

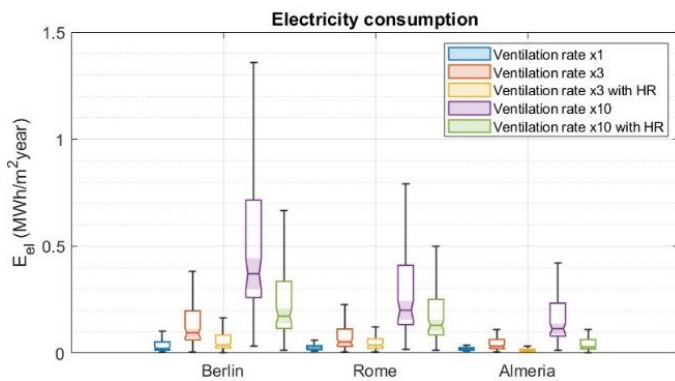


Fig. 10 – Electricity needs for all the case studies investigated

The benefits achieved during the cooling season, due to the free cooling effect, as shown in Fig. 9, are, in fact, counterbalanced by the highest consumption during the heating season. Lower electricity consumption increases are, on the other hand, detected in the case of adoption of PS1.1 (yellow bars) and PS2.1 (green bars). These reductions are smaller in magnitude with respect to those shown in the case of Fig. 7 and Fig. 8, due to the higher consumption of the fans connected to the HR adoption (higher duct system pressure drops).

5. Conclusions

In the present manuscript, the effectiveness of the ventilation rates proposed by the current ANSI/ASHRAE Standard 62.1-2019 in dealing with the Covid-19 contagion risk is investigated. To carry out this analysis, the Wells-Riley model (Riley, et al., 1978), largely adopted in the literature to evaluate the Covid-19 contagion risk, was implemented in a purpose -developed MATLAB routine. By means of this tool, all the building categories presented in the ANSI/ASHRAE Standard 62.1-2019,

applied to a purpose -conceived case study, were studied by considering, for each space type, the related crowding indexes, the occupancy schedules, and the outdoor air ventilation rates suggested by the standard. By doing so, it was possible to assess the Covid-19 contagion risk in the case of the presence of infected people in the room for each of the investigated building typologies, as a function of diverse pivotal parameters (exposure time to virus, typology of the facial mask worn, etc.). Aiming at reducing the Covid-19 contagion risk associated with the scenarios investigated, and with the aim of providing useful insights and design criteria for ventilation systems, higher outdoor air flow rates were tested by assessing their effect in terms of infection probability. Finally, by exploiting a dynamic simulation model, purposely developed by means of a Building Energy Modeling (BEM) approach, the energy implications of the proposed ventilation strategies were assessed. From the analyses carried out, the key considerations are:

- The ventilation rates values proposed in the current ANSI/ASHRAE Standard 62.1-2019 are not capable of ensuring a safe indoor environment in the case of no face mask worn. Specifically, an infection risk probability higher than 1 % (value considered as safe) is almost always reached by the analysis conducted, regardless of the considered exposure time. The same is true for surgical mask adoption, which gives lower infection risk probability, but is very often still higher than the safe threshold.
- The current standard adoption returns a very low contagion risk probability only in the case of all occupants wearing a FFP2 mask.
- The adoption of higher ventilation rates (x3 and x10) always returns interesting infection risk reductions, ranging from between 30 to 50 % and 65 to 80 %, respectively. Nevertheless, x3 ventilation is viable only for an exposure time to the virus of 1 hour, whereas in the case of 2 and 6 hours, the resulting contagion risk is always higher than 1 %.
- Ten times augmented ventilation vs. ANSI/ASHRAE Standard 62.1-2019 values reduces the contagion risk below 1 % for both 1- and 2-hour exposure times, whereas 6 hours is often still too high.

- By increasing ventilation, it is possible to reduce the Covid-19 risk to under 1 %, without wearing face masks only for 1- and 2- hour attendance times, whereas, in the case of 6 hours, this is not possible. Consequently, in the case of certain space types characterized by long occupancy times (e.g., classrooms), further solutions should be adopted.
- From the energy point of view, the proposed ventilation strategies return remarkable electricity demand increases. In this framework, x3 ventilation proves to be the best trade-off solution.
- The adoption of a heat recovery device allows for a remarkable reduction of the energy impact of the proposed ventilation strategies, making both x3 and x10 ventilations more feasible than the same solutions without the HR.

From the results obtained, it is possible to conclude that the existing normative does not provide an adequate amount of outdoor air to ensure a low Covid-19 contagion risk in enclosed spaces for the wellbeing and comfort of occupants. In this framework, the augmentation of the outdoor air flowrate is proven to be a good solution to adopt. Nonetheless, such an action is highly energy-consuming, requiring the adoption of heat recovery devices. Otherwise, it would be unviable from an energy and economic point of view.

Acknowledgement

This research has been co-funded by the Italian Ministry of Research through the NEXT. COM (Prot. 20172FSCH4) "Towards the NEXT generation of Multiphysics and multidomain environmental COMfort models: theory elaboration and validation experiment" project, within the PRIN 2017 program. The authors wish to thank their project colleagues for their constructive feedback and collaboration.

Nomenclature

A_z	Net area of the zone
BEM	Building Energy Modeling
b_r	Breathing rate
D	Exposure time to the virus
ER	Quanta emission Rate
g_{ee}	Electrical equipment power load
g_l	Lighting power load intensity
$g_{l,p}$	Latent heat gain per person
$g_{s,p}$	Sensible heat gain per person
n	Inhaled quanta
N	Number of people in the room
P	Infection Probability
PS	Proposed System
q_c	Average quanta concentration
R_a	Outdoor airflow rate per area
R_p	Outdoor airflow rate per person
RS	Reference System
V	Room Volume
V_{bz}	Breathing-zone ventilation
V_{out}	Outdoor air ventilation flow rate

References

- Agarwal, N., C. S. Meena, B. P. Raj, L. Saini, A. Kumar, N. Gopalakrishnan, A. Kumar, N. B. Balam, T. Alam, N. R. Kapoor, and V. Aggarwal. 2021. "Indoor air quality improvement in COVID-19 pandemic: Review." *Sustainable Cities and Society* 70: 102942. doi: <https://doi.org/10.1016/j.scs.2021.102942>
- ASHRAE. 2019. *ASHRAE Standard 62.1-2019 Ventilation for Acceptable Indoor Air Quality*.
- Balocco, C., and L. Leoncini. 2020. "Energy Cost for Effective Ventilation and Air Quality for Healthy Buildings: Plant Proposals for a Historic Building School Reopening in the Covid-19 Era." *Sustainability* 12(20): 8737. doi: <https://doi.org/10.3390/su12208737>
- Barone, G., A. Buonomano, C. Forzano, and A. Palombo. 2016. "WLHP Systems in Commercial Buildings: A Case Study Analysis Based on a Dynamic Simulation Approach." *American Journal of Engineering and Applied Sciences* 9(3): 659-668. doi: <https://doi.org/10.3844/ajeassp.2016.659.668>

- Barone, G., A. Buonomano, C. Forzano, G. F. Giuzio, and A. Palombo. 2020. "Passive and active performance assessment of building integrated hybrid solar photovoltaic/thermal collector prototypes: Energy, comfort, and economic analyses." *Energy* 209: 118435. doi: <https://doi.org/10.1016/j.energy.2020.118435>
- Burki, T. K. 2022. "Omicron variant and booster COVID-19 vaccines." *The Lancet Respiratory Medicine* 10: e17. doi: [https://doi.org/10.1016/S2213-2600\(21\)00559-2](https://doi.org/10.1016/S2213-2600(21)00559-2)
- Campbell, F., B. Archer, H. Laurenson-Schafer, Y. Jinnai, F. Konings, N. Batra, B. Pavlin, K. Vandemaele, M. D Van Kerkhove, T. Jombart, O. Morgan, and O. le Polain de Waroux. 2021. "Increased transmissibility and global spread of SARS-CoV-2 variants of concern as at June 2021." *Eurosurveillance* 26(24): 2100509.
- Castaldo, V. L., I. Pigliautile, F. Rosso, F. Cotana, F. De Giorgio, and A. L. Pisello. 2018. "How subjective and non-physical parameters affect occupants' environmental comfort perception." *Energy and Buildings* 178: 107-29. doi: <https://doi.org/10.1016/j.enbuild.2018.08.020>
- Emmerich, S. J., D. Heinzerling, J.-I. Choi, and A. K. Persily. 2013. "Multizone modeling of strategies to reduce the spread of airborne infectious agents in healthcare facilities." *Building and Environment* 60: 105-15. doi: <https://doi.org/10.1016/j.buildenv.2012.11.013>
- Faulkner, C. A., J. E. Castellini, W. Zuo, D. M. Lorenzetti, and M. D. Sohn. 2021. "Investigation of HVAC operation strategies for office buildings during COVID-19 pandemic." *Building and Environment* 207B: 108519. doi: <https://doi.org/10.1016/j.buildenv.2021.108519>
- Guo, M., P. Xu, T. Xiao, R. He, M. Dai, and S. L. Miller. 2021. "Review and comparison of HVAC operation guidelines in different countries during the COVID-19 pandemic." *Building and Environment* 187: 107368. doi: <https://doi.org/10.1016/j.buildenv.2020.107368>
- Li, C., and H. Tang. 2021. "Study on ventilation rates and assessment of infection risks of COVID-19 in an outpatient building." *Journal of Building Engineering* 42: 103090. doi: <https://doi.org/10.1016/j.job.2021.103090>
- Li, Y., H. Qian, J. Hang, X. Chen, P. Cheng, H. Ling, S. Wang, P. Liang, J. Li, S. Xiao, J. Wei, L. Liu, B. J. Cowling, and M. Kang. 2021. "Probable airborne transmission of SARS-CoV-2 in a poorly ventilated restaurant." *Building and Environment* 196: 107788. doi: <https://doi.org/10.1016/j.buildenv.2021.107788>
- Miller, S. L., W. W. Nazaroff, J. L. Jimenez, A. Boerstra, G. Buonanno, S. J. Dancer, J. Kurnitski, L. C. Marr, L. Morawska, and C. Noakes. 2021. "Transmission of SARS-CoV-2 by inhalation of respiratory aerosol in the Skagit Valley Chorale superspreading event." *Indoor Air* 31: 314-23. doi: <https://doi.org/10.1111/ina.12751>
- Mokhtari, R., and M. Hossein Jahangir. 2021. "The effect of occupant distribution on energy consumption and COVID-19 infection in buildings: A case study of university building." *Building and Environment* 190: 107561. doi: <https://doi.org/10.1016/j.buildenv.2020.107561>
- Pan, Y., C. Du, Z. Fu, and M. Fu. 2021. "Re-thinking of engineering operation solutions to HVAC systems under the emerging COVID-19 pandemic." *Journal of Building Engineering* 43: 102889. doi: <https://doi.org/10.1016/j.job.2021.102889>
- Pavilonis, B., A. M. Ierardi, L. Levine, F. Mirer, and E. A. Kelvin. 2021. "Estimating aerosol transmission risk of SARS-CoV-2 in New York City public schools during reopening." *Environmental Research* 195: 110805. doi: <https://doi.org/10.1016/j.envres.2021.110805>
- Peng, Z., A. L. Pineda Rojas, E. Kropff, W. Bahnfleth, G. Buonanno, S. J. Dancer, J. Kurnitski, Y. Li, M. G. L. C. Loomans, L. C. Marr, L. Morawska, W. Nazaroff, C. Noakes, X. Querol, C. Sekhar, R. Tellier, T. Greenhalgh, L. Bourouiba, A. Boerstra, J. W. Tang, S. L. Miller, and J. L. Jimenez. 2022. "Practical Indicators for Risk of Airborne Transmission in Shared Indoor Environments and Their Application to COVID-19 Outbreaks." *Environmental Science & Technology* 56: 1125-37. doi: <https://doi.org/10.1021/acs.est.1c06531>
- Peng, Z., and J. L. Jimenez. 2021. "Exhaled CO₂ as a COVID-19 Infection Risk Proxy for Different Indoor Environments and Activities." *Environmental Science & Technology Letters*.

- Riley, E. C., G. Murphy, and R. L. Riley. 1978. "Airborne spread of measles in a suburban elementary school." *American Journal of Epidemiology* 107: 421-32. doi: <https://doi.org/10.1093/oxfordjournals.aje.a112560>.
- Risbeck, M. J., M. Z. Bazant, Z. Jiang, Y. M. Lee, K. H. Drees, and J. D. Douglas. 2021. "Modeling and multiobjective optimization of indoor airborne disease transmission risk and associated energy consumption for building HVAC systems." *Energy and Buildings* 253: 111497. doi: <https://doi.org/10.1016/j.enbuild.2021.111497>
- Schibuola, L., and C. Tambani. 2021a. "High energy efficiency ventilation to limit COVID-19 contagion in school environments." *Energy and Buildings* 240: 110882. doi: <https://doi.org/10.1016/j.enbuild.2021.110882>
- Schibuola, L., and C. Tambani. 2021b. "Performance comparison of heat recovery systems to reduce viral contagion in indoor environments." *Applied Thermal Engineering* 190: 116843. doi: <https://doi.org/10.1016/j.applthermaleng.2021.116843>
- Sha, H., X. Zhang, and D. Qi. 2021. "Optimal control of high-rise building mechanical ventilation system for achieving low risk of COVID-19 transmission and ventilative cooling." *Sustainable Cities and Society* 74: 103256. doi: <https://doi.org/10.1016/j.scs.2021.103256>
- Shrubsole, C., S. Dimitroulopoulou, K. Foxall, B. Gadeberg, and A. Doutsis. 2019. "IAQ guidelines for selected volatile organic compounds (VOCs) in the UK." *Building and Environment* 165: 106382. doi: <https://doi.org/10.1016/j.buildenv.2019.106382>
- Srivastava, S., X. Zhao, A. Manay, and Q. Chen. 2021. "Effective ventilation and air disinfection system for reducing coronavirus disease 2019 (COVID-19) infection risk in office buildings." *Sustainable Cities and Society* 75: 103408. doi: <https://doi.org/10.1016/j.scs.2021.103408>
- Sun, C., and Z. Zhai. 2020. "The efficacy of social distance and ventilation effectiveness in preventing COVID-19 transmission." *Sustainable Cities and Society* 62: 102390. doi: <https://doi.org/10.1016/j.scs.2020.102390>
- Xu, Y., J. Cai, S. Li, Q. He, and S. Zhu. 2021. "Airborne infection risks of SARS-CoV-2 in U.S. schools and impacts of different intervention strategies." *Sustainable Cities and Society* 74: 103188. <https://doi.org/10.1016/j.scs.2021.103188>
- Zheng, W., J. Hu, Z. Wang, J. Li, Z. Fu, H. Li, J. Jurasz, S. K. Chou, and J. Yan. 2021. "COVID-19 Impact on Operation and Energy Consumption of Heating, Ventilation and Air-Conditioning (HVAC) Systems." *Advances in Applied Energy* 3: 100040. doi: <https://doi.org/10.1016/j.adapen.2021.100040>

Design of Energy-Neutral Smart Buildings: An Ontological Framework to Integrate LCA, BIM and PLM

Tarun Kumar – CPDM, Indian Institute of Science, Bangalore, India – tarunkumar@iisc.ac.in

Monto Mani – CST & CPDM, Indian Institute of Science, Bangalore, India – montoman@iisc.ac.in

Abstract

The smart built environment (SBE) exhibits a dynamic integration between the physical and digital environment, where the physical elements, such as spaces, walls, windows, doors, roof, and floor, interact with the digital sensing elements, such as sensors, actuators, control systems, and networking systems. Energy neutrality is a concept dealing with the lifecycle energy performance of energy-saving sensing devices integrated into the SBE, such as the smart sensor-actuator system (SSAS). Ontology is a concept of representing and organising information (and their inter-relationships) about a specific domain with the intention of managing complexity, enhancing understanding, and promoting problem-solving skills. Employing semantic web technologies, a framework for designing and simulating energy-neutral, sensor-embedded smart buildings is proposed, which exhibits an ontological integration of Lifecycle Assessment (LCA), Building Information Modelling (BIM), and Product Lifecycle Management (PLM). A preliminary implementation of the proposed framework is demonstrated using OWL (Ontological Web Language) in Protégé software. After that, a design interaction matrix between buildings (and their components), building designers, product designers, and lifecycle practitioners is developed to provide efficiency, optimisation, and sustainability in the design process. This integration framework would streamline the design process, providing a collaborative simulation platform for cross-field designers to enhance the environmental performance of the SBE. In the future, this framework could be employed to create a robust real-time integrated IoT-based platform for designing and modelling energy-neutral smart buildings.

1. Introduction

The design and modelling of smart buildings is a complex process compared to conventional buildings (Kumar & Mani, 2019; Panteli et al., 2020). The

smart built environment dynamically integrates the physical and digital environments, with physical elements—such as spaces, walls, windows, doors, roofs, floors, lights, HVAC and so on—interacting with digital sensing elements such as sensors, actuators, control systems, and networking systems (Dasgupta, 2018; Kumar et al., 2022). The challenges in this interactive relationship stem from the need for a real-time information exchange between physical and digital environments, emphasising the importance of decisions made during the early stages of building design. For example, luminaire technology (LED/CFL), integrated occupancy sensors, and real-time interactions (or feedback) are critical for occupant comfort, well-being, and energy efficiency in the lighting subsystem of smart buildings (Khanna et al., 2019; Kumar et al., 2018; Nair et al., 2018 and 2019). Despite recent advances in information technology and computational intelligence, the architecture, engineering, construction, and operations (AECO) industry manifests a substantial digital divide in technology adoption (Ayinla & Adamu, 2018; Saka et al., 2022). The computing industry's technical know-how, such as semantic web technologies, could be leveraged in the AECO industry to bridge this burgeoning gap (Pauwels et al., 2017).

Smart building design (SBD) is a cross-functional domain involving multiple stakeholders, including building designers (architects, civil engineers, structural engineers), computer and electronic engineers, sensor designers, control engineers, LCA practitioners, interaction designers and data scientists (Kumar & Mani, 2017a). As a result, incorporating smart sensor-actuator systems (SSAS) into the construction, information, operation, and control systems of smart buildings takes time and resources. The SBD requires a constant knowledge exchange and

information feedback from cross-functional domains to optimise performance. LCA, BIM, and PLM are domains involved in various SBD stages but are fragmented in process/data integration and stakeholder management, resulting in data redundancy, complexity, and inefficiency.

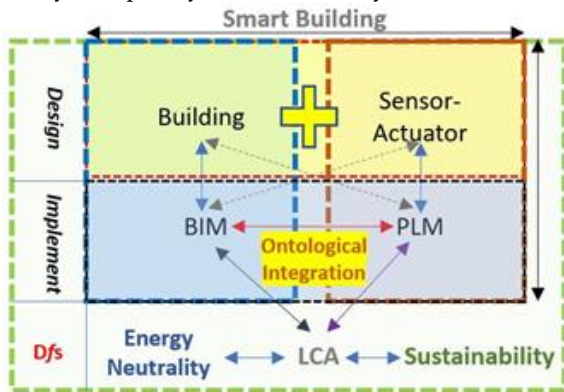


Fig. 1 – Design of energy-neutral smart buildings: conceptual structure of the research study integrating LCA, BIM and PLM

This paper proposes a framework for designing and modelling energy-neutral, sensor-embedded smart buildings using an ontological integration of LCA, BIM and PLM employing semantic web technologies. Fig. 1 presents the conceptual structure of the study.

Integrating collaborative knowledge of various designers and domains—at the early design phase of a smart building—is critical for synchronising the different design methodologies adopted by each stakeholder. Stakeholders (designers and modellers) use field-specific design and implementation methodologies from their respective domains at various stages of the design process. As a result, a comprehensive framework defining the criteria for combining data from multiple fields into a single collaborative platform that supports the inter-accessibility of data from all stakeholders involved in designing and modelling a smart building is needed. Such a framework reduces the limitations of disconnected data by creating an ontology-based linked data model for smart building design using semantic web technologies.

1.1 Energy Neutrality in Smart Buildings

Energy Neutrality is a concept dealing with energy payback associated with energy-saving sensing devices such as smart sensor-actuator systems (SSAS)

over their lifecycle (Kumar & Mani, 2017b). Often, the energy involved over the lifecycle of an SSAS could be more than the energy-saving it yields, depending on the connected load (Kumar & Mani, 2017a). Smart buildings are those integrated with SSAS aimed at improving the productivity of the building occupants, saving energy, and information management. With smart buildings becoming increasingly complex, energy neutrality computations can provide an insight into the appropriate design and integration of smart sensor-actuator systems. Earlier studies into energy neutrality have revealed that the design of the SSAS in its entirety (electronics, housing, fixtures, wiring) has a significant impact on its total embodied energy (Kumar & Mani, 2017a and 2017b). The SSAS could be viewed as products integrated into buildings, with their lifecycle design influencing their effective integration in buildings, which ultimately affects the sustainability performance of smart buildings.

1.2 Lifecycle Assessment

Lifecycle assessment (LCA) is a method to assess the environmental impacts of a product (such as SSAS) throughout its lifecycle, including extraction, manufacturing, use/operation, and end-of-life stages (ISO, 2006). LCA methodology is one of the industry-accepted and scientific methods to assess the sustainability of a product (Jensen et al., 1997; Röck et al., 2018). It considers the inflow and outflow of mass, energy, and emissions through various product lifecycle stages. ISO 14040-14044 is the international standard that describes the framework and guidelines for conducting an LCA. The different phases according to ISO 14040:2006 are: 'Goal and scope definition', 'Lifecycle inventory analysis (LCI)', 'Lifecycle impact assessment (LCIA)', 'Interpretation phase' and 'Reporting and review phase' (ISO, 2006). The definition of 'system boundary' and 'functional units' are essential steps to conduct an LCA of any product. The databases used are Ecoinvent, GaBi, USDA, ELCD, Agri-footprint, etc. The prominent software used is Gabi, SimaPro, Umberto, openLCA, and so on.

1.3 Building Information Modelling

Widely used in the AECO industry, Building Information Modelling (BIM) is an integrated infrastructural data management process that shares and increases the transparency of building data in its designing, construction, and management (Ghaffarianhoseini et al., 2017; Volk et al., 2014). BIM is a three-dimensional modelling process for developing a built environment as a digital representation of physical built elements and spaces (Ghaffarianhoseini et al., 2017). Moreover, BIM actively supports design and management decision-making at all phases of the building lifecycle, including planning, design, construction, and management stages, thus providing a collaborative platform for all the stakeholders by enhancing the information flow. The software tools for conducting BIM are Autodesk Revit, ArchiCAD, NavisWorks, Trimble Connect, and VectorWorks Architect.

Table 1 – A brief comparison of LCA, BIM and PLM

	LCA	BIM	PLM
Industry	Sustainability assessment	AECO industry	Manufacturing industry
Goal	Interested in environmental impacts	Building design construction and management	Product lifecycle management
Model & data	Lifecycle model & database	3D virtual models & BIM data	3D Product model & CAD data
Stakeholders	LCA practitioners, compliance authorities, designers & researchers	Shared repository between architects, engineers, and managers	Designers, engineers, manufacturers, researchers

1.4 Product Lifecycle Management

Product Lifecycle Management (PLM) is an extensive data management system for managing the entire life of a product. It is a collaborative activity that integrates product management and stakeholders across its lifecycle (Lämmer & Theiss, 2015). The product's data flows through initial design conception to detailed engineering design, manufacturing, packaging, distribution, usage, service (maintenance), and end-of-life phases. It is critical to centralise a product's information throughout its

lifecycle to facilitate cross-domain knowledge exchange. The approach adopted in PLM primarily focuses on improving product efficiency in its design, economic value, environmental impact, and social outreach to promote the decision-making process, especially during early design decisions. Table 1 compares LCA, BIM, and PLM and lays the conceptual foundation for their integration.

1.5 Ontology and Semantics

Ontology is a machine-readable (formal) specification of conceptualisation for representing and organising information in a specific domain to manage complexity, improve understanding, and promote problem-solving ability (W3C, 2004). By converting complex systems into simple processes, ontology creates a shared and collaborative platform in the information sciences, allowing knowledge to be used in widespread cross-domain functionality that can be searched and queried via the internet. It also explicitly manages knowledge bases by systematically organising their specification—in terms of concepts, classes, properties, relations, definition, function, constraints, axiom, rules, and categories—and displaying logical reasoning and web semantics in data description and structural layout (for example, knowledge graph).

The family of ontologies (formal knowledge representation languages) are created in Web Ontology Language (OWL), based on the Semantic Web domain (Antonioni & Van Harmelen, 2004; W3C, 2004). The design of OWL is a build-up version of the Resource Description Framework (RDF). Semantic web technologies (OWL and RDF) promote mapping and analysis of data to create meaningful knowledge-bases and promote information interoperability across domains. In general terms, the primary function of semantic web technologies is the creation of an interlinkage (of language with different formats) that integrates different frameworks adopted from cross-functional fields and data collected from multiple sources in varied (non-standardised) protocols. Hence, ontologies authored in formal languages (such as OWL) are the connecting bridges across multiple data formats to extract common (and unambiguous) meaningful information, characterising the knowledge in class, objects, and

their inter-relativity, functions, attributes, and hierarchies. From the semiotic perspective, any language (machine-readable or English) consists of three distinct fields: a) syntactics (objective: the set of rules and grammatical structure), b) semantics (subjective: the arrangement of vocabulary in a structured format to generate its meaning and expression), and c) pragmatics (contextual implication: inference and implication, context-dependent). Similarly, semantic web technologies have triples for knowledge management and modelling semantic data. The semantic triples consist of three entities which are as follows: (a) subject (entity); (b) predicate (attribute); and (c) object (value-model) to compose a common machine-interpretable statement about the semantic database. Therefore, this makes ontological languages (e.g., OWL) an integration layer to standardise the cross-functional knowledge-base. For the effective design of smart buildings, the integration of LCA, BIM, and PLM is necessitated. The 'smart building design' domain could benefit immensely by leveraging the power of ontology and semantics to integrate SSAS into buildings, thereby making them more sustainable. Hence, Ontology and semantic web technologies provide an appropriate collaborative platform for such a cross-domain integration.

2. Integrated Ontological Framework

An integrated ontological framework is proposed in Fig. 2 to integrate LCA, BIM and PLM at various levels, i.e., L1-data integration layer, L2-data exchange layer, L3-software implementation layer, L4-design implementation layer, L5-stakeholder integration layer, and L6-domain integration layer. An ontological knowledge integration framework across these layers (L1-L6) provides a consolidated framework for the collaborative design of energy-neutral smart buildings. The three vertices of the triangular layers represent the LCA (sustainability domain), the BIM (building domain), and the PLM (product design domain), respectively. In the L1 layer, LCA data is integrated with product and building data. In layer L2, LCA, BIM and PLM exchange formats are consolidated to form a machine-interpretable, formal, and explicit data layer. Then, these data are fed into

an integrated software environment that combines the LCA, BIM and PLM capabilities (L3).

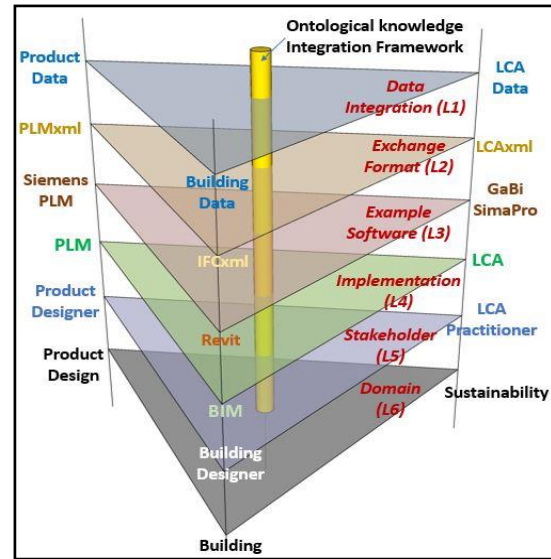


Fig. 2 – A model framework for the ontological integration of BIM, PLM and LCA for the design of energy-neutral smart buildings

After that, a design implementation layer (L4) is envisaged with data processing and knowledge integration capabilities. The L4 layer leads to a collaborative design platform(L5) comprising subject experts, i.e., LCA practitioners, architects and product designers. A single cross-functional design team may replace these designers in the future. Finally, the domain level integration of sustainability, building design, and product design is completed at layer L6, resulting in an inter-disciplinary domain for smart building design.

3. Implementation in Protégé

This preliminary framework for LCA-BIM-PLM integration is modelled on Protégé software using the ontological web language (OWL). The XML version used for the data integration is XML version 1.0. The data modelling vocabulary used is RDFS (Resource Description Framework Schema). The model framework structure comprises: - 'Entity', 'Classes', 'Object properties', 'Annotation properties', 'Data properties' and 'Individual by class'. 'Design_Smart_Buildings' is the main class in 'Owl: Things', and 'LCA', 'BIM', and 'PLM' are subclasses, as shown in Fig. 3.

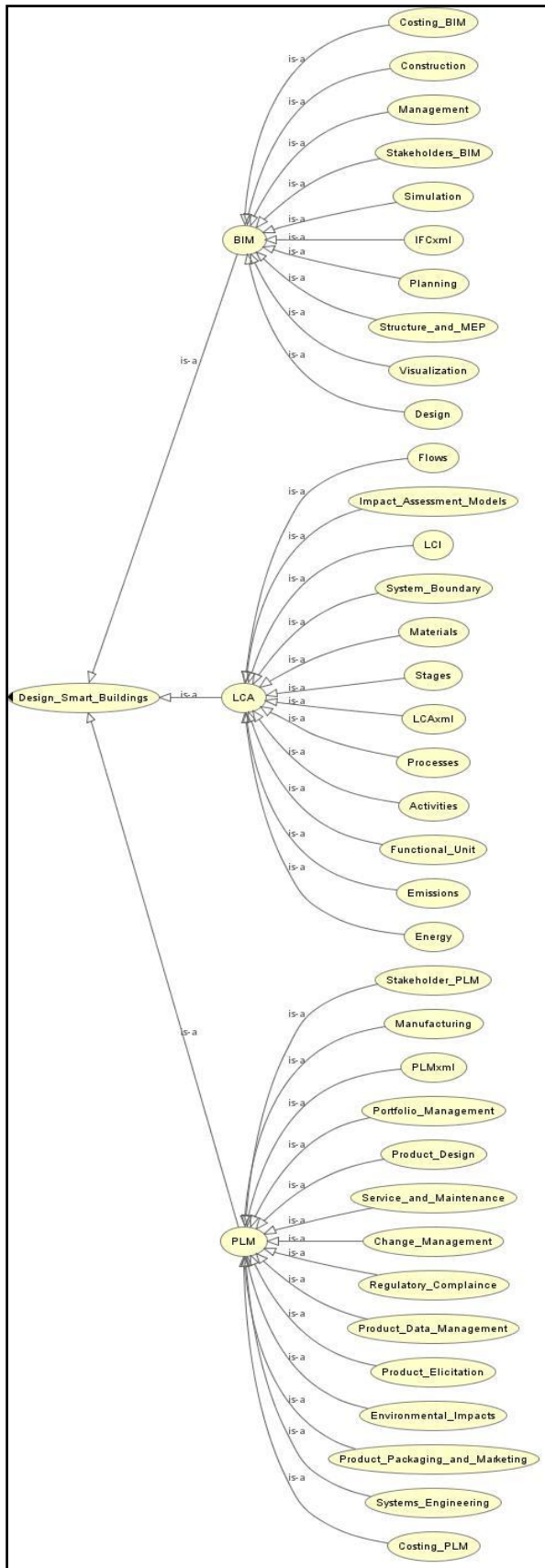


Fig. 3 – Preliminary implementation of the Model LCA-BIM-PLM framework for the design of smart buildings in Protégé Software

This framework schema can be saved in RDF/XML syntax, Turtle syntax, OWL/XML syntax, OBO syntax, Manchester/OWL syntax, OWL functional syntax, and LaTeX JSON-LD syntax. The ‘reasoner’ used for querying is ELK 0.4.3. ‘OWLviz’ is used for visualisation, while ‘OntoGraf’ is used for creating the graph. DL query and SPARQL 1.1 semantic query languages are used to access, retrieve, and manipulate data in RDFS. A Java code is generated to interface, translate, and bridge the semantic web ontology with the logic programming domain.

Each class/subclass can have their object, data, and annotation properties connected by relationships. Each instance in this framework can be designed as a standalone smart building with all the above-mentioned characteristics. These unique instances of smart buildings could be accessed via the web and would form a smart building database known as the ‘Internet of Buildings’ (IoB).

4. Discussions

As shown in Table 2, column V1 represents the lifecycle of data through ‘data’, ‘information’, ‘knowledge’, ‘insight and wisdom’ and ‘design and optimisation’ stages. The rows represent the integration between LCA, BIM and PLM domains.

Table 2 – OWL-based ontological integration framework for LCA, BIM and PLM to design energy-neutral smart buildings

	V1	V2	V3	V4	V5
			LCA	BIM	PLM
H1	Data	Processing and Apply Syntax	ILCD	IFC	JT
H2	Information	Meaning and Semantics	LCA XML	IFC XML	PLM XML
			Integrate Data Format		
			Ontological Integration by OWL		
H3	Knowledge	Cross Domain Integration	LCA	BIM	PLM
			K_{n1}	K_{n2}	K_{n3}
H4	Insight and Wisdom	New Knowledge Generation	Knowledge Integration		
			Shared Conceptualisation		
H5	Design and Optimisation		Creative Innovations		
			Resource Efficient and Energy-Neutral Design		
	Smart Buildings				

It should be noted that appropriate transformations are applied to each stage. H1 represents the data processing and application of syntax for data integration. Existing data in the LCA, BIM and PLM industries are fragmented. Recently, work on standardising data formats within the domains has started, e.g., ILCD format in LCA, IFC data format in BIM, and JT format in PLM. The inter-operability of such cross-domain datasets is low due to multiple formats, multiple software platforms and different protocols. The eXtended Markup Language (XML) can solve this problem by applying user-defined specific rule sets (Syntax) to make it machine-interpretable and independent of software and hardware platforms. In this framework, the LCA, BIM and PLM data are converted to XML format, ready to be processed and queried.

Once the cross-domain data is syntactic and formal (machine-interpretable), the question of data semantics (meaning of such data) arises. In the H2 stage, the ontological web language (OWL) is used to semantically integrate this data and reduce ambiguity in its meaning. The processing of cross-functional data with semantic web tools would transform the data into chunks of useful information, which is still far away from a consolidated knowledge stage. In the H3 stage, when these chunks of information are integrated vertically in their respective domain, it becomes knowledge (e.g., Kn1 in LCA, Kn2 in BIM, Kn3 in PLM). In the next stage (H4), these knowledge sets are integrated through an ontological knowledge-integration framework to form a consolidated design knowledge set that provides valuable insights into smart building design and modelling. This acquired wisdom backed by empirical and integrated data, constitutes the breeding ground for 'shared conceptualisation' and 'new' knowledge. The designer (of smart buildings) would use this 'new knowledge' to improve designs, create innovations and provide optimisations for energy-neutrality in the H5 stage. Moreover, the design and optimisation (H5) stage would provide a feedback loop for the data stage (H1), further improving the data requirements, new data collection, data filtering and data integration processes. The capability of the H5 stage to provide a reinforcement feedback loop is not only limited to H1 stage, but it can also give feedback to H2, H3, H4 and H5 stage.

This framework facilitates multi-variate assessment of smart building performance in terms of energy, functionality, and operability before finalising the design by creating a 'design schema' as a transitional framework between the building's physical and digital (geo-spatial and energy-related) information. Additionally, this meta-framework comprehensively characterises a smart built environment integrated with a sensing system, allowing designers (and stakeholders) to evaluate the design using a hybrid simulation platform, and then make necessary early-design decisions regarding building performance, sensor-actuator integration, energy efficiency, and human-building interactions (HBI).

4.1 Design Implications

This ontological integration framework provides for the interactions (and feedback) between various designers, researchers and stakeholders involved in designing energy-neutral smart buildings. A design interaction matrix captures the interactions between buildings (and their functional components), and designers (of building, products, and sustainability) are captured by a design interaction matrix, as shown in Table 3. B(i) and B(j) represent smart buildings. B(i) is the superset containing elements from individual building components to the whole building system. 'Building designer' set D(B) consists of architects, civil engineers, structural engineers, and various consultants involved in the BIM process. Whereas D(P) represents the product designer set of smart sensor-actuator systems and energy-saving appliances.

Table 3 – Design interaction matrix for the ontological integration of BIM, PLM and LCA for energy-neutral smart buildings

$B(i) \rightarrow B(j)$ $\forall B(i) \subseteq B(j)$	B(j)	D(B)	D(P)	S(L)
B(j)	$B(j) \rightarrow B(j)$	$B(j) \rightarrow D(B)$	$B(j) \rightarrow D(P)$	$B(j) \rightarrow S(L)$
D(B)	$D(B) \rightarrow B(j)$	$D(B) \rightarrow D(B)$	$D(B) \rightarrow D(P)$	$D(P) \rightarrow S(L)$
D(P)	$D(P) \rightarrow B(j)$	$D(P) \rightarrow D(B)$	$D(P) \rightarrow D(P)$	$D(P) \rightarrow S(L)$
S(L)	$S(L) \rightarrow B(j)$	$S(L) \rightarrow D(B)$	$S(L) \rightarrow D(P)$	$S(L) \rightarrow S(L)$

To add the sustainability layer to the smart building design, S(L) indicates the LCA practitioners who perform the sustainability assessment of the system.

The diagonal of this matrix is the self-interactions in the B(j), D(B), D(P) and S(L). The first cell represents the interaction between buildings B(i) and B(j), which opens the possibilities of inter-building communication and smart city integration. This matrix is skew-symmetric, as the D(B)→B(j) interaction is not the same as B(j)→D(B) interaction, but rather is opposite in direction.

The ontological integration framework can assist these interactions between stakeholders in designing better smart buildings. In future, these interactions can be automated, and the D(B), D(P) and S(L) designers can be integrated to form one single set of designers, known as 'Smart Building Designers'. Such cross-platform designers would further improve the design framework, resulting in smart buildings that are both energy- and resource-efficient.

5. Conclusions

Based on the ontological integration of the three participating domains, this LCA-BIM-PLM integrated framework provides a plausible solution for designing an energy-neutral smart building system. A preliminary implementation of this ontological framework is demonstrated in Protégé software with the help of OWL. Furthermore, a design interaction matrix is created between buildings (and their components), building designers, product designers, and lifecycle practitioners, allowing for increased efficiency, optimisation, and sustainability in the building design and simulation process, which is further enhanced by reinforcing feedback loops.

The proposed framework would improve the environmental performance of smart buildings by streamlining the design and simulation process, providing a collaborative platform for cross-field designers. In the future, a robust real-time platform for designing and modelling energy-neutral smart built environments could be developed using this framework as its foundation.

References

- Antoniou, G., and F. Van Harmelen. 2004. "Web Ontology Language: Owl." In *Handbook on Ontologies*: 67–92. Springer.
- Ayinla, K. O., and Z. Adamu. 2018. "Bridging the Digital Divide Gap in BIM Technology Adoption." *Engineering, Construction and Architectural Management* 25(10): 1398–1416. doi: <https://doi.org/10.1108/ECAM-05-2017-0091>
- Dasgupta, A. 2018. *Towards a Unified Framework for Smart Built Environment Design: An Architectural Perspective*. Virginia Tech.
- Ghaffarianhoseini, A., J. Tookey, A. Ghaffarianhoseini, N. Naismith, S. Azhar, O. Efimova, and K. Raahemifar. 2017. "Building Information Modelling (BIM) Uptake: Clear Benefits, Understanding Its Implementation, Risks and Challenges." *Renewable and Sustainable Energy Reviews* 75: 1046–1053. doi: <https://doi.org/10.1016/j.rser.2016.11.083>
- ISO. 2006. *ISO 14040: Environmental Management—Life Cycle Assessment—Principles and Framework*. International Organization for Standardization.
- Jensen, A. A., J. Elkington, K. Christiansen, L. Hoffmann, B. T. Moller, and A. Schmidt. 1997. "Life-Cycle Assessment (LCA)-a Guide to Approaches." *European Communities*. <https://www.eea.europa.eu/publications/GH-07-97-595-EN-C/Issue-report-No-6.pdf>
- Khanna, A., S. Arora, A. Chhabra, K. K. Bhardwaj, and D. Kumar Sharma. 2019. "IoT Architecture for Preventive Energy Conservation of Smart Buildings BT - Energy Conservation for IoT Devices: Concepts, Paradigms and Solutions." edited by Mamta Mittal, Sudeep Tanwar, Basant Agarwal, and Lalit Mohan Goyal, 179–208. Singapore: Springer Singapore. doi: https://doi.org/10.1007/978-981-13-7399-2_8
- Kumar, T., and M. Mani. 2017a. "An Energy-Neutrality Based Evaluation into the Effectiveness of Occupancy Sensors in Buildings: An Integrated Life-Cycle Study." In *Design to Thrive Proceedings PLEA 2017*, 2:2579–86. NCEUB 2017
- Kumar, T., and M. Mani. 2017b. "Life Cycle Assessment (LCA) to Assess Energy Neutrality in Occupancy Sensors." In *Research into Design for Communities*: 105–16. doi: https://doi.org/10.1007/978-981-10-3521-0_9

- Kumar, T., and M. Mani. 2019. "Discerning Occupant Psychosocial Behaviour in Smart Built Environment and Its Design." In *Proceedings of the 1st ACM International Workshop on Urban Building Energy Sensing, Controls, Big Data Analysis, and Visualization - UrbSys'19*: 69–76. doi: <https://doi.org/10.1145/3363459.3363534>
- Kumar, T., R. R. Rao, P. C. Ramamurthy, and M. Mani. 2018. "Safety of Light Emitting Diode (LED) Based Domestic Lighting in Rural Context." In *2018 15th IEEE India Council International Conference (INDICON)*: 1–5. Doi: <https://doi.org/10.1109/INDICON45594.2018.8987093>
- Kumar, T., R. Srinivasan, and M. Mani. 2022. "An Emergy-Based Approach to Evaluate the Effectiveness of Integrating IoT-Based Sensing Systems into Smart Buildings." *Sustainable Energy Technologies and Assessments* 52: 102225. doi: <https://doi.org/https://doi.org/10.1016/j.seta.2022.102225>
- Lämmer, L., and M. Theiss. 2015. "Product Lifecycle Management." In *Concurrent Engineering in the 21st Century: Foundations, Developments and Challenges*. doi: https://doi.org/10.1007/978-3-319-13776-6_16
- Nair, S., R. Rao, T. Kumar, G. G. Prasad, M. Kumar, P. K. Henna, A. Saifudeen, and M. Mani. 2019. "Design of a Do-It-Yourself (DIY) Based Solar-Powered LED Lighting System for Training and Empowering Rural Youth." In *ICoRD 2019*: 451–60. doi: https://doi.org/10.1007/978-981-13-5974-3_39
- Nair, S., R. R. Rao, T. Kumar, G. G. Prasad, M. Kumar, P K. Henna, A. Saifudeen, and M. Mani. 2018. "'Roshini' - Developing a DIY Rural Solar Light: Utilizing Products at End-of-Life (EoL) Stage." In *2018 IEEE Global Humanitarian Technology Conference (GHTC)*: 1–6. doi: <https://doi.org/10.1109/GHTC.2018.8601891>
- Panteli, C., A. Kylili, and P. A Fokaides. 2020. "Building Information Modelling Applications in Smart Buildings: From Design to Commissioning and beyond A Critical Review." *Journal of Cleaner Production* 265: 121766. doi: <https://doi.org/https://doi.org/10.1016/j.jclepro.2020.121766>
- Pauwels, P., S. Zhang, and Y.-C. Lee. 2017. "Semantic Web Technologies in AEC Industry: A Literature Overview." *Automation in Construction* 73: 145–65. doi: <https://doi.org/https://doi.org/10.1016/j.autcon.2016.10.003>
- Röck, M., A. Hollberg, G. Habert, and A. Passer. 2018. "LCA and BIM: Visualization of Environmental Potentials in Building Construction at Early Design Stages." *Building and Environment* 140: 153–61. doi: <https://doi.org/https://doi.org/10.1016/j.buildenv.2018.05.006>
- Saka, A. B., D. W. M. Chan, and A.-M. Mahamadu. 2022. "Rethinking the Digital Divide of BIM Adoption in the AEC Industry." *Journal of Management in Engineering* 38(2): 4021092.
- Volk, R., J. Stengel, and F. Schultmann. 2014. "Building Information Modeling (BIM) for Existing Buildings—Literature Review and Future Needs." *Automation in Construction* 38: 109–27.
- W3C. 2004. "OWL Web Ontology Language Semantics and Abstract Syntax." Edited by P. Patel-Schneider, P. Hayes, and I. Horrocks. W3C. <https://www.w3.org/TR/owl-semantics/semantics-all.html>

Assessing the Performance of a Simplification Algorithm for Urban Building Energy Modeling in Multi-Objective Optimization

Federico Battini – Free University of Bozen-Bolzano, Italy – federico.battini@natec.unibz.it

Giovanni Pernigotto – Free University of Bozen-Bolzano, Italy – giovanni.pernigotto@unibz.it

Andrea Gasparella – Free University of Bozen-Bolzano, Italy – andrea.gasparella@unibz.it

Abstract

Urban Building Energy Modeling and Multi-Objective Optimization are two very computationally intensive applications of Building Performance Simulation. In this research, a simplification algorithm developed to speed up thermal simulations at urban scale was tested to assess its performance in optimization studies. Since the algorithm showed good accuracy at the individual building level, it was applied to standalone buildings, considering a set of energy efficiency measures and all the possible combinations of four objectives, i.e., heating and cooling needs, thermal comfort and costs. The algorithm showed adequate performance in finding the optima with the same inputs for most of the considered buildings and combinations of objectives in different climatic conditions, allowing the simulation time to be reduced to one third.

1. Introduction

In 1965, Gordon E. Moore stated that the number of transistors on an integrated circuit would have increased at a rate of roughly a factor of two per year, at least over ten years (Moore, 1965). Nowadays, such a prediction, known as Moore's law, is still true, and it means that the power of computers is approximately doubling every couple of years. Thanks to such exponential increases in computing resources, two fields of Building Performance Simulation *BPS* have been gaining more and more interest in recent years: Multi-Objective Optimization *MOO* and Urban Building Energy Modeling *UBEM*. Rather than offering a one-design solution, *MOO* provides the flexibility of choosing from a set of optimal solutions with a more realistic decision-making process (Costa-Carrapiço et al., 2020). On the other hand, *UBEM* aims at finding an aggregated

and simplified way of estimating the operational energy needs of groups of buildings, overcoming the limitations of single building modeling (Reinhart & Davila, 2015).

The major computational cost of *MOO* and *UBEM* is the main drawback that they have in common. Regardless of other technical aspects, such as the modeler's skills and knowledge, being too computationally demanding is the first hurdle preventing their widespread employment in common practice. In addition, it is also the main reason why most of the *UBEM* studies present in the literature investigate retrofit or design scenarios (Ang et al., 2020) rather than performing *MOO*. Haneef et al. (2021) carried out one of the few studies combining *UBEM* and *MOO*. Considering a residential district of around a hundred buildings, they examined different sets of renovation measures for the building envelope and found the Pareto front with regarding three objectives, i.e., energy, economic and sustainability performances.

In a previous work (Battini et al., 2021), we proposed a simplification algorithm for *UBEM* to speed up the simulation time limiting the accuracy loss at hourly and building scale. The algorithm simplifies any arbitrarily shaped building into a representative shoebox to estimate the building's indoor temperatures and thermal loads. Since the procedure showed good precision in assessing the building's performance at individual level, it could also be used to expedite other aspects of *BPS*, such as *MOO*. Given these premises, the aim of the present work is to assess the capabilities of the simplification in performing *MOO*. A batch of standalone buildings were selected to test the procedure and they were simulated in three climates. The optimization was carried out considering energy efficiency measures

pertaining only the building envelope respect to up to four objectives, i.e., heating needs, cooling needs, indoor thermal comfort, and economic performance. The objectives were considered one, two, three and four at a time, in order to evaluate the algorithm's reliability with all possible target combinations.

2. Methodology

2.1 Simplification Algorithm

The simplification, or “shoeboxing”, algorithm is capable of converting a building of any shape into a shoebox. Thus, from a detailed or starting model, a simplified or shoebox model is obtained. The process to be employed for simplifying each building present in an urban model into its representative shoebox has three steps:

1. *Shoebox generation*: by solving a non-linear system of three equations in three unknowns, the dimensions of the shoebox are found from the starting building geometry.
2. *Radiation modeling*: opaque surfaces are placed on a portion of each window of the simplified model, in order to reduce the amount of incoming radiation and reproduce the effect of the contextual and self-shadings simulated in the detailed model. To size such equivalent shading surfaces, a radiation analysis is performed on both models to compute obstruction ratios for each orientation and floor.
3. *Building adjacency*: adiabatic surfaces are used to account for adjacent buildings.

A more in-depth description of the shoeboxing process can be found in a previous work by the authors (Battini et al., 2021). Once obtained, detailed and simplified models are characterized by the same non-geometrical features.

The procedure does not depend on specific tools to be developed, hence it can be reproduced with any software having the right capabilities. In this work, Rhinoceros and Grasshopper were employed for the geometrical conversion, Ladybug Tools SDK was used for creating the energy models, and EnergyPlus was utilized as BPS tool. The programs were coupled by automating the entire process thanks to custom-made Python scripts.

2.2 Multi-Objective Optimization

2.2.1 Buildings selection for testing

The simplification algorithm developed was first tested on 3072 buildings of complex shape built out of polyominoes (Golomb, 1994) to guarantee complex and non-repetitive shapes. Moreover, to assess its prediction capabilities under different boundary conditions, every building geometry obtained and its related simplified model were simulated in three climates, i.e., Bolzano and Messina, Italy, and Denver, US.

Since performing a MOO is already largely computationally and time-consuming, a set of buildings were chosen from the ones already generated. Fig. 1 reports the boxplots for the relative annual differences between detailed and simplified models in the three climates. The results are reported as a function of the number of floors of each building and show how, for both targets, the simplified model prediction always falls within $\pm 20\%$ difference. Five buildings for each target (i.e., heating and cooling) were chosen for each climate, thus thirty building were used in the MOO. In order to employ representative buildings in this work, starting from the relative annual differences obtained by the previous study, buildings corresponding to the minimum, first quartile, median, third quartile and maximum difference were selected. In this way, it was possible to study buildings whose performances are different but also representative of the batch which they were picked from. Among the starting 3072 possibilities, Fig. 2 reports the buildings selected for the analysis. Instead of simulating all buildings in the three climates, each building was simulated in the same climate from which it was selected. Thus, ten buildings were simulated per each climatic condition.

2.2.2 Optimization

The aim of the present optimization is to test whether the detailed and simplified building models' non-dominated solutions match in terms of inputs. Thus, the optima found should have the same values for the inputs rather than the outputs.

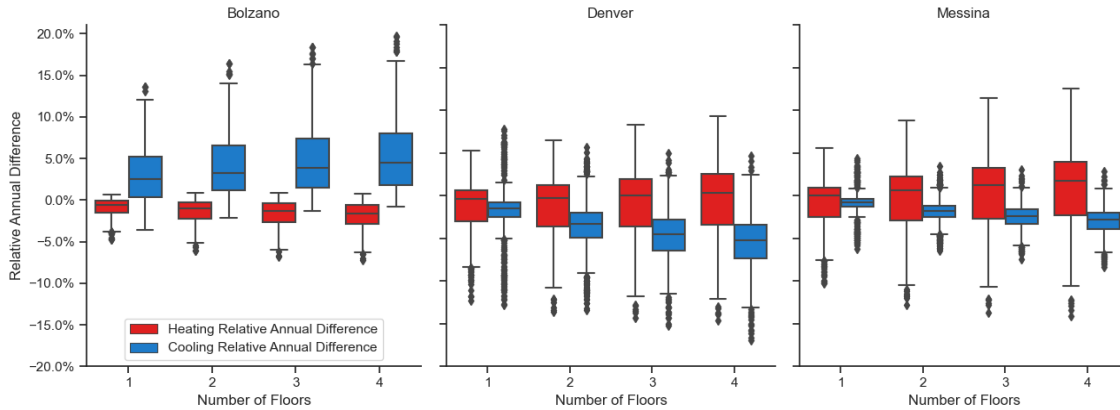


Fig. 1 – Boxplots for annual heating and cooling needs relative differences depending on buildings' number of floors for the entire building

Since the algorithm was developed for urban scale applications, the variables considered in this first study only focus on the envelope. Since in *UBEM*, the information regarding the systems is usually not available, retrofit or design scenarios mainly pertain to the buildings' envelope. Thus, three variables were considered:

- insulation type: all external opaque surfaces are characterized by the same composition, three types of insulation were selected, i.e., XPS, mineral wool, and cellulose fiber.
- insulation thickness: the thickness of the type of insulation varied from 2 to 20 cm with a step of 2 cm.
- type of window: five different types of windows were chosen, such as double glazing with air filling, double glazing with argon filling and

high solar factor, double glazing with argon filling and low solar factor, triple glazing with argon filling and high solar factor, and triple glazing with argon filling and low solar factor.

In Table 1, the variables considered are reported along with their properties and related investment costs. As far as insulation is concerned, the investment cost per square meter was computed in function of the thickness s according to the formulas reported for each type of material. The investment costs considered in this study for the opaque and transparent envelope are the same as those employed by Haneef et al. (2021) and Pernigotto et al. (2017). Given the low number of combinations, a full factorial analysis was carried out and all possibilities were simulated.

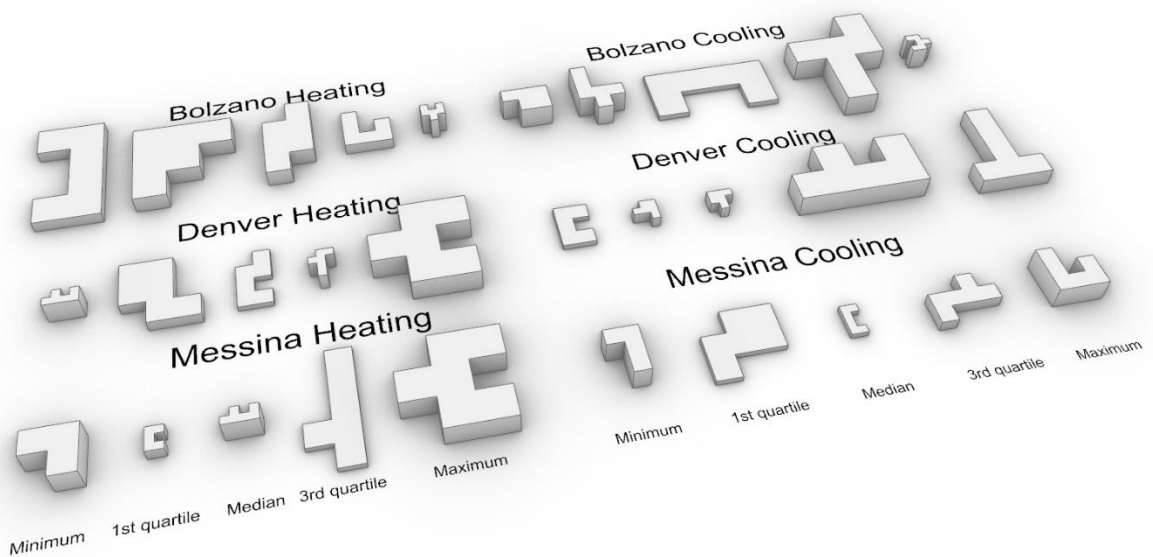


Fig. 2 – Selection of buildings for each target and climate

Table 1 – Variables for MOO

Insulation				
Insulation	Thermal conductivity [$\text{W m}^{-1} \text{K}^{-1}$]	Density [kg m^{-3}]	Specific heat [$\text{J kg}^{-1} \text{K}^{-1}$]	Investment cost [€ m^{-2}]
XPS	0.035	30	1450	$112.5 \cdot s + 55.6$
Mineral wool	0.038	130	1030	$213.6 \cdot s + 70.2$
Cellulose fiber	0.045	160	2000	$363.7 \cdot s + 74.6$
Windows				
Window	Glass transmittance [$\text{W m}^{-2} \text{K}^{-1}$]	SHGC [-]	Investment cost [€ m^{-2}]	
Double glazing air filling	2.72	0.76	247.30	
Double glazing argon filling high SHGC	1.14	0.61	404.33	
Double glazing argon filling low SHGC	1.10	0.35	439.06	
Triple glazing air filling high SHGC	0.61	0.58	477.65	
Triple glazing air filling low SHGC	0.60	0.34	454.49	

Thus, the real Pareto solutions were found, since no optimization algorithm was used.

To test the simplification capabilities as broadly as possible, the heating demand, cooling demand, thermal comfort and economic performance were considered as the objectives to be minimized. The heating and cooling needs were accounted as annual energy needs expressed in megawatt hour by summing up the hourly needs. Thermal comfort was evaluated as the annual average of the hourly results for the Predicted Percentage of Dissatisfied *PPD*, since it is one of the suggested methods by UNI EN ISO 7730 (UNI, 2006) for long-term evaluations of comfort conditions. The costs were considered by computing the Net Present Value *NPV* of the building by means of an economic analysis with a lifespan of 30 years according to UNI EN 15459-1 (UNI, 2018). The optimal solutions were found for all the possible combinations of objectives, thus from one at a time to all four together, resulting in 15 combinations. In this way, it was possible to assess the performance of the procedure with a variable number of objectives and non-dominated solutions.

For each case, the optimal solutions found for the detailed and simplified models were compared. First, the total number of optima was counted. Then, it was checked for the presence of non-matching solutions as follows: (i) the solutions that were found as optima for the detailed model which were dominated for the simplified one were counted as optima not found, (ii) the solutions that were labeled as non-dominated for the simplified model that were not optima for the detailed one were considered as wrongly found optima. On top of these two absolute

values, for each combination of objectives, the error rate in performing a right choice or a wrong choice with respect to the total number of real optima was computed.

3. Results and Discussion

Even though the aim of this work is to assess if the detailed and simplified models result in having the same input values for the optimal solutions, the simulation outputs for heating and cooling needs, and the *PPD* for the detailed and simplified models were visually compared.

Fig. 3 and Fig. 4 show that the simplified models tend to underestimate the heating needs and overestimate the cooling ones. Such behavior was present also in the previous work from which the buildings were selected. However, since prior to this research the algorithm was tested focusing mainly on the buildings' shape rather than varying the thermophysical properties of the envelope, it was not possible to state that such a tendency could be true in all cases. Fig. 5 reports the boxplots with the *PPD* distribution for all the combinations for the buildings considered. Compared with the thermal needs, the distributions of the annual average *PPDs* for the simplified and detailed models are much more similar.

From Figs. 3, 4 and 5, it is clear that the differences between detailed and shoebox models are independent of the starting building's shape. Thus, to be consistent with previous research, the results for the optimization were compared in the three climates to assess the procedures' weaknesses more in detail.

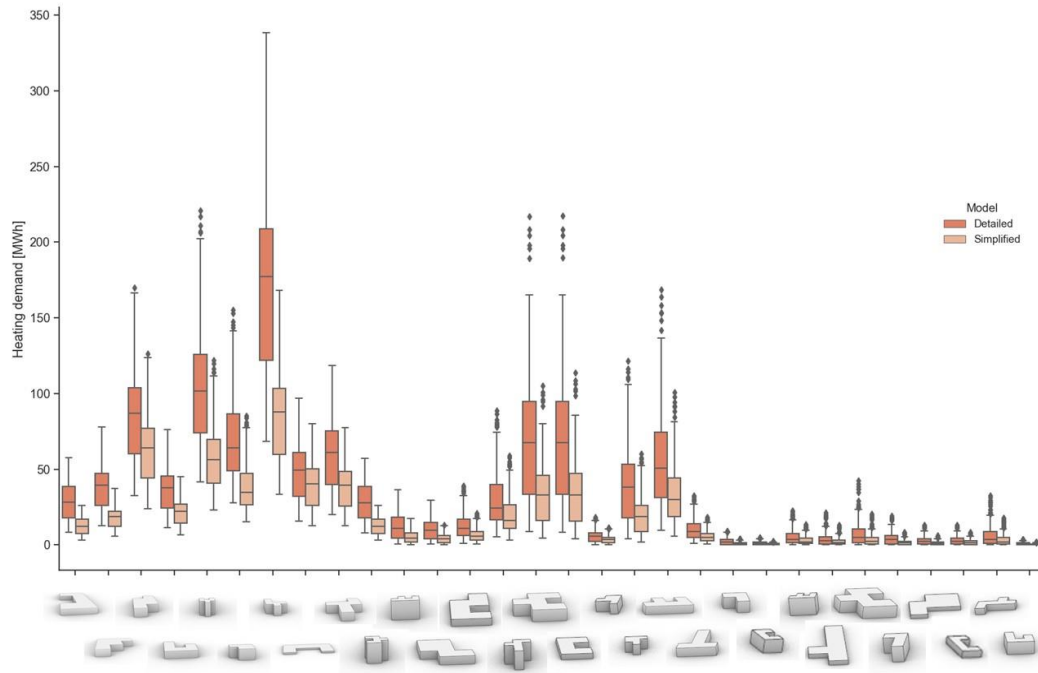


Fig. 3 – Annual heating needs boxplots for detailed and simplified models of each building for all input combinations

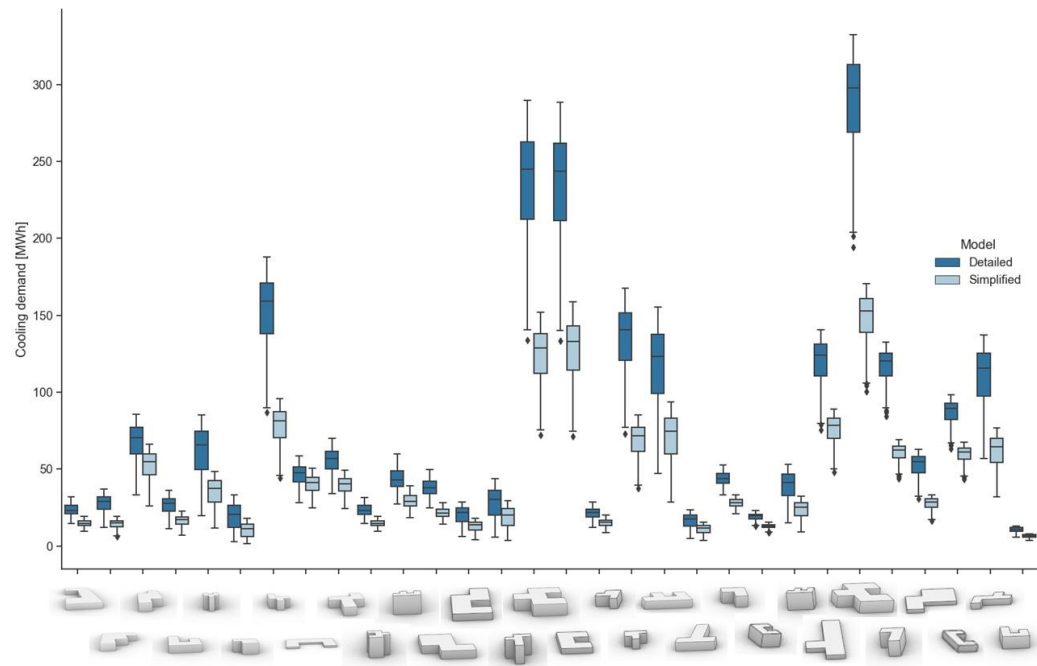


Fig. 4 – Annual cooling needs boxplots for detailed and simplified models of each building for all input combinations

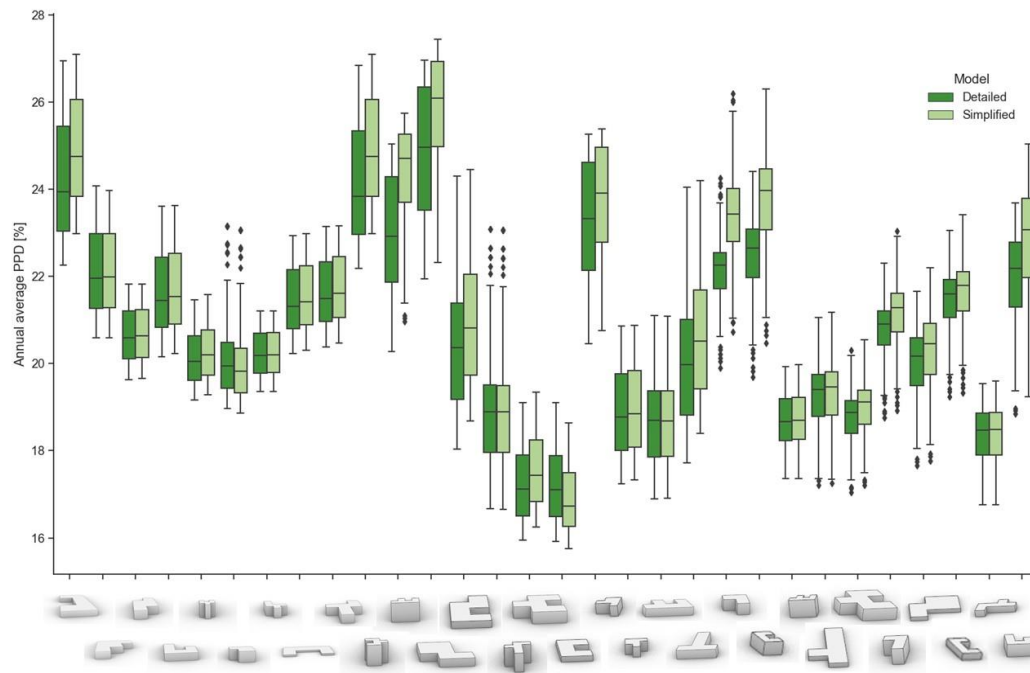


Fig. 5 – PPD boxplots for detailed and simplified models of each building for all input combinations

Table 2 reports the results for all combinations of objectives in the three climates. To visually understand in which cases the algorithm is performing better, the cells reporting the objectives considered were color-coded according to the right or wrong error rates. The combinations of objectives were colored in green if both error rates were lower or equal to 10 %, yellow if at least one of them was larger than 10 % and lower or equal to 20 %, and red if at least one of the two errors was greater than 20 %. In this way, it is possible to have a quick understanding of the reported tabular results.

The number of optimal solutions found for the detailed models is greatly affected not only by the number of objectives but also by the type of objectives considered. When antagonist objectives such as heating and cooling are in the same optimization problem, the number of optimal solutions increases much more compared with other cases. Since the NPV is related to both heating and cooling annual needs, including the economic performance leads to an increase of optima as well. Even though from Fig. 5 it seems that, for detailed and simplified models, the distributions for the annual average thermal comfort could be similar, Table 2 reports higher error rates when thermal comfort is included among the objectives, mainly for the climates of Bolzano and Denver. Generally, in all climates, low error

rates are reported when having one, three or four objectives. Thus, the algorithm's performance in finding the right optimal solutions is more accurate when there is a unique solution (i.e., one objective) or the number of optima is very large.

In the climate of Bolzano, the higher error rates occur when the economic and comfort objectives are optimized. When they are coupled with the cooling needs for the simplified models, not every optimum is found. On the other hand, coupling them with the heating needs leads to mainly wrongly labeled optima. As far as the climate of Denver is concerned, the results obtained are very similar to those of Bolzano. Even though thermal comfort and costs still yield the least accurate outcomes, there is an overall reduction of the error rates, except for the analysis with thermal comfort as sole objective.

Finally, the climate of Messina is the one yielding the most accurate optimization predictions, even for the heating demand, which is not a target output for this type of climate. Overall, for standalone buildings, the algorithm is three times faster in performing energy simulations for the buildings considered. Thus, the time required to run an optimization for each of these buildings was cut to one third. Even though, in some cases, the errors are still not negligible, the algorithm's performance in finding a set of optimal solutions is adequate for the purpose.

Table 2 – Optimal solutions comparison in the three climates

Bolzano						
Objectives	Total real optima	Total not found optima	Total wrongly labeled optima	Right choice error [%]	Wrong choice error [%]	Average number of optima
Heating	10	0	0	0.00	0.00	1.00
Cooling	10	0	0	0.00	0.00	1.00
Costs	10	0	0	0.00	0.00	1.00
Comfort	10	4	4	40.00	40.00	1.00
Comfort-Costs	115	36	28	31.30	24.35	11.50
Cooling-Comfort	101	19	0	18.81	0.00	10.10
Cooling-Costs	169	13	0	7.69	0.00	16.90
Heating-Comfort	99	2	50	2.02	50.51	9.90
Heating-Cooling	289	0	0	0.00	0.00	28.90
Heating-Costs	353	1	42	0.28	11.90	35.30
Cooling-Comfort-Costs	403	52	0	12.90	0.00	40.30
Heating-Cooling-Comfort	299	0	1	0.00	0.33	29.90
Heating-Cooling-Costs	1025	5	0	0.49	0.00	102.50
Heating-Comfort-Costs	503	0	52	0.00	10.34	50.30
Heating-Cooling-Comfort-Costs	1047	5	1	0.48	0.10	104.70
Denver						
Heating	10	1	1	10.00	10.00	1.00
Cooling	10	0	0	0.00	0.00	1.00
Costs	10	2	2	20.00	20.00	1.00
Comfort	10	4	4	40.00	40.00	1.00
Comfort-Costs	332	50	17	15.06	5.12	33.20
Cooling-Comfort	153	16	1	10.46	0.65	15.30
Cooling-Costs	80	5	0	6.25	0.00	8.00
Heating-Comfort	87	5	16	5.75	18.39	8.70
Heating-Cooling	256	8	2	3.13	0.78	25.60
Heating-Costs	405	8	14	1.98	3.46	40.50
Cooling-Comfort-Costs	477	56	1	11.74	0.21	47.70
Heating-Cooling-Comfort	259	8	3	3.09	1.16	25.90
Heating-Cooling-Costs	912	13	3	1.43	0.33	91.20
Heating-Comfort-Costs	578	9	31	1.56	5.36	57.80
Heating-Cooling-Comfort-Costs	918	13	3	1.42	0.33	91.80
Messina						
Heating	10	0	0	0.00	0.00	1.00
Cooling	10	1	1	10.00	10.00	1.00
Costs	10	0	0	0.00	0.00	1.00
Comfort	10	0	0	0.00	0.00	1.00
Comfort-Costs	38	0	0	0.00	0.00	3.80
Cooling-Comfort	15	0	1	0.00	6.67	1.50
Cooling-Costs	30	2	0	6.67	0.00	3.00
Heating-Comfort	284	1	1	0.35	0.35	28.40
Heating-Cooling	290	1	3	0.34	1.03	29.00
Heating-Costs	615	5	7	0.81	1.14	61.50
Cooling-Comfort-Costs	38	0	0	0.00	0.00	3.80
Heating-Cooling-Comfort	297	0	1	0.00	0.34	29.70
Heating-Cooling-Costs	1014	6	7	0.59	0.69	101.40
Heating-Comfort-Costs	1067	4	6	0.37	0.56	106.70
Heating-Cooling-Comfort-Costs	1081	3	4	0.28	0.37	108.10

4. Conclusion

In this work, the performance of a simplification algorithm developed for *UBEM* was tested in order to speed up the simulation time of building-level *MOO*. From a previous study, a group of buildings was chosen to perform a *MOO*, and energy efficiency measures and four objectives were selected. Heating and cooling needs, thermal comfort and investment costs were considered as objectives. To test the capabilities of the simplification in finding the right optimal solutions, all possible combinations of objectives were counted, and the buildings were simulated in three different climates.

Overall, it was possible to reduce to one third the thermal simulation time, obtaining adequate results for almost all combinations of objectives, regardless of the climatic condition considered. More specifically, the error rates in choosing the right optima were lower than 10 % for more than half of the combinations of objectives considered. Except for four cases, it was always possible to limit the error rate to maximum 20 %. Nonetheless, since the optimal solutions are related to the prediction accuracy of the algorithm, improving the precision of the simplification procedure will lead to more exact solutions. For this reason, a new configuration of the algorithm modeling the incoming radiation on a monthly basis is under development by the authors.

Acknowledgement

This research has been partially developed in the framework of the Internal Project of the Free University of Bozen-Bolzano TESES-Urb ("Techno-economic methodologies to investigate sustainable energy scenarios at urban level", CUP: I54I19001130005)

References

- Ang, Y. Q., Z. M. Berzolla, and C. F. Reinhart. 2020. "From concept to application: A review of use cases in urban building energy modeling." *Applied Energy* 279: 115738. doi: <https://doi.org/10.1016/j.apenergy.2020.115738>
- Battini, F., G. Pernigotto, and A. Gasparella. 2021. "Development of a shoeboxing approach for Urban Building Energy Modeling." In *Proceedings of the VI International High Performance Buildings Conference at Purdue*, West Lafayette, IN, US.
- Costa-Carrapiço, I., R. Raslan, and J. N. González. 2020. "A systematic review of genetic algorithm-based multi-objective optimisation for building retrofitting strategies towards energy efficiency." *Energy and Buildings* 210: 109690. doi: <https://doi.org/10.1016/j.enbuild.2019.109690>
- Ente Nazionale Italiano di Normazione (UNI). 2006. *EN ISO 7730 - Ergonomia degli ambienti termici - Determinazione analitica e interpretazione del benessere termico mediante il calcolo degli indici PMV e PPD e dei criteri di benessere termico locale*.
- Ente Nazionale Italiano di Unificazione (UNI). 2018. *UNI EN 15459-1 - Energy performance of buildings - Economic evaluation procedure for energy systems in buildings - Part 1: Calculation procedures, Module M1-14*.
- Golomb, S. W. 1994. *Polyominoes: Puzzles, Patterns, Problems, and Packings*. Princeton, New Jersey: Princeton University Press.
- Haneef, F., G. Pernigotto, A. Gasparella, and J. H. Kämpf. 2021. "Application of Urban Scale Energy Modelling and Multi-Objective Optimization Techniques for Building Energy Renovation at District Scale." *Sustainability* 13(20): 11554. doi: <https://doi.org/10.3390/su132011554>
- Moore, G. E. 1965. "Cramming more components onto integrated circuits." *Electronics* 38(8).
- Pernigotto, G., A. Prada, F. Cappelletti, and A. Gasparella. 2017. "Impact of Reference Years on the Outcome of Multi-Objective Optimization for Building Energy Refurbishment." *Energies* 10(11): 1925. doi: <https://doi.org/10.3390/en10111925>
- Reinhart, C., and C. Davila. 2015. "Urban building energy modeling - A review of a nascent field." *Building and Environment* 97: 196-202. doi: <https://doi.org/10.1016/j.buildenv.2015.12.001>

Application of a Simplification Algorithm for Urban Building Energy Modeling to Complex-Shaped Educational Buildings

Matteo Merli – Free University of Bozen-Bolzano, Italy – matteo.merli@stud-extra.unibz.it

Federico Battini – Free University of Bozen-Bolzano, Italy – federico.battini@natec.unibz.it

Giovanni Pernigotto – Free University of Bozen-Bolzano, Italy – giovanni.pernigotto@unibz.it

Andrea Gasparella – Free University of Bozen-Bolzano, Italy – andrea.gasparella@unibz.it

Abstract

To reduce greenhouse gases emissions related to the building sector and to make informed decisions about sustainable building design and urban planning, building energy simulation should be adopted as a supporting tool by designers and policy makers. However, since building simulation is extremely time-consuming, its application is limited in daily design work. This research aims at testing a new simplification algorithm proposed for Urban Building Energy Modeling to reduce the computational complexity of thermal models in favor of the simulation speed without compromising accuracy. The procedure was applied on two educational buildings of complex shapes located in Bolzano, Italy. Results show that the simplified models reduced the simulation time up to 135 times, with building level relative annual deviations lower than 6 %.

1. Introduction

In the building professional sector, Building Energy Modeling *BEM* can serve to design an energy efficient building or to verify its compliance with local, regional or national energy codes, as well as the actual energy performance. The former requires the use of *BEM* as an early design tool to support design tasks aiming at finding the best cost-effective solutions. At this stage of the design process, standard inputs and boundary conditions are conventionally used and a short calculation time is essential to compare multiple alternatives. The latter bypasses the analysis of different scenarios and focuses on the final simulation output, comparing it to a reference benchmark. In this case, the models are prepared in accordance with codes or technical standards, and a high degree of calculation accuracy is expected.

Overall, since accurate modeling procedures and iterative design processes require a large amount of time and computational resources, simplification workflows can be employed to speed up these kinds of simulations. However, most of the simplification techniques present in the literature have been developed for Urban Building Energy Modeling, *UBEM*, rather than *BEM*. Indeed, since *UBEM* is very computationally intensive, it is necessary to introduce such methods in order to perform urban scale simulations.

Even though *UBEM* is a relatively new field of study aiming at designing and optimizing urban energy systems and planning urban development, several tools, such as CitySim, SimStadt, umi, CityBES, URBANopt and TEASER, have already been released. Nonetheless, in recent years, different types of simplification algorithms intended to ease *UBEM* computing resources have been proposed. Different to the tools listed above, which fully comprise the *UBEM* workflow, these algorithms are only meant to replace the simulation stage.

In 2013, Dogan and Reinhart developed a fully automated and accelerated method capable of abstracting building massing into a meaningful group of simplified box-unit (shoebox) thermal models (Dogan & Reinhart, 2013), which they later named Shoeboxer (Dogan & Reinhart, 2017). In 2019, inspired by the idea of the Shoeboxer, Zhu et al. (2019) developed the Building Blocks Energy Estimation *BBEE* method for assessing building thermal demand at the district level by combining a *BBEE* algorithm and energy databases.

In this work, a new algorithm, developed by Battini et al. (2021b), which simplifies every building energy model into a representative simplified shoe-

box, was tested at the individual building level. The aim is to evaluate the algorithm's performance in estimating the energy use and accelerating the simulation of complex-shape buildings by applying it to two educational buildings in Bolzano, Italy.

2. Methodology

The process followed in order to assess the performance of the shoeboxing algorithm on the buildings considered is made of several steps. (i) case study introduction and data gathering, (ii) detailed geometry and energy modeling, (iii) calibration against monitored temperature profiles, (iv) application of the algorithm, and (v) model simulation and comparison.

2.1 Case Study

The two case studies are two educational buildings located in Bolzano, Italy. The first one is a kindergarten, called "Positano", built in 2009, while the second one is a primary school, called "Langer", built in 2014. Fig. 1 shows the location of the two buildings in the city of Bolzano. As reflected in their year of construction, both buildings are located in the western part of the city, in which new neighborhoods have been built over the past few decades. Positano kindergarten is a three-storey building, one of which is underground, and it is located in a district in which it is surrounded by residential buildings of up to 6 floors in height.



Fig. 1 – Locations of the two buildings in Bolzano, Italy

On the other hand, Langer primary school, which has three floors above ground and one underground, faces high residential buildings from North-East to South and open agricultural areas to the west.

2.2 Detailed Building Energy Modeling

Rhinoceros3D and Grasshopper were used to model the buildings' geometry in compliance with the technical floorplan drawings provided by the Municipality of Bolzano, allowing a characterization of the outer shell with windows and external fixed shades, as well as the subdivision of the internal spaces into different zones. Multi-zonal building energy models were prepared according to two main factors: construction assemblies and use of space. Adjacent spaces with similar properties were merged into a single zone, i.e., a single massing model with no internal partitions. Since each level includes spaces with similar functions, Positano was modeled with one thermal zone per floor. On the other hand, Langer school was subdivided into 12 thermal zones, according to the different functions and shapes of the school.

To model the urban context, the geometries of surrounding buildings' up to 200 m distance away have been imported into Rhinoceros3D with the aid of Gismo, a Grasshopper plug-in which enables automatic generation of urban environment and terrain geometry through a connection with the OpenStreetMap website.

The conversion from massing models to thermal zones was conducted using Ladybug Tools, an open-source suite of plug-ins for Grasshopper, and the characterization of the energy models was automated thanks to eppy, a Python scripting language for EnergyPlus which allows rapid and selective modification of EnergyPlus input files.

The energy certifications provided by the Municipality of Bolzano were used to define the construction elements (opaque and transparent) making up the envelope of the buildings. Occupancy profiles, people density, plug loads and lighting power densities were provided by the school administrations or obtained during in-situ surveys. Since the city of Bolzano belongs to the climate zone E, the heating period was set from the 15th of October to the 15th of

April, in accordance with Italian law. For Positano, the heating setpoint was set to 21 °C, based on the real temperature data available. On the other hand, for Langer primary school, the heating setpoint was set equal to 22 °C, in accordance with the information received by the school administration. The daily schedules of occupancy were determined combining information from the schools' administration and suggestions based on technical standards, such as UNI CEN/TR 16798-6 (2018) and ASHRAE 90.1 (2013). The density of people per square meter was estimated using the technical standard UNI 10339 (1995). The infiltration rates were set equal to 0.17 ach, according to the results of a previous experimental study in which indoor conditions were monitored in a classroom at Positano kindergarten (Dugaria et al., 2021). The ventilation rates were initially estimated by means of the calculation proposed in the technical standard UNI 10339 (1995), while the ventilation schedules were obtained by estimating the window openings depending on the variation of CO₂ concentration detected by dedicated sensors. Thanks to already-performed monitoring campaigns, it was possible to have data from one sensor in one classroom for the ground and first floors in Positano and one sensor in one classroom in Langer. Moreover, in the primary school, all the thermal zones, except the classrooms and the hallway, are equipped with a

controlled mechanical ventilation system. Thus, for these thermal zones, a decision was made to use the design ventilation rates and schedules reported in the energy certification. Finally, as regards the shades, a dynamic solar based control with a setpoint of 300 W/m² was hypothesized, in accordance with what was found by Roberts et al. (2022), limiting their activation to the period from February 15th to October 31st in both buildings. The values for the internal loads and controls for all the zones of both buildings are reported in Table 1.

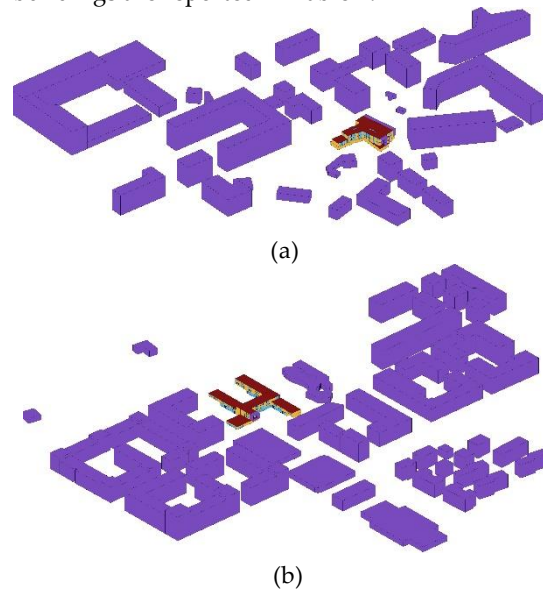


Fig. 2 – 3D geometrical models of the buildings with context: (a) Positano kindergarten and (b) Langer primary school

Table 1 – Internal loads, HVAC system controls and shading control settings for type of zone in the two buildings

	Zone	Lighting power [W/m ²]	People [people/m ²]	Ventilation rate [ach]	Infiltration rate [ach]	Heating setpoint [°C]	Shading setpoint [W/m ²]
Positano	Underground	5.71	0.1	2.82	0.17	21	–
	Ground	4.25	0.17	1.72	0.17	21	300
	First	5.24	0.26	1.86	0.17	21	300
Langer	Basement	1.5	0.08	1.5	0.17	22	–
	Hallway	2.65	0.12	1.64	0.17	22	300
	Canteen	2.55	0.6	3.36	0.17	22	300
	Classrooms	3.8	0.3	2.42	0.17	22	300
	Library	3.95	0.3	3.03	0.17	22	300
	Gym	2.4	0.2	2.87	0.17	22	300
	Auditorium	5	0.6	1.83	0.17	22	300

2.3 Calibration

Both models were calibrated against the real indoor air temperature data available for two kindergarten classrooms for the whole year 2019 for Positano and of one classroom from 11th April 2019 for Langer. The calibration was performed using the weather file of Bolzano from the year 2019 only on the zones for which data were available. For Positano, the ground and first floor were calibrated, while for Langer, the zone in which the monitored classroom is present. For the primary school, the result of the calibration was then applied to the other zones without mechanical ventilation.

The models were calibrated considering as variables the ventilation rate and people density. Both variables ranged from -50 % to +50 %, with a step of 10 %, starting from the nominal values computed according to standards. Table 2 reports all the values employed for the calibration for the zones considered. For each zone, a full factorial calibration was carried out, resulting in 121 simulated models for each case. The hourly Root Mean Square Error *RMSE* was computed between the simulated and monitored temperature during the period of interest for the calibration, i.e., the heating season, from the 15th of October to the 15th of April. Since for Langer no data were available for the first period of the year, the school's classroom was calibrated only considering the last months of the year.

In the present study, since no data were available about the heating system and its rated power, an ideal heating system characterized by an unlimited power was employed. For this reason, the simulated temperatures will always be greater or equal to the setpoint, even though the monitored temperature profiles can be lower. In order to cope with such discrepancies and to pick the most suitable combination of inputs from the calibration, the minimum seasonal *RMSE* was found. Then, all the combinations yielding a *RMSE* within 5 % difference from the minimum were considered. Among these combinations, the one with the lowest *RMSE* closest to the nominal ventilation rate was selected. In this way, it was possible to prevent choosing a combination with too low or too high a ventilation rate, which could undermine annual prediction accuracy for the heating demand. Indeed, since the simulated temperatures cannot be below the setpoint, changing the ventilation rate can lead to very limited improvements in the *RMSEs* of the temperature profiles, while having a huge impact on the heating demand.

2.4 Application of the Simplification Algorithm

Once the detailed building energy models were calibrated, the simplification algorithm was used to obtain as many shoebox energy models as the number of thermal zones making up the detailed models.

Table 2 – Ranges and values for calibration per zone

Positano – Ground Floor											
	-50 %	-40 %	-30 %	-20 %	-10 %	0 %	10 %	20 %	30 %	40 %	50 %
Ventilation rate [ach]	0.86	1.05	1.25	1.44	1.63	1.72	1.82	2.01	2.2	2.4	2.59
People [people/m ²]	0.08	0.1	0.12	0.14	0.16	0.17	0.18	0.19	0.2	0.21	0.22
Positano – First Floor											
Ventilation rate [ach]	0.93	1.13	1.34	1.55	1.75	1.86	1.96	2.17	2.37	2.58	2.78
People [people/m ²]	0.13	0.16	0.19	0.22	0.25	0.26	0.27	0.3	0.33	0.36	0.39
Langer – Classroom											
Ventilation rate [ach]	1.21	1.48	1.75	2.02	2.29	2.42	2.56	2.83	3.09	3.36	3.63
People [people/m ²]	0.15	0.18	0.22	0.25	0.28	0.3	0.32	0.35	0.38	0.42	0.45

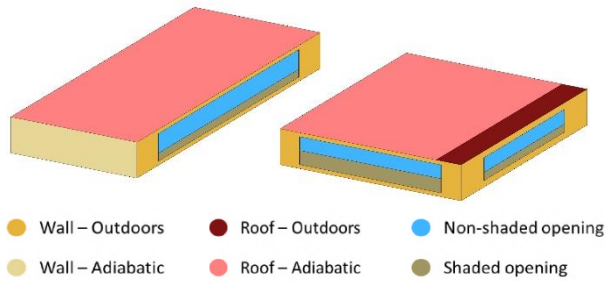


Fig. 3 – Example of shoebox models with boundary conditions

A comprehensive overview of the operations executed by the algorithm can be found in the work by Battini et al. (2021b). Nonetheless, the main steps can be summarized as follows:

1. Incident radiation analysis on the windows of the detailed energy model, subdivided for each cardinal direction by considering a $\pm 45^\circ$ tolerance range. The ratio between the annual incident radiation on each façade and the one calculated for a reference box unit is set as shading factor in order to take into account the share of radiation obstructed by self-shading and external objects.
2. Shoebox generation based on three geometrical indicators employed to solve a system of equations, in which the three dimensions of the shoebox are the unknowns. The shoebox's apertures are generated according to the same window-to-wall ratio calculated for each orientation of the related thermal zones ($\pm 45^\circ$ tolerance range).
3. Calculation of the adjacent surface area portions for each thermal zone that are in contact with other thermal zones. Since the algorithm generates freestanding buildings, the inter-building partitions are treated as adiabatic surfaces, assuming no heat flow between touching thermal zones.
4. Shoebox aperture surface reduction according to the shading factor that was calculated for each orientation. The reduction is implemented by substituting a part of transparent surface with an opaque element having the same thermophysical properties of the window.

Once the shoeboxes were obtained, the same non-geometrical properties of the starting thermal zone were assigned to the related shoebox.

2.5 Detailed and Simplified Model Comparison

Different to the procedure followed in the calibration process, in which temperatures were used to compare the monitored and simulated profiles, the comparison between detailed and simplified models was performed on the heating needs. Although energy simulations commonly adopt Typical Meteorological Year (TMY) weather files, the same weather file with the climatic data of Bolzano for the year 2019 employed for the calibration was utilized to assess the algorithm's performance.

As regards heating needs, the comparison metrics selected for this purpose are: (i) the absolute difference of the annual energy needs, (ii) the relative difference of the annual energy needs and (iii) the *RMSE*, calculated with a time step of 1 hour. Since shoeboxes are generally smaller than the starting geometry, their heating demand was multiplied by a scaling factor to take into account the reduction of floor area that is part of the simplification process.

3. Results and Discussion

3.1 Calibration

Table 3 reports the outcomes of the calibration, in which people densities do not correspond to the ones computed from the standards, while the values for ventilation rates are the same. This is because, even though the lowest *RMSEs* obtained were the ones with the greatest ventilation rates, as stated in Section 2.5, values closer to the ones computed following the standards would have been chosen if within 5 % difference.

Table 3 – Calibration results

	Ventilation rate [ach]	People density [people/m ²]
Positano – Ground floor	1.72	0.08
Positano – First floor	1.86	0.16
Langer – Classroom	2.42	0.25

Indeed, the *RMSEs* showed differences in the order of hundredths or thousandths of degree, hence negligible. The combination of inputs obtained from the calibration process was also used in the simplified models for the comparison.

3.2 Simplification Results

The annual energy demands for space heating are reported in Table 4.

For Positano kindergarten, the simplified model's total annual heating demand is equal to 30.13 MWh, 1.69 MWh more compared with the detailed model's results. In relative terms, the total deviation of the detailed model is equal to -5.62 % compared with the simplified one.

Regarding each thermal zone, the underground floor shoebox underestimates the heating demand, although only slightly, while the ground and first floor shoeboxes overestimate it by a deviation that does not exceed 2.06 MWh. As regards *RMSEs*, even though they are low for all floors, the underground floor shoebox shows the best performance in terms of hourly deviation from the detailed thermal zone's heating demand prediction.

For Langer primary school, the simplified model's

total annual heating demand prediction is equal to 153.21 MWh, which is 7.05 MWh greater than the detailed model's predicted results. In relative terms, the total deviation is equal to +4.60%. Analyzing the results for each thermal zone, only the basement and the canteen underestimate the heating demand, while the rest of the shoeboxes overestimate the annual heating demand by a deviation that varies for each zone. Classrooms, gym and auditorium shoeboxes show the best performances, overestimating no more than 13.10 % in relative terms, or 0.88 MWh in absolute terms. The library's ground floor shoebox overestimates the predicted heating demand of the detailed model by 27.30 %, which is, however, one of the lowest heating needs (only 4.89 MWh). On the other hand, although the library's first floor heating demand is below average, it is characterized by a deviation of 6.20 %.

Table 4 – Heating needs prediction comparison

		Detailed - Heating [MWh]	Simplified - Heating [MWh]	Absolute difference [MWh]	Relative difference [%]	RMSE [kWh]
Positano	Underground	7.41	6.91	0.49	-7.16%	0.08
	Ground	9.05	9.18	-0.13	1.40%	0.79
	First	11.97	14.03	-2.06	14.68%	0.42
	TOTAL	28.43	30.13	-1.69	5.62%	0.89
Langer	Basement	19.91	17.97	1.95	-10.80%	0.33
	Hallway	33.03	36.25	-3.22	8.90%	0.61
	Canteen	10.71	10.62	0.08	-0.80%	0.31
	First Floor Classroom1	10.46	11.34	-0.88	7.80%	0.19
	First Floor Classroom2	8.15	8.42	-0.28	3.30%	0.06
	First Floor Classroom3	2.69	2.98	-0.29	9.80%	0.06
	Second Floor Classroom1	9.80	10.00	-0.20	2.00%	0.04
	Second Floor Classroom2	3.02	3.47	-0.45	13.10%	0.09
	Library Ground Floor	4.89	6.73	-1.83	27.30%	0.42
	Library First Floor	8.96	9.56	-0.59	6.20%	0.12
	Gym	22.29	22.92	-0.63	2.70%	0.25
	Auditorium	12.26	12.94	-0.69	5.30%	0.16
	TOTAL	146.16	153.21	-7.05	4.60%	1.38

Table 5 – Recorded simulation time and comparison

		Simulation time [s]		
Positano	Underground		4.01	
	Ground floor		5.16	
	First Floor		5.43	
	Simplified	Total	14.60	134.78x
	Detailed		1967.64	faster
Langer	Basement		3.97	
	Hallway		5.18	
	Canteen		4.83	
	First Floor Classroom1		4.83	
	First Floor Classroom2		4.85	
	First Floor Classroom3		4.51	
	Second Floor Classroom1		4.85	
	Second Floor Classroom2		4.79	
	Library Ground Floor		4.80	
	Library First Floor		4.88	
	Gym		5.19	
	Auditorium		4.83	
	Simplified	Total	53.54	8.18x
	Detailed		438.14	faster

The results of both case studies showed that shoeboxes can predict fairly well the heating needs of the detailed thermal zones. Moreover, for both buildings, the sum of the shoeboxes' predictions achieves high accuracy in estimating the global annual heating demand of the buildings detailed.

Even though results about temperatures have not been reported, the temperature profiles of the simplified models are generally underestimated throughout the entire year (i.e., leading to larger heating needs), with larger discrepancies in the summer period. This is mainly because, in general, the shoeboxing procedure leads to smaller thermal zones having a lower thermal capacity and it models the incoming radiation starting from a fixed obstruction ratio for the whole year. Indeed, in order to yield even more accurate results, the modeling of the external shadings should be improved since the surrounding context has a different impact on the air node heat balance during the year, i.e., it has a greater influence in summer (Battini et al., 2021a). Table 5 reports the simulation runtime of detailed and simplified models. Regardless of the building

considered, the shoebox simulation time takes between 3 and 5 seconds. Summing up the time required by the simplified models for each building and considering the simulation time of the whole building models, the simplified building models reduced the computing time of the energy simulation by 134.78 and 8.18 times for Positano and Langer, respectively. Such discrepancies in time reduction are due to the time required for the detailed models to be simulated. Indeed, the speed of the detailed model's simulation mostly depends on the shape of the thermal zones and the external shading objects. Even though Positano kindergarten is composed of only three thermal zones, all of them are characterized by a complex shape, while Langer primary school is mostly composed of parallelepiped-shaped thermal zones. Moreover, the number of surfaces representing the urban context in Positano is approximately 3.5 times the one in Langer.

4. Conclusion

In this work, a new simplification algorithm capable of properly estimating the energy use of complex-shape buildings reducing the simulation time was tested. The algorithm can convert every building of whatever shape and geometry into a representative shoebox energy model. The conversion involves the simplification of the building geometry, apertures and adjacencies, and the transformation of the buildings' obstructions into shading opaque elements.

To test the procedure at the individual building level, two educational buildings of complex shape located in Bolzano, Italy, were studied, i.e., Positano kindergarten and Langer primary school. Firstly, both buildings were modeled in detail in terms of geometry, construction assemblies, internal loads, schedules and surrounding context. Then, they were calibrated thanks to monitored indoor temperature data of the schools' classrooms considering the two variables characterized by the largest uncertainty: ventilation rates and people densities. Afterwards, the simplification algorithm was applied to obtain shoeboxes from the detailed thermal zones. Finally, detailed and simplified models were simulated in EnergyPlus using the same weather file and

the simulation results were analyzed and compared. The comparison highlighted that, in both case studies, the simplification algorithm is able to convert complex-shape building thermal zones into shoeboxes that can predict their annual heating demand with high accuracy and through significantly faster energy simulations. In general, the heating needs are slightly overestimated by the shoeboxes, leading to total overestimates equal to 5.62 % and 4.60 %, for Positano kindergarten and Langer school, respectively. Since shoeboxes have proven to be more capable of predicting thermal behavior of the detailed building model in winter rather than in summer, the implementation of new solutions for managing the incoming radiation is needed as further research. In terms of computing time, the simplified models' energy simulations were 135 and 8 times faster compared with the detailed ones for Positano and Langer, respectively. The significantly faster simulations achieved by the shoeboxes, together with their high accuracy in predicting the detailed model's energy performance, allow this simplification algorithm for building level applications to be used.

Acknowledgement

This research was developed thanks to the Geology, Civil Protection and Energy Office of the Municipality of Bozen-Bolzano, within the framework of the Project IndAIR-Edu – “Indoor Air Quality and Ventilation Effectiveness in Educational Buildings” (CUP: I56C18000180005; Free University of Bozen-Bolzano, Faculty of Science and Technology, RTD call 2018).

References

- ASHRAE 2013. *ASHRAE 90.1-2013. Standard energy standard for buildings except low-rise residential buildings*.
- Battini, F., G. Pernigotto, and A. Gasparella. 2021a. “A parametric analysis of the impact of thermophysical, geometry and urban features on the energy demand of a simplified building shoebox model.” In *Proceedings of Building Simulation 2021*, Bruges, Belgium
- Battini, F., G. Pernigotto, and A. Gasparella. 2021b. “Development of a shoeboxing approach for Urban Building Energy Modeling.” In *Proceedings of the VI International High Performance Buildings Conference at Purdue*, West Lafayette, IN, US.
- Dogan, T., and C. Reinhart. 2013. “Automated conversion of architectural massing models into thermal 'shoebox' models.” In *Proceedings of Building Simulation 2013*, Chambéry, France.
- Dogan, T., and C. Reinhart. 2017. “Shoeboxer: An algorithm for abstracted rapid multi-zone building energy model generation and simulation.” *Energy and Buildings* 140: 140-153. doi: <https://doi.org/10.1016/j.enbuild.2017.01.030>
- Dugaria, S., G. Pernigotto, and A. Gasparella. 2021. “Indoor conditions in educational buildings: the case of Bolzano schools.” In *ASHRAE Topical Conference Proceedings*, Athens, Greece.
- Roberts, J. A., G. De Michele, G. Pernigotto, A. Gasparella, and S. Avesani. 2022. “Impact of active façade control parameters and sensor network complexity on comfort and efficiency: A residential Italian case-study.” *Energy and Buildings* 255: 111650. doi: <https://doi.org/10.1016/j.enbuild.2021.111650>
- UNI. 1995. *UNI 10339:1995. Air-conditioning systems for thermal comfort in buildings: general, classification and requirements. offer, order and supply specifications*.
- UNI. 2018. *UNI CEN/TR 16798-6:2018. (2018). Energy performance of buildings - ventilation for buildings - part 6: Interpretation of the requirements in en 16798-5 -1 and en 16798-5-2 - calculation methods for energy requirements of ventilation and air conditioning systems*.
- Zhu, P., D. Yan, H. Sun, J. An, and Y. Huang. 2019. “Building Blocks Energy Estimation (BBEE): A method for building energy estimation on district level.” *Energy and Buildings* 185: 137-147. <https://doi.org/10.1016/j.enbuild.2018.12.031>

Numerical Investigation of Radiation Efficiency of a Cross-Laminated Timber Floor

Marco Caniato – Free University of Bozen-Bolzano, Italy – marco.caniato@unibz.it

Nicola Granzotto – Free University of Bozen-Bolzano, Italy – nicolagranzotto74@gmail.com

Federica Bettarello – University of Trieste, Italy – fbettarello@units.it

Arianna Marzi – Free University of Bozen-Bolzano, Italy – arianna.marzi@natec.unibz.it

Paolo Bonfiglio – Materiacustica srl, Italy – paolo.bonfiglio@materiacustica.it

Andrea Gasparella – Free University of Bozen-Bolzano, Italy – andrea.gasparella@unibz.it

Abstract

Cross-Laminated Timber (CLT) is a building technology that is becoming increasingly popular due to its sustainability and availability. Nevertheless, CLT structures present some challenges, especially in terms of both structure-borne and airborne insulation. In this paper, a 200 -mm CLT floor was characterized in the laboratory, according to ISO standards, by using a standard tapping machine in order to understand its vibro-acoustic behavior in terms of radiation efficiency for structural excitation. In particular, experimental tests were compared to analytical prediction models available in the literature to check the accuracy of simulation methods in the prediction of the radiation capability of CLT structures.

1. Introduction

In recent years, the use of timber as a construction material in the building sector has been increasing. Sustainable edifices made exclusively with timber or refurbishment of conventional heavyweight houses using new timber structures are common in most cities. In view of this, the use of wooden components and, in particular, Cross Laminated Timber (CLT) elements has greatly increased in the past decade. Timber has a number of advantages: it is an eco-friendly material, well suited for thermal comfort and a fast-track on-site construction process, featuring the possibility of implementing existing structures thanks to its reduced weight. However, its acoustic simulations lack a complete description, since the literature does not always provide reliable methods capable of predicting reliable

values as regards acoustic performance. From this perspective, further studies are needed to develop and improve prediction models of CLT floor sound and vibrational behavior (Yang et al., 2021; Zhang et al., 2020). Among all available parameters, one worthy of investigation is represented by radiation efficiency. Indeed, the sound radiation index is of paramount importance for understanding and simulating the behavior of these elements (Kohrmann, 2017).

A recent study (Jansson, 2021) has shown how the use of software and calculation models, currently available for the study of the characteristics of multilayer systems, are not reliable when wooden structures are used. For this reason, it is of paramount importance not only to know the characteristics of the materials, but also their radiation efficiency.

However, the study of this parameter, in relation to the characterization of CLT floors, is still partially incomplete.

Hence, to design CLT structures with good acoustic insulation, there is the need to characterize the sound radiation of the vibrating elements.

The radiation efficiency can be computed using dedicated equations or simulated using Finite Elements Methods. In this paper, this latter approach is used to verify if, with reference CLT floor, the method can be used and if it could provide reliable and robust results.

2. Material and Methods

2.1 Description of Investigated CLT Floor

This paper presents the results of a numerical investigation of the radiation efficiency of a CLT floor with a thickness of 200 mm and a size of 4155 mm x 3000 mm, measured in a laboratory built in accordance with the ISO 10140 series standards, using a standardized tapping machine (B&K 3297) as mechanical source (Fig. 1).



Fig. 1 – Investigated CLT floor mechanically excited using a standardized tapping machine

The laboratory was built to minimize flanking transmission and, in particular, it features a volume of transmitting room of 50.9 m³ and a volume of the receiving room of 60.63 m³.



Fig. 2 – Picture of the available acoustic facility

A grid of accelerometers was used to monitor the acceleration levels. Precisely, the measurement pattern is described in Fig. 3.

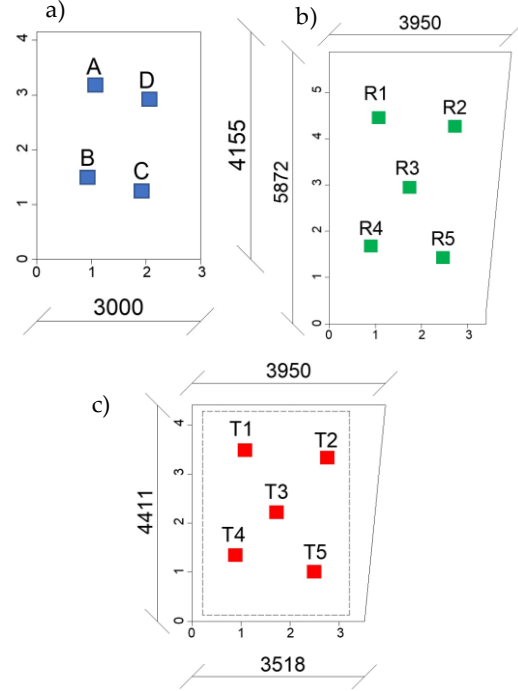


Fig. 3 –Tapping machine positions (a); microphone positions in the receiving room; (b) accelerometer position in the receiving room (c)

The radiation efficiency was measured using following expression:

$$\sigma_{rad} = \frac{W_{rad}}{\rho_0 c_0 S \langle v^2 \rangle_{s,t}} \quad (1)$$

where W_{rad} [W] is the radiation power, ρ_0 [kg/m³] is the air density, c_0 [m/s] is the speed of sound, S [m²] is the floor surface, $\langle v^2 \rangle_{s,t}$ is the average square vibration velocity on the receiving side. The radiation power was evaluated using the average sound pressure level (Svantek 958) and the reverberation time in the receiving room. The averaged squared velocity was measured using accelerometers (Dytran 3023) mounted on the bottom side of the CLT floor.

2.2 Description of Numerical Approaches

As previously described, CLT floor is made of five layers (having a thickness of 4 cm each and density of around 420 kg/m³). It is well known in the literature that each layer is an orthotropic solid and a comprehensive analysis requires the knowledge of 9 independent parameters (3 Young's modulus, 3 shear modulus and three Poisson's ratio). Table 1 summarizes values of mechanical parameters utilized as input data of investigated numerical approaches.

Parameters in Table 1 were used for layers 1, 3 and 5. Layers 2 and 4 were modeled using the same parameters in a 90-degree-rotated coordinate system. In the following sessions, two different numerical approached will be described.

Table 1 – Mechanical properties of each CLT layer

E [GPa]	G [GPa]	ν [-]	η [-]
$E1=11$	$G12=0.69$	0.14	0.01
$E2=0.37$	$G13=0.069$	0.33	0.01
$E3=0.37$	$G23=0.69$	0.14	0.01

2.2.1 Hybrid FEM-Analytical model I

A statistical radiation efficiency model was implemented, based on the modal-average formulations, using frequency-dependent stiffness properties as input data. Such a statistical approach requires some additional assumptions: (a) high modal density and modal overlap over the entire frequency range (b) the sound power is only radiated by resonant modes; (c) the resonant modes are uncorrelated; (d) equipartition of modal energy can be applied. The radiation efficiency can be calculated as:

$$\sigma_{\text{ortho}}(\omega) = \frac{L_x L_y}{\pi^2 n_d} \int_0^{\pi/2} \sigma(\omega, \phi) k_B \frac{\partial k_B}{\partial \omega} d\phi. \quad (2)$$

where L_x and L_y are the lateral size of the CLT floor, $\sigma(\omega, \phi)$ the radiation efficiency calculated using Leppington's formulation (Leppington et al., 1982), n_d the plate modal density and k_B the structural bending wave propagating in the plate. At any propagation angle ϕ , the direction-dependent bending wavenumber can be estimated from the wavenumber components along the principal directions k_{Bx} and k_{By} , by applying a well-established orthotropic elliptic model.

To summarize, if the wavenumber components, along with the principal directions k_{Bx} and k_{By} are known together with the size and the plate density, the radiation efficiency can be calculated.

In the present research, the wavenumbers k_{Bx} and k_{By} were determined using a simplified finite element model (implemented in Comsol Multiphysics) and the Inhomogeneous Wave Correlation (IWC). In particular, two finite element models of freely

suspended CLT beams (1 m long) in x and y directions are solved when a unit force in z direction is exerted on a side of the beam.

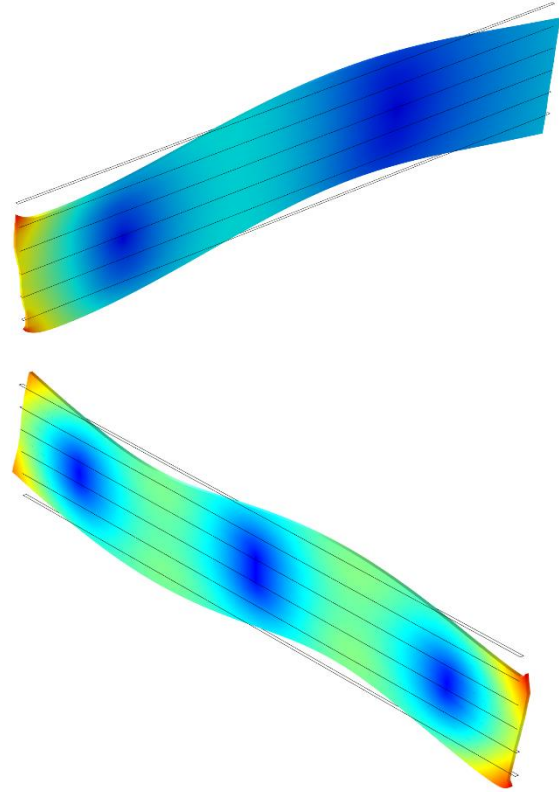


Fig. 4 – FEM models of CLT beams for the extraction of the structural wavenumbers along the principal directions

Once each model is solved, the z direction complex displacement is computed along each beam on a set of equally spaced points (1cm of spacing has been considered). By applying the IWC method, it is possible to determine the dispersion relation (the wavenumber as a function of the frequency) in both principal directions (Fig. 5).

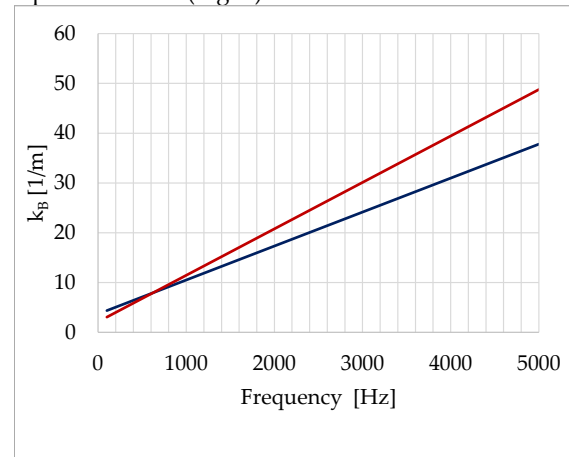


Fig. 5 – Computed structural wave numbers along the principal directions

2.2.2 Hybrid FEM-Analytical model II

The second hybrid method requires a two-step procedure:

1. A FEM model of the entire floor is solved for a mechanical point excitation. In this case, the three different simulations were considered according to the positions of the tapping machine during experimental.
2. Once the model is solved, the z direction complex velocity is computed on a grid of equally spaced points (5 cm of spacing was considered). The mean-squared velocity in Eq. 1 can be directly calculated as the average of the squared velocity, while radiated power of Eq. 1 has been computed using the Discrete Calculation Method (DCM) (Santoni et al., 2019):

$$W_{\text{rad}} = \sum_i \left[\text{Re}(Z_{ii}) |v_i|^2 + \sum_j \text{Re}(Z_{ij} v_i v_j^*) \right] \quad (3)$$

where Z_{ii} and Z_{ij} are the self- and cross-radiation impedances, respectively.

2.2.3 Accuracy

In order to estimate the quality of the fit, a standard deviation is calculated by taking into consideration the measured values as the average data (μ) for each of n frequency bands (1/3 octave) and the calculated values as experimental ones (Eq. 3):

$$\sigma_{\text{dev}} = \sqrt{\frac{1}{N} \sum_{i=1}^n (x_i - \mu)^2} \quad (3)$$

In addition, the mean difference is computed (Eq. 4):

$$\Delta_{\text{mean}} = \frac{1}{N} \sum_{i=1}^n |x_i - \mu| \quad (4)$$

3. Results

Experimental radiated sound power and structural velocity levels are shown in Fig. 6.

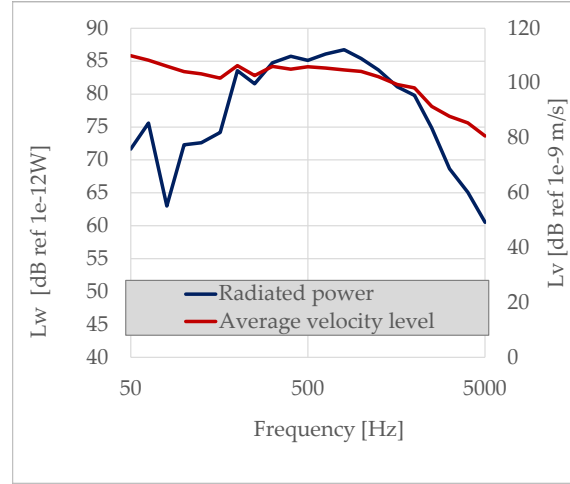


Fig. 6 – Experimental radiated sound power and structural velocity levels

The comparison between experimental values and numerical models of the radiation efficiency is shown in Fig. 7.

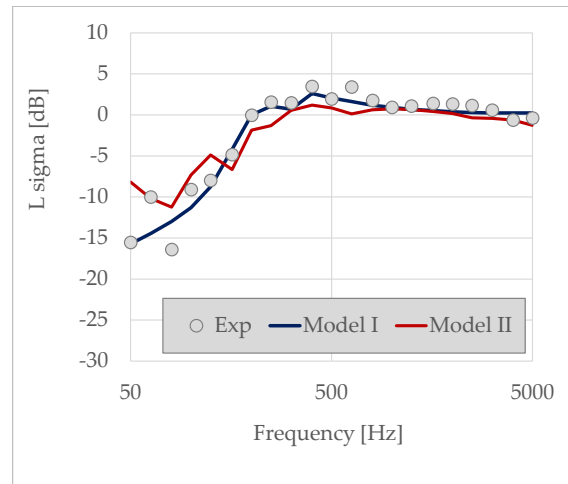


Fig. 7 – Radiation efficiency. Comparison between different simulation approaches

From the curves in the previous graph, it is possible to observe satisfactory accuracy of both simulation techniques. The average absolute differences are equal to 1 dB and 1.8 dB for Model I and Model II when compared with experimental tests. In particular, model II is able to investigate modal behavior of the plate. Fig. 8 depicts the modal resonances of the full floor at frequencies of up to around 150 Hz.

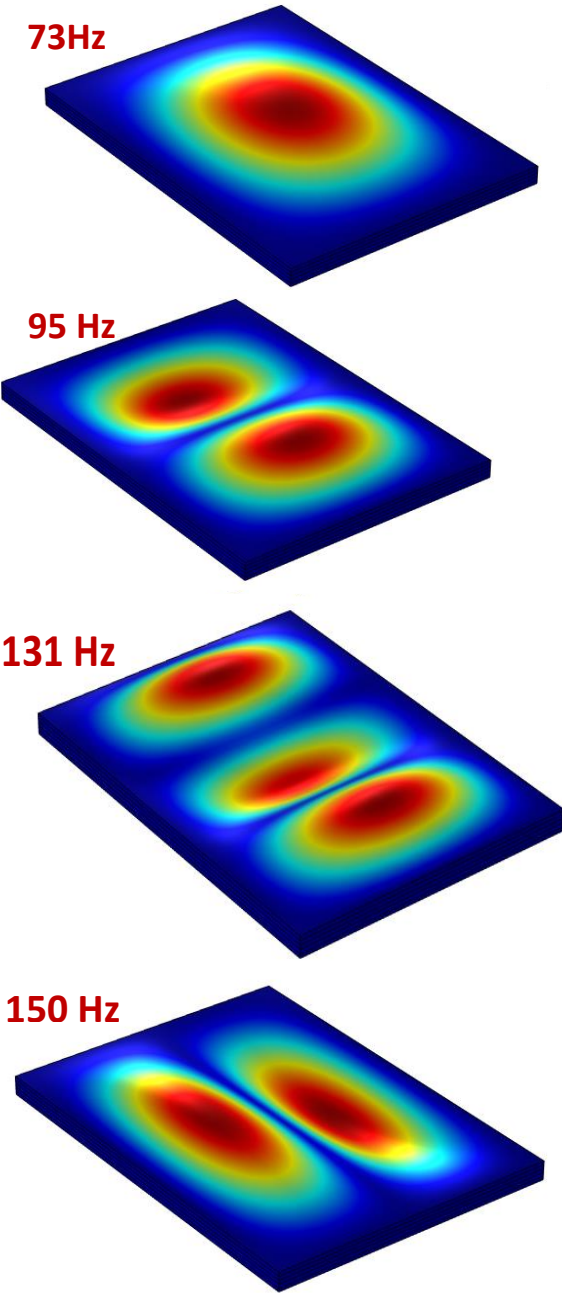


Fig. 8 – Model eigenfrequencies determined using a full 3D FEM model

Furthermore, deviations (i.e., arithmetic differences) between experimental data and numerical simulations are depicted in Fig. 9. From the comparison, it is possible to observe a better capability of Model I to simulate the radiation efficiency of the CLT structure, while both methodologies show higher deviations at frequencies lower than 125 Hz, which is the frequency region governed by resonant modes of the floor and it is highly dependent on

boundary conditions, generally difficult to implement in simplified numerical models.

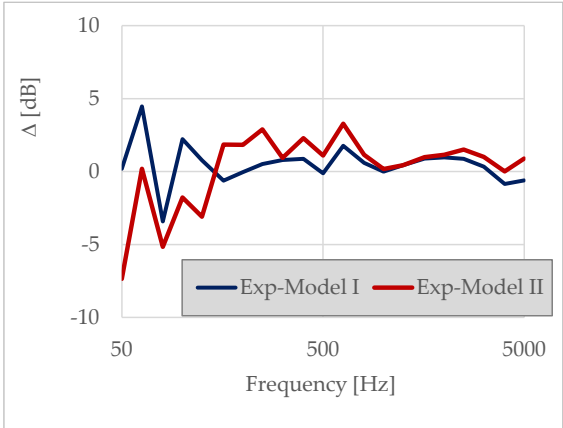


Fig. 9 – Deviations between experimental data and numerical simulations

In Table 2, the simulation accuracy is reported. It can be noticed that model I presents better values than model II, mostly because of low frequency values differences reported in Fig. 9.

Table 2 – Accuracy for different numerical methods

<i>Numerical thod</i>	<i>me- Dev.st</i>	Δ_{mean}
Model I	0.91	0.74
Model II	1.72	1.47

4. Conclusion

In this paper, two different numerical approaches were utilized for the prediction of the radiation efficiency of a Cross-Laminated Timber frame for building constructions. Results were compared with experimental tests carried out in a dedicated laboratory. The accuracy of proposed methodologies was proved to be between 1 and 2 dB in terms of average radiation efficiency level. The implementation of both methodologies is straightforward and requires knowledge of the mechanical properties of the orthotropic timber material. Future work will be devoted to extension of the proposed numerical formulations to different acoustic and mechanical excitations.

Acknowledgement

This work was financed by the European Interreg BIGWOOD project, IT AT 1081 CUP: I54I18000300006.

Nomenclature

Symbols

W_{rad}	radiation power (W)
ρ_0	air density (kg/m^3)
c_0	speed of sound (m/s)
S	floor surface (m^2)
$\langle v_2 \rangle_{s,t}$	is the average square vibration velocity on the receiving side (m/s)
E	Young's modulus (GPa)
G	Shear modulus (GPa)
ν	Poissino ratio (-)
η	Loss factor (-)
L_x	dimension (m)
L_y	y-direction size dimension (m)
$\sigma(\omega, \phi)$	radiation efficiency (-)
η_d	plate modal density (-)
k_B	structural bending wave propagating in the plate (m^{-1})
ϕ	propagation angle (rad)
Z	radiation impedances (rayls)

Subscripts/Superscripts

x	x-direction
y	y-direction

References

- ISO. 2021. *ISO 10140-3:2021; Acoustics—Laboratory Measurement of Sound Insulation of Building Elements—Part 3: Measurement of Impact Sound Insulation..*
- Jansson, L. 2021. “Estimating Impact Noise through Cross Laminated Timber Floors Using the Transfer Matrix Method”. In *Proceedings of the INTER-NOISE 2021*.
- Kohrmann, M. 2017. *Numerical Methods for the Vibro-Acoustic Assessment of Timber Floor Constructions*. Technische Universität München: München, Germany.
- Leppington, F. G., E. G. Broadbent, and K. H. Heron. 1982. “The acoustic radiation efficiency of rectangular panels”. *Proceedings of the Royal Society of London A: Mathematical, Physical and Engineering Sciences* 82: 245–71.
- Yang, Y., C. Fenemore, M. J. Kingan, and B. R. Mace. 2021. “Analysis of the vibroacoustic characteristics of cross laminated timber panels using a wave and finite element method”. *Journal of Sound and Vibration* 494: 115842.
- Zhang, X.; X. Hu, H. Gong, J. Zhang, and Z. Lv, and W. Hong. 2020. “Experimental study on the impact sound insulation of cross laminated timber and timber-concrete composite floors”. *Applied Acoustic* 161: 107173.

Assessment of Contagion Risk due to Covid-19 for a Multi-Zone Building Model of Offices

Riccardo Albertin – Free University of Bozen-Bolzano, Italy – riccardo.albertin@natec.unibz.it

Alessandro Pernici – Free University of Bozen-Bolzano, Italy – alessandro.pernici@natec.unibz.it

Giovanni Pernigotto – Free University of Bozen-Bolzano, Italy – giovanni.pernigotto.unibz.it

Andrea Gasparella – Free University of Bozen-Bolzano, Italy – andrea.gasparella.unibz.it

Abstract

In this research, a probabilistic model was applied to a building model of a public building located in Bolzano, Italy, for the assessment of the airborne contagion risk due to Covid-19. Different ventilation strategies were investigated in terms of risk reduction, as well as the effectiveness of the Pfizer vaccine. TRNSYS and TRNFLOW models of the public building were created to evaluate the internal airflows, necessary to calculate Covid-19 concentrations in the offices. Both building and airflow models were calibrated against measurement data collected with temperature sensors located in some of the building offices and hallways, prior to coupling with a Monte Carlo model for the risk assessment process. The results were reported in terms of infection risk, both for occupants located in the same office, as well as for occupants in adja-

cent spaces. It was observed that the current operational modes of both natural and mechanical ventilation are able to limit the spread of Covid-19 only in case of vaccination coverage presence and if the Delta variant is considered. If vaccination coverage is not present or if the Omicron variant is concerned, a higher frequency of windows opening, and a schedule based on occupancy profiles for mechanical ventilation should be adopted.

1. Introduction

In the literature, some references about airborne contagion risk assessment due to Covid-19 are available. One example is given by the work of Buonanno et al. (2020a), on which the “Airborne Infection Risk Calculator” (AIRC) is based, for risk



Fig. 1 – Case study building located in Bolzano, Italy

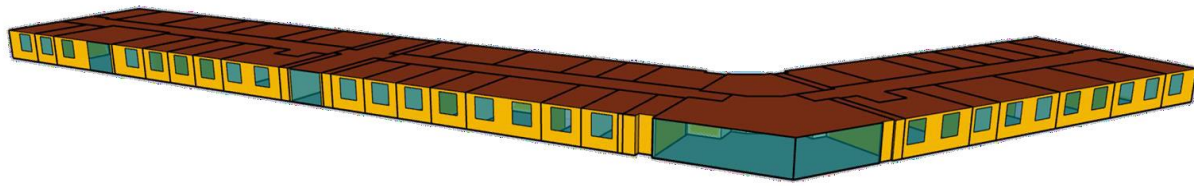


Fig. 2 – 3D model of the second floor of the case study building

assessment due to airborne diseases, including Covid-19. The AIRC tool, as well as other works regarding risk assessment for airborne contagion due to Covid-19, have some limitations. Firstly, it is possible to perform risk assessment only for one room at a time, not considering in this way potential infections in adjacent rooms due to the spread of the Covid-19 virus through doors, or ducts in the mechanical ventilation system. Secondly, one of the major assumptions needed to perform risk assessment is static conditions. For this reason, in Albertin et al. (2022a), a Monte Carlo model was developed to overcome the aforementioned limitations. The probabilistic method proposed is based on the coupling of TRNSYS and TRNFLOW, a building simulation software and a plugin for the evaluation of airflows and infiltrations, respectively, and an algorithm based on the AIRC tool developed in MATLAB® environment. The airflows evaluated with the building and airflow models were utilized for the calculation of Covid-19 con-

centrations in the internal zones of the building. Then, a Monte Carlo model was used to evaluate the risk of infection for the occupants under different environmental conditions by simulating several scenarios 1000 times each. The whole process was subsequently enhanced in Albertin et al. (2022b), giving the possibility of also considering different Covid-19 variants (Alpha, Delta, Omicron), vaccines (AstraZeneca, Pfizer, Moderna), air purifiers and other features.

In this work, the enhanced version of the probabilistic model is further expanded with the Page algorithm for the randomized creation of occupancy profiles for each occupant and applied to a public building containing offices.

2. Case Study

The case study selected for this work is part of the second floor of a public office (Fig. 1) located in via

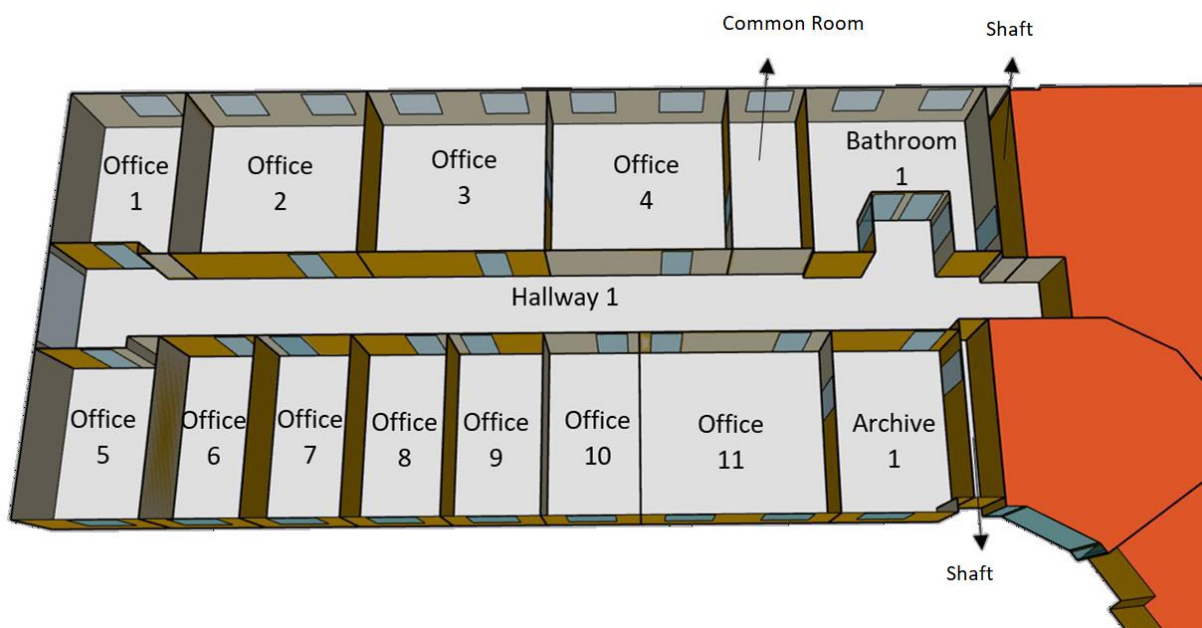


Fig. 3 – Highlight of the second floor of the office block selected for the risk assessment

Vincenzo Lancia, Bolzano, Italy. The second floor is composed of three blocks, and the one selected for the risk assessment is represented in detail in Fig. 3. The surface area of the block is about 564 m², for an internal height of 2.7 m and, therefore, a total internal volume of 1523 m³.

Different ventilation systems are installed for each block, with a low air-flow velocity setting, integrated dehumidification system and crossflow heat recovery unit. However, it has been observed that the mechanical ventilation system is not utilized during working hours, especially in summer, due to issues regarding thermal comfort. For this reason, mechanical ventilation is operative only early in the morning, during lunch hours and in the evening after 6 pm.

All the office windows are composed of a double-glazed glass and an aluminium frame. Given their large dimension and proximity to a busy street, a source of air pollution and acoustic discomfort, it has been observed that the windows are rarely opened and just for short periods of time.

Temperature, relative humidity, and CO₂ sensors are present in three different offices to monitor the environmental parameters (offices 4, 8 and 9 in Fig. 3), and only temperature sensors are present in the relative adjacent rooms for calibration and validation purposes. The sensors used are ONSET HOBO MX1102A for the three offices and ONSET HOBO U12-013 for the adjacent rooms.

3. Model Development

3.1 Building Model

An existing model of the case study building developed in TRNYS was adapted for the calculation of the internal airflows and infiltrations prior to coupling with the probabilistic model. While, in the original model, several rooms were characterized in detail, including offices, bathrooms, hallways, archives, etc. (Fig. 2), in the model used for the risk assessment, only one of the three blocks of the building was considered (Fig. 3). In the selected block, eleven offices, one archive, a hallway, one bathroom, a common room and two shafts are located. As mentioned before, CO₂ was monitored in

three offices (offices 4-8-9), while the temperature was also monitored in some adjacent spaces (offices 3-7-10, the hallway and the common room). The data collected from the adjacent rooms was used to set the boundary conditions of the three main offices during the calibration process. The period selected for calibration goes from November 30th to December 15th, 2021, while the validation was carried out in the period starting from December 15th to December 24th of the same year. Calibration and validation were performed on the measured temperature.

The occupancy profiles were randomly determined with the Page stochastic algorithm, based on the occupancy probability profiles proposed by ASHRAE standards. An occupancy profile was created in this way for each occupant of the block, considering in the process the day of the week (weekday, Saturday, Sunday) and the hour of the day. With the Page algorithm, it was possible to account for short moment of absence from the office, as well as long periods of absence usually related to sickness or holidays.

The airflow evaluation was carried out with TRNFLOW, a plugin for TRNSYS, based on the software COMIS. Two external nodes were added to the TRNFLOW model (a.k.a. airflow network, or AFN), one for each external side where windows are present. Pressure coefficients were chosen accordingly to the TRNFLOW manual for a semi-sheltered building. Infiltrations were modeled with the *crack* component, both for closed windows and for doors, while internal and external airflows (present in the case of an open window and/or door), with the *large opening* component. Four different opening profiles for the opening and closing of the windows were extrapolated from the data collected in the monitored offices, and then assigned to all the internal spaces. Finally, the *test data* component was used to model the mechanical ventilation, with a constant rate of fresh air supply when active.

3 design variables were considered during the calibration process, and these are related to each component: for the *crack* component, the air mass flow coefficient, the discharge coefficient for the *large opening* component and the ventilation efficacy for the *test data* component were considered. After

calibration, the AFN was used to evaluate both infiltrations and airflows in the block considered for risk assessment.

3.2 Occupancy Scenarios

Some hypotheses regarding the occupancy of the offices were formulated. Firstly, it was supposed that all the occupants of the building were susceptible subjects (i.e., people that can be infected by Covid-19). Only one person was infected and contagious at the start of the risk assessment process: an occupant of office 3 (Fig. 3). In all offices, only one person was present at a time, with the exception of offices 2-3-4, where 2 persons could be present at the same moment according to their occupancy profiles. In total, during occupancy hours, 15 people could be simultaneously present in the block considered for risk assessment. Occupancy hours were scheduled to be from 8 am to 12 pm in the morning, and then from 1 pm to 5 pm in the afternoon. The occupants of the offices did not move from one space to another: whenever an office was scheduled to be empty, the occupants were supposed to be outside the block.

Doors were considered usually closed and briefly open only whenever a change in the occupancy status of a given office occurred (i.e., an occupant entered/left the office according to its occupancy profile). Windows were also observed to be usually closed. Since the expected state of the windows when open was the tilted position, an opening fraction of 30 % was considered for the windows when open. This was necessary to limit the airflows evaluated by the *large opening* component of the AFN, avoiding an overestimation of the air change rate for the internal spaces.

4. Monte Carlo Analysis

The Monte Carlo model used for the risk assessment analysis was based on a previous model, developed for a set of three university classrooms in the Free University of Bozen-Bolzano (Albertin et al., 2022a), where it was used to evaluate the airborne risk of contagion for the students and professors of the classrooms for different scenarios.

Some ventilation strategies were investigated in terms of risk reduction, as well as the effect of mask utilization. The probabilistic model was subsequently enhanced in Albertin et al. (2022b), to consider different Covid-19 variants (Delta and Omicron), vaccines (AstraZeneca, Pfizer and Moderna), and the effect of air purifiers, as well. In this work, the Monte Carlo model was adapted to the office building and further enhanced with the Page algorithm for the creation of randomized occupancy profiles for each occupant. The probabilistic nature of the Page algorithm could be fully exploited within the Monte Carlo method, whose simplified schematic is represented in Fig. 4.

The process started with the definition of a scenario, by selecting the ventilation strategy, the presence of vaccine coverage, Covid-19 variants, etc. Then, each scenario was evaluated 1000 times, in this work referred as *iterations*. An iteration consists of a series of simulations, each one representing a day. During the simulations, the airflow database was used to calculate the concentration of Covid-19 in the offices, and, thus, the dose received by the occupants (Buonanno et al., 2020b). Thanks to the dose, it was possible to account on a day-to-day basis for newly infected occupants, who would contribute towards increasing Covid-19 concentrations in the block in the next simulations. The simulations stopped when it was not possible to have new infections, meaning that the infected occupants were either no longer contagious or kept outside the block.

In this chapter, the risk assessment model is described in detail, highlighting the differences with respect to previous works.

4.1 Scenario Definition

The risk assessment process begins with the definition of the scenario. The ventilation strategies considered for the given scenario were automatically implemented in the TRNSYS model, as well as in the AFN, changing the parameters used for the evaluation of both infiltrations and airflows. The building model was then used to create a database of airflows under different conditions (windows and/or door opened or closed). The database was used during the simulation phase to dynamically

evaluate the concentrations for each office, necessary for calculating the dose received by the occupants, and thus, to identify new infections.

4.2 Scenario Evaluation Process

Each scenario was evaluated with 1000 iterations. An iteration started with a random process for assigning a quanta emission rate value (QR, where a quantum is defined as “the dose of airborne droplet nuclei required to cause infection in 63 % of susceptible persons” in Buonanno et al., 2020b) to each occupant. The process was also carried out for the occupants that were not infected to save computational time. During a simulation, if a subject was not infected, his or her QR was considered to be zero. The QR was then switched to the value assigned only for those occupants that were infected during a simulation. The QR values were randomly selected with a lognormal distribution curve whose parameters depended on the activity performed by each occupant (Buonanno et al., 2020b). The activities were subdivided into primary and secondary activity.

The time allocated to the secondary activity was randomly chosen with a Gaussian distribution, with a process ensuring that the primary activity was carried out at least 70 % of the time. Two values of QR were then randomly extracted for the occupants, one for each activity, and subsequently weighted with the time allocated to the respective activities, and finally added up.

In a similar process, two other values were ran-

domly assigned to all the occupants during the initial phase of an iteration: asymptomatic status and vaccination status.

Asymptomatic status was determined once again for all the occupants, infected or not. Early categorization was performed randomly with a normal distribution curve whose parameters were set according to Ma et al. (2021). Those occupants categorized as asymptomatic and who would get infected during a simulation would increase the Covid-19 concentrations in the block during the whole contagious period, without ever being kept outside the building.

Table 1 – List of activities with relative parameters for the log-normal distribution curve

Activity	Log Mean	Log Standard Deviation	Type
Resting-breathing	-0.43	0.73	Primary
Standing-speaking	1.08	0.72	Secondary

Finally, vaccination status was randomly extracted. All the occupants were categorized in this way as fully vaccinated (2 doses received), partially vaccinated (1 dose received) or not vaccinated. The number of occupants in each category was automatically assigned to match the vaccination coverage according to the global database of Covid-19 vaccinations (Mathieu et al., 2021). The vaccination

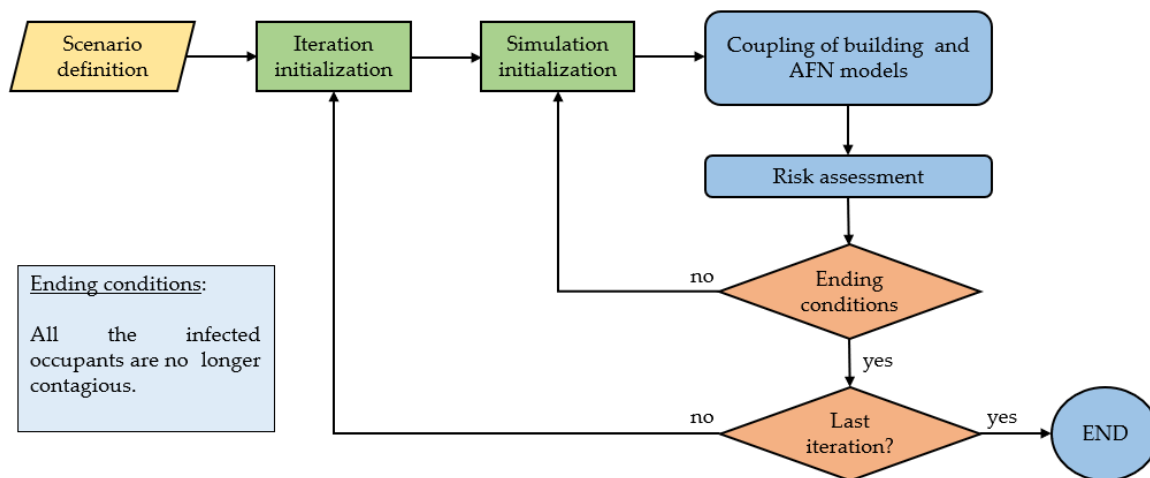


Fig. 4 – Scheme of the Monte Carlo model utilized for the risk assessment process

coverage selected represents the situation in Italy on November 1st, 2021, with 72 % fully vaccinated, 5.8 % partially vaccinated and 22.2 % not vaccinated. Furthermore, the effectiveness of each vaccination category depends on the typology of Covid-19 variants considered, and on the vaccine selected: Pfizer, Moderna, AstraZeneca (Andrews et al., 2022). The effectiveness of the vaccine selected can then vary from occupant to occupant, and it was used to randomly select the subjects who were immune to airborne contagion due to Covid-19 for a given iteration. For example, a fully vaccinated occupant with 2 doses of Moderna had a higher probability of being immune to the Delta variant compared with an occupant with only one dose of AstraZeneca.

Before the start of the simulations, some hypotheses were formulated: all the occupants were not infected and were susceptible to Covid-19 contagion, except for one occupant in office 3, who was already infected, asymptomatic, and contagious. The initial concentrations of Covid-19 in all the internal spaces of the block were equal to zero.

At this stage, the simulations started and were performed until the ending condition is met, which signified the end of the iteration. At the end of each iteration, the number of infected occupants in office 3 and in the whole block were counted, obtaining a distribution of 1000 values. It was then possible to calculate the likelihood of having one or more infected subjects both for the office where the first infected was located (office 3) and for the other offices of the block. The distinction was important, since having new infections in adjacent spaces meant that it was possible for the Covid-19 virus to spread from one room to another, increasing the chances of unacceptable outcomes.

4.3 Risk Assessment

During a simulation, the airflows evaluated with the AFN were utilized to dynamically calculate Covid-19 concentrations in all the internal environments of the block considered. Then, at the end of each day, the dose received by the occupants was calculated, taking into consideration the occupancy profile of each subject and Covid-19 concentration in the respective office. Finally, with the

dose received it was possible to calculate the probability of infection for each occupant (Buonanno et al., 2020a), and thus, to randomly account for new infections at the end of each day. Those occupants that were selected as not infectable during the assessment of the vaccination status always had a probability of infection equal to zero for the given iteration.

For each newly infected occupant, the contagious period was randomly determined, as well as the symptom onset day. The process is reported in detail in Albertin et al. (2022b). The occupants that were infected and that were outside the contagious period cannot be infected again during an iteration. The simulations were repeated until all the occupants were no longer contagious. At this stage, the final number of infected occupants was computed for each office and the iteration came to an end.

5. Simulation Plan

A total of 27 scenarios were evaluated with the Monte Carlo model by considering different natural and mechanical ventilation strategies, Covid-19 variants, and the presence of vaccination coverage with the Pfizer vaccine.

There were 3 natural ventilation strategies considered for the scenarios: (1) all the windows were always closed; (2) the opening of the windows was set by profiles based on measured data; (3) the windows were open for 10 minutes every hour and during the lunch break. There were also 3 mechanical ventilation strategies: (1) always inactive; (2) active outside occupancy hours as observed during the monitoring period (7 – 8 am, 12 – 13 pm, 5 – 6 pm); (3) active during occupancy hours (8 am – 12 pm, 1 – 5 pm). Two Covid-19 variants were considered, (a) Delta and (b) Omicron, respectively. Finally, the efficacy of vaccines was investigated by comparing the case where (a) all the people were not vaccinated or (b) with vaccination coverage, performed with the Pfizer vaccine. Cases were coded, with a sequence of two numbers, both in range 1-3, representing respectively the natural and mechanical ventilation strategy considered, followed by a letter D or O, respectively, for the Delta and Omicron variants, or O/D if the case was

valid for both variants. Finally, the last member of the sequence was a number: 1 when vaccination coverage was present, and 0 when not. As, for example, code 13O1 represents the case with windows always closed (natural ventilation strategy number 1), mechanical ventilation active during occupancy hours (mechanical ventilation strategy number 3), Omicron variant and vaccination coverage present.

6. Results

The results were reported as the likelihood of having a specific number of newly infected subjects by considering all offices:

- L0, refers to the likelihood of not having new infections,
- L1, refers to the likelihood of having exactly one new infection,
- L2, refers to the likelihood of having exactly two new infections,
- L2+, refers to the likelihood of having more than two new infections.

Furthermore, the likelihood values were colored in shades of red and green, where red represents the lower value, and green the highest value for L0. The colours were inverted for the metrics L1, L2, L2+. In this way, it was easily possible to identify the scenarios with the best and worst possible outcome thanks to the colors of each row in Table 2.

To this end, it was possible to identify the worst-case scenario as 11D/O0. In this case, the windows are always closed, allowing only a small amount of fresh air (infiltrations) to enter the building through the cracks and small openings, since the mechanical ventilation is always inactive, too. Furthermore, in this case, vaccination coverage is not present. The result is a likelihood of 50 % of having a new infection in the block. Most of the time, the infection will occur inside the same office (L1 ~ 27 %) but it can also happen in other rooms, too (L2 ~ 9 %; L2+ ~ 14 %). By taking into consideration the case that represents the actual conditions of the block regarding both mechanical and natural ventilation strategies, in the case of vaccine coverage not being present (22D/O0), the results are similar to the worst-case scenario, with a probability of 42 %

of having at least one new infection. The coupling of mechanical and natural ventilation is able to reduce the probability of infection in adjacent rooms from ca. 23 % to 17 %. In the case of windows being opened often, and the mechanical ventilation being active during occupancy hours (case 33D/O0), it is possible to reduce the probability of new infection even further to 25 % (half with respect to the worst-case scenario), and the probability of new infections in adjacent offices to 7 %. The efficacy of vaccination coverage strongly depends on the Covid-19 variant considered. By looking at the table, it is possible to observe how vaccinations are a valid substitute for the optimal ventilation strategies (i.e., strategy number 3 for both mechanical and natural ventilation) when the Delta variant is considered. In fact, the scenario with windows always closed and mechanical ventilation always inactive (11D1) is comparable with the best-case scenario without vaccination coverage (33D/O0). If all the possible counter measures are taken (scenario 33D1), it is possible to reduce the probability of new infections to 10 %, and the probability of having new infections in adjacent rooms to almost 0 %. For the Omicron variant, the considered vaccines are not as effective as for the Delta variant. In this case, the results are slightly better if compared with the scenarios without vaccination coverage.

7. Conclusion

In this work, a Monte Carlo method for the assessment of airborne contagion risk due to Covid-19 was applied to some offices contained in a public building, taking into consideration different ventilation strategies, two Covid-19 variants, and the presence of vaccine coverage. It was observed that the current strategies regarding both window utilization and mechanical ventilation are not able to prevent the spread of Covid-19 virus from office to office. Vaccination coverage alone is able to reduce the risk of contagion due to Covid-19 to acceptable values only when it is a case of the Delta variant.

Table 2 – Likelihood of having exactly 0 (L0), 1 (L1), 2 (L2), or more (L2+) newly-infected occupants for each scenario

Scenario Code	L0 (%)	L1 (%)	L2 (%)	L2+ (%)
11D/O0	50	27	9	14
12D/O0	56	29	7	8
13D/O0	65	24	8	4
21D/O0	54	29	9	9
22D/O0	58	26	9	8
23D/O0	65	21	8	6
31D/O0	70	20	6	4
32D/O0	73	21	4	2
33D/O0	75	19	5	2
11D1	74	19	4	2
12D1	79	18	3	1
13D1	85	13	2	0
21D1	81	16	2	1
22D1	77	18	3	2
23D1	86	12	2	0
31D1	87	12	1	0
32D1	88	11	1	0
33D1	90	8	1	0
11O1	60	25	8	7
12O1	62	25	8	6
13O1	70	21	6	3
21O1	62	24	7	7
22O1	65	24	6	5
23O1	73	21	3	3
31O1	72	21	5	3
32O1	73	21	5	2
33O1	82	14	3	2

In fact, if the Omicron variant is considered instead, the only proper way to contain the spread of the virus is to combine vaccination coverage with an increase in opening frequency of windows, and to adopt an appropriate schedule for mechanical ventilation, preferably based on occupancy profiles.

Acknowledgement

This study was funded by the Free University of Bolzano-Bozen within the “Ventilation and Indoor Air Quality in Offices: Monitoring and Improvement” project (CUP: I55F21002050005) and performed with the support of the Geology, Civil Protection and Energy Office of the Municipality of Bozen-Bolzano.

References

- Albertin, R., G. Pernigotto, and A. Gasparella. 2022a. “Assessment Of The Covid-19 Contagion Risk In University Classrooms With TRNSYS And TRNFLOW Simulations.” *Proceedings of IAQ 2020*, May 4-6, 2022, Athens, Greece.
- Albertin, R., G. Pernigotto, and A. Gasparella. 2022b. “Contagion Risk Assessment For COVID-19 Variants With A Dynamic Approach For A Multizone Building Model Of University Classrooms.” *Proceedings of Herrick Conferences*, July 10-14, 2022, West Lafayette, United States.
- Andrews, N., J. Stowe, F. Kirsebom, S. Toffa, T. Rieckard, E. Gallagher, C. Gower, M. Kall, N. Groves, A. M. O’Connell, D. Simons, P. B. Blomquist, A. Zaidi, S. Nash, N. Iwani Binti Abdul Aziz, S. Thelwall, G. Dabrera, R. Myers, G. Amirthalingam, S. Gharbia, ... J. Lopez Bernal. 2022. “Covid-19 Vaccine Effectiveness against the Omicron (B.1.1.529) Variant.” *The New England journal of medicine*, NEJMoa2119451. doi: <https://doi.org/10.1056/NEJMoa2119451>
- Buonanno, G., L. Morawska, and L. Stabile. 2020a. “Quantitative assessment of the risk of airborne transmission of SARS-CoV-2 infection: Prospective and retrospective applications.” *Environ-*

- ment international* 145: 106112. doi: <https://doi.org/10.1016/j.envint.2020.106112>
- Buonanno, G., L. Stabile, and L. Morawska. 2020b. "Estimation of airborne viral emission: Quanta emission rate of SARS-CoV-2 for infection risk assessment." *Environment international* 141: 105794. doi: <https://doi.org/10.1016/j.envint.2020.105794>
- Ma, Q., J. Liu, Q. Liu, L. Kang, R. Liu, W. Jing, Y. Wu, and M. Liu. 2021. "Global Percentage of Asymptomatic SARS-CoV-2 Infections Among the Tested Population and Individuals with Confirmed COVID-19 Diagnosis: A Systematic Review and Meta-analysis." *JAMA network open* 4(12): e2137257. doi: <https://doi.org/10.1001/jamanetworkopen.2021.37257>
- Mathieu, E., H. Ritchie, E. Ortiz-Ospina, M. Roser, J. Hasell, C. Appel, C. Giattino, and L. Rod s-Guirao. 2021. "A global database of COVID-19 vaccinations." *Nature human behaviour* 5(7): 947–953. doi: <https://doi.org/10.1038/s41562-021-01122-8>

Impact of Visual, Thermal, and Indoor Air Quality Conditions on Students' Wellbeing and Learning Performance in a Primary School of Bolzano, Italy

Giovanni Demozzi – Free University of Bozen-Bolzano, Italy – giovanni.demozzi@gmail.com

Luca Zaniboni – University of Trento & Free University of Bozen-Bolzano, Italy – luca.zaniboni@unitn.it

Giovanni Pernigotto – Free University of Bozen-Bolzano, Italy – giovanni.pernigotto@unibz.it

Andrea Gasparella – Free University of Bozen-Bolzano; Italy – andrea.gasparella@unibz.it

Abstract

Poor Indoor Environmental Quality *IEQ* conditions, defined by the four environmental comfort domains (thermo-hygrometric, visual, Indoor Air Quality *IAQ* and acoustic), can cause not only discomfort to building occupants, but also lack of concentration, and harmful and unhealthy status. In this work, visual, thermal and *IAQ* conditions in a primary school located in Bolzano, Italy, were analysed to assess their impact on students' learning performance. After a survey in the school, which included measurements of illuminance, luminance, optical properties of materials, air temperature and CO₂ concentration, some simulation models were developed. Through a Radiance model, daylight metrics (e.g., Daylight Factor and Daylight Autonomy) and glare metrics (e.g., Daylight Glare Index and Daylight Glare Probability) were calculated. Furthermore, the melanopic illuminance was simulated to evaluate the non-visual effects of light on children's circadian cycles. In addition to that, EnergyPlus simulations allowed an evaluation of the long-term indoor air quality and thermal comfort conditions, which were used to estimate the students' potential performance loss according to some models in the literature. Interventions on shading devices and *HVAC* system controls were suggested, in order to optimize *IEQ*, with a minimization of performance loss and energy consumption.

1. Introduction

Indoor Environmental Quality *IEQ*, defined by the combination of the four environmental comfort domains (thermo-hygrometric, visual, Indoor Air

Quality *IAQ*, and acoustic), must be carefully guaranteed in places such as schools, where people spend a considerable amount of their lifetime. In fact, poor environmental conditions can lead to discomfort in the occupants, and even to poor learning and work performance (UNI EN 15251:2007, UNI EN 16798-1:2019). Furthermore, recent studies in the literature suggest taking comfort from a multi-domain point of view into account (Schweiker et al., 2020; Toftum, 2002; Torresin et al., 2018).

As regards visual comfort, several studies in the literature found this fundamental for indoor wellbeing, since it also affects psychological and psychophysical conditions, as well as circadian rhythms and people's performance (Aries et al., 2010; Cajochen et al., 2005; Khanie et al., 2016; Stevens & Rea, 2001; Webb, 2006; Zaniboni et al., 2022).

As far as the circadian rhythms are concerned, the first models of sensitivity to circadian light were defined in 2001 by Brainard et al. (2001) and Thapan et al. (2001). Later, Rea et al. (2005; 2011) proposed an empirical model of human circadian response based on the neuroanatomy and neurophysiology of the retina and on the results of psychophysical studies. In this model, the concept of Circadian Stimulus *CS*, which represents the relative effectiveness of circadian light, was introduced. According to Rea et al. (2005; 2011), a *CS* of 0.3 in the morning is suitable for the promotion of a good circadian cycle.

Figueiro et al. (2016) highlighted that, in order to stimulate the circadian rhythm, a high circadian stimulus with bright, bluish-white light must be received in the morning, while a low circadian sti-

mulus with dim, yellowish-white light is preferable in the evening. In this way, both levels of alertness and sleep quality are improved. Nevertheless, as Figueiro et al. (2016) discovered, several aspects must be taken into careful consideration to have a correct CS trend during the day:

1. spectral power distribution of light sources has to be characterized, not relying exclusively on Correlated Colour Temperatures $CCTs$;
2. both vertical illuminance E_v and only horizontal illuminance E_h on the work plane have to be considered;
3. the fact that illuminance level influences CS more than CCT has to be remembered.

As regards IAQ , CO_2 concentration is the main parameter usually monitored. In fact, even if CO_2 is not classified as a pollutant by the World Health Organization, it can be considered a good proxy of the Indoor Air Quality (López et al., 2021). As Bakó-Biró et al. (2012) stated, large CO_2 concentrations have been proven to reduce pupils' attention and vigilance, thus negatively affecting memory and concentration.

Similar effects can be generated by thermal discomfort. Indeed, as observed by Porras-Salazar et al. (2018), thermal discomfort in classrooms can reduce the ability of students to perform typical school tasks, and has an impact on their performance scores.

Given these premises, this study aimed to discuss the impact of visual and thermal aspects and IAQ on students' wellbeing and learning performance. The structure of the research was two-fold. The first part focused on the visual and non-visual effects of light on learning performance of students. The second part, on the other hand, concerned thermal comfort and IAQ , quantifying the pupils' expected performance loss in agreement with the models by Porras-Salazar et al. (2018) and Wargocki et al. (2019).

2. Case Study

This study features a primary school located in Bolzano, Italy. The building, opened in 2014, has a simple and linear architectural form, with a fully glazed atrium on a central square, a place of meeting and social gathering for the neighborhood community. The structure is organized into two sectors connected by a central element.

Fifteen classrooms, each with an area of about 50 m^2 , are on the first and second floors. Classrooms are illuminated by large windows equipped with internal light curtains, and with ceiling tube LED lamps. This analysis focused on three classrooms, north, south and east-oriented.



Fig. 1 – Internal northern classroom view

3. Photopic and Melanopic Analysis

3.1 Survey and Building Model

During the survey, performed on October 23rd, 2019, the following information was collected:

- every surface's color, with reflected luminous fluxes, incident luminous fluxes, reflectance, and chromatic coordinate (Y_{xy}), obtained by means of a portable spectrophotometer;
- illuminance values on students' task area, measured with a luxmeter;
- luminance and luminance maps considering students' typical viewpoints, measured with a spot luminance meter and a calibrated digital camera.

These data were used as inputs for the development of Radiance models.

3.2 Photopic Simulation Model

The Radiance models were developed using Rhinoceros and Grasshopper, with the Ladybug and Honeybee plugins. Urban and natural contexts were imported using Blender. A 2019 actual meteorological year was employed first to compare the simulated results with the measurements, and then for annual simulations.

The following analyses were performed:

- Image-based point-in-time simulations to detect glare risks for students and teacher and validate the model against measured data.*

The pupils are supposed to change frequently their view, looking at the desk or at the teacher alternatively. Thus, the selected visual task area was not limited to the desk, but also included the frontal view. Furthermore, the teacher's view of the classroom was included as well. 15 comparisons between simulated Daylight Glare Probability *DGP* values and those calculated from the luminance maps collected with the calibrated digital camera were carried out.

- Calculation of daylight metrics:* assessment of the Daylight Factor *DF*, with CIE overcast sky, and of dynamic daylight metrics, such as Daylight Autonomy *DA*, continuous Daylight Autonomy *cDA*, Useful Daylight Illuminance *UDI*, and spatial Daylight Autonomy *sDA*. In both cases, a 210-point squared grid (0.5 m x 0.5 m x 0.7 m) on the task area of seated students was used, in agreement with the EN 12464-1.
- Annual calculation of eDGP*, in particular, considering students looking at the window.
- Annual shading and lighting switch profiles*, suggesting, respectively, if venetian blinds need to be adopted or not and whether lights need to be turned on during the year and at which intensity level.

3.2.1 Results

The following figures show some of the results obtained through the simulations described in Section 3.2. Fig. 2 and Fig. 3 show a comparison between the *DGP* calculated from a *HDR* camera luminance map and the simulated one in the eastern classroom. As can be noticed, both gave a value of 0.20, demonstrating the accuracy of the developed Radiance model.

Table 1 shows the Daylight Factors for the three

classrooms considered. Except for the south-oriented classroom, it can be noticed that *DF* is larger than 4 %, in agreement with the current requirements set by Italian law for these types of buildings.

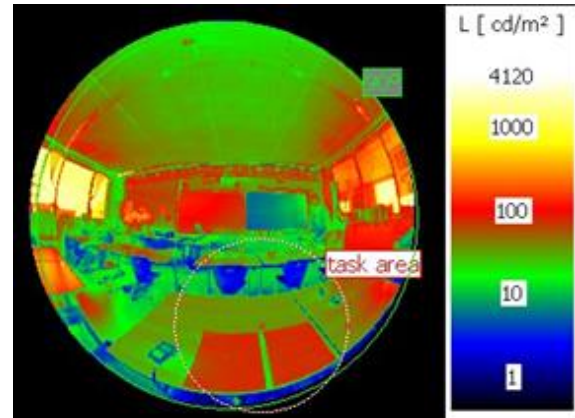


Fig. 2 – Eastern classroom – measured luminance map and student's view *DGP* = 0.20

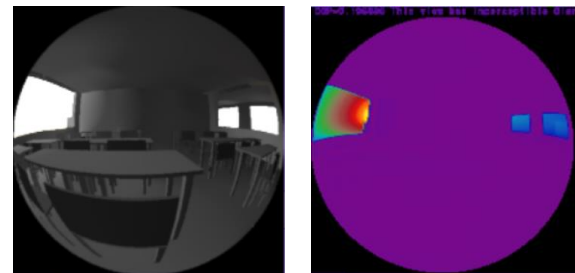


Fig. 3 – Eastern classroom – simulated luminance map and student's view *DGP* = 0.20

Table 1 – Daylight factor

	Northern classroom	Southern classroom	Eastern classroom
<i>DF</i> _{average}	4.4 %	3.2 %	4.2 %

Figs. 4-6 show the values of *DA*, *cDA* and *UDI* for the east-oriented classrooms. As can be noticed, the portion of the room closer to the windows shows a large value of *DA* and *cDA*; however, the natural illuminance can be excessive, as can be observed considering the *UDI* shown in Fig. 6.

Table 2 summarizes the dynamic daylight metrics for all three classrooms. The eastern classroom shows the highest values of *DA*, *cDA* and *sDA*, while the south-oriented one is characterized by the minimum ones. This is due to the exposure, the effects of reflectance of nearby buildings and the absence of high obstacles.

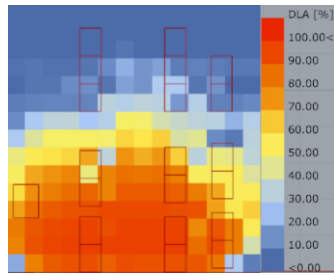


Fig. 4 – Eastern classroom – DA

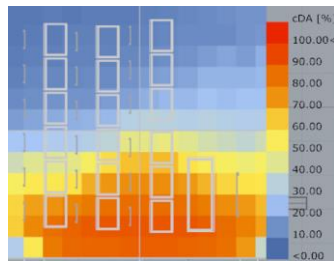


Fig. 5 – Eastern classroom – cDA

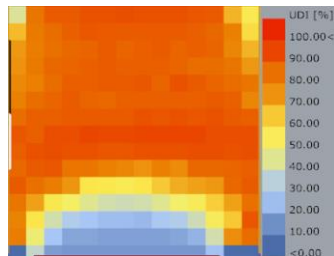


Fig. 6 – Eastern classroom – UDI

Table 2 – Dynamic daylight metrics

	Northern classroom	Southern classroom	Eastern classroom
$DA_{average}$	30.9 %	20.9 %	40.1 %
$cDA_{average}$	60.3 %	40.1 %	63.8 %
$UDI_{average100-2000lx}$	85.0 %	47.9 %	70.8 %
sDA	31.6 %	22.6 %	40.9 %

Finally, Figs. 7-9 represent the annual distribution of $eDGP$ calculated for the view of a student in the centre of the room, recommended usage of shading devices and light switch for the eastern classroom. As can be noticed, the risk of glare is frequently encountered, in particular, during autumn and spring. Therefore, the presence of shadings is here recommended. The same applies to the south-oriented classroom.

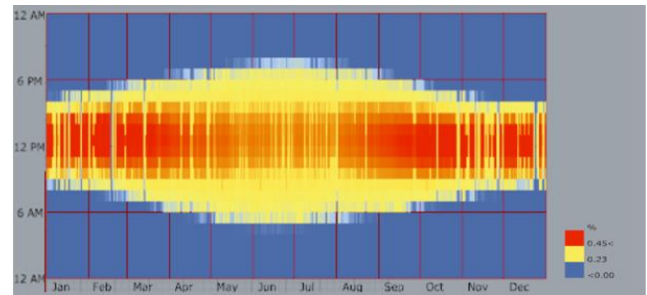


Fig. 7 – Eastern classroom annual DGP

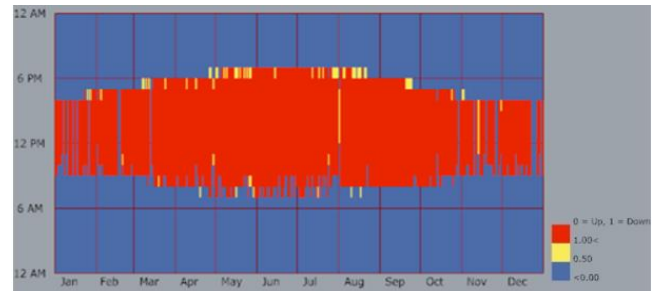


Fig. 8 – Eastern classroom annual shading device

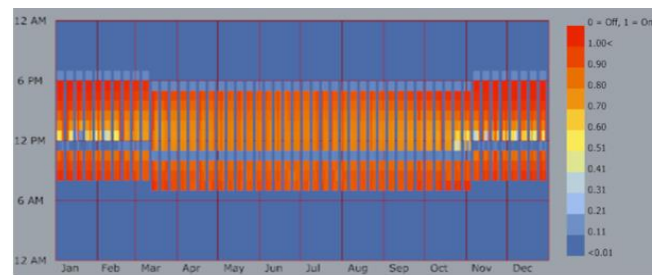


Fig. 9 – Eastern classroom annual lighting switch

3.3 Melanopic Simulation Model

The melanopic illuminance was computed using Lark, a Grasshopper plugin released by Inanici et al. (2015). In order to perform a simplified monthly calculation, a representative day for each month was considered, in accordance with Klein (1976). For the sake of comparison, the analysis was performed using both a CIE clear sky and a climate-based sky.

Within this computation, the light stimulus was evaluated vertically (e.g., in the direction of gaze) by means of six virtual sensors placed across a regularly spaced analysis grid of nine points, at a height of 1.2 m (seated person eye level). All the simulations were set with the same hourly time intervals during the occupational period, i.e., from 8 am to 4 pm.

After the calculation of Rea's melanopic illuminance, the three classrooms were analyzed, verifying if a CS value of 0.3 was achievable for at least 1 h in the early part of the day.

3.3.1 Results

In all three classrooms, melanopic illuminance was unevenly distributed and quite low. This was particularly true for the positions far away from windows and during winter months, as shown in Fig. 10 and Fig. 11 for the eastern classroom. This condition risks not allowing a shift in the biological clock of the occupants. Results from annual calculations indicated that roughly 1/2 of the area in the northern classroom, 1/2 of the area in the southern classroom, and 1/3 of the area in the eastern classroom did not benefit from melanopic illuminance all year long.

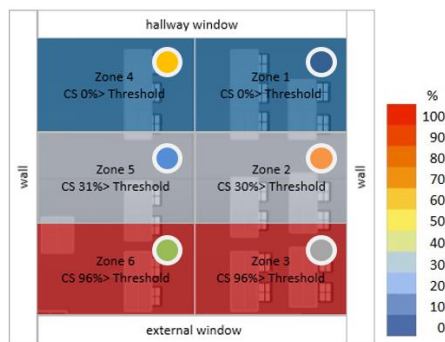


Fig. 10 – Eastern classroom sensor position and percentage of threshold exceedance over the year

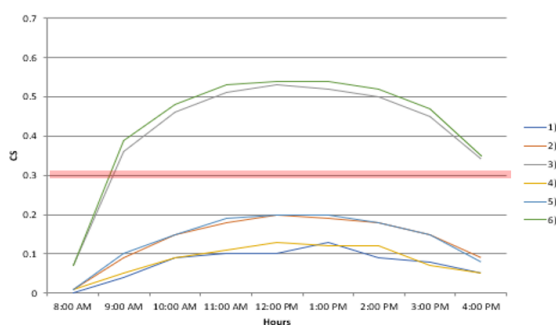


Fig. 11 – Eastern classroom CS trend on January 17th

4. CO₂ and Thermal Analysis

4.1 Survey and Building Model

A monitoring campaign was performed in one of the three classrooms, specifically the southern one, measuring air temperatures and CO₂ concentrations from November to December 2019, with a 10-minute time step.

An EnergyPlus model was developed using a 2019 actual meteorological year and including the surrounding urban context. The thermophysical properties of the building envelope (material thermal conductivity, thickness, density and specific heat capacity) were taken from the technical report and the CasaClima building energy certificate. As regards the glazing system, double glazed low-e windows were modeled with WINDOW by the Lawrence Berkeley National Laboratory (LBNL), considering a window gap of 0.016 m, with a mixture of 90 % argon and 10 % air.

Internal gains were estimated considering the 9 luminaires of 166 W each installed, the presence of 100-W electric equipment (laptop and beamer), and occupants (ASHRAE Handbook of Fundamentals), with a metabolic rate of 1.2 met (as suggested in EN ISO 7730 for sedentary activities), clothing of 1 clo, and in agreement with the school official occupancy schedules. An overall CO₂ generation rate of 0.00002 m³/s was set, and a reference of 400 ppm CO₂ concentration.

Infiltration and ventilation rates were set according to Table 3. Specifically, typical opening schedules of windows were simulated according to the information given by school teachers. Similarly, the control of the shading devices was set in agreement with the typical behavior communicated by school teachers, also considering lowering the shadings when the direct radiation incident on the window is larger than 150 W.

The model calibration was performed manually, varying the infiltration rate, the carbon dioxide generation and the optic properties of obstacles and internal shadings.

4.2 Simulated Configurations and Outputs

The EnergyPlus simulations were computed with four different controls for the HVAC systems:

- *Standard*: simulation of the heating period with heating setpoint of 20 °C and natural ventilation;
- *VAR1*: simulation of the same *Standard* configuration with an additional cooling system with a cooling setpoint of 26 °C;
- *VAR2*: simulation of the same *Standard* configuration with the addition of a Mechanical Ventilation System *MVS* supplying 5 h⁻¹ (i.e., 11 l/s/person during hours of occupation);
- *VAR3*: the combination of *VAR1* + *VAR2*.

Table 3 – Natural and mechanical ventilation in the different configurations

	Standard	VAR1	VAR2	VAR3
Infiltration (Always present)	0.05 h ⁻¹	0.05 h ⁻¹	0.05 h ⁻¹	0.05 h ⁻¹
Tilt open (Occupancy period)	0.1 h ⁻¹	0.1 h ⁻¹	-	-
Windows completely open (Lunch break, after lessons)	5 h ⁻¹	5 h ⁻¹	-	-
MVS (Occupancy period)	-	-	5 h ⁻¹	5 h ⁻¹

Simulated CO₂ concentrations and Fanger PMVs were correlated to pupils' performance loss according to the model developed by Porras-Salazar et al. (2018) and Wargocki et al. (2019). Diverse learning activities were considered, including typical schoolwork tasks, such as arithmetical calculations, reading and comprehension exercises, psychological tests measuring cognitive skills and the abilities needed to perform schoolwork (i.e., tests measuring concentration, memory and response time, results of aptitude and national tests examining progress in learning, results of midterm and final exams and end-of-year grades). Short-term sick leave rates were evaluated as well.

4.2.1 Results

As may be observed in Fig. 12, if no mechanical ventilation is used (as in the *Standard* and *VAR1* configurations), the level of CO₂ concentration exceeds those recommended in EN 16798-1:2019 for school environments (i.e., category I). As reported in Table 4, this issue led to important losses, especially in “*speed and reaction time*” and “*national and aptitude tests and exams*” scores.

On the whole, simulations revealed that the main performance loss of pupils in all the four configurations is due to thermal discomfort, up to 20 %. This result is consistent with Sarbu et al. (2015), who reported that occupants are more sensitive to temperature variations than to CO₂ concentration variations.

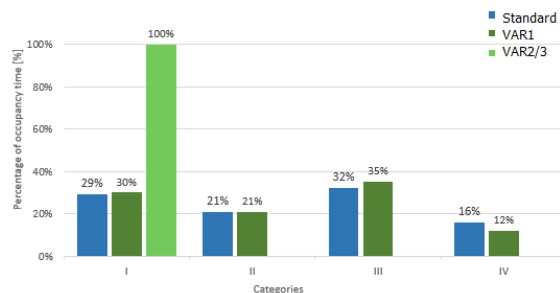


Fig.12 – Share of occupied time in the different IAQ categories in accordance with EN 16798-1:2019

Table 4 – Different configurations and maximum performance losses

	max % performance losses	Standard	VAR1	VAR2	VAR3
Speed or reaction time		12 %	12 %	0 %	0 %
Accuracy		2 %	2 %	0 %	0 %
National and aptitude tests and exams		16 %	16 %	0 %	0 %
Daily attendance		4 %	4 %	0 %	0 %
Thermal discomfort		22 %	21 %	16 %	16 %

5. Discussion and Conclusion

This study uses experimental monitoring and dynamic simulation to assess *IEQ* in three classrooms of a case study school in Bolzano, evaluating the impact on students' wellbeing and learning performance.

In the first part of the study, related to the visual and non-visual analysis of classroom lighting conditions, several issues were identified. In fact, not all environments were well illuminated by daylight (due to the building configuration and to the presence of nearby buildings and mountains), and the risk of glare occurred all year round in east and south-oriented classrooms. For this reason, it was found advisable to adopt shading devices and dimmed daylight systems controlled by a photo-sensor in order to solve issues of glare and lack of daylight. Also, timed control artificial lighting, compensating for the lack of daylight, could be beneficial. These recommendations can be considered to be in agreement with what has been suggested in other works in the literature (e.g., Akashi et al., 2013; Choi et al., 2020).

As regards the non-visual effects of light, it was found that in all three classrooms, melanopic illuminance was unevenly distributed and quite low, especially for the east-oriented classroom, with the risk of not allowing a proper shift in the biological clock of the occupants.

The second part of the study revealed that the main performance loss (from 16 % to 22 %) of the pupils is due to thermal discomfort. In this respect, a potential measure could be the adoption of a local thermostat for controlling the room temperature, avoiding typical problems of overheating in winter months, with positive effects on the energy consumption and pupil performance.

Furthermore, mechanical ventilation was found necessary to ensure good *IAQ* conditions for students. In this framework, an integrated control of the *HVAC* system could be helpful to further improve both environmental quality and energy performance.

Acknowledgement

This thesis was partially developed in the framework of the internal project "IndAIR-Edu – Indoor Air Quality and Ventilation Effectiveness in Educational Buildings" of the Free University of Bozen-Bolzano. The authors kindly thank the Geology, Civil Protection and Energy Office of the Municipality of Bolzano, in particular the engineer Francesca Roberti, for supporting this research, and the management team of A. Langer school.

References

- Akashi, Y., and J. Neches. 2013. "Detectability and acceptability of illuminance reduction for load shedding." *Journal of the Illuminating Engineering Society*: 3-13. doi: <https://doi.org/10.1080/00994480.2004.10748422>
- Aries, M. B., J. A. Veitch, and G. R. Newsham. 2010. "Windows, view, and office characteristics predict physical and psychological discomfort." *Journal of environmental psychology* 30(4): 533-541. <https://doi.org/10.1016/j.jenvp.2009.12.004>
- ASHRAE. 2017. *ASHRAE Handbook-Fundamentals*.
- Bakó-Biró, Z., D. J. Clements-Croome, N. Kochhar, H. B. Awbi, and M. J. Williams. 2012. "Ventilation rates in schools and pupils' performance." *Building and Environment* 48. doi: <https://doi.org/10.1016/j.buildenv.2011.08.018>
- Brainard, G. C., J. P. Hanifin, J. M. Greeson, B. Byrne, G. Glickman, E. Gerner, and M. D. Rollag. 2001. "Action Spectrum for Melatonin Regulation in Humans: Evidence for a Novel Circadian Photoreceptor." *Journal of Neuroscience* 21(16): 6405-6412. doi: <https://doi.org/10.1523/JNEUROSCI.21-16-06405.2001>
- Cajochen, C., M. Munch, S. Kobialka, K. Krauchi, R. Steiner, P. Oelhafen, S. Orgul, and A. Wirz-Justice. 2005. "High sensitivity of human melatonin, alertness, thermoregulation, and heart rate to short wavelength light". *The journal of clinical endocrinology & metabolism* 90(3): 1311-1316. doi: <https://doi.org/10.1210/jc.2004-0957>

- Choi, K., and H. J. Suk. 2020. "The gradual transition from blue-enriched to neutral white light for creating a supportive learning environment." *Building and Environment* 180: 107046. doi: <https://doi.org/10.1016/j.buildenv.2020.107046>
- EnergyPlus. 2019. "Weather data". EnergyPlus website (<https://energyplus.net/weather>), accessed on June 2019.
- European Committee for Standardization. 2005. *EN ISO 7730. Ergonomics of the Thermal Environment - Analytical Determination and Interpretation of Thermal Comfort Using Calculation of the PMV and PPD Indices and Local Thermal Comfort Criteria*. Belgium: Brussels.
- European Committee for Standardization. 2007. *EN 15251. Indoor environmental input parameters for design and assessment of energy performance of buildings addressing indoor air quality, thermal environment, lighting and acoustics*. Belgium: Brussels
- European Committee for Standardization. 2011. *EN 12464-1. Light and lighting - Lighting of work places - Part 1: Indoor work places*. Belgium: Brussels
- European Committee for Standardization. 2019. *EN 16798-1. Energy performance of buildings - Ventilation for buildings - Part 1: Indoor environmental input parameters for design and assessment of energy performance of buildings addressing indoor air quality, thermal environment, lighting and acoustics*. Belgium: Brussels
- Figueiro, M. G., K. Gonzales, and D. Pedler. 2016. "Designing With Circadian Stimulus." *Lighting Design and Application*: 31–33.
- Klein, S. A. 1977. "Calculation of monthly average insolation on tilted surfaces." *Solar energy* 19(4): 325-329. doi: [https://doi.org/10.1016/0038-092X\(77\)90001-9](https://doi.org/10.1016/0038-092X(77)90001-9)
- López, M. J. R., G. Guyot, B. Golly, M. Ondarts, F. Wurtz, and E. Gonze. 2021. "Relevance of CO2-based IAQ indicators: Feedback from long-term monitoring of three nearly zero-energy houses." *Journal of Building Engineering* 44: 103350. doi: <https://doi.org/10.1016/j.jobe.2021.103350>
- Porras-Salazar, J. A., D. P. Wyon, B. Piderit-Moreno, S. Contreras-Espinoza, and P. Wargocki. 2018. "Reducing classroom temperature in a tropical climate improved the thermal comfort and the performance of elementary school pupils." *Indoor Air* 28. doi: <https://doi.org/10.1111/ina.12501>
- Rea, M. S., M. G. Figueiro, A. Bierman, and R. Hamner. 2011. "Modelling the spectral sensitivity of the human circadian system." *Lighting Research and Technology*. doi: <https://doi.org/10.1177/1477153511430474>
- Rea, M. S., M. G. Figueiro, J. D. Bullough, and A. Bierman. 2005. "A model of phototransduction by the human circadian system." *Brain Research Reviews* 50(2): 213-228. doi: <https://doi.org/10.1016/j.brainresrev.2005.07.002>
- Sarbu, I., and C. Pacurar. 2015. "Experimental and numerical research to assess indoor environment quality and schoolwork performance in university classrooms." *Building and Environment*. doi: <https://doi.org/10.1016/j.buildenv.2015.06.022>
- Sarey Khanie, M., J. Stoll, W. Einhaeuser, J. Wienold, and M. Andersen. 2016. "Gaze responsive visual comfort: New findings on gaze behaviour in a daylit office space in relation to glare"(No. CONF, pp. 373-384). *Cie Central Bureau*.
- Schweiker, M., E. Ampatzi, M.S. Andargie, R. K. Andersen, E. Azar, V. M Barthelmes, and S. Zhang. 2020. "Review of multi-domain approaches to indoor environmental perception and behaviour." *Building and Environment* 176: 106804. doi: <https://doi.org/10.1016/j.buildenv.2020.106804>
- Stevens, R. G., and M. S. Rea. 2001. "Light in the built environment: potential role of circadian disruption in endocrine disruption and breast cancer." *Cancer Causes & Control* 12(3): 279-287. doi: <https://doi.org/10.1023/A:1011237000609>
- Thapan, K., J. Arendt, and D. J. Skene. 2001. "An action spectrum for melatonin suppression: evidence for a novel non-rod, non-cone photoreceptor system in humans." *Journal of Physiology*. doi: <https://doi.org/10.1111/j.1469-7793.2001.t01-1-00261>
- Toftum, J. 2002. "Human response to combined indoor environment exposures." *Energy and*

- buildings* 34(6): 601-606. doi: [https://doi.org/10.1016/S0378-7788\(02\)00010-5](https://doi.org/10.1016/S0378-7788(02)00010-5)
- Torresin, S., G. Pernigotto, F. Cappelletti, and A. Gasparella. 2018. "Combined effects of environmental factors on human perception and objective performance: A review of experimental laboratory works." *Indoor air* 28(4): 525-538. doi: <https://doi.org/10.1111/ina.12457>
- Wargocki, P., J. A. Porras-Salazara, S. Contreras-Espinoza. 2019. "The relationship between classroom temperature and children's performance in school." *Building and Environment* 157: 197-204. doi: <https://doi.org/10.1016/j.buildenv.2019.04.046>
- 157
- Webb, A. R., 2006. "Considerations for lighting in the built environment: Non-visual effects of light." *Energy and Buildings* 38(7): 721-727. doi: <https://doi.org/10.1016/j.enbuild.2006.03.004>
- Zaniboni, L., M. Sarey Khanie, G. Pernigotto, J. Toftum, A. Gasparella, and B.W. Olesen. 2022. "Lighting conditions in physiotherapy centres: A comparative field study." *Lighting Research & Technology*: 14771535211046521. doi: <https://doi.org/10.1177%2F14771535211046521>

Performance Simulation of Desiccant Wheel under Dynamic Conditions: Comparison between Detailed and Simplified Models

Simone Dugaria – Free University of Bozen-Bolzano, Italy – simone.dugaria@unibz.it

Andrea Gasparella – Free University of Bozen-Bolzano, Italy – andrea.gasparella@unibz.it

Abstract

In the last few decades, European countries have been facing an increasing demand for active air-conditioning (cooling and dehumidification) in the summer period. As a good alternative to energy demanding vapor compression cooling-based air dehumidification, building HVAC systems integrating desiccant-based dehumidification has drawn increasing attention. These technologies offer the possibility to significantly reduce the energy requirement for air dehumidification and post-heating due to excessive cooling. In fact, air-conditioning systems that use solid or liquid desiccant offer the interesting capacity of separating dehumidification and sensible cooling of air and realizing high-energy-efficiency systems. However, the complexity perceived by technicians towards the design of air-conditioning systems based on these technologies actually limits their adoption in HVAC systems, mainly due to the difficulties in predicting the performance of the desiccant devices, which is the crucial component of the system. On the one hand, many simplified approaches commonly adopted to simulate and optimize the dehumidification performance are based on steady-state models and their reliability under unsteady conditions is questionable; on the other hand, accurate detailed models available for the design and development of components do not turn out to be particularly suitable for simulation of energy systems, due to their high computational cost. The present work focuses on desiccant wheels, whose performance is not only directly related to the properties of the sorption material, but also depends strongly on operating conditions, such as rotational speed, regeneration temperature and inlet air conditions, which are typically non-stationary in real application. In this context, the purpose of this paper is to assess the reliability of a simplified model to predict the behavior of a desiccant wheel under dynamic conditions. To do so, a detailed model of a desiccant wheel is developed and validated against experimental data available in the literature. Finally, a comparison between the devel-

oped detailed model and the simplified model under dynamic conditions is carried out.

1. Introduction

The adoption of new and efficient dehumidification technologies as an alternative to condensation is attracting increasing interest, both in civil application and industrial production. Compared with the traditional vapor compression dehumidification method, the absorption dehumidification method can save up to 40 % energy (Du & Lin, 2020) and make full use of renewable energy sources. Moreover, adsorption dehumidification systems allow improved control of systems with advantages for occupants' thermohygrometric comfort. As clearly discussed in many review papers (Ge et al., 2014; Daou et al., 2006; Sultan et al., 2015), desiccant wheel systems are attracting increasing interest because they offer advantages over other air conditioning systems, such as the possibility of:

- i) using water as a natural refrigerant and other environmentally-friendly desiccant materials (such as silica gel and zeolites);
- ii) making energy-efficient cooling systems that work with the sensitive and latent loads, the application of which is possible under different environmental conditions;
- iii) meeting the requirements of miniaturization and being less subject to corrosion compared with the liquid desiccant system (in which the liquid and air directly interact);
- iv) integrating low-grade heat sources (such as solar energy, geothermic energy and waste heat), hence significantly reducing the operating costs;

- v) overcoming the discontinuous problem of the fixed-bed desiccant cooling system.

The rotary desiccant wheel is a relatively mature technology, yet its wide application is still limited due to the complexity perceived by technicians towards the design of air-conditioning systems based on this technology. The design of HVAC systems based on this technology is quite complex because of the difficulties in predicting the performance of the desiccant wheel, which is the crucial component of the system. In fact, the performance of the desiccant wheel is critical to the capability, size and cost of the whole system (De Antonellis et al., 2010). Desiccant wheel performance strongly depends on regeneration temperature on the revolution speed, inlet airflow conditions (temperature, humidity and flow rate) and on the coupled heat and mass transfer within the desiccant. These aspects greatly complicate the development of models which can accurately predict the performance of a desiccant wheel under non-stationary conditions without incurring in high computational load and complexity. On the one hand, many detailed desiccant wheels models have been based on a detailed physical approach and they are particularly suitable for the development and design of components (Ge et al., 2008); on the other hand, simplified approaches based on practical correlations (Angrisani et al., 2012; De Antonellis et al., 2015; Jurinak, 1982; Panaras et al., 2010) are commonly used to simulate and optimize the dehumidification performance, but their reliability under unsteady conditions is questionable. The purpose of this work is to assess the reliability of simplified models to predict the behavior of a desiccant wheel under dynamic conditions. The rotary desiccant dehumidifier model contained in the TESS Component Libraries for Trnsys18™ was chosen to represent the simplified models based on the correlations. A detailed model of a desiccant wheel was developed and validated against experimental data available in the literature and, finally, a comparison between these two models was carried out. A desiccant wheel is a cylindrical rotating device generally consisting of a structure of several channels. The channels run in the axial direction of the wheel and are parallel to each other. Depending on the manufacturing process, they can have usually a rectangular, triangular or sinusoidal shape. The

structure is made by supporting material impregnated with an adsorbent substance (desiccant) in a typical content f of 70–80 %. The most widespread support materials are paper, aluminium, synthetic fibers or plastic, while common adsorbents are silica gel, zeolite and activated alumina (De Antonellis et al., 2015).

In its basic configuration, the wheel is divided into two sections, where the air streams are arranged in counter-flow. In the process section, the air stream is dehumidified and undergoes heating. In the regeneration section, an air stream is heated before passing through the wheel to increase its moisture-holding capacity; the regeneration air stream passing through the wheel removes vapor from the desiccant material and exits cooled and humidified. A diagram of a desiccant wheel is shown in Fig. 1.

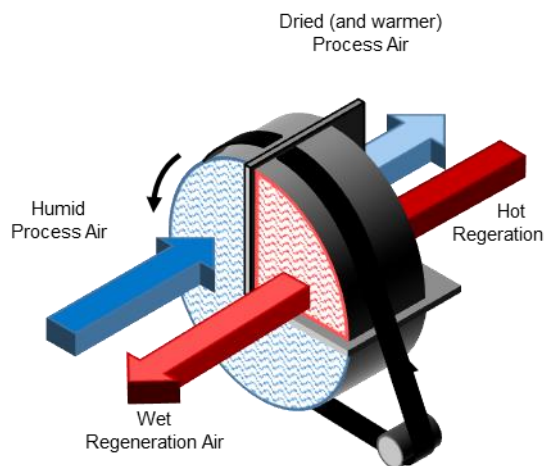


Fig. 1 – Diagram of a desiccant wheel

2. Model Description

Two models were considered in this paper to simulate the performance of a desiccant wheel such as the one shown in Fig. 1. In the first defined detailed model, the coupled heat and mass transfer within the wheel is modeled in detail. The simplified model is a correlation-based model that can immediately provide output conditions without the need to specify detailed parameters of the desiccant wheel.

In the detailed model, to reflect the actual transfer processes occurring in the desiccant wheel, a gas and solid side resistance was applied, where also the solid side heat conduction and mass diffusion

resistances were considered. Compared with only gas-side resistance models, gas and solid side resistance models are more related to the actual process in the desiccant wheel (Ge et al., 2008). However, the diffusion and adsorption processes inside the desiccant are lumped into the mass and heat transfer coefficients. The precision of these models is considered satisfactory because the desiccant layer is rather thin (Ge et al., 2008). The model also takes also into account heat and mass transfer from the desiccant to the air stream and the developing temperature and velocity profiles along the desiccant wheel channels.

The numerical analysis is based on the following assumptions:

- Heat and mass transfer from the wheel to the surroundings are negligible;
- The channels are considered identical and uniformly distributed throughout the wheel;
- Supporting and desiccant materials are evenly distributed in the layer.
- The properties of the dry desiccant material, as well as of the supporting material are constant;
- Heat and mass transfer between adjacent channel are negligible: temperature and moisture content gradients in circumferential and radial directions are not considered;
- The hygroscopic capacity of supporting material is negligible compared with the adsorbent;
- The inlet air conditions are uniform and the air flow is one-dimensional;
- Air leakages between the two streams are negligible;
- Heat conduction in humid air is negligible;
- Pressure loss of the air stream is negligible for heat and mass transfer processes (the thermodynamic properties are unaffected)
- Axial heat conduction and mass diffusion in the air are small compared with convective processes;
- The vapor enters the pores, diffuses in the pores, and, meanwhile, is adsorbed.
- The influence of the pressure drop in axial direction on heat and mass transfer is neglected;
- The heat of adsorption is set free in the layer immediately when the vapor enters the porous layer and is partially convected into air stream.

The schematics of a channel segment in the desiccant wheel is shown in Fig. 2.

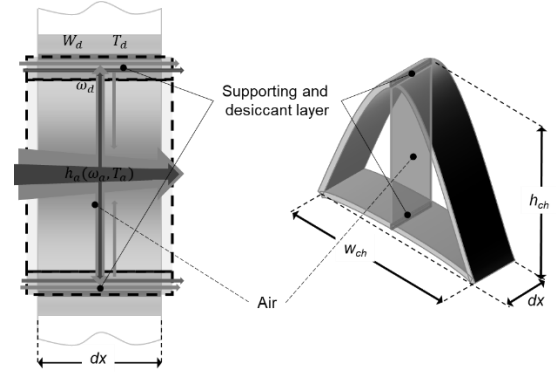


Fig. 2 – Schematic of the control volume in a channel segment (right) and mass and energy transfers in a control volume (left)

In the detailed model, one channel segment with an infinitesimal length dx is selected as the control volume (Fig. 2 - left). The control volume is separated into two nodes, one is the humid air in the channel and the other is the layer composed of supporting and desiccant materials (Fig. 2 - right). The layer of supporting and desiccant material is shared by two channels: therefore, the thickness of the layer in one control volume is half of its actual value and the middle of this layer is considered to be adiabatic. Referring to Fig. 2, the following laws were applied to the infinitesimal control volume.

Mass balance of water in the desiccant material and adsorbed water:

$$\begin{aligned} \rho_a \varepsilon A_{ch} (1-f) \frac{\partial \omega_d}{\partial t} + \rho_d (1-\varepsilon) A_{ch} (1-f) \varphi \frac{\partial W}{\partial t} \\ = \rho_a \varepsilon A_{ch} (1-f) D_{eff} \frac{\partial^2 \omega_d}{\partial x^2} \\ + \rho_d A_{ch} (1-f) D_s \frac{\partial^2 W}{\partial x^2} \\ + h_m P_{ch} (\omega_d - \omega_a) \end{aligned} \quad (1)$$

Energy balance for the desiccant material, supporting material and adsorbed water:

$$\begin{aligned} \rho_s (1-\varepsilon) A_{ch} (1-f) c_{p,s} (1-\varphi) \frac{\partial T_d}{\partial t} \\ + \rho_d (1-\varepsilon) A_{ch} (1-f) c_{p,d} \varphi \left(\frac{\partial T_d}{\partial t} - \frac{\lambda_d}{\rho_d c_{p,d}} \frac{\partial^2 T_d}{\partial x^2} \right) \\ = h_{th} P_{ch} (T_a - T_d) \\ + h_m P_{ch} (\omega_a - \omega_d) c_{p,v} (T_a - T_d) \\ - h_m P_{ch} (\omega_a - \omega_d) (1-\eta) i_{ad} \end{aligned} \quad (2)$$

Mass balance of water in the air stream:

$$\rho_a f A_{ch} \left(\frac{\partial \omega_a}{\partial t} + u \frac{\partial \omega_a}{\partial x} \right) = h_m P_{ch} (\omega_d - \omega_a) \quad (3)$$

Energy balance in the air stream:

$$\begin{aligned} \rho_a f A_{ch} (c_{p,a} + \omega_a c_{p,v}) \left(\frac{\partial T_a}{\partial t} + u \frac{\partial T_a}{\partial x} \right) \\ = h_{th} P_{ch} (T_d - T_a) \\ + h_m P_{ch} (\omega_d - \omega_a) c_{p,v} (T_d - T_a) \\ - h_m P_{ch} (\omega_d - \omega_a) \eta i_{ad} \end{aligned} \quad (4)$$

To solve the system of partial differential equations, a set of boundary and initial conditions is needed. Assuming adiabatic and impermeable boundaries at the entrance and exit flow channel leads to a negligible error: according to Simonson and Besant (1997), the transfer area at the inlet and outlet of the wheel correspond to less than 0.1 %. Therefore, the following relationships apply for the support and desiccant layer:

$$\begin{aligned} \left. \frac{\partial T_d}{\partial x} \right|_{x=0} = \left. \frac{\partial T_d}{\partial x} \right|_{x=L} = 0 \\ \left. \frac{\partial \omega_d}{\partial x} \right|_{x=0} = \left. \frac{\partial \omega_d}{\partial x} \right|_{x=L} = 0 \end{aligned} \quad (5)$$

The temperature, humidity ratio and velocity boundary conditions for the air are given by Dirichlet boundary conditions periodically switching between process and regeneration air stream:

$$\begin{aligned} T_a(0, t) &= \begin{cases} T_{p,inlet} \\ T_{r,inlet} \end{cases} \\ \omega_a(0, t) &= \begin{cases} \omega_{p,inlet} \\ \omega_{r,inlet} \end{cases} \\ u_a(0, t) &= \begin{cases} u_{p,inlet} \\ u_{r,inlet} \end{cases} \end{aligned} \quad (6)$$

Assuming uniform initial temperature and humidity ratio of the air and of the support and desiccant, we have:

$$\begin{aligned} T_a(x, 0) &= T_{a0} \\ \omega_a(x, 0) &= \omega_{a0} \\ T_d(x, 0) &= T_{d0} \\ \omega_d(x, 0) &= \omega_{d0} \\ W(x, 0) &= W_0 \end{aligned} \quad (7)$$

Additional equations are needed to solve the initial-boundary-value problem.

The equilibrium water uptake in the desiccant material can be expressed by a general sorption curve

that directly links the water uptake W to the relative humidity.

The isosteric heat of adsorption i_{ad} of silica gel calculate using the equation recommended by San (1993). The effective diffusion coefficient D_{eff} accounts for both molecular diffusion and Knudsen diffusion. However, as reported by Pesaran and Mills (1987), since most of the pores of silica gel are less than $100 \cdot 10^{-10}$ m, ordinary diffusion can be ignored in usual silica gel applications. The surface diffusion D_s is evaluated with the relationship proposed by Pesaran and Mills (1987).

The heat transfer coefficient h_{th} is derived from the local Nusselt, calculated following equation of Niu and Zhang (2002). Assuming a sinusoidal geometry for the channel, the Nusselt number for the fully developed flow and the equivalent diameter were calculated through the correlations proposed by Kakaç et al. (1987). The mass transfer coefficient h_m was derived from the Sherwood number.

Given the initial and boundary condition, the partial differential equations system of the four non-linear and coupled heat and mass transfer equations is implemented and solved in Matlab™ environment.

In the simplified model developed by Howe (1983) and based on the original work of Jurinak (1982), the outlet air conditions (humidity ratio and temperature) are provided through two combined potentials $F1$ and $F2$ for a silica gel desiccant defined in the following way:

$$F1 = \frac{-2865}{T^{1.490}} + 4.344 \omega^{0.8624} \quad (8)$$

$$F2 = \frac{T^{1.490}}{6360} + 1.127 \omega^{0.07969} \quad (9)$$

In order to obtain the process air outlet condition, Eqs. (8) and (9) should be numerically solved to get the corresponding values of temperature and humidity ratio. The model computes the values of $F1$ and $F2$ for a given set of design conditions of both the process and regeneration streams, then uses an iterative process to guess and then converge to the values of the outlet conditions.

3. Validation and Model Comparison

To validate the models, the model results were compared with the experimental data of a commercial desiccant wheel produced by the Japanese manufacturer Seibu Giken Co. Ltd. (Kodama et al., 1993) available in the literature. The supporting layer of the wheel in consideration is made of ceramic porous fiber paper, impregnated with silica gel. The constant thermophysical properties and geometrical parameters of the wheel are listed in Table 1.

Table 1 – Thermophysical and geometrical parameters assumed for the simulation

Angle of regeneration	90°
Desiccant material	Silica gel type A
Porosity	0.4
Volume ratio of desiccant in the layer	0.7
Supporting material	Ceramic fiber sheets
Channel pitch (w x h)	3.2 x 1.8 mm
Wheel diameter	320 mm
Wheel length	200 mm
Rotation speed	6 rph

The structure contains between 70 % and 80 % type A silica gel. The regeneration zone occupies a quarter of the frontal area of the wheel, while the remaining area is dedicated to process air dehumidification. There is 20 mm of brass between the two zone with no air flow. However, the presence of these two separators was not considered in the detailed model. All three experimental series were obtained at the optimum wheel speed, equal to 6 rph.

Table 2 reports the experimental data used in the comparison for the inlet process air conditions. For the inlet regeneration conditions, the same humidity ratio of the process air and a constant regeneration temperature of 140°C is assumed.

Table 2 – Experimental inlet conditions for the process air (Kodama et al., 1993)

	Series 1	Series 2	Series 3
Temperature	24.4 °C	23.7 °C	23.3 °C
Humidity ratio	14.2 g/kg	8.9 g/kg	7.3 g/kg

The $F1$ and $F2$ potentials of the simplified model were calculated by taking as reference the outlet conditions for process and regeneration air from another series of data of the same experiments taken under similar conditions (Kodama et al., 1993). Then, these potentials were used to evaluate the output conditions for the three series considered here. The two models were compared under dynamic conditions with varying inlet air temperature and humidity. The other model inputs (regeneration temperature, rotation speed, air flow rate) were kept constant, as were the characteristics of the desiccant wheel. In order to provide a representative input for a real application, inlet temperature and humidity ratio are generated from a monitoring data set obtained from a weather station installed at the Free University of Bozen-Bolzano. The sampling time is 1 minute.

4. Results and Discussion

Fig. 3 and Fig. 4 show the outlet process air humidity ratio and temperature as a function of the angular position. These figures provide a graphical comparison of the experimental and simulated outlet conditions as function of the angle. The data depicted in these figures refer to Series 1 (in blue) Series 2 (in red) and Series 3 (in green). The experimental angular values are plotted with markers, the dashed line is the angular distributions obtained from the detailed model, while the dotted lines refer to the outputs of the simplified model. It has to be mentioned that the plotted angular distributions of the detailed model are those obtained once the transient period has ended and the outlet conditions have reached stable values.

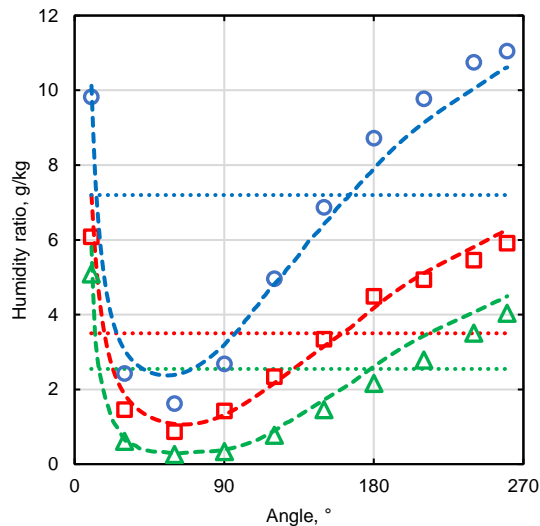


Fig. 3 – Angular distribution of the humidity ratio of processed air at the outlet

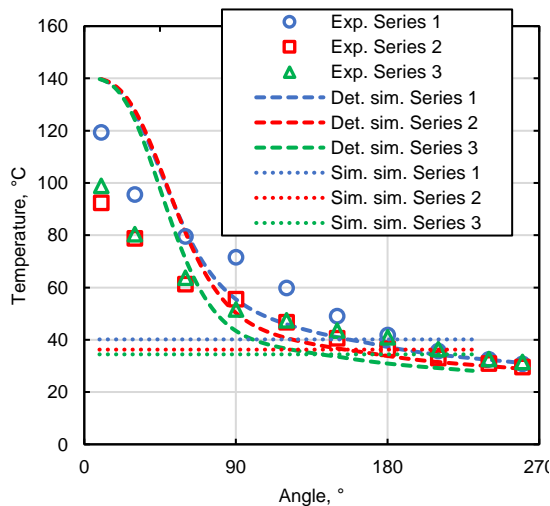


Fig. 4 – Angular distribution of the temperature of process air at the outlet

The detailed model is able to capture the physics of the problem and reproduce with fidelity the angular distribution of the outlet humidity ratio; however, the errors obtained for the single angular values of the humidity ratio may be significant (up to 47 %). The angular distribution of the outlet temperature differs more from the experimental data than does the humidity ratio. The largest differences between simulated and experimental values occur at the first angular positions where the transition between regeneration and process has just occurred. For all the experimental series, the detailed model underestimates the average temperature and humidity ratio of the outlet process air (calculated as the average of

the angular values). The difference in the process air average outlet conditions between simulated and the experimental values is always below 12 % (largest error for Series 1) for the humidity ratio and 10 % for the temperature (largest error for Series 2).

Regarding the simplified model, as shown in Fig. 3 and Fig. 4, this cannot provide the angular distribution of temperature and humidity ratio, but only a constant value corresponding to the average outlet conditions of the process air leaving the desiccant wheel. Comparing the values provided by the simplified model against the experimental data for Series 1 and Series 3, we have an overestimation of the output humidity ratio, with an error of 5 % and 21 %, respectively, while for Series 2, the model overestimates the dehumidification capacity of the wheel (difference in the outlet humidity ratio equal to 4 %). The temperature in the outlet process air is always underestimated by the simplified model with an error ranging between 31 % and 36 %.

The two models were compared under dynamic conditions with varying inlet air temperature and humidity. The other model inputs (regeneration temperature, rotation speed, air flow rate) were kept constant, as were the characteristics of the desiccant wheel. The humidity ratio profile obtained from the two models of the are shown in Fig. 5.

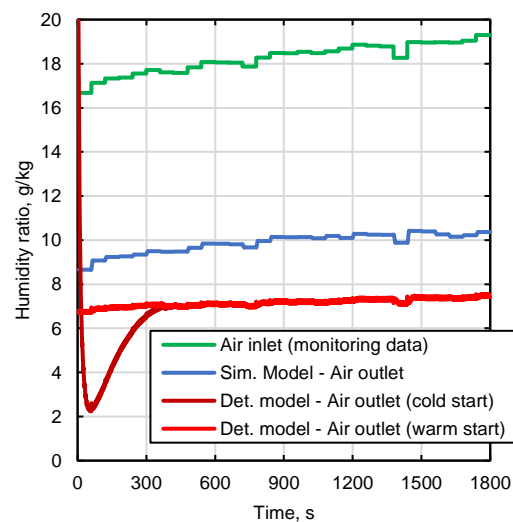


Fig. 5 – Inlet and outlet humidity ratio under dynamic conditions

Although involving a significant difference in terms of absolute values, simplified and detailed model (warm start) return similar trends for outlet air conditions. This is true when the initial wheel state in the detailed model is derived from an earlier operation state (warm start). On the other hand, if a cold start is considered (the initial state of the wheel is assumed to be in equilibrium with the environment), the detailed model reproduces typical transient trends and, once exhausted (after about 400 s), it leads to the reconciliation of the profiles with those obtained with the warm start.

5. Conclusion

A detailed and a simplified model of a desiccant wheel were implemented. The performance of the desiccant wheel simulated by the two models was compared against experimental data. Both models are able to provide the humidity of the air leaving the wheel with small errors. Within the limits of the conditions considered in this study, the simplified model presents larger errors in simulating the outlet temperature in comparison with the detailed model. Comparison under dynamic conditions shows that the simplified model cannot reproduce any transient regime of the desiccant wheel. This limitation may lead to errors in the prediction of output conditions, especially in the cold start case, as evidenced by the simulations conducted. However, once the steady state condition is reached, the simplified model returns results with trends similar to the detailed model with significant computational cost savings.

The main limitations of the simplified model considered in this study are related to the fact that it must be initialized with reference conditions that are bound to rotational speed of the wheel, regeneration conditions and air flow rate. This implies that the simplified model can return reliable results only when the simulated conditions are similar to the reference conditions under consideration.

Acknowledgement

This study was funded by the Free University of Bolzano-Bozen within the Ventilation and Indoor Air Quality in Offices: Monitoring and Improvement" project (CUP: I55F21002050005).

Nomenclature

Symbols

A_{ch}	Cross sectional area of the channel (m^2)
c_p	Isobaric specific heat ($J\ kg^{-1}\ K^{-1}$)
D_{eff}	Effective diffusivity ($m^2\ s^{-1}$)
D_s	Surface diffusivity ($m^2\ s^{-1}$)
f	Area ratio of flow passage in the channel
h_m	Mass convection coefficient ($kg\ m^{-2}\ s^{-1}$)
h_{th}	Heat convection coefficient ($W\ m^{-2}\ K^{-1}$)
i_{ad}	Isotheric heat of adsorption ($J\ kg^{-1}$)
P_{ch}	Perimeter of the flow passage (m)
t	Time (s)
T	Temperature (K)
u	Air velocity in the flow passage ($m\ s^{-1}$)
W	Water uptake in the desiccant ($kg_w\ kg_d^{-1}$)
x	Axial coordinate
ϵ	Porosity
η	Fraction of ads. heat convected to air
λ	Thermal conductivity ($W\ m^{-1}\ K^{-1}$)
ρ	Mass density ($kg\ m^{-3}$)
ω	Humidity ratio ($kg_v\ kg_{da}^{-1}$)

Subscripts/Superscripts

a	Air
d	Desiccant material
s	Supporting material
v	Water vapor

References

- Angrisani, G., C. Roselli, and M. Sasso. 2012. "Experimental Validation of Constant Efficiency Models for the Subsystems of an Unconventional Desiccant-Based Air Handling Unit and Investigation of Its Performance." *Applied Thermal Engineering* 33–34: 100–108. doi: <https://doi.org/10.1016/j.applthermaleng.2011.09.018>
- Daou, K., R. Wang, and Z. Xia. 2006. "Desiccant Cooling Air Conditioning: A Review." *Renewable and Sustainable Energy Reviews* 10(2): 55–77. doi: <https://doi.org/10.1016/j.rser.2004.09.010>
- De Antonellis, S., M. Intini, and C. M. Joppolo. 2015. "Desiccant Wheels Effectiveness Parameters: Correlations Based on Experimental Data." *Energy and Buildings* 103: 296–306. doi: <https://doi.org/10.1016/j.enbuild.2015.06.041>
- De Antonellis, S., C. M. Joppolo, and L. Molinaroli. 2010. "Simulation, Performance Analysis and Optimization of Desiccant Wheels." *Energy and Buildings* 42(9): 1386–93. doi: <https://doi.org/10.1016/j.enbuild.2010.03.007>
- Du, Z., and X. Lin. 2020. "Research Progress of Rotary Desiccant Wheel Optimization Technology." *IOP Conference Series: Earth and Environmental Science* 512(1): 012181. doi: <https://doi.org/10.1088/1755-1315/512/1/012181>
- Ge, T. S., Y. J. Dai, and R. Z. Wang. 2014. "Review on Solar Powered Rotary Desiccant Wheel Cooling System." *Renewable and Sustainable Energy Reviews* 39: 476–97. doi: <https://doi.org/10.1016/j.rser.2014.07.121>
- Ge, T. S., Y. Li, R. Z. Wang, and Y. J. Dai. 2008. "A Review of the Mathematical Models for Predicting Rotary Desiccant Wheel." *Renewable and Sustainable Energy Reviews* 12(6): 1485–1528. doi: <https://doi.org/10.1016/j.rser.2007.01.012>
- Howe, R. R. 1983. "Model and Performance Characteristics of a Commercially-Sized Hybrid Air Conditioning System Which Utilizes a Rotary Desiccant Dehumidifier." Madison: University of Wisconsin--Madison.
- Jurinak, J. J. 1982. "Open Cycle Desiccant Cooling—Component Models and System Simulations." PhD Thesis, Madison ProQuest Dissertations Publishing.
- Kakaç, S., R. K. Shah, R. K. Shah, and W. Aung. 1987. *Handbook of Single-Phase Convective Heat Transfer*. A Wiley-Interscience Publication. Wiley.
- Kodama, A., M. Goto, T. Hirose, and T. Kuma. 1993. "Experimental Study of Optimal Operation for a Honeycomb Adsorber Operated with Thermal Swing." *Journal of Chemical Engineering of Japan* 26(5): 530–35. doi: <https://doi.org/10.1252/jcej.26.530>
- Niu, J. L., and L. Z. Zhang. 2002. "Heat Transfer and Friction Coefficients in Corrugated Ducts Confined by Sinusoidal and Arc Curves." *International Journal of Heat and Mass Transfer* 45(3): 571–78. doi: [https://doi.org/10.1016/S0017-9310\(01\)00177-6](https://doi.org/10.1016/S0017-9310(01)00177-6)
- Panaras, G., E. Mathioulakis, V. Belessiotis, and N. Kyriakis. 2010. "Experimental Validation of a Simplified Approach for a Desiccant Wheel Model." *Energy and Buildings* 42(10): 1719–25. doi: <https://doi.org/10.1016/j.enbuild.2010.05.006>
- Pesaran, A. A., and A. F. Mills. 1987. "Moisture Transport in Silica Gel Packed Beds—Theoretical Study." *International Journal of Heat and Mass Transfer* 30(6): 1037–49. doi: [https://doi.org/10.1016/0017-9310\(87\)90034-2](https://doi.org/10.1016/0017-9310(87)90034-2)
- San, J.-Y. 1993. "Heat and Mass Transfer in a Two-Dimensional Cross-Flow Regenerator with a Solid Conduction Effect." *International Journal of Heat and Mass Transfer* 36(3): 633–43. doi: [https://doi.org/10.1016/0017-9310\(93\)80039-W](https://doi.org/10.1016/0017-9310(93)80039-W)
- Simonson, C., and R. Besant. 1997. "Heat and Moisture Transfer in Desiccant Coated Rotary Energy Exchangers: Part I. Numerical Model." *HVAC&R Research* 3(4): 325–50. doi: <https://doi.org/10.1080/10789669.1997.10391381>
- Sultan, M., I.I. El-Sharkawy, T. Miyazaki, B. Baran Saha, and S. Koyama. 2015. "An Overview of Solid Desiccant Dehumidification and Air Conditioning Systems." *Renewable and Sustainable Energy Reviews* 46: 16–29. doi: <https://doi.org/10.1016/j.rser.2015.02.038>

BIM and Mixed Reality for Visualizing Building Energy Data

Dietmar Siegele – Fraunhofer Italia, Italy – dietmar.siegele@fraunhofer.it

Paola Penna – Fraunhofer Italia, Italy – paola.penna@fraunhofer.it

Ilaria Di Blasio – Fraunhofer Italia, Italy – ilaria.diblasio@fraunhofer.it

Michael Riedl – Fraunhofer Italia, Italy – michael.riedl@fraunhofer.it

Abstract

The visualization of building energy data is an open topic, intuitive approaches are rare and new concepts are required to handle big data collected by more and more sensors or even derived from energy simulation results. The interpretation of data, either derived from a monitoring system or from building simulation analysis, can be difficult to handle. Combining geometrical data and energy data into a visualization interface could be a promising way to help designers and facility managers to better understand the use of different spaces, enabling a higher efficiency of building management. In this paper, an application for visualizing monitoring data or simulation results by means of Mixed Reality and BIM is presented. For the purpose, a doll's house concept (third-person observer) has been adopted as a container for the visualization of energy data in a geometrical context. Time-series based interactive diagrams, derived from monitoring system or simulation results, are integrated into geometrical holograms of buildings or parts of buildings (like floors) and they allow intuitive working. Moreover, multi-user scenarios applying cloud anchors are supported. The geometrical models are retrieved by applying Building Information Modelling (BIM).

1. Introduction

One of the main challenges in modern Building Energy Management Systems (BEMS) is related to the visualization of measurement data (Ramelan et al., 2021). Internet of Things (IoT) initiatives produce a large amount of collected data that have become difficult to handle because of the difficulties related to the interpretation of the data and moreover to their visualization before interpretation can take place. In addition, the visualization of simulation results can be difficult to interpret if not

connected directly to a geometrical context. Thus, in the area of BEMS, combining geometrical data and measurement or simulation data into one interface is a main research topic. Integrating real time collection of occupancy data, such as location and behavior, into a BIM model could help facility management (FM) to better understand the use of different spaces, enabling a higher efficiency of building management. Mixed Reality (MR) can be even more useful because it allows virtual information to be displayed in real world, making data interpretation easier. In recent literature, several works deal with new approaches for visualizing monitoring or simulation data in a more intuitive ways, mainly using BIM as a container for information (Gerrish et al., 2017; Marzouk et al., 2014; Truong et al., 2017) as well as using augmented reality (AR) and scanning a QR-code for displaying on-site sensor data (Mylonas et al., 2019). This paper proposes a new approach for visualizing energy or indoor comfort data in a geometrical context, imported from BIM, by combining a doll's house concept (third-person observer) with a real-world concept that was initially proposed in (Siegele et al., 2021). This concept does not only allow a very intuitive exploration of data, but it paves the way for a multi-user interface approach, where several users, at the same place or distributed, can explore data together on-site or off-site. Moreover, in the case of a monitoring infrastructure, by using QR-code scanning, it is possible to check the data of specific sensors on-site directly.

Mixed Reality (MR) has already been applied in different areas of building construction. Most of the time the classical approach for visualization is used: information is overlaid on real world geometry, like by (Riexinger et al., 2018) or

(Schweigkofler et al., 2018). The benefits of using MR and Augmented Reality (AR) have been proved to be efficient for supporting the most critical working phase on the building site. Indeed, this has been tested by several Horizon projects, such as BIM4EEB (BIM4EEB, 2022) and BIMplement (BIMplement Project H2020, 2022). Another interesting application of AR is for supporting the design phase, by visualizing the simulation results in a more intuitive way. (Fukuda et al., 2019) developed a new AR-based methodology for intuitively visualizing indoor thermal environment benefits leads by different renovation design alternatives, based on computational fluid dynamics simulation results. (Carneiro et al., 2019) presented an approach for guiding occupant behavior by visualizing the effects of their preferences on light distribution and energy consumption in an office space by means of virtual reality (VR).

The use of MR and AR for visualizing time-series based data in order to overcome the difficulties of handling a large amount of data derived from the IoT infrastructure has been slightly investigated. Such a concept was presented by (Jang et al., 2019), who used a time-series graph like on a screen. However, this does not allow interaction with the data. Moreover, in a multi-user scenario this approach is non-intuitive. Another concept was proposed by (Aftab et al., 2017). They overlaid shading areas or lines on the geometry (floors, walls) to visualize real-time information about the building. Today's IoT-approaches focus on single-point measurement. Another interesting approach is presented by (Dave et al., 2018). The authors developed a platform that integrates the built environment data with IoT sensors and BIM, which provides information about energy usage, occupancy and user comfort. In this context, multi-point measurement (like thermal imaging) is rarely used and only these kinds of measurements benefit from such an approach. This is likely also the reason why (Aftab et al., 2017) only presented a concept without results of a real use case. It is also very difficult from a technical point of view to reach the necessary accuracy of indoor positioning to achieve this with AR devices (Minnecci et al., 2019; Siegele et al., 2020). Other approaches, related to the different possibilities of visualizing energy efficiency

concepts by means of Virtual Reality (VR), were proposed by (Häfner et al., 2014). They used interactive charts to visualize time-series-based data. However, it was only presented in VR and the representation of the building structure was rudimentary. Applications for MR-devices (like HoloLens), are rare.

An application for studying the improvement of HVAC systems in learning factories was proposed by (Czarski et al., 2020). However, no time-series data was visualized in that context. A third-person perspective on-site was presented by (Liu et al., 2020) for visualizing data of a thermal imaging camera that measures the temperature of a façade (and thus the energy efficiency). However, this concept was not based on MR, but on AR by using a tablet.

To visualize measurement data with BIM models, several approaches are available. In the literature they are mainly defined as Digital Twins, even if usually not the complete features of a Digital Twin are proposed. The process for integrating indoor comfort data collected by a monitoring system through the application of a BIM-based model was described by (Penna et al., 2019).

The present work tries to overcome the limitations of time-series data visualization by proposing a digital multi-user interface realized by means of MR for localizing measurement data in a geometrical context, realized through BIM. Moreover, this approach also allows the visualization of the results coming from energy simulation software (i.e., IDA ICE, TRNSYS; EnergyPlus etc.). The approach shows a concept of exploring and analyzing monitoring and simulation data in an intuitive way and, at the same time, of giving the possibility to several users to visualize the data off-site and on-site.

This research is structured as follows: first, we present the adopted method by describing the software used, the proposed software architecture and the implemented features. Second, in the Results section, we describe how the application is working and what can be done with it. Consequently, in the Discussion section, we discuss the impact of our proposed software architecture. Moreover, we discuss how the software architecture can be extended and we propose how industrial standards (IFC, OpenXR) must move to provide such inter-

faces in a more general way applicable to a broader audience.

2. Materials And Methods

The application, which we developed for visualizing sensors and simulation data into a geometrical context, is based on the implementation of a proxy, which represents a data hub. An open API using REST is implemented, with which the gap between data and Mixed Reality is closed. The software architecture of our application is shown in Fig. 1.

As shown in Fig. 1, either the data derived from sensors or from energy simulation analysis are stored and saved in a time-series database. Regarding the monitoring infrastructure, we use LoRaWAN technology, because it allows the use of battery-driven sensors and it has a high coverage. In the same way, building energy simulation data can be evaluated by means of any simulation platform (i.e., Energyplus, TRNSYS, IDA ICE etc.) and results are stored in a time-series database. We used the time-series database *InfluxDB* (InfluxDB, 2022). In general, all kind of time-series databases, if they provide an API, can be used after implementing it into the proxy. We use the REST interface provided by *InfluxDB* to query the data from the database.

We use Unity (Unity Real-Time Development Platform, 2022) to develop the Mixed Reality (MR) application that is based on the Microsoft Mixed Reality Toolkit (MRTK 2.7) (MRTK-Unity Developer Documentation, 2022) and is designed by means of the OpenXR architecture (OpenXR Overview, 2022). Thus, it can also be used on other XR-compatible devices.

We get the models for different environments from BIM models by using the FBX file format, which is a proprietary file format owned by Autodesk. FBX is not a standard format when using BIM. We did not use the industrial file standard IFC, which is usually used for data exchange when working with BIM, because it has some significant disadvantages when used in a non-BIM environment like Unity. A main issue is that textures are not stored in the file, but also information on how e.g., two walls are connected, is not explicitly stored in the file. This

makes it very difficult to use the IFC file format to exchange visual information. Moreover, also the FBX format allows us to store metadata with the model.

This aspect has high relevance for visualizing monitoring data, as in the BIM model, where the unique identifiers (ID) of the sensors are stored as metadata. With this ID, a link between the model and the database is created. In this way, it is easy to assign sensor data in Unity to the corresponding geometry. The ID consists of abbreviations that include the city, the street, the street number, the building part/lot, the floor, the room, and an incremental sensor number.

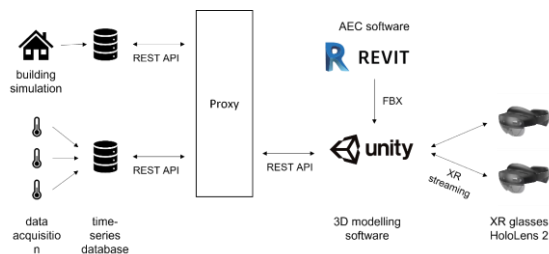


Fig. 1 – Software architecture

To catch specific data from a sensor in an on-site environment, QR-codes are used. *OpenCV for Unity* asset (OpenCv for Unity, 2022) is used to realize this feature. The QR-codes are generated from the ID introduced above.

For visualizing the time-series data in Unity we use *Asset Graph and Chart* (Graph and Chart, 2022). It enables us to visualize real-time data by adding data streams in a programmatic way.

The application itself can run stand-online on a XR-device, like the Microsoft HoloLens 2. However, for better graphics (shading) and better performance, we apply XR streaming. Multiple devices can be operated at the same time, while using the concept of persisting virtual content in the real-world. We share the actual position and orientation of the doll's house model by applying *Azure Spatial Anchors*. The position is stored in a *CosmosDB* database. On the XR device, a localization process is carried out, where the MRTK supports a coarse localization by using Wi-Fi and BLE signatures. The localization itself is realized by matching landmarks.

In the XR application several features are implemented:

Doll's house view of BIM-imported model with display of real-time data and time-series-based interactive diagram, derived from monitoring system or simulation results, as part of the hologram. In the model, values like temperature, humidity or CO₂ concentration are shown as numbers. Occupancy can be displayed with avatars.

Scanning of QR-codes in an on-site environment for reading data of a specific sensor (real-time and time-series-based diagram) and localization of the sensor in the doll's house-view of the model.

Multi-user sessions for the doll's house view for interactive sessions with several persons.

3. Results

The application is run on a Microsoft HoloLens 2 and the result of the developed XR application is shown in Fig. 2. This is the doll's house mode, where a flat within a building is visible. In each room, indoor air quality (IAQ) sensors are installed, whose real-time values can be visualized as tooltips based on the MRTK. The tooltips change their orientation and size according to the position of the viewer and allow an intuitive and clear view of the data. Occupancy can be visualized with avatars in the corresponding rooms. Not only IAQ data can be visualized, but any kind of data measured in the selected rooms or simulated by means of energy simulation software. At the moment, our concept concentrates all data measured from different sensors in one room to a single tooltip. A set of buttons allows control of the model, and the doll's houses are freely scalable and rotatable through the vertical axis. In the future, also a concept of zones will be added to visualize bigger models without dedicated rooms, i.e., shopping centers.



Fig. 2 – View of doll's house with real-time values

In Fig. 3 we show a screenshot of the XR application with a time-series-based diagram. It can be interactively controlled by using finger gestures. Sliding backwards and forwards in time is enabled by this feature. In the future, these diagrams will be enhanced by adding i.e., shading colors to visualize comfort or safety areas. E.g., the CO₂ output can be assisted by using traffic light colors to quickly identify critical rooms or zones and time ranges. co



Fig. 3 – View of doll's house with time-series-based diagrams

The user can also change the building, as shown in Fig. 4, where we visualize the floor of an office building.

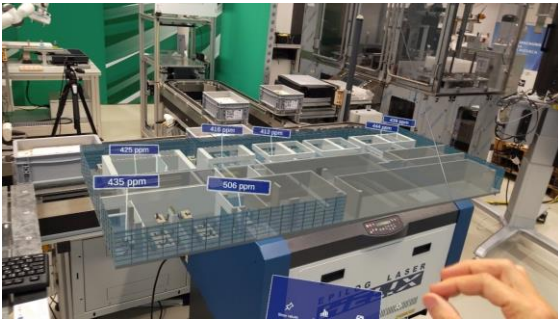


Fig. 4 – View of doll's house of a different building

When on-site, the feature of Fig. 5 can be used by a facility manager. Scanning a QR-code assigned with the ID of the sensors allows an additional hologram with the time-series based interactive diagram to appear. In addition, in the geometrical model the position of the sensor is highlighted as a tooltip, which is not visible in the figure presented. On-site orientation for the user is significantly improved by this feature. To allow free movement on-site, the hologram shown in Fig. 3 can also be detached and follows the user automatically. Moreover, an arrow always shows the position of the doll's house, if it is not in the field of view of the user.

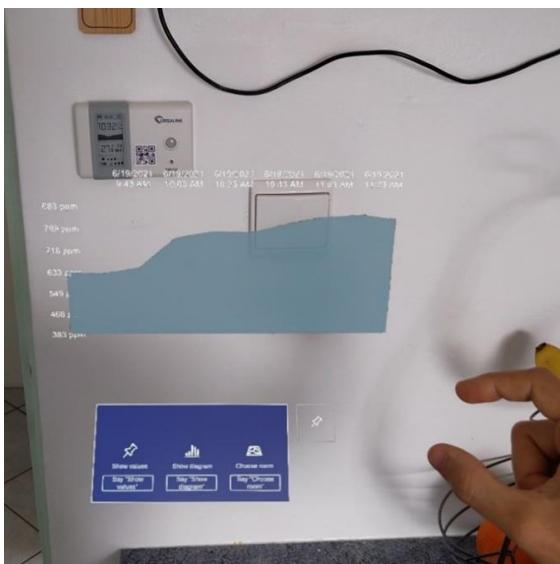


Fig. 5 – Time-series-based diagram assigned to a sensor

4. Discussion

Displaying time-based data in MR devices provides a very intuitive option of showing data in an interactive way. In the multi-user mode people can

use the application, e.g., in a workshop to discuss aspects on data collected.

By this paper we want to present the principal concept of displaying time-series-based data in MR devices. There is a need to implement several additional features before it can be tested in a real-world scenario, like in the facility management. The diagram to display data must be improved. For now, it is not possible to choose different timestep sizes or to scale the diagram on the time axis. Here, we need also to develop new ways to apply e.g., hand gestures or speech recognition for activating these advanced features. For now, it is also not possible to load a BIM model dynamically into the application. This must be done manually in Unity. It is also necessary to manually export the BIM model into the FBX file format. This aspect can be particularly problematic: developing complex interfaces, which would be necessary for these tasks, is very difficult in MR. There is, so far, no common guideline available, as to how such a task – which, using a PC and a mouse, may take a matter of minutes – can be carried out on an MR device.

Additional features for a real application should include comments and drawings. In the future, a real-time coupling with the BIM model should also be achieved. However, implementing these features requires XR streaming and a server-based software architecture.

5. Conclusion

In this paper, we presented a concept of an XR application for visualizing data in building energy management systems. Using time-series-based interactive diagrams integrated into a geometrical hologram of a zone can help to improve the usability of such applications. Using time-series-based databases allows fast querying of data, and thus provides a seamless integration into the overall experience.

In the further development, we want to get rid of the QR-codes on the sensors by implementing a BIM-based navigation algorithm for pre-positioning in combination with cloud anchors (based on landscapes) for an accurate positioning

within a room (the same approach we use for robotic applications (Follini et al., 2020). This will allow even better immersion and usability. In addition to the time-series based diagrams, we will add additional diagram types. We want to add additional features for visualization, like better visibility of sensors with sprites and surface shading for multi-point data or simulation data. In the long term, we want to achieve a close-to-real-time import of the BIM model, where we target a server-based solution as an application on its own (automatic conversion from Revit-files or IFC to FBX or similar).

Acknowledgement

The research leading to these results has received funding from the European Regional Development Fund (Fondo Europeo di Sviluppo Regionale FESR Alto Adige 2014-2020) under the Grant Agreement n. FESR1141 CUP B54E20002030001.

References

- Aftab, M., S. Chi-Kin Chau, and M. Khonji. 2017. "Enabling Self-Aware Smart Buildings by Augmented Reality." In *Proceedings of ACM International Conference on Future Energy Systems (e-Energy)* 2018.
- BIM4EEB. "BIM4EEB: BIM Based Toolkit for Efficient rEnovation in Buildings." Accessed January 2022. <https://www.bim4eeb-project.eu/>
- BIMplement Project H2020. "Towards a Learning Building Sector by Setting up a Large-Scale and Flexible Qualification Methodology Integrating Technical, Cross-Craft and BIM Related Skills and Competence." Accessed January 2022. <https://www.bimplement-project.eu/>
- Carneiro, J.P., A. Aryal, and B. Bacerik-Gerber. 2019. "Influencing Occupant's Choices by Using Spatiotemporal Information Visualization in Immersive Virtual Environments." *Building and Environment* 150: 330-338. doi: <https://doi.org/10.1016/j.buildenv.2019.01.024>
- Czarski, M., Y. T. Ng, M. Vogt, M. Juraschek, B. Thiede, P.S. Tan, S. Thiede, and C. Herrmann. 2020. "A Mixed Reality Application for Studying the Improvement of HVAC Systems in Learning Factories." *Building and Environment* 150: 330-338. doi: <https://doi.org/10.1016/j.promfg.2020.04.039>
- Dave, B., A. Buda, A. Nurminen, and K. Främling. 2018. "A Framework for Integrating BIM and IoT through Open Standards." *Automation in Construction* 95: 35-45. doi: <https://doi.org/10.1016/j.autcon.2018.07.022>
- Follini, C., V. Magnago, K. Freitag, M. Terzer, C. Marcher, M. Riedl, A. Giusti, and D. T. Matt. 2020. "BIM-Integrated Collaborative Robotics for Application in Building Construction and Maintenance." *Robotics* 10: 2. doi: <https://doi.org/10.3390/robotics10010002>
- Fukuda, T., K. Yokoi, N. Yabuki, and A. Motamedi. 2019. "An Indoor Thermal Environment Design System for Renovation Using Augmented Reality." *Journal of Computational Design and Engineering* 6: 179-188. doi: <https://doi.org/10.1016/j.jcde.2018.05.007>
- Gerrish, T., K. Ruikar, M. Cook, M. Johnson, M. Phillip and C. Lowry. 2017. "BIM Application to Building Energy Performance Visualisation and Management: Challenges and Potential." *Energy and Buildings* 144: 218-228. doi: <https://doi.org/10.1016/j.enbuild.2017.03.032>
- Graph And Chart. Unity Asset Store. Accessed January 2022. <https://assetstore.unity.com/packages/tools/gui/graph-and-chart-78488>
- Häfner, P., J. Seeßle, J. Dücker, M. Zienthek, and F. Szeliga. 2014. "Interactive Visualization of Energy Efficiency Concepts Using Virtual Reality." In *Proceedings of Conference and Exhibition of the European Association of Virtual and Augmented Reality* 2014. doi: <http://dx.doi.org/10.2312/eurovr.20141346>
- InfluxDB. "InfluxDB: Open-Source Time Series Database ". InfluxData. Accessed January 2022. <https://www.influxdata.com/>
- Jang, H., M. Choi, S. Lee, J. Lee, and S. Park. 2019. "Building Energy Management System Based on Mixed Reality for Intuitive Interface." In *Proceedings of the 2019 2nd International Conference on Electronics Technology ICET 2019*, 483-486.

- Liu, F., T. Jonsson, and S. Seipel. 2020. "Evaluation of Augmented Reality-Based Building Diagnostics Using Third Person Perspective." *ISPRS International Journal of Geo-Information* 9: 53. doi: <https://doi.org/10.3390/ijgi9010053>
- Marzouk, M., and A. Abdelaty. 2014. "Monitoring Thermal Comfort in Subways Using Building Information Modeling." *Energy and Buildings* 84: 252–257. doi: <https://doi.org/10.1016/j.enbuild.2014.08.006>
- Minnecci, G., A. Schweigkofler, C. Marcher, G. Pasetti Monizza, T. Tillo, and D. Matt. 2019. "Computer Vision Approach for Indoor Location Recognition Within an Augmented Reality Mobile Application." In *Proceedings of the Lecture Notes in Computer Science (including subseries Lecture Notes in Artificial Intelligence and Lecture Notes in Bioinformatics)* 11792: 45–53.
- MRTK-Unity Developer Documentation. Mixed Reality Toolkit. Accessed January 2022. <https://docs.microsoft.com/en-us/windows/mixed-reality/mrtk-unity/?view=mrtkunity-2021-05>
- Mylonas, G., C. Triantafyllis, and D. Amaxilatis. 2019. "An Augmented Reality Prototype for Supporting IoT-Based Educational Activities for Energy-Efficient School Buildings." *Electronic Notes Theoretical Computer Science* 343: 89–101. doi: <https://doi.org/10.1016/j.entcs.2019.04.012>
- OpenXR Overview. The Khronos Group. Accessed January 2022. <https://www.khronos.org/openxr/>
- OpenCV for Unity. Unity Asset Store. Accessed January 2022. <https://assetstore.unity.com/packages/tools/integration/opencv-for-unity-21088>
- Penna, P., G. L. Regis, A. Schweigkofler, C. Marcher, and D. Matt. 2019. "From Sensors to BIM: Monitoring Comfort Conditions of Social Housing with the KlimaKit Model." In *Proceedings of the Lecture Notes in Computer Science (including subseries Lecture Notes in Artificial Intelligence and Lecture Notes in Bioinformatics)*, 11792: 108–115.
- Ramelan, A., F. Adriyanto, C. Hermanu, M. H. Ibrahim, J. S. Saputro, and O. Setiawan. 2021. "IoT Based Building Energy Monitoring and Controlling System Using LoRa Modulation and MQTT Protocol". *IOP Conference Series: Materials Science and Engineering* 1096: 012069. doi: <https://doi.org/10.1088/1757-899x/1096/1/012069>
- Riexinger, G., A. Kluth, M. Olbrich, J.-D. Braun, and T. Bauernhansl. 2018. "Mixed Reality for On-Site Self-Instruction and Self-Inspection with Building Information Models." In *Proceedings of the Procedia CIRP*, 72: 1124–1129.
- Schweigkofler, A., G. Pasetti Monizza, E. Domi, A. Popescu, J. Ratajczak, C. Marcher, M. Riedl, and D. Matt. 2018. "Development of a Digital Platform Based on the Integration of Augmented Reality and BIM for the Management of Information in Construction Processes." In *IFIP Advances in Information and Communication Technology*, 540: 46–55.
- Siegele, D., U. Di Staso, M. Piovano, C. Marcher, and D. T. Matt. 2020. "State of the Art of Non-Vision-Based Localization Technologies for AR in Facility Management." *Lecture Notes in Computer Science* 12242: 255–272. doi: https://doi.org/10.1007/978-3-030-58465-8_20
- Siegele, D., P. Penna, and M. Riedl. 2021. "Visualizing Building Energy Measurement Data in Mixed Reality Applying B.I.M." *Lecture Notes in Computer Science* 12980: 255–272. doi: https://doi.org/10.1007/978-3-030-87595-4_18
- Truong, H., A. Francisco, A. Khosrowpour, J. E. Taylor, and N. Mohammadi. 2017. "Method for Visualizing Energy Use in Building Information Models." *Energy Procedia* 142: 2541–2546. doi: <https://doi.org/10.1016/j.egypro.2017.12.089>

Impact of Solar Radiation Modelling on the Simulated Building Energy Performance in the Climate of Bolzano, Italy

Giovanni Pernigotto – Free University of Bozen-Bolzano, Italy – giovanni.pernigotto@unibz.it

Alessandro Prada – University of Trento, Italy – alessandro.prada@unibz.it

Aleksandr Gevorgian – Free University of Bozen-Bolzano, Italy – aleksandr.gevorgian@natec.unibz.it

Andrea Gasparella – Free University of Bozen-Bolzano, Italy – andrea.gasparella@unibz.it

Abstract

We can mainly identify two groups of models in the literature to calculate solar irradiance incident on building envelope surfaces: *horizontal diffuse irradiance models*, to distinguish beam and diffuse horizontal components and *irradiance models for tilted surfaces*, to determine the irradiance incident on inclined surfaces. Due to the fact that solar irradiance data are different depending on location, climatic condition and topographic factors, there is no uniform solar irradiance model that can provide the same level of accuracy worldwide. Furthermore, this is even more critical in mountain areas, characterized by terrain complexity and the presence of specific local climatic conditions affecting solar radiation distribution.

In this research, the performance of 22 horizontal diffuse irradiance models and 12 irradiance models for tilted surfaces was assessed to check their suitability for application in mountain regions. The analysis was carried out in the Italian Alps, specifically, in the city of Bolzano, using as a reference the global solar irradiance data collected for both horizontal and vertical surfaces. Moreover, the energy needs for space heating and cooling of 48 simplified building configurations were simulated to quantify the impact of solar irradiance models on the simulated building energy performance.

1. Introduction

Nowadays, architects and engineers increasingly rely on building energy simulation tools to design more and more energy-efficient buildings. In this context, precise modeling of solar irradiance on building components is crucial, especially when simulating the thermal behavior of buildings. Various mathematical and empirical models have been

developed and proposed in the literature in the last few decades, for both the subdivision of global horizontal solar irradiance into beam and diffuse components (horizontal diffuse irradiance models) and for estimating solar irradiance on tilted surfaces (irradiance models for tilted surfaces). Examples include isotropic models, as cited by (Duffie & Beckman, 1991), and anisotropic models (Gueymard, 1987; Klucher, 1979; Muneer & Kinghorn, 1997; Perez et al., 1990; Robledo & Soler, 1998). Comparisons and modifications to these models and their application to specific regions have also been undertaken (Behr, 1997; Remund et al., 2003).

Despite the availability of many models, these were primarily derived from flat regions, and their results are to some extent location-dependent. Indeed, accuracy issues might be found when these irradiance models are used in a mountain region, where orographic complexity may cause a wide variety of inclines, introduce shades and reflections influencing meteorological parameters and contributing to the formation of local climate conditions. In this case, the success in providing adequate solar irradiance information would depend on the model's accuracy and reliability of input parameters. As a consequence, these models should be validated in each location by comparing experimental data with the predicted ones (Loutzenhiser et al., 2007). Validation is indeed essential for quantifying output uncertainty, whose propagation in building performance simulation models can also depend on the building's characteristics (Prada et al., 2015).

In this research, the accuracy of solar irradiance models on simulated building energy performance was investigated for a mountain climate, i.e., Bolzano, Italy. Specifically, 22 horizontal diffuse irradi-

ance models were coupled with 12 irradiance models for tilted surfaces, obtaining 264 combinations. The different profiles of calculated solar irradiance incident on the building envelope surfaces were used as input in TRNSYS 18 for the simulation of the energy performances of a dataset of 48 simplified residential buildings. This set was defined by changing insulation level and thermal inertia of opaque components, window surface and orientation, and kind of glazing system, focusing on their solar heat gain coefficient (*SHGC*). Finally, minimum and maximum monthly and annual deviations in heating and cooling needs for the simulated dataset of 48 buildings were discussed, employing statistical analysis to correlate the differences in energy performance prediction to the building envelope features.

2. Case Study

2.1 Location and Weather Station

Bolzano is a municipality in the Italian Alpine region (46.500° N, 11.350° E), located specifically in a

basin where the Sarntal Valley, the Eisacktal Valley, and the Adige Valley meet. Almost 110,000 people live in this city on an area of about 30 km². Although the city centre is located at an altitude of 268 m, the municipality spreads from 232 m to more than 1600 m above sea level.

The weather station considered in this study is installed on the flat roof of the A2 Building at NOI TechPark in Bolzano (46.479° N, 11.331° E, about 25 m high), in the southern and industrial neighborhood of the city (Fig. 1).

As shown in Fig. 2, the weather station is equipped with 5 Delta-T SPN1 Sunshine Pyranometers able to measure both global and diffuse irradiance - one installed horizontally and four installed vertically towards the main cardinal directions. Furthermore, the weather station includes 5 LiCor Photometric Sensors (1 horizontal + 4 vertical, as for the SPN1 Sunshine Pyranometers) and an EKO ASI 16 sky camera (not used in this work). The 5 SPN1 Sunshine Pyranometers collect solar data with a 1-minute time discretization and the period considered in this analysis ranges from April 2021 to March 2022.

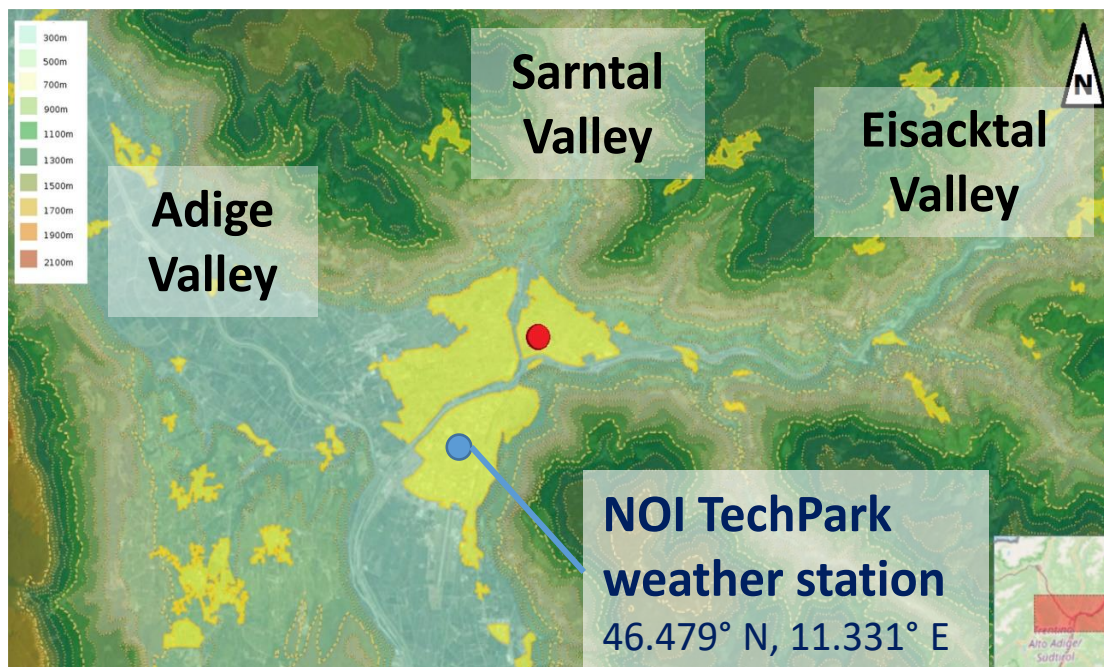


Fig. 1 – Basin of Bolzano: the different colors (light green to brown) indicate the altitude, while the yellow indicates the urban areas (map developed starting from Geobrowser Maps by the Autonomous Province of Bolzano). The red dot in the picture on the left indicates the University campus, while the blue dot highlights the position of the weather station at NOI TechPark considered in this research.

Table 1 – Solar irradiance models

ID	Horizontal diffuse irradiance models	ID	Irradiance models for tilted surfaces
1	Erbs et al. (1982)	A	Liu & Jordan (1960)
2	Orgill & Hollands (1977)	B	Burgler (1977)
3	Reindl et al. (1990a) – Model 1	C	Temps & Coulson (1977)
4	Reindl et al. (1990a) – Model 2	D	Klucher (1978)
5	Reindl et al. (1990a) – Model 3	E	Hay & Davies (1980)
6	Lam & Li (1996)	F	Ma & Iqbal (1983)
7	Boland et al. (2008)	G	Skartveit & Olseth (1986)
8	Hawladar (1984)	H	Gueymard (1986)
9	De Miguel et al. (2001)	I	Reindl et al. (1990b)
10	Karatasou et al. (2003)	J	Perez et al. (1990)
11	Chandrasekaran & Kumar (1994)	K	Muneer (2006) – Model 1
12	Oliveira et al. (2002)	L	Muneer (2006) – Model 2
13	Soares et al. (2004)		
14	Muneer et al. (1984)		
15	Spencer (1982)		
16	Chendo & Maduekwe (1994) – Model 1		
17	Chendo & Maduekwe (1994) – Model 2		
18	Skartveit & Olseth (1987)		
19	Maxwell (1987)		
20	Perez et al. (1992) – Model 1		
21	Perez et al. (1992) – Model 2		
22	Perez et al. (1992) – Model 3		



Fig. 2 – Weather station installed at NOI TechPark in Bolzano

3. Simulation

3.1 Solar Irradiance Models

As a follow-up to previous research on this topic (Pernigotto et al., 2015, 2016 and 2022; Prada et al.,

2014a and 2014b), we focused on the same set of 22 horizontal diffuse irradiance models and 12 irradiance models for tilted surfaces previously analyzed (Table 1). The two groups of irradiance models were combined, for a total of 264 alternatives.

3.2 Dataset of 48 Building Configurations

48 simplified buildings were used for the assessment of the impact of the solar irradiance models on the simulated energy needs for space heating and space cooling. All 48 configurations are characterized by the same geometry and have a single thermal zone, with a square floor area of 100 m², an internal height of 3 m, and the façades oriented towards the main cardinal directions. In each building, all windows are positioned on the same façade. Both sides of the vertical walls and the internal side of the roof have a solar absorptance of 0.3, while the external side of the roof and the internal side of the floor have 0.6.

All opaque components are made of a two-layer structure with insulating polystyrene on the external side and an internal massive layer, whose thermal resistance is about $0.8 \text{ m}^2 \text{ K W}^{-1}$. The polystyrene has a thermal conductivity of $0.04 \text{ W m}^{-1} \text{ K}^{-1}$, a density of 40 kg m^{-3} , and a specific heat capacity of $1470 \text{ J kg}^{-1} \text{ K}^{-1}$. The massive layer can be either timber (thickness: 0.10 m ; thermal conductivity: $0.13 \text{ W m}^{-1} \text{ K}^{-1}$; density: 399 kg m^{-3} ; specific heat capacity: $1880 \text{ J kg}^{-1} \text{ K}^{-1}$) or concrete (thickness: 0.30 m ; thermal conductivity: $0.37 \text{ W m}^{-1} \text{ K}^{-1}$; density: 1190 kg m^{-3} ; specific heat capacity: $840 \text{ J kg}^{-1} \text{ K}^{-1}$). The window systems are composed of double-pane glazing with a U -value of $1.1 \text{ W m}^{-2} \text{ K}^{-1}$ and a timber frame (20 % of the window area) with a U -value of $1.2 \text{ W m}^{-2} \text{ K}^{-1}$.

Internal gains and ventilation rate are kept constant, with values representative of residential buildings (UNI, 2014) and equal, respectively, to 4 W m^{-2} , half radiative and half convective, and to 0.3 air changes per hour (ACH). An ideal system maintains the internal air temperature between 20°C and 26°C , i.e., the heating and the cooling setpoints. Conventional limits of heating and cooling seasons for the climate of Bolzano were neglected, assuming ideal space heating and cooling available all year.

A summary of the variables considered in the set of 48 buildings is reported in Table 2. Further details about this dataset of buildings can be found in (Pernigotto et al., 2021).

Table 2 – Variables describing the buildings in the dataset

Insulation thickness and U -value	Materials and thermal inertia c	Window size and WWR ratio	Window SHGC	Window orientation
5 cm ($U = 0.45 \text{ W m}^{-2} \text{ K}^{-1}$)	Timber ($c = 75 \text{ kJ m}^{-2} \text{ K}^{-1}$)	14.5 m^2 (WWR = 48.5 %)	0.35	East
15 cm ($U = 0.21 \text{ W m}^{-2} \text{ K}^{-1}$)	Concrete ($c = 300 \text{ kJ m}^{-2} \text{ K}^{-1}$)	29.1 m^2 (WWR = 97.1 %)	0.61	South
				West

3.3 Methodology

As a first step, focus was placed on the data collected by the SNP1 Sunshine Pyranometers of NOI TechPark weather station, performing a quality check to identify missing entries and outliers (e.g., values exceeding the solar constant and positive values before dawn and after dusk). Post-processed solar data, still with 1-minute time discretization, were further manipulated to obtain hourly profiles of solar irradiation, expressed in watt-hours per square meter in agreement with the typical convention adopted in weather data for building performance simulation (e.g., the EnergyPlus .epw weather files). Minor missing entries (i.e., one or few hours of missing solar irradiation data) were fixed by either linear or cyclic interpolation, depending on the length of the missing data series. Missing data entries longer than a day, on the other hand, were not fixed and simply discarded from the analysis.

In the second step, the capabilities of the 264 pairs of solar irradiance models were assessed using the measured solar data as a reference. Specifically, for each one of the 264 combinations of horizontal diffuse irradiance models and irradiance models for tilted surfaces, the hourly profiles of global solar horizontal irradiation of the selected period (April 2021 - March 2022) were used as inputs to determine the global and the diffuse solar irradiation on four vertical surfaces oriented towards the main cardinal directions. These estimated hourly profiles of global and diffuse solar irradiation were then compared to the measured ones, calculating for each orientation the Mean Absolute Error (MAE) in order to identify the best and the worst-performing pairs of models. As regards the last step, the energy performances of the 48 reference building configurations were simulated in TRNSYS 18, using the best and the worst-performing pairs of solar irradiance models as inputs.

4. Result Analysis and Discussion

4.1 Step 1 – Quality Check on the Dataset of Solar Irradiation Measurements

Thanks to the quality check performed, it was found that, for the analyzed period (April 2021 – March 2022), the missing and wrong 1-minute entries had only minor impacts on the annual series, without continuous gaps longer than 1 hour. This ensured a robust basis for the comparisons performed in the next steps.

4.2 Step 2 – Comparison Between Simulated and Measured Solar Irradiation Values

4.2.1 Accuracy in the prediction of vertical diffuse solar irradiance

Table 3 shows the best and the worst-performing pairs of irradiance models, determined for each orientation according to the Mean Absolute Error (MAE) for the diffuse vertical irradiance values. It can be noticed that each orientation has a given pair of models optimizing the prediction of the diffuse vertical irradiance. Specifically, the pairs A10 (Liu & Jordan + Karatasou models) for the south orientation, A15 (Liu & Jordan + Spencer models) for the east one, H6 (Gueymard + Lam & Li models) for the north one, and B8 (Burgler + Hawlader models). The largest MAEs are found for east and west orientations, as expected, considering the geography of the location (Fig. 1). As regards the worst-performing pairs of models, for south and east orientations, the largest errors are found with the pair F20 (Ma & Iqbal + Perez Model 1) while D20 (Klucher + Perez Model 1) is the worst-performing pair for north and west orientations. MAE values are lower than about 15 Wh m⁻² in case of the best-performing pairs and even larger than 70 Wh m⁻² for the worst-performing ones.

Analyzing the horizontal diffuse irradiance models, which are most frequently found among the best-performing ones, we can list the Soares model for the south orientation, the Perez Model 1 for the east and the west orientations, and the Muneer model for the north. Some of these models, optimal for a

given orientation, are the worst-performing ones for another. For instance, the Perez model 1 is the worst-performing for south and north orientations, the Soares model is the worst-performing model for the east one, and the Spencer model gives the worst estimates of vertical diffuse irradiance for the west orientation.

4.2.2 Accuracy in the prediction of vertical global solar irradiance

Table 4 shows the same analysis as in Section 4.2.1 considering MAEs calculated for the global solar irradiation on the vertical surfaces. As regards the best-performing models, G16 (Skartveit & Olseth + Chendo & Manduekwe Model 1), B20 (Burgler + Perez Model 1), H14 (Gueymard + Muneer) and B20 (Burgler + Perez Model 1) were identified, respectively, for south, east, north and west orientations. The pairs of worst-performing solar irradiance models were, instead, C20 (Temps & Coulson + Perez Model 1) for the south-oriented surface, F13 (Ma & Iqbal + Soares) for the east-oriented one, D20 (Klucher + Perez Model 1) for the north one, and F15 (Ma & Iqbal + Spencer) for the west one. As can be noted, when global solar irradiance is considered, the best- and worst-performing models are different to those found for the diffuse solar irradiance. Looking at the MAEs, larger values are generally observed compared to the previous analysis on the diffuse solar irradiance. Focusing on the best-performing models in global irradiance analysis, it can be seen that slightly larger MAEs are found for south and north-oriented vertical surfaces (i.e., respectively 24.8 versus 12.7 Wh m⁻² and 9.8 versus 7.9 Wh m⁻²). On the contrary, very large errors are observed for east and west orientations, with MAEs larger than 120 and 150 Wh m⁻². The same trends can be identified analyzing the results of the worst-performing models, with MAEs similar to those observed in the diffuse irradiance analysis for south and north orientations (i.e., 61.9 versus 75 Wh m⁻² and 57.5 versus 61.6 Wh m⁻²) and much larger for the east and west ones (i.e., 184.1 versus 71.8 Wh m⁻² and 207.9 versus 58.6 Wh m⁻²). On the whole, it can be concluded that a good level of accuracy can be obtained in the estimation of the incident global irradiance for south and north-oriented vertical walls,

while larger errors are more frequently found for east and west orientations due to the presence of close natural obstacles.

As regards irradiance models for tilted surfaces, the Liu & Jordan model (south orientation), the Burgler Model (east and west orientations), and the Perez model (north orientation) can be seen as the most frequently found among the best-performing ones. Regardless of orientation, the worst-performing model most frequently encountered is the Ma & Iqbal model.

4.2.3 Comparison with another weather station

Table 5 reports the main findings of a former analysis (Pernigotto et al., 2022) focusing on another Bolzano weather station installed on top of one of the buildings of the university campus in the city center (46.498° N, 11.349° E) and performed over a

three-year period (2018, 2019 and 2021). By comparing the MAEs reported in Table 4 with those in Table 5, it can be commented that larger errors are generally encountered in the prediction of solar irradiance in the location of the city center weather station. This is true for all vertical orientations except the eastern one. Indeed, studying the natural obstacles in the two locations, it can be seen that they are taller for the NOI TechPark weather station as far as the east orientation is concerned, while for the university weather station in the city center, they are more relevant for the west one. Again, each orientation has specific best and worst-performing pairs of solar irradiance models, which are typically different from those identified for the NOI TechPark weather station, except for the best-performing models for the west orientation and the worst-performing one for the north one.

Table 3 – Best and worst-performing pairs of solar irradiance models: diffuse irradiance

Best-performing pairs of irradiance models MAEs (Wh m ⁻²)				Worst-performing pairs of irradiance models MAEs (Wh m ⁻²)			
South	East	North	West	South	East	North	West
A10	A15	H6	B8	F20	F20	D20	D20
Liu & Jordan + Karatassou	Liu & Jordan + Spencer	Gueymard + Lam & Li	Burgler + Hawladar	Ma & Iqbal + Perez Model 1	Ma & Iqbal + Perez Model 1	Klucher + Perez Model 1	Klucher + Perez Model 1
12.7	15.1	7.9	14.8	75.0	71.8	66.1	58.6

Table 4 – Best and worst-performing pairs of solar irradiance models: global irradiance

Best-performing pairs of irradiance models MAEs (Wh m ⁻²)				Worst-performing pairs of irradiance models MAEs (Wh m ⁻²)			
South	East	North	West	South	East	North	West
G16	B20	H14	B20	C20	F13	D20	F15
Skartveit & Olseth + Chendo & Manduekwe Model 1	Burgler + Perez Model 1	Gueymard + Muneer	Burgler + Perez Model 1	Temps & Coulson + Perez Model 1	Ma & Iqbal + Soares	Klucher + Perez Model 1	Ma & Iqbal + Spencer
24.8	121.7	9.8	150.2	61.9	184.1	57.5	207.9

Table 5 – Best and worst-performing pairs of solar irradiance models: global irradiance. Comparison with the analysis performed in Pernigotto et al. (2022) with respect to the UNIBZ weather station (46.498° N, 11.349° E) for the years 2018, 2019 and 2021

Best-performing pairs of irradiance models				Worst-performing pairs of irradiance models			
MAEs (Wh m ⁻²)				MAEs (Wh m ⁻²)			
South	East	North	West	South	East	North	West
H18	C20	J18	B20	I15	F15	D20	F18
Gueymard + Skartveit & Olseth	Temps & Coulson + Perez Model 1	Perez et al. + Skartveit & Olseth	Burgler + Perez Model 1	Reindl et al. + Spencer	Ma & Iqbal + Spencer	Klucher + Perez Model 1	Ma & Iqbal + Skartveit & Olseth
43.8	79.3	26.1	165.3	67.4	130.6	79.9	384.1

4.3 Step 3 – Analysis of Building Energy Performance

Table 6 reports the minimum and the maximum deviations found by simulating the energy performances for the considered dataset of buildings with the different pairs of solar irradiance models. Specifically, considering the results described in Section 4.2, the following 7 pairs of models were selected for this analysis:

1. Burgler + Perez Model 1 (B20)
2. Temps & Coulson + Perez Model 1 (C20)
3. Klucher + Perez Model 1 (D20)
4. Ma & Iqbal + Soares (F13)
5. Ma & Iqbal + Spencer (F15)
6. Skartveit & Olseth + Chendo & Manduekwe Model 1 (G16)
7. Gueymard + Muneer (H14)

The largest heating need deviations are within 5 kWh m⁻² m⁻¹ and are registered in the coldest months of the year (i.e., January, December), as expected. As regards the whole simulated period, the largest heating need deviations range from 1.4 to 17.7 kWh m⁻² a⁻¹. Higher sensitivity to the choice of solar irradiance models is often found in those configurations with poorly insulated massive walls (i.e., concrete structures with 5 centimeters of insulation), and large south-oriented windows with high *SHGC*.

The cooling needs are characterized by monthly deviations within or around 4 kWh m⁻² m⁻¹, usually occurring during the summer (i.e., June). Considering the whole simulated period, cooling needs deviations range from 3 to 23 kWh m⁻² a⁻¹. This time, the largest deviation occurs for building configuration with well-insulated lightweight walls (i.e., timber walls with 15 centimeters of insulation), and large west-oriented windows with high *SHGC*.

Table 6 – Minimum and maximum monthly deviations of heating and cooling needs for the simulated dataset of 48 buildings

Time	Heating need deviations [kWh m ⁻²]		Cooling need deviations [kWh m ⁻²]	
	min	max	Min	max
Jan 2022	0.3	4.8	0.0	3.8
Feb 2022	0.3	3.2	0.0	3.5
Mar 2022	0.0	1.8	0.0	3.3
Apr 2021	0.0	0.7	0.0	2.0
May 2021	0.0	0.1	0.0	3.4
Jun 2021	0.0	0.0	1.1	4.2
Jul 2021	0.0	0.0	0.9	3.9
Aug 2021	0.0	0.0	0.7	3.0
Sep 2021	0.0	0.0	0.3	2.3
Oct 2021	0.0	1.3	0.0	4.1
Nov 2021	0.2	3.5	0.0	2.3
Dec 2021	0.3	4.9	0.0	1.5
Period	1.4	17.7	3.1	22.9

Fig. 3 depicts the cumulative distribution functions of the annual energy needs for space heating and cooling simulated for the 48 buildings. As can be seen, a larger variability of the findings is recorded

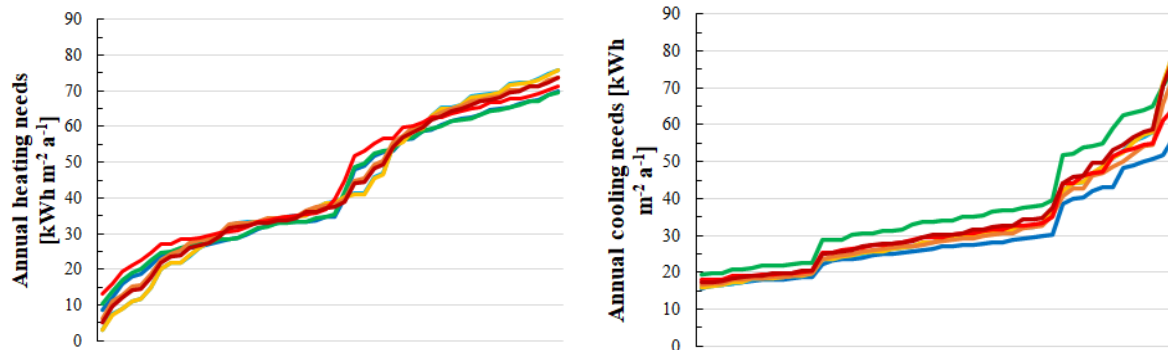


Fig. 3 - Cumulative distribution functions of the annual heating and cooling energy needs simulated for the 48 buildings with the following solar irradiance models: **B20** (Burgler + Perez Model 1), **C20** (Temps & Coulson + Perez Model 1), **D20** (Klucher + Perez Model 1), **F13** (Ma & Iqbal + Soares), **F15** (Ma & Iqbal + Spencer), **G16** (Skartveit & Olseth + Chendo & Manduekwe Model 1), and **H14** (Gueymard + Muneer)

5. Conclusion

This research assessed the capabilities of 22 horizontal diffuse irradiance models and 12 irradiance models for tilted surfaces for the calculation of the solar irradiance incident on the building envelope in mountain environments, which are characterized by complex irradiation patterns depending on the orography and the multiple terrain reflections. Solar irradiance calculated by all combinations of horizontal diffuse irradiance models and irradiance models for tilted surfaces were compared with diffuse and global irradiance measured in the Alpine location of Bolzano, Italy, during the period between April 2021 – March 2022 on four vertical surfaces oriented towards the main cardinal directions. Through the analysis of hourly Mean Absolute Errors, the best and the worst-performing pairs of models were first identified for each orientation and then used in TRNSYS simulations determine the energy needs for space heating and cooling for a dataset of 48 simplified buildings.

We found that:

- The performances of the pairs of solar irradiance models can be very different, depending on the orientation considered. In particular, the east and west orientations were found to be the most critical ones for the case study considered. Furthermore, varying accuracy can be expected for diffe-

rent locations in the same mountain valley or basin.

- None of the models in the literature was found able to ensure the same level of accuracy for all the four vertical cardinal orientations.
- The impact of the selection of solar irradiance models on the simulated energy performance is affected by the building's features.

Taking into consideration the main findings listed above, further developments of this research will involve testing potential modifications of the studied solar irradiance models to increase their capabilities when applied in mountain environments, in particular in the considered case study location of Bolzano, Italy.

Acknowledgement

This research was funded by the internal project of the Free University of Bozen-Bolzano “SOMNE - Bolzano Solar Irradiance Monitoring Network” (CUP: I56C18000930005; CRC Call 2018).

References

- Behr, H. D. 1997. "Solar radiation on tilted south oriented surfaces: Validation of transfer-models." *Solar Energy* 61(6): 399-413. doi: [https://doi.org/10.1016/S0038-092X\(97\)00081-9](https://doi.org/10.1016/S0038-092X(97)00081-9)
- Duffie, A. J., and W. A. Beckman. 1991. *Solar Engineering of Thermal Processes* (4th ed.). Wiley, Hoboken.
- Gueymard, C. 1987. "An Anisotropic Solar Irradiance Model for Tilted Surfaces and Its Comparison with Selected Engineering Algorithms." *Solar Energy* 38(5): 367-386. doi: [https://doi.org/10.1016/0038-092X\(87\)90009-0](https://doi.org/10.1016/0038-092X(87)90009-0)
- Klucher, T. M. 1979. "Evaluation of models to predict insolation on tilted surfaces." *Solar Energy* 23(2): 111-114. doi: [https://doi.org/10.1016/0038-092X\(79\)90110-5](https://doi.org/10.1016/0038-092X(79)90110-5)
- Loutzenhiser, P. G., H. Manz, C. Felsmann, P. A. Strachan, T. Frank, and G. M. Maxwell. 2007. "Empirical validation of models to compute solar irradiance on inclined surfaces for building energy simulation." *Solar Energy* 81(2): 254-267. doi: <https://doi.org/10.1016/j.solener.2006.03.009>
- Muneer, T., and D. Kinghorn. 1997. "Luminous efficacy of solar irradiance: Improved models." *International Journal of Lighting Research and Technology* 29(4): 185-191. doi: <https://doi.org/10.1177/14771535970290040401>
- Perez, R., P. Ineichen, R. Seals, J. Michalsky, and R. Stewart. 1990. "Modeling Daylight Availability And Irradiance Components From Direct And Global Irradiance." *Solar Energy* 44(5): 271-289. doi: [https://doi.org/10.1016/0038-092X\(90\)90055-H](https://doi.org/10.1016/0038-092X(90)90055-H)
- Pernigotto, G., A. Prada, P. Baggio, A. Gasparella, and A. Mahdavi. 2015. "Impact of solar irradiation models on simulated hourly energy performance of buildings." In *Proceedings of Building Simulation 2015*, Hyderabad, India.
- Pernigotto, G., A. Prada, P. Baggio, A. Gasparella, and A. Mahdavi. 2016. "Solar irradiance modelling and uncertainty on building hourly profiles of heating and cooling energy needs." In *Proceedings of the IV International High Performance Buildings Conference at Purdue*, West Lafayette, IN, U.S.
- Pernigotto, G., A. Gasparella, and J.L.M. Hensen. 2021. "Assessment of a weather-based climate classification with building energy simulation." In *Proceedings of Building Simulation 2021*, Bruges, Belgium.
- Pernigotto, G., A. Prada, and A. Gasparella. 2022. "Assessment Of The Accuracy Of Solar Irradiance Models In Mountain Locations: The Case Of Bolzano, Italy." In *Proceedings of the VII International High Performance Buildings Conference at Purdue*, West Lafayette, IN, U.S.
- Prada, A., G. Pernigotto, A. Gasparella, and A. Mahdavi. 2014a. "Combined effects of diffuse fraction and tilted surface radiation models." In *Proceedings of ECPPM 2014 - 10th European Conference on Product & Process Modelling*, Vienna, Austria.
- Prada, A., G. Pernigotto, P. Baggio, A. Gasparella, and A. Mahdavi. 2014b. "Effect of Solar Radiation Model on the Predicted Energy Performance of Buildings." In *Proceedings of the III International High Performance Buildings Conference at Purdue*, West Lafayette, IN, U.S.
- Prada, A., G. Pernigotto, F. Cappelletti, and A. Gasparella. 2015. "Impact of solar irradiation models on building refurbishment measures from multi-objective optimization." In *Proceedings of Building Simulation 2015*, Hyderabad, India.
- Robledo, L., and A. Soler. 1998. "Modeling Irradiance on Inclined Planes with an Anisotropic Model." *Energy* 23(3): 193-201. doi: [https://doi.org/10.1016/S0360-5442\(97\)00083-2](https://doi.org/10.1016/S0360-5442(97)00083-2)
- Remund, J., W. Lucien, and J. Page. 2003. "Chain of algorithms to calculate advanced radiation parameters." In *Proceedings of ISES Solar World Congress*, Goteborg, Sweden.
- UNI (Ente Nazionale Italiano di Normazione). 2014. *UNI/TS 11300-1:2014 - Energy performance of buildings Part 1: Evaluation of energy need for space heating and cooling*, Milan, Italy: UNI.

Effect of the Time Interval Base on the Calculation of the Renewable Quota of Building in an Alpine Context

Margherita Povolato – University of Trento, Italy – margherita.povolato@unitn.it

Alessandro Prada – University of Trento, Italy – alessandro.prada@unitn.it

Paolo Baggio – University of Trento, Italy – paolo.baggio@unitn.it

Abstract

The European goal of decarbonization drives design toward high-performance buildings that maximize the use of renewable sources. Hence, the European RED II Directive (EU, 2018) and the Italian decree (DL 8/11/2021) raise the minimum renewable share in new buildings and major renovations. In this framework, an air-source heat pump (ASHP) combined with an on-site photovoltaic system (PV) is one of the most popular solutions. However, the effectiveness of this heating system in mountainous contexts is not taken for granted, since the harsh climate induces both an increase in heating requirements and a deterioration of heat pump performance. For these reasons, energy simulation is a useful tool for understanding energy behavior and evaluate strategies to ensure the best energy savings. Currently, the renewable quota verification involves a quasi-steady state calculation on a monthly basis. However, this implies the use of the national grid as a battery through the net metering mechanism. The actual share of renewable coverage in the absence of expensive electric storage will necessarily be lower. This work analyzes the actual renewable share achievable in a new building in a mountainous area. Five representative locations in the province of Trento were initially identified through a cluster analysis. The renewable share was evaluated through a coupled dynamic simulation of the building and the energy systems. The results show how the calculated renewable share in this building changes according to the time interval used to close the balance with the grid. The evaluation of the renewable quota (QR) was carried out not only closing the balance by the hour or sub-hour but also by the month.

1. Introduction

Despite the recent increase in efficiency investment, the International Energy Agency (IEA, 2021) states that buildings' lifecycles are responsible, directly and indirectly, for about 37 % of global energy and process-related CO₂ emissions. According to the European Directive 2018/2001 (EU, 2018) and to Legislative Decree n.199/2021 (DL 8/11/2021), heat pump and renewable equipment deployment seems to be one of the most effective and the most economical solutions for reducing buildings' carbon footprint.

In the absence of electric batteries, a certain level of the renewable share is assured by the direct use of the PV production for heat pump operation. Nevertheless, the mismatch between the solar availability (during the day) and the building energy demand (mostly during the evening) is one of the main challenges to reach a high renewable share. Different solutions have been studied in the literature to increase the renewable quota of the system, such as energy storage and control strategies to match the building load to the solar availability (Fisher et al., 2017; Luthander et al., 2015). In (Pinamonti et al., 2020) the authors showed how the use of simple rule-based controls can lead to the reduction of up to 17 % of the energy withdrawn from the grid. Similarly, in (Franzoi et al., 2021a), the benefit of renewable energy communities in self-consumption of PV production emerges. What is not yet clear is whether the mandatory limits on renewable quotas are achievable without these measures. Moreover, the regulation currently provides for the calculation based on balance closure on a monthly basis, thus ensuring within the month the possibility of balancing between the

energy delivered in the central hours of the day and that withdrawn during the night, in a net metering scheme. Another research question therefore involves how much the real self-consumption of renewable energy of buildings that comply with the regulatory constraint in the absence of net metering and expensive electric batteries is.

This work therefore focuses on the analysis of a new residential building equipped with a low temperature heating system, thermal storage and a heat pump coupled with a PV system.

The single-family building (MF) analyzed represents a typical Italian building (Capozza et al., 2014), whose thermal properties meet mandatory constraints for new construction or major renovations.

2. Methodology

This paper studies the energy behavior of the MF building, to estimate the renewable quota. The goal is to verify whether the minimum share (DL 8/11/2021) of total primary energy covered by renewable primary energy is also achievable in a mountain context. The building and the HVAC systems are modeled in (TRNSYS v.17), as shown in the figure below.

2.1 Climate Conditions

The paper specifically analyzes the Alpine climate context of northern Italy. Five municipalities were selected by (Ceccolini et al., 2020), as a result of a clustering of the climate data of the municipalities of Trentino, in northern Italy (Fig. 2). Trento is located in the Italian climatic zone E, with heating

degree days from 2101 Kd to 3000 Kd; while the other municipalities are in zone F, with heating degree days over 3001 Kd (DPR 412/93).

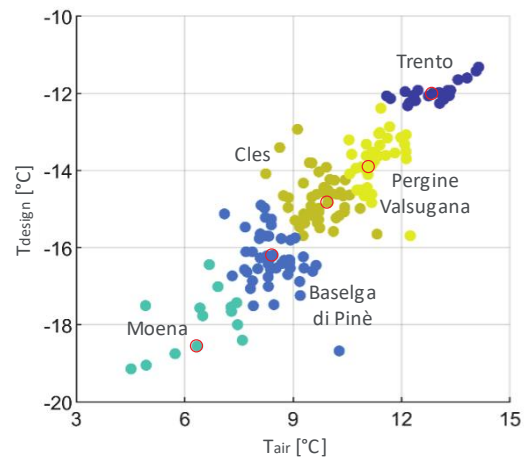


Fig. 2 – Identification of the 5 clusters of Trentino municipalities from the analysis of the average annual temperature and of the design temperature

Climate data are those of UNI 10349-1:2016 standard (UNI, 2016a), but for locations not included in the list, the solar irradiation of the nearest main city is assumed. Pergine Valsugana and Baselga di Pinè are related to Trento, whereas Cles and Moena are nearest to Bolzano.

Table 1 – Climatic data for the 5 municipalities of Trentino

Cluster	Municipalities	Lat	Alt	T _{design}	T _{air}
1	Trento	46.04	194	-12	12.9
2	Pergine V.	46.04	482	-14	11.4
3	Cles	46.22	658	-15	10.1
4	Baselga di Pinè	46.08	964	-16	8.8
5	Moena	46.23	1184	-18	6.4

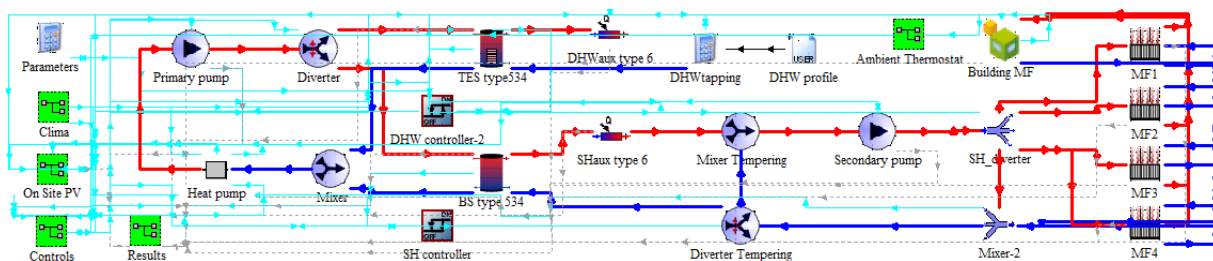


Fig. 1 – Layout of the developed TRNSYS model

2.2 Case Study Building

The MF building is composed of 2 floors, each with an area of around 88 m². The thermal characteristics are close to the limits of transmittance required by the current local legislation (DPP 13/07/2009). To reach a high-performance level, the building has 15 cm of extruded polystyrene (EPS) insulation on the external walls, 12 cm on the roof and well-insulated windows. The 4 thermal zones, 44 m² each, are identified by splitting the building along the west to the east axis in order to have uniform solar gains in the zone.

Table 2 presents the geometrical characteristics and the thermal properties of the building.

Table 2 – Geometrical characteristics and thermal properties of the single-family building

Geometrical characteristics		MF
Floors	/	2
Apartments	/	1
A _{FloorL}	m ²	104.86
A _{FloorN}	m ²	87.99
VolumeN	m ³	527.91
A _{w,N}	m ²	8.4
A _{w,S}	m ²	8.4
A _{w,E-W}	m ²	8.4
Height/ _{1 floor}	m	3
Thermal properties		MF
U _{floor}	Wm ⁻² K ⁻¹	0.366
U _{wall}	Wm ⁻² K ⁻¹	0.183
U _{roof}	Wm ⁻² K ⁻¹	0.225
U _{window}	Wm ⁻² K ⁻¹	0.8

2.3 HVAC System

The HVAC system (Fig. 3) consists of an inverter-driven heat pump (HP), a buffer storage tank (BS) for space heating (SH), and one for thermal energy storage (TES) for domestic hot water (DHW) preparation. The heat pump has a rated capacity of 7.18 kW for source temperature 7 °C and sink 35 °C. The emission terminals for SH are radiant panels fed with an inlet temperature of the hot water of 35 °C in the design conditions. The supply temperature to the radiant panels, as well as the BS and the HP setpoint temperatures, are controlled by an outdoor reset control. The setpoint temperature of the TES is 50 °C. The temperatures of the BS and TES determine the activation of the heat pump and are controlled by a proportional control.

The building is also provided with a photovoltaic system, inclined 20° on the south pitch of the roof. There are 7 modules connected in series, resulting in a peak power of 2.94 kW and an overall area of 12 m² (i.e., roughly 12.5 % of the roof surface).

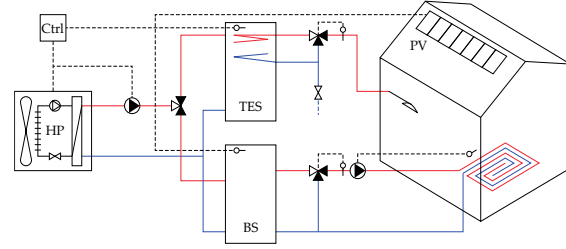


Fig. 3 – Heating system

2.4 Control Strategy

The single-family building is analyzed with and without self-consumption (SC) maximization strategies.

In the first scenario (*bas*), there is no advanced control strategy. A basic control is used, whereby the thermal storages are fully charged when a temperature set-point change occurs.

In the second scenario (*enh*), a rule-based control strategy (RBC) is adopted to maximize the SC of PV generation. The BS and TES set-points are raised, in case of PV energy surplus. This strategy, for inverter-driven air-to-water heat pump, was proposed by (Pinamonti et al., 2020).

2.5 Renewable Primary Energy Quota

Although the dynamic energy simulation uses a time step of 1 minute, the calculation of the renewable energy quota is performed closing the balance on a monthly basis (Eq. 1), according to the Italian standard (UNI 2016b). In addition, Eq. 2 and Eq. 3 show the calculation of the renewable quota closing the balance on an hourly basis, according to the current net metering scheme, and on the minute (i.e., the time step), respectively.

$$QR_{mo.} = \frac{\sum_{months} \min(\int_{mo.} Load; \int_{mo.} PV)}{\sum_{months} \int_{mo.} Load} \quad (1)$$

$$QR_{ho.} = \frac{\sum_{hours} \min(\int_{ho.} Load; \int_{ho.} PV)}{\sum_{hours} \int_{ho.} Load} \quad (2)$$

$$QR_{mi.} = \frac{\sum_{minutes} \min(\int_{mi.} Load; \int_{mi.} PV)}{\sum_{minutes} \int_{mi.} Load} \quad (3)$$

3. Results and Discussion

This section presents the results of the dynamic simulation, for both scenarios. The analysis performed allows an understanding of the extent to which the different interval affects the QR. Furthermore, the results are represented according to the different site elevations, thus showing the role of climate severity.

3.1 Annual Renewable Quota (*bas*)

The calculated quota of renewable energy over the total primary energy increases by 12 % ÷ 17 % in the 5 locations, changing the balance closure interval from a minute to a month (Fig. 4). This shows how the regulatory constraint of 60 % (monthly basis), with no storage batteries, corresponds to an actual renewable share of about 50 %.

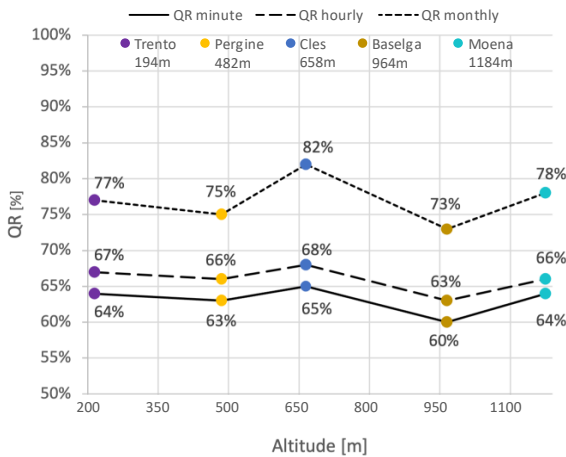


Fig. 4 – Annual values of QR minute, QR hourly and QR monthly: TRNSYS results for the MF building (*bas*)

The hourly and minute calculation has almost similar values with less marked deviations. The differences are much more evident if QRminute or QRhourly is compared with QRmonthly. Between the monthly renewable share and the minute one there is an average difference of about 13 %. The greatest difference is in Cles, Baselga and Moena, the municipalities with a harsher climate.

The renewable share calculated on a monthly basis is obviously greater than that on a minute basis, because the assumed on-site exchange allows the grid to be used as a virtual battery (within the month).

It can be noted that the percentage of QR decreases as the altitude of the municipalities increases, and, consequently, the design and the outdoor air temperature is lower. However, two anomalous behaviors are found for Cles and Moena. This is due to the higher solar radiation (UNI, 2016a).

3.2 Self-Consumption (*bas*)

Figs. 5 to 9 present the comparison between the monthly load profile (blue bars) and PV generation (orange bars) and the self-consumed energy based on a one-minute balance (yellow bars). The representation is made for each climate analyzed. In addition, the graphs show the self-consumption factor (SCF) and load coverage factor (LCF). The former is defined as the ratio of self-consumed PV energy vs the total PV energy generated. LCF, on the other hand, represents the fraction of PV energy used over the electricity absorbed by the HP and auxiliary systems. The LCF index differs from QRminute because it estimates only the renewable electricity share, neglecting both the renewable electricity taken from the grid, as well as the air source energy of the HP.

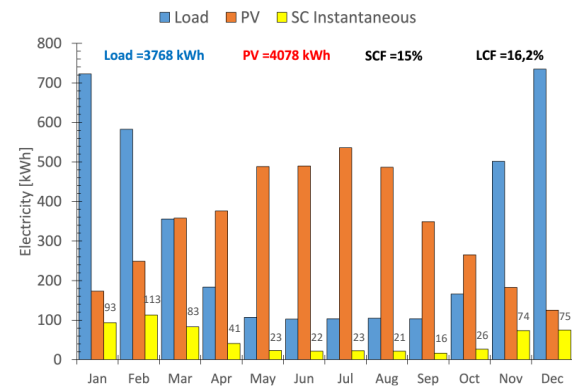
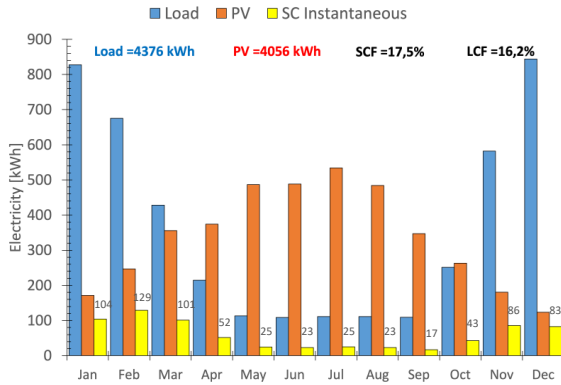
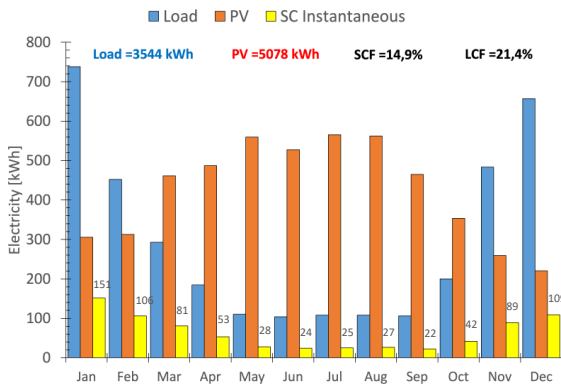
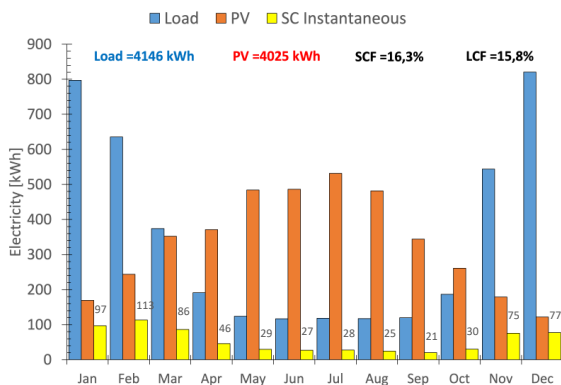
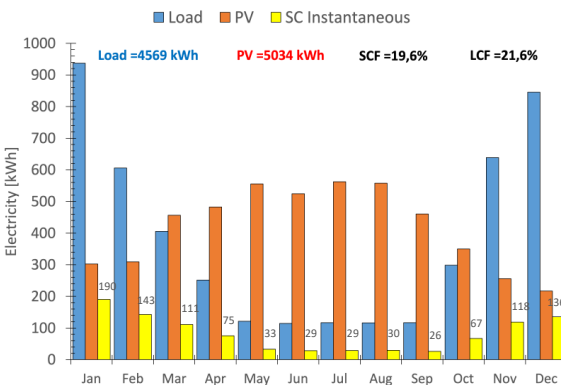


Fig. 5 – Energy profiles and SC minute based on Trento (*bas*)


 Fig. 6 – Energy profiles and SC minute based on Pergine (*bas*)

 Fig. 7 – Energy profiles and SC minute based on Cles (*bas*)

 Fig. 8 – Energy profiles and SC minute based on Baselga (*bas*)

 Fig. 9 – Energy profiles and SC minute based on Moena (*bas*)

Obviously, the load profile does not coincide with that of PV production. The largest gains from PV are during the summer period and during the day-time. This contrasts with the monthly demand profile and the daily habits of households, which consume more in the evening hours.

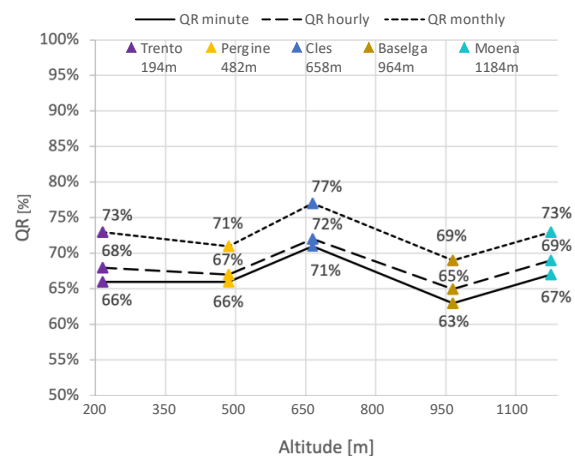
If self-consumption based on a monthly balance were shown, in summer, the yellow bar would coincide with the blue bar (self-consumption equal to load) and, in winter, with the orange one (self-consumption equal to PV generation). As already mentioned, closing the balance with an interval of a month implies balancing between the energy injected into the network in the central hours and that taken during the night in a net-metering scheme, that is, exploiting the grid as a virtual battery, albeit with the constraint of using all the stored energy within the month.

By calculating the actual SC of renewable energy, in the absence of net-metering and electric batteries, lower renewable quotas would be achieved.

As shown in the graphs, SCF ranges from a minimum of 15 % to a maximum of 20 % (17 % average), while LCF ranges from 16 % to 22 % (18 % average). The highest values are obtained in Moena. High LCF and SCF values mean that the electricity load is mostly covered by PV panels.

3.3 Annual Renewable Quota (*enh*)

To increase the SC, in the second scenario, the rule-based control strategy is applied. Comparing the results in Fig. 10 with those in Fig. 4, QRminute and QRhourly increase, while QRmonthly decreases.


 Fig. 10 – Annual values of QR minute, QR hourly and QR monthly: TRNSYS results for the MF building (*enh*)

The graph firstly highlights a lower variability (5 % ÷ 7 %) between the QR evaluated on a monthly basis compared with the minute-evaluated QR. This demonstrates the ability of the adopted control in optimizing the use of the PV generation. QRminute improves by about 3 % because the instantaneous consumption of PV energy rises, and grid withdrawal decreases by about 4 %. In contrast, the QRmonthly decreases as rule-based control results in an increased load (Figure 11). However, in the monthly balance calculation all the PV production was already self-consumed also in the *bas* scenario, since the grid acts as a battery. Therefore, the higher load of the rule-based control corresponds to a higher withdrawal from the grid and, consequently, to a QR decrement. Summing up, the difference between the instantaneous values and the monthly one is lower. In the first scenario, the gap is about 13 %, while in the second one, it is about 6 %.

3.4 Self-Consumption (*enh*)

Figure 11 shows the effects of the enhanced control strategy (*enh*) for the municipality of Trento. Compared with the *bas* scenario (Fig. 5), the profile of instantaneous self-consumption changes.

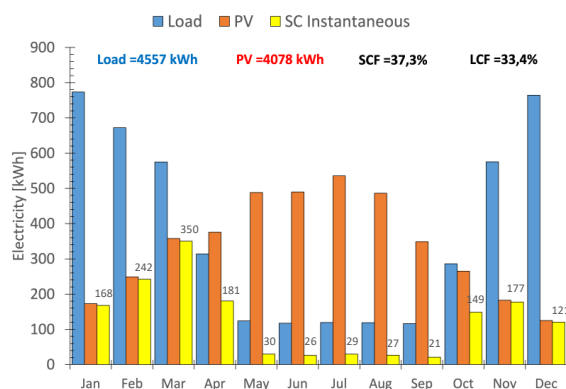


Fig. 11 – Energy profiles and SC minute based on Trento (*enh*)

The PV generation remains the same, since the system has not been upgraded, but improved. On the other hand, consumption increases slightly (from 3768 kWh to 4557 kWh) due to the control system. The demand profile rises simultaneously with the increase in self-consumption of the energy produced. With the basic control strategy, SCF and LCF are 15 % and 16,2 %; while with the rule-based control are 37.3 % and 33.4 %. This then

demonstrates the capability of the control to directly use the PV production, reducing power exchange with the grid.

3.5 Discussion

As the results show, the interval used for balance closure greatly affects QR value. This is especially true if enhanced control strategies aimed at maximizing self-consumption are not employed. However, these enhanced controls are not (currently!) rewarded by the calculation method adopted by Italian law. However, the ongoing changes on the billing scheme for electric power that will soon introduce the hourly based balance calculation will undoubtedly reward the enhanced control scheme with a reduced energy cost.

Looking at both scenarios (*bas* and *enh*), the QR limit of 60 % is easily reached even in the harsh climates analyzed.

The building is close to being a zero-energy building on an annual basis at all locations investigated, as demonstrated by the energy matching chart (Luthander et al., 2015). The solid line in Fig. 12 connects all points where SCF is equal to LCF, implying that annual PV production is equal to annual load. A point above the bisector means that the annual PV generation is greater than the annual consumption of the building.

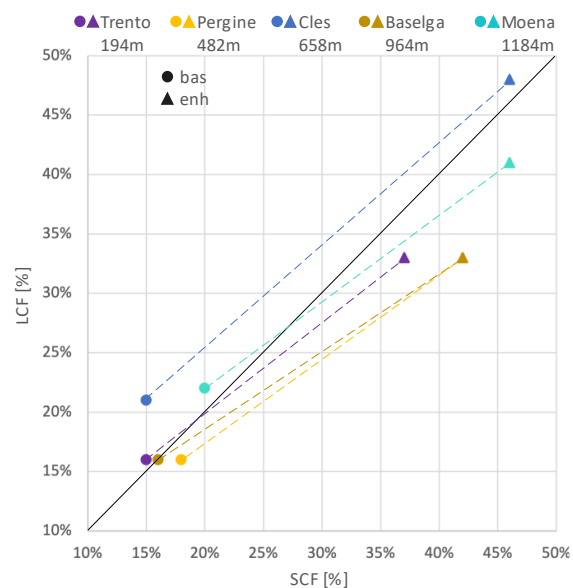


Fig. 12 – Comparison between *bas* (circle) and *enh* (triangle) through matching chart

The graph then shows how the control simultaneously increases SCF and LCF. However, there is a tendency for SCF to increase more than LCF, due to the slight increase in consumption. However, it should be emphasized how this is done by installing a cheap controller. A higher performance is achievable with (more expensive) batteries, which allow a better match of the building load to the solar availability.

4. Conclusions

The results show that 60 % renewable share is easily achieved in a new building, even in the mountainous areas analyzed.

If no control strategies aimed at maximizing self-consumption are employed, achieving a monthly QR of 60 % means an actual renewable share of about 13 % less, whereas, using an enhanced control strategy, the actual renewable share is about 6 % less than the monthly balance.

By closing the balance on a monthly basis, advanced control strategies are not rewarded. In fact, the pursuit of self-consumption often leads to an increase in energy demand, which, by closing the budget on a monthly basis, can lead to a reduction in the renewable share.

These controls, however, are beneficial in terms of reduced exchanges with the grid. In Trento, there is a 22.3 % increase in PV self-consumption and a 17.2 % increase in PV coverage of electricity consumption if the balance is closed on a minute or hourly basis. Taking all 5 municipalities into consideration, SCF rises by about 26 % and LCF by about 19 %.

Acknowledgement

This research was funded by the MIUR-Italian Ministry of Education, Universities and Research (PRIN 2017) grant number 2017KAAECT within the framework of FLEXHEAT project “The energy FLEXibility of enhanced HEAT pumps for the next generation of sustainable buildings”.

Nomenclature

Symbols

A	Surface (m ²)
A _{Floor} L	Gross surface (m ²)
A _{Floor} N	Net surface (m ²)
ASHP	Air-Source Heat Pump
BAS	Base control strategy
BS	Buffer Storage
ENH	Enhanced Control Strategy
HP	Heat Pump
LCF	Load Cover Factor
MF	Single-family
PV	Photovoltaic
QR	Quota of renewable primary energy
SC	Self-Consumption
SCF	Supply Cover Factor
T _{air}	Air-dry bulb temperature (°C)
T _{design}	Design temperature (°C)
TES	Thermal Energy Storage
U	Thermal transmittance (Wm ⁻² K ⁻¹)
V	Volume (m ³)

Subscripts/Superscripts

ho.	Hour
mi.	Minute
mo.	Month
w,E-W	East and West-oriented windows
w,N	North-oriented windows
w,S	South-oriented windows

References

- Capozza, A., F. Carrara, M. Gobbi, F. Madonna, and F. Ravasio. 2014. *Analisi tecnico-economica di interventi di riqualificazione*.
- Ceccolini, C., N. Franzoi, A. Prada, and P. Baggio. 2020. *Scenario di penetrazione delle pompe di calore per il riscaldamento e la produzione acqua calda sanitaria*.
- European Parliament (EU). 2018. *Renewable Energy Directive (RED II), Directive (EU) 2018/2001 of the European Parliament and of the Council of 11 December 2018 on the promotion of the use of energy from renewable sources*.
- Fisher, D., and H. Madani. 2017. “On heat pumps in smart grids: A review.” *Renewable and*

- Sustainable Energy Reviews* 70: 342–357. doi: <https://doi.org/10.1016/j.rser.2016.11.182>.
- Franzoi, N., A. Prada, S. Veronesi, and P. Baggio. 2021. "Enhancing PV Self-Consumption through Energy Communities in Heating-Dominated Climates." *Energies* 14: 4165. doi: <https://doi.org/10.3390/en14144165>
- Italian Government. 2021. DL 8/11/2021. *Decreto legislativo 8 novembre 2021, n. 199. Attuazione della direttiva (UE) 2018/2001 del Parlamento europeo e del Consiglio, dell'11 dicembre 2018, sulla promozione dell'uso dell'energia da fonti rinnovabili*.
- International Energy Agency (IEA). 2021. *Tracking Buildings 2021; Tracking Report*; IEA, Paris, France. Accessed March 30, 2022. <https://www.iea.org/reports/tracking-buildings-2021>
- Luthander, R., J. Widén, D. Nilsson, and J. Palm. 2015. "Photovoltaic self-consumption in buildings: A review." *Applied Energy* 142: 80–94. doi: <https://doi.org/10.1016/j.apenergy.2014.12.028>
- Pinamonti, M., A. Prada, and P. Baggio. 2020. "Rule-Based Control Strategy to Increase Photovoltaic Self-Consumption of a Modulating Heat Pump Using Water Storages and Building Mass Activation." *Energies* 13: 6282. doi: <https://doi.org/10.3390/en13236282>
- President of the Italian Republic. 1993. DPR 412/93. *Decreto del presidente della Repubblica 412/93 – Regolamento recante norme per la progettazione, l'installazione, l'esercizio e la manutenzione degli impianti termici degli edifici ai fini del contenimento dei consumi di energia*.
- Province of Trento. 2009. DPP 13 13/07/2009. *Decreto del presidente della provincia 13 luglio 2009, n. 11-13/Leg - Disposizioni regolamentari in materia di edilizia sostenibile in attuazione del titolo IV della legge provinciale 4 marzo 2008, n.1 (Pianificazione urbanistica e governo del territorio)*.
- TRNSYS Version 17. Madison, U.S.A.: Solar Energy Laboratory, University of Wisconsin-Madison. Accessed February-3, 2022. <https://www.trnsys.com>
- UNI (Ente italiano di unificazione). 2016a. UNI 10349-1 – *Riscaldamento e raffrescamento degli edifici - Dati climatici - Parte 1: Medie mensili per la valutazione della prestazione termo-energetica dell'edificio e metodi per ripartire l'irradianza solare nella frazione diretta e diffusa e per calcolare l'irradianza solare su di una superficie inclinata*.
- UNI (Ente italiano di unificazione). 2016b. UNI TS 11300-4 – *Prestazioni energetiche degli edifici - Parte 5: Calcolo dell'energia primaria e della quota di energia da fonti rinnovabili*.

Innovative Approaches for Teaching BPS: First Implementations of Business Game-Like Activities

Andrea Gasparella – Free University of Bozen-Bolzano, Italy – andrea.gasparella@unibz.it

Abstract

Experiential Learning (ExL) has long been considered a useful and necessary tool in educational courses in several different fields, including engineering. Nevertheless, traditional didactical approaches have prevailed, in particular, in Bachelor and Master Engineering programs, at least in Italy.

This implies the focus is kept more on theoretical aspects even for disciplines in which practical activities and learning by doing could provide the necessary competence for students to enter the job market promptly. Furthermore, ExL is recognized as providing a more immersive educational environment, capable of increasing participation and motivation in students.

One of the techniques introduced by the ExL consists of roleplaygames, some of which in the form of business games. This work reports about the main outcomes from an initial implementation of a business game-like approach to train perspective building envelope and energy systems designers. In particular, the game is intended to train students in the use of building simulation, showing what the potential and the peculiarities of the job can be when approaching the market. In addition, since it is commonly recognized that, while BPS is widely used in teaching and research, it is not widespread among practitioners, the game was also conceived to promote BPS use in practice.

The main features, including constraints and critical points, of the implementations within a university course in an Energy Engineering study program are described together with some suggestions for future improvements.

1. Introduction

Experiential Learning (ExL) is commonly defined as a teaching approach based on learning from experience, as opposed to a more traditional and formal education, which is mostly focused on the presentation of somehow abstract concepts by the

teacher. Indeed, the relevant difference does not refer to the abstraction, rather than to the approach, which requires the learner to assume an active role in the learning process.

Even if it is indisputable that ExL can contribute to filling the gap between theoretical knowledge and practical skills and competences that is so often observed in many higher educational programs, the focus is more on the process of creating and acquiring knowledge.

Nevertheless, the experience itself, which is often included in many study programs at least in the form of traineeships and internships, is not enough. As introduced through the foundational theories of experiential learning by Dewey, Freire, James, Lewin, and Rogers, a transformation of the experience is required.

In the Experiential Learning Theory, introduced by Kolb and Kolb (2009, 2017), two dialectically related modes of grasping experience—Concrete Experience (CE) and Abstract Conceptualization (AC)—as well as two dialectically related modes of transforming experience—Reflective Observation (RO) and Active Experimentation (AE) - are combined in a cyclic and iterative process.

In this respect, the theoretical concepts provided by the teacher in the traditional model are still required to support knowledge development, even if it emerges more and more from an interactive relation between teacher and learners, and between reflection and experience.

This also leads to some extent to a larger engagement of the learner. In addition, due to the constructivist nature of the learning process, learning outcomes are the result of a personal interpretation by the learner.

Finally, this is compatible with a more recursive interaction between theory and practice, and compatible with a process of gradual development

of knowledge, in which foundational concepts are not necessarily provided prior to the practical experimentation.

It seems there is a general consensus towards the broad effectiveness of ExL in achieving all learning outcomes, namely knowledge, skills and competences (or responsibility/autonomy, according to the definition of the European Qualification Network). In educational areas and levels, such as Bachelor and Master Engineering programs, where it is important the student be trained to not only to acquire theoretical skills but also to take a more practical attitude towards problem solving, design, decision making, etc., this appears of crucial importance.

However, in many cases, only some of the tools proposed by the ExL are implemented. As an example, Baker et al. (2012) confirm that, despite the robust use of experiential learning in fields such as agricultural education, “experiential learning” and “experiential education” have mainly been used to describe teaching approaches such as field work experiences, internships, outdoor education, adventure education, vocational education, lab work, simulations, and games (Itin, 1999).

In this framework, the implementation of ExL concepts in courses dealing with Building Physics and Building Performance Simulation is described as necessary by Beausoleil-Morrison et al. (2015), to “develop the necessary knowledge and skills to effectively apply BPS tools”, to the point that “this must be recognized in the way we teach the discipline”.

The above reasons led to the adoption of ExL practices within a course in Building Physics and Building Energy Simulation in a Master program in Energy Engineering at the Free University of Bolzano (Gasparella, 2017). Not only was BPS awareness and competence improved through the implementation of numerical solutions to the theoretical governing equations, but the learning of the theoretical foundations of BP itself was enhanced by the development of the solution approaches with the use of a spreadsheet, instead of working with already available simulation tools. This allowed combining experientially the application of the concepts with introducing the students

to the use and understanding of BPS. The students were also asked to apply BPS in small groups and develop a project to be presented and discussed at the final exam.

Although BPS is a powerful tool for designing, operating, and renovating buildings, its use in professional design practice seems to be less common than expected and to lack professionals able to work with it, independently of the efforts put into simplifying interfaces and integrating functionalities within the most common design tools (Soebarto et al., 2015).

With the additional goal of increasing the awareness and readiness of graduates to use BPS tools once entering the job market, it made sense to extend and rationalize the use of ExL techniques, turning the project work into a business game, or at least to start moving in that direction.

Business simulation games are roleplay games introduced in the 1950s to train students in business schools. As reported by Jackson (1959), they derived from the war games used in Germany in mid-19th century and later in Japan, in preparation for World War II. Business games are generally based on strategic decisions that imply some consequences for the players, providing direct feedback for their decisions and actions. In addition, detailed rules and realistic complexity are required to mirror real applicative contexts. Competition among teams is often included to engage participants and improve interactions within the groups. Specialized games can focus only on some areas of business management. Faria (1990) reported a rapid spread of the tools in the US in the thirty years from 1960 and 1990, even if a wide expansion potential was still present.

The use of business game-like tools in the field of BP and BPS, as in other engineering and technical areas is not well documented.

IBPSA, the International Building Performance Simulation Association, has introduced a Student Modeling Competition taking place within the biennial Building Simulation conference, since 2013. So far, five competitions have taken place (namely in 2013, 2015, 2017, 2019 and 2021). In the 2013 edition, the students were asked to use simulation to design an energy-positive house, limiting only the building geometry and focusing

on energy, under constraints on comfort and IAQ. In 2015, the focus was on an office building, and on designing and testing a mixed-mode ventilation strategy. In 2019, a more structured case was proposed, considering an existing historical building, with peculiar constraints limiting the possible interventions, and asking the students to undergo a 5-step approach (simulation pentathlon) from simulating the existing building to optimize the overall building performance (including multi-objective optimization). The 2021 edition focused on low-tech buildings and on the use of simulation to improve comfort, while preserving the energy efficiency.

In this work, a preliminary report is presented on the attempt to implement a business game-like task in the above-mentioned course in Building Physics and Building Energy Simulation in the Master program in Energy Engineering at the Free University of Bolzano. The existing project work was reorganized and proposed in the form of a game, with small groups competing and comparing their solutions in public presentations during the course.

The game focused on the renovation of a residential building. It was organized into four phases, asking the students to refine the project through the introduction of additional and contrasting objectives, and building on top of the results of a preliminary evaluation of the baseline configuration. The activity required the students to use a BPS tool, with only basic preliminary knowledge, while theoretical foundations related to BP and to the numerical solutions of the governing equations were provided in parallel, considering further applications of the ExL approach, as described in Gasparella (2017).

2. Methods

2.1 Experiential Learning Experiences

An ExL integrated teaching method for a course dealing with Building Physics and Building Performance Simulation within a Master program in Energy Engineering had been under development and testing for ten years at the time of writing this

paper. In approximately 90 hours, the fundamentals of building physics and modeling are presented, together with the main aspects of thermal comfort and indoor air quality. The course starts illustrating the thermodynamic balance of the indoor air volume, according to the model called “air node balance”.

The definition of the boundary conditions for solving the balance requires characterizing the unsteady thermal conduction in the envelope components, which in turn can be determined only through the surface balances, so through the analysis of convection, long and short wave radiation interactions at the external and internal surfaces for opaque and transparent envelope elements, and so on.

For each of the mentioned processes (i.e., conduction, convection, radiation), the main controlling equations are defined and their numerical or analytical solutions discussed, to end with a step-by-step implementation of a detailed model in a general productivity spreadsheet environment. As a result, at the end of the course, the students are able to develop a comprehensive simulation tool that, despite the limitations in the computational efficiency proper of a spreadsheet, can compare favorably to the most widespread tools available on the market in terms of both detail and accuracy.

In short, the student has the opportunity of applying the theoretical foundations, experiencing through simulation the behavior and relevance of each different process, and its contribution to the overall performance, observing the outcomes, conceptualizing the findings and actively interacting with the experimental environment, while understanding the inner operation of BPS tools.

The learning circle encompassing the four phases of Concrete Experience (CE), Reflective Observation (RO), Abstract conceptualization (AC), Active experimentation (AE) is therefore entirely implemented and repeated iteratively while progressing with the analysis of the different aspects.

2.2 Towards a Business Game

A business game is a roleplay game in which the player/learner has to perform tasks and obtain

results/feedback typical in professional practice, generally in the managerial field. In particular, the learner is expected to apply knowledge, skills and capabilities to evaluate alternatives and make decisions.

In the case of graduate students in Energy Engineering with a focus on Building Physics and Building Energy Systems, it is likely that in their professional activities they have to contribute to or directly perform the design of buildings, analyzing energy-related aspects, optimizing investment, and maximizing comfort conditions. They are expected to deploy the skills and competences necessary to (i) simulate performance, (ii) verify reliability of results, (iii) analyze outcomes and evaluate their sensitivity to the design parameters, (iv) optimize contrasting objectives, (v) make sensible proposals and find trade-offs, (vi) present and discuss with clients or other consultants, (vii) manage time and resources devoted to the analysis, understanding costs and benefits, in the different design phases.

To this aim, the project originally included in the exam assignments has been redesigned to serve as a sort of roleplay game.

The students had to start working on an assigned project in small teams of 3-4 persons, as if they were a design studio in charge of renovating an existing residential building and giving advice to a client. Students in a team could have different roles but also discuss ideas and methods.

A simulation tool was shortly introduced during the first weeks of the course and students got familiar with it through a guided example presented by some teaching assistants, who had been former students in the same course.

One of a couple of different buildings (Fig. 1) were randomly assigned to each of the nine teams.

Both buildings were detached houses, with two storeys for a three-person family. The envelope was typical of the '60s, therefore lacking any insulation and adopting single pane glazing. The buildings had different internal layouts, different orientations (main axis East to West or North to South), and different locations (Bolzano, Italy – cold winter and warm to hot summer, or Graz, Austria – with colder winter and slightly milder summer as in Fig. 2).

Shade cast from nearby buildings is also included in the evaluation in order to promote careful analysis of the context.

Even if non-thermal energy performances were not considered, students were encouraged to maximise daylight as a preference from the owner. While guaranteeing minimum access to daylight through the prescription of a minimum WWR was requested, increasing window size, changing their position and redefining the internal layout was allowed.

Students were asked to proceed to the following steps:

- (i) Analysis of the baseline case,
- (ii) Assessment of the energy impact of intervention measures,
- (iii) Definition of cost-effective solutions, and
- (iv) Assessment and improvement of thermal comfort and indoor air quality.

Data to perform the economic analysis (costs for the different interventions, including windows resizing and repositioning, layout redesign and shades installation) were provided after phase (ii). Input and requisites for the comfort analysis were provided after the cost-effective optimization in phase (iii).

At the end of phases (ii), (iii) and (iv), the teams were asked to give a short presentation (10-15 minutes) to the other groups (three times in total), receiving comments and answering questions. This represented a novelty compared with the original project work, which was mainly discussed at the end of the course and only with the examiner.

In two rounds after the second and third presentations, all teams were also asked to evaluate each other's work, selecting the best one for each of four categories (i) presentation; (ii) innovation; (iii) comprehensiveness; (iv) performance. From the preferences expressed in the two rounds, a ranking list was formed for each of the evaluation categories, and updated with the teacher and teaching assistants' evaluations. Four teams were commended as the best in one of the categories and one as overall winner for the game.

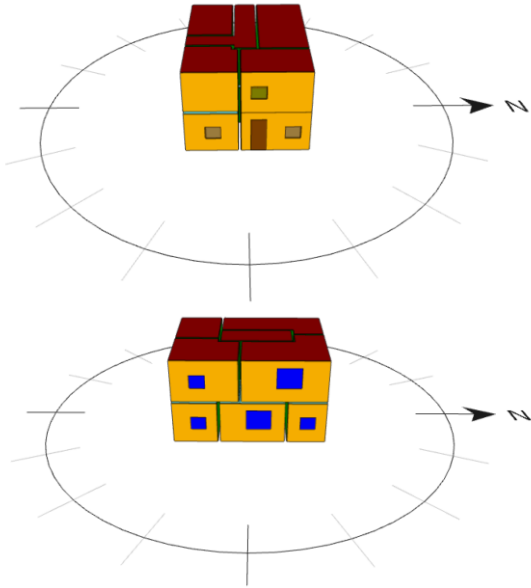


Fig. 1 – Residential buildings for the business game. The cases of Bolzano (above) and Graz (below)

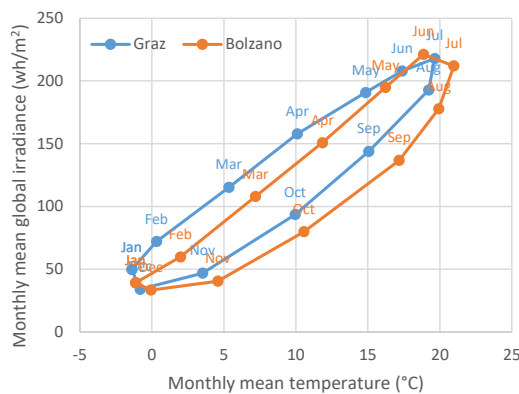


Fig. 2 – Reference climatic conditions (air temperature and global irradiance on the horizontal) in Bolzano and Graz

3. Results and Discussion

As for the outcomes of the adoption of the game, an initial evaluation concerns the students' behavior and strategies. In particular, some interesting techniques were observed among those implemented to overcome limitations in the calculation capabilities and minimize the required efforts. Most of the groups developed a customized approach to assessing the combined effect of different intervention measures and to adding optimization objectives in an efficient way. Some of noticeable strategies adopted in the different phases are reported below:

- (i) The preliminary analysis of the baseline configuration was generally conducted through a multi-zone simulation. One of the teams, however, ran free-floating simulations considering individual rooms, to point out specific critical points from peculiar temperature profiles. Some teams also included daylight evaluation, even if not explicitly requested.
- (ii) Most of the teams decided to redefine the layout and window position, to optimize both the distribution of spaces and the access to solar gains and daylight. In many cases, preliminary parametric evaluations were performed with different window sizes.
- (iii) Some teams minimized the cost of a full sensitivity analysis on each of the intervention measures, establishing a preference order. They selected the most influential interventions, adopting parametrically the most extreme levels allowed for each. They then kept the order in the optimization steps. Some others increased the level of each intervention at a time (such as the insulation thickness), stopping when the marginal improvement was reduced to below a certain percentage, and moving to the next with the same approach.
- (iv) Energy optimization followed generally from either the simple combination of the preferred levels of the different intervention measures, or a sequential approach. That foresaw the optimization of the most impacting intervention, adding on top of it the second best, and so on. In some cases, students seemed more aware of the possible non-linear interaction effects, so solutions related to the previous intervention level were explored again after adopting the new one.
- (v) Cost optimization was mostly based on the evaluation of the economic performance (simple payback period) of the energy optimized configurations. Subsequently a reduction in the investment cost and so in the payback was attempted through the decrease or removal of some of the interventions, such as of the reduction of the insulation thickness or moving back to single or double pane glazing from double or triple, respectively. Some

groups decided to cap the economic indicators.

- (vi) Comfort (thermal and IAQ) was generally only assessed verifying the compatibility of the renovated configuration(s) with the prescribed comfort category. In some cases, when overheating issues were highlighted, some control strategies dealing with increased natural ventilation or with some refined assumptions about the occupant's behavior and presence were considered. Somewhat surprisingly, some of the teams simply decided to adopt air conditioning.

Presentations deserve a special mention. Presentations proved to be a good tool not only to engage the participation and practice some soft skills, such as communication strategies, but also to self-assess the quality of the work. Reiteration led to an increased quality level: some groups were motivated to increase the number of simulations, explore different solutions, use different approaches, and in general to verify their own results, and refine the presentation strategy. Overall, presenting and discussing among peers and with the support of the teacher and assistants proved to be effective in reinforcing, together with the game itself, the effectiveness of the different steps in the learning cycle, and improving the overall outcomes of the course.

Some general pros and cons can be listed as follows. As concerns the positive aspects:

- (i) A simulation tool was learned through its direct use, with little need for training but some hours to develop a guided test case together with the students;
- (ii) A more competitive context and an early start was able to increase collaboration and team working within groups with respect to the original project work. Some level of specialization of the members of a group was observed;
- (iii) The business game promoted a more practical mind-set, more aware of real-life limitations and more sensitive to a client's perspective, forcing students to consider aspects they would not be fully aware of otherwise;

- (iv) Multi-objective optimization without the availability of optimization tools, which could have been considered detrimental, turned out to be quite beneficial. It forced the students to develop empirical approaches to assess sensitivity and refine solutions;
- (v) Public discussion and multi-step development allowed the comparison of the intermediate achievements of the groups, stimulating students to improve their approaches and recognize the limitations of the proposals.

Some negative outcomes or aspects to improve on have that have been identified are:

- (i) The game had to start even earlier than the theoretical lessons to be able to provide adequate insight into the involved phenomena. That is accepted in ExL but would require deepening the phase of abstract conceptualization and the support for the teams and students;
- (ii) Some of knowledge and skills required to develop the project are partially missing, such as those related with the economic evaluation. This could require in the future a multi-disciplinary approach in which the business game encompasses different courses;
- (iii) A significant amount of time had to be allocated during the course, in particular for autonomous work, which might lead to compression of some parts and overloading of the students;
- (iv) MOO without reliance on optimization tools led to sub-optimal solutions and possibly to inconsistencies between the findings of different groups;
- (v) The structure of the business game still needs to be refined, and some dynamics and roles/responsibilities introduced more clearly.
- (vi) The evaluation grid needs to be improved to support the conceptualization phase and generate more competition among groups.

4. Conclusion

This work reports on the implementation of a business game-like task in a university course in Building Physics and Building Energy Simulation

for a Master program in Energy Engineering at the Free University of Bolzano. The course had already been designed and organized to take advantage of some ExL techniques. In particular, BP and BES concepts and competences were already developed in a learning cycle approach, implementing and experimenting on the theoretical foundations presented in class through the development of a simulation spreadsheet including all the relevant aspects contributing to the building dynamic energy behaviour.

In this framework, a project work was designed in the form of a business game, with small groups competing and comparing the solutions proposed in a series of presentations to the class. The game focused on the renovation of a small residential building. It was organized into four phases, asking the students to refine the project by adding progressively contrasting objectives, such as energy, costs, and comfort.

The activity required the students to use a BPS tool, with only basic preliminary knowledge, while theoretical foundations related to BP and to the numerical solutions of the governing equations were still being provided in parallel, as described in Gasparella (2017).

Overall, the attempt improved the quality of the experiential learning approach proposed in the course, stimulating greater participation and promoting a deeper awareness of the main concepts, skills and competences required in the field. The business game represented a step forward regarding the usual project work, in particular because of its structured approach, the focus on a couple of reference cases only, the presentations and interactions occurring after each phase and the discussion within and among the groups.

There is still a significant amount of work to do in order to:

- (i) Provide more structured rules and roles, to make the game more realistic and engaging.
- (ii) Consolidate the features of the case studies in order to facilitate the development of some parts which would have needed more information and to simplify the verification.
- (iii) Involve professionals in the definition of the case study (to make them more realistic as

from point i) and possibly also in the discussion and evaluation of the results

- (iv) Extend the game to other universities and introduce “finals” levels involving the best groups from each university

Acknowledgements

The activities described in the paper could not have been developed without the passionate and tireless contribution of Federico Battini and Riccardo Albertin, former students in the course and PhD candidates at the time of the implementation of the business game-like approach described in this work, who also served as teaching assistants.

References

- Baker, M. A., J. S. Robinson, and D. A. Kolb. 2012. “Aligning Kolb’s Experiential Learning Theory with a Comprehensive Agricultural Education Model.” *Journal of Agricultural Education* 53(4): 1–16. doi: <https://doi.org/10.5032/jae.2012.04001>
- Beausoleil-Morrison, I., C. J. Hopfe, D. Crawley, and R. Rawal. 2015. “Teaching Building Performance Simulation through a Continuous Learning Cycle.” Proceedings of Building Simulation 2015 - 14th Conference of International Building Performance Simulation Association, Hyderabad, India, December 7-9.
- Faria, A. J. 1990. “Business Simulation Games after Thirty Years: Current Usage Levels in the United States.” *Guide to Business Gaming and Experiential Learning*.
- Gasparella, A. 2017. “Building Physics and Building Simulation: An Integrated Approach to Educational Programs.” *Applied Mechanics and Materials* 887: 117–128. doi: <https://doi.org/10.4028/www.scientific.net/amm.887.117>
- Itin, C. M. 1999. “Reasserting the philosophy of experiential education as a vehicle for change in the 21st century.” *The Journal of Experiential Education* 22(2): 91-98. doi: <https://doi.org/10.1177/105382599902200206>

- Jackson, J. R. 1959. "Learning from Experience in Business Decision Games." *California Management Review* 1(2): 92-107. doi: <https://doi.org/10.2307/41165351>
- Kolb, A. Y., and D. A. Kolb. 2009. "The Learning way: Meta-Cognitive Aspects of Experiential Learning." *Simulation Gaming* 40: 297-327. doi: <https://doi.org/10.1177/1046878108325713>
- Kolb, A. Y., and D. A. Kolb. 2017. "Experiential Learning Theory as a Guide for Experiential Educators in Higher Education." *ELTHE: A Journal for Engaged Educators* 1 (1): 7-44.
- Soebarto, V., C. J. Hopfe, D. Crawley, and R. Rawal. 2015. "Capturing the Views of Architects about Building Performance Simulation to be used During Design Processes." Proceedings of Building Simulation 2015 - 14th Conference of International Building Performance Simulation Association, Hyderabad, India, December 7-9.